PROCEEDINGS OF SPIE

Photonics Applications in Astronomy, Communications, Industry, and High-Energy Physics Experiments 2019

Ryszard S. Romaniuk
Maciej Linczuk
Editors

26 May – 2 June 2019
Wilga, Poland

Organized by
Institute of Electronic Systems, Faculty of Electronics and Information Technologies,
Warsaw University of Technology (Poland)

Sponsored by
PSP—Photonics Society of Poland • Committee of Electronics and Telecommunications, Polish Academy of Sciences • ARIES—Accelerator Research and Innovation for European Science and Society (CERN, EU H2020) • PKOpto—Polish Committee of Optoelectronics of SEP—The Association of Polish Electrical Engineers • EuroFusion Collaboration • EuroFusion Poland

Published by
SPIE

Volume 11176

Part Three of Three Parts

Proceedings of SPIE 0277-786X, V. 11176

SPIE is an international society advancing an interdisciplinary approach to the science and application of light.

The papers in this volume were part of the technical conference cited on the cover and title page. Papers were selected and subject to review by the editors and conference program committee. Some conference presentations may not be available for publication. Additional papers and presentation recordings may be available online in the SPIE Digital Library at SPIEDigitalLibrary.org.

The papers reflect the work and thoughts of the authors and are published herein as submitted. The publisher is not responsible for the validity of the information or for any outcomes resulting from reliance thereon.

Please use the following format to cite material from these proceedings:
Author(s), "Title of Paper," in *Photonics Applications in Astronomy, Communications, Industry, and High-Energy Physics Experiments 2019*, edited by Ryszard S. Romaniuk, Maciej Linczuk, Proceedings of SPIE Vol. 11176 (SPIE, Bellingham, WA, 2019) Seven-digit Article CID Number.

ISSN: 0277-786X
ISSN: 1996-756X (electronic)

ISBN: 9781510630659
ISBN: 9781510630666 (electronic)

Published by
SPIE
P.O. Box 10, Bellingham, Washington 98227-0010 USA
Telephone +1 360 676 3290 (Pacific Time) · Fax +1 360 647 1445
SPIE.org
Copyright © 2019, Society of Photo-Optical Instrumentation Engineers.

Copying of material in this book for internal or personal use, or for the internal or personal use of specific clients, beyond the fair use provisions granted by the U.S. Copyright Law is authorized by SPIE subject to payment of copying fees. The Transactional Reporting Service base fee for this volume is $21.00 per article (or portion thereof), which should be paid directly to the Copyright Clearance Center (CCC), 222 Rosewood Drive, Danvers, MA 01923. Payment may also be made electronically through CCC Online at copyright.com. Other copying for republication, resale, advertising or promotion, or any form of systematic or multiple reproduction of any material in this book is prohibited except with permission in writing from the publisher. The CCC fee code is 0277-786X/19/$21.00.

Printed in the United States of America by Curran Associates, Inc., under license from SPIE.

Publication of record for individual papers is online in the SPIE Digital Library.

SPIEDigitalLibrary.org

Paper Numbering: *Proceedings of SPIE* follow an e-First publication model. A unique citation identifier (CID) number is assigned to each article at the time of publication. Utilization of CIDs allows articles to be fully citable as soon as they are published online, and connects the same identifier to all online and print versions of the publication. SPIE uses a seven-digit CID article numbering system structured as follows:

- The first five digits correspond to the SPIE volume number.
- The last two digits indicate publication order within the volume using a Base 36 numbering system employing both numerals and letters. These two-number sets start with 00, 01, 02, 03, 04, 05, 06, 07, 08, 09, 0A, 0B … 0Z, followed by 10-1Z, 20-2Z, etc. The CID Number appears on each page of the manuscript.

Contents

xvii *Authors*

xxiii *Conference Committee*

xxvii *Introduction*

Part One

CONFERENCE OVERVIEW

11176 02 **Photonics applications and web engineering: WILGA 2019 (Invited Paper)** [11176-1]

PHOTONICS APPLICATIONS

11176 03 **CIR fast approximation for closed space VLC transmission with the use of a trained artificial neural network** [11176-3]

11176 04 **Pre-equalization versus post-equalization of the VLC LEDs (Invited Paper)** [11176-5]

11176 05 **Overview of the measuring systems where a continuously altered light source plays a key role: Part II (Invited Paper)** [11176-11]

11176 06 **Jones matrix mapping of polycrystalline networks of layers of main types of amino acids** [11176-16]

11176 07 **Expansion of the operating spectral range of the optical processor** [11176-18]

11176 08 **Stochastic deterministic methods for processing signals and images in optical electronic systems** [11176-51]

11176 09 **Neurocomputer architecture based on spiking neural network and its optoelectronic implementation** [11176-53]

11176 0A **Improved x-ray fluorescent wavelength dispersive spectrometer** [11176-55]

11176 0B **Application of evolutionary algorithms to DWDM optical networks design** [11176-64]

11176 0C **Application of infrared and high-speed cameras in diagnostics of CNC milling machines: case study** [11176-69]

11176 0D **Interference systems as photonic crystals** [11176-74]

11176 0E **Machine vision system for quality control of molded plastic packaging** [11176-77]

11176 0F **The approach for improvement of knowledge bases organization in optical data networks cluster** [11176-78]

11176 0G **The use of optically controlled transparent and blockchain technology for the processing of large-scale data arrays** [11176-79]

11176 0H **Deep learning for rectification of radial distortion image** [11176-81]

11176 0I **Exploitation of PLC controller to maintain the illuminance of outdoor lighting in the work place at the required level** [11176-86]

11176 0J **Acceleration of heavy ions to multi-GeV energies by an ultra-intense laser (Invited Paper)** [11176-87]

11176 0K **From face identification to emotion recognition** [11176-88]

11176 0L **3D imaging methods in quality inspection systems (Invited Paper)** [11176-91]

11176 0M **The information technology for image filtering and storing obtained under low light conditions** [11176-96]

11176 0N **A sensing device for color immediate detection of medium-distant objects on the horizon** [11176-99]

11176 0O **Research of optoimmittance logical elements** [11176-100]

11176 0P **Optical force and optical torque action in birefringent medium under the total internal reflection** [11176-102]

11176 0Q **The impact of rain on performance of visible light communication** [11176-116]

11176 0R **Spectrometric data analysis of a capillary sensor of fuel photo-stability working with high power light emitting diode at 365 nm** [11176-118]

11176 0S **The visualization quality improvement method of x-ray images with locally concentrated features (IMRI-method)** [11176-126]

11176 0T **Forming thermal imaging system field of view with afocal lens cap** [11176-130]

11176 0U **Optimization analysis for image-based steganography using generative adversarial networks (Invited Paper)** [11176-134]

11176 0V **The impact of fog on performance of visible light communication** [11176-136]

11176 0W **Evaluation of the possibility of using RGB image analysis to co-firing process** [11176-142]

11176 0X **Optoimmittance logic elements** [11176-147]

11176 0Y **Road lighting control options** [11176-152]

11176 0Z **The use of 3D imaging to determine the orientation and location of the object based on the CAD model** [11176-158]

11176 10 **Grounds for mechatronic system development of the optical devices position dynamic stabilization of a mobile terrestrial robotic system** [11176-160]

11176 11 **Development and research of a radio measuring device with a frequency output signal based on a pyroelectric primary converter** [11176-162]

11176 12 **Structural organization of video informative systems on light-emitting diodes** [11176-169]

11176 13 **Distributed optoelectronic system of environmental monitoring in a real-time mode** [11176-170]

11176 14 **Visualization of measurements in the Microsoft Visual Studio environment** [11176-172]

11176 15 **Experimental research of hydroluminescence in the cavitating flow of mineral oil** [11176-173]

11176 16 **Fiber optic interface channels for united data and power supply transmission for neutral interaction application in signal transmission networks** [11176-175]

11176 17 **Calibration of vision systems** [11176-176]

11176 18 **Robotic station for vision inspection of product quality** [11176-180]

11176 19 **Defect detection in steel materials using sensors based on fiber Bragg gratings** [11176-191]

11176 1A **Adaptive oriented filtration of digital images in the spatial domain** [11176-212]

11176 1B **Elaboration of pyramidal methods applying computation technique “rough-fine” image identification** [11176-216]

11176 1C **Analysis of the properties of measuring elongation systems using uniform Bragg gratings as measuring transducers** [11176-221]

11176 1D **Criterion of spatial resolution of imaging system** [11176-223]

11176 1E **Double-sided self-apodization effect in chirped tapered fiber Bragg gratings** [11176-264]

11176 1F **Analysis of the inscription imperfections and its influence on the Bragg grating spectral responses** [11176-265]

11176 1G **Numerical analysis of the spectral response of Fibonacci-like phase-shifted fiber Bragg gratings** [11176-266]

11176 1H **Superstructure FBGs induction through applying of the pressing force** [11176-267]

11176 1I **Theory of photoreactive effect in bipolar and MOSFET transistors** [11176-270]

11176 1J **Video signals integrator: configuration database (Invited Paper)** [11176-271]

11176 1K **Simultaneous monitoring of the phenomena of CD, Crosstalk, and OSNR in the physical layer of the optical network with the use of convolutional neural networks** [11176-275]

COMPUTATIONAL INTELLIGENCE

11176 1L **Computationally efficient index generation unit using a Bloom filter** [11176-4]

11176 1M **Paraphrase generation and evaluation: a view from the trenches** [11176-9]

11176 1N **Neural network approach to numeric array sorting** [11176-12]

11176 1O **Analysis and specification of consistency rules for UML diagrams** [11176-26]

11176 1P **The new C++ serialization library supporting backward and forward compatibility** [11176-27]

11176 1Q **Widget detection on screenshots using computer vision and machine learning algorithms** [11176-28]

11176 1R **Analysis of electrical patterns activity in artificial multi-stable neural networks** [11176-39]

11176 1S **DDoS-attack detection using artificial neural networks in Matlab** [11176-42]

11176 1T **Computer modeling of dissemination of informational influences in social networks with different strategies of information distributors** [11176-44]

11176 1U **Machine learning models for predicting customer decision in motor claims settlement (Invited Paper)** [11176-48]

11176 1V **ESD problems in embedded systems** [11176-59]

11176 1W **The efficient algorithm for mapping next generation sequencing reads to reference genome** [11176-61]

11176 1X **Parallel multiple blocked methods of Bickart type** [11176-117]

11176 1Y **Method of data anomaly detection in the process of mobile applications installation** [11176-144]

11176 1Z **Applying artificial intelligence for cellular networks optimization** [11176-146]

11176 20 **Improvement of the learning process of the automated speaker recognition system for critical use with HMM-DNN component** [11176-153]

11176 21 **Reliable frequent itemsets mining with actor-based Apriori algorithm** [11176-168]

11176 22 **Transformation of polygonal description of objects into functional specification based on three-dimensional patches of free forms** [11176-198]

11176 23 **Information technology for creation of semantic structure of educational materials** [11176-200]

11176 24 **Method for defining conceptual classes in the description of use cases** [11176-203]

11176 25 **Information technology for evaluation of innovation indicators influence and investment activity on competitiveness of the region** [11176-205]

11176 26 **Optimization of web-application performance** [11176-210]

11176 27 **Information technology in creating intelligent chatbots** [11176-246]

11176 28 **Method and algorithm of the piecewise-hyperplane clusterization using tools of pseudo-inverse matrices** [11176-247]

Part Two

BIOMEDICAL APPLICATIONS

11176 29 **The model and simulations of device generating the electromagnetic field in measurements monitoring the vital functions of cultured cells** [11176-15]

11176 2A **Information model for forecasting of violation reparative osteogenesis of long bonds** [11176-21]

11176 2B **Determination of the time of occurrence of superficial damage to human biological tissues on the basis of colorimetry and fuzzy estimates of color types** [11176-30]

11176 2C **Formation of information medical environment in different levels** [11176-31]

11176 2D **Information model of individual rehabilitation program efficacy in disabled persons with cardiovascular diseases** [11176-32]

11176 2E **Methodology for flight crew psycho-physiological status forecasting** [11176-33]

11176 2F **Possibility of determining the cause of the snore by instrumental methods** [11176-34]

11176 2G **An approach to quality evaluation of embryos based on their geometrical parameters** [11176-35]

11176 2H **Biometric hand tremor identification on graphics tablet** [11176-36]

11176 2I **Peculiarities of red blood cells motion under the action of vertical spin of evanescent wave** [11176-37]

11176 2J **Non-native speech recognition using audio style transfer** [11176-49]

11176 2K **Automatic liver detection algorithm on CT images** [11176-50]

11176 2L **Quality analysis of dermatoscopic images thresholding with malignant melanoma** [11176-67]

11176 2M **Influence of probe pressure on human skin spectrophotometric measurements** [11176-68]

11176 2N **Modular control system for behavioral experiments** [11176-71]

11176 2O **Design of portable optoelectronic devices for optogenetic research of mice brain** [11176-105]

11176 2P **Selection of metals in biomems applications** [11176-112]

11176 2Q **Method of indicators forecasting of biomedical images using a parallel-hierarchical network** [11176-122]

11176 2R **Multispectral environmental monitoring of phytoplankton pigment parameters in aquatic environments** [11176-123]

11176 2S **Objective EMG signal models comparison for gait diagnostics** [11176-132]

11176 2T **The mathematical model of frequency gas transducer based on transistor structure with NDR for diagnosis of helicobacter pylori strains** [11176-140]

11176 2U **Assessment of adaptive algorithms effectiveness for suppression of powerline harmonics in EEG signals** [11176-179]

11176 2V **Acetylcholinesterase-based biosensing solutions for the detection of organophosphorus pesticides** [11176-183]

11176 2W **Multi-objective noisy-based deep feature loss for speech enhancement** [11176-184]

11176 2X **Formalization of the stages of diagnostic and therapeutic measures in decision support systems in medicine** [11176-186]

11176 2Y **Visualisation of biological tissues with the use of LED source illumination** [11176-187]

11176 2Z **Singular approach to the analysis of Jones matrix images of biological crystals networks** [11176-214]

11176 30 **Methods and means of "single-point" phasometry of microscopic images of optical-anisotropic biological objects** [11176-215]

11176 31 **Method for determination of laminar boundary layer of airflow in the upper respiratory tract** [11176-234]

11176 32 **Application of EMG-signal phase portraits for differentiation of musculoskeletal system diseases** [11176-235]

11176 33 **Prognosis of efficacy of medical and social rehabilitation in disabled individuals with respiratory diseases** [11176-237]

11176 34 **Model of electronic public health management on the example of the territorial community of Vinnytsia region** [11176-249]

ASTRONOMY, PLANETARY GEODESY, AND SPACE ENGINEERING

11176 35 **One class SVM for building detection on Sentinel-2 images** [11176-6]

11176 36 **Quasar clustering based on their parameterization data** [11176-7]

11176 37 **Optimization of quasar parametrization using genetic algorithms** [11176-8]

11176 38 **Comparison of mathematical morphology with the local multifractal description applied to the image samples processing** [11176-29]

11176 39 **Analysis of cloudiness by intensity segmentation and clustering** [11176-43]

11176 3A **A passive sensing device for a cloud on the skyline detection (Invited Paper)** [11176-57]

11176 3B **Modelling of soft fault propagation in sequential circuits by fuzzy-logic simulations (Invited Paper)** [11176-73]

11176 3C **Simulation of CubeSat caliber particle detector "MiRA_ep" response to energetic electrons and protons using GEANT4 package (Invited Paper)** [11176-94]

11176 3D **Creation of training dataset for Sentinel-2 land cover classification** [11176-106]

11176 3E **Design of fine guidance system (FGS) for ARIEL mission (Invited Paper)** [11176-119]

11176 3F **Design of the MERTIS pointing unit for BEPI COLOMBO mission** [11176-121]

11176 3G **Concept of an SDR radio transceiver for HyperSat microsatellite platform** [11176-193]

11176 3H **Space robot equipped with compliant linear actuator on end effector: simulations results** [11176-219]

11176 3I **Analysis of relativistic effects in GNSS measurements based on calculation of metric tensor components and comparison with existing models** [11176-220]

11176 3J **STIX IDPU: very efficient and reliable controller for a scientific instrument (Invited Paper)** [11176-229]

11176 3K **Design of DPU and PSU for ESA JUICE Submillimeter Wave Instrument (SWI)** [11176-230]

11176 3L **Utilization of design features of the particle telescope STEP-F and solar x-ray spectrophotometer SphinX for exploration of the Earth's radiation belt properties** [11176-231]

11176 3M **Post-processing tools for land cover classification of Sentinel-2** [11176-232]

11176 3N **Regional warning centre of Warsaw in heliogeophysical prediction service laboratory: space weather service in Poland (Invited Paper)** [11176-238]

11176 3O **Space weather usage of LOFAR PL610 station** [11176-239]

11176 3P **On the legality of appropriation of space resources** [11176-240]

11176 3Q **Design and development of scientific satellite instrumentation according to Space 4.0 approach: the advantages and dangers (Invited Paper)** [11176-241]

11176 3R **Design and test of magnetorquer in PCB technology for nanosatellites** [11176-244]

11176 3S **Electronic box structural analyses for a space flight** [11176-251]

11176 3T **Trial as a pragmatic and systematic approach for assessing new solutions in crisis management and rescue operations** [11176-253]

11176 3U **Design of the radiator for detection part of the Submillimeter Wave Instrument (SWI) of JUICE mission** [11176-255]

11176 3V **Microgravity testbed for the development of space robot control systems and the demonstration of orbital maneuvers** [11176-256]

11176 3W **Concept of the platform architecture for data integration from the Border Guard observation systems** [11176-257]

11176 3X **Planetary penetrator control electronics design concept** [11176-259]

11176 3Y **Planetary penetrator electromagnetic drive design concept** [11176-260]

11176 3Z **Design and tests of sunsensor based on 2D position sensitive detector** [11176-261]

11176 40 **Optimization of angular rotation control for high accuracy and repeatability mirror positioning system of space hyperspectral spectrometer DESIS** [11176-262]

Part Three

NUCLEAR FUSION AND HIGH ENERGY PHYSICS

11176 41 **Implementation of OMTF trigger algorithm with high-level synthesis (Invited Paper)** [11176-22]

11176 42 **Automatic management of local bus address space in complex FPGA-implemented hierarchical systems** [11176-23]

11176 43 **Geometry and dynamics in heavy-ion collisions seen by the femtoscopy method (Invited Paper)** [11176-75]

11176 44 **IPbus bus functional model in universal VHDL verification methodology** [11176-76]

11176 45 **Preliminary dynamic analysis of the forces on the COMPASS-U tokamak foundations** [11176-89]

11176 46 **Synchronization between computation and acquisition parts in the GEM detector-based measurement system** [11176-108]

11176 47 **Detecting nuclear debris with the forward proton detectors at the LHC** [11176-110]

11176 48 **Extracting the top-quark mass and Yukawa coupling from the threshold scan at CLIC** [11176-148]

11176 49 **Preliminary mechanical analysis of the COMPASS-U central solenoid** [11176-150]

11176 4A **Communication model for multi-level control, management, and acquisition firmware-software implementations for tokamak plasma diagnostics systems** [11176-155]

11176 4B **Pion-kaon femtoscopy in Therminator 2 model** [11176-166]

11176 4C **Kaon femtoscopy in STAR** [11176-167]

11176 4D **GEM detector charge signals sequencer implementation for WEST experiment** [11176-194]

11176 4E **GEM-based technology for plasma diagnostic application** [11176-250]

11176 4F **Design and development of soft x-ray diagnostics based on GEM detectors at IPPLM (Invited Paper)** [11176-252]

11176 4G **Basics of numerical simulations of the signals from GEM detector** [11176-254]

11176 4H **Tracking with deep neural networks** [11176-268]

11176 4I **On the exclusive jet measurements at the LHC** [11176-277]

11176 4J **Using ALFA detectors for the LHC beam background measurements** [11176-278]

MATERIAL ENGINEERING

11176 4K **Towards increasing of lateral dimension of Molybdenum disulphide MoS_2** [11176-2]

11176 4L **Screen printed graphene electrodes for voltammetric dopamine determination** [11176-10]

11176 4M **Photoluminescence properties of ZnSe:Al, ZnSe:Cu nanoparticles obtained by chemical synthesis** [11176-19]

11176 4N **Nanostructure with periodic position dependent electron effective mass** [11176-20]

11176 4O **Preparation of n-CuO nanostructural films by thermal oxidation/PVD method** [11176-24]

11176 4P **Angles between matrices and between polynomials in analysis of electrical circuits (Invited Paper)** [11176-40]

11176 4Q **Photocatalytic properties of nanosilver-doped TiO_2 powders** [11176-58]

11176 4R **Influence of annealing on electronic properties of thin AlN films deposited by magnetron sputtering method on silicon substrates** [11176-60]

11176 4S **Determination of the activation energy of the relaxation time of the composite cellulose: synthetic ester with a high water content** [11176-63]

11176 4T **Characterization of CuO nanorods** [11176-65]

11176 4U **Influence of high temperature annealing on AC electric properties of SiO_2 thin layers implanted with In and Sb ions** [11176-66]

11176 4V **Analysis of metrological properties of the measurement system to study changes in the resistance of nanocomposite carbon-palladium thin films under the influence of hydrogen** [11176-70]

11176 4W **Modeling of the percolation phenomenon of disordered two-dimensional systems** [11176-90]

11176 4X **Technology and characterization of ISFET structures with graphene membrane** [11176-93]

11176 4Y **Prediction method of input parameters impacting of dimensional accuracy of high aspect ratio holes obtained by using EDD** [11176-95]

11176 4Z **AlGaN/GaN HEMTs for the purposes of electronic applications** [11176-97]

11176 50 **Cutting force prediction in ball-end milling of Ni-Ti alloy** [11176-101]

11176 51 **The application of high-speed camera registration for analysis of the chip breaking methods in the machining of nickel-based alloys** [11176-104]

11176 52 **AC conductivity activation energy of composite cellulose-synthetic ester MIDEL 7131-water nanodrops** [11176-107]

11176 53 **The numerical analysis of the electric field distribution behind the three-layer wall** [11176-114]

11176 54 **Thin film capacitors made of various metals for impedance sensing technique** [11176-115]

11176 55 **The investigation of transparent electrodes made with ultrasonic spray coater** [11176-120]

11176 56 **Preparation of MoS_2 films for sensor applications** [11176-125]

11176 57 **Modeling of burrs during drilling of titanium alloy** [11176-127]

11176 58 **Fabrication antennas with 2D and 3D printing technologies: review** [11176-129]

11176 59 **Utilizing sugar-based material in additive manufacturing** [11176-131]

11176 5A **Optimization of cutting data of nickel-based sintered materials turning** [11176-133]

11176 5B **Mechanical and thermal properties of ABS/iron composite for fused deposition modeling** [11176-135]

11176 5C **Manufacturing stretchable conductive interconnects on fabric substrates: development of a technology** [11176-145]

11176 5D **Analysis of the creation process of the chip during the orthogonal turning of pure titanium using a high-speed camera** [11176-149]

11176 5E **Analysis of the material model of C45 steel for the simulation of the machining process** [11176-157]

11176 5F **Manufacturing methods and challenges in structural electronics** [11176-177]

11176 5G **Effect of sonication process and solvent type on ageing of silver ink for aerosol jet printing** [11176-182]

11176 5H **Controlling of gold nanoparticles by the help of transverse spin momentum of evanescent waves in biomedical applications** [11176-190]

11176 5I **Screen-printed ion-selective electrode for potassium determination** [11176-263]

11176 5J **The analysis of sensitivity and nonlinearity parameters of selected signal conditioners for resistance measurement** [11176-41]

11176 5K **Distributed measurement data collecting system with mobile packet transmission** [11176-46]

11176 5L **Multi-channel temperature measurement system with remote dashboard for electric vehicle** [11176-47]

11176 5M **Influence of RES sources on the location of distribution points in the MV network** [11176-54]

11176 5N **Development of a non-standard system of microwave quadripoles parameters** [11176-80]

11176 5O **The role of equipotential bondings as a measure of protection against electric shock by the example of special installations** [11176-83]

11176 5P **An indoor tracking system and pattern recognition algorithms as key components of IoT-based entertainment industry** [11176-85]

11176 5Q **Automatization of measurements in the stability and linearity tests of direct current-current transducer (DCCT)** [11176-113]

11176 5R **Acoustic sensor optimization for SMART technologies** [11176-128]

11176 5S **Comparative analysis of packet scheduling algorithms in IPv4 and IPv6 networks** [11176-137]

11176 5T **Analysis of wireless network security for data transmission performance** [11176-138]

11176 5U **Strain gauge sensor for the Internet of Things** [11176-151]

11176 5V **Generalized model of optimal development of the production system based on optimal aggregation methodology** [11176-154]

11176 5W **High speed buffer devices on the base of push-pull current amplifiers** [11176-159]

11176 5X **High directivity microstrip couplers for impedance transforming** [11176-165]

11176 5Y **Numerical method for processing frequency measuring signals from microelectronic sensors based on transistor structures with negative differential resistance** [11176-171]

11176 5Z **Forecasting and evaluation of voltage conditions in a low-voltage power grid with a large share of prosumer installations** [11176-188]

11176 60 **Logic correctness of control algorithms for mechatronic discrete systems with parallel processes** [11176-206]

11176 61 **Comparison of high-level programming languages efficiency in embedded systems** [11176-208]

11176 62 **Selection of the calculus system base for ADC and DAC with weight redundancy** [11176-218]

11176 63 **Correlation method for calculation of weight coefficients of artificial neural-like networking hydraulic units' diagnostic systems** [11176-224]

11176 64 **Mobile distribution point architecture concept of ICT infrastructure** [11176-258]

Authors

Numbers in the index correspond to the last two digits of the seven-digit citation identifier (CID) article numbering system used in Proceedings of SPIE. The first five digits reflect the volume number. Base 36 numbering is employed for the last two digits and indicates the order of articles within the volume. Numbers start with 00, 01, 02, 03, 04, 05, 06, 07, 08, 09, 0A, 0B...0Z, followed by 10-1Z, 20-2Z, etc.

Abisheva, Akmaral, 1A
Abramowicz, Adam, 5X
Adamenko, Volodymyr O., 3C
Adamiec, J., 3R
Aleksandrowicz, S., 38
Aleksiejuk, Konrad, 3X, 3Y
Amirgaliyev, Yedilkhan, 1B, 1X, 2A, 2T, 5W
Amirgaliyeva, Saltanat, 2Q
Angelsky, Oleg V., 5H
Antomonov, Michail Yu., 2C
Antypenko, Ruslan V., 3C
Araszkiewicz, Piotr, 1H
Arokiasamy, Aldrin Wilfred, 0U
Arshidinova, Mukaddas, 09, 2R, 4N
Askarova, Nursanat, 1Y
Avrunin, Oleg G., 2F, 2H, 31
Azarov, Olexiy D., 5W, 62
Azarova, Larysa E., 23
Bachinsky, Viktor T., 06
Badziak, Jan, 0J
Bąkała, Jarosław, 3C
Balner, V., 49
Balovsyak, Serhiy V., 1A
Baraban, Mariya V., 0M
Baraban, Serhii V., 27, 5N
Baran, Jędrzej, 3S, 3X, 3Y
Baranowski, J. M., 4K
Barciński, Tomasz, 3S, 3X, 3Y
Barmak, Olexander V., 23, 28
Barylak, Jaromir, 3C, 3L
Bashkow, Evgeniy A., 1X
Basmadji, Fatina Liliana, 3V
Bednarek, Jakub, 61
Belikov, Konstantin A., 60
Belka, Radosław, 4Q, 5P
Ber, K., 3J, 3K
Bevz, Olexander M., 0M
Bezsmertna, Halyna V., 2A, 2D, 33
Bezsmertnyi, Yurii O., 2A, 2D, 33
Bezuglyi, Andrii I., 2X
Białek, A., 3U
Bialyk, Ihor M., 3I
Biedrzycki, Rafał, 0B
Bilichenko, Victor V., 63
Bilozertseva, Violetta I., 0D
Bisikalo, Oleg V., 1Z
Blaszczak, Urszula J., 2Y
Błaut, Paweł, 0I, 5O
Błocki, J., 45, 49
Bogach, Ilona V., 0M
Bogachuk, Volodymyr V., 11, 63
Bogomolov, Sergii V., 5W, 62
Boguszewski, Pawel, 2N
Bojarczuk, Juliusz, 1E, 1F, 1G
Borecki, Michal, 0N, 0R, 3A
Borovska, Taisa M., 5V
Borovytsky, Volodymyr N., 1D
Borowik, Grzegorz, 1J
Borowska, Joanna, 2N
Brawata, Sebastian, 1J, 3W, 64
Breiter, Michał, 1P
Brytavskyi, Ievgen V., 4M
Buchowicz, Andrzej, 1J
Bućwińska, Agnieszka, 17
Bugubayeva, Alina, 08, 13, 33
Bujwan, W., 3J, 3K
Bukowiecka, Danuta, 1J
Bulygina, Olena V., 2E
Burdeynyy, Volodymyr M., 4N
Bykov, Mykola M., 20
Caban, Piotr A., 4K, 4X, 4Z
Cepelak, Michal, 5U
Chang, Xin, 0K
Chęciński, Karol, 1Q
Cherepinina, Yana, 24
Chernetchenko, Dmytro V., 1R
Chernyaschuk, Natalia L., 1B, 2A
Chernyshova, Maryna, 46, 4A, 4D, 4E, 4F, 4G
Chmaj, Grzegorz, 3V
Chodun, R., 4R
Choroszucho, Agnieszka, 53, 61
Chwastowski, Janusz J., 47
Chyzh, Igor G., 0T
Cichocki, Andrzej, 3B, 3J
Ciepielewski, P., 4K
Cieśla, Krzysztof, 47
Czaplińska, Katarzyna, 1H
Czapski, Paweł, 3G
Czarnacka, Karolina, 4U
Czarski, Tomasz, 46, 4A, 4D, 4F, 4G
Czerwosz, Elżbieta, 4O, 4T
Dąbrowska, Anna Maria, 5J
Dacko, Adam, 3S
Dąda, Anna, 0I, 5O
Dąmbski, Marcin, 1U
Danys, Lukas, 0Q, 0V, 5R
Darmetko, M., 3J

Daszkiewicz, Marek, 05
Dawgul, M., 4L
Denissova, Nataliya, 07
Derevyanchuk, Oleksandr V., 1A
Diduszko, R., 4O
Dmitrieva, Olga A., 1X
Domański, Jarosław, 0J
Doroshchenkov, Gennadii D., 0A, 12
Dovgun, Andriy Ya., 30
Drin, Yaroslav M., 06, 30
Drzewiecki, W., 38
Dubolazov, Olexander V., 06, 2Z, 30
Dudnik, Oleksiy V., 3C, 3L
Duk, Mariusz, 11, 5W
Dumiszewska, Ewa, 4K, 4Z
Duskazaev, Gali, 0O
Dusza, Jacek J., 2S
Dyakonenko, Nina L., 0D
Dybowska-Sarapuk, Ł., 5C
Dziedzic, Bartosz, 4J
Dzierżak, Róża, 0S, 2Q
Erland, Paula, 4I
Fedotov, Alexander K., 4U
Filatova, Anna E., 0S, 2X
Firek, Piotr, 4R, 4X, 56
Flis, Adam, 2N
Fodchuk, Igor M., 1A
Foks-Ryznar, Anna, 3T
Forc, Mateusz, 1Q, 2J
Franczyk, Emilia, 57, 5E
Franus, Wiktor, 1M, 1U
Frasunek, Przemysław, 1J
Gaca, Jaroslaw, 4Z
Galas, Jacek, 05
Galochkin, Olexander V., 2Z
Garcia, J. P., 3K, 3U
Garmash, Volodymir V., 0M
Gąska, Michał, 1J, 2N, 46, 4A, 4D, 4F
Gęca, Mateusz, 0R
Gerasymova, Iryna G., 2E
German, Ivanna I., 2Z
Gertsiy, Alexander A., 1B
Gołaszewski, Arkadiusz, 5X
Golonko, Piotr, 61
Goździuk, Magdalena, 29
Grabowski, Andrzej, 64
Grądz, Żaklin M., 2R
Grenda, Bogdan, 3W
Grimm, O., 3J
Grishin, Dmitry I., 5V
Gromaszek, Konrad, 22, 23, 24, 25, 60
Gromny, Ewa, 3D, 3M
Grudziński, Dariusz T., 58
Gryko, Lukasz, 2Y
Grzeczka, Agnieszka, 3W
Gubarev, Aleksandr P., 60
Gumiński, Marek, 42
Hacek, P., 49
Hajovsky, Radovan, 5U
Hanasz, Stanisław, 3G
Hanpantsurova, Oksana S., 60
Harasim, Damian, 16
Hartogh, P., 3K, 3U
Havlicek, J., 45
Hernández, Iván Gallego, 2S
Homolinskyi, Victor O., 2F
Hotra, Oleksandra, 2L, 2M
Hraniak, Valerii F., 63
Hromadka, J., 45, 49
Hryniewicz, Krzysztof, 37
Huskova, Nadiia H., 1X
Iaremyn, Stanislav Yu., 2A
Ivanets, Olga B., 2E
Ivanskyi, Dmytro I., 0P, 2I, 5H
Ivasyuk, Igor D., 2Q
Iwański, Jacek, 64
Jabłoński, Michał, 1Q
Jakhno, Oleg M., 15
Jakubowska, Małgorzata, 2V, 4L, 55, 59, 5C, 5I
Janczak, Daniel, 2V, 4L, 5C
Jankowska-Śliwińska, J., 4L
Jaros, Rene, 0Q, 0V
Jarosiński, Jakub, 1J
Jarykbassov, Daniyar, 24
Jastrzebski, Pawel, 1J
Jędrzejewski, Konrad, 2U
Jenerowicz, Małgorzata, 38, 3D
Jewartowski, Blazej, 1J
Juchnikowski, G., 3J, 3R
Jurkiewicz, Rafał, 1J
Kaczorek, Tadeusz, 4P
Kahankova, Radana, 5R
Kalimoldayev, Mashat, 06, 0G, 1S, 2C, 3I, 5V, 63
Kalizhanova, Aliya, 0D, 0F, 0M, 0P, 16, 26, 2Z
Kalychak, Yuriy I., 39
Kamiński, Jarosław, 64
Karnakova, Gayni, 27
Kasprowicz, Grzegorz H., 1J, 2N, 3G, 3W, 46, 4A, 4D, 4E, 4F, 64
Katewicz, Ewelina, 1J, 64
Katsyv, Samoil Sh., 63
Kęczkowska, J., 4O, 4Q
Khomyuk, Victor V., 1N
Khudaieva, Sofiia, 2F
Kierczyński, Konrad, 4S
Kierzkiewicz, Maciej, 2K
Kirichek, Oleksii V., 32
Kisała, Piotr A., 0D, 0G, 0M, 1I
Klimek, Jacek, 0D, 0F, 0G, 5N
Knapska, Ewelina, 2N
Knignitska, Tatyana V., 30
Knyps, Piotr, 4K, 4Z
Kobylianskyi, Oleksandr V., 2H, 2T
Kobylyanska, Iryna M., 20
Kociubiński, Andrzej, 06, 07, 29, 2A, 4M, 4N
Koegl, S., 3J
Kokriatskaia, Natalia I., 1B, 2Q
Kolarik, Jakub, 0Q, 0V, 5R
Kolasiński, Piotr, 4A, 4D, 4F
Kolesnytskyj, Oleh K., 09

Kolobrodov, Mykyta S., 07
Kolobrodov, Valentin H., 07, 0T
Kołodziej, L., 55, 59
Koltunowicz, Tomasz N., 4U
Komada, Paweł, 0T, 0X, 12, 13, 15, 1Y, 1Z, 2T, 5Y
Kondracka, Kinga, 4X
Kondrusik, Wiktoria, 1H
Korba, P., 3K
Korwin-Pawlowski, Michael L., 3A
Kostiuk, Dmytro V., 15
Kotlik, Mariusz, 64
Kotyra, Andrzej, 0W, 1A, 1B, 1D, 26, 2Z, 30, 62
Kovalenko, Alexander S., 2C
Kovalenko, Sergii V., 2G
Kovalenko, Svitlana M., 2G
Kovaliuk, Dmytro O., 26
Kovaliuk, Oleh O., 26
Kovtun, Viacheslav V., 20
Kowalczyk, M., 03
Kowalczyk, M., 50
Kowalik, P., 03
Kowaliński, Mirosław, 3C, 3L
Kowalska-Strzęciwilk, Ewa, 46, 4A, 4E, 4F, 4G
Kowalski, Tomasz, 3S
Kozak, Lyudmila M., 2C
Kozbakova, Ainur, 0T, 15, 1N, 2E, 30
Kozdrowski, Stanisław, 0B
Kozhemiako, Andrii V., 13, 1N, 1S
Kozlovska, Tetiana I., 2D
Kozłowski, Mirosław, 4O, 4T
Kozłowski, Tomasz, 05
Krak, Iurii V., 23, 28
Krawczyk, Rafał D., 46, 4A, 4D, 4F
Krawczyk, S., 4V
Krekoten, Evgen G., 31
Krivoruchko, Ivan A., 2A
Kroitor, Olga P., 1A
Krosman, K., 1V
Krucker, S., 3J
Krupiński, Michał, 35, 38, 3D, 3M
Kruszewski, Michał, 42, 44
Krylyk, Liudmyla, 27
Kryszczyński, Tadeusz, 05
Krzemiński, Jakub, 5G
Kucharczyk, Marcin, 4H
Kucheruk, Volodymyr Yu., 1Z
Kudin, Hrygorii I., 28
Kudriavtsev, Dmytro, 27
Kukharchuk, Vasyl V., 63
Kuklewski, Michał, 3G
Kulakov, Pavel I., 1Z
Kulchytskyi, Bohdan V., 1S
Kulias, Anatolii I., 23
Kuligowski, P., 3K
Kulish, Sergiy M., 31
Kunbolat, Algazy, 07
Kuncicky, Lumir, 0Y
Kungurtsev, Oleksii, 24
Kupershtein, Leonid M., 1N, 1S
Kurylenko, Iryna V., 2D, 33
Kuśmirek, Wiktor, 1Q, 1W
Kutsenko, Alexander S., 2G
Kutsman, Vladislav V., 09
Kuzmenko, Liliia V., 0G
Kuzovik, Vyacheslav D., 2E
Kvaterniuk, Olena, 2B, 2R
Kvaterniuk, Serhii, 2B, 2R
Kvyetnyy, Roman N., 0M
Kyrylashchyk, Svitlana A., 5W, 62
Lazarev, Alexander A., 0O
Lazarev, Igor V., 3C
Lenty, Bartosz, 0E
Lepak, Łukasz, 1Q
Lesko, Oleksandr Yo., 34
Lewandowski, Jakub, 2Y
Lewiński, Stanisław, 35, 3D, 3M
Lin, Chenghong, 36
Linczuk, Maciej, 02
Linczuk, Paweł, 46, 4A, 4D, 4F, 4G
Lishchynska, Lyudmyla B., 0O, 0X
Litwin, Dariusz, 05
Luhovskyi, Alexandr F., 15
Lyashenko, Artem V., 2H
Lysenko, Gennadii L., 0G
Lytyuga, Oleksandr P., 08
Machno, M., 4Y
Maciejewski, Marcin, 31, 32, 33
Mądry, J., 3Z
Majdan, Paweł, 3W
Makal, Jaroslaw, 5Q
Malinovskyi, Vadim, 0F, 16
Malinowski, Bartosz, 3P
Malinowski, Karol, 46, 4A, 4F, 4G
Malinowski, Radosław, 35, 3D, 3M
Małkiewicz, Krzysztof, 64
Malyk, Igor V., 2Z
Mamyrbaev, Orken, 28, 62
Mandebura, Anastasiia, 2R
Mandebura, Svyatoslav, 2R
Mankiewicz, Lech, 2N
Manziuk, Eduard O., 28
Markowski, Konrad, 1E, 1F, 1G, 1H
Markowski, Piotr, 64
Martinek, Radek, 0Q, 0V, 5R
Martyniuk, Tatiana B., 1N, 1S
Matras, A., 4Y
Matyjasiak, Barbara, 3N, 3O
Mazurek, Gustaw, 3W
Mazurek, Paweł, 3W
Mazurets, Olexander V., 23
Mazurkiewicz, Tomasz, 1L
Megel, Yuriy Y., 2G
Meleshko, Yelyzaveta V., 1T
Melnyk, Roman A., 39
Michalowski, P. P., 4K
Michalska, M., 3J
Michalska, Magdalena, 1X, 2L, 2M
Mielnik, Dariusz, 3W
Miettinen, E.-P., 3K
Miller, Piotr, 5M, 5Z

Mishalov, Volodymyr D., 06
Mokanyuk, Olexander, 2B
Motrich, Artem V., 06
Mrozek, T., 1K
Mrozowski, Piotr, 64
Mulawka, Jan J., 2K
Mumladze, Georgij R., 2X
Murat, Kacper, 1F
Musiał, Jacek, 3X, 3Y
Mustetsova, Olena, 2F
Mykytenko, Volodymyr I., 0T
Nalbach-Moszynska, Małgorzata, 1J
Nebava, Mykola I., 34
Neumann, Łukasz, 1U
Niderla, Norbert, 1F
Niepostyn, S., 1O
Nitka, Arkadiusz, 0Z
Nitsuk, Yury A., 4M
Nochnichenko, Ihor V., 15
Nosova, Tatyana V., 32
Nosova, Yana V., 31
Novak, Tomas, 0Y
Novikova, Nataliia, 24
Nowak, Kacper, 48
Nowak, Robert M., 1M, 1P, 1Q, 1U, 1W, 2J
Nowakowska-Langier, K., 4R
Nowakowski, Artur, 3D, 3M
Nowosielski, W., 3K
Nurseitova, Karlygash, 12, 1I, 1Z, 5Y
Odaiska, Khrystyna S., 1A
Okal, Paweł, 4W
Olchowik, Monika, 2K
Olejnik, Arkadiusz, 0N, 3A
Omiotek, Zbigniew, 2B, 2C, 2D, 2E, 2F, 2G, 2H, 2I
Orazalieva, Sandugash, 10, 5N
Orleanski, Piotr, 3F, 3Q
Ormanbekova, Ainur, 32, 34, 5H
Ortwein, R., 45
Osadchuk, Iaroslav O., 11, 1I, 2T
Osadchuk, Oleksandr V., 11, 1I, 2T, 5N, 5Y
Osadchuk, Vladimir S., 11, 1I, 2T
Ostrowski, S., 55, 59
Ovcharenko, Aleksander P., 0D
Ozeranskyi, Volodymyr, 27
Palamarchuk, Mykhaylo I., 2H
Pałgan, T., 3U
Palma, P., 3H
Pan, Zhihao, 0H
Panas, Patryk, 0M, 0O, 0P
Panek, R., 45, 49
Pankiewicz, Patryk, 1W
Parkot, Katarzyna, 18
Pastuszak, Grzegorz, 1J
Patel, N., 45
Pavlov, Sergii V., 06, 22, 2A, 2Q, 33
Pavlyukovich, Natalia, 2Z, 30
Pavlyukovich, Olexander V., 2Z, 30
Pawelski, Daniel, 1J
Pawlowska, Diana, 4C
Paziewska-Nowak, A., 4L
Pęksyk, Jakub, 1E
Pepłowski, Andrzej, 2V, 5C, 5I
Perlicki, K., 1K
Petruk, Vasil, 2B, 2R
Pietrzak, Robert, 3F
Pijanowska, D., 4L
Pijarski, Paweł, 5M
Pilarczyk, Rafal, 2W
Pinaieva, Olga Yu., 26
Piórek, Izabella, 5I
Plucinska, Renata, 2U
Podgórski, Piotr, 3C
Podsiadły, B., 5B
Polak, S., 3U
Polhul, Tetiana D., 1Y
Povoroznyuk, Anatoliy I., 0S, 2X
Poźniak, Krzysztof T., 1J, 3B, 3W, 46, 4A, 4D, 4F, 64
Pożoga, Mariusz, 3N, 3O
Prysyazhnyuk, Petro V., 2Z
Przewłoka, Aleksandra, 4X
Pshenychnyi, Olexiy O., 1A
Puścian, Marek, 21
Pustovit, Grigorii P., 0A
Rabenda, Marcin, 14
Raczyński, T., 4L, 5C
Radzewicz, Czesław, 2O
Radziak, Kamil, 05
Radzikowski, Kacper, 1Q, 2J
Rakhmetullina, Saule, 13, 2R, 31
Rakytyanska, Hanna, 2B
Rataj, Mirosław, 3E, 3F, 3U, 40
Reshetnyak, Maria, 24
Rogalski, Przemysław, 52
Romaniuk, Ryszard S., 02, 12, 16, 1R, 1Y, 1Z, 3B
Romanko, Olha, 25
Romanyuk, Oksana A., 2C
Romanyuk, Olexander N., 22
Romanyuk, Svitlana O., 13
Rosiński, Wojciech, 3W
Rudyk, Andrii V., 5N
Rumian, Ksenia, 5A
Rusakov, Konstantin, 2O
Rutkowski, K., 3K
Rybicki, Marcin, 3D, 3M
Rybus, Tomasz, 3V
Rychlik, Arkadiusz, 0N, 3A
Ryzenko, Jakub, 3T
Sakypbekova, Meruyert, 4M
Salem Nasser Mohamed, Mohamed, 1N
Sarkisova, Yuliya V., 06
Savina, Nataliia B., 25, 34
Savytskyi, Anton Y., 5Y
Sawicki, Daniel, 0W, 1R, 1S, 1T, 39, 5S, 5T
Selegrat, Monika, 2S
Seletska, Olena O., 11, 1I, 2T
Selivanova, Karina G., 2H
Semenets, Valerii V., 32
Semenov, Andriy O., 1Z, 5N, 5Y
Semenova, Olena O., 1Z, 5N
Sereja, Klara, 5Z

Sestak, D., 45, 49
Severilov, Victor A., 5V
Seweryn, Karol, 3H, 3V
Sewiolo, Mateusz, 5Q
Shevchuk, Andrey V., 13
Shevchuk, Viktor I., 2D, 33
Shtofel, Dmytro H., 2X
Shushliapina, Natalia O., 31
Sichko, Tetiana V., 2Q
Sidor, Karol, 0I, 5M, 5O
Siegieda, Tomasz, 5J
Sienkiewicz, Piotr, 3W
Sioma, Andrzej, 0C, 0L
Siuzdak, J., 04
Skalski, A., 5B
Skarbek, Władysław, 0H, 0K, 0U, 2W
Skarżyński, Kacper, 5G
Skorupski, Krzysztof, 08, 09, 0A, 19, 1C
Skup, Konrad R., 3E, 3J, 3K
Slanina, Zdenek, 0Q, 0V, 0Y, 5R, 5U
Słoma, Marcin, 58, 59, 5B, 5F, 5G
Słowik, Jakub, 5S
Ślusarczyk, Łukasz, 57, 5D, 5E
Smailova, Saule, 11, 1T, 20, 23, 25
Smolarz, Andrzej, 1N, 27, 28, 34
Smółkowski, Adam, 1U
Smyk, Sebastian, 5T
Sobiecki, Mateusz, 3E
Sokal, E., 3R
Sokansky, Karel, 0Y
Sokół, Grzegorz, 1J
Soltys, Iryna V., 2Z, 30
Sopivnyk, Ruslan V., 2E
Sosnowski, J., 1V
Stakhov, Oleksiy Y., 5W, 62
Stämm, S., 3U
Stankiewicz, Jacek M., 53
Staszewski, Rafał, 47
Steckiewicz, Adam, 53
Stepanchenko, Olha M., 3I
Stepaniuk, Dmytro S., 1B, 2Q
Stępińska, Izabela, 4T
Stepniak, G., 04
Stobiecki, Paweł, 3W
Stonio, Bartłomiej, 56
Strikova, Tetiana O., 08
Struniawski, Jarosław, 1J, 64
Strutynskyi, Serhii, 10
Struzikiewicz, Grzegorz, 0C, 51
Suchańska, M., 4O
Sumorek, Mateusz, 61
Sydoruk, Oleh O., 13
Sylwester, Janusz, 3C, 3L
Syzdykpayeva, Aigul, 2B, 2D, 2F, 2H
Szmidt, Jan, 3A, 4R, 4X, 56
Szymajda, Waldemar, 64
Szymański, Paweł, 4B
Talakh, Mariya V., 30
Tarnovskyi, Mykola H., 0A, 12
Taube, Andrzej, 56
Teklinska, Dominika, 4Z
Tepliakova, Irina V., 4M
Teplova, Olena Yu., 2D
Timchenko, Leonid I., 1B, 2Q
Tkachuk, Vladyslav M., 2I
Tomasik, Lukasz, 3N, 3O
Tomka, Yuriy Ya., 2Z, 30
Topyła, Dominik, 1F
Troianovska, Tatyana I., 22
Trzebińska, Karolina, 3T
Tsymbal, Serhii V., 63
Turgunbekov, Azat, 60
Turgynbekov, Yerbol, 22
Tushnytskyy, Ruslan B., 39
Tuzhanskyi, Stanislav Ye., 1D
Twardowski, Bartłomiej, 1M, 1Q
Tyburska, Agata, 1J, 64
Tymchik, Sergii, 2F
Tymchyk, Grygorij S., 07, 0T
Tymińska, Joanna, 3T
Ulichev, Oleksandr S., 1T
Ursan, Maksym I., 13
Ushenko, Alexander G., 06
Ushenko, Vladimir A., 06
Ushenko, Yuriy A., 2Z, 30
Vanchuliak, Oleg Ya., 06
Vasazhenko, Nataliia O., 34
Vernigora, Inna V., 5V
Voitovych, Olesia P., 1S
Voytsekhovskaya, Elena V., 0O
Voznyak, Oleksandr M., 5N
Vyatkin, Sergey I., 22
Wąchal, P., 49
Walendziuk, Wojciech, 5J, 5L, 5U
Wałpuski, Bartłomiej, 5F
Walter, Piotr, 2V
Wang, Le, 2J
Wasiewicz, Piotr, 36, 37
Waskiewicz, M., 4R
Wawer, Piotr, 3E, 3F
Wawrzaszek, A., 38
Wawrzaszek, R., 3R, 3Z, 40
Wawrzusiak, Radosław, 1J
Wawrzyniak, Zbigniew M., 2S, 3W, 64
Wawrzyński, Paweł, 1Q
Wereszko, Błażej, 3W
Winiarski, Maciej, 2N
Winkler, M., 3J, 3K
Wojcik, Marek, 4Z
Wójcik, Waldemar, 10, 20, 2X, 3I, 5H, 5V, 63
Wojeński, Andrzej, 3W, 46, 4A, 4D, 4F, 4G, 64
Wojtkowski, Wojciech, 5K, 5L
Wolter, Marcin, 4H
Woźniczak, Tomasz, 3C
Wróblewski, G., 55, 59
Wronka, Halina, 4O, 4T
Wrzosek, Emil, 3T
Yarovyi, Andrii A., 1Y, 27
Yeraliyeva, Bakhyt, 39
Yerkeldessova, Gulzada, 1D

Yezerskyi, Nikita V., 3C
Yoshie, Osamu, 2J
Yusupova, Gulbahar, 1R
Zabolotna, Natalia I., 30
Zabołotny, Wojciech M., 1J, 3W, 41, 42, 46, 4D, 4F, 64
Zajac, Andrzej, 2Y
Zarębska, Arleta, 1G
Żarnecki, Aleksander F., 48
Zarzeczny, D., 2P, 54
Zavolovitch, Alina Y., 06
Zawistowski, Paweł, 1M, 1U
Zawistowski, T., 3R
Zayukov, Ivan V., 34
Zbroszczyk, Hanna Paulina, 43
Zdunek, K., 4R
Zębala, Wojciech, 57, 5A
Zenkova, Claudia Y., 0P
Zhemchuzhkina, Tatyana V., 32
Zhunissova, Ulzhalgas, 0S, 2G, 2I, 2X
Zielińska, Agata, 3C
Zieliński, Tomasz, 19, 1C
Zlepko, Alexandra S., 2X
Zlepko, Sergii M., 2D, 32, 33
Żukociński, Mateusz, 5X
Żukowski, Jakub, 61
Zviahin, Oleksander S., 5Y
Zwęgliński, Tomasz, 3T
Zych, M., 4L, 5C
Zychowicz, Łukasz, 19, 1C

Implementation of OMTF trigger algorithm with High-Level Synthesis

Wojciech M. Zabołotny[a,b]

[a]Warsaw University of Technology, Institute of Electronic Systems, ul. Nowowiejska 15/19, 00-665 Warszawa, Poland
[b]University of Warsaw, Institute of Experimental Physics, ul. Pasteura 5, 02-093 Warszawa, Poland

ABSTRACT

The paper presents the implementation of the Overlap Muon Track Finder algorithm using the High-Level Synthesis (HLS). That algorithm has been previously implemented in a highly optimized VHDL code. Therefore, comparison of the implementations based on VHDL code, and on HLS provides an assessment of the suitability of HLS for implementation of complex algorithms. Additionally, analysis of the correlation between the HLS code and parameters of the produced solution gives suggestions regarding the correct implementation of typical data-processing algorithms in HLS.

Keywords: HLS, FPGA, OMTF, Trigger algorithm, Logic synthesis, VHDL

1. INTRODUCTION

High-Level Synthesis[1] draws the attention of many system designers and FPGA developers. It has created a hope that C programmers will be able to efficiently implement algorithms in FPGA. The previous experiments with HLS applied to the stream heap-sorting system[2] have shown, that for such simple algorithms usage of HLS in certain conditions may result in better performance, than thoroughly handcrafted HDL code. Even though HLS was not able to achieve the shortest possible Initialization Interval (II) of the pipelined design, for more relaxed requirements, it provided the solution with significantly smaller resource consumption. Those results encouraged testing the suitability of the HLS approach to more complex algorithms. The good candidate is the Overlap Muon Track Finder algorithm,[3] that was carefully optimized both regarding the resource usage and achievable speed of processing.

2. STRUCTURE OF THE ALGORITHM

The Overlap Muon Track Finder (OMTF) algorithm has been developed for the upgrade of the muon trigger in the CMS experiment, and has been used during the LHC Run 2.[4] The OMTF algorithm is described in detail in the articles Ref. 3 and Ref. 5, and the theory behind it is shortly described in Ref. 6. In the CMS detector, the bunches of accelerated particles collide roughly every 25 ns. Those collisions are called bunch crossings (BX). The muons produced during the collision are passing through the CMS detector and generating the electrical signals, called hits in the 18 layers of the detector. The task of the algorithm is to find the transversal momentum p_T of those muons. The algorithm uses averaged tracks (patterns) generated in physical simulations for different values of p_T and finds the track that is best matched to the observed set of hits. The main concept of the algorithm is shortly presented in Figure 1. The PDF values are based on the logarithm of the probability that the muon with particular p_T generates hit with the particular azimuthal angle. The precalculated PDF values are stored in lookup tables.

The block diagram of the hardware that performs the OMTF algorithm is shown in Figure 2. The following is a short and simplified description of the algorithm explaining the structure of the hardware implementation. The full description may be found in the referenced articles.[3,5]

- In the first stage, the hits recorded in specially selected "reference layers" are analyzed. They are ordered by priority. From each BX up to 4 hits from those layers, so-called "reference hits", with highest priorities are taken and used as a basis for track reconstruction.

Further author information: (Send correspondence to W.M.Z.)
W.M.Z.: E-mail: wzab@ise.pw.edu.pl, Telephone: +48 22 234 7717

Photonics Applications in Astronomy, Communications, Industry, and High-Energy Physics Experiments 2019, edited by Ryszard S. Romaniuk, Maciej Linczuk, Proc. of SPIE Vol. 11176, 1117641
© 2019 SPIE · CCC code: 0277-786X/19/$21 · doi: 10.1117/12.2536258

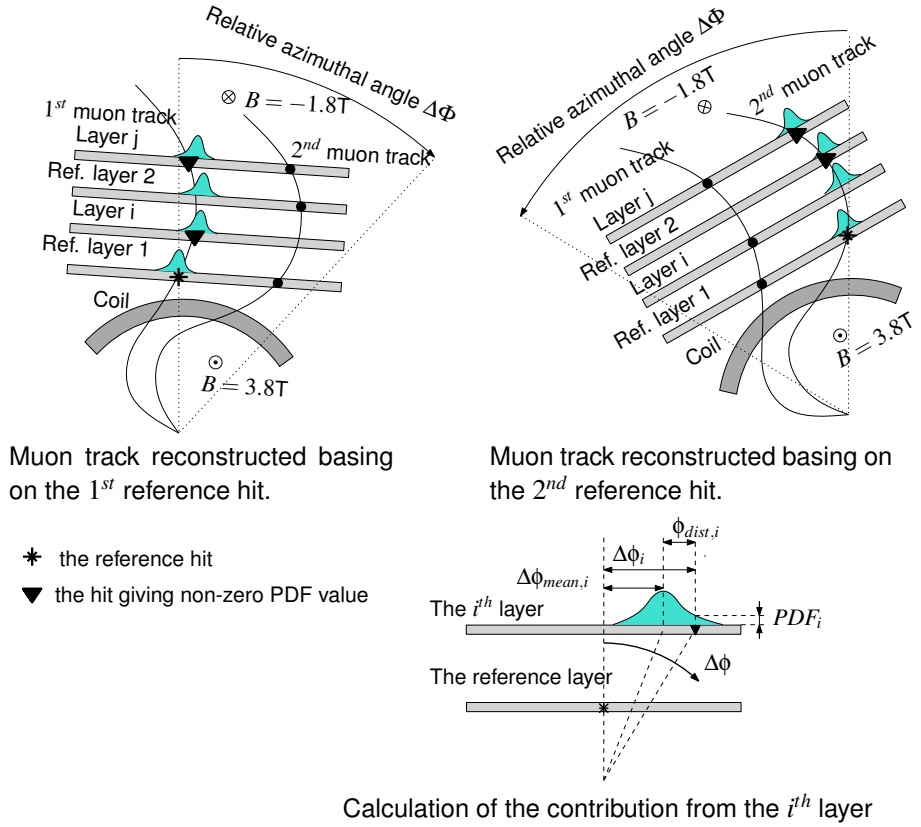

Figure 1: Reconstruction of two muon tracks with OMTF algorithm. Two reference hits from the first reference layer are used. Each of them is associated with another muon track. The lower figure shows how the PDF contribution from the particular detector layer is calculated. The figure is reproduced with minimal modifications from the Open Access publication Ref. 5 according to the CC-BY 4.0 license.[7]

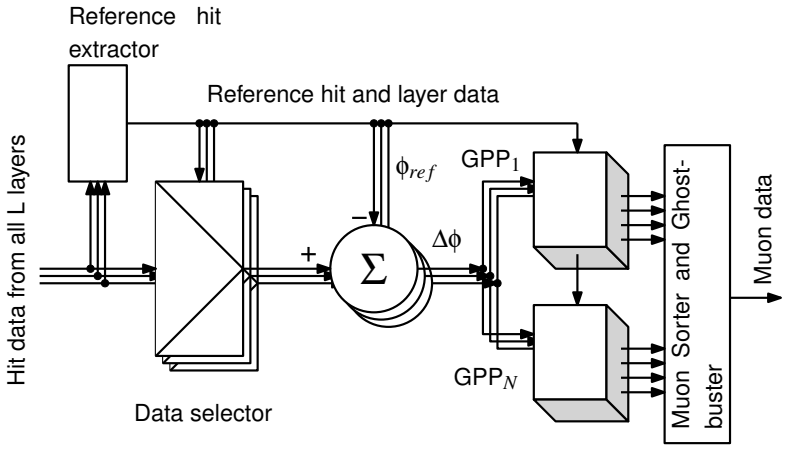

Figure 2: Block diagram of the OMTF algorithm implementation. The GPP (Golden Pattern Processor) units are matching the delivered hits with the individual sets of track patterns. The figure is reproduced with minimal modifications from the Open Access publication Ref 5 according to the CC-BY 4.0 license.[7]

- Next, the detector links, that are likely to provide the hits belonging to the muon track associated with the selected "reference hit" are selected. The azimuthal angle ϕ_{ref} of the reference hit is subtracted from the azimuthal angle ϕ of those hits, forming the $\Delta\phi$ values.
- Further processing is done in parallel for multiple patterns corresponding to different values of the p_T and different sign of the charge of the muon*
  - For each layer, the average bending of the muon track $\Delta\phi_{mean}$ is taken, and the hit nearest to the pattern track is selected.
  - From the lookup table, the PDF contribution from each layer is found (as shown in Figure 1).
  - The sum of PDF contributions from all layers and the number of contributing layers is calculated†.
- Finally, the pattern with the highest number of contributing layers and the highest total PDF is selected.

The internal structure of the block calculating the total PDF for the single track pattern is shown in Figure 3.

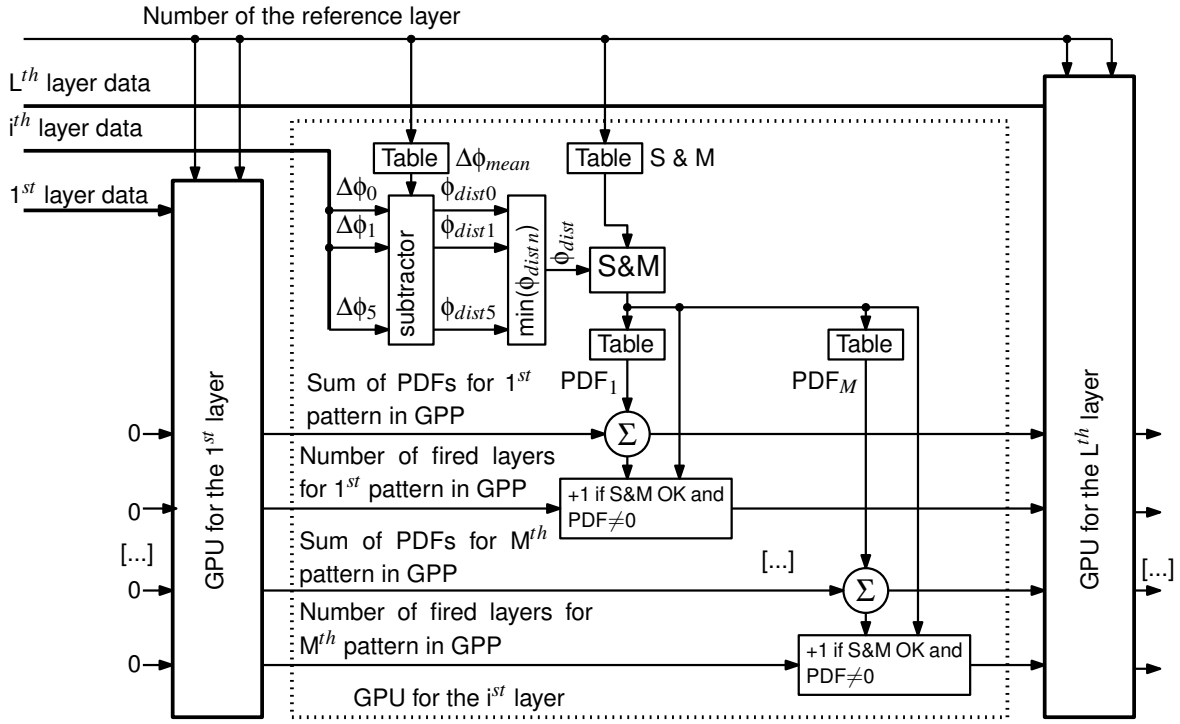

Figure 3: Implementation of the single GPP handling M patterns. The Golden Pattern Unit (GPU) is the block which analyses hits in a single layer. L is the number of layers, M is the number of patterns in the set of patterns handled in the GPP. "S&M" (shift & mask) are the blocks used to scale $\Delta\phi$ depending on the PDF distribution width. The figure is reproduced with minimal modifications from the Open Access publication Ref. 5 according to the CC-BY 4.0 license.[7]

The OMTF algorithm was created and initially tested as a C++ program. Then it was carefully translated into the parameterized high-level HDL description,[3,8] tested and optimized. The whole iterative process requiring multiple iterations is described in Ref. 5. Certain modifications required repeated retuning of delays in parallel branches of the algorithm. That process was especially time-consuming and error-prone, and therefore for future similar systems, an automated tool has been created.[9]

*To minimize resource consumption, the patterns are grouped in sets containing 2 or 4 patterns, that are processed simultaneously.

†Layers belonging to one type of detectors - the DT, are analyzed as pairs in a special way. The details are described in Ref. 3

```
#include <stdint.h>
#include <stdio.h>
#include <string.h>
#include <ap_int.h>
static ap_uint<1> sdin[128];
static int first = 0;
int prior_enc(ap_uint<1> load,
              ap_uint<1> ref_hit_bits[GP_N_OF_REF_HITS])
{
#pragma HLS PIPELINE II=1
#pragma HLS UNROLL
#pragma HLS ARRAY_PARTITION variable=sdin complete
#pragma HLS ARRAY_PARTITION variable=ref_hit_bits complete
    int i;
    int found = -1;
    if (load) {
        first = 0;
        for (i = 0; i < GP_N_OF_REF_HITS; i++)
            sdin[i] = ref_hit_bits[i];
    }
    for (i = 0; i < GP_N_OF_REF_HITS; i++) {
        if ((i >= first) && (found == -1)) {
            if (sdin[i]) {
                first = i + 1;
                found = i;
            }
        }
    }
    return found;
}
```

Figure 4: The simplest and "naive" HLS implementation of the priority encoder used to select the "reference hit". That code resulted in unacceptable Initialization Interval.

3. PREPARATION OF THE HLS IMPLEMENTATION

The features described in the previous section, make the OMTF algorithm an ideal object for HLS implementation. If such implementation is reliable and successful, the development cycle could be significantly reduced, because any modification of the algorithm done in C could be quickly and automatically translated into the FPGA code.

All experiments have been performed using the Vivado HLS 2018.3 environment. The computer used for tests was equipped with Intel Xeon CPU E5-2623 v4 working at 2.60 GHz clock frequency. The pattern definition used for tests consisted of 20 pattern sets, containing 52 track patterns in total.

The HLS source code was the C/C++ reimplementation of the OMTF algorithm. The design was tested in simulations using the same test data sets that were used for testing of the HDL implementation. The testbench for C simulations was created basing on the original testbench written for the HDL implementation. That testbench also has been modified to allow testing of the HDL code generated by HLS synthesis.

3.1 Initial HLS implementation

To achieve similar functionality, as in the original, the design was supposed to be implemented in pipeline architecture with Initialization Interval equal to 1 and the clock frequency equal to 160 MHz (4 clock periods per BX to test up to 4 reference hits). Correct operation of the code in C simulations was achieved without problems. However, ensuring proper synthesis and implementation was more complicated.

The first version of the code, written without considering specific features of the FPGA hardware, resulted in very high Initialization Interval values - up to 128. The analysis of the problem has shown that the priority encoder used to select the reference hit with the highest priority requires reimplementation. The original "naive" code is shown in Figure 4. To improve the Initialization Interval, the encoder has been decomposed into a two-level hierarchical structure described with the code shown in Figure 5. Similarly, it was necessary to implement a hierarchical sorter finding the best-matched pattern on the output of the algorithm.

Unfortunately, the implementation shown in Figure 5 has exposed a serious problem. The C simulations of the whole algorithm have produced correct results for the test data. Synthesis and the implementation didn't generate any critical warnings or errors. However, simulations of the generated HDL code resulted in corrupted output. Not all reference hits were processed. Resolving the problem was complicated by the fact that the code generated by HLS is huge and almost illegible. Additionally, each synthesis and implementation of the complete algorithm took even up to 12 hours.

Fortunately, the problem was again associated with the priority encoder, that could be easily extracted as an individual block and tested separately. However, to correctly integrate the extracted priority encoder with its testbench, it was necessary to add the interface definitions (*#pragma HLS INTERFACE*). It appeared that forgetting to remove them before the compilation of the whole design resulted in an increase of Initialization Interval from 1 to 4[‡]. The final version of the priority encoder that works correctly with II=1 both in C simulations and as the HLS-produced HDL code is shown in Figure 6.

[‡]That problem may be solved by creating the separate wrapper for the block and specifying interfaces in the wrapper.

```
#include <stdint.h>
#include <stdio.h>
#include <string.h>
#include <ap_int.h>
#include <ap_utils.h>
static ap_uint<8> code = 0;
ap_uint<1> sdin[128];

void prior_sub_enc(ap_uint<1> rhb[8], ap_uint<4> *code)
{
#pragma HLS LATENCY max=0
#pragma HLS INLINE
#pragma HLS UNROLL
    *code = 8;
    for (int i = 0; i < 8; i++) {
        if (rhb[i] == 1) {
            *code = i;
            break;
        }
    }
}

int prior_enc(ap_uint<1> load,
              ap_uint<1> ref_hit_bits[128])
{
#pragma HLS PIPELINE II=1
#pragma HLS UNROLL
#pragma HLS ARRAY_PARTITION variable=ref_hit_bits complete
#pragma HLS ARRAY_PARTITION variable=sdin complete
    ap_uint<4> sub_code[16];
#pragma HLS ARRAY_PARTITION variable=sub_code complete
    if (load == 1) {
        for (int i = 0; i < 128; i++) {
            sdin[i] = ref_hit_bits[i];
        }
    } else {
        if (code < 128)
            sdin[code] = 0;
    }
    code = 128;
    for (int i = 0; i < 16; i++) {
        prior_sub_enc(&sdin[8 * i], &sub_code[i]);
        if (sub_code[i] < 8) {
            code = i * 8 + sub_code[i];
            break;
        }
    }
    return code;
}
```

Figure 5: The initial hierarchical HLS implementation of the priority encoder used to select the “reference hit”. That code has correct II=1 and behaves correctly in C simulation, but produces the HDL code that does not work correctly.

```
#include <stdint.h>
#include <stdio.h>
#include <string.h>
#include <ap_int.h>
#include <ap_utils.h>
static ap_uint<1> sdin[128];
void prior_sub_enc(ap_uint<1> rhb[8], ap_uint<4> *code) {
#pragma HLS LATENCY max=0
#pragma HLS INLINE
#pragma HLS UNROLL
        *code = 8;
        for (int i = 0; i < 8; i++) {
                if (rhb[i] == 1) {
                        *code = i;
                        break;
                }
        }
}

int prior_enc(ap_uint<1> load, ap_uint<1> ref_hit_bits[128]) {
#pragma HLS PIPELINE II=1
#pragma HLS UNROLL
#pragma HLS ARRAY_PARTITION variable=ref_hit_bits complete
#pragma HLS ARRAY_PARTITION variable=sdin complete
        ap_uint<4> sub_code[16];
        int code = 0;
#pragma HLS ARRAY_PARTITION variable=sub_code complete
        code = 128;
        for (int i = 0; i < 16; i++) {
                prior_sub_enc(&sdin[8 * i], &sub_code[i]);
                if (sub_code[i] < 8) {
                        code = i * 8 + sub_code[i];
                        break;
                }
        }
        if (load == 1) {
                for (int i = 0; i < 128; i++) {
                        sdin[i] = ref_hit_bits[i];
                }
        } else {
                if (code < 128)
                        sdin[code] = 0;
        }
        return code;
}
```

Figure 6: The final hierarchical HLS implementation of the priority encoder used to select the “reference hit”. That code has correct II=1, behaves correctly in C simulation, and produces correct HDL code.

Table 1: Comparison of the source code complexity for HDL and HLS approaches. It can be seen that the HLS reduced the number of files and lines of the code roughly by a factor of 3. The analysis excludes the automatically generated files with definitions of patterns and similar constant values and structures.

Form of description]	Files	Code	Comment	Comment %	Blank	Total
HDL (VHDL)	21	1724	787	31.3%	302	2813
HLS	7	564	260	31.6%	78	902

In the whole process of correcting the HLS implementation, it was important that the reference HDL implementation existed. Obtaining Initialization Interval equal to 1 (II=1) was really difficult and required significant effort. Without the knowledge that the optimized HDL implementation is able to work at II=1, it was easy to come to the conclusion that the problem can't be solved with a pipeline with so short II.

4. RESULTS AND DISCUSSION

It was possible to obtain the correct working implementation of the OMTF algorithm using the HLS synthesis. The implementation is based on a pipelined architecture with parallel branches, but the whole task of equalization of the delays in parallel branches was correctly handled by the HLS tool. It is a significant advantage, that seriously reduces the risk of errors and effort to maintain the design.

4.1 Code complexity

Use of HLS also allows significant complexity of the source code. Table 1 compares the amount of code needed to implement the HDL and HLS versions of the algorithm. It is also worth to emphasize that the C/C++ description is better legible and easier to maintain by a software engineer not skilled in FPGA programming. However, in case of problems with the generated HDL code, the FPGA related skills may be important. They may be also useful to prepare the C/C++ code best suited for FPGA implementation.

4.2 Time of compilation

The HLS and HDL approaches differ significantly regarding the time of compilation. For huge and complex designs like OMTF, the HLS synthesis and implementation may be significantly increased. The values obtained on Xeon-equipped computer used for tests were as follows

- **For HDL (VHDL) implementation**
  - Synthesis: 53 minutes
  - Implementation: 20 minutes
  - **Total: 73 minutes**
- **for HLS implementation**
  - Synthesis: 430 minutes
  - Implementation: 248 minutes
  - **Total: 678 minutes**

Due to the long compilation, it may be important to provide the possibility to decompose a large design into smaller blocks and prepare testbenches for all of them. Without a possibility to test both in C and in produced HDL the "priority encoder" it would be impossible to isolate and fix the problems described in section 3.1. It is important, that for smaller blocks the HLS synthesis and implementation times are much shorter. Therefore, it is very important to test parts of the design with smaller blocks and perform the final HLS compilation after resolving all problems exposed during testing of smaller blocks.

Table 2: Resource usage and minimal clock period in FPGA (predicted values after HLS synthesis and final values after implementation).

	LUT	FF	BRAM	Min. clock period
Available	433200 (100%)	866400 (100%)	2940 (100%)	6.125 ns
Synthesis	12174356 (2810%)	1348296 (155%)	720 (24%)	7.480 ns
Implementation	123964 (29%)	112240 (13%)	720 (24%)	5.925 ns

Table 3: Comparison of the results of synthesis based on HLS and HDL description of the OMTF algorithm.

Design method	Slice LUTs	Slice Registers	F7 Muxes	F8 Muxes	Slices	LUT as Logic	LUT as Memory	Block RAM Tile
HLS	123964 (28.6%)	112240 (12.9%)	437 (0.2%)	33 (0.03%)	39312 (36.3%)	106900 (24.7%)	17064 (9.8%)	360 (24.49%)
HDL	114791 (26.5%)	92845 (10.7%)	272 (0.13%)	39 (0.04%)	40607 (37.5%)	108905 (25.1%)	5886 (3.4%)	360 (24.49%)

The obtained results of HLS synthesis suggested that the design can't be implemented both regarding the required clock frequency and FPGA occupancy. Fortunately, the optimizations performed during the implementation significantly reduced the critical path and resource occupancy. The results of HLS synthesis and implementation are presented in Table 2.

4.3 Resource consumption and performance

Both HDL and HLS-based designs are capable of working at clock 160 MHz with Initialization Interval equal to 1. However, they differ in latency:

- The latency of HDL-based design: 38 clock periods
- The latency of HLS-based design: 54 clock periods (significantly higher, but acceptable)

The resource consumption of both designs is shown in Table 3. Both methods give similar FPGA occupancy.

5. CONCLUSIONS

The results obtained during the development and testing of the HLS-based implementation of the OMTF algorithm have exposed certain advantages and disadvantages of such an approach. They are listed below.

Advantages of HLS implementations:

- It is possible to translate the algorithm implemented in C/C++ into FPGA implementation.
- The source code is smaller than in HDL-based design, easier to understand and maintain.
- It is easier to test the algorithm as the C/C++ program than in HDL simulation.
- The HLS ensures correct synchronization of data in parallel paths of the pipelined design.

Possible problems with HLS implementations:

- Not all algorithms correctly working in C/C++ are correctly translated into synthesizable HDL code.

- Preparation of C/C++ code for the HLS implementation may require knowledge about the operation of FPGAs.
- The correct results of the C simulation do not warrant the correct operation of the final HDL implementation.
- For complex designs, the synthesis and implementation times of the design may be significantly increased.
- The generated HDL code is huge and illegible. It makes almost impossible debugging that code in case of erroneous operation.

It may be stated that indeed the HLS allows implementing even complex algorithms in FPGA, based on the C or C++ description of the algorithm. It seems, that the basic implementation may be produced even by a software engineer with minimal FPGA skills. However, when really high performance is needed, the deep knowledge of FPGA capabilities and limitations is very important. The organization of C code and selection of options (HLS pragmas) may significantly affect the results. Automated generation of HDL code by HLS tools may reduce the amount of human work needed to maintain complex designs (e.g., eliminating the need to manually adjust latencies in parallel branches). In theory testing of algorithms in C simulations should increase the speed of development based on iterative testing and corrections. Unfortunately, the very annoying finding that results of C simulation may sometimes disagree with the behavior of the generated HDL code, imposes frequent verification in HDL simulations. In connection with long times of HLS compilation, that may significantly slow down the development process. Hopefully, the HLS is a quickly developing technology, and probably the problem may be eliminated in future versions.

HLS seems to be a promising technology, however, its usage for complex designs must be carefully evaluated regarding benefits and losses.

ACKNOWLEDGMENTS

The author thanks all the members of the Warsaw CMS group who participated in the development of the original OMTF algorithm.

Work partially supported by statutory funds of Institute of Electronic Systems. OMTF project is supported by National Science Centre, Poland, grant UMO-2015/19/B/ST2/0286

REFERENCES

[1] Xilinx, "Vivado design suite user guide, high-level synthesis." https://www.xilinx.com/products/design-tools/vivado/integration/esl-design.html [Online; accessed 29-April-2018].

[2] Zabołotny, W. M., "Implementation of heapsort in programmable logic with high-level synthesis," *Proc.SPIE* **10808**, 108084C (Oct. 2018).

[3] Zabolotny, W. and Byszuk, A., "Algorithm and implementation of muon trigger and data transmission system for barrel-endcap overlap region of the CMS detector," *Journal of Instrumentation* **11**, C03004–C03004 (Mar. 2016).

[4] Konecki, M. A., "The CMS Level-1 muon triggers for the LHC Run II," Tech. Rep. CMS-CR-2018-227, CERN, Geneva (Sep 2018).

[5] Bluj, M., Buńkowski, K., Byszuk, A., Doroba, K., Drabik, P., Górski, M., Kalinowski, A., Kierzkowski, K., Konecki, M., Miętki, P., Okliński, W., Olszewski, M., Poźniak, K., Zabołotny, W., Zawistowski, K., and Żarnecki, G., "From the Physical Model to the Electronic System — OMTF Trigger for CMS," *Acta Physica Polonica B Proceedings Supplement* **9**(2), 181 (2016).

[6] Bunkowski, K., "The algorithm of the CMS Level-1 Overlap Muon Track Finder trigger," *Nuclear Instruments and Methods in Physics Research Section A: Accelerators, Spectrometers, Detectors and Associated Equipment* (Oct. 2018).

[7] "Attribution-sharealike 4.0 international." https://creativecommons.org/licenses/by-sa/4.0/ [Online; accessed 29-April-2019].

[8] Zabolotny, W. M. et al., "FPGA implementation of overlap MTF trigger: preliminary study," *Proc. SPIE* **9290**, 929025–929025–11 (2014).

[9] Zabołotny, W. M., "Automatic latency equalization in VHDL-implemented complex pipelined systems," *Proc.SPIE* **10031**, 10031 – 10031 – 12 (2016).

Automatic management of local bus address space in complex FPGA-implemented hierarchical systems

Wojciech M. Zabołotny[a], Marek Gumiński[a], and Michał Kruszewski[a]

[a]Institute of Electronic Systems, Warsaw University of Technology, ul. Nowowiejska 15/19, 00-665 Warszawa, Poland

ABSTRACT

The FPGA-implemented data acquisition and processing systems are usually configured via local bus providing access to internal control and status registers. Management of the address space of that local bus is a well known and non-trivial problem, especially in complex hierarchical systems. Even though various solutions have been already proposed, it seems that there is still a need for an open, portable address management system, capable of operation with different local bus technologies and various control interfaces. This paper presents a proposition for such a system. The multi-level hierarchy of nested blocks with internal control and status registers is supported. The blocks and registers may be implemented as single instances or vectors of multiple instances. The structure of the system is described with the XML file. The generated address map may be stored in various formats compatible with different control interfaces (e.g., IPbus or AXI). The proposed solution is compatible with the design flow based on parametrized high-level HDL implementation of the FPGA firmware.

Keywords: FPGA, Control interface, Address space, Wishbone, VHDL

1. INTRODUCTION

Complex digital data processing systems in FPGA chips are often created by connecting separate blocks developed and maintained by different teams. The correct cooperation of those blocks depends on a good definition of their interconnection both regarding the datapath and the control interfaces. In this paper, we concentrate on the solution that helps to create a clear and scalable organization of the control infrastructure. That requires good isolation of different blocks. It should be possible to add a new block or to modify the existing block without requiring significant modification of other blocks. The interconnections between the blocks should be as simple as possible. The number of separately used signals should be minimized. Generally, the problem may be decomposed into two main tasks. The first of them is the allocation of the address space so that each block is given the appropriate amount of register addresses. The second one is providing the address decoders, and bus interconnects, that are efficiently handled by the synthesis tools.

2. PREVIOUS SOLUTIONS

Of course, the problem of efficient management of internal control infrastructure in FPGAs is well known and many solutions are already existing.

2.1 "Internal Interface" and "Component Internal Interface"

Probably one of the most sophisticated solutions are the "Internal Interface" (II)[1,2] and the later object-oriented version the "Component Internal Interface" (CII).[3–5] They are widely used in the electronic systems prepared for TESLA,[6] FLASH,[7] CMS[1] and many other experiments. They are mainly oriented on controlling the FPGA systems from Java, C++ or Matlab, and internally they are using a VME-like interface. Both II and CII give sophisticated possibilities to access complex data structures (matrices of arbitrary length, sets of bit vectors, etc.). However, the price is high complexity of internal FPGA logic, that results in high resource consumption and long critical path. Unfortunately, both those solutions are not Open Source, and therefore they can't be freely adopted by any user.

Further author information: (Send correspondence to W.M.Z.)
W.M.Z.: E-mail: wzab@ise.pw.edu.pl, Telephone: +48 22 234 6693

Photonics Applications in Astronomy, Communications, Industry, and High-Energy Physics Experiments 2019, edited by Ryszard S. Romaniuk, Maciej Linczuk, Proc. of SPIE Vol. 11176, 1117642
© 2019 SPIE · CCC code: 0277-786X/19/$21 · doi: 10.1117/12.2536259

2.2 Address generators and decoding infrastructure provided by FPGA development environments

The development environment provided by FPGA vendors like Xilinx, or Intel (formerly Altera) provide tools supporting the management of the local AXI or Avalon bus. Xilinx offers the Block Design function in their Vivado[8] environment, while Intel offers Platform Designer[9] in their Quartus[10] environment. Figure 1 shows a simple system designed in Xilinx Vivado, containing blocks interconnected via the local AXI bus. Figure 2 shows the address table generated automatically by that tool. For such a simple system it may be an ideal solution with the graphical presentation of block's interconnections. Unfortunately, it becomes very difficult to manage when the complexity of the system grows and especially when the number of blocks or nested subblocks is parameterized. It also heavily relies on GUI and therefore is not fully compatible with purely HDL-based or script-driven development flow.

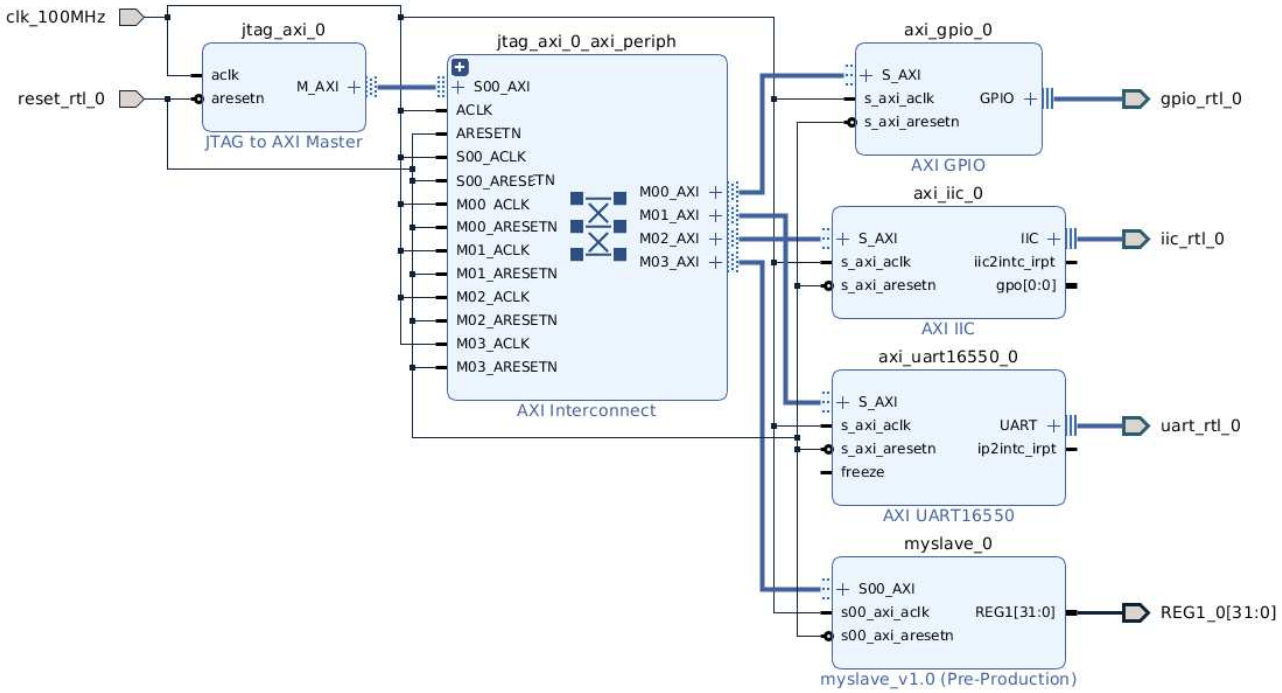

Figure 1: Simple system created in Block Designer in Xilinx Vivado environment.

Address Editor

Cell	Slave Interface	Base Name	Offset Address	Range	High Address
jtag_axi_0					
Data (32 address bits : 4G)					
axi_gpio_0	S_AXI	Reg	0x4000_0000	64K	0x4000_FFFF
axi_iic_0	S_AXI	Reg	0x4080_0000	64K	0x4080_FFFF
axi_uart16550_0	S_AXI	Reg	0x44A0_0000	64K	0x44A0_FFFF
myslave_0	S00_AXI	S00_AXI_reg	0x44A1_0000	64K	0x44A1_FFFF

Figure 2: The address allocation for the simple system from figure 1.

2.3 IPbus

One of the buses widely used in FPGA-implemented data processing systems is IPbus.[11] It is especially well suited for systems controlled via the Ethernet network. IPbus offers quite a sophisticated system for informing the software about the allocation of addresses. The XML-formatted address tables may reflect a complex hierarchy of blocks, registers, and bitfields. Unfortunately, IPbus provides only minimal support for the creation of address decoders for already existing address tables.[12] An attempt to generate IPbus address tables for a parameterized HDL design was the "adr_gen" system.[13] It uses a single IPbus slave with multiple control (read/write) and status (read only) registers to connect the user-specified hierarchical system. The system description must be written in Python language, using classes provided by "adr_gen". That system, however, separated the local bus interface from the user logic and required connecting multiple signals in HDL. Another disadvantage was the assignment of all slaves to the continuous range of addresses. That resulted in the suboptimal assignment of addresses in case of groups (vectors) of identical blocks, as such group was not aligned to the 2^N boundary and the generated address decoders were not fully optimized. The "adr_gen" system, however, could also be used to connect the user logic to the AXI bus using the AXI4 slave automatically generated by the Vivado "Create a new AXI4 Peripheral" command.

2.4 Wishbone slave generator

The Wishbone slave generator (wbgen2)[14] is a tool that is oriented on the automated generation of Wishbone slave IP cores in VHDL or Verilog, that implements registers, memory blocks or FIFOs. The slave is described in a C-like language. Basing on that description the tool automatically generates the address map for the slave, the VHDL/Verilog code with full implementation of the slave, the C headers that may be used by the software and also the documentation in the HTML format.

The wbgen2 is a fully open solution. It's disadvantage however is that it does not support the hierarchy of blocks, neither the vectors of registers.

3. THE ADDR_GEN_WB SYSTEM FOR LOCAL BUS MANAGEMENT

Basing on the review of existing solutions, we have decided to create our own system, aimed at combining the best features of all of them while remaining as simple as possible. The proposed system may be considered a reimplementation in Python[15] of the "wbgen2" tool (the original was written in Lua[16] language), with added support for a hierarchy of nested blocks and possibility to create groups (vectors) of registers and nested blocks.

3.1 Selection of the local bus

As the local control bus, the Wishbone[17] bus was chosen. It is used in the classic single mode. In this mode, it may control both the Wishbone and IPbus slaves, which gives access to multiple open IP cores. It is possible to control the local bus from the IPbus master. Additionally, there are bridges providing control of the Wishbone bus from other busses like Avalon[18] or AXI.[19–21] Therefore, such selection of local bus ensures high versatility and flexibility of the created control infrastructure, which is desirable, even though it provides lower performance than pure AXI bus.

3.2 Architecture of the created control system

The created control system has a tree architecture and is shown in Figure 3. Please note, that this figure shows only the control interconnections, fully ignoring the datapath transmitting the processed data. On the top level, the local bus is controlled by one or more Wishbone bus masters. The Local Wishbone node (see Figure 4) contains the Wishbone crossbar,[22] that delivers the WB bus to a single slave servicing local control and status signals, and optionally to the lower level slaves. The system supports also the groups (vectors) of identical slaves. For them, the arrays of lower level WB busses are created. The blocks can be nested, and the number of levels is limited only by the FPGA resources, the maximum acceptable length of critical path and by the capability of the address space. The critical path may be shortened by selecting the registered mode in the WB crossbar. That increases the maximum acceptable bus clock speed but introduces additional latency in the bus transactions.

For systems that use different clocks in different parts of the design, addr_gen_wb offers also the clock domain crossing (CDC) block that is optimized for single read/write transactions.

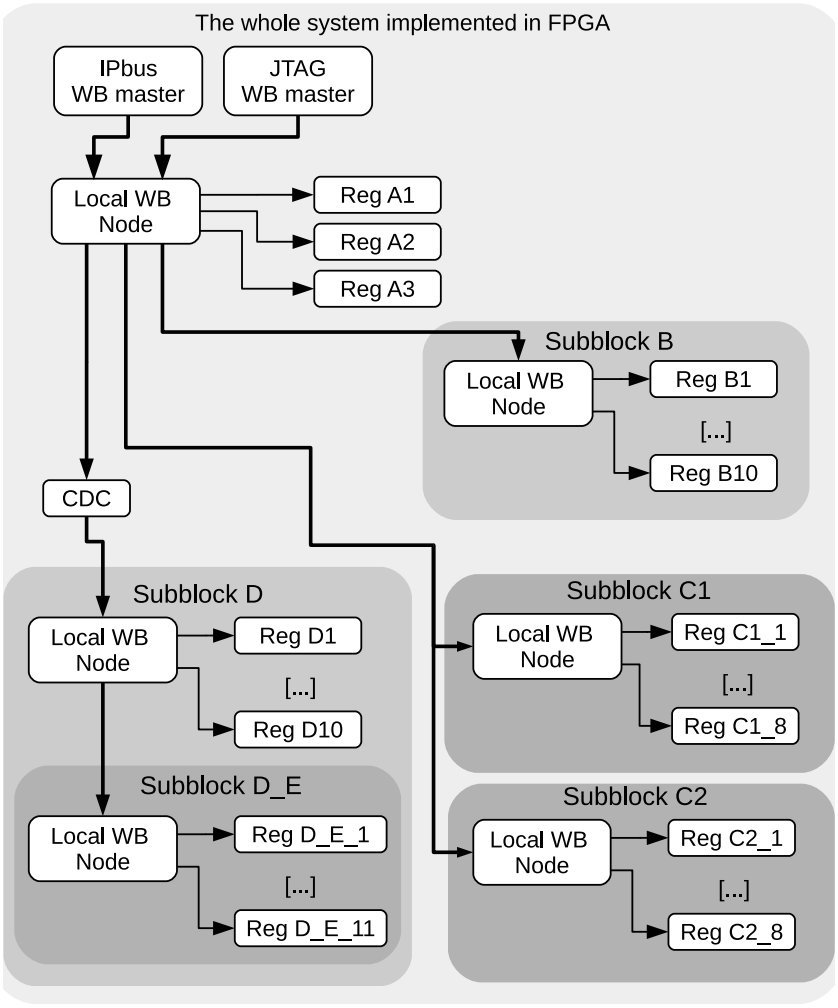

Figure 3: The block diagram of an example system built in the FPGA using the adr_gen_wb environment. The CDC block provides the clock domain crossing functionality. It allows subblocks D and D_E to run with another clock than the rest of the system.

The presented architecture maximally simplifies routing of signals between the bus interface and the user logic. The only control signals that are routed between the blocks are the two records implementing the WB bus. The signals associated with slave registers are connected to the corresponding ports generated in the local WB node.

3.3 Description of the system

The system is described in XML format. The top entity "sysdef" contains multiple definitions of "block" entities. One of them is selected as the top-level block using the "top" attribute of "sysdef" entity. The "masters" attribute of the "sysdef" entity defines the number of WB masters controlling the local bus (default value is 1). In each "block" multiple status (read only - "sreg") and control (read/write - "creg") registers may be defined. Two status registers are always automatically generated. The first of them, "ID" contains the CRC32 checksum of the name of the block. The second of them, "VER" contains the time of the system generation. The block may also contain multiple subblocks, defined by "subblock" child nodes. Their "type" attribute should be set to the name of the nested block. The "name" attribute defines the name of the particular instance. It is also possible to connect a nested node that is not generated by addr_gen_wb as "blackbox" child node. In that case, it is required to specify via the "addrbits" attribute the number of lower address bits used by that block for internal addressing. Both registers and nested blocks may be defined as groups. The number of group members

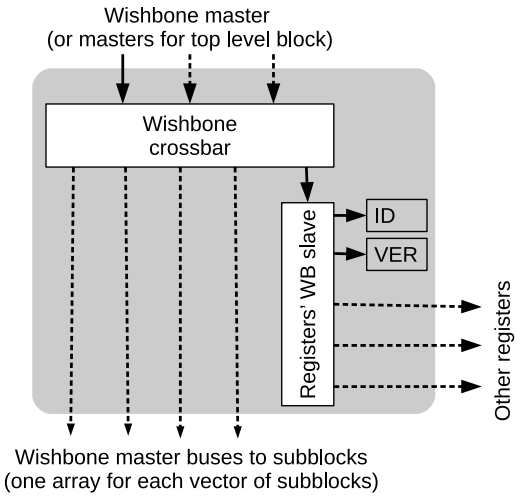

Figure 4: The generated WB interface to be included in the user's block.

```
<sysdef top="MAIN">

<block name="SYS1">
  <creg name="CTRL" desc="Control register" stb="1">
    <field name="START" width="1"/>
    <field name="STOP" width="1"/>
  </creg>
  <sreg name="STATUS" desc="Status register" ack="1" />
  <creg name="ENABLEs" desc="Link enable registers" reps="10" default="0x0"/>
</block>

<block name="MAIN">
  <subblock name="LINKS" type="SYS1" reps="5"/>
  <blackbox name="EXTERN" type="EXTTEST" addrbits="10" reps="3" />
  <sreg name="INS" desc="Input registers" reps="2" ack="1" />
  <creg name="CTRL" desc="Control register in the main block" default="0x11" stb="1">
    <field name="CLK_ENABLE" width="1"/>
    <field name="CLK_FREQ" width="4"/>
    <field name="PLL_RESET" width="1"/>
  </creg>
</block>

</sysdef>
```

Figure 5: Example of the description of the system for addr_gen_wb environment.

is specified with "reps" attribute. In registers, it is possible to define the bitfields. In that case, the addr_gen_wb generates the appropriate record type and functions for conversion between the std_logic_vector and that type. For status registers, it is possible to add the "ack" signal that is asserted for one clock pulse when the value is read. For control registers, it is possible to generate the "stb" signal, that is asserted for one clock pulse whenever the new value is written.

The example of the system definition is shown in Figure 5 and the VHDL package generated for the "MAIN" block is shown in Figure 6.

The addr_gen_wb automatically generates the VHDL sources of the local WB nodes (see Figure 7), that should be instantiated into the user's block, as shown in Figure 3.

3.4 Algorithm for allocation of addresses

To enable optimal implementation of address decoders the address space for each block requiring the K addresses, where $0 < K \leq 2^N$ is aligned to the 2^N boundary so that N bits are used for internal addressing in the block. To ensure efficient utilization of the address space, the required size of the address space for each block is calculated, traversing the system description from the most nested blocks to the top. After that, the blocks are ordered in the order of decreasing size of their address space, and their base addresses are set with the proper alignment.

```
library ieee;
use ieee.std_logic_1164.all;
use ieee.numeric_std.all;
library work;
use work.wishbone_pkg.all;

package MAIN_wb_pkg is

subtype t_INS is std_logic_vector(31 downto 0);
type t_INS_array is array(0 to 1) of t_INS;

type t_CTRL is record
  CLK_ENABLE:std_logic_vector(0 downto 0);
  CLK_FREQ:std_logic_vector(3 downto 0);
  PLL_RESET:std_logic_vector(0 downto 0);
end record;

function stlv2t_CTRL(x : std_logic_vector) return t_CTRL;
function t_CTRL2stlv(x : t_CTRL) return std_logic_vector;
end MAIN_wb_pkg;
```

```
package body MAIN_wb_pkg is
function stlv2t_CTRL(x : std_logic_vector) return t_CTRL is
variable res : t_CTRL;
begin
  res.CLK_ENABLE := std_logic_vector(x(0 downto 0));
  res.CLK_FREQ := std_logic_vector(x(4 downto 1));
  res.PLL_RESET := std_logic_vector(x(5 downto 5));
  return res;
end stlv2t_CTRL;

function t_CTRL2stlv(x : t_CTRL) return std_logic_vector is
variable res : std_logic_vector(31 downto 0);
begin
  res := (others => '0');
  res(0 downto 0) := std_logic_vector(x.CLK_ENABLE);
  res(4 downto 1) := std_logic_vector(x.CLK_FREQ);
  res(5 downto 5) := std_logic_vector(x.PLL_RESET);
  return res;
end t_CTRL2stlv;
end MAIN_wb_pkg;
```

Figure 6: The VHDL package generated by addr_gen_wb for the "MAIN" block from Figure 5. The dedicated t_CTRL record type is created for the CTRL control register with bitfields. The array type t_INS_array is created for the group of registers "INS".

```
library ieee;
use ieee.std_logic_1164.all;
use ieee.numeric_std.all;
library work;
use work.wishbone_pkg.all;
use work.MAIN_wb_pkg.all;

entity MAIN_wb is
  port (
    slave_i : in t_wishbone_slave_in;
    slave_o : out t_wishbone_slave_out;
    EXTERN_wb_m_o : out t_wishbone_master_out_array(0 to 2);
    EXTERN_wb_m_i : in t_wishbone_master_in_array(0 to 2);
    LINKS_wb_m_o : out t_wishbone_master_out_array(0 to 4);
    LINKS_wb_m_i : in t_wishbone_master_in_array(0 to 4);

    INS_i : in  t_INS_array;
    INS_i_ack : out std_logic;
    CTRL_o : out  t_CTRL;
    CTRL_o_stb : out std_logic;

    rst_n_i : in std_logic;
    clk_sys_i : in std_logic
    );

end MAIN_wb;
-- [...]
-- (Implementation of the entity is omitted)
```

Figure 7: The declaration of the local WB node generated by addr_gen_wb for the "MAIN" block from Figure 5

.

3.5 Generation of the address table for software

Currently, addr_gen_wb generates the IPbus compatible XML address tables that may be later on used directly by the C++ or Python programmes. The addr_gen_wb also generates the address tables in the form of Forth words, that may be used by the J1B Forth CPU[23] for automatic initialization after power-up and interactive diagnostics at the runtime. The information about the tree of blocks and registers and their addresses is stored in the addr_gen_wb internal data structures. Therefore, it is easy to use that information to generate the address map in any required format.

3.6 Results and conclusions

The described addr_gen_wb environment ensures automated allocation of the addresses for registers in the complex, hierarchical data processing systems implemented in the FPGA and using the Wishbone local control bus. It also supports the automated generation of the VHDL code implementing the local Wishbone node interfaces, providing convenient access to the signals associated with all local registers in each node, and routing of lower level WB busses to the nested blocks. The addr_gen_wb supports groups (vectors) of registers and identical blocks. That's a crucial functionality for HDL-oriented development of complex parameterized designs. For registers split into multiple bitfields, dedicated record types, together with access functions are generated.

The blocks comprising the system are well isolated regarding their interconnection with the control bus. That facilitates development and maintaining of systems assembled from blocks developed different teams independently. That's an essential feature in electronics created e.g., for High Energy Physics experiments.

```
<node id="MAIN">
  <node id="EXTERN[0]" address="0x00000000" module="file://EXTERN_address.xml"/>
  <node id="EXTERN[1]" address="0x00000400" module="file://EXTERN_address.xml"/>
  <node id="EXTERN[2]" address="0x00000800" module="file://EXTERN_address.xml"/>
  <node id="LINKS[0]" address="0x00001000" module="file://SYS1_address.xml"/>
  <node id="LINKS[1]" address="0x00001010" module="file://SYS1_address.xml"/>
  <node id="LINKS[2]" address="0x00001020" module="file://SYS1_address.xml"/>
  <node id="LINKS[3]" address="0x00001030" module="file://SYS1_address.xml"/>
  <node id="LINKS[4]" address="0x00001040" module="file://SYS1_address.xml"/>
  <node id="ID" address="0x00001080" permission="r"/>
  <node id="VER" address="0x00001081" permission="r"/>
  <node id="INS[0]" address="0x00001082" permission="r"/>
  <node id="INS[1]" address="0x00001083" permission="r"/>
  <node id="CTRL" address="0x00001084" permission="rw">
    <node id="CLK_ENABLE" mask="0x00000001"/>
    <node id="CLK_FREQ" mask="0x0000001e"/>
    <node id="PLL_RESET" mask="0x00000020"/>
  </node>
</node>
```

Figure 8: The address table in IPbus-compatible XML format generated by addr_gen_wb for the "MAIN" block from Figure 5.

```
: %/ $0 ;
: %/#EXTERN %/ $0 + swap $400 * + ;
: %/#LINKS %/ $1000 + swap $10 * + ;
: %/#LINKS_ID %/#LINKS $0 + ;
: %/#LINKS_VER %/#LINKS $1 + ;
: %/#LINKS_CTRL %/#LINKS $2 + ;
: %/#LINKS_CTRL.START %/#LINKS_CTRL $1 $0 ;
: %/#LINKS_CTRL.STOP %/#LINKS_CTRL $2 $1 ;
: %/#LINKS_STATUS %/#LINKS $3 + ;
: %/#LINKS#ENABLEs %/#LINKS + $4 + ;
: %/_ID %/ $1080 + ;
: %/_VER %/ $1081 + ;
: %/#INS %/ + $1082 + ;
: %/_CTRL %/ $1084 + ;
: %/_CTRL.CLK_ENABLE %/_CTRL $1 $0 ;
: %/_CTRL.CLK_FREQ %/_CTRL $1e $1 ;
: %/_CTRL.PLL_RESET %/_CTRL $20 $5 ;
```

Figure 9: The address table in J1B-compatible Forth format generated by addr_gen_wb for the "MAIN" block from Figure 5.

The addr_gen_wb has been successfully used in the development of FPGA firmware for the GBTX[24] emulator for CBM[25,26] experiment. It is also planned as a tool to integrate various blocks in the future CRI[27] firmware for the CBM experiment.

Sources of the addr_gen_wb system are available in the Github repository 28.

ACKNOWLEDGMENTS

Work supported by statutory funds of Institute of Electronic Systems.

REFERENCES

[1] Pozniak, K. T., Bartoszek, M., and Pietrusinski, M., "Internal interface for RPC muon trigger electronics at CMS experiment," in [*Proc. SPIE*], Romaniuk, R. S., ed., **5484**, 269–282 (July 2004).

[2] Poźniak, K. T., "Internal interface i/o communication with fpga circuits and hardware description standard for applications in hep and fel electronics ver. 1.0," (2005). Available from the website https://flash.desy.de/reports_publications/tesla_reports/tesla_reports_2005/ [Online; accessed 29-April-2019].

[3] Drabik, P., Pozniak, K. T., Bunkowski, K., Zawistowski, K., Byszuk, A., Bluj, M., Doroba, K., Górski, M., Kalinowski, A., Kierzkowski, K., Konecki, M., Królikowski, J., Oklinski, W., Olszewski, M., Skala, A., and Zabołotny, W. M., "Object oriented hardware-software test bench for OMTF diagnosis," in [*Proc. SPIE*], Romaniuk, R. S., ed., **9662**, 96622P (Sept. 2015).

[4] Drabik, P. and Pozniak, K. T., "Maintaining complex and distributed measurement systems with component internal interface framework," in [*Proc. SPIE*], Romaniuk, R. S. and Kulpa, K. S., eds., **7502**, 75022C (June 2009).

[5] Zagoździńska, A., Poźniak, K. T., and Drabik, P. K., "Selected issues of the universal communication environment implementation for CII standard," in [*Proc. SPIE*], Romaniuk, R. S., ed., **8008**, 80080N (June 2011).

[6] "Tesla technology collaboration." https://tesla-new.desy.de/ [Online; accessed 29-April-2019].

[7] "Free-electron laser flash." https://flash.desy.de/ [Online; accessed 29-April-2019].

[8] "Vivado design suite - hlx editions." https://www.xilinx.com/products/design-tools/vivado.html [Online; accessed 29-April-2019].
[9] "Intel quartus prime pro edition user guide, platform designer." https://www.intel.com/content/dam/www/programmable/us/en/pdfs/literature/ug/ug-qpp-platform-designer.pdf [Online; accessed 29-April-2019].
[10] "Intel quartus prime software suite, overview." https://www.intel.com/content/www/us/en/software/programmable/quartus-prime/overview.html [Online; accessed 29-April-2019].
[11] "IPbus." https://ipbus.web.cern.ch/ipbus/ [Online; accessed 29-April-2019].
[12] "Automatically generating IPbus address decoder firmware from uHAL address table." https://ipbus.web.cern.ch/ipbus/doc/user/html/firmware/addressDecoders.html [Online; accessed 29-April-2019].
[13] "Adr_gen - automatic address generator." https://github.com/wzab/wzab-hdl-library/tree/master/addr_gen [Online; accessed 29-April-2019].
[14] "Wishbone slave generator." https://www.ohwr.org/project/wishbone-gen [Online; accessed 29-April-2019].
[15] "Python." https://www.python.org [Online; accessed 29-April-2019].
[16] "The programming language Lua." https://www.lua.org/ [Online; accessed 29-April-2019].
[17] "SoC interconnection: WISHBONE." https://opencores.org/howto/wishbone [Online; accessed 29-April-2019].
[18] "Avalon/wishbone :: Overview." https://opencores.org/projects/avalon-wishbone-bridge [Online; accessed 29-April-2019].
[19] "Simple axi4-lite bridges for ipbus and wishbone." https://opencores.org/projects/ax4lbr [Online; accessed 29-April-2019].
[20] "Wb2axip: A pipelined wishbone b4 to axi4 bridge." https://github.com/ZipCPU/wb2axip [Online; accessed 29-April-2019].
[21] "Wishbone to axi bridge (vhdl)." https://github.com/qermit/WishboneAXI [Online; accessed 29-April-2019].
[22] "Platform-independent core collection, wishbone crossbar." https://ohwr.org/project/general-cores/blob/master/modules/wishbone/wb_crossbar [Online; accessed 29-April-2019].
[23] "Forth based system for afck board initialization and diagnostics." https://github.com/wzab/AFCK_J1B_FORTH [Online; accessed 29-April-2019].
[24] "GBTX manual." https://espace.cern.ch/GBT-Project/GBTX/Manuals/gbtxManual.pdf [Online; accessed 29-April-2019].
[25] "CBM - The Compressed Baryonic Matter experiment." http://www.fair-center.eu/for-users/experiments/cbm.html [Online; accessed 26-October-2015].
[26] Ablyazimov, T., Abuhoza, A., Adak, R. P., and etal, "Challenges in QCD matter physics –the scientific programme of the Compressed Baryonic Matter experiment at FAIR," *The European Physical Journal A* **53**(3), 60 (2017).
[27] Zabołotny, W. M., Byszuk, A. P., Gumiński, M., Emschermann, D., Kasprowicz, G. H., Hutter, D., Poźniak, K. T., and Romaniuk, R. S., "CRI board for CBM experiment: preliminary studies," in [*Proc. SPIE*], Romaniuk, R. S. and Linczuk, M., eds., **10808**, 108083X, SPIE, Wilga, Poland (Oct. 2018).
[28] Zabołotny, W. M., "adr_gen_wb.py - register access for hierarchical wishbone connected systems," (2017). https://github.com/wzab/addr_gen_wb [Online; accessed 29-April-2019].

Invited Paper

Geometry and Dynamics in Heavy-Ion Collisions Seen by the Femtoscopy Method

Hanna Paulina Zbroszczyk

Warsaw University of Technology, Faculty of Physics,
Koszykowa 75, 00-662 Warsaw, Poland

ABSTRACT

Geometry and dynamics of the source produced as a results of heavy-ion collisions at high energies can be studies via femtoscopy method. Correlations of two particles at small relative momentum are sensitive to the effects of Quantum Statistics and the Final State Interactions. They allow one to study the space-time properties of the source which are of the order of 10^{15} m and 10^{-23} s, respectively. Beam Energy Scan (BES) program conducted at the Relativistic Heavy Ion Collider (RHIC) covers an important part of the QCD Phase Diagram with beams of Au ions accelerated to relativistic velocities. Already completed first phase of the BES program uses heavy-ions collided in the energy range measured in the reference frame of center of mass from 7.7 to 200 GeV. This is a baryon-rich region that can be studied via femtoscopy methods with baryons. On one hand meson-meson correlations are the most commonly studied and baryon-baryon systems together with two-meson and meson-baryon correlations provide a complete information about source parameters. On the other hand the measurements of non-identical particle combinations complement our knowledge about space-time asymmetries during emission process. Physics of heavy-ion collisions is successfully deduced basing on studies of the properties of the particle-emitting source and how they change with different collision energies. Such studies include various centralities of the collision. In this paper, the STAR preliminary results including femtoscopic systems of various particle combinations such as protons, pions and kaons produced as a results of Au+Au collisions at BES energies are discussed

Keywords: Heavy-ion collision, femtoscopy, correlations

1. INTRODUCTION

Solenoidal Tracker At RHIC (STAR) is an experiment realized at Relativistic Heavy Ion Collider (RHIC) at Brookhaven National Laboratory (BNL), Upton. The main goal of the STAR experiment is to study the properties of matter created under extreme conditions (such as pressure, density) and thus to learn about interactions between hadrons. For almost 20 years, STAR has been collecting data from various collisions of different ions at different energies: 7.7, 11.5, 19.6, 27, 39, 62.4, 130, and 200 GeV. The highest collision energy of Au nuclei is $\sqrt{s_{NN}} = 200$ GeV and it enables a measurement of hot and dense matter after QGP formation. The Beam Energy Scan (BES) program,[1,2] which first part includes colliding energies below $\sqrt{s_{NN}} = 62.4$ GeV, is mainly focused on exploration of the QCD phase transition between Quark Gluon Plasma (QGP) and a hadron gas and also to search for the Critical Point (CP) between first order phase-transition and cross-over transition described by Quantum Chromodynamics (QCD).

2. DETAILS OF ANALYSIS

In order to define a femtoscopic correlation function,[3,4] in the case of identical particle combinations Lonitudinally Co-Moving System (LCMS) is used which is defines as $p_{L,1} + p_{L,2} = 0$. $p_{L,1}$ and $p_{L,2}$ are longitudinal components of momentum for single particles. Using LCMS system the correlation function is defined using $Q_{\text{inv}} = \sqrt{(p_1 - p_2)^2 - (E_1 - E_2)^2}$ variable. In the case of nonidentical particle combinations Pair Rest Frame (PRF) reference is used which defined $k^* = p_1 = -p_2$ variable. PRF reference can be also used for identical

Further author information:
H.P.Z.: E-mail: hanna.zbroszczyk@pw.edu.pl, Telephone: +48 22 234 58 51

Photonics Applications in Astronomy, Communications, Industry, and High-Energy Physics Experiments 2019,
edited by Ryszard S. Romaniuk, Maciej Linczuk, Proc. of SPIE Vol. 11176, 1117643
© 2019 SPIE · CCC code: 0277-786X/19/$21 · doi: 10.1117/12.2536695

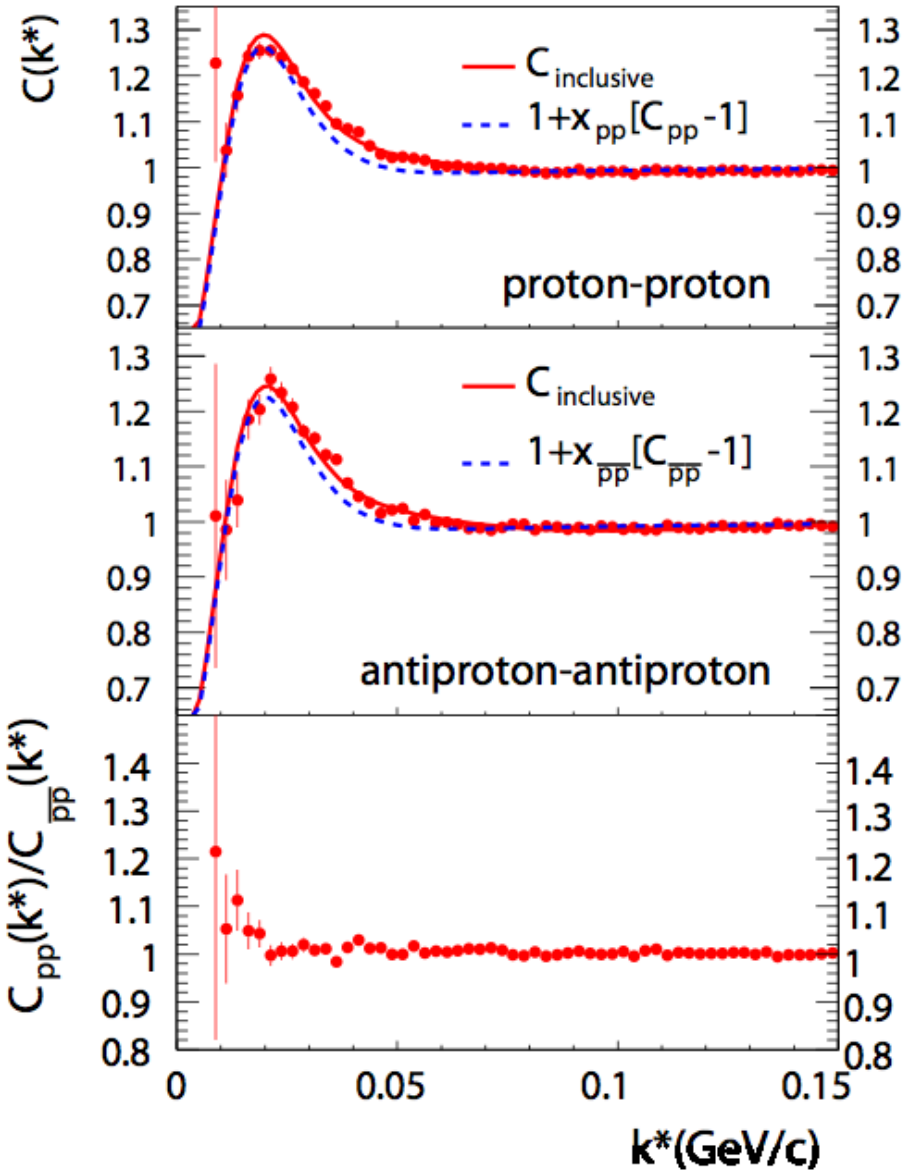

Figure 1. Proton-proton (top), antiproton-antiproton (middle) and the ratio of these correlation functions (bottom) for $\sqrt{s_{NN}} = 200$ GeV[5]

pairs of particles and then $Q_{\rm inv} = 2k^*$.

The difenition of the correlation functions is as follows: $C(k^*) = \frac{A(k^*)}{B(k^*)}$ or $C(Q_{\rm inv}) = \frac{A(Q_{\rm inv})}{B(Q_{\rm inv})}$. Correlated pairs of particles (from the same event enter) enter the numerator $A(k^*)$ or $A(Q_{\rm inv})$ and uncorrelated pairs of particles (from different events) enter the denominator $B(k^*)$ or $B(Q_{\rm inv})$ of the correlation function. All particles are measured and identified with two detectors: the Time Projection Chamber (TPC) and the Time of Flight (TOF). The centrality selection is determined basing on the uncorrected primary charged particle multiplicity measured in the pseudorapidity region ($|Y| = \frac{1}{2} ln \frac{E+p_z}{E-p_z} < 0.5$) as given by the TPC detector. The centrality classes are defined by the fraction of this multiplicity distribution. The centrality class defined as $0 - 10\%$ corresponds to the most central collisions calculated in amount of up to 10% of the total hadronic cross section of the collision,

while the $70-80\%$ bin is related to the most peripheral collisions. All particles are identified using the energy loss in the detector (dE/dx). Minimum Bias Au+Au collisions in amount of almost 200 millions events obtained as a collisions at the energy $\sqrt{s_{NN}} = 200$ GeV (within the centrality up to 80%) events gathered in year 2010 are divided into three centrality classes: central (0-10%), midcentral (10-30%), and peripheral (30-80%). In the case of BES data the same definitions of centrality classes were used.
Pions are chosen in the transverse momentum range: $0.2 < p_T < 1.2$ GeV/c and kaons within $0.2 < p_T < 1.2$ GeV/c. Protons and antiprotons are chosen in the transverse momentum range: $0.4 < p_T < 2.5$ GeV/c. All particles are taken from the rapidity interval $|y| < 0.5$. Each track is extrapolated to the primary vertex. If the shortest distance between track and the vertex exceeds 1 cm, the track is excluded from analysis chain. This removes a significant fraction of non-primary track candidates. Information derived from TOF detector allows one to estimate the mass of particle, we require the mass square of pions to be between 0.01 and 0.03 GeV/c^2, of kaons within 0.21 and 0.28 GeV/c^2 and of protons to be between 0.76 and 1.03 GeV/c^2. The particle purity is not taken into account as it is estimated as almost 100%. The effect of tracks-splitting and -merging are also taken into account.

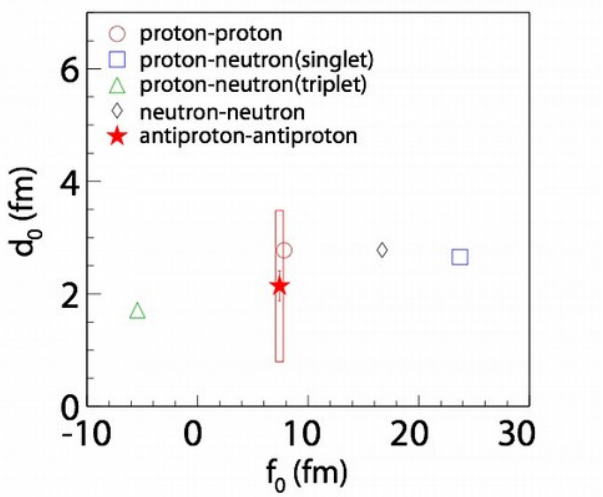

Figure 2. Parameters of strong interactions for different hadron pairs[5]

3. GEOMETRY OF COLLISION

As a result of heavy-ion collision there is created a hot and dense system which produces different types of particles. Using femtoscopic methods it is possible to learn about both: geometrical and dynamical properties of the source. Geometrical parameters are related to sizes and dynamical ones to space-time emission sequence of particles of different species. Femtoscopy enables to study space characteristics of source emitting pairs of particles. Thus, it is impossible to explore information related to the whole source but rather to its part emitting considered pairs of particles. It explains why source sizes extracted from various studies are different depending on considered system. So the geometry of heavy-ion collision can be studied via femtoscopic parameters describing source sizes of emission areas.

3.1 RESULTS FOR $\mathrm{Au}+\mathrm{Au}$ COLLISIONS AT $\sqrt{s_{NN}} = 200$ GeV

Figure 1 presents the measured correlation functions of proton-proton, antiproton-antiproton, and the ratio of proton-proton and antiproton-antiproton for collision energy $\sqrt{s_{NN}} = 200$ GeV. Correlation functions for baryon-baryon and antibaryon-antibaryon pairs are assumed to be consistent with each other within uncertainties.[5] The scattering length, f_0 is an parameter that describes low-energy scattering and d_0 is defines as the effective range of strong interaction between two particles. From these studies parameters f_0 and d_0 are estimated for antiproton-antiproton pairs and they are found to be consistent with those for proton-proton pairs (Fig. 2).

Source sizes in the case of two protons or two antiprotons were found as $R_{pp} = 2.75 \pm 0.01(stat) \pm 0.04(syst.)fm$ and $R_{\bar{p}\bar{p}} = 2.80 \pm 0.02(stat) \pm 0.03(syst.)fm$.

3.2 RESULTS FOR Au + Au COLLISIONS FOR BES PROGRAM

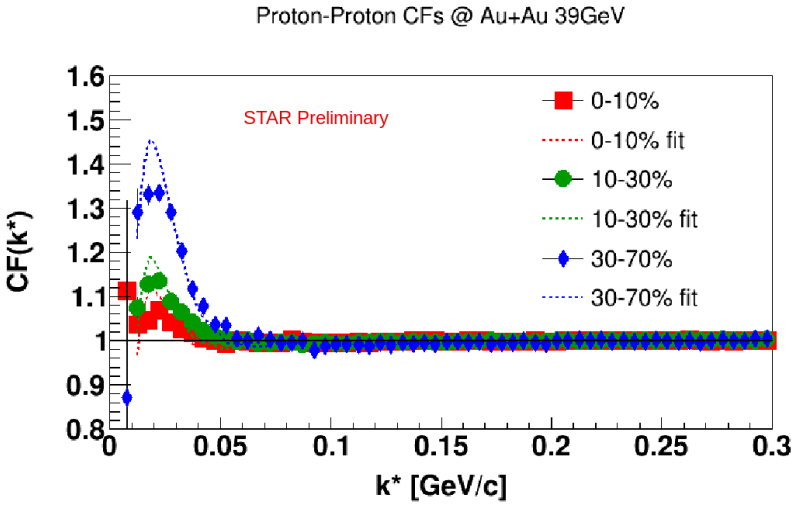

Figure 3. Proton-proton correlation functions for different centrality classes for $\sqrt{s_{NN}} = 39$ GeV,[67]

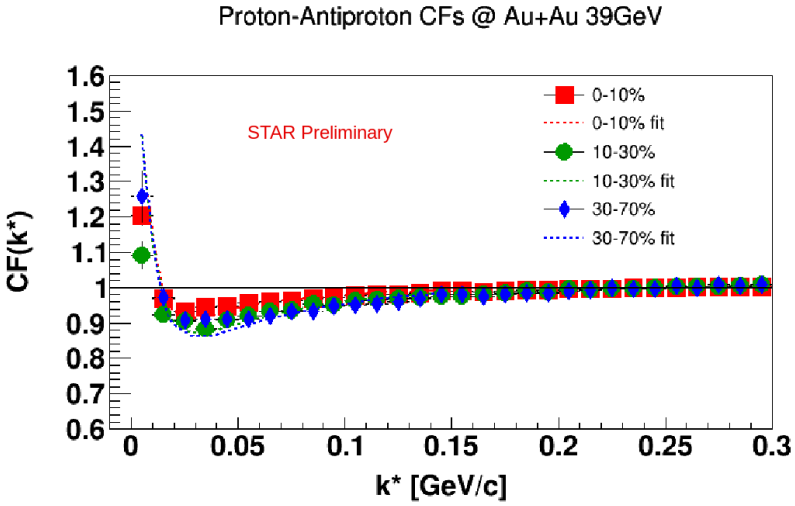

Figure 4. Proton-antiproton correlation functions for different centrality classes for $\sqrt{s_{NN}} = 39$ GeV,[67]

Figure 3 shows results of proton-proton correlation functions for $\sqrt{s_{NN}} = 39$ GeV for three different centralities. Figure 4 presents results for proton-antiproton correlation functions for the same centrality classes. Centrality dependence is clearly seen. Table 1 discusses the centrality dependence of protons and antiprotons source sizes measured for identical and non-identical pairs. These results for identical pairs are consistent with each other within uncertainties, however discrepancies between identical and non-identical baryon pairs occur due to the measurements of residual correlations coming from weakly-decayed particles which were not removed from measured correlation functions. Table 2 presents results of proton-proton, antiproton-antiproton and proton-proton systems for different collision energies where residual correlation correction should be done.

Presented results indicate that source size strongly depends on collision centrality (in the case of more central collisions bigger source is produced indicated by a weaker correlation signal while in the case of more peripheral

Table 1. Source sizes R_{inv} for various baryon (antibaryon) pairs with statistical and systematic uncertainties (due to purity correction only).

Centrality	$R_{inv}\, p-p\ [fm]$	$R_{inv}\, \bar{p}-\bar{p}\ [fm]$	$R_{inv}\, p-\bar{p}\ [fm]$
$0-10\%$	$4.00 \pm 0.15 \pm 0.02$	$3.82 \pm 0.20 \pm 0.03$	$3.39 \pm 0.12 \pm 0.14$
$10-30\%$	$3.61 \pm 0.13 \pm 0.17$	$3.68 \pm 0.15 \pm 0.11$	$2.69 \pm 0.10 \pm 0.12$
$30-70\%$	$2.72 \pm 0.07 \pm 0.07$	$2.95 \pm 0.11 \pm 0.08$	$2.56 \pm 0.09 \pm 0.12$

Table 2. Source sizes R_{inv} for various baryon pairs with error bars: statistical and systematic ones due to purity correction.

$\sqrt{s_{NN}}\,[GeV]$	$R_{inv}\, p-p\ [fm]$	$R_{inv}\, p-\bar{p}\ [fm]$
7.7	$3.59 \pm 0.16 \pm 0.19$	–
11.5	$3.66 \pm 0.08 \pm 0.05$	$3.30 \pm 0.42 \pm 0.28$
19.6	$3.82 \pm 0.15 \pm 0.06$	$3.32 \pm 0.25 \pm 0.13$
27	$3.80 \pm 0.12 \pm 0.08$	$3.49 \pm 0.25 \pm 0.16$
39	$4.00 \pm 0.15 \pm 0.02$	$3.39 \pm 0.12 \pm 0.14$

collisions smaller source and stronger correlation is measured). Radii of source depends also on energy collision: in the case of collision for higher collision energy bigger source and weaker correlation is registered.

4. DYNAMICS OF COLLISION

Dynamics of the collision can be studies using femtoscopic methods using only nonidentical particles combinations. It is possible to study emission sequence in the case of distinguishable particles. Collision dynamics can be related to space and time aspects. Femtoscopy method is sensitive to the emission asymmetries related to the spatial shifts (particles of different types statistically are emitted from different areas of the emission source) and to the time intervals between emissions of two different particles. However it is impossible to distinguish whether space and / or time asymmetry is deduced. In the case of such studies measured correlation function is determined using Spherical Harmonics decomponents. Thus, it is possible to study two components: $C00(k^*)$ which is consistent with one-dimensional correlation function $C(k^*)$ and $C11(k^*)$ which is sensitive to the possible asymmetries in the emission process. Figure 5 shows correlation functions ($C11$ components) for pion-kaon systems for various collision centralities for collision energy $\sqrt{s_{NN}} = 39$ GeV. Figure 6 shows correlation functions ($C11$ components) for pion-kaon systems for various collision energy for BES program. All $C11$ functions are different from zero value for small k^* intervals. It confirms emission asymmetries proving than lighter particles (pions) are statistically emitted closer to the systems center and / or earlier than heavier particles (kaons). The reason of such asymmetries is caused by flow phenomenon which affects differently particles with different masses.

5. SUMMARY

In this paper there are presented results describing geometrical and dynamical properties of source produced during heavy-ion collisions. In the context of geometrical properties results of the proton-proton, antiproton-antiproton, and proton-antiproton femtoscopy for Au + Au collisions at $\sqrt{s_{NN}}$ =200 GeV and at BES program at STAR are discussed. Except source sizes these studies delivere the scattering length (f_0) and effective range (d_0) parameters of strong interaction of protons and antiprotons. From studies performed in the frame of BES program, invariant source sizes are extracted for proton-proton, proton-antiproton and antiproton-antiproton pairs. The effect of residual correlations in the case of not taking them into account would be reflected in discrepancies between the source sizes estimated for identical and non-identical combinations of protons and antiprotons. Presented results underline significance of changing source sizes with different collision centrality of collision energy. In the context of geometrical properties results of pion-kaon correlations are discussed. They prove that emission differences of distinguishable particles can have their origin in both: spatial and time

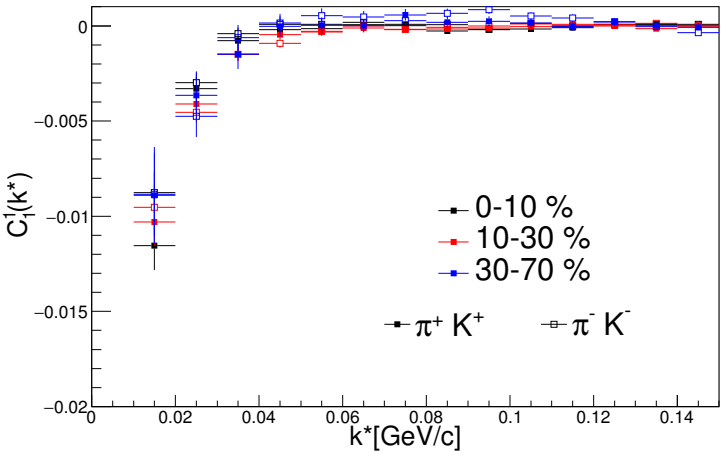

Figure 5. Pion-kaon correlation functions for different centrality classes for $\sqrt{s_{NN}} = 39$ GeV[7]

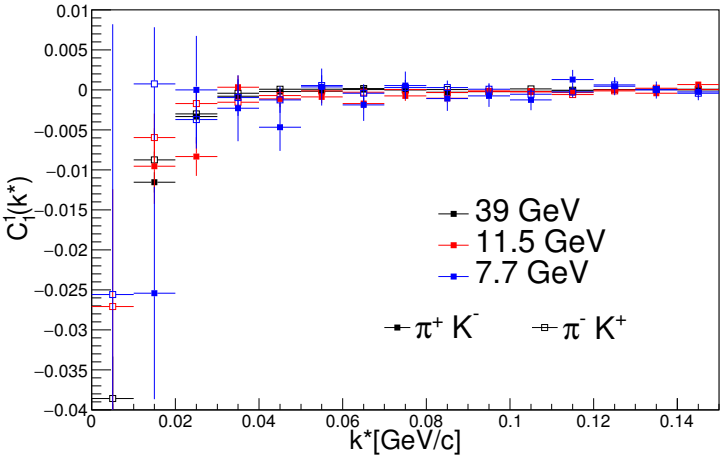

Figure 6. Pion-kaon correlation functions for different collision energies for BES program[7]

components. Both of them are the result of different emission properties for particles with different masses. Shown results confirm that lighter particles are in average emitted closer to the systems center and /or earlier than heavier ones.

ACKNOWLEDGMENTS

This work was supported by the Grant of National Science Centre, Poland, No: 2017/27/B/ST2/01947.

REFERENCES

[1] G. Odyniec *et al.*, J. Phys. **G37**, 094028 (2010)
[2] M.M.Aggarwal *et al.*, arXiv:1007.2613v1
[3] V.G. Grishin, G.I. Kopylov, M.I. Podgoretskii, Sov. J. Nucl. Phys. **13** (1971) 638
[4] R. Lednicky, V. L. Lyuboshitz, Sov. Journ. Nucl. Phys. **35** (1982) 770
[5] L. Adamczyk *et al.*, Nature **527** (2015) 345-348
[6] H. Zbroszczyk *et al.*, Proceedings of Workshop on Particle Correlations and Femtoscopy, to be published in Acta Phys. Polonica B (accepted)
[7] S. Siejka *et al.*, Nucl.Phys. **A982** (2019) 359-362

IPbus Bus Functional Model in Universal VHDL Verification Methodology

Michał Kruszewski

Institute of Electronic Systems, Warsaw University of Technology, ul. Nowowiejska 15/19, 00-665 Warszawa, Poland

ABSTRACT

Simulation-based functional verification is an important part of a Field-Programmable Gate Array (FPGA) design flow. It is desirable of test bench to be written quickly, with high abstraction and in understandable way. The paper describes IPbus Bus Functional Model (BFM) that has been implemented in the Universal VHDL Verification Methodology (UVVM) test bench infrastructure. It also presents a simple example how the module should be used.

Keywords: IPbus, UVVM, BFM, VHDL, FPGA

1. INTRODUCTION

The importance of electronic design verification has been growing for several years. It is roughly estimated that todays verification accounts for about 50-70% of development effort.[1,2] Growing design complexity entails demand for highly abstracted testing environments.

There are two leading approaches for Hardware Description Language (HDL) projects verification, simulation-based and formal. Formal verification is the process of proving or disproving the correctness of a design using mathematical methods, without the need to simulate a design. Formal methods are known to significantly reduce the verification time, however they require expensive tools (e. g. Questa - Siemens' Mentor Graphics or Incisive - Cadence) and well-educated verification engineers. As a result it is mostly affordable and implemented by big Application-Specific Integrated Circuit (ASIC) vendors. On the other side of the market, there are small and medium FPGA design companies and university projects that still build their verification strategy on the simulation-based approach.

Writing well thought test benches in a custom way is as hard as writing well thought design. However, understanding a test bench written is a custom way is harder than writing one by yourself. It is expected of any good test bench of any complexity to be:

- simple to write,
- simple to execute, debug and understand,
- simple to understand and modify by anyone,
- simple to understand reports and results.

In order to achieve these requirements some informal and formal standards have been established. The most popular and being the first standardized is the Universal Verification Methodology (UVM).[3] It is built on the Open Verification Methodology (OVM), which combined the Advanced Verification Methodology (AVM) with the Universal Reuse Methodology (URM) and concepts from the e Reuse Methodology (eRM). The UVM consists of a set of application programming interfaces (APIs) that defines a base class library (BCL) definition used to develop modular, scalable, and reusable components for functional verification environments. Both the APIs and BCL are based on the IEEE standard for SystemVerilog.[4] This is some kind of difficulty, especially in the Europe, where Very High Speed Integrated Circuits Hardware Description Language (VHDL) still dominates.[2] There are of course possibilities to co-simulate VHDL with SystemVerilog, however it requires from engineers to be fluent in both languages and limits the number of potential fast simulation engines only to the commercial ones. To overcome these drawbacks some open source initiatives such as Open Source VHDL Verification Methodology (OSVVM)[5] and UVVM[6] have been started.

Further author information: (Send correspondence to M. Kruszewski)
E-mail: mkruszew@mion.elka.pw.edu.pl, Telephone: +48 22 234 77 44

Photonics Applications in Astronomy, Communications, Industry, and High-Energy Physics Experiments 2019, edited by Ryszard S. Romaniuk, Maciej Linczuk, Proc. of SPIE Vol. 11176, 1117644
© 2019 SPIE · CCC code: 0277-786X/19/$21 · doi: 10.1117/12.2536696

1.1 UVVM

Universal VHDL Verification Methodology (UVVM) is a free and open source methodology and library for making very structured VHDL-based test benches. UVVM has actually copied a few of the principles from UVM and could thus be seen as a simplified VHDL version of UVM, only in a familiar language, being component oriented and simpler to use and understand.[7] It was launched by Norway company named Bitvis in 2016. UVVM has an extremely low user threshold, and at the same time has advanced options available when needed for more complex test benches.[8] It consists of the following elements:

- UVVM Utility Library,
- VHDL Verification Component (VVC) framework,
- BFMs for the most popular buses like AXI4-Lite, AXI-Stream, Avalon MM etc.,
- VVCs to be used with UVVM VVC framework that may be combined with BFMs.

UVVM has been tested with Modelsim, Riviera-PRO and GHDL,[9] and should thus also work with Questa and Active-HDL.[7] It should generally run perfectly well with any VHDL-2018 compatible simulator. European Space Agency (ESA) is now backing UVVM through a contract of more than 250k euro for an extension of UVVM, and may recommend their suppliers to use UVVM for FPGA verification (unless they already have a good internal solution).[10]

1.2 IPbus

The IPbus protocol is an IP-based protocol for controlling hardware devices.[11] It assumes the existence of a virtual bus with 32-bit word addressing and 32-bit data transfer. It has a strong emphasis on simplicity and reliability, as well as ease and compactness of implementation. In order to reduce hardware resource usage, the complexity has been pushed into the software client-layer. IPbus protocol version 2.0 offers its user 8 types of distinct transactions:[12]

1. read transaction,
2. write transaction,
3. non-incrementing read transaction - useful for reading from a FIFO,
4. non-incrementing write transaction - useful for writing to a FIFO,
5. read/modify/write bits transaction - useful for setting or clearing bits,
6. read/modify/write sum transaction - useful for subtracting or adding values to a register,
7. configuration space read transaction - operates on separate address space,
8. configuration space write transaction - operates on separate address space.

IPbus is a complete suite of software and firmware that consists of the following components.

- IPbus firmware - a module that implements the IPbus protocol within end-user hardware,
- ControlHub - a software application that mediates simultaneous hardware access from multiple uHAL clients, and implements the IPbus reliability mechanism over UDP,
- uHAL - the Hardware Access Library (HAL) providing an end-user C++/Python API for IPbus reads, writes and read/modify/write transactions.

IPbus protocol is often used in High Energy Physics (HEP) experiments, for instance Compressed Baryonic Matter (CBM) at GSI Helmholtz Centre for Heavy Ion Research.[13]

2. IMPLEMENTATION

The implemented IPbus BFM has the following features:

- To carry out a transaction user needs to call only one procedure ipbus_transact.
- It supports all IPbus transaction types except configuration space read and write transactions as they operate on separate address space.
- It supports all IPbus transaction info codes.
- It provides user with dedicated functions for defining each type of transaction, so that user does not have to know the IPbus packet format.
- It uses transactor entity from the ipbus_firmware[14] repository so it tests part of the ipbus firmware by the way.
- By using transactor entity from the ipbus_firmware[14] repository, in case of any transaction errors, bus errors or bus timeouts, a simulation exactly resembles a situation that would happen in the hardware.

Unfortunately it is not free of drawbacks that also should be mentioned:

- User has to explicitly define proper length of the IPbus transaction body. Proper means long enough. This is due to the VHDL standard[15] that does not allow constraining record elements based on value assignment during declaration. However transaction body is always 1 word longer (because of the transaction address) than the transaction data, so it should not be hard for a user to determine proper body length. In case of improper length (too short) runtime error occurs during simulation.
- It should not be used to measure the IPbus transaction latency. The implementation skips some operations that are normally performed by the IPbus firmware, so using it for estimation or evaluation of the IPbus transactions duration leads to underestimation.

The model has been implemented in the UVVM_Community_VIPs[16] repository. It consists of two files located in the vip_ipbus/src directory ipbus_transactor_wrapper.vhd and ipbus_bfm_pkg.vhd. File ipbus_transactor_wrapper.vhd defines a wrapper entity for the transactor entity from the ipbus library. The role of this wrapper is solely to reduce the amount of typing needed to instantiate the transactor from the ipbus library. This is achieved by two custom types (t_ipbus_transactor_inputs and t_ipbus_transactor_outputs) that encapsulates respectively IPbus specific inputs and outputs. The difference between ports of the transactor and its wrapper is shown in the Listing 1.

Listing 1: Comparison of the transactor and transactor_wrapper ports.

```
entity transactor is
  port(
    clk : in std_logic; -- IPbus clock
    rst : in std_logic; -- Sync reset
    ipb_out  : out ipb_wbus; -- IPbus bus signals
    ipb_in   : in ipb_rbus;
    ipb_req  : out std_logic; -- Bus arbitrator signals
    ipb_grant: in std_logic;
    trans_in : in ipbus_trans_in; -- Interface to packet buffers
    trans_out: out ipbus_trans_out;
    cfg_vector_in  : in std_logic_vector(127 downto 0);
    cfg_vector_out : out std_logic_vector(127 downto 0)
  );
end transactor;

entity ipbus_transactor_wrapper is
  port (
    clk : in std_logic; -- IPbus clock
```

```
    rst : in std_logic; -- Sync reset
    ipbus_transactor_inputs  : in t_ipbus_transactor_inputs;
    ipbus_transactor_outputs : out t_ipbus_transactor_outputs
  );
end ipbus_transactor_wrapper;
```

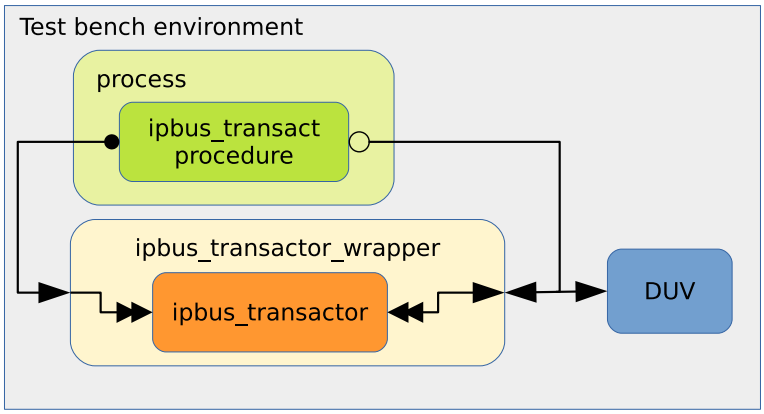

Figure 1: Simple test bench structure with single DUV.

The IPbus BFM can be used in test benches of different complexity. Figure 1 shows the simplest scenario with single Device Under Verification (DUV). Filled circle on the ipbus_transact procedure means that the procedure only drives the signals. Unfilled circle, on the other hand, means that the procedure only observes the signals. Arrows stand for signals connection to the entity ports. Double arrows on some ports indicate already mentioned port encapsulation.

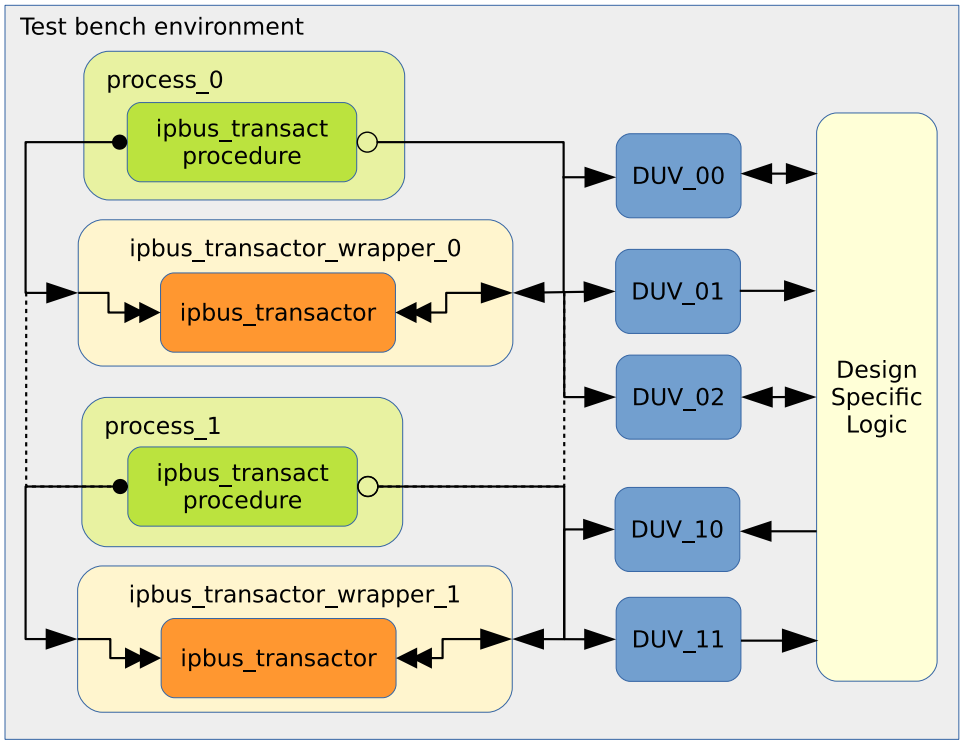

Figure 2: Possible advanced test bench structure.

Figure 2 presents more sophisticated test bench structure possible to implement with the IPbus BFM. What is important

to notice is the fact, that single process with ipbus_transact procedure can cooperate with different ipbus_transactor_wrappers. It can be dynamically changed as simulation time passes by. The only limitation is that single process can not cooperate with multiple ipbus_transactor_wrappers in parallel (in the same time). The dynamic change of process and ipbus_transactor_wrapper pairs is represented in the figure with fine dashed lines.

3. EXAMPLE USAGE

Three libraries need to be compiled in order to use implemented IPbus BFM: IPbus,[14] UVVM[6] and UVVM_Community_VIPs.[16] The installation is one-time process (not including updates), and it takes few minutes as compilation scripts are available in the repositories. * Simple template for a test bench with IPbus BFM is provided in the UVVM_Community_VIPs[16] repository in vip_ipbus/template directory (file simple_tb_template.vhd). It instantiates ipbus_transactor_wrapper entity and defines necessary signals. In case of testing single entity, user only needs to instantiate the entity of a DUV, define DUV specific signals, assign value to a request transaction using dedicated functions, call ipbus_transact procedure and check response transaction or other signals driven by the DUV. In vip_ipbus/tb directory there is a test bench (file ipbus_bfm_tb.vhd) that was used for debugging IPbus BFM. It was also based on the simple_tb_template.vhd template. Listing 2 shows what needs to be added in the test bench by the user to verify DUV behavior in case of particular transaction when DUV is already instantiated.

Listing 2: .

```
-- Signal can be declared in any declarative part that accepts signals declarations.
-- Use dedicated functions for defining transaction signals.
-- Assigning can be done in any place that accepts signal assignment.
signal rmw_bits_request_transaction : t_ipbus_transaction(bodyy(0 to 2))
       := ipbus_rmw_bits_transaction(X"00000000", X"00000004", X"F0000000");

-- Procedure can be called in any place that accepts procedure calls.
ipbus_transact(rmw_bits_request_transaction,
               response_transaction,
               ipbus_transactor_inputs,
               ipbus_transactor_outputs,
               clk);
-- Check response or any application specific signals.
check_value(ipb_control_regs(0), X"F0000004", FAILURE,
            "Checking read/modify/write bits transaction.");
```

Figure 3 shows console output for transaction from the Listing 2. There is an information about the simulation time when transaction has started, finished as well as IPbus packet header log for request and response transactions.

```
UVVM: ID_BFM                    1904.0 ns  IPbus BFM              ipbus_transact()
UVVM:                                                             Request Transaction:
UVVM:                                                               HEADER:
UVVM:                                                                 Protocol version: 2
UVVM:                                                                 Transaction ID:   0
UVVM:                                                                 Word count:       1
UVVM:                                                                 Type ID:          rmw_bits
UVVM:                                                                 Info code:        outbound_request
UVVM: ID_BFM                    2384.0 ns  IPbus BFM              ipbus_transact() completed
UVVM:                                                             Response Transaction:
UVVM:                                                               HEADER:
UVVM:                                                                 Protocol version: 2
UVVM:                                                                 Transaction ID:   0
UVVM:                                                                 Word count:       1
UVVM:                                                                 Type ID:          rmw_bits
UVVM:                                                                 Info code:        req_handled_successfully
UVVM: ID_POS_ACK                2384.0 ns  TB seq.                check_value() => OK, for slv x"F0000004"'. 'Checking read/modify/write bits transaction.'
```

Figure 3: Sample console output.

*Script for compiling UVVM library (compile-uvvm.sh) is available in the GHDL[9] repository. In case of default install path it is located in the /usr/local/lib/ghdl/vendors directory. Script for compiling IPbus library[14] is available as the pull request https://github.com/ipbus/ipbus-firmware/pull/100. Script for compiling UVVM_Community_VIPs[16] is not yet available, but compile-uvvm.sh script can be easily adjusted for this purpose.

4. CONCLUSIONS

Verification plays crucial role in the FPGA design. Well organised test bench infrastrcture increases efficiency as well as project quality. Thanks to the open source initiatives like UVVM, engineers can write test benches in uniform, understandable way and reuse modules already implemented by others. The described IPbus BFM is just a small part of a much larger whole, but it may help designers to save a lot of time or maybe even money.

REFERENCES

[1] Oliveira, M. F., Kuznik, C., Le, H. M., Große, D., Haedicke, F., Mueller, W., Drechsler, R., Ecker, W., and Esen, V., "The system verification methodology for advanced TLM verification," in [*Proceedings of the eighth IEEE/ACM/IFIP international conference on Hardware/software codesign and system synthesis - CODES+ISSS '12*], 313, ACM Press, Tampere, Finland (2012). http://dl.acm.org/citation.cfm?doid=2380445.2380497.

[2] Foster, H., "The 2018 Wilson Research Group ASIC and FPGA Functional Verification Study," tech. rep. https://www.mentor.com/products/fv/events/the-2018-wilson-research-group-asic-and-fpga-functional-verification-study.

[3] "IEEE Standard for Universal Verification Methodology Language Reference Manual," tech. rep., IEEE. http://ieeexplore.ieee.org/document/7932212/.

[4] "IEEE Std 1800™-2012 (Revision of IEEE Std 1800-2009) IEEE Standard for SystemVerilog—Unified Hardware Design, Specification, and Verification Language," 1315.

[5] "Open Source VHDL Verification Methodology." http://osvvm.org/.

[6] UVVM, "Open Source VHDL Verification Library and Methodology: for very efficient VHDL verification of FPGA and ASIC - resulting also in a significant quality improvement - UVVM/UVVM," (Apr. 2019). https://github.com/UVVM/UVVM.

[7] Tallaksen, E. and As, B., "Invited Paper: UVVM — The Fastest Growing FPGA Verification Methodology Worldwide!," 6 (Mar. 2019). https://osda.gitlab.io/19/tallaksen.pdf.

[8] "A free library for good testbench checking functionality | LinkedIn." https://www.linkedin.com/pulse/free-library-good-testbench-checking-functionality-espen-tallaksen/?trk=mp-reader-card.

[9] "VHDL 2008/93/87 simulator. Contribute to ghdl/ghdl development by creating an account on GitHub," (Apr. 2019). https://github.com/ghdl/ghdl.

[10] Tallaksen, E., "UVVM - Universal VHDL Verification Methodology. Setting a standard for VHDL testbenches," (Apr. 2018). https://indico.esa.int/event/232/contributions/2159/.

[11] Larrea, C. G., Harder, K., Newbold, D., Sankey, D., Rose, A., Thea, A., and Williams, T., "IPbus: a flexible Ethernet-based control system for xTCA hardware," *Journal of Instrumentation* **10**, C02019–C02019 (Feb. 2015). http://stacks.iop.org/1748-0221/10/i=02/a=C02019?key=crossref.ae8332d93ce3ed23f23295860b52bb3e.

[12] Frazier, R., Iles, G., Magrans de Abril, M., Newbold, D., Rose, A., Sankey, D., and Williams, T., "The IPbus protocol: version 2.0," (Dec. 2013). https://svnweb.cern.ch/trac/cactus/browser/trunk/doc/ipbusprotocolv20.pdf.

[13] Zabołotny, W. M., Byszuk, A. P., Gumiński, M., Emschermann, D., Kasprowicz, G. H., Hutter, D., Poźniak, K. T., and Romaniuk, R. S., "CRI board for CBM experiment: preliminary studies," in [*Photonics Applications in Astronomy, Communications, Industry, and High-Energy Physics Experiments 2018*], Romaniuk, R. S. and Linczuk, M., eds., 57, SPIE, Wilga, Poland (Oct. 2018). https://www.spiedigitallibrary.org/conference-proceedings-of-spie/10808/2501415/CRI-board-for-CBM-experiment-preliminary-studies/10.1117/12.2501415.full.

[14] "Firmware that implements a reliable high-performance control link for particle physics electronics, based on the IPbus protocol: ipbus/ipbus-firmware," (Apr. 2019). https://github.com/ipbus/ipbus-firmware.

[15] "IEEE Standard VHDL Language Reference Manual," *IEEE Std 1076-2008 (Revision of IEEE Std 1076-2002)* , c1–626 (Jan. 2009).

[16] UVVM, "Repository for the UVVM community to share VIPs. Contribute to UVVM/UVVM_community_vips development by creating an account on GitHub," (Apr. 2019). https://github.com/UVVM/UVVM_Community_VIPs.

Preliminary dynamic analysis of the forces on the COMPASS-U tokamak foundations

R. Ortwein[a], J. Blocki[a], J. Hromadka[b], N. Patel[b], D. Sestak[b], J. Havlicek[b], R. Panek[b]

[a]Institute of Nuclear Physics of the Polish Academy of Sciences, ul. Radzikowskiego 152 31-342 Cracow, Poland
[a]Institute of Plasma Physics of the Czech Academy of Sciences, Za Slovankou 1782/3, 182 00 Praha, Czech Republic

ABSTRACT

The COMPASS-U tokamak (B_t = 5 T, I_p = 2 MA, R = 0.894 m, a = 0.27 m) is currently under design at IPP CAS (Institute of Plasma Physics of the Czech Academy of Sciences). One of the design challenges is to design sufficiently strong foundations to support even the highest forces that are generated during plasma disruption events. The worst, found up to now, scenario has been considered in order to simulate the response of the main tokamak components and to calculate the force transmitted to the foundations. A 3D model has been built in the ANSYS Workbench software including the cryostat support, the vacuum vessel, the poloidal field coils and their supports. The forces have been calculated via global electromagnetic model. Integrated values of the forces and torques have been spread onto surfaces of the parts. The modal superposition method has been utilized for the integration, based on the first 100 vibration modes. Rayleigh damping model with the fraction of critical damping of 2% was used. The reaction forces transmitted to the foundations have been obtained providing input for the civil design work.

Keywords: Tokamak, COMPASS-U, plasma, disruption, ANSYS, electromagnetic forces, foundations

1. INTRODUCTION

The COMPASS Upgrade (COMPASS-U)[1] is currently in the design phase in the IPP CAS. The major and minor radiuses of the COMPASS-U torus are 0.89 m and 0.27 m (Fig. 1), compared to 0.56 m and 0.18 m for the previous COMPASS tokamak[2,3]. The mass of the new structure is approximately 250 tons and reinforcement of the existing foundations is necessary. The values of maximum forces transmitted to the foundations need to be evaluated. For this purpose only the worst case scenario of the electromagnetic loads was used - occurring during plasma disruption. As the design work is still ongoing, the worst possible disruption scenario has not been found yet as it requires running large numbers of parametric studies. In the present study the worst scenario found up to now was used to predict the dynamic response of the structure. In the final stage of the design, when the worst disruption scenario will be known the dynamic analysis will be repeated.

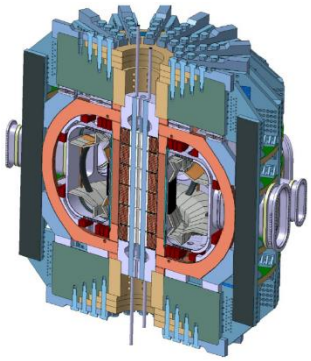

Figure 1. The general view of the COMPASS-U tokamak

Photonics Applications in Astronomy, Communications, Industry, and High-Energy Physics Experiments 2019, edited by Ryszard S. Romaniuk, Maciej Linczuk, Proc. of SPIE Vol. 11176, 1117645
© 2019 SPIE · CCC code: 0277-786X/19/$21 · doi: 10.1117/12.2536740

During disruption event the plasma touches or gets near the inner wall of the vacuum vessel (VV) causing significant currents and thus significant electromagnetic forces. The whole disruption event happens within milliseconds during which the forces are reaching several mega Newtons and more. Such fast changing loads require taking into account the inertial effects in order to correctly predict the reactions in the supports that are transmitted to the foundations. The, so called, dynamic amplification factor (DAF) is often used to describe the influence of the inertial effects w.r.t. the static response. DAF for 1D system is defined as the ratio of the dynamic deflection to the static one[4-5], which is equivalent to the ratio of the dynamic reaction to the static reaction – $k \cdot u_{dyn} / k \cdot u_{stat}$. The dynamic amplification factor is in the range between 1 and 2. The maximum value of 2 is reached for an undamped system loaded with a step force[6]. In reality a step force cannot be realized, as it would require infinite power and no damping.

Several approaches are possible for the dynamic analysis of tokamaks, for which the vacuum vessel is the most often analyzed part. Common approach is related to modeling of only a segment of the geometry and assuming periodic symmetry - to decrease the computational cost (simulation time). In the early stage of the ITER tokamak design a coarse model of $1/5^{th}$ and $1/10^{th}$ of the vacuum vessel's circumference was used[7]. Another approach consisted of using 1D elements (spring + damper + mass) to model the magnet system and the vacuum vessel and was applied for sensitivity studies in transient analysis for ITER[8]. In order to take into account the asymmetric loads that arise for example during disruption events full 360^{o} shell models of the VV were often used for ITER[9-12]. Another - mixed - approach was used in[13], where the vacuum vessel of ITER was modeled with solid elements and the ports with shell elements. In order to decrease the computational cost the substructuring (Guyan reduction) method[14] was adopted. In the paper[15] the component mode synthesis CMS[14] was used, and the vacuum vessel was modeled as $1/9^{th}$ (40^{0}) segment modeled in two ways with shells and with solid elements.

In this work solid modeling in 3D is adopted taking into account a simplified model of the full 360^{0} structure in order to account for not axisymmetric loads resulting from plasma disruption scenarios. The model includes not only the vacuum vessel but as well the bottom part of the cryostat, on which the VV is supported, and the main support for toroidal field (TF), poloidal field (PF) coils and the central solenoid (CS). Such approach allows studying the global dynamic scenario, in which forces from the central solenoid and poloidal field coils contribute to the dynamic reactions in the foundations. Such global dynamic modeling approach, including the main tokamak support in the geometry and involving the forces from the PF coils, the VV and the CS, to the best of the Authors knowledge, have not been done yet for any tokamak.

The paper is organized into 6 chapters. In the 2^{nd} one the FEM model of the COMPASS-U tokamak is described together with the modeling assumptions. The electromagnetic model used to find the Lorentz forces during plasma disruption and the forces for the worst possible scenario (found up to now as the design is still ongoing) are described in the 3^{rd} chapter. The results of the modal analysis are given in the 4^{th} chapter, and the results of the transient analysis in the last 5^{th}.

2. THE FEM MODEL OF THE COMPASS-U TOKAMAK

The geometry included in the FEM model consists of the vacuum vessel, its supporting legs, the main support (for TF and PF coils) and the bottom part of the cryostat (Fig. 2a, 2b). The geometry of the VV was modeled without any details - such as port extensions, as they play very minor role in the disruption scenario. The vacuum vessel was divided into four parts (Fig. 2c) denoted: TOP, BOT (bottom), HFS (high field side) and LFS (low field side) in order to account for the inhomogeneous distribution of the Lorentz forces within the VV during the disruption event. With LFS being the area with the smallest radius, HFS the inside area of the outer layer, TOP the inside areas of the top "lid" and BOT the inside area of the bottom "lid". The forces were applied via "remote force" feature of ANSYS Workbench.

The PF coils and the CS were not modeled explicitly, as the design is still ongoing and the connection details were not finalized yet. However the dynamic forces resulting from the central solenoid and PF coils were taken into account. In order to apply the forces from the central solenoid and the poloidal field coils the areas of the contact with the main support were imprinted into the geometry as shown in Fig. 3a, 3b and Fig. 4a. The forces from the central solenoid were applied to the main support via 16 areas from top and bottom (Fig. 4a). The meshed model is shown in Fig. 4b.

Two materials were used in the analysis, the Inconel 625 for the VV and the 304 stainless steel for all the other parts (Table 1). The maximum operation temperature was assumed for the vacuum vessel – namely 500^{0}C, and all the other parts were at the cryogenic temperature of -196^{0}C (77 K).

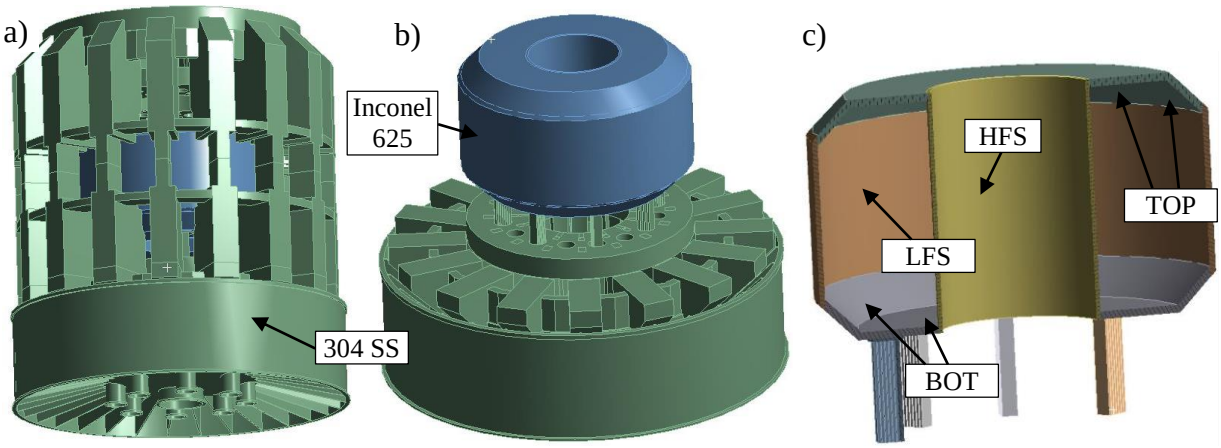

Figure 2. a) General view of the model of COMPASS-U tokamak; b) View on the vacuum vessel and its support; c) Divisions of the VV into 4 parts: TOP, BOT, HFS, LFS

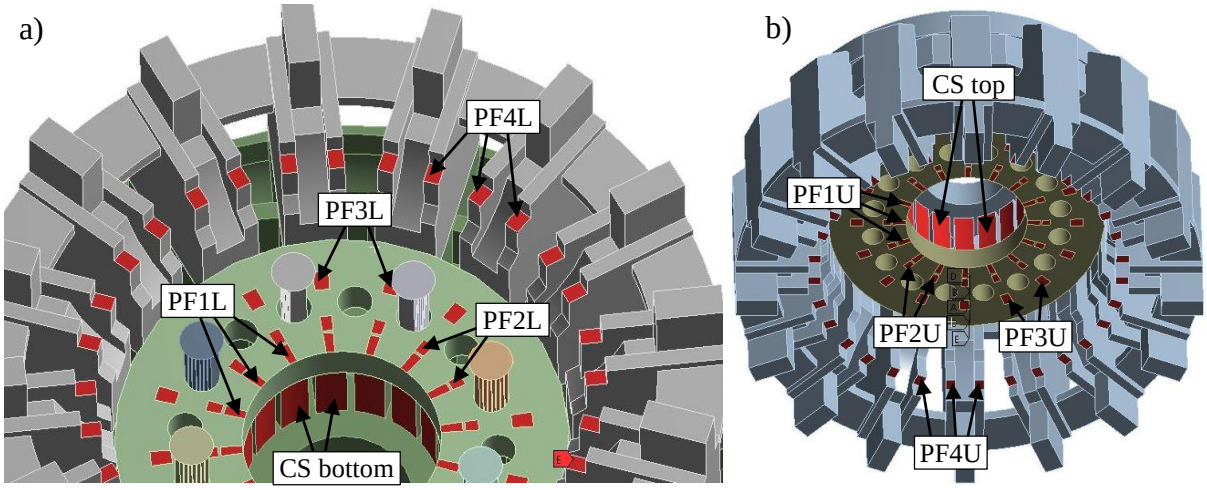

Figure 3. a) Areas of contact beween the holders of the poloidal field coils PF1L÷PF4L and the bottom part of the main support; b) Areas of contact beween the holders of the poloidal field coils PF1U÷PF4U and the top part of the main support

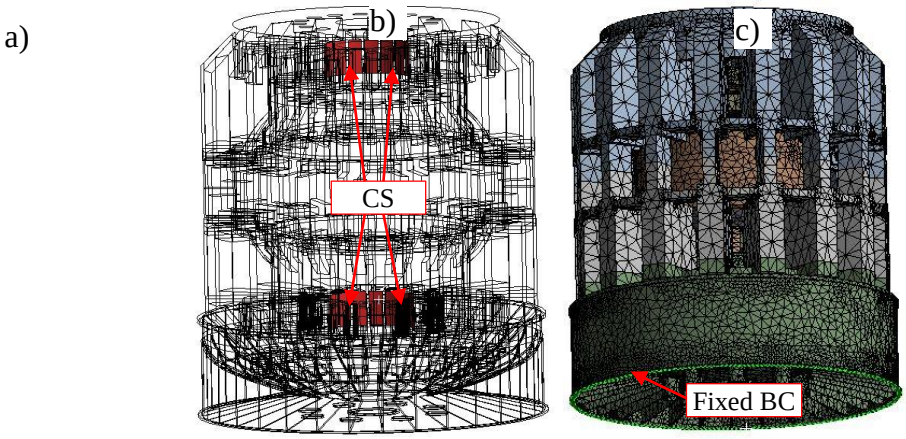

Figure 4. a) Areas of contact between the central solenoid and the main support; b) Finite element mesh of the first model (354554 nodes, 192053 elements)

Table 1. Material properties used for the transient structural analysis of the COMPASS-U tokamak

Number	Material	Young's modulus	Poisson's ratio	Density
1	Inconel 625	181[16] GPa (at 500 °C)	0.302[16] (at 500 °C)	8440[16] kg/m^3
2	Stainless steel 304	205[17] GPa (at 20 °C)	0.278[17]	7860[17] kg/m^3

The boundary conditions consisted of fixing the outer ring of the bottom part of the cryostat (Fig. 4b). The electromagnetic loads coming from the disruption are described in the 4th chapter.

3. ELECTROMAGNETIC SIMULATIONS OF THE PLASMA DISRUPTIONS

The forces for the transient structural analysis were sought via 2D axisymmetric model shown in Fig. 5. In addition to the central solenoid, poloidal field coils, the vacuum vessel, the plasma column was modeled as having circular cross-section. In the scenario shown in Fig. 5 the plasma current was quenching near the top stabilizing plate. This configuration was related to two possible current scenarios in the central solenoid and in the poloidal field coils, namely:

- DHSC: D-shaped plasma, high triangularity, small plasma, lower X-point
- DLSF: D-shaped plasma, low triangularity, small plasma, higher X-point

Similar plasma quench could occur near the bottom stabilizing plate with analogous two configuration of currents: DHSC, DLSF. These 4 scenarios were considered in the electromagnetic study, out of which the quench with the top stabilizing plate with DHSC current configurations was considered for the dynamic analysis.

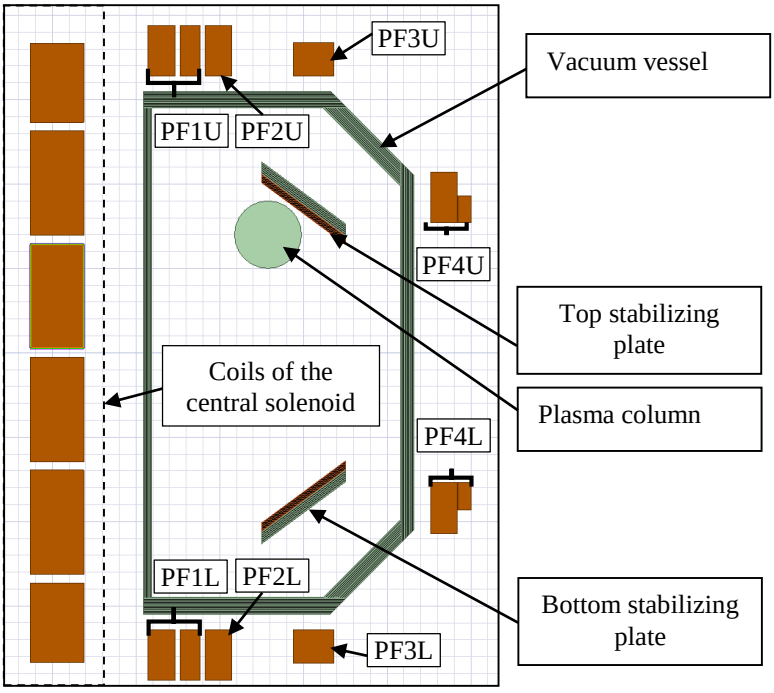

Figure 5. 2D axisymmetric model used to compute the electromagnetic forces during plasma disruptions

Only the circumferential component of the current was nonzero in the plasma disruption analysis, resulting in non-zero forces only in the radial and axial directions: F_R, F_Z. The resulting distributions of electromagnetic forces was not included directly, but equivalent loads were sought. The geometrical center of the vacuum vessel was used as the reduction point for all the forces. The equivalent forces and torques were calculated based on the formulas:

$$\vec{F}_{eqv}(t) = \iiint_V \left(\vec{j} \times \vec{B}\right) dV \quad (1)$$

$$\vec{M}_{eqv}(t) = \iiint_V \vec{r} \times \left(\vec{j} \times \vec{B}\right) dV \quad (2)$$

where $\vec{j}$ is the current density, $\vec{B}$ is the magnetic field vector and $\vec{r}$ is the position vector from the center of the VV (chosen reduction pole).
Due to axisymmetric distribution of the radial force in PF coils and in the vacuum vessel the net force calculated from Eq. 1 was non-zero only in the axial direction (F_Z). The net torque calculated from Eq. 2 was equal to zero.

The whole electromagnetic analysis was performed over 0.5 seconds. The resulting forces in the four parts of the VV are plotted in Fig. 6; after about 200 ms all the forces were already close to 0. The maximum values were reached in the first 400 μs (Fig. 7) with the force in the top part reaching -3.72 MN and in high field side 2.72 MN. The total force in the central solenoid is shown in Fig. 8. The increase rate from 1.56 MN to 4 MN was rather slow compared to the forces in the VV. The forces in the poloidal field coils are shown in Fig. 9. Here the decay took for the coils PF1U and PF3U took 500 ms. The rate of change for the forces in PF coils was much smaller compared to the forces in the VV. The extreme values of the axial force in PF coils were 4.33 MN for the coil PF3U and -8.06 MN for PF1U.

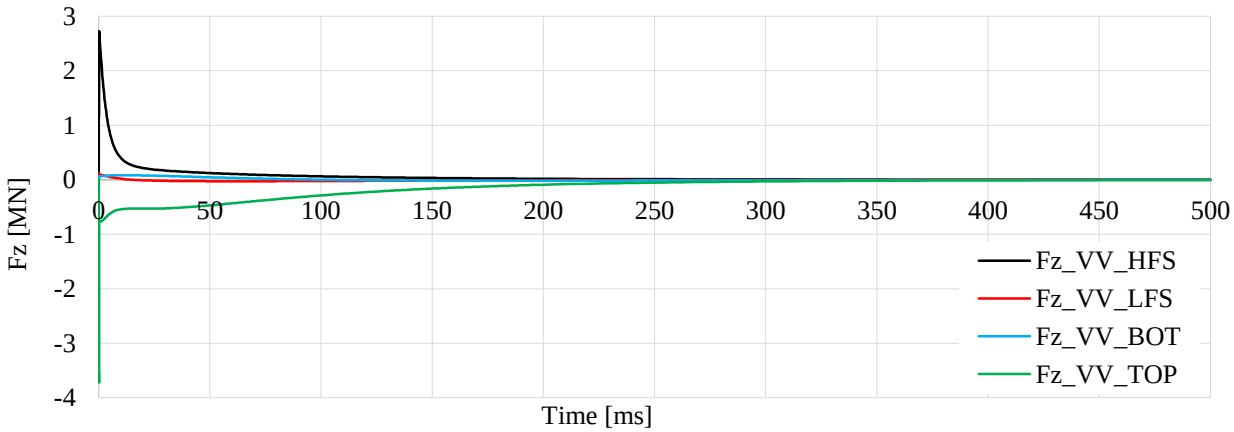

Figure 6. Total axial forces in the: BOT, TOP, LFS and HFS parts of the VV during the "top DHSC" plasma quench

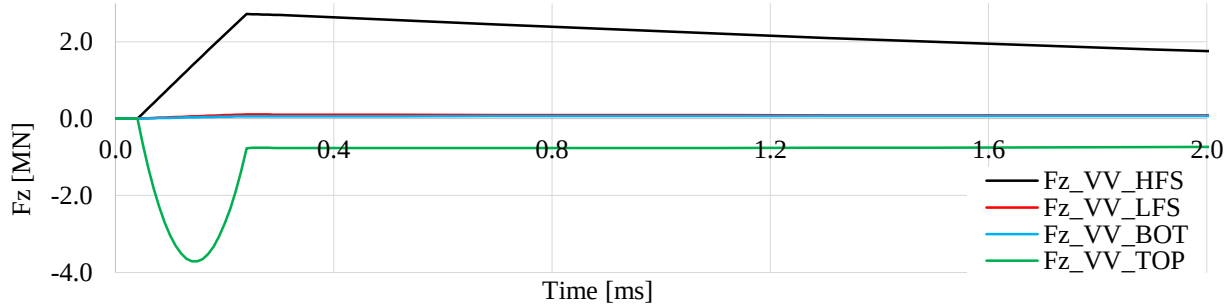

Figure 7. Total axial forces in the: BOT, TOP, LFS and HFS parts of the VV during the "top DHSC" plasma quench; first 1.2 ms of the event

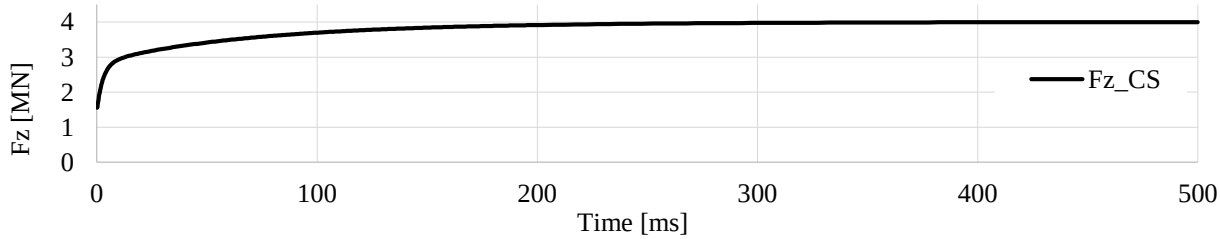

Figure 8. Total axial force in the central solenoid during the "top DHSC" plasma quench

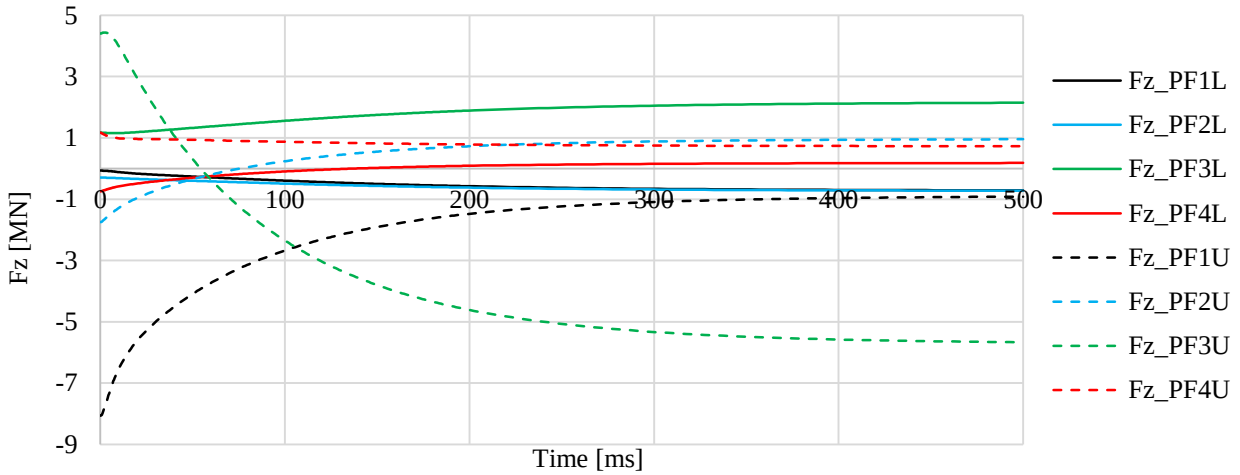

Figure 9. Total axial forces in the poloidal field coils during the "top DHSC" plasma quench

4. RESULTS OF THE MODAL ANALYSIS

The dynamic analysis was performed in the ANSYS Workbench software. The first step in performing the dynamic analysis consisted of the linear modal analysis to find out the relevant frequencies and mode shapes. As the mode superposition method was used for the transient analysis, 100 vibration modes were sought to, later on, construct the transient solution. The results of the modal analysis are listed in Table. 2. The first resonant frequency was 14 Hz, and the 100th 194.1 Hz. For the modes from 13th to 66th the frequency did not change much and was in the range 86.1÷88.2 Hz. The shape of the 1st vibration mode is shown in Fig. 10. The mobilized mass for the 100 vibration modes was 98.8 % indicating that sufficient number of modes were found.

Table 2. Results of the modal analysis performed on the model with the mesh shown in Fig. 4b

Mode	Freq. [Hz]	Mode	Freq. [Hz]	Mode	Freq. [Hz]	Mode	Freq. [Hz]	Mode	Freq. [Hz]
1	14.02	11	81.62	74	174.24	84	190.39	94	192.49
2	14.04	12	81.81	75	181.28	85	190.66	95	192.97
3	16.47	13÷66	86.14÷88.15	76	181.31	86	190.84	96	193.19
4	21.21	67	91.90	77	182.06	87	190.93	97	193.30
5	21.21	68	91.92	78	185.88	88	191.28	98	193.43
6	28.25	69	105.29	79	189.10	89	191.50	99	193.78
7	57.40	70	105.33	80	189.16	90	191.71	100	194.06
8	57.44	71	119.56	81	189.43	91	191.94		
9	58.02	72	145.08	82	189.87	92	192.17		
10	76.21	73	173.37	83	190.15	93	192.41		

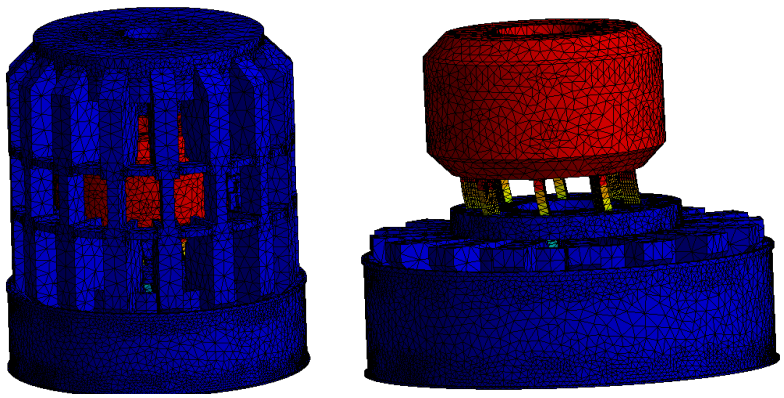

Figure 10. The shape of the 1st vibration mode, displacement magnification 20x

5. TRANSIENT DYNAMIC ANALYSIS

In order to realistically simulate the dynamic response of the tokamak frequency damping of the Rayleigh[18] type was included in the analysis. The damping ratio[6] (fraction of critical damping) was chosen in conservative way as equal to 2 % similarly as for vertical displacement events for ITER[19]. The Rayleigh damping scheme assumes the damping as proportional to mass and stiffness and is characterized by two coefficients: α and β:

$$[C] = \alpha [M] + \beta [K] \tag{3}$$

The coefficients α and β can be calculated based on the equation[20]

$$\varsigma_n = \frac{\alpha}{4} \frac{1}{\pi \cdot f_n} + \beta \pi \cdot f_n \tag{4}$$

where f_n is the n-th resonant frequency and ς_n is the damping ratio corresponding to the frequency f_n
Solving the Eq. 4 for the coefficients α and β assuming the lowest and the highest modal frequencies gives the following formulas[20]:

$$\alpha = 4\pi\varsigma_n \frac{f_{\min} \cdot f_{\max}}{f_{\min} + f_{\max}} \tag{5}$$

$$\beta = \frac{\varsigma_n}{\pi (f_{\min} + f_{\max})} \tag{6}$$

The damping parameters calculated from Eq. 5 and Eq. 6 were α=3.29, β=3.06e-5 (ς_n=0.02; f_{min}=14.02 Hz, f_{max} =194.06 Hz after Tab. 2). The resulting damping ratio (Eq. 4) is plotted in Fig. 11. The damping ratio was bounded to max. 2%, but for certain frequencies it was as small as 1%.

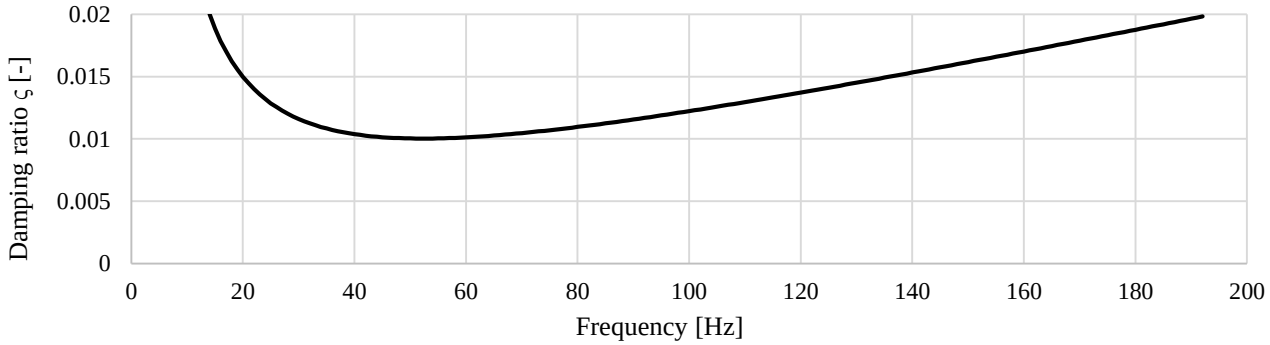

Figure 11. Damping ratio used for the dynamic analysis of the COMPASS-U tokamak, α=3.29, β=3.06e-5

Due to the considerable computational effort the transient analysis was performed in two steps. First by integrating almost the entire force range with large integration step, and secondly focusing only on the range with the maximum reaction force and integrating with smaller time step. The results of the first integration with 1 ms time step and 300 ms end time are shown in Fig. 12. In the 2nd analysis only 50 ms were analyzed with 10 μs integration step (Fig. 13). The maximum force was 1.9 MN and the minimum -2.26 MN. The reaction has to be augmented by the weight of the structure – 217 tons, so the maximum reaction force equals 4.07 MN, and minimum -0.09 MN (Fig. 13). The foundations have to carry an equivalent of 407 tons, so 1.87 times more than the mass of the structure. As the minimum reaction force was negative, the structure could lift from the ground during the analyzed disruption event. But as the weight of the whole tokamak structure was not included in the model, with 250 tons the weight will be sufficient to counteract the upward dynamic forces.

The maximum total deformation and the maximum von Mises stress are plotted as function of time in Fig. 14 and Fig. 15. With the maximum deformation of 2.7 mm and maximum von Mises stress of 202 MPa occurring at 3.2 ms. The corresponding maximum deformation and maximum von Mises stresses at 3.2 ms are shown in Fig. 16. The maximum reaction was reached at different time, after 7 ms (Fig. 13).

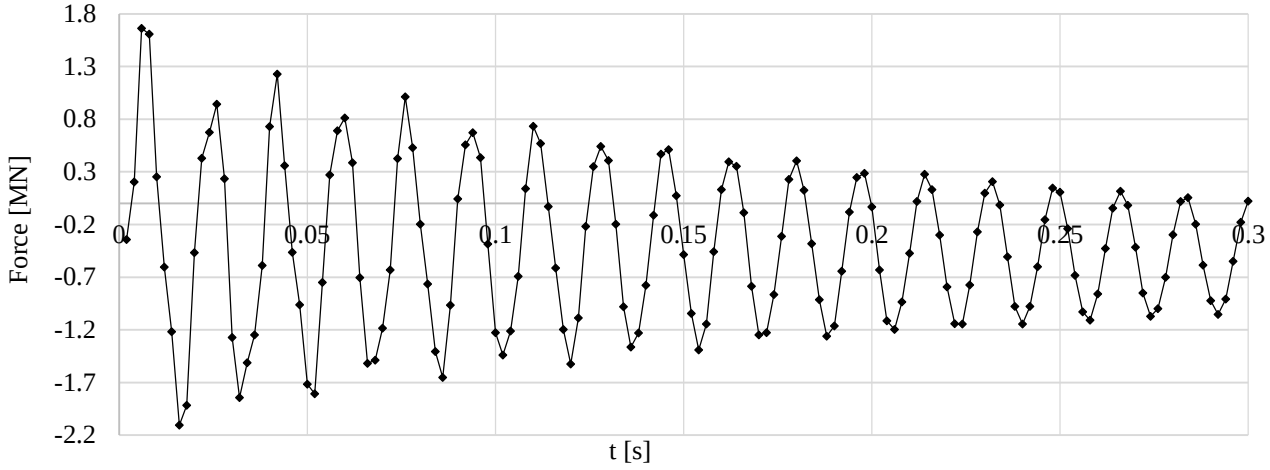

Figure 12. Force F_Z transmitted to the foundations – reaction from the support, analysis time 300 ms, time step 1 ms

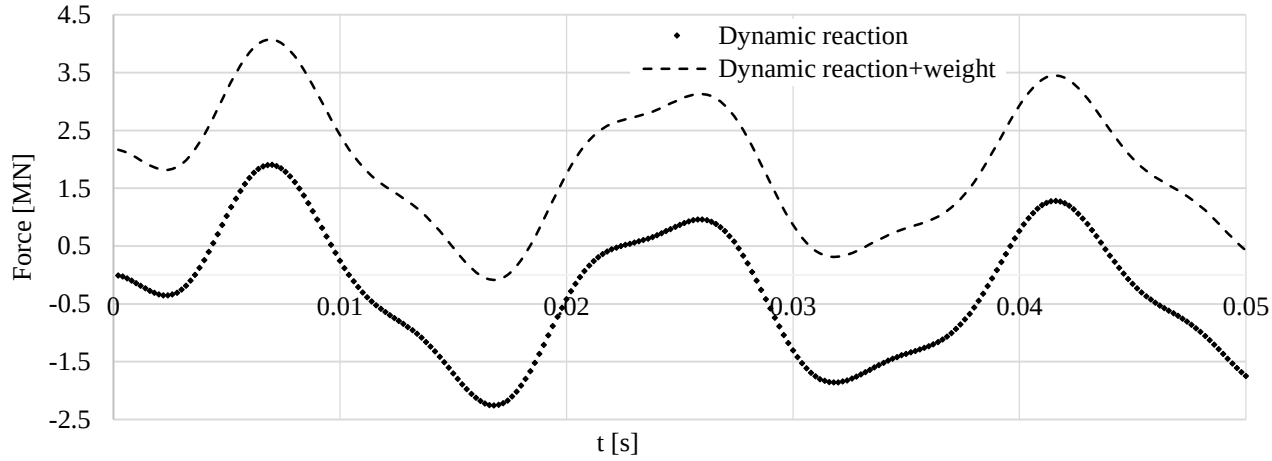

Figure 13. Force F_Z transmitted to the foundations – reaction from the support, analysis time 50 ms, time step 10 μs

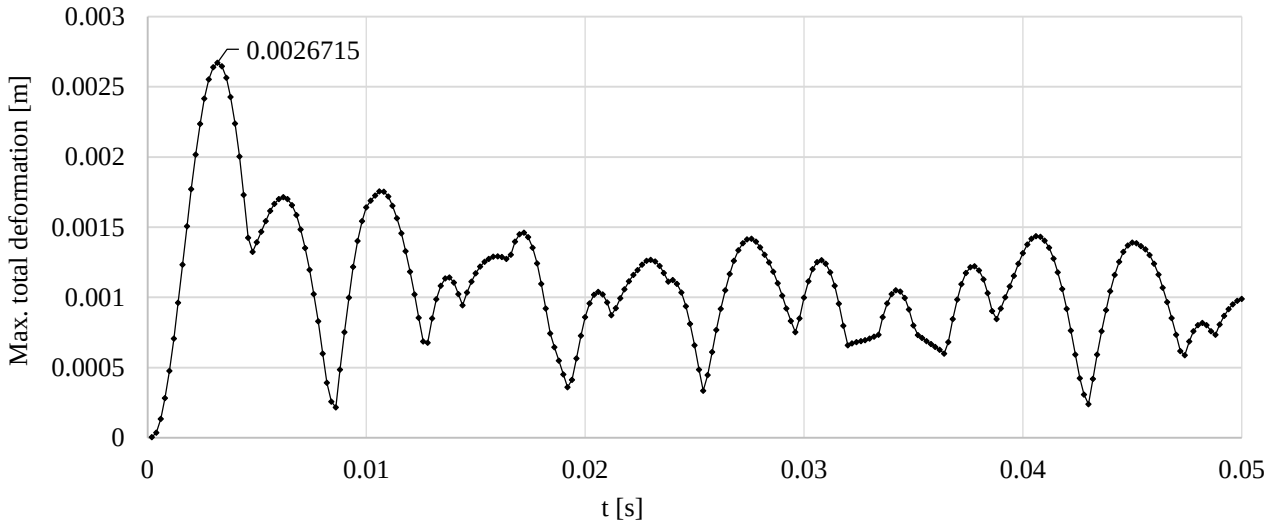

Figure 14. Maximum total deformation during the transient analysis, end time 50 ms, time step 10 μs

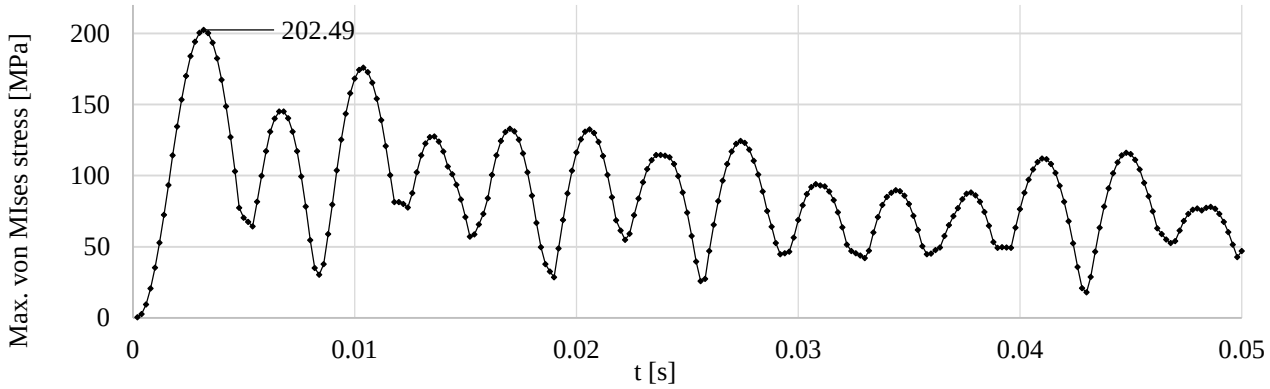

Figure 15. Maximum von Mises stress during the transient analysis, end time 50 ms, time step 10 μs

a b

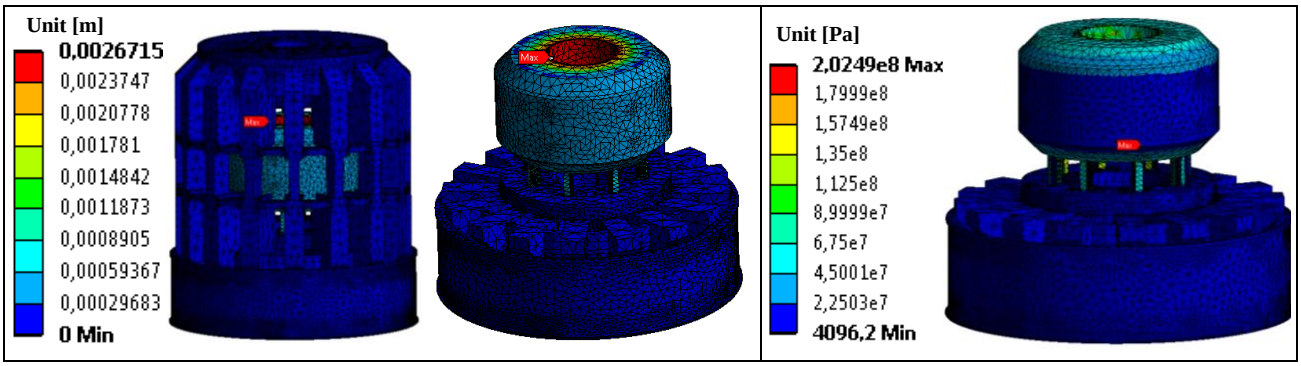

Figure 16. a) Maximum total deformation of the model for 3.2 ms time; b) Maximum von Mises stress for 3.2 ms time

6. CONCLUSIONS & FUTURE WORK

The response of the COMPASS-U tokamak to the dynamic electromagnetic loads resulting from plasma quench was found. Based on the results the following conclusions were drawn:

1. Only the axial forces contribute to the reactions in the support – so to the forces transmitted to the foundations.
2. The force transmitted to the foundations was found to be 4.07 MN, thus equivalent to 407 tons of dead mass.
3. The maximum deformations and stresses during the disruption were completely acceptable and of no danger to the tokamak structure.

In the following stage of the project the analysis will be repeated for the real worst case scenario found after number of parametric studies based on plasma equilibria and the electromagnetic simulations. The electromagnetic forces will be applied to the actual geometry and as transient 3D fields, not only as global equivalents.

ACKNOWLEDGEMENTS

This work has been carried out within the framework of the project COMPASS-U: Tokamak for cutting-edge fusion research (No. CZ.02.1.01/0.0/0.0/16_019/0000768) and co-funded from European structural and investment funds.

REFERENCES

[1] Panek, R., Markovic, T., Cahyna, P., Dejarnac, R., Havlicek, J., Horacek, J., Hron, M., Imrisek, M., Junek, P., Komm, M., Sestak, D., Urban, J., Varju, J., Weinzettl, V., Adamek, J., Bilkova, P., Bohm, P., Dimitrova, M., Hacek, P., Kovarik, K., Krbec, J., Mlynar, J., Podolnik, A., Seidl, J., Stockel, J., Tomes, M., Zajac, F.,

Mitosinkova, K., Peterka, M., Vondracek, P., the COMPASS team, “Conceptual design of the COMPASS upgrade tokamak”, Fusion Engineering and Design 123, 11–16 (2017)
[2] Panek, R., Adamek, J., Aftanas, M., Bilkova, P., Bohm, P., Brochard, F., Cahyna, P., Cavalier, J., Dejarnac, R., Dimitrova, M., Grover, O., Harrison, J., Hacek, P., Havlicek, J., Havranek, A., Horacek, J., Hron, M., Imrisek, M., Janky, F., Kirk, A., Komm, M., Kovarik, K., Krbec, J., Kripner, L., Markovic, T., Mitosinkova, K., Mlynar, J., Naydenkova, D., Peterka, M., Seidl, J., Stockel, J., Stefanikova, E., Tomes, M., Urban, J., Vondracek, P., Varavin, M., Varju, J., Weinzettl, V., Zajac, J., the COMPASS team, “Status of the COMPASS tokamak and characterization of the first H-mode” Plasma Phys. Control. Fusion 58 014015 (2016)
[3] Panek, R., Bilykova, O., Fuchs, V., Hron, M., Chraska, P., Pavlo, P., Stockel, J., Urban, J., Weinzettl, V., Zajac, J., Zacek,F., “Reinstallation of the COMPASS-D tokamak in IPP ASCR”, Czechoslovak Journal of Physics 56 Suppl. B (2006)
[4] Pitcher, C. S., Barnsley, R., Feder, R., Hu, Q., Loesser, G. D., Lyublin, B., Padasalagi, S., Pak, S., Reichle, R., Sato, K., Udintsev, V. S., Walker, C., Walsh, M., Zhai, Y., “Nuclear engineering of diagnostic port plugs on ITER”, Fusion Engineering and Design 87, 667–674 (2012)
[5] Vacas, C., Rodriguez, E., Guirao, J., Iglesias, S., Udintsev, V., Pak, S., Maquet, P., Roces, J., Casal, N., “The choice of dynamic amplification factors for the ITER generic port plugs during disruptions”, Fusion Engineering and Design 98-99, 1652–1655 (2015)
[6] Chopra, A. K., [Dynamics of structures], Pearson, Prentice-hall International Series I Civil Engineering and Engineering Mechanics, 2016
[7] Weissenburger, D., “Dynamic analysis of eddy currents and forces in the TFTR vacuum vessel due to plasma disruptions”, IEEE Transactions on Magnetics 21(6), 2347 – 2350 (1985)
[8] Tado, S., Kitamura, K., Itou, Y., Koizumi, K., Tada, E., Tsunematsu, T., „Dynamic analysis of the tokamak support system in ITER”, Fusion Engineering and Design 41(1-4), 421-429 (1998)
[9] Martinez, J. M., Jun, C., H., Portafaix, C., Alekseev, A., Sborchia, C., Choi, C. H., Albin, V., Borrelly, S., Cambazar, M., Gaucher, T., Sfarni, S., Tailhardat, O., “Structural damages prevention of the ITER vacuum vessel and ports by elasto-plastic analysis with regards to RCC-MR”, Fusion Engineering and Design 98–99, 1552–1555 (2015)
[10] Martinez, J.-M., Jun, C. H., Portafaix, C., Choi, C.-H., Ioki, K., Sannazzaro, G., Sborchia, C., Cambazar, M., Corti, Ph., Pinori, K., Sfarni, S., Tailhardat, O., Borrelly, S., Albin, V., Pelletier, N., “Structural analysis of the ITER Vacuum Vessel regarding 2012 ITER Project-Level Loads”, Fusion Engineering and Design 89, 1836–1842 (2014)
[11] Martinez, J.-M., Alekseev, A., Sborchia, C., Choi, C. H., Utin, Y., Jun, C. H., Terasawa, A., Popova, E., Xiang, B., Sannazaro, G., Lee, A., Martin, A., Teissier, P., Sabourin, F., Caixas, J., Fernandez, E., Zarzalejos, J. M., Kim, H.-S., Kim, Y. G., Privalova, E., Du., S, Wang, S., Albin, V., Gaucher, T., Borrelly, S., Cambazar, M., Sfarni, S., “ITER VV structural analysis completion during manufacturing phase”, Fusion Engineering and Design 109–111, 688–692 (2016)
[12] Takeda N., Shibanuma, K., “Dynamic analysis of ITER tokamak using simplified model for support structure”, Journal of Plasma and Fusion Research 80(11), 988-990 (2004)
[13] Martino F. D., Pou, J. A., Scholer, T., Frano, R. L., Aquaro, D., “Simplified models of the ITER vacuum vessel for global seismic analyses”, Fusion Engineering and Design 136, 1354–1358 (2018)
[14] “ANSYS Mechanical APDL Substructuring Analysis Guide”, <https://www.sharcnet.ca/Software/Ansys/16.2.3/en-us/help/ans_substr/Hlp_G_substrTOC.html> (11 April 2019)
[15] Blocki, J., Combescure, D., Mazzone, G., “Assessment of the dynamic behaviors of the ITER Vacuum Vessel”, Fusion Engineering and Design 88, 1938-1941 (2013)
[16] “Special Metals Corporation”, Inconel Alloy 625 <http://www.specialmetals.com/assets/smc/documents/alloys/inconel/inconel-alloy-625.pdf> (12 April 2019)
[17] Ledbetter, H. M., Weston, W. F., Naimon, E. R., “Low temperature elastic properties of four austenitic stainless steels”, Journal of Applied Physics 46(9), 3855–3860 (1975)
[18] Rayleigh, L., [Theory of Sound], Dover, 1945
[19] “ITER Vacuum Vessel Load Specification, 2013, <http://zingkashing.dx.am/ITER_Vacuum_Vessel_Load_Specification_2F52JY_v3_3.pdf> (16 April 2019)
[20] Cruz, C., Miranda, E., “Evaluation of the Rayleigh damping model for buildings”, Engineering Structures 138, 324-336 (2017)

Synchronization between computation and acquisition parts in the GEM detector based measurement system

Pawel Linczuk[ab], Wojciech M. Zabolotny[b], Andrzej Wojenski[b], Rafal D. Krawczyk[bc], Krzysztof T. Pozniak[b], Maryna Chernyshova[a], Tomasz Czarski[a], Michal Gaska[b], Grzegorz Kasprowicz[b], Ewa Kowalska-Strzeciwilk[a], Karol Malinowski[a]

[a]Institute of Plasma Physics and Laser Microfusion, Warsaw, Poland
[b]Warsaw University of Technology, Institute of Electronic System, Warsaw, Poland
[c]CERN, Geneva, Switzerland

ABSTRACT

The presented system is used for monitoring of the plasma impurities in the tokamak. It is done by measuring radiation in Soft X-Ray range with the use of a GEM-based detector. Acquired data is transferred through the whole system with low latency. Presented system can be divided into many parts - detector, analog electronics, FPGA, PCIe transmission line and computer system with high-performance CPU. This work will concentrate on synchronization between FPGA, which write data to the memory on the CPU side and computational part, which is executed in the computer. In long-running measurements, there is a synchronization problems which can arise. There is a difference in variables based on which the execution time of both parts is dependent. Working on measurements of radiation of plasma impurities requires limits in terms of latency. This paper presents reasons, descriptions and solutions for such problems.

Keywords: plasma diagnostics, GEM system, data processing

1. INTRODUCTION

There is being conducted an extensive research concentrated on energy production from the nuclear fusion. One of the methods currently developed is based on exploitation of the tokamak plasma. To make the reaction efficient, plasma inside the device has to remain stable at certain conditions. One of the obstacles, which could prevent it, is related to the presence of tungsten impurities in plasma originating from tokamak chamber components. If they accumulate, they can lower efficiency and eventually cause a disruption, which stops the reaction and may even damage the device. There is a need for monitoring those impurities with low latency and real-time manner, which can lead to improvement of the experiment control. The details are described in [1,2,3].

The presented system implements such a functionality by measurement of the soft X-ray radiation emitted by impurities in range 0.1 to 20 keV. It uses a detector based on Gas Electron Multiplier (GEM) foils. Measured signals are sent through analog and digital electronics. At the end of the processing path, the FPGA sends detected chunks of signals to the PC, where the computation part is implemented[4,5].

The presented system is built to measure[5] and compute[6] raw samples to provide high-quality measurements. Due to possible signal distortions[7], other solutions like Time Over Threshold (ToT) value can result in errors in computations. More details about the computation part are provided in [6,8]. The GPU-implemented algorithm is also considered[9].

This architecture, with such separate parts, generates a kind of producer-consumer problem. The solution was found for global trigger mode with double buffering[3]. The serial mode improves latency possibilities, removes the need for additional buffers but brings new challenges regarding extreme cases, which are described in more detail in this paper.

Photonics Applications in Astronomy, Communications, Industry, and High-Energy Physics Experiments 2019,
edited by Ryszard S. Romaniuk, Maciej Linczuk, Proc. of SPIE Vol. 11176, 1117646
© 2019 SPIE · CCC code: 0277-786X/19/$21 · doi: 10.1117/12.2536777

Figure 1: Simplified architecture of the system. More details about transmission between FPGA and PC (yellow part in the figure) is described in [10]. More details about the whole architecture are described in [3].

2. MEASUREMENT SYSTEM

The architecture of the system and data path is described in figure 1. Data path consists of a DMA engine implemented in FPGA[10]. On the CPU side, there are dedicated threads distributed between available cores. Each of them has assigned tasks like:

1. handling acquired chunks of data, validity checking, and data distribution through the system by task queue,
2. acquiring task from queue and spawning computation threads,
3. writing of the data produced by the computation part.

Measurement data is gathered from each of the pixels of the detector. Signals are sampled by Analog Digital Converters and handled in FPGA continuously. Stream from each pixel is called a channel. If one of the measurement samples rise above the trigger level (adjustable by user), raw samples are packed into data chunks. The one used in software processing is made of 40 raw signal samples. Chunks are packed in events, which are single logical data packets grouped and sent from FPGA. The system is capable of working with two different triggering algorithms called global and local, which have different events definition.

First one works by gathering chunks of data from all channels at once if on one or more of the channels signal samples crossed the trigger level. This algorithm was widely tested and described in previous works[11,12]. It provides good solution for integration and installation of the system. The synchronization of chunks between channels is convenient for algorithm testing. Gathering data from channels which do not have signal data can provide much information about measurement quality. With this mode, problems like interferences from the environment or incorrect installation of shielding can be checked. However, in this mode, triggering of the single channel generates a huge stream of data. Samples are sent in events of 64 channels multiplied by 40 samples and metadata[5]. Data is ordered by acquisition time. It means that in memory, the first samples of all channels are written first, then the second samples, and so on. This layout is inconvenient for memory access in the signal processing algorithm, which needs to process a single chunk of data per channel.

Additionally, data gathered from FPGA needs further reordering before transposition. Due to those problems double buffering (described earlier in [3]) was introduced. In this mode, events are huge and can require much computation, even if there are not many channels with measured X-ray based signals. That can result in increased latency of the whole data path.

Local triggering sends the events containing only data chunks corresponding to the single channel in which samples have crossed the trigger level. That lowers much the need for memory bandwidth and provides the much better concentration of signal data. Data send in a single event consists single chunk of 40 samples and metadata, which are optimally laid in memory for signal processing algorithm. With this solution, there is no need for double buffering and transposition.

In the considered implementation described in [10] data must be continuously read. Subsequent chunks of data are stored in the cyclic buffer (readout architecture is described in figure 2). There is a single thread

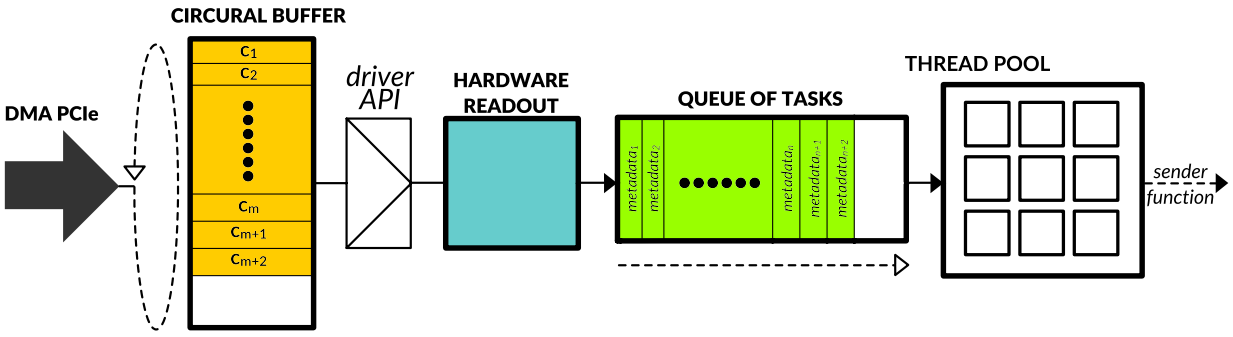

Figure 2: Simplified architecture of the data path. This solution only propagates the metadata through the system, which provides a zero-copy solution not achievable earlier. More details are described in [3].

dedicated to check the integrity of downloaded data and to properly distribute metadata of the chunk to the worker thread pool - which processes data with algorithms used for histograms generation.

Earlier work presented the possibility of a system working in firm real-time with global triggering algorithm[12] and 10 ms latency from signal detection in the FPGA to its storage in the memory file system. However, this research did not concentrate on the extreme cases of the measurements in the serial mode.

3. SYNCHRONISATION PROBLEM

The crucial requirement for the data distribution path is to maximize data path throughput, amount of correctly computed output histograms, and to minimize latency. There is much effort to ensure the quality of output data. The path should handle correctly overloads in different parts.

The efficiency of different parts depends on different variables. In terms of latency, the FPGA part does not consider the complexity of signals in processed chunks. Amount of data sent through PCIe does not depend on the number of pulses registered in the single chunk of 40 samples (must be one or more). That means that the number of samples and signals detected within it are not linearly dependent. However computational part highly depends on the complexity of registered pulses within a single chunk. For example, a chunk with only one pulse is faster to calculate than pileup of multiple pulses. That can result in differences between time of acquisition with storage in cyclic buffer and generation time of algorithmic computations output.

There are few possibilities regarding differences in performance of considered parts:

1. FPGA part is slower than the computational part,
2. FPGA part is comparable with the computational part,
3. FPGA part is faster than the computational part.

4. PROPOSED SOLUTION

The first situation is not dangerous for the continuity of computations. If data is not sent through the PCIe, it means that there is no data to be processed. Even if data is sent, the computational part can handle it. There is enough time to finish processing and to wait for the next chunk of the data. No additional action has to be performed to ensure stable operation.

The second and third situations can be dangerous. In those situations, we have to consider the priority of the transfer to circular buffer or pool of computation threads.

If the transfer has the priority, we have to notify the working thread, that data has been overwritten. That can be done by checking the metadata of the chunk at the start and the end of processing of the buffer. If data got overwritten, the metadata would change, resulting in rejection of calculated results. In the worst case scenario, the circular buffer may be almost full. That would result in repeated overwriting and invalidation of the data received by the computational thread. In this state, system does not generate any output due to continuous invalidation.

Another solution is to assign higher priority to computational threads. If the data in circular buffer is not processed yet by computational threads, it can't be overwritten with the newly acquired data. Due to the need of continuous writing of the data, FPGA has to overwrite the last written chunk of data. This situation is called a stall state and is presented in figure 3a. As soon as the computational part ends processing and frees a slot in the circular buffer, FPGA transfer can resume regular operation.

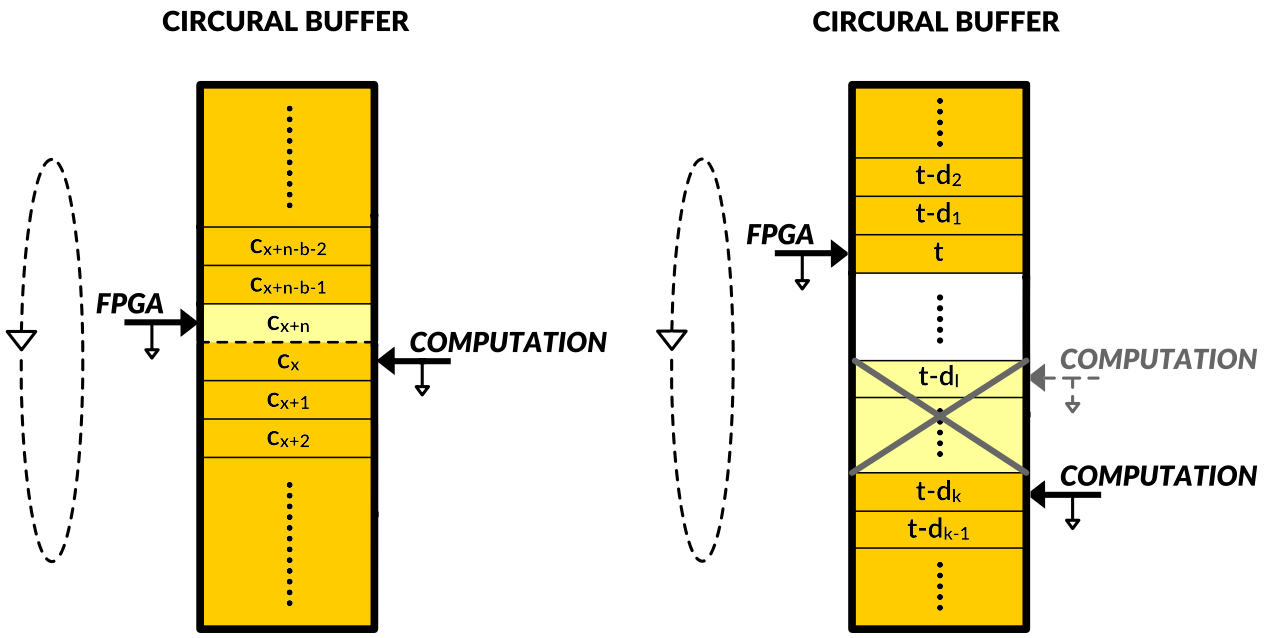

(a) Single packet overflow situation with the higher priority of computational part. Computation part is executing slower or in equal speed to the FPGA part writing new data to the buffer. c is an indicator for the data packet, n is the number of packets stored between computation and acquisition parts pointers, b is the number of lost packets or data overwrites. In this situation, before the computation part is able to produce the result and free a slot in the circular buffer, FPGA overwrites the last available slot b times.

(b) Simplified situation with limited latency of computation. It is the timestamp of the current time. $d_1, d_2, ..., d_k, ..., d_l$ are delays between the time of storing in a circular buffer and the actual time. l is the index of the last chunk stored in the circular buffer and k is the index which computation part could compute adding own latency of processing, but still in the limits of the set latency. In this case, the computing part pointer is moved from l to k and $l - k$ packets were discarded.

Figure 3: Schematic of solutions for data distribution problems. In both parts of the figure, there is a state of circular buffer presented. The pointer of current reading/writing is shown as a horizontal arrow for FPGA and computational parts. Pointers are incremented in the downward direction (indicated by the arrow pointing downward).

To prevent hidden continuity errors in computation threads, there should be a flag marking the chunk as overwritten by FPGA in the stall state. To improve the quality of the results, instead of a flag, the counter of overwrites can be stored (The counter must implement "saturation". When it reaches its maximum value, it does not wrap to zero and remains constant). That provides information about the number of lost packets due to the overload of the buffer.

Such a situation is likely to occur when the system works in offline mode. Then its computational threads should compute all available data. However, plasma is a dynamic process. The latency may need to be limited to ensure the validity of the measured data. In such a real-time mode, acquisition thread should check timestamps of the ready to compute chunks of data. If the waiting time rises above a pre-set level, chunk should be confirmed as computed and freed for overwriting. The level should be equal to the maximally allowed latency decreased by the maximum of the transmission time and computation time. Such a packet of events should be treated as lost. This situation is presented in figure 3b.

5. CONCLUSIONS

System description and differences in triggering algorithms is presented. Elimination of double buffering is achieved by switching to the serial triggering algorithm, which enables lowering the overall data path latency. This solution, however, complicates the integration at different throughputs of the FPGA and computational parts. The efficiency of both of them depends on different variables. Possible problems are presented with a discussion of their importance. The proposed solutions are described including the higher priority of the computation part, the overwriting of data and discarding chunks of data which can't be processed in the latency limit.

ACKNOWLEDGMENTS

This work has been carried out within the framework of the EUROfusion Consortium and has received funding from the Euratom research and training programme 2014-2018 and 2019-2020 under grant agreement No 633053. The views and opinions expressed herein do not necessarily reflect those of the European Commission. This scientific work was partly supported by Polish Ministry of Science and Higher Education within the framework of the scientific financial resources in the years 2014-2019 allocated for the realization of the international co-financed project.

REFERENCES

[1] Mazon, D., Jardin, A., Malard, P., Chernyshova, M., Coston, C., Malard, P., O'Mullane, M., Czarski, T., Malinowski, K., Faisse, F., Ferlay, F., Verger, J., Bec, A., Larroque, S., Kasprowicz, G., Wojenski, A., and Pozniak, K., "SXR measurement and W transport survey using GEM tomographic system on WEST," *Journal of Instrumentation* **12**, C11034 (2017).

[2] Chernyshova, M., Czarski, T., Malinowski, K., Kowalska-Strzeciwilk, E., Pozniak, K., Kasprowicz, G., Zabolotny, W., Wojenski, A., Kolasinski, P., Mazon, D., and Malard, P., "Conceptual design and development of GEM based detecting system for tomographic tungsten focused transport monitoring," *Journal of Instrumentation* **10**, P10022 (2015).

[3] Linczuk, P., Krawczyk, R. D., Zabolotny, W. M., Wojenski, A., Pozniak, K. T., Chernyshova, M., Czarski, T., Gaska, M., Kasprowicz, G., Kowalska-Strzeciwilk, E., and Malinowski, K., "Data distribution and dispatching software for processing measurement data acquired with SXR GEM-based system," *Proc.SPIE* **10808** (2018).

[4] Kasprowicz, G., Zabolotny, W. M., Pozniak, K., Chernyshova, M., Czarski, T., Gaska, M., Kolasinski, P., Krawczyk, R., Linczuk, P., and Wojenski, A., "Multichannel Data Acquisition System for GEM Detectors," *Journal of Fusion Energy* (Jun 2018).

[5] Wojenski, A., Pozniak, K., Kasprowicz, G., Kolasinski, P., Krawczyk, R., Zabolotny, W., Chernyshova, M., Czarski, T., Malinowski, K., and Mazon, D., "Multichannel measurement system for extended SXR plasma diagnostics based on novel radiation-hard electronics," *Fusion Engineering and Design* **123**, 727 – 731 (2017).

[6] Czarski, T., Chernyshova, M., Malinowski, K., Pozniak, K., Kasprowicz, G., Kolasinski, P., Krawczyk, R., Wojenski, A., Linczuk, P., Zabolotny, W., Jardin, A., Mazon, D., Jakubowska, K., Boutoux, G., Burgy, F., Hulin, S., and Batani, D., "Measuring issues in the GEM detector system for fusion plasma imaging," *Journal of Instrumentation* **13**, C08001 (2018).

[7] Wojenski, A., Pozniak, K., Mazon, D., and Chernyshova, M., "FPGA-based novel real-time evaluation and data quality monitoring system for tokamak high-performance GEM soft X-ray diagnostic," *Journal of Instrumentation* **13**, P12024 (2018).

[8] Krawczyk, R. D., Czarski, T., Linczuk, P., Wojenski, A., Kolasinski, P., Gaska, M., Chernyshova, M., Mazon, D., Jardin, A., Malard, P., Poźniak, K., Kasprowicz, G., Zabolotny, W., Kowalska-Strzeciwilk, E., and Malinowski, K., "The software-defined fast post-processing for GEM soft x-ray diagnostics in the Tungsten Environment in Steady-state Tokamak thermal fusion reactor," *Review of Scientific Instruments* **89**, 063504 (2018).

[9] Krawczyk, R., Czarski, T., Linczuk, P., Wojenski, A., Chernyshova, M., Pozniak, K., Mazon, D., Kolasinski, P., Kasprowicz, G., Zabolotny, W., Gaska, M., Kowalsaka-Strzeciwilk, E., Malinowski, K., Jardin, A., and Malard, P., "Parallel computing in soft X-rays plasma diagnostic systems for thermal fusion reactors—feasibility studies for GPUs," *Concurrency and Computation: Practice and Experience* , e5235 (2019).

[10] Zabołotny, W. M., "DMA implementations for FPGA-based data acquisition systems," *Proc.SPIE* **10445** (2017).

[11] Linczuk, P., Krawczyk, R., Wojenski, A., Zabolotny, W., Pozniak, K., Chernyshova, M., Czarski, T., Kolasinski, P., Kasprowicz, G., Gaska, M., Kowalska-Strzeciwilk, E., and Malinowski, K., "Performance evaluation of developed GEM-based X-Ray diagnostic system," *Acta Physica Polonica B, Proceedings Supplement* **11**.

[12] Linczuk, P., Krawczyk, R., Wojenski, A., Zabolotny, W., Chernyshova, M., Pozniak, K., Czarski, T., Gaska, M., Kasprowicz, G., Kolasinski, P., Kowalska-Strzeciwilk, E., and Malinowski, K., "Latency and throughput of online processing in Soft X-Ray GEM-based measurement system," *Journal of Instrumentation* **14**, C05001 (2019).

Detecting Nuclear Debris with the Forward Proton Detectors at the LHC

Krzysztof Cieśla*, Rafał Staszewski, and Janusz J. Chwastowski

Institute of Nuclear Physics Polish Academy of Sciences, ul. Radzikowskiego 152, 31-342 Kraków, Poland

ABSTRACT

The already existing forward proton detectors are considered in the context of the heavy ion collisions. The potential of such detectors in measuring the nuclear debris originating from de-excitation of colliding ions is presented. The apparatus geometric acceptance for different nuclei is studied. Also, the influence of the Fermi motion and experimental conditions is considered. A possibility of the reconstructing of collision the impact parameter from the measurement of the nuclear fragments is discussed.

1. INTRODUCTION

The Large Hadron Collider[1] is equipped with dedicated forward detectors allowing the registration of protons scattered in diffractive or electromagnetic interactions. Due to very small scattering angles of such a proton and the required precision these detectors are installed very far away from the interaction point. In addition, the use of the Roman Pot technology allows placing them very close to the proton beams.

The LHC physics programme is not only devoted to the studies of the proton–proton interactions. The possibilities of accelerating heavy ion beams have already resulted in many measurements of proton–lead and lead–lead collisions (see for example[2] and references therein).

The sketch of an ultrarelativistic interaction of two heavy nuclei is depicted in Fig. 1. In the most common case, the impact parameter of the collision has a non-zero value. Therefore, only a part of the nucleons belonging to one nucleus collides with a part of the nucleons in the other nucleus. The actively participating nucleons in the interaction are called the participant nucleons (or participants), in contrast to the spectator nucleons (or spectators).

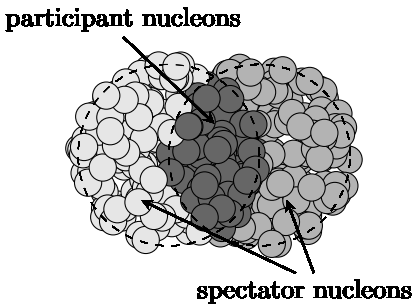

Figure 1. A schematic diagram of a ultrarelativistic heavy ion collision (view perpendicular to the relative velocities).

The time-scale of the ultrarelativistic ion collision is much shorter than that of the interactions within the nuclei. Thus, the spectators are essentially left intact during the nucleus–nucleus collision. Typically, they are

*Presented at XLIV-th IEEE-SPIE Joint Symposium Wilga 2019 by K. Cieśla
Further author information:
K. Cieśla: Krzysztof.Ciesla@ifj.edu.pl
R. Staszewski: Rafal.Staszewski@ifj.edu.pl
J. J. Chwastowski: Janusz.Chwastowski@ifj.edu.pl

Photonics Applications in Astronomy, Communications, Industry, and High-Energy Physics Experiments 2019, edited by Ryszard S. Romaniuk, Maciej Linczuk, Proc. of SPIE Vol. 11176, 1117647
© 2019 SPIE · CCC code: 0277-786X/19/$21 · doi: 10.1117/12.2536782

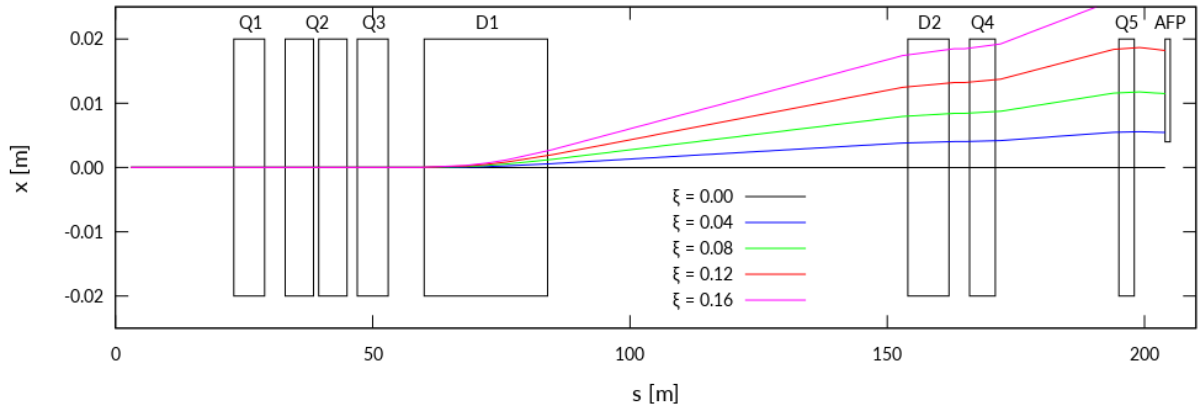

Figure 2. Trajectories of diffractively scattered proton in the LHC magnetic fields; x is the horizontal coordinate of the trajectory with respect to the nominal orbit, s is the distance from the interaction point along the orbit, ξ is the relative energy loss of a proton.

scattered into the accelerator beam pipe and escape the acceptance of the central detectors, similarly to the forward protons. The present work tries to answer whether and to what extent the forward proton detectors at the LHC can be used with heavy ion beams.

2. FORWARD PROTON DETECTORS

Several systems of forward proton detectors are currently installed at the LHC, including: TOTEM,[3] CT-PPS,[4] ALFA[5] and AFP.[6] All of these detectors are deployed about 200 m away from their corresponding interaction points. The AFP and CT-PPS detectors approach the beams horizontally, the ALFA ones vertically, whereas TOTEM has both types of the detectors. The considerations presented below use the AFP detectors. However, the results are expected to be qualitatively similar for other horizontal detectors. The potential application of the vertical ones is not covered within this work.

The AFP (ATLAS Forward Proton) detectors[6] are a sub-system of the ATLAS experiment located at the LHC Interaction Point 1. It consists of four stations – two on each outgoing beam, with the near stations placed 205 m and the far ones 217 m away from the interaction point. The AFP makes use of the Roman Pot mechanism allowing the horizontal insertion of the detectors into the accelerator beam pipe. Each station contains a tracking detector of four planes of the 3D Silicon sensors.[7] Additionally, the far stations can be equipped with quartz-based Cherenkov time-of-flight counters, which are not relevant to the present study.

Before being detected by the AFP, a diffractively scattered proton passes through the LHC magnetic lattice:

- The Q1 – Q3 triplet of quadrupole magnets responsible for the final focusing and the emittance matching of the beams, providing the high luminosity of collisions.
- The two dipole magnets: D1 and D2. D1 separates the incoming and the outgoing beams, whereas D2 accommodates them within the corresponding beam pipes of the machine.
- The Q4 and Q5 quadrupole magnets are used to match the beam optics in the interaction region to the rest of the ring.

The momentum of the diffractively scattered proton is slightly different from that of the beam proton. During the interaction, the proton is scattered at a very small angle and also looses some part of its energy. The small scattering angles imply that the distribution of the transverse momentum of the diffractively scattered protons is very steep. Therefore, the scattered proton trajectory and hence the position in the forward detector is mainly

determined by the proton energy. The transverse momentum leads only to a moderate smearing of protons position.

The relative energy loss of a proton is defined as $\xi = 1 - E_{proton}/E_{beam}$. The higher is its value the larger is the curvature of scattered proton trajectory (and hence the displacement from the nominal beam orbit) in the magnetic field. Therefore, such particles can be registered by detectors placed close to the beam. As an example, Fig. 2 shows the trajectories of protons with different energy values, here specified by the relative energy loss. Also, the LHC magnetic lattice and the AFP detector are sketched in this figure.

The kinematic range in which the measurements are possible can be quantified by the value of the geometric acceptance defined as a function of the proton relative energy loss and its transverse momentum, averaged over the azimuthal angle. Naturally, the acceptance depends on the exact settings of the magnetic fields, the so-called machine optics, and on the position of the detector with respect to the beam.

An example of the acceptance plot, calculated for the design LHC optics[8] is depicted in Fig. 3. The presented results were obtained using the Mad-X programme.[9] One can see that the AFP detectors can register the protons that lost between 2% and 12% of their energy and gained less than 2.5 GeV of transverse momentum.

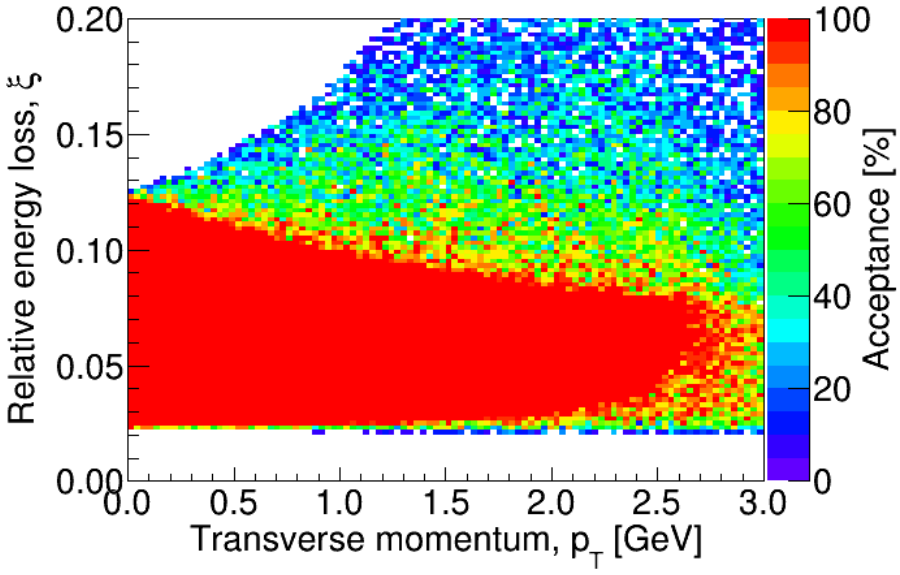

Figure 3. Geometric acceptance of the AFP detectors for diffractive protons.

3. ACCEPTANCE FOR SPECTATOR FRAGMENTS

After the interaction of ultrarelativistic heavy ions, the spectator nucleons are left in a very strange state. Before the collision the nucleons were a part of the nucleus and were interacting with other nucleons belonging to it. Then, the participating nucleons are "taken away" and the spectators are left as members of an highly unstable ensemble, which subsequently decays into lighter fragments. In order to assess the geometric acceptance of the detectors for the spectator fragments, it is assumed that all the nuclei lighter than the projectiles can possibly be produced without paying any attention to the known abundances of particular isotopes.

The AFP detector stations are positioned far away from the interaction point, therefore the first step is to check which produced debris can reach them before a potential decay. The spectators move with velocity close to the speed of light and their Lorentz factor is $\gamma = 2751$ (for the lead beam and the LHC magnets set as for 6500 GeV proton beams). Then, the proper time of a nucleus before it reaches the AFP detector is about 0.3 ns. Fig. 4 presents the half-life times of the known nuclei[†]. It is clear that the vast majority of the nuclei could reach the detectors before decaying.

[†]This and other plots in this paper are presented in a non- standard way, as a function of the atomic number Z and

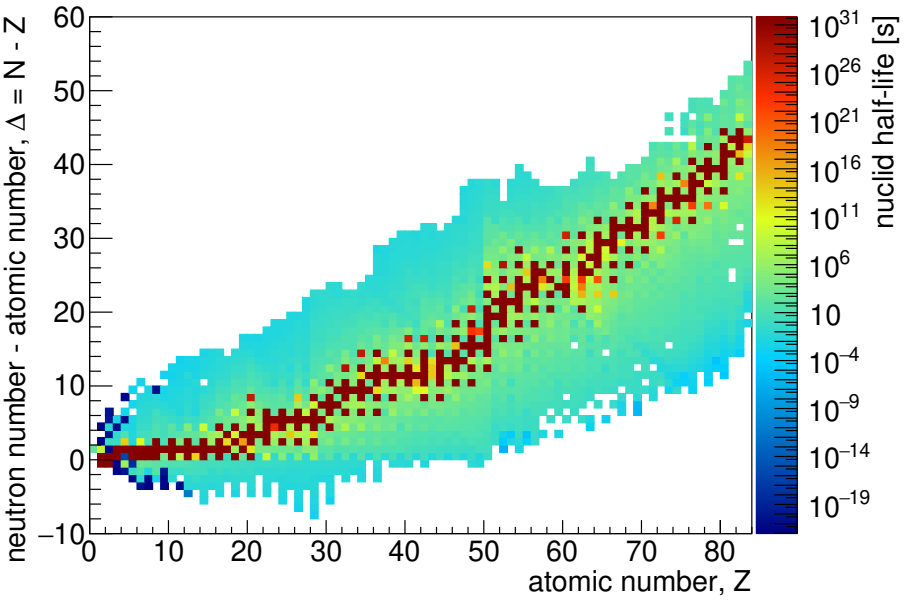

Figure 4. Half-life of known nuclei.[10]

Neglecting the internal motion of the nucleons within the nucleus energy of each of nucleons is the same and equal to the energy of the beam divided by the mass number of the beam particles: $E_N = E_b/A_b$. Assuming that the spectators are left intact in the collision, a spectator fragment with mass number A would have the energy equal to $A \cdot E_N$. The internal motion of the nucleons can be described by introducing the Fermi-gas model of a nucleus. In the rest frame of the nucleus, the density of nucleon states is given by $\mathrm{d}n \sim p^2\mathrm{d}p$. Therefore, in the simulation the absolute value of the momentum of each nucleon was randomly drawn from a quadratic distribution between zero and the Fermi momentum of 250 MeV. The direction of the momentum of each nucleon was assumed to be isotropically distributed. The momentum of a given fragment was calculated as a vector sum of the momenta of all its nucleons. Finally, the nucleus momentum was Lorentz-transformed into the laboratory frame.

Simulation of the nuclear fragments transport was done using the MAD-X program. The setting for the lead beams were deployed, obtained assuming that the beam of fully ionised ${}^{208}_{82}Pb$ ions is accelerated to the energy of 2.56 TeV per nucleon, which corresponds to 6.5 TeV energy protons. The LHC optics of $\beta^* = 0.8$ m[8] was taken, which corresponds to the LHC Run 2 heavy ion operations. Trajectories of ions different from lead were simulated by scaling their momenta to the momentum of a lead ion that would have same trajectory in the magnetic field. This procedure is possible because the trajectory in the magnetic field depends effectively on the ratio of the particle momentum to its charge.

Neglecting the spreads due to the beam emittance and the Fermi motion, a nucleus with a given A and Z will hit the AFP detectors in a well defined position. Since the dipole magnets bend the beam in the horizontal direction, then the x-coordinate of the nuclear fragment trajectory plays the major role in the present considerations. One should recall that for the safety reasons the detector is positioned at some distance with respect to the beam and that there is additional dead material of the Roman Pot floor.

Fig. 5a shows the horizontal positions of all nuclei at 211 m from the interaction point, which is in the middle between the two AFP stations. Naturally, the position of ${}^{208}_{82}Pb$ ($\Delta = 44$) and all nuclei with the same A/Z ratio (*i.e.* the same Δ/Z ratio) is equal to zero. Nuclei with less neutrons per proton are deflected outside the LHC ring, similarly to diffractive protons, thus can be registered in the AFP detectors, whereas nuclei containing more neutrons per proton are deflected towards the LHC centre escaping the detection. Nuclei with A/Z very different from that of the lead can be lost in the LHC apertures and not reach 211 m at all.

the difference of the number of neutrons, N, and the atomic number, $\Delta = N - Z = A - 2Z$, where A is the mass number.

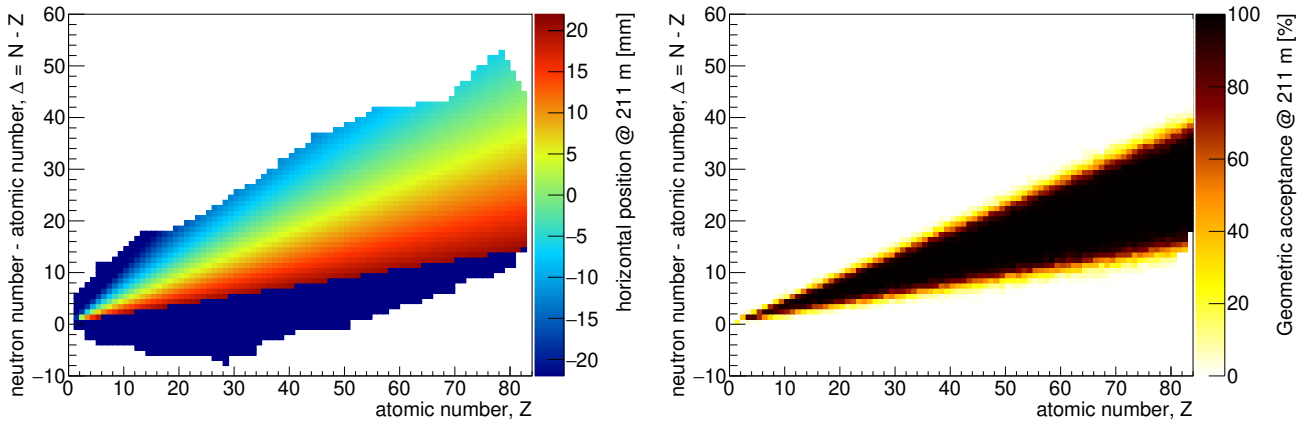

(a) (b)

Figure 5. (a) Horizontal position of nuclei at 211 m from the ATLAS interaction point. The nuclei lost in the LHC apertures are drawn in dark blue. (b) AFP acceptance for nuclear debris.

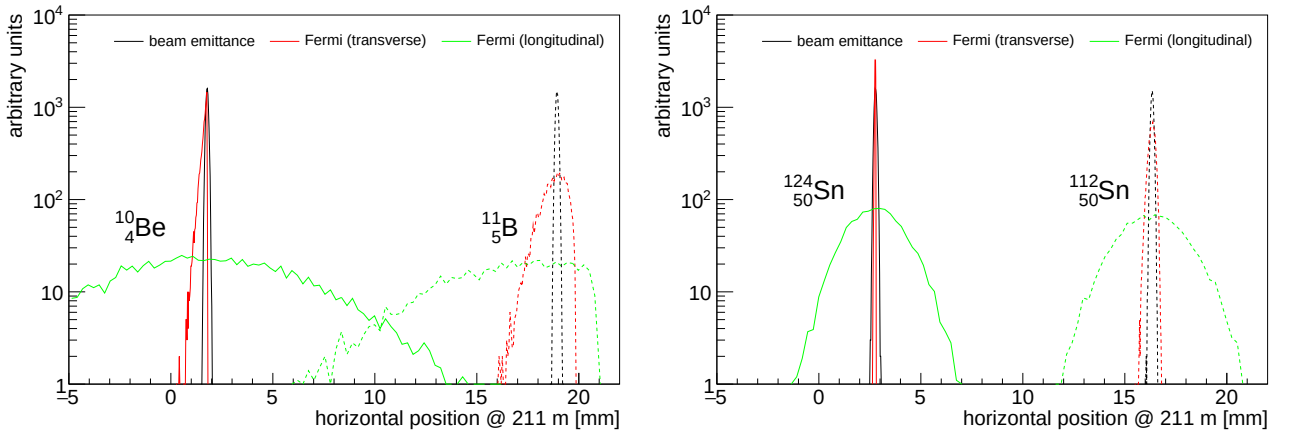

(a) (b)

Figure 6. Effects of the beam emittance and the Fermi motion on the fragment position in AFP for selected light (a) and heavy (b) nuclei.

For the emittance value of 1.233 µm,[8] the lead beams at the interaction point have the angular spread of 24 µrad, while the interaction vertex distribution has the transverse spread of 13 µm and the longitudinal one of 5.5 cm. The horizontal width of the beam at 211 m from the interaction point, σ_x, is 134 µm. This width is taken as a usual unit of the distance between the detector and the beam. In the following, it was assumed that the sensitive area of the sensor is placed 3 mm from the centre of the beam. This distance covers about $19\sigma_x$ and a 0.5 mm-long distance between the active detector edge and outer wall of the Roman Pot floor.

Fig. 5b shows the acceptance to detect a given nucleus as a function of Z and Δ. The obtained results were averaged over the distributions of the momenta discussed before and the Gaussian spreads of the LHC beams (spatial and angular).

Although, the AFP detectors were not thought to detect the nuclear debris, their acceptance covers a significant part of the nuclei spectrum. This is particularly true for the heavier nuclei, where for a given Z more than a half of known nuclei can be potentially detected. With decreasing Z value the range of the accepted masses linearly decreases.

A study of the influence of various factors on the position of the selected ions at the distance of 211 m away from the interaction point is presented in Fig. 6. As can be observed, the effects of the beam spreads and those due to the transverse component of the Fermi motion are quite small. As it was anticipated the position smearing

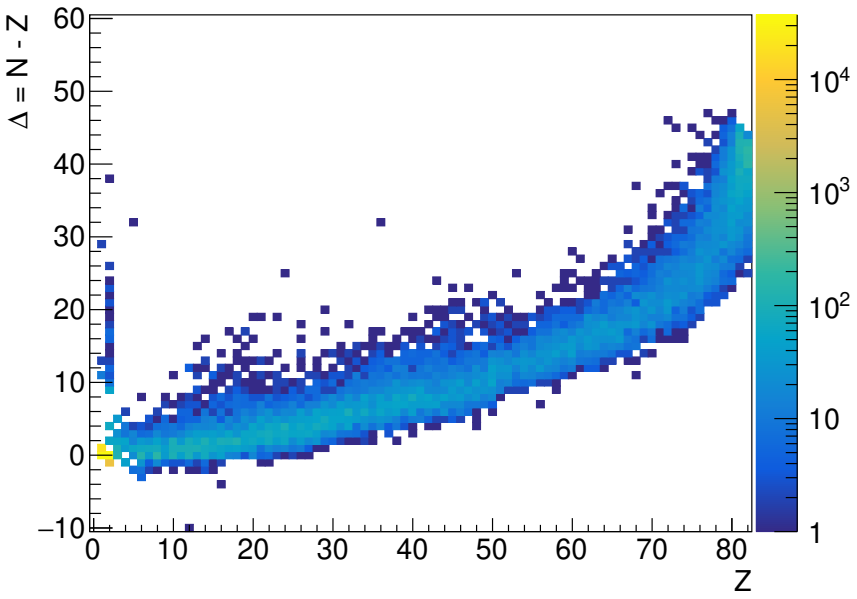

Figure 7. Abundance of nuclear fragments produced in PbPb collisions simulated using DPMJET.

is dominated by the longitudinal Fermi motion magnified by the Lorentz boost. This effect is stronger for lighter nuclear debris.

4. TOWARDS THE CENTRALITY DETERMINATION

The discussion concerning the details of the fragmentation process is outside the scope of the present study, see for example[11–15] and references therein. In order to study how the measurement of fragments can be used to get information about the central state, a simulation of PbPb collisions using the DPMJET Monte Carlo event generator[12] was performed. For each simulated event, the generator reports a list of produced particles, including the spectator fragments. The distribution of the produced fragments is presented in Fig. 7.

Each event is generated with a known, however, random value of the impact parameter. Fig. 8a presents the correlation between the impact parameter value and the sum of mass numbers of all[‡] produced nuclear fragments. As expected, there is a strong dependence between these two variables – the more peripheral the event, the more spectators are produced. However, not all fragments are within the acceptance of the forward detectors.

Fig. 8b shows the same correlation, but here the sum runs only over the fragments registered in the forward proton detectors [§]. One can notice that some correlation is still present, but it is not as strong as the one shown in Fig. 8a. In addition, a clear picture of two components added together is visible. One correlation is similar to the original one, while the other one with $\sum A$ scaled down.

The initial state of the PbPb collision is to a first approximation symmetric with respect to the p_z sign. However, the fluctuations of the ions shape and those related to the fragmentation of the spectator systems can break this symmetry. All this can cause an asymmetry between the fragments produced in the two hemispheres of a given ion-ion interaction. This is illustrated in Fig. 9 showing the correlation between the sum of A measured on the two sides. One can observe two component picture. On one side a large fraction of events with $\sum A$ on both sides correlated. The central dependence is approximately symmetric, however, very broad. In addition, a large fraction of events is characterised by extremely asymmetric values of $\sum A$ in opposite hemispheres. Based

[‡]For technical reasons, free protons and neutrons are not counted. However, the spectator neutrons still can be registered in the zero degree calorimeters.

[§]For the results based on the DPMJET simulation, the acceptance of the forward proton detectors is taken into account in an approximate way based on their A/Z ratio.

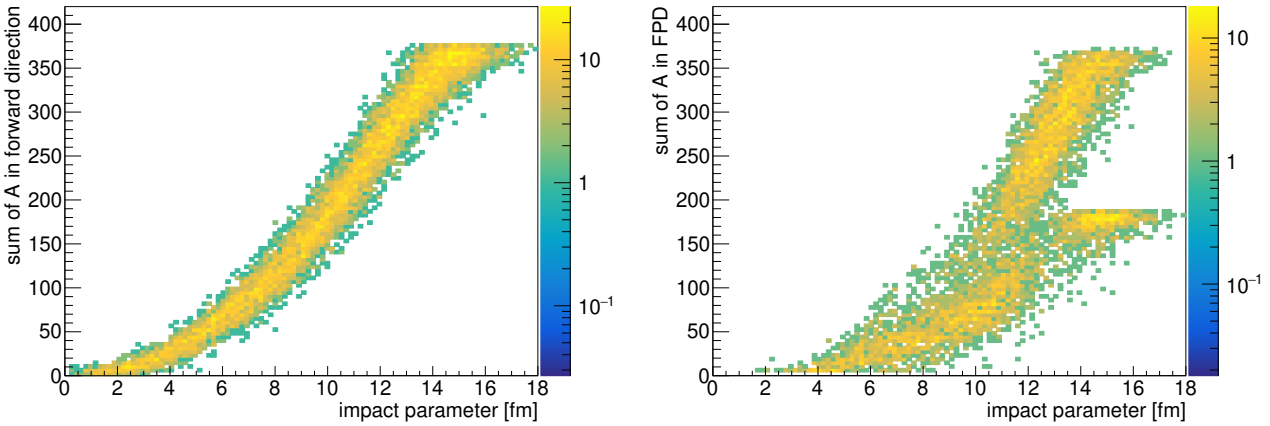

(a) (b)

Figure 8. Correlation between the impact parameter of the collision and the sum of mass numbers of: (a) all produced nuclear fragments, (b) nuclear fragments within the acceptance of forward proton detectors.

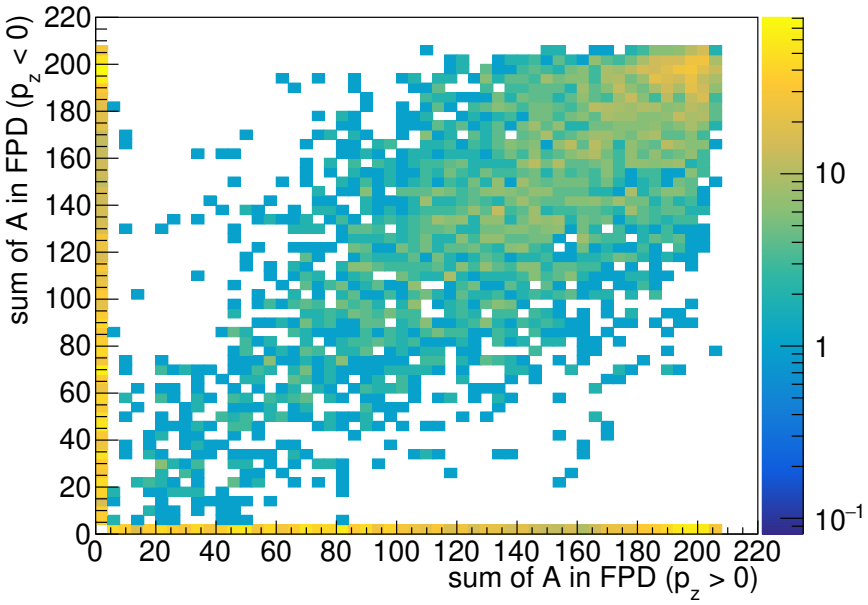

Figure 9. Correlation between the sum of mass numbers of nuclear fragments within the acceptance of forward proton detectors belonging to the oposite hemispheres of the reaction.

on this result, two classes of events can be distinguished: events with nuclear fragments measured on both sides (double tag) and only on one side (single tag). It is worth mentioning that for the double-tag events, the $\sum A$ of the fragments measured on both sides are correlated. The width of this correlation reflects the correlation between the impact parameter (common for the whole event) and the measurements on each side.

It is interesting to ask what is the probability that a given event will be of either type. This value depends on the impact parameter and is depicted in Fig. 10. For the most central events, the probability of observing any fragments in the forward detectors is to a good approximation zero. This comes from the fact that in such collisions only the lightest spectator fragments, which will escape the registration, can be formed. With increasing value of the impact parameter the probability of the single-tag events increases. However, at about 12 – 14 fm, it drops down, which corresponds to a peak in the probability for double-tag events.

Fig. 11 presents the correlations between the impact parameter and the sum of A for measured fragments for the two types of events separately. A correlation between the two variables is visible in both cases, which

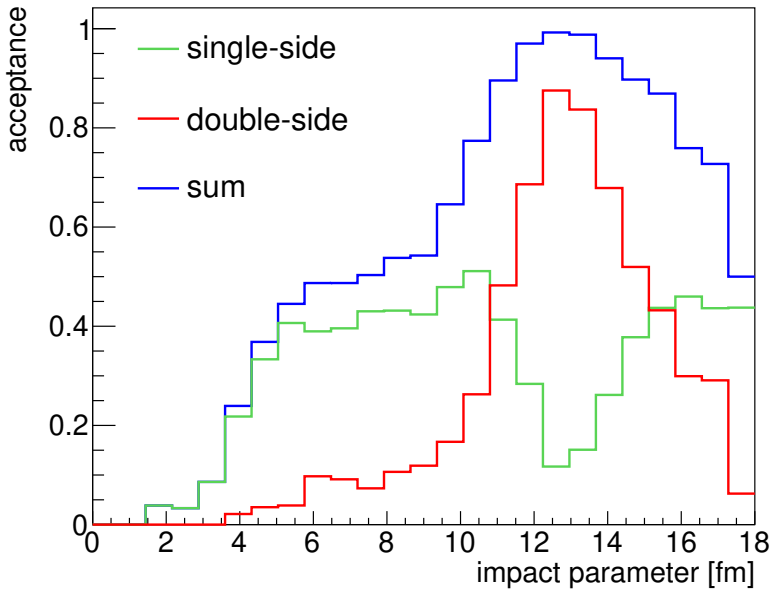

Figure 10. Acceptance for events with nuclear fragments being measured in forward proton detectors.

demonstrates that the proposed method can be used for centrality determination.

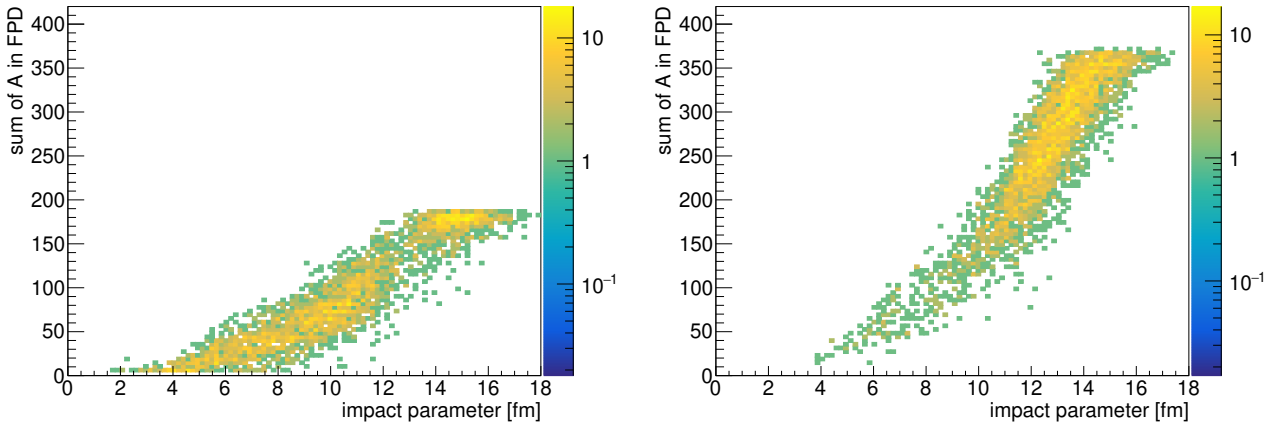

(a) (b)

Figure 11. Correlation between the impact parameter of the collision and the sum of mass numbers of nuclear fragments within the acceptance of forward proton detectors for (a) single-tag and (b) double-tag events.

5. SUMMARY AND CONCLUSIONS

In the presented study it was shown that the existing forward proton detectors at the LHC provide an interesting possibility of detecting nuclear debris emerging from the collision of two heavy ions. This possibility could be used for a measurement of abundances of various fragments produced in heavy-ion collisions.

Another interesting feature offered by such detectors is a measurement of the centrality of PbPb collisions. Different centralities result in different signals generated by the produced nuclear debris. Such a measurement would be independent of and complementary to other commonly used methods. It should be underlined that with the use of several forward detectors that would provide much larger acceptance, in comparison to the discussed case, a direct measurement of the number of spectators and hence the determination of the number of

participants could be possible, see also.[16] However, the present work shows that one can get information about the centrality even with the limited acceptance of already existing detectors.

Finally, it is worth mentioning that measurements of spectators using the Roman Pot detectors could be considered not only for ion–ion collisions, but also for proton–ion or lepton–ion interactions. However, the fragmentation of a nucleus excited by a proton or a virtual photon can be very different from the fragmentation of the spectator system discussed in this paper. Therefore, this topic requires a dedicated study to understand what could be a possible physics motivation for such measurements and what experimental setup would be needed.

ACKNOWLEDGMENTS

We gratefully acknowledge discussions with S. Tarafdar and A. Milov on these topics.
This work was supported in part by Polish National Science Center grant no. 2015/19/B/ST2/00989.

REFERENCES

[1] Evans, L. and Bryant, P., "LHC Machine," *JINST* **3**, S08001 (2008).
[2] Antinori, F. et al., "Proceedings, 27th International Conference on Ultrarelativistic Nucleus-Nucleus Collisions (Quark Matter 2018)," *Nucl. Phys.* **A982**, pp.1–1066 (2019).
[3] TOTEM Collaboration, "The TOTEM Experiment at the CERN Large Hadron Collider," *JINST* **3**, S08007 (2008).
[4] CMS-TOTEM Collaboration, "CMS-TOTEM Precision Proton Spectrometer," Tech. Rep. CERN-LHCC-2014-021, TOTEM-TDR-003, CMS-TDR-13 (Sep 2014).
[5] ATLAS Collaboration, "ATLAS Forward Detectors for Measurement of Elastic Scattering and Luminosity," Tech. Rep. ATLAS-TDR-18, CERN-LHCC-2008-004 (2008).
[6] ATLAS Collaboration, "Technical Design Report for the ATLAS Forward Proton Detector," Tech. Rep. CERN-LHCC-2015-009. ATLAS-TDR-024 (May 2015).
[7] Grinstein, S. et al., "Beam Test Studies of 3D Pixel Sensors Irradiated Non-Uniformly for the ATLAS Forward Physics Detector," *Nucl. Instrum. Meth.* **A730**, 28–32 (2013).
[8] "LHC Optics Web Home." (http://cern.ch/lhcoptics).
[9] "MAD – Methodical Accelerator Design." (https://mad.web.cern.ch/mad/).
[10] Audi, G. et al., "The NUBASE2016 evaluation of nuclear properties," *Chinese Physics* **C41** (2016).
[11] Ferrari, A., Sala, P. R., Ranft, J., and Roesler, S., "Cascade particles, nuclear evaporation, and residual nuclei in high-energy hadron - nucleus interactions," *Z. Phys.* **C70**, 413–426 (1996).
[12] Roesler, S., Engel, R., and Ranft, J., "The Monte Carlo event generator DPMJET-III," in [*Advanced Monte Carlo for radiation physics, particle transport simulation and applications. Proceedings, Conference, MC2000, Lisbon, Portugal, October 23-26, 2000*], 1033–1038 (2000).
[13] Olson, D. L. et al., "Factorization of fragment-production cross sections in relativistic heavy-ion collisions," *Phys. Rev.* **C28** (1983).
[14] Frankland, J. D. et al., "Fragment production in central heavy ion collisions: Reconciling the dominance of dynamics with observed phase transition signals through universal fluctuations," in [*Proceedings, 40th International Winter Meeting on Nuclear Physics (Bormio 2002): Bormio, Italy, January 21-26, 2002*], (2002).
[15] Jacak, V. et al., "Fragment production in intermediate energy heavy ion reactions," *Phys. Rev. C* **35**, 1751–1788 (1987).
[16] Tarafdar, S., Citron, Z., and Milov, A., "A Centrality Detector Concept," *Nucl. Instrum. Meth.* **A768**, 170–178 (2014).

Extracting the top-quark mass and Yukawa coupling from the threshold scan at CLIC

Kacper Nowak[a] and Aleksander F. Żarnecki[a]

[a]University of Warsaw, Faculty of Physics, ul. Pasteura 5, 02-093 Warsaw, Poland.

ABSTRACT

The Compact Linear Collider (CLIC) is a concept for a next-generation accelerator at CERN, colliding electrons and positrons at energies up to several TeV. One of the main goals at the initial CLIC running stage is the measurement of the top-quark mass and width in a scan of the beam energy through the pair production threshold. However, the shape of the threshold cross section depends not only on the top-quark mass but also on other model parameters as the top-quark width, top Yukawa coupling and the strong coupling constant.

We study the expected precision of the top-quark mass determination from the threshold scan. We use the most general fit approach with all relevant model parameters taken into account. In addition, we take the normalisation uncertainty into account as well as the expected constraints on the top Yukawa coupling and strong coupling constant from earlier experiments. We demonstrate that even in the most general approach the top-quark mass can be extracted with statistical precision of the order of 20 to 30 MeV. Additional improvement is expected if the running scenario is optimized. We also address the feasibility of the top Yukawa coupling determination from the threshold scan.

Keywords: CLIC project, top-quark physics, threshold scan, top-quark mass, top Yukawa coupling

1. INTRODUCTION

The research programs of the future linear e^+e^- colliders include a wide range of measurements related to top quark. Precise measurement of the top-quark mass is of particular importance, as it is essential for the understanding of the Higgs mechanism, electroweak symmetry breaking and for constraining many "new physics" scenarios. Both the International Linear Collider (ILC)[1] and the Compact Linear Collider (CLIC)[2,3] are expected to provide an opportunity to extract the top-quark mass from the measurement of the $t\bar{t}$ pair-production threshold around $\sqrt{s} = 350$ GeV. Detailed simulation studies were performed for ILC[4] and CLIC[5] showing that with cross section measurements at 10 different values of collision energy, each with 10 fb^{-1} of data, a statistical accuracy of the order of 20 MeV can be obtained on the top-quark mass. However, the shape of the threshold cross section is also sensitive to other model parameters: the top-quark width, its Yukawa coupling and the strong coupling constant. Uncertainties on these parameters together with systematic effects were shown to result in the total expected uncertainty on the top-quark mass of the order of 50 MeV.[6] However, only the two-parameter fits to the threshold scan data were considered in this study.

Discussed in this contribution is the more general approach to the top-quark mass measurement at the threshold based on the simultaneous fit of all model parameters and the normalisation, taking also the possible constraints from earlier measurements into account. We examine constraints on the data normalisation, the strong coupling constant and the top Yukawa coupling required to extract the top-quark mass with the statistical precision of the order of 30 MeV. Further improvement of the measurement should be possible by optimizing the threshold scan scenario.[7] Although the study was carried out in the framework of the CLICdp Collaboration presented results are more general and should apply to possible measurement at ILC as well.

Further author information: (Send correspondence to Kacper Nowak)
Kacper Nowak: E-mail: k.nowak27@student.uw.edu.pl
Aleksander F. Żarnecki: E-mail: zarnecki@fuw.edu.pl

Photonics Applications in Astronomy, Communications, Industry, and High-Energy Physics Experiments 2019,
edited by Ryszard S. Romaniuk, Maciej Linczuk, Proc. of SPIE Vol. 11176, 1117648
© 2019 SPIE · CCC code: 0277-786X/19/$21 · doi: 10.1117/12.2536861

2. REFERENCE SCENARIO

The first stage of CLIC will allow an energy of 380 GeV to be reached, giving access to most Higgs boson and top quark measurements.[8] In the first CLIC running stage with 1 ab^{-1} of total integrated luminosity,[9] a dedicated scan of 100 fb^{-1} is planned at the $t\bar{t}$ threshold. The baseline scenario of the threshold scan, considered for both ILC and CLIC, assumes running at 10 equidistant energy points taking 10 fb^{-1} of data for each value of $\sqrt{s}$. Example of such a measurement is presented in Fig. 1. The solid curve represents the theoretical cross section predictions including the effects of the initial state radiation (ISR) and the CLIC luminosity spectra. For the presented study the "Low Charge" luminosity spectrum optimised for the threshold scan was used.[6] Large sets of simulated measurement (pseudo-data) were generated taking into account the expected statistical uncertainties of the data points. The overall top-pair event reconstruction efficiency of 70.2%, including the relevant branching fractions, was assumed,[5] and the background contribution remaining after the event selection procedure corresponding to the cross section of 73 fb.

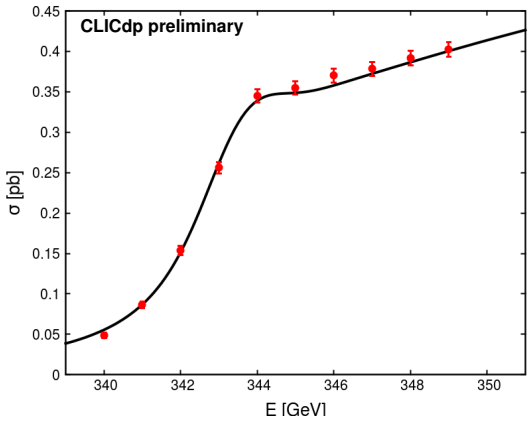

Figure 1. Reference scenario for the top-quark threshold scan. The error bars on the simulated data points show the expected statistical uncertainties of the cross section measurements assuming total integrated luminosity of 10 fb^{-1} per measurement and event selection efficiency of 70.2%.[5]

3. FIT METHOD

To calculate the cross section templates the program `QQbar_threshold`,[10] taking into account NNNLO QCD calculations[11] and other corrections[12–14] was used. The templates were generated for different values of the top-quark mass*, m_t, top-quark width, Γ_t, top Yukawa coupling (relative to the SM value), y_t, and of the strong coupling constant, α_s. Independent variations of all parameters were considered around the nominal values of $\tilde{m}_t = 171.5$ GeV, $\tilde{\Gamma}_t = 1.37$ GeV, $\tilde{y}_t = 1$ and $\tilde{\alpha}_s(M_Z^2) = 0.1185$. These templates are used to fit the parameter values to the simulated measurement results. For estimate of the theoretical uncertainties, we vary the renormalisation scale, μ, used in the cross section calculations, between 60 GeV and 120 GeV (the nominal value is $\tilde{\mu} = 80$ GeV). We also assume 2% uncertainty on the expected background cross contribution. For a proper estimate of systematic effects, the corresponding variations were only applied in the pseudo-data generation and not in the fit.

For each generated pseudo-data set and each considered cross section template the χ^2 value is calculated from the formula

$$\chi^2(\vec{p},\alpha) = \sum_i \left(\frac{m_i - \alpha\cdot\mu_i(\vec{p})}{\sigma_i}\right)^2 + \left(\frac{\alpha-1}{\Delta}\right)^2 + \sum_j \left(\frac{p_j - \tilde{p}_j}{\sigma_{p_j}}\right)^2 \quad (1)$$

where m_i and σ_i are the measured cross section values with their statistical uncertainties, $\mu_i(\vec{p})$ denotes the template cross section values for corresponding collision energies and given parameter set $\vec{p} = (m_t, \Gamma_t, \alpha_s, y_t^2)$,

*PS mass scheme[15] is used for the top-quark mass definition.

and α is the template normalisation factor. The second term in the χ^2 formula corresponds to the normalisation constraint, where we consider different values of the relative normalisation uncertainty Δ. The normalisation factor α can be evaluated for each template separately, by solving the minimisation condition $\frac{\partial \chi^2}{\partial \alpha} = 0$. The third term represents possible constraints on the model parameters p_j resulting from the earlier measurements with uncertainty σ_{p_j}. In this study, we consider possible external constraints for α_s and y_t only.

The values of the top-quark mass and other parameters can then be extracted from the fit of the polynomial χ^2 dependence on the components of $\vec{p}$

$$\chi^2_\alpha(\vec{p}) = \sum_{i=0}^{N}\sum_{j=0}^{N} A_{i,j}\, p_i p_j \tag{2}$$

where χ^2_α is the χ^2 value minimised w.r.t. normalisation factor α, N is the number of considered model parameters and i, j are parameter indexes ($i, j = 1 \ldots N$). $A_{i,j}$ is the symmetric matrix of coefficients of N-dimensional parabola. To simplify the formula, we define $p_0 \equiv 1$ (the linear part is thus given by $2A_{0,j}p_j$ and the constant part is $A_{0,0}$). The values of parameters $A_{0,0}, \ldots, A_{n,n}$ are found by solving a set of linear equations, when we use χ^2_α values calculated for different parameter sets $\vec{p}$ as input. The fitted values of $A_{0,0}, \ldots, A_{n,n}$ are then used to extract the parameter values minimising the $\chi^2_\alpha(\vec{p})$, their expected uncertainties and correlation coefficients.

Results of the two parameter fit (top-quark mass and width) to about 4000 pseudo-data sets simulated for the reference threshold scan scenario (see Fig. 1) are presented in Fig. 2. The distribution of fit results is well described by the 2-D Gaussian profile; results of the profile fit to the data are indicated by the one, two and five sigma contours[†] in Fig. 2.

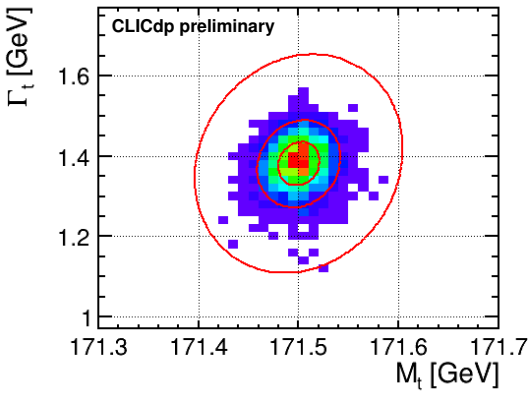

Figure 2. Results of the two-parameter fits to the top threshold scan, for sets of pseudo-data generated for nominal parameter values, $\tilde{m}_t = 171.5$ GeV and $\tilde{\Gamma}_t = 1.37$ GeV. One, two and five sigma contours represent the 2-D gaussian distribution fitted to the presented results.

4. VALIDATION

To ensure that our fit algorithm gives proper results we repeated the fit procedure for sets of pseudo-data generated with non-standard templates. Shown in Fig. 3 are the distributions of the fitted top-quark mass from the two-parameter fit (2D) and the fitted top Yukawa coupling parameter from the four-parameter fit (4D), for the pseudo-data sets generated using cross-section templates with different values of these parameters. For both the top-quark mass and Yukawa coupling variations, fit results follow very closely the input parameter values.

Shown in Fig. 4 are the distributions of the top-quark mass uncertainty and the top-quark width uncertainty, resulting from the two-parameter fits to a large set of pseudo-data generated with a nominal template. These

[†]Note that for the 2-D Gaussian distribution about 61%, 14% and 0.0004% of events are expected outside 1σ, 2σ and 5σ contours, respectively.

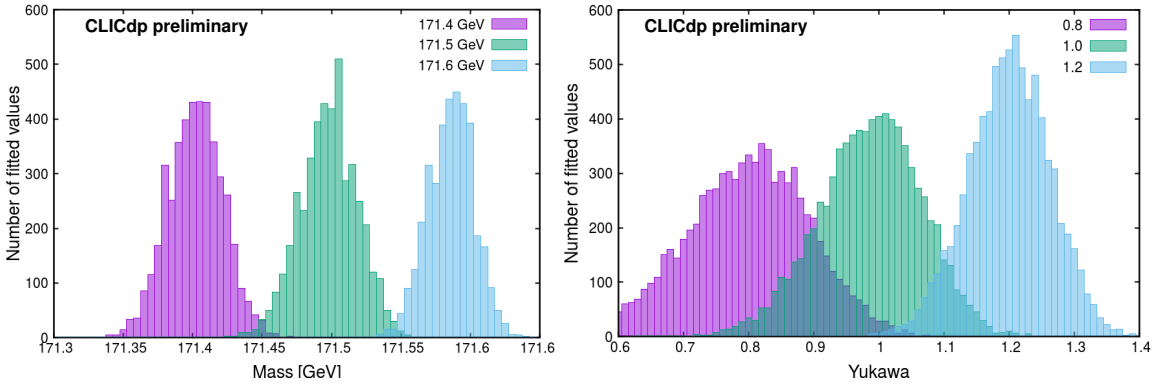

Figure 3. Histograms of fitted values for the top-quark mass (left) and top Yukawa coupling (right). Different histograms corresponds to the pseudo-data sets generated using cross-section templates with different values of the corresponding model parameter, as indicated in the plot.

uncertainties are calculated from the parameter covariance matrix, based on coefficients of the polynomial χ^2 parameterisation described by Eq. 2. In the ideal case they should match the Gaussian widths of the parameter distributions. For the considered 2-D fit configuration (top-quark mass vs top-quark width, see Fig. 2), fits to the marginalized parameter distributions result in σ_{m_t}=21 MeV and σ_{Γ_t}=54 MeV. These uncertainties are in a very good agreement with results of the previous study.[6] The uncertainties estimated from the covariance matrix of the fit tend to be systematically lower, which can most likely be attributed to the assumed shape of the χ^2 function, neglecting the possible higher-order terms. Still, we can conclude that our fit method reproduced nicely the input parameter values and gives realistic uncertainty estimates.

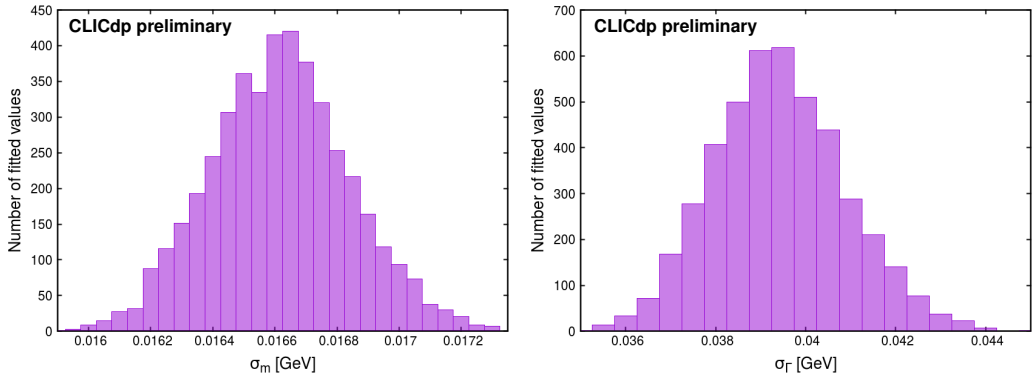

Figure 4. Distributions of the top-quark mass uncertainty (left) and the top-quark width uncertainty (right), from the two-parameter fits to a set of pseudo-data generated from the nominal template.

5. RESULTS

As mentioned above, all studies presented so far considered at most two-parameter fits to the threshold scan data. Our approach, thanks to its simple, semi-analytical form, allows us to perform fits with more free model parameters. Moreover, we can add additional constraints on the selected parameters to make the fit reflect the expected experimental situation better. The constraint that clearly influences the fit results is the assumed uncertainty on the data normalisation[‡], Δ (see Eq. 1). This influence is clearly visible in Fig. 5, which shows the expected statistical precision of the top-quark mass determination as a function of the normalisation uncertainty. Four different fit configurations are considered: two-dimensional fit of mass and width (2D), fit of mass, width

[‡]This uncertainty also includes the possible overall normalisation uncertainty of the theoretical prediction.

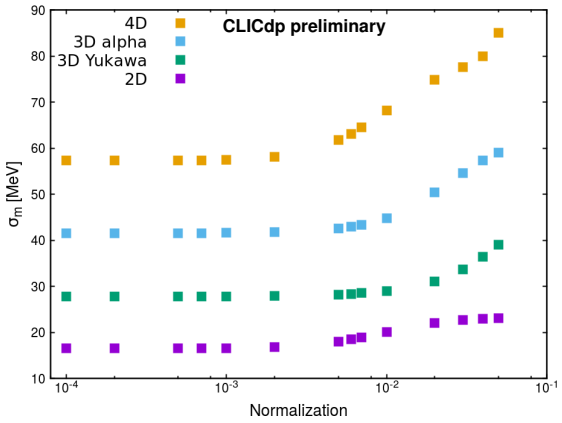

Figure 5. Statistical uncertainty on the top-quark mass as a function of the normalisation uncertainty. Four fit configurations are considered, see text for details.

and strong coupling (3D alpha), fit of mass, width and Yukawa coupling (3D Yukawa), and the simultaneous fit of the top-quark mass, width, strong coupling and Yukawa coupling (4D). Please note that normalisation is always fitted as an additional parameter, as described in Sec. 3. To allow for the most precise top-quark mass determination, the overall normalisation of the data (and theory) has to be known on sub-percent level. Also visible in Fig. 5 is the effect of adding more model parameters in the fit. While the statistical uncertainty on the top-quark mass below 20 MeV can be easily achieved when we use the 2D fit procedure (i.e. mass and width fit only), the uncertainty increases significantly when other parameters (strong coupling or Yukawa coupling) are added to the fit. However, the strong coupling constant is not a "free" parameter, and we have to take into account that it can be constrained from other measurements. This is shown in Fig. 6, where the top-quark mass uncertainty from the 3D fit (with mass, width and strong coupling as free parameters, as well as normalisation) is plotted as a function of the strong coupling and normalisation uncertainties. To be able to extract the mass with 20 MeV precision, the strong coupling constant has to be known to better than 0.0004 and uncertainty of 0.001 (current world average) would only allow to reach precision of the order of 30 MeV.

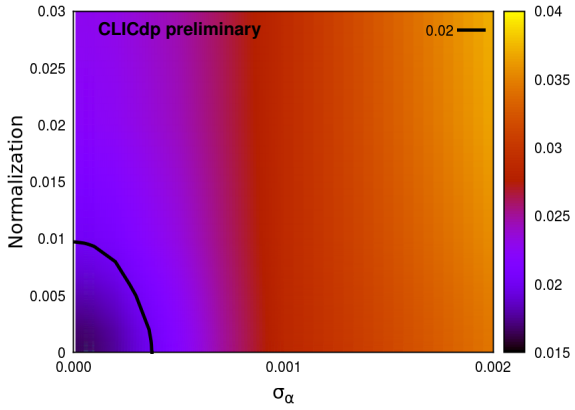

Figure 6. Expected statistical uncertainty on the top-quark mass as a function of the uncertainty of strong coupling constant and normalisation. Results from the fit of mass, width and the strong coupling (3D). Color maps are obtained using a linear interpolation algorithm.

The conclusions change significantly, if we include Yukawa coupling as an additional parameter in the fit. As shown in Fig. 7 (left), if no constraints are imposed on Yukawa coupling, the top-quark mass can not be extracted

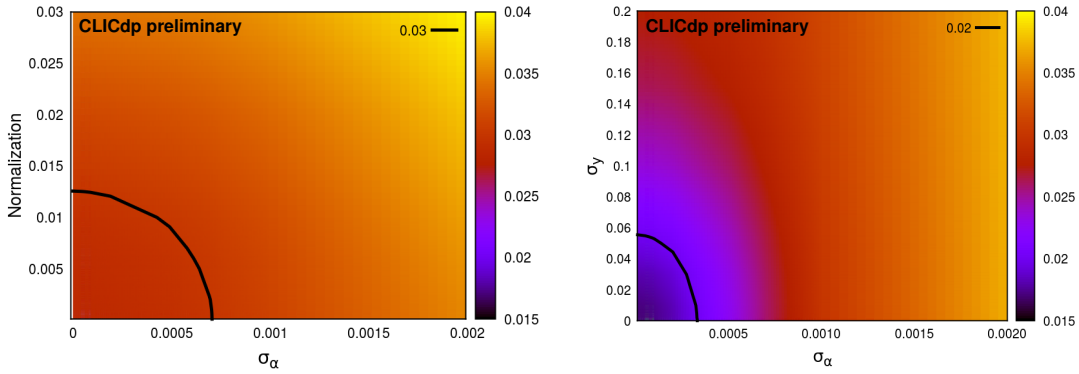

Figure 7. Expected statistical uncertainty on the top-quark mass from the fit involving all considered model parameters (4D). Left: as a function of the strong coupling constant and normalisation uncertainties, assuming no constraints on the Yukawa couplin. Right: as a function of the strong coupling constant and Yukawa coupling uncertainties, assuming normalisation uncertainty, $\Delta = 10^{-3}$.

with precision better than 28 MeV, even for negligible uncertainties in normalisation and strong coupling (refer also to Fig. 5). To be able to extract the mass with precision of the order of 20 MeV, Yukawa coupling has to be constrained from other measurement to about 5% and the strong coupling constant has to be known to better than 0.0003.

As the top-quark pair-production cross section depends on the top Yukawa coupling, the threshold scan data can also be used to constrain its value. We studied the statistical precision of the Yukawa coupling determination from the 4D fit as a function of the assumed normalisation and strong coupling uncertainties. Results presented in Fig. 8 indicate that contribution from the Yukawa coupling can be observed with high significance (above 5σ, i.e. with statistical precision below 0.2). Assuming the normalisation is known at per-mille level and the strong coupling is independently measured to better than 0.0003, statistical precision on the Yukawa coupling of the order of 10% should be feasible.

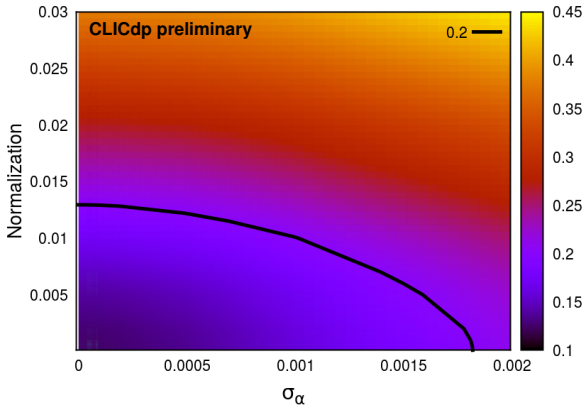

Figure 8. Expected statistical uncertainty on the top Yukawa coupling from the fit involving all considered model parameters (4D), as a function of the strong coupling constant and normalisation uncertainties. The black line indicates the parameter range where we can expect 5σ significance.

6. SYSTEMATIC EFFECTS

The systematic uncertainties of the threshold cross section measurements are likely to limit the ultimate precision of the top-quark mass determination. Various sources of uncertainties have been investigated[6] and the combined systematic uncertainties on the top-quark are expected to be in the range 30 MeV to 50 MeV. Here, we estimate the size of systematic effects in the top Yukawa coupling determination from the threshold scan. We repeated the 4-D fit procedure for pseudo-data sets generated with different systematic variations, as discussed in Sec. 3. Results are presented in Fig. 9. Variation of the renormalisation scale, μ, has a negligible effect on the Yukawa coupling fit results. However, the assumed uncertainty on the background contribution of 2% results in about 15% systematic uncertainty in the determination of the top Yukawa coupling. One can conclude that the systematic effects will be important for constraining the top Yukawa coupling from the threshold scan and should be studied in more detail.

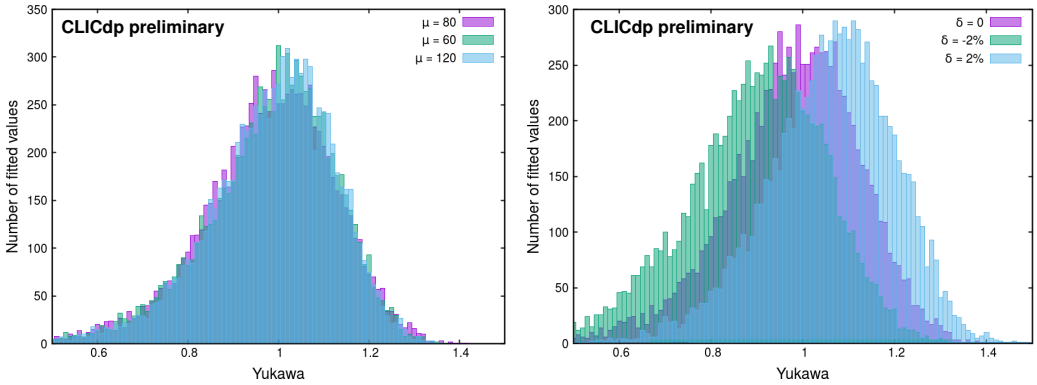

Figure 9. Histograms of the fitted top Yukawa coupling from the fits involving all considered model parameters (4D). Different histograms correspond to the pseudo-data sets generated with systematic variations of the renormalisation scale μ (left) and of the background level (right), as indicated in the plot.

7. CONCLUSIONS

We presented the general approach to the analysis of the top-quark pair-production threshold scan results, which is used to extend the results of the recent CLICdp study.[6] A simultaneous fit of all relevant model parameters and normalisation is performed, taking into account possible constraints from other measurements. Results based on large sets of simulated measurements show that the statistical precision of top-quark mass measurement of the order of 30 MeV can be easily obtained, while reducing this uncertainty further is only possible, if uncertainties on the normalisation, strong coupling constant and the Yukawa coupling are sufficiently low. In particular, to reduce the statistical uncertainty to the level of 20 MeV, the Yukawa coupling needs to be known to about 5%.

Top threshold scan data can be also used to constrain the top Yukawa coupling. Statistical precision of the order of 10% can be obtained, provided the normalisation is known at per-mille level and the strong coupling to better than 0.0003. If this is the case, determination of the Yukawa coupling from the threshold scan data will be limited by theoretical uncertainties and systematic effects.

ACKNOWLEDGMENTS

This work was carried out in the framework of the CLICdp Collaboration. We are grateful to collaboration members for fruitful discussions and comments received to the manuscript.

REFERENCES

[1] "The International Linear Collider Technical Design Report - Volume 2: Physics," (2013). ILC-Report-2013-040, arXiv:1306.6352.

[2] Linssen, L. et al., eds., [*Physics and Detectors at CLIC: CLIC Conceptual Design Report*], CERN (2012). CERN-2012-003.

[3] Charles, T. K. et al., "The Compact Linear Collider (CLIC) - 2018 Summary Report," *CERN Yellow Rep. Monogr.* **1802**, 1–98 (2018).

[4] Horiguchi, T., Ishikawa, A., Suehara, T., Fujii, K., Sumino, Y., Kiyo, Y., and Yamamoto, H., "Study of top quark pair production near threshold at the ILC." `arXiv:1310.0563` (2013).

[5] Seidel, K., Simon, F., Tesar, M., and Poss, S., "Top quark mass measurements at and above threshold at CLIC," *Eur. Phys. J.* **C73**, 2530 (2013).

[6] Abramowicz, H. et al., "Top-Quark Physics at the CLIC Electron-Positron Linear Collider." `arXiv:1807.02441` (Submitted to JHEP) (2018).

[7] Nowak, K. and Zarnecki, A. F., "Prospects for improving top-quark mass measurement precision at future e+e- colliders," *Proc.SPIE* **10808**, 10808 – 10808 – 8 (2018).

[8] Boland, M. J. et al., "Updated baseline for a staged Compact Linear Collider." CERN-2016-004, `arXiv:1608.07537` (2016).

[9] Robson, A. and Roloff, P., "Updated CLIC luminosity staging baseline and Higgs coupling prospects." CLICdp-Note-2018-002, `arXiv:1812.01644` (2018).

[10] Beneke, M., Kiyo, Y., Maier, A., and Piclum, J., "Near-threshold production of heavy quarks with QQbar_threshold," *Comput. Phys. Commun.* **209**, 96–115 (2016).

[11] Beneke, M., Kiyo, Y., Marquard, P., Penin, A., Piclum, J., and Steinhauser, M., "Next-to-Next-to-Next-to-Leading Order QCD Prediction for the Top Antitop S-Wave Pair Production Cross Section Near Threshold in e^+e^- Annihilation," *Phys. Rev. Lett.* **115**(19), 192001 (2015).

[12] Beneke, M., Maier, A., Piclum, J., and Rauh, T., "Higgs effects in top anti-top production near threshold in e^+e^- annihilation," *Nucl. Phys.* **B899**, 180–193 (2015).

[13] Beneke, M., Piclum, J., and Rauh, T., "P-wave contribution to third-order top-quark pair production near threshold," *Nucl. Phys.* **B880**, 414–434 (2014).

[14] Beneke, M., Jantzen, B., and Ruiz-Femenia, P., "Electroweak non-resonant NLO corrections to $e^+e^- \to W^+W^-b\bar{b}$ in the $t\bar{t}$ resonance region," *Nucl. Phys.* **B840**, 186–213 (2010).

[15] Beneke, M., "A Quark mass definition adequate for threshold problems," *Phys. Lett.* **B434**, 115–125 (1998).

Preliminary mechanical analysis of the COMPASS-U Central Solenoid

P. Wąchal[a], J. Błocki[a], J. Hromadka[b], P. Hacek[b], D. Sestak[b], V. Balner[b], R. Panek[b],

[a]Institute of Nuclear Physics of the Polish Academy of Sciences, ul. Radzikowskiego 152 31-342 Cracow, Poland
[a]Institute of Plasma Physics of the Czech Academy of Sciences, Za Slovankou 1782/3, 182 00 Praha, Czech Republic

ABSTRACT

The COMPASS-U (Bt = 5 T, Ip = 2 MA, R = 0.894 m, a = 0.27 m) will be the successor of the COMPASS tokamak which is the main experimental facility of the Tokamak Department at the Institute of Plasma Physics of the Czech Academy of Sciences. The mail goals of this project will be to enlarge the COMPASS operational space and improve its performance. Additionally, COMPASS-U will examine some of the important challenges in the Plasma Exhaust Physics (PEX).

The COMPASS Upgrade requires a new design of the whole structure of the device. Central Solenoid is one of the most important parts of the tokamak in the design process. In this paper we present preliminary stage of Central Solenoid mechanical analysis. Mechanical analysis using Finite Element Method (FEM) includes calculations with 2D axisymmetric numerical model of the one layer of full conductor and conductor with cooling holes configurations. Furthermore, mechanical analyses of the whole stack of eight coils in different configurations are presented. The analysis takes into account the most vital phases of the magnet's operation like cooling down and powering of the magnet. Results for stack of eight coils are presented for scenario: premagnetization of coils (t=3.26 s) without plasma. Calculated scenario is an extreme case of loading for maximal possible parameters. Optimization of mechanical design was not done yet and it is planned in further steps of tokamak design.

Keywords: COMPASS-U, tokamak, finite element method, mechanical analysis

1. INTRODUCTION

The COMPASS Upgrade is a project which has a purpose to upgrade an existing tokamak at Institute of Plasma Physics of the Czech Academy of Sciences (IPP CAS). This will allow to enlarge operational space and improve performance of COMPASS device. The COMPASS-U tokamak will replace the existing device and will use infrastructure from its predecessor[1]. This project is foreseen in the European fusion program, and also in world-wide program after shut-down of Alcator C-Mod. The COMPASS-U tokamak will represent a versatile device which has an advantage for scaling towards ITER (International Thermonuclear Experimental Reactor) and DEMO (DEMOnstration Power Station)[1]. Moreover, COMPASS-U allows to achieve of H-mode of plasmas configuration and it is relevant for further ITER study[2]. Additionally, from scientific side this project will be very important.

The relevant parameters of COMPASS-U are: major radius 0.894 m, minor radius 0.27 m, plasma current 2 MA and toroidal field 5 T. One of the most important systems of COMPASS-U is magnet system. The COMPASS-U magnet system will include toroidal field (TF) coils, poloidal field (PF) coils and central solenoid (CS) coils. For the conductor material in TF, PF and CS coils oxygen-free high conductivity (OFHC) copper will be used. Use of this type of material and cooling down to liquid nitrogen temperature (LNT) give possibility to minimalize energy requirements and decrease of Ohmic losses[1]. This paper shows a development of the central solenoid design as one of the most import parts of the magnet system as well as of the whole structure of the tokamak. In order to investigate proposed geometry of the central solenoid the preliminary mechanical analysis was performed. For this reason 2D axisymmetric analysis was conducted for different configurations of conductor. Results from mechanical analysis show stresses and displacements caused by cooling down and powering of the magnet. Pre-compression of magnet at this stage of design is not taken into consideration.

Photonics Applications in Astronomy, Communications, Industry, and High-Energy Physics Experiments 2019, edited by Ryszard S. Romaniuk, Maciej Linczuk, Proc. of SPIE Vol. 11176, 1117649
© 2019 SPIE · CCC code: 0277-786X/19/$21 · doi: 10.1117/12.2536881

2. CENTRAL SOLENOID

At this stage of design of the central solenoid it is assumed that this magnet comprises eight coils (modules) with oxygen-free high conductivity copper conductor material. Each coil is pancake wound with a single OFHC conductor. The central solenoid must provide sufficient amount of the volt-seconds needed to induce and maintain adequate plasma current. This type of magnet provides total magnetic flux up to 5.2 Vs to create plasma current up to 2 MA[1]. In the previous approaches of design some cases with different coils configurations were checked i.e. with six coils in the central solenoid structure. The cooling of the coils to LNT is foreseen by holes inside the conductor in each turn. Each coil will have its own current leads. In the assembly of the CS inserts from G-10 between particular modules will be foreseen as one of the possible materials for this application. Whereas, ceramic inserts on the top and bottom of central solenoid are predicted. The main role of this ceramic inserts will be provide pre-stress in central solenoid. To fulfill space between each turn in coils and provide electrical insulation use of insulation is needed. Eight stacks of the central solenoid coils are closed into inner and outer tube which will be simultaneously a cover of the CS. The general view of the cross section of COMPASS-U tokamak model is depicted in Figure 1.

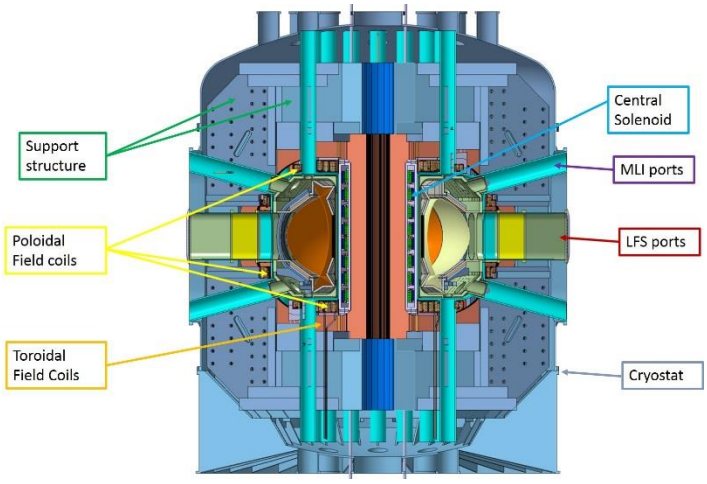

Figure 1. General view of the cross section of COMPASS-U tokamak.

3. MECHANICAL ANALYSIS FOR ONE CONDUCTOR LAYER

3.1 2D Finite element model of the one conductor layer

The 2D finite element model was prepared based on the current central solenoid geometry which was designed at Institute of Plasma Physics of the CAS. First stage of the preliminary analysis includes two cases: 1) one conductor layer with holes and insulation and 2) one full conductor layer with insulation. Finite element models used in the analysis are depicted in Figure 2 and Figure 3. The main dimensions for all cases are inner radius IR, outer radius OR of the layer, height h, width w of the conductor and radius of the cooling holes r. The thickness of the epoxy layers is 1 and 3 mm in axial and radial directions, respectively. These dimensions are presented in Table 1.

Table 1. Main dimensions of used models.

Parameter	Case 1)	Case 2)
IR [mm]	380	380
OR [mm]	465	465
Conductor height h [mm]	21	21
Conductor width w [mm]	19	19
Hole radius r [mm]	4.5	-

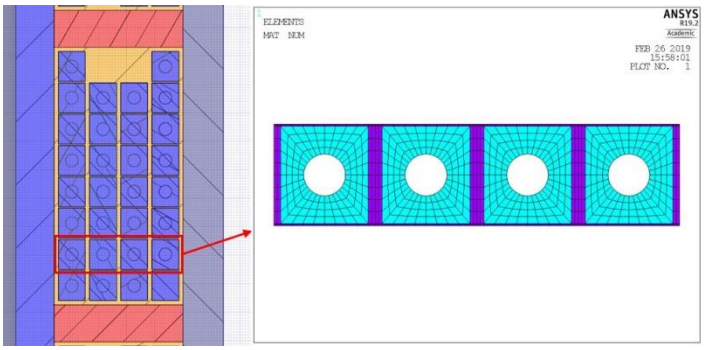

Figure 2. Finite element model of the one conductor layer with holes and insulation.

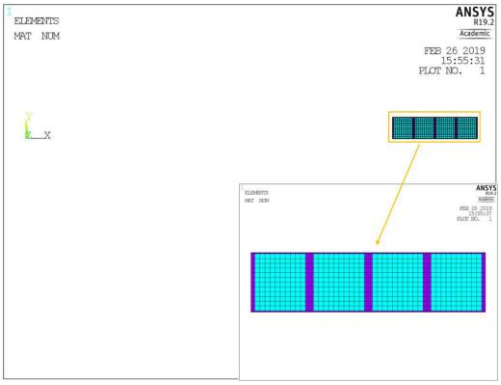

Figure 3. Finite element model of the one full conductor layer with insulation.

For calculations the ANSYS APDL code was used[3]. The PLANE182 element type was used in mechanical analysis which has ability to model 2D axisymmetric structures. Mentioned feature was used for modeling axisymmetric model for one layer. This element type has four nodes and displacements in X and Y direction as degrees of freedom[3].

3.2 Material properties

At this stage of the mechanical analysis for conductor material the OFHC copper[4] was chosen and for epoxy the Permaglass was used[5]. Material properties which were utilized in this analysis are shown in Table 2.

Table 2. Material properties used in the analysis.

Material	Material property	Value
OFHC copper	E [GPa]	130
	ν [-]	0.31
	ρ [kg/m^3]	8900
Permaglass xe - type xe2/1	E [GPa]	42
	ν [-]	0.3
	ρ [kg/m^3]	2100

Using OFHC copper as a conductor and cooling down to LNT gives low Ohmic losses which affect on achievable magnetic field[1].

3.3 Loads and boundary conditions

First, preliminary mechanical analysis was done for two cases of the one conductor layer. This approach is useful to gain knowledge about deformation and stress states in these cases and should give conclusions which will be helpful for the further analysis of the eight coil stack. Moreover, this approach is needed to check the method of application of the volumetric force loading. At this stage the only load from electromagnetic volumetric force in radial direction was considered. In these cases, integral radial load from a volumetric radial load is equal to F_{total}= 15.2 MN for whole 14 layers in the coil. Only 1/14 part of F_{total} was used because calculations were conducted for one layer. Between integral radial load and volumetric radial load there is a dependency:

$$F_{total} = \int_v F_{vol,r}(r)\,dV \tag{1}$$

The volumetric radial force distribution is given by equation:

$$F_{vol,r}(r) = \frac{F_{vp}}{(OR - IR)} \cdot (OR\text{-}r) \tag{2}$$

We assume that $F_{vol,r}(OR) = 0$ and $F_{vol,r}(IR) = Fvp$ and the function $F_{vol,r}(r)$ is linear. After substitution (2) into (1) we get:

$$F_{total} = F_{vp} \int_v \frac{OR\text{-}r}{OR\text{-}IR} dV \tag{3}$$

Where $F_{vol,r}(r)$ is the electromagnetic volumetric force distribution in radial direction, r is the radius at particular point and OR, IR are outer and inner radius, respectively. F_{vp} is the peak value of volumetric force. For case with full conductor, equation (3) can be directly calculated, but for more complex shapes this approach could bring some difficulties in the solution. Consequently, equation (1) can also be expressed in the numerical approach:

$$F_{total} = F_{vp} \sum_{i=1}^{en} \frac{OR\text{-}r_i}{OR\text{-}IR} \Delta v_i \tag{4}$$

To determine maximum value of F_{vp}, F_{total} should be divided by expression of sum $\sum_{i=1}^{en} \frac{OR\text{-}r_i}{OR\text{-}IR} \Delta v_i$. Then, calculated value of F_{vp} can be introduced to equation (2). Electromagnetic analysis was done at Institute of Plasma Physics of the CAS to calculate needed electromagnetic loads in mechanical analyses. As boundary conditions displacement in axial direction at the bottom of the turn was blocked for two cases. Loads and boundary conditions are depicted in Figure 4.

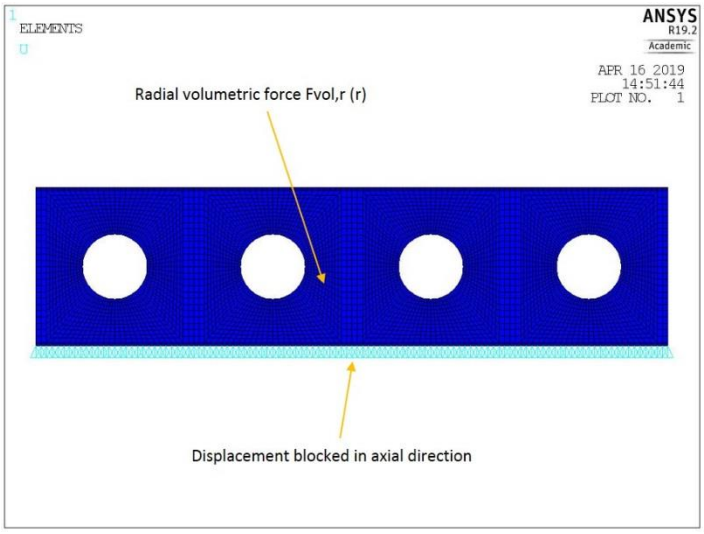

Figure 4. Loads and boundary conditions used in the analysis.

3.4 Results

Calculations were done for two cases 1) one conductor layer with holes and insulation, and 2) one conductor layer with insulation. Results in map of hoop stresses and radial displacements are shown in Figure 5 and Figure 6.

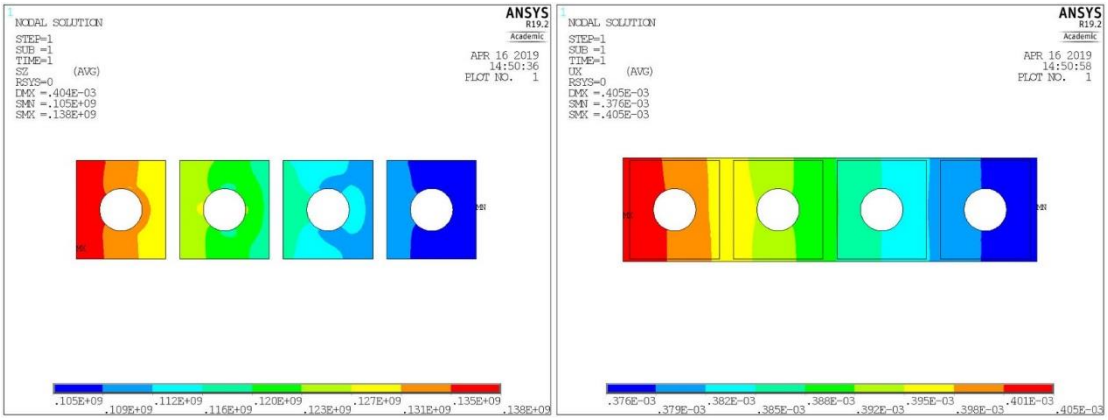

Figure 5. Hoop stress and radial displacement for case 1.

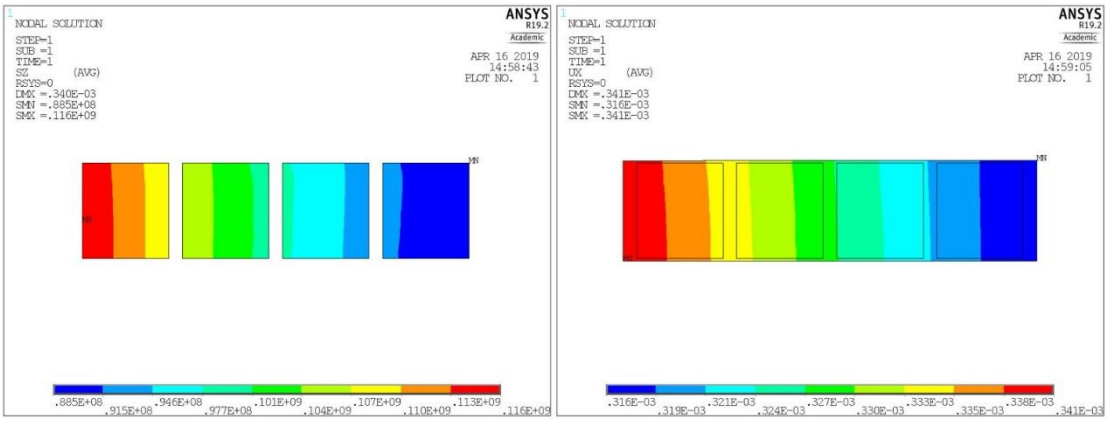

Figure 6. Hoop stress and radial displacement for case 2.

Table 3. Results for two cases presented as a maximum values of hoop stress and radial displacement.

Case	Max hoop stress [MPa]	Max radial displacement [mm]
Case 1	138	0.40
Case 2	116	0.34

In Table 3 maximum hoop stresses and radial displacements are shown. Comparing volumes for each of the coils it can be noted that for case 1 this value is $3.5614 \cdot 10^{-3}$ m^3 and for case 2 is equal to $4.2368 \cdot 10^{-3}$ m^3, respectively. Hoop stresses for case 1 are higher than for case 2 because of smaller volume of the conductor and by this smaller amount of material which withstands electromagnetic force. Similar to hoop stresses the radial displacements for case 1 are higher than in case 2. Von Mises stresses are 139 and 117 MPa, for case 1 and case 2, respectively. Stress results show that for this type of loads plastic deformation does not occur (yield strength for OFHC copper is equal to 324 MPa[4]). This analysis shows what order of magnitude are stresses in above cases. Application of cooling holes can improve cooling of conductor but increases the risk of higher stresses in case with only electromagnetic load.

4. MECHANICAL ANALYSIS OF THE CENTRAL SOLENOID

4.1 Geometry and 2D finite model of central solenoid

Next step of the preliminary mechanical analysis was to calculate the eight coils in stack configuration. Finite element model was based on the geometry which was prepared at IPP CAS. Geometry of CS is shown in Figure 7. The structure of the CS includes among others inner legs of TF coils, inner and outer tubes which will enclose impregnated coils, inserts from G-10 (or other selected material) which are responsible for transmission of axial force between coils. Space between each conductor turn will be filled by insulation which at this stage is in the phase of selection of a suitable material.

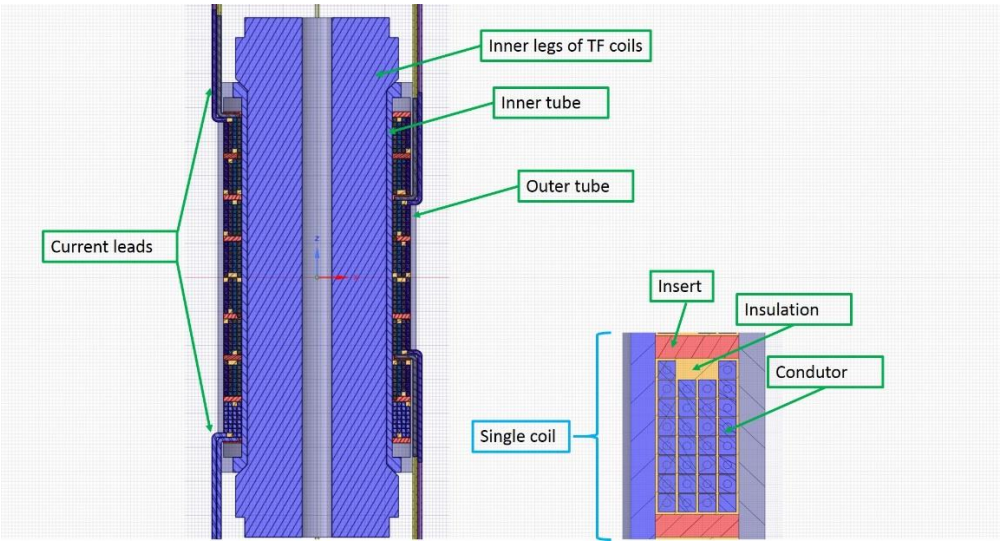

Figure 7. Cross section of the central solenoid and single coil.

Numerical model with eight coils with mesh is shown in Figure 8. Between coils inserts from G-10 material were modeled. Each insert is 26 mm thick and 91 mm wide. Only in the middle of the central solenoid insert is not modeled like in CAD model. Current leads are not modeled in this analysis.

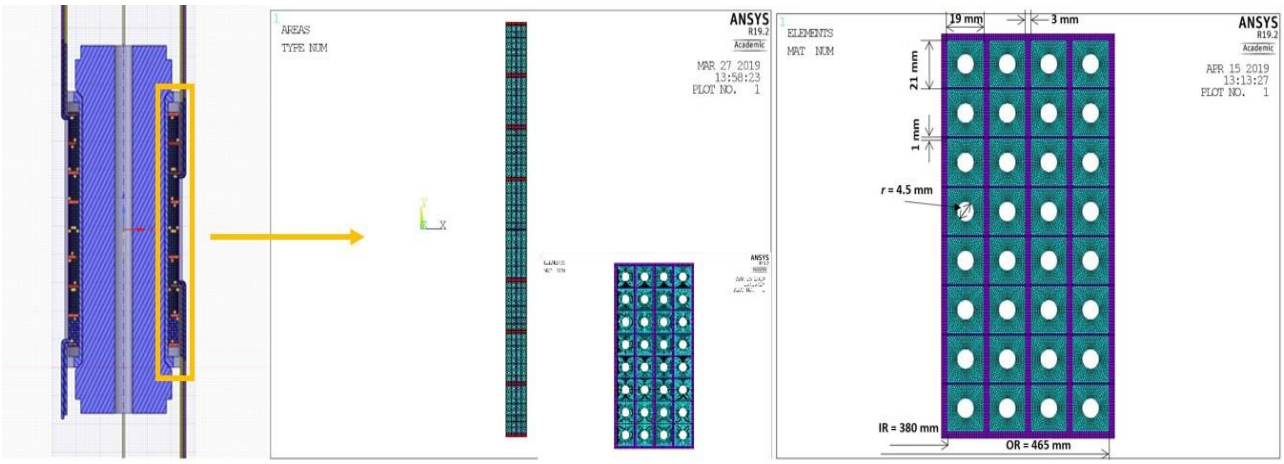

Figure 8. Cross section of central solenoid (CAD model) and finite element model of eight coils stack (with zoom on the one coil view).

In Table 4 main dimensions of the eight coil stack are shown. Inner and outer radius was counted from inner and outer edge of the extreme conductors. Also, in Table 4 radius of cooling holes is shown.

Table 4. Main dimensions of the eight coil stack and conductor.

Parameter	Eight coils
IR [mm]	380
OR [mm]	465
Height h [mm]	1656
Width w [mm]	85
Hole radius r [mm]	4.5

Conductor have dimensions 19 mm width and 21 mm height. Each of conductor turn has the same cross section for particular holes configuration. Similarly, dimensions of the G-10 layers were used. G-10 layer between coil turns has 3 mm and 1 mm thick in radial and axial direction, respectively. In case with elliptical holes, dimensions of ellipse are 10 mm major axis which is aligned in axial direction (cooling holes are elongated in axial direction) and 8.1 mm minor axis which is belonging to radial direction. Also, as in case with one conductor layer the PLANE182 was used to simulate 2D axisymmetric magnet structure[3].

4.2 Material properties

Material properties used in preliminary analysis are described in Table 5. Isotropic material properties were assumed for OFHC copper and orthotropic for G-10 which was selected as an epoxy layer and inserts[6,7]. For OFHC copper elastic properties was selected at room temperature (RT)[8]. This analysis contains thermal load because of cooling down of a CS structure. Thus, is needed to determine mean thermal expansion from RT to LNT (300-80 K range) for each used material. Mean thermal expansion at RT to LNT is shown in Table 5. This parameter was obtained for above mentioned range for OFHC copper and G-10 materials based on the literature[6,8].

Table 5. Material properties used in eight stack analysis.

Material	Material property	Value at 300 K	Value at 300-80 K range
OFHC copper	E [GPa]	125	-
	ν [-]	0.346	-
	ρ [kg/m^3]	8900	-
	α [10^{-6}/K]	-	14
G-10	E_x [GPa]	16.5	-
	E_y [GPa]	16.5	-
	E_z [GPa]	18.6	-
	ν_{xy} [-]	0.2	-
	ν_{xz} [-]	0.2	-
	ν_{yz} [-]	0.2	-
	G_{xy} [GPa]	6.87	-
	G_{xz} [GPa]	7.75	-
	G_{yz} [GPa]	7.75	-
	α_x [10^{-6}/K]	-	9.65
	α_y [10^{-6}/K]	-	28.97
	α_z [10^{-6}/K]	-	9.65
	ρ [kg/m^3]	1800	

4.3 Loads and boundary conditions

To closer study mechanical behavior of CS with an extended number of loads, the eight coils stack was modeled and particular coils were loaded by volumetric radial force in radial and axial directions. Each coil has its own load which is a result of acting magnetic field. In Figure 9 magnetic field distribution for scenario premagnetization of coils, no plasma and description of coils in CS with boundary conditions has been shown. Among three plasma scenarios (others are: End of flat-top, no plasma; and End of flat-top, 2MA plasma disruption) this one is marked by the largest forces acting on the CS in radial directions.

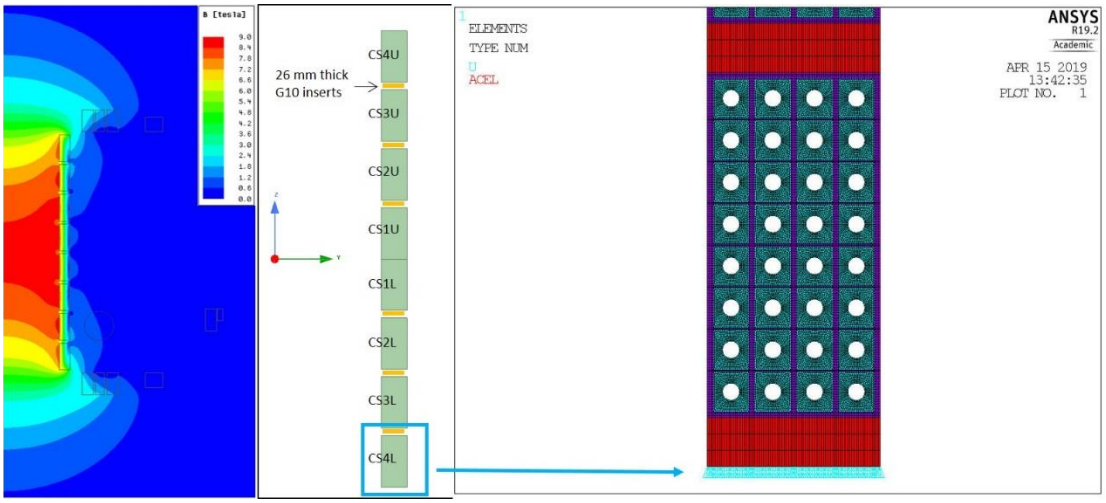

Figure 9. Magnetic field distribution with description of particular coils in CS structure and boundary conditions in coils stack.

Table 6. Electromagnetic force values in radial and axial directions for particular coils of CS.

Parameter	F_R [N]	F_z [N]
CS1L	1.53E+07	3.06E+05
CS1U	1.53E+07	-3.06E+05
CS2L	1.50E+07	1.11E+06
CS2U	1.50E+07	-1.11E+06
CS3L	1.41E+07	2.77E+06
CS3U	1.41E+07	-2.77E+06
CS4L	1.26E+07	8.33E+06
CS4U	1.26E+07	-8.33E+06

The highest values of volumetric forces in radial direction are in central part of the CS (CS1L and CS1U coils, depicted in Figure 9). This is due to the highest magnetic field in this part of magnet as is it shown in Figure 9. In this scenario coils are loaded symmetrically in axial direction, so globally axial net force is equal to zero. In Table 6 radial and axial electromagnetic force values are depicted. The same way of application of radial volumetric force was used as was described in Chapter 3.3. Axial force is independent from radius, so axial volumetric load is calculated as F_z divided by particular coil volume. The analysis was done without pre-compression step. Calculations take into account three kind of loads: cooling down from RT to liquid nitrogen temperature (thermal load TL), volumetric forces in radial and axial directions (EM) and self-weight (SW). The whole structure of eight coil stack was simply supported at the bottom side (displacements blocked in axial direction). Simple support was used for both cases with different shape of holes.

4.4 Results

Thermal and electromagnetic loads have significant contribution to stress state of the CS structure. To check stress and displacement states at these conditions analysis for RT and LNT was performed. Additionally, self-weight was considered. Two cases were taken into account: coils with conductor with circular cooling holes and coils with elliptical cooling holes.

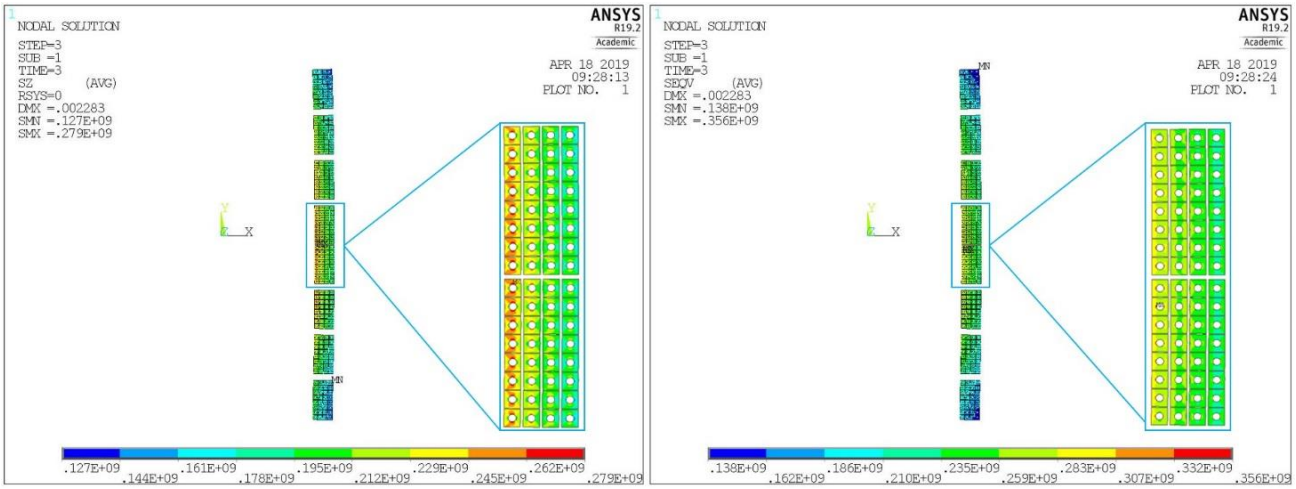

Figure 10. Hoop stress and von Mises stress for the conductor at RT (TL+EM+SW) – conductor with circular cooling holes (with zoom in CS1L/CS1U coils).

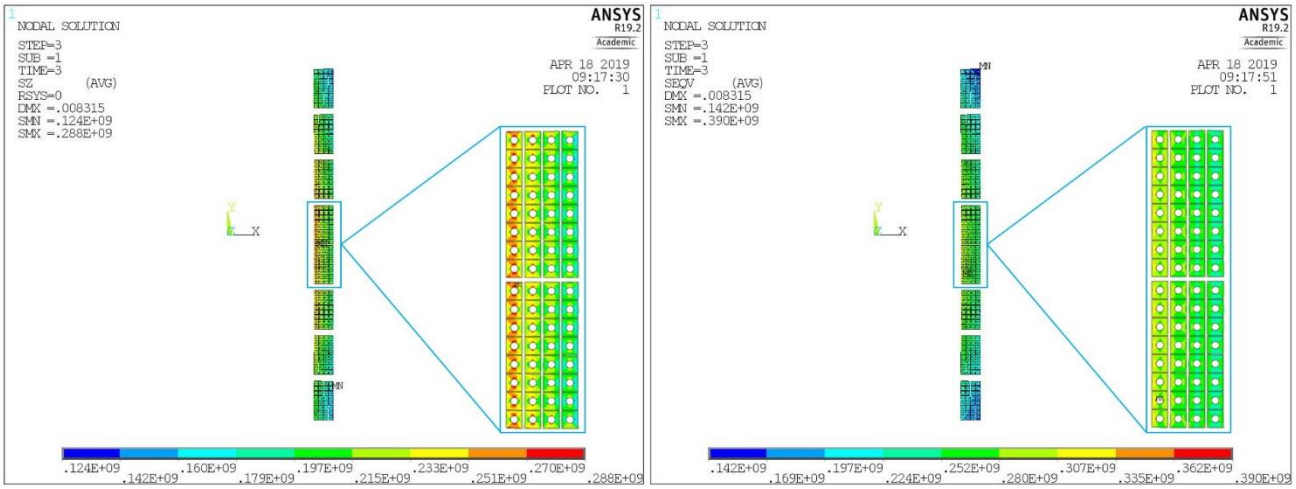

Figure 11. Hoop stress and von Mises stress for the conductor at LNT (TL+EM+SW) – conductor with circular cooling holes (with zoom in CS1L/CS1U coils).

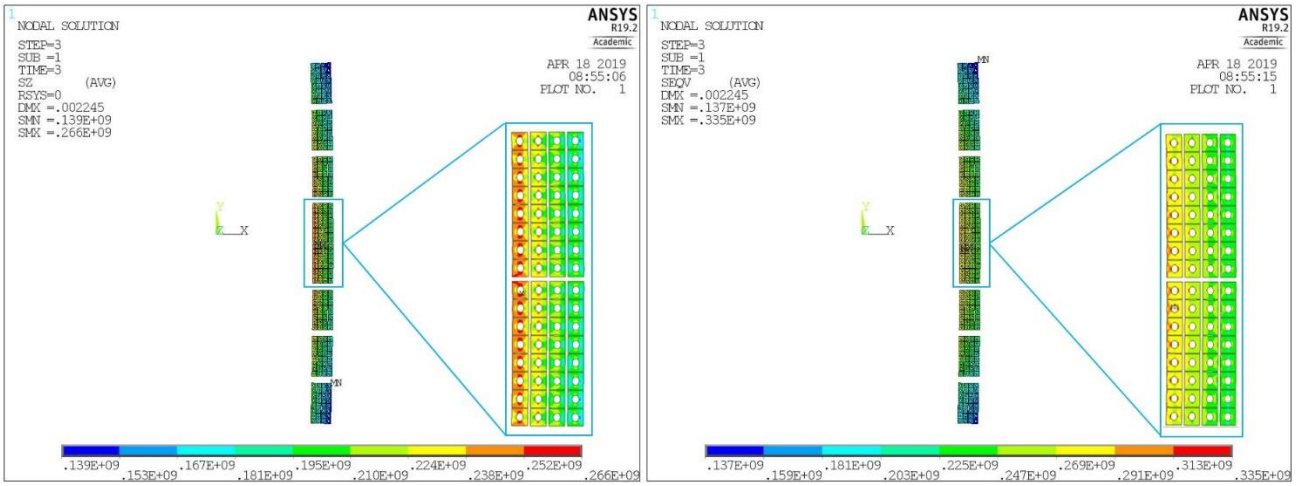

Figure 12. Hoop stress and von Mises stress for the conductor at RT (TL+EM+SW) – conductor with elliptical cooling holes (with zoom in CS1L/CS1U coils).

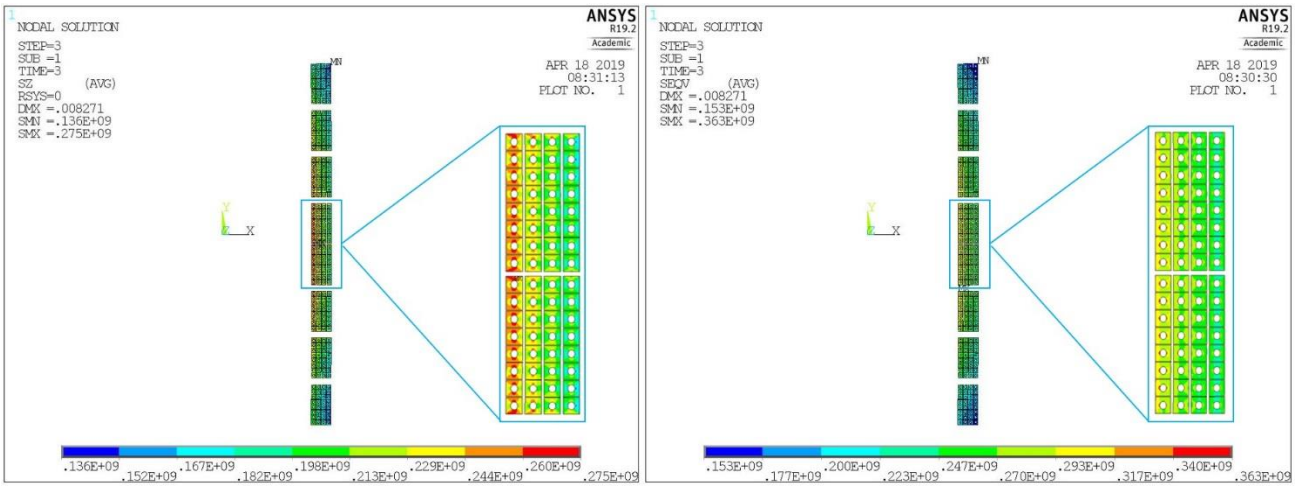

Figure 13. Hoop stress and von Mises stress for the conductor at LNT (TL+EM+SW) – conductor with elliptical cooling holes (with zoom in CS1L/CS1U coils).

In above cases in Figure 10 to Figure 13, hoop and von Mises stresses are depicted. Calculations have been performed for two temperatures RT and LNT. The mechanical analysis shows that hoop stresses have major role in material stress state, which usually occurs for axisymmetric structures. Comparing two above cases it can be seen that for conductor with circular holes maximum hoop stress reaches value 288 MPa at LNT. Values of hoop stress in case with elliptical holes are lower compared to case with circular holes, maximum hoop stresses reaches value 275 MPa. What is worth mentioning that axial stresses are also high due to volumetric axial force. The highest values for axial stresses occurred in compression direction and are equal to -221/-267 MPa at RT and LNT, respectively for circular holes. For elliptical holes axial stresses reach values -174/-210 MPa at RT and LNT, respectively. The location of the largest axial stresses is near the edge region of the holes at central part of central solenoid.

From conducted calculations it can be noticed that von Misses stresses (in this case 390 MPa) are higher than yield strength for circular holes at LNT. For OFHC material yield strength is equal to 378 MPa at 77 K and 316 MPa at 300 K for 60% cold work copper[8]. For elliptical holes von Misses stresses (in this case 363 MPa) are lower than yield strength at LNT, but are close to acceptable value. At RT for two considered cases von Misses stresses are higher than yield strength for OFHC material at this temperature and are equal to 356 and 335 MPa, for circular and elliptical holes, respectively.

From insulation point of view shear stresses have rather low values. For case with circular holes at 80K min/max values are equal to -21.8/21.8 MPa and for elliptical holes are mostly the same -22.3/22.2 MPa.

Results for RT and LNT show that the electromagnetic load has the highest influence on the stress state for above cases. The thermal stresses caused by difference in thermal expansion for each material are much smaller than those that are caused by electromagnetic forces. The above preliminary analysis shows the need for further optimization of the central solenoid structure.

It should be noted that these calculations do not take into account inner and outer tubes in which coils will be placed. Ceramic inserts with tubes play role in axial pre-load of CS coils. Furthermore, at present the value of axial pre-stress is unknown. Axial pre-stress will have influence on CS work. Further analysis should show how CS will work with above additional condition.

Radial and axial displacements (min/max) which are presented in Table 7 show that change of the conductor cross section shape (with the same cross-sectional area $A_1 = 3.35 \cdot 10^{-4}$ m^2 for circular holes and $A_2 = 3.35 \cdot 10^{-4}$ m^2 for elliptical holes) does not increase maximum displacement values. For comparison $A = 3.99 \cdot 10^{-4}$ m^2 for full conductor. Moreover, this approach with elliptical holes can increase stiffness in radial direction and can improve cooling of the conductor. For case with circular holes, after cooling down the CS structure to 80 K, the min/max radial displacements are equal to -1.41/ -1.11 mm. In the next steps, after EM loads and self-weight these displacements remain negative and are equal to -0.85/ -0.31 mm. It is similar in the case with elliptical holes. For case with circular holes radial displacements for first and last step of loading are shown in Figure 14.

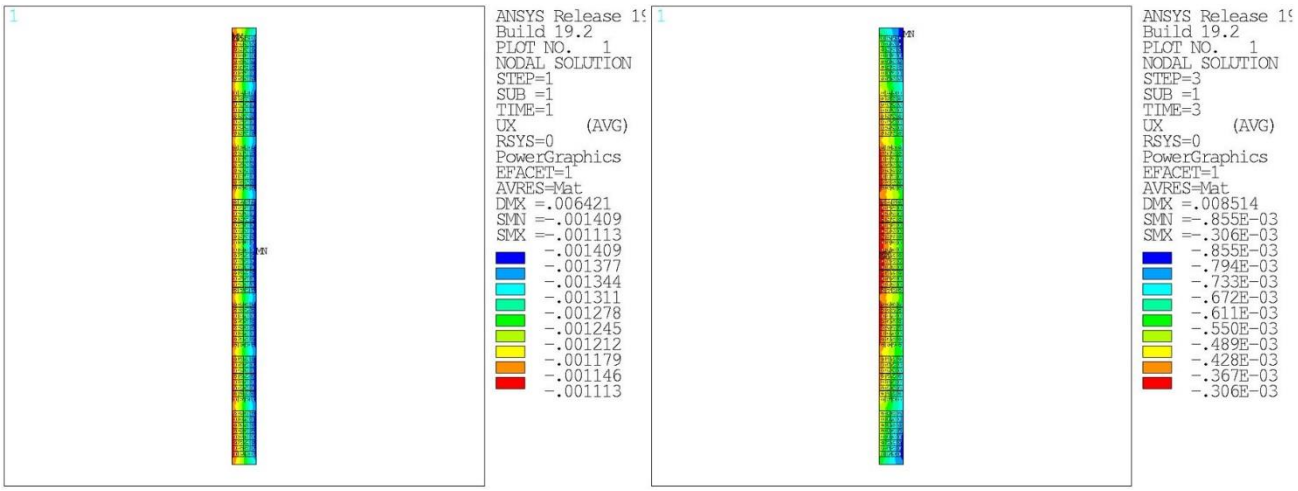

Figure 14. Radial displacements at LNT for first and last step of loading (TL on the left) and (TL+EM+SW on the right).

Table 7. Minimum and maximum radial and axial displacements at 80K and 300K.

Case	Min/Max radial displacement [mm] at 80 K	Min/Max axial displacement [mm] at 80 K	Min/Max radial displacement [mm] at 300 K	Min/Max axial displacement [mm] at 300 K
Conductor with circular holes	-0.85/-0.31	-8.5/0	0.49/0.83	-2.2/0
Conductor with elliptical holes	-0.86/-0.31	-8.4/0	0.49/0.83	-2.2/0

The use of holes with various shapes is influenced by many factors, for example, the method and technology of manufacturing and their influence on the structure of the magnet. Obtained results can be helpful in further analysis of CS and also give more information about direction of design CS coils and its cooling.

5. CONCLUSIONS

The preliminary mechanical analysis has been presented in this paper. Electromagnetic loads were also included in the performed analysis. The loading method which allows transfer of electromagnetic loads to mechanical structure has been checked and developed. 2D axisymmetric models were used to study behavior of the central solenoid under particular conditions. Obtained results from cases of the one layer of the conductor and eight coil stack provide answer what is the order of magnitude of stresses and displacements is under radial electromagnetic (only load for the case with one layer of the conductor), thermal and self-weight loads. Preliminary mechanical analysis of eight coil stack shows that coils reach yield stress for OFHC material in several cases. Calculated stress in the copper material is too high and should be lowered to 200-240 MPa maximally. There are several ways to decrease stress state in the conductor material. From mechanical point of view decrease of stress in CS could be done by optimize of the structure (smaller cooling holes, composite wrap around the CS coils or only around the 1st innermost layer). Another way to decrease stress state is lower V·s requirement which would lower stress by ~20% (this is feasible with non-inductive current drive or optimized heating scheme during the plasma current ramp-up). Additionally, lower top performance plasma current from 2 MA to 1.8 MA which would further lower stress by ~20%. What is important to note, pre-stress load at this stage of design is not known. In further analysis this magnitude should be introduced and checked.

Different shapes of cooling holes in the conductor were proposed. Configurations of cross section of the conductor showed differences in stress state. Selection of the shape of the cooling holes should take into account both the state of stress and other aspects such as the method of cooling.

ACKNOWLEDGEMENTS

This work has been carried out within the framework of the project COMPASS-U: Tokamak for cutting-edge fusion research (No. CZ.02.1.01/0.0/0.0/16_019/0000768) and co-funded from European structural and investment funds.

REFERENCES

[1] Panek R., Markovic T., Cahyna P., Dejarnac R., Havlicek J., Horacek J., Hron M., Imrisek M., Junek P., Komm M., Sestak D., Urban J., Varju J., Weinzettl V., Adamek J., Bilkova P., Bohm P., Dimitrova M., Hacek P., Kovarik K., Krbec J., Mlynar J., Podolnik A., Seidl J., Stockel J., Tomes M., Zajac F., Mitosinkova K., Peterka M., Vondracek P., "Conceptual design of the COMPASS upgrade tokamak", Fusion Engineering and Design 123, 11–16 (2017)
[2] Panek, R., et. al., "Status of the COMPASS tokamak and characterization of the first H-mode", Plasma Phys. Control. Fusion 58 (2016) 014015 (9pp).
[3] "ANSYS_Mechanical_APDL_Element_Reference", 2019.
[4] "Oxygen-free high conductivity Copper, Hard, UNS C10200", http://www.matweb.com/search/DataSheet.aspx?MatGUID=0db21ddedce14e16993ee5cbdf97878d&ckck=1 (10 April 2019).
[5] "Permaglass data sheet", http://www.permali.co.uk (10 April 2019).
[6] Bradley P., Radebaugh R., "Properties of selected materials at cryogenic temperatures", NIST publications, June 17, 2013.
[7] "G-10 Fiberglass Epoxy Laminate Sheet", http://www.matweb.com/search/datasheet.aspx?matguid=8337b2d050d44da1b8a9a5e61b0d5f85&ckck=1 (10 April 2019).
[8] Simon N. J. et al., "Properties of Copper and Copper Alloys at Cryogenic Temperatures", Final report. United States: N. p., 1992. Web.

Communication model for multi-level control, management and acquisition firmware-software implementations for tokamak plasma diagnostics systems

A. Wojenski[1*], P. Linczuk[1,2], R. Krawczyk[1,3], P. Kolasinski[1], M. Gaska[1], K. T. Pozniak[1], G. Kasprowicz[1], M. Chernyshova[2], T. Czarski[2], E. Kowalska-Strzeciwilk[2], K. Malinowski[2]

[1]Warsaw University of Technology, Institute of Electronics Systems, Nowowiejska 15/19, 00-665 Warsaw, Poland
[2]Institute of Plasma Physics and Laser Microfusion, Hery 23, 01-497 Warsaw, Poland
[3]CERN, 1211 Geneva 23, Switzerland

*Contact e-mail: A.Wojenski@elka.pw.edu.pl

ABSTRACT

The paper describes the communication model implemented for tokamak plasma diagnostics systems. The approach was tested for the SXR measurement system working with the GEM detector. The model describes the interfaces used for integration of various firmware and software implementations, done in the system. The purpose of the applications is to control and manage the system with acquisition of measurement data. The applications are often design by various authors, therefore it is necessary to create a common communication model, for easy integration and upgrades of the components in the system.

Keywords: System modeling, FPGA, Verilog/VHDL, HDL, GEM detector, SXR plasma diagnostics, modular measurement system, tokamak

1. INTRODUCTION

Complex measurement systems, for example used in plasma physics tokamak experiments, often contains various types of embedded firmware, gateware and software. Each of them is developed by specialists from certain topics, e.g. FPGA programmers, low-level software designers, embedded system designers, electronics teams (e.g. FPGA, microcontrollers). The whole system contains therefore a large number of applications, that are highly specialized and often need to interact with each other. In the paper is presented the model approach for implementation of complete soft X-ray measurement system for use in tokamak environment [1, 2].

2. APPLICATION MODEL IMPLEMENTED IN GT-SXR SYSTEM

The GEM Tomography Soft X-ray (GT-SXR) measurement system is containing various components, in order to make the whole system acquiring the data from the GEM detector in form of raw signals. The GEM can contain up to 128 measurement channels. For the moment, it's working with 112-channel readout board design. In contains various hardware elements, that needs to be properly programmed and configured [3]:

- FPGA boards with data acquisition algorithms
- Analog and digital front-end boards (AFE and ADB)
- System triggering unit with data consolidator in for of PCI-Express switch (8-to-1)
- High voltage unit [4]
- Low voltage system management [5]

Photonics Applications in Astronomy, Communications, Industry, and High-Energy Physics Experiments 2019, edited by Ryszard S. Romaniuk, Maciej Linczuk, Proc. of SPIE Vol. 11176, 111764A
© 2019 SPIE · CCC code: 0277-786X/19/$21 · doi: 10.1117/12.2536890

The complete description of the system can be found in [6-7]. On top of that, there is a need of the applications that would manage the system for the startup (boot process) and further acquiring the data. For this, several low-level applications were designed:

- FPGA/FMC Configuration software (FCS) – required for low-level interaction with the hardware and FPGAs [8]
- HV configuration software – required for the low-level communication with high voltage unit (voltage and protections configurations)
- Low voltage control software – required for proper working of analog boards (AFE and ADB)

Since the system is acquiring the data from the GEM detector in real-time, therefore specialized readout software from the FPGAs needs to be additionally designed [9, 10]. This part of software should be also automatically deployed upon measurement process start with automated data registration and storage.
Those applications are designed and run locally on the system. However, multiple parameters can be configurated by the user. Therefore, it is necessary to design in a model a common interface to exchange the parameters between front-end backend applications - that could be either Matlab algorithms [11], standalone data processing algorithms [12] or external complex data storage and diagnostics control software. In addition, the system should be designed in a way that a complete path of boot-up and initialization process should be performed automatically.
The complete software layout model is presented in Fig. 1.

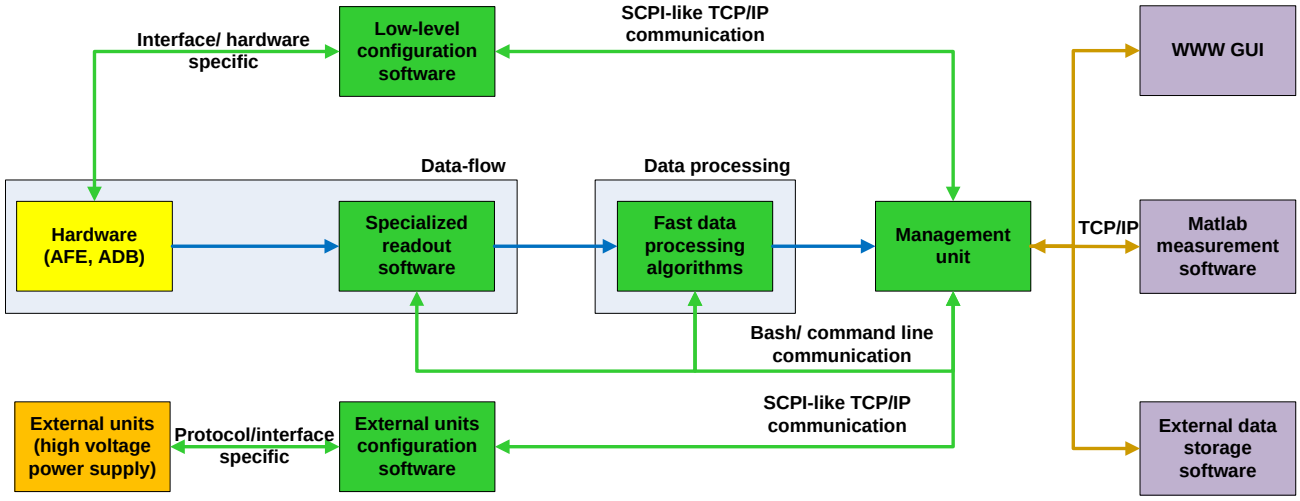

Fig. 1 Complete software layout and communication model used in GT-SXR measurement system

The software organization model can be divided into several parts:

- Low-level software for hardware configuration
- Software for external units' management (i.e. high voltage unit, low voltage power supply)
- Specialized readout software
- Management unit for the integration of front-end and back-end, including:
  - Communication standard for data exchange between components

3. LOW-LEVEL SOFTWARE COMPONENTS COMMUNICATION MODEL IN GT-SXR SYSTEM

As stated in section 2, there are several main components, that can be considered as a base component in the GT-SXR system. In order to easily integrate the different types of components in the system, including various developers from different specifications, the communication layout needs to be described.
The first block is the low-level software that communicates directly with hardware. Such components from one side are implementing protocols drivers (i.e. PCI-Express, USB, RS-232, USB-FIFO) and local interfaces e.g. I2C, SPI.

However, this software often performs a set of actions, in proper sequence, to initialize the system. For top level management unit this functionality should to be accessed from a high-level abstraction logic, pointing only to the specific actions or functions. In order to meet that requirement, for the local integration, two types of interfaces are available:

- Command line invoking the software, with high abstraction level functions,
  e.g. "-configure adb_board -offset 100", "-dma_size 100 -dma_timeout 200"
- Set of bash scripts, containing list of actions in a command line mode with parameter. The management unit can then run complex scripts from simple bash files, e.g. "program_fpga.sh", "init_afe_boards.sh 2"

This type of interface allows to divide the work between hardware, software and mixed-type specialists for easy integration.
Software for external units' management can be developed in a similar way. However, the external units can have their own setup routines already implemented, therefore the application that implements protocol driver from one side, and command line support can often be sufficient to control such units [4].
More complex in term of the management is an optimized readout software that read the raw signal data from the detector and sends it to local storage or computation algorithms. A high-performance example of the application can be found in [9, 10]. This part of software is strictly related with hardware implementation, in this case with the FPGA design and embedded PC resources. The algorithms are invoked from the management software. The management software is using direct command line execution, based on the internal state of the system. The system must be in advance prepared for the measurement (waiting for trigger state), before the readout software can be started. The configuration (by front-end application) of this software part is often unavailable, since it is designed in most optimal way in scope of performance.
The similar rules of design also apply to the standalone algorithms. They need to be designed in a robust way, accepting only measurement data and producing results, e.g. to the file. The design must also be tuned to meet the PC architecture features and cannot be easily modified in term of data processing path. However, the algorithms can support input parameters for the data computation stage, e.g. trigger level, size of clusters [12].
For the complete integration of the mentioned components additional software is required, indicated in section 2 as management unit (dispatcher) for the integration of front-end and back-end applications. The dispatcher integrates execution of all the mentioned codes from one place. From one side it implements specific calls to the models (e.g. invoking bash scripts). From the other side it contains slots for attaching front-ends. Also, the dispatcher software can contain logic, like finite state machine or status memory, indicating at which stage of the configuration or processing the measurement system is. The front-end sockets can be designed in various ways, e.g.:

- Shared memory
- Dedicated API
- Network connection (local or remote)

For the GT-SXR system, the TCP/IP socket communication is used. The network communication model is based on SCPI-like commands syntax, including:

- Setting parameters
- Reading parameters
- Error codes reporting

The benefit of using TCP/IP communication is that it is mostly independent of used hardware and operating system. In addition, it can be run locally or allow remote connections. The local communication can be used for WWW GUI interface, and the remote connection (e.g. sockets) can be used for the GT-SXR system for connecting the Matlab algorithmic interface. In addition, it allows easy integration with other external components.
The network communication protocol in SCPI form was also designed as a backend interface system for the other components: FCS software and external units (HV power supply). This approach is flexible in term of e.g. tests, the access to the components routines can be done from simple Telnet terminal. The additional benefit of this is also that the whole set of routines can be tested, while the top-level management software is under development.

4. SUMMARY

The presented software model allows to divide work on the complex systems, between various teams or specialists. The main model components are: hardware configuration support, external units support, data readout application and top-level management unit. The internal communication on the low-level side is done by the command line execution of application or on bash scripts preset. All of the components allow also for the internal TCP/IP communication based on SCPI-like messages with status and errors reporting. The top-level dispatcher unit manages whole software, additionally by implementing finite state machine logic, for status of the system tracing. The dispatcher unit allows easy extension of the system and interfacing with other external components, like front-ends (Matlab, WWW GUI) or high-level data managements systems used in big research facilities.

REFERENCES

[1] Kasprowicz, G., et al., „Multichannel Data Acquisition System for GEM Detectors", (2018) Journal of Fusion Energy, pp. 1-13, DOI: 10.1007/s10894-018-0167-0

[2] Chernyshova, M., et al., „Conceptual design and development of GEM based detecting system for tomographic tungsten focused transport monitoring", (2015) Journal of Instrumentation, 10 (10), art. no. P10022, DOI: 10.1088/1748-0221/10/10/P10022

[3] Wojenski, A., et al., „Multichannel measurement system for extended SXR plasma diagnostics based on novel radiation-hard electronics", (2017) Fusion Engineering and Design, 123, pp. 727-731, DOI: 10.1016/j.fusengdes.2017.04.134

[4] Gąska, M., et al., „High-voltage Power Supply for GEM Detectors" Proceedings of Acta Physica Polonica Supplement, vol. 11, (2018), DOI: 10.5506/APhysPolBSupp.11.781

[5] Gąska, M., et al., „Protection system for electronic measurement system for hot tokamak plasma diagnostics", Elektronika - Konstrukcje, Technologie, Zastosowania, vol. 8, (2017)

[6] Wojenski, A., et al., „FPGA-based GEM detector signal acquisition for SXR spectroscopy system", (2016) Journal of Instrumentation, 11 (11), art. no. C11035, DOI: 10.1088/1748-0221/11/11/C11035

[7] Wojenski, A., et al., „Multichannel reconfigurable measurement system for hot plasma diagnostics based on GEM-2D detector", (2014) Nuclear Instruments and Methods in Physics Research, Section B: Beam Interactions with Materials and Atoms, 364, pp. 49-53, DOI: 10.1016/j.nimb.2015.06.022

[8] Wojenski, A., et al., „Diagnostic-management system and test pulse acquisition for WEST plasma measurement system", (2014) Proceedings of SPIE - The International Society for Optical Engineering, 9290, art. no. 929029, DOI: 10.1117/12.2074967

[9] Linczuk, P., et al., „Data distribution and dispatching software for processing measurement data acquired with SXR GEM-based system", (2018) Proceedings of SPIE - The International Society for Optical Engineering, 10808, art. no. 1080841, DOI: 10.1117/12.2501510

[10] Linczuk, P., et al., „Latency and throughput of online processing in Soft X-Ray GEM-based measurement system", (2019) Journal of Instrumentation, vol. 14 (05), art. no. C05001, DOI: 10.1088/1748-0221/14/05/C05001"

[11] Czarski, T., et al., „Algorithms development for the GEM-based detection system", (2016) Proceedings of SPIE - The International Society for Optical Engineering, 10031, art. no. 100313Z, DOI: 10.1117/12.2249573

[12] Krawczyk, R.D., et al., „The software-defined fast post-processing for GEM soft x-ray diagnostics in the Tungsten Environment in Steady-state Tokamak thermal fusion reactor", (2018) Review of Scientific Instruments, 89 (6), art. no. 063504, DOI: 10.1063/1.5022131

Pion-kaon femtoscopy in Therminator 2 model

Paweł Szymański[a]

[a]Faculty of Physics, Warsaw University of Technology

ABSTRACT

Two particle femtoscopy allows one to study the properties of the particle-emitting source. From non-identical particle correlations one can obtain information about the asymmetry in emission process of particles of different types. Theoretical studies based on Therminator 2 model adapted for collision energies from the Beam Energy Scan program at STAR allow one to investigate the dependence of source sizes and emission asymmetry.

Keywords: THERMINATOR 2, Femtoscopy, Correlations, Beam Energy Scan, Pions, Kaons

1. INTRODUCTION

THERMINATOR,[1] the THERMal heavy-IoN generATOR, is a Monte Carlo generator invented to study the statistical production of particles created in relativistic heavy-ion collisions. It implements various thermal models of particle production with single freeze-out. Beam Energy Scan program (BES),[2] launched at the Solenoid Tracker at RHIC (STAR), is designed to study the phase diagram of nuclear matter. It uses gold ion collisions at Relativistic Heavy-Ion Collider (RHIC) at collision energy ($\sqrt{s_{NN}}$) in range from 7.7 up to 62.4 GeV.

2. THERMINATOR 2 MODEL

THERMINATOR model takes a number of parameters to specify a collision energy. There are thermodynamic parameters:

- Temperature (T) [MeV]
- Chamical Potentials:
  - Baryon (μ_B) [MeV]
  - Strangeness (μ_S) [MeV]
  - Third component of isospin (μ_{I_3}) [MeV]

Thermodynamic parameters are presented in Table 1. They are calculated in work.[3]

Also there are geometrical and dynamical parameters:

- mean lifetime (τ) [fm]
- source size at freeze-out (ρ_{max}) [fm]
- transverse velocity (V_T)

They are estimated using statistical methods (Table 2).

Further author information:
E-mail: pawel.szymanski.dokt@pw.edu.pl

Photonics Applications in Astronomy, Communications, Industry, and High-Energy Physics Experiments 2019,
edited by Ryszard S. Romaniuk, Maciej Linczuk, Proc. of SPIE Vol. 11176, 111764B
© 2019 SPIE · CCC code: 0277-786X/19/$21 · doi: 10.1117/12.2536925

Table 1. Thermodynamic parameters of THERMINATOR model.[3]

$\sqrt{s_{NN}}[GeV]$	T [MeV]	μ_B [MeV]	μ_S [MeV]	μ_{I_3} [MeV]
7.7	139.0	406.4	93.4685	-10.5677
11.5	150.1	303.2	69.9562	-7.9697
19.6	156.2	196.8	45.6875	-5.2882
27	157.6	149.0	34.7938	-4.0845
39	158.4	106.9	25.1974	-3.0241
62.4	158.8	68.9	16.5409	-2.0676

Table 2. THERMINATOR 2 parameters for BES energies.

$\sqrt{s_{NN}}[GeV]$	τ [fm]	ρ_{max} [fm]	V_T
7.7	8.3	8	0.65
11.5	8.35	8	0.8
19.6	8.75	8.2	0.85
27	8.75	8.85	0.8
39	8.6	8.7	0.75
62.4	9.4	9	0.75

3. FEMTOSCOPY

The correlation function is defined as a ratio of probability of observing two particles with momenta $\vec{p_1}$ and $\vec{p_2}$ at the same place and time ($P_2(\vec{p_1}, \vec{p_2})$) to the product of probabilities of observing such particles independetly ($P_1(\vec{p_1})$ and $P_1'(\vec{p_2})$):

$$C(\vec{p_1}, \vec{p_2}) = \frac{P_2(\vec{p_1}, \vec{p_2})}{P_1(\vec{p_1})P_1'(\vec{p_2})} \tag{1}$$

3.1 Non-identical particle femtoscopy

Correlation of non-identical particles arises from Final State Interactions: Coulomb and / or strong forces. The Coulomb interaction is dominant in case of pion-kaon system (Figures 1(a) and 1(b)). The correlation between particles is calculated in the Pair Rest Frame (PRF) system. The k^* (Equation 2) is the particle momentum in Pair Rest Frame.

$$k^* = p_1^* = -p_2^* \tag{2}$$

3.2 Spherical Harmonics

One of the most advanced representations of the correlation function is spherical harmonic decomposition, where three dimensional correlation function is converted into infinite set of one dimensional components.[4–8] The correlation function ($C(\vec{k^*})$) is defined as:

$$C(\vec{k^*}) = \sqrt{4\Pi} \sum_{lm} C_l^m(\vec{k^*}) Y_l^m(\theta, \phi) \tag{3}$$

$$C_l^m(\vec{k^*}) = \int C(\vec{k^*}, \theta, \phi) Y_l^m(\theta, \phi) d\phi d(\cos\theta) \tag{4}$$

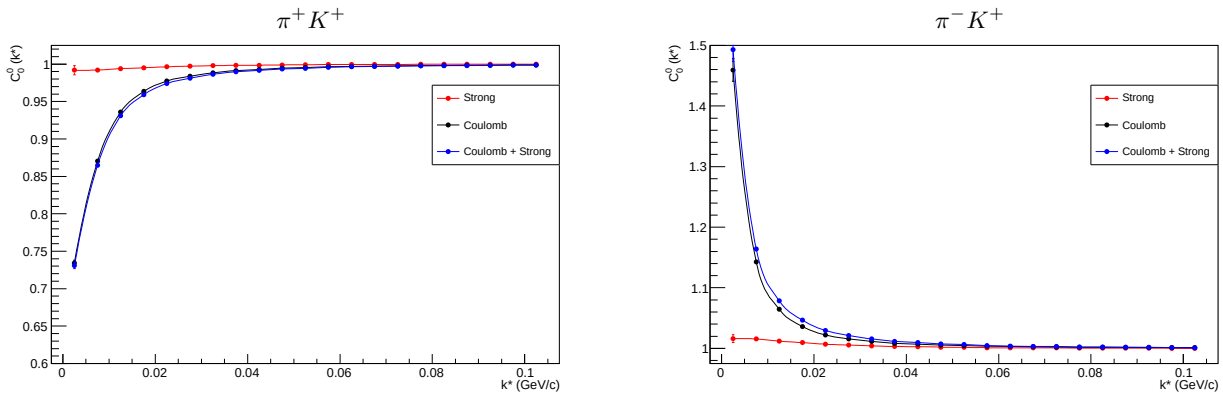

(a) (b)

Figure 1. FSI effect on correlation for π^+K^+ (a) and π^-K^+ (b).

where θ and ϕ — polar and azimuthal angles, respectively.

Component C_0^0 is sensitive to the system size and $\Re C_1^1$ is sensitive to the emission asymmetry.[8]

3.3 Time and space asymmetry

Asymmetries in space-time emission process are seen in non-identical particle femtoscopy.[9] It can be explained considering space and time asymmetries separately (Figure 2). When particles are emitted from the same positions but at different times, time asymmetry takes place. If faster particle is emitted earlier ($t_1 < t_2$), the *moving away* scenario occurs. In this scenario particles interact shorter and correlation effect is weaker. The *catching up* scenario occurs in the case of faster particle emitted later then particles interact longer and their correlation effect is stronger. There are similar scenarios in the case of space asymmetry, but one considers if faster particle is emitted closer to the center of the source or further.

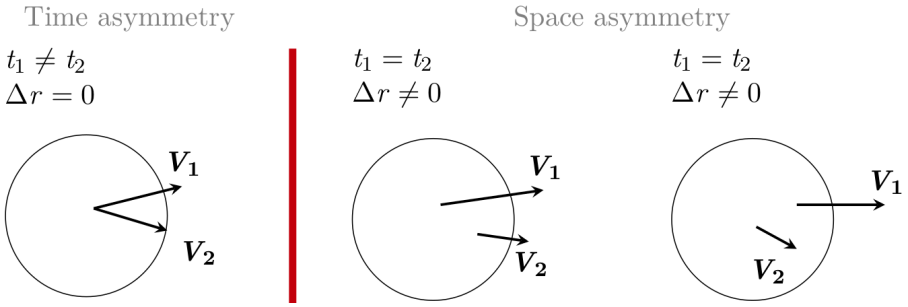

Figure 2. Two types of asymmetry — time and space.

4. RESULTS

In this work to calculate correlation function for positive pion and positive kaon pairs data generated from THERMINATOR 2 model are used. Number of events generated for BES energies are shown in Table 3.

4.1 Spherical harmonics

Figure 3 presents C_0^0 components for π^+K^+ pairs for BES energies. There is a visible dependence on collision energy of these functions. $\Re C_1^1$ components for π^+K^+ pairs are shown in Figure 4. These plots show a clear signal of emission asymmetry.

Table 3. THERMINATOR 2 parameters for BES energies.

$\sqrt{s_{NN}}$ [GeV]	# of events
7.7	19 500
11.5	10 000
19.6	10 000
27	8 000
39	8 000
62.4	6 000

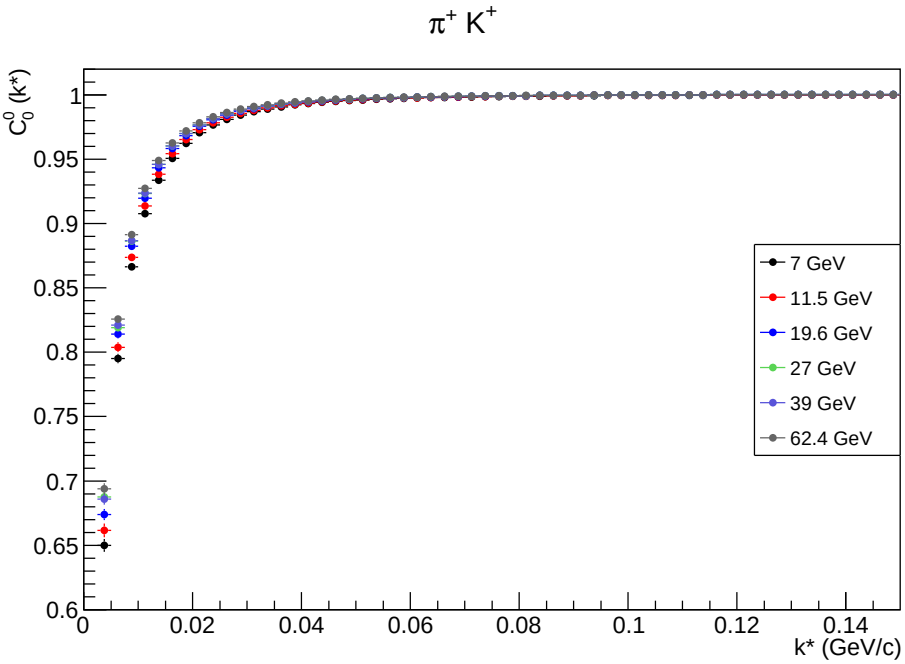

Figure 3. Spherical harmonics C_0^0 components for π^+K^+ pairs for different energies $\sqrt{s_{NN}}$ of most central (0-5%) Au+Au collisions for data from THERMINATOR 2 model.

4.2 Energy dependence

To extract space-time information about the system, a fitting procedure is applied. To perform this procedure the CorrFit tool is used.[10] For the fitting procedure the gaussian source distribution is assumed.

The STAR experiment measured the size of the $\pi - K$ emission source (R) as $(12.5 \pm 0.4^{+2.2}_{-3})$ fm and emission difference (μ) as $(-5.6 \pm 0.6^{+1.9}_{-1.3})$ fm, for Au+Au collisions at $\sqrt{s_{NN}} = 130$ GeV[11] and emission source (R) as $(13.0^{+0.3+2.5}_{-0.2-0.9})$, emission difference ($\mu$) as $(-10.6^{+0.5+0.5}_{-0.6-7.8})$ at $\sqrt{s_{NN}} = 200$ GeV.[12] Sizes of emission sources, extracted from functions presented in Figure 3, as a function of collision energy $\sqrt{s_{NN}}$ are presented in Figure 5. For lower energies sizes of the source are smaller than the size measured in the STAR experiment for $\sqrt{s_{NN}} = 130$ GeV. There is a visible dependence of size of the source on the collision energy. Figure 6 shows emission asymmetry, extracted from functions presented in Figure 4, in function of collision energy $\sqrt{s_{NN}}$. Obtained emission asymmetry is bigger than this measured in the STAR experiment at energy $\sqrt{s_{NN}} = 130$ GeV. Data from THERMINATOR 2 model shows dependence of emission asymmetry on the collision energy.

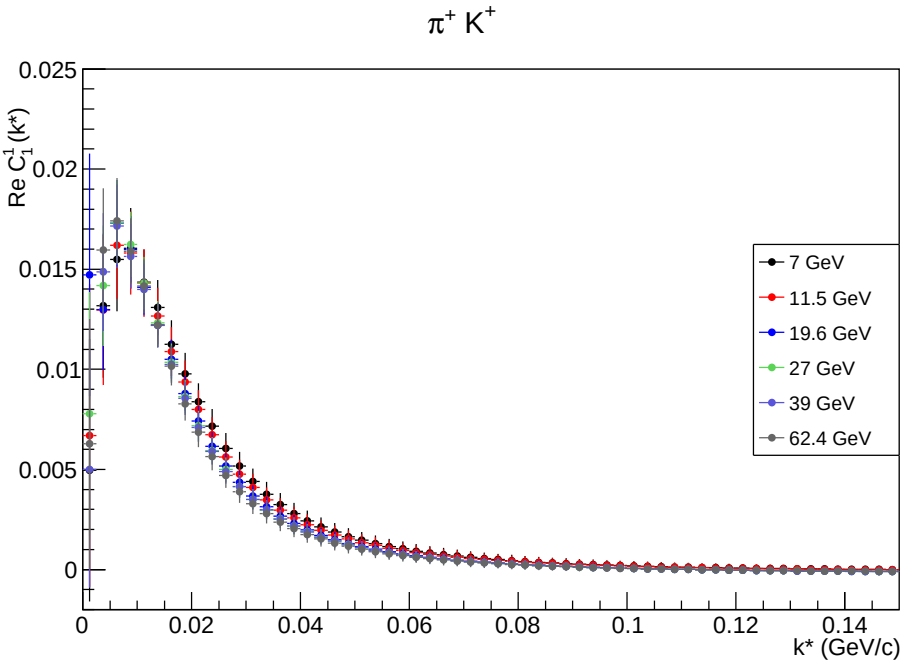

Figure 4. Spherical harmonics C_1^1 components for π^+K^+ pairs for different energies $\sqrt{s_{NN}}$ of most central (0-5%) Au+Au collisions for data from THERMINATOR 2 model.

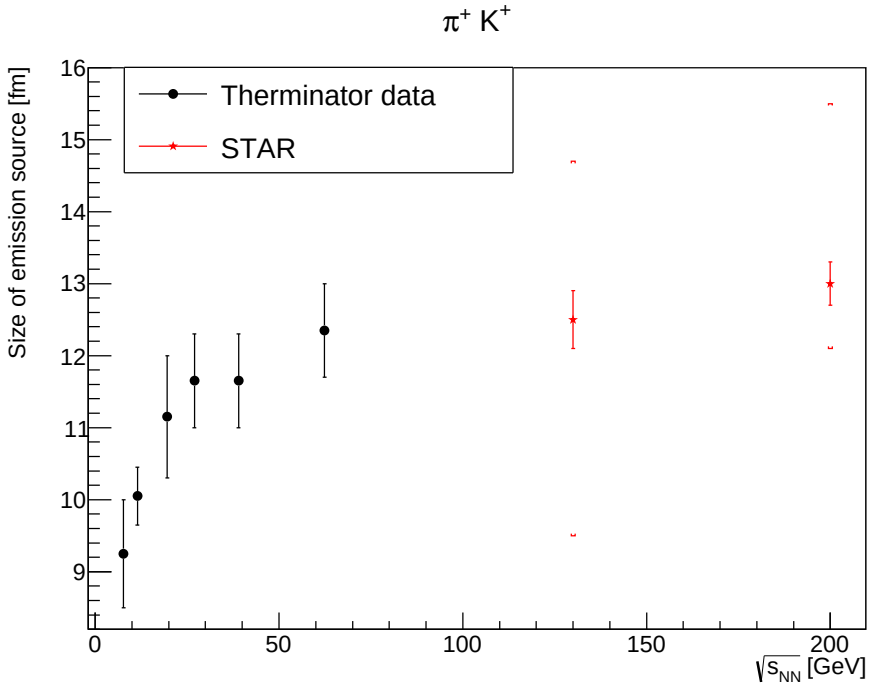

Figure 5. Size of emission sources in function of collision energy for π^+K^+ system from THERMINATOR model - black points. Size obtained by STAR Collaboration for 130 GeV[11] and 200 GeV[12] - red star.

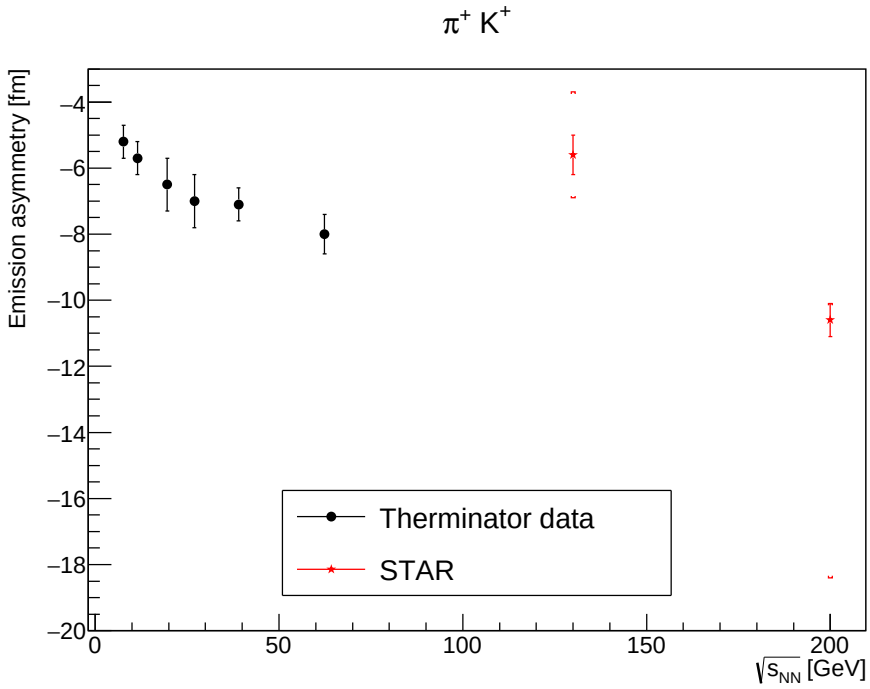

Figure 6. Emission asymmetry in function of collision energy for π^+K^+ system from THERMINATOR model - black points. Emission asymmetry obtained by STAR Collaboration for 130 GeV[11] and 200 GeV[12] - red star.

5. SUMMARY

In this proceedings, the results of pion-kaon femtoscopy for Au+Au collisions at energies $\sqrt{s_{NN}} = 7.7-62.4$ GeV generated from THERMINATOR 2 are presented. The size of the source and emission asymmetry obtained from THERMINATOR 2 data are also presented.

A clear signal of asymmetry in emission process is observed for analyzed energies. Negative values of emission asymmetry point out that most of the pions are emitted closer to the center of the source and/or later than most of the kaons. Size of emission source and emission asymmetry show dependency on collision energy $\sqrt{s_{NN}}$. Source sizes are similar to this obtained in the STAR experiment, but emission asymmetry is bigger than this obtained in the STAR experiment at $\sqrt{s_{NN}} = 130$ GeV. Emission parameters obtained by the STAR experiment have large systematic uncertainties. They are calculated by using CMSGauss source model. To obtain the parameters for data from THERMINATOR 2 model, the LCMSGauss source model was used. This may be the reason for differences in the obtained parameters.

ACKNOWLEDGMENTS

This work was supported by the grant: UMO-2017/27/B/ST2/01947 supported by National Science Centre, Poland (NCN)

REFERENCES

[1] Chojnacki, M., Kisiel, A., Broniowski, W., and Florkowski, W. *Comput.Phys.Commun.* **183**, 746–773 (2012).
[2] Odyniec, G. *J. Phys.: Conf. Ser.* **455**, 012037 (2013).
[3] Seniut, M., "Therminator generator adaptation to the consitions of RHIC and FAIR experimental complexes," *Engineer's Thesis* (2017).
[4] Danielewicz, P. and Pratt, S. *Phys. Lett. B* **618**, 60 (2005).
[5] Danielewicz, P. and Pratt, S. *Phys. Rev. C* **75**, 034907 (2007).
[6] Chajecki, Z. and Lisa, M. *Phys. Rev. C* **78**, 064903 (2008).

[7] Kisiel, A. and Brown, D. *Phys. Rev. C* **80**, 064911 (2009).
[8] Kisiel, A. *Phys. Rev. C* **81**, 064906 (2010).
[9] Lednicky, R. *Phys. Lett, B* **18**, 30 (1996).
[10] Kisiel, A. *Nukleonika (Suplement 2)* **49**, 81–83 (2004).
[11] STAR Collaboration *Phys. Rev. Lett.* **91**, 262302 (2003).
[12] Kisiel, A., "Studies of non-identical meson-meson correlations at low relative velocities in relativistic heavy-ion collisions registered in the STAR experiment," *Ph.D. Thesis* (2004).

Kaon femtoscopy in STAR

Diana Pawlowska (for the STAR Collaboration)

Faculty of Physics, Warsaw University of Technology,
Koszykowa 75, 00-662 Warsaw, Poland

ABSTRACT

Properties of nuclear matter can be studied by relativistic heavy-ion collisions in high energy experiments like STAR. One of the methods to learn about properties of nuclear matter is femtoscopy, which relies on information carried by the particles produced in the collisions. Using femtoscopic observables, the source parameters related to space-time characteristics, are provided. During heavy-ion collisions mostly pions are produced and therefore pion femtoscopy is a particularly a useful tool. High statistics data sets from RHIC have also made possible to study the strange particle correlations. The lightest strange hadrons are charged and neutral kaons.
In this report, one-dimensional correlation functions of kaon system in Au+Au collisions at $\sqrt{s_{NN}} = 200$ GeV measured by the STAR experiment at RHIC will be presented.

Keywords: kaon femtoscopy, STAR, correlation function

1. INTRODUCTION

1.1 The STAR experiment

The Solenoidal Tracker At RHIC (STAR) is one of large detector assemblies built in Relativistic Heavy Ion Collider (RHIC) in Brookheaven National Laboratory (BNL). The main purpose of building such a detector is to study the properties of strongly interacting matter at high enegies and finding Quark-Gluon Plasma (QGP) signatures.

1.2 Beam Energy Scan program

Beam Energy Scan (BES) is a comprehensive program realized by all experiments of the RHIC complex. It was launched in 2010 to study the Quantum Chromodynamics Phase Diagram at different chemical potential (μ_B) and temperature (T) values. In the first phase ended in 2014, gold ions were collided at energies $\sqrt{s_{NN}} = 7.7$, 11.5, 14.5, 19.6, 27, 39, 62.4 and 200 GeV. The second phase, started in 2019, covers the energy range below $\sqrt{s_{NN}} = 30$ GeV, where the QGP signatures seem to change or even disappear [1, 2].
The main goals of the BES program include:

- to study phase diagram at different energies and find areas in which QGP signatures are turned off,
- to find a critical point between crossover and the first-order phase transition,
- to examine the area between the hadronic and quark-gluon matter.

1.3 Hanbury Brown and Twiss interferometry

The basic idea behind femtoscopy is known as intensity interferometry, which was began by the work of Hanbury Brown and Twiss, who created the method that has been converted to examine the particle emitting source (sizes about 10^{-15} m) by measuring a momentum distributions. In the original method the angular size of the astronomical objects using the Michelson interferometry are measured [3].

Further author information:
E-mail: diana.pawlowska@fizyka.pw.edu.pl

Photonics Applications in Astronomy, Communications, Industry, and High-Energy Physics Experiments 2019,
edited by Ryszard S. Romaniuk, Maciej Linczuk, Proc. of SPIE Vol. 11176, 111764C
© 2019 SPIE · CCC code: 0277-786X/19/$21 · doi: 10.1117/12.2536926

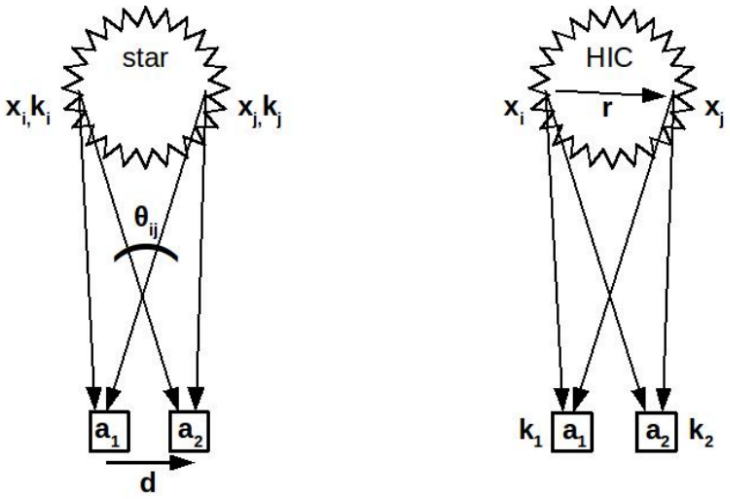

Figure 1: Schematic diagram of intensity interferometry used in astronomy (left) and particle physics (right) [4].

1.4 Correlation functions

According to the definition, the correlation function is expressed by the ratio of probability of observing two particles with specific momenta $\vec{p_1}$ and $\vec{p_2}$ at the same place and time to the product of probabilities of finding these two particles separately [5]:

$$C_2(\vec{p_1}, \vec{p_2}) = \frac{P_2(\vec{p_1}, \vec{p_2})}{P_1(\vec{p_1})P_1(\vec{p_2})} \tag{1}$$

Whereas, the experimental correlation function is created as a ratio of two distributions A(q_{inv}) and B(q_{inv}) - Eq.2. The A(q_{inv}) is the signal distribution obtained by counting all registered pairs with a given momentum, q_{inv}, from the same collision. The B(q_{inv}) is the background distribution, where pairs are constructed from the combining particles from different collisions.

$$C(q_{inv}) = \frac{A(q_{inv})}{B(q_{inv})} \tag{2}$$

$$q_{inv} = \sqrt{(\vec{p_1} - \vec{p_2})^2 - (E_1 - E_2)^2} \tag{3}$$

The correlation function can be studied as a function of k^*. This variable for particles with identical masses is equal to [6]:

$$k^* = \frac{q_{inv}}{2} \tag{4}$$

2. KAON CORRELATION FUNCTION

The shape of the identical kaons correlation function depends on :

- Quantum Statistical effects (QS)
- Final State Interactions (FSI):
  - Coulomb Interaction (COUL)
  - Strong Interaction (SI)

Kaons are described by Bose-Einstein statistics, which increases the probability of finding two particles with the same quantum state. In the case on like-sign charged kaons, a strong negative correlation is observed due to the Coulomb repulsion - Fig.2a. In case of the neutral kaons, the Coulomb interaction is absent, but strong interaction need to be taken into account - Fig.2b.

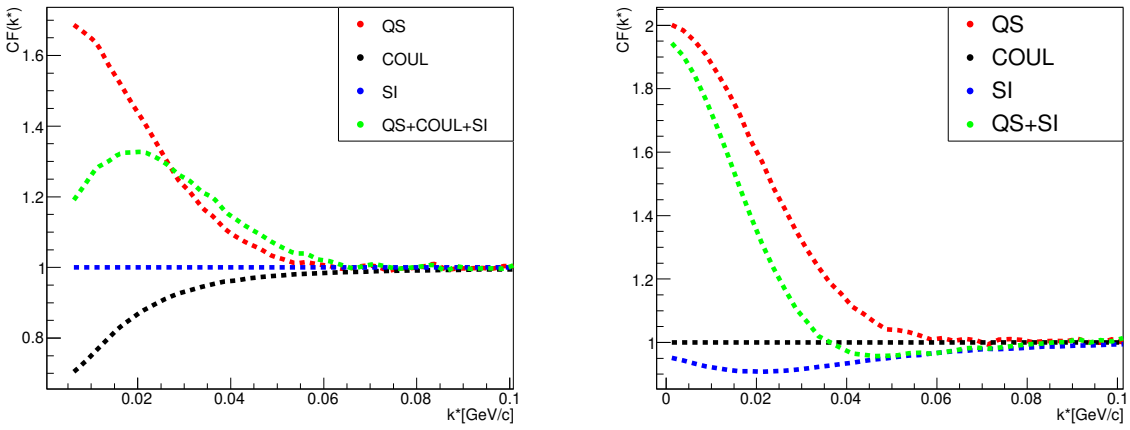

(a) Like-sign charged kaons

(b) Neutral kaons

Figure 2: Correlation function CF(k*) of the kaon pairs from Therminator model for central Au+Au collisions at $\sqrt{s_{NN}} = 200$ GeV [7]. It includes: QS (red dotted line), COUL (black line, the Coulomb source radius is 5 fm), SI (blue line) and all together (green line).

2.1 Parameterization of the correlation function

To investigate the time-space characteristics of the particle-emitting source, including its size (R_{inv}), parameterization of the correlation function is performed. The analytic function is adapted to the one-dimensional experimental correlation function (we assume the simplest case for two identical bosons) expressed in the Eq.5, taking into account only Quantum Statistics correlations. In addition, it is assumed that the source has a spherical shape and Gaussian density distribution:

$$C(q_{inv}) = 1 + \lambda \exp[-R_{inv}^2 q_{inv}^2] \tag{5}$$

where: λ - the correlation strength.

It is also important to include strong interaction into the fit of the $K_S^0 K_S^0$ correlation function. It can be done using Lednicky and Lyuboshitz model [8] by modifying Eq.5 as follows:

$$C(q_{inv}) = 1 + \exp[-R_{inv}^2 q_{inv}^2] + \alpha \left[\left| \frac{f(k^*)}{R_{inv}} \right|^2 + \frac{4\Re f(k^*)}{\sqrt{\pi} R_{inv}} F_1(q_{inv} R_{inv}) - \frac{2\Im f(k^*)}{R_{inv}} F_2(q_{inv} R_{inv}) \right] \tag{6}$$

$$F_1(z) = \int_0^z dx \frac{\exp[x^2 - z^2]}{z} \tag{7}$$

$$F_2(z) = \frac{1 - \exp[-z^2]}{z} \tag{8}$$

The s-wave $K_S^0 K_S^0$ scattering amplitude $f(k^*)$ is dominated by the near threshold s-wave isoscalar and isovector resonances $f_0(980)$ and $a_0(980)$.

2.2 Armenteros-Podolanski plot

The Armenteros-Podolanski plot describes the kinematic properties of the V^0 candidates (neutral reconstructed particle). It reflects dependence of the relative transverse momentum of decay products (q_T) on the longitudinal momentum asymmetry ($\alpha = (p_L^+ - p_L^-)/(p_L^+ + p_L^-)$), where p_L^+ and p_L^- are the longitudinal momenta of positive and negative daughter, respectively - Fig.3:

- decay products of the $K_S^0 \rightarrow \pi^+ + \pi^-$ have the same mass and therefore their momenta are distributed symmetrically on average,
- for $\Lambda^0 \rightarrow p + \pi$ the proton (antiproton) takes on average a larger part of the momentum and as a result the distribution is asymmetric.

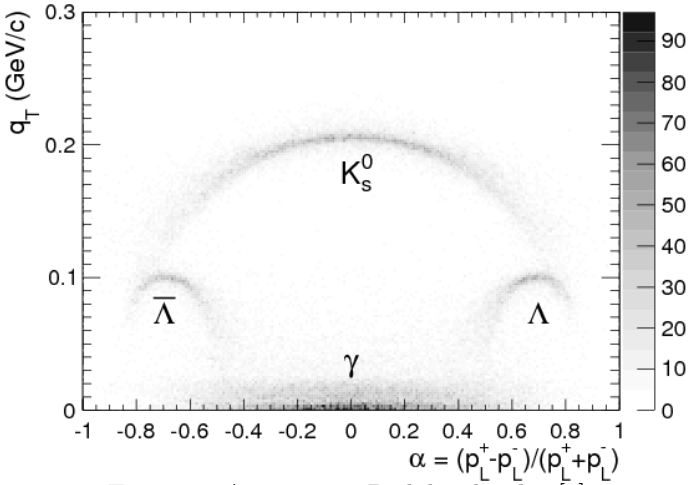

Figure 3: Armenteros-Podolanski plot [9].

3. DATA SELECTION

In this study, minimum-bias (0-80% centrality) Au+Au collisions at $\sqrt{s_{NN}}$ = 200 GeV were analyzed. The kaon identification was performed using the information from two detectors, namely the Time Projection Chamber (TPC) and the Time-Of-Flight (TOF). Table 1 shows cuts for π^+ and π^- (daughter particles of the V^0 candidates). Cuts for neutral kaons are presented in Table 2.

Table 1: Daughter cuts

Cut	π^+	π^-
p_T [GeV/c]	0.2-1.2	0.2-1.2
DCA to the primary vertex [cm]	>1.3	>1.3
minimum TPC hits	15	15
$\lvert n_{\sigma\pi}\rvert$	<3	<3
$\lvert n_{\sigma K}\rvert$	>3	>3
$\lvert n_{\sigma p}\rvert$	>3	>3

Table 2: Neutral kaon cuts

Cut	K_s^0
p_T [Gev/c]	0.2-1.5
$\lvert\eta\rvert$	<0.5
V^0 DCA to the primary vertex [cm]	0-0.3
DCA of daughters [cm]	0-0.3
decay lenght [cm]	>0.2
Armenteros q_T [GeV/c]	0.12-0.22
Armenteros $\lvert\alpha\rvert$	<0.7
mass range [GeV/c^2]	0.488-0.51
mass from PDG 2016 [GeV/c^2]	0.498±0.006

The experimantal Armenteros-Podolanski plot is shown on Fig.4. Signal region of K^0_S candidates is symmetric. Furthermore, other particles, e.g. Λ and $\overline{\Lambda}$, are not noticeable.

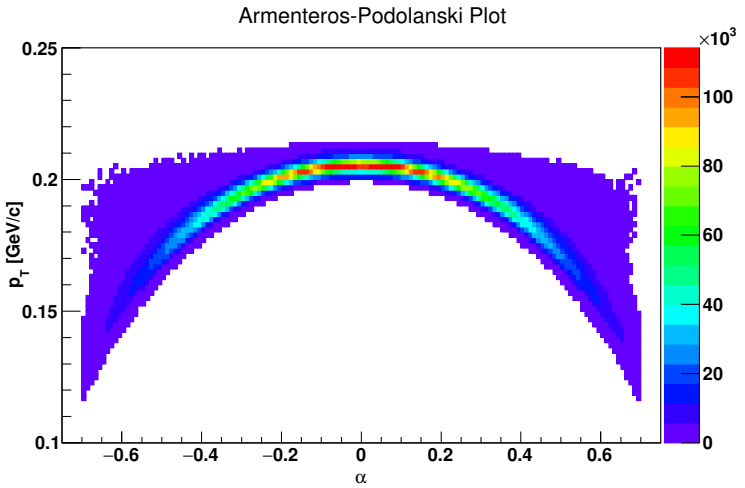

Figure 4: Armenteros-Podolanski plot for K^0_S candidates in Au+Au collisions at $\sqrt{s_{NN}}$= 200 GeV.

3.1 Purity correction

The pair purity, $PairPurity(q_{inv})$, is independent of q_{inv} in the range of considered invariant four-momentum difference. The pair purity is calculated as:

$$PairPurity(q_{inv}) = \frac{S}{S+B}(p_{T,i}) \times \frac{S}{S+B}(p_{T,j})$$

where: S is a signal (number of K^0_s in the specificnrange of distribution of invariant mass), B is a background (number of other particles in this range of distribution of invariant mass) and $p_{T,i}$, $p_{T,j}$ - transverse momentum of first and second in the pair K^0_s. As a result, an average value of 88% is used to correct the correlation function. The raw correlation functions are corrected for the $K^0_sK^0_s$ pair purity according to the expression:

$$C_{corrected}(q_{inv}) = \frac{C_{measured}(q_{inv}) - 1}{PairPurity(q_{inv})} + 1$$

4. RESULTS

Figure 5 shows $K^0_sK^0_s$ correlation functions with Gaussian fit before and after correcting for pair purity measured for minimum bias (0-80%) Au+Au collisions at $\sqrt{s_{NN}} = 200$ GeV. Before purity correction a weaker correlation (smaller values of λ parameter) is observed as compared to this after purity correction.

Numerical calculations presented in Table 3 and Table 4 show the smaller values of source's radii after corrections (larger statistical uncertainties) and different values of λ parameter (larger for correlations after purity corrections).

Table 3: Radii of the particle emitting source before purity correction.

Centrality	Radii [fm]	λ
0-80%	5.08 ± 0.19	0.630 ± 0.051

Table 4: Radii of the particle emitting source after purity correction.

Centrality	Radii [fm]	λ
0-80%	4.72 ± 0.20	0.701 ± 0.056

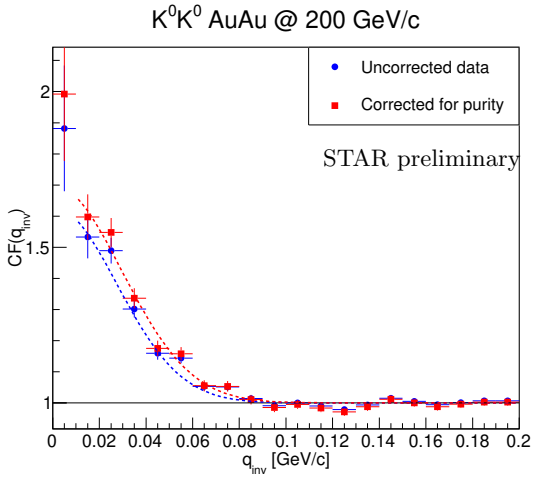

Figure 5: The $K^0_S K^0_S$ correlation functions together with fits before (the blue points) and after (the red points) purity corrections for minimum bias events (0-80%) for $\sqrt{s_{NN}} = 200$ GeV. The uncertainties are statistical only.

4.1 Comparison with previous result

In 2006 STAR Collaboration published the first statistically meaningful results from two-K^0_S femtoscopy in Au+Au collisions at $\sqrt{s_{NN}} = 200$ GeV [10]. In that analysis, events from the Zero Degree Calorimeter (ZDC) and the Central Trigger Barrel (CTB) data sets were used. The radii of the effective source was obtained as 5.02 ± 0.61 fm from Gaussian fit.

Comparing previous results with those obtained from this analysis, similar source sizes are determined. As it possible to notice in the Figure 6, the shape of the correlation functions before and after applying the purity correction is similar.

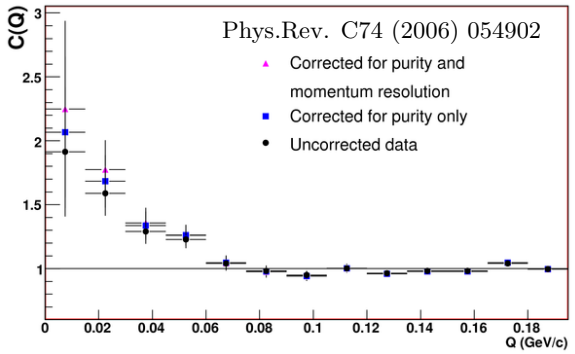

(a) The $K^0_S K^0_S$ correlation function from central Au+Au collisions at $\sqrt{s_{NN}} = 200$ GeV. Uncorrected data are described by the solid circles, after purity correction - the squares, after purity and momentum resolution correction - the triangles. The uncertainties in the results are statistical only.

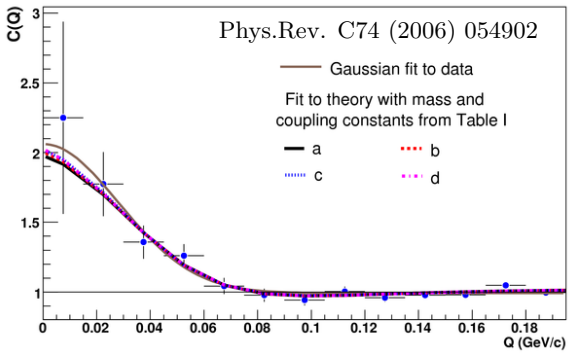

(b) Fits to the $K^0_S K^0_S$ experimental correlation function. The uncertainties in the results are statistical only.

Figure 6: Previous STAR result [10].

5. SUMMARY

In this proceedings, neutral kaon one-dimensional femtoscopic measurements at the STAR experiment have been presented. The analysis has been done for minimum bias (0-80%) Au+Au collisions at $\sqrt{s_{NN}} = 200$ GeV.

The neutral kaon correlation functions were parameterized by Gaussion fit. The purity correction for neutral kaons slightly reduces the size of the measured particle-emitting source and increases the statistical uncertainties. Comparison with previous result shows similar values of radii and shape of the function.

ACKNOWLEDGMENTS

This work was supported by the grant: UMO-2017/27/B/ST2/01947 supported by the National Science Centre, Poland (NCN)

REFERENCES

[1] Odyniec, G., "Future of the Beam Energy Scan program at RHIC," *EPJ Web Conf.* (2015).

[2] Adams, J., et al., "Studying the Phase Diagram of QCD matter at RHIC," (March 2014).

[3] Hanbury Brown, R. and Twiss, R., "A new type of interferometer for use in radio astronomy," *Phil. Mag.* (1954).

[4] Steinpreis, M., "Neutral kaon femtoscopy in Pb-Pb collisions at $\sqrt{s_{NN}} = 2.76$ TeV at the LHC with ALICE," (2014). Ph.D thesis.

[5] Zbroszczyk, H., "Studies of baryon-baryon correlations in relativistic nuclear collisions registered at the STAR experiment," (2008). Ph.D thesis.

[6] Lednicky, R., "Correlation femtoscopy," *Nucl.Phys.* (2006).

[7] Chojnacki M., Kisiel A., Florkowski W., Broniowski W., "Therminator 2: Thermal heavy ion generator 2," *Comput.Phys.Commun.* (2012).

[8] Lednicky, R. and Lyuboshitz, V., "Final-state interaction effect on pairing correlations between particles with small relative momenta," *Sov.J.Nucl.Phys* (1982).

[9] Aamodt, K., et al., "Strange particle production in protonproton collisions at $\sqrt{s_{NN}} = 0.9$ TeV with ALICE at the LHC," *Eur. Phys. J. C* (2011).

[10] Abelev, B. I., et al., "Neutral kaon interferometry in Au+Au collisions at $\sqrt{s_{NN}} = 200$ GeV," *Phys. Rev. C* (2006).

GEM detector charge signals sequencer implementation for WEST experiment

Piotr Kolasiński[a*], Krzysztof Poźniak[a], Tomasz Czarski[b], Maryna Chernyshova[b], Michał Gąska[a], Paweł Linczuk[b,a], Grzegorz Kasprowicz[a], Rafał Krawczyk[a,c], Andrzej Wojeński[a], Wojciech Zabołotny[a]
[a]Institute of Electronics Systems, ul. Nowowiejska 15/19, 00-665 Warsaw, Poland
[b]Institute of Plasma Physics and Laser Microfusion, 23 Hery Street, 01-497 Warsaw, Poland
[c]CERN, 1211 Geneva 23,Switzerland

ABSTRACT

This paper focuses on implementation of the charge signal sequencer in FPGA chip dedicated for GEM detector. First is described structure of GEM detector for WEST experiment developed by IPPLM and Warsaw University of Technology. Then the article explains why signal sequencer is needed in the new system and shortly presents how it works. It collects data from all detector channels and sends it out in unambiguous order to PC. It plays a big role in a data pipeline. Proper order of data improves parameters of the system, decreases the latency and simplifies computations on PC side. The article explains technical aspects of the implementation like architecture, blocks, dataflow or configuration features. In the end, there are presented results of the implementation.

Keywords: FPGA, GEM, sequencer, measurement system, tokamak, Xilinx

1. INTRODUCTION

Gas Electron Multiplier (GEM) detectors are very useful in detecting the high rate of soft X-ray, gamma radiation or ionizing particles [1], [7][7]. They allow monitoring the behaviour of the plasma and capturing parameters like rotation speed, ion temperature or impurity concentration. Therefore GEM detectors are used as a part of measurement systems in tokamaks. Better understanding plasma behaviour in tokamak will help to keep it stable for a longer time. Extending this process with correct control system, eventually, will be a next step to generate and deliver energy from fusion reactions.

Such system was developed for WEST experiment by IPPLM and Warsaw University of Technology [2]. The main goal of the system is to diagnose plasma impurities radiation. Requirements, for control purposes, include low latency feedback real-time mode, fast charge calculations (< 1 ms.) and collecting all raw data coming from the GEM detector [3]. Additionally for diagnostic, equally important, is fast readout system. Whole developed system and firmware was prepared and designed to achieve all those requirements. Detector developed for WEST experiment can be classified as a second revision detector. First revision was designed for JET experiment [4], [5], [6], [11].

The system can be divided into a few basic parts. Concept of full data flow is depicted on fig 1. [7] and hardware block design diagram on fig. 2 [8], [9], [10]. At beginning, data is processed by analog part of the system. GEM detector detects the radiation and then electric signals are amplified and filtered on AFE and ADB boards. Next, signals from all channels (128) are converted to digital values by A/D converters with frequency 125 MHz and effective number of bits equal to 10 (ENOB).

* p.kolasinski@elka.pw.edu.pl; phone +48 22 234 79 54; fax +48 22 825 23 00; www.ise.pw.edu.pl

Photonics Applications in Astronomy, Communications, Industry, and High-Energy Physics Experiments 2019, edited by Ryszard S. Romaniuk, Maciej Linczuk, Proc. of SPIE Vol. 11176, 111764D
© 2019 SPIE · CCC code: 0277-786X/19/$21 · doi: 10.1117/12.2537002

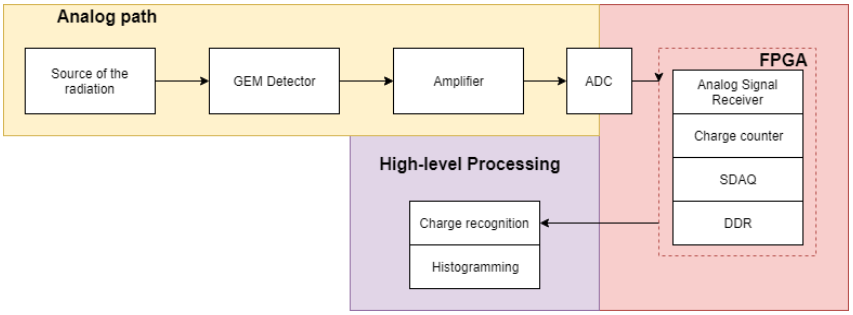

Figure 1. Dataflow in the measurement system for WEST experiment.

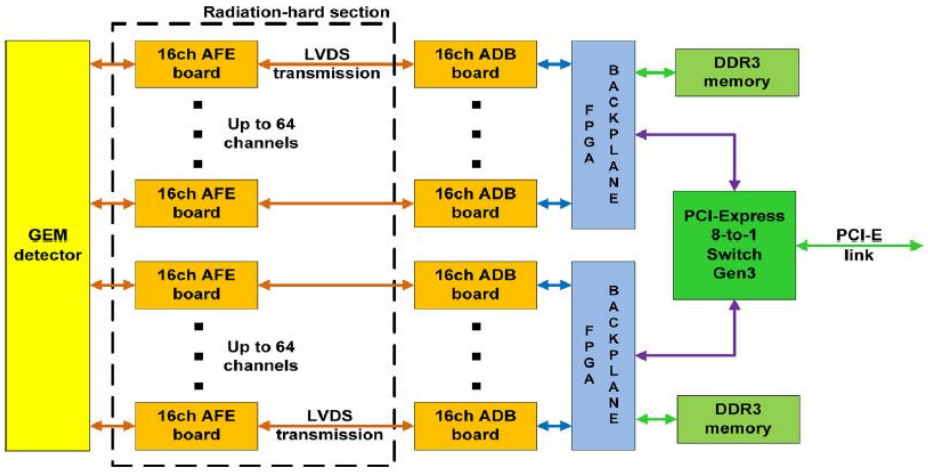

Figure 2. Hardware block diagram of the measurement system for WEST experiment.

Data from ADC is pre-processed in FPGA chips (fig. 3). To have access to raw data in PC, FPGA processing is limited only to crucial algorithms like identifying the events and computing their energy. Those algorithms are executed for data from every channel in parallel. After basic processing, FPGA sorts the data and sends it to DDR memory [11]. Correct, fast sorting algorithm is essential for next processing steps. Low latency and fast processing on PC side can be achieved thanks to high quality delivered data. PC gets the data sorted by time and by channel [12]. On PC are done more complex algorithms like charge calculations or histogramming [13], [14].

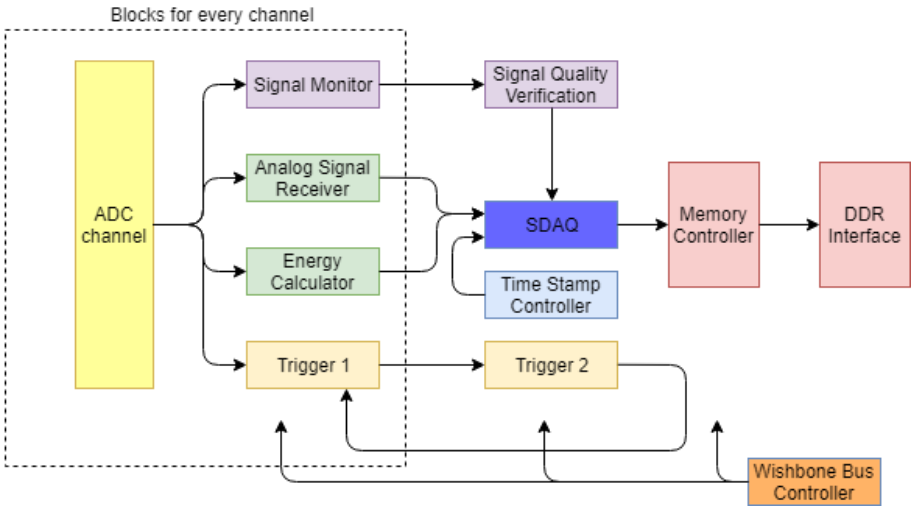

Figure 3. FPGA dataflow in the measurement system for WEST experiment.

2. CHARGE SIGNAL SEQUENCER

The sequencer (fig. 4) is a crucial part of the data pipeline. It has big impact on latency of the system. By delivering sorted data to PC, it simplifies calculation at the next stages.

Sequencer takes the data from all channels concurrently, sorts it in chronological, unequivocal order and sends to the output [12], [15]. Every sample is wrapped into a frame, which has four fields: status bits for storing useful information, channel number, time of the sample and raw data. First three fields create identifier of the event and frame.

Data, to save resources, is stored in the buffers. Every channel has its own buffer. In the same time, identifiers go to the sorter, where are sorted by time and, if the time of incoming samples is equal, by position.

At the end, identifier at the output of the sorter is concatenated with the proper data read from channel buffer and then are transferred to the next block. More about sequencer concept can be found in [16], [17].

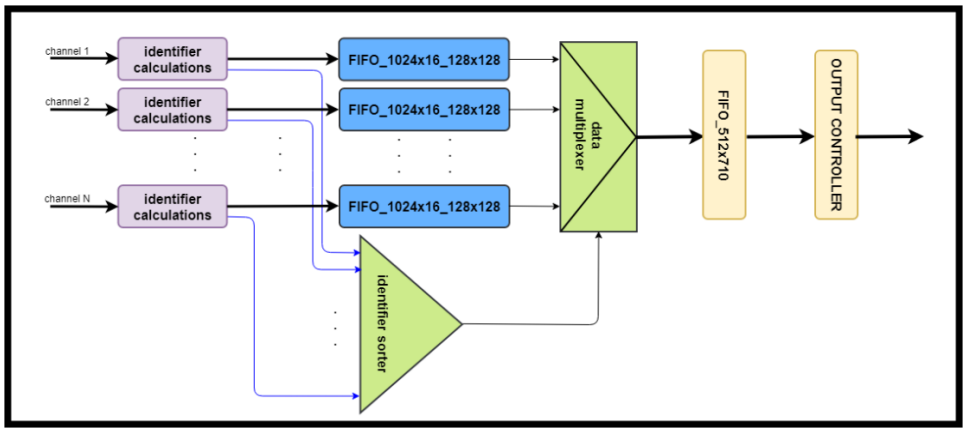

Figure 4. Basic dataflow structure of the sequencer algorithm.

3. CHARGE SIGNAL SEQUENCER – HARDWARE IMPLEMENTATION FOR WEST EXPERIMENT

Block diagram of implemented design is depicted on fig. 5. On the picture can be distinguished four blocks. Enable Controller is responsible for correct interpretation of enable signals and configuration of the rest blocks. Channel Mapping block adjusts hardware data channels to the logic representation in a PC control unit. Heart of the algorithm is placed in Sequence Calculator block, where sorting processing is done. The last block in the pipeline, Output Controller, receives data from sequencer and sends it to the output buffer. It is also responsible for sending any configuration or status frames to inform PC about current state of the sequencer. In next paragraphs are described all blocks in details.

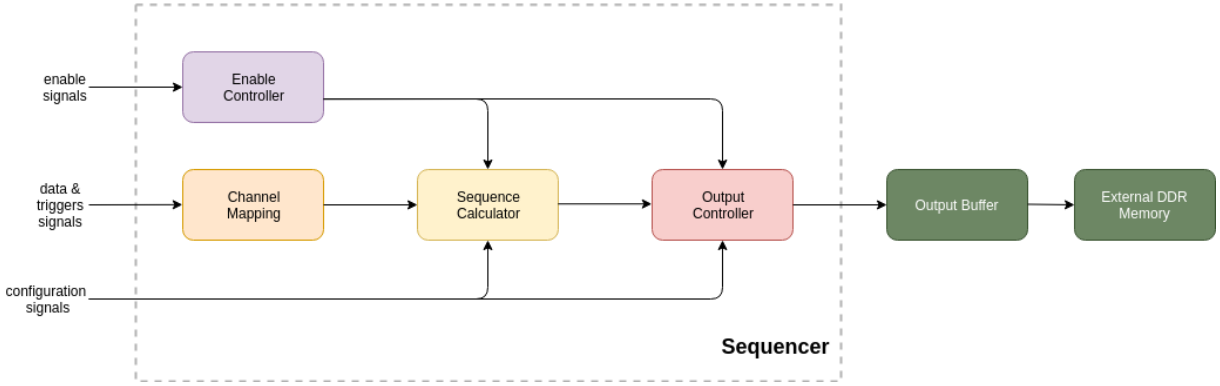

Figure 5. Block diagram of the sequencer algorithm implementation in FPGA.

Enable Controller contains only glue logic signals. It receives from PC four enable signals (trig_en, extAlgEnSignalEnable, acq_enable, extAlgEn) and based on those signals it makes control decisions. Trig_en can be treated as reset signal. Low

level on that signal resets all registers. It should be toggled after every measurement process. Next signal in hierarchy, extAlgEnSignalEnable, configures source of a trigger (external or internal). Settings next two signals high, finally causes that the sequencer is ready to receive the data.

It can be noticed, that sequence of setting on/off those enable signals in correct order is very important. Beside controlling enable states, controller based on a status of the measurement process, sends request to other modules to send GetLastPacket status frame to PC. That status informs about finished whole process of taking measurements.

Next block, Channel Mapping, connects hardware channels with control signals on PC side and logic layout in the sequencer. Because placing hardware channels depends on many parameters like pads layout, place of AFE card, it is important to do mapping before starting any measurement process. Additionally the mapping block connects channel triggers with corresponding to them data channels. The last task which is done in that block is mapping enable signals to all used channels. Currently from the PC come enable signals where every signal is responsible for activating/deactivating sixteen channels. In the Channel Mapping block, enable signals are connected with correct channels individually.

The Sequence Calculator block is responsible for sorting process. Diagram of the block is depicted on fig. 6. Timestamp Calculator submodule counts the clock cycles, when enable signals is on. Currently timestamp counter uses 64 bits. Timestamp value is shared with Identifier Calculator submodule.

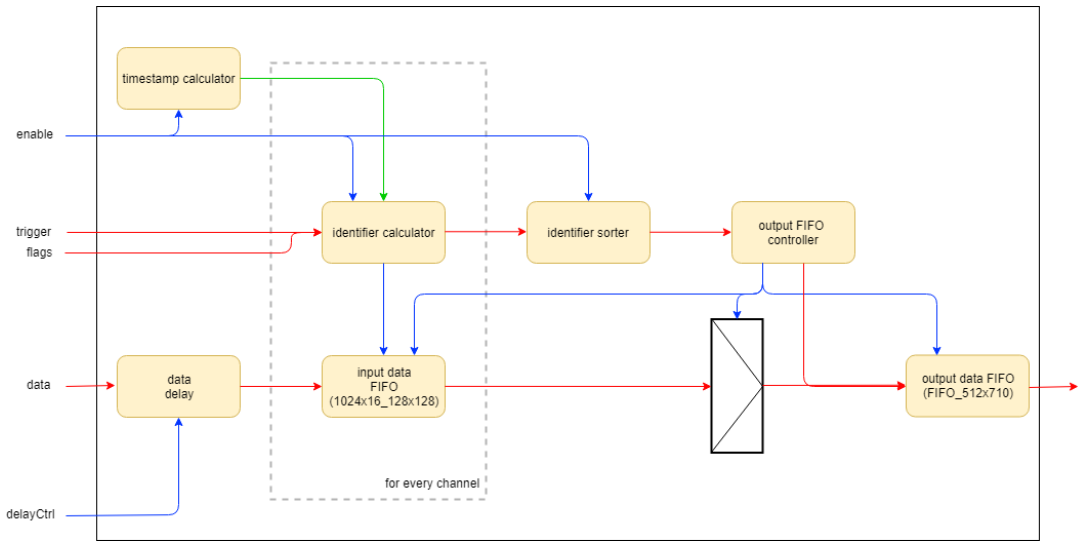

Figure 6. Block diagram of the Sequence Calculator submodule.

Data Delay submodule adds a delay path to data signals. Algorithms used in a pipeline before the sequencer can cause that data can come to the sequencer a few cycles earlier than trigger. To compensate those differences and align data signals to triggers, sequencer adds dummy delay. The delay value can vary between 0 – 15 and is equal to all channels. The setting comes from PC.

When the enable signal allows taking measurements, time counter works and data and trigger appear on the inputs of the block, the next stage is to detect the event, mark it, and wrap it into a frame. Frame for WEST experiment contains four fields: status bits, timestamp, position and data. Lengths of fields are as following:

- status bits: 24 bits (not used currently)
- timestamp: 64 bits
- position: 6 bits (on a single board can be placed up to 64 channels)
- data: 640 bit (40 samples and every is 16-bits length)

To sum up, currently every frame is 710 bits length (64 + 6 + 640, status bits not used).

Identifier is created as a sum of three fields: timestamp, position and status flags if applicable. Every identifier is sent to Identifier Sorter submodule and data to channel input FIFO memory.

In case of detecting event, all data has to be written to channel's FIFO. It is being written for 40 cycles. However the readout from the FIFO memory of whole event data has to be as fast as possible. Therefore as the channel FIFO is used asymmetric FIFO, where input is configured as 16 bit length with 1024 word deep and output as 128 bit length with 128 words deep. That configuration means that it takes only 5 clock cycles to read whole even data. Input word deep of the memory (1024) allows saving more than 20 events, so in the same time that number of events from only one channel can be processed by identifier sorter. With the last data sample sending to memory event identifier is being sent to Identifier sorter.

Identifier Sorter (fig. 7) is built from expanded modified comparators called Basic Sorting Block. First comparator checks if currently output register in the BSB stores the valid data. If yes, the comparator does not do any more steps in ongoing cycle. If the register is empty, the comparator controller checks if any data is available at the input ports from 2 previous comparator blocks. If no, does not do any more steps in ongoing cycle. If yes, controller checks if the data is available only on one port or both. If on one port, then that data is taken over and control signals are send to a previous BSB from which the data was taken. If on both input port is valid data, controller checks which data came earlier and that one is taken. If on both input ports, timestamp are the same, priority has an identifier with lower channel number.

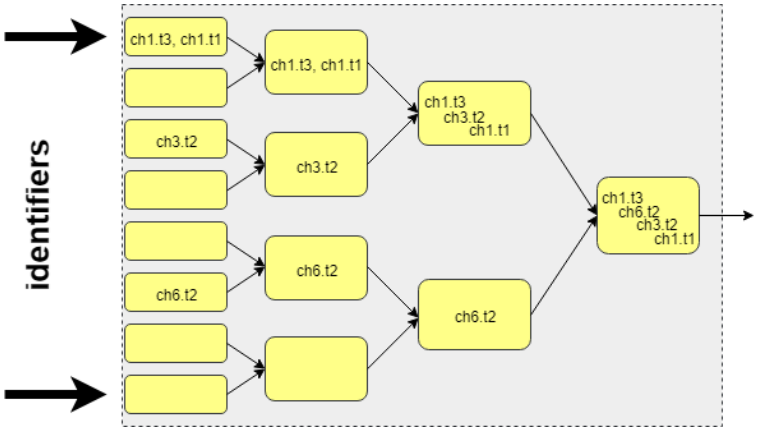

Figure 7. Block diagram of the Identifier Sorter.

At the output of the last BSB block in the sorter, identifiers are sorted by time and by channel. Output FIFO controller, based on data in the identifier, properly drives the multiplexer, which inputs are connected to outputs of all data FIFOs. After configuring the multiplexer, controller needs 5 cycles to read all event data, concatenate it with data from identifier and save it in the output FIFO memory, which length is equal to length of data and identifier together (710 bit). This is the last stage of the sorting algorithm. Data stored in the output FIFO can be read by Output Controller module and prepared to send to the next output buffer.

Input data width of the output buffer is 256 bits, so output of sorter has to be adjusted to that width. Therefore during preparing output data, the frame is extended from 710 to 768 bits (fig. 8).

To the frame is added one filed - header, which informs PC about first bits of the frame. It simplifies the algorithms on PC side.

And new frame is configured as following:

- header: 32 bits
- status bits: 24 bits
- timestamp: 64 bits
- position: 8 bits (on a single board up to 64 channels, but extended to 8, just for adjusting purposes)
- data: 640 bit (40 samples and every is 16-bits length)

Because the frame at this stage contains 768 bits, it means, that to send whole frame to the output buffer, are needed 3 cycles. AXI4-Lite stream interface is used.

32 bits - header	24 bits – status bits	8 bits - position	64 bits - timestamp	128 bits – data: MSB [0] → [7] LSB
256 bits – data: MSB [8] → [23] LSB				
256 bits – data: MSB [24] → [39] LSB				

Figure 8. Output frame structure.

The output buffer has some limited size. Data from output buffer goes directly to an external memory. External memory driver reads always whole output buffer even, if it does not store any relevant data. Therefore it is important to mark end of valid data in every buffer readout. That set of valid data (frames) stored in output buffer is defined as packet. Packet size has to be smaller or equal to output buffer size.

The Output Controller block beside adjusting frame to the output buffer interface, additionally controls number of events in packet, sends status frames (GetLastPacket, EndOfPacket) and controls TimeOut feature (fig. 9).

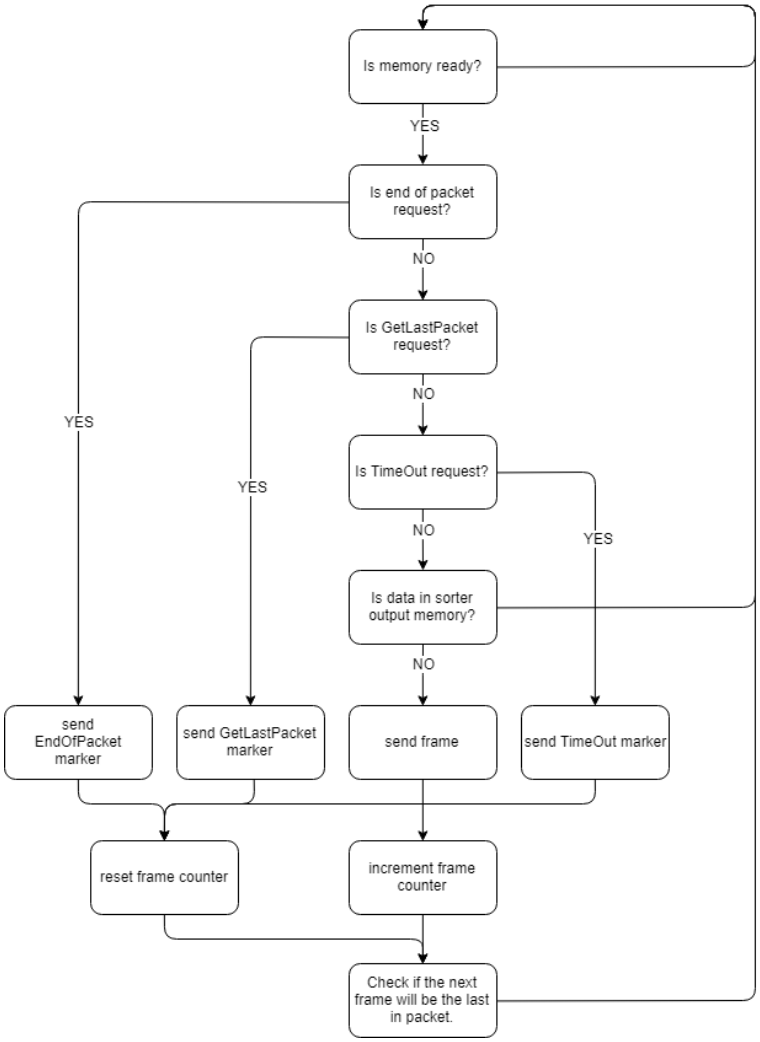

Figure 9. Decision flow diagram of the output controller.

PC can set parameter like MaxPacketSize. This parameter defines packet size and depends on memory configuration or process parameters. When number of sent events exceeds MaxPacketSize, it has to be sent EndOfPacket marker (3x256

bits with pattern 0xFAFA). This informs where in the packet is placed the last valid data. After marker position, all data should be thrown away.

GetLastPacket marker (3x256 bits with pattern 0xF1F1) is sent when all planned measurements were done. First, the PC switches off the enable signal. In response for that sequence, FPGA chip sends GetLastPacket marker to unambiguously inform PC where is end of valid data in last sent packet. After that marker, any read data is invalid and can be thrown away. After sending data marker, sequencer is set in the reset mode and measurement process is finished. To start it again, whole process of starting measurements and configuring and enabling modules is necessary.

TimeOut feature is used in cases, when any event does not come for a longer time. PC should be informed about such breaks. Therefore TimeOut parameter is set by PC, and every that time, if no data is ready for send, sequencer sends empty packet with only TimeOut marker (3x256 bits with pattern 0xFAFA).

Every standard frame or status frame has a priority order. At the beginning of sending frame to the output buffer, firstly is checked, if output buffer is ready to get new data. If no, controller waits for the next cycle. If yes, controller checks if was request for marker EndOfPacket. If yes, that marker is sent and event counter in the packet is reset. This process closes the current packet. Any new data will go to the next packet. This marker has priority, because in every packet should be stored information where end of valid data is. Exceptions is only when GetLastPacket marker is sent in the packet. If there is no request for EndOfPacket, next is checked if is request for GestLastPacket. If yes, that marker is sent. Sending this packet finishes whole measurement process. The lower priority has TimeOut request. If that request is in the system, that markers is sent. At the end is checked if data is available in output FIFO in sequencer. If yes this event data is read, formed into output frame format and sent. Then event counter in packet is incremented and, if applicable, is created request to send EndOfPacket marker. This ends of procedure sending data to output buffer and this is the last process in the charge signal sequencer block.

4. RESULTS OF IMPLEMENTATION

Sequencer was implemented in xc7a200tffg1156-2 chip with VHDL language. IP cores were used for generating memory blocks. Block works with frequency of 80 MHz. Details about used resources are presented in tab. 1. Because of lack of RAM block, which were used for other algorithms in the design, it was crucial to develop architecture which uses as less as possible those blocks. Therefore between next levels in the identifier sorter there are no buffers. Additionally the same reason causes missing input buffers to the sequencer. To process the one frame 5 clock cycles is needed, so every 62.5 ns. new frame (with event) can be written to the output buffer. It gives bandwidth of $16*10^6$ events/second and $768*16*10^6$ bits/second. Developed architecture is optimised for WEST experiment.

Table 1. Results of implementation. Used resources by the sequencer module in the FPGA.

Name	Slice LUTs (134600)	Slice Registers (269200)	Block RAM Tile (365)	LUT as Logic (134600)	LUT as Memory (46200)	Slice (33650)	LUT Flip Flop Pairs (134600)
west_backplane_top	93371	150951	251.5	85672	7699	33151	52243
dbg_hub (dbg_hub_CV)	436	721	0	412	24	264	247
inst_sorter_top (sorter_top)	28129	62068	138	27105	1024	12540	19162
MapSys.sorter_chan_mapping_gen_inst ...	0	0	0	0	0	0	0
sorter_inst (LPM_BSORTER)	26312	60818	138	25288	1024	11952	18054
sorter_out_ctrl_inst (sorter_out_ctrl)	1814	1245	0	1814	0	647	1098

5. SUMMARY

Article presents implementations of charge signal sequencer algorithm dedicated for WEST experiment in Xilinx FPGA chip. Block was written in VHDL language. Article in details describes data types used in the sequencer, data flow, configuration signals, interface between block and PC and subblocks configuration. Implemented algorithm was tested and waits for real environment measurements.

REFERENCES

[1] D. Mazon, et al., GEM detectors for WEST and potential application for heavy impurity transport studies, Journal of Instrumentation, 11 (8), 2016

[2] D. Mazon, M. Chernyshova, G. Jiolat, et al., Design of soft-X-ray tomographic system in WEST using GEM detectors, FUSION ENGINEERING AND DESIGN, 96-97, Pages: 856-860, 2015

[3] M. Chernyshova, et al., Conceptual design and development of GEM based detecting system for tomographic tungsten focused transport monitoring, Journal of Instrumentation, 10 (10), 2015

[4] WM Zabołotny, et al., FPGA and Embedded Systems Based Fast Data Acquisition and Processing for GEM Detectors, Journal of Fusion Energy, 1-10, 2018

[5] G. Kasprowicz., et al., Fast ADC based multichannel acquisition system for the GEM detector, Proc. SPIE, 8454, 84540M, 2012

[6] K. T. Pozniak., et al., FPGA based charge fast histogramming for GEM detector, Proc. SPIE 8903, 89032F, 2013

[7] T. Czarski, et al., Data processing for soft X-ray diagnostics based on GEM detector measurements for fusion plasma imaging, Nuclear Instruments and Methods in Physics Research, 364, 54-59, 2015

[8] P. Linczuk, et al., Latency and throughput of online processing in Soft X-Ray GEM-based measurement system, Journal of Instrumentation, 14 (05), 2019

[9] A. Wojenski, et al., Multichannel measurement system for extended SXR plasma diagnostics based on novel radiation-hard electronics, Fusion Engineering and Design, 123, 727-731, 2017

[10] P. Linczuk, et al., Performance Evaluation of Developed GEM-based X-Ray Diagnostic System, Acta Physica Polonica B, Proceedings Suppleent, 2018

[11] P. Kolasinski, et al., Modeling and implementation of the GEM detector charge signals sequencer for the hot plasma tokamak fast diagnostics system, Przegląd Telekomunikacyjny + Wiadomości Telekomunikacyjne, 4, 86-91, 2018

[12] P. Kolasinski, et al., Serial Data Acquisition for GEM-2D detector, Proc. SPIE, 9290, 92902H, 2014

[13] R. D. Krawczyk, et al., Introducing parallelism to histogramming functions for GEM systems, Proc. SPIE, 9662, 96622N, 2015

[14] T. Czarski, et al., Charge cluster identification for multidimensional GEM detector structures, Proc. SPIE, 10808, 108084E, 2018

[15] T. Czarski, et al., Serial data acquisition for the X-ray plasma diagnostics with selected GEM detector structures, Journal of Instrumentation, 10 (10), 2015

[16] P. Kolasinski, et al., Matlab-based modeling of GEM diagnostic data sequencer, Proc. SPIE, 10808, 108083Z, 2018

[17] P. Kolasinski, et al., FPGA based fast, low latency serialization system for measurement data, Elektronika : konstrukcje, technologie, zastosowania, 58 (8), 40 – 45, 2017

GEM based technology for plasma diagnostic application

E. Kowalska-Strzęciwilk[a], M. Chernyshova[a], G. Kasprowicz[b]
[a]Institute of Plasma Physics and Laser Microfusion, 01-497, Warsaw, Poland; [b]Warsaw University of Technology, Institute of Electronic Systems, Warsaw, Poland;

ABSTRACT

Many types of micropattern gas detectors (MPGD) have been used as tracking detectors in experiments with high-energy particle physics and imaging detectors, especially in the case of soft X-rays. Several advantages like high count rate capability, good spatial and energy resolution, low cost and possibility of constructing large area detectors with very small dead area make these detectors very attractive in field of particle physics. The paper presents the designing, construction and assembling of two prototype Triple Gas Electron Multiplier (Triple-GEM) detectors. These were developed for high-resolution X-ray spectroscopy measurements for tokamak plasma to serve as plasma monitoring in soft X-ray region for the WEST tokamak.

Keywords: X-ray detectors, Gas electron multipliers, Soft X-ray, Plasma physics diagnostics, Micropattern gaseous detectors (MSGC, GEM, THGEM, RETHGEM, MHSP, MICROPIC, MICROMEGAS etc);

1. INTRODUCTION

Constantly new requirements for soft-X ray (SXR) radiation detection causes intensive work on new types of detectors that would fulfill conditions required in physical research and measurement methods used in various fields of science. Many works are dedicated to detectors, but the scope of applications for various types of Gas Electron Multiplier (GEM) detectors has become more and more extensive in recent years and includes areas not only in the field of high energy elementary particle physics, but also in medicine, biology and fine arts such as paintings[1]. Applying the GEM detectors it is possible to measure either an intensive gamma flux in radiotherapy or a weak flux of X-rays coming from radioactive waste, as well as to monitor the high intensity beam for hadron therapy[2,3]. Furthermore it can examine tokamak plasma through SXR measurements and the correction of neutron detection, that opens a possibility to use this technology for applications of neutron spallation sources[2].

In view of limited spatial resolution and precision of several technologies those are capable to get a digital X-ray image with a good efficiency in the very high rates, MPGD technology can provide these capabilities by many representatives, with the most effective one - Gas Electron Multiplier[4].

While still in a development stage, a detection system based on GEM technology has been proposed to be used as SXR tomographic system for tokamaks[4-9]. It is expected that detectors constructed based on the GEM technology will help to solve the basic limitations on the dimension, spatial position and required energy sensitivity imposed on any X-ray detector for the tokamak plasma. One of the most important goals is to design a system based on GEM technology to detect plasma impurities, such as tungsten emission. As it is known, tungsten is one of the main candidates for tokamak plasma processing materials for the future fusion reactor ITER[8], it has been also applied on the WEST device, where an actively cooled tungsten divertor will be installed. Therefore, an effective system is needed to monitor level of tungsten impurities in the plasma, those excess can lead to plasma disruption.

In this paper, some technological aspects of the design of such detecting system for SXR application on the example of two types of GEM detectors will be presented. These two GEM detectors, called vertical and horizontal, are going to be put inside the vertical and outside of the horizontal ports in order to compose a complete tomography system to be installed and exploited on the WEST tokamak[7,8,10]. More details on the overall design is given in the paper[10].

Photonics Applications in Astronomy, Communications, Industry, and High-Energy Physics Experiments 2019,
edited by Ryszard S. Romaniuk, Maciej Linczuk, Proc. of SPIE Vol. 11176, 111764E
© 2019 SPIE · CCC code: 0277-786X/19/$21 · doi: 10.1117/12.2537543

2. STRUCTURE OF GEM DETECTORS FOR X-RAY MEASUREMENTS

GEM detector was developed in the late nineties by scientists for applications in particle and X-ray detection. The main problem with gas counters is that a large detector with fine anode spacing and high voltage applied encounters substantial risk of electrical breakdown due to the high electric fields between the collecting anodes. For GEM detectors this situation is essentially improved by operation with decoupled stages of electron multiplication and charge collection.

This type of gaseous detectors was invented by Fabio Sauli in 1997[4]. The basis of the GEM detector is a Kapton foil of thickness of 50 μm with the copper clad on both sides (5 μm thickness), densely perforated with regularly-spaced and precisely shaped holes shown in Figure 1 with all the dimensions of the standard double-conical holes. The schematic view of a detector containing two GEM multiplication stages is presented in Figure 2. Figures 2(a)-(b) show a schematic cross section of the detector with one GEM foil. These drawings present a typical Single-GEM (S-GEM) detector with one GEM foil. In Figure 2(a) there is a detector cross section with a window plane at the top and a reading anode plane at the bottom where the window and detector electrodes are under a high negative electrical potential applied, and the reading anode plane is kept at zero potential.

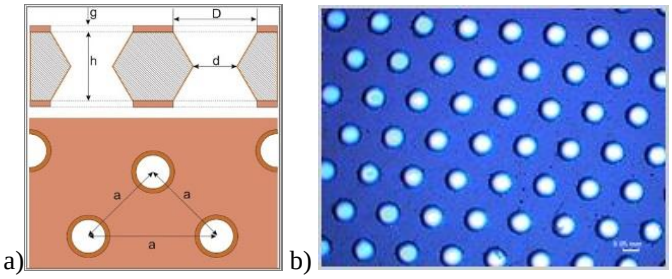

Fig. 1. (a) The outer diameter of the hole D = 70 μm, inner diameter of the hole d = 50 μm, the thickness of Kapton *h* = 50 μm, the layer of copper *g* = 5 μm and the pitch between holes *a* = 140 μm. (b) GEM foil (Al) under microscope[10,11].

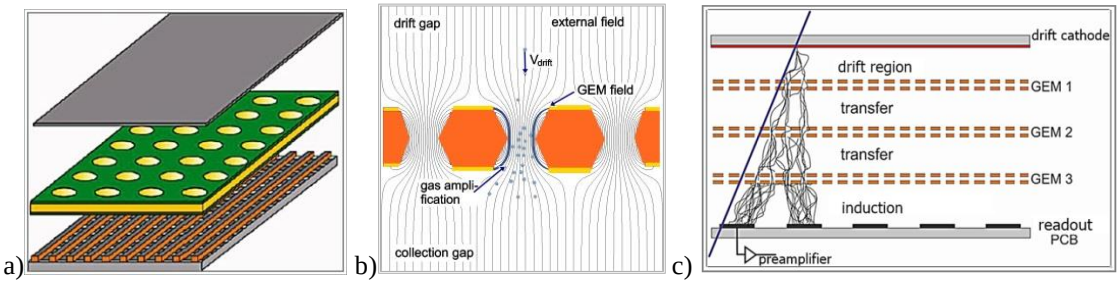

Fig. 2. (a) The detector with one GEM foil (Single-GEM). (b) Cross-sectional view of a GEM foil showing the electric field and equipotential lines in the region inside the holes. (c) scheme of a created electron avalanche in T-GEM detector with the amplification concept shown[12,13].

Figure 2(b) shows an enlarged view of the electric field configuration inside and near the holes in the GEM foils. Multiplication of free electrons and ions occurs within the strong field region inside the holes. Figure 2(c) shows a typical Triple-GEM detector (T-GEM) and electron avalanche with illustration of the amplification concept.
Below the drift cathode there is the drift region. This is usually the largest gap (usually 3-15 mm) in the detector where a gas ionization takes place. A charged particle or a photon that interacts with the gas in the drift region produces ionization clusters of positive ions and electrons. Due to the applied electric field, the cluster of positive ions drifts towards the cathode, while the electron cluster drifts towards the holes of the first GEM foil. Here charge is multiplied and while the amplified electron charge drifts toward the second GEM foil a great percentage of positive ions produced in the holes is captured by the upper GEM electrode. So multiplication channel is quickly released and ready to multiply new electron clusters. These is also some percentage of multiplied electrons those are captured by the lower GEM electrode. A similar process occurs on the other GEM foils. In the case of such detectors (three GEM foils) an electron charge multiplying is repeated on subsequent foils. An electron multiplication factor, detector gain, depends, thus, exponentially on the sum of

the three GEM voltages. Beneath the third GEM foil, multiplied electron cluster induces a current pulse on an anode pad. Readout electronics discriminates, shapes this signal and counts it with the estimated electron charge (particle/photon energy), so that a digital information on the measured radiation is visualized and stored.

3.CONCEPTUAL DESIGN AND ASSEMBLY OF THE GEM DETECTOR CHAMBER

3.1 Conceptual design

The aim of this study was to design a new diagnostics focused on the metal impurities radiation monitoring, particularly tungsten emission, by SXR measurements. Study of the impurities distribution in tokamaks motivated to construct the system of detection based on the GEM technology. In the Figures 3-4 the first prototype of GEM foils is shown with the design of two detecting systems (vertical and horizontal). It was estimated that the total active surface of these two detectors is of 200x20 mm^2 and 254x20 mm^2, respectively. The first step of technological process was the choice of materials for detector chamber. Particular attention should be paid to the selection of materials that would work under special conditions, such as magnetic field, high temperature, neutron radiation or any interference of various types. Moreover, these materials can not disrupt its operation, so to build a detector only certified materials could be used, such as those passed outgassing and ageing test, radiation hardness as well as having appropriate electrical properties.

a)

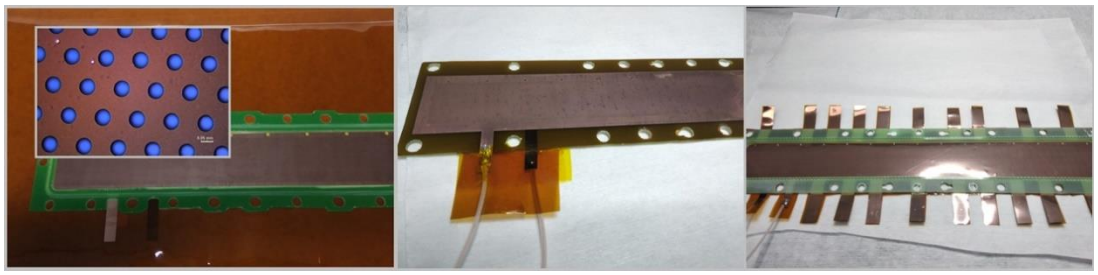

b)

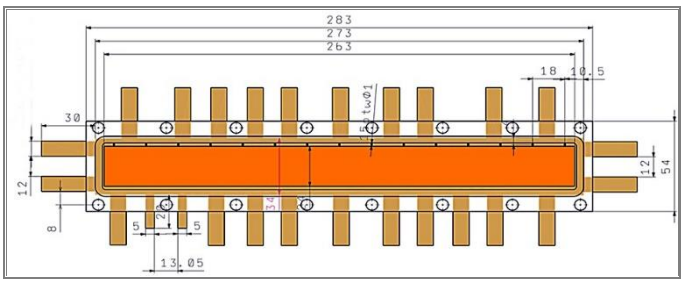

Fig. 3. (a) The GEM foil with an active area of 200x20 mm^2 glued onto frames made of epoxy glass - such a foil was applied in our final vertical detector and (b) the scheme of designed GEM foil for one of the final detectors (horizontal) with an active area of 263x20 mm^2 and additional holes outside the active area to increase the free movement of working gas in detector.

The first step before the final selection of the materials for the detector frames and the cassette consisted of performing several tests with various materials such as “white” and “black” ertacetal, two types of fiberglass (Isoval, Voltadur) and epoxyglass TSE-3.

Finally the following elements were selected:

- three types of GEM foils: standard double-conical or cylindrical holes foil with copper surface, light standard double-conical holes foil with less amount of copper and standard double-conical holes foil with aluminium cladding instead of copper (active area of 260x20 mm^2, 200x20 mm^2, 100x100 mm^2);
- as material of the detector window one-side thin aluminized Mylar foil (Polyethylene Terephthalate) of 5 μm thickness was chosen in order to minimize the low energy photon absorption;
- as mounting glue Araldite AY 103/HY 991 was used, which is ideal for bonding very smooth and low-absorbency surfaces and which retains its transparency even after drying;

- two gas compositions were selected: the Ar:CO_2 and Ar:CO_2:CF_4 mixtures.

In addition, it was necessary to design a suitable GEM foil geometry for the developed horizontal and vertical detectors (Fig. 3(b)).

a) 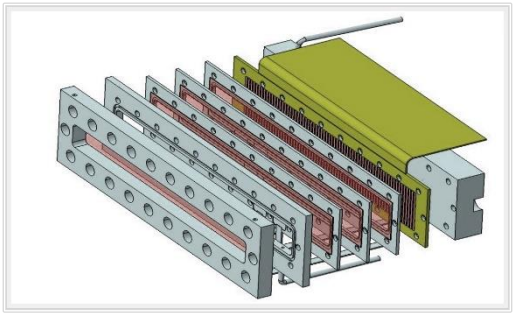 b) 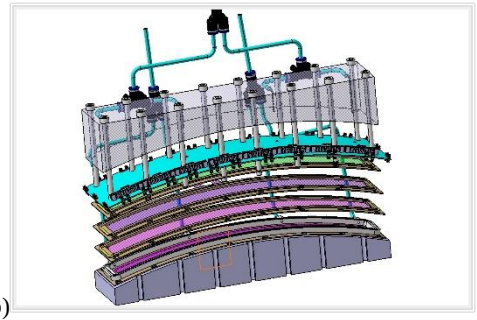

Fig. 4. (a) Schematic structure of the T-GEM X-ray detectors for poloidal tomography: frames of the vertical detector with strip plane (green plate); (b) schematic of designed frames for horizontal detector.

After designing the GEM foil geometry and support, a detector chamber structure was worked out with all the frames. In Figures 4(a)-(b), the frames scheme for the vertical and horizontal detector is shown. The T-GEM geometry proposed for the SXR diagnostics in the WEST project allows achieving a high total gas gain, with a very low probability of discharging.

3.2 Assembling

The first step of the assembly of the detector is a stretching of Mylar foil, which serves as window and cathode of the detector, and gluing it on the window frame. This process consists of mechanically stretching of Mylar foil by hands and sticking the edges of the foil to a frame or by using a special stretching device. The same process is used whilst stretching and gluing GEM foils, which is illustrated in Figure 5. The pictures below show how the stretched foil looks like during the stretching process in the typical handmade process (Fig. 5(a) and on the stretching device (Fig. 5 (b)). The whole process of stretching takes place at the room temperature but gluing process is conducted in an oven at 40-50^{0}C. Mylar and GEM foils remain smooth and flat after this process. The handmade method seems to be easier and more effective for Mylar foil but for the GEM foil the method with the use of a stretching device results in flatter and uniform surface, i.e., after stretching process the GEM foil is much better stretched and retains this property even after the gluing process on the frame.

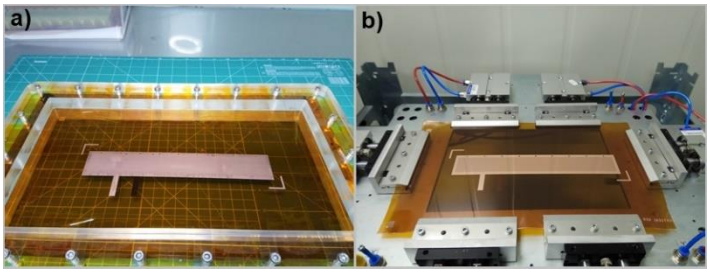

Fig.5. (a) The process of stretching the window film on the intermediate frames (thickness - 12 μm and 5 μm) and (b) process of stretching the window film on the stretching device.

All detector frames are made of Isoval or Voltadur epoxyglass material. Earlier tests show that epoxy is a better material for the detector frames as the frame made of Ertacetal changes its dimensions under the influence of heat. This can be explained by the fact that thermal expansion coefficient is higher for Ertacetal in comparison with the epoxyglass, therefore, as a result the frame undergoes larger thermal strain and deformation. The studies showed that the state of internal stress (residual) also affects the flatness and stiffness of the frames[15].

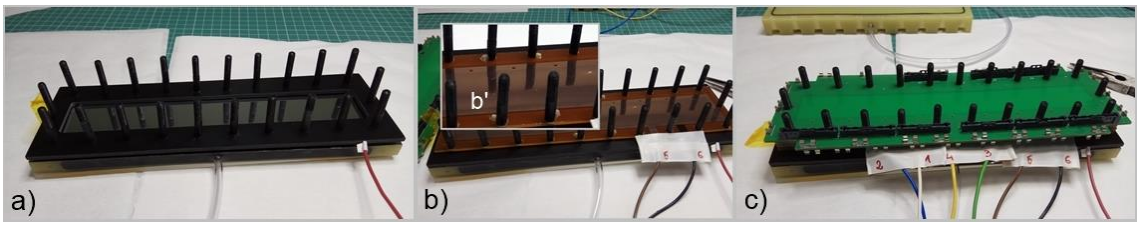

Fig. 6. The assembly process of the TGEM detector: (a) assembly of the drift gap frame, (b)-(b') assembly of GEM foils with contacts, (c) assembly of the PCB readout plate.

The next step was to combine all the frames, O-rings and the readout board together. Figure 6 shows the assembling of the vertical detector. As the first this process is undergone by a window frame with Mylar foil and intermediate frame (Fig.6(a)), then, the frame with a GEM foil (Fig. 6(b))with a certain type of element, such as eccentricity, which helping to expand the side walls of the frames to maintain the GEM foil flatness (Fig. 6(b')) and the last one is the readout plate (Fig.6(c)). The same process takes place in the case of the horizontal detector. Figure 7 shows the process of assembling the horizontal detector. One of the differences between the vertical and horizontal detectors is that the window frame in the horizontal detector is very thin as in the case of a ready-made curve frame it would be difficult to glue ideally the Mylar foil on this surface. Therefore, the window frame is separate and is very thin in order to improve the flatness of the window. The another important difference is the detector's curvature.

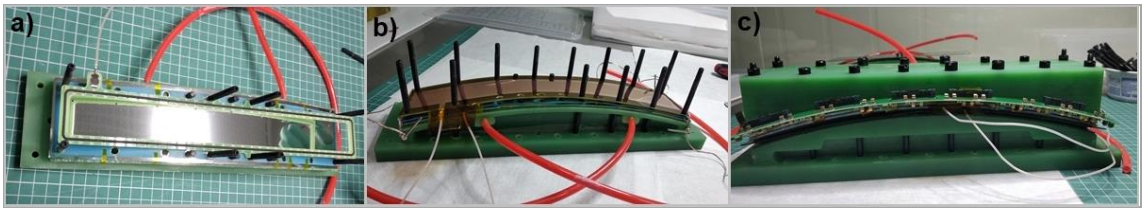

Fig. 7. The assembly process of the curve TGEM detector.

One of the last stages of detector assembly is its connection with the cassette (Fig. 8). The connecting elements are the backplane connecting signal tapes with the reading plate, which have to be checked beforehand for damage and conductivity. The final stage, however, is the installation of electromagnetic interference shielding, i.e. steel shielding in the part between both PCB plates. At the end, the detector tests were carried out with electronics that has been constructed specially for the needs of the plasma physics experiment and of the various functionality of the detector itself.

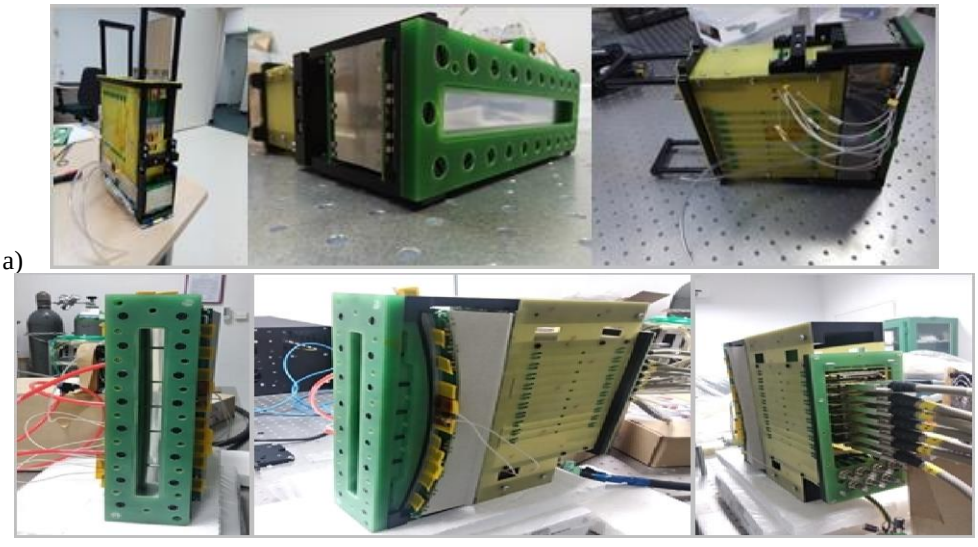

Fig.8. The final vertical (a) and horizontal detectors (b) with the cassettes.

Finally, two vertical and horizontal GEM detectors were constructed, which have been tested at the laboratory. At the moment, the vertical one is already mounted on the WEST project. The horizontal detector is still undergoing the final tests and validation before its installation on the tokamak to complete the tomography system.

4. SUMMARY

The conceptual design of the GEM detectors developed for SXR applications is finalized for the two detectors composing the complete tomography system for the WEST project. Summarizing, the technology of assembling GEM detector and technology of GEM and Mylar foil bonding was developed. Both horizontal and vertical T-GEM detector prototypes were assembled. In order to optimize the detection efficiency of the selected X-ray energy, a study of the mixture of gases and materials on the detector window was carried out. Therefore, two mixtures of gases were accepted: $Ar:CO_2$ and $Ar:CO_2:CF_4$ as well as one-sided aluminized Mylar window was approved as window material. All parts of the detector are replaceable. So eventual damaged parts of GEM detectors can be replaced and fixed quickly of low cost. Final materials and assembling procedures were selected and developed successfully. Preliminary tests of the prototype detector allowed us to continue work on the design and development of the final detectors (vertical and horizontal), with the result of vertical detector installation on the WEST project for the first measurements of the plasma radiation during the upcoming experimental campaign.

ACKNOWLEDGMENTS

This scientific work was partly supported by Polish Ministry of Science and Higher Education within the framework of the scientific financial resources in the year 2018 allocated for the realization of the international co-financed project.

REFERENCES

[1] A. Zielińska et al., Journal of Instrumentation, Vol. 8, (2013) P10011.
[2] F. Murtas, Applications of triple GEM detectors beyond particle and nuclear physics. JINST 9 (2014) doi:10.1088/1748-0221/9/01/C01058.
[3] M. Bucciantonio et al., Development of a fast proton range radiography system for quality assurance in hadrontherapy. Vienna Conference on Instrumentation, Vol. 732, 21 December 2013, (2013) 564–567.
[4] F. Sauli, GEM: A new concept for electron amplification in gas detectors, Nucl. Instr. and Meth. A 386 (1997) 531.
[5] M. Chernyshova et al., „Development of GEM gas detectors for X-ray crystal spectrometry," JINST 9 (2014) C03003.
[6] J. Rzadkiewicz et al., „Design of T-GEM detectors for X-ray diagnostics on JET," Nucl. Instrum. Meth. A 720 (2013) 36.
[7] D. Mazon et al., „Soft x-ray tomography for real-time applications: present status at Tore Supra and possible future developments," Review of Scientific Instruments 83 (2012) 063505.
[8] M. Chernyshova et al., „Conceptual design and development of GEM based detecting system for tomographic tungsten focused transport monitoring," JINST 10 (2015) doi:10.1088/1748-0221/10/10/P10022.
[9] T. Nakano et al., „Determination of tungsten and molybdenum concentrations from an X-ray range spectrum in JET with the ITER-like wall configuration," J. of Physics B: At. Mol. Opt. Phys. 48, (2015) p. 144023.
[10] M. Chernyshova et al., „GEM detector development for tokamak plasma radiation diagnostics: SXR poloidal tomography," Proc. SPIE, Photonics Applications in Astronomy, Communications, Industry, and High-Energy Physics Experiments 9662 (2015) 966231.
[11] M. Chernyshova et al., "Advantages of Al based GEM detector aimed at plasma soft−semi hard X-ray radiation imaging", Fusion Engineering and Design, In Press, (2019).
[12] F. Sauli, The gas electron multiplier (GEM): Operating principles and applications. Vol. 805,(2016), P.2–24.
[13] D. Mazon et al., „Design of soft-X-ray tomographic system in WEST using GEM detectors", Fusion Engineering and Design, Vol. 96–97, (2015), p. 856–860.
[14] M. Alfonsi et al., The triple-GEM detector for the M1R1 muon station at LHCb, IEEE Nucl. Sci. Symp. Conf. Rec. 2 (2005) 811.Y1212–1215.
[15] E. Kowalska-Strzeciwilk et al., „Technological aspects of GEM detector design and assembling for soft X-ray application" Vol. 10031, (2016), id. 100313Y 8 pp.

Design and development of soft X-ray diagnostics based on GEM detectors at IPPLM

Maryna Chernyshova[*a], Tomasz Czarski[a], Ewa Kowalska-Strzęciwilk[a], Karol Malinowski[a], Krzysztof T. Poźniak[b], Grzegorz Kasprowicz[b], Wojciech M. Zabołotny[b], Andrzej Wojeński[b], Rafał D. Krawczyk[b,c], Paweł Linczuk[a,b], Piotr Kolasiński[b], Michał Gąska[b]
[a]Institute of Plasma Physics and Laser Microfusion, Hery 23, 01-497 Warsaw, Poland; [b]Warsaw University of Technology, Institute of Electronic Systems, Nowowiejska 15/19, 00-665 Warsaw, Poland; [c]CERN, 1211 Geneva 23, Switzerland

ABSTRACT

The search for new technologies in the field of plasma diagnostics entails the increasing demands on the radiative stability of the used materials due to development and usage of fusion facilities, where the study of processes occurring during the interaction of radiation with matter has become particularly important. Currently, a new X-ray imaging detection technology is required for tokamaks such as ITER. X-ray detectors that are being used in existing equipment may rapidly degrade due to large neutron fluxes characteristic for the tokamak environment.

Despite the relatively wide use of semiconductor detectors to record SXR radiation (generally ionizing radiation), gas detectors are promising candidates that are suited much better for use in future fusion reactors given their resistance to neutron radiation. The most promising representative of the new gas detector class is the so called Gas Electron Multiplier (GEM), which is characterized by high amplification factor of the primary charge that is originated from photon absorption. Its main advantages are the compactness of the detector, good temporal and spatial resolutions, the ability to discriminate against photon energy and better neutron resistance compared to existing systems. All this makes such a detection system a potentially better candidate for soft X-ray measurements in the ITER and DEMO reactors. In this work, a new type of detection system based on GEM technology was proposed for soft X-ray measurements in the ITER reactor-oriented research, which is being developed at IPPLM.

Keywords: Nuclear instruments and methods for hot plasma diagnostics; X-ray detectors; Electron multipliers (gas); Micropattern gaseous detectors (MSGC, GEM, THGEM, RETHGEM, MHSP, MICROPIC, MICROMEGAS, InGrid, etc.).

1. INTRODUCTION

Current energy generation methods are not able to meet long-term global needs, and environmental pollution from fossil fuel combustion and nuclear waste complicates the already difficult environmental situation in the world. Therefore, one of the most important tasks of the present civilization is to research and develop new “clean” energy sources. One such alternative energy production method is based on nuclear fusion, i.e. on the fusion reaction of lightweight nuclei, for which a fusion reactor is currently being developed, in which fusion energy on industrial scale is expected to be obtained through controlled fusion.

Despite lengthy and costly research, however, the development of an efficient fusion reactor has proved to be a much more complex task than the development of a nuclear fission reactor. The main efforts of scientists are now aimed at investigating the plasma-chamber wall interaction, developing materials with low induction activity to be used as wall elements, as well as creating technologies that will make the reactor economically viable. One of the tasks associated with the study of the plasma-wall interaction is to study the process of the formation and behavior of plasma contamination.

Basic information on impurities is obtained by studying linear emission of impurities. The solution of most contamination problems depends to a decisive degree on the knowledge of the dynamics of impurities emission in time and space (in the

[*]maryna.chernyshova@ipplm.pl

Photonics Applications in Astronomy, Communications, Industry, and High-Energy Physics Experiments 2019, edited by Ryszard S. Romaniuk, Maciej Linczuk, Proc. of SPIE Vol. 11176, 111764F
© 2019 SPIE · CCC code: 0277-786X/19/$21 · doi: 10.1117/12.2537832

cross-section of the plasma chord). This leads to an understanding of the impact of impurities on plasma confinement and discharge scenarios and should enable better assessment of plasma status and optimization of discharge parameters for future fusion reactors.

X-ray spectroscopy used for this purpose is a recognized, effective and powerful tool in plasma diagnostics. Measurement of such radiation (in the 0.1-20 keV range) is a standard way of obtaining valuable information on particle transport and MHD (MagnetoHydroDynamics) phenomena. Currently, a new X-ray imaging detection technology is required for tokamaks such as ITER. X-ray detectors that are being used in existing equipment may rapidly degrade due to large neutron fluxes characteristic for the tokamak environment, as observed during fusion tests on the TFTR equipment in the USA during the experimental campaign on deuterium-tritium mixture[1].

Despite the relatively wide use of semiconductor detectors to record SXR radiation (generally ionizing radiation), gas detectors are promising candidates that are suited much better for use in future fusion reactors given their resistance to neutron radiation. Several new gas detectors, that are commonly called MicroPattern Gaseous Detectors (MPGDs), have been proposed and developed in this field. The most promising representative of this class is the detector called Gas Electron Multiplier (GEM)[2,3], which is characterized by high amplification factor of the primary charge that is originated from photon absorption. As a result, the interest in GEM-based detectors is growing steadily, and the possible use of GEM detectors now goes beyond the area of high energy physics. The main advantages of GEM technology are the compactness of the detector, good temporal and spatial resolutions, the ability to discriminate against photon energy and better neutron resistance compared to existing systems. All this makes such a detection system a potentially better candidate for soft X-ray measurements in the ITER and DEMO reactors.

In this work, a new type of detection system based on GEM technology was proposed for soft X-ray measurements in the ITER reactor-oriented research. These detectors are planned to be used to monitor plasma impurity in research projects and scientific programmes to support the construction of the ITER experimental reactor and ultimately achieve an effective fusion reaction.

2. DEVELOPMENT OF GEM-BASED GAS DETECTORS FOR SPECTROMETER ON JET TOKAMAK

Tokamak plasma X-rays come from continuous radiation (e.g., bremsstrahlung) and linear radiation. In particular, on the JET tokamak, in addition to continuous radiation, intense linear one is emitted by highly ionized tungsten and nickel impurities that escaped from structural materials during plasma discharge. Therefore, the main purpose of such a detection system is to measure the spectra of X-rays, with high resolution, coming from characteristic lines of impurities present in the plasma of tokamak and to ensure the monitoring of this radiation. This measurement is very important as it can provide accurate information on key plasma parameters such as impurities concentration, ion temperature and toroidal rotation velocity[4,5].

In fusion devices with magnetic confinement of plasma, high-resolution diagnostics of SXR radiation is applied in specific energy ranges of photons. Therefore, two independent measurement paths were prepared for high resolution bent crystal spectrometer on the JET tokamak to monitor plasma emission spectra. Each of the measurement paths was designed to monitor plasma emission spectra in certain ranges of photon energy, which correspond to specific orders of diffraction of used crystals[6]. The first diagnostic channel was designed to monitor the radiation emitted by tungsten ions, mainly W^{46+} with an energy of about 2.4 keV, observed in the first order of diffraction (the most intense W radiation is in the energy ranges of ~250 eV and ~2.5 keV photons[7,8]). This measurement channel allows simultaneous recording of continuous radiation emitted in narrow ranges of energy defined by the spectrometer geometry and corresponding to the first three orders of diffraction. The second measurement channel was dedicated to monitoring the radiation emitted by nickel ions Ni^{26+} with an energy of about 7.8 keV observed in the second diffraction order. This detection channel also enables the recording of continuous radiation with photon energies suitable for the first, second and third order of diffraction, and intensities determined by the electron temperature of the plasma.

In order to record characteristic emission lines of impurities and continuous radiation in a wide range of energy, this spectrometer required two independent detection systems with high counting speed and very good spatial resolution in one dimension, suitable for spectrometer parameters. In addition, it was important to obtain an energy resolution of the detection technique used, which would allow the identification of photons from different reflection orders. It should be noted that this was not possible for the previous detection system used on the KX1 spectrometer. The information extracted

from all spectral diffraction orders (the continuous radiation spectrum) should also have allowed a better estimation of the plasma state.

During realization of this research programme focused on the development of future ITER reactor, in particular on materials for the plasma face components and the divertor (ITER-Like Wall programme), and therefore, on the observation of the level of tungsten contamination, a new technique of detection of impurities was proposed[9,10,16].

Triple-GEM-based detection modules have been designed and built to meet the requirements of SXR radiation monitoring on the JET tokamak[5,11]. The following requirements were used during the design: large detection area (suitable for large plasma volumes and spectrometer geometry), high SXR photon conversion factor in the drift/conversion area of the detector, good signal-to-noise ratio provided by the high amplification of the detector charge and satisfied energy resolution (20-30%). X-rays monitoring required also good spatial resolution (appropriate to the characteristics of the spectrometer), time resolution corresponding to plasma dynamics and high repeatability and measurement stability at high radiation intensities.

GEM technology enables separation of gas amplification structure and readout electrode[12]. An additional advantage of such a structure is that only a fast electron component of avalanches in gas drifts in the direction of the readout electrode strips, which significantly reduces the effect of the spatial charge caused by positive ions. After the gas amplification stage, the next structure is the electrode that reads the signal from the stripes in order to position and energy-sensitive measurement of the diffraction profile appropriate for the specific SXR energy range. Each strip of the electrode is assigned to an acquisition electronics channel, together those form an electronic system.

The signals generated on the strip electrode contain all the information necessary to evaluate the energy and to reconstruct the position of the absorbed photons[13,14]. Due to the diffusion of the charge during the drift and amplification stages, the final electron cloud in the induction gap already spreads onto several readout strips. Such a group creates a cluster for a given single quantum absorption event of incident radiation. Therefore, an important measurement issue is the determination of the charge and position of the cluster (i.e. the energy and position of the photon), through its identification by means of a developed data processing algorithm.

Within this work preparation of the procedure of data acquisition and processing, the development of algorithms determining the energy and position of photon, which are crucial for obtaining correct physical results were performed. It should be noted that the preparation of appropriate algorithms for obtaining physical parameters and checking the results produced by the electronics module is necessary during the development of the diagnostic tool. Therefore, in the next stage of development of the acquisition system, the preparation and verification of the physical correctness of the results of the so-called serial data acquisition, which was developed for the purposes of laboratory research, was done[14]. This allowed to record all signal samples exceeding the trigger level independently for each measuring channel and, therefore, to increase throughput, which resulted in an increase in the detector's measurement performance. In addition, the effect of the developed acquisition procedure resulted in obtaining of a correct distribution of the cluster charge value, which directly corresponds to the energy spectra of the X-ray source.

In the course of this work, during laboratory tests, the operation of detectors was studied with an ^{55}Fe radiation source. Typical energy distributions were obtained for the whole detector operating at a gas charge amplification above 10^3 with an energy resolution (FWHM) of 23%. The linear dependence of the cluster charge on the photon energy was confirmed in the energy range corresponding to iron isotope source line with the energy of about 5.9 keV and in the range of plasma radiation selected by diffraction on a crystal with a width of ~20 eV by means of the KX1 spectrometer.

Also the stability of the detector during short-term exposure to rapid changes in X-ray flux intensity was verified using an X-ray generator. For this purpose, a sequence of 20-second exposures separated by a few minutes interval of time was used. Such a time structure corresponded to the time sequence of the detector's operation on the JET tokamak. These tests were dictated by the dependence of the GEM detector amplification on the charge accumulated on the dielectric in the GEM film holes, since the time constant of charging the Kapton depends strongly on the density of current flowing locally through the GEM film. Decrease of the amplification gain at low intensity measured in the direction of decreasing radiation intensity indicated that the GEM film charging processes caused by avalanche current in the gas determined the detector's susceptibility to radiation intensity variation. The results of the measurements of the evolution of the amplification of the detector charge showed a relatively good stability of the amplification in the range of the spectrometer radiation intensity.

After laboratory tests and preliminary tokamak results, and after optimization of the final mechanical construction of the detectors, they were installed on the KX1 spectrometer on the JET tokamak. The purpose of processing the signals obtained

from the detectors was to measure the energy and position distribution of photons for the exposure time of 10 ms. The GEM detectors developed are being actively used in data acquisition and measurements of plasma contamination radiation and determination of plasma parameters on the JET tokamak.

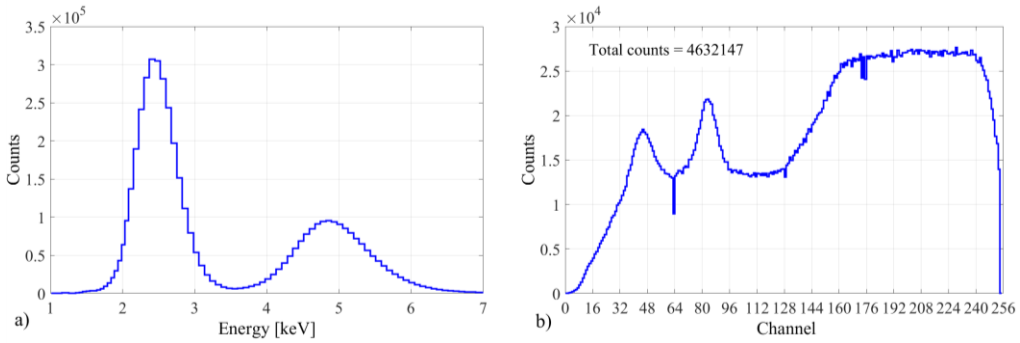

Figure 1. Characteristics of plasma radiation imaging for JET tokamak discharge: (a) energy spectrum accumulated over time, (b) position distribution accumulated over time[13].

The results obtained for the plasma discharge recorded by the detector in the first measurement channel (W lines) are shown in the Figure 1. Since for bent crystal spectrometer the distribution of the charge position of the cluster also corresponded to the energy defined by crystal diffraction, it was crucial to use the energy resolution capability of the detectors used to distinguish between first and second orders of diffraction for tokamak plasma diagnostics[15,16]. It has been shown that the on-line system separates the continuous and linear X-rays from the different diffraction orders and provides the energy spectra for each readout channel. This innovative functionality of the developed X-ray diagnostics enabled precise analysis of spectra corresponding to different ions of plasma contamination.

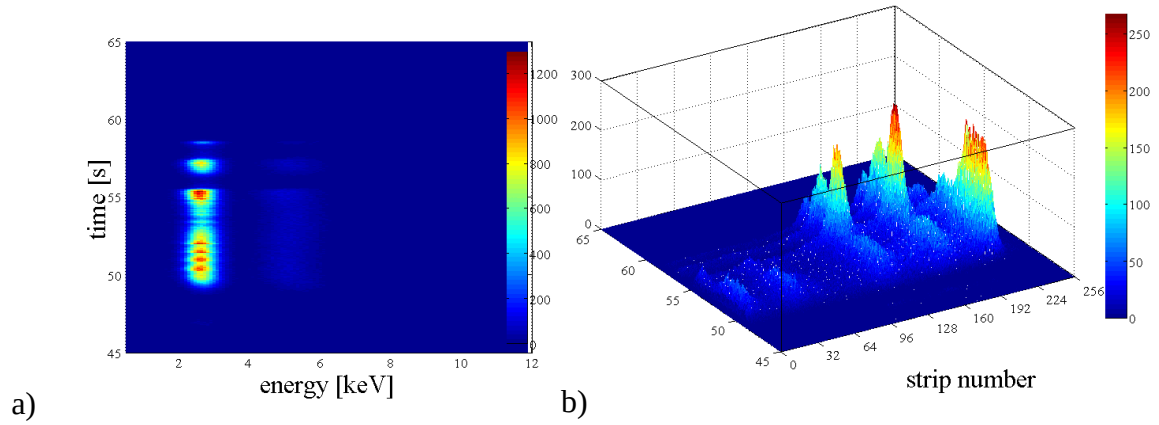

Figure 2. Time dependence of photon energy distribution for all channels (a) and corresponding time dependence of photon intensity (b) for individual detector channels during the discharge on JET tokamak with time resolution of 10 ms (exposure time). Both parts of the figure represent the total X-ray spectrum from all diffraction orders[6].

Figure 2 illustrates how the tungsten monitoring system works during a plasma discharge on the JET tokamak. The time dependency of the energy spectrum of radiation is accumulated for all readout strips/detector channels for 10 ms exposure time (Figure 2 (a)). The two lines are clearly visible at 2.4 keV and 4.8 keV, relating respectively to the first (lines of characteristic radiation of the W^{46+} ion and other W ions of similar ionization as well as continuous radiation) and the second order of crystal diffraction (continuous radiation). Figure 2 (b) shows the time evolution of the number of photons for each measuring channel during 20 seconds of the plasma discharge. It should be noted that these data have been processed in real time as part of individual histogramming (energy distributions and positions of registered photons) for each channel.

The data obtained from the developed detectors correlated well with the plasma process. The supplied detection system has identified, for the first time, diffraction profiles corresponding to different spectral orders of crystal reflection for KX1 diagnostics, thus providing accurate information on the emission of continuous and characteristic radiation from plasma

contamination. These results indicate that the developed Triple-GEM detectors are an innovative scientific and research tool of high utility and importance for plasma radiation measurements in the SXR range. This was also confirmed by the results of the work presented in[16]. The development of the issues discussed above can be found in publications[6,9,10,13-15,17].

3. DESIGN AND DEVELOPMENT OF GEM-BASED GAS DETECTORS FOR DIRECT RECORDING OF PLASMA RADIATION IN DIFFICULT TOKAMAK CONDITIONS

The problem of metal impurities also applies to the WEST project[18] in which an actively cooled tungsten divertor is implemented. Because of the coupling between impurities transport and MHD activity, which can lead to accumulation of impurities in the plasma[19], this is particularly dangerous in the case of long-term tokamak impulses (target discharges on the WEST tokamak). Therefore, an appropriate diagnostic tool is required to monitor the level of impurities and to reconstruct their distribution.

In the framework of this work, a GEM-based detection system for the ITER-oriented WEST tokamak has been proposed as a dedicated SXR radiation tomography system with energy differentiation[20-30]. Detectors based on this technology were designed to meet the requirements of dimensional limitations, to be sensitive to the spatial location of X-rays and their energy (i.e. the basic features required of any tokamak plasma X-ray detector), to offer a sufficiently large detection area matched to a dedicated diagnostic port, to have good spatial resolution, high signal-to-noise ratio, photon energy estimation capability and neutron resistance. It should be emphasized that the developed tomography system will allow distinguishing the energy of photons; such information has been inaccessible to the former tomography system on the WEST tokamak. Combining spectral information about plasma radiation with good spatial resolution of detection will provide basic information about the state of the plasma.

The proposed tomography based on GEM detectors will be used for impurities studies, especially tungsten. Therefore, the main objective of the new X-ray diagnostics was to ensure monitoring of radiation emitted by highly ionized metal impurities, focusing on emission in the range of 2-4 keV.

It is expected that the system of two GEM detectors, located in the vertical and horizontal ports[20], will register the energy of SXR photons together with the reconstruction of their location, i.e. enabling poloidal plasma tomography with the resolution of energy. The detectors are positioned to cover the maximum total viewing angle available for each port in order to achieve both optimal spatial resolution and optimal internal structure of the detection chamber. Numerous physical, technical and logistical problems had to be solved, taking into account the space limitations and operating conditions of the detection system, such as high ambient temperature, expected magnetic field distributions, etc. In addition, as the viewing angle for both ports is quite large (~25° and ~32°), the parallax effect had to be taken into account. Therefore, the drift gap of the inner chamber of the detector was optimized to minimize the shift in the visible position of plasma radiation observed for two different viewing lines (tomographic lines)[30].

Since the system is designed to test tungsten impurities and MHD activity, the following time resolution requirements have been set: the detection system should be capable of achieving a transport range of impurities with a resolution of at least 1 kHz and should record the slowest MHD activity at 10 kHz. With regard to the spatial scale, it was estimated that the resolution of 1 cm for the entire plasma volume is satisfactory to obtain a good tomographic image that will contain accurate information about the magnetic axis, the inversion radius of the sawtooth and the gradient distribution of the impurities.

In accordance with these requirements, a conceptual design of the detector's detection chamber was prepared. The chosen design of the triple GEM cascade allowed achieving high total gas multiplication with very low probability of spontaneous discharges. Due to the strongly reduced effect of space charges in the sequential amplification process, high efficiency could also be achieved. The quantum detection performance has been adapted to the energy of interest by simulating the photon absorption performance of different gas mixtures and detector window materials. The expected efficiency of detection of the M line of W X-rays (2.4 keV) was ~20%.

In the meantime, in order to support the ongoing design and construction phases, as well as the design and development of processing electronics and the completion of the final detection system for poloidal tomography, a significant research was conducted to study the basic characteristics of the detector and the final preparation of the detector for the foreseen experimental conditions by means of tests using a model detector (with a similar configuration) and simulation of the detector signals. In this way, the detector's operation was examined on many levels[20,23,24,31,32].

The GEM technology allows building a gas detector with a relatively high gain operating steadily at radiation fluxes up to 10^{11} cps^{-1} m^{-2}. However, due to the requirement of energy discrimination in tokamak applications, the detector should operate in proportional mode with a stable, relatively low gas gain (~10^3) over a wide dynamic range to prevent discharges and saturation of the spatial charge[31,32]. To verify these limitations, the detection capability of two GEM hole geometries using a copper anode X-ray tube emitting photons with ~8 keV energy (K Cu line) was examined. The detector was exposed to a collimated beam perpendicular to its window and the effective electron amplification as a function of the absorbed photon flux was determined (Figure 3).

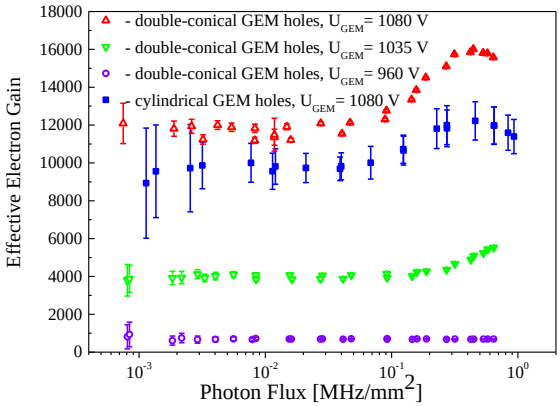

Figure 3. Effective electron amplification as a function of photon flux for double conical and cylindrical GEM foil holes[24].

In addition to the laboratory tests, the tokamak tests were planned and conducted of a model detector that was introduced to the experimental conditions of the operating ASDEX Upgrade (AUG) device for the first preliminary GEM-based diagnostic tests. The aim was to take into account the challenges related to the operation of the detector in an arduous radiation environment[21].

The experiments were conducted in two phases. In the first phase, the detection system was exposed only to background radiation (neutron, gamma and hard X-ray (HXR)). In this phase, the detector had no direct view of the plasma and was placed close to HXR diagnostics. It has been tested both without and with neutron shielding. Then, in the second phase, the system was moved to SXR, where in addition its detection surface was exposed to SXR photons, through a direct view of the central plasma.

The obtained spectral results indicated that the observed low energy shoulder in the detector spectrum can be interpreted as a contribution from high-energy photons. Such high energy photons may also induce emission from some elements present in the elements of the gas detection chamber or in its immediate vicinity, causing characteristic fluorescence lines that contribute to the spectrum observed. In the SXR area, the main candidate, among the detector chamber materials, may be copper in GEM foils with $K_{\alpha 1}$ line of 8.05 keV (the line at 8 keV was observed in the spectrum for the entire detection area at the very beginning of the discharge at a lower SXR photon flux).

Since the neutron beams from the plasma cause a mixed field of radiation that accompanies the transmission of neutrons through the environment, additional laboratory tests were planned and conducted of the detector's operation under the influence of neutron fluxes from ^{241}Am-Be source[22]. Their aim was to check the elements of the detection system which, as a result of neutron interaction, could become a source of electromagnetic radiation of various origins, such as gamma, X-rays, etc. Thus, by placing a neutron source near the detector window, the spectrum of an uncovered (non-removable casing) radioactive source was measured, which showed a peculiarity at about 8 keV, overlapping with a monotonically decreasing "tail" (that was also observed for the data from the AUG tokamak), created under the influence of illumination. In order to prove the origin of this peak, various tests were performed, the results of which confirmed that the peak was originated from Cu fluorescence in the detector chamber and was most probably caused by gamma radiation from a neutron induced activation reaction of aluminum (^{27}Al(n,γ)^{28}Al), the source casing material. The total attenuation of these gamma rays by means of a lead shield effectively removed the observed peak, indicating its non-neutron origin in the detector chamber.

It is worth mentioning that before and after irradiation of the detector, background radiation was recorded without any radioactive source in order to check its possible changes. The background intensity after irradiation turned out to be about

four times higher than at the beginning of the tests. This number relatively characterized the neutron induced radioactivity of the detector materials, which was not significant in comparison with the detector signal intensity during exposure on the whole detector surface. On the other hand, however, during the irradiation process, the background signal may also come from the own gamma rays emitted by the radioactive source. Thus, secondary products from the neutron reaction may be important, contributing to the neutron detector signal.

In order to estimate the possible influence of neutron flux on the regular GEM detector signal and to understand the mechanism of neutron interaction with detector materials, simulations using the GEANT4 toolkit[33] were initiated and developed. As a result of the simulations, the intensity of the most common emerging radiation in the function of neutron energy, which accompanies the neutron interactions, was obtained. It was found that the most frequent nuclear reactions induced by neutrons are as follows (n,γ), (n,p), (n,d), (n,α), (n,n'). Basically, for all particles, their number increases with the neutron energy, with a clear interaction starting at about 0.1 MeV of the neutron energy. Since the generated particles can continue to interact with the materials of the detector and the gas, they can eventually create high-energy electrons inside the detector before they leave the detector or are absorbed in its chamber. In fact, they can be additionally dissipated by the materials of the detector and the gas, ionizing neutral atoms and losing energy. These interactions produce low energy electrons (~1-10 keV) that can be trapped in the detector and recorded as a regular signal, which is undesirable when GEM detectors are used for SXR diagnostics.

Therefore, a further simulation of the evolution of the reaction products was carried out and the spectra of energy of the formed particles for neutrons with energy of 2.45 MeV, inseparably connected with the deuterium plasma, were calculated[22]. In terms of charged particles, the expected response of the detector is quite predictable, so simulations of the final detector signal, which can be recorded, were conducted for gamma rays, for two energies: 0.6 and 1.33 MeV, and three interactions of interest for the operation of the GEM detector: photoelectric effect, Compton scattering and the effect of the creation of electron-positron pairs. All effects are produced by high-energy electrons inside the detector. Tracking all the interactions in the detector that cause the appearance of the electron finally in the drift/conversion gap, the energy distributions of electrons were obtained and is shown in Figure 4 (a). The electrons of the presented energy distribution can be completely trapped in the drift gap of the detector and recorded as a regular signal, which can be mistakenly considered as SXR photons of different energies. The origin of primary electrons for the used experimental system on AUG tokamak is illustrated on Figure 4 (b) in the function of energy of the absorbed photon. In addition to air in the front of the detector window, the main materials contributing to the signal were copper and the detector's working gas.

The simulations were used not only to consider the interaction of incident radiation with the detector elements, but also to optimize the design of the inner chamber of the detector and its performance[25].

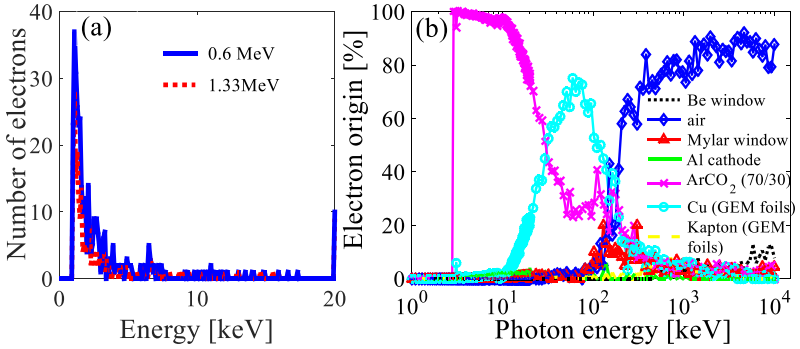

Figure 4. (a) Simulated spectra of produced electrons that have appeared in the detector drift gap for photons of 0.6 and 1.33 MeV energies. (b) Contribution of various basic materials/gases present during the experiment on the AUG tokamak in the formation of the electron in the drift gap in the function of energy of the absorbed photon[22].

One of the important operating parameters of the detector is its energy resolution. Therefore, simulation studies were conducted to assess the energy resolution of a triple GEM detector for a 5.9 keV X-ray quanta[26]. The calculations were performed using the numerical tool Garfield++ in two stages. In the first stage, the conversion of photons in the drift area into multiple primary electrons (δ electrons), which are the source of electron avalanches in the GEM detector, was simulated. This allowed obtaining a distribution of the number of primary electrons generated in the drift area by quantum X using the numerical tool Heed[34].

In the second stage, the primary electrons from the resulting quantitative distribution became the source of electron avalanches propagated through the whole volume of the GEM detector. The distribution of the obtained signals produced a spectrum corresponding to a peak with energy of 5.9 keV, which allowed determining the theoretical energy resolution of the detector at the level of 16.77%. For comparison, experimental measurements of signals from the model GEM detector were also carried out. The results of the calculations were found to match well with the experimental data.

In this way, it was available to study the influence of individual elements of the detector's chamber on its energy efficiency. The knowledge gained allowed for a better understanding of experimental observations and their influence on the deterioration of recorded energy resolution, accompanying the process of recording and processing signals.

The progress of this research on the issues discussed above and the obtained results can be found in the following publications[20-29,35-40].

4. WORK ON DETECTORS TO IMAGE X-RAY RADIATION ORIGINATED FROM TOKAMAK'S PLASMA

Excellent imaging capabilities for MPGD-based detectors[41] which, due to their wide application, conquer various fields (e.g.[42,43]), can also be used for direct imaging of plasma radiation. For example, using 2D toroidal GEM-based imaging and combining it with GEM-based poloidal tomography makes possible obtaining 3D information that should be available to study the interaction between tungsten impurities and MHD activity. Combined with advanced electronics, these detectors offer excellent spatial and temporal resolution, as well as the ability to obtain a charge spectrum from which it is possible to reproduce the photon spectrum. In this way, additional 3D information can be used to determine the boundary conditions of 2D tomography, direct imaging, MHD simulation testing (synthetic diagnostics) or to use 3D tomography. The spectral resolution provided by the system can be used to determine the boundary conditions of the tungsten transport codes.

As it is known, tungsten ion transport interacts with MHD activity and this interaction is a full three-dimensional phenomenon (e.g. 3D tungsten redistribution in NTM (Neoclassical Tearing Mode) or internal kink mode instabilities due to, for example, plasma rotation or off-axis ICRH (Ion Cyclotron Resonance Heating)). Proper identification of the mode and its location, as well as the spatial distribution of tungsten, would be more accurate thanks to diagnostics that guarantees obtaining of such 3D effects. In this respect, this diagnostics could be beneficial because a third detector, which would be a two-dimensional detector observing a poloidal cross-section, would provide access to the required 3D information, and would be complementary to standard poloidal tomography. It can be used both to effectively identify limits of 2D tomography in simple cases with axial-symmetric SXR emissions, as well as to validate 3D effects in a synthetic diagnostics approach, or to be used as direct 3D tomography. It must be said that the activity of W and MHD cannot be considered independent, therefore spectral resolution and 3D information are complementary if detailed physical examinations are to be carried out. Moreover, it is expected that electrons accelerated during magnetic reconnection processes, i.e. sawtooth, or during the discharge disruption caused by massive gas injections should produce a strongly anisotropic signal, to measure which a toroidal camera is excellently suited. Therefore, common use of toroidal detector with poloidal detectors would allow for better quantification of radiation anisotropy, and thus, both better quantification of the responsible electric field and better spatial location of accelerated electrons. Of course, such radiation would be visible at higher energy levels, but early observations suggest that it should be visible on SXR signals.

It should be noted that gas detectors based on GEM technology have additional advantages that are important for the current task, such as compactness, but a large detection area, and operational and flexible geometry, which is very important due to the limited available space around the tokamak chamber. In addition, external conditions such as magnetic field will not prevent the detector from operating effectively[44,30]. Other advantages include ~20 ns single photon measurement time (reasonable time resolution will allow solving the problem of plasma dynamics (~100 μs)), relatively low cost, and as mentioned above, spatial separation of charge transfer/amplification and charge accumulation processes (i.e. signal readout), which allows for good 2D resolution (up to 50 μm[45]).

So far, an extensive research was conducted to optimize the response of GEM detectors. These include electrode configurations, detection chamber materials choice, geometry of holes in GEM foils, applied voltages for optimal field distribution, and gas flow rate and mixture composition. Micropattern readout is another important element of GEM detectors. It is responsible for the effective extraction of the collected charge from the electron cloud and its proper transfer to the electronic circuit. Selecting the geometry of the readout plane is important for the spatial resolution of the detector that was studied in[13,14,46].

In the case of intensive radiation sources such as tokamak plasma, there are events with multiple photons at the same time, which are lost during histogramming. This is due to the fact that simultaneous photons can appear in the same electronic channel, common for a group of connected pixels, even being recorded in different places on the readout plane. It is associated with the ambiguity of processing such a multi-hit event. A potential solution would be to have smaller and independent pixels for unambiguous reconstruction of the position and energy of the registered photons. This may not be practical, however, because thousands of pixels are needed for good spatial resolution even on a relatively small detection area.

In order to determine the limit values for the considered readout structures in relation to the unambiguous determination of the charge cluster produced by the photon and its position on the anode plane, this type of measurements was carried out for all readout structures[46]. The results are shown in Figure 5 together with the extrapolated intensity of the X-ray generator.

Since tokamak plasma is a very bright source of SXR radiation, it can produce a very intense photon flux on the detector surface, which reaches over 10^5-10^7 cps mm^{-2} depending on the heating power, impurities present in the plasma and the detector system. Considering that high spatial resolution imaging of tokamak plasma would require a huge number of pixels directly connected to the readout electronics channels, it would be more appropriate to develop a readout structure with reduced independent electronics channels. Therefore, for the purpose of plasma imaging, the structure of the UXV readout, taking into account its further development and optimization, can be considered as a promising basic configuration for the construction of anode electrodes with the required characteristics.

With the high radiation fluxes mentioned above, there is a high probability of overlapping signals in time and space, which may prevent the identification of charge clusters from the detector signals, and this means a loss of information about the energy and number of photons. In order to improve the performance of the detector, a procedure of separation of overlapping pulses for the same electronic channel has been developed, so that it can be implemented in real time data processing[47]. The developed algorithm separates the superimposed signals caused by a relatively slow electronic circuit. The separation of overlapping pulses has been successfully introduced and verified for simulation experiments. The procedure is effective when the primary GEM pulses do not overlap. The expected improvement in time resolution is about ~50 ns compared to ~500 ns previously achieved for shaped detector signals. This can significantly improve the performance of the GEM detector by implementing an algorithm in the FPGA module (or by processing signals in quasi online mode).

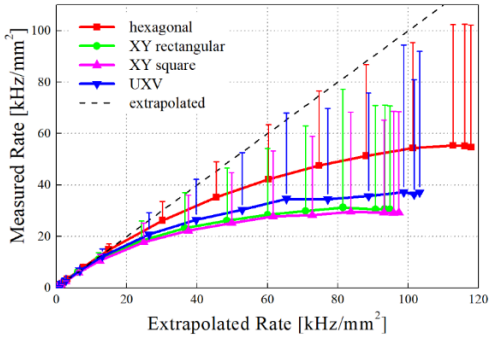

Figure 5. The deviation of the photon flux measured by the GEM detector from the extrapolated flux for all the readout structures. The total number of indistinguishable events is marked as error bars. Extrapolated flux (dashed grey line) was obtained from independent verification of the linearity of the X-ray generator[46].

Since plasma radiation has a very high intensity and covers a wide range, the detection section of the developed diagnostics must be adapted to the experimental environment. It should not only thoroughly examine the radiation, but ideally, it should not provide any additional parasitic signals from the interaction of detector elements with incident radiation, e.g. fluorescence emission from photon-sensitive chamber elements. Therefore, the detector components must be designed so as not to interfere with the original signal.

The X-ray spectrum from the plasma in the Soft-Semi-Hard (S-SH) area of the radiation consists of a wide part of continuous radiation mixed with the emission from heavy impurities. Such a spectrum usually extends above the absorption edge of the copper (~9 keV), in particular for the ITER reactor, the basic material used so far for the production of GEM films, what could lead to a parasitic fluorescence signal. Recently, very preliminary studies on the adaptation of GEM foil

with reduced copper have been launched[48] based on a chromium adhesive layer. However, the energy of the Cr K_α line is 5.411 keV, reaching the target energy range of photons. In addition, the fluorescence yield of Cr layers is also high due to relatively high Z, equal to ~0.35 for Cr and ~0.5 for Cu[49] as well as the effect of photon absorption.

In this work, aluminum as a top metallic layer of GEM foil was proposed in order to use them for tokamak plasma imaging in the S-SH X-ray range. A lower absorption coefficient of Al compared to Cu above 2 keV leads to a lower radiation effect for Al film, and in addition, the fluorescence yield of Al is less than 0.05[49]. In one of the recent papers[50], for the first time, according to the best knowledge of the authors, the newly developed GEM aluminum foils (with an adhesive layer of Cr) proposed have been pretested for use in plasma X-ray imaging in the S-SH range.

In order to compare the influence of different materials on radiation imaging, simulations of a GEM response using GEANT4 (Figure 6 (a)) were performed. It was shown that the intensity of parasitic fluorescence lines varies strongly depending on the material used in the detection chamber.

Since direct imaging imposes a perpendicular direction on incident radiation, it requires that the contribution of all unwanted signals from the interaction of detector materials with incident radiation be minimized. Therefore, the detectors were tested for different radiation sources (fluorescent lines) to verify the spectral performance of two detectors differing only in GEM foil material. The results of the tests are shown in Figure 6 (b-d). The presented dependencies show an undesirable influence of Cu material. Even with an aluminum GEM-based detector that has copper only on the readout board, Cu contributes to the overall signal (peak at ~8 keV on both drawings). The spectrum derived from Cu GEM foil exhibits a line of copper K- series (wide peak at ~8 keV with a Ar escape peak at ~5 keV). The measured spectra were consistent with the results of the simulation. This provided important information about the origin of the detector signal, with both the material and type of interaction been explained. This also confirmed the conclusion that Al is a more suitable material for the use in the detector for plasma imaging.

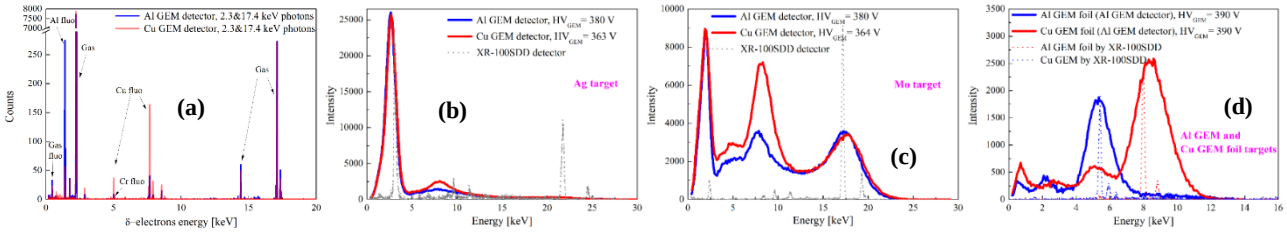

Figure 6. (a) Simulations of δ electrons spectra for incident photons of 2.3 and 17.4 keV. Measured spectra for the following material targets: (b) Ag, (c) Mo, and (d) Cu GEM and Al GEM foils (L, K-edge of Mo) for Al and Cu GEM foils[50].

Moreover, the aspect of neutron interaction with the detection chamber material and with surrounding materials in a fusion experiment, as a source of background radiation, should be taken into account (which is a separate and broad issue[21,22]). In short, comparing the activation of Al and Cu by the full spectrum of neutrons produced in fusion devices, it turns out that Al material is more suitable for fusion applications also under its neutron interaction, since its active cross-section for activation is several times smaller than in the case of Cu. It also disperses several times less neutrons than Cu in almost the entire neutron range, except for 1-3 MeV, where this ratio is relatively higher (by 30-40%) than for Cu. In addition, the cross-sections of the radiation capture (n,γ), which is a very intensive reaction for thermal neutrons, are about 10 times smaller for Al than for Cu atoms.

5. SUMMARY

This work summarizes the achievements of the team at IPPLM in the development of a new global SXR measurement system based on GEM gas detectors. This work was initiated and is currently ongoing to support an ITER-oriented research programme, in order to develop a useful and effective detector for research in plasma physics through observation and analysis of radiation measurement. The main objective of this work was to develop, construct and study new GEM-based detectors for high resolution bent crystal spectrometer, tungsten transport tomography in ITER-oriented tokamaks and plasma radiation imaging.

The presented achievements showed that the proposed diagnostics can be used to measure SXR in tokamak plasma conditions. This diagnostics is intended to be used in future fusion reactors, as it takes into account the harshness of the operating conditions and eliminates the weaknesses of currently used SXR semiconductor detectors.

REFERENCES

[1] Séguin, F.H., et al., "Radiation-hardened x-ray imaging for burning-plasma tokamaks," Review of Scientific Instruments 68, 753 (1997).
[2] Sauli, F., "The gas electron multiplier (GEM): Operating principles and applications," Nuclear Instruments and Methods in Physics Research Section A 805, 2-24 (2016).
[3] Buzulutskov, A.F., "Radiation Detectors Based on Gas Electron Multipliers (Review)," Instruments and Experimental Techniques 50(3), 287–310 (2007).
[4] Hill, K.W., et al., "A spatially resolving x-ray crystal spectrometer for measurement of ion-temperature and rotation-velocity profiles on the Alcator C-Mod tokamak", Review Scientific Instruments 79, 10E320 (2008).
[5] Zastrow, K.-D., et al., "Deduction of central plasma parameters from line-of-sight averaged spectroscopic observations," Journal of Applied Physics 70, 6732 (1991).
[6] Chernyshova, M., et al., "Development of GEM gas detectors for X-ray crystal spectrometry," Journal of Instrumentation 9, C03003 (2014).
[7] Zemtsov, I., et al., "Modelling of tungsten behavior in plasma of t-10 tokamak," Physics of Atomic Nuclei 81(7), 1042-1047 (2018).
[8] Pütterich, T., et al., "Modelling of measured tungsten spectra from ASDEX Upgrade and predictions for ITER," Plasma Physics and Controlled Fusion 50, 085016 (2008).
[9] Rzadkiewicz, J., et al., "Design of T-GEM detectors for X-ray diagnostics on JET," Nuclear Instruments and Methods in Physics Research A 720, 36 (2013).
[10] Jakubowska, K., et al., "Development of a 1D Triple GEM X-ray detector for a high-resolution X-ray diagnostics at JET," Proceedings of the 38th EPS Conference on Plasma Physics 2011, 716 (2011).
[11] Bartiromo, R., et al., "JET high resolution bent crystal spectrometer," Review of Scientific Instruments 60, 237 (1989).
[12] Bachmann, S., et al., "Charge amplification and transfer processes in the gas electron multiplier," Nuclear Instruments and Methods in Physics Research Section A 438, 376 (1999).
[13] Czarski, T., et al., "Data processing for soft X-ray diagnostics based on GEM detector measurements for fusion plasma imaging," Nuclear Instruments and Methods in Physics Research Section B 364, 54-59 (2015).
[14] Czarski, T., et al., "Serial data acquisition for the X-ray plasma diagnostics with selected GEM detector structures," Journal of Instrumentation 10, P10013 (2015).
[15] Shumack, A.E., et al., "X-Ray Crystal Spectrometer Upgrade for ITER-like wall experiments at JET," Review of Scientific Instruments 85, 11E425 (2014).
[16] Nakano, T., et al., "Determination of tungsten and molybdenum concentrations from an X-ray range spectrum in JET with the ITER-like wall configuration," Journal of Physics B: Atomic, Molecular and Optical Physics 48, 144023 (2015).
[17] Pozniak, K.T., et al., "FPGA based charge fast histogramming for GEM detector," Proc. SPIE 8903, 89032F (2013).
[18] Bucalossi, J., et al., "The WEST project: Testing ITER divertor high heat flux component technology in a steady state tokamak environment," Fusion Engineering and Design 89(7-8), 907-912 (2014).
[19] Sertoli, M., et al., "Modification of impurity transport in the presence of saturated (m,n) = (1,1) MHD activity at ASDEX Upgrade," Plasma Physics and Controlled Fusion 57(7), 075004 (2015).
[20] Chernyshova, M., et al., "Conceptual design and development of GEM based detecting system for tomographic tungsten focused transport monitoring," Journal of Instrumentation 10, P10022 (2015).
[21] Chernyshova, M., et al., "Gaseous electron multiplier-based soft X-ray plasma diagnostics development: Preliminary tests at ASDEX Upgrade," Review of Scientific Instruments 87(11), 11E325 (2016).
[22] Chernyshova, M., et al., "GEM detectors development for radiation environment: neutron tests and simulations," Proc. SPIE 10031, 100313X (2016).
[23] Chernyshova, M., et al., "Development of GEM detector for tokamak SXR tomography system: Preliminary laboratory tests," Fusion Engineering and Design 123, 877-881 (2017).
[24] Chernyshova, M., et al., "Study of the optimal configuration for a Gas Electron Multiplier aimed at plasma impurity radiation monitoring," Fusion Engineering and Design 136, 592-596 (2018).
[25] Chernyshova, M., et al., "Development of GEM detector for plasma diagnostics application: simulations addressing optimization of its performance," Journal of Instrumentation 12, C12034 (2017).

[26] Malinowski, K., et al., "Simulation of energy spectrum of GEM detector from an x-ray quantum," Journal of Instrumentation 13, C01018 (2018).
[27] Mazon, D., et al., "Design of soft-X-ray tomographic system in WEST using GEM detectors," Fusion Engineering and Design 96-97, 856-860 (2015).
[28] Zienkiewicz, P., et al., "Data management software concept for WEST plasma measurement system," Proc. of SPIE 9290, 92902B-1 (2014).
[29] Wojenski, A., et. al., "Diagnostic-Management System and Test Pulse Acquisition for WEST Plasma Measurement System," Proc. of SPIE 9290, 929029-1 (2014).
[30] Chernyshova, M., et al., "GEM detector development for tokamak plasma radiation diagnostics: SXR poloidal tomography," Proc. of SPIE 9662, 966231-1 (2015).
[31] Sauli, F., "Development and applications of gas electron multiplier detectors," Nuclear Instruments and Methods in Physics Research A 505, 195-198 (2003).
[32] Ball, M., et al., "Ion backflow studies for the ALICE TPC upgrade with GEMs," Journal of Instrumentation 9, C04025 (2014).
[33] Agostinelli, S., et al., "Geant4 - a simulation toolkit," Nuclear Instruments and Methods in Physics Research A 506, 250 (2003).
[34] Smirnov, I.B., "Modeling of ionization produced by fast charged particles in gases," Nuclear Instruments and Methods in Physics Research A 554, 474 (2005).
[35] Mazon, D., et al., "SXR measurement and W transport survey using GEM tomographic system on WEST," Journal of Instrumentation 12, C11034 (2017).
[36] Jardin, A., et al., "Tomographic capabilities of the new GEM based SXR diagnostic of WEST," Journal of Instrumentation 11, C07006 (2016).
[37] Wojenski, A., et al., "Concept and current status of data acquisition technique for GEM detector–based SXR diagnostics," Fusion Science and Technology 69, 595-604 (2016).
[38] Wojenski, A., et al., "Multichannel reconfigurable measurement system for hot plasma diagnostics based on GEM-2D detector," Nuclear Instruments and Methods in Physics Research B 364, 49-53 (2015).
[39] Wojenski, A., et al., "FPGA-based GEM detector signal acquisition for SXR spectroscopy system," Journal of Instrumentation 11, C11035 (2016).
[40] Mazon, D., et al., "GEM detectors for WEST and potential application for heavy impurity transport studies," Journal of Instrumentation 11, C08006 (2016).
[41] Bachmann, S., et al., "High rate X-ray imaging using multi-GEM detectors with a novel readout design," Nuclear Instruments and Methods in Physics Research A 478, 104 (2002).
[42] Zielinska, A., et al., "X-ray fluorescence imaging system for fast mapping of pigment distributions in cultural heritage paintings," Journal of Instrumentation 8, P10011 (2013).
[43] Veloso, J.F.C.A., et al., "Energy resolved X-ray fluorescence imaging based on a micropattern gas detector," Spectrochimica Acta Part B: Atomic Spectroscopy 65(3), 241-247 (2010).
[44] Blatt, S., et al., "Charge transfer of GEM structures in high magnetic fields," Nuclear Physics B Proceedings Supplement 150, 155-158 (2006).
[45] Bressan, A., et al., "Beam tests of the gas electron multiplier," Nuclear Instruments and Methods in Physics Research Section A 425(1-2), 262-276 (1999).
[46] Chernyshova, M., et al., "2D GEM based imaging detector readout capabilities from perspective of intense soft X-ray plasma radiation," Review of Scientific Instruments 89, 10G106 (2018).
[47] Czarski, T., et al., "Measuring issues in the GEM detector system for fusion plasma imaging," Journal of Instrumentation 13, C08001 (2018).
[48] Mindur, B., et al., "Performance of a GEM detector with copper-less foils," Journal of Instrumentation 12, P09020 (2017).
[49] Krause, M.O., "Atomic radiative and radiationless yields for K and l shells," J. Phys. Chem. Ref. Data 8, 307 (1979).
[50] Chernyshova, M., et al. "Advantages of Al based GEM detector aimed at plasma soft−semi hard X-ray radiation imaging," Fusion Engineering and Design, https://doi.org/10.1016/j.fusengdes.2019.01.153 (2019).

Basics of numerical simulations of the signals from GEM detector

Karol Malinowski*[a], Maryna Chernyshova[a], Tomasz Czarski[a], Ewa Kowalska-Strzęciwilk [a], Paweł Linczuk[a,b], Andrzej Wojeński[b],
[a]Institute of Plasma Physics and Laser Microfusion, Hery Street 23, 01-497 Warsaw, Poland;
[b]Warsaw University of Technology, Institute of Electronic Systems, Nowowiejska 15/19, 00-665 Warsaw, Poland

ABSTRACT

The Gas Electron Multiplier (GEM) is a detector used to register ionizing radiation, e.g., soft X-rays. The detector of this type, built and developed at the IPPLM institute, allows registering X-rays in the energy range of 2-20keV and determining its intensity in time, as well as its spatial position and energy. Simulating the work of such a detector, performed in parallel to experimental research, and sometimes preceding it, allows for optimization of construction and operation parameters of this detector with respect to the requirements set in the experiment, and allows for a better understanding of the physical processes occurring in the detector. The paper presents how simulations are performed, i.e. describes applied programs, main stages of simulation such as the construction of a three-dimensional model of the detector for calculations, the efficiency of X-ray detection, its conversion to primary electrons and the process of avalanche formation. Finally, the results obtained in this way are also presented.

Keywords: gaseous ionization detector, GEM detector simulation, X-ray detector

1. INTRODUCTION

The GEM detector[1] is used in many physical experiments. Detectors constructed in our laboratory are used in particular in tokamak research[2]. The general scheme of the GEM detector is shown in Figure 1. The principle of operation of such a detector is as follows. An X-ray quantum of a certain energy (e.g. 6 keV) falls on the detector window, passes through it and reaches the first gas area (drift). Here, with a certain probability, the radiation is absorbed by the photoelectric effect (dominant in the soft X-ray region), as a result of which ionization electrons (photoelectron and Auger electrons) are created, which then, as a result of ionization, cause the formation of a certain number (tens to hundreds) of electrons. These electrons are pulled by an electric field (1-4kV/cm) onto the GEM foil. Such foil is a dielectric on both sides covered with copper (electrodes), in which holes are made with a diameter of 50 um and a distance between them of 140 um. The electrons fly through holes of the foil, where the electric field has a much higher value (>50kV/cm), allowing for the multiplication of electrons (Townsend discharge). This process takes place three times in general (3 foils) giving a total amplification of 10^3-10^4. The last electrode (readout) receives such a number of electrons that it is possible to register by electronic circuits[3].

Simulating the operation of such a detector requires the use of at least several specialized programs. This paper presents simulations performed using free, non-commercial software developed in several research centers, including CERN. These programs allow simulating virtually the entire process of detector operation, including its structure (geometry, materials used), applied voltage and parameters of incident X-rays.

2. SOFTWARE USED FOR SIMULATION

The basic and most important program, Garfield++[4], used to simulate GEM-based detectors was developed many years ago. This is a program for constructing detailed simulations of multiple aspects of drift chambers with gaseous media. For a given electric field it allows simulating drift and the whole process of creating an avalanche of electrons in the gas. The program also uses, among others, two other programs: Magboltz and Heed. Magboltz[5,6] counts the transport properties of electrons in gas mixtures, and the program Heed[7] allows simulating the ionization pattern produced along

*karol.malinowski@ifplim.pl

Photonics Applications in Astronomy, Communications, Industry, and High-Energy Physics Experiments 2019, edited by Ryszard S. Romaniuk, Maciej Linczuk, Proc. of SPIE Vol. 11176, 111764G
© 2019 SPIE · CCC code: 0277-786X/19/$21 · doi: 10.1117/12.2537950

the track of relativistic charged particles. Heed can also be used for the simulation of x-ray photoabsorption. The conversion of x-rays in the drift volume into a number of primary electrons, which are a source of electron avalanches in the GEM device, can be simulated using either program Degrad or Heed. Degrad[8] is a program developed by S. Biagi, using an accurate Auger cascade model for interaction of photons and particles with gas mixtures in electric and magnetic fields.

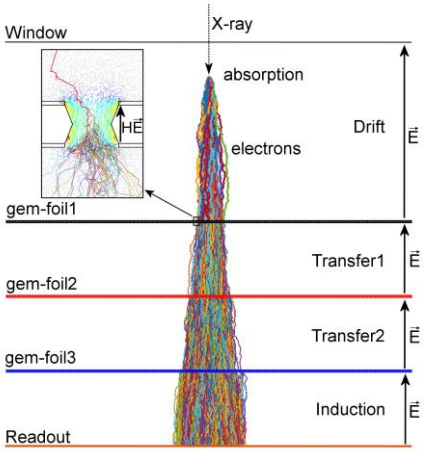

Figure 1. Operating scheme of GEM-based detector.

Although Garfield++ allows the calculation of electron propagation for simple geometries of electric fields, for more complex fields, such as the GEM detector, it is necessary to use external programs. In this work two free programs Gmsh[9] and Elmer[10] were used. Gmsh is a finite-element mesh (FEM) generator, used to define a geometry and split it into many small elements so that the finite element method can be applied in the calculation of electrostatic fields. Elmer is a finite element analysis program. This program is used to calculate the electric field throughout space in a device geometry for a mesh previously generated by Gmsh. This three-dimensional map of the electric field is then loaded into the Garfield++ program.

Another program used in simulations of the GEM detector signals is GEANT4[11]. The GEANT4 program (for GEometry ANd Tracking) is a platform for "the simulation of the passage of particles through matter," using Monte Carlo methods. In our case, it allows calculating the efficiency of X-ray detection by the detector or to predict the appearance of various undesirable signals resulting from the interaction of X-ray radiation with the tested detector.

3. CALCULATION OF THE GRID AND FIELD MAP

Since the GEM detector structure is reproducible in X and Y directions, i.e. along the perforated foil surface, and the detector surface itself is very large (e.g. 10x10cm^2) compared to the distance between the holes (140um), in the Gmsh program, only a small slice ("cell") of the detector structure is created, which covers the entire space along the Z axis and a small fragment along the XY surface. In the cell structure, the volume of gas, kapton and copper on the kapton are determined, as well as the surface of the electrodes on the window and the readout. Such a cell at a later stage of the simulation is duplicated and arranged next to each other in an ordinary or mirror way, creating any large structure in X and Y directions. Figure 2 shows such a cell made in the Gmsh program. The fragments of the GEM foil in the cell are moved relative to each other, which causes that when the detector is assembled, the holes of the first (black), second (red) and third (blue) foils are positioned relative to each other as shown on the right side of the image.

Then, using the Gmsh program, the FEM method is applied to generate a mesh, in whose nodes the value of the electric field is later counted. Mesh generation is one of the most important elements of the simulation. The mesh must be more dense in areas with a high gradient of the field, i.e. in the area of a hole in the GEM foil, and as rarely as possible in areas with little variation of the field, as the calculation time of the electron avalanche grows with node number. Therefore, an

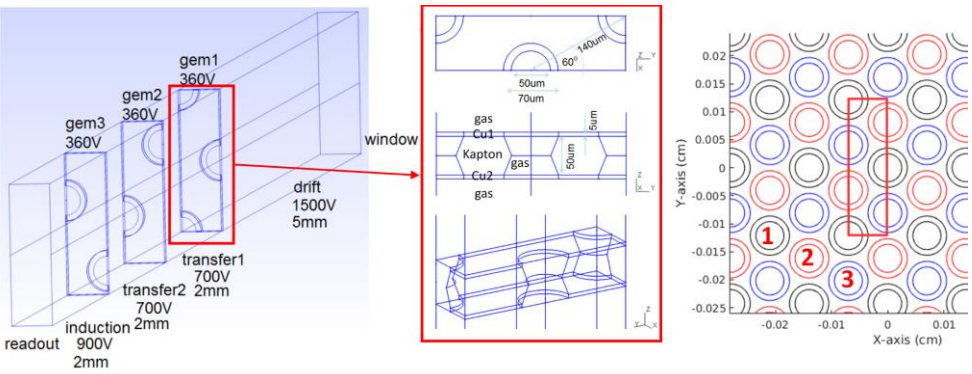

Figure 2. View of a 3-foils GEM detector cell created in the Gmsh software. On the left, there is a view of the entire cell with exemplary voltages, in the middle - a detailed view of the GEM foil, on the right - a single cell forming, through a mirror fold, the entire three-layered detector structure.

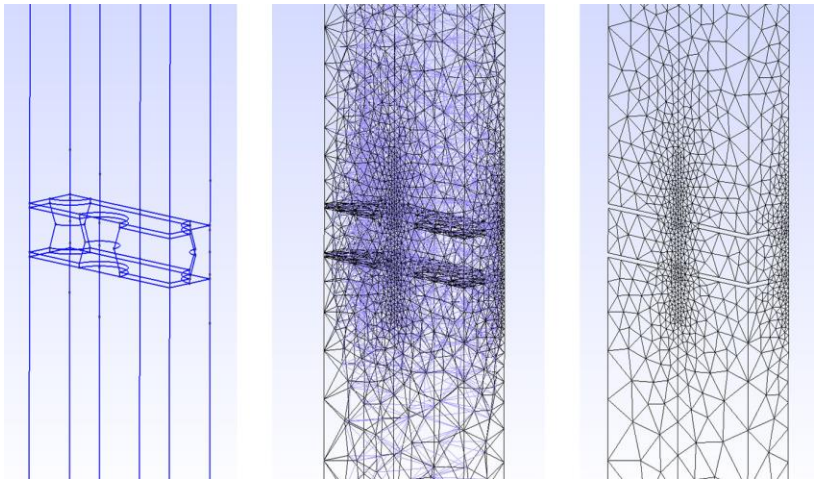

Figure 3. Example of a mesh for a GEM detector cell made with Gmsh. On the left there is a view of the edge of the structure, in the middle - a 3D-view of the mesh, on the right - a view of the mesh on the cell surface.

optimum between the density of the mesh (accuracy of calculations) and the smallest number of mesh nodes (speed of calculations) is sought. An example of the mesh used for the calculations is shown in Figure 3.The Elmer program calculates voltage values for mesh nodes. Relative permittivity values for gas, kapton and copper and voltage values for all electrodes shall be given as input parameters in addition to the mesh. Figure 4 shows the resulting electric field map for the GEM cell. It can be seen that the field value in the hole reaches about $5*10^6$ V/m (compared to $7.2*10^6$ V/m of the nominal field between the foil electrodes).

4. CONVERSION OF X-RAYS INTO PRIMARY ELECTRONS

The absorption of X-rays in the GEM detector, as described in the introduction, occurs with a certain probability, different for different radiation energies. Additionally, only photons absorbed in the drift area, i.e. in the first gas area behind the detector window, give the correct signal. The whole process of converting X-rays into a cloud of electrons, the so-called primary ones, which initiate the creation of a whole avalanche of electrons in the detector, is quite complex[12]. In general, the absorption of the radiation quanta occurs as a result of the photoelectric effect, creating ionization electrons, i.e. photoelectrons and Auger electrons, which then lose their energies by ionizing gas atoms along their trajectories and in effect cause the formation of a certain number of free electrons, which are the beginning of an avalanche and therefore measured electric signal. For energy above 3.2keV (Ar K-shell binding energy), with some

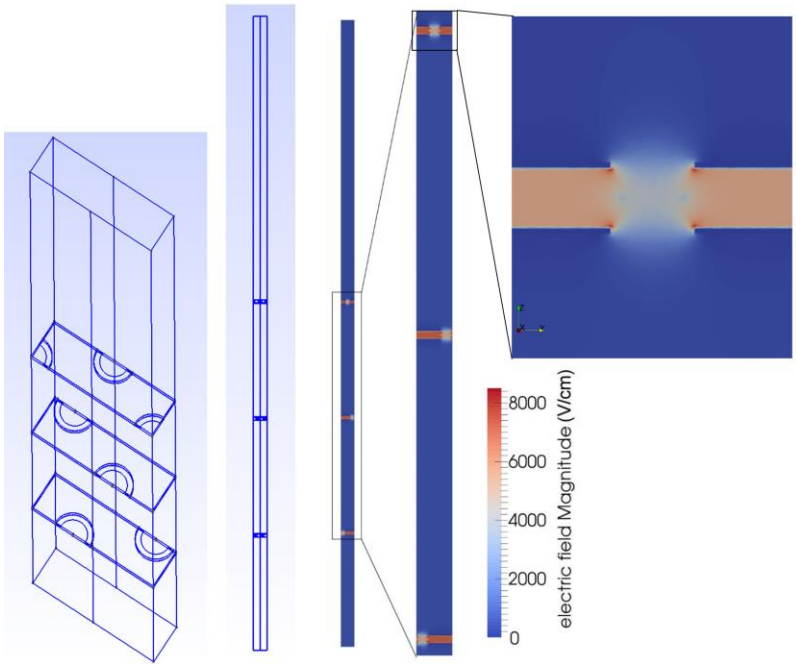

Figure 4. View of a GEM detector cell (created in Gmsh) and its electric field distribution (calculated in Elmer).

probability, during the interaction of quantum X with the Argon atom, filling up the vacancy on the K-shell, instead of the emission of the Auger electron with energy of 3 keV is accompanied by the escape of this energy outside the atom in the form of a fluorescent photon. Therefore, sometimes the total energy of the primary electrons has 3keV less energy and in effect at the output of the detector one gets the signals correspondingly 3keV less. Figure 5 shows the X-ray absorptions of 1 to 10 keV photons in the 5 mm drift area of the detector for the basic gas mixture Ar/CO_2 70/30 and for comparison with the two other mixtures. This dependence was obtained by means of the GEANT4 program. You can see that the detector has the highest detection efficiency for energy of 1-7 keV. The first one, visible on the diagram, the absorption edge at 1.5keV energy results from the radiation transmission through the detector window with the Al layer (the binding energy of the K-shell is 1.56 keV), and the second one at the energy of 3.2 keV is connected with the binding energy of electrons in the K-shell of Ar, which is a component of the gas mixture.

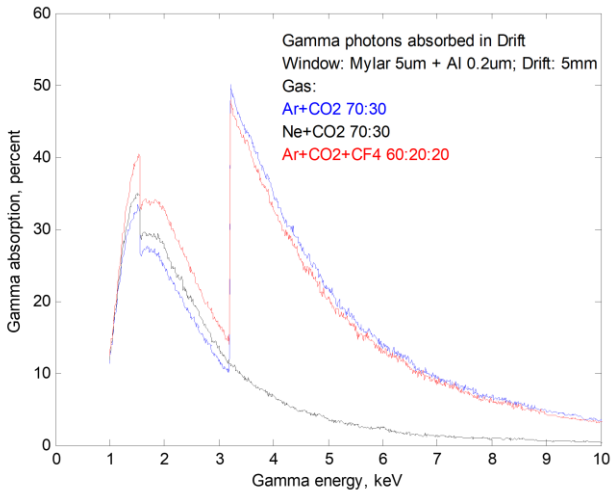

Figure 5. Absorption of X-rays with energies of 1 to 10 keV in the GEM detector with different gas mixtures.

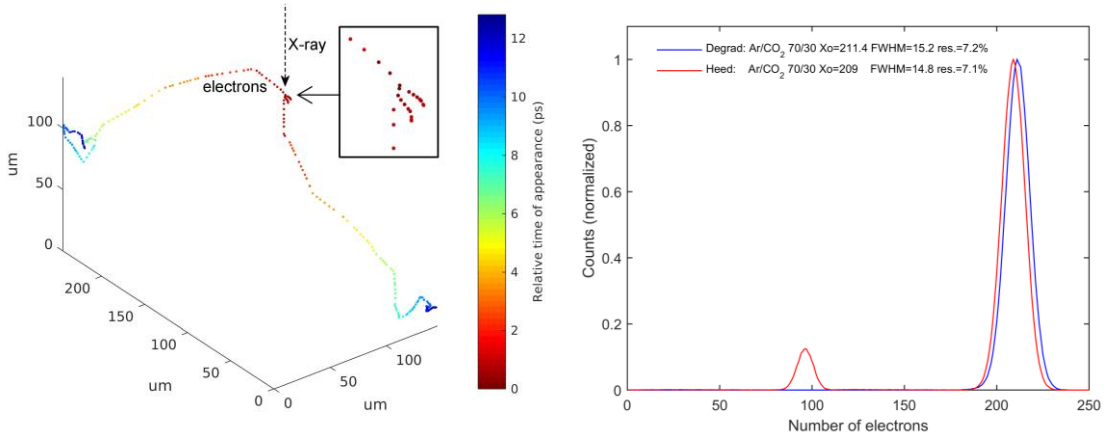

Figure 6. An example, calculated in Heed, of spatial position of primary electrons generated by the absorption of the x-ray quantum with energy of 5.9 keV in the argon atom in the gas mixture Ar/CO_2 70/30 (on the left) and distributions of the number of primary electrons produced for this absorption calculated by Heed and Degrad (on the right)[11].

Figure 6, on the left, shows an example of the Heed program's spatial distribution of the cloud of electrons created by the absorption of X-rays in the gaseous area of drift. In this case, free electrons appeared along the trajectory of four ionization electrons - one photoelectron and 3 Auger electrons. Figure 6, on the right, shows the distribution, calculated by two programs, of the number of primary electrons produced by the absorption of the quanta X with an energy of 5.9 keV (energy from the test source ^{55}Fe) in the drift area of the gas mixture of the GEM detector. As can be seen, this number is variable, with an average value of about 210 electrons for the dominant process and 96 electrons for the less probable process with the escape of the argon fluorescence photon.

5. SIMULATION OF THE SIGNALS ON READOUT

In the next step, the data from Gmsh and Elmer, i.e. the geometry and distribution of the electric field, are used as input for the avalanche simulation of the GEM detector by means of Garfield++. Data obtained from the Heed program, i.e. position, energy and number of electrons, serve as parameters for electrons initiating an avalanche. Simulations were performed for gas mixture Ar/CO_2 70/30 and voltage on GEM foils V_{GEM}=380V. The remaining parameters, i.e. the values of voltages and distances between the foils, were changed to check the influence of these changes on the parameters of the output signals. Figure 7 shows an avalanche obtained from Garfield++ program for a single electron and a total avalanche from 209 electrons, corresponding to the avalanche caused by the registration of X-ray quanta of

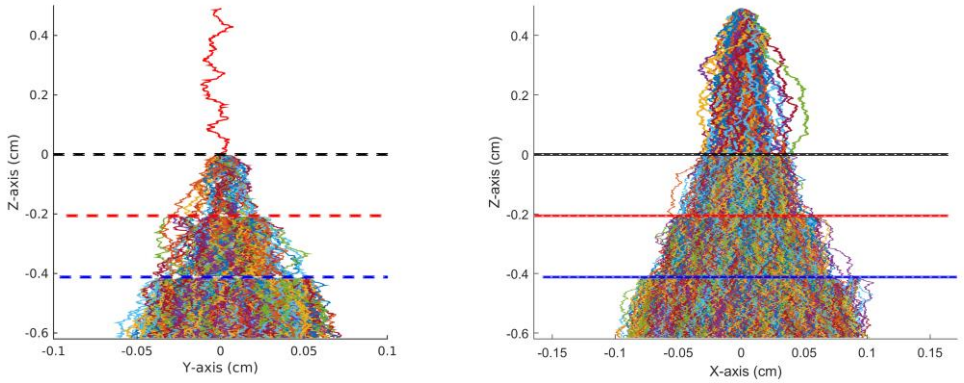

Figure 7. An example of simulated electron avalanche from one (left) and 209 (right) primary electrons calculated by means of Garfield++.

5.9 keV energy by the detector. The size (FWHM) of the electron cloud on the readout electrode is approximately 0.5mm. The exact density distributions of the electrons on the readout, for different configurations of the distance between the foils, are shown in Figure 8. The creation of an electron avalanche causes not only their multiplication and enlargement of their spatial area, but also their extension in time. Figure 9 shows the time distributions of the electrons when they reach the readout for different voltage configurations and foils distances. The presented time is calculated in relation to the appearance of primary electrons in the drift area. The obtained electron gains range from 3300 to 5400.

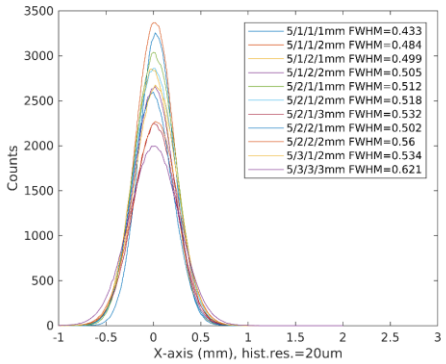

Figure 8. The spatial distribution (along X-axis) of electrons density on readout electrode of the GEM detector, performed for different spatial configuration and for fixed values of electric field: D/T1/T2/I = 1200/2000/2500/4500 V/cm, V_{GEM}=380V, calculated by means of Garfield++.

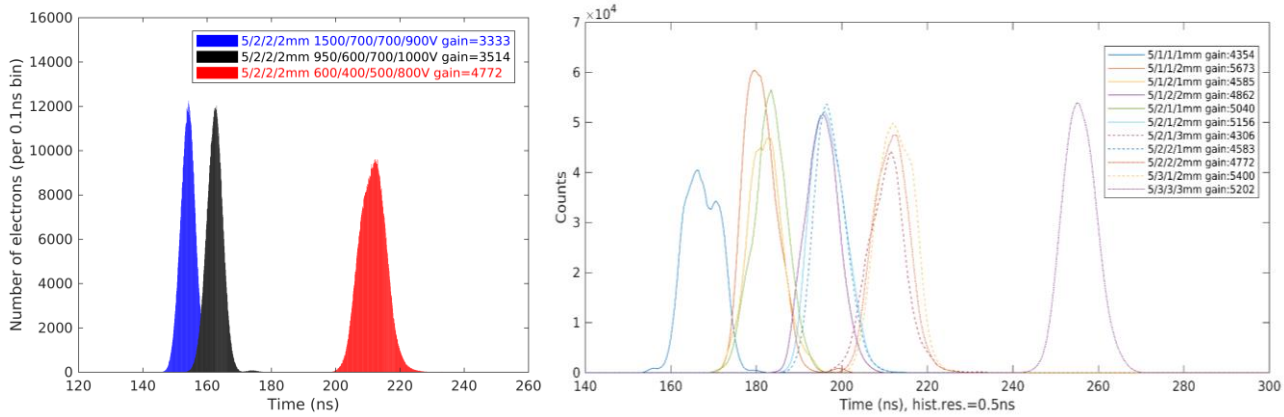

Figure 9. Results of signal simulations (from 209 primary electrons) on Readout electrode of GEM detector, performed for three different voltage configurations (left) and for different spatial configuration, for fixed values of electric field D/T1/T2/I = 1200/2000/2500/4500 V/cm and V_{GEM}=380V (right).

6. SUMMARY

The set of programming tools presented in the paper allows simulating virtually all the work of the GEM detector, from the X-ray quanta to the appearance of an electrical signal on the reading electrode. The obtained results can be helpful in optimizing the detector for specific requirements, such as maximizing gain, temporal or spatial resolution, or assisting in the selection of voltage at the electrodes. Simulations are also useful for a better understanding of the physical processes involved in converting X-rays quanta into electrical signals in the GEM detector.

ACKNOWLEDGMENTS

This scientific work was partly supported by Polish Ministry of Science and Higher Education within the framework of the scientific financial resources in the years 2014-2019 allocated for the realization of the international co-financed project.

REFERENCES

[1] Sauli, F., "The gas electron multiplier (GEM): Operating principles and applications," Nucl. Instrum. Meth. A805, 2-24 (2016).
[2] Chernyshova, M., Malinowski, K., Czarski, T. et al., "Gaseous electron multiplier-based soft x-ray plasma diagnostics development: Preliminary tests at ASDEX Upgrade," Rev. Sci. Instrum. 87, 11E325 (2016).
[3] Czarski, T., Chernyshova, M., Pozniak, K. T. et al., "Data processing for soft x-ray diagnostics based on GEM detector measurements for fusion plasma imaging," Nucl. Instrum. Meth. B 364, 54-59 (2015).
[4] Schindler, H., Veenhof, R. et al., "Garfield++," http://garfieldpp.web.cern.ch/garfieldpp.
[5] Biagi, S., "Magboltz," http://magboltz.web.cern.ch/magboltz/.
[6] Biagi, S., "Monte Carlo simulation of electron drift and diffusion in counting gases under the influence of electric and magnetic fields," Nucl. Instr. and Meth. A 421, 234–240 (1999).
[7] Smirnov, I. B., "Modeling of ionization produced by fast charged particles in gases," Nucl. Instr. Meth. A 554, 474-493 (2005).
[8] Biagi, S., "Degrad," http://magboltz.web.cern.ch/magboltz/.
[9] Geuzaine, C., Remacle, J.-F., "Gmsh: A 3-D finite element mesh generator with built-in pre- and post-processing facilities," Int. J. Numer. Meth. Eng. 79, 1309–1331 (2009).
[10] C. I. C. for Science, "Elmer: Open Source Finite Element Software for Multiphysical Problems," http://www.csc.fi/english/pages/elmer.
[11] Agostinelli, S. et al., "Geant4 - a simulation toolkit," Nucl. Instrum. Methods. A 506, 250–303 (2003).
[12] Malinowski, K., Chernyshova, M., Czarski, T. et al., "Simulation of energy spectrum of GEM detector from an x-ray quantum," JINST 13, C01018 (2018).

Tracking with Deep Neural Networks

Marcin Kucharczyk[a] and Marcin Wolter[a]

[a]Institute of Nuclear Physics PAN, Kraków, Poland

ABSTRACT

High Energy Physics experiments require fast and efficient methods to reconstruct the tracks of charged particles. Commonly used algorithms are sequential and the CPU required increases rapidly with a number of tracks. Neural networks can speed up the process due to their capability to model complex non-linear data dependencies and finding all tracks in parallel.

In this paper we describe the application of the Deep Neural Network to the reconstruction of straight tracks in a toy two and three-dimensional models. It is planned to apply this tracking method to the experimental data taken by the MUonE experiment at CERN.

Keywords: Deep Neural Networks, Machine Learning, tracking, HEP

1. INTRODUCTION

Particle detectors used in High Energy Physics (HEP) require an efficient and fast reconstruction of charged particle tracks. Effective tracking algorithms are used in HEP experiments for years (for example the Kalman Filter[1]), but they are sequential and the CPU required increases rapidly with the track density. Machine learning algorithms, especially Deep Neural Networks, can speed up the reconstruction process thanks to their capability to model complex non-linear data dependencies and to parallelize easily.

Our goal is to test and eventually use the track finding techniques based on machine learning. They are planned to be applied to the experimental testbeam data taken in 2017 and 2018 by the MUonE experiment,[2] planned to be operating at the SPS accelerator at CERN. The experiment supposes to measure a hadronic correction to the anomalous muon magnetic moment in order to increase the sensitivity to the potential New Physics phenomena which may cause an observed discrepancy with respect to the Standard Model predictions. The Deep Neural Networks may provide fast and efficient pattern recognition which is the most crucial step in the track reconstruction procedure.

The track reconstruction is performed for two and three-dimensional models. Preliminary results from a two-dimensional toy model were shown at KUKDM 2019 conference,[3] in this article the results for two dimensional reconstruction are added.

2. TRACK RECONSTRUCTION

Our aim is to test on a simple toy example, whether we are able to reconstruct a particle track without using the sequential tracking algorithms, but reconstructing the track parameters at once using the deep neural network. This approach was tested on a simple two-dimensional model and than extended into three dimensions.

Further author information: e-mail: marcin.kucharczyk@ifj.edu.pl, marcin.wolter@ifj.edu.pl

Photonics Applications in Astronomy, Communications, Industry, and High-Energy Physics Experiments 2019,
edited by Ryszard S. Romaniuk, Maciej Linczuk, Proc. of SPIE Vol. 11176, 111764H
© 2019 SPIE · CCC code: 0277-786X/19/$21 · doi: 10.1117/12.2538197

2.1 Reconstruction in 2D

To avoid computational problems and excessive use of CPU the two-dimensional 28×28 pixel toy model with straight particle tracks has been developed. A random noise and pixel inefficiency has been added to make the model more realistic.

The model is later extended into three dimensions, which required the use of a cluster of Graphic Processor Units (GPU).

Based on the research presented by the HEP.TrkX project[4] in[5,6] we have built a neural network that processes the raw detector data without any intermediate steps. In this straight-forward approach we have used the convolutional neural network (CNN)[7] to find the straight tracks in the toy model. A straight track in two-dimensional space can be described by the equation representing a straight line, i.e., $y = ax + b$, with slope a and intercept b (see Figure 1). The neural network is trained to return these two parameters for each track.

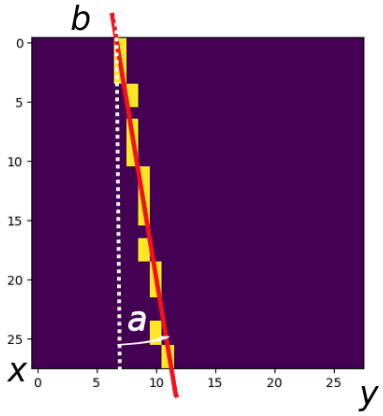

Figure 1. Single track event.

The CNNs proved to be very powerful in the image recognition tasks and are routinely used in many image and video recognition tasks. The CNN network is implemented using a KERAS[8] library with tensorflow[9] as a backend. The network consists of two convolutional layers (*Conv2D*) with a 3×3 convolution window followed by the *MaxPooling* layer and than by another two convolutional layers. The single *Dropout* layer suppresses the overtraining, and the final regression is performed in the *Dense* layer with 400 nodes. In total the neural network has over 2 million trainable parameters. The detailed description of different types of layers in the KERAS package can be found in.[8]

A network described above is capable to reconstruct events with a single track. For events with multiple tracks an additional layer is needed, which transforms the output of the neural network into a sequence of track parameters. The multi-track finding problem might be treated similar to the image-captioning, where the descriptions of tracks (i.e. track parameters) are analogous to the text captions assigned to the various patterns seen in the image.[10] For that purpose the Long Short Term Memory (LSTM)[11] layer is added. A CNN extracts all relevant features from the input image and LSTM stacked on top of the convolutional layers emits track parameters for each track in sequence, enabling finding parameters of multiple tracks (see Figure 2).

After performing the neural network reconstruction the hits which are not further than five pixels from the track reconstructed by the neural network are selected. They are used to fit a track using the robust fit implemented in the ROOT[12] framework. The robust fit allows to drop the outliers and redo the fit with fewer hits. This procedure is repeated until either the minimal number of hits is reached (in our case 70% of the input hits) or all the outliers not fitting to the track are removed. This fit, performed after the neural network pattern recognition, should be able to improve the resolution of track reconstruction.

2.2 Reconstruction in 3D

The extension into 3-dimensions is quite straight-forward, the 2D convolutional layers have to be replaced by 3D layers and the size of the network is increased due to the higher complexity of tracking in 3D.

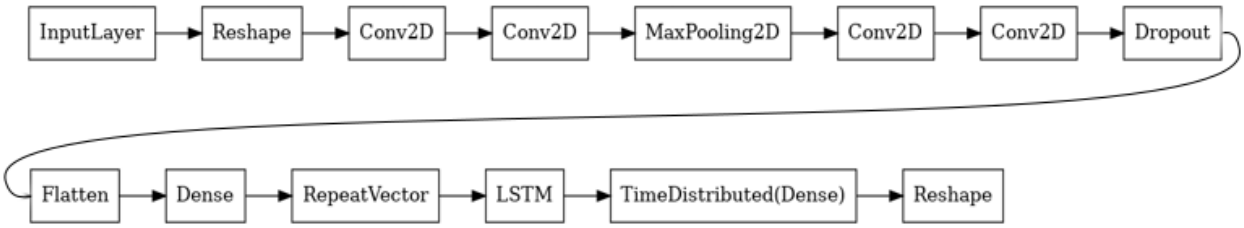

Figure 2. Deep neural network with convolutional layers followed by a dense and LSTM layers is trained to reconstruct track parameters for a variable number of tracks.

After a couple of tests the following network architecture was chosen: the network consists of two convolutional layers (*Conv3D*) with 32 3×3×3 convolution windows which are followed by the *MaxPooling3D* layer and than by another two convolutional layers, each having 128 3×3×3 convolution windows. The *Dropout* layer suppresses the overtraining, and the final regression is performed in the *Dense* layer with 400 nodes. It is then followed by the *LSTM* layer, which allows the multiple track reconstruction (see Figure 3).

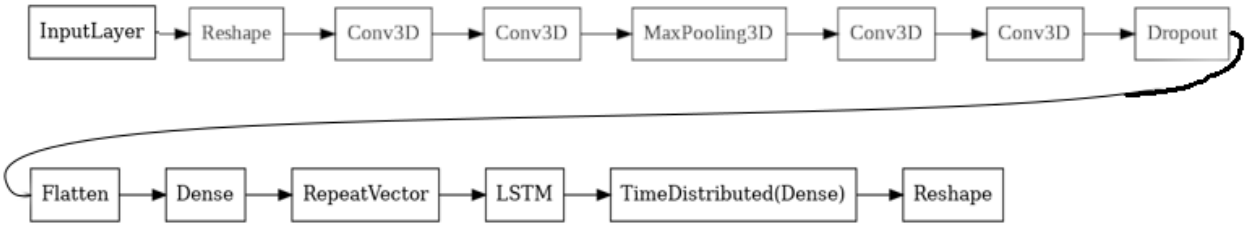

Figure 3. Deep neural network with convolutional layers followed by a dense and LSTM layers trained to reconstruct track parameters in the three-dimensional space.

The neural network used for three-dimensional pattern recognition has over 28 million trainable parameters, 14 times more than the network used for the 2D-tracks.The efficient training of such a network is possible only on clusters of Graphic Processor Units (GPU). For testing the 3D reconstruction algorithms the Google GPU support[13] was used.

The training was performed on events with two straight tracks with 90% pixel efficiency and various noise levels. The events needed for training were generated "on flight", during the network training and used only once, since the generation time was negligible comparing to the time used for training. The network geometry was not optimized for the track reconstruction purposes due to the lack of time and computer resources needed for multiple training. Also, for a feasibility study,

It was found, that this network can not be trained directly on the events containing noise, since in that case the training does not converge. Instead, a special training procedure is developed, in which the noise level is increased steadily during the training procedure:

1. pre-training on events with no additional noise using the Stochastic Gradient Descent (SGD) optimizer,[14] which performs the first training in 16 epochs,
2. training (max 512 epochs or stopping in case of no progress, typically about 150 epochs) using the adaptive learning rate optimization algorithm ADAM[15] designed specifically for training deep neural networks, which allows much faster training rate,

3. post-training again with an SGD optimizer, performing the final tuning of the network in 16 epochs,
4. after training the noise level is increased and the already trained network is trained again, but on events with higher noise level (go to point 2).

The training is stopped after a desired noise level is reached.

3. RESULTS

The track reconstruction was performed first on a two-dimensional toy model, which allows a relatively fast pattern recognition. In the next step the bigger network was tested on three-dimensional model.

3.1 Reconstruction in 2D

The track reconstruction was done first for events with a single track. In the next step the analysis was repeated for events with three tracks.

Single track events

In the first step of our analyses we have tested the performance of the convolutional neural network without LSTM layer on single track events. The pixel efficiency was set to 70% and the noise varied in the range between 0 and 30%. The noise level is defined as the probability of a single pixel not belonging to the track to generate a false signal. The example events with various noise levels are shown in Figure 4.

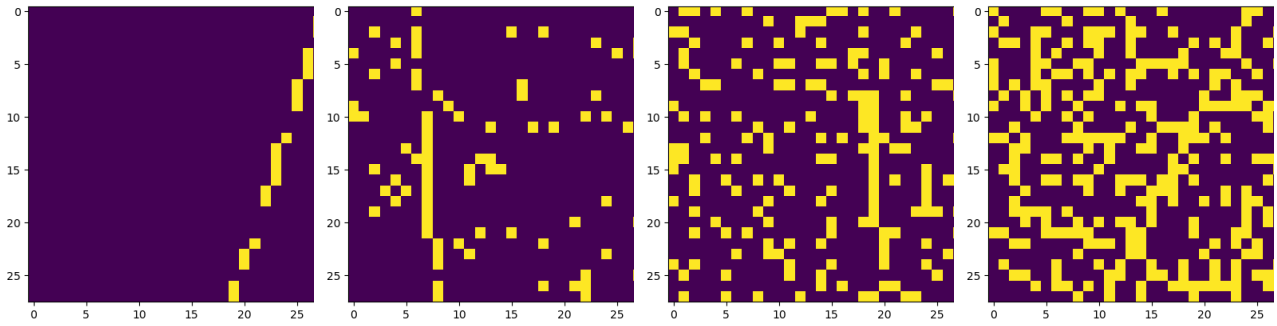

Figure 4. Single track events with pixel efficiency 70% and a noise level at 0%, 10%, 20% and 30% (from left to right).

Figure 5 shows the distribution of a difference between the reconstructed and true track parameters (slope and intercept) for events with no noise and with a high, 30% noise. The Gaussian is fitted to these distributions and the width of the Gaussian is taken as a measure of the resolution. The results for various noise levels are shown in Figure 6.

The track reconstruction accuracy is very good for events with no noise and degrades for higher noise levels. The robust fit applied after the neural network pattern recognition does not improve the resolution significantly.

The track is assumed to be properly reconstructed, when the deep neural network finds a track, which is not further than five pixels from the true track at any point. The reconstruction efficiency is defined as a ratio of reconstructed track to the total number of generated tracks. For the events without noise the reconstruction efficiency, shown in Figure 6, reaches over 99% and drops down to 84% for 30% noise.

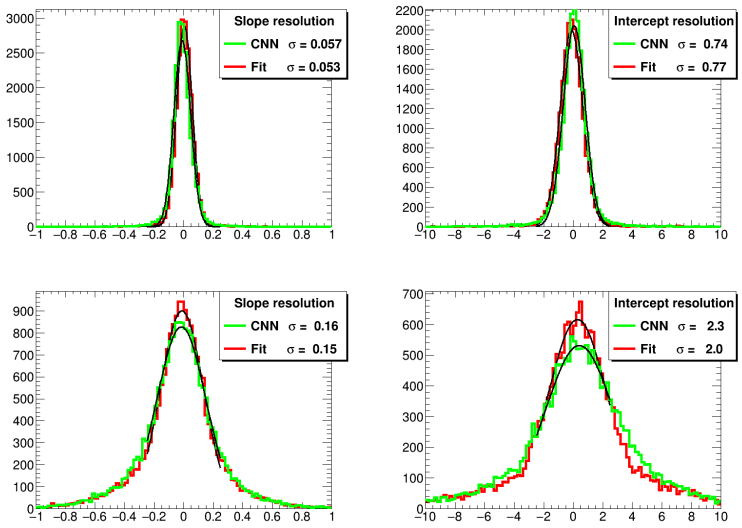

Figure 5. Resolution of the slope (left column) and intercept (right column) for the single track events with a pixel efficiency 70% and a noise level at 10% (upper row) and at 30% (lower row).

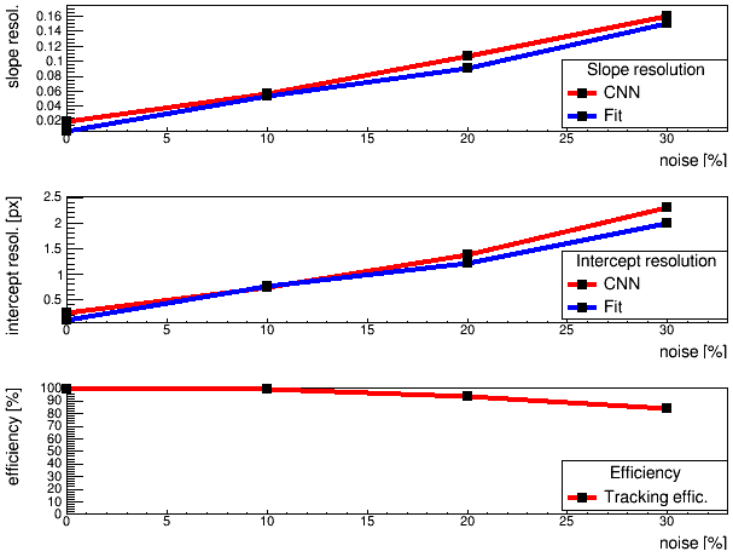

Figure 6. Track slope resolution obtained by the neural network and the robust fit (upper plot), track intercept resolution (middle plot) and the reconstruction efficiency for single track events (bottom plot) for noise levels at 0%, 10%, 20% and 30%.

Events with multiple tracks

In the next step the LSTM layer was added to the network as described in Section 2. This layer allows to reconstruct events with multiple tracks. Example events with three tracks are shown in Figure 7.

The pattern recognition with three tracks at high noise levels is not an easy task, the tracks are barely visible by eye. So, it is not astonishing, that the reconstruction efficiency goes down to about 50% for 30% noise. At 10% noise the efficiency is still reasonable (76%) and for events with no noise it reaches 92%. The resolution is significantly worse than for single track events (see Figures 8 and 9).

The example events with three tracks and various noise levels are shown in Figure 10. For events with higher noise some tracks remain not reconstructed or they are reconstructed poorly. However, a high 30% noise and

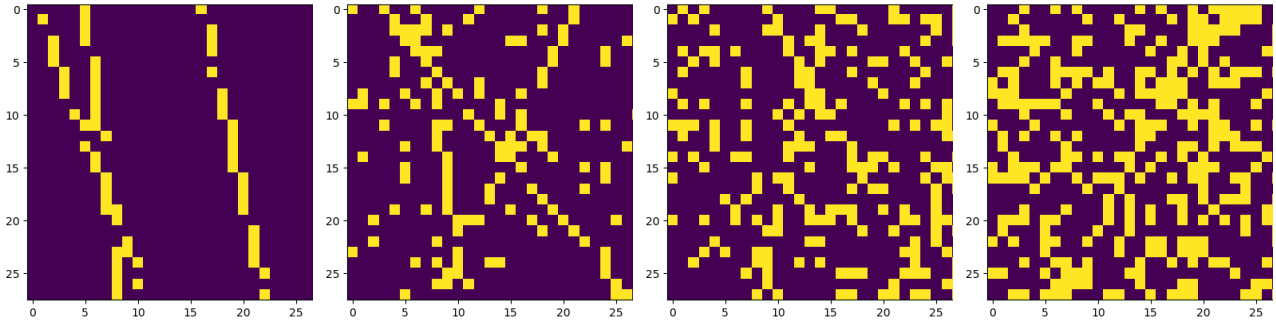

Figure 7. Three track events with pixel efficiency 70% and a noise level at 0%, 10%, 20% and 30% (from left to right).

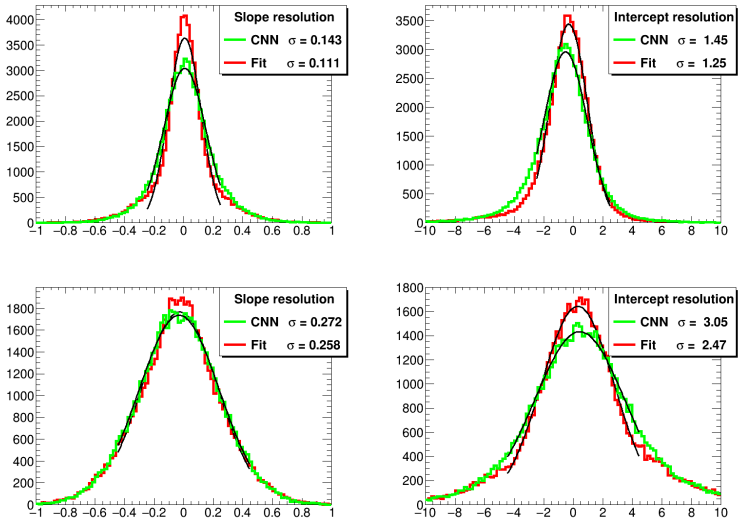

Figure 8. Resolution of the slope (left column) and intercept (right column) for three track events with pixel efficiency of 70% and a noise level at 10% (upper row) and 30% (lower row).

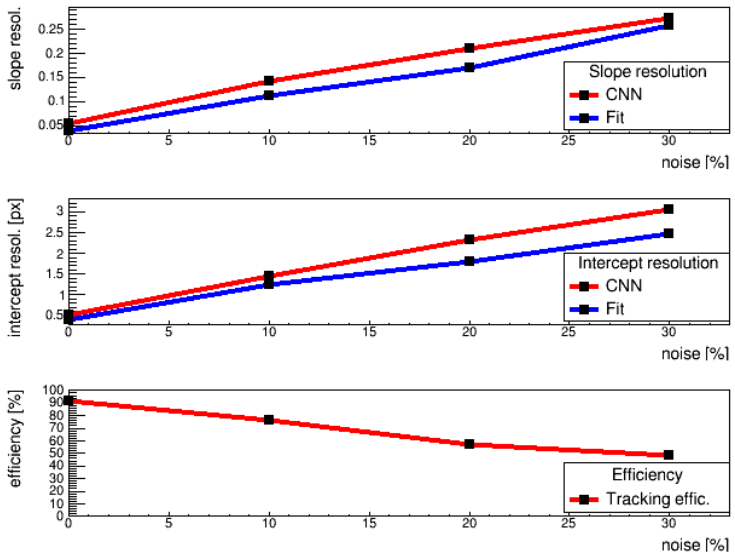

Figure 9. Track slope resolution obtained by the neural network and the robust fit (upper plot), track intercept resolution (middle plot) and the reconstruction efficiency for events with three tracks (bottom plot) for noise levels at 0%, 10%, 20% and 30%.

relatively low efficiency of 70% are extreme conditions for the pattern recognition algorithm.

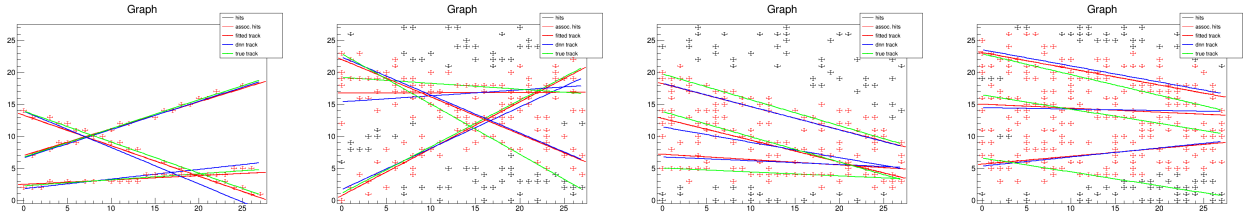

Figure 10. Example three track events with tracks reconstructed using neural network (blue) and the robust fit (red) together with true tracks (green). Hits marked in red were used for fitting. The events were generated with no noise, 10% noise, 20% noise and 30% noise (from left to right).

3.2 Reconstruction in 3D

The pattern recognition in three dimensions is more complicated than for a much simpler 2D model, therefore the acceptable noise levels must be lower. The track reconstruction was performed for noise levels between 0 and 20%. In Figure 11 the track reconstruction resolution for different noise levels is shown. The resolution becomes worse with the increasing noise level, but the neural network reconstruction remains quite accurate even for events with high noise.

The reconstruction efficiency is defined similarly as for 2D model, i.e. the track is counted as reconstructed if it is at every point closer than 5 pixels to the true track. The efficiency is quite flat at the level of 96% even for noise level up to 5% and it drops down to 76% for a high, 20% noise. The reconstruction resolution is stable for noise levels below 5%, than it becomes worse.

Figure 12 shows example events with reconstructed and true tracks plotted. It should be emphasized, that the deep neural network tracking performs quite well event at high noise producing reasonable results.

4. CPU CONSUMPTION

The neural network requires a lot of CPU time for training, but once trained the CPU used by a pattern recognition is relatively low comparing to the standard methods. The Table 1 shows the amount of CPU needed

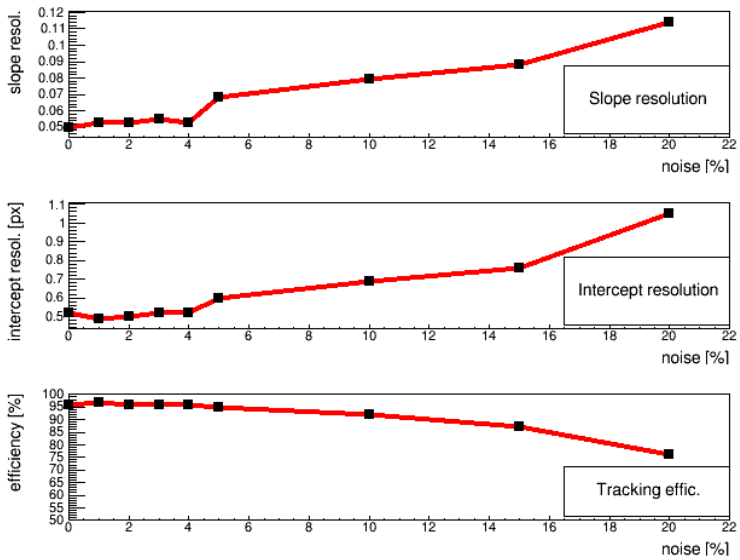

Figure 11. Slope resolution obtained by the neural network (upper plot), track intercept resolution (middle plot) and the reconstruction efficiency for three-dimensional events (bottom plot) for noise levels between 0% and 20%.

for the network training and the actual pattern recognition for three track events and 10% noise in the two-dimensional model. The CPU consumption is compared to the ROOT robust fit for the same sample. It should be emphasized that the fit requires about 50 times more CPU than the neural network pattern recognition.

The neural network training for three-dimensional model was performed using the GPU support. The entire training for five noise levels required 318 minutes on Google GPU cluster. The later application of the trained network took very little time comparing to the time required for training.

	CPU usage (arbitrary units)
Neural network training	399
Neural network pattern recognition	9
ROOT robust fit	482

Table 1. CPU consumption (in arbitrary units) by the neural network pattern recognition and robust fit for three track events with 10% noise in two-dimensional model.

This results show that the neural network pattern recognition can significantly reduce the computing resources used by the tracking algorithms.

5. APPLICATION IN FUTURE EXPERIMENTS

As the algorithms applied have been proven to be successful on a toy Monte Carlo model with three tracks, they are planned to be used in more realistic conditions using a test beam data for the MUonE experiment planned to be operating at the SPS accelerator at CERN.[2] It is characterized by a relatively low occupancy, however, due to the limited acceptance and very low angles of outgoing particles, a separation between electron and muon after an elastic scattering is not straightforward and needs efficient and very precise track reconstruction algorithms. Therefore, in order to achieve the physics goal, which is a measurement of the hadronic contribution to the anomalous muon magnetic moment with an uncertainty at the level of 0.05%, the Deep Neural Network methods are going to be applied and tested with respect to the commonly use site, collecting a data sample of about 1.4 billion of events. Figure 13 shows the concept of the MUonE setup. It is a modular system consisting of 16 silicon microstrip layers, 2 carbon targets and an electromagnetic calorimeter. The modules are separated by a relative distance of 1 m from each other and spaced by air.

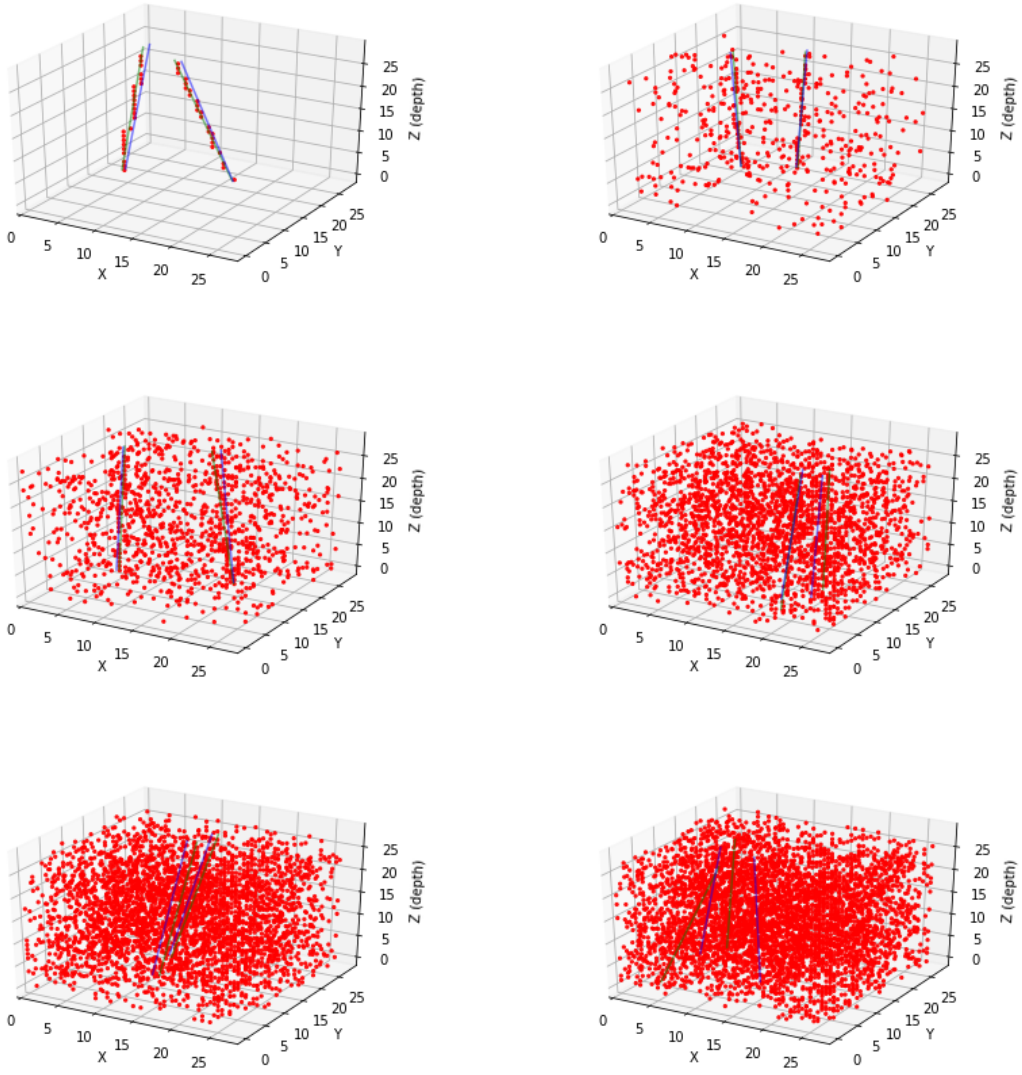

Figure 12. Example three-dimensional events with tracks reconstructed using neural network (blue) together with true tracks (green). The events were generated with no noise (upper left plot), 2% noise (upper right plot), 5%noise (middle left plot), 10% noise (middle right plot), 15% noise (lower left plot) and 20% noise (lower right plot).

There are three tracks to be reconstructed in the detector, i.e. the direction and momentum of the incident muon and directions of the outgoing electron and muon. Therefore, according to no CPU time limit and relatively low detector occupancy expected, the goal of the pattern recognition is a maximum possible track reconstruction efficiency. At the first stage the pattern recognition is performed in the xz and yz projections, by constructing pairs from all the combinations of hits in x and y layers separately. For each pair of hits a two-dimensional lines in xz or yz projections are determined, and all the hits within a certain window are then collected. The best selected combinations of the hits constituting two-dimensional lines in xz or yz projections are fitted.

In the next step such two-dimensional lines are combined into three-dimensional track candidates treated as a seed for the track fitting. After the selection applying some quality requirements they are fitted using MINUIT minimization package,[16] with all the hits collected within a certain window with respect to the initial three-dimensional line.

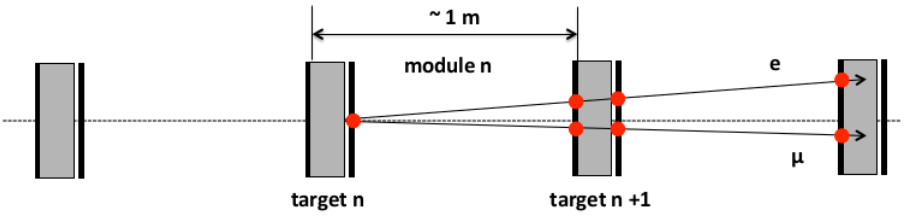

Figure 13. Concept of the MUonE detector final layout, where the input beam enters the detector from the left. Thick black lines denote the tracking modules. Figure adopted from.[2]

The collections of reconstructed tracks are used to search for events of the muon-electron scattering. All combinations of track pairs are checked to intersect in one of the targets within a certain window. Then the third track incoming to the target close to the intersection point is added. For the three tracks initially compatible with muon-electron scattering a global least square fit is performed.

It should be emphasized, that there is still a room for improvement at the level of patter recognition and track reconstruction, which may finally provide higher precision and efficiency. A natural candidate to be used is a very fast and parallel Deep Neural Networks method, allowing in principle to perform the pattern recognition "at once", having at the same time a great potential for increasing the precision and efficiency.

6. CONCLUSIONS

The neural network algorithm was proven to be successful when applied to the toy model, both in two and in three dimensions. We plan to test it in more realistic conditions using a testbeam data taken by the MUonE experiment. Therefore, in order to reduce the CPU timing and increase efficiency of the overall tracking reconstruction procedure, the Deep Neural Network methods are going to be applied and tested with respect to the commonly used procedures.

The 2D toy model doesn't require much computing power, but if extended to more realistic 3D conditions the GPU cluster is needed to speed up the network training.

ACKNOWLEDGMENTS

The work was supported in part by Polish Government grant 2017/25/B/ST2/01234 and ACK CYFRONET computing grant lhcbflav08.

REFERENCES

[1] Frühwirth, R., "Application of kalman filtering to track and vertex fitting," *Nuclear Instruments and Methods in Physics Research Section A: Accelerators, Spectrometers, Detectors and Associated Equipment* **262**(2-3), 444–450 (1987).

[2] Abbiendi, G. and al., "Measuring the leading hadronic contribution to the muon $g-2$ via μe scattering," *European Physical Journal C* **77**, 139 (2017).

[3] Kucharczyk, M. and Wolter, M., "Track finding with deep neural networks," Konferencja Użytkowników Komputerów Dużej Mocy, Zakopane 2019 http://www.cyfronet.krakow.pl/kdm19.

[4] Calafiura, P., "Hep advanced tracking algorithms with cross-cutting applications (project hep.trkx)."

[5] Farrell, S., Anderson, D., Calafiura, P., Cerati, G., Gray, L., Kowalkowski, J., Mudigonda, M., Spentzouris, P., Spiropoulou, M., Tsaris, A., et al., "The hep. trkx project: deep neural networks for hl-lhc online and offline tracking," in [*EPJ Web of Conferences*], **150**, 00003, EDP Sciences (2017).

[6] Farrell, S., Calafiura, P., Mudigonda, M., Anderson, D., Vlimant, J.-R., Zheng, S., Bendavid, J., Spiropulu, M., Cerati, G., Gray, L., et al., "Novel deep learning methods for track reconstruction," *arXiv preprint arXiv:1810.06111* (2018).

[7] LeCun, Y., Bengio, Y., and Hinton, G., "Deep learning," *nature* **521**(7553), 436 (2015).
[8] Chollet, F. et al., "Keras: Deep learning library for theano and tensorflow," (2015).
[9] Abadi, M., Barham, P., Chen, J., Chen, Z., Davis, A., Dean, J., Devin, M., Ghemawat, S., Irving, G., Isard, M., et al., "Tensorflow: A system for large-scale machine learning," in [*12th {USENIX} Symposium on Operating Systems Design and Implementation ({OSDI} 16)*], 265–283 (2016).
[10] Vinyals, O., Toshev, A., Bengio, S., and Erhan, D., "Show and tell: A neural image caption generator," in [*Proceedings of the IEEE conference on computer vision and pattern recognition*], 3156–3164 (2015).
[11] Hochreiter, S. and Schmidhuber, J., "Long short-term memory," *Neural computation* **9**(8), 1735–1780 (1997).
[12] Brun, R. and Rademakers, F., "ROOT: An object oriented data analysis framework," *Nucl. Instrum. Meth.* **A389**, 81–86 (1997).
[13] "Google colaboratory," https://colab.research.google.com.
[14] Robbins, H. and Monro, S., "A stochastic approximation method," *The annals of mathematical statistics* , 400–407 (1951).
[15] Kingma, D. P. and Ba, J., "Adam: A method for stochastic optimization," *arXiv preprint arXiv:1412.6980* (2014).
[16] James, F. and Roos, M., "Minuit: a system for function minimization and analysis of the parameter errors and corrections," *Comput. Phys. Commun.* **10**(CERN-DD-75-20), 343–367 (1975).

On the Exclusive Jet Measurements at the LHC

Paula Erland[a]

[a]Institute of Nuclear Physics PAS, Radzikowskiego 152, 31-342 Cracow, Poland

ABSTRACT

Properties of the exclusive jet production process are briefly described. A need for a dedicated trigger algorithms for studies of such process in the LHC experiments is explained. Influence of the machine luminosity leveling – a change of the betatron function and crossing angle – on the scattered proton position in the AFP is discussed. Finally, impact of pile-up and optics on the expected algorithm efficiency is estimated.

Keywords: LHC, ATLAS, AFP, jet, exclusive, trigger, HLT

1. INTRODUCTION

In this paper some aspects of the exclusive jet measurement at the LHC are discussed. Exclusive jet production (see Feynman diagram in Figure 1) is a very rare and interesting process, which is still quite poorly known.[1] It can be described by:

- two jets: usually produced centrally (at small rapidity),
- two protons: scattered at small angles (few hundreds μrad from the beam axis),
- rapidity gap between the central system and the scattered protons.

A term "exclusivity" means that all final state particles can be measured. This implies a strong relation of the kinematics of the central state and the scattered protons. High luminosity at the LHC gives a hope to significantly measure properties of the exclusive jet production in ATLAS[2] and CMS/TOTEM[3,4] experiments. In this paper a stress will be put on the ATLAS detector but the conclusions should remain valid also for CMS.

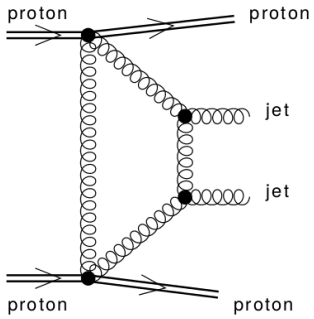

Figure 1: Leading Feynman diagram of the exclusive jet production: two gluon jets, two scattered protons and a presence of a "screening" gluon to make exchange colourless.

Jets can be detected by the ATLAS central detector but the forward scattered protons escape its acceptance region through the beam pipe opening. This underlines a need for a dedicated set of detectors installed far away from the interaction point. For the ATLAS interaction point (IP1) these are the ATLAS Forward Proton (AFP)[5] detectors.

Further author information:
Paula Erland: E-mail: paula.erland@ifj.edu.pl

Photonics Applications in Astronomy, Communications, Industry, and High-Energy Physics Experiments 2019, edited by Ryszard S. Romaniuk, Maciej Linczuk, Proc. of SPIE Vol. 11176, 111764I
© 2019 SPIE · CCC code: 0277-786X/19/$21 · doi: 10.1117/12.2539024

AFP system consists of two Roman pot stations (Near and Far) on each side of ATLAS. They are located symmetrically on both sides of the IP1 at the distance of about 210 m from it. The detectors are horizontally inserted into the LHC beam-pipe up to few millimetres from the beam. Detectors located on the ATLAS C side are positioned in the vicinity of beam 1 whereas the ones on the A side close to beam 2. Each station contains four Silicon Tracker planes (SiT), which provide a precise measurement of the scattered proton trajectory position (spatial resolution of a single plane was measured to be about 6 μm and about 30 μm in x and y respectively[6]). Far stations host also the Time of Flight (ToF) detectors. The main goal of ToF modules is to reduce the backgrounds, via the measurement of the arrival time of a proton combined with the interaction vertex reconstruction. The timing resolution is expected to be of about 30 ps.[6]

For obvious reasons the LHC magnetic lattice influences the scattered proton trajectory and one has to take into account the following elements:

- two dipole magnets (D1-D2) for beam separation (bending),
- five quadrupole magnets (Q1-Q5) for beam focusing,
- two collimators (TCL4, TCL5) for magnet protection.

Settings of these elements, called the accelerator optics, come from the requirements of the experiments in terms of luminosity and the LHC machine protection and may differ between the runs. The properties of various LHC optics are discussed in Ref.[7]gnuplot plot sqrt from column in bash script

In order to fulfil the exclusivity criteria all stable particles should be measured. For the exclusive jet production, both scattered protons need to be within the AFP acceptance.[8] It means that the energy of the jet system is expected to be between about 300 and 1300 GeV. As was shown in *e.g.* Ref.,[9] the cross section for such jets is expected to be about few μb. This means taking the data in the high pile-up conditions, *i.e.* in a situation when multiple pp interactions occur during one bunch crossing.

As was discussed in,[10] the main gnuplot plot sqrt from column in bash scriptbackgrounds for the exclusive jet production are due to a non-diffractive and single diffractive processes overlaid with scattered protons originating from the minimum-bias pile-up events. The most common backgrounds are shown in Figure 2.

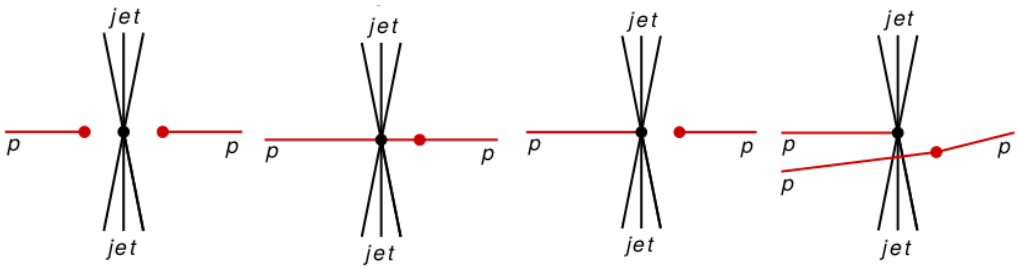

(a) (b) (c) (d)

Figure 2: Backgrounds to the exclusive jet production: (a) non-diffractive jets + 2 protons from 2 different pile-up vertices, (b) non-diffractive jets + 2 protons from the same pile-up vertex, (c) single diffractive jets + proton from pile-up, (d) single diffractive jets + proton from pile-up.

The cross-section for the non-diffractive jet production is the highest one among the processes with a hard scale – the jets are copiously produced in ATLAS. Due to the limited trigger and data acquisition bandwidths not all of these events can be saved for analysis. In ATLAS, events are selected at two trigger steps called level-1 (L1) and High Level Trigger (HLT).[2] Due to the storage limitation certain thresholds were introduced at the L1 and HLT stages. Events not fulfilling these criteria are prescaled, *i.e.* only a fraction of them is saved. For jets, the selection is usually based on the minimum transverse momentum, (p_T), of a jet. For data taken in years 2015-2018 (the so-called Run2 period) these thresholds were set to 100 GeV at L1 and about 440 GeV at HLT.[9] For the future data taking (starting from Run3), these limits may be even higher. Since the cross-section for

exclusive jets is very small and steeply falling with increasing jet p_T, it is necessary to accept all events being within the detector acceptance. Since, as was discussed above, this results in jets with p_T staring from 150 GeV, a dedicated trigger algorithm has to be used. In the this paper the focus will be on the HLT items.

Considered algorithm consists of two parts:

1. comparison of the "proton" position computed from the di-jet system kinematics to a real proton position as registered in AFP,
2. comparison of the jet vertex and the one reconstructed using the AFP Time-of-Flight system.

The idea of the first part is to match the position of "proton" which is calculated using the proton properties inferred from the jet kinematics to that of the proton actually registered in the AFP station. The jet observables (p_T, energy, rapidity and azimuthal angle) are measured by ATLAS. From all jets in the event two with the highest p_T are selected. At this step the vertex is not requited as it is expected that high p_T jets should not originate from two independent vertices.

Using the jet observables the di-jet system mass (M_{jj}) and rapidity (y_{jj}) are computed. Next, a relative energy loss ($\xi_{A,C}$) of a proton scattered into the ATLAS A/C hemisphere is calculated as:

$$\xi_{A,C} = \exp(\pm y_{jj}) \frac{M_{jj}}{2E_{beam}}.$$

The estimated properties of a hypothetical scattered proton are used to simulate its transport through the LHC magnetic lattice and to calculate its trajectory position in the AFP station. Next, this hypothetical position (p_{jet}) and the registered one (p_{proton}) are compared. If the predicted position is close enough to the measured one, the event is accepted by the trigger. In presented work the default selection criteria used in the current ATLAS trigger algorithm were chosen. It was required that the difference between the two positions in $x(y)$ direction are smaller than 2(2.5) mm and the radius $R = \sqrt{(p^x_{proton} - p^x_{jet})^2 + (p^y_{proton} - p^y_{jet})^2} < 2$ mm. Therefore, the effective cut is the one on the radius. These criteria could be optimized to reject as much of the background as possible while keeping majority of the signal.

The second part of the exclusive jet trigger uses the comparison of the interaction vertex position calculated from the AFP measured times of flight of the scattered protons and that of the jet vertex reconstructed in ATLAS. A "proton vertex" can be computed as: $Z_p = (t_A - t_C)\frac{c}{2}$ and then compared to the jet system related one: $Z_p - z_{jet}$.

The first part of this trigger algorithm strongly depends on the changes of the LHC optics or the jets kinematics. In this paper, a discussion about the influence of the LHC optics and presence of pile-up is presented.

2. IMPACT OF THE LHC OPTICS

In order to collect a large amount of data required by physics analysis, the LHC tries to maximize the luminosity. There are few methods to achieve this. One uses the relation of the betatron function at IP, (β^*), and the instantaneous luminosity. The luminosity is inverse proportional to the β^* value. Another method hinge on the crossing angle levelling (θ_C). It is an angle at which the beams are crossing at the interaction point*. The range of possible changes is limited by the long range beam-beam separation (required to ensure good beam lifetimes) and by the mechanical aperture of the beam pipe. In order to keep the luminosity high, the LHC decided to adjust both β^* and θ_C during the data taking.

In order to study the levelling influence on the reconstruction of the proton position two β^* values, typically used during Run2, were considered: $\beta^* = 30$ cm and $\beta^* = 40$ cm. It was checked that the resulting proton positions for a given crossing angle are exactly the same. Therefore, all further analysis are done only for $\beta^* = 30$ cm.

*In this paper the "crossing angle" is denoted as and angle between the nominal z beam axis and the z direction of the beam. In literature such angle is sometimes called "half crossing angle".

In contrast to the β^* levelling, a significant differences are observed while applying a change of θ_C. This is clearly visible in Figure 3 (left) where the proton positions in the AFP for the three different values of the crossing angle (140, 160 and 180 μrad) are shown. Except from the focal point located around $x_{AFP} = -4$ mm, which is expected to be independent of the machine optics,[11] the change of θ_C moves the protons along y-axis. At -20 mm from the beam centre $(0, 0)$, which is typically an edge of the AFP detector acceptance at high mass, the difference is about few millimetres. This shows the needed to make trigger algorithm optics-dependent.

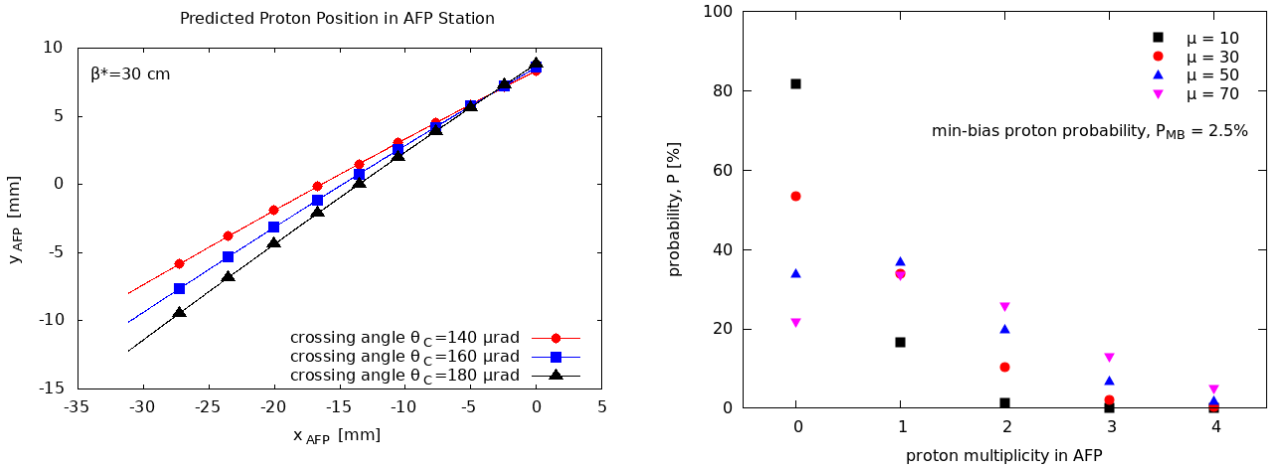

Figure 3: **Left:** proton position in the AFP detector for β^*=30 cm and various values of crossing angle: 140, 160 and 180 μrad. **Right:** proton multiplicity in the AFP detector for various pile-up conditions. The probability of registering a minimum-bias proton in the AFP is assumed to be of 2.5%.

3. IMPACT OF PILE-UP

In this section the impact of the pile-up environment on the presence of the scattered protons in AFP and its influence on the jet kinematics is briefly discussed.

The presence of additional protons increases the chance of an event to be accepted by the trigger. The multiplicity of protons visible in AFP for a given pile-up is shown in Figure 3 (right). The plot was prepared under the assumption that a chance of the minimum-bias proton registration in the AFP is 2.5%. A more detailed discussion about the probability of having the scattered protons in the AFP detector can be found in *e.g.* Ref.[12] As can be seen from the figure, for pile-up of 10 the chance to have more than one proton is negligible. However, at $\mu = 30$ it increases to about 15% and at $\mu = 50$ it is of about 30%. This can decrease the background rejection power due to combinatorics as the chance that one of two (three, ...) registered protons will match the one from jet kinematics increases.

Another consequence of the non-zero pile-up environment is its impact on the jet reconstruction. In order to study such effect Monte Carlo samples containing signal (exclusive jets; generated by FPMC[13]), background (non-diffractive jets; generated by Pythia8[14]) and pile-up (minimum bias events; generated by Pythia 8) were prepared. The jets were reconstructed using the anti-kT algorithm implemented in the FastJet tool.[15] Two values of the jet radius were used: R = 0.4 and 1.0. The choice was to match the most popular settings used by the ATLAS Collaboration for jet analyses.

The trigger efficiency, *i.e.* the number of events triggered by the used algorithm to the number of all events having the double AFP tag, as a function of the pile-up value is shown in Figure 4. Proton was assumed to be tagged if its x position in AFP was smaller than -2.5 mm, which reflects Run 2 data-taking conditions. Top plots are for the signal and bottom ones for the non-diffractive jet background. The value of pile-up was fixed, *i.e.* no Poisson smearing was applied. The selection criteria result the pure selection efficiency (*i.e.* at $\mu = 0$) of about 75% for anti-kT with $R = 0.4$ and 80% for $R = 1.0$. The difference is due to the presence of a third (fourth, ...) jet in the event which influences the properties of kinematics of a "proton" reconstructed from jets.

The pile-up interactions cause more particles to be present in a registered event. In consequence, the jets have usually higher p_T and slightly different rapidity w.r.t. the $\mu = 0$ situation. In case of signal this significantly worsens the efficiency, especially in the case of anti-kT with $R = 1.0$. In case of background, slightly more events are selected at higher pile-up values. The major effect is the presence of multiple protons (see Fig. 3 (right)). Nevertheless, the rejection power stays at the level of few permille, typically below 0.5%. The fluctuations are of a statistical nature (the background sample contained 100 000 events).

It is worth mentioning that ATLAS and CMS Collaborations provided special algorithms[16] for the suppression of the pile-up effects on the jet reconstruction. It is clear that such a correction is a must also for the exclusive jet trigger, but such studies are beyond the scope of this paper.

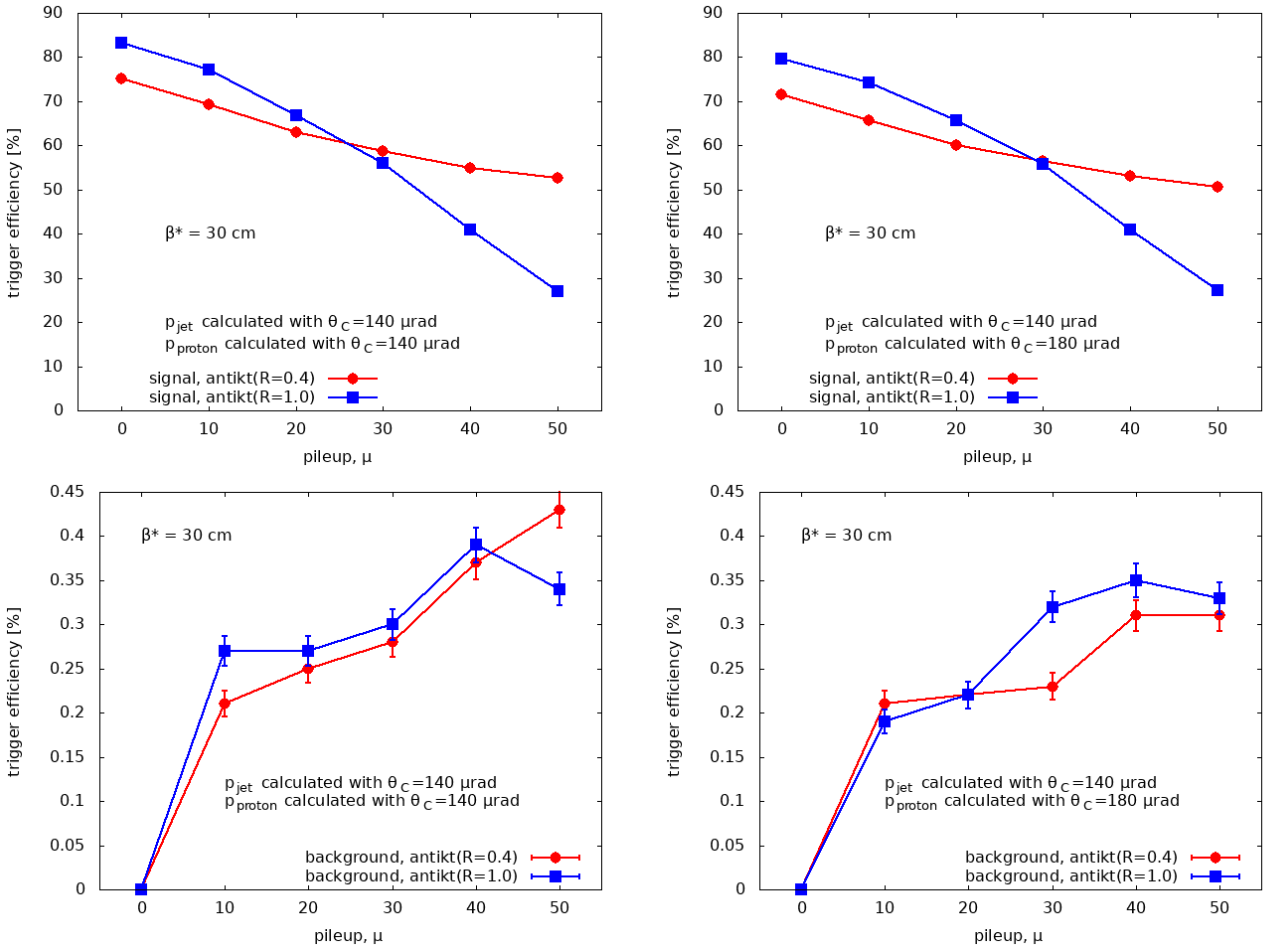

Figure 4: Efficiency of HLT exclusive jet trigger algorithm for signal (exclusive jets, **top**) and background (non-diffractive jets, **bottom**) as a function of pile-up for two settings of anti-kT algorithm. **Left** plots are for exact optics. On the **right** plot "real" protons were transported with θ_C of 180 μrad whereas "jet protons" with $\theta_C = 140$ μrad which reflects effect of luminosity leveling.

4. SUMMARY

The data delivered by the LHC provided a chance to measure properties of the exclusive jet production process. With the current experimental set-up, this can be done by ATLAS and CMS/TOTEM Collaborations, since both jets and scattered protons should be measured. In case of ATLAS, a dedicated trigger algorithms at the L1 and HLT levels have to be used.

One of important HLT algorithms uses a correlation between the jet and the scattered proton kinematics. Due to the fact that protons are measured about 200 m from the interaction point, they have to travel through the LHC magnets which have a profound impact on their trajectories. This is taken into account in the proton tracking tools.

In this paper, it is shown how a new feature of the LHC machine – the luminosity levelling – impacts the trigger efficiency. A change of β^* seems to have no effect, contrary to the change of the crossing angle of the beams. In such a case, when θ_C is changed from 140 μrad to 180 μrad, the efficiency drops by few percent. At zero pile-up the efficiency is about 75% for anti-kT with $R = 0.4$ and 80% if $R = 1.0$ is used. Simultaneously, non-diffractive background is strongly suppressed – only less then 0.5% of events is accepted.

Presence of high pile-up greatly modifies the signal efficiency since it changes the jet kinematics. Hence, the use of the pile-up suppression algorithms in the jet reconstruction is a must. Its effect on the trigger algorithm should be studied in detail by both Collaborations.

Acknowledgements

This work has been partially supported by the Polish Ministry of Science and Higher Education under the "Diamentowy Grant" programme (0138/DIA/2017/46). The author would like to thank dr Maciej Trzebiński and prof. Janusz Chwastowski for suggestions, discussions and comments.

REFERENCES

[1] Akiba, K. et al., "LHC Forward Physics," *J. Phys.* **G43**, 110201 (2016).
[2] Aad, G. et al., "The ATLAS Experiment at the CERN Large Hadron Collider," *JINST* **3**, S08003 (2008).
[3] Chatrchyan, S. et al., "The CMS Experiment at the CERN LHC," *JINST* **3**, S08004 (2008).
[4] Anelli, G. et al., "The TOTEM experiment at the CERN Large Hadron Collider," *JINST* **3**, S08007 (2008).
[5] Adamczyk, L. et al., "Technical Design Report for the ATLAS Forward Proton Detector," Tech. Rep. CERN-LHCC-2015-009. ATLAS-TDR-024 (May 2015).
[6] Lange, J. et al., "Beam tests of an integrated prototype of the ATLAS Forward Proton detector," *JINST* **11**(09), P09005 (2016).
[7] Trzebinski, M., "Machine Optics Studies for the LHC Measurements," *Proc. SPIE Int. Soc. Opt. Eng.* **9290**, 929026 (2014).
[8] Trzebinski, M., "Hard Diffraction with Proton Tagging at the LHC," *Acta Phys. Polon.* **B46**(8), 1499 (2015).
[9] Aaboud, M. et al., "Measurement of inclusive jet and dijet cross-sections in proton-proton collisions at $\sqrt{s} = 13$ TeV with the ATLAS detector," *JHEP* **05**, 195 (2018).
[10] "Exclusive Jet Production with Forward Proton Tagging," Tech. Rep. ATL-PHYS-PUB-2015-003, CERN, Geneva (Feb 2015).
[11] Staszewski, R., Trzebinski, M., and Chwastowski, J., "Dynamic Alignment Method at the LHC ," *Advances in High Energy Physics* **2012**, Article ID 428305 (2012).
[12] Staszewski, R., *Study of Diffraction with the ATLAS detector at the LHC*, PhD thesis, IRFU, SPP, Saclay (2012).
[13] Boonekamp, M., Dechambre, A., Juranek, V., Kepka, O., Rangel, M., Royon, C., and Staszewski, R., "FPMC: A Generator for forward physics," (2011).
[14] Sjostrand, T., Mrenna, S., and Skands, P. Z., "A Brief Introduction to PYTHIA 8.1," *Comput. Phys. Commun.* **178**, 852–867 (2008).
[15] Cacciari, M., Salam, G. P., and Soyez, G., "FastJet User Manual," *Eur. Phys. J.* **C72**, 1896 (2012).
[16] Aaboud, M. et al., "Pile-up subtraction and suppression for jets in ATLAS," *ATLAS-CONF-2013-083* (2013).

Using ALFA Detectors for the LHC Beam Background Measurements*

Bartosz Dziedzic on behalf of the ATLAS Collaboration†

Institute of Nuclear Physics Polish Academy of Sciences
Radzikowskiego 152, 31-342 Kraków, Poland

ABSTRACT

This paper presents background measurements performed during special runs with high β^* optics at injection energy using ALFA detectors in the ATLAS experiment at the LHC. Such special runs require specific collimation scheme which reduces beam-induced background. Hence, complex preparation including simulations and tests had to be performed. This document discusses results of tests with different collimation schemes and background measurement during final data taking. In particular one of the runs was devoted to test a new type of collimators based on crystal channelling effect, that were used during physics data taking for the first time at the LHC.

Keywords: ATLAS experiment, ALFA detector, beam background, collimation, LHC

1. INTRODUCTION

Forward detectors at the LHC are designed to register protons scattered at very small angles. Such protons escape the acceptance of the main LHC detectors through the beam pipe and traverse the machine magnetic lattice accompanying the proton bunches. To measure precisely the scattering angles of such protons the detectors have to be placed in the immediate vicinity of the proton beam. Typically, the distance is of the order of a few millimetres from the beam centre. Therefore, such detectors are exposed to backgrounds that are in-time with the beam – coherent backgrounds called the beam halo. On the other hand, the forward detectors can be used as a great tool for measurements of such backgrounds.

The paper is organised as follows. The next section introduces the ALFA detectors at the ATLAS experiment. Section 3 describes the beam conditions during the test and physics runs. The proton beam collimation is discussed in Section 4. Section 5 gives the details of the performed test runs, while Section 6 describes the physics runs. The observations are discussed in Section 7 which is followed by the summary.

2. ALFA DETECTORS AND THE TRIGGER SYSTEM

ALFA (Absolute Luminosity For ATLAS)[1] is a forward detector that is a subsystem of the ATLAS Experiment.[2] This detector is designed to measure the absolute luminosity of the LHC, making use of the elastically scattered protons. It is an ensemble of eight detectors installed inside four Roman Pot stations placed symmetrically at a distance of about 240 m from the ATLAS interaction point (IP). The closer (or NEAR) stations are located about 237 meters away from the IP, while the further (FAR) ones are positioned 245 meters away from the IP. The Roman Pot technology allows insertion of the detector into the beam pipe and positioning it in the vicinity of the proton beam. The detectors move along the vertical direction (perpendicular to the LHC ring plane) so that there are a few milimeters between the detector and the beam centre. This distance is measured in units of the local beam width. Due to the operation very close to the proton beam, the Roman Pots are controlled only from CERN Control Center (CCC) and only in close co-operation of the LHC operators and Collimation Working Group (CWG).

Each Roman Pot station houses an upper and a lower detector. Each detector consists of two parts – a Main Detector (MD) and an Overlap Detector (OD). The MDs are used for tracking protons scattered at very small angles, while the ODs are used to determine the relative alignment between the upper and lower detectors. The detectors are shown in Fig. 1.

*Presented at XLIV-th IEEE-SPIE Joint Symposium Wilga 2019 by B. Dziedzic: e-mail bartosz.dziedzic@ifj.edu.pl

†Copyright 2019 CERN for the benefit of the ATLAS Collaboration. Reproduction of this article or parts of it is allowed as specified in the CC-BY-4.0 license

Photonics Applications in Astronomy, Communications, Industry, and High-Energy Physics Experiments 2019, edited by Ryszard S. Romaniuk, Maciej Linczuk, Proc. of SPIE Vol. 11176, 111764J
© 2019 SPIE · CCC code: 0277-786X/19/$21 · doi: 10.1117/12.2539808

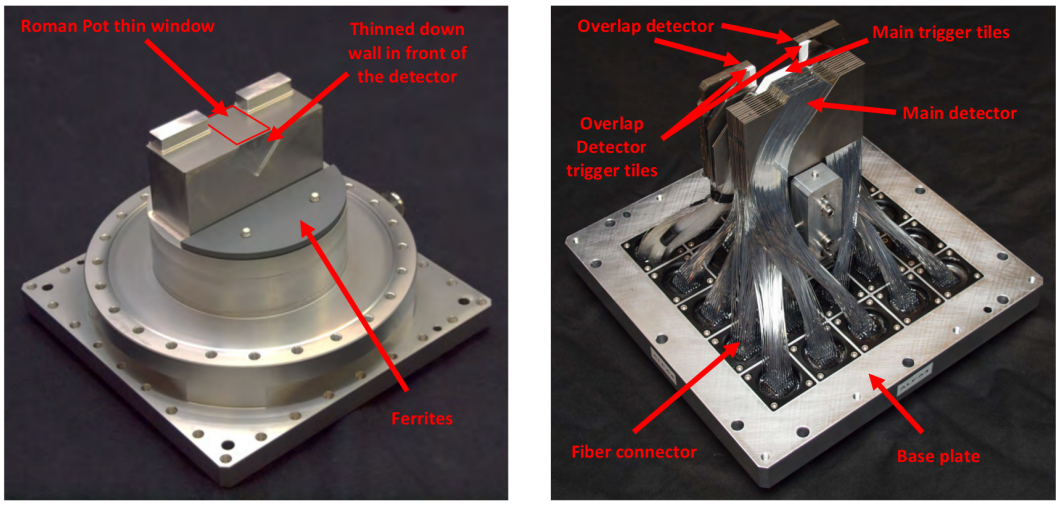

Figure 1. The Roman Pot (left picture) and ALFA detector including MD and OD (right picture).[3]

The Main Detector consists of ten double layers of scintillating fibres oriented alternatingly at the angle of $\pm 45^\circ$ with respect to the vertical direction. Each layer contains 64 squared fibres coated with a thin layer of aluminium. The size of a single fibre is 0.5×0.5 mm^2, and the resolution of the track position measurement is about 30 µm. The Overlap Detectors consist of two parts placed symmetrically on the MD sides. Each of them contains three layers of staggered scintillating fibres, 32 fibres each. The fibres are the same as those in MDs.

Behind each MD there are two 3 mm thick scintillating tiles used for triggering. Only a coincidence of both tiles generates the trigger signal. For the ODs, only single tiles are used for triggering. As each detector can send only a single trigger signal at the time, the prioritisation of triggers is applied – MD has higher priority than OD, thus if OD and MD generate triggers simultaneously, only MD trigger is sent to ATLAS Central Trigger Processor (CTP) over the 280 m long cable.[4]

The time of flight of a scattered proton is 800 ns. The trigger signal propagation takes 1030 ns and its processing on the detector and the CTP side takes 423 ns. This sums up to 2253 ns in total while the maximum ATLAS latency is 2175 ns.[3] To solve this problem a new VME module was developed – ALFA_CTPIN. This module is responsible for fast decoding of the trigger signals and reduces the total time by 135 ns resulting in the total time of 2118 ns.[3] ALFA_CTPIN required firmware upgrade and clock frequency increase of the digital front-end, thus latency was reduced by 12.5 ns. It also procvided an opportunity to reduce LEMO cables' length saving another 21 ns. 102.5 ns was saved directly on signal processing in ALFA_CTPIN module. The sources of the latency are presented in Table 1.

ALFA_CTPIN allows a measurement of the frequency of the produced trigger signals, providing information within 1.5 s long periods of time. Moreover, the rates are measured for each LHC bunch crossing separately. Therefore, it may be used as a basic tool for the machine background determination.[5]

3. BEAM CONDITIONS FOR ALFA RUNS

The data for both the test and physics runs were taken at the LHC proton beam injection energy of 450 GeV. The chosen optics used different betatron function [‡] values in x and y directions: $\beta_x^* = 50$ m, $\beta_y^* = 100$ m. During the test runs, both beams contained four colliding proton bunches. The physics runs used either six colliding isolated bunches or five colliding isolated bunches with a sixth non-colliding one. The non-colliding bunch was used to estimate the beam-related background (section 6). During data taking the ALFA detectors were positioned at the distance of $3\sigma = 4.5$ mm from the beam center. In all runs, the beams collided head on.

[‡]The betatron measures the distance after which the beam doubles its transverse dimensions. It is a function of the distance along the beam orbit.

Table 1. Comparison of latency before and after ALFA_CTP installation

Run2 before ALFA_CTPIN installation		**Run2 after ALFA_CTPIN installation**	
Source of latency	**Latency [ns]**	**Source of latency**	**Latency [ns]**
Time of flight	800	Time of flight	800
Scintillator	3	Scintillator	3
Photomultiplier	6	Photomultiplier	6
LEMO-cables (tunnel)	25	LEMO-cables (tunnel)	10
MAROC2 (analog FE)	13	MAROC2 (analog FE)	13
Digital Front End	50	Digital Front End	37.5
Air-core-cable	1030	Air-core-cable	1030
LEMO-cables (USA15)	15	LEMO-cables (USA15)	10
MDOD separation	60	ALFA_CTPIN	37.5
NIM to LVDS	5		
CTPIN logic	25		
CTP PITbus upgrade	50		
CTP functionality	125	CTP functionality	125
CTP OUT upgrade	25	CTP OUT upgrade	25
New position of outer stations	21	New position of outer stations	21
TOTAL	**2253**	**TOTAL**	**2118**

4. BEAM COLLIMATION SYSTEM DESIGN

The trajectories of the LHC beams are controlled by a large number of superconducting magnets. This set of magnets is called the cold aperture. In some sections, where high radiation levels are reached, the machine uses classical high-temperature magnets – the warm aperture regions. As there are always some regular and inevitable beam losses, it is very important to limit them to the warm aperture regions. Thus, a complex beam collimation system is essential. One should notice that the collimation system operation leads to the background reduction and optimisation which are of primary importance also for the forward detectors. The CWG in cooperation with experimental groups works on simulations of different collimations schemes according to the requests. It should be stressed that in some situations (as in the case of the ALFA high β^* runs) the physics background optimisation is a very complicated process and it may take long time to achieve an acceptable background level.[6]

The LHC tunnel hosts more than 100 collimators. The majority of them is installed within two machine sections – IR3 and IR7. Those are devoted to the off-momentum particles and the betatron cleaning, respectively. Some additional collimators are installed within the experimental insertions, transfer lines, beam dump and around injectors.[7] A schematic layout of the LHC collimation system is presented in the Fig. 2.

Collimators are organized in a multistage system. This means that all collimators are divided into groups:

- primary (TCP - Target Collimator, Primary),
- secondary (TCSG - Target Collimator, Secondary, Graphite),
- tertiary (TCTP - Target Collimator, Tertiary, Pick-up),
- absorbers (TCL - Target Collimator, Long Absorber, TCLA - Target Collimator, Long, Active Absorber).

Each of the above groups is designed to fulfill a different task. TCPs, TCSGs and TCLAs are installed in the cleaning insertion regions (IR3, IR7). Primary collimators are those closest to the beam and are cleaning the primary beam halo coming from regular beam losses. Primary collimators also cause the secondary beam halo and the hadron showers (see Fig. 3). The secondary collimators are devised to clean the secondary halo. They are closed to distances not smaller than those for the primary halo collimators. Naturally, the TCSGs scatter

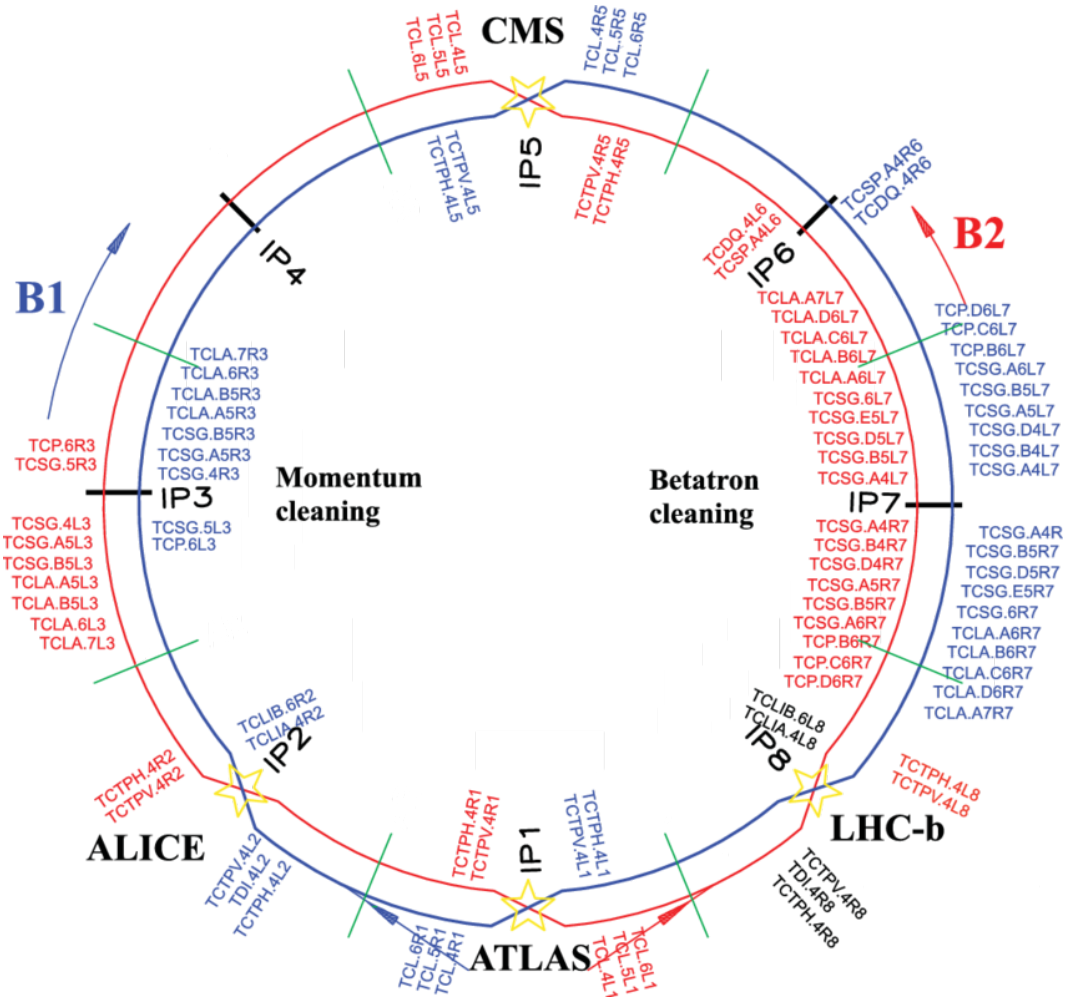

Figure 2. Layout of the collimation system.[7]

stray protons inducing thus the tertiary beam halo and hadronic showers which are caught by the absorbing collimators (TCLAs). The tertiary collimators are installed upstream of the experimental areas to protect their equipment and magnets. The physics debris absorbers (TCLs) are installed downstream of the experimental areas.[7]

5. ALFA TEST RUN SETUP

The aim of the test was to find the optimal collimation scheme allowing for efficient data taking, providing low beam-induced background level. During the test runs, the unprescaled rates of the following triggers were monitored on-line: triggers from each MD detector, an elastic trigger and a systematic trigger. The elastic trigger uses a simple logic to estimate the rate of elastic events (see Fig. 4). The systematic trigger delivers an estimation of the background level.

The first test run was performed on 8th of November 2017. The detectors were located 3σ from the beam centre. Each of seven schemes started with a beam scraping lasting about 3–5 minutes. During beam scraping, the TCTPs were inserted into 3σ position until the readings of Beam Loss Monitors (BLMs) stabilised. Meanwhile, the TCLAs and TCTPs were set in the positions according to prepared schemes. Then, the TCPs were retracted to the 5.5σ position. For each test, data were collected over a period of 30 minutes.

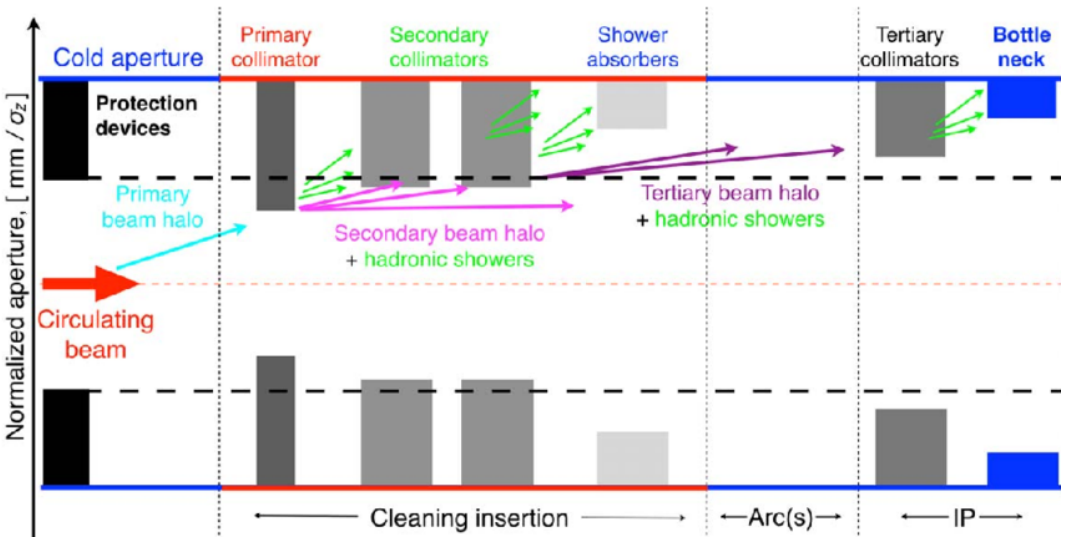

Figure 3. Multistage collimation scheme.[7]

After every scraping procedure, the MD trigger rate increased very quickly. It reached a level of 10 kHz in about one minute. The elastic trigger rate was 50-200 Hz, depending on the chosen configuration and the TCLAs and TCTPs settings, while the expected value from simulations was of order of 10 Hz.

The second test run was performed two weeks later. Six collimator settings schemes were tested. Apart from a new collimation schemes including scraping up to 2.0σ and the Roman Pot positions in 3.5σ, an increase of the RF voltage from 6.6 to 12 MV and different tunes of the octupole magnets were tested. Only one of the tested schemes looked promising in the on-line monitoring. This scheme was repeated for the 3σ Roman Pot positions. The MD trigger rate was lower than 500 Hz up to 15 minutes after the scraping while the elastic trigger rate was below 10 Hz. Unfortunately, further off-line analysis showed that none of the schemes could be used for physics data taking because the background levels were still too high.

The third test run was performed in May 2018. Three schemes were devised. For that test the TCPs were in fixed positions of 3σ and during the scraping the TCTPs and TCLAs were moved to the 2σ positions. After the scraping the TCTPs and TCLAs were retracted to 2.5σ positions. The RF voltage was increased from the nominal value of 6 MV to 12 MV to avoid debunching effects. The elastic trigger rate stayed below the expected level of 10 Hz for only a few seconds. Two minutes after the scraping, the elastic trigger rate exceeded few hundred Hz. The MD trigger rates exceeded 10 kHz within less than three minutes. Further off-line analysis confirmed high level of the irreducible background proving that also these schemes were not proper for the physics data taking.

The fourth test was performed in October 2018. For that test all vertical collimators were inserted to positions $2.5\text{-}3.0\sigma$, while the RF voltage was reduced to 4 MV. The elastic trigger rate was changing between 10 Hz and 15 Hz for almost 40 minutes, while the MD trigger rate of each of the detectors did not exceed 1 kHz. Further off-line analysis demonstrated that this scheme can be used for the physics data taking.

6. PHYSICS DATA TAKING SETUP

To collect physics data, the fourth set of settings discussed above were used (i.e. multistage collimation). They are referred in the following as Setting 1. In addition, the so-called crystal channelling collimation tests were performed, and these settings are called Setting 2. Table 2 presents the collimators' positions during data taking with the collimation policy as described according to collimation Settings 1 and Setting 2.

LHC Fill 7284 was devoted to the multistage collimation scheme, and the procedure leading to the data taking was as follows. Once the beam was set by the LHC operators, the initial scraping was performed – the

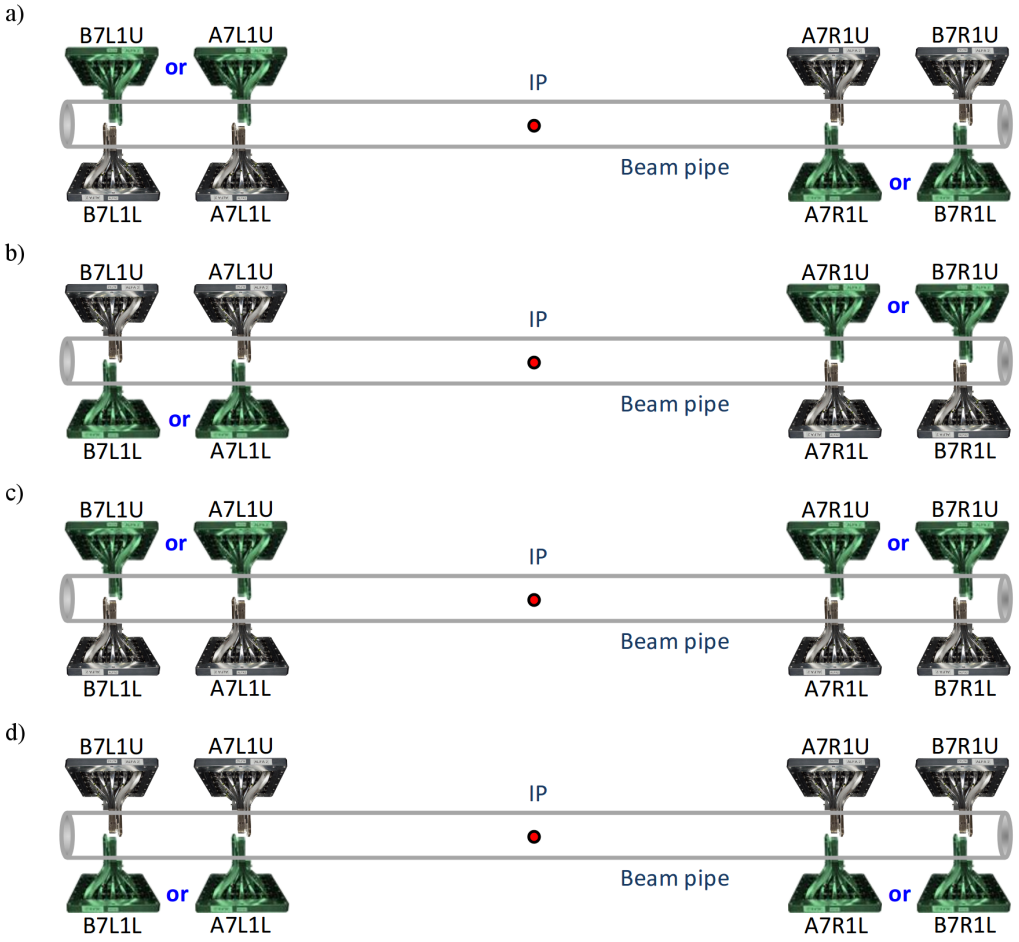

Figure 4. Elastic trigger logic and the systematic trigger logic.[8] Logic a) and b) correspond to elastic trigger patterns, while c) and d) show the systematic trigger patterns.

TCLA.A6 and TCP.C6 were moved to 2.0σ and 3.0σ positions, respectively, and then the positions of the other collimators were set according to the values listed in Table 2. When the BLM rates stabilised, the ALFA Roman Pots were moved into their operation positions, i.e. 3.0σ. Then the TCLA.A6 and TCP.C6 collimators were retracted to the data taking position – 4.0σ and 2.5σ respectively (Table 2). During the data taking the elastic and systematic trigger rates were monitored. The systematic trigger rate rose slowly, and when it reached the elastic one, approximately every hour, beam re-scraping was required. When the elastic rate after the re-scraping fell below 10 Hz, the beam was dumped and refill of the LHC was requested. The data-taking run took about four hours.

LHC Fill 7289 was devoted to the crystal collimation scheme. The initial scraping procedure was similar to that mentioned above. After initial scraping, the TCLA.A6 collimators were retracted from 2.5σ to 2.7σ and the crystal collimators were inserted to the 2.5σ position. After all the parameters stabilised the Roman Pots were inserted to the 3.0σ positions. Positions of the collimators for data taking with the use of crystal collimators are presented in Table 2. The systematic trigger rate increased much more slowly than in the multistage collimation scheme case and the data taking lasted for over three hours without a re-scraping request.

Table 2. Collimators positions in σ for runs with multistage collimation scheme (Setting 1) and for run with crystal collimation scheme (Setting 2).

Collimator	Plane	IR	Setting 1	Setting 2
TCLA.A6	V	7	2.5	2.7
TCLA.A5	V	3	2.7	2.7
TCTPV.4L2	V	2	2.7	2.7
TCTPV.4R8	V	8	2.7	2.7
TCTPV.4L2	V	1	2.7	2.7
TCTPV.4R8	V	5	2.7	2.7
TCLA.C6	V	7	2.7	2.7
TCP.D	V	7	3.0	3.0
TCP.6	H	3	5.3	5.3
All TCSGs	H	3	6.3	6.3
All TCSGs	H	3	9.0	9.0
TCP.C6	H	7	4.0	4.0
TCSG.B4	H	7	5.0	5.0
TCSG.6	H	7	5.0	5.0
TCLA.B6	H	7	8.0	8.0
TCLA.A7	H	7	8.0	8.0
Crystal	V	7	n/a	2.5
Roman Pots	V	1/5	3.0	3.0

7. BACKGROUND MEASUREMENT

During physics data taking with the multistage collimation, each beam contained an additional non-colliding isolated bunch to measure the beam-induced background. This approach was repeated for the run with the crystal collimation scheme.

During the run with the multistage collimation scheme, the rates seen by the detectors on one side of the IP were comparable. However, the ratio of the readings on the left and right sides of the IP was nearly constant and close to 2. The interpretation was that beam2 (Fig. 2) gave twice as much background as beam1. The beam-induced background was growing constantly over time. The off-line analysis showed the irreducible elastic background contribution of about 0.5%.

During the run with crystal collimation scheme, the ratio of the readings on the left and right sides of the IP was measured as well. Its value was close to the inverse of the one observed for the multistage collimation scheme. Moreover, the differences in the MD trigger rates between the detectors on the right side was much higher than that for ones on the left side, or for the multistage collimation. The rates from each of the Main Detectors on the left side of the Interaction Point were almost the same.

It is interesting to point out that for these runs, contrary to those with the multistage collimation scheme, the difference between the beams was observed not only in the trigger rates, but also in the spatial distributions of the measured tracks. The off-line analysis showed that the irreducible background for crystal is about 1.5%, 3 times higher than for the multistage collimation.

8. SUMMARY

After almost one year of preparation, the ATLAS-ALFA detector took data at the LHC injection energy with high β^* optics. For runs where multistage collimation was used, the background growth over time forced re-scraping roughly every hour. Beam-related background patterns look similar on each side of the IP.

During the special runs the crystal collimators were tested. The growth of the trigger rates during those runs was much slower, thus re-scraping was not required for over three hours of data taking. There was a strong asymmetry in the beam-related background pattern, that requires further investigation.

Off-line analysis showed the irreducible elastic background was about 0.5% and 1.5% for multistage and crystal collimation respectively.

The usefulness of the crystal collimation scheme during high β^* runs requires further off-line analysis. Conclusions from the discussed measurements will be used for preparation of the high β^* runs expected in the future.

REFERENCES

[1] The ALFA Collaboration, "The ALFA roman pot detectors of ATLAS," *Journal of Instrumentation* **11**(11), P11013 (2016).

[2] The ATLAS Collaboration, "The ATLAS experiment at the CERN large hadron collider," *Journal of Instrumentation* **3**(08), S08003 (2008).

[3] Jakobsen, S., "ALFA latency for Run1 and expectations for Run2," Tech. Rep. ATL-COM-LUM-2013-018, CERN, Geneva (Jul 2013).

[4] Korcyl, K., "ALFA detector: timing and trigger," Proc. SPIE 89032-K1 (2013).

[5] Iwanski, W., Jakobsen, S., Korcyl, K., and Oechsle, J., "Functionality and performance of the ALFA_CTPIN module," *PoS* **TWEPP-17**, 142 (2017).

[6] Garcia Morales, H., Bruce, R., Burkhardt, H., Deile, M., Jakobsen, S., Mereghetti, A., and Redaelli, S., "Special Collimation System Configuration for the LHC High-Beta Runs," MOPML012 (2018).

[7] Redaelli, S., "Beam cleaning and collimation systems," CERN Yellow Report CERN-2016-002, pp.403-437 (2016).

[8] Jakobsen, S., "Commissioning of the Absolute Luminosity For ATLAS detector at the LHC," (2013). CERN-THESIS-2013-230.

Towards increasing of lateral dimension of Molybdenum disulfide MoS_2

P.Knyps[a], P.A.Caban[a], P.Ciepielewski[a], P. P.Michalowski[a], E.Dumiszewska[a] and J.M.Baranowski[a]
[a]Institute of Electronic Materials Technology, Warsaw, Poland

ABSTRACT

The growth process of molybdenum disulfide (MoS_2) films on SiO_2, Al_2O_3 and BN substrates is presented. Samples were measured by Raman spectroscopy and Secondary Ion Mass Spectrometry to investigate mechanism of increase lateral dimensions and quality of the grown material. The size of obtained layers is crucial for further processing and application into current microelectronic devices. Considering all the substrates used in sulfurization process of molybdenum layers, hexagon Boron Nitride (hBN) is the most promising material. It is the result of its high crystalline quality and lack of oxygen atoms, which diffuse to surface during production process in 750°C and disallow to increase dimensions of MoS_2. Described method of sulfurization creates possibility of production of that material on large area substrates and easy integration with other two dimensional compounds like graphene, WS_2, SiC, hBN for new types of electronic applications.

Keywords: Molybdenum disulfide, Large-scale MoS_2 layers, Sulfurization of Mo, Raman scattering, Secondary Ion Mass Spectrometry

1. INTRODUCTION

Actual trends of miniaturization in microelectronics also drive toward thin atomic layer materials. Discovery of graphene and its extraction by A. Geim and K. Novoselov in 2004 showed that monolayers materials can be used as a crucial part of microelectronic devices. Other 2D materials - transition metal dichalcogenides (TMDs), like WS_2 and MoS_2 have received great attention and have emerged as an attractive group of nano-scale materials due to their unparallel properties [1]. Their electronic features like tunable band gap, electrical conductivity and transparency make them great candidates for optoelectronic and nano-electronic applications, such as photodetectors, photovoltaic cells, transistors and sensors. Molybdenum disulfide is well known material commonly used in industry, but recently also its electronic properties have been investigated. MoS_2 is a two-dimensional crystal with strong in-plane covalent bonding and weak out of plane van der Waals one. The easiest method to get MoS_2 monolayers is the mechanical exfoliation of bulk material. But this technique is not efficient for obtaining large area uniform 2D material appropriate for mass fabrication. Another method also successfully used to produce large area layers of MoS_2 is chemical vapour deposition (CVD). In that method direct growth of 2D materials is achieved on substrate with thin metal deposited in physical vapour deposition system. In that paper we describe technology of sulfurization of molybdenum deposited on different substrates such as SiO_2, Al_2O_3 and BN.

Motivation of the present work is the great success of other 2d material - graphene. It's high electrical conductivity ($\sim 10^4\ \Omega^{-1}\ cm^{-1}$) [2], electron mobility of 15000 $cm^2 \cdot V^{-1} \cdot s^{-1}$ [3] and high transparency (97.7% transmittance in the visible spectrum) [4] have been recognized in monolayer graphene and predestine graphene for various applications, including solar cells [5], flexible electronics [6], transparent electrodes [7] and energy storage [8].

Among many various 2D materials, molybdenum disulfide (MoS_2) has been also receiving much research attention. Because of its electronic properties few atomic layer MoS_2 has good potential applications in micro and optoelectronics, and flexible devices. MoS_2 is a relatively quite common material, it is chemically inert and the band gap 1,8eV [9] is well matched to the solar spectrum, which creates great possibility to implement this material into smart electronic devices like Internet of Things (IoT) and sensors [9][10].

2. EXPERIMENTAL

One focused on production of electronic materials always must keep in mind that there is interaction between material quality, production process efficiency and costs. Chemical vapour deposition (CVD) is a technique that contain

Photonics Applications in Astronomy, Communications, Industry, and High-Energy Physics Experiments 2019,
edited by Ryszard S. Romaniuk, Maciej Linczuk, Proc. of SPIE Vol. 11176, 111764K
© 2019 SPIE · CCC code: 0277-786X/19/$21 · doi: 10.1117/12.2533912

depositing of a solid material from a gaseous phase when chemical reaction occurs between gasses and heated substrates. Precursor gases are transported into the reaction chamber at low temperatures. When they come into contact with a heated substrate, they react or decompose forming a solid phase which is deposited onto the substrate. The substrate temperature, gas flows and pressure in reactor are critical parameters and can determine what reactions will take place.

From many different methods of production of MoS_2 [11] we used sulfurization of molybdenum atomic layer, which helps to improve the uniformity on large areas substrates. In that method synthesis of MoS_2 is divided into two technological stages. First one is deposition of a thin layer of Molybdenum on different types, 2 inch diameter substrates. We used SiO_2, Al_2O_3 and BN on sapphire. It was carried out in e-beam evaporation in Kurt Lesker PVD system. Deposition of Mo metal was done under 5×10^{-7} Thor pressure. Evaporated Mo film ranged from 0.4nm to 2.0nm in thickness. Deposition rate is maintain on very low level 0,010-0,020Å/s and samples are mounted on rotating disc to obtain high uniformity of layer thickness. RMS parameter of surface roughness is 0,3nm.

After that, sputtered samples with Mo layer were placed in Chemical Vapour Deposition (CVD) reactor for sulfurization to form MoS_2 film. H_2S was used as precursor of Sulfur and H_2 as carrier gas. The sulfurization process took place at 750°C temperature for 15 minutes. H_2S flow was closed after the growth and reaactor was cooled down to room temperature. Excess Sulfur atoms from the surface of sample were evaporated by annealing sample in 150°C for 30 minutes.

3. RESULTS

To characterize the MoS_2 layers during Mo deposition and sulfurization processes different techniques were used. Raman measurements were performed on Renishaw in Via Raman Microscope using 532nm wavelength laser light. To avoid the destruction of MoS_2 layers, power was reduced below 0.1 mW and size of a spot was about 0.5μm in diameter The laser was focused on sample using ×100 objective and numerical aperture NA=0.9 in a backscattering geometry. Secondary Ion Mass Spectrometry measurements were done on a CAMECA SC Ultra instrument under ultra-high vacuum bellow $4x10^{-10}$ mbar. Optical profilometry was done on 3D non-contact optical Bruker profilometer for analysis of surface quality.
Molybdenum layers were deposited with thickness ranging from 0,40 nm up to 2,0 nm which correspond to 1-5 atomic layers. However after sulfurization process and SIMS analysis, the thickness was reduced to 0,40 nm. That resulted from the fact that under MoS_2 layer was unreacted molybdenum material. Quality and roughness of deposited metal was proper for further CVD process, what is shown on Figure 1.

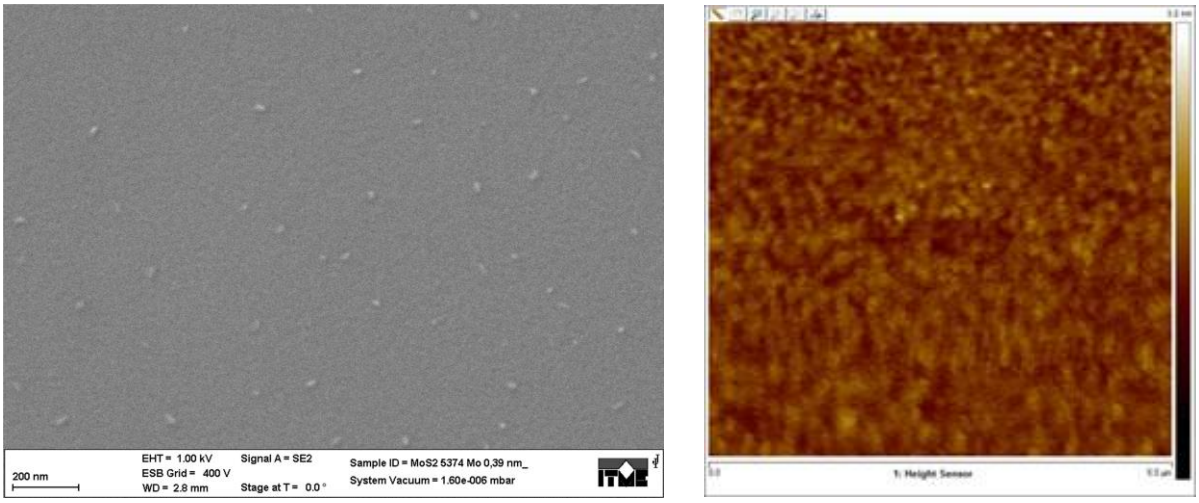

Figure 1. Scanning electron microscopy image (left) and atomic force microscopy (right) of deposited molybdenum 0,40 nm layer on Al_2O_3 substrate.

Raman spectroscopy is optical, contactless method to identify molecules in sample and its characteristic structural fingerprint. In our work this technique was used to analyze the number of atomic layers in thin MoS_2. It was described [12] that the frequencies of the Raman $E^1{}_2g$ and A_{1g} peaks are dependent on the MoS_2 thicknesses in the range of 1-4

monolayers. Difference of these mode increases from 19 cm^{-1} for monolayer to 25 cm^{-1} for bulk material (more than 4 atomic layers).
Analysing Raman spectra of MoS_2 grown on SiO_2 (Figure 2) we can state that the crystalline quality of the Sample A (MoS_2 on SiO_2/Si,) is unsatisfying – peaks intensity is low and FWHM value largest from all three analysed samples. The frequency difference is 24 cm^{-1} which corresponds to thickness of four layers of MoS_2. Sample B (MoS_2 deposited on Al_2O_3) has much better quality - peaks are more intense and narrower. The frequency difference is 22 cm^{-1} which indicates two layers of MoS_2. MoS_2 grown on BN/Al_2O_3) has the highest quality and the frequency difference is 23 cm^{-1} which indicates two and three layers of MoS_2.

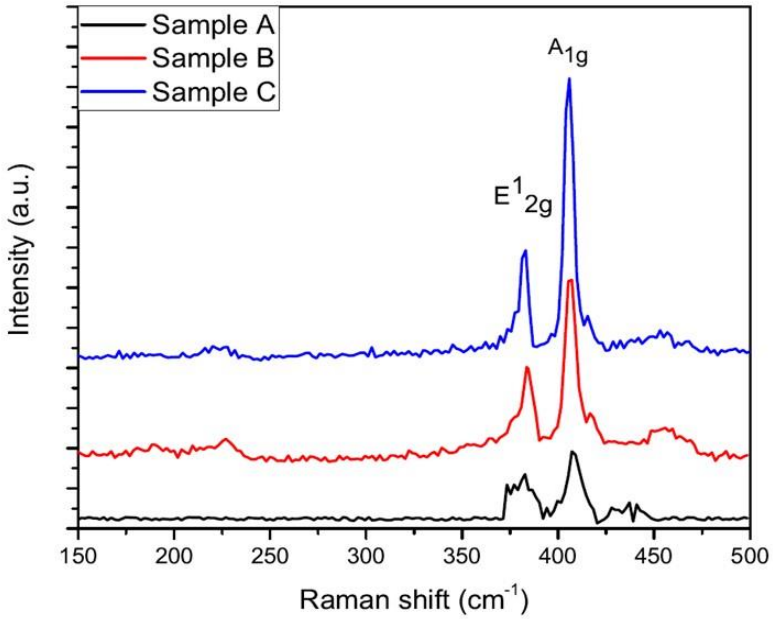

Figure 2. Raman spectrum of MoS_2 layers deposited on different substrates: Sample A: MoS_2/SiO_2/Si, sample B: MoS_2 on sapphire (Al_2O_3), sample C: MoS_2 on BN grown on Al_2O_3.

Additional analysis of Raman mapping of MoS_2 grown on Al_2O_3 was done (Figure 3). Energy difference between E_{2g} and A_{1g} Raman modes from 22,8 cm^{-1} to 23,6 cm^{-1} indicate of islands from 2 to 3 atomic layers of MoS_2. Intensity map of mode A_{1g} (Figure 3 right) shows continuity of MoS_2 layer, measured value exist in every point of the sample.

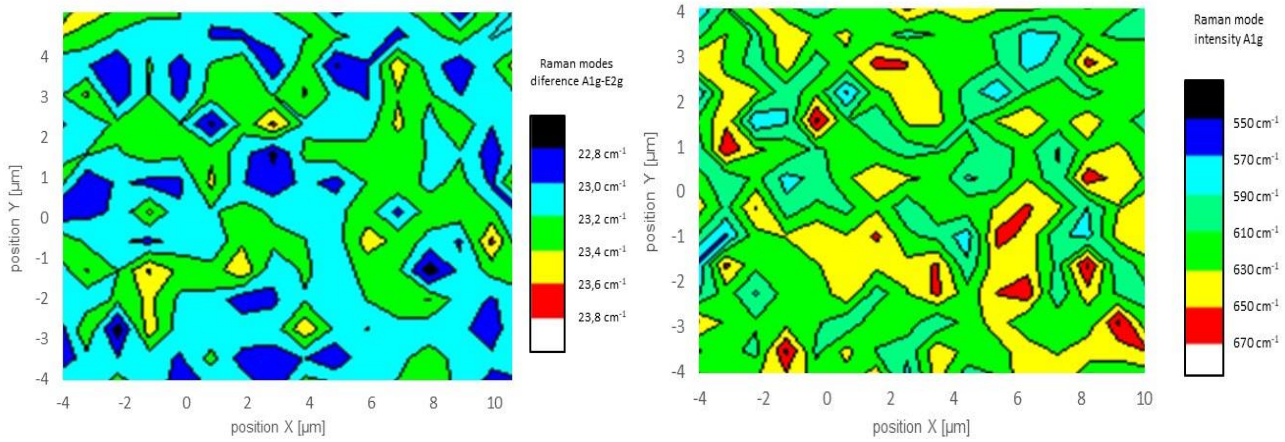

Figure 3. Map of Raman modes difference A_{1g}-E_{2g} (left) and Raman mode A_{1g} intensity (right) MoS_2 on Al_2O_3.

In our work we focused on growth of MoS_2 on large areas substrates – minimum 2 inch diameter, because only such wafers are compatible with other technological processes like CVD, photolithography and spin coating. First substrate used for deposition of MoS_2 was cheap and widely used 20nm thick SiO_2 layer on Silicon wafers. That creates possibility for easy integration of new 2-dimension material with technology developed for many years and still being the leading ones in microelectronics. Unfortunately expansion of atomic layers on SiO_2 substrate stopped on triangle shapes with 40% surface coverage. The change of the used substrate into sapphire significantly increased quality of layer (Figure 2) and also helped to enlarge their area size (Figure 5). Raman spectrums from different points on 2-inch wafer confirm existence of MoS_2 on about 80% of their area. Only region close to flats cut (point 1 and 2 on Figure 4) have weak Raman signal from peaks E_{2g} and A_{1g} – it is caused by disturbed gas flow in CVD reactor close to wafer cut during sulfurization.

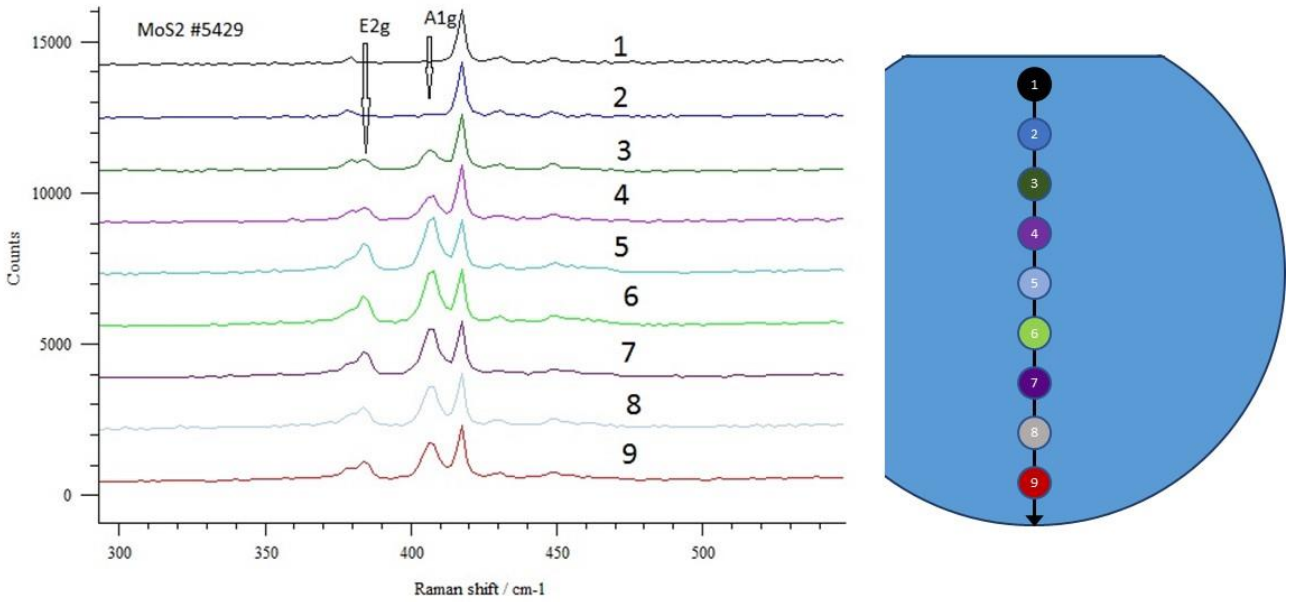

Figure 4. Map of Raman modes difference A_{1g}-E_{2g} (left) and Raman mode A_{1g} intensity (right) MoS_2 on Al_2O_3

Secondary Ion Mass Spectrometry (SIMS) images for samples made on different substrates clearly shows differences in quality of MoS_2 layers and their lateral dimensions. Precise dedicated procedures were established for analyzed material, because atomic layers must be treated in very delicate way and bombardment by ions with energy as low as necessary. SIMS imagining mode allows to identify MoS_2 phase, amorphous MoS oxide and oxygen on the sample.

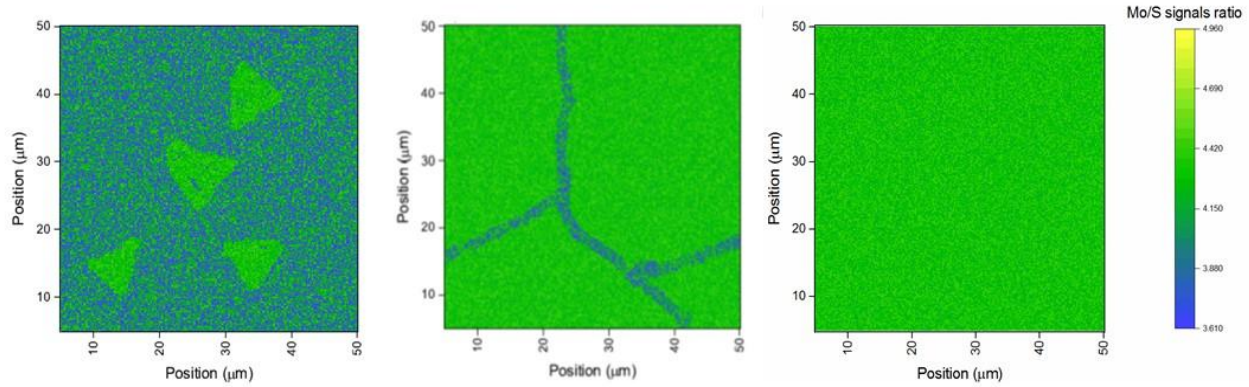

Figure 5. SIMS distribution map of signal from ratio of Mo to S elements. Samples from left to right: Sample A: $MoS_2/SiO_2/Si$, sample B: MoS_2 on sapphire (Al_2O_3), sample C: MoS_2 on BN grown on Al_2O_3.

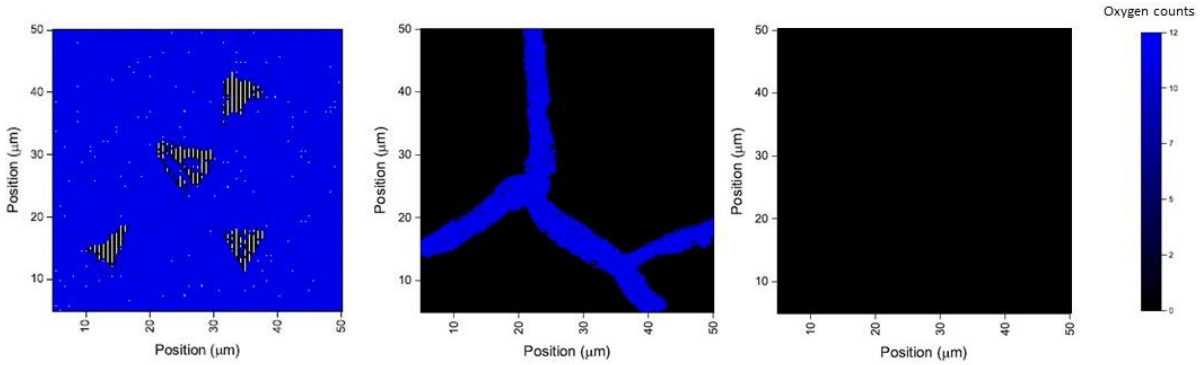

Figure 6. SIMS distribution map of signal from oxygen. Samples in the same order as on Figure 5.

It has been demonstrated that the oxygen released from a substrate reduces the size of MoS_2 domains. Characteristic triangle shapes (Figure 5) are visible on left image. Their growth on SiO_2 covers up to 40% of the area, while using sapphire as a substrate increases coverage area to 90%. Sapphire is much more stable oxide than SiO_2. If BN/Al_2O_3 is used as a substrate no oxidation takes place (Figure 6) and homogenous layers of MoS_2 are formed.

4. CONCLUSIONS

Our latest technological work demonstrated possibility to growth Molybdenum Disulfide with good quality and continuity on large area substrates. From different types of substrates hexagonal Boron Nitride on Al_2O_3 seems to be most appropriate to CVD sulfurization, because it is free from oxygen atoms. The 2 nm thick hBN layer on sapphire reduce oxygen diffusion to the grown MoS_2 film and allow for produce continuous and uniform layers on 2-inch substrates.

ACKNOWLEDGEMENTS

This work was supported by the European Union's Horizon 2020 research and innovation programme under grant agreement no. 785219.

REFERENCES

[1] Ramakrishna Matte, H. S. S., Gomathi, A., Manna, A. K., Late, D. J., Datta, R., Pati, S. K., & Rao, C. N. R. (2010). MoS_2 and WS2 analogues of graphene. Angewandte Chemie International Edition, 49(24), 4059-4062.
[2] Allen, M. J., Tung, V. C., & Kaner, R. B. (2010). Honeycomb Carbon: A Review of Graphene. Chemical Reviews, 110(1), 132–145. doi:10.1021/cr900070d
[3] Geim, A. K., & Novoselov, K. S. (2007). The rise of graphene. Nature Materials, 6(3), 183–191. doi:10.1038/nmat1849
[4] Falkovsky, L. A. (2008). Optical properties of graphene. In Journal of Physics: Conference Series (Vol. 129, No. 1, p. 012004). IOP Publishing.
[5] Soldano, C., Mahmood, A., & Dujardin, E. (2010). Production, properties and potential of graphene. Carbon, 48(8), 2127–2150. doi:10.1016/j.carbon.2010.01.058
[6] Tran, T. S., Dutta, N. K., & Choudhury, N. R. (2018). Graphene inks for printed flexible electronics: Graphene dispersions, ink formulations, printing techniques and applications. Advances in Colloid and Interface Science, 261, 41–61. doi:10.1016/j.cis.2018.09.003
[7] Woo, Y. (2018). Transparent Conductive Electrodes Based on Graphene-Related Materials. Micromachines, 10(1), 13. doi:10.3390/mi10010013
[8] Zang, X. (2018). Graphene-Based Flexible Energy Storage Devices. Graphene, 175–199. doi:10.1016/b978-0-12-812651-6.00007-0

[9] Chang, H.-Y., Yogeesh, M. N., Ghosh, R., Rai, A., Sanne, A., Yang, S., … Akinwande, D. (2015). Large-Area Monolayer MoS_2 for Flexible Low-Power RF Nanoelectronics in the GHz Regime. Advanced Materials, 28(9), 1818–1823. doi:10.1002/adma.201504309

[10] Borecki, M., L., M., Beblowska, M., Szmidt, J., Szmidt, M., Duk, M., Jakubowski, A. (2011). Intelligent Photonic Sensors for Application in Decentralized Wastewater Systems. Waste Water - Evaluation and Management. doi:10.5772/16136

[11] Li, X., & Zhu, H. (2015). Two-dimensional MoS_2: Properties, preparation, and applications. Journal of Materiomics, 1(1), 33–44. doi:10.1016/j.jmat.2015.03.003

[12] Li, H., Zhang, Q., Yap, C. C. R., Tay, B. K., Edwin, T. H. T., Olivier, A., & Baillargeat, D. (2012). From Bulk to Monolayer MoS_2: Evolution of Raman Scattering. Advanced Functional Materials, 22(7), 1385–1390. doi:10.1002/adfm.201102111

Screen printed graphene electrodes for voltammetric dopamine determination

T. Raczyński*[a], D. Janczak [a], J. Jankowska-Śliwińska [b], M. Dawgul [c], A. Paziewska-Nowak [c], D. Pijanowska [c], M. Zych [a], M. Jakubowska [a]

[a]Institute of Metrology and Bioengineering, Faculty of Mechatronics, Warsaw University of Technology, A. Boboli 8 St., 02-525 Warsaw, Poland

[b]Institute of Electron Technology, Department of Micro- and Nanotechnology of Wide Bandgap Semiconductors, Aleja Lotników 32/46 St., 02-668 Warsaw, Poland

[c]Maciej Nałęcz Institute of Biocybernetics and Biomedical Engineering, Polish Academy of Sciences, Ks. Trojdena 4 St., 02-109 Warsaw, Poland

* tomasz.raczynski.stud@pw.edu.pl

ABSTRACT

In this work, new graphene-based screen-printed electrodes are proposed as a new, cheaper alternative to more common electrodes for determination of dopamine. Electrodes were designed, manufactured and tested to look for correlations between different graphene weight percentages used in electrodes and oxidation peaks and sensitivity in dopamine determination. All electrodes were tested using cyclic voltammetry. For a reference, graphite electrodes were tested. With sensitivity of 0.0161 µA/µM and detection limit of 5.549 µM those electrodes showed potential promise in use of graphene for electrode material. In electrodes manufacturing, Laroflex® and PMMA based vehicles were mixed in with graphene platelets with diameters ranging over 2 µm and thickness between 8-15 nm. Initial tests with electrodes screen printed with graphene layers of 150 µM showed very low response. 0.0077 µA/µM sensitivity and 11.970 µM detection limit were achieved with Laroflex® based electrodes. Further testing with thicker layers gave more impressive results with detection limit going as low as 1.349 µM and 0.1343 µA/µM sensitivity. Such results bring those electrodes to comparable level with other electrodes available.

Keywords: Graphene, sensors, screen printing, dopamine, voltammetry

1. INTRODUCTION

Dopamine is a catecholamine, that functions as a neurotransmitter in human brain. It is released by neurons grouped in distinct pathways, responsible for motor functions, executive functions and reward- and aversion-related cognition. Disturbances of dopamine functions, shortage of dopamine or even death of dopamine neurons is linked with chorea, Parkinson's disease, addictions, schizophrenia and attention deficit hyperactivity disorder[1]. Due to the severity of these conditions, precise determination of dopamine concentration is very important. There are many different methods used for dopamine determination: spectrophotometry[2], chromatography[3], fluorometry[4] but the most common are electroanalytical methods[5]. Electroanalytical methods are rapid, simple, have high sensitivity and don't require expensive equipment. There is diverse range of materials used in manufacturing of electrodes for electroanalytical measurements, but recently, carbon-based nanomaterials have been more widely used. Such materials have relatively inert electrochemistry, high electrocatalytic activity and wide potential window[6]. One of the most recent and most attractive nanomaterials is graphene. It has wide range of uses in medicine[7] or in electronics[8,9]. It is biocompatible[10], has highly developed surface area and can yield better results than GCE[11]. When used in combination with polymer it can create flexible and conductive material. With proper application such material can be used as electrodes for voltammetric measurements[12]. There are many ways to manufacture such electrodes, but screen printing, being reliable, quick and cost-effective, is one with most potential for mass production and future development. There is a lot of research on screen printed graphene electrodes[13] but there is no information that would help to develop it as a large-scale technology. One of such information is correlation between weight percentage of graphene in paste and sensitivity and limit of detection of voltammetric measurements. For this

Photonics Applications in Astronomy, Communications, Industry, and High-Energy Physics Experiments 2019, edited by Ryszard S. Romaniuk, Maciej Linczuk, Proc. of SPIE Vol. 11176, 111764L
© 2019 SPIE · CCC code: 0277-786X/19/$21 · doi: 10.1117/12.2535784

research, dopamine was chosen as an analyte, because it is widely tested neurotransmitter. Thanks to that, there are many different sensors to compare with when it comes to performance.

2. EXPERIMENTAL METHODS

2.1. Materials

Type C graphene nanoplatelets were purchased from Cheap Tubes Inc (USA). They have particle diameter of over 2 µm, thickness of 8-15 nm and surface area of 500-700 m^2/g. Two different types of vehicle were chosen: solution of PMMA in butyl carbitol acetate and Laroflex® solution in diethylene glycol butyl ether acetate. Silver polymer paste type L-121 was used. Both vehicles and silver paste were manufactured in Institute of Metrology and Biomedical Engineering of Warsaw University of Technology. Dielectric paste 5018A was bought from Dekorglass.
For experimentation, NaH2PO4, KCl and dopamine hydrochloride (DA) were purchased from Sigma Aldrich, 0.1 M NaOH was purchased from Avantor.

2.2. Preparation of graphene pastes

To prepare the graphene paste, graphene nanoplatelets were mixed with chosen vehicle to form a slurry. Specific amounts of graphene and vehicle were used to create pastes with desired weight percentage of graphene in whole paste. Graphene slurry then was mixed in mortar for 15 minutes. Afterwards, paste was processed by Exakt three-roll-mill 80E with 5 µm gap to eliminate agglomerates and achieve uniform consistency. There were multiple pastes prepared to examine prospective correlation between paste contents and parameters of electrodes (Table 1).

Table 1. Types of prepared pastes and names of electrodes manufactured

Graphene weight percentage [%wt]	Vehicle type	Paste label
12.5	PMMA based	T3
18	PMMA based	T11
20	PMMA based	T6
10	Laroflex® based	T1
15	Laroflex® based	T2
20	Laroflex® based	T3
22	Laroflex® based	T7

2.3. Electrodes manufacturing

Graphene electrodes consisted of three screen printed layers on PMMA foil. Each layer was screen printed using Auriel Automation screen printer C920. They were printed via specially prepared 68 T polyester screens and a stencil. After printing conductive silver layer, electrodes were cured for 20 minutes in 120°C using SLW 53 STD POL-EKO-APARATURA oven. On conductive layer, dielectric layer was printed and cured using UV dryer UN60001-0002 Technigraf. After that, graphene layer was printed, and cured for 20 minutes in 120°C using oven. Printing screens were designed to print multiple electrodes at once with working layer of 1.5x6.5 mm.

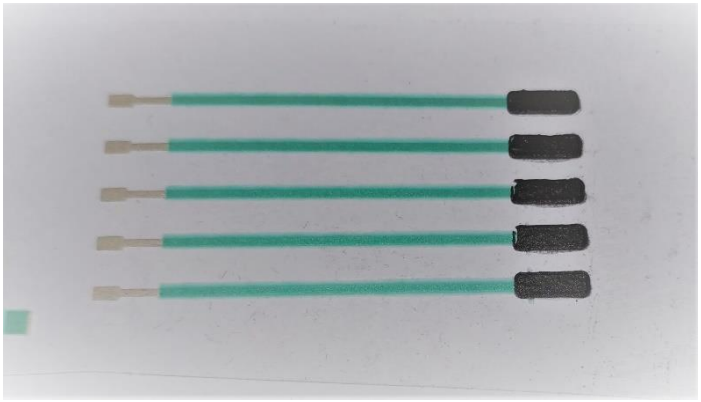

Figure 1. Screen printed electrodes

2.4. Voltammetric measurements

To conduct the experiments, based on literature[14–17], 7.5 pH 0.1 M phosphate buffer saline (PBS) was prepared. NaH2PO4 and KCl were measured and mixed with distilled water. PH of solution was measured using Ion Analyser MeterLab PHM250. To bring pH of solution up to 7.5 small portions of 0.1 M NaOH were added. As analyte, solution of 0.1 mM dopamine hydrochloride in distilled water was prepared.

During each experiment, 3 ml of PBS was deoxidized for 20 minutes using nitrogen gas. Three electrodes: reference saturated calomel electrode, counter platinum electrode and working graphene electrode were cleaned with distilled water and connected to PalmSens Electrochemical Sensor Interface (Figure 2).

First, 10 scans of cyclic voltammetry were prepared to clean electrodes from any chemical impurities. Based on literature[14,16,18], oxidation peak of dopamine was expected to be around 0.1 – 0.3 V, so electrodes with signal noise in that range were discarded. Then differential pulse voltammetry (DPV) were performed. Best parameters were decided to be, scan range – -0.5 ÷ 1 V, potential step – 0.005 V, pulse potential – 0.2 V, time of pulse – 0.07 s and scan rate – 0.03 V/s.

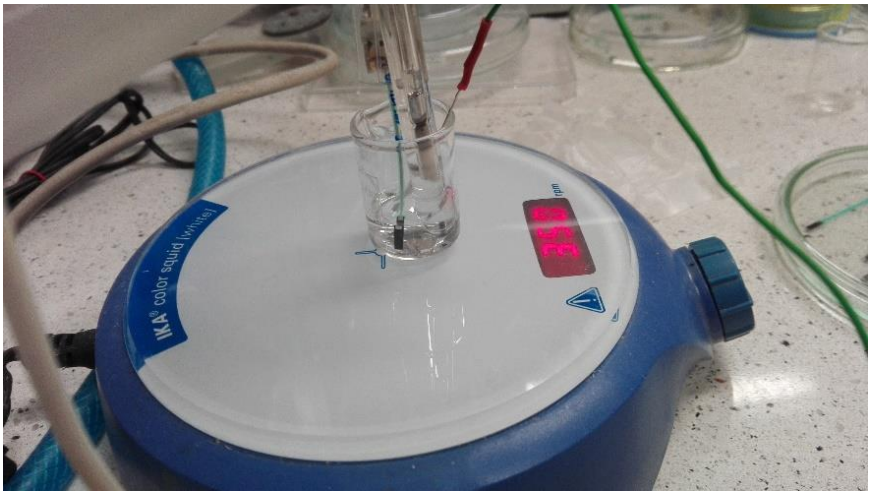

Figure 2. Setup used for voltammetric measurements

After each scan, dopamine solution was added to acquire dopamine concentrations of 10 µM, 25 µM, 50 µM, 100 µM.

3. RESULTS AND DISCUSSION

For reference, graphite electrodes (GP) made in Institute of Biocybernetics and Biomedical Engineering Polish Academy of Sciences. They were successful in determining dopamine in range of 5-200 µM. Dopamine oxidation peak started a 0.2 V, but at higher concentrations of dopamine, it had drifted towards 0.2 V (Figure 3). After analysis, limit of detection was calculated to be 5.549 µM and sensitivity to be 0.0161 µA/µM (Figure 4).

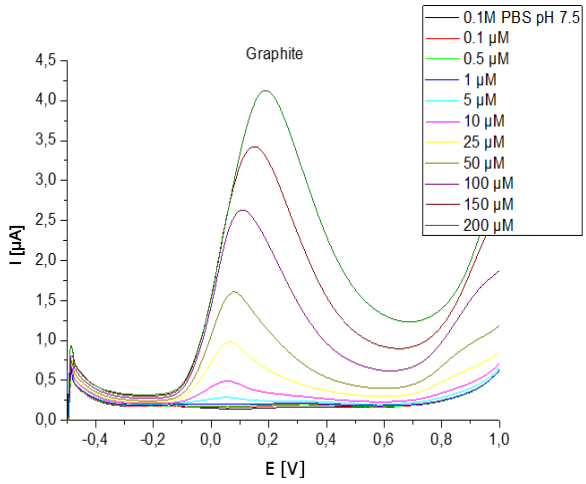

Figure 3. Exemplary voltammograms obtained with the use of differential pulse voltammetry by means of graphite electrode for dopamine solutions in concentration range 0.1 ÷ 200 µM.

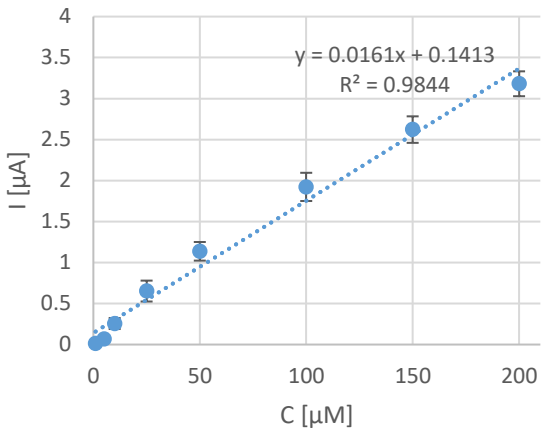

Figure 4. Calibration curve based on DPV measurements of graphite electrode

Afterwards, different graphene electrodes were tested. Sensors screen printed using screens and paste T1 showed very low response: limit of detection of 11.9703 µM and sensitivity of 0.0077. Such low results were attributed to thin graphene layer of 150 µm compared to 400 µm of graphite electrodes. To improve quality of electrodes, electrodes screen printed through stencil were prepared with 400 µm graphene layer. New electrodes showed much better results (Table 2). When increasing graphene weight percentage, increase of sensitivity can be observed. The drawback of such operation is that with increase of graphene amount, paste becomes thicker and thicker, which precludes it from possibility of screen printing. With Laroflex®, pastes with graphene wt% higher than 22%, paste become very hard to print and for PMMA based pastes, pastes with wt% over 18% are too thick to print. With graphene layer thickness of 400 µm of, limit of detection also improved. Very high values with PMMA based vehicle are caused by low repeatability of electrodes printed with too thick pastes. For further research, paste T7 should be used. It has best limit of detection, which can be further increased with improved repeatability of electrodes. It also has very good sensitivity (Figure 5), being still able to screen print with that paste. Those electrodes have also low average peak potential and with increased concentration of dopamine, peak potential does not change (Figure 6).

Table 2. Types of prepared pastes and names of electrodes manufactured

Name	GNP [%wt]	Vehicle	Sensitivity [µA/µM]	LOD [µM]	Av. Peak potential [V]	R^2
T1	10	Laroflex®	0.00988	42.206	0.3125	0.9729
T2	15	Laroflex®	0.0116	10.872	0.2775	0.9985
T3	20	Laroflex®	0.0687	5.370	0.056	0.9969
T7	22	Laroflex®	0.1343	1.349	0.0512	0.9979
T12	12.5	PMMA	0.0668	30.770	0.0417	0.9833
T11	18	PMMA	0.1217	185.680	0.039	0.9938
T6	20	PMMA	0.2074	90.816	0.0574	0.9914

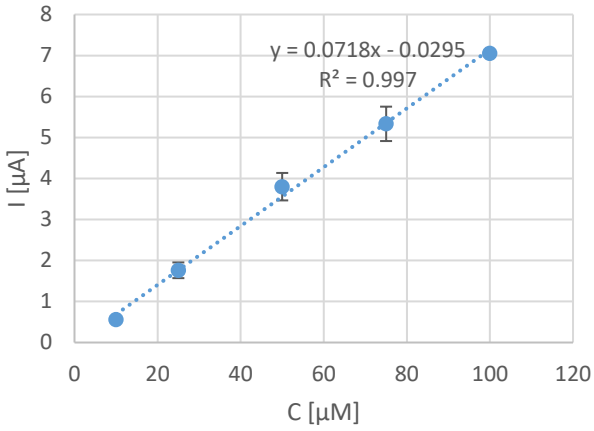

Figure 5. Calibration curve based on DPV measurements of T3 graphene electrode

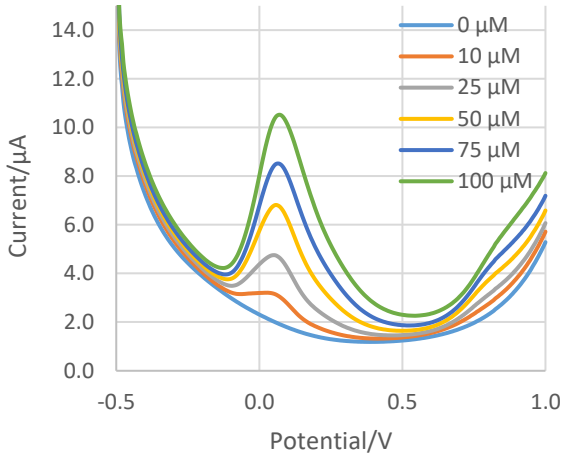

Figure 6. Exemplary voltammograms obtained with the use of differential pulse voltammetry by means of T3 graphene electrode for dopamine solutions in concentration range 10 ÷ 100 µM.

With achieved performance, screen printed graphene electrodes can be used in laboratories for determination of dopamine. In comparison with other dopamine electrodes (Table 3) it has lower sensitivity but initial limit of detection, which is improvable, is promising. The main advantage of those electrodes is its' very low production cost. Cost of sheet of 50 screen printed electrodes is dozens of times lower than single GCE.

Table 3. Comparison of prepared electrodes and existing electrodes

Name	Sensitivity [µA/µM]	LOD [µM]	Av. Peak Potential [V]	R^2
T7	0.1343	1.349	0.0512	0.9979
GP	0.0161	5.549	0.05	0.9844
Cu_2O/graphene/GCE[19]	3.4425	0.36	0.3	0.9997
CuO/CPE[20]	1.342	0.055	0.16	0.996
Graphene/Pt/GCE[21]	0.9695	0.03	0.272	0.9976
GO/GCE[22]	0.482	0.5	0.22	0.997

4. CONCLUSIONS

This article presents new electrodes, that can be used for voltammetric measurements. Graphene nanoplatelets were used to create pastes with different graphene weight percentages. They were tested using voltammetric method of differential pulse voltammetry. Research showed that with increase of weight percentage of graphene, sensitivity and limit of detection was increased. Due to increasing thickness of paste, best paste still suitable for printing, was paste with 22 wt% and Laroflex® based vehicle. Further improvements could be made in repeatability of electrodes lowering theirs limit of detection. Presented research could be continued to create biosensors[23] or find new parameters for other analytes.

5. REFERENCES

[1] Kim, J.-H., Auerbach, J. M., Rodríguez-Gómez, J. A., Velasco, I., Gavin, D., Lumelsky, N., Lee, S.-H., Nguyen, J., Sánchez-Pernaute, R., Bankiewicz, K. and McKay, R., "Dopamine neurons derived from embryonic stem cells function in an animal model of Parkinson's disease," Nature **418**(6893), 50–56 (2002).

[2] Hormozi Nezhad, M. R., Tashkhourian, J. and Khodaveisi, J., "Sensitive spectrophotometric detection of dopamine, levodopa and adrenaline using surface plasmon resonance band of silver nanoparticles," J. Iran. Chem. Soc. **7**(S2), S83–S91 (2010).

[3] Guan, C. ., Ouyang, J., Li, Q. ., Liu, B. . and Baeyens, W. R. ., "Simultaneous determination of catecholamines by ion chromatography with direct conductivity detection," Talanta **50**(6), 1197–1203 (2000).

[4] Ebru Seçkin, Z. and Volkan, M., "Flow injection fluorescence determination of dopamine using a photo induced electron transfer (PET) boronic acid derivative," Anal. Chim. Acta **547**(1), 104–108 (2005).

[5] Lai, G.-S., Zhang, H.-L. and Han, D.-Y., "Electrocatalytic oxidation and voltammetric determination of dopamine at a Nafion/carbon-coated iron nanoparticles-chitosan composite film modified electrode," Microchim. Acta **160**(1–2), 233–239 (2008).

[6] Temoçin, Z., "Modification of glassy carbon electrode in basic medium by electrochemical treatment for simultaneous determination of dopamine, ascorbic acid and uric acid," Sensors Actuators B Chem. **176**, 796–802 (2013).

[7] Młyńczak, M., Zyliński, M., Janczak, D., Jakubowska, M., Niewiadomski, W. and Cybulski, G., "Graphene electrodes for long-term impedance pneumography - a feasibility study," 514–517 (2018).

[8] Kopyt, P., Salski, B., Olszewska-Placha, M., Janczak, D., Sloma, M., Kurkus, T., Jakubowska, M. and Gwarek, W., "Graphene-Based Dipole Antenna for a UHF RFID Tag," IEEE Trans. Antennas Propag. **64**(7), 2862–2868 (2016).

[9] Olszewska-Placha, M., Salski, B., Janczak, D., Bajurko, P. R., Gwarek, W. and Jakubowska, M., "A Broadband Absorber With a Resistive Pattern Made of Ink With Graphene Nano-Platelets," IEEE Trans. Antennas Propag. **63**(2), 565–572 (2015).

[10] Pinto, A. M., Gonçalves, I. C. and Magalhães, F. D., "Graphene-based materials biocompatibility: A review," Colloids Surfaces B Biointerfaces **111**, 188–202 (2013).

[11] Pumera, M., "Graphene-based nanomaterials and their electrochemistry," Chem. Soc. Rev. **39**(11), 4146 (2010).

[12] Janczak, D., Peplowski, A., Wroblewski, G., Gorski, L., Zwierkowska, E. and Jakubowska, M., "Investigations of Printed Flexible pH Sensing Materials Based on Graphene Platelets and Submicron RuO_2 Powders," J. Sensors **2017**, 1–6 (2017).

[13] Cinti, S. and Arduini, F., "Graphene-based screen-printed electrochemical (bio)sensors and their applications: Efforts and criticisms," Biosens. Bioelectron. **89**, 107–122 (2017).

[14] Adekunle, A. S., Agboola, B. O., Pillay, J. and Ozoemena, K. I., "Electrocatalytic detection of dopamine at single-walled carbon nanotubes–iron (III) oxide nanoparticles platform," Sensors Actuators B Chem. **148**(1), 93–102 (2010).

[15] Anithaa, A. C., Lavanya, N., Asokan, K. and Sekar, C., "WO3 nanoparticles based direct electrochemical dopamine sensor in the presence of ascorbic acid," Electrochim. Acta **167**, 294–302 (2015).

[16] Fan, Y., Lu, H.-T., Liu, J.-H., Yang, C.-P., Jing, Q.-S., Zhang, Y.-X., Yang, X.-K. and Huang, K.-J., "Hydrothermal preparation and electrochemical sensing properties of TiO2–graphene nanocomposite," Colloids Surfaces B Biointerfaces **83**(1), 78–82 (2011).

[17] Kim, Y.-R., Bong, S., Kang, Y.-J., Yang, Y., Mahajan, R. K., Kim, J. S. and Kim, H., "Electrochemical detection of dopamine in the presence of ascorbic acid using graphene modified electrodes," Biosens. Bioelectron. **25**(10), 2366–2369 (2010).

[18] Argüello, J., Leidens, V. L., Magosso, H. A., Ramos, R. R. and Gushikem, Y., "Simultaneous voltammetric determination of ascorbic acid, dopamine and uric acid by methylene blue adsorbed on a phosphorylated zirconia–silica composite electrode," Electrochim. Acta **54**(2), 560–565 (2008).

[19] Zhang, F., Li, Y., Gu, Y., Wang, Z. and Wang, C., "One-pot solvothermal synthesis of a Cu2O/Graphene nanocomposite and its application in an electrochemical sensor for dopamine," Microchim. Acta **173**(1–2), 103–109 (2011).

[20] Reddy, S., Kumara Swamy, B. E. and Jayadevappa, H., "CuO nanoparticle sensor for the electrochemical determination of dopamine," Electrochim. Acta **61**, 78–86 (2012).

[21] Sun, C.-L., Lee, H.-H., Yang, J.-M. and Wu, C.-C., "The simultaneous electrochemical detection of ascorbic acid, dopamine, and uric acid using graphene/size-selected Pt nanocomposites," Biosens. Bioelectron. **26**(8), 3450–3455 (2011).
[22] Gao, F., Cai, X., Wang, X., Gao, C., Liu, S., Gao, F. and Wang, Q., "Highly sensitive and selective detection of dopamine in the presence of ascorbic acid at graphene oxide modified electrode," Sensors Actuators B Chem. **186**, 380–387 (2013).
[23] Pepłowski, A., Janczak, D. and Jakubowska, M., "Stabilization of glucose-oxidase in the graphene paste for screen-printed glucose biosensor," 11 September 2015, 96624H, International Society for Optics and Photonics.

Photoluminescence Properties of ZnSe:Al, ZnSe:Cu Nanoparticles Obtained by Chemical Synthesis

Irina V. Tepliakova[a], Yury A. Nitsuk[a], Ievgen V. Brytavskyi[a], Andrzej Kociubiński*[b], Meruyert Sakypbekova[c]
[a]I.I.Mechnikov Odessa National University, Dvoryanskaya Str., 2, 65082 Odessa, Ukraine; [b]Lublin University of Technology, Nadbystrzycka 38D, 20-618 Lublin, Poland; [c]Al-Farabi Kazakh National University, Al-Farabi 71 Avenue, Almaty, Republic of Kazakhstan

ABSTRACT

This work represents an effective method for synthesis and doping of ZnSe nanocrystals with elements of group 3 and transition elements. The structure of crystals and their average size are determined. The spectra of optical density and photoluminescence were studied, and a comparative analysis of characteristics of the obtained nanoparticles with their bulk analogs was carried out.

Keywords: ZnSe nanoparticles, photoluminescence, optical properties, biomedical labeling, luminescent labels, colloidal synthesis

1. INTRODUCTION

Semiconductor nanocrystals of A2B6 group are promising materials for semiconductor electronics, biomedical imaging and disinfection. Existing synthesis methods make it possible to obtain nanocrystals with a narrow size distribution, specified surface morphology and high stability. The ability to control the band gap and the luminescence wavelength makes these nanocrystals useful for optoelectronics. Luminescent semiconductor nanoparticles with wide absorption spectrum and pronounced luminescence peaks in the visible and near-IR regions are very promising for medical diagnostics [1].

Among the semiconductor crystals of the A2B6 group, the most studied are CdS and CdSe. Cheap and simple method of obtaining, as well as high quantum yield of radiation in the visible region of the spectrum can be mentioned as the main advantages of these materials [1,2,3]. A serious disadvantage of these materials is their cytotoxicity. Therefore, it is advisable to use nanocrystals of selenide and zinc sulfide for biomedical applications. In order to be used as markers for fluorescence tomography, nanocrystals must have effective radiation in red and near-IR regions [4,5,6]. It is known that aluminum and copper impurities are effective activators of radiation in these regions in bulk ZnSe crystals. Therefore, the study of the optical and luminescent properties of ZnSe:Al and ZnSe:Cu nanocrystals is relevant [7,8].

2. FORMULATION OF THE PROBLEM

The purpose of this work is to find a way to control the spectral position of the longwave radiation bands of ZnSe nanocrystals by doping them with aluminum and copper impurities, to establish the nature of optical and luminescent transitions in ZnSe, ZnSe:Al and ZnSe:Cu nanocrystals.

3. MAIN RESEARCH MATERIAL

In this work, zinc selenide nanocrystals were studied, which were obtained by a chemical method using commercial reagents from the Merck Company. The source of zinc ions was zinc chloride, and the source of selenium ions was sodium selenosulfate. For doping with aluminum or copper, a 1% solution of aluminum chloride or copper chloride was added to a 10% solution of zinc chloride. The synthesis of nanoparticles was carried out in 1 ml of a 5% gelatin solution and had the following form [8,9,10]:

$$ZnCl_2+Na_2SeSO_3 \rightarrow ZnSe\downarrow+Na_2SO_3+Cl_2\uparrow \quad (1)$$

*akociub@semiconductor.pl

Photonics Applications in Astronomy, Communications, Industry, and High-Energy Physics Experiments 2019, edited by Ryszard S. Romaniuk, Maciej Linczuk, Proc. of SPIE Vol. 11176, 111764M
© 2019 SPIE · CCC code: 0277-786X/19/$21 · doi: 10.1117/12.2536248

$$ZnCl_2+Al_2Cl_3+Na_2SeSO_3 \rightarrow ZnSe{:}Al\downarrow+Na_2SO_3+Cl_2\uparrow \quad (2)$$

$$ZnCl_2+CuCl_2+Na_2SeSO_3 \rightarrow ZnSe{:}Cu\downarrow+Na_2SO_3+Cl_2\uparrow \quad (3)$$

After removing residual reaction products, a colloidal solution of nanoparticles was deposited on a quartz substrate and placed in an oven until the polymer film dried. For X-ray diffraction and SEM studies, the solution was deposited on silicon substrates. On X-ray diffractograms, the dominant peaks were identified, which correspond to the (111), (220), (311) planes in ZnSe (Fig. 1, according to JCPDS 96-900-8858). Similar planes were found in ZnSe: Al and ZnSe: Cu nanocrystals.

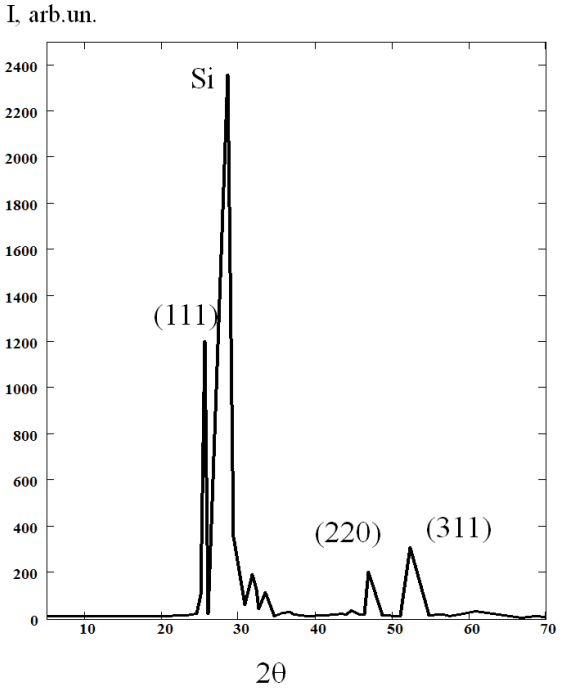

Figure 1. XRD image of ZnSe nanocrystals

Tabela 1. Optical characteristics of ZnSe, ZnSe:Al, ZnSe:Cu nanocrystals in region of optical absorption edge

Sample	The type of nanocrystalls	E_g, eV	ΔE_g, eV	R, nm
1	ZnSe, 0.05% $ZnCl_2$, 0.05% Na_2SeSO_3	3.63	0.95	4.3
2	ZnSe, 0.03% $ZnCl_2$, 0.03% Na_2SeSO_3	3.78	1.1	4
3	ZnSe:Al, 0.03% $ZnCl_2$+0.001% Al_2Cl_3, 0.03% Na_2SeSO_3	3.76	1.08	4.1
4	ZnSe:Al, 0.03% $ZnCl_2$+0.002% Al_2Cl_3, 0.03% Na_2SeSO_3	3.71	1.03	4.2
5	ZnSe:Cu, 0.05% $ZnCl_2$+0.001% $CuCl_2$, 0.05% Na_2SeSO_3	3.54	0.86	4.6
6	ZnSe:Cu, 0.05% $ZnCl_2$+0.002% $CuCl_2$, 0.05% Na_2SeSO_3	3.44	0.76	4.8
7	ZnSe:Cu, 0.05% $ZnCl_2$+0.003% $CuCl_2Cl_3$, 0.05% Na_2SeSO_3	3.38	0.7	5

For comparison, bulk ZnSe, ZnSe: Al and ZnSe: Cu crystals obtained by diffusion doping of Al and Cu impurities at various temperatures of growth were studied. The temperature varied from 750 to 900°C.

The optical density and photoluminescence spectra were investigated to establish the nature of optical and luminescent transitions in studied nanocrystals as well as to determine the average size of nanoparticles and the concentration of an optically active impurity. For this purpose, the sets of samples with different ratio of initial and impurity components were selected (Table 1).

The optical density spectra were measured using a MDR-6 monochromator with diffraction gratings of 2400 lines/mm for the ultraviolet, 1200 lines/mm for the visible and near-IR spectral regions and 600 lines/mm for the IR region. A photomultiplier tube FEU-100 was used as a radiation detector.The photoluminescence spectra were measured on an ISP-51 prism spectrograph. The registration of radiation was carried out with a FEU-100 photomultiplier tube and IR photoresistor. The luminescence was excited by Edison Opto Corporation LEDs with radiation peaks at 375, 400, 460, 550 and 640 nm and a pulsed nitrogen ILGI-503 laser with a wavelength of 331.7 nm.

4. OPTICAL DENSITY STUDY

The optical density spectra of undoped ZnSe nanocrystals are shown in Fig. 2. It has been established that a decrease in the concentration of the initial zinc chloride and sodium selenosulfate from 0.1 g / ml to 0.01 g / ml leads to a shift of the band gap towards high energies from 3.3 to 3.78 eV, which is confirmed by the colloidal solution color change from pale yellow to colorless [11,12,13].

The average radius of the nanoparticles was estimated in the effective mass approximation by the change in the band gap (ΔE_g) compared to bulk crystals, using the formula [9,33]:

$$R = \frac{h}{\sqrt{8\mu\Delta E_g}} \tag{4}$$

Here h is Planck's constant; $\mu = ((m_{e*})^{-1} + (m_{h*})^{-1})^{-1}$, where $m_{e*} = 0.19m_e$, $m_h* = 0.8m_e$ are, respectively, the effective masses of an electron and a hole in zinc selenide; m_e is the mass of a free electron; ΔE_g is the difference between the band gap in the nanoparticle and the bulk ZnSe crystal (2.68 eV). The results of calculations are presented in Table 1.

SEM images of sample 2 are presented in Fig. 2. The formation of nanoparticles with a size of 10-12 nm observed. The difference between calculated and observed size of crystalines could be explained by agglomeration of smaller grains into larger clusters that are 2-3 times bigger than single nanocrystal. Doping with aluminum or copper shifts the optical absorption edge to lower energies (Fig. 3, Fig. 4). In this case, the magnitude of the shift increases with growth of dopant concentration. A similar low-energy shift is observed in bulk ZnSe: Al and ZnSe: Cu crystals (Fig. 5, Fig. 6).

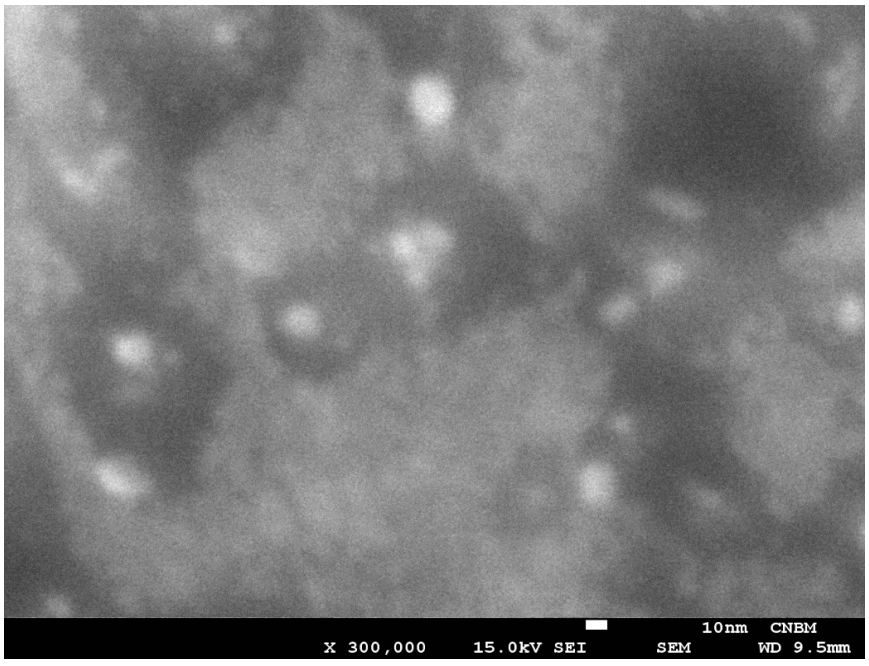

Figure 2. SEM –image of ZnSe nanocrystals (Sample 2)

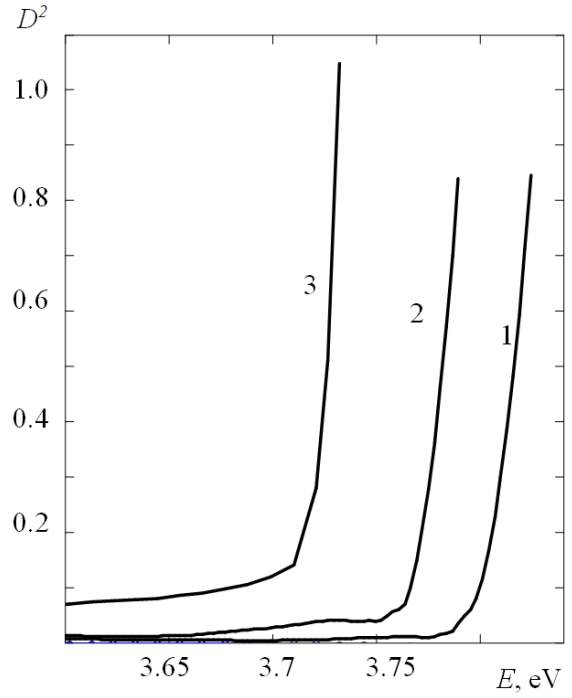

Figure 3. Optical absorption spectra of (1) ZnSe nanocrystals and (2, 3) ZnSe:Al nanocrystals. The Al2Cl3 dopant concentrations are 2% (2) and 5% (3).

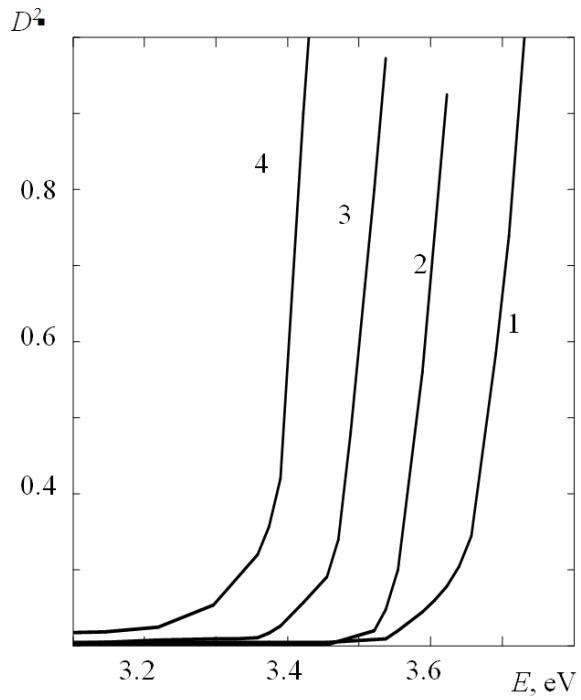

Figure 4. Optical absorption spectra of (1) ZnSe nanocrystals and (2, 3, 4) ZnSe:Cu nanocrystals. The CuCl2 dopant concentrations are 2% (2), 3% (3) and 5% (4).

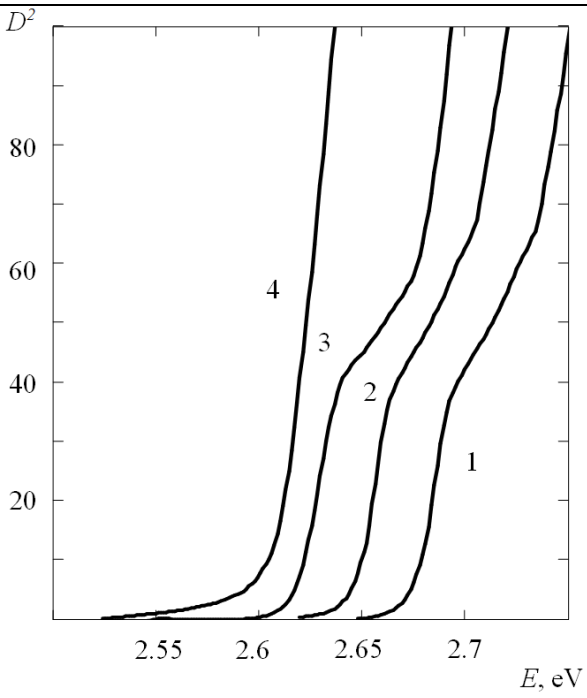

Figure 5. Optical absorption spectra of (1) ZnSe single crystals and (2, 3, 4) ZnSe:Al single crystals. The annealing temperatures are 800 (2), 850 (3) and 900°C (4).

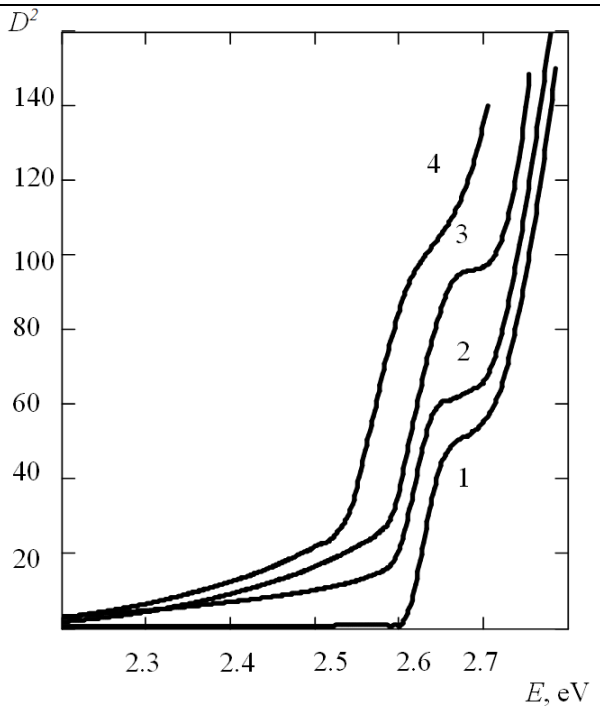

Figure 6. Optical absorption spectra of (1) ZnSe single crystals and (2, 3, 4) ZnSe:Cu single crystals. The annealing temperatures are 800 (2), 850 (3) and 900°C (4).

This shift cannot be explained only by the particle size increase. In bulk crystals, such a shift is explained by inter-impurity Coulomb interaction, which is a characteristic of group III elements [10, 11] and transition element impurities [12–16]. Using the relation [10]

$$\Delta E_g = 2 \cdot 10^5 \left(\frac{3}{\pi} \right)^{1/3} \frac{eN^{1/3}}{4\pi\varepsilon_0\varepsilon_s}, \quad (5)$$

where: e – electron charge, N – concentration of an aluminum or copper impurity in cm^{-3}, $\varepsilon_s = 8.33$ is the static dielectric constant of zinc selenide. The concentration of aluminum and copper in the studied ZnSe: Al nanocrystals (samples 3-4) was calculated from the value of the shift of the band gap between undoped ZnSe nanoparticles (sample 1 or 2). The maximum concentration of optically active aluminum impurity was $2 \cdot 10^{19}$ cm^{-3} in nanocrystals containing 0.002% Al_2Cl_3. When the concentration of Al_2Cl_3 decreases to 0.001% the concentration of the optically active aluminum impurity decreases to $8 \cdot 10^{17}$ cm^{-3} respectively. . High concentrations of optically active copper impurities indicate the effective incorporation of copper atoms into the zinc sublattice in case of this doping method. The concentration of optically active copper impurity varies from $2 \cdot 10^{19}$ to $4 \cdot 10^{20}$ cm^{-3} with an increase in the concentration of $CuCl_2$ from 0.001 to 0.003% in samples 5-7 [14,15,16].

5. INVESTIGATION OF LONG-WAVELENGTH PHOTOLUMINESCENCE

Investigation of ZnSe nanocrystals photoluminescence spectra has shown the presence of broad photoluminescence bands localized in the 550-850 nm region. The change in the temperature of nanocrystals from 300 to 430 K did not cause a shift in the studied spectra. The position of the spectra remained unchanged even with a change in the band gap width of nanocrystals. The presence of a number of bends and a large (~ 150 nm) half-width of the bands indicate their non-elementary nature. The spectra modeling by elementary Gaussian components program revealed a series of elementary emission lines localized at 580, 600, 630, 680, 700, 750 and 800 nm (Fig. 7a). The identical elementary emission lines were observed earlier in bulk ZnSe single crystals (Fig. 7b) [18,31,32].

Emission at a wavelength of 580 nm appears due to associative native defects $(V_{Zn}V_{Se})^-$. The emission line at a wavelength of 600 nm appears due to associative defects $(V_{Zn}D_{Se})^-$ where the donor is either V_{Se} or an uncontrolled donor impurity, an VII group element, for example, Cl, Br, I. The other emission lines were associated with defects $(V_{Zn}D_{Zn})^-$ with different distances between donors and acceptors. Here the donor, according to [18], is the uncontrolled Al, In, Ga impurities [17,18,19].

Doping with aluminium during the growth of nanocrystals leads to an increase of the emission intensity in the 500-1000 nm region. Further increase of the emission intensity with increasing Al_2Cl_3 concentration is explained by an increase of the donor impurity concentration in investigated nanocrystals [20,21,22].

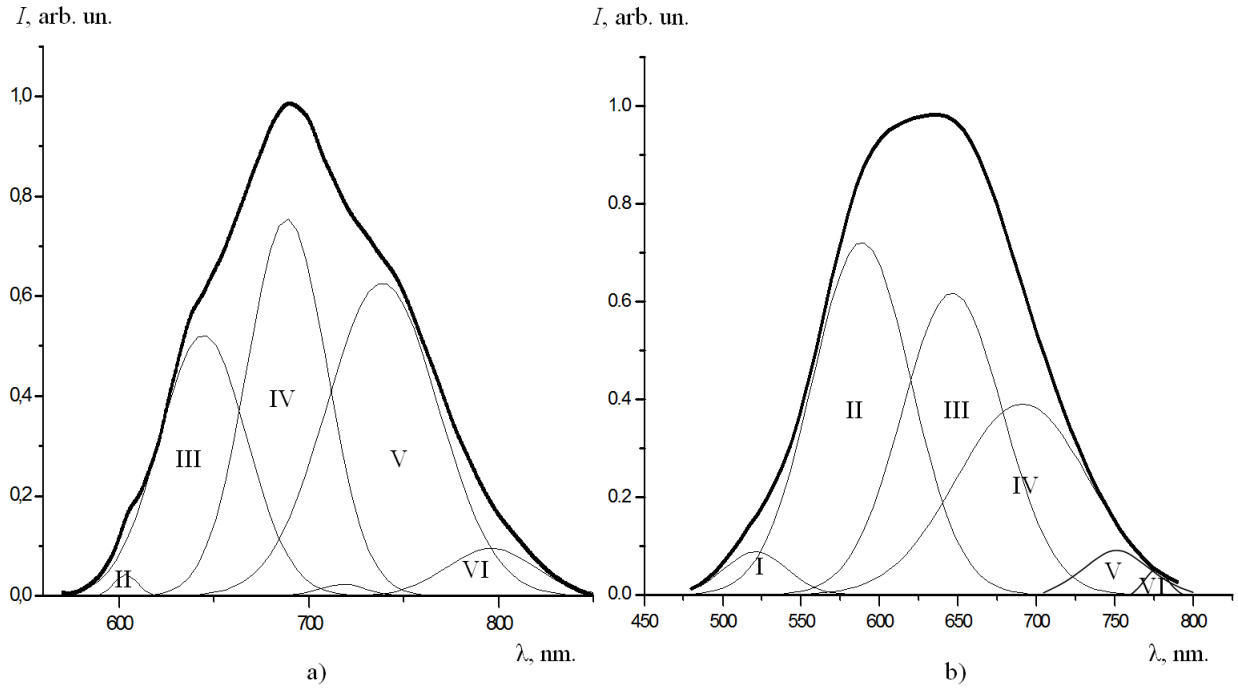

Figure 7. Photoluminescence spectra of (a) ZnSe nanocrystals and (b) single crystals [11]

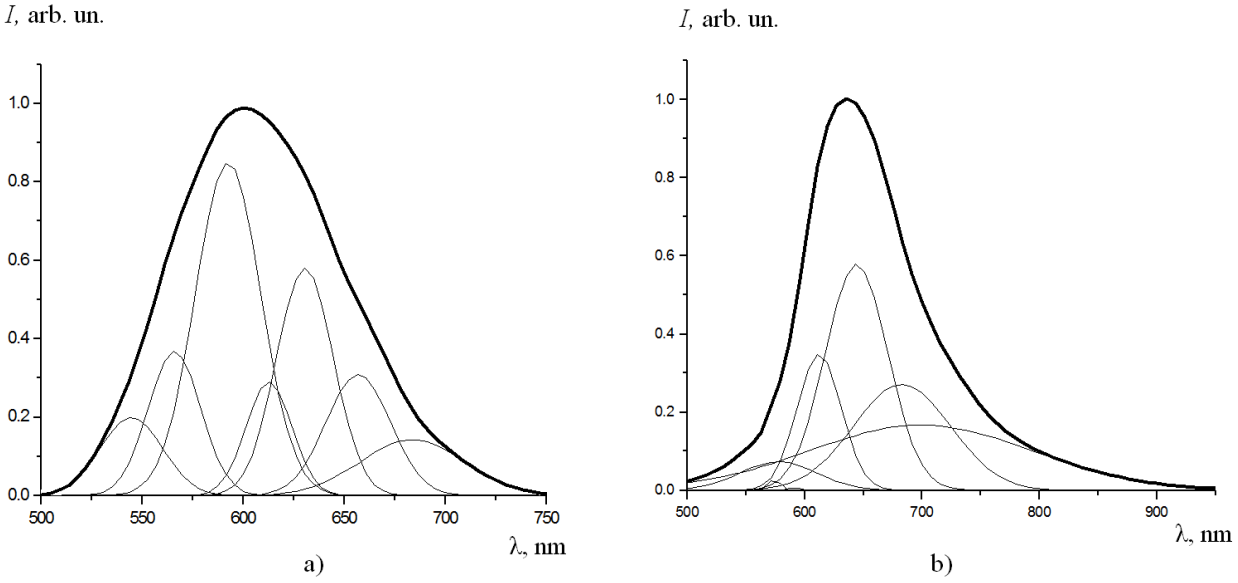

Figure 8. Photoluminescence spectra of (a) ZnSe:Al single crystals and (b) nanocrystals

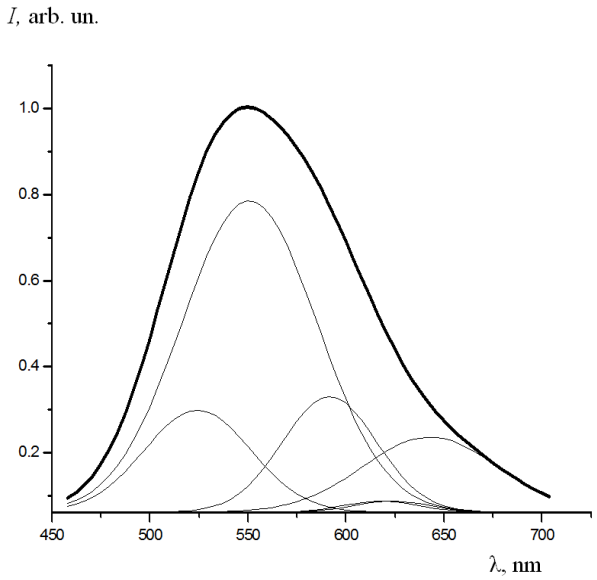

Figure 9. Photoluminescence spectra of ZnSe:Cu nanocrystals (Sample 5)

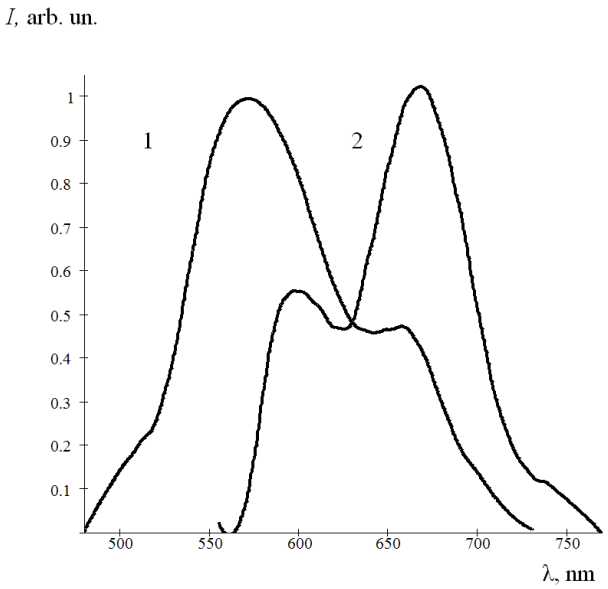

Figure 10. Photoluminescence spectra of ZnSe:Cu single crystals. Tmeas=77 (1) and 300 K (2)

In the emission spectra of ZnSe:Al nanocrystals, elementary emission lines are emitted at 580, 600, 630, 680, and 700 nm (Fig. 8 b). The same emission lines were detected in bulk crystals of ZnSe:Al (Fig. 8 a) [28,29,30].

It was found that a change of Al_2Cl_3 concentration and the choice of the stabilizing matrix type do not lead to a shift of the elementary and integral emission lines to the short-wave or long-wave region. The change in technological conditions leads to a change in the intensity of the elementary emission lines, which is explained by the redistribution of the concentration of native and impurity defects that create the associative centers. The shift of the emission integrated maximum to the smaller wavelengths region with increasing Al_2Cl_3 concentration from 0.001 to 0.002% can be explained by increasing in the intensity of the elementary emission line at 600 nm due to associative defects $(V_{Zn}Cl_{Se})$ [23.24]$^{-}$.

Doping of ZnSe nanocrystals with copper during the growth process leads to a shift of the emission spectra to the shortwave region. The photoluminescence spectra of ZnSe:Cu nanocrystals with a $CuCl_2$ concentration of 0.001–0.003% are broad non-elementary emission bands localized in the region of 500–750 nm (Fig. 9). The decomposition of the spectrum into elementary Gaussian components allowed us to identify a series of lines with maxima at 520, 540, 590, 660 nm. Elementary radiation lines with such maxima are not observed in undoped ZnSe nanocrystals. In bulk ZnSe: Cu crystals at T = 300 K, the emission bands at 590 and 660 nm are also detected. In bulk crystals he emission band at 550 nm at T = 77 K is observed. According to [18], the emission lines in bulk crystals and polycrystalline ZnSe films are not connected with isolated Cu_{Zn}, but are caused by the complexes. The emission line at 520 nm is due to transitions $(Cu_{Zn}^{-}, V_{Se}^{+})^{-}$. The radiation line at 540–550 nm is associated with transitions within the associative center $(Cu_{Zn}^{-}, Cl_{Se}^{+})^{-}$ [19]. The emission line at 660 nm is due to radiative transitions involving doubly charged copper ions within the donor-acceptor pair $(Cu_{Zn}^{2-}, Cl_{Se}^{+})^{-}$ [19,20]. The emission line at 590 nm is most likely due to transitions involving a doubly charged copper ion and a single-charged selenium vacancy within the center $(Cu_{Zn}^{2-}, V_{Se}^{+})^{-}$ [18]. A further increase in the concentration of copper chloride to 0.005% and more leads to strong absorption in the near-IR region and concentration quenching of the observed radiation lines, and the colloidal solutions of the nanoparticles become dark gray in color [25,26, 27].

6. CONCLUSION

ZnSe, ZnSe: Al, ZnSe: Cu nanoparticles with a diameter of up to 4 nm were successfully synthesized using "green" synthesis method and organic stabilizing agents. The nature of radiation transitions in ZnSe and ZnSe: Al, ZnSe: Cu nanocrystals have been established. It was experimentally confirmed that the emission lines caused by the luminescence on donor – acceptor pairs in nanocrystals are identical to the emission lines in bulk crystals. This proves that ZnSe: Al

and ZnSe: Cu nanocrystals can be effectively used as a material for biomedical visualization, optoelectronics, etc. due to both optical and luminescent properties, and simplicity and low cost of fabrication technology.

ACKNOWLEDGMENTS

The authors are grateful to Professor I.R. Yatsunsky from Adam Mickiewicz Poznań University for SEM images and discussion of the results.

REFERENCES

[1] Gaubas, E., Brytavskyi, I., Ceponis, T., Jasiunas, A., Kalesinskas, V., Kovalevskij, V., Meskauskaite, D., Pavlov, J., Remeikis, V., Tamulaitis, G., Tekorius, A., „In situ variations of carrier decay and proton induced luminescence characteristics in polycrystalline CdS," Journal of Applied Physics 115, 243507 (2014).

[2] Gaubas, E., Borschak, V., Brytavskyi, I., Čeponis, T., Dobrovolskas, D., Juršėnas, S., Kusakovskij, J., Smyntyna, V., Tamulaitis, G., Tekorius, A., "Nonradiative and Radiative Recombination in CdS Polycrystalline Structures," Advances in Condensed Matter Physics 2013, 917543 (2013).

[3] Gaubas, E., Brytavskyi, I., Ceponis, T., Kalendra, V., Tekorius, A., „Spectroscopy of Deep Traps in Cu_2S-CdS Junction Structures," Materials 5(12), 2597–2608 (2012).

[4] Peng, X., Schlamp, M. C., Kadavanich, A. V., Alivisatos, A. P., "Epitaxial growth of highly luminescent CdSe/CdS core/shell nanocrystals with photostability and electronic accessibility," Journal of the American Chemical Society 119(30), 7019–7029 (1997).

[5] Dabbousi, B. O., Rodriguez-Viejo, J., Mikulec, F. V., et al., "(CdSe)ZnS core-shell quantum dots: synthesis and characterization of a size series of highly luminescent nanocrystallites," Journal of Physical Chemistry B 101(46), 9463–9475 (1997).

[6] Han, D., Song, C., Li, X., "Synthesis and Fluorescence Property of Mn-Doped ZnSe Nanowires," J. Nanomaterials 22, 1-4 (2010).

[7] Smyntyna, V. A., Skobeeva, V. M., "Photoactivation of luminescence in CdS nanocrystals," Beilstein Journal of Nanotechnology 5, 355-359 (2014).

[8] Suyver, J. F., van der Beek, T., Wuister, S. F., Kelly, J. J., Meijerink, A., "Luminescence of nanocrystalline ZnSe:Cu," Applied Physics Letters 79, 401 (2001).

[9] Bouley, J.C., "Blanconnier, P., Hermann, A., "Luminescence in highly conductive n-type ZnSe," J. Appl. Phys. 46(8), 3549- 3555 (1975).

[10] Vaksman, Yu. F., Nitsuk, Yu. A., Purtov, Yu. N., Shapkin, P. V., "Native and Impurity Defects in ZnSe:In Single Crystals Prepared by Free Growth," Semiconductors 35(8), 920-926 (2001).

[11] Nitsuk, Yu. A., "Diffusion of chromium and impurity absorption in ZnS crystals," Functional Materials 20(1), 10-14 (2013).

[12] Nitsuk, Yu. A., Vaksman, Yu. F., "Optical absorption and diffusion of iron in ZnS single crystals," Functional Materials 19(2), 75-79 (2012).

[13] Nitsuk, Yu. A., „Energy states of a Cr^{2+} ion in ZnSe crystals," Semiconductors 47(6), 736-739 (2013).

[14] Nitsuk, Yu. A., "Optical absorption of vanadium in ZnSe single crystals," Semiconductors 48(2), 142-147 (2014).

[15] Nitsuk, Yu. A., "Study of the impurity photoconductivity and luminescence in ZnSe:Ni crystals in the visible spectral region," Semiconductors 46(10), 1265-1269 (2012).

[16] Serdyuk, V. V., Korneva, N. N., Vaksman, Yu. F., "Studies of Long-Wave Luminescence of Zinc Selenide Monocrystals," Phys. Stat. Sol.(a) 91, 173-183 (1985).

[17] Morozova, N. K., Karetnikov, I. A., Blinov, V. V., Gavrishchuk, E. M., "A study of luminescence centers related to copper and oxygen in ZnSe," Semiconductors 35(1), 24-32 (2001).

[18] Kukk, P., Palmre, O., Mellikov, E., "The structure of recombination centres in activated ZnSe phosphors," Phys. Stat. Sol A 70(1), 35-42 (1982).

[19] Bryant, F. G., Manning, P. S., "Radiation damage and decay characteristics of zinc selenide emission bands," J. Phys. Chem. Solids. 35(1), 97-101 (1974).

[20] Azarov, O. D., Dudnyk, V., Kaduk, O. V., Smolarz, A., Burlibay, A., "Method of correcting of the tracking ADC with weight redundancy conversion characteristic," Proceedeings of SPIE 9816, Optical Fibers and Their Applications 2015, 98161V (2015).

[21] Azarov, O. D., Murashchenko, O. G., Chernyak, O. I., Smolarz, A., Kashaganova, G., "Method of glitch reduction in DAC with weight redundancy," Proceedeings of SPIE 9816, Optical Fibers and Their Applications 2015, 98161T (2015).
[22] Azarov, O. D., Dudnyk, V., Duk, M., Porubov, D., "Static and dynamic characteristics of the self-calibrating multibit ADC analog components," Proceedeings of SPIE 8698, Optical Fibers and Their Applications 2012, 86980N (2013).
[23] Azarov, O. D., Chernyak, A. I., Chernyak, P. A., "Class of numerical systems for pipeline bit sequential development of multiple optoelectronic data streams," Proceedeings of SPIE 4425, Selected Papers from the International Conference on Optoelectronic Information Technologies, (2001).
[24] Osadchuk, A., Osadchuk, I., Smolarz, A., Kussambayeva, N., "Pressure transducer of the on the basis of reactive properties of transistor structure with negative resistance," Proceedeings of SPIE 9816, Optical Fibers and Their Applications 2015, 98161C (2015).
[25] Osadchuk, O., Osadchuk, V., Osadchuk, I., „The Generator of Superhigh Frequencies on the Basis Silicon Germanium Heterojunction Bipolar Transistors," 13th International Conference on Modern Problems of Radio Engineering, Telecommunications and Computer Science (TCSET), 336-338 (2016).
[26] Semenov, A. O., Osadchuk, A.V., Osadchuk, I. A., Koval, K. O., Prytula, M. O., "The chaos oscillator with inertial non-linearity based on a transistor structure with negative resistance," Proceedings of the International Conference Micro/Nanotechnologies and Electron Devices (EDM), 17th International Conference of Young Specialists, (2016).
[27] Rovira, R. H., Pavlov, S. V., Kaminski, O. S., Bayas, M. M., "Methods of Processing Video Polarimetry Information Based on Least-Squares and Fourier Analysis," Middle-East Journal of Scientific Research 16 (9), 1201-1204 (2013).
[28] Zabolotna, N. I., Pavlov, S. V., Ushenko, A. G., Karachevtsev, A. O., Savich, V. O., et al. "System of the phase tomography of optically anisotropic polycrystalline films of biological fluids," Proceedeings of SPIE 9166, Biosensing and Nanomedicine VII, 916616 (2014).
[29] Zabolotna, N. I., Pavlov, S. V., Ushenko, A. G., Sobko, O. V., Savich, V. O., „Multivariate system of polarization tomography of biological crystals birefringence networks," Proceedeings of SPIE 9166, Biosensing and Nanomedicine VII, 916615 (2014).
[30] Wójcik, W., Smolarz, A., [Information Technology in Medical Diagnostics], London, July 11, Taylor &Francis Group CRC Press Reference (2017).
[31] Vassilenko, V., Valtchev, S., Teixeira, J. P., Pavlov, S., "Energy harvesting: an interesting topic for education programs in engineering specialities," Internet, Education, Science (IES-2016), 149-156 (2016).
[32] Krak, Y. V., Barmak, A. V., Bagriy, R. A., Stelya, I. O., "Text entry system for alternative speech communications," Journal of Automation and Information Sciences 49(1), 65–75 (2017).
[33] Kryvonos, Iu. G., Krak, Y. V., Barmak, O .V., Bagriy, R. O., "Predictive text typing system for the Ukrainian language," Cybernetics and systems analysis 53(4), 495-502 (2017).

Nanostructure with periodic position dependent electron effective mass

Volodymyr M. Burdeynyy[a], Andrzej Kociubiński*[b], Mukaddas Arshidinova[c]
[a]Vinnytsia National Technical University, Khmel'nyts'ke Hwy, 95, 21000 Vinnytsia, Ukraina;
[b]Lublin University of Technology, Nadbystrzycka 38D, 20-618 Lublin, Poland; [c]Al-Farabi Kazakh National University, Al-Farabi 71 Avenue, Almaty, Republic of Kazakhstan

ABSTRACT

This communication has been dedicated to spectral properties of system composing of periodic arrays of layers which form superlattice with electron effective mass dependent on coordinate inside of each layer. We considered one dimensional model which admits to obtain the exact solution of wave equation. The position dependent mass inside the layer was represented by the linear function. We has found wave functions in their explicit and exact forms as well as the secular equation for the energy eiguen values. The energy spectrum of electrons as expected manifests properties typical for periodic nanostructures.

Keywords: superlattice; electron spectrum, position-dependent mass, Schrödinger equation

1. INTRODUCTION

For a long time yet semiconductors superlattices turned out [1] one of the most important functional elements of a lot of nanoelectronics devices such as pillar lasers structures or light emitting diodes et cet. In the last decades considerable progress based on molecular beam epitaxy methods or STM and AFM technologies allows to create numerous nanosystems, superlattices among them, with demanded spectral properties. As a rule, electron energetic spectrum consists of relatively narrow minibands which are formed due to the periodic modulation of the basic properties of supperlattice components such as the conduct band bottom and the valence band top in semiconductor heterojunctions or, for example, periodic doping semiconductor layers. Significant advances in nanoscience have opened the way for synthesis materials, for example, one-dimensional semiconductotr nanostructures [2], with exceptional properties which can allow to construct and produce electronic and optoelectronic devices based on completely new conceptions. Due to technology progress, we can't exclude possibility to create periodic structure like above mentioned examples by space modulation of electron effective mass. That is why a study of spectral properties of system with periodic position-dependent mass can be really interesting enough.

The quantum mechanics of a particle with an effective coordinate-dependent mass for a long time has been and continues to be the subject of a considerable number of studies. This fact is motivated by various circumstances. One of them involves the fun damental quantum dynamics principles related to the conception of mass. The quantum mechanics was created and built up for a particle whose mass as function of generalized coordinates is some constant. When the particle mass becomes position dependent the problem of operator ordering appears [3,4]. The fact is that the operator of linear moment can be positioned in different places in operator of the kinetic energy conducting to some ambiguity in explicit form of Hamiltonian. Considerable relevance of the problem can be confirmed by the fact that even founders of basics quantum conseptions have dedicated their attention and contributed a lot to its resolution. However the ordering ambiguity problem has no complete and final treatment yet. That is why researches of position dependent mass particle have serious reasons for quantum theory. On the other hand, the intensive development of nanotechnology, in the first place of energy bands engineering, fabrication of compositionally graded crystals, heterostructures transfer the above mentioned problem from a purely scientific plane to the practical one in order to create materials with predetermined and predictable properties, which are often determined by the effective mass. Among them we have to point out the density of states, coefficient of optical absorption, transport mobility and other mass sensitive parameters. Than in connection with the foregoing it will be interesting to study some special models of positon-dependent mass systems which admit the exact solution. One of the models is represented in this communication.

*akociub@semiconductor.pl

Photonics Applications in Astronomy, Communications, Industry, and High-Energy Physics Experiments 2019, edited by Ryszard S. Romaniuk, Maciej Linczuk, Proc. of SPIE Vol. 11176, 111764N
© 2019 SPIE · CCC code: 0277-786X/19/$21 · doi: 10.1117/12.2536249

2. DESCRIPTION OF MODEL. MODIFICATED WAVE EQUATION

We considered the layered periodic structure with the axis aliened along axis X. Inside of the layer the electron spectrum is parabolic with the isotropic effective mass in plane of layer and the mass dependent on coordinate X in the direction of superstructure axis. Position dependence of electron effective mass in its natural form appears in nonuniform solid state systems, when due to the coordinate dependent chemical composition some modification requires not only crystal field potential but also the kinetic energy operator. In order to study the effect of mass modification only we proceed from the assumption that the mass of charge carriers in their one-dimensional motion admits to be given by the expression:

$$m(x) = m_0 f(x) \tag{1}$$

where $f(x)$ is a function whose choice will be specified in the below following text.

Note that the explicit form of the kinetic energy operator, due to the above mentioned ambiguity, continues to be discussed intensively in the literature, for example, one can refer to works [3,4]. As it is quite well-known nearly the extreme points of non degenerated energetic bands accordingly to the Wannier theorem [5] the envelope factor of the wave function obeys a Schrödinger-like equation. However, the formal substitution of expression (1) instead the effective electron mass in this equation can not be accepted because this change conducts to the non-hermitian form of the Hamilton's operator. Then the above sub lined ambiguity of the operators ordering appears.

The nature of this ambiguity is quite obvious and lies in the fact the kinetic energy operator no longer commutes with the momentum linear operator $\hat{p}_x = -i\hbar\partial_x$ if the particle's mass $m(x)$ becomes position dependent. Consequently, the problem of momentum linear operator and particle mass ordering appears and demands its resolution. A natural correction of the kinetic energy operator can be reduced to representation [6,7,8] of the kinetic term by the symmetrized form, namely:

$$\hat{H}_c = \frac{1}{4}\left[\frac{1}{m(x)}\hat{p}_x^2 + \hat{p}_x^2\frac{1}{m(x)}\right] \tag{2}$$

but even this choice does not fix the ordering problem.

That is why the number of alternative forms have been proposed. One of the most commonly used approach to organize the momentum and mass operators has been suggested by von Roos [9,10] and can be given as follows:

$$\hat{H}_c = \frac{1}{4}\left[m^{\eta}(x)\hat{p}_x m^{\varepsilon}(x)\hat{p}_x m^{\rho}(x) + m^{\rho}(x)\hat{p}_x m^{\varepsilon}(x)\hat{p}_x m^{\eta}(x)\right] \tag{3}$$

where the parameters ε, ρ, η must satisfy the condition $\varepsilon + \rho + \eta = -1$. Beginning from this expression a lot of concrete models have been proposed and explored. Unfortunately, the early written symmetrical and very simple Hamiltonian does not fit into the scheme recommended by von Ross. This term was added to the von Ross's formula in order to include in consideration the symmetrized or Weyl ordered operator.

In this paper, we prefer to use frequently applied by a lot of authors, see for example works [11,12,14], values, namely $\varepsilon = -1$, $\rho = 0$ and $\eta = 0$, correspond to the Ben Daniel-Duke model [15]. Accordingly to the review [16] this choice allows to conserve the fundamental properties of Hamiltonian and considerable simplifies resolution of wave equation due to the more simple form of effective potential.

Because of the fact that in plane electron movement is free, in the wave equation the commonly used method of separation of variables can be applied. After this approach has been realized and assuming Ben Daniel-Duke's proposal we will have for the Schrödinger equation the following expression:

$$-\frac{\mathrm{h}^2}{2m_0}\partial_x\frac{1}{f(x)}\partial_x\Psi = E\Psi \tag{4}$$

where $\Psi \equiv \Psi(x)$ describes the motion along the superstructure axis and $E = \mathrm{E} - E(\vec{k})$ – energy counted from the energetic band corresponding to the free in plane motion.

Since we try to find an explicit and exact solution of equation (4) further consideration demands to specify the function $f(x)$ which describes coordinate dependence of particle's mass. There are a lot references [16] where some general forms of functions which provide the exact solutions of wave equation (4) have been established. In addition to these general forms in the extensive bibliography one can found some concrete examples where these exact solutions have been explicitly established and corresponding energy eigenvalues have been determined. Here we refer to the studies represented in the paper [5,14,17], where exact solutions of Schrödinger equation with mass given in terms of hyperbolic functions have been found and widely discussed. By the authors of works [12,13,14] the cases relative to description of mass in terms of polynomial functions were thoroughly investigated. Three coordinate distributions of masses combined with modified Morse's and Kratzer's potentials received complete treatment in the paper [17] where the authors applying the point canonical transformation method have found the wave equation exact solutions. A number of authors, see for references[17], develop the super symmetry theory in its operator methods. By using this approach they resolved the eigen functions and eigen values problems for a wide set of special mass distributions.

If exclude the ordering problem, to our knowledge, a majority of studies has been dedicated to resolution of wave equation with position-dependent mass given in terms of some smooth functions. However, for layered systems, such as superlattices, mass distribution is periodic and it can also manifest some sharp change into interfaces. That is why in this paper we try at least slightly to expand the list of exact solutions of position dependent mass problem considering the model which in our opinion could be relevant to nanostructures and other applications. Thus we treat the one-dimensional quantum dynamics of the particle with position dependent effective mass represented by the periodical function given as follows [23,24]:

$$f(x) = \frac{\kappa(x-nL)}{L} + 1 \; ; \; x \in [nL,(n+1)L] \; ; \; n \in Z \tag{5}$$

Accordingly to this choice parameter m_0 is the mass in the left point of period. We also assume that $k \geq 0$. The case corresponding to values $-1 < k \leq 0$ after changing $x \to -x$ admits to apply the below described approach.

Due to the coefficients of Schrödinger equation (4) are periodical functions with the period L its solutions have to satisfy to certain boundary conditions. Having recourse to Floquet theorem [19] we can write the first boundary condition as follows:

$$\Psi(x)\big|_{x=0} = e^{iqL}\,\Psi(x)\big|_{x=L} \tag{6}$$

Concerning the second one it comes up of probability's flux density continuity, that is:

$$\frac{1}{m_0 f(x)}\partial_x\Psi(x)\bigg|_{x=0} = e^{iqL}\,\frac{1}{m_0 f(x)}\partial_x\Psi(x)\bigg|_{x=L} \tag{7}$$

Here q is the wave vector which runs quasi continuous values into the first Brillouin zone $-\frac{\pi}{L} < q \leq \frac{\pi}{L}$

It is convenient to apply the method of coordinate transformation [4] in order to resolve the Couchy's problem (4),(6),(7). Hence we introduce a dimensionless variable y determining it by the expression [25,26]:

$$y = \frac{\kappa}{L} x + 1 \tag{8}$$

By substituting the formula (8) into the equation (4) we rewrite it as follows:

$$-\frac{\mathrm{h}^2}{2m_0}\left(\frac{\kappa}{L}\right)^2 \partial_y \frac{1}{y} \partial_y \Psi = E\Psi \tag{9}$$

In order to simplify the last and below written equations we assume a notice:

$$Q^2 = \frac{2m_0 E}{\mathrm{h}^2}\left(\frac{L}{\kappa}\right)^2 \tag{10}$$

Than we finally obtain

$$y\partial_y^2 \Psi - \partial_y \Psi + Q^2 y^2 \Psi = 0 \tag{11}$$

The equation (11) is the main result for further consideration.

3. WAVE FUNCTIONS AND EIGEN VALUES OF ENERGY

The system of fundamental solutions of equation (11) can be expressed in terms of the Bessel $J_\nu(\xi)$ and Neumann $N_\nu(\xi)$ functions. According to the reference book [19] we have such general solution:

$$\Psi(y) = AyJ_{2/3}\left(\frac{2}{3}Qy^{3/2}\right) + ByN_{2/3}\left(\frac{2}{3}Qy^{3/2}\right) \tag{12}$$

Substitution (12) in the boundary conditions (6) and (7) leads to the following system of equations for coefficients A and B:

$$\begin{cases} Ay_0 J_{2/3}\left(\frac{2}{3}Qy_0^{3/2}\right) + By_0 N_{2/3}\left(\frac{2}{3}Qy_0^{3/2}\right) = \\ \qquad = e^{iqL}\left[Ay_L J_{2/3}\left(\frac{2}{3}Qy_L^{3/2}\right) + By_L N_{2/3}\left(\frac{2}{3}Qy_L^{3/2}\right)\right] \\ \frac{1}{y_0}\frac{\partial}{\partial y_0}\left[Ay_0 J_{2/3}\left(\frac{2}{3}Qy_0^{3/2}\right) + By_0 N_{2/3}\left(\frac{2}{3}Qy_0^{3/2}\right)\right] = \\ \qquad = e^{iqL}\frac{1}{y_L}\frac{\partial}{\partial y_L}\left[Ay_L J_{2/3}\left(\frac{2}{3}Qy_L^{3/2}\right) + By_L N_{2/3}\left(\frac{2}{3}Qy_L^{3/2}\right)\right] \end{cases} \tag{13}$$

where the notice

$$y_L = 1 + \kappa \tag{14}$$

was introduce.

The dispersion equation can be obtained in the standard way, namely, equaling to zero the system (13) determinant. To simplify the final result one can apply expressions corresponding to the Vronskian of equation (11), as well as the Vronskian relative to the Bessel equation independent solutions [20]. In this way we have found:

$$\frac{6}{\pi}CosqL = y_L\left[J_{2/3}\left(\frac{2}{3}Qy_L^{3/2}\right)\partial_{y_0}N_{2/3}\left(\frac{2}{3}Qy_0^{3/2}\right)-\partial_{y_0}J_{2/3}\left(\frac{2}{3}Qy_0^{3/2}\right)N_{2/3}\left(\frac{2}{3}Qy_L^{3/2}\right)\right]+$$
$$+y_0\left[J_{2/3}\left(\frac{2}{3}Qy_0^{3/2}\right)\partial_{y_L}N_{2/3}\left(\frac{2}{3}Qy_L^{3/2}\right)-\partial_{y_L}J_{2/3}\left(\frac{2}{3}Qy_L^{3/2}\right)N_{2/3}\left(\frac{2}{3}Qy_0^{3/2}\right)\right]+ \quad (15)$$
$$+\frac{(y_L^2-y_0^2)}{y_0y_L}\left[J_{2/3}\left(\frac{2}{3}Qy_L^{3/2}\right)N_{2/3}\left(\frac{2}{3}Qy_0^{3/2}\right)-J_{2/3}\left(\frac{2}{3}Qy_0^{3/2}\right)N_{2/3}\left(\frac{2}{3}Qy_L^{3/2}\right)\right]$$

After specifying all the derivates we have come to the master equation in its final form, namely:

$$\frac{6}{\pi}CosqL = \frac{2(y_L^2-y_0^2)}{y_0y_L}\left[J_{2/3}\left(\frac{2}{3}Qy_L^{3/2}\right)N_{2/3}\left(\frac{2}{3}Qy_0^{3/2}\right)-J_{2/3}\left(\frac{2}{3}Qy_0^{3/2}\right)N_{2/3}\left(\frac{2}{3}Qy_L^{3/2}\right)\right]-$$
$$-Q\sqrt{y_0}y_L\left[J_{2/3}\left(\frac{2}{3}Qy_L^{3/2}\right)N_{5/3}\left(\frac{2}{3}Qy_0^{3/2}\right)-J_{5/3}\left(\frac{2}{3}Qy_0^{3/2}\right)N_{2/3}\left(\frac{2}{3}Qy_L^{3/2}\right)\right]- \quad (16)$$
$$-Qy_0\sqrt{y_L}\left[J_{2/3}\left(\frac{2}{3}Qy_0^{3/2}\right)N_{5/3}\left(\frac{2}{3}Qy_L^{3/2}\right)-J_{5/3}\left(\frac{2}{3}Qy_L^{3/2}\right)N_{2/3}\left(\frac{2}{3}Qy_0^{3/2}\right)\right]$$

Approximate solutions of equation (16) can be obtained for two asymptotic cases, In the first case, taking into account the asymptotic expansions of the Bessel and Neumann functions [20], we come to the equation:

$$\frac{1}{2}\left[(y_L)^{1/4}+(y_L)^{-1/4}\right]Cos\left[\frac{2}{3}Q(y_L^{3/2}-1)\right]=CosqL \quad (17)$$

where the terms of order Q^{-1} and superior ones have been neglected. Let us point out that multiplicative factor in equation (16) satisfies to the condition $(y_L^{1/4}+y_L^{-1/4})/2\geq 1$ for all the actual values of parameter κ. Hence the equation (16) always has solutions. By resolving the equation (16), we have obtained:

$$E_n(q)=\frac{\mathrm{h}^2}{2m_0}\left(\frac{3\kappa}{2L(y_L^{3/2}-1)}\right)^2\left\{\pi n+arcCos\left[\frac{2CosqL}{y_L^{1/4}+y_L^{-1/4}}\right]\right\}^2 \quad (18)$$

Regarding the expression (16) and comparing it with the well known results of State Solid Theory [21] we make sure that periodic and linear modulation of particle mass produces the effect similar to the action of periodic potential of perfect crystal whose impact on the electron spectrum comes to the renormalization of the particle mass and formation of energetic bands. Accordingly to Eq. (18), that is for highly exited states , subbands reduce to non dispersed energetic levels and the electron moves in such a way as if its effective mass was constant and renormalized, as follows [27]:

$$m_{eff}=\frac{4}{9\kappa^2}m_0(y_L^{3/2}-1)^2 \quad (19)$$

It is quite obvious that the explicit form of mass renormalization depends on peculiarities of model and the last expression only can be valid for the mass modification determined by Eqs. (1), (5).

In order to verify validity of this result we considered the special case corresponding to limit $\kappa \to 0$.Due to the definitions (1) and (5) the particle mass becomes position independent if κ is equal to zero. Than we have to receive a free particle energy spectrum. Indeed in the case $\kappa = 0$ from equation (15) comes out

$$\lim_{\kappa \to 0} E_n(q) = \frac{\mathrm{h}^2}{2m_0}\left(q + \frac{\pi n}{L}\right)^2 \tag{20}$$

Passing to the extended Brillouin's scheme we naturally obtain the parabolic dispersion law inherent to the free particle.

Returning to the result (17) we note that the periodic modulation of the effective mass by some coordinate dependent function in relation to the energy eigen values plays the same role as the periodic potential, namely, the spectrum splits in allowed energy zones, in each of which the energy is a continuous function of the wave vector. Consequently, one can pass to conclusion that one of the way to expand technologic possibilities of zone spectrum engineering consists in the periodic modulation of the position dependent mass

The width W_n of allowed zone is determined by the expression:

$$W_n = \frac{\pi^2 \mathrm{h}^2 (2n+1)}{2m_0}\left(\frac{3\kappa}{2L(y_L^{3/2}-1)}\right)^2\left(1 - \frac{2}{\pi}\arccos\frac{2}{y_L^{1/4}+y_L^{-1/4}}\right) \tag{21}$$

while the forbidden zone gap E_{gn} has been found as follows:

$$E_{gn} = \frac{\pi^2 \mathrm{h}^2}{m_0}\left(\frac{3\kappa}{2L(y_L^{3/2}-1)}\right)^2\left(n + \frac{1}{2} + \frac{1}{\pi}\arccos\frac{2}{y_L^{1/4}+y_L^{-1/4}}\right) \tag{22}$$

It is interesting to note that neglecting by the dispersion one can obtain the results identical to ones corresponding to the well known problem of the particle in the rectangular potential well [22].

In the second case, that is, if $Qy_L^{1/2} = 1$, after applying the expansion of cylindrical functions in series and restricting us by the main terms only, we have

$$E(q) = \frac{10\mathrm{h}^2}{m_0}\left(\frac{\kappa}{L}\right)^2\left(\frac{1+CosqL}{1+(1+\kappa)^3}\right) \tag{23}$$

Consequently lowly laid branches of energy spectrum is analogous to the energy bands peculiar for the well-known in the Solid State Physics model of the nearest neighbours. It is easy also to see that for small values of wave number, the spectrum admits parabolic approximation with inverted scheme of quadratic energetic band and averaged electron mass which can be in obvious manner determined by correspondent expansion in series of equation (23)

4. CONCLUSION

In the context of the superlattice formed by periodic array of layers with effective mass dependent on coordinate into each of them, electron quantum dynamics has been studied. Assuming that the electron mass inside layer can be expressed as linear function of coordinate aligned along the superlattice axis, effective wave equation has been found in such special mathematic form that allows to obtain its exact solutions. These exact solutions were established not only for eigenfuntion but for secular equation too. The mentioned equation was found by joint applying of boundary conditions and the Floquet theorem and it shows the structure typical for well-known in Solids State Physics

Shrödinger's equations with periodic coefficients such as Kronig-Penney model for example [21,22]. However its solution in explicit form could only be found for two limits.

One of these cases corresponds to dimensionless wave number much more than one. In this case the dispersion law clearly shows the features of superlattice electron spectrum, namely, it consists of energetic subbands separated by forbidden zones. Characteristic properties such as subbands and forbidden zone widths depend on sublattice basic parameters that are period L and angular coefficient κ. Due to these peculiarities the creation of structures with predictable spectral properties becomes possible. The electron spectrum for highly situated energetic subbands turns out weakly depended on wave number and reveals behavior appropriated to one-dimensional rectangular well. The result points out that electron can be considered as the particle confined inside of the layer.

In the case correspondent to the wave number much less than one electron dispersion law is similar to the energetic spectrum in the nearest neighborhoods approximation with the renormalized effective mass and consists of one inverted energetic band.

The obtained results can be also applied to the frequency spectrum of layered photonic crystals with periodic and linear modulation of dielectric permeability.

REFERENCES

[1] Weisbuch, C., Vinter, B., [Quanum Semiconductor structures], New York, Academic Press (1993).
[2] Fang, X., Bando, Y., Guatam, U. K., Zhai, T., Gradečak, S., Golberg, D., "Heterostructures and superlattices in one-dimensional nanoscale semiconductors," J. Mater. Chem. 19, 5683-5689 (2009).
[3] Levy-Leblond, J. M., "Position-dependent effective mass and Galilean invariance," Phys.Rev. A 52, 1845 (1995).
[4] Koç, R., Saym, S.,"The Schrödinger equation with position-dependent mass," J.Phys.A: Math.Theor.-43, 455203 (2010).
[5] Cunha, M. S., Christiansen, H. R., "Analityc results in the position-dependent mass Schrödinger problem," Comm. in Theoretical Physics, 1-14 (2013).
[6] Gora, T., Williams, F., "Theory of Electronic States and Transport in Graded Mixed Semiconductors," Phys.Rev. 177, 1179 (1969).
[7] Bastard, G., Furdyna J. K., Mucielski, J., "Landau levels and cyclotron resonance in graded mixed semiconductors," Phys.Rev. B12, 4356-4359 (1975).
[8] Bastard, G., "Superlattice band structure in the envelope-function approximation," Phys.Rev. B24, 5693 (1981).
[9] Von Roos, O., "Position-dependent effective masses in semiconductor theory," Phys. Rev. B27, 7547 (1983).
[10] Von Roos, O., Mavromatis, H., "Position-dependent effective masses in semiconductor theory," II,Phys. Rev. B31, 2294 (1985).
[11] Barranco, M. M. Pi, Gatica S. M., Hermandes, E. S., Navarro, J., "Structure and energetic of mixed ^{4}He-^{3}He drops," Phys.Rev. B56, 8997 (1997).
[12] Peter, A. J., Navaneethakrishnan, K., "Effects of position-dependent mass and dielectric function of a hydrogenic donor in a quantum dot," Physica E : Low-dimensional Systems and Nanostructures 40(9), 2747-2751 (2008).
[13] Koç, R., Saym, S., "Remarks on the solution of the position-dependent mass Schrödiger equation," J.Phys.A: Math.Theor. 43, 455203 (2010).
[14] Alvarez, C. D. E., "Exactly Solvable Potentials and Romanovski Polynomials in Quantum Mechanics," Thesis for MS degree, Universidad Autónoma de San Luis Potosí, Mexico (2007).
[15] Ben Daniel, D. J., Duke, C.B., "Position-Charge Effects in Electron Tunneling," Phys. Rev., 152, 683-692 (1966).
[16] Christiansen, H. R., Cunha, M.S., "Energy eigenfunctions for position-dependent mass particles in a new class of molecular Hamiltonians," J. of Math. Phys., 1-32 (2014).
[17] Ramazan, S., Tezcan, C., "Exact solution of Schrödinger equation for modified Kratzer's molecular potential with the position-dependent mass," International Journal of Modern Physics E 17(07), 1327-1334 (2008).

[18] Guo-Xing, J. U., Chang-Ying, C. A. I., Zhong-Zhou R. E. N., "Generalized Harmonic Oscillator and Schrödinger Equation with Position-Dependent Mass," Communications in Theoretical Physics 51(5), 797 (2009).
[19] Kamke, E., [Differentialgleichungen, lösungsmethoden and lösungen], Leipzig, (1959).
[20] Abramovwitz, M., Stegun I. A., "Handbook of Mathematical Functions with formulas, graphs and mathematical tables," New York, NBS (1964).
[21] Ashcroft, N.W., Mermin N. D., [Solid State Physics], Holt, Rinehart and Winston, New York, (1976).
[22] Flügge, S., "Practical Quantum Mechanics," V1, Springer-Verlag (1971).
[23] Wojcik, W., Kisala, P., „Source: The application of inverse analysis in strain distribution recovery using the fibre bragg grating sensors," Metrology and Measurement Systems 16(4), 649-660 (2009).
[24] Wojcik, W., Gromaszek, K., Kotyra, A., et al., „Pulverized coal combustion boiler efficient control," Przeglad Elektrotechniczny 88(11B), 316-319 (2012).
[25] Zabolotna, N. I., Wojcik, W., Pavlov, S. V., et al., „Diagnostics of pathologically changed birefringent networks by means of phase Mueller matrix tomography," Optical Fibers and Their Applications 2012 Book Series: Proceedings of SPIE 8698, UNSP 86980E (2013).
[26] Krak, Y. V., Barmak, A. V., Bagriy, R. A., Stelya, I. O., "Text entry system for alternative speech communications," Journal of Automation and Information Sciences 49(1), 65-75 (2017).
[27] Kryvonos, I. G., Krak, I. V., Barmak, O. V., Bagriy, R. O., "Predictive text typing system for the Ukrainian language," Cybernetics and systems analysis 53(4), 495–502 (2017).

Preparation of n-CuO nanostructural films by thermal oxidation/PVD method

E.Czerwosz[1], H.Wronka[1], M.Kozłowski[1], R.Diduszko[1], J.Kęczkowska[2], M.Suchańska[2]

[1] Sieć Badawcza Łukaszewicz - Instytut Tele- i Radiotechniczny ,03-450 Warszawa, ul.Ratuszowa 11, Poland

[2] Politechnika Świętokrzyska, al. Tysiąclecia P.P. 7, 25-314 Kielce, Poland

ABSTRACT

CuO films compose of copper oxide nanorods and nanograins with fcc type of structure have been prepared by multistep PVD / thermal oxidation method at different temperatures of annealing (400, 500and 600 ^{o}C). Ni-C nanocatalyst films was the factor lowering temperature and duration time of thermal oxidation (in comparison with literature data for similar methods) in which nanorods have been obtained. Obtained nanostructural films (composed of 1D and 2D objects) were characterized with XRD, SEM, EDX and Raman spectroscopy. All applied methods proved that the CuO nanostructural film is formed due to thermal oxidation of prepared multilayer film.

Keywords: copper oxide, thermal oxidation, PVD

1. INTRODUCTION

Copper oxide (CuO) is a semiconducting material which could be used in many applications such as a photovoltaic solar cells [1-3],some gases (e.g. H_2, H_2O_2, NH_3) sensors [4-6] and photothermal material [7]. CuO are p-type semiconductors with band gaps 1.5 – 1.8 eV for indirect transition and 1.9 eV for direct transition which are close to the ideal energy gap for solar cells and allows for good solar spectral absorption due to this direct band gap. CuO thin films are prepared by various techniques such as chemical vapor deposition (VCD), vacuum evaporation, electro-deposition, sputtering process, electron-beam evaporation, chemical solution deposition (CSD) [8-11]. Some authors show that copper oxide can be produced by thermal oxidation of copper [12-15]. In the paper [12] by Plascencia et al. it was presented that copper oxidation in the temperature range of 300 –1000°C can be realized. They also showed that the oxidation was followed by logarithmic law of surface diffusion at 300–500°C, and by parabolic law of diffusion of copper ions through oxide layer at 600–1 000°C. It was also shown that dense and compact layer of single phase CuO was formed at the oxygen pressure lower than the equilibrium potential for Cu/Cu, and the rate of the oxidation under this condition was increased with increasing oxygen pressure [13].

The nanomaterials based on CuO have the fundamental and practical importance. The well-defined CuO nanostructures with various morphologies are fabricated and many synthesis techniques are developed to prepare different assemblies of CuO building blocks. The chemical and physical properties of CuO are dependent on its size and shape. The synthesis methods of various CuO nano and microstructures with controllable morphology are proposed. CuO nanostructures such as nanorods, nanowires, nanoneedles, nanoribbons, spheroidal, hollow spheres, have been observed depending on the methods and its technological parameters.

CuO can be obtained on various substrates what enables to use it in many devices. CuO can be applied in sensors (gaseous and liquid), photovoltaic cells, photothermal elements, photoelectrochemical devices, photocatalytic devices as well as in superconductors.

In the paper [16] an obtaining of copper oxides through deposition of copper thin film (300 nm) on a glass slide and their subsequent thermal treatment by direct oxidation in an open atmosphere as a function of oxidation temperature. Thin films of copper were deposited on a glass substrates by evaporation technique from a copper wire. These films firstly were annealed for 60 min., and then they were oxidized in the oven in rising temperature (from 250 to 400^{o}C).

In this paper we present the new technology of CuO nanostructural films preparation. These films are prepared on different substrates in several steps where the last step is the thermal oxidation. We observe that CuO nanostructural

Photonics Applications in Astronomy, Communications, Industry, and High-Energy Physics Experiments 2019, edited by Ryszard S. Romaniuk, Maciej Linczuk, Proc. of SPIE Vol. 11176, 111764O
© 2019 SPIE · CCC code: 0277-786X/19/$21 · doi: 10.1117/12.2536328

films are formed during oxidation of Cu film deposited on Ni-C nanocatalyst film prepared firstly on various substrates and oxidation time is 0.5hour what is much shorter than time applied in other cited papers.

2. EXPERIMENTAL METHODS

The thickness of films was measured using scanning electron microscopy (SEM). The thickness measurements were carried out on the cross-section of the layers deposited on Si substrate. The morphology and topography of the films were studied with the JEOL JSM-7600F field emission scanning microscope operating at 5 keV incident electron beam energy, equipped with SE (Secondary Electron) detector. The quantitative analyses of the chemical composition were checked by Energy Dispersive X-ray (EDX) method using X-MAX Silicon Drift Detector (Oxford Instruments) coupled with the SEM.

The XRD measurements were performed with a Rigaku SmartLab 3kW diffractometer, equipped with Dtex 1D detector, using CuKa radiation ($\lambda \approx 1.5418$ Å).

The Raman spectra measurements were carried out using automated micro-Raman Nicolet Almega XR spectrometer (Thermo Scientific). The measurements were carried out in ambient temperature for the excitation wavelength of 532nm. A laser beam with a power of approximately 2.5 mW was used. Spectra acquisition was performed for spectral range 100-4000 cm-1.

The method of preparation of nanostructural films (composed of 1D and 2D objects) is innovative and was patented by us.

The Ni-C nanocatalyst films were prepared by physical vapor deposition (PVD) method from two separated sources containing fullerite C_{60} (99,995 % purity Sigma-Aldrich) and nickel acetate. This method was patented and described in paper [17]. The content of Ni in such nano-catalyst film was ~3,5 wt. %. It was also shown that Ni has a form of nanograins with diameter of few nanometers and these nanograins are placed in carbonaceous matrix what prevents the agglomeration of Ni nanograins into bigger objects.

Thin films of copper were deposited on a top of nanocatalyst Ni-C films prepared on a various substrates (Al foil with thickness 0.1mm or plate with thickness 2mm, n-Si wafer) by PVD method. The Cu layer was grown at a dynamic vacuum of $5x\ 10^{-5}$ mbar using as a source the Cu metal. The prepared samples description is shown in Tab.1. The thickness of the sample S0-Si prepared on the Si wafer was ~270nm (Fig.1b) while the nanocatalst Ni-C films thickness in this sample was ~170nm (Fig.1a). Taking into account the same technological parameters for S0-Al film we can suppose that the thickness of this film is similar to the thickness of film prepared on Si wafer.

These multilayer films were placed in the furnace and heated gradually with various heating rate up to final temperature (400, 500, 600 ^{o}C) for 30 min. at the air atmosphere. The thickness of films prepared in this way cannot be determined because of high roughness of these films. We also prepared the samples annealed at the temperature 200 and 300 o C, but all used methods showed the presence of metallic copper phase in the studied samples.

Tab.1 Sample's description

Sample no	substrate	Final oxidation temperature [^{o}C]	Oxidation duration time [hour]	Cu/Ni-C film thickness [nm]
S0- Al	Al	-	-	
S1-Al	Al foil	400	0,5	
S2-Al	Al foil	500	0,5	
S3-Al	Al foil	600	0,5	
S0-Si	n-Si			~270
S1-Si	n-Si	400	0,5	
S2-Si	n-Si	500	0,5	
S3-Si	n-Si	600	0,5	

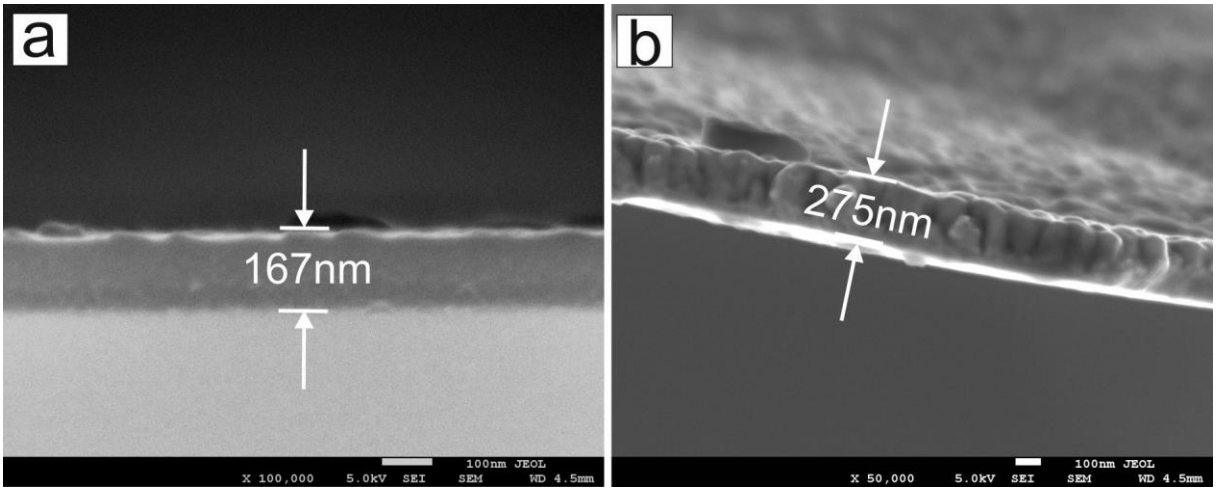

Fig.1 SEM image of the cross-section of films a) Ni-C nanocatalyst, b) Cu/Ni-C nanocatalyst

3. RESULTS AND DISCUSSION

The results of XRD studies are presented in Fig.2 and Fig.3. In Fig.2 the XRD diffraction patterns of the series of samples prepared on a Al substrates are shown. The XRD diffraction pattern of S0-Al sample (Fig.2a) presents reflections from the Al substrate (marked with the symbol "*") interpreted accordingly to ICDD 4-787 pattern. The aluminum has the structure of fcc type and the lattice constant a = 4.049 Å. The peaks marked with the symbol "+" are attributed to metallic Cu layer (ICDD 4-836) with the structure of fcc type and lattice constant a = 3.615 Å. The diffraction pattern of S1-Al sample (Fig.2b) annealed at 400 ° C contains reflections from the Al substrate but peaks belonging to diffraction from CuO of tenorite copper oxide phase (marked with "o") are found either. Accordingly to ICDD 48-1548, this CuO compound has C2/c monoclinic structure and lattice constants a = 4.688 Å , b = 3.423 Å, c = 5.132 Å, β = 99.5º. Presented inFig.2c XRD diffraction pattern of the sample S3-Al annealed at 600 ° C has similar character and beside of Al origin peaks (marked with "*") presents also peaks connected to CuO crystallites (marked with "o").

Fig.3 presents results of XRD studies for series of films prepared on Si wafer. XRD diffraction pattern of the sample S0-Si is shown in Fig.3a. The reflections from metallic Cu layer (marked with the symbol "+") are observed. Accordingly to ICDD 4-836 pattern this film has the structure of fcc type with the lattice constant a = 3.615 Å. XRD diffraction pattern of the sample S1-Si annealed at 400 ° C shows peaks belonging to reflections from the CuO -tenorite copper oxide phase (marked with "o"). This CuO has C2/c monoclinic structure with lattice constants a = 4.688 Å , b = 3.423 Å, c = 5.132 Å, β = 99.5º (ICDD 48-1548). The XRD diffraction pattern of the sample S3-Si annealed at 600 ° C similarly to previous sample contains peaks from the CuO phase. The higher noises level is connected to a smaller CuO grains size for this than for sample S1-Al.

These XRD results prove that due to the thermal oxidation process CuO with fcc type of structure is formed only. No other types of copper oxides was observed while studying XRD patterns. At the oxidation temperature 400 ° C no trace of metallic Cu was found yet.

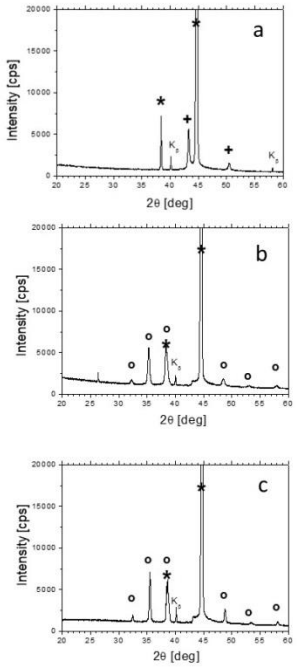

Fig.2 X-ray diffraction patterns of the samples prepared on the aluminum foil: a) S0-Al; b) S1-Al; c) S3-Al

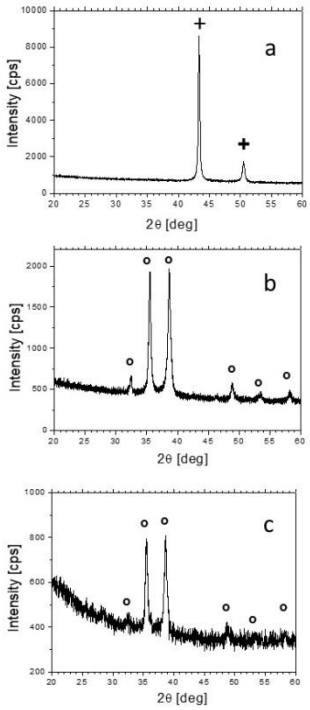

Fig.3 X-ray diffraction patterns of the samples prepared on the Si wafer: a) S0-Si; b) S1-Si; c) S3-Si

SEM images of prepared samples are presented in Fig.4 and Fig.5. In Fig.4 the samples prepared on alumina substrates and in Fig. 5 the samples on Si wafer are shown. The size of grains in S0 samples prepared on different substrates is different. The grains obtained on the Si wafer are bigger then grains observed on Al substrate. XRD patterns showed that these grains are Cu grains. The thermal oxidation process leads to a growth of two kind of grains: first are rounded and second are elongated with rode-like shape (nanorods) with micro or nanometers sizes. Accordingly to XRD results these all objects are copper oxides (CuO with fcc type of structure).

In Fig.4 the nanostructural objects (nanorods) with length from few hundreds of nanometers up to few micrometers are found. The diameter of nanorods changes from 30nm to 100nm respectively for annealing temperature 400 and 600° C. It should be noticed that longer objects are formed in processes with lower oxidation temperatures what corresponds with lower annealing ratio (~13deg/min) while the processes with the highest used annealing temperature leads to formation of shorter nanorods (the annealing ratio was 20 deg/min). Similar effect is observed for films obtained on Si wafer. Although the length of obtained nanorods is much lower (few tens of nanometers) the effect has the same character. Lower annealing ratio causes the growth of longer nanoobjects. Fig.5d shows that the growth of nanorods at the annealing ratio 20deg/min didn't started at all. The influence of the substrate on the nanorods growth is also visible.

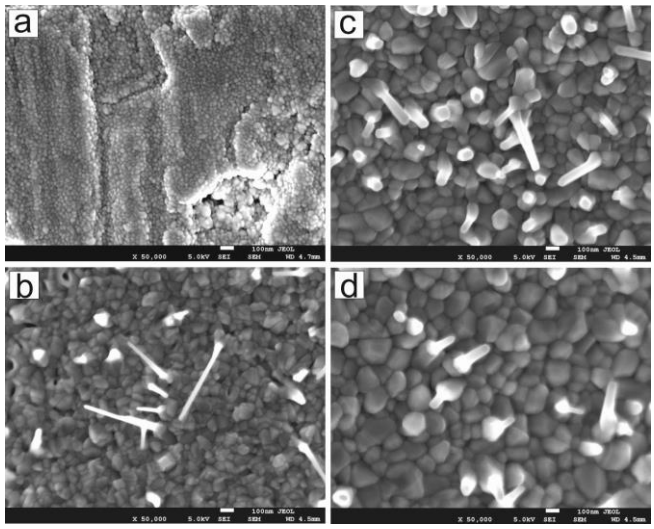

Fig.4 SEM images of samples prepared on alumina foil: a) S0 – Al; b) S1-Al; c) S2-Al; d) S3-Al films

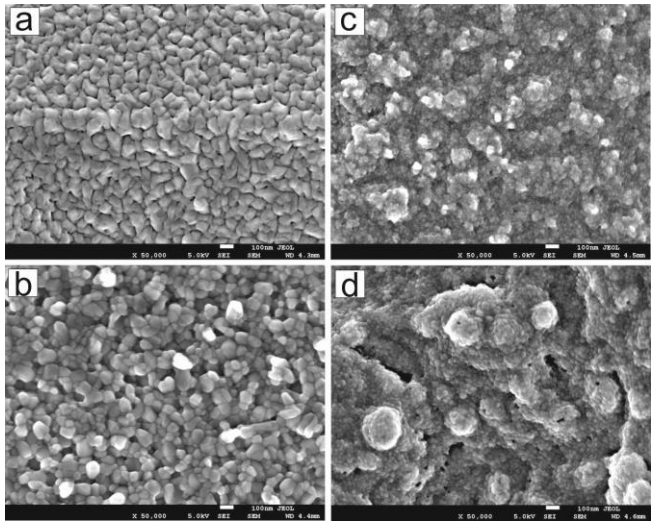

Fig.5 SEM images of samples prepared on Si wafer : a) S0 – Si; b) S1- Si; c) S2- Si; d) S3- Si films

The grain's size analysis for samples obtained on silicon is presented in Fig.6. The size of grains is smaller for sample obtained at the temperature 600° C (average 60nm) than for grain's size for the sample prepared at 400° C (150nm). This results are consistent with XRD results for these samples where higher lever of noises is observed for the sample S3-Si what is connected to lower size of nanograins of CuO.

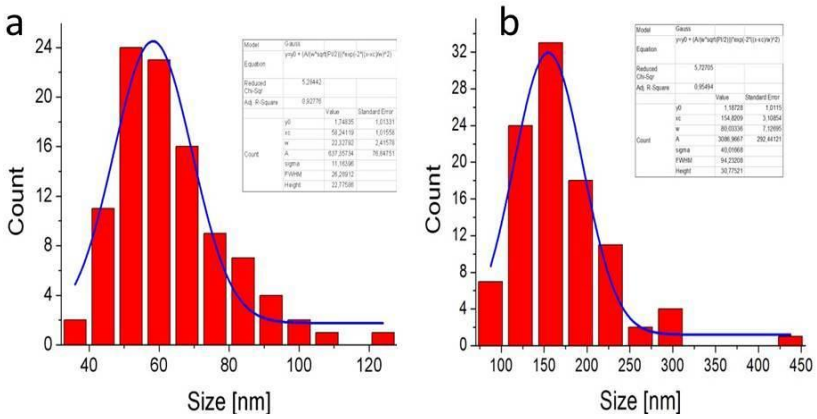

Fig.6 Grains size analysis for the samples: a) S3-Si, b) S1-Si

The samples prepared on aluminum exhibit an ability for a formation of longer nanorods then the samples prepared on silicon. This effect could be connected to the much higher thermal conductivity and thermal capacity of Al than these relevant properties of Si. It seems, when taking in account the XRD and SEM results, that CuO growth has a volumetric character with this exception that nanorods are formed on the film surface where the temperature is lower.

In paper [18] it was shown that for many thermal oxidation methods with Cu substrate the growth of various CuO nanorods needs temperature 400-700 °C and the annealing time no less than one hour. These methods require usually the oxygen or air flow through the oven what intensifies the nanorods density. In our case any substrate which is suitable for applied annealing temperature can be used, the heating atmosphere was the air and no flow was applied.

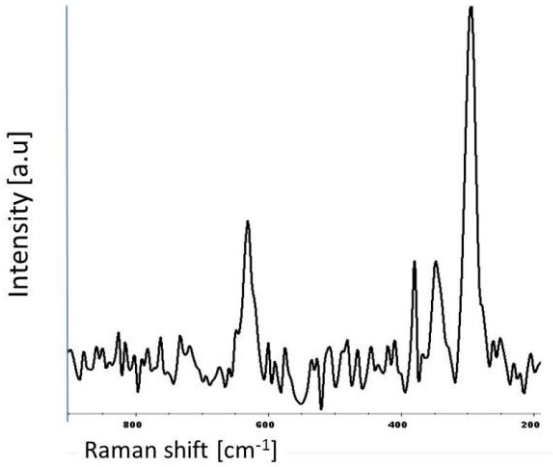

Fig.7 Raman spectrum of S1-Al sample.

The existence of CuO phase in the annealed films confirm also the Raman spectra. In the paper [19] the detailed analysis of vibrational properties of CuO and its Raman spectra were presented. The Raman spectra of CuO has three active vibrational modes reflected in the bands placed at 296 (A_g), 346 (B_g) and 631 (B_g) cm^{-1}. In the A_g and B_g Raman modes only the oxygen atoms move, with displacements in the b-direction (b- direction is along lattice b axe) for A_g and

perpendicular to the b-axis for B_g modes. In CuO, where the only internal parameter is the y-coordinate of the O site, the strongest Raman peak corresponds to the fully symmetrical A_g mode where the O atoms move along b.

The example of Raman spectrum for S1-Al sample (annealed at 400 °C) is presented in Fig. 7. The observed Raman band positions are 296, 348 and 632 cm^{-1}. This sample contained the longest CuO nanorods. In this Raman spectrum the strongest observed band is attributed to A_g mode connected to the vibration of oxygen atoms along b lattice axe. In paper [20] it was stated that the red shift and broadening of the Raman spectra of CuO nanocrystal are mainly due to size effects. When the grain size decreases the band's position is shifted toward lower wavelength. For example the band placed at 631 cm^{-1} moves up to 621 cm^{-1} when the grain size decreases from few hundreds of nanometers to 10nm. In the case of S1-Al sample almost no shift is observed what confirms SEM observation.

4. CONCLUSIONS

The CuO films were successfully prepared by multi step PVD/thermal oxidation method. CuO film were annealed at temperatures 400°C, 500°C, and 600°C. Variation in the form of obtained nanostructural films indicated temperature and annealing ratio dependence in sizes and shapes of 1D and 2D CuO (nanorods and nanograins) nanostructural objects.

The temperature and duration time of preparation of nanostructural films (composed of 1D and 2D objects) were lower than reported in literature regarding similar methods.

Thermal oxidation is a simple, efficient and low-cost method for synthesizing 1D CuO nanostructures and it is suitable for batch fabrication and mass production. The achieved 1D CuO nanostructures can be obtained in a form of nanorods with different length and diameter what is connected to the temperature and annealing ratio of thermal oxidation process. In addition, the morphology, density, diameter and length ofthe1D CuO nanostructures can be easily tailored by adjusting other synthesis parameters (Ni content in initial film, thickness of Cu film and type of topography of substrate).

REFERENCES

1. A. Bhaumik, A. Haque, P. Karnati, M.F.N. Taufique, R. Patel, K. Ghosh, Copper oxide based nanostructures for improved solar cell efficiency, Thin Solid Films 572 , 126–133(2014)
2. R.P. Wijesundera, Fabrication of the CuO/Cu2O heterojunction using an electrodeposition technique for solar cell applications, Semicond. Sci. Technol. 25, 045015-20(2010)
3. Yusheng Xia, Xuxin Pu, Jie Liu, Jie Liang, Pujun Liu, Xiaoqing Li and Xibin Yu, CuO nanoleaves enhance the c-Si solar cell efficiency, J. Mater. Chem. A, 2, 6796 - 6800(2014)
4. Aixia gu, Guangfeng Wang, Xiaojun Zhang, Bin Fang, Synthesis of CuO nanoflower and its application as a H2O2 sensor, Bull. Mater. Sci., 33(1), 17–20(2010)
5. O. Şişman, N. Kılınç, Z.Z. Öztürk, H2 sensing properties of Cu2O nanowires on glass substrate, Procedia Engineering 120, 1170 – 1174(2015)
6. Bhuvaneshwari S. and N. Gopalakrishnan, CuO Mesostructures As Ammonia Sensors, AIP Conference Proceedings 1942, 050114 1-4(2018)
7. H.H.Afify, S.E.Demian, M.A.Helal, F.A. Mahmoud, Sprayed CuO film on glass and aluminum substrates for photothermal application, Indian Journal of Pure& Appl.Phys., 37 , 379-383(1999)
8. Lim YF, Chua CS, Lee CJJ, Chi D. Sol–gel deposited Cu2O and CuO thin films for photocatalytic water splitting. Physical Chemistry Chemical Physics, 16 (47), 25928-25934 (2014)
9. Lin CY, Lai YH, Mersch D, and Reisner E. Cu2O/NiOx nanocomposite as an inexpensive photocathode in photoelectrochemical water splitting. Chemical Science, 3 (12) (2012) 3482-3487.
10. Zhang Z, and Wang P. Highly stable copper oxide composite as an effective photocathode for water splitting via a facile electrochemical synthesis strategy. Journal of Material Chemistry, 6 (22), 2456-2464 (2012)
11. Paracchino A, Mathews N, Hisatomi T, Stefik M, Tilley SD, and Gratzel M. Ultrathin films on copper (I) oxide water splitting photocathodes: a study on performance and stability, Energy & Enviromental Science, 5, 86738-681(2012) .
12. N.J.Tannyan, G. Plascencia and T. Utigard High Temperature Oxidation of Copper and Copper Aluminum Alloys. Canadian Metallurgical Quarterly, 41(2), 213–218(2002) .

13. A. Strawbridge, R. A. Rapp, The Role of Reactive Elements on Scale Growth in High-Temperature Oxidation of Pure Nickel, Iron, Cobalt, and Copper I . Oxidation Kinetics and Scale Morphology, J. Electrochem. Soc., 141, 1905-15(1994)
14. Xuchuan Jiang, Thurston Herricks, and Younan Xia, CuO Nanowires Can Be Synthesized by Heating Copper Substrates in Air, Nano Lett.,. 2(12) , 1333-1338(2002)
15. Jei-Pil WANG, W. D. CHO, Oxidation Behavior of Pure Copper in Oxygen and/or Water Vapor at Intermediate Temperature, ISIJ International, 49(12), 1926–1931(2009)
16. D. Santos-Cruz, S.A. Mayén-Hernández, F. de Moure-Flores, J. Campos-Álvarez, Mou Pal, J. Santos-Cruz, CuO_X thin films by direct oxidation of Cu films deposited by physical vapor deposition, Results in Physics 7, 4140–4144(2017)
17. E.Czerwosz, P.Dłużewski, M.Kozlowski, M.Nowicki, A.Richter, Topographical and morphological studies of the superficial structure changes during the growth of heterogeneous carbonaceous films with Ni nano-crystals inclusion, Vacuum 74, 311-315 (2004)
18. Qiaobao Zhang, Kaili Zhang, Daguo Xu, Guangcheng Yang, Hui Huang, Fude Nie, Chenmin Liu, Shihe Yang, CuO nanostructures: Synthesis, characterization, growth mechanisms, fundamental properties, and applications, Progress in Materials Science 60, 208–337(2014)
19. L. Debbichi, M. C. Marco de Lucas, J. F. Pierson, and P. Krüger, Vibrational Properties of CuO and Cu4O3 from First-Principles Calculations, and Raman and Infrared Spectroscopy, J. Phys. Chem. C., 116, 10232−10237(2012)
20. J. F. Xu, W. Ji, Z. X. Shen, W. S. Li, S. H. Tang, X. R. Ye, D. Z. Jia X. Q. Xin, Raman Spectra of CuO Nanocrystals, J. Raman Spectrosc. ,30, 413–415 (1999)

Angles between matrices and between polynomials in analysis of electrical circuits

Tadeusz Kaczorek
Białystok University of Technology, Faculty of Electrical Engineering,
Wiejska 45D, 15-351 Białystok

ABSTRACT

The notions of angles between matrices and between polynomials of linear electrical circuits are introduced. In analysis of angles between state matrices of linear electrical circuits the Hadamard product of two matrices is applied. The angles between matrices and their functions are also addressed. The angles between two polynomials of transfer matrices of electrical circuits are analyzed and some new properties are established.

Keywords: angle between matrices, polynomials, matrix function, linear, electrical circuit

1. INTRODUCTION

A dynamical system is called positive if its trajectory starting from any nonnegative initial state remains forever in the positive orthant for all nonnegative inputs. An overview of state of the art in positive theory is given in the monographs [3, 11]. Variety of models having positive behavior can be found in engineering, especially in electrical circuits [19], economics, social sciences, biology and medicine, etc. [3, 11].

The positive electrical circuits have been analyzed in [5-7, 9, 10, 12-14, 17]. The constructability, observability and reachability of standard and positive electrical circuits has been addressed in [6, 12], the decoupling zeros in [7] and minimal-phase positive electrical circuits in [9]. A new class of normal positive linear electrical circuits has been introduced in [10]. Positive fractional linear electrical circuits have been investigated in [13] and positive unstable electrical circuits in [14]. Infinite eigenvalue assignment by output-feedback for singular systems has been analyzed in [8]. Zeroing of state variables in descriptor electrical circuits has been addressed in [17]. Controller synthesis for positive linear systems with bounded controls has been investigated in [1]. Stability of continuous-time and discrete-time linear systems with inverse state matrices has been analyzed in [18,2] and the transfer matrices with positive coefficients of standard and fractional positive systems in [20].

In this paper the notions of angles between matrices and polynomials of linear electrical circuits will be introduced and their basic properties will be investigated.

The paper is organized as follows. In section 2 the basic definitions and properties of positive electrical circuits are recalled. The angles between matrices of linear electrical circuits are introduced and their properties are analyzed in section 3. The angles between matrices and their functions are addressed in section 4.The angles between two polynomials are introduced and their properties are investigated in section 5. Concluding remarks are given in section 6.

The following notation will be used: $\Re$ - the set of real numbers, $\Re^{n\times m}$ - the set of $n\times m$ real matrices, $\Re_+^{n\times m}$ - the set of $n\times m$ real matrices with nonnegative entries and $\Re_+^n = \Re_+^{n\times 1}$, M_n - the set of $n\times n$ Metzler matrices (real matrices with nonnegative off-diagonal entries), I_n - the $n\times n$ identity matrix.

2. POSITIVE ELECTRICAL CIRCUITS

Consider the linear continuous-time electrical circuit described by the state equations

$$\dot{x}(t) = Ax(t) + Bu(t)\,, \tag{2.1a}$$

$$y(t) = Cx(t) + Du(t)\,, \tag{2.1b}$$

Photonics Applications in Astronomy, Communications, Industry, and High-Energy Physics Experiments 2019,
edited by Ryszard S. Romaniuk, Maciej Linczuk, Proc. of SPIE Vol. 11176, 111764P
© 2019 SPIE · CCC code: 0277-786X/19/$21 · doi: 10.1117/12.2536466

where $x(t) \in \Re^n$, $u(t) \in \Re^m$, $y(t) \in \Re^p$ are the state, input and output vectors and $A \in \Re^{n \times n}$, $B \in \Re^{n \times m}$, $C \in \Re^{p \times n}$, $D \in \Re^{p \times m}$.

It is well-known [19] that any linear electrical circuit composed of resistors, coils, capacitors and voltage (current) sources can be described by the state equations (2.1). Usually as the state variables $x_1(t), \ldots, x_n(t)$ (the components of the state vector $x(t)$) the currents in the coils and voltages on the capacitors are chosen.

Definition 2.1. [19] The electrical circuit (2.1) is called (internally) positive if $x(t) \in \Re_+^n$ and $y = y(t) \in \Re_+^p$, $t \in [0,+\infty]$ for any $x_0 = x(0) \in \Re_+^n$ and every $u(t) \in \Re_+^m$, $t \in [0,+\infty]$.

Theorem 2.1. [19] The electrical circuit (2.1) is positive if and only if

$$A \in M_n,\ B \in \Re_+^{n \times m},\ C \in \Re_+^{p \times n},\ D \in \Re_+^{p \times m}. \tag{2.2}$$

Theorem 2.2. [19] The linear electrical circuit composed of resistors, coils and voltage sources is positive for any values of the resistances, inductances and source voltages if the number of coils is less or equal to the number of its linearly independent meshes and the direction of the mesh currents are consistent with the directions of the mesh source voltages.

Theorem 2.3. [19] The linear electrical circuit composed of resistors, capacitors and voltage sources is not positive for all values of its resistances, capacitances and source voltages if each its branch contains resistor, capacitor and voltage source.

Theorem 2.4. [19] The *R*, *L*, *C*, *e* electrical circuits are not positive for any values of its resistances, inductances, capacitances and source voltages if at least one its branch contains coil and capacitor.

Definition 2.2. [19] The positive electrical circuit is called asymptotically stable if

$$\lim_{t \to \infty} x(t) = 0 \text{ for any } x_0 \in \Re_+^n. \tag{2.3}$$

Theorem 2.5. [19] The positive electrical circuit is asymptotically stable if and only if:

1) All coefficients of the characteristic polynomial

$$\det[I_n s - A] = s^n + a_{n-1}s^{n-1} + \ldots + a_1 s + a_0 \tag{2.4}$$

are positive, i.e. $a_k > 0$ for $k = 0,1,\ldots,n-1$.

2) There exists strictly positive vector $\lambda^T = [\lambda_1 \quad \cdots \quad \lambda_n]^T$, $\lambda_k > 0$, $k = 1,\ldots,n$ such that

$$A\lambda < 0. \tag{2.5}$$

3. ANGLES BETWEEN STATE MATRICES OF LINEAR ELECTRICAL CIRCUITS.

In this section the angle between two matrices will be defined and used in linear electrical circuits.

To any given matrix $A = [a_{ij}] \in R^{n \times m}$ the following two corresponding vectors can be define

$$\overline{A} = [a_{11} \ldots a_{1m} \ \ a_{21} \ldots a_{2m} \ \ a_{31} \ldots a_{nm}]^T \in \Re^{nm} \tag{3.1a}$$

and

$$\hat{A} = [a_{11} \ldots a_{n1} \ \ a_{21} \ldots a_{n2} \ \ a_{31} \ldots a_{nn}]^T \in \Re^{nm} \tag{3.1b}$$

T denotes the transpose.

Using the vectors of the matrices $A \in \Re^{n \times m}$ and $B = [b_{ij}] \in \Re^{n \times m}$ we may defined the following scalar product of the two matrices.

Definition 3.1. The scalar

$$(\overline{A},\overline{B}) = (\hat{A},\hat{B}) = \sum_{i=1}^{n}\sum_{j=1}^{m} a_{ij}b_{ij} \tag{3.2}$$

is called the scalar product of the matrices A and B.

In particular case if $A = B$ then

$$(\overline{A},\overline{A}) = (\hat{A},\hat{A}) = \left|\overline{A}\right|^2 = \left|\hat{A}\right|^2 = \sum_{i=1}^{n}\sum_{j=1}^{m} a_{ij}^2 > 0 \tag{3.3}$$

for any nonzero matrix $A \in \Re^{n\times m}$.

Using (3.2) and (3.3) we may defined the angle φ between two given matrices A and B of the same dimensions.

Definition 3.2. The angle defined by

$$\varphi = \varphi_{A,B} = \arccos\frac{(\overline{A},\overline{B})}{\left|\overline{A}\right\|\overline{B}\right|} = \arccos\frac{(\hat{A},\hat{B})}{\left|\hat{A}\right\|\hat{B}\right|}, \quad 0 < \varphi < \pi \tag{3.4a}$$

is called the angle φ between the matrices A and B.

The relation (3.4a) can be equivalently written in the form

$$\cos\varphi = \cos\varphi_{A,B} = \frac{(\overline{A},\overline{B})}{\left|\overline{A}\right\|\overline{B}\right|} = \frac{(\hat{A},\hat{B})}{\left|\hat{A}\right\|\hat{B}\right|}. \tag{3.4b}$$

From (3.4b) it follows the following conclusion.

Conclusion 3.1.

$$\cos\varphi_{A,B} = \cos\varphi_{B,A} \text{ and } \cos\varphi_{-A,-B} = \cos\varphi_{B,A}. \tag{3.5}$$

In particular case if $\overline{B} = \overline{A}$ then from (3.4b) we have $\cos\varphi = 1$ and $\varphi = 0$.

Example 3.1. Find the $\cos\varphi$ between the following matrices

$$A = \begin{bmatrix} 1 & -2 \\ 0 & 1 \\ 2 & 3 \end{bmatrix}, \quad B = \begin{bmatrix} 0 & 2 \\ 1 & 0 \\ -1 & 1 \end{bmatrix}. \tag{3.6}$$

In this case

$$\overline{A} = [1 \ -2 \ 0 \ 1 \ 2 \ 3]^T, \ \overline{B} = [0 \ 2 \ 1 \ 0 \ -1 \ 1]^T \tag{3.7a}$$

and

$$\hat{A} = [1 \ 0 \ 2 \ -2 \ 1 \ 3]^T, \ \hat{B} = [0 \ 1 \ -1 \ 2 \ 0 \ 1]^T. \tag{3.7b}$$

Using (3.2), (3.3), (3.4b) and (3.7) we obtain

$$(\overline{A},\overline{B}) = (\hat{A},\hat{B}) = -3, \quad \left|\overline{A}\right|^2 = \left|\hat{A}\right|^2 = 19, \ \left|\overline{B}\right|^2 = \left|\hat{B}\right|^2 = 7 \tag{3.8a}$$

and

$$\cos\varphi = \cos\varphi_{A,B} = \frac{(\overline{A},\overline{B})}{\left|\overline{A}\right\|\left|\overline{B}\right|} = \frac{(\hat{A},\hat{B})}{\left|\hat{A}\right\|\left|\hat{B}\right|} = -\frac{3}{\sqrt{19}\sqrt{7}} = -0.260\,. \tag{3.8b}$$

Consider the following two matrices of the same dimensions

$$A = [a_{ij}] \in \Re^{n\times m}, \quad B = [b_{ij}] \in \Re^{n\times m} \tag{3.9}$$

Definition 3.3. The matrix defined by

$$A \circ B = \begin{bmatrix} a_{11}b_{11} & \cdots & a_{1m}b_{1m} \\ \cdots & \cdots & \cdots \\ a_{n1}b_{n1} & \cdots & a_{nm}b_{nm} \end{bmatrix} \in \Re^{n\times m} \tag{3.10}$$

is called the Hadamard product of the matrices (3.9) [16].

Theorem 3.1. If the Hadamard product (3.10) of the matrices (3.9) is zero matrix then the angle φ between the matrices (3.9) is equal to $\frac{\pi}{2}$.

Proof. From Definitions 3.1 and 3.3 it follows that $A \circ B = 0$ implies

$$(\overline{A},\overline{B}) = \sum_{i=1}^{n}\sum_{j=1}^{m} a_{ij}b_{ij} = 0\,. \tag{3.11}$$

In this case from (3.4b) we obtain $\cos\varphi = 0$ and $\varphi = \frac{\pi}{2}$. □

Example 3.2. Using (3.9) for the matrices

$$A = \begin{bmatrix} 1 & 0 & -2 \\ 0 & -1 & 3 \end{bmatrix}, \quad B = \begin{bmatrix} 0 & 1 & 0 \\ 2 & 0 & 0 \end{bmatrix} \tag{3.12}$$

we obtain

$$A \circ B = \begin{bmatrix} 0 & 0 & 0 \\ 0 & 0 & 0 \end{bmatrix} \tag{3.13}$$

and

$$(\overline{A},\overline{B}) = \sum_{i=1}^{2}\sum_{j=1}^{3} a_{ij}b_{ij} = 0\,. \tag{3.14}$$

Therefore, by Theorem 3.1 the angle between the matrices (3.12) is equal $\frac{\pi}{2}$.

Theorem 3.2. The angle φ between the matrices $A = [a_{ij}] \in \Re^{n\times m}$, $B = [b_{ij}] \in \Re^{n\times m}$ satisfies the condition $\cos\varphi \geq 0$ if and only if

$$(\overline{A},\overline{B}) = \sum_{i=1}^{n}\sum_{j=1}^{m} a_{ij}b_{ij} \geq 0 \tag{3.15a}$$

and $\cos\varphi < 0$ if and only if

$$(\overline{A},\overline{B}) = \sum_{i=1}^{n}\sum_{j=1}^{m} a_{ij}b_{ij} < 0\,. \tag{3.15b}$$

Proof. Note that if (3.15a) is satisfied then from (3.4b) it follows that $\cos\varphi \geq 0$ since $\left|\overline{A}\right| > 0$ and $\left|\overline{B}\right| > 0$.

Proof of (3.15b) is similar. □

A matrix $A = [a_{ij}] \in \Re^{n \times m}$ is called the Metzler matrix if $a_{ij} \geq 0$ for $i \neq j$, $i, j = 1,...,n$. The set of $n \times n$ Metzler matrices will we denoted by M_n. By Theorem 2.5 the Metzler matrix is asymptotically stable (Hurwitz) if and only if there exists a strictly positive vector $\lambda = [\lambda_1,...,\lambda_n]$, $\lambda_k > 0$, $k = 1...,n$ such that the condition (2.5) is satisfied.

Examples of electrical circuits with Metzler state matrix A are given in [19].

Theorem 3.3. The angle φ between two asymptotically stable Metzler matrices $A = [a_{ij}] \in M_n$, $B = [b_{ij}] \in M_n$ satisfies the condition $0 < \varphi < \frac{\pi}{2}$.

Proof. From (2.5) it follows that the diagonal entries a_{ii} and b_{ii} for $i = 1...,n$ of asymptotically stable Metzler matrices *A* and *B* are negative. In this case the condition (3.15a) is satisfied and $0 < \varphi < \frac{\pi}{2}$. □

Example 3.3. Consider the following two asymptotically stable Metzler matrices

$$A = \begin{bmatrix} -2 & 1 \\ 0 & -3 \end{bmatrix}, \quad B = \begin{bmatrix} -1 & 1 \\ 0 & -1 \end{bmatrix}. \tag{3.16}$$

Using (3.2), (3.4b) and (3.16) we obtain

$$\overline{A} = \begin{bmatrix} -2 \\ 1 \\ 0 \\ -3 \end{bmatrix}, \ \overline{B} = \begin{bmatrix} -1 \\ 1 \\ 0 \\ -1 \end{bmatrix}, \ (\overline{A}, \overline{B}) = 6, \ \left|\overline{A}\right|^2 = 14, \ \left|\overline{B}\right|^2 = 3 \tag{3.17}$$

and

$$\cos\varphi = \frac{(\overline{A}, \overline{B})}{\left|\overline{A}\right|\left|\overline{B}\right|} = \frac{6}{\sqrt{14}\sqrt{3}} = 0.926 \tag{3.18}$$

This confirms the thesis of Theorem 3.3

Example 3.4. Find the $\cos\varphi$ between asymptotically stable Metzler matrix *A* given by (3.16) and the unstable Metzler matrix

$$B = \begin{bmatrix} 1 & 1 \\ 0 & 2 \end{bmatrix}. \tag{3.19}$$

In this case we obtain

$$\overline{A} = \begin{bmatrix} -2 \\ 1 \\ 0 \\ -3 \end{bmatrix}, \ \overline{B} = \begin{bmatrix} 1 \\ 1 \\ 0 \\ 2 \end{bmatrix}, \ (\overline{A}, \overline{B}) = -7, \ \left|\overline{A}\right|^2 = 14, \ \left|\overline{B}\right|^2 = 6 \tag{3.20}$$

and

$$\cos\varphi = \frac{(\overline{A},\overline{B})}{\left|\overline{A}\right\|\overline{B}|} = \frac{-7}{\sqrt{14}\sqrt{6}} = -0.764\,, \quad \frac{\pi}{2} \le \varphi \le \pi \tag{3.21}$$

Theorem 3.4. Consider the electrical circuits shown in Fig. 3.1 with given parameters *R*, *L*, *C* for two choices of the components of their state vectors. The angles between two matrices corresponding to different choice of the state variables in state vectors is the same

$$\cos\varphi_k = \frac{(\overline{A}_{k1},\overline{A}_{k2})}{\left|\overline{A}_{k1}\right\|\overline{A}_{k2}|} = -\frac{2}{\frac{L}{R^2C}+\frac{C}{L}+\frac{L}{C}} \quad \text{for } k = 2,3,4\,. \tag{3.22}$$

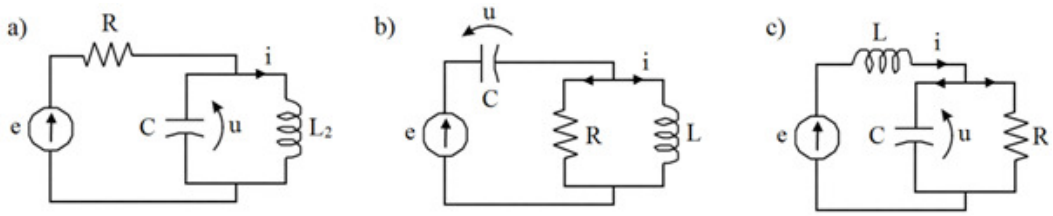

Figure 3.1. Electrical circuits.

Proof. Using (3.4b) and taking into account that

$$A_{21} = \begin{bmatrix} -\frac{1}{RC} & -\frac{1}{C} \\ \frac{1}{L} & 0 \end{bmatrix}, \quad A_{22} = \begin{bmatrix} 0 & \frac{1}{L} \\ -\frac{1}{C} & -\frac{1}{RC} \end{bmatrix}$$

we obtain

$$\overline{A}_{21} = \begin{bmatrix} -\frac{1}{RC} \\ -\frac{1}{C} \\ \frac{1}{L} \\ 0 \end{bmatrix}, \quad \overline{A}_{22} = \begin{bmatrix} 0 \\ \frac{1}{L} \\ -\frac{1}{C} \\ -\frac{1}{RC} \end{bmatrix} \tag{3.23}$$

and

$$\cos\varphi_2 = \frac{(\overline{A}_{21},\overline{A}_{22})}{\left|\overline{A}_{21}\right\|\overline{A}_{22}|} = -\frac{2}{\frac{L}{R^2C}+\frac{C}{L}+\frac{L}{C}} \tag{3.24}$$

since

$$\left|\overline{A}_{21}\right| = \left|\overline{A}_{22}\right| = \sqrt{\left(\frac{1}{RC}\right)^2 + \left(\frac{1}{L}\right)^2 + \left(\frac{1}{C}\right)^2}\,.$$

Proof for $k = 3.4$ is similar. □

Remark 3.1. For the electrical circuit shown in Fig. 3.2 the angle between two matrices A_{11} and A_{12} is given by

$$\cos\varphi_1 = \frac{(\overline{A}_{11}, \overline{A}_{12})}{\left|\overline{A}_{11}\right\|\overline{A}_{12}\right|} = -\frac{2}{\frac{R^2C}{L}+\frac{L}{C}+\frac{C}{L}} < 0 \tag{3.25}$$

and is different from the ones of Fig. 3.1.

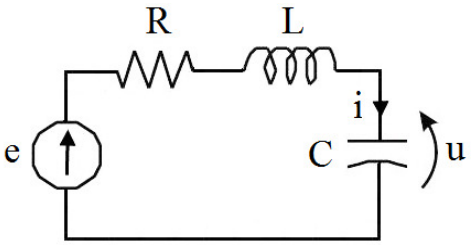

Figure 3.2. Electrical circuit.

Now let us consider the angles between the state matrices of the electrical circuits A_{k1} and their inverses A_{k1}^{-1} for $k = 1,...,4$.

Taking into account that for the electrical circuit shown in Fig. 3.2

$$A_{11} = \begin{bmatrix} 0 & \frac{1}{C} \\ -\frac{1}{L} & -\frac{R}{L} \end{bmatrix} \text{ and } A_{11}^{-1} = \begin{bmatrix} -RC & -L \\ C & 0 \end{bmatrix} \tag{3.26}$$

we obtain

$$\overline{A}_{11} = \begin{bmatrix} 0 \\ \frac{1}{C} \\ -\frac{1}{L} \\ -\frac{R}{L} \end{bmatrix}, \quad \overline{A}_{11}^{-1} = \begin{bmatrix} -RC \\ -L \\ C \\ 0 \end{bmatrix} \tag{3.27a}$$

and

$$\cos\overline{\varphi}_1 = \frac{(\overline{A}_{11}, \overline{A}_{11}^{-1})}{\left|\overline{A}_{11}\right\|\overline{A}_{11}^{-1}\right|} = -\frac{\frac{C}{L}+\frac{L}{C}}{\sqrt{\left(\frac{1}{C}\right)^2+\left(\frac{1}{L}\right)^2+\left(\frac{R}{L}\right)^2}\sqrt{(RC)^2+L^2+C^2}} < 0\,. \tag{3.27b}$$

For the electrical circuit shown in Fig. 3.1a we have

$$\overline{A}_{21}=\begin{bmatrix}-\dfrac{1}{RC}\\ -\dfrac{1}{C}\\ \dfrac{1}{L}\\ 0\end{bmatrix},\quad \overline{A}_{21}^{-1}=\begin{bmatrix}0\\ L\\ -C\\ -\dfrac{L}{R}\end{bmatrix} \tag{3.28a}$$

and

$$\cos\overline{\varphi}_2=\frac{(\overline{A}_{21},\overline{A}_{21}^{-1})}{\left|\overline{A}_{21}\right\|\overline{A}_{21}^{-1}\right|}=-\frac{\dfrac{C}{L}+\dfrac{L}{C}}{\sqrt{\left(\dfrac{1}{RC}\right)^2+\left(\dfrac{1}{L}\right)^2+\left(\dfrac{R}{L}\right)^2}\sqrt{L^2+C^2+\left(\dfrac{L}{R}\right)^2}}<0\,. \tag{3.28b}$$

In a similar way for the electrical circuit shown in Fig. 3.1b we obtain

$$\overline{A}_{31}=\begin{bmatrix}-\dfrac{1}{RC}\\ \dfrac{1}{C}\\ -\dfrac{1}{L}\\ 0\end{bmatrix},\quad \overline{A}_{31}^{-1}=\begin{bmatrix}0\\ -L\\ C\\ -\dfrac{L}{R}\end{bmatrix} \tag{3.29a}$$

and

$$\cos\overline{\varphi}_3=\frac{(\overline{A}_{31},\overline{A}_{31}^{-1})}{\left|\overline{A}_{31}\right\|\overline{A}_{31}^{-1}\right|}=-\frac{\dfrac{C}{L}+\dfrac{L}{C}}{\sqrt{\left(\dfrac{1}{RC}\right)^2+\left(\dfrac{1}{L}\right)^2+\left(\dfrac{1}{C}\right)^2}\sqrt{L^2+C^2+\left(\dfrac{L}{R}\right)^2}}<0\,. \tag{3.29b}$$

For the electrical circuit shown in Fig. 3.1c we obtain

$$\overline{A}_{41}=\begin{bmatrix}-\dfrac{1}{RC}\\ \dfrac{1}{C}\\ -\dfrac{1}{L}\\ 0\end{bmatrix},\quad \overline{A}_{41}^{-1}=\begin{bmatrix}0\\ -L\\ C\\ -\dfrac{L}{R}\end{bmatrix} \tag{3.30a}$$

and

$$\cos\overline{\varphi}_4=\frac{(\overline{A}_{41},\overline{A}_{41}^{-1})}{\left|\overline{A}_{41}\right\|\overline{A}_{41}^{-1}\right|}=-\frac{\dfrac{C}{L}+\dfrac{L}{C}}{\sqrt{\left(\dfrac{1}{RC}\right)^2+\left(\dfrac{1}{C}\right)^2+\left(\dfrac{1}{L}\right)^2}\sqrt{L^2+C^2+\left(\dfrac{L}{R}\right)^2}}<0\,. \tag{3.30b}$$

Conclusion 3.1. From comparison of (3.28b) and (3.29b) we have $\cos\overline{\varphi}_2=\cos\overline{\varphi}_4$ and all $\cos\overline{\varphi}_k$, $k=1,2,3,4$ are negative.

The above considerations can be extended to linear electrical circuits for $n>2$.

Theorem 3.5. Let $A \in \Re_+^{n\times n}$ and $B \in \Re_+^{n\times n}$ be $n\times n$ real matrices with nonnegative entries and at least one positive entry:

1) The angle $\varphi_{A,B}$ between the matrices A and B satisfies the condition

$$0 < \varphi_{A,B} < \frac{\pi}{2} \tag{3.31a}$$

2) The angle φ_{A,A^k} between the matrices A, A^k, $k = 1,2,...$ satisfies the condition

$$0 < \varphi_{A,A^k} < \frac{\pi}{2} \text{ for } k = 0,1,... \tag{3.31b}$$

Proof. Note that the Hadamard product of the matrices $A = [a_{ij}] \in \Re_+^{n\times n}$ and $B = [b_{ij}] \in \Re_+^{n\times n}$ is positive

$$A \circ B = \sum_{i=1}^{n} \sum_{j=1}^{m} a_{ij} b_{ij} > 0 \tag{3.32}$$

and from (3.4) we have

$$\cos\varphi_{A,B} > 0 \text{ and } 0 < \varphi_{A,B} < \frac{\pi}{2} \tag{3.33}$$

since $\left|A\right\|B\right| > 0$.

The proof of (3.31b) is similar since $A^k \in \Re_+^{n\times n}$ for $k = 0,1,...$ □

Remark 3.1. If $B = A \in \Re_+^{n\times n}$ then $\varphi_{A,A} = 0$.

Theorem 3.6. The angle φ between the Metzler Hurwitz matrix $A \in M_n$ and its inverse A^{-1} satisfies the condition

$$0 < \varphi < \frac{\pi}{2}. \tag{3.34}$$

Proof. From (3.4b) we have

$$\cos\varphi = \frac{(\overline{A}, \overline{A}^{-1})}{\left|\overline{A}\right\|\overline{A}^{-1}\right|}. \tag{3.35}$$

By assumption the matrix $A \in M_n$ is Hurwitz and it satisfies the condition (2.5). The strictly positive vector λ can be chosen as $\lambda = A^{-1}c$ for $c \in \Re_+^n$ strictly positive. Taking into account that for the Metzler Hurwitz matrix A we have $-A^{-1} \in \Re_+^{n\times n}$ and from (3.35) and (2.5) we obtain (3.34) since $\cos\varphi > 0$. □

Example 3.5. Consider the Metzler matrix

$$A = \begin{bmatrix} -2 & 1 & 0 \\ 2 & -3 & 1 \\ 0 & 1 & -3 \end{bmatrix} \tag{3.36}$$

which is Hutwitz since the condition (3.25) is satisfied for

$$\lambda = A^{-1}c = \frac{1}{10}\begin{bmatrix} 8 & 3 & 1 \\ 6 & 6 & 2 \\ 2 & 2 & 4 \end{bmatrix}\begin{bmatrix} 1 \\ 1 \\ 1 \end{bmatrix} = \frac{1}{5}\begin{bmatrix} 6 \\ 7 \\ 4 \end{bmatrix},\ c = \begin{bmatrix} 1 & 1 & 1 \end{bmatrix}^T. \tag{3.37}$$

Using (3.35), (3.36) and (3.37) we obtain

$$\overline{A} = [-2\ \ 1\ \ 0\ \ 2\ \ -3\ \ 1\ \ 0\ \ 1\ \ -3]^T,\quad \overline{A}^{-1} = -\frac{1}{10}[8\ \ 3\ \ 1\ \ 6\ \ 6\ \ 2\ \ 2\ \ 2\ \ 4]^T$$

$$(\overline{A}, \overline{A}^{-1}) = -\frac{1}{10}(-16+3+12-18+2+2-12) = \frac{25}{10} > 0 \tag{3.38}$$

and from (3.31) $\cos\varphi > 0$ and $0 < \varphi < \frac{\pi}{2}$ since $\left|\overline{A}\right\|\overline{A}^{-1}\right| > 0$.

Example 3.6. Consider the electrical circuit shown in Fig. 3.3 with given resistances R_1, R_2, R_3, inductances L_1, L_2 and source voltages e_1, e_2.

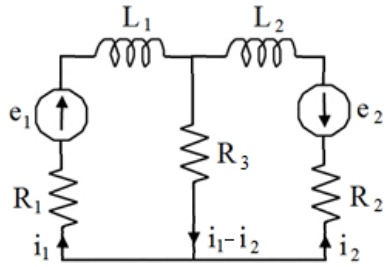

Figure 3.3. Electrical circuit.

Using the Kirchhoff's laws we may write the equations

$$\begin{aligned} e_1 &= (R_1 + R_3)i_1 - R_3 i_2 + L_1 \frac{di_1}{dt}, \\ e_2 &= (R_2 + R_3)i_2 - R_3 i_1 + L_2 \frac{di_2}{dt}. \end{aligned} \tag{3.39}$$

The equations (3.39) can be written in the form

$$\frac{d}{dt}\begin{bmatrix} i_1 \\ i_2 \end{bmatrix} = A\begin{bmatrix} i_1 \\ i_2 \end{bmatrix} + B\begin{bmatrix} e_1 \\ e_2 \end{bmatrix} \tag{3.40a}$$

where

$$A = \begin{bmatrix} -\frac{R_1 + R_3}{L_1} & \frac{R_3}{L_1} \\ \frac{R_3}{L_2} & -\frac{R_2 + R_3}{L_2} \end{bmatrix},\quad B = \begin{bmatrix} \frac{1}{L_1} & 0 \\ 0 & \frac{1}{L_2} \end{bmatrix}. \tag{3.40b}$$

For $R_k > 0$, $k = 1,2$ and $L_i > 0$, $i = 1,2$ the matrix A is Metzler Hurwitz matrix and its inverse has the form

$$A^{-1} = -\frac{1}{R}\begin{bmatrix} (R_2 + R_3)L_1 & R_3 L_2 \\ R_3 L_1 & (R_1 + R_3)L_2 \end{bmatrix},\quad R = R_1(R_2 + R_3) + R_2 R_3. \tag{3.41}$$

The angle $\varphi_{A,A^{-1}}$ between the matrices A and A^{-1} is given by

$$\varphi_{A,A^{-1}} = \arccos\frac{(\overline{A}, \overline{A}^{-1})}{\left|\overline{A}\right\|\overline{A}^{-1}\right|} = \arccos\left\{\left[2\frac{(R_1 + R_3)(R_2 + R_3)}{R} - \frac{R_3^2}{R}\left(\frac{L_1}{L_2} + \frac{L_2}{L_1}\right)\right]\frac{1}{\left|\overline{A}\right\|\overline{A}^{-1}\right|}\right\} \tag{3.42a}$$

where

$$\left|\overline{A}\right|^2 = \left(\frac{R_1 + R_3}{L_1}\right)^2 + 2\left(\frac{R_3}{L_2}\right)^2 + \left(\frac{R_2 + R_3}{L_2}\right)^2,$$
$$\left|\overline{A}^{-1}\right|^2 = \left(\frac{(R_2 + R_3)L_1}{R}\right)^2 + R_3^2\left(\frac{L_1^2 + L_2^2}{R}\right)^2 + \left(\frac{(R_1 + R_3)L_2}{R}\right)^2. \tag{3.42b}$$

In particular case when $L_1 = L_2$ we obtain

$$\varphi_{A,A^{-1}} = \arccos\frac{2}{\left|\overline{A}\right\|\overline{A}^{-1}\right|}. \tag{3.43}$$

Example 3.7. Consider the electrical circuit shown in Fig. 3.4 with given resistances R_1, R_2, inductance *L*, capacitance *C* and source voltage *e*.

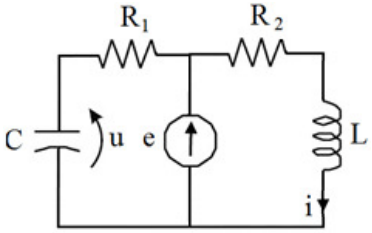

Figure 3.4. Electrical circuit.

Using the Kirchhoff's laws we may write the equations

$$\begin{aligned} e &= u + R_1 C\frac{du}{dt} \\ e &= R_2 i + L\frac{di}{dt} \end{aligned} \tag{3.44}$$

which can be written in the form

$$\frac{d}{dt}\begin{bmatrix} u \\ i_2 \end{bmatrix} = A\begin{bmatrix} u \\ i_2 \end{bmatrix} + Be \tag{3.45a}$$

where

$$A = \begin{bmatrix} -\frac{1}{R_1 C} & 0 \\ 0 & -\frac{R_2}{L} \end{bmatrix}, \quad B = \begin{bmatrix} \frac{1}{R_1 C} \\ \frac{1}{L} \end{bmatrix}. \tag{3.45b}$$

From (3.45b) it follows that the electrical circuit is positive and asymptotically stable.

The inverse matrix of *A* has the form

$$A^{-1} = \begin{bmatrix} -R_1 C & 0 \\ 0 & -\frac{L}{R_2} \end{bmatrix}. \tag{3.46}$$

The angle $\varphi_{A,A^{-1}}$ between the matrices A and A^{-1} is given by

$$\varphi_{A,A^{-1}} = \arccos \frac{(\overline{A}, \overline{A}^{-1})}{\left\|\overline{A}\right\|\left\|\overline{A}^{-1}\right\|} = \frac{2}{\sqrt{2+\left(\frac{R_1R_2C}{L}\right)^2+\left(\frac{L}{R_1R_2C}\right)^2}} \tag{3.47}$$

and $0 < \varphi_{A,A^{-1}} < \frac{\pi}{2}$.

4. ANGLES BETWEEN MATRICES AND THEIR FUNCTIONS

Let $T \in \Re^{n\times n}$ be a nonsingular matrix which transforms the matrix $A \in \Re^{n\times n}$ to its diagonal form

$$T^{-1}AT = \mathrm{diag}[\lambda_1,...,\lambda_n], \tag{4.1}$$

where λ_k, $k = 1,...,n$ are the eigenvalues of the matrix A.

Let $f(\lambda)$ be a scalar function well defined on the spectrum of the matrix A, i.e. $f(\lambda_k)$ has finite values for $k = 1,...,n$.

Then the matrix function $f(A) \in \Re^{n\times n}$ can be written in the form [4, 15]

$$f(A) = T\,\mathrm{diag}[f(\lambda_1),...,f(\lambda_n)]T^{-1}. \tag{4.2}$$

Example 4.1. The characteristic polynomial of the matrix

$$A = \begin{bmatrix} -2 & 1 \\ 2 & -3 \end{bmatrix} \tag{4.3}$$

has the form

$$\det[I_2\lambda - A] = \begin{vmatrix} \lambda+2 & -1 \\ -2 & \lambda+3 \end{vmatrix} = \lambda^2 + 5\lambda + 4 \tag{4.4}$$

and its zeros are $\lambda_1 = -1$, $\lambda_2 = -4$. Therefore, the spectrum of the matrix (4.3) is {-1, -4}.

The matrix T transforming the matrix (4.3) to its diagonal form is

$$T = \begin{bmatrix} 1 & -1 \\ 1 & 2 \end{bmatrix} \tag{4.5}$$

since

$$T^{-1}AT = \frac{1}{3}\begin{bmatrix} 2 & 1 \\ -1 & 1 \end{bmatrix}\begin{bmatrix} -2 & 1 \\ 2 & -3 \end{bmatrix}\begin{bmatrix} 1 & -1 \\ 1 & 2 \end{bmatrix} = \begin{bmatrix} -1 & 0 \\ 0 & -4 \end{bmatrix}. \tag{4.6}$$

Using (4.2) in particular case for $f(A) = e^{At}$ and (4.3) we obtain

$$e^{At} = \exp\begin{bmatrix} -2 & 1 \\ 2 & -3 \end{bmatrix} = \begin{bmatrix} 1 & -1 \\ 1 & 2 \end{bmatrix}\begin{bmatrix} e^{-t} & 0 \\ 0 & e^{-4t} \end{bmatrix}\begin{bmatrix} \frac{2}{3} & \frac{1}{3} \\ -\frac{1}{3} & \frac{1}{3} \end{bmatrix} = \begin{bmatrix} \frac{2}{3}e^{-t}+\frac{1}{3}e^{-4t} & \frac{1}{3}(e^{-t}+e^{-4t}) \\ \frac{2}{3}(e^{-t}-e^{-4t}) & \frac{1}{3}e^{-t}+\frac{2}{3}e^{-4t} \end{bmatrix}. \tag{4.7}$$

Using (3.4a) we may define the angle φ between the matrices A and $f(A)$ as follows

Definition 4.1. The angle defined by

$$\varphi = \arccos \frac{(\overline{A}, \bar{f}(A))}{\left|\overline{A}\right\| \bar{f}(A)|} \tag{4.8}$$

is called the angle between the matrices A and $f(A)$.

In particular case for $f(A) = A^{-1}$ we have

$$\varphi = \arccos \frac{(\overline{A}, \overline{A}^{-1})}{\left|\overline{A}\right\| \overline{A}^{-1}|} . \tag{4.9}$$

Example 4.2. (Continuation of Example 4.1). Find the angle between the matrices A^{-1} and A, e^{At} for (4.3).

In the first case taking into account that for (4.3)

$$A^{-1} = \begin{bmatrix} -2 & 1 \\ 2 & -3 \end{bmatrix}^{-1} = -\frac{1}{4}\begin{bmatrix} 3 & 1 \\ 2 & 2 \end{bmatrix} \tag{4.10}$$

and using (3.4b) we obtain $\overline{A} = [-2,1,2,-3]$ and $\overline{A}^{-1} = -\left[\frac{3}{4}, \frac{1}{4}, \frac{1}{2}, -\frac{1}{2}\right]^T$

$$\cos\varphi = \frac{(\overline{A}, \overline{A}^{-1})}{\sqrt{\left|\overline{A}\right|^2}\sqrt{\left|\overline{A}^{-1}\right|^2}} = \frac{\frac{7}{4}}{\sqrt{18}\sqrt{\frac{5}{8}}} = 0.39 , \ \varphi = 67.1° . \tag{4.11}$$

In the second case taking into account (4.8) and (4.7) we obtain $e^{\overline{A}t} = \left[\frac{2}{3}e^{-t} + \frac{1}{3}e^{-4t}, \frac{1}{3}(e^{-t} - e^{-4t}), \frac{2}{3}(e^{-t} - e^{-4t}), \frac{1}{3}e^{-t} + \frac{2}{3}e^{-4t}\right]^T$ and

$$\cos\varphi = \frac{(\overline{A}, e^{\overline{A}t})}{\sqrt{\left|\overline{A}\right|^2}\sqrt{\left|e^{\overline{A}t}\right|^2}} = \frac{-\frac{2}{3}e^{-t} - \frac{13}{3}e^{-4t}}{\sqrt{18}\sqrt{\frac{1}{3}(10e^{-2t} - 2e^{-5t} + 10e^{-8t})}} < 0 , \ t \geq 0 , \ \frac{\pi}{2} < \varphi < \pi . \tag{4.12}$$

These considerations can be extended to [4,15]:

1) any matrix functions well-defined on the spectrum of the matrix A,
2) any two matrix functions well-defined on the spectrum of the matrix A,
3) any two matrix functions well-defined on the spectrum of the matrix A and B, respectively.

5. ANGLES BETWEEN POLYNOMIALS

In this section the angles between two polynomials of linear electrical circuits will be defined and their basic properties will be established.

Consider the polynomials in variable s

$$\begin{aligned} p(s) &= p_n(s) = a_n s^n + a_{n-1}s^{n-1} + ... + a_1 s + a_0 \\ q(s) &= q_n(s) = b_m s^m + b_{m-1}s^{m-1} + ... + b_1 s + b_0 \end{aligned} \tag{5.1}$$

with constant coefficients a_i, $i = 0,1,...,n$ and b_j, $j = 0,1,...,m$.

Definition 5.1. The scalar

$$\big(p(s), q(s)\big) = \int_a^b p(s)q(s)ds \tag{5.2}$$

where a, b are given real numbers, is called the scalar product of the polynomials (5.1).

In particular case if $p(s) = q(s)$ then

$$\big(p(s), p(s)\big) = \int_a^b [p(s)]^2 ds \tag{5.3}$$

and

$$|p(s)| = \sqrt{p(s), p(s)} \tag{5.4}$$

is the module of the polynomial $p(s)$.

Using (5.2) and (5.4) we may define the angle φ between the polynomials (5.1)

Definition 5.2. The angle defined by

$$\varphi = \varphi_{p,q} = \arccos \frac{p(s), q(s)}{|p(s)\|q(s)|} \quad \text{for} \quad 0 < \varphi < \pi \tag{5.5}$$

is called the angle φ between the polynomials (4.1).

The formula (5.5) can be equivalently written in the form

$$\cos\varphi = \cos\varphi_{p,q} = \frac{\big(p(s), q(s)\big)}{|p(s)\|q(s)|}. \tag{5.6}$$

In particular case if $p(s) = q(s)$ then from(5.6) we have $\cos\varphi = 1$ and $\varphi = 0$.

Example 5.1. Find the $\cos\varphi$ between the following polynomials

$$p(s) = s^2 + 2s + 3 \text{ and } \quad q(s) = 2s + 1 \tag{5.7}$$

for $a = 1$ and $b = 2$.

Using (5.3), (5.4) and (5.7) we obtain

$$\begin{aligned} \big(p(s), q(s)\big) &= \int_1^2 p(s)q(s)ds = \int_1^2 (s^2 + 2s + 3)(2s + 1)ds \\ &= \int_1^2 (2s^3 + 5s^2 + 8s + 3)ds = \frac{1}{2}s^4 + \frac{5}{3}s^3 + 4s^2 + 3s\Big|_1^2 = 34.167 \end{aligned} \tag{5.8}$$

$$\begin{aligned} |p(s)|^2 &= \int_1^2 [p(s)]^2 ds = \int_1^2 (s^2 + 2s + 3)^2 ds = \frac{1}{5}s^5 + s^4 + \frac{10}{3}s^3 + 6s^2 + 9s\Big|_1^2 = 71.533 \\ |q(s)|^2 &= \int_1^2 [q(s)]^2 ds = \int_1^2 (4s^2 + 4s + 1)ds = \frac{4}{3}s^3 + 2s^2 + s\Big|_1^2 = 16.333 \end{aligned} \tag{5.9}$$

and

$$\cos\varphi = \frac{(p(s), q(s))}{|p(s)||q(s)|} = \frac{34{,}167}{\sqrt{34{,}182}} = 0.995\,. \tag{5.10}$$

From (5.6) it follows that

$$\cos\varphi_{p,q} = \cos\varphi_{q,p} \tag{5.11}$$

and

$$\cos\varphi_{-p,-q} = \cos\varphi_{p,q}\,. \tag{5.12}$$

Let us consider the transfer function of linear electrical circuit of the form

$$T(s) = \frac{n(s)}{d(s)} \tag{5.13}$$

where

$$n(s) = b_m s^m + b_{m-1} s^{m-1} + \ldots + b_1 s + b_0\,, \tag{5.14}$$

$$d(s) = s^n + a_{n-1} s^{n-1} + \ldots + a_1 s + a_0\,. \tag{5.15}$$

The inverse transfer function of (5.13) has the from

$$T^{-1}(s) = \frac{d(s)}{n(s)}\,. \tag{5.16}$$

From (5.5) applied to (5.13) and (5.16) we have the following conclusion.

Conclusion 5.1. The angle $\varphi_{n,d}$ between the polynomials (5.14) and (5.15) and the angle φ_T of (4.13) and $\varphi_{T^{-1}}$ of (4.16) satisfy the equalities

$$1)\quad \varphi_{n,d} = \varphi_{d,n}\,, \tag{5.17}$$

$$2)\quad \varphi_T = \varphi_{T^{-1}}\,. \tag{5.18}$$

In particular case for

$$T(s) = \frac{1}{d(s)} \tag{5.19}$$

we have

$$\varphi_T = \varphi_{T^{-1}} = \varphi_{1,d} = \varphi_{d,1}\,. \tag{5.20}$$

Remark 5.1. Note that if zeros of the polynomials (5.14) and (5.15) have negative real parts (the polynomials are asymptotically stable) when the angle $\varphi_{d,n}$ between the polynomials $d(s)$ and $n(s)$ has the same sign for all nonnegative $a \geq 0$ and $b \geq 0$ in (5.2) and (5.3). In this case we may assume for example $a = 0$ and $b = 1$.

Example 5.1. Find the angle of the transfer function

$$T(s) = \frac{n(s)}{d(s)} = \frac{2s+4}{s^2+4s+3} \tag{5.21}$$

with the poles $s_1 = -1$, $s_2 = -3$ and zero $z_1 = -2$.

Using (5.3), (5.4) and (5.21) we obtain

$$\big(n(s),d(s)\big)=\int_0^1(2s+4)(s^2+4s+3)ds=\int_0^1(2s^3+12s^2+22s+12)ds=27.5$$

$$\big|n(s)\big|^2=\int_0^1(2s+4)^2ds=\int_0^1(4s^2+16s+16)ds=25.333 \tag{5.22}$$

$$\big|d(s)\big|^2=\int_0^1(s^2+4s+3)^2ds=\int_0^1(s^4+8s^3+22s^2+24s+9)ds=30.533$$

and

$$\cos\varphi_{n,d}=\frac{\big(n(s),d(s)\big)}{\big|n(s)\big\|d(s)\big|}=\frac{27{,}5}{\sqrt{773{,}509}}\approx 0.988\,. \tag{5.23}$$

Example 5.2. (Continuation of Example 3.6) Consider the electrical circuit shown in Fig. 3.4 for $R_1=R_2=1$, $R_3=2$ and $L_1=L_2=1$.

In this case the matrices (3.40b) have the forms

$$A=\begin{bmatrix}-3 & 2\\ 2 & -3\end{bmatrix},\quad B=\begin{bmatrix}1 & 0\\ 0 & 1\end{bmatrix} \tag{5.24}$$

As the output y of the electrical circuit we choose

$$y=i_1+i_2=C\begin{bmatrix}i_1\\ i_2\end{bmatrix}\ \text{ and }\ C=\begin{bmatrix}1 & 1\end{bmatrix}. \tag{5.25}$$

The transfer matrix $T(s)$ of the electrical circuit has the from

$$T(s)=C\big[I_2s-A\big]^{-1}B=\begin{bmatrix}1 & 1\end{bmatrix}\begin{bmatrix}s+3 & -2\\ -2 & s+3\end{bmatrix}^{-1}\begin{bmatrix}1 & 0\\ 0 & 1\end{bmatrix}=\frac{1}{s^2+6s+5}\begin{bmatrix}s+5 & s+5\end{bmatrix}. \tag{5.26}$$

The angle φ_{T_1} of the transfer function

$$T_1(s)=\frac{s+5}{s^2+6s+5} \tag{5.27}$$

is equal to

$$\varphi_{T_1}=\arccos T_1(s)=\arccos\frac{s+5}{s^2+6s+5}=10{,}63^\circ \tag{5.28}$$

since

$$\big(n(s),d(s)\big)=\int_0^1(s+5)(s^2+6s+5)ds=46.417$$

$$\big|n(s)\big|^2=\int_0^1(s+5)^2ds=30.333 \tag{5.29}$$

$$\big|d(s)\big|^2=\int_0^1(s^2+6s+5)^2ds=73.533.$$

6. CONCLUDING REMARKS

The notions of angles between matrices and between polynomials of linear electrical circuits have been introduced and investigated. In analysis of angles between state matrices of linear electrical circuits the Hadamard product of two matrices has been applied and some basic properties of the angles between matrices of linear electrical circuits have been established (Theorems 3.1-3.6). The angles between matrices and their functions have been also introduced (Definition 4.1). The angles between two polynomials are defined (Definition 5.2). Some basic properties of transfer functions of linear electrical are analyzed and some new properties have been also established. The considerations are illustrated by examples of linear electrical circuits. The considerations can be extended to fractional linear electrical circuits.

Acknowledgment

The studies have been carried out in the framework of work No. S/WE/1/2016 and financed from the funds for science by the Polish Ministry of Science and Higher Education.

REFERENCES

[1] Ait Rami M. and Tadeo F., "Controller synthesis for positive linear systems with bounded controls," IEEE Transactions on Circuits and Systems 54(2), 151-155 (2007).
[2] Boyd S., El Ghaoui L., Feron E. and Balakrishnan V., Linear Matrix Inequalities in System and Control Theory, Society for Industrial and Applied Mathematics (SIAM) (1994).
[3] Farina L. and Rinaldi S., Positive Linear Systems; Theory and Applications. J. Wiley, New York (2000).
[4] Gantmacher F.R., The Theory of Matrices, Chelsea (1974).
[5] Kaczorek T., "A class of positive and stable time-varying electrical circuits, " Electrical Review 91(5), 121-124 (2015).
[6] Kaczorek T., "Constructability and observability of standard and positive electrical circuits," Electrical Review 89(7), 132-136 (2013).
[7] Kaczorek T., "Decoupling zeros of positive continuous-time linear systems and electrical circuits," Advances in Systems Science. Advances in Intelligent Systems and Computing 240, Springer, 1-15 (2014).
[8] Kaczorek T., "Infinite eigenvalue assignment by output-feedback for singular systems," Int. J. Appl. Math. Comput. Sci. 14(1), 19-23 (2004).
[9] Kaczorek T., "Minimal-phase positive electrical circuits," Electrical Review 92(3), 182-189 (2016).
[10] Kaczorek T., "Normal positive electrical circuits," IET Circuits Theory and Applications 9(5), 691-699 (2015).
[11] Kaczorek T., Positive 1D and 2D Systems. Springer-Verlag, London (2002).
[12] Kaczorek T., "Positive electrical circuits and their reachability," Archives of Electrical Engineering 60(3), 283-301 (2011).
[13] Kaczorek T., "Positive fractional linear electrical circuits," Proc. SPIE 8903, Art. No 3903-35.
[14] Kaczorek T., "Positive and stable electrical circuits with state matrices," Archives of Electrical Engineering 67(3), 563-578 (2018).
[15] Kaczorek T., "Positive unstable electrical circuits," Electrical Review 88(5a), 187-192 (2012).
[16] KaczorekT., Vectors and Matrices in Automation and Electrotechnics, WNT, Warszawa (1998) (in Polish).
[17] Kaczorek T., "Zeroing of state variables in descriptor electrical circuits by state-feedbacks," Electrical Review 89(10), 200-203 (2013).
[18] Kaczorek T. and Borawski K., "Stability of continuous-time and discrete-time linear systems with inverse state matrices," Measurement Automation Monitoring 62(4), 132-135, (2016).
[19] Kaczorek T. and Rogowski K., Fractional Linear Systems and Electrical Circuits, Studies in Systems, Decision and Control 13, Springer (2015).
[20] Kaczorek T. and Sajewski L., Transfer matrices with positive coefficients for standard and fractional positive linear systems. Proc. of MMAR, Międzyzdroje (2018).

Photocatalytic properties of nanosilver-doped TiO_2 powders

R. Belka[a], J. Kęczkowska[a]
[a] Kielce University of Technology, 25-314 Kielce, al. Tysiąclecia P.P. 7.

ABSTRACT

The article presents the impact of adding nanocolloidal silver to titanium dioxide (TiO_2) on the photocatalytic properties of the resulting mixture. Titanium dioxide layers, being the mixture of rutile and anatase, were obtained using the sol-gel method. The sol-gel method employed is relatively simple and inexpensive. What is more, it enables to modify properties and phase composition of the material obtained. The photocatalytic properties of the obtained samples were tested by measuring the absorbance of active substance solutions in the form of Methyl Orange (MO) and a steroid hormone, i.e. β-estradiol. It was proved TiO_2 powders with colloidal silver admixture had a higher catalytic efficiency.

Keywords: TiO_2, anatase phase, rutile phase, sol-gel method, Raman spectroscopy, photocatalytic properties of TiO_2

1. INTRODUCTION

The development of industry entails generation of wastewater having complex chemical composition, containing dangerous, carcinogenic and mutagenic substances. Despite the availability of many physical, chemical and biological methods, treating such wastewater has still been an important problem especially when the wastewater contains degradation-resistant substances and the ones toxic for microbes [1-2]. This is why it is so important and desirable to look for new ways of pollution removal from wastewater, including but not limited to effective, available and affordable technology.

Both the reference works [3-7] and the implemented solutions indicate Advanced Oxidation Processes (AOP), employing high oxidation potential (2.8 V) of the hydroxyl radicals OH* created in the reaction environment, are used more and more often to treat wastewater containing complex and not readily biodegradable organic compounds. In such conditions organic pollutants are decomposed into chemicals of a simpler chemical form, and finally they are mineralised to CO_2 and H_2O. One of processes classified as AOP is a heterogeneous photocatalysis using titanium dioxide. An example of using the photocatalytic properties of TiO_2 is employing it to remove residues of medication, hormones and steroids from wastewater [8-11].

The efficiency and effectiveness of the photocatalytic organic pollution decomposition reaction in the presence of titanium dioxide are conditional on the radiation intensity, irradiation duration, solution oxygenation degree, temperature, pH value, concentration of the pollution removed and the concentration of the photocatalyst and its physico-chemical properties.

Thanks to its photocatalytic properties, titanium oxide (IV) is a compound of very high application potential. According to the reference works, amorphous titanium oxide form is almost inactive for photocatalysis [12]. The most active form of titanium oxide for photocatalysis is considered anatase [13–16]. Rutile displays much lower photocatalytic activity than anatase which results from a higher temperature required to obtain it [14, 17]. It was proved also [18, 19] the mixture of anatase (70-75%) and rutile (30-25%) has a much higher photocatalytic activity than pure anatase.

To improve catalytic properties of TiO_2, oxide layers can be enriched with different elements (metal ions or non-metal atoms). The valence of the metal ions introduced is decisive for TiO_2 activity. According to reference works, modifying titanium oxide with metal ions of the identical charge as Ti ion results in changed interactions between metal atoms. For example, adding Ce^{4+} ions to titanium oxide reduces photoactivity which results from increased speed of charge carrier recombination [20]. However, if metal ions with the valence lower than Ti^{4+} are introduced into TiO_2 structure (e.g. Y^{3+}, La^{3+}, Nd^{3+}, Pd^{2+}), a new energy state appears near the edge of the photocatalyst valence band. This results in extending the recombination process for the electron-hole pairs [21, 22]. The non-metals improving TiO_2 photoactivity include e.g. carbon, sulphur, boron, phosphorus, fluorine and iodine [23-27]. Admixing element atoms to TiO_2 can lead to narrowing the band gap, appearance of new energy states and oxygen vacancies. The band gap narrowing results from shifting the maximum radiation absorption towards higher wavelengths and replacing e.g. by sulphur or nitrogen. New band gaps are created as a result of admixing carbon or nitrogen to titanium dioxide.

*j.keczkowska@tu.kielce.pl

Photonics Applications in Astronomy, Communications, Industry, and High-Energy Physics Experiments 2019,
edited by Ryszard S. Romaniuk, Maciej Linczuk, Proc. of SPIE Vol. 11176, 111764Q
© 2019 SPIE · CCC code: 0277-786X/19/$21 · doi: 10.1117/12.2536619

At present, high research interest is enjoyed by the systems where TiO_2 is modified by two atom types at the same time [29, 30]. For bimetallic admixtures, the catalytic, electron and optical properties differ frequently from the properties of pure metallic constituents [31].

2. EXPERIMENTAL

2.1. Samples preparation

The studied titanium dioxide (TiO_2) powders were obtained using a sol-gel method. The first stage was preparing a solution (a sol). The sol preparation process is based on the well-known sol-gel method where the precursor of TiO_2 was titanium tetraisopropoxide, i.e. $Ti(OCH(CH_3)_2)_4$, TTIP. The solution was prepared as follows: 10 ml TTIP was pipetted (pipetting duration 50 minutes) to the flask containing a mixture of 60 ml of distilled water (or a water solution of a colloidal silver, ensuring the final concentration of Ag content) and 90 ml of isopropanol, with catalytic substances added (acetic acid). The stabiliser for the colloidal solution was acetyloacetone (AcAcH) in the amount of ca. 3.5 ml. The obtained solutions were stirred intensely in room temperature for 120 min using a magnetic pendulum model MS11HS. Next, the samples were dried for a couple of days. In the second stage, the gel was calcinated in 550^{o}C for several hours. The detailed information on the process parameters and the list of studied samples is presented in Table 1.

Table 1. List of the samples with the technological process parameters

Sample symbol	H_2O :TTIP stoichiometry	TTIP:AcAcH stoichiometry	Acid type and quantity	Ag content [%]	Calcination time at 550^{o}C
T1	6:1	1:1	Nitric acid – 2 ml	0	~100 min
T3			Acetic acid – 20ml	0	~100 min
T4				1	~ 240 min
T5				0.5	~240 min

2.2. Experimental setup

To determine the phase composition of the prepared samples, the tests were carried out with the Raman spectrometry. The Raman spectra measurements were carried out using automated micro-Raman Nicolet Almega XR spectrometer (Thermo Scientific). The measurements were carried out in ambient temperature for the excitation wavelength of 532 nm. A laser beam with a power of approximately 2.5 mW was used. Spectra acquisition was performed for spectral range 100-4000 cm^{-1}. Measurements were made in a micro mode using the integrated BX51 microscope (Olympus).

To determine photocatalytic properties, the method of measuring the absorbance of the solution was used. Transmittance measurements were carried out using spectrophotometer Jasco V-670, in the range of 200–800 nm, with the resolution of 1 nm. The solutions were placed in standard quartz cuvettes with 10 mm optical path length. It was assumed the absorbance values, according to Beer-Lambert law, are proportional to the concentration of the analyzed substances.

3. RESULTS

3.1. Raman spectra

Raman Spectroscopy is a useful method of identification, enabling to distinguish the anatase phase from the rutile phase. Standard group theory analysis suggests that the Raman active modes of TiO_2 are distributed into the irreducible representations as $A_{1g}+2B_{1g}+3E_g$ and as $A_{1g}+B_{1g}+B_{2g}+E_g$ for anatase and rutile respectively [32, 33]. In the rutile spectrum, there are three main bands of positions: 605, 439 and 226 cm^{-1}, as well as weaker bands of positions 570, 404 cm^{-1} [34]. The Raman spectra of TiO_2 anatase show a strong band at about 143 cm^{-1} and four other bands at 197, 399, 513 and 639 cm^{-1}, which come from the optical vibration modes belonging to the $E_g(\nu6)$, $E_g(\nu5)$, $B_{1g}(\nu4)$, $A_{1g}+B_{1g}(\nu3+\nu2)$ and $E_g(\nu1)$ irreducible representations [35, 36].

Raman spectra of the examined samples, together with the reference spectrum, were presented in figure 1. These spectra can be assigned to the anatase phase without the presence of the rutile or brookite phases, in line with the XRD analysis [33]. It was observed that the calcination temperature increase results in the appearance of bands characteristic of rutile phase in the spectra of the studied samples. In the Raman spectrum of sample 1, obtained in the lowest calcination temperature, solely a band with the peak at about ~143 cm^{-1} ($E_g(\nu6)$ mode) was observed which can be interpreted as a band characteristic of anatase phase.

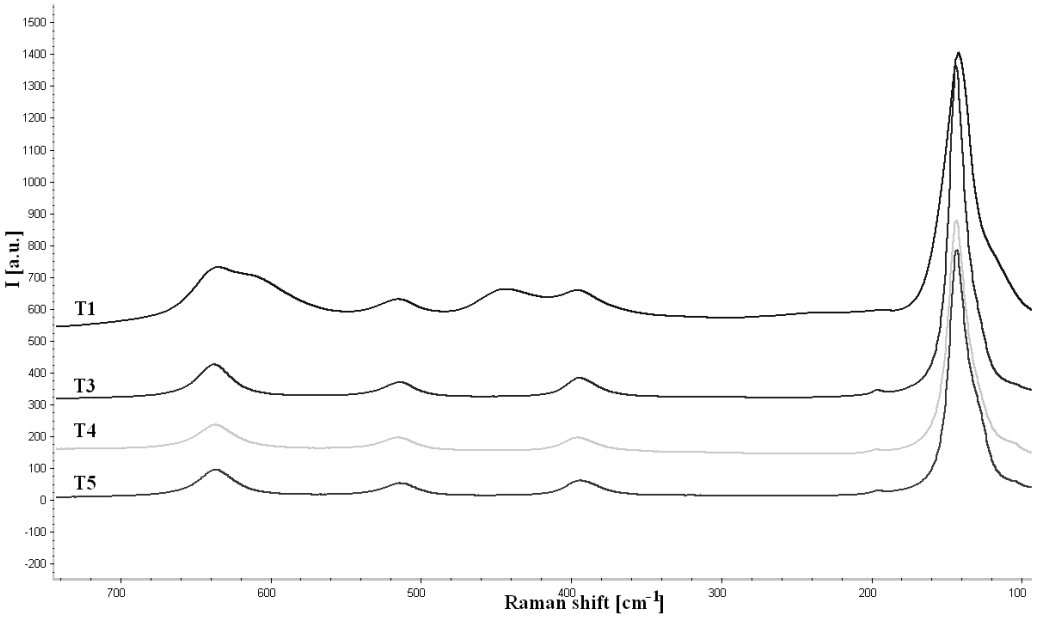

Figure 1. Raman spectra for samples 1–5 in spectral region: 100–800 cm^{-1}.

To determine the dominant band parameters of E_g(ν6) mode (characteristic of anatase), the obtained spectra were decomposed into constituent bands using Voigt function. The dominant band parameters (FWHM — full width at half maximum, peak position, intensity) are presented in table 2.

Table 2. Band analysis of Raman spectra (where: FWHM — full width at half maximum, I — intensity, ω — peak position)

Sample	T1			T3			T4			T5		
Mode	ω [cm^{-1}]	I [a.u.]	FWHM	ω [cm^{-1}]	I [a.u.]	FWHM	ω [cm^{-1}]	I [a.u.]	FWHM	ω [cm^{-1}]	I [a.u.]	FWHM
E_g(ν6)	142	520	4.1	143	1600	1.61	143	720	1.46	142	736	1.47
E_g(ν5)	196	0.66	3.8	-	-	-	-	-	-	-	-	-
B_{1g}(ν4)	394	35	14	394	100	13	395	45	14	393	49	14
Rutil	443	36	18	-	-	-	-	-	-	-	-	-
A_{1g}+B_{1g} (ν3+ν2)	515	27	13	515	82	12	516	41	14	515	40	14
Rutil	603	37	20	-	-	-	-	-	-	-	-	-
E_g(ν1)	637	60	18	638	166	14	637	75	15	637	82	14

3.2. Studying photocatalytic properties

Photocatalytic properties were studied based on the decomposition of the azo dye, i.e. Methyl Orange ($C_{14}H_{14}N_3NaO_3S$, MO) and on the steroid hormone β-estradiol (Estra-1,3,5(10)-triene-3,17β-diol) – both Sigma Aldrich. To determine the photocatalytic properties of the obtained samples, the method of measuring absorbance of solutions of substances subject to catalytic degradation was employed.

Photocatalytic decomposition of Methyl Orange (MO)

The four samples with the volume of 20 ml each were made from the water solution of MO with the 0.0025% wt. concentration. ~ 25±2 mg of T3, T4 and T5 photocatalysts were added to three of them. The T1 sample, due to the presence of rutile, was not taken into account in catalytic studies. The fourth sample was a reference one (with no photocatalyst added). Next, the solutions prepared in this way were exposed to UVA light (λ>320nm) 80W for 5 days. Absorption spectra of solutions after 5 days of exposure to light are presented in figure 2. It was found out the concentration of the catalysed substance (MO) was lowest when the catalyst in the form of TiO_2 with 1% by weight of Ag added was used (sample T4). According to the measurements, it was ~ 53.5% of the initial value, when compared to ~63.7% for T5 sample (TiO_2 + 0.5% by weight of Ag) and ~72.3% for pure TiO_2 (T3). Based on the results obtained, it

can be claimed the introduction of small amounts of colloidal silver to the prepared sol increased the efficiency of titanium oxide photocatalytic reaction.

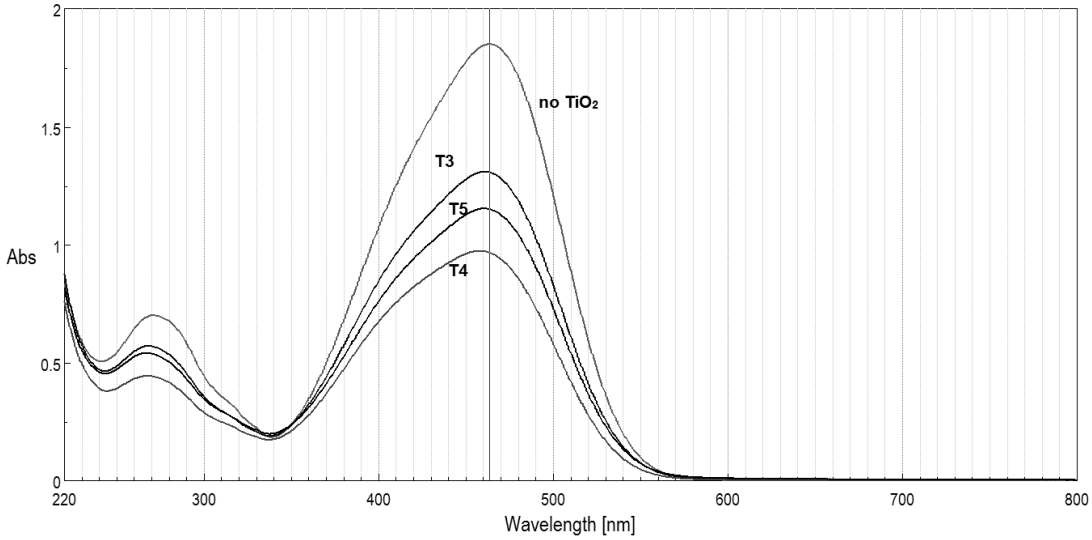

Figure 2 Absorption spectra of solutions after 5 days of exposure to light.

Figure 3 illustrates the influence of irradiation on changing the absorbance/MO concentration. The obtained results indicate the photocatalytic processes were clearly faster when photocatalysts with nanosilver admixture where used. Simultaneously, they prove the photocatalysis process does not take place if there is no irradiation. Nanosilver is not an independent reaction catalyst, but gets active in the presence of optical radiation.

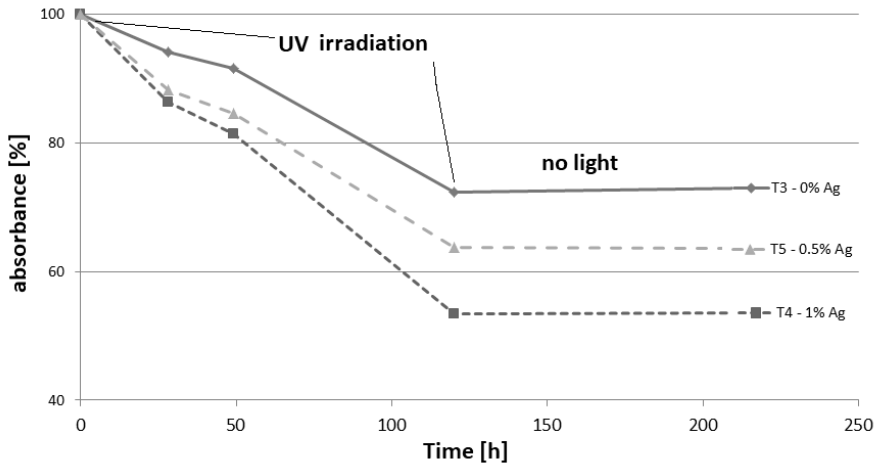

Figure 3. Change of absorbance versus irradiation time.

Photocatalytic degradation of the steroid hormone, β-estradiol

The hormone solutions in the mixture of water and isopropanol were prepared with the concentration of 0.01% by weight, and equal amounts (50mg ± 2 mg) of photocatalysts T3, T4 and T5 added. The isopropyl alcohol ensured efficient hormone solubility which is insufficient when pure water is used. The solutions prepared in this way were exposed to light for 14 days. Measurements were carried out after 1, 5, 9 and 14 days of irradiation.
The received absorbance spectra for individual samples are presented in fig. 4. In the absorbance spectrum, two bands characteristic of β-estradiol were observed with the peak at 279 nm and 288 nm [38].

a)

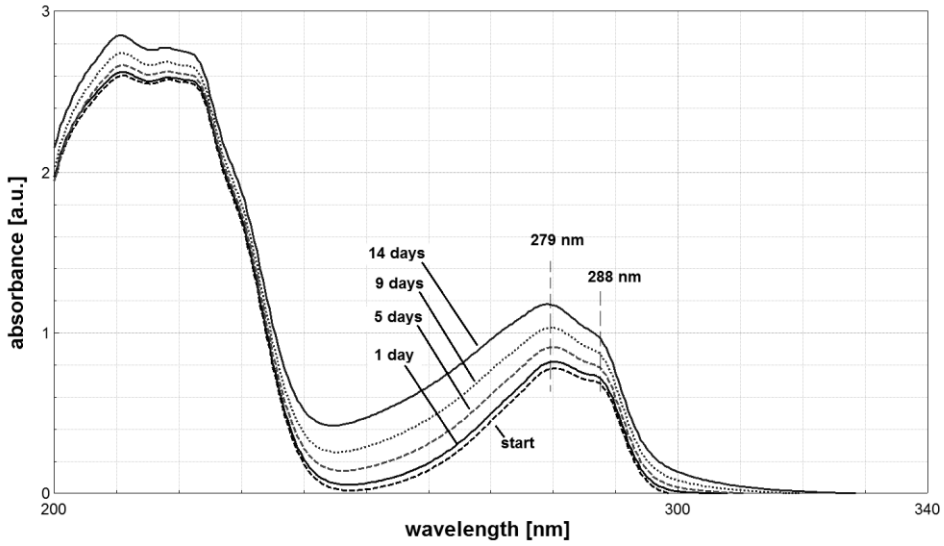

b)

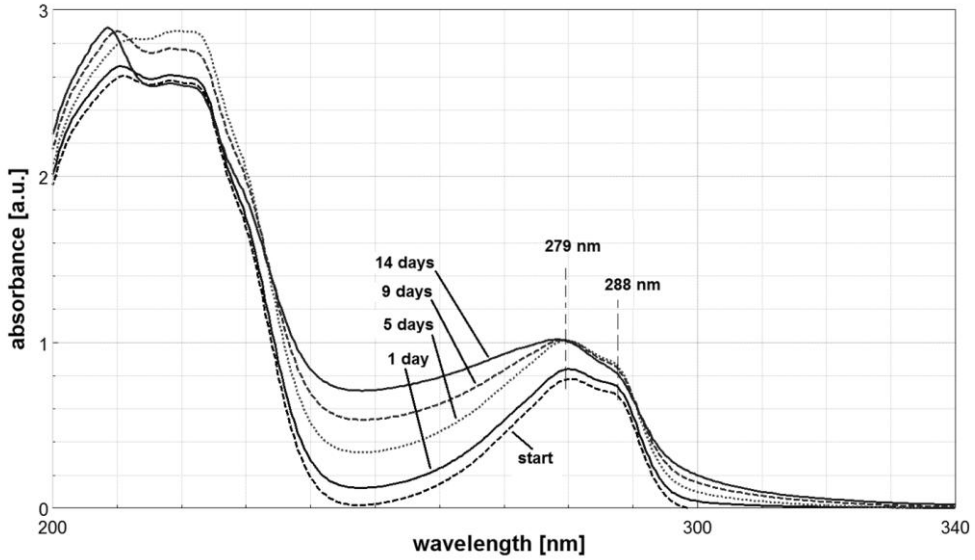

Figure 4. Absorption spectra for β-estradiol solutions containing pure TiO_2 catalyst (a), and 1% Ag-doped catalyst (b) after 0, 1, 5, 9 and 14 days of irradiation.

Absorption spectra point to some transformations of an unspecified type underwent by the hormone in the photocatalyst presence. Absorbance grows instead of decreasing which is connected with the appearance of an additional and relatively wide band with the peak at ca. 265 nm. Consequently, based thereon it is not possible to determine if a complete decomposition/oxidation of the hormone takes place here, as for MO. The said transformation seems more conspicuous for samples with the photocatalyst with Ag admixture. To visualise changes better, the differential analysis of spectra was used, calculating the fourth derivative of the spectrum with the appropriately selected parameters of Savitzky-Golay filter which enabled to eliminate the slowly-changing component connected with the additional band. The results presented in figure 5 enable to determine that also in this case the bands characteristic of the hormone have a reduced intensity at 279 and 288 nm.

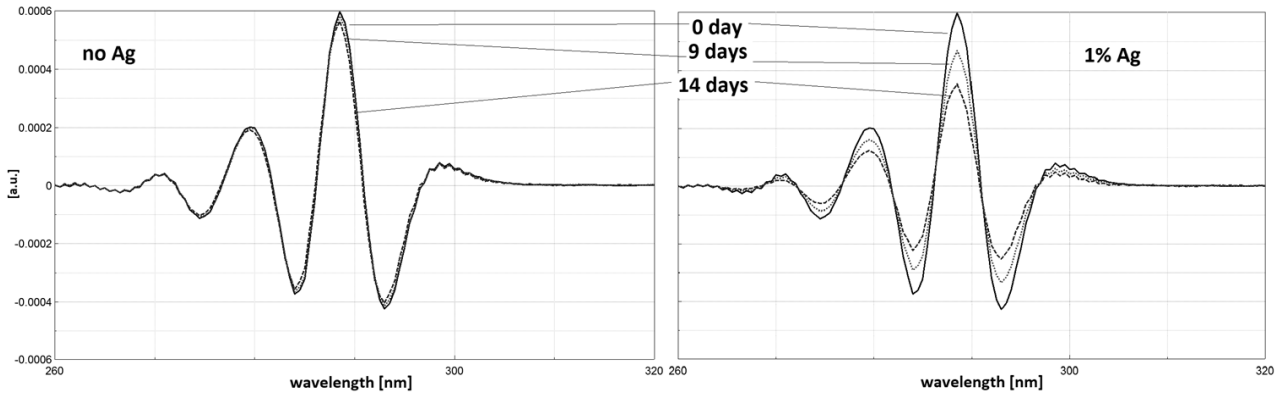

Figure 5. Analysis of the fourth derivative of the solution containing T3 (left) and T4 (right) photocatalysts.

Examinations revealed that for T4 catalyst (1% Ag) the intensity of the fourth derivative band at 279 nm fell by 44%, and at 288 nm by 47%. To compare, for T3 catalyst (no Ag) the decrease was 1.3% and 2.5% respectively.

4. CONCLUSIONS

The measurements carried out confirm higher photocatalytic efficiency of titanium dioxide in the presence of silver. It should be kept in mind the optical and catalytic properties of TiO_2/Ag composites are conditional primarily on the size and shape of particles. This is why the colloidal silver solution was used in the titanium oxide admixing process. The parameters modifying the size and shape of the obtained nanoparticles include e.g. temperature, reducing reagents used, type of dispersed phase and stabilizer type used. According to reference works [39–40], in the setups with no surfactant added and with no pH control, the metal ions adsorbed from the surface are reduced to silver. Metallic "islands" are created on titanium oxide surface and their rapid growth can lead to covering the whole surface. The mechanism of increasing titanium dioxide photocatalytic properties in the presence of colloidal nanosilver has not been fully known and requires further research works. It can be supposed, however, it may be connected with a plasmon photocatalytic effect taking place in multi-function ceramic and metallic nanocomposites. According to the reference work [41], the presence of plasmon phenomena may support the photocatalytic process due e.g. to sensitising the semi-conductor phase caused by the surface resonance, more effective charge separation in the presence of Schottky barrier, more effective charge transport (the so-called fast lane), supporting adsorption processes and, last but not least, the thermocatalytic processes accompanying this phenomenon.

ACKNOWLEDGEMENTS

The optical research was performed using equipment co-founded by the European Regional Development Fund (METROLAB project, UDA-RPSW.02.01.00-26-010/12). The Raman research was performed using equipment co-founded by the European Regional Development Fund within the Innovative Economy Operational Programme 2007-2013 (No POIG 02.02.00-26-023/08-00).

REFERENCES

[1] Kolpin, D. W., Furlong, E. T., Meyer, M. T., Thurman, E. M., Zaugg, S. D., Barber, L. B., Buxton, H. T., "Pharmaceuticals, hormones, and other organic wastewater contaminants in u.s. Streams, 1999-2000: a national reconnaissance," Environ. Sci. Technol. 36, 1202-1211 (2002).

[2] Sun, W. L., Qu, Y. Z., Yu, Q., Ni, J. R., "Adsorption of organic pollutants from coking and papermaking wastewaters by bottom ash," J. Hazard. Mater. 154, 595-601 (2008).

[3] Munter, R., "Advanced Oxidation Processes–Current Status and Prospects," Proc. Estoninian Acad. Sci. Chem. 50(2), 59-80 (2001).

[4] Oller, I., Malato, S., Sánchez-Pérez, J. A., "Combination of Advanced Oxidation Processes and biological treatments for wastewater decontamination - A review," Sci. Total Environ. 409(20), 4141-66 (2011).

[5] Stasinakis, A. S., "Use of selected advanced oxidation processes (AOPS) for wastewater treatment – a mini review," Global Nest J. 10(3), 376-385 (2008).
[6] Tong, A., Braund, R., Warren, D., Peake, B., "TiO_2-assisted photodegradation of pharmaceuticals - a review," Open Chem. 10(4), 989-1027 (2012).
[7] Sun, W. L., Li S., Mai J. X., Ni J. R., "Initial photocatalytic degradation intermediates/pathways of 17a-ethynylestradiol: Effect of pH and methanol," Chemosphere 81, 92-99 (2010).
[8] Pelaez, M., Nolan, N. T., Pillai, S. C., Seery, M. K., Falaras, P., Kontos, A. G., Dunlop, P. S. M., Hamilton, J. W. J., Byrne, J. A., O'Shea, K., et al., "A Review on the Visible Light Active TitaniumDioxide Photocatalysts for EnvironmentalApplications," Appl. Catal. B 125, 331–349 (2012).
[9] Rizzo, L., Meric, S., Guida, M., Kassinos, D., Belgiorno, V., "Heterogenous photocatalytic degradation kinetics and detoxification of an urban wastewater treatment plant effluent contaminated with pharmaceuticals," Water Res. 43, 4070–4078 (2009).
[10] Zhang, Y., Zhou, J. L., Ning, B., "Photodegradation of estrone and 17bestradiol in water," Water Res. 41, 19-26 (2007).
[11] Ohko, Y., Iuchi, K. I, Niwa, C., Tatsuma, T., Nakashima, T., Iguchi, T., Kubota, Y., Fujishima, A., "17 beta-estradiol degradation by TiO_2 photocatalysis as a means of reducing estrogenic activity," Environ. Sci. Technol. 36, 4175-4181 (2002).
[12] Carp, O., Huisman, C. L., Reller, A., "Photoinduced reactivity of titanium dioxide," Prog. Solid State Chem. 32, 33 (2004).
[13] Janus, M., Inagaki, M., Tryba, B., Toyoda, M., Morawski, A. W., „Carbon-modified TiO_2 photocatalyst by ethanol carbonization," Appl. Catal. B 63, 272-276 (2006).
[14] Inagaki, M., Nonaka, R., Tryba, B., Morawski, A. W., „Dependence of photocatalytic activity of anatase powders on their crystallinity," Chemosphere 64, 437 (2006).
[15] Li, Y. F., Liu, Z. P., „Particle size, shape and activity for photocatalysis on titania anatase nanoparticles in aqueous surroundings," J. Am. Chem. Soc. 133(39), 15743-52 (2011).
[16] Belka, R., Kęczkowska, J., "A new preparation method of rutile-anatase TiO_2 coatings for photocatalytic application," Proc. SPIE 10808, 108084H (2018).
[17] Grzechulska-Damszel, J., Morawski, A. W., Grzmil, B., „Thermally Modified Titania Photocatalysts for Phenol Removal from Water," Inter. J. Photoenergy ID 96398, 1-7 (2006).
[18] Ohno, T., Tokieda, K., Higashida, S., Matsumura, M., „Synergism between rutile and anatase TiO_2 particles in photocatalytic oxidation of naphthalene," Appl. Catal. A 244, 383-391 (2003).
[19] Muggli, D. S., Ding, L., "Photocatalytic performance of sulfated TiO_2 and Degussa P-25 TiO_2 during oxidation of organics," Appl. Catal. B: Env. 32, 181-194 (2001).
[20] Lin, J., Yu, J. C., "An investigation on photocatalytic activities of mixed TiO_2-rare earth oxides for the oxidation of acetone in air," J. Photochem. Photobiol. A 116, 63-67 (1998).
[21] Mozia, S., Heciak, A., Morawski, A. W., „Preparation of Fe-modified photocatalysts and their application for generation of useful hydrocarbons during photocatalytic decomposition of acetic acid," J. Photochem. Photobiol. A 216, 275-282 (2010).
[22] Tryba, B., Piszcz, M., Morawski, A. W., „. Photocatalytic activity of TiO_2-WO_3 composites," Int. J. Photoenergy ID 297319, 1 (2009).
[23] Janus, M., Choina, J., Morawski, A. W., "Azo dyes decomposition on new nitrogen-modified anatase TiO_2 with high adsorptivity," J. Hazard. Mater. 166, 1-5 (2009).
[24] Ohno, T., Mitsui T., Matsumura, M., "Photocatalytic Activity of S-Doped TiO_2 Photocatalyst Under Visible Light," Chem. Lett. 32(4), 364-365 (2003).
[25] Zaleska, A., Sobczak, J. W., Grabowska, E., Hupka, J., „Preparation and photocatalytic activity of boron-modified TiO_2 under UV and visible light," Appl. Catal. B 78, 92-100 (2007).
[26] Korosi, L., Dekany, I., "Preparation and invetsigationof structural and photocatalytic properties of phosphate modified titanium dioxide," Colloids Surf. A 280, 146-154 (2006).
[27] Yu, J.,C., Yu, J., Ho, W., Jiang, Z., Zhang, Z., "Effects of F^- Doping on the Photocatalytic Activity and Microstructures of Nanocrystalline TiO_2 Powders," Chem. Mater. 14, 3808-3816 (2002).
[28] Hong, X. T., Luo, Z. P., Batteas, J. D., "Enhanced visible-light absorption and dopant distribution of iodine-TiO_2 nanoparticles synthesized by a new facile two-step hydrothermal method," J. Solid State Chem. 184, 2244-9 (2011).
[29] Wang, X., Lim, T. T., "Solvothermal synthesis of C-N codoped TiO_2 and photocatalytic evaluation for bisphenol A degradation using a visible-light irradiated LED photoreactor," Appl. Catal. B 100(1-2), 355-364 (2010).

[30] Song, S., Hong, F. Y., He, Z. Q., Wang, H. Y., Xu, X. H., Chen, J. M., "Influence of zirconium doping on the activities of zirconium and iodine co-doped titanium dioxide in the decolorization of methyl orange under visible light irradiation," Appl. Surf. Sci. 257, 10101-10108 (2011).
[31] Evangelisti, C., Schiavi, E., Aronica, L. A., Caporusso, A. M., Vitulli, G., Bertinetti, L., Martra, G., Balerna, A., Mobilio, S., "Bimetallic Gold-Palladium vapour derived catalysts: The role of structural features on their catalytic activity," Journal of Catalysis 286, 224-236 (2012).
[32] Bersani, D., Lottici, P. P., Ding, X. Z., "Phonon confinement effects in the Raman scattering by TiO_2 nanocrystals," Appl. Phys. Lett. 72, 73-75 (1998).
[33] Belka, R., Kęczkowska, J., Diduszko, R., "Structural investigation of anatase prepared at different calcination temperatures of sol-gel process", Proc. SPIE 10031, 1003108 (2016)
[34] Glass, B. P., Fries, M., "Micro-Raman spectroscopic study of fine-grained, shock-metamorphosed rock fragments from the Australasian microtektite layer," Meteoritics and Planetary Science 43(9), 1487-1496 (2008).
[35] Ohsaka, T., Izumi, F., Fujiki, Y., "Raman spectrum of anatase, TiO_2," Journal of Raman Spectroscopy 7, 321-324 (1978).
[36] Zhang, W. F., He, Y. L., Zhang, M. S., Yin, Z., Chen, Q., "Raman scattering study on anatase TiO_2 nanocrystals," Journal of Physics D: Applied Physics 33, 912-916 (2000).
[37] Zhang, F., Guan N., Li Y., Zhang X., Chen J., Zeng, H., "Control of morphology of silver clusters coated on titanium dioxide during photocatalysis," Langmuir 19, 8230-8234 (2003).
[38] Yilmaz, B., Kadioglu, Y., "Determination of 17 β-estradiol in pharmaceutical preparation by UV spectrophotometry and high performance liquid chromatography methods," Arabian Journal of Chemistry 10(1), S1422-S1428 (2017).
[39] Liu, S. X., Qu, Z. P., Han, X. W., Sun, C. L., "A mechanism for enhanced photocatalytic activity of silver-loaded titanium dioxide," Catal. Today 93–95, 877–884 (2004).
[40] Li, F. B., Li, X. Z., "The enhancement of photodegradation efficiency using Pt–TiO_2 catalyst," Chemosphere 48, 1103–1111 (2002).
[41] Zhang, X., Chen, Y.L., Liu, R. and Tsai, D.P. "Plasmonic photocatalysis," Reports on Progress in Physics 76 (4), 046401 (2013).

Influence of annealing on electronic properties of thin AlN films deposited by magnetron sputtering method on silicon substrates

P. Firek*[a], M. Waskiewicz[a], K. Zdunek[b,c], J. Szmidt[a], R. Chodun[b], K. Nowakowska-Langier[c]
[a]Warsaw University of Technology, Institute of Microelectronics and Optoelectronics, Koszykowa 75, 00-662 Warszawa, Poland; [b]Warsaw University of Technology, Faculty of Materials Science and Engineering, Woloska 141, 02-507 Warsaw, Poland; [c]The Andrzej Soltan Institute for Nuclear Studies (IPJ), 05-400 Otwock-Swierk, Poland

ABSTRACT

The AlN films were deposited using magnetron (ϕ = 100 mm) and pulse power supplier (f = 100 kHz, with modulation of f = 2 kHz; current 3 A). Deposition processes were carried out at pressure of 2 Pa and using Ar/N_2 gas mixture. The films were deposited on n-type silicon wafers located in parallel to aluminum target, keeping substrate-target distance at 15 cm. Round, titanium electrodes were evaporated on the top of deposited layers. Thus, metal-insulator-semiconductor (MIS) structures were created with aluminum nitride thin films playing the role of the insulator. Measurements of current-voltage (I-V) characteristics of MIS structures after annealing in different temperatures (300°C, 500°C), allowed to determine the leakage current density and critical electric field intensity (E_{BR}) of investigated layers. Capacitance-voltage (C-V) measurements of the structures allowed to obtain the dielectric constant value (ε_{ri}) of the films. Ellipsometric measurements allowed to obtain properties of deposited layer like thickness (29 nm), refraction index (1.855) and energy band gap (5.667 eV). Films' microstructure was additionally studied using scanning electron microscope (SEM) and grazing X-ray diffraction (GXRD).

*pfirek@elka.pw.edu.pl

Keywords: aluminum nitride, thin film, annealing, magnetron sputtering, electrical properties,

1. INTRODUCTION

AlN films presents very interesting properties as e.g., isomorphous crystallographic structure, high resistivity (~10^{13} Ω cm) [1, 2], wide bandgap (6.2eV) [3, 4, 5, 6], high thermal conductivity (3.2 W/cm · K) [7]. Its melting temperature is greater than 2000 °C and the relative permittivity is about 9 [6]. All this makes AlN useful in the area of electronic, optical and acoustic applications [8, 9, 10].

Aluminum Nitride can be produced by various plasma deposition techniques [11], molecular beam epitaxy (MBE) [12], Chemical Vapor Deposition (CVD) [13], pulsed laser deposition (PLD) methods [14]. AlN deposited by magnetron sputtering method is also an attractive dielectric for electronic device application material e.g. for use with Silicon Carbide (SiC) substrates for high temperature and high-power devices [1, 2, 3, 15, 16, 17, 18]. For this purpose, in addition to the development of the AlN deposition method, preparation of layers with good electronic properties at elevated temperatures is necessary.

The development of advanced technologies is based also on the development of advanced materials, their processing [19], as well as the development of new solutions for devices [20], [21], and systems [22].

2. EXPERIMENTAL DETAILS

The AlN layers were synthesized by using two magnetrons (diameter 100mm), which were built at the Faculty of Materials Science and Engineering Warsaw University of Technology, operating in the Gemini system. In this experiment aluminum target (thickness 8mm) was used. To supply the guns 10 kW power adapter (200 kHz) switched between guns with the frequency of 2 kHz was used. Deposition processes were carried out at the pressure of 2 Pa using Ar/N_2 gas mixture and 3 A average current. The films were deposited on n-type silicon wafers located in parallel to the target, keeping substrate-target distance at 9 cm. After deposition, the thickness

Photonics Applications in Astronomy, Communications, Industry, and High-Energy Physics Experiments 2019, edited by Ryszard S. Romaniuk, Maciej Linczuk, Proc. of SPIE Vol. 11176, 111764R
© 2019 SPIE · CCC code: 0277-786X/19/$21 · doi: 10.1117/12.2536649

and refractive index of AlN layers were measured by means of ellipsometry (Horiba Jobin Yvon, UVISEL FUV 190 nm - 880 nm). Other samples were tested using Scanning Electron Microscope (SEM) and grazing X-ray diffraction (GXRD).

Round, titanium electrodes were evaporated on the top of deposited layers. Thus, metal-insulator-semiconductor (MIS) structures were created with aluminum nitride thin films playing the role of the insulator. Measurements of current-voltage (I-V) characteristics of MIS structures after annealing in different temperatures (300°C, 500°C), allowed to determine extraction of several electronic parameters (e.g. relative dielectric constant ε_{ri}, flat band voltage V_{FB}, leakage current density J_l or critical electric field intensity E_{BR}). Using titanium as electrodes' material allowed annealing MIS structures in Ar atmosphere for 30 minutes in different temperature (300°C and 500°C). This made it possible to determine changes in electrical parameters after the annealing process.

3. RESULTS

In Figure 1 the magnetron sputtering setup is presented. Fig. 2 presents the typical SEM images of the AlN layers deposited using magnetron sputtering of aluminum target. Obtained films are dense, nanocrystalline and their structure strongly depends on process parameters like e.g. Ar+N mixture pressure. The column character of layers decreases with decreasing of the pressure.

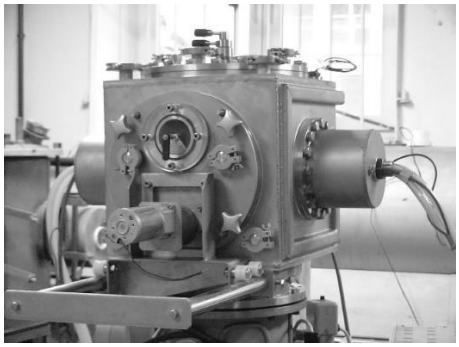

Figure 1. Magnetron Sputtering Setup.

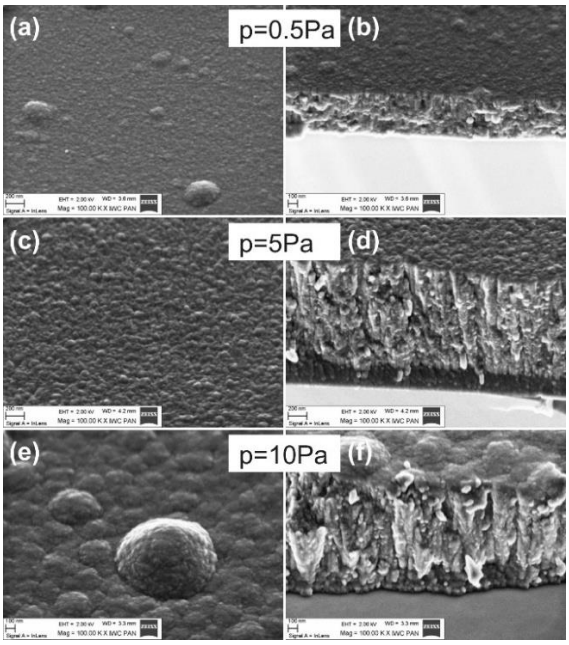

Figure 2. SEM images of AlN films. (a) (c) (e) Surface morphology of AlN film prepared with 0.5 Pa, 5 Pa and 10 Pa Ar/N2 gas pressure. (b) (d) (f) Cross-sectional image of AlN film prepared with 0.5 Pa, 5 Pa and 10 Pa Ar/N2 gas flow.

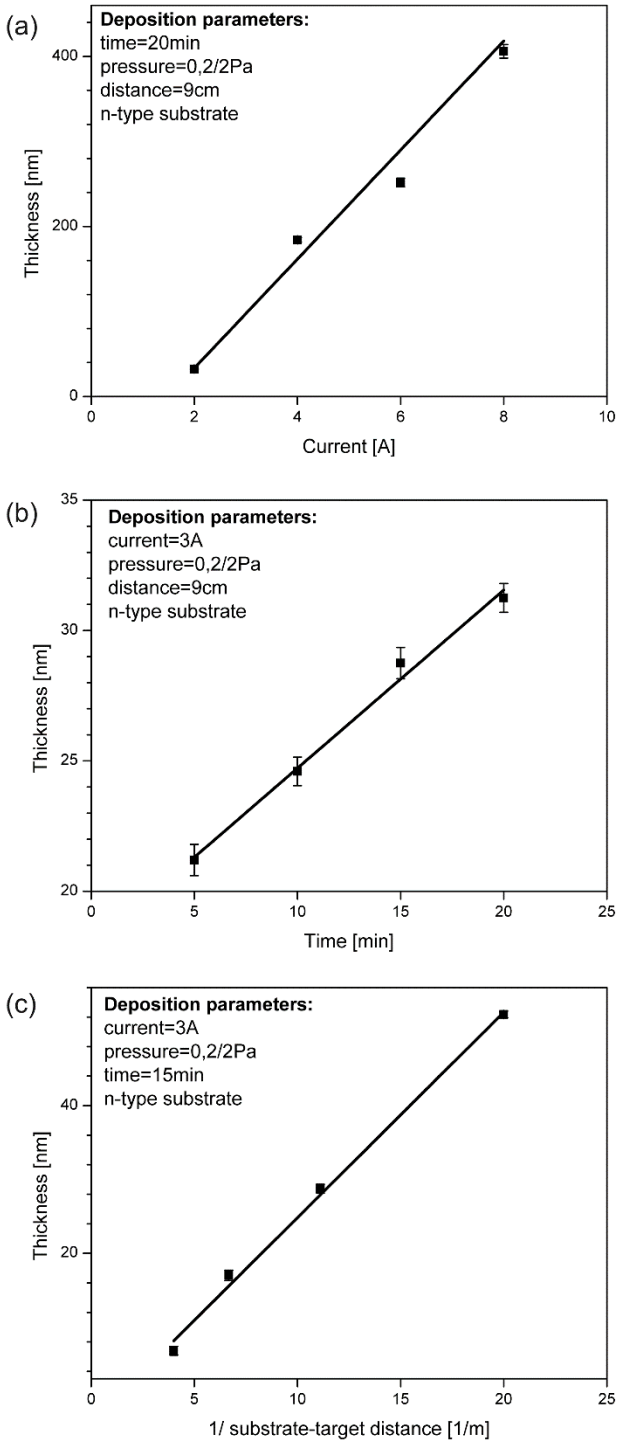

Figure 3. Ellipsometry results. (a) AlN thickness as a function of deposition current. (b) AlN thickness as a function of deposition time. (c) AlN thickness as a function of inversed target-substrate distance.

Fig. 3 shows influence of current, time and target - substrate distance on layer thickness. Thickness of obtained layers increases lineary with the increasing of deposition time and value of sputtering current, in case of target-

substrate distance dependence is reversed. Similar properties of the deposition process were shown in [23]. Refracting index of this layer is 1.85 and it is higher than obtained results in [24] (deposited by MOCVD – 1.65) subsequently lower than presented in other publications, where AlN layers were deposited by RF magnetron sputtering, like [23] (2.1), [25] (1.9-2.1). Energy bandgap before annealing was about 5,7 eV and it is slightly less than the value shown in [23]. GXRD investigations show that preferred direction of AlN crystallites is <002> (Fig. 4). The obtained diffraction value of lattice properties of synthesized AlN layers corresponds to the literature and a =3.12 nm and c = 5.02 nm.

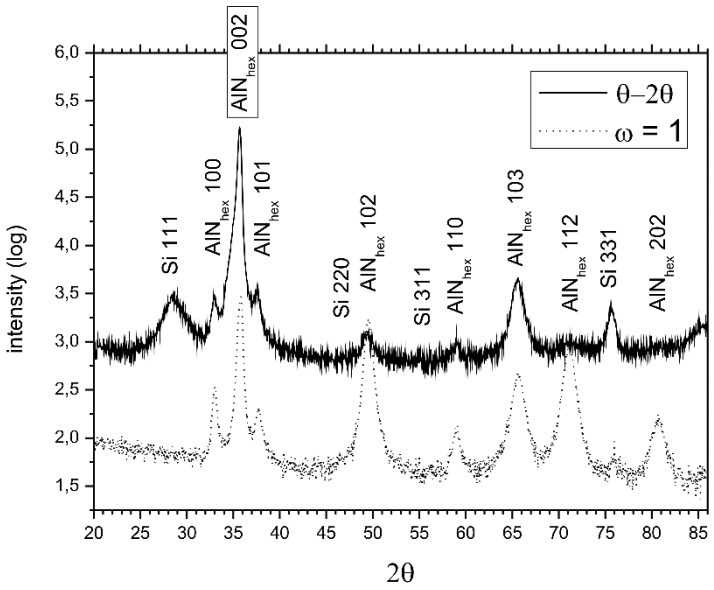

Figure 4. GXRD diffraction results.

The values of AlN layers were specified based on the electrical measurements. Evaluated parameters are collected in Table 1. Typical electric capacitance-voltage characteristics (C-V) of fabricated MIS structures are shown in Figure 5. These curves were measured at the frequency of 100kHz. Before annealing of the structures, C-V measurements were very repeatable, there was no hysteresis loop and flat band voltage V_{FB} was about 0.1V and relative dielectric constant ε_{ri} was around 5.5 (value of this parameter is lower than in other publications, eg. about 8 in [24] where AlN was deposited by MOCVD and 9.1 in [26]). Figure 6 presents typical results of I-V measurements before annealing. In all cases curves demonstrate symmetrical character and are repeatable. Majority portion of measured curves show leakage current density below 40 nA/cm^2 (for 5V) which is comparable with published values [23] and critical electric field intensity about 2.5 MV/cm which is better than published in [27] but lower than the value in [23] (4 - 12MV/cm).

Table 1. Extracted parameters of AlN layers before and after annealing in 300ºC.

Parameter	Temperature of annealing	
	-	300ºC
X_i [nm]	29	
ε_{ri}	5.5	4.3
C_{FB} [pF]	159	137
V_{FB} [V]	0.1	0.1
ΔV_H [V]	0.05	0
Q_{eff} [C/cm2]	$-1.68 \cdot 10^{-7}$	$-1.32 \cdot 10^{-7}$

After the first annealing (300°C, 30min, Ar) C-V curves were changed but they were still repeatable. Dielectric constant after this process was 4.3 and flat band voltage V_{FB} was still about 0.1V. There was a noticeable change in the leakage current density (I-V characteristics after annealing - Fig. 6) and it is below 10 nA/cm^2 (for 5V). It is important that part of the measured structures that were originally characterized by high values of leakage current presents improvement of their dielectric properties This type of I-V characteristics are shown in Figure 7.

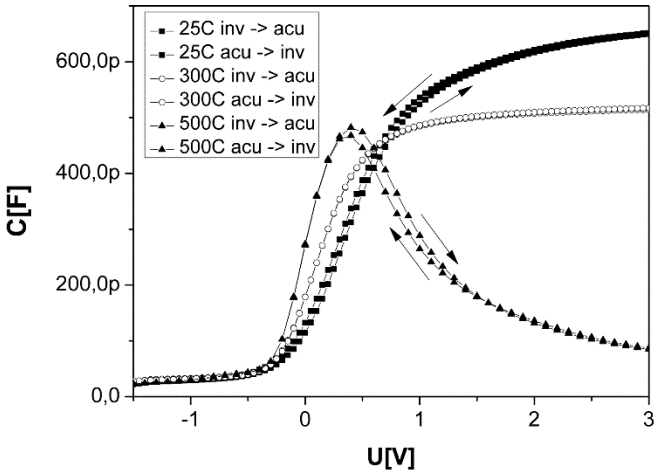

Figure 5. Typical Capacitance-Voltage characteristics of AlN layers before and after annealing in 300ºC and 500 ºC.

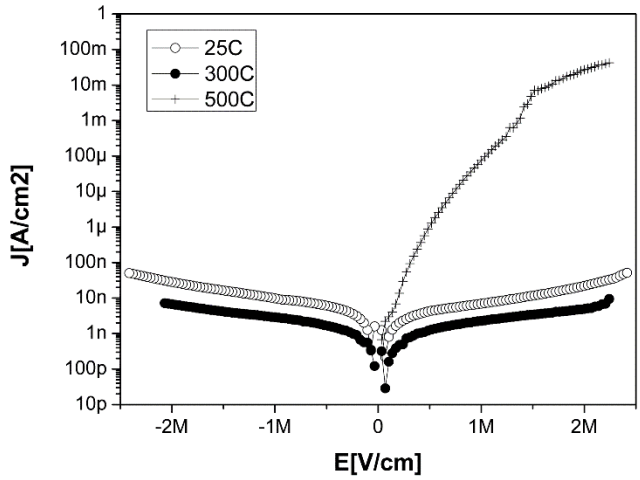

Figure 6. Typical Current-Voltage characteristics of AlN layers before and after annealing in 300ºC and 500 ºC.

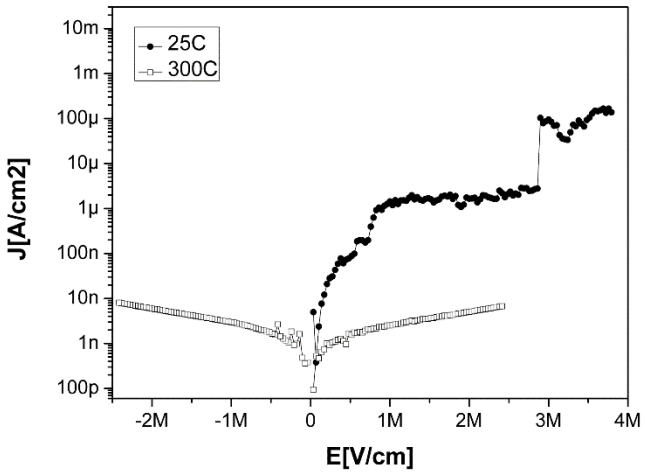

Figure 7. Improvement of Current-Voltage characteristic after annealing in 300ºC.

After the last annealing process (500°C, 30min, Ar) the leakage current was increased. It was impossible to obtain dielectric constant value of this sample. In Figure 5 leakage character of annealed structures is presented. This huge leakage current was also confirmed by I-V characteristics for this structure on Figure 6.

4. CONCLUSIONS

The AlN films obtained as a result of the magnetron sputtering of Al target, show nanocrystalline structure. Thermal annealing process (300°C) in argon atmosphere, improve the electrical properties. Simultaneously after annealing in temperature 500°C increasing of leakage current was observed.

It can be concluded that the studies on fabricated layers are very promising. The electrical parameters have the potential to allow their use in MISFET structures as a gate insulator. This is a particularly interesting topic in terms of systems to work at elevated temperatures. AlN seems to be a good material for applications in electronics in combination with silicon carbide.

REFERENCES

[1] Gielisse, P., “Wide Bandgap Materials in Future Electronic Applications,” Proc. of XXIV International Conference IMAPS Poland, 115-123 (2000).

[2] Mohammad, S. N. and Morkoc, H., “Progress and Prospects of Group-III Nitride Semiconductors,” Progress in Quantum Electronics 20(No. 5/6), 361-525 (1996).

[3] Venkataraj, S., Severin, D., Drese, R., Koerfer, F. and Wuttig, M., “Structural, optical and mechanical properties of aluminium nitride films prepared by reactive DC magnetron sputtering,” Thin Solid Films Vol. 502 No. 1, 235-239 (2006).

[4] Galca, A. C., Stan, G. E., Trinca, L. M., Negrila, C. C. and Nistor, L. C., “Structural and optical properties of c-axis oriented aluminum nitride thin films prepared at low temperature by reactive radio-frequency magnetron sputtering,” Thin Solid Films Vol. 524 No. 1, 328-333 (2012).

[5] Ababneh, A., Schmid, U., Hernando, J., Sánchez-Rojas, J. L. and Seidel, H., “The influence of sputter deposition parameters on piezoelectric and mechanical properties of AlN thin films,” Materials Science and Engineering B Vol. 172 No. 3, 253-258 (2010).

[6] Rowland, L. B., Kern, R. S., Tanaka, S. and Davis, R.F., “Aluminum nitride/silicon carbide multilayer heterostructure produced by plasma-assisted, gas-source molecular beam epitaxy,” Applied Physics Letters Vol. 62 No. 25, 3333-3335 (1993).

[7] Belkerk, B.E., Soussou, A., Carette, M., Djouadi, M. A. and Scudeller, Y., "Structural-dependent thermal conductivity of aluminium nitride produced by reactive direct current magnetron sputtering," Applied Physics Letters Vol. 101, 151908-1 - 151908-4 (2012).
[8] Assouar, M. B., Elmazria, O., Hakiki, M. and Alnot, P., "Study of acoustical and optical properties of AlN films for saw and baw devices: correlation between these properties," Integrated Ferroelectrics Vol. 82 No.1, 45-54 (2006).
[9] Caban, P., Rudzinski, M., Wojcik, M., Gaca, J. and Strupinski, W., "Growth of aluminium nitride with linear change of ammonia flow," Journal of Crystal Growth Vol. 414, 81-86 (2015).
[10] Firek, P., Wáskiewicz, M., Stonio, B. and Szmidt, J., "Properties of AlN thin films deposited by means of magnetron sputtering for ISFET applications," Materials Science-Poland Vol. 33 No. 4, 669–676 (2015).
[11] Szmidt, J., "Electronic Properties of Nanocrystalline Layers of Wide-Band-Gap Materials," Chaos. Solitons & Fractals Vol. 10 No. 12, 2099-2152 (1999).
[12] Davis, R. F., Paisley, M. J., Sitar, Z., Kester, D. J., Ailey, K. S. and Wang, C., "Deposition of III-N Thin Films by Molecular Beam Epitaxy," Microelectronics Journal Vol. 25(8), 661-674 (1994).
[13] Choy, K. L., "Chemical vapour deposition of coatings," Progress in Materials Science 48, 57–170 (2003).
[14] Baek, J., Ma, J., Becker, M. F., Keto, J. W. and Kovar, D., "Correlations between optical properties, microstructure, and processing conditions of Aluminum nitride thin films fabricated by pulsed laser deposition," Thin Solid Films 515, 7096–7104 (2007).
[15] Casady, J. B. and Johnson, R. W., "Status of Silicon Carbide (SiC) as a Wide-Bandgap Semiconductor for High-Temperature Applications: A Review," Solid-State Electronics Vol. 39 No. 10, 1409-1422 (1996).
[16] Chalker, P. R., "Wide Bandgap Semiconductor Materials for High Temperature Electronics," Thin Solid Films Vol. 343 4, 616-622 (1999).
[17] Borecki M., et al., "Large-area transparent in visible range silicon carbide photodiode," Proc. SPIE 8903, 89030H (2013).
[18] Sochacki M., et al., "Interface traps in Al/HfO_2/SiO_2/4H-SiC metal-insulator-semiconductor (MIS) structures studied by the thermally-stimulated current (TSC) technique," Microelectronic Engineering 157, 46-51 (2016)
[19] Król, K., Sochacki, M., Turek, M., Żuk, J., Przewlocki, H. M., Gutt, T., Borowicz, P., Guziewicz, M., Szuber, J., Kwoka, M., Kościelniak, P. and Szmidt, J., "Influence of Phosphorus Implantation on Electrical Properties of Al/SiO_2/4H-SiC MOS Structure," Materials Science Forum Vol. 821-823, 496-499 (2015).
[20] Sochacki, M. and Szmidt, J., "Dielectric films fabricated in plasma as passivation of 4H-SiC Schottky diodes," Thin Solid Films Vol. 446 No. 1, 106-110 (2004).
[21] Firek, P. and Szmidt, J., "MISFET structures with barium titanate as a dielectric layer for application in memory cells," Microelectronics Reliability Vol. 51 No. 7, 1187-1191 (2011).
[22] Borecki, M., "The fiber optic sensor with D type head synthesis," Proceedings of SPIE Optical Fibers Vol. 5952, 324-328, (2005).
[23] Adam, T., Kolodzey, J., Swann, C. P., Tsao, M. W. and Rabolt, J. F., "The electrical properties of MIS capacitors with AlN gate dielectrics," Applied Surface Science 175-6, 428-435 (2001).
[24] Szmidt, J., Sokołowska, A., Olszyna, A., Werbowy, A. and Pawłowski, P., "Electronic properties of nanocrystalline BN and AlN films deposited on Si and GaAs - a comparision," Diamond and Related Materials 8 2-5, 391-397 (1999).
[25] You, Y. Z. and Kim, D., "Influence of incidence angle and distance on the structure of aluminum nitride films prepared by reactive magnetron sputtering," Thin Solid Films 515, 2860-2863 (2007).
[26] Gould. R. D. and Awan, S. A., "Dielectric properties of AlN_x thin films prepared by RF magnetron sputtering of Al using a N_2/Ar sputtering gas mixture," Thin Solid Films 469 70, 184-918 (2004).
[27] Oliveira, C., Massi, M., Santos, S. G., Otani, C., Maciel, H. S. and Mansano, R. D., "Dielectric characteristics of AlN film grown by d.c.-magnetron sputtering discharge," Diamond and Related Materials 10, 1317-1321 (2001).

Determination of the activation energy of the relaxation time of the composite cellulose - synthetic ester with a high water content

Konrad Kierczyński*[a]
[a] Department of Electric Devices and High Voltage Technology, Lublin University of Technology, 38a, Nadbystrzycka Str., 20-618 Lublin, Poland;

ABSTRACT

The paper presents the results of the conductivity testing of Weidmann electrotechnical pressboard, with a moisture content of 5% by weight impregnated with MIDEL 7131 synthetic ester. Frequency and temperature dependencies of AC conductivity were determined on the basis of experimental results. The approximations of the frequency dependencies of conductivity were made with a step of 100 points per decade. The frequency dependencies of approximated conductivity waveforms at all measuring temperatures were shifted by means of the energy of activating the conductivity to a temperature of 293 K (reference temperature in electrical engineering). Arrhenius graphs were also drawn up, from which the energy activation of relaxation time and the value of the R^2 determination coefficient for the selected conductivities were determined. Approximations of Arrhenius's graphs indicate high accuracy, as evidenced by the values of the coefficient of determination close to one. It has been found that the value of the activation energy of relaxation time varies within a very narrow range, which indicates that in the entire frequency range conduction is carried out according to the same mechanism - hopping conductivity.

Keywords: synthetic ester, pressboard, AC conductivity, activation energy, moisture content, composite, water nanoparticle, power transformer

1. INTRODUCTION

In high-voltage power transformers, electrotechnical pressboard impregnated with insulating oil is used as insulation. During exploitation, the insulation in the transformer undergoes aging phenomena, during which cellulose depolymerization occurs [1, 2]. The insulation temperature and the moisture level have a big influence on the aging of the cellulose insulation. Temperature has a significant impact not only in power transformers [3]. The basic source of moisture in the insulation of solid transformers is moisture coming from the outside, which dissolves in the transformer oil and then absorbed by cellulose. This is due to the fact that the solubility of water in cellulose is more than a thousand times higher than in transformer oil [4]. Moisture in pressboard gather from the initial level about 0.8% by weight to as much as 5% by weight. This increase is detrimental to the quality of paper and oil insulation of power transformers and has a huge impact on its reliability.

High demands on insulation cause displacement of insulation oils from their use in power transformers. Synthetic esters are an increasing proportion of fluids used in this type of devices. The biggest advantages of synthetic esters compared to mineral oils is the relatively high water solubility without significant deterioration of dielectric properties, much higher ignition temperature and biodegradability [5, 6]. Devices that use this type of liquids due to their properties can work in places where a possible explosion poses a large ecological threat and in large human centers.

The problem of moisture gathering in the solid component of power transformers containing oil or synthetic ester makes it very important to determine it precisely. To determine the moisture content in paper-oil insulation of hermetic energy transformers filled with synthetic ester, the same test methods should be used as for transformers filled with mineral oil. Non-destructive electrical methods are most often used for this. These methods can be divided into two groups - time domain measurements using direct voltage and frequency measurements using alternating voltage. The group of measurements in the time domain includes the RVM (Return Voltage Measurement) method [7, 8] and PDC (Polarization Depolarization Current) [9, 10]. The second group includes the FDS method (Frequency Domain Spectroscopy) [11, 12].

Analysis of dielectric relaxation processes in time and frequency domains was based on a number of models, each of which had more or less reliable physical justification. Some of them do not find experimental confirmation.

*k.kierczynski@pollub.pl; phone +48 815384328

Photonics Applications in Astronomy, Communications, Industry, and High-Energy Physics Experiments 2019, edited by Ryszard S. Romaniuk, Maciej Linczuk, Proc. of SPIE Vol. 11176, 111764S
© 2019 SPIE · CCC code: 0277-786X/19/$21 · doi: 10.1117/12.2536660

The electrical properties of the synthetic ester differ from those of the insulating oil, therefore a test cycle should be carried out of composite the cellulose - synthetic ester - water nanoparticles. So far, a series of tests has been carried out using the PDC method, presented, for example, in works [13-15]. Currently, much attention is devoted to the study of many different materials, with different research methods [16-19].

In work [20, 21] 12, it was established that water in cellulose is precipitated in the form of nanoparticles with dimensions of about 2.32 nm, containing about 220 molecules of water.This is consistent with the sufficient condition for the formation of nanoparticles [22, 23] which is that oil and water do not enter chemical reactions, they are not mutually soluble and the surface tension of water is much higher than that of synthetic ester. This means that moistened impregnated insulation oil should be treated as a cellulose composite - synthetic ester - water nanoparticles.

In works [20, 24–26] a quantum mechanical phenomenon of electron tunneling between the potential wells created by water nanoparticles for the analysis of the dependence of conductivity, dielectric permittivity and tangent of the composite loss angle cellulose - insulation oil - water nanoparticles on frequency, temperature and moisture content was applied. The results obtained in the analysis allowed for the development of methods for converting the above-mentioned parameters, obtained at any measurement temperature in the range of 10 °C - 80 °C to a reference temperature of 20 °C.

The aim of this work was to develop a new method to determine the activation energy value of the relaxation time of the composite cellulose - synthetic ester - water nanoparticles in a wide range of frequencies. For testing, as an example, a sample of pressboard with a water content of 5% by weight was selected. Such a choice is caused by the fact that reaching such moisture content may lead to a catastrophic failure of the power transformer. To analyze the obtained experimental results, the model of jump conductivity (electron tunneling) on direct and alternating current will be used, which proved excellent during the analysis of direct and alternating current results of conductivity tests of the composite cellulose - synthetic ester - water nanoparticles.

2. DETAILS EXPERIMENTAL

Synthetic ester MIDEL 7331 produced by MIDEL and the pressboard produced by Weidman were used in the research. The cut out round sample of the pressboard with a radius of 8 cm with a thickness of 1.5 mm was dried in a vacuum at 353 K for 48 hours. Knowing the mass of the dried sample of the pressboard, you can calculate the mass of the sample with a specific moisture content. Knowing the weight of a sample with a certain moisture, the sample is exposed to atmospheric air. The sample absorbs moisture from the atmosphere increasing its mass. After reaching the appropriate mass, which response to a moisture content of 5% by weight the sample is dropped into a hermetic container in which a new synthetic ester is located. The sample was seasoned for 6 months at room temperature. This was to establish a thermodynamic equilibrium between pressboard, synthetic ester and moisture.

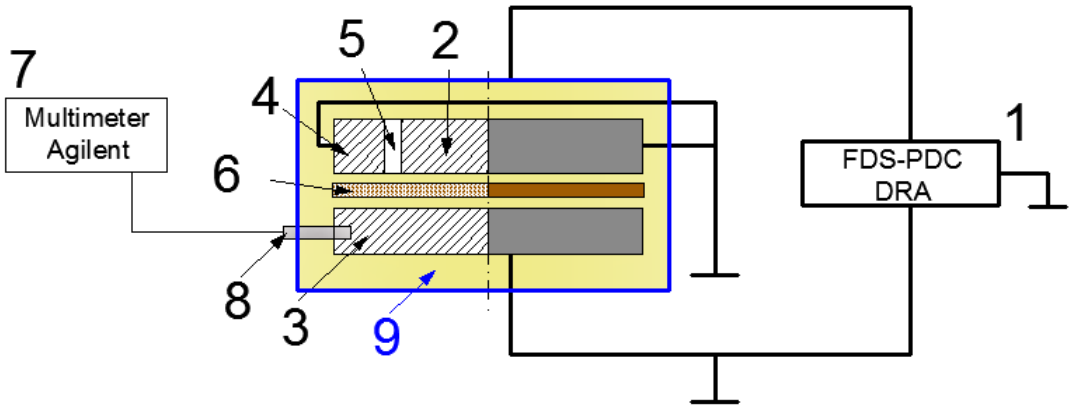

Figure 1. Block diagram of the stand for direct current measurements of the electrical properties of the liquid-solid insulation, 1 – FDS-PDC Dielectric Response Analyser (Dirana meter); 2 – voltage electrode; 3 – measuring electrode; 4 – protective electrode; 5 – insulator; 6 – pressboard impregnated with synthetic ester; 7 – Agilent temperature meter, 8 – PT 1000 temperature sensor; 9 – climatic chamber.

The FDS method was used for the measurements. The tests were carried out using a three-electrode measuring capacitor, the diagram of which is shown in Figure 1. Between the voltage electrode (3) and measuring electrode (4) was placed a moistened sample of pressboard prepared in the manner described above. The whole is placed in a hermetic vessel and is poured with the ester. The prepared vessel is placed in a climatic chamber. The accuracy of maintaining the temperature in the climatic chamber was ± 0.1 °C. After reaching the set temperature, the climatic chamber sustains it for many hours. At the same time, the temperature of the measuring capacitor is monitored by means of the PT 1000 sensor and the Agilent temperature meter. The Dirana meter produced by Omicron was used to measure AC properties the FDS method. The FDS meter automatically selects the measurement time based on the preset measurement frequencies. In the research, the frequency dependences of conductivity at temperatures of 253 K, 273 K, 283 K, 293 K, 303 K, 313 K and 323 K were determined.

The basics of the method of AC analysis of the dielectric response (FDS method) are based on the analysis of the second Maxwell equation (generalized Amper's law). It shows that in real dielectric materials the density of electric current consists of a conduction current vector with the density j_R, and a offset current vector with a density j_C, so that[27]:

$$\oint(\vec{H}\cdot d\vec{l}) = j_C + j_R \tag{1}$$

where: H – vector of magnetic field strength; dl – length vector, tangent to the integration circuit; j_C – vector of the offset current density; j_R – conduction current density vector.

In the FDS method, the forcing electric field is sinusoidal with a pulsation ω. The instantaneous value of the electric field intensity is:

$$E = E_0 \sin(\omega \cdot t) \tag{2}$$

where: E – instantaneous value of the electric field intensity; E_0 – amplitude of the electric field intensity; ω – pulsation; t – time; f – frequency.

The offset current current density, entering the second Maxwell equation[27]:

$$\vec{j}_C(\omega) = \frac{\partial \vec{D}}{\partial t} = (\vec{D} = \varepsilon_0 \varepsilon \vec{E}) = \omega \varepsilon' \varepsilon_0 E_0 \sin(\omega t - \frac{\pi}{2}) \tag{3}$$

where: D – electric induction vector; ε_0 – dielectric permittivity of the vacuum; ε` – relative dielectric permittivity.

Dielectric permittivity ε 'describes the dielectric's ability to polarize and is, in most cases, a function of frequency, temperature and moisture.

Density of conduction current, entering the second Maxwell equation[27]:

$$\vec{j}_R(\omega) = \sigma(\omega, T, X)E = \sigma(\omega, T, X)E_0 \sin(\omega t) \tag{4}$$

where: σ – conductivity, T –temperature, X – moisture in wt. %, E_0 – the electric field intensity; ω – pulsation; t – time

Meters, used to measure AC parameters of electrical systems, so-called impedance meters, perform measurements of two basic characteristic values. These are Z impedance values and phase shift angle φ. The impedance value is determined based on the measured values of the supply voltage applied to the capacitor and the current flowing through the dielectric according to the formula:

$$Z = \frac{U}{I} \tag{5}$$

where: U - amplitude of voltage supplying the measurement system; I - amplitude of current intensity.

The angle of the phase shift φ is determined on the basis of the time offset between the zero crossing points of the instantaneous values of voltage and current intensity and the measurement frequency. Next, with the help of appropriate calculation algorithms, the meter numerically determines the parameters of the RC parallel circuit, such as the resistance R, the capacity C, and the tangent of the loss angle (tanδ) by the formulas:

$$R = \frac{Z}{\cos\varphi} \tag{6}$$

$$C = \frac{\sin\varphi}{\varpi Z} \tag{7}$$

$$\tan\delta = \frac{1}{\tan\varphi} \tag{8}$$

For laboratory measurements using the FDS method, a parallel-plate capacitor is most often used. On the basis of the R and C values, taking into account the geometrical dimensions of the dielectric material, using the formulas[28] material parameters are calculated - conductivity and relative dielectric permittivity, entering the formulas (3), (4):

$$\sigma(\omega, T, X) = \frac{d}{R \cdot S} \tag{9}$$

where: σ-conductivity; *R* - resistance; *d* - dielectric thickness; *S* - cross-section area of the dielectric.

$$\varepsilon' = \varepsilon'(\omega, T, X) = \frac{C}{C_0} \tag{10}$$

Where: ε` - relative dielectric permittivity, *C* - capacity, C_0 - vacuum capacitor capacity.

The analysis of the formulas (6) - (8) shows that the phase shift angle is one of the basic characteristics of the insulating material that serves, together with the impedance, for the calculation of capacitance, resistance, loss tangent and material parameters - permittivity and conductivity. In the further part of the work we will focus only on one material parameter - AC conductivity, the value of which was calculated using formula (9) using formulas (5) - for impedance and (6) - for resistance.

3. DETERMINATION OF THE ENERGY ACTIVATION OF RELAXATION TIME

Figure 2 presents, in the form of points, experimental results of the conductivity of cellulose-synthetic ester-water nanoparticles composite with a moisture content of 5% by weight determined from FDS measurements in the measurement temperature range from 253 K to 323 K. Measuring points, from figure 2, are placed three per decade. To obtain the values between the measurement points, needed in further analysis, a new method of polynomial approximation, proposed in the paper, was used[29]. This work also proposed a method of converting the frequency dependence of conductivity, obtained at any temperature, to the reference temperature of 293 K (20 °C) assumed in electrical engineering. Using this method, approximations of the frequency dependencies of conductivity, shown in Figure 2 in the form of continuous lines, were made. Approximations were made with a step of 100 points per decade. The high quality approximation is indicated by the values of the determination coefficients, the lowest of which is $R^2 = 0.999996$ for the course at the temperature $T = 293$ K. In the area of the lowest frequencies, conductivity is an almost constant value that can be considered as a DC conductivity. Only for the lowest measuring temperature of 253 K, the conductivity even at the lowest frequency has not yet obtained a fixed value.

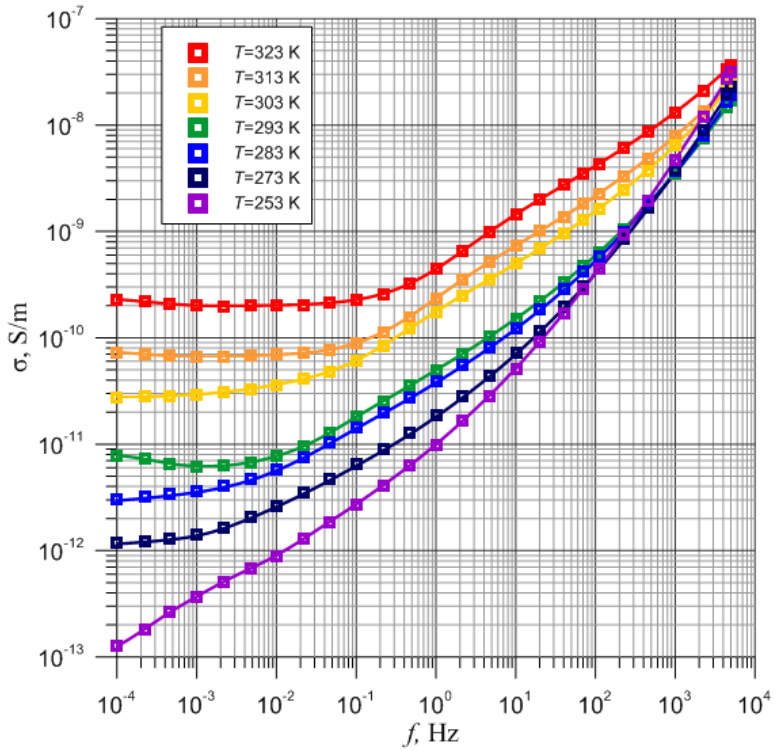

Figure 2. Frequency dependence of the conductivity of the composite cellulose - synthetic ester - water nanoparticles with a moisture content of 5% by weight for various measuring temperatures in the range of 235-323 K. Points - experimental results; solid lines - polynomial approximation.

It should be noted that the steady conductivity value increases with increasing temperature. This is related to the occurrence of temperature dependence of conductivity. As frequency increases, the transition from the fixed value to the increase in conductivity is visible. Conductivity begins to increase faster and then there is an almost imperceptible slowdown in its growth. The starting point of the increase in conductivity moves as the temperature increases into the area of higher frequencies. It is related to the temperature dependence of relaxation time, described by the formula [30, 31]:

$$\tau = \tau_0 \exp\left(\frac{\Delta W_\tau}{kT}\right) \tag{11}$$

where: ΔW_τ – energy activation of relaxation time; τ_0 – number factor.

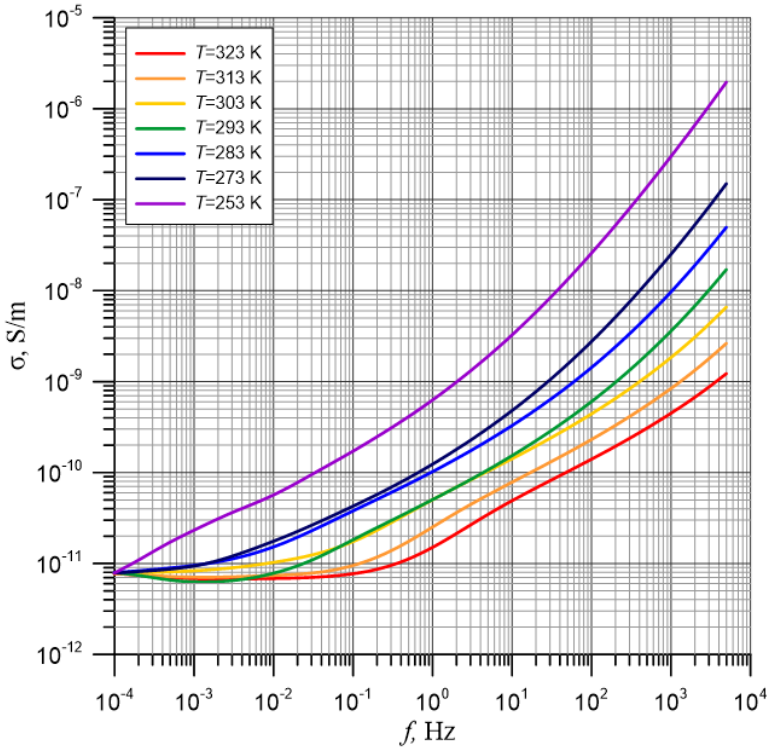

Figure 3. Frequency dependencies of approximated runs of conductivity of the composite cellulose - synthetic ester - water nanoparticles with a moisture content of 5% by weight for measuring temperatures: 253 K, 273 K, 283 K, 293 K, 303 K, 314 K and 323 K, shifted by the energy of activation of the conductivity to a temperature of 293 K.

As can be seen from Figure 3, waveforms for temperatures, smaller than 293 K, are shifting to the area of higher conductivity, while for temperatures higher than 293 K - to the area of lower conductivities. After shifting all the curves to the reference temperature (293 K), it can be seen that in the conductivity range from 10^{-9} to $2*10^{-11}$ there are all temperature waveforms. For the four selected conductivity values in this range, on the basis of the waveforms presented in Figure 3, Arrhenius plots are presented, shown in Figure 4. Approximations of Arrhenius plots indicate their high accuracy, because the determination coefficients, determined for them, presented in Table 1, are from 0.958 and higher. On the basis of Arrhenius's graphs, the activation energy of relaxation time was determined for each of them, the values of which are presented in Table 1. The value of the activation energy of relaxation time for four selected conductivities from the range (10^{-9} – $2*10^{-11}$) S/m changes in very narrow range from a minimum of 0.641 eV to a maximum of 0.739 eV. The average value of the activation energy of relaxation time is (0.695 ± 0.0398) eV.

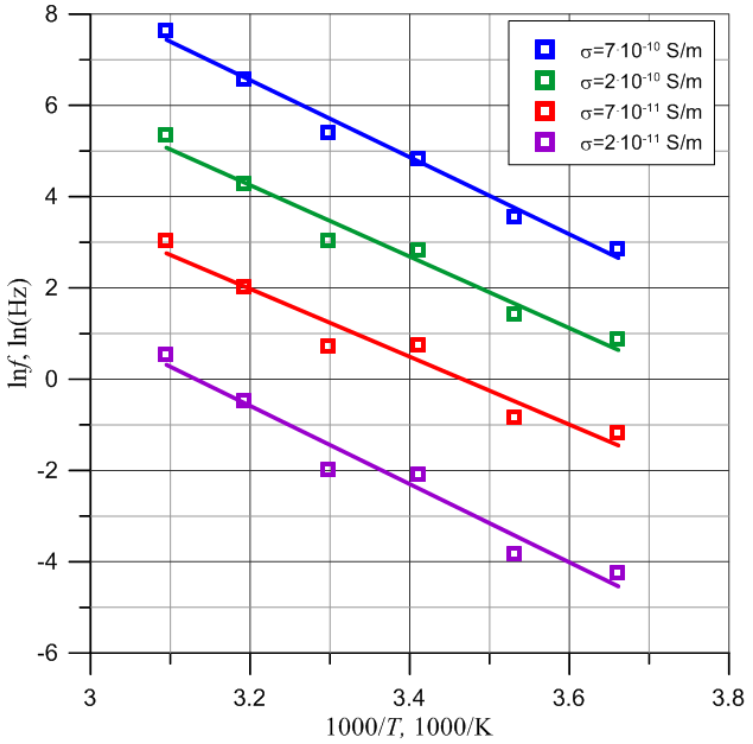

Figure 4. Arrhenius plots for AC conductivity for selected conductivities

Table 1. Numerical values of activation energy of relaxation time for 4 conductivities, R^2 determination coefficients and uncertainty of type A measurements.

σ, S/m	Δ*E*, eV	R^2, a. u.
$2 \cdot 10^{-11}$	0,739	0,958
$7 \cdot 10^{-11}$	0,641	0,949
$2 \cdot 10^{-10}$	0,675	0,968
$7 \cdot 10^{-10}$	0,728	0,987
Average	0,695	0,966
Standard deviation	0,0398	0,0139

4. CONCLUSIONS

The paper presents the results of AC electrical parameters of Weidmann's pressboard, used in power transformers as a fixed element of paper-oil insulation. The moisture content in the pressboard impregnated with the MIDEL 7131 synthetic ester was 5% by weight. The tests were carried out by Omirron's Diran meter in the frequency range from 10^{-4} Hz to 5000Hz and temperatures from 253 K to 323 K. Frequency and temperature dependencies of AC conductivity were determined on the basis of experimental results. The approximations of the frequency dependencies of conductivity were made with a step of 100 points per decade. The frequency dependencies of approximated conductivity waveforms for all measuring temperatures were shifted by means of the activating energy of the conductivity to the temperature 293 K (reference temperature in electrical engineering). Arrhenius plots were also drawn, from which the activation energy of the relaxation time for selected conductivities and the value of the determination coefficient R^2 were determined. Approximations of Arrhenius's plots are indicative of high accuracy, as evidenced by the values of the coefficient of determination, whose minimum value is 0.958. The value of activation energy of the relaxation time varies in a very narrow range from a minimum of 0.641 eV to a maximum of 0.739 eV, and the average value of the relaxation time activation energy is (0.695 ± 0.0398) eV. It has been proved in this way that the activation energy of the relaxation time does not

depend on the frequency. Throughout the entire frequency range, the conductivity of the electric current is carried out according to the same mechanism - hopping conductivity.

ACKNOWLEDGEMENT

This research was partially funded from the statute tasks of the Lublin University of Technology, at the Faculty of Electrical Engineering and Computer Science, S-28/E/2018, entitled "Researches of electrical, magnetic, thermal and mechanical properties of modern electrotechnical and electronic materials, including nanomaterials and electrical devices and their components, in order to determination of suitability for use in electrical engineering and to increase the efficiency of energy management." and S-280/E/2018, entitled "Electrical properties of insulating materials cellulose-transformer oil".

REFERENCES

[1] Jalbert, J., Rodriguez-Celis, E., Duchesne, S., Morin, B., Ryadi, M. and Gilbert, R., "Kinetics of the production of chain-end groups and methanol from the depolymerization of cellulose during the ageing of paper/oil systems. Part 3: extension of the study under temperature conditions over 120 °C," Cellulose **22**(1), 829–848 (2015).

[2] Gilbert, R., Jalbert, J., Duchesne, S., Tétreault, P., Morin, B. and Denos, Y., "Kinetics of the production of chain-end groups and methanol from the depolymerization of cellulose during the ageing of paper/oil systems. Part 2: Thermally-upgraded insulating papers," Cellulose **17**(2), 253–269 (2010).

[3] Frivaldsky, M., Cuntala, J., Spanik, P. and Kanovsky, A., "Investigation of thermal effects and lifetime estimation of electrolytic double layer capacitors during repeated charge and discharge cycles in dedicated application," Electr. Eng. **100**(1), 11–25 (2018).

[4] Oommen T. V., "Moisture Equilibrium in Paper Oil Systems," Proc. 16th Electr. Insul. Conf. (1983).

[5] CIGRE Working Group A2.35., "Experiences in service with new insulating liquids, CIGRE Brochure No 436" (2010).

[6] Havriliak, S. and Havriliak, S. J., "Dielectric and mechanical relaxation in materials : analysis, interpretation, and application to polymers," Hanser Publishers (1997).

[7] Saha, T. K., "Review of time-domain polarization measurements for assessing insulation condition in aged transformers," IEEE Trans. Power Deliv. **18**(4), 1293–1301 (2003).

[8] Dey, D., Chatterjee, B., Chakravorti, S. and Munshi, S., "Importance of denoising in dielectric response measurements of transformer insulation: An uncertainty analysis based approach," Measurement **43**(1), 54–66 (2010).

[9] Saha, T. K. and Purkait, P., "Investigation of polarization and depolarization current measurements for the assessment of oil-paper insulation of aged transformers," IEEE Trans. Dielectr. Electr. Insul. **11**(1), 144–154 (2004).

[10] Wolny, S. and Kędzia, J., "The assessment of the influence of temperature of selected parameters of the approximation method of depolarization current analysis of paper–oil insulation," J. Non. Cryst. Solids **356**(11–17), 809–814 (2010).

[11] Jaya, M., Geissler, D. and Leibfried, T., "Accelerating Dielectric Response Measurements on Power Transformers—Part I: A Frequency-Domain Approach," IEEE Trans. Power Deliv. **28**(3), 1469–1473 (2013).

[12] Tao Zhang, Xiaoqin Li, Haoyun Lv and Xiaorui Tan., "Parameter Identification and Calculation of Return Voltage Curve Based on FDS Data," IEEE Trans. Appl. Supercond. **24**(5), 1–5 (2014).

[13] Kierczynski, K., Zukowski, P., Sebok, M. and Gutten, M., "Comparison of DC conductivity of the insulating oil and moisturized electrical pressboard impregnated with insulating oil," 2018 ELEKTRO, 1–4, IEEE (2018).

[14] Zenker, M. and Kierczynski, K., "Comparison of DC conductivity of the synthetic ester and a composite of cellulose, synthetic ester, water nanoparticles," Adv. Top. Optoelectron. Microelectron. Nanotechnologies IX **10977**, I. Cristea, M. Vladescu, and R. D. Tamas, Eds., 128, SPIE (2018).

[15] Kierczyński, K., Subocz, J., Żukowski, P. and Zenker, M., "The influence of temperature on the AC conductivity of a composite pressboard-synthetic ester-water nanoparticles," Photonics Appl. Astron. Commun. Ind. High-Energy Phys. Exp. 2018, R. S. Romaniuk and M. Linczuk, Eds., 160, SPIE (2018).

[16] Pogrebnjak, A., Goncharov, A., Yunda, A., Shelest, I., Swic, A. and Lebedynskyi, I., "Structural Features Of The Formation Of Multicomponent And High-Entropy Transition Metal Nitride Films," High Temp. Mater. Process. An Int. Q. High-Technology Plasma Process. **22**(1), 7–15 (2018).

[17] Bondariev, V., Zukowski, P., Luhin, V. G. and Voitov, I. V., "Thermogravimetric Analysis Of The

$(FeCoZr)_X(CaF_2)_{(100-X)}$ Nanocomposite," High Temp. Mater. Process. An Int. Q. High-Technology Plasma Process. **21**(4), 289–298 (2017).
[18] Alekseev, V. A., Usoltcev, V. P., Yuran, S. I. and Shulmin, D. N., "Complex For Monitoring Of Sewage Optical Density Changes," Devices Methods Meas. **9**(1), 7–16 (2018).
[19] Kabanau, D. M., Lebiadok, Y. V., Shpak, P. V., Zhuk, S. M. and Stashkevich, S. P., "Device Based On Gainassb Leds For Measurement Of Water Concentration In Oil," Devices Methods Meas. **8**(2), 142–150 (2017).
[20] Żukowski, P., Kołtunowicz, T. N., Kierczyński, K., Subocz, J. and Szrot, M., "Formation of water nanodrops in cellulose impregnated with insulating oil," Cellulose **22**(1), 861–866 (2015).
[21] Zukowski, P., Koltunowicz, T. N., Kierczynski, K., Subocz, J., Szrot, M. and Gutten, M., "Assessment of water content in an impregnated pressboard based on DC conductivity measurements theoretical assumptions," IEEE Trans. Dielectr. Electr. Insul. **21**(3), 1268–1275 (2014).
[22] Pogrebnjak, A. D., Ivashchenko, V. I., Skrynskyy, P. L., Bondar, O. V., Konarski, P., Załęski, K., Jurga, S. and Coy, E., "Experimental and theoretical studies of the physicochemical and mechanical properties of multi-layered TiN/SiC films: Temperature effects on the nanocomposite structure," Compos. Part B Eng. **142**, 85–94 (2018).
[23] Pogrebnjak, A. D. and Beresnev, V. M., "Nanocoatings nanosystems nanotechnologies," Bentham Books (2012).
[24] Żukowski, P., Kołtunowicz, T. N., Kierczyński, K., Rogalski, P., Subocz, J., Szrot, M., Gutten, M., Sebok, M. and Jurcik, J., "Permittivity of a composite of cellulose, mineral oil, and water nanoparticles: theoretical assumptions," Cellulose **23**(1), 175–183 (2016).
[25] Żukowski, P., Kołtunowicz, T. N., Kierczyński, K., Rogalski, P., Subocz, J., Szrot, M., Gutten, M., Sebok, M. and Korenciak, D., "Dielectric losses in the composite cellulose–mineral oil–water nanoparticles: theoretical assumptions," Cellulose **23**(3), 1609–1616 (2016).
[26] Żukowski, P., Kierczyński, K., Kołtunowicz, T. N., Rogalski, P. and Subocz, J., "Application of elements of quantum mechanics in analysing AC conductivity and determining the dimensions of water nanodrops in the composite of cellulose and mineral oil," Cellulose **26**(5), 2969–2985 (2019).
[27] Landau, L. D., Lifshitz, E. M. and Pitaevskiĭ, L. P., "Electrodynamics of continuous media," Butterworth-Heinemann (1984).
[28] Halliday, D. and Resnick, R., "Physics, Part II. ," John Wiley & Sons, New York (1978).
[29] Żukowski, P., Kołtunowicz, T. N., Kierczyński, K., Subocz, J., Szrot, M., Gutten, M., Sebok, M. and Jurcik, J., "An analysis of AC conductivity in moist oil-impregnated insulation pressboard," IEEE Trans. Dielectr. Electr. Insul. **22**(4), 2156–2164 (2015).
[30] Psarras, G. C., Manolakaki, E. and Tsangaris, G. M., "Dielectric dispersion and ac conductivity in—Iron particles loaded—polymer composites," Compos. Part A Appl. Sci. Manuf. **34**(12), 1187–1198 (2003).
[31] Kudryashov, M. A., Mashin, A. I., Logunov, A. A., Chidichimo, G. and De Filpo, G., "Frequency dependence of the electrical conductivity in Ag/PAN nanocomposites," Tech. Phys. **57**(7), 965–970 (2012).

Characterization of CuO nanorods

Izabela Stępińska, Mirosław Kozłowski, Elżbieta Czerwosz, Halina Wronka
Tele and Radio Research Institute, Ratuszowa 11, 03-450 Warsaw, Poland

ABSTRACT

The molecular and crystalline structure of a new type of nanomaterial were presented. The method consisting of two stages - physical vapor deposition from the gas phase and thermal oxidation - contains layers with Cu_xO nanostructures especially CuO nanorods. High-resolution electron transmission microscopy and infrared spectroscopy measurements allowed for the determination of the crystalline and molecular structure of examined films. HRTEM research shows that nanorods are made of CuO, while infrared spectroscopy studies confirm the existence of CuO and Cu_2O phase layers in the structure. The obtained material is widely used in various fields of science, including electronics, photovoltaics, sensors and biomedical engineering.

Keywords: CuO, nanorods, TEM, FTIR, PVD, thermal oxidation

1. INTRODUCTION

Transition metal oxides are the basis of different functional materials with significant scientific and industrial importance. Copper oxide (Cu_xO) has been of great interest in recent years. In the form of various nanostructures (one or two dimensional), it attracts attention due to its intriguing properties and a wide range of applications. As a semiconductor with an energy gap of 2 eV and 1.2 eV for Cu_2O and CuO [1] respectively, it is a good candidate for photovoltaics or optoelectronics. In particular, it is used in detection of gases [2,3], lithium-ion batteries [4], solar cells [5], supercapacitors [6]. In gas sensors, it can be used to detect gases such as NO_2, H_2S, CO or NH_3, in a wide range of temperatures. CuO nanoparticles are also known for their ability to destroy pathogenic microorganisms and bacteria resistant to antibiotics. These properties have led to the development of numerous approaches in many areas of biomedicine, such as special anti-microbial surfaces, wound bandages and modified medical garments. Such nanostructures can affect the development of intelligent systems for pathogen detection and treatment of infections of various origins. In ref. [7], authors report on the potential destructive effects of CuO foil nanorods decorated with folate on a breast cancer cells, inducing apoptosis and limiting the migration of these cells without noteworthy toxic effects on healthy cells. Another well-known application of CuO nanostructures in medicine today are glucose sensors. From the literature, the possibilities of using CuO nanorods in very sensitive and selective non-enzymatic glucose detectors are known. Their action is based on the oxidation of glucose particles on the electrode without the participation of enzymes or other natural catalysts. Amperometric studies of electrode response to changes in glucose concentrations in various environments, including human serum, are the subject of works [8,9]. Sensors using Cu_xO nanostructures are characterized by high sensitivity, a wide range of glucose detection, good selectivity, repeatability and stability at low manufacturing costs compared to enzymatic biosensors.

Copper oxide nanostructures are well described in the literature, and a wide range of information on their synthesis and properties has been available for a long time. Of particular interest is copper oxide in the form of nanorods. In this form it has a large specific surface area, it shows higher absorption, e.g. photons in photovoltaic devices, increasing their efficiency. Similarly in gas detection, a higher probability of absorption gives a better and faster response. In turn, due to its shape and high ratio of length to diameter (the so-called 'aspect ratio') it can be used as a source of electrons in the field emission.

The most commonly used synthesis techniques of Cu_xO nanostructures are physical and chemical deposition from the gas and liquid phases. Examples of the former are the methods using physical vapor depression (PVD) and chemical vapor deposition (CVD) processes. Methods using physical phenomena include RF sputtering (radio frequency), static discharge, thermal vapor deposition, thermal oxidation, epitaxy from molecular and electron beams [10-14]. In case of these processes, Cu_xO nanostructures are formed from a source of pure copper or Cu_xO compounds in the form of a solid or powder target which is vaporized or sprayed, sometimes assisted with ion bombardment or electron beam, thermal heating or laser radiation. CVD processes with numerous modification including atmospheric pressure, assisted plasma

Photonics Applications in Astronomy, Communications, Industry, and High-Energy Physics Experiments 2019,
edited by Ryszard S. Romaniuk, Maciej Linczuk, Proc. of SPIE Vol. 11176, 111764T
© 2019 SPIE · CCC code: 0277-786X/19/$21 · doi: 10.1117/12.2536667

[15-17] have also become popular and are used to achieve the desired Cu_xO stoichiometry. In the synthesis from the liquid phase are mainly used electrodeposition techniques, hydro- and sol-thermal, sol-gel [18-21].
In this article we present a characterization of CuO nanorods obtained by innovative two step method consisting of PVD process in which nanocatalyst C-Ni film was prepared on Cu substrate and next the thermal oxidation of prepared in first step sample. The result of such process is the layer of CuO nanorods placed on Cu substrate. The method was elaborated and patented in our Institute and it allows for preparation of the CuO nanorods film on copper surface. The nanorods distribution density can be steer by content of Ni in nanocatalyst Ni-C film. In this paper we show most typical CuO film and it characterization by SEM, TEM, STEM, ED (electron diffraction) and FTIR methods.

2. EXPERIMENTAL

A synthesis method of CuO nanorods contains two stages: the PVD process and next the heating of the initial PVD film in the air in the temperature range of 400-650°C. The carbon-nickel nanocomposite film (C-Ni) obtained in the previously developed technology [22], in the PVD process, modified the copper surface during thermal oxidation in the air.
The thin C-Ni film consisting of a nickel nanograins embedded in a carbonaceous matrix was deposited on a clean Cu surface. In the next step films were heated at different temperatures in the air for 0.5 hour. As a result of such process the Cu surface is covered with a complex structure containing CuO nanorods with diameters 60-120 nm and lengths up to 10 μm.
Molecular and crystalline structure as well as surface topography on each preparation step of films was investigated with different techniques.
The topography of layers obtained at different temperatures was analyzed by scanning electron microscopy (SEM) with the JEOL JSM-7600F field emission scanning microscope operating at 5 keV incident electron beam energy, equipped with secondary electron (SE) detector.
transmission electron microscope (TEM) and scanning transmission electron microscope (STEM) methods were applied to study details of the structure of nanorods. These investigations were performed with the Talos F200X high resolution TEM operating at 200keV incident electron beam energy equipped with EDX Spectrometer (Bruker). TEM worked in normal and high resolution (HRTEM) mode. Focus ion beam (FIB) technique was used to get information about films structure from the surface down to the substrate level. To protect the film surface against a gallium ion beam cutting a platinum layer was deposited.
The molecular structure was studied by Fourier-transform infrared (FTIR) spectroscopy. FTIR spectra were obtained with ThermoScientific Nicolet iS10 FTIR spectrometer, using ATR (Attenuated Total Reflection) technique, in the spectral range 500 - 4000 cm^{-1}, with a resolution of 4 cm^{-1}.

3. RESULTS AND DISCUSSION

3.1 Topography of CuO nanorods film.

Fig. 1 shows surface imaging for a typical C-Ni film before (Fig.1a) and after (Fig.1b) thermal oxidation at annealing temperature of 650°C and oxidation process duration time 30 mins. The C-Ni film deposited on a pure Cu substrate is characterized by a surface with a low roughness and a fine-grained structure. Thermal oxidation in the air of the initial film causes chemical reaction of the copper substrate with oxygen, resulting in Cu_xO nanostructures. The average length of nanorods (Fig.1c) ranges from 1 to several μm, and the diameter reaches several dozen nm.

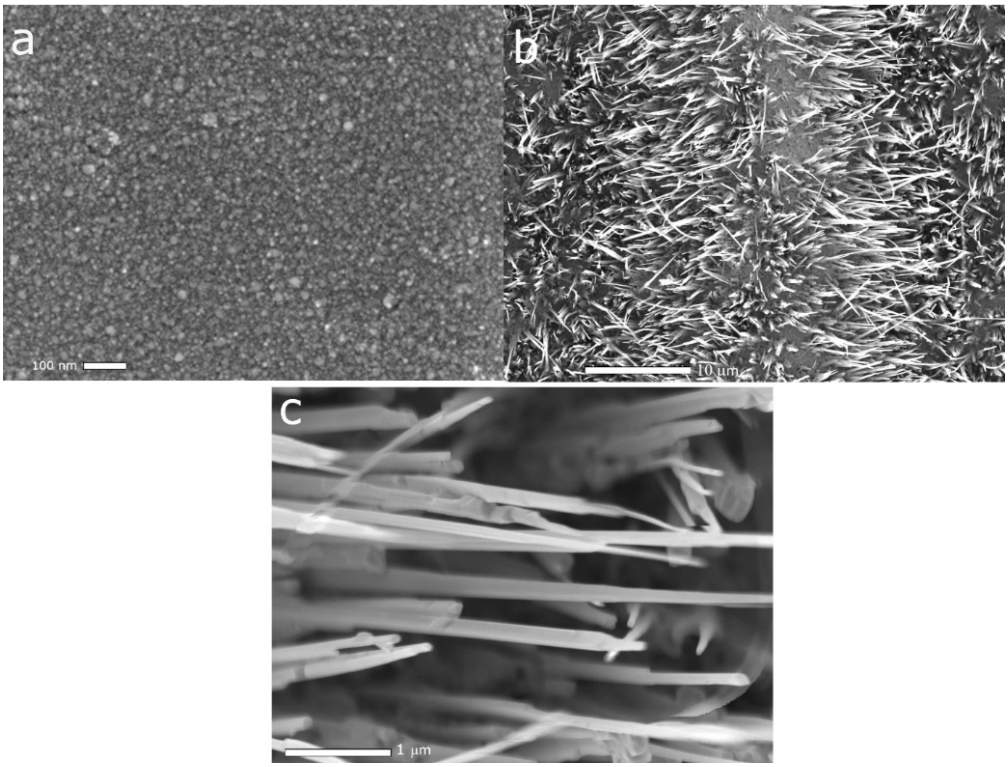

Fig. 1 SEM images of C-Ni film's surface a) before and b) after thermal oxidation, c) CuO nanorods.

3.2 Crystalline structure of CuO nanorods.

HRTEM studies were performed to identify the crystalline structure of CuO nanorods. The investigated material was obtained by removing the film from copper surface straight onto the microscopic carbonaceous mesh. Fig. 2a shows TEM images of CuO nanorods found on such a membrane (Fig. 2). It can be observed that the nanorods are of various thickness, some of them are fused together (Fig.2a). Obtained nanorods have diameter between 60-180 nm, but thinner ones are also observed. The length of nanorods is up to 10 µm or more. HRTEM investigation was conducted on a single CuO nanorod and consisted of the analysis of the crystalline structure, morphology, and chemical composition. A fragment of a single nanorod with a diameter of ~30 nm illustrates Fig. 2b, on which the crystalline planes are clearly visible. The measured interplanar distance is 0.27 nm. This value corresponds to the interplanar distance [110] for CuO (value equal to 0.274 nm according to the ICDD standard 03-065-2309). Fig. 2c shows the X-ray microanalysis made with TEM. Observations are made for Cu for K and L lines, and oxygen.

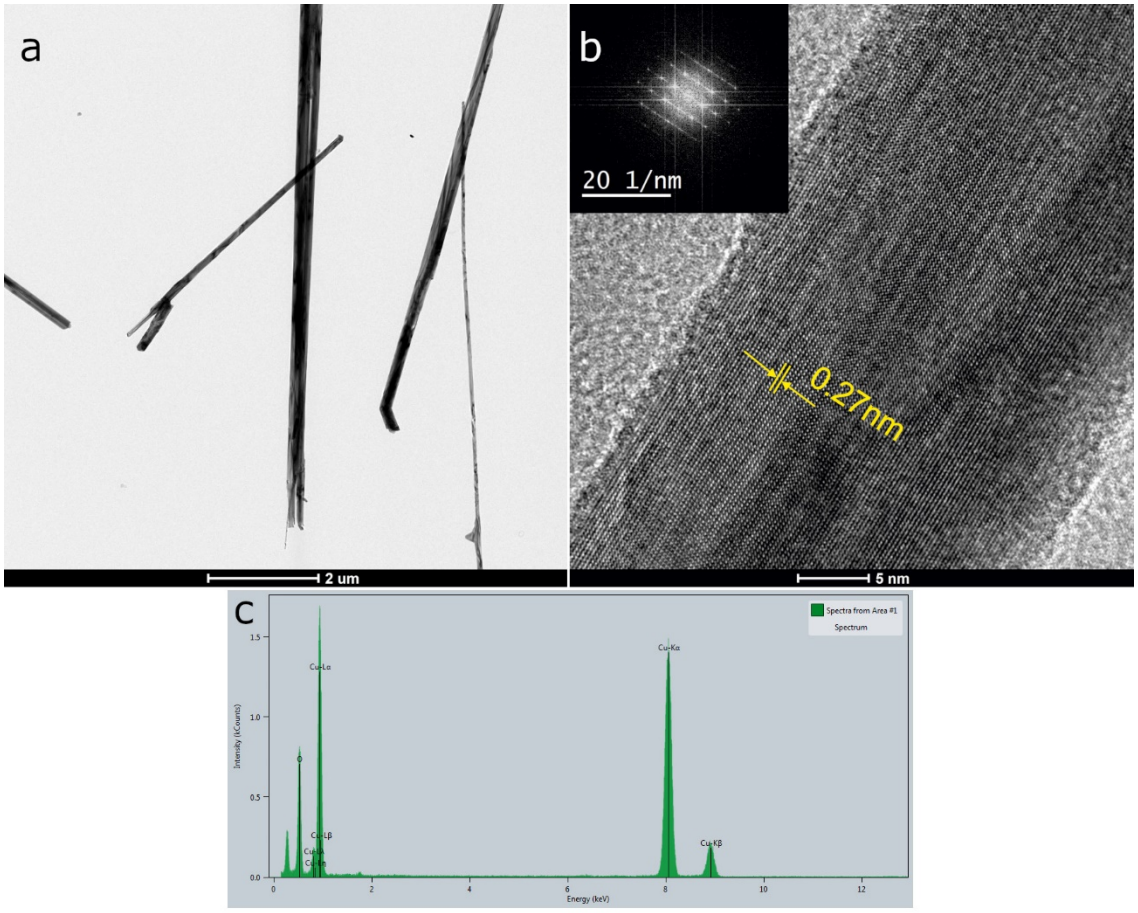

Fig. 2. a) TEM image of CuO nanorods formed after thermal oxidation at 650 °C for 30 min, b) high resolution image of CuO nanorods together with electron diffraction image obtained by inverse Fourier transform (FFT) from this image, c) EDX spectrum of a single nanorod CuO

Fig. 3 presents the results of studies from different detectors used in TEM and correlated with the graph of crystalline structure analysis and chemical composition along the yellow line marked on Fig. 3c. Fig. 3a shows the distribution of chemical elements of the investigated material: Cu and O, with the ratio of copper to oxygen being 80 to 20% which is typical for CuO structure (Fig. 3d). It can be noticed that nanorods are evenly composed of these elements, they are homogeneous and do not contain any precipitates with a different chemical composition. Fig. 3b is an image from the HAADF detector (High Angle Annular Dark Field) and shows the chemical contrast connected with the differential in the atomic number Z.

Fig. 3c is an image from the DF4 detector (Dark Field) which is a mix of chemical and diffraction contrast in the crystalline structure. The analysed CuO nanorods are homogeneous objects in the relation to the atomic number Z. Therefore, differences visible on the image from DF4 result from the variable crystallographic orientation. The lighter and darker areas correspond to different crystallographic orientations of the same material - material with the same chemical composition.

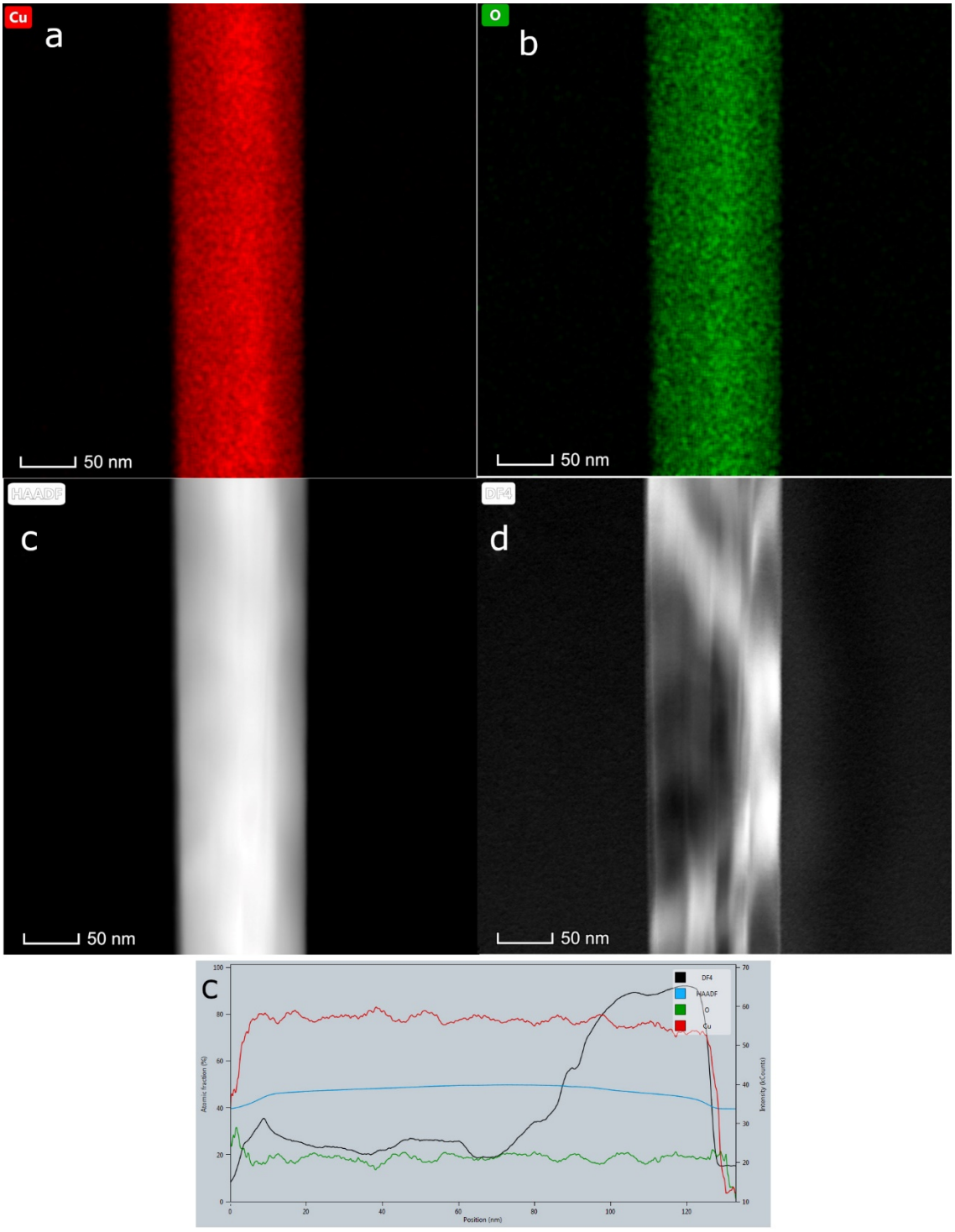

Fig. 3 STEM imaging of a single CuO nanorods, a) maps of Cu and O distribution, b) material contrast so-called *Z* contrast in HAADF mode, c) diffraction contrast in DF4 mode, d) change of oxygen and copper concentration along the selected line (yellow) of analysis and change of material and diffraction contrast along the same line.

Fig. 4 illustrates SEM imaging of cross section of CuO nanorods film after FIB preparation method. There was observed that nanorods' growth begin very deep inside the film. But more studies should be done referring to growth mechanism.

But more studies should be done referring to growth mechanism. Understanding the mechanisms is crucial to optimize the growth conditions and thus achieve the desired size, morphologies, and structures of CuO nanorods. However, the growth processes and the corresponding mechanisms reported in literature studies are somewhat divergent and equivocal.

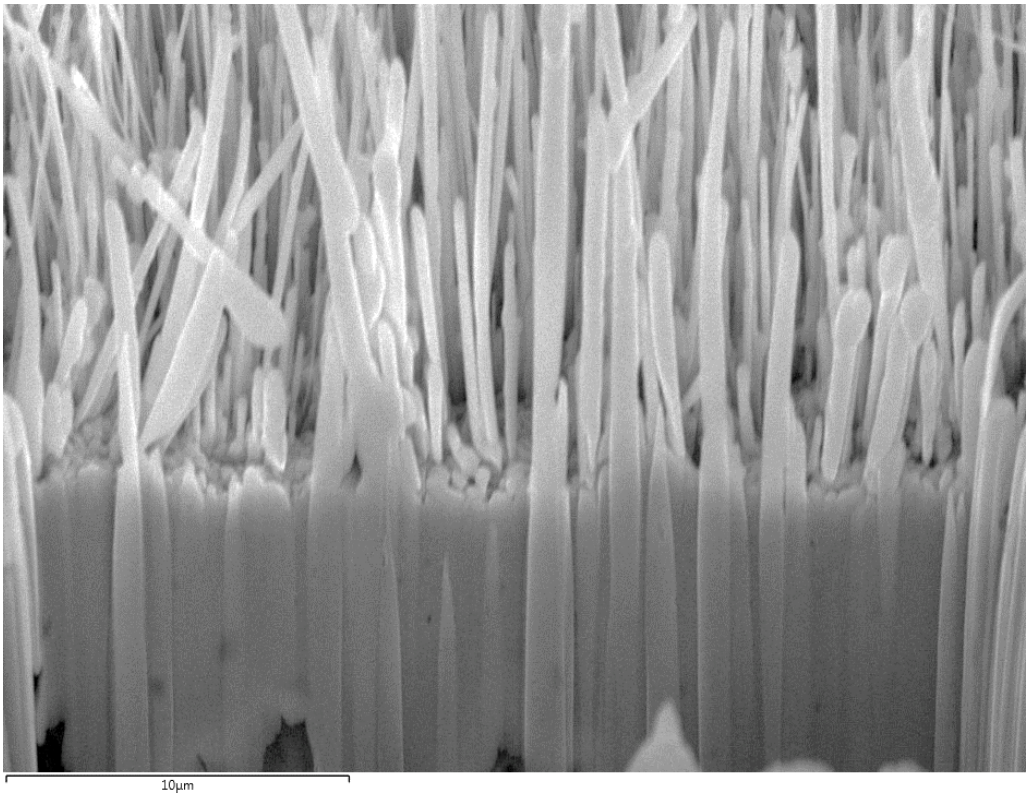

Fig. 4. TEM cross sectional analysis of CuO nanorods film.

3.3 Molecular structure of CuO nanorods

From the literature it is known that the basic infrared absorption bands that reveal the oscillation modes of CuO nanostructures appear in the spectral range below 1000 cm^{-1} [23, 24].

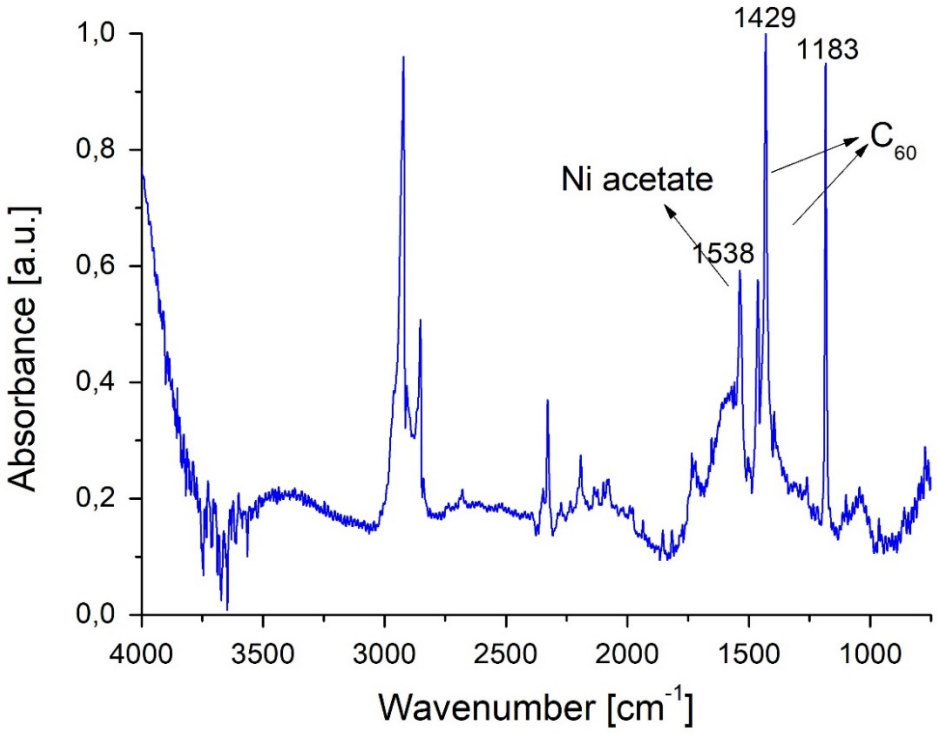

Fig. 5 FTIR spectrum of initial C-Ni film

Fig. 5 shows an example spectrum for the C-Ni initial film. On the graph, clear bands at 1183 and 1429 cm^{-1}, related to stretching vibrations and asymmetric deformation vibrations of pentagons of C_{60} fullerene molecules are observed [25, 26]. It is connected to the incomplete decomposition of fullerite in PVD processes. The spectrum also shows characteristic band for nickel acetate at 1538 cm^{-1} [27], which would mean that the residue of acetate after PVD process exists on the C-Ni film.

The oscillational modes in the CuO nanorods network are related to the relative motion of Cu and O atoms, which contain asymmetric Cu-O stretching vibration and asymmetric O-Cu-O bending vibration. FTIR spectrum of prepared CuO nanorods is shown as Fig. 6. The high-frequency mode around 461 cm^{-1} is reported as Cu-O stretching along the $[\bar{1}01]$ direction and the mode at 540 cm^{-1} is attributed to Cu-O stretching along [101] direction [28, 29].

The band at 626 cm^{-1} can be attributed to the stretching vibrations Cu(I)-O, occurring, according to literature data, around 625 cm^{-1} [30]. This can confirm the existence of the Cu_2O phase. Small shifts in the frequency of vibrations may be related to the presence of Ni atoms, which is a component of the initial C-Ni layer. In [31], it was shown that the presence of atoms of another metal (La) in the CuO structure caused slight shifts in the absorption bands.

In the FTIR spectrum for films obtained in the thermal oxidation process, bands with wavenumber higher than the CuO vibration modes are observed, an i.e. band around 876 cm^{-1}. In work [32], there was also observed band at 881 cm^{-1} for vibrations coming from Cu-OH structures. These bands are associated with the occurrence of various forms of copper compounds with oxygen and hydrogen occurring in the form of nanostructures. The bands in the region from 1000-1500 cm^{-1} are associated C–O stretch and C–H bending vibrations modes of the hydroxyl group combined with copper atoms. There is also a band at 1637 cm^{-1} corresponds to C=O stretching vibration of the -CHO functional groups and broad band around 3400 cm^{-1} connected to -OH stretching vibration. Bands in the range of 2850-2950 cm^{-1} are attributed to vibrations modes of C-H.

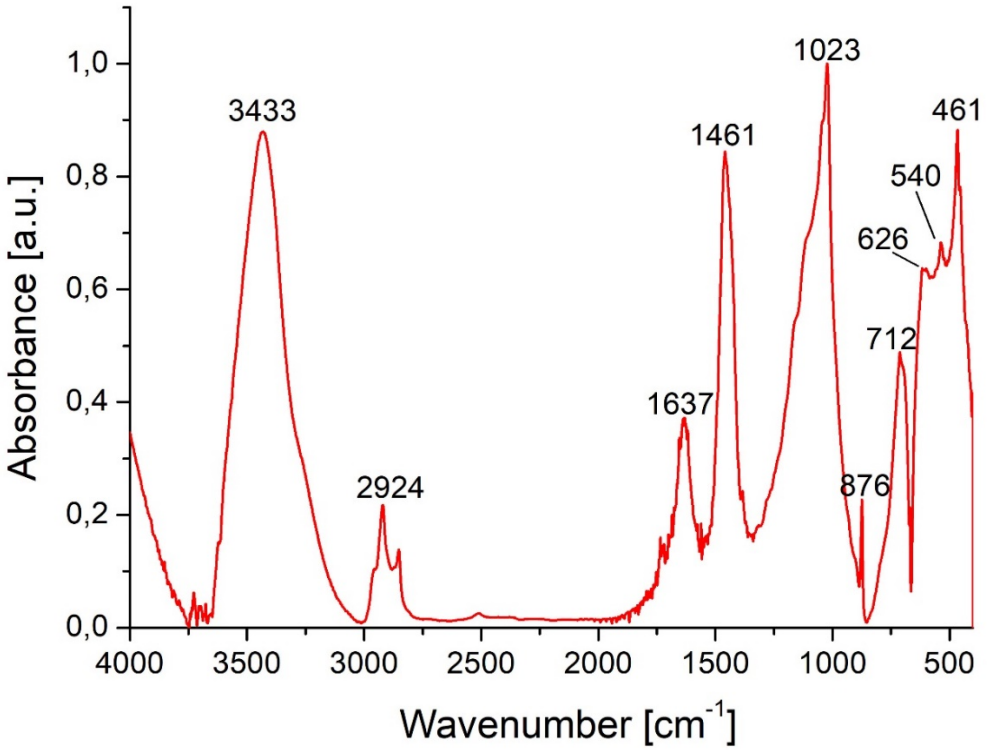

Fig. 6 FTIR spectrum of CuO nanorods

4. CONCLUSIONS

In this work the crystalline and molecular structure of CuO nanorods synthesized by PVD and thermal oxidation methods was studied. FTIR studies prove that films after thermal annealing in the air are composed of Cu_xO nanostructures. The characteristic bands for CuO (461, 540 cm^{-1}) and Cu_2O (626 cm^{-1}) phase occurred. HRTEM studies for single nanorod exhibited that interplanar distances in [110] plane of 0.27nm which is the interplanar distance for CuO.

In summary, we shown that Cu-O film obtained by our method consist mainly of CuO nanorods. The trace of Cu_2O was detected by FTIR method. The film of nanorods is dense and nanorods are aligned and growing perpendicularly to the copper surface.

ACKNOWLEDGMENT

This work was supported by the Ministry of Science and Higher Education.

REFERENCES

[1] Filipic, G., Cvelbar, U., “Copper oxide nanorods: a review of growth,” Nanotechnology, 23, 194001-16 (2012).

[2] Yang, Ch., Su, X., Xiao, F., Jian, J., Wang, J., “Gas sensing properties of CuO nanorods synthesized by a microwave assisted hydrothermal method,” Sensor Actuat B-Chem, 158, 299– 303 (2011).

[3] Li, Y., Liang, J., Tao, Z., Chen, J., “CuO particles and plates: Synthesis and gas-sensor application.” Mater. Res. Bull., 43, 2380–2385 (2008).

[4] Rai, A. K., Anh, L. T., Gim, J., Mathew, V., Kang, J., Paul, B. J., Singh, N. K., Song, J., Kim, J., “Facile approach to synthesize CuO/reduced graphene oxide nanocomposite as anode materials for lithium-ion battery,” J. Power Sources, 244, 435–441 (2013).

[5] Kidowaki, H., Oku, T., Akiyama, T., Suzuki, A., Jeyadevan, B., Cuya, J., "Fabrication and characterization of CuO-based solar cells," J. Mater. Sci. Res., 1, 138–143 (2012).
[6] Shinde, S. K., Dubal, D. P., Ghodake, G. S., Gomez-Romero, P., Kimc, S., Fulari, V. J., "Influence of Mn incorporation on the supercapacitive properties of hybrid CuO/$Cu(OH)_2$ electrodes," RSC Adv, 5, 30478–30484 (2015).
[7] Ahir, M., Bhattacharya, S., Karmakar, S., "Tailored-CuO-nanowire decorated with folic acid mediated coupling of the mitochondrial-ROS generation and miR425-PTEN axis in furnishing potent anti-cancer activity in human triple negative breast carcinoma cells," Biomaterials, 76, 115–132 (2016).
[8] Zhang Y., Liu, Y., Sub, L., Zhang, Z., Huo, D., Hou, C., Lei, Y., "CuO nanowires based sensitive and selective non-enzymatic glucose detection," Sensor Actuat B-Chem, 191, 86– 93 (2014).
[9] Liu, X., Yang, W., Chen, L., Jia, J., "Three-dimensional copper foam supported CuO nanowire arrays: an efficient non-enzymatic glucose sensor," Electrochim Acta, 235, 519–526 (2017).
[10] Chu, C. L., Lu, H. C., Lo, C. Y., Lai, C. Y., Wang, Y. H., "Physical properties of copper oxide thin films prepared by dc reactive magnetron sputtering under different oxygen partial pressures," Phys. B, 404, 4831–4834 (2009).
[11] Santra, K., Sarkar, C. K., Mukherjee, M. K., Ghosh, B., "Thin Solid Films, Copper oxide thin films grown by plasma evaporation method," 213, 226–229 (1992).
[12] Vila, M., Diaz-Guerra, C., Piqueras, J., "Optical and magnetic properties of CuO nanorods grown by thermal oxidation," J. Phys. D: Appl. Phys., 43, 135403-13 (2010)
[13] Zhang, Q., Xu, D., Zhou, X., Wu, X., Zhang, K., "Solar Hydrogen Generation from Water Splitting Using ZnO/CuO Hetero Nanostructures," Enrgy Proced, 61, 345– 48 (2014).
[14] Kawwam, M., Alharbi, F. H., Kayed, T., Aldwayyan, A., Alyamani, A., Tabet, N., Lebbou, K., "Characterization of CuO(1 1 1)/MgO(1 0 0) films grown under two different PLD backgrounds," Appl. Surf. Sci., 276, 7–12 (2013).
[15] Medina-Valtierra, J., Frausto-Reyes, C., Camarillo-Martinez, G., Ramirez-Ortiz, J. A., "Complete oxidation of isopropanol over Cu_2O_3 (paramelaconite) coating deposited on fiberglass by CVD," Appl. Catal. A, 356, 36–42 (2009).
[16] Ramirez-Ortiza, J., Ogura, T., Medina-Valtierra, J., Acosta-Ortiz, S. E., Bosch, P., Reyes, J. A., Lara, V. H., "A catalytic application of Cu_2O and CuO films deposited over fiberglass," Appl. Surf. Sci., 174, 177–184 (2001).
[17] Ghodselahi, T., Vesaghi, M. A., Shafiekhani, A., Baghizadeh, A., Lameii, M., "XPS study of the Cu@ Cu_2O core-shell nanoparticles," Appl. Surf. Sci., 255, 2730–2734 (2008).
[18] Xu, M., Wang, F., Ding, B., Song, X., Fang, J., "Electrochemical synthesis of leaf-like CuO mesocrystals and their lithium storage properties," RSC Adv., 2, 2240–2243 (2012).
[19] Yuan, G. Q., Jiang, H. F., Lin, C., Liao, S. J., "Shape- and size-controlled electrochemical synthesis of cupric oxide nanocrystals," J. Cryst. Growth, 303, 400–406 (2007).
[20] Cao, M. H., Hu, C. W., Wang, Y. H., Guo, Y. H., Guo, C. X., Wang, E. B., "A controllable synthetic route to Cu, Cu2O, and CuO nanotubes and nanorods," Chem. Commun., 15, 1884–1885 (2003).
[21] Liu, L., Hong, K., Hu, T., Xu, M., "Synthesis of aligned copper oxide nanorod arrays by a seed mediated hydrothermal method," J. Alloys Compd., 511, 195–197 (2012).
[22] Czerwosz E., Dłużewski P., Nowakowski R., Wronka H., "Studies of structural changes in C60 C70:Ni layers annealed under oxidative conditions," Vacuum, 48(3-4), 357-361 (1997).
[23] Xu, Y., Chen, D., Jiao, X., "Fabrication of CuO Pricky Microspheres with Tunable Size by a Simple Solution Route," J. Phys. Chem. B ,109, 13561-13566 (2005).
[24] Dar, M. A., Nam, S. H., Kim, Y. S., Kim, W. B., "Synthesis, characterization, and electrochemical properties of self-assembled leaf-like CuO nanostructures," J Solid State Electrochem, 14, 1719–1726 (2010).
[25] Byszewski, P., Klusek, Z., "Some properties of fullerenes and carbon nanotubes," Opto-Electron Rev., 9(2), 203-210 (2001).
[26] Jing, D., Pan, Z., "Molecular vibrational modes of C60 and C70 via finite element method," Eur. J. Mech. A-Solid, 28, 948-954 (2009).
[27] Guan, H., Zhou, W., Fu, S., Shao, C., Liu, Y., "Electrospun nanofibers of NiO/SiO2 composite," J. Phys. Chem. Solids, 70, 1374–1377 (2009).
[28] Borgohain, K., Singh, J. B., Rama, M. V., Rao, Z., Shripathi, T., Mahamuni, S., "Quantum size effects in CuO nanoparticles," Phys. Rev. B, 61, 11093-11096 (2000).
[29] Sahai, A., Goswami, N., Kaushik, S. D., Tripathi, S., "Cu/Cu2O/CuO nanoparticles: Novel synthesis by exploding wire technique and extensive characterization," Appl Surf Sci, 390, 974-983 (2016)
[30] Khan, M. A., Ullah, M., Iqbal, T., Mahmood, H., Khan, A., Shafique, M., Majid, A., Ahmed, A., Khan, N. A., "Surfactant Assisted Synthesis of Cuprous Oxide (Cu2O) nanoparticles via Solvothermal Process," Nanoscience and Nanotechnology Research, 3(1) 16-22 (2015).

[31] Varughese, G., Rini, V., Suraj, S. P., Usha, K. T., “Characterisation and optical studies of copper oxide nanostructures doped with lanthanum ions,” Advances in Materials Science, 14(4), 49-60 (2014).
[32] Henrist, C., Traina, K., Hubert, C., Toussaint, G., Rulmont, A., Cloots, R., “Study of the morphology of copper hydroxynitrate nanoplatelets obtained by controlled double jet precipitation and urea hydrolysis,”. J. Cryst. Growth., 254, 176-187 (2003).

Influence of high temperature annealing on AC electric properties of SiO_2 thin layers implanted with In and Sb ions

Karolina Czarnacka*[a], Tomasz N. Koltunowicz[a], Aleksander K. Fedotov[b]

[a] Department of Electric Devices and High Voltage Technology, Lublin University of Technology, Lublin, Poland

[b] Belarusian State University, Minsk, Belarus

ABSTRACT

This paper presents results of AC measurements of resistance R_p, phase angle θ, capacity C_p and loss tangent tgδ in dependences on frequency and temperature for InSb-SiO_2/Si nanocomposite, immediately after preparation and annealed at 1273 K. The material was obtained by the In^+ and Sb^+ ions implantation into a SiO_2 thin layer. Using obtained parameters frequency dependence of conductivity σ, real and imaginary components of permittivity were determined. This work refers to the hopping mechanism of conductivity and relaxation mechanisms of prepared material.

Keywords: thin films, ion implantation, dielectric properties, relative permittivity, hopping transport

1. INTRODUCTION

The constant trend in both basic and engineering research are nanocomposite materials and thin-film materials [15]. This is due to the possibility of interference in their structure at the atomic level, which affects the total change in properties compared to the macro scale [10, 16]. The creation of the nanostructure causes changes in mechanical [12] and chemical [14] as well as optical [11], electric [13] and magnetic [17] properties.

Wide-range AC current measurements of electrical properties, combined with structural tests give a lot of information on the mechanisms of electric charge transfer [18]. So far, it has been established that in nanocomposites of the metal-dielectric type, with grain structure, there is a step change of charges between neighboring metal nanorods that create wells of potential [4, 5]. The occurrence of this mechanism determines the occurrence of phenomena such as non-coil inductance, voltage resonance phenomena or current resonance [6, 9]. The occurrence of these dependencies results from the construction of the material being tested and processes such as annealing [1, 2, 8]. Nanocomposite materials with dielectric matrix SiO2 with both metal and silicon nanoparticles [3, 11] in recent years have attracted attention due to the possibility of use in optoelectronic devices.

The purpose of this work was to perform AC measurements of electrical quantities, i.e. resistance R_p, phase shift angle θ and capacitance C_p in function of frequency and temperature of the InSb-SiO_2/Si nanocomposite before and after high temperature annealing. On this basis, the conductivity σ of this material and the real and imaginary components of dielectric permittivity were determined. On this basis, the mechanism of electric charge transfer in the tested material and the influence of measurement parameters on the obtained quantities are described.

2. EXPERIMENTAL

The object of the study was a nanocomposite material with the structure InSb-SiO_2/Si obtained by the use of implantation of antimony Sb and indium In ions. The ions were implanted with energy of 200 keV at a dose of 8×10^{15} cm^{-2} into a layer of SiO_2 with a thickness of 300 nm. The silica layer was obtained by heating the p-type silicon substrate. The doses of ions chosen in this way made it possible to obtain a depth distribution of approx. 110 nm from the surface of SiO_2 and their volume concentration of approx. 1.2×10^{21} cm^{-3}.

Measurements of AC electric values were carried out on the measurement stand described in paper [7]. The electrical quantities were determined as a function of frequency (50 Hz - 10^6 Hz) and temperature (40 K – 375 K).

*karolina.czarnacka@pollub.edu.pl; phone +48 81-538-43-26; fax +48 81-538-45-75

Photonics Applications in Astronomy, Communications, Industry, and High-Energy Physics Experiments 2019, edited by Ryszard S. Romaniuk, Maciej Linczuk, Proc. of SPIE Vol. 11176, 111764U
© 2019 SPIE · CCC code: 0277-786X/19/$21 · doi: 10.1117/12.2536668

The measurements were made immediately after fabrication and after annealing at high temperature T_a=1273 K. The measured values were resistance R_p, angle of phase shift θ, tangent of dielectric loss tanδ and capacity C_p. On this basis, the relative dielectric permittivity ε_r, the lossiness ε" of the tested material and its conductivity σ were calculated.

3. RESULTS AND DISCUSSION

Fig. 1 shows the frequency dependence of the capacity C_p of the InSb-SiO_2/Si nanocomposite at several measurement temperatures before and after annealing at T_a = 1273 K. As can be seen before annealing in the low frequency range to around 10^4 Hz, the capacity is practically constant. With further increase in frequency, the capacity is rapidly decreasing. The annealing caused that this decrease shift into the higher frequency range.

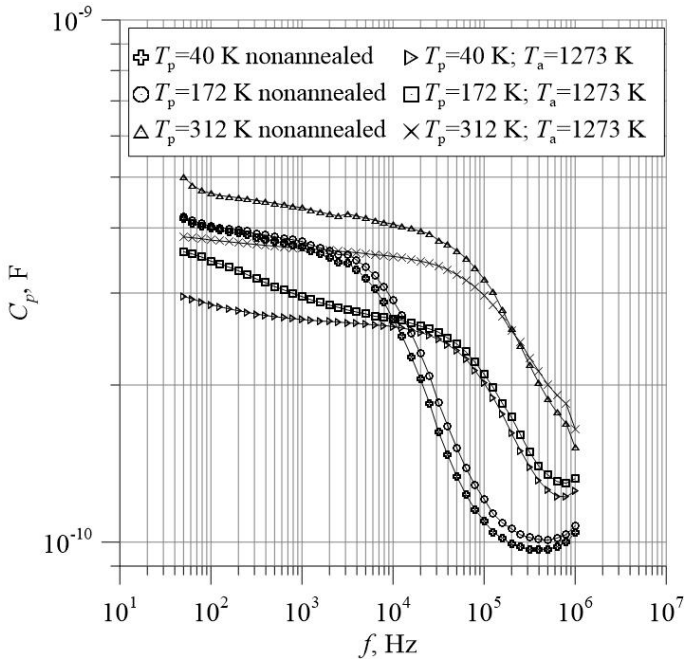

Fig. 1. Temperature and frequency dependence of the capacity C_p of InSb-SiO_2/Si nanocomposite before and after annealing at T_a=1273 K for selected measuring temperatures T_p

Fig. 2 presents the frequency and temperature dependence of dielectric loss tangent of the tested material before and after high temperature annealing. As can be seen in Fig. 2 for the sample not annealed in the low frequency range to about 10^3 Hz, for all measuring temperatures the tangent tgδ value rapidly decreases and then shows a parabolic shape. This indicates a relaxing mechanism of dielectric losses. The dielectric losses of the preheated material are also characterized by a relaxation mechanism, while in the low frequency range the losses are practically constant and the maximum is shifted in the high frequency range above 10^5 Hz.

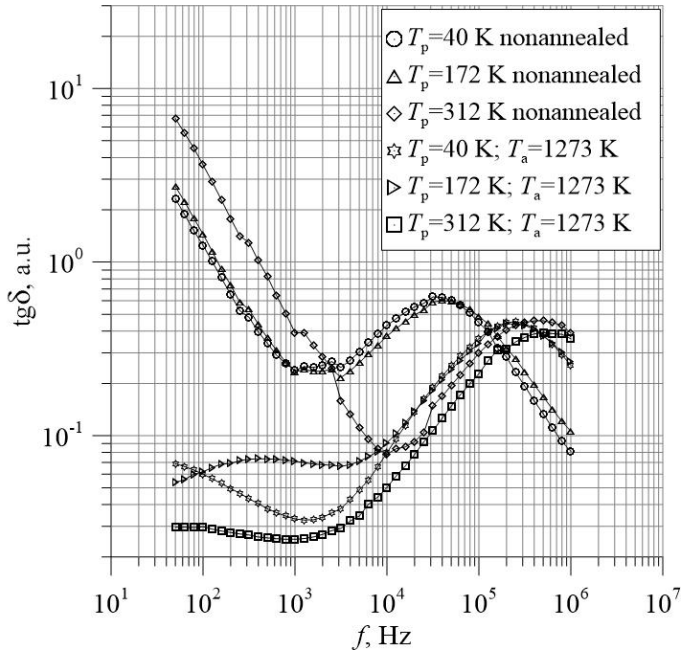

Fig. 2. Temperature and frequency dependence of the loss tangent tgδ of InSb-SiO_2/Si nanocomposite before and after annealing at T_a=1273 K for selected measuring temperatures T_p

The analysis of the dependence of the phase shift angle on the frequency and temperature of the nanocomposite directly after receiving, as is presented in Fig. 3, shows that the angle of the phase shift decreases from nearly zero to almost -90°. This type of phase shift determines the capacitive behavior of the tested material. Annealing caused that the phase shift angle in the low frequency range reaches a constant value almost -90°. This dependence still retains its capacitive character but is close to currents resonance. In the same frequency range, the dielectric losses of the annealed sample are the smallest.

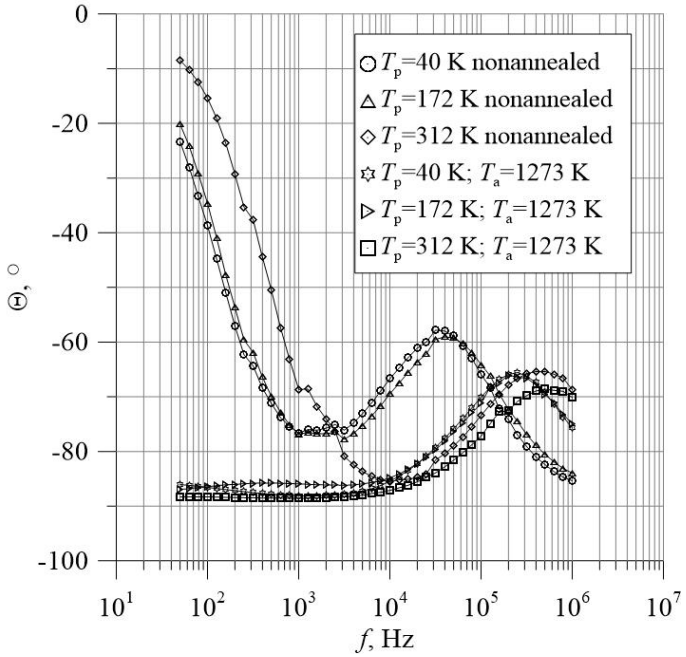

Fig. 3. Temperature and frequency dependence of the phase shift angle θ of InSb-SiO_2/Si nanocomposite before and after annealing at T_a=1273 K for selected measuring temperatures T_p

On the basis of obtained capacity Cp values and geometric dimensions of the tested nanocomposite, the relative permittivity ε_r was determined. The frequency and temperature dependence of the relative permittivity of the InSb-SiO_2/Si nanocomposite is shown in Fig. 4a. For non-annealed samples, a sudden drop in permittivity ε_r with a frequency in the range from about 10^3 Hz to about 10^5 Hz can be seen. With a further increase in frequency, the permittivity ε_r decreases mildly to an almost constant value. In the case of annealed sample, the rapid decrease in permittivity ε_r is shifted to the higher frequency range.

In order to further analyze the dielectric properties of the obtained nanocomposite, the frequency-temperature dependences of the imaginary component of permittivity ε" were developed. These dependencies are shown in the Fig. 4b. In the case of an non-annealed sample, its lossiness ε" rapidly decreases in the low frequency range to about 10^3 Hz and then a small parabolic dependency is visible. In addition, parabolic loss changes coincide with the decrease in relative permeability. This proves dipole polarization.

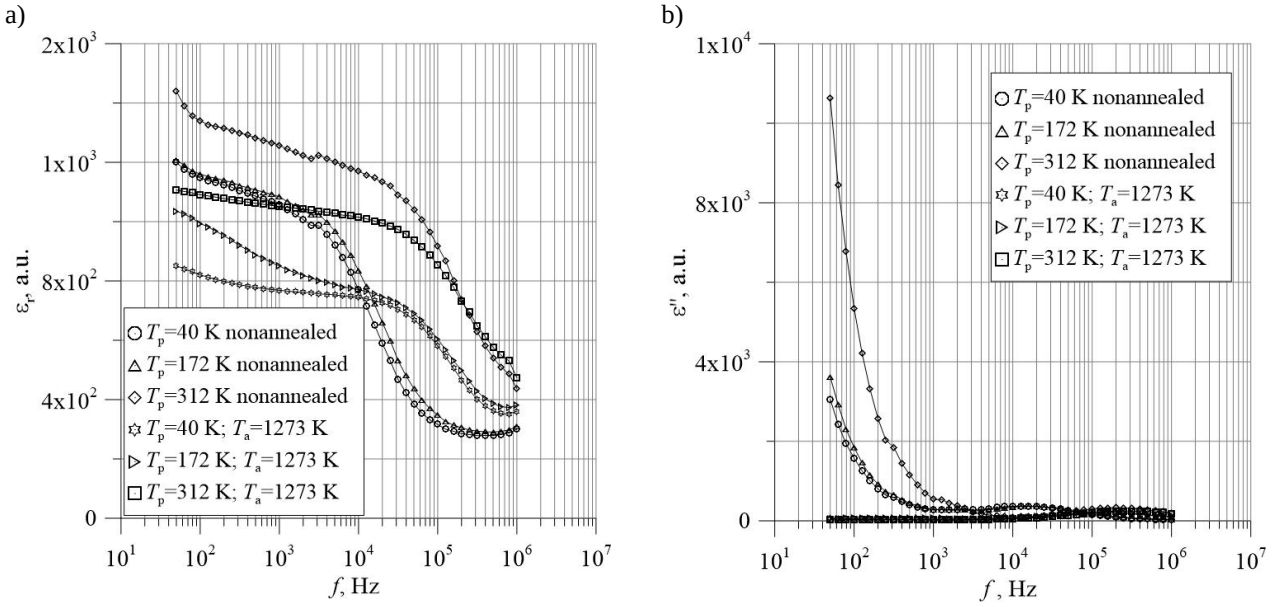

Fig. 4. Temperature and frequency dependence of a) relative dielectric permittivity ε_r and b) a) imaginary component of permittivity ε" of InSb-SiO_2/Si nanocomposite before and after annealing at T_a=1273 K for selected measuring temperatures T_p

Fig. 5 shows the frequency and temperature dependence of conductivity σ. In both cases (non-annealed alnd annealed sample) an increase in conductivity with frequency is visible. For an non-annealed sample, the increase is two orders of magnitude, and for an high temperature annealed sample the increase of conductivity is almost five orders. This demonstrates the hopping transport mechanism of electric charges. Nanocomposite materials with a metal-dielectric structure in their structure contain nanodimentional potential wells, in this case they are the inclusion of antimony and indium. With high concentrations of metallic nanocrystals or structural defects (ie wells), the distances between them allow electron tunneling. The hopping exchange of electrons between neutral wells causes the formation of dipoles, which arrange themselves under the influence of the external electric field and additional polarity occurs. From here there are parabolic changes in the lossiness ε" of material.

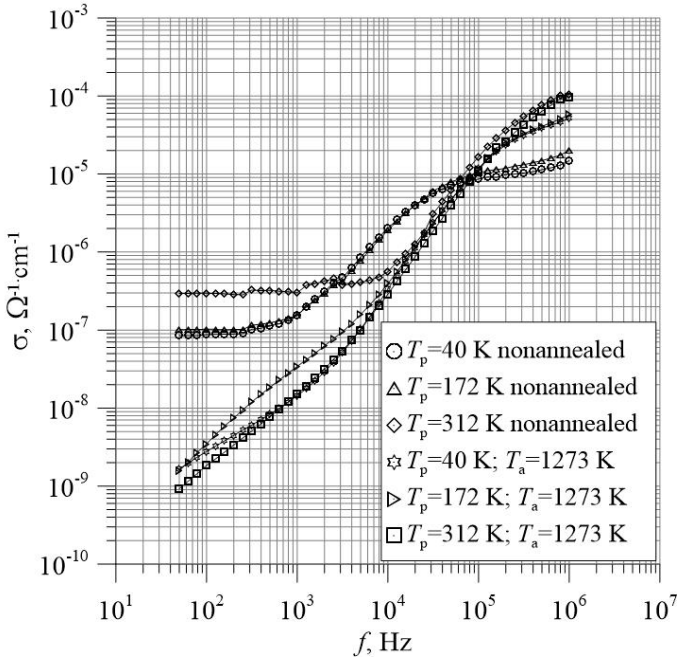

Fig. 5. Temperature and frequency dependence of conductivity σ of InSb-SiO_2/Si nanocomposite before and after annealing at T_a=1273 K for selected measuring temperatures T_p

4. CONCLUSIONS

Granular nanocomposite with the structure of InSb-SiO_2/Si obtained by the implantation of antimony and indium ions into the silica surface on the silicon substrate was the subject of the presented research. As a result of AC measurements of electrical properties, it was found that high temperature annealing of the material causes slight changes in material properties. It has been shown that the material exhibits an hopping mechanism of charge transfer, which causes dipolar polarization. Losses are of a relaxation nature and have the smallest value in the low frequency range for the annealed sample.

REFERENCES

[1] Boiko, O., "Ferromagnetic alloy—ferroelectric ceramic nanocomposites for nanoelectronics: the influence of a heat treatment on electrical properties." High Temp Mater Process 21(3), 251–259 (2017).

[2] Bondariev, V., Zukowski, P., Luhin, V., Voitov, I. V., "Thermo-gravimetric analysis of the nanocomposite $(FeCoZr)_x(CaF_2)_{(100-x)}$," High TempMater Process 21(4), 289–298 (2017).

[3] Czarnacka, K. , Koltunowicz, T.N., Zukowski, P., Fedotov, A.K., "Dielectric properties of multi-layer nanocomposites SiO_x/ZrO_2 after high temperature annealing," Ceramics International vol. 45, 6499-6502 (2019).

[4] Fedotov, A., Mazanik, A., Svito, I., Saad, A., Fedotova, V., Czarnackad, K. and Koltunowicz, T. N., "Mechanisms of carrier transport in $Cu_x(SiO_2)_{1-x}$ nanocomposites manufactured by ion-beam sputtering with Ar ions," Acta Phys. Pol. A vol. 128 n.5, 883-886 (2015).

[5] Koltunowicz, T. N., "Dielectric properties of $(CoFeZr)_x(PZT)_{100-x}$ nanocomposites produced with a beam of argon and oxygen ions," Acta Phys. Pol. A vol. 125 n. 6, 1412-1414 (2014).

[6] Koltunowicz, T. N., “Inductive type properties of FeCoZr-CaF_2 and FeCoZr–PZT nanocomposites,” J. Mater. Sci. Mater. Electron. vol. 26 n. 9, 6450-6457 (2015).

[7] Koltunowicz, T. N., “Test Station for Frequency-Domain Dielectric Spectroscopy of Nanocomposites and Semiconductors,” J. Appl. Spectrosc. Vol. 82 n. 4, 653–658 (2015).

[8] Kołtunowicz, T. N., Zhukowski, P., Fedotov, A. K., Larkin, A. V., Patryn, A., Andryevskyy, B., Saad, A., Fedotova, J. A. and Fedotova, V. V., “Influence of matrix type on negative capacitance effect in nanogranular composite films FeCoZr-insulator,” Elektron. ir Elektrotechnika vol. 19 n. 4, 37-40 (2013).

[9] Koltunowicz, T. N., Zukowski, P., Czarnacka, K., Bondariev, V., Boiko, O., Svito, I. A. and Fedotov, A.K., “Dielectric properties of nanocomposite $(Cu)_x(SiO_2)_{(100-x)}$ produced by ion-beam sputtering,” J. Alloys Compd. Vol. 652, 444–449 (2015).

[10] Koltunowicz, T.N., Bondariev, V., Odnodvorets, L.V., Protsenko, S.I., Shumakova, M., Tkach, O.P., "Electrophysical properties of granular film alloys," Vacuum vol. 164, 165-169 (2019).

[11] Komarov, F., Vlasukova, L., Greben, M., Milchanin, O., Zuk, J., Wesch, W., Wendler, E. and Togambaeva, A., “Structural and optical properties of silicon layers with InSb and InAs nanocrystals formed by ion-beam synthesis,” Nucl. Instruments Methods Phys. Res. Sect. B Beam Interact. with Mater. Atoms vol. 307, 102–106 (2013).

[12] Maksakova, O.V., Simoẽs, S., Pogrebnjak, A.D., Bondar, O.V., Kravchenko, Y.O., Koltunowicz, T.N., Shaimardanov, Z.K., “Multilayered ZrN/CrN Coatings with Enhanced Thermal and Mechanical Properties,” J. Alloys Compd. vol. 776, 679-690 (2019).

[13] Pantsialeyeu, K.U., Krautsevich, A.U., Rovba, I.A., Lysenko, V.I., Vorobey, R.I., Gusev, O.K., Zharin, A.L., “Analysis Of The Electrophysical And Photoelectric Properties Of Nanocomposite Polymers By The Modified Kelvin Probe,” Devices and Methods of Measurements 8(4), 386-397 (2017).

[14] Pogrebnjak, A. D., Kobzev, A. P., Gritsenko, B. P., Sokolov, S., Bazyl, E., Sviridenko, N. V., Valyaev, A. N. and Ivanov, Y. F., “Effect of Fe and Zr ion implantation and high-current electron irradiation treatment on chemical and mechanical properties of Ti-V-Al alloy,” J. Appl. Phys. 87(5), 2142–2148 (2000).

[15] Pogrebnjak, A.D., Beresnev, V.M., "Nanocoatings Nanosystems Nanotechnologies," Bentham Science, Oak Park, (2012).

[16] Yakimchuk, D. V., Kaniukov, E. Yu., Demyanov, S. E., Bundyukova, V. D., Dzeinak, A. V., Makoed, I. I., Arzumanyan, G. M., Doroshkevich, N. V., Mamatkulov, K. Z., Sivakov, V., "Dependence Of The Surface-Enhanced Raman Scattering Signal On The Shape Of Silver Nanostructures Grown In The SiO_2/n-Si Porous Template, Devices and Methods of Measurements vol. 8 n. 3, 228–235 (2017).

[17] Zhukowski, P., Sidorenko, J., Kołtunowicz, T. N., Fedotova, J. A. and Larkin, A. V., “Magnetic properties of nanocomposites $(CoFeZr)_x(Al_2O_3)_{1-x}$,” Prz. Elektrotechniczny vol. 86 n. 7, 296-298 (2010).

[18] Zukowski, P., Kołtunowicz, T., Partyka, J., Fedotova, Y. A. and Larkin, A. V., “Hopping conductivity of metal-dielectric nanocomposites produced by means of magnetron sputtering with the application of oxygen and argon ions,” Vacuum vol. 83 Supplement 1, S280-S283 (2009).

Analysis of metrological properties of the measurement system to study changes in the resistance of nanocomposite carbon-palladium thin films under the influence of hydrogen

S. Krawczyk*[a]
[a] The Tele and Radio Research Institute , Ratuszowa 11 Street,03-450 Warsaw, Poland

ABSTRACT

Nanocomposite carbon-palladium thin films were prepared by PVD method on ceramic (Al_2O_3) substrates by our group at Tele & Research Institute in Warsaw. Resistance of these films changed under the influence of hydrogen at different concentration of this gas. Set-up for measurements of resistance changes due to gas influence was designed and built. The set-up is composed of measurement chamber, gas flow controllers, valves and specially devoted to this experiment computer system with SkSysM program developed by the author.
In this paper, the measurement system and its metrological properties are described. The uncertainty of measurement of the system during experimental procedure of resistance changes measurements for C-Pd films under influence of hydrogen is described. The uncertainty of measurements, illustrated with the experimental errors for dynamic and static conditions of experiment is also discussed.
Keywords: thin films, carbon, palladium, measurement of resistance, uncertainty.

1. INTRODUCTION

In the Tele and Radio Research Institute nanostructural carbon-palladium thin films (C-Pd) are prepared [1-3].These films are prepared by Physical Vapor Deposition(PVD) method on ceramic (Al_2O_3) substrates by our group. Resistance of these films change due to presence of hydrogen. It is well known that effective sensing materials to sense hydrogen are based on palladium (Pd) [4-6]. Sensors based on palladium have drawbacks as hysteresis behavior in electrical resistance caused by adsorption of hydrogen in the structure of Pd [7]. Nanostructural carbon-palladium thin films have smaller hysteresis behavior than sensor based on bulk palladium so are promising materials for sensing application.

The author build special measuring system devoted to examination of resistance changes of nanocomposite carbon-palladium, thin films under influence of hydrogen concertation. In this paper, the measurement system and its metrological properties are described. The further procedure of calculating the uncertainty of measurement and the uncertainty budget of measurements as well as error analysis illustrated with the experimental errors for dynamic and static conditions of experiment are also discussed.

2. EXPERIMENTAL

2.1 Experimental set-up

The measurements were carried out in a special chamber (Fig2a), having electrical feedthrough, gas flow inlet and outlet. Measurement chamber was part of special set up to examine C-Pd films.

Fig.2a shows measurement chamber and measurement set-up. Mass flow controllers controlled the flow rate. SkSysM application installed on controller computer measured changes of resistance of nanocomposite carbon-palladium, thin films under influence of hydrogen and control timings of hydrogen and airflow over the samples. Fig. 1 shows interface of SkSysM application. The data of measured resistance application are collected on controlling computer. In each process of measure changes resistance of C-Pd films, influenced by hydrogen and synthetic air, were collected 1500 samples of resistance measure. The hydrogen concentration was 3,85 percent hydrogen in nitrogen and

Photonics Applications in Astronomy, Communications, Industry, and High-Energy Physics Experiments 2019,
edited by Ryszard S. Romaniuk, Maciej Linczuk, Proc. of SPIE Vol. 11176, 111764V
© 2019 SPIE · CCC code: 0277-786X/19/$21 · doi: 10.1117/12.2536684

the total gas flow rate was constant at 50 ml/min. We performed experiments at room temperature and atmospheric pressure.

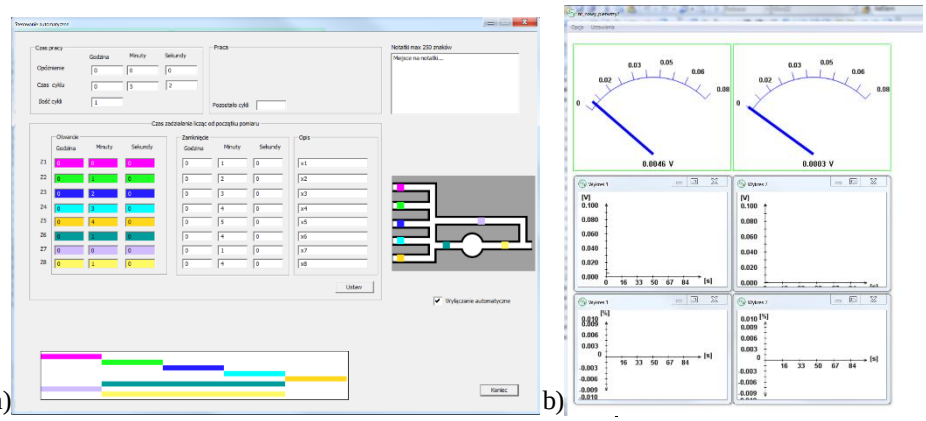

a) b)

Fig.1 Interface of SkSysM application: *a –controlling part, b – measuring part.*

SkSysM application consists of two parts. The first measuring part shows in real time measurement results. Measurement results are shown as analog gauges and plots. Plots show real and relative changes of measured quantities.

The second part of SkSysM application allows to setting up: number of measurements cycles and timings. Operator can decide how many cycles of measurement should be done. The measurement last cycle duration time can be also steered.. It also should decided when during measure cycle the appropriate values should turn on and turn off.

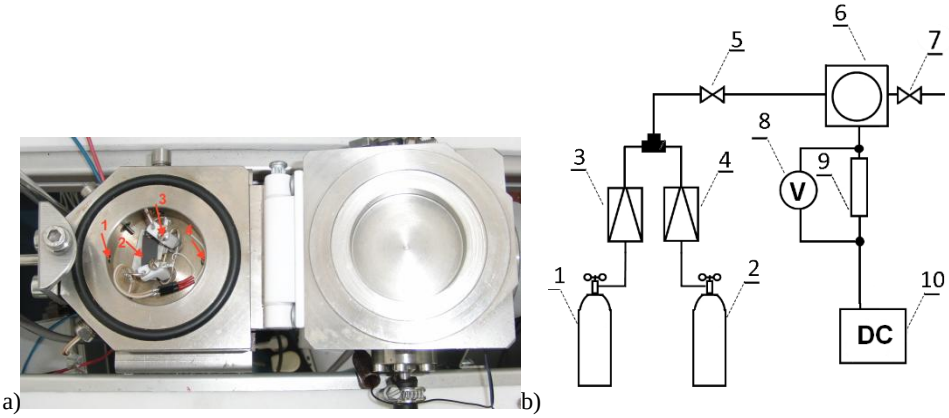

a) b)

Fig.2 Measurment chamber a): *1- flow inlet, 2-C-Pd film,3- measure holder of film,4- flow outlet*, measurmetn set-up b):*1 – hydrogen,2 – synthetic air, 3,4 – mass flow controlers, 5,7 – valves, 7 – measurment chamber, 8 – computational measurment system, 9 – reference resistor, 10 – power supply.*

Resistance was measured by indirect method with known reference resistor. Figure Fig.3 shows schema of electrical connection.

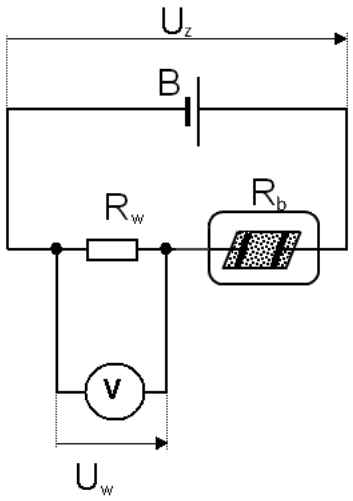

Fig.3 Schema of electrical connections in measurement system of C-Pd resistance films for indirect method:*U_z – supply voltage, R_w – reference resistance, R_b – examined model resistance, U_w – voltage drop on reference resistor.*

Examined resistance was calculated by equation (1).

$$R_b = \frac{(U_z - U_w) * R_w}{U_w} \quad (1)$$

Where: U_z – supply voltage, R_w – reference resistance, R_b – examined resistance, U_w – voltage drop on reference resistor.

Measurement system measured voltages U_z and U_w and clculating R_b according to equation (1) with known resistance R_w.

2.2 Measurement of resistance for model resistor

To calculate static uncertainty of measuring system we carried out measurements of resistance for model resistor with known resistance and uncertainty. We used two identical resistors, one as examined model resistor and second as reference resistor. The experiment was performed without gas flow in the measurement chamber. Measurements were done for eleven resistors with resistance: 0.1, 1, 10, 100, 1000, 10000, 100000, 500000, 1000000 kΩ and uncertainty 0.1%. 1500 samples of resistance measurements for all examined resistors were collected.

2.3 Measurement of resistance of C-Pd films

We chose samples of C-Pd films to perform the experiment. We prepared these samples by PVD method applying with two sources. The first source containing fullerene C60 and the second one containing palladium acetate were used. The film was deposited on the alundum substrate. The Static resistance of sample was 0,355kΩ.

The Experiment for hydrogen sensing was performed by measuring the electrical resistance of C-Pd film during their interaction with hydrogen and next with the synthetic air.

Firstly, we start the flow hydrogen over sample in measuring chamber by turn on the flow in a flow mass controller. All experiment was steering by SkSysM application installed on computer. After specified time, when the sample's resistance reached a steady state, the hydrogen flow stopped and discharge of the films took place by flow synthetic air in specified time. before experiment in SkSysM application Operator sets up timings of flows gases.

The Scanning Electron Microscopy (SEM) and Transmission Electron Microscopy (TEM) were used to characterize a structure and a morphology of studied films. Fig.4 Shows changes of resistance C-Pd film influenced by presence of hydrogen in ambient atmosphere.

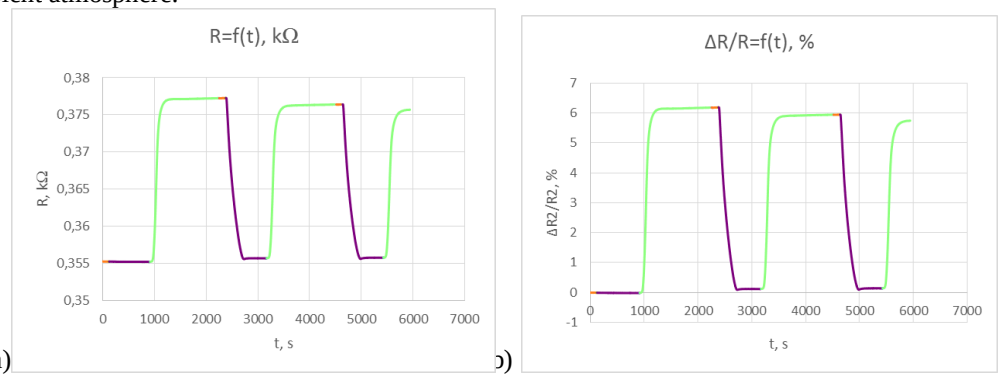

a) b)

Fig.4 The changes of resistance C-Pd film influenced by presence of hydrogen in the ambient atmosphere

3. UNCERTAINTY OF MEASURE

To calculate uncertainty of measured C-Pd films resistance under influence of hydrogen we have to know what is uncertainty of measure resistance our measuring system. First we examined measuring system with model resistor with known resistance and uncertainty. Next, we calculated uncertainty of measure resistance our measurement system using well-known rules [8]. In such case we knew uncertainty of measure resistance measuring system, then we could calculate uncertainty of measured resistance C-Pd films. We calculated uncertainty of measure resistance C-Pd films in steady state, without presence hydrogen over the film and dynamic state when hydrogen is present.

The applied method of indirect method of measurement introduce three possible source of uncertainty of measure voltages U_z, U_w and uncertainty of resistance reference resistor. This is the reason why we have to calculate uncertainty of measuring system, use combined uncertainty [8]. When a measurement has more than one identifiable source of measurement uncertainty, then the combined standard uncertainty (u_c) must be calculated. Generally, a two steps process is used to calculate the combined standard uncertainty. The first step determined uncertainties measured directly and the second step combined the uncertainties using summation in quadrature, known as root sum of the squares [9].

With these Two-method type A and type B the uncertainties of measurements can be calculated directly. The purpose of the Type A and Type B classification is to indicate the two different ways of evaluating uncertainty components. Type A uncertainty is the "evaluation of a component of measurement uncertainty by a statistical analysis of measured quantity values obtained under defined measurement conditions [9]. Type B uncertainty is the "evaluation of a component of measurement uncertainty determined by means other than a Type A evaluation of measurement uncertainty" [8]. Type A uncertainty is calculated according to equation (2). The producer of devices or resistors gives type B uncertainty.

$$u_A(X) = \sqrt{\frac{\sum_{i=1}^{n}(X_i - \bar{X})}{n(n-1)}} \tag{2}$$

Uncertainties measured directly were calculated using equations (3).

$$u(X) = \sqrt{u_A^2(X) + u_B^2(X)} \tag{3}$$

Combined uncertainties were calculated using summation in quadrature given by formula (5).

$$u(R_b) = \sqrt{\left(\frac{\sigma R_b}{\sigma R_w}\right)^2 u^2(R_w) + \left(\frac{\sigma R_b}{\sigma U_z}\right)^2 u^2(U_z) + \left(\frac{\sigma R_b}{\sigma U_w}\right)^2 u^2(U_w)} =$$

$$\frac{1}{U_w^2}\sqrt{(U_z-1)^2 u^2(R_w)U_w^2 + R_w^2 u^2(U_z)U_w^2 + R_w^2 U_z^2 u^2(U_w)} \ldots\ldots \quad \ldots\ldots (5)$$

3.1 Uncertainty of measuring resistance of resistor

To calculate uncertainty of measured resistance by measuring system we used data collected accordingly to paragraph 2.2. The voltage Uncertainties measured directly were evaluated following the formulas (2) and (3). Uncertainties of resistance of references resistors was calculated accordingly to formula (4).

$$u(R_w) = \frac{R_{nom} \times 0{,}1\%}{\sqrt{3}} \quad (4)$$

Where R_{nom} – nominal resistance reference resistors.

Combined uncertainty of measured resistance by measuring system was calculated using equation (5), where: $u(R_w)$ – uncertainty resistance of reference resistor, $u(U_z)$ – uncertainty of measure supply voltage, $u(U_w)$ – uncertainty of measure drop voltage on reference resistor.

Fig.5 shows results of evaluation combined uncertainties of measure resistance by measuring system and Tab1.shows values.

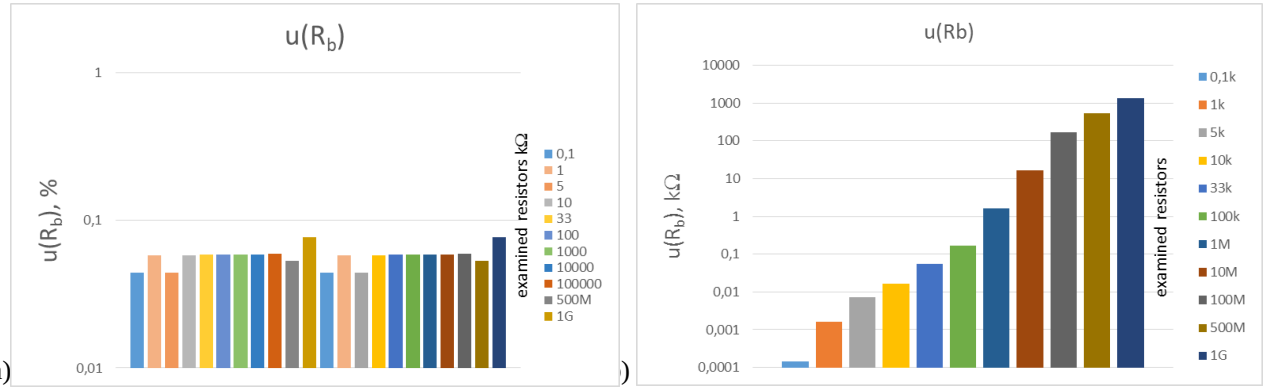

`Fig.5 Combined uncertainties of measured resistance by measuring system: *a – relative values, b– real values*

Tab.1 Values of uncertainties of measure resistance

Resistance, kΩ	0,1	1	5	10	33	100	1000	10000	100000	500M	1G
$u(R_b)$, %	0,044	0,058	0,044	0,058	0,059	0,059	0,059	0,059	0,060	0,054	0,077
u(Rb), kΩ	0,000	0,001	0,002	0,01	0,02	0,06	0,59	5,92	59,76	259,23	682,42

3.2 Uncertainty of measuring resistance of nanostructural carbon-palladium thin films

To calculate uncertainty of measured resistance by measuring system we used data collected accordingly to paragraph 2.3. There are two possible sources of uncertainty; first uncertainty of measuring system and second unknown uncertainty of C-Pd film. According to rules described in paragraph 3 at first we evaluated direct uncertainty of measure resistance C-Pd films following formula (2) and next we evaluated combined uncertainty follow formula (3), where $u_A(x)$ - uncertainty of measure resistance C-Pd films and $u_B(X)$ – combined uncertainty of measure resistance by measuring system evaluated in paragraph 3.1. Fig.6 shows results of evaluation of combined uncertainties of measure resistance C-Pd films in static and dynamic state table Tab.2shows values.

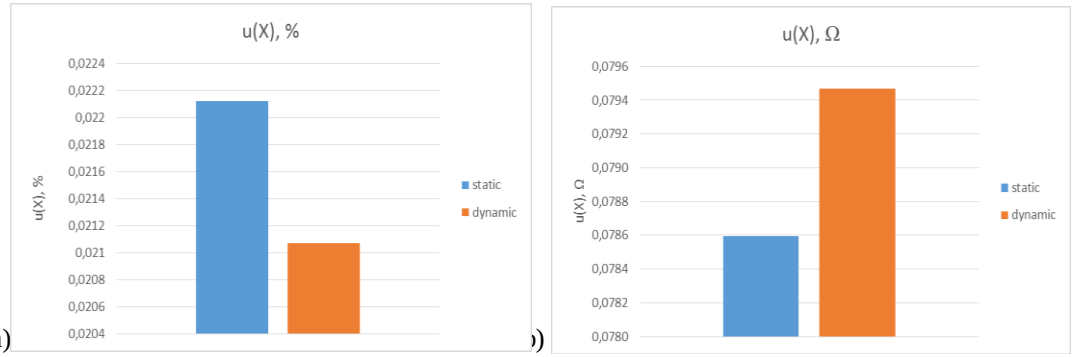

a) b)

Fig.6 Combined uncertainties of measure resistance C-Pd films:*a – relative values, b – real values*

Tab.2 Values of uncertainties of measure resistance C-Pd films

	Static	Dynamic
u(X), %	0,044	0,058
u(X), Ω	0,0786	0,0795

4. CONCLUSIONS

In this paper , the measurement system and its metrological properties were described as well as the uncertainty of measurement of the system during experimental procedure resistance changes of C-Pd films under influence of hydrogen was discussed. The method of uncertainty calculation for was presented. This method concerned the measuring system to examine nanocomposite carbon-palladium thin films prepared by PVD method on ceramic (Al_2O_3) substrates.

The Evaluation of uncertainty of measured resistance using described here measuring system shows that this device has very low uncertainty for wide spectra of measuring resistance.

The Examination of changes of resistance C-Pd films under hydrogen and synthetic air shows that uncertainty of resistance C-Pd films is changing due to presence or not hydrogen in ambient atmosphere. Real values of uncertainty of resistance C-Pd films are bigger in dynamic state. It is connected with a bigger resistance of C-Pd films in a dynamic state. The Relative values of uncertainty of resistance C-Pd films are smaller when the sample was placed in atmosphere-containing hydrogen.

Acknowledgment

The author thanks prof. E.Czerwosz for stimulating discussions as well as for both prof. E.Czerwosz and Ms H.Wronka for preparation of C-Pd samples.

REFERENCES

[1] Kowalska E., Czerwosz E., Kozłowski M., Surga W., Radomska J., Wronka H, „Structural, thermal, and electrical properties of carbonaceous films containing palladium nanocrystals", J. Therm. Anal. Calorim., 101(2), 737–742(2010)

[2] Kozłowski M., Czerwosz E., Dłużewski P., Kowalska E., Radomska J., Wronka H., "Nanostructural C-Pd coatings obtained in 2-steps PVD/CVD technological process", JAMME, 37, 304 (2009)

[3] Kozłowski M., Czerwosz E., Kowalska E, Kamińska A., "Investigation of Pd content in C-Pd films for hydrogen sensor applications", J. Therm. Anal. Calorim., (2011)

[4] Lee E., Min J., Lee E., Noh J., Hyoun J., Jung B., Lee W., "Hydrogen gas sensing performance of Pd–Ni alloy thin films. Thin Solid Films", 519,880–884(2010)

[5] Noh L. -S., Lee J. M., "Low-Dimensional Palladium Nanostructures for Fast and Reliable Hydrogen Gas Detection", Sensors,11, 825–851 (2011)

[6] Zhang D., Sun Y., Jiang C., Zhang Y., "Room temperature hydrogen gas sensor based on palladium decorated tin oxide/molybdenum disulfide ternary hybrid via hydrothermal route", Sens. Actuators B Chem., 242,15–24 (2017)

[7] Lewis F. A. "The Palladium-Hydrogen System a Survey of Hydride Formation and the Effects". Platin. Met. Rev.;26,20–27(1982)

[8] Hugh W, Coleman W., Glenn S. Jr., "Experimentation, Validation, and Uncertainty Analysis for Engineers", John Wiley & Sons, Inc.,3(2009)

[9] International vocabulary of metrology – Basic and general concepts and associated terms ,JCGM 200,(2012)

Modeling of the percolation phenomenon of disordered two-dimensional systems

Paweł Okal*
Dept. of Electric Devices and High Voltage Technology, Lublin University of Technology,
38a, Nadbystrzycka Str., 20-618 Lublin, Poland;

ABSTRACT

The article presents the examination method of the percolation phenomenon by modeling occurring in the metal-dielectric nanocomposites of electron tunneling phenomena. This method using the full high voltage discharge phenomenon. Nanocomposites are materials composed of two types of phases, dielectric and metallic. Metallic phase elements are random distributed on the dielectric matrix. The probability is congruous to normal distribution and nanoparticles sized are not the same. The quantum tunneling phenomenon makes possible the current flow without direct contact between neighboring nanoparticles. The point of the studied phenomenon is the step change conductivity during direct current flow. This step change depends on concentration of metallic phase is called percolation threshold. Due to this phenomenon percolation has become the subject of nanomaterials research. Due to the similarity, the incomplete high-voltage discharges phenomenon in air was used to study percolation. In the model, the air is the dielectric medium. Iron discs simulate the metallic phase. The two-dimensional matrix where he discs will be placed of a dielectric material was made. A random point generator to create coordinates where metal discs will be placed was used. The voltage increase is controlled by the created electronic system connected to a stepper motor that drives the autotransformer. The voltage rise speed is 2 kV / s. Metal disks size 3mm, 6mm, 8mm, 10mm and 14mm were used. The test consists in reading the voltage value at which the dielectric matrix is punctured for different contents of the metallic phase. The inverse of the read voltage is the conductivity value of the entire system. When the content of metal discs is low, the conductivity of the system is low. After exceeding a certain concentration value, there is a step decrease in conductivity. . The point at which a step change in conductivity occurs is called the percolation threshold. To determine the percolation point, dielectric matrices were measured for different contents of the metallic phase. A series of measurements was created that differed in the concentration of metallic discs (the area of the discs in relation to the surface area between the electrodes). For each of them, the breakdown voltage value was measured and a graph of the reversal of this voltage from concentration was created. The result of the test was the direct determination of the percolation threshold value from the obtained graph.

Keywords: percolation, percolation modeling

1. INTRODUCTION

The issue of percolation appeared for the first time in the mid-1940s and the first theoretical article was published in 1952 by Hiroshi Fujita. However, S. R. Broadbent and J.M. Hammersley[1] are considered pioneers whose publications and research included percolation issues. They started research in connection with their new class of mathematical problems. These problems concerned the description of liquid flow through porous bi-and multi-phase media. This problem is intensively studied by mathematicians and physicists from its introduction to literature. The reason for this is the very wide application of this concept in many fields of science, starting from the aforementioned flow of liquids through porous material, spreading diseases in the population, ending with communication, electron transport, jumps of various length, conductivity etc. The number of subsequent publications regarding percolation theory in both books and scientific articles is constantly growing. The number of practical applications is also increasing.

*p.okal@pollub.com

Photonics Applications in Astronomy, Communications, Industry, and High-Energy Physics Experiments 2019,
edited by Ryszard S. Romaniuk, Maciej Linczuk, Proc. of SPIE Vol. 11176, 111764W
© 2019 SPIE · CCC code: 0277-786X/19/$21 · doi: 10.1117/12.2536741

Nanocomposites are disordered systems. Describing these systems as well as modeling phase transitions is very problematic for physicists. Conducting research in this area is justified because they provide the most information about real phenomena at the nanometer scale. It is currently a very dynamically developing branch of science due to the increasing demand for materials with a complex structure and specific physical[2, 3] properties, chemical[4, 5] properties, optical, mechanical properties[6], electrical properties, ferromagnetic[7] properties, photoelectric[8] properties, conductivity[9] properties surface potential tests[10] etc. The production of nanocomposites with specific properties is a complicated process using many techniques, eg plasma techniques, vacuum-arc deposition[11], ion beam sputtering[12], magnetron sputtering[13], ultrasonic cavitation[14, 15]. These are materials currently widely used in technology, medicine, military, space, air technology and other industries.

In the 1950s a phenomenon called a metal-dielectric transition was described whose experimentation was confirmed experimentally. It was found that at the nanometer scale, in the systems composed of metallic and dielectric phases such as the nanocomposite, quantum phenomena related to electron tunneling occur. In micrometer composites the metallic phase particles had to form a metallic path to make the conductivity different from zero. In the case of nanocomposites this was not necessary.

Quantum tunneling is an extraordinary type of guidance. Electrons in materials with high resistance, tunnel between potential wells. If the participation of other types of conductivity, i.e. ionic conductivity or electron and hole conductivity in semiconductors are reduced, electron tunneling occur. From the Schrodinger wave equations it follows that there is an area outside the potential well where is non-zero probability the electron exist. This is basics for the occurrence of the quantum of electron tunneling phenomenon. The probability of the presence of the valence electron outside the potential well at a distance r from the barrier is described by the formula[16]:

$$\Psi^2 = \exp(-2\alpha r) \tag{1}$$

Where: α - inverse of the radius of the location of the electron; r - distance from the potential well where the electron is located:

$$\alpha^{-1} \cong R_B \tag{2}$$

Where: Rb - the radius of the location of the electron in the potential well, otherwise called the Bohr radius.

Using this fact, on the nanometer scale one can conclude that there is a non-zero probability that the electron tunneling from the first well to the next one. Important fact is the electrons jumps between potential wells below the potential barrier. The electron takes external thermal energy ΔW which is smaller than the potential barrier voltage. Without the involvement of external factors, the direction of electron tunneling is random and unorganized. When the external electric field operates, the direction of tunneling becomes orderly. This is due to the Debye factor:

$$\exp\left(\pm\frac{e\cdot r\cdot E}{k\cdot T}\right) = \sinh\left(\frac{e\cdot r\cdot E}{k\cdot T}\right) \tag{3}$$

Where: e - charge of the electron, r - distance between the neutral atom from which the electron is tuned and the positive ion to which it jumps (tunnel); E - intensity of electric field; K - Boltzman's constant; T – temperature.

It follows from this formula that when the external electric field is activated, the vast majority of electrons tunnel in the direction opposite to the external electric field. Electrons tunnel between potential wells in two different ways. The first case concerns the poor location of electrons. Because this phenomenon occurs at temperatures close to the temperature of liquid helium, it is not taken into account in the following article. The second mechanism occurs in the case of a strong electron location and high temperatures. Nevill Mott was the author and precursor of this theory. He dealt with the tunneling of electrons in disordered semiconductors and dielectrics. The formula below describes the conductivity between neighboring potential wells:

$$\sigma = \sigma_0 \exp\left(-2\alpha r - \frac{\Delta W}{kT} \right) \tag{4}$$

Analyzing the above given formula, in the mechanism of tunneling between neighboring wells, the conductivity strongly depends on the temperature. The activation energy, resulting from the formula (4), results from the fact that the electron usually jumps from the lower energy level in the first well potential to a higher level in the second well. In nanocomposites, the distance between potential wells is a function of the N concentration resulting from formula (4):

$$r \approx N^{-\frac{1}{3}} \tag{5}$$

Formulas [3] [4] show that the conductivity is non-linear. It follows that conductivity is faster than linear increases with the concentration of wells of potentials. Mott calculated[16] that the change in the conductivity type occurs then, the concentration of the potential wells will be large enough that the radius will be less than 2.5 Bohr radius.

$$r \cong 2{,}5 R_B \tag{6}$$

There will be a transition from the dielectric type conductivity characterized by a positive temperature coefficient of conductivity $d\sigma / dT > 0$ for the conductivity of the metallic type with $d\sigma / dT < 0$.
The transition from the dielectric conductivity at low contents to the metallic type in the area of high content wells is related to the phenomenon of percolation threshold. Below this threshold, along with the increase of the metallic phase the increase in the conductivity of the nanocomposite is very small, while the increase in conductivity increases severely above the percolation threshold.

The phenomenon of percolation and percolation threshold covers a wide range of issues related to the flow of electric current in spatial networks and in the manufactured of metal-dielectric type nanomaterials. Until now networks consisting of various resistive, resistive-capacitive and even inductive-resistive-capacitive elements have been used to model the phenomenon of percolation. Models were created based on the fact that the elements were placed in the nodes of the network and connected with each other. When a continuous path was created in the network in such a way that there is a way to transfer current from one end of the network to another through network elements. Then we talk about the connection which is called the percolation channel. When some nodes are broken, their resistance will be infinite. At some point during intersections between nodes, all percolation channels will be interrupted. Then the conductivity of the system as in the current value will be 0 while the change point of these properties of the whole system will be called the percolation threshold. This state in networks composed of passive elements can be achieved in two ways. In the first of them, randomly defined nodes are eliminated. In the second case, the segments connecting the nodes are crossed. There are also other ways to model the phenomenon of percolation. There were, for example, attempts to conduct electric current conduction through randomly mixed spheres of identical dimensions, some of which were made of metal, and some - from insulating material. Gradually increasing the content of metallic balls we achieve a rapid increase in the current from virtually zero which corresponds to going through the percolation threshold. This means that in the ball mixture a percolation channel was created in which the metallic balls in contact connect the two contacts connected to the power source. Both in network and ball models below the percolation threshold, the current does not flow. This means that the resistance below the percolation threshold reaches an infinite value.
Unfortunately both the network and ball models do not allow for determining the percolation channel route. In addition, the models do not take into account that in nanocomposites, current conduction is also below and below the percolation threshold, and as the content of the metallic phase increases the conductivity of the material increases (patterns 4,5).

2. RESEARCH AND ANALYSIS

To explore the phenomenon of percolation a two-dimensional model was created. This model was based on the phenomenon of a complete high voltage discharge in the air. The idea of the model was the random arrangement of metal disks that model the metallic phase on the dielectric matrix. The air between the disks determine a dielectric phase. This assumption is very similar to quantum tunneling in nanocomposites. Comparing the high-voltage discharges in the air and

quantum tunneling, one can notice the similarity of both phenomena. In the nanocomposite, as the distance between nanoparticles of the metallic phase decreases, the probability of electron tunneling between potential wells increases. Similarly with a full high voltage discharge in the air. As the distance between the metal discs decreases, the value of the jump voltage decreases. As can be seen from equations 4 and 5, concentration directly affects the conductivity of a metal-type nanocomposite dielectric. Concentration is inversely proportional to conductivity. The high-voltage discharge in the air is a macroscopic phenomenon and electron quantum tunneling is a nanometer phenomenon. The scale of these phenomena is completely different but the underlying conductivity allows modeling of tunneling by means of high voltage discharges in the air.

The created model is two-dimensional. A matrix with randomly generated coordinates of points was created. These are places where metal discs representing the metallic phase will be placed. Coordinates of points were generated using a computer program. A random point generator was used as well as developed algorithms that avoided conflict in the surrounding environment so that they would not have a common part. The matrix thus generated was placed on a dielectric basis of high strength. This limits the analysis of the phenomenon to two axes. The size of the matrix is 25 cm by 22.5 cm. This value is limited by the maximum generator AC voltage which is 155.6 kV.

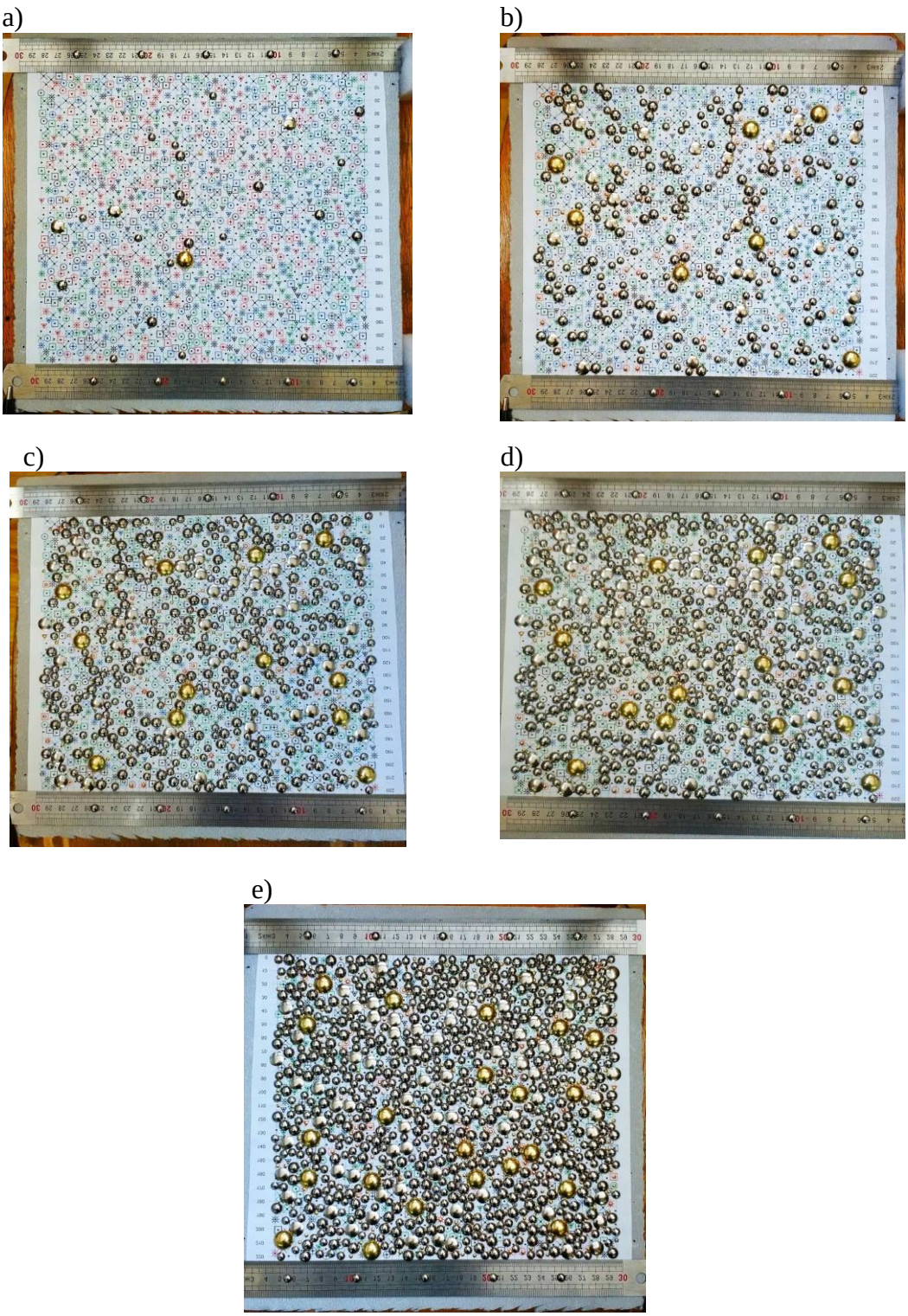

Figure 1. Positions of metallic discs modeling "nanoparticles" for different concentration: a) 2,21%; b) 16,18%; c) 32,59%; d) 54,38%; e) 68,96%.

The metal discs have sizes: 3mm, 6mm 8mm 10mm and 14mm. Their amount is consistent with the normal distribution as it occurs in nanocomposites and nanomaterials. High voltage was generated by using a high voltage transformer. Two flat electrodes were placed parallel at a distance of 22.5 cm. The transformer had an electronic circuit[17] that controlled its operation so that the voltage would grow at 2 kV / s.
During the voltage increase a jump occurred. This jump occurred in the air, between the flat electrodes along the path of the least resistance. This resistance was reduced by the presence of metal discs. The test was based on the readout of the voltage of the jump voltage for the ever-increasing infiltration - less and less inter-electrode space. The study used 980 disks that were divided into 32 groups. In each series the size distribution of the discs was also close to normal. By adding another group of disks, the fill value was increased by 1,79-2,28%. Measurements were repeated 3 times and the results were averaged. In this way, the jump voltage characteristic was obtained depending on the filling.

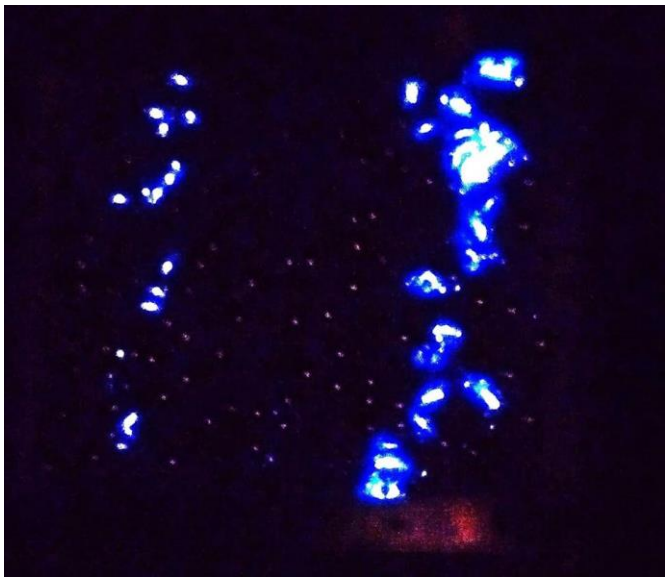

Figure 2. Registration of percolation channels in the darkroom for 67% concentration.

The test proved that with the increase in the concentration of "nanoparticles" the voltage value between the electrodes decreases. Fig. 3 shows the relationship between the inverse of the breakdown voltage and the concentration of metal disks. In addition, different sizes of metal disks were used. Their distribution is close to normal and this was determined based on the analysis of nanocomposites.

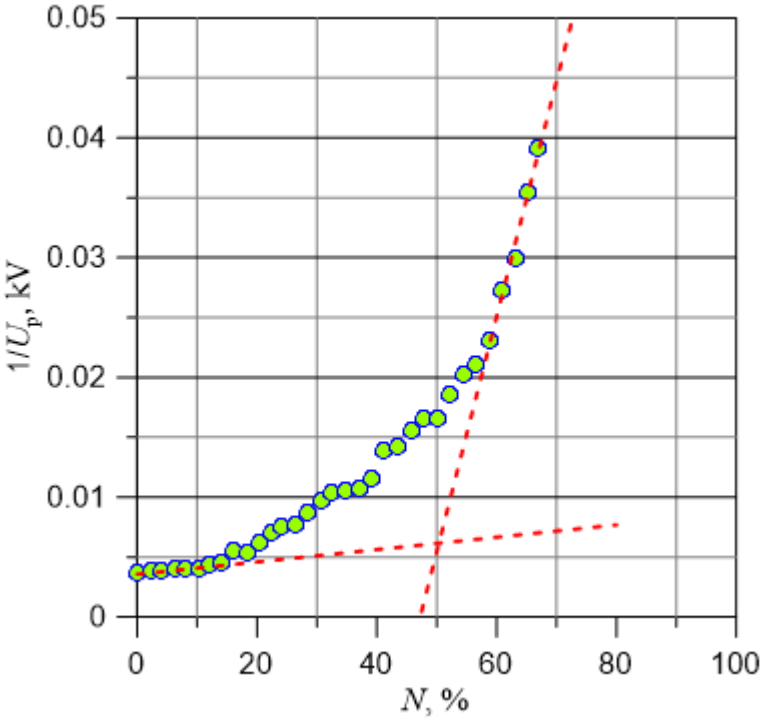

Figure 3. Graph of the inverse of the breakdown voltage and concentration.

As the concentration of the metallic phase increases, the voltage of the jump decreases. Exactly the same happens in nanocomposites, where along with the increase of nanoparticles, the conductivity of the system increases. The first part of the characteristic refers to the area of low concentration. The increase in conductivity in this part is small. This can be interpreted as a type of dielectric conductivity. For a certain characteristic point, after exceeding a given concentration, there is a sudden change in conductivity. In the following, the characteristics are linear again. This section is equivalent to metallic conductivity. The point of concentration in which the abrupt change in conductivity is the point of percolation. This point was determined by approximation of the linear sections of the characteristic and constitutes 51%. It should be noted that below the percolation threshold, i.e. in the dielectric conductivity, the conductivity is different from 0. The current flow is possible as in nanocomposites, also below the percolation threshold, which gives the model advantage over others. The second advantage of this model is the ability to determine the percolation channel route. Network and ball models based on the flow of electric current do not allow this to deviate from the actual systems (see patterns 4.5).

3. CONCLUSION

The model of percolation analysis in metal-type dielectric nanocomposites is presented. The model was based on high voltage electrical discharge in the air. The metallic phase of the nanocomposite is modeled by metal discs. Random dots on the matrix were generated for the named disks. A test stand was built to measure flashover voltage. From the above measurements, the relationship between the changeover voltage and the concentration was formed. By approximating the straight lines in the graph, the percolation threshold was estimated. It was established that the voltage decreases with the concentration of "nanoparticles". In addition, percolation channels were recorded during discharges in the form of photographs.

REFERENCES

[1] Broadbent, S. R., Hammersley J. M., "Percolation Processes I. Crystals and Mazes," Mathematical Proceedings of the Cambridge Philosophical Society, 53(3), 629-641 (1957).

[2] Zukowski, P., Koltunowicz, T., Partyka, J., Wegierek, P., Komarov, F. F., Mironov, A. M., Butkievith, N., Freik, D., "Dielectric properties and model of hopping conductivity of GaAs irradiated by H+ ions," Vacuum, 81(10), 1137-1140 (2007).

[3] Khezri, K.,Fazli, Y., "Synthesis and Characterization of Poly (styrene-co-butyl acrylate)/Silica Aerogel Nanocomposites by in situ AGET ATRP: Investigating Thermal Properties," High Temperature Materials and Processes, 36(10), 955-962 (2017).

[4] Kołtunowicz, T. N., Zhukowski, P., Fedotova, V. V., Saad, A. M., Fedotov, A, K., "Hopping Conductance in Nanocomposites (Fe0.45Co0.45Zr0.10)x(Al2O3)1-x Manufactured by Ion-Beam Sputtering of Complex Target in Ar+O2 Ambient," Acta Physica Polonica A, 120(1), 39-42 (2011).

[5] Fedotov, A. S., Shepelevich, V., Poznyak, S., Tsybulskaya, L., Mazanik, A., Svito, I., Gusakova, S., Zukowski, P., Koltunowicz, T. N., "Simulation of polycrystalline bismuth films Seebeck coefficient based on experimental texture identification," Materials Chemistry and Physics, 177(1), 413-416 (2016).

[6] Pogrebnjak, A. D., Il'yashenko, M. V., Kaverin, M. V., Shypylenko, A. P., Pshyk, A. V., Beresnev, V. M., Kitik, G. V., Erdybayeva, N. K., Makhmudov, N. A., Kolisnichenko, O. V., Tyurin, Yu. N., Shpak, A. P., "Physical and Mechanical Properties of the Nanocomposite and Combined Ti-N-Si/WC-Co-Cr та Ti-N-Si/(Cr3C2)75-(NiCr)25 Coatings," Journal of Nano- and Electronic Physics, 1(4), (2009).

[7] Koltunowicz, T. N., P. Zukowski, P., Boiko, O., Saad, A., Fedotova, J. A., Fedotov, A. K., Larkin, A., Kasiuk, J., "AC Hopping Conductance in Nanocomposite Films with Ferromagnetic Alloy Nanoparticles in a PbZrTiO3 Matrix," Journal of Electronic Materials, 44(7), 2260-2268 (2015).

[8] Pantsialeyeu, K. U., Krautsevich, A. U., Rovba, I. A., Lysenko, V. I., Vorobey, R. I., Gusev, O. K., Zharin, A. L., " Analysis of the electrophysical and photoelectric properties of nanocomposite polymers by the modified Kelvin probe," Devices and Methods of Measurements, 8(4), 386-397 (2017).

[9] Kołtunowicz, T. N., Zhukowski, P., Fedotova, V. V., Saad, A. M., Larkin, A. K., "The features of real part of admittance in the nanocomposites (Fe45Co45Zr10)x(Al2O3)100-x manufactured by Ion-Beam Sputtering Technique with Ar Ions," Acta Physica Polonica A, 120(1), 35-38 (2011).

[10] Tyavlosky, A. K., Zharin, A. L., Gusev, O. K., Varabei, R. I., Muhurov, N. I., Sharonov, G. V., Pantsialeyeu, K. U., "Analysis of surface defects of aluminum and its alloys with a scanning Kelvin probe," Devices and Methods of Measurements, 8(1), 61-76 (2017).

[11] Gorbachov, L.A, Pogrebnjak, A. D., Kuzema, O. S., "Formation of new Phases and Local High Temperatures in Nanoscaled Areas During Cyclic Fracture of Steel," Journal of Nano- and Electronic Physics, 1(4), (2009).

[12] Svito, I. A., Fedotov, A. K., Saad, A., Zukowski, P., Koltunowicz, T. N., "Influence of oxide matrix on electron transport in (FeCoZr)x(Al2O3)1-x nanocomposite films," Journal of Alloys and Compounds, 699(1), 818–823 (2017).

[13] Zhukowski, P., Kołtunowicz, T. N., Fedotova, J. A., Larkin, A. V., "An effect of annealing on electric properties of nanocomposites (CoFeZr)x(Al2O3)1-x produced by magnetron sputtering in the atmosphere of argon and oxygen beyond the percolation threshold," Przegląd Elektrotechniczny, 86(7), 157-159 (2010).

[14] Xuan, Y., Jia, S., Nastac, L., "Processing and Microstructure Characteristics of As-Cast A356 Alloys Manufactured via Ultrasonic Cavitation during Solidification," High Temperature Materials and Processes, 36(4), 381-387 (2017).

[15] Xuan, Y., Zhang, D., Nastac, L., "An Experimental and Modeling Investigation of Al-based Nanocomposites Manufactured via Ultrasonic Cavitation and Solidification Processing," High Temperature Materials and Processes, 5(8), 16022-16031 (2018).

[16] Mott, N. F., Davis, E. A., [Electron Processes in Non-Crystalline Materials], Clarendon Press, Oxford (1979).

[17] Dudrik, J., Marcel, B., Špánik, P., "Soft switching full-bridge PWM DC/DC converter using secondary snubber," Journal of Electrical and Electronics Engineering, 2(1), (2009).

Technology and characterization of ISFET structures with graphene membrane

Kinga Kondracka*[a], Piotr Firek[a], Piotr Caban[b], Aleksandra Przewłoka[b], Jan Szmidt[a]
[a]Warsaw University of Technology, Institute of Microelectronics and Optoelectronics, Koszykowa 75, 00-662 Warszawa, Poland;
[b] Institute of Electronic Materials Technology

ABSTRACT

Graphene due to its properties, such as high sensitivity and biocompatibility finds application in instruments that are used to cooperation with organic substances. At the same time, from the point of view of sensory devices, it is a material with high absorption potential that is able to improve sensitivity and selectivity of these devices. Another benefit of graphene application may be to use its properties in connection with ISFET – Ion Sensitive Field Effect Transistor, which operation principle is based mostly on detection of changes in hydrogen ions concentration.

ISFET transistors ale produced in MOS technology, the difference between them and classic MOSFET (Metal-Oxide-Semiconductor Field Effect Transistor) structures is gate area, where gate metallization was replaced with reference electrode submerged in solution applied in this area. Properties of the solution determine transistor's action. It is possible to make modifications in gate area of the structure which effects in changes of transistor's properties. Example of such a modification may be application of graphene layer, which properties may significantly improve detecting capabilities of ISFET devices. For the needs of the research described in this work, graphene was deposited in gate area of transistors through transfer from cooper and germanium surfaces.

To check correctness of ISFETs with graphene layer work, current – voltage characteristics of them were determined. Standard I-V characteristics with SiO_2 as gate dielectric were compared with these where gate area was enriched with a graphene layer. Structures with graphene mostly worked properly. Thanks to the results presented in this work, it is possible to carry out further experiments using this structures and organic substances.

Keywords: ISFET, graphene, membrane, I-V characteristics

1. INTRODUCTION

At present, the growing Internet of Things market is causing the development of new optical and electronic sensors. Sensing elements [1] and advanced sensor systems [2] requires appropriate microelectronic technologies. ISFET transistors are ion-sensitive field effective transistors which principle of operation is similar to MOSFET, but due to different construction it differs in possible applications. ISFET transistors find use as sensors in agriculture, environmental protection [3], or biology [4][5]. The studies carried out so far indicate the possibility of detecting cell viability with the help of the ISFET transistor [6], but still sensitivity and biocompatibility of devices based on this structure need improvement. Such improvement may be provided by the use of graphene and its compounds as a layer deposited on the transistor. Graphene has good electrical conductivity, high surface area, high strength, good elastic properties, good thermal conductivity and ease of functionalization. It has various applications in energy storage devices, fuel cells and what is most important in case of this work – sensors. It is used in biomedical applications such as diagnosis or drug delivery [7]. It is known for being a good candidate as pH sensor [8][9] what is a common point for it and ISFET transistors. This paper will discuss the stages of adaptation of the ISFET transistor for biological application by applying graphene to it and the electrical characterization of such a structure.

Photonics Applications in Astronomy, Communications, Industry, and High-Energy Physics Experiments 2019, edited by Ryszard S. Romaniuk, Maciej Linczuk, Proc. of SPIE Vol. 11176, 111764X
© 2019 SPIE · CCC code: 0277-786X/19/$21 · doi: 10.1117/12.2536746

2. MATERIALS AND METHODS

2.1 Transistors

ISFETs are field effect transistors that are sensitive to the change in hydrogen ions concentration, and are therefore able to detect pH changes. This is possible due to the fact that the ISFET construction is similar to the typical MOSFET transistor, the difference however occurs in the gate area, where metallization is replaced by a solution with a reference electrode immersed in it.

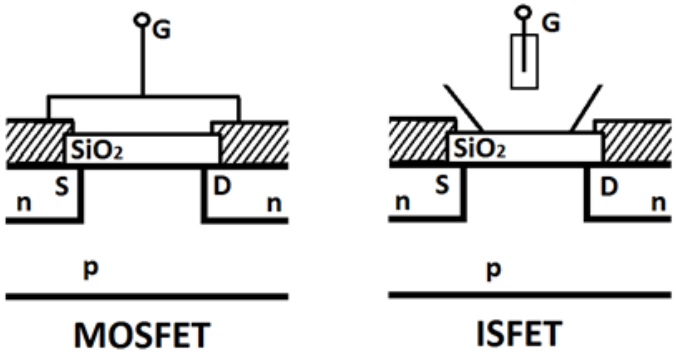

Figure 1. Comparison of MOSFET (left) and ISFET (right) transistors.

ISFET is able to indicate the change of ion concentration in the area of the gate by changing the width of the channel, and thus the value of current flowing through it. Such transistors are made in the standard MOS technology, the process of their production has been described in section 2.3. Both in the basic SiO_2 form as the gate oxide and with the modifications, it is used as a sensor for various types of applications, among others - biological. One of the possible modifications is the use of the graphene layer, which makes it possible to improve the biocompatibility of the gate area, the adhesion of the cells, their survival and the electrical effect on the transistor.

2.2 Graphene

Graphene is a flat structure composed of carbon atoms, connected in hexagons. The material resembles a honeycomb shape, and because it has a one-atomic thickness, it is approximately a two-dimensional structure. Graphene is of interest to the industry due to its various properties, including electrical and mechanical. The special properties of graphene such as high electrical conductivity, mechanical strength, thermal stability and larger surface area makes them suitable for various applications as sensors, electronic devices, composite materials, catalysts [10]. Apart from this, graphene and graphene based materials have found increasing applications in biomedical field for imaging [11], biosensing [12], drug delivery, [13], photothermal cancer therapy [14] and tissue engineering [15]. The basal planar structure and high surface area allows graphene to act as a template for the delivery of biological molecules and drugs. Use of graphene as a tissue engineering scaffold has recently gained interest after graphene was found to promote the attachment and proliferation of several mammalian cell lines [16]. Also, graphene oxide (GO) and graphene sheets has been reported in the context of antibacterial activity [17].

2.3 Production

The ISFET transistors are made almost identically like MISFET transistors, only the metallization step in the gate area is omitted. A detailed description of the transistor production process and graphene application procedure are described below.

The production of such a transistor can be made in standard MOS technology. Silicon p-type ground plates with an orientation <100> and resistivity of 1-10 Ωcm are used. At the beginning, the impurities and the natural oxide produced on the silicon are removed. After exposing the silicon monocrystal, the plate is subjected to oxidation in an atmosphere of water vapor. The oxide that was created as a result of this process serves as a mask for the source and drain diffusion process (a).

The next stage is the first photolithography. The positive emulsion is centrifuged on the plate and then heated for 30 min. Then the emulsion is irradiated, and a pattern is formed on the tile, which is then induced in the developer, after which the plate is rinsed in deionized water. After additional hardening of the photoresist pattern on the plate, it is etched in a hydrofluoric acid buffer solution, which results in the desired pattern in the oxide. After this process, the photoresist is removed with acetone, and the plate rinsed and dried on the centrifuge.

Drains and sources are produced in a technological furnace with a phosphorus diffusion chamber. At the beginning, previously unveiled areas are oxidized, then in the process of pre-diffusion, phosphorus is introduced, and finally during the so-called re-diffusion phosphorus diffuses with the enamel layer to the previously exposed silicon in drainage and source areas (b). The phosphorus is removed in the HF solution without significantly affecting the field oxide.

The next step is the second photolithography, the course of which is similar to the first, in this case, however, it is necessary to center the mask. During this photolithography, in the mask, the channel areas are additionally exposed.

After the above-mentioned treatments it is necessary to remove residual reagents, remove organic and metallic contaminants. As a result of cleaning, an oxide is formed on the surface of the plate, it is removed in the HF solution. Thanks to these preparations, the plate is ready to produce on it a gate dielectric. The dielectric is the SiO_2 layer, which is obtained during thermal oxidation in the furnace (c).

The third photolithography goes like the previous ones, this time the windows in the mask reflect the contacts (d). After its completion, windows for contacts are exposed in the silicon layer (e). Then, aluminum is vaporized on the plate in the vacuum chamber and the last, fourth photolithography is carried out. In this photolithography metallization shapes are mapped on the mask. Metallization is also removed from the gate area because this area remains exposed in the ISFET transistor (f).

The plate is then cut into single transistors and graphene is transferred to their gate areas. In the case of the structures analyzed in this article, graphene transferred from cooper and germanium were used.

The first step is to create a graphene layer with CVD method [18] on transition metals such as copper or germanium. Then the transition metal with graphene is coated with the PMMA polymer and the copper layer is etched with ammonium persulfate. Graphene along with PMMA is applied to the SiO_2 layer of the transistor. Finally, the PMMA layer is etched, so that we get a transistor with a graphene layer in the gate area. Deposition of graphene was completed at the Institute of Electronic Materials Technology.

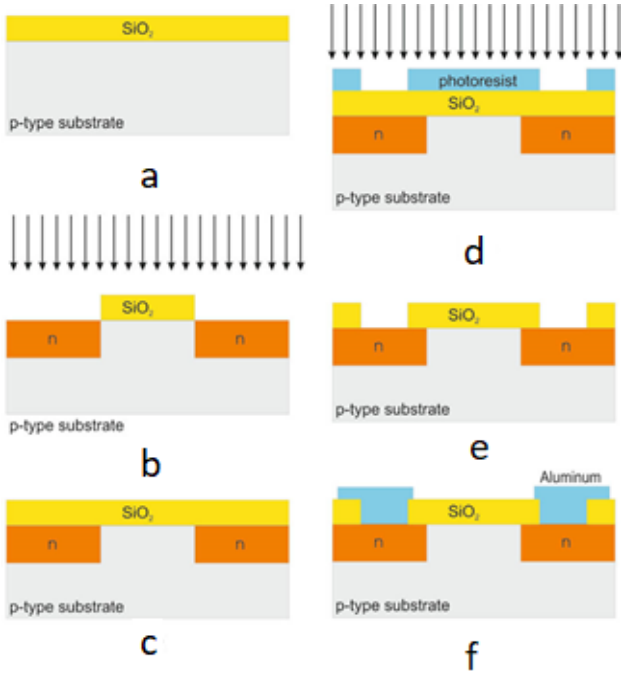

Figure 2. Production of ISFET transistor

2.4 Measurements

In order to check the correct operation of the transistors after graphene application, their current-voltage characteristics were determined, both output and transition. As a solution applied to the gate area of the structures, deionized water was used. In order to make such a measurement possible, it is necessary to use a special measuring station, where the transistor is placed in a 3D measuring cell with tube through which the solution is supplied to the transistor. To facilitate the connection of contacts in the transistor with voltage sources and measuring devices, as well as the supply of the solution, the transistor is connected to a PCB dedicated to it.

A voltage was supplied between the source and the drain, in the range 0-5V, for each subsequent value of this voltage the voltage supplied between the source and the gate was also changed in the range of 0-5 V for the output and transitional characteristics. These measurements were carried out at the Institute of Microelectronics and Optoelectronics of the Warsaw University of Technology.

3. RESULTS

To check the correctness of transistors after applying graphene, 10 structures were used, 6 of them had graphene transferred from copper and 4 transferred from germanium. Both of these groups showed the correct operation of the transistors. The individual pieces showed some disturbances, probably due to the transistors being assembled to PCB boards after the graphene was applied to them. On the basis of these results, it can be stipulated that the application of the graphene layer does not worsen the general mode of operation of the ISFET transistor at an electric angle, the level of available current values have not diminished. In the case of graphene transferred from germanium, the currents were slightly higher than for copper, but the order of magnitude remained the same. Due to the fact that the experiment aimed at checking the correctness of the operation of devices made in a particular technology, the sample size was small, therefore it is difficult to tell if the previously described difference is a rule or only a matter of specific devices.

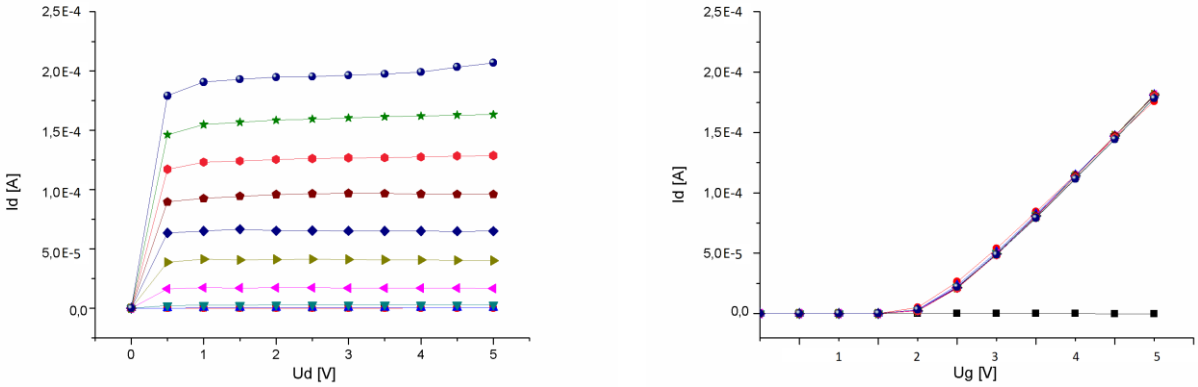

Figure 3. Output (left) and transitional (right) I-V characteristics of ISFET transistor with graphene layer transferred from cooper.

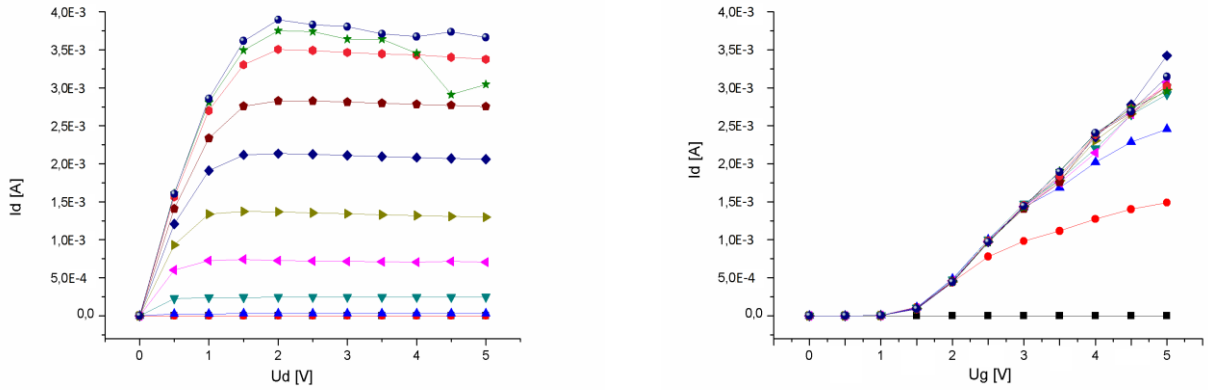

Figure 4. Output (left) and transitional (right) I-V characteristics of ISFET transistor with graphene layer transferred from germanium.

4. CONCLUSIONS

Obtained results shows that structures with graphene transferred from germanium presents better properties than this where graphene from cooper was transferred. Applying the graphene layer to the ISFET transistor does not change its electrical properties, it is possible to proceed to the next stage of testing this type of devices, i.e. to apply biological material to them. The influence of graphene properties on the interaction between the transistor and the biological substance will be checked. As stated in the section with results, several transistors did not work properly, but it probably resulted from the fact that after applying graphene, transistors were subjected to assembly operations, after which they were not cleaned due to the possibility of damage to the applied graphene layer. In the future, an attempt is made to apply graphene to the transistor already mounted to the PCB, in order to avoid the additional possibility of damaging the transistor or applied layer during possible operations at the transistor.

REFERENCES

[1] Borecki M., et al., "Large-area transparent in visible range silicon carbide photodiode," Proc. SPIE 8903, 89030H (2013).
[2] Borecki M., Korwin-Pawlowski M.L., Bebłowska M., "A method of examination of liquids by neural network analysis of reflectometric and transmission time domain data from optical capillaries and fibers," IEEE Sensors Journal 7, 1208-1213 (2008).
[3] Poghossian, A., Baade, A., Emons, H. and Schöning, M. J., “Application of ISFETs for pH Measurement in Rain Droplets,” Sensors and Actuators B Chemical 76, 634-638 (2001).
[4] Lee, C. S., Kim, S. K. and Kim, M., “Ion-sensitive field-effect transistor for biological sensing,” Sensors 9(9), 7111–7131 (2009).
[5] Firek P., et al., "ISFET structures with chemically modified membrane for bovine serum albumin detection," Circuit World 44, 45-50 (2018).
[6] Arafa, H., Obahiagbon, U., Kullman, D., Domínguez, F., Magee, A. and Christen, J. B., "Characterization and application of a discrete quartz extended-gate ISFET for the assessment of tumor cell viability," Proc. IEEE Healthcare Innovation Point-Of-Care Technologies Conference (HI-POCT), 62-65 (2016).
[7] Gurunathan, S., Kim, J. H., “Synthesis, toxicity, biocompatibility, and biomedical applications of graphene and graphene-related materials,” International journal of nanomedicine 11, 1927–1945 (2016).
[8] Kiani, M. J., Ahmadi, M. T., Karimi Feiz Abadi, H., Rahmani, M., Hashim, A. and Che Harun, F. K., “Analytical modelling of monolayer graphene-based ion-sensitive FET to pH changes,” Nanoscale research letters 8(1), 173 (2013).

[9] Firek P., et al., "Properties of AlN thin films deposited by means of magnetron sputtering for ISFET applications," Materials Science-Poland 33, 669–676 (2015).
[10] Robinson, J. T., Tabakman, S. M., Liang, Y., Wang, H., Casalongue, H. S., Vinh, D. and Dai, H., "Ultrasmall Reduced Graphene Oxide with High Near-Infrared Absorbance for Photothermal Therapy," Journal of the American Chemical Society 133(17), 6825-6831 (2011).
[11] Gollavelli, G., Ling, Y. C., "Multi-functional graphene as an in vitro and in vivo imaging probe," Biomaterials 33(8), 2532-2545 (2012).
[12] Du, D., Wang, L., Shao, Y., Wang, J., Engelhard, M. H. and Lin Y., "Functionalized Graphene Oxide as a Nanocarrier in a Multienzyme Labeling Amplification Strategy for Ultrasensitive Electrochemical Immunoassay of Phosphorylated p53 (S392)," Analytical Chemistry 83(3), 746-752 (2011).
[13] Zhang, L., Xia, J., Zhao, Q., Liu, L. and Zhang, Z., "Functional graphene oxide as a nanocarrier for controlled loading and targeted delivery of mixed anticancer drugs," Small 6, 537–544 (2010).
[14] Yang, K., Zhang, S., Zhang, G., Sun, X., Lee, S. T. and Liu, Z., "Graphene in Mice: Ultrahigh In Vivo Tumor Uptake and Efficient Photothermal Therapy," Nano Letters 10(9), 3318-3323 (2010).
[15] Chen, G. Y., Pang, D. W. P., Hwang, S. M., Tuan H. Y. and Hu, Y. C., "A graphene-based platform for induced pluripotent stem cells culture and differentiation," Biomaterials 33(2), 418-427 (2012).
[16] Agarwal, S., Zhou, X., Ye, F., He, Q., Chen, G. C. K., Soo, J., Boey, F., Zhang, H. and Chen P., "Interfacing live cells with nanocarbon substrates," Langmuir 26(4), 2244-2247 (2010).
[17] Hu, W., Peng, C., Lv, M., Li, X., Zhang, Y., Chen, N., Fan, C. and Huang Q., "Protein Corona-Mediated Mitigation of Cytotoxicity of Graphene Oxide," ACS Nano 5(5), 3693-3700 (2011).
[18] Losurdo, M., Giangregorio, M. M., Capezzuto, P. and Bruno, G., "Graphene CVD growth on copper and nickel: Role of hydrogen in kinetics and structure," Physical Chemistry Chemical Physics 13, 20836-43 (2011).

Prediction method of input parameters impacting of dimensional accuracy of high aspect ratio holes obtained by using EDD

M. Machno*[a], A. Matras[b]

[a]Rail Vehicles Institute, [b]Production Engineering Institute, Mechanical Faculty, Cracow University of Technology, Avenue Jana Pawła II 37, PL 31-864 Cracow, Poland

ABSTRACT

This paper deals with the optimization of technological parameters (such as discharge voltage, current amplitude, time of impulse) to improve a dimensional accuracy of high aspect ratio holes obtained by using electrical discharge drilling (EDD). High aspect ratio holes characterize aspect ratio length to diameter of hole above 10 and diameter less than 1 mm. Due to drilling the holes included difficulties, especially in case applying difficult–to–machine materials as workpiece. In the first part of the article, based on the results analysis of experimental research, a mathematical model is developed. The second part of the study presents the results analysis of method prediction of selected process parameters which influence the technological factors such as linear tool wear, material removal rate and conicity angle.

Keywords: Electrical Discharge Drilling (EDD), deep hole, difficult–to–machine material, prediction method, RSM.

1. INTRODUCTION

Nowadays, the industry is focused on the producing of parts which characterize smaller dimensions with much better properties and made of difficult–to –machine advanced materials such as titanium and nickel alloy, ceramics and composite[1-4]. Manufacturing technologies of drilling microholes (with diameter in the range 8 – 500 μm and aspect ratio above 20:1) in these materials, are needed in aeroplane and automotive industry[5,6]. Fabrication of the holes in difficult–to–machine materials by using conventional methods is very challenging, especially in case reaching of high precision and accuracy machined parts and shapes[7-10]. Due to a non–conventional methods are used to machine these materials.

In case performing of holes, electrical discharge drilling (EDD) is one of the most used effective techniques to drill, especially high aspect ratio holes (above 20:1) with small diameters (less than 1 mm)[11-12]. In EDD process material is removed by the action of electrical discharges between electrodes (one of the electrodes is a workpiece and the second one is a tool) in a narrow gap. It gives the possibility to machine regardless of the material hardness. The electrical sparks make possible to remove the material by melting and evaporation of workpiece and material electrode. The work material and tool electrode are immersed in dielectric liquid[13-14]. The main advantages of EDD process include: simple tooling and its capability of drilling multiple holes simultaneously, lack of burrs, ability to drill on tilted surfaces[15].

When the drilling microholes, insufficient flushing area between electrodes can contribute to accumulate debris particles at the bottom of hole. The accumulated debris generates secondary discharges which lead to poor shape accuracy holes such as hole taper and hole dilation, increase of tool wear (side and end), low material removal rate[13,16]. In case the holes characterize large aspect ratio, the problem of debris removal can be solved with applying different electrode movements (planetary or rotary) or vibration assisted methods[16,17].

*magdalena.machno@mech.pk.edu.pl; phone +48 12 374 36 56; fax +48 12 374 36 56; mech.pk.edu.pl

Photonics Applications in Astronomy, Communications, Industry, and High-Energy Physics Experiments 2019, edited by Ryszard S. Romaniuk, Maciej Linczuk, Proc. of SPIE Vol. 11176, 111764Y
© 2019 SPIE · CCC code: 0277-786X/19/$21 · doi: 10.1117/12.2536749

To understand and to improve EDD process, the influence of process parameters on the technological factors are analyzed[15,18]. Results of analysis are used to optimize EDD process parameters. Selecting process parameters with appropriate values plays an important role to obtain high material removal rate, low tool wear, high quality of surface (low surface roughness parameter) and high accuracy of holes. Many researchers deal with optimizing parameters (such as current amplitude, time of the impulse, duty cycle, voltage) by using various optimization techniques[19,20]. These techniques include: RSM, ANOVA, GRA, TOPSIS, Fuzzy logic, artificial neutral network (ANN), Taguchi techniques[19,21-27].

In this study, the optimized method is presented that involves the prediction of input parameters (such as current amplitude, time of the impulse and discharge voltage). The proposed method is determined on basis of the experimental tests. In the first part of the article, the results experimental research of EDD are presented. The experimental tests involve the impact of process parameters on the linear tool wear, taper angle and drilling speed. The second part of the paper presents using of optimization method such as RSM (Response Surface Methodology) to obtain high drilling speed, low linear tool wear and satisfactory taper angle. RSM is a one of the numerous statistical method which is widely applied to optimize the process parameters.

2. RESEARCH METHODOLOGY

The experimental research included EDD high aspect ratio holes (aspect ratio of length to diameter is above 10). Inconel 718 alloy was selected as workpiece. The chemical composition and major mechanical properties of this alloy are presented in Table 1 and 2, respectively.

Table1. Chemical composition of Inconel 718 (wt. %).

	Ni	**Cr**	**Fe**	**Nb**	**Mo**	**Ti**	**Al**	**Co**	**Mn**	**C**	**Si**	**P**
Max.	55.00	21.00	Balance	4.75	2.80	0.65	0.20	1.00	0.35	0.08	0.35	0.015
Min.	50.00	17.00		5.50	3.30	1.15	0.80	-	-	-	-	-

Table2. Thermal properties of Inconel 718.

Density (kg/m^3)	8190
Heat capacity (J/kgK)	0.2T(°C)+ 421.7
Thermal conductivity (W/(mK)	0.015T(°C) + 11.002
Melting temperature (K)	1573.15

The EDM drilling research was carried on the test stand designed for this purpose (Fig. 1). The sample with special tool guide attachment was performed to carry out the experimental tests (Fig. 2a). The special equipment was used to place the ceramic tool guide which enabled to minimize influence of electrode vibrations and to provide eccentricity on the drilling (Fig. 2b). An additional technological pad was applied on the underside of the sample due to avoid problems with through drilling. The all drilling tests were performed with using copper tubular electrode, an external and an internal diameter was 0.4 mm and 0.2 mm (respectively).

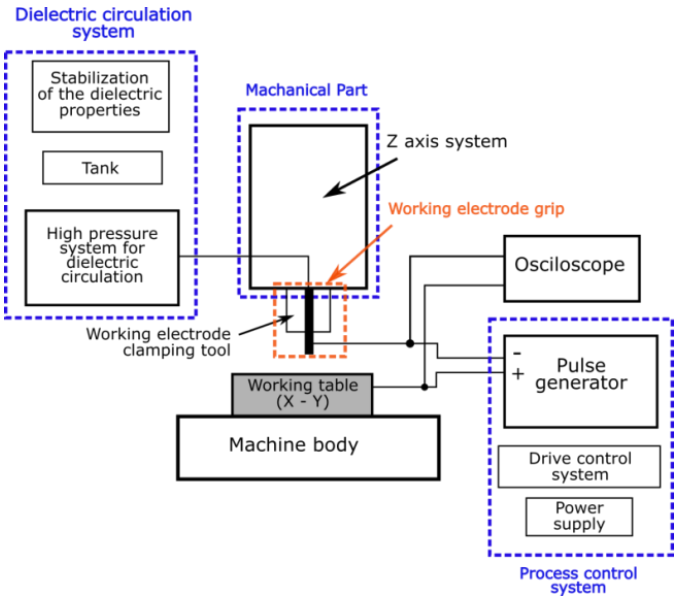

Figure 1.Scheme of the test stand.

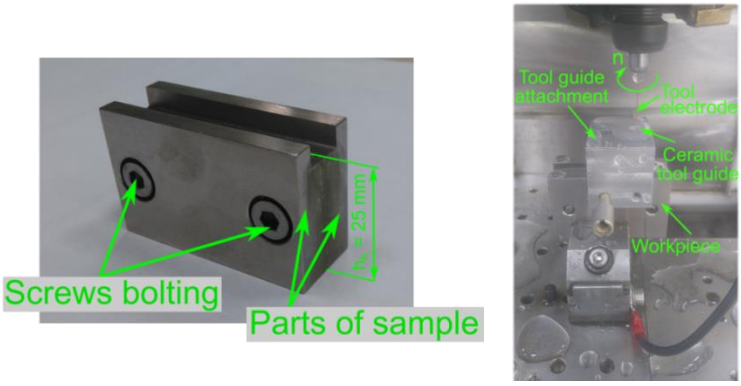

a) b)

Figure 2. a) Image of special prepared sample, b) experimental set up.

The research was performed according to the theory of experiment, by three-level rotatable research plan containing input and output parameters which are presented in Table 3.

Table 3. Input and output parameters of research.

Input parameters	**Min.**	**Max.**
Time of the impulse t_i (μs)	100	1000
Current amplitude I (A)	3	4.65
Discharge voltage U (V)	80	120
Out parameters		
Linear tool wear EW (%)		
Taper angle tap_α		
Drilling speed v (μm/s)		

During the research was applied:

- gap thickness, S = 50 μm,
- dielectric inlet pressure, p_{in} = 8 MPa,
- electrode rotation speed, n = 400 rpm,
- time of drilling t_d (t_d = 45 min or shorter in case achieving of through hole),
- deionized water with low electrical conductivity as dielectric fluid.

The goal of the experimental research constitutes to examine the impact of process parameters (such as current amplitude, time of the impulse, discharge voltage) on drilling efficiency, linear tool wear and taper angle. The linear tool wear *EW* is calculated, according to the following formula:

$$\mathrm{EW} = \frac{h_t}{h_h} \cdot 100\,\% \tag{1}$$

where: h_t –shortening of the electrode and h_h – hole depth. The taper angle tap_α is calculated from the following equation:

$$\mathrm{tap}_\alpha = \frac{(D_{in} - D_{out})}{2 \cdot h_h} \tag{2}$$

where: D_{in} – input diameter and D_{out} – output diameter of hole.

After drilling of holes the parts of sample were separated, what enabled the dimensional shape accuracy analysis of holes and measurement of diameters along hole depth (Fig. 3).

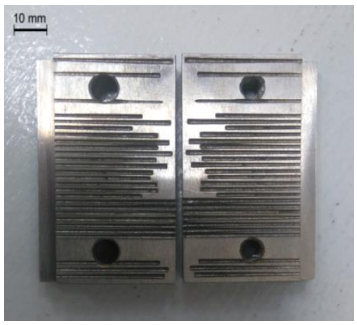

Figure 3. Image of seperated parts of sample.

3. ANALYSIS OF HOLE DIMENSIONAL SHAPE ACCURACY

The obtained holes shape characterizes 'reverse conicity' (value of output diameter D_{out} is higher than value of input diameter D_{in}). This phenomena can be result by accumulation of debris in machining area. Insufficient interelectrode and side gap flushing during process can cause secondary discharge between debris and side hole at hole bottom. For the reason the output diameter of hole can be increased. In case drilling the hole with high aspect ratio, significant depth of hole with small diameter (less than 1 mm) can cause strenghtened flushing difficulties of gap.

The higher drilling speed *v* is obtained during increasing values of discharge voltage *U* and current amplitude *I*. It is related to obtain higher discharge energy in single discharge. The drilling speed includes in the range v = 6 – 13 μm/s. The increase of current also affects on the increase of hole depth and higher drilling speed. However, the linear tool wear is in the range EW = 20 – 80 %. The increase of *EW* is observed with longer impulse time duration t_i and applying current amplitude above I = 4 A. It is related to obtain increasing of hole depth and amount unremoved debris when applying current amplitude above I= 4 A. But longer time of the impulse can lead to longer time of electrical discharge in single impulse. Higher hole depth and higher amount of debris can cause increase of linear tool wear.

The values of taper angle tap_α involve the range -0.0012 ÷ -0.012. The minus sign informs of the hole reverse conicity. Higher taper angle is obtained during applying higher current amplitude I (Fig. 4a, 4b) and shorter time of the impulse t_i (Fig. 5a, 5b). The increase of current impacts of higher energy in single discharge what can cause higher amount of debris in drilling area. Increasing hole depth can hinder the evacuating of debris from gap and their accumulation can be intensified. Then, occurring secondary discharges can cause the increase of hole output diameter. It can be result using deionized water as dielectric fluid which can be treated as weak electrolyte. Applying shorter time of the impulse can be caused removing material by simultaneous interaction of electrochemical dissolution and electrical discharges. For shorter impulse time duration the hole depth is increased in comparison to applying longer time of the impulse. In this case, evacuating debris can be insufficient.

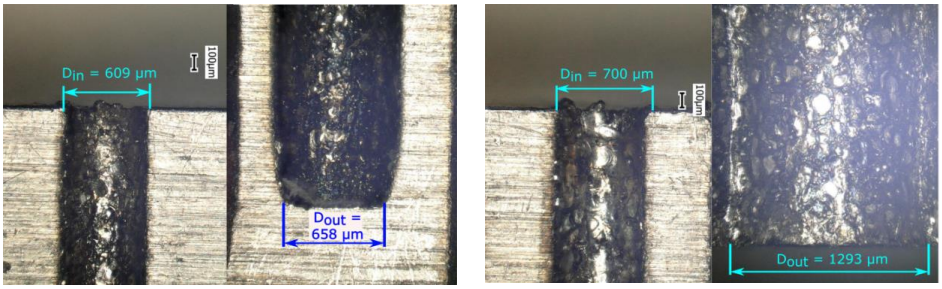

a) I = 3 A b) I = 4.65 A

Figure 4. Images of holes cross – section during applying extreme values of current amplitude I, constant drilling parameters: t_i = 550 µs and U = 100 V.

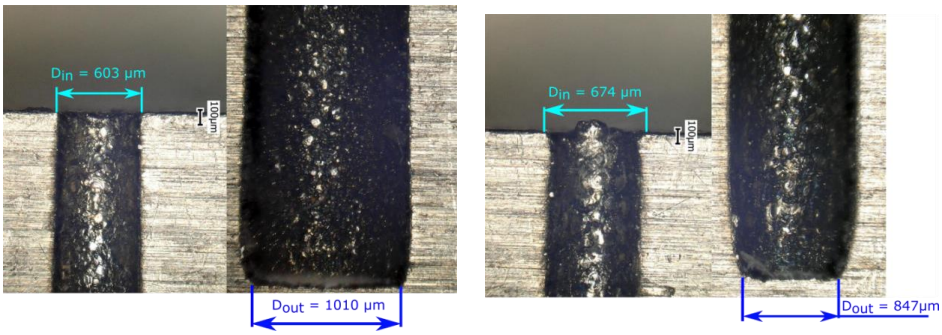

a) t_i = 100 µs b) t_i = 1000 µs

Figure 5. Images of holes cross – section during applying extreme values of time of the impulse t_i, constant drilling parameters: I = 3.83 A and U = 100 V.

4. OPTIMIZATION OF PROCESS PARAMETERS BY USING RESPONSE SURFACE METHODOLOGY (RSM)

On the basis of the analysis results, mathematical models with regression equations for taper angle tap_α, linear tool wear EW, drilling speed v and input diameter of hole D_{in}, including the impact of impulse time duration, current amplitude and discharge voltage, were developed (Fig. 6). The analysis of variance for tap_α, EW, v and D_{in} involves determining the coefficient such as P, S and R-Sq (p-value (P), square root of the MSE (S) and coefficient of determination (R-Sq). Then, to perform the optimization of process parameters, the Response Surface Methodology was used. The defined regression equations (3-6) were the following:

$$tap_\propto = -0.05208 - 0.00006523 \cdot U + 0.00001894 \cdot t_i + 0.03028 \cdot I - 0.0000000144 \cdot t_i^2 - 0.0045679 \cdot I^2 \quad (3)$$

$$EW = 34.4771 + 0.459469 \cdot U - 0.0715096 \cdot t_i - 11.3576 \cdot I - 0.00111031 \cdot U \cdot t_i + 0.0547356 \cdot t_i \cdot I \quad (4)$$

$$v = 19.0526 + 0.0924384 \cdot U + 0.00602294 \cdot t_i - 12.6648 \cdot I + 2.02255 \cdot I^2 - 0.0000848881 \cdot U \cdot t_i \quad (5)$$

$$D_{in} = 879.42 - 15.437 \cdot U + 0.71678 \cdot t_i + 127.572 \cdot I + 0.077658 \cdot U^2 - 0.0001583 \cdot t_i^2 - 0.129566 \cdot t_i \cdot I \quad (6)$$

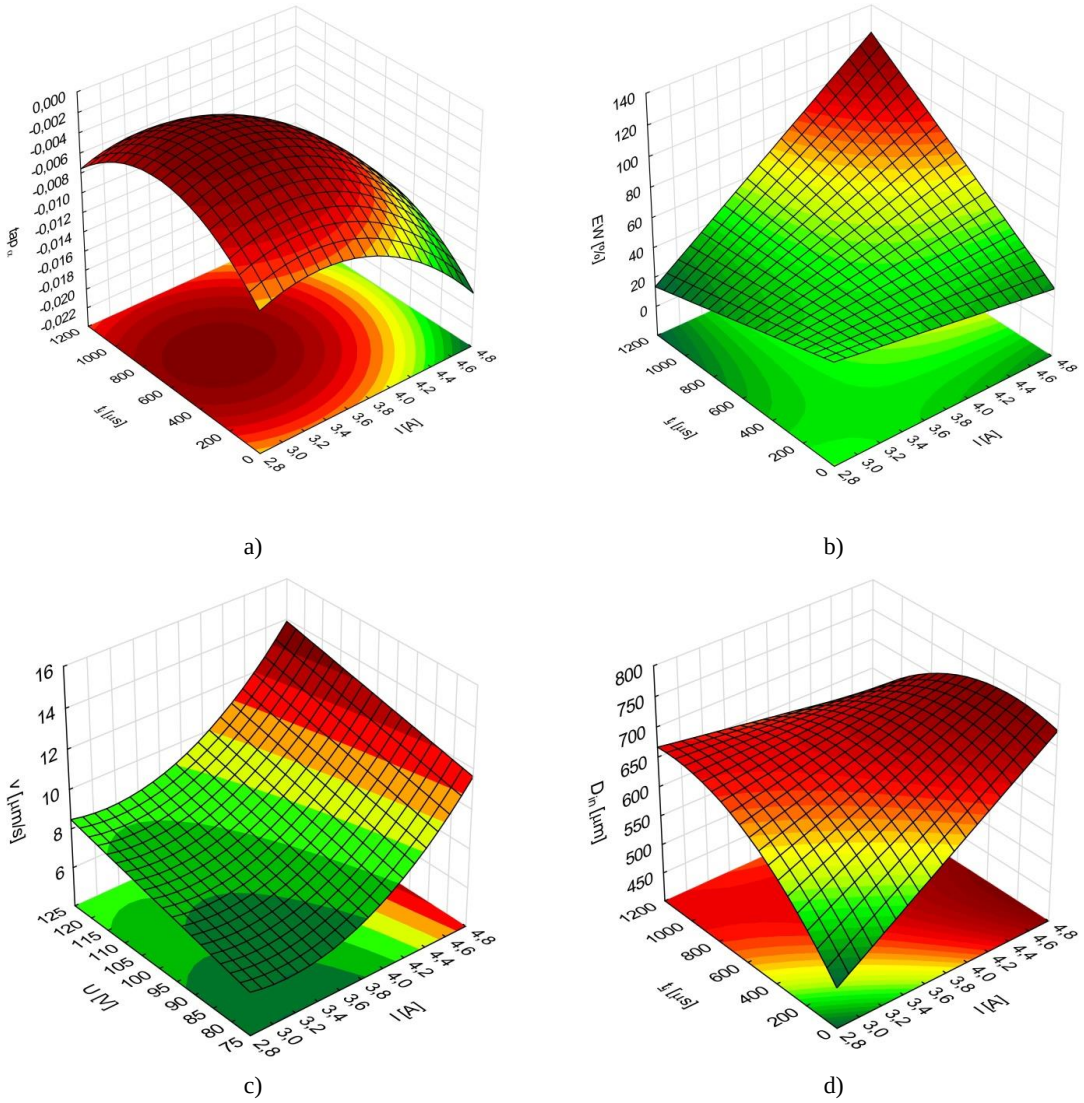

Figure 6. Graph representing relations between: a) taper angle tap_α and time of the impulse t_i and current amplitude I, b) linear tool wear EW and time of the impulse t_i and current amplitude I, c) drilling speed v and discharge voltage U and current amplitude I, d) input diameter of hole D_{in} and time of the impulse t_i and current amplitude I.

The impact of impulse time duration t_i and current amplitude I on the taper angle tap_α and the values of input diameter D_{in}, is presented in Graphs 6a and 6d, respectively. The analysis of results shows the increase of linear tool wear EW with extending of time of the impulse t_i and increasing of current amplitude I (Fig. 6b). Application of longer time of the impulse causes increase of tool wear flank. After drilling with application of t_i = 550 µs, the diameter of tool tip is about 20 % smaller than the nominal value of tool diameter. However, in case applying t_i = 282 µs, the diameter of tool tip is about 10 % smaller than the nominal value of diameter. In addition, when applying t_i = 550 µs the tool wear flank occurs on the longer part of tool flank in comparison to applying t_i = 282 µs. It can be result accumulation higher amount of debris in machining area and higher secondary discharges. For longer time of the impulse, time of occurring electrical discharges in single impulse is also longer. These phenomena can affect on strengthened tool wear (side and end). The relation EW (t_i, I) is presented in the Graph 6b. However, the drilling speed increases with increasing of discharge voltage and current amplitude what is related to high discharge energy in this case (Fig. 6c).

Created mathematical models are used to the optimization of input parameters values. The determined ranges of values of optimised factors are such as: input diameter of hole $D_{in} = 700^{+10}_{-10}$ µm, maximum possible taper angle in the range $0 \geq$

$tap_\alpha \geq$ - 0.004, maximum possible drilling speed and minimum possible linear tool wear. On the basis of optimization results the process parameters are defined as follows: U = 120 V, t_i = 588µs, I = 3.65 A. The optimization graph is shown in the Figure 7.

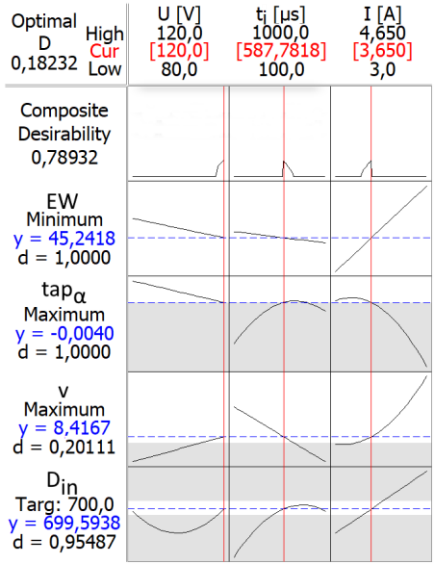

Figure 7. Graph representing the relation between input parameters and optimized factors (*EW*, tap_α, *v*, D_{in}).

5. SUMMARY

In this paper the mathematical model for predicting of values of EDD process parameters which can enable to improve values of technical factors such as input diameter D_{in}, taper angle tap_α, drilling speed *v* and linear tool wear *EW*. To perform mathematical model and optimization of input parameters, the Response Surface Method (RSM) was used. On based the obtained optimization results, the values the process parameters should be such as: U = 120 V, t_i = 588 µs, I = 3.65 A.

The results of experimental research analysis concerning electrical discharge drilling of high aspect holes (aspect ratio length to diameter of hole above 10 and diameter less than 1 mm) in Inconel 718 alloy, have shown:

1. During the drilling process, at the hole bottom debris accumulates. Debris can cause secondary discharges which contribute to extend output diameter of hole.
2. The phenomenon in machining area cause defect of hole shape such as 'reverse conicity' ($D_{in} < D_{out}$).
3. Applied values of process parameters (*U*, t_i and *I*) cause the values range of hole input diameter constitutes 603 – 739 µm.
4. Linear tool wear increases with increasing of impulse time duration and current amplitude and drilling speed increases with increasing of discharge voltage and current amplitude.

REFERENCES

[1] Zębala, W., Gawlik, J., Matras, A., Struzikiewicz, G., Ślusarczyk, Ł., "Research of surface finish during titanium alloy turning," Key Engineering Materials 581, 409-414 (2014).

[2] Skoczypiec, S., Machno, M., Bizoń, W., "The Capabilities of Electrodischarge Microdrilling of High Aspect Ratio Holes in Ceramic Materials", Management and Production Engineering Review 6, 61–69 (2015).

[3] Słodki, B., Struzikiewicz, G., Ślusarczyk, Ł., "Influence of cutting fluid conditions and cutting parameters on the chip form in turning of titanium and steel alloys," Key Engineering Materials 686, 74-79 (2015).

[4] Bilek, O., Hrdina, J., Lukovics, I., Pero, R., Samek, D., "Improved shape of rotating grinding wheels for high speed grinding," Tehnicki Vjesnik, 21(1), 63-68 (2014).

[5] Antar, M., Chantzis, D., Marimuthu, S., Hayward, P., "High Speed EDM and Laser Drilling of Aerospace Alloys", Procedia CIRP 42, 526-531 (2016).
[6] Ślusarczyk, Ł., "The construction of the milling process simulation models," Proc. of SPIE 10031, 1-7 (2016).
[7] Zabel, A., Heilmann, M., "Deep hole drilling using tools with small diameters—Process analysis and process design", CIRP Annals 61(1) , 111-114 (2012).
[8] Bílek, O., Fojtl, L., Pata, V., Cop, J., "Supramolecular structure of polymers and its effect on surface quality of injection molded parts using various surface quality of cavities,: Manufacturing Technology 16(5), 874-879 (2016).
[9] Struzikiewicz, G., Otko, T., "Dependence of shape deviations and surface roughness in the hardened steel turning," Key Engineering Materials 581, 443-448 (2014).
[10] Matras, A., Zębala, W., Kowalczyk, R., "Precision milling of hardened steel with CBN tools," Key Engineering Materials 581, 12-187 (2014).
[11] Unune, R. D., Chandrakant Kumar, Harlal, Ch. N., Mali, S., "Accuracy and quality of micro-holes in vibration assisted micro-electro-discharge drilling of Inconel 718," Measurement 135, 424-437 (2019).
[12] Lipiec, P., Machno, M., Skoczypiec, S.: "The Experimental Research on Electrodischarge Drilling of High Aspect Ratio Holes in Inconel 718," AIP Conference Proceedings 1960, 1-6 (2018).
[13] Ekmekci, B., Sayar, A., "Debris and consequences in micro electric discharge machining of micro-holes," International Journal of Machine Tools and Manufacture 65, 58-67 (2013).
[14] Munz, M., Risto, M., Haas, R., "Specifics of flushing in electrical discharge drilling," Procedia CIRP 6, 83-88 (2013).
[15] Kuppan, P., Narayanan, S., Oyyaravelu, R., Balan, A. S. S., "Performance Evaluation of Electrode Materials in Electric Discharge Deep Hole Drilling of Inconel 718 Superalloy," Procedia Engineering 174, 53-59 (2017).
[16] Ferraris, E., Castiglioni, V., Ceyssens, F., M. Annoni, M., Lauwers, B., Reynaerts, D., "EDM drillling of ultra-high aspect ratio micro holes," CIRP Annals 62(1), 191-194 (2013).
[17] Ayesta, I., Flañoa, O., Izquierdo, B., Sanchez, J. A., Plaz, S., "Experimental study on debris evacuation during slot EDMing," Procedia CIRP 42, 6-11 (2016).
[18] Kuppan, P., Rajadurai, A., Narayanan, S., "Influence of EDM process parameters in deep hole drilling of Inconel 718," The International Journal of Advanced Manufacturing Technology 38(1-2), 74-84 (2007).
[19] Das, M. H., Kumar, K., Barmana, T. Kr., Sahooa, P., "Application of Artificial bee Colony Algorithm for Optimization of MRR and Surface Roughness in EDM of EN31 tool steel," Procedia Materials Science 6, 741-751 (2014).
[20] Ay, M. , Çaydaş, U. , Hasçalık, A. "Optimization of micro-EDM drilling of inconel 718 superalloy," Int J Adv Manuf Technol 66, 1015-1023 (2013).
[21] Paswan, K., Chattopadhyaya, S., Pramanik, A., "Review Paper on Machining of Metal Matrix Composite and Optimizing Methods used in Electrical Discharge Machining," Materials Today Proceedings 5, 24428-24438 (2018).
[22] Kowalczyk, M., "Application of the Monte Carlo method for the optimization of surface roughness during precise turning of NiTi shape memory alloy," Proc. of SPIE 10808, 1-9 (2018).
[23] Kowalczyk, M., "Application of Taguchi method to optimization of surface roughness during precise turning of NiTi shape memory alloy," Proc. of SPIE 104455, 1-10 (2017).
[24] Ciszkiewicz, A., Milewski, G., „Path planning for minimally-invasive knee surgery using a hybrid optimization procedure," Comput Methods Biomech Biomed Engin 21, 47-54 (2018).
[25] Matras, A., Zębala, W., Machno, M., "Research and Method of Roughness Prediction of a Curvilinear Surface after Titanium Alloy Turning," Materials 12(3), 502 (2019).
[26] Lin, Y.-Ch., Wang, A-Ch., Wang, D.-A., Chen Ch.-Ch., "Machining performance and optimizing machining parameters of Al2O3–TiC ceramics using EDM based on the Taguchi method," Materials and Manufacturing Processes 24(6), 667-674 (2009).
[27] Struzikiewicz, G., Zębla, W., Rumian K., "Application of Taguchi method to optimization of cutting force and temperature during turning of difficult to cut materials," Key Engineering Materials 686, 114-118 (2016).

AlGaN/GaN HEMTs for the purposes of electronic applications

Piotr A. Caban*[a], Marek Wojcik[a], Jaroslaw Gaca[a], Piotr Knyps[a], Dominika Teklinska[a], Ewa Dumiszewska[a]

[a] Lukasiewicz Research Network - Institute of Electronic Materials Technology, Wolczynska 133, 01-919 Warsaw, Poland

ABSTRACT

Aluminium nitride is particularly interesting due to its unique properties such as a wide and direct band gap as well as high thermal conductivity. High quality AlN epitaxial layers are needed in UV devices and are used as a buffer layer in the deposition of HEMTs. Its quality has an impact on further deposition as well as two dimensional electron gas properties for AlGaN/GaN HEMTs. It was observed that AlN has crucial impact on electrical as well as structural properties of AlGaN/GaN heterostructures.

Keywords: AlN, GaN. HEMT, AlGaN/GaN, MOVPE, buffer layer

1. INTRODUCTION

Development of high frequency electronics, high power and high temperatures, requires semiconductor materials that are characterized by resistance to high intensity of the electromagnetic field, high power break, high mobility of carriers and high thermal conductivity. The largest application possibilities in high-frequency and high-power instruments are provided by silicon carbide (SiC) and gallium nitride (GaN) and its compounds.

HEMT (High Electron Mobility Transistor) type transistors, whose operation is based on the generation and use of two-dimensional electron gas with high carrier mobility, generated in the AlGaN / GaN heterojunction, are used in such modern wireless telecommunications devices today as modern devices for monitoring and environmental protection [1], security systems, also to fight against terrorism (generators and Terahertz radiation detectors), as well as in modern navigation systems, in particular in radar systems [2]. The use of sapphire as a substrate crystal is associated with the necessity of using a two-stage growth process. After the low-temperature nucleation from GaN, high-temperature growth occurs. Unfortunately, obtaining high-resistive GaN layers requires special technological treatments and does not guarantee resistivity at the expected level. The solution is the use of an aluminum nitride layer (AlN), which as a buffer layer or a nucleation layer has made that layer useful for further GaN epitaxy and most of further UV applications [3] . In such a condition AlN layer properties determines quality of further epilayers and finally mobility of two dimensional electron gas - 2DEG . The AIN nucleation layer is of particular importance in preparation of a final heterostucture. During its growth, the time and temperature of its recrystallization should be precisely monitored [4]. The basic objective of the research is the application of the homogeneous AlN generation technology using the MOVPE method using a) a linear change in ammonia flow and at b) a constant ammonia flow in the HEMT transistor. The intermediate objective is to determine stable technological conditions, weakly dependent on the growth parameters of low temperature AlN nucleation layer, which lead to the creation of the best epitaxial structure of the transistor with high homogeneity of the surface and expected parameters of two-dimensional electron gas on the AlGaN / GaN heterojunction [3].

Amano et al. [5] in his older publication reported process of islands fusion which is normally called coalescence. This process start with the deposition of the nuclei of the substrate surface and then its expansion in the two dimensions until they connect together to formed continuous layer. Furthermore coalescence thickness (time) can be also defined based on the reflectance measurements [6,7,8]. In this experiment the coalescence will be defined on measurements of topography only. In such case when the coalescence process is finished the islands connect one to another creating surface on which we observed only pits between them. Based on the aforementioned definition the growth after finished coalescence is described as two-dimensional (2D), whereas the one just before as three-dimensional (3D).

In the case of two-dimensional growth crucial parameter which determine this mode of growth is high reactor temperature (T_R) >1200˚C during AlN deposition. In the used epitaxial reactor this high T_R corresponds to the

Photonics Applications in Astronomy, Communications, Industry, and High-Energy Physics Experiments 2019, edited by Ryszard S. Romaniuk, Maciej Linczuk, Proc. of SPIE Vol. 11176, 111764Z
© 2019 SPIE · CCC code: 0277-786X/19/$21 · doi: 10.1117/12.2536751

temperature of the susceptor surface (T_S) measured by emissivity corrected pyrometry (EpiTT). Based on those consideration it can be concluded that in this aspect temperature is the most important technological parameter [9, 10]. Moreover, deposited layers of AlGaN/GaN heterostructure were characterized by Atomic Force Microscopy (AFM), High Resolution X-ray Diffraction (HRXRD), Hall effect measurements and Defect Selective Etching (DSE).

2. EXPERIMENT

Substrates used in this experiment were 2-inch double side polished (0001)-oriented Al_2O_3 (sapphire) substrates with off-cut up to 0.2˚ to m-plane. AlN-based structures growth was performed in an AIX 200/4 RF-S metal organic vapor phase epitaxy low-pressure reactor (MOVPE). The precursors gases used for deposition of appropriate layers were ammonia (NH3) and trimethylaluminium (TMAl), whereas hydrogen (H_2) was used as a carrier gas. All samples with the deposited 20 nm thick AlN nucleation layer was prepared in the identical growth conditions. For both low and high temperature of deposition of the nucleation layer the reactor pressure was 50 mbar. By using a Laytec EpiCurve TT system the in situ sample curvature and reflectance measurements were performed. Subsequently AlN layers were grown at high T_R of 1200 ^oC at constant NH_3 flux equal V/III ratio 50, 100, 150, 205, 255, 305 and with linearly ramping the NH3 flux what delivers layer with V/III ratio from 100 to 10 during deposition time [4]. On AlN buffers prepared like that 1 μm thick GaN layer was growth at the reactor pressure 50 mbar followed by thin AlN and then 20nm $Al_{0.2}Ga_{0.7}N$ to obtain AlGaN/GaN heterostructure.

As a measurement tool for surface morphology analysis a Veeco Dimension V SPM with NanoScope V Controller was used. It was crucial that measurements were performed just after unload the sample from the reactor and in the air at room temperature. The images were appropriate processed using NanoScope analysis software (flattened and plain). The Root Mean Square (RMS) roughness parameter was estimate based on the measured valleys and peaks on the surface of the measured samples.

2DEG characterization of AlGaN/GaN heterostructures were performed using HMS-3000 Hall effect measurement system working at room temperature.

Defect Selective Etching (DSE) was performed in the molten eutectic of KOH-NaOH [11]. After this etching the defects present in epitaxial layers can be defined easily based on the images obtained using Scanning Electron Microscopy (SEM). According to the literature it is commonly known that each type of defects in the crystallographic structure has a different rate of etching [12]. Among all types of dislocations present in the AlN epitaxial layers threading etch dislocations have the lowest etch rate. Based on this one can be concluded that they will revealed as a small pits, whereas screw and mixed as a larger ones due to its higher etch rate. In spite of those differences all samples need to be etched at the same conditions to revealed dislocation for comparison between different samples with similar thickness of the epi-layer.

Furthermore, the analysis of the structure of the AlN epitaxial layers was performed using a SmartLab X-ray diffractometer equipped with a 9 kW rotating Cu anode (α = 0.15405 nm). The radial and angular diffraction profiles were set down for the following incident optics setting: cross beam optics CBO unit, Ge(220) × 2 monochromator, open Soller slit, and on the receiving side: Soller slit open and Soller slit 5.0 deg. For obtaining wide range of information about samples there were adjusted in such a way that the c-axis was parallel to the φ-axis of the goniometer. This featured lead to carrying out the radial and angular scans of the (00l) reciprocal lattice spots for l = 2, 4, 6. Normally such XRD measurements of the AlN films are performed using the mosaic model of crystals [13, 14]. However in this case was assumed that the AlN layer include crystallites (mosaic blocks), which each and every was coherently scatters X-rays. In this research the dimension of the mosaic blocks was identify in the growth direction (radial correlation length) as $L^{\perp}$ and in the direction perpendicular to the growth (lateral correlation length) as $L^{\parallel}$. The presence of defects in the epitaxial layer was observed as the broadening of the angular scan of the symmetric reflections 00l of AlN grown on c-plane sapphire on the X-ray curves. This broadening is controlled by the tilt and the lateral correlation length. As the broadening of the reciprocal lattice spot due to tilted crystallites is proportional to the scattering order and a broadening due to the lateral correlation length is independent of the scattering vector, a graphical separation of these two effects is possible by recording higher order reflections and performing a separation analogous to the Williamson - Hall plot [15].

3. RESULTS

In the process of deposition of the high temperature AlN layer, which is strongly correlated with the nucleation layer, depending on the V / III value, several effects may appear: - for the V / III value > 255: there is no lateral growth (Fig. 1a), - for the values V / III <100; 255):hexagonal AlN inclusions appear (Fig. 1b) - for V / III values <50; 100): few hexagonal precipitations are present - for V / III values below 50: the surface takes on an hexagonal structure (Fig. 1c). After applying a linear change in ammonia flow (for values in the V / III range = 100 to 10), it is possible to make the process of depositing the high temperature AlN layer independent of the nucleation layer.

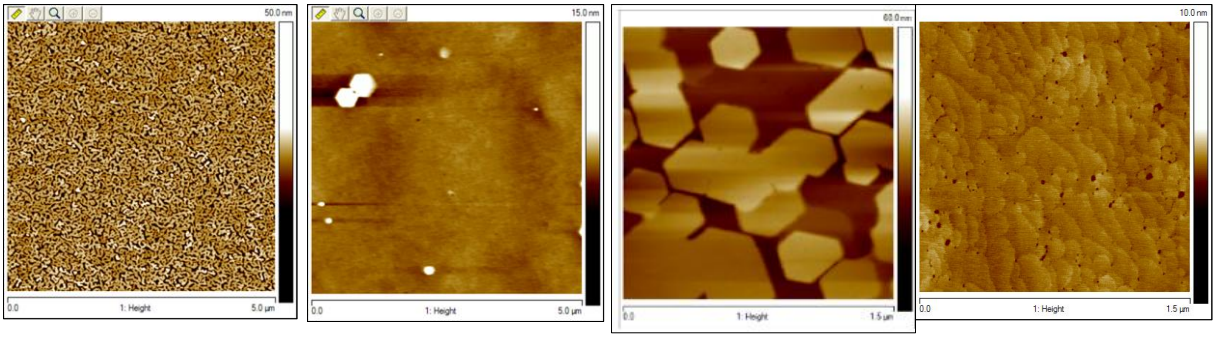

Figure 1. The surface morphology of high temperature AlN layer deposited at V/III ratio: a) 305, b) 100, c) 10 and d) linear change of ammonia flux.

Further analysis was performed for AlGaN / GaN heterostructures deposited on AlN buffer layers demonstrated above. The list of analyzed samples (V/III ratio for AlN , AlN buffer thickness, AlN growth rate) and Hall effect measurement results for AlGaN / GaN heterostructures (Figure 2) are presented in Table 1.

Surface roughness was investigated and it was noticed that RMS for all of the investigated samples varies from 0.3nm for samples A, C, D, E, F, G, increases to 0.4 for sample B.

The value of 2DEG mobility, one of the most important parameter determining the suitability of the heterostructure for application in real device, shows that samples from B to G can be qualified as potentially meeting expectation for HEMTs. Sample A is diverging from the other values, what is more, 2DEG concentration is higher than in the case of other samples. It can be assumed that the main reason is the interaction of the AlN layer directly on GaN and indirectly on 2DEG from AlGaN/GaN heterojunction. It seems that resistivity of GaN is a point for that deviation. I can be assumed that for the Sample A, the GaN layer is less resistant then for others. Confirmation of this fact can only be the fabrication of the device and breakdown voltage measurements.

It need to be emphasis that besides the surface topography, the selection of best growth conditions should be concluded depend on both and defect selective etching and XRD measurements. For this research d_{AlGaN} - the length of the correlation in the direction of growth in the AlGaN layer [Å], d_{AlN} - length of the correlation in the direction of growth in the AlN layer [nm], x - composition of the $Al_{(1-x)}Ga_xN$ layer (Table 2). It was confirmed that the composition of AlGaN layer is rather stable and do not depend on growth conditions of previous layers despite sample E and F where correlation length and AlGaN composition is lower than for the other samples . On the other hand Al correlation length is not stable and the worst results was obtained for AlN grown using decrease of ammonia flux.

The obtained results show that the overall defect density varies from sample to sample from 2.5×10^9 for sample B and 3.5×10^9 cm^{-2} for sample A to 7.4×10^9 cm^{-2} for sample G (Tab. 2). It can be concluded that the defect density was similar in both cases, but the manner in which the etching process was performed showed the presence of voids in the volume of the layer what can be observed in Figure 3.

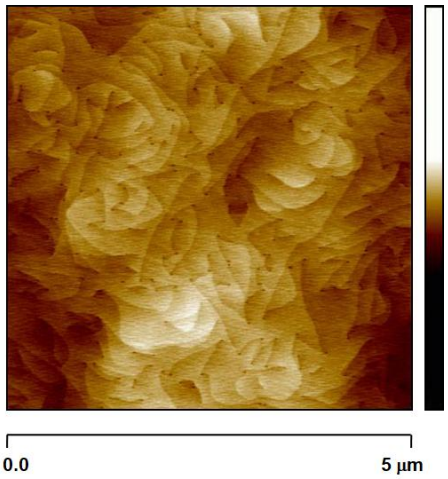

Figure 2. The surface morphology of typical AlGaN/GaN HEMTs grown on AlN buffer (sample A).

Table 1. AlN buffer growth properties (thickness and the growth rate) correlated with AlGaN/GaN 2DEG properties.

	V/III	d_{AlN} [nm]	V_{AlN} [nm/s]	µ [cm^2/Vs]	N [cm^{-2}]
A	100 -> 10	320	0.27	1095	1.3e13
B	50	316	0.17	1589	7.8e12
C	100	326	0.18	1904	7.2e12
D	150	356	0.26	1702	7.0e12
E	205	319	0.17	1859	8.1e12
F	255	318	0.17	1900	7.3e12
G	305	318	0.17	1518	7.8e12

Table 2. Calculated results of defects selective etching (Etch Pits Density) and lattice parameters for AlN layers calculated using Williamson-Hall plots [15]

	d_{AlGaN} [Å]	d_{AlN} [nm]	$Al_xGa_{1-x}N$	EPD = 10^9 [cm^{-2}]
A	22	105	0,75	3.8
B	16	110	0,74	2.5
C	14	170	0,75	6.5
D	22	130	0,75	4.7
E	16	137	0,69	4.1
F	17	133	0,70	6.7
G	21	110	0,75	7.4

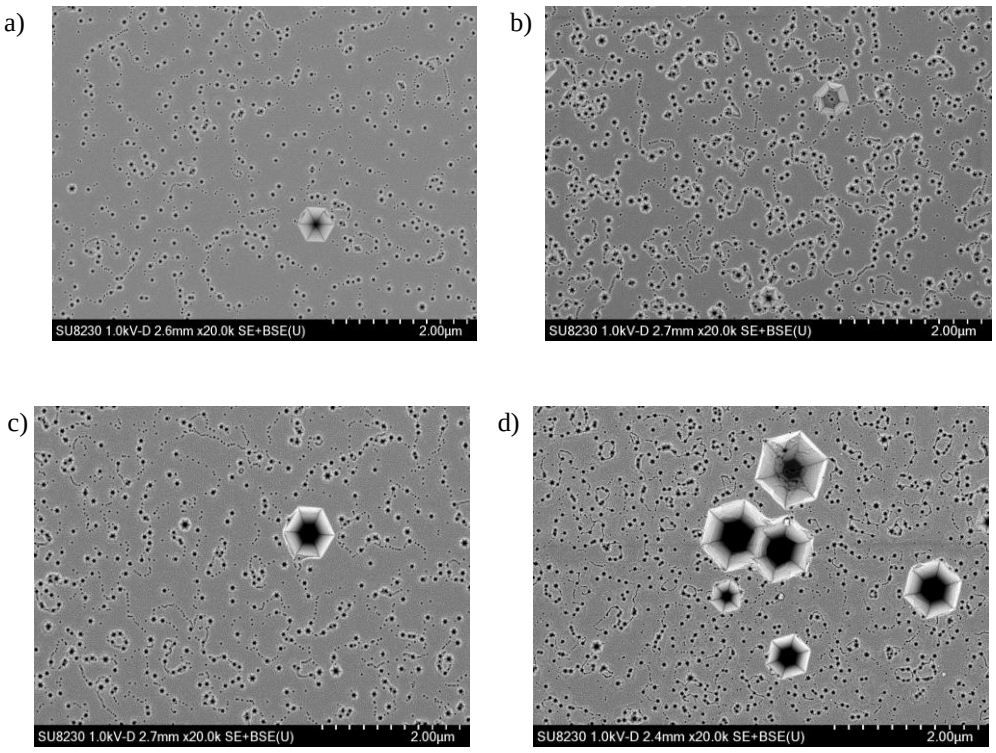

Figure 3. SEM images of AlGaN/GaN surface grown on AlN buffers: a) sample A, b) sample D, c) sample E, d) sample G after DSE.

4. SUMMARY

The HEMT layers produced have a similar value of surface roughness (RMS ~ 0.3nm) that does not depends on the shape of the AlN despite the AlN grown at low V/III ratio. This is due to the applied GaN growth conditions, in particular the growth condition of GaN layer allows for quick transition from 3D to 2D growth mode. GaN layers are rather highly resistive despite layer grown on AlN buffer grown at decreasing ammonia flux. Its high quality decrease resistivity of further epilayer. Electrical parameters describing 2DEG enable a further fabrication of the device and determines the most appropriate technology for layer production of AlN buffer layer for applications in the HEMTs applications. Further development requires determination of transistor breakedown voltage and correlation with X-ray results. However it is known that the breakdown voltage of the F type structure is know to be greater than 40V for 5um drain-source distance and will be published soon.

This work was supported by the Danish Strategic Research Foundation in the frame of project Semiconductor Materials for Power Electronics.

REFERENCES

[1] Firek, P., Cichomski, M., Waskiewicz, M., Piwoński, I., & Kisielewska, A. (2018). ISFET structures with chemically modified membrane for bovine serum albumin detection. Circuit World, 44(1), 45–50

[2] Dobrzański, L. (2016). Monolityczny mikrofalowy układ scalony GaN/AlGaN. ELEKTRONIKA - KONSTRUKCJE, TECHNOLOGIE, ZASTOSOWANIA, 1(6), 8–11

[3] Borecki, M., Prus, P., & Korwin-Pawlowski, M. L. (2019). Capillary Sensor with Disposable Optrode for Diesel Fuel Quality Testing. Sensors, 19(9), 1980

[4] Caban, P., Rudzinski, M., Wojcik, M., Gaca, J., & Strupinski, W. (2015). Growth of aluminium nitride with linear change of ammonia flow. Journal of Crystal Growth, 414, 81–86

[5] Amano, H., Sawaki, N., Akasaki, I., & Toyoda, Y. (1986). Metalorganic vapor phase epitaxial growth of a high quality GaN film using an AlN buffer layer. Applied Physics Letters, 48(5), 353–355

[6] Kueller, V., Knauer, A., Zeimer, U., Kneissl, M., & Weyers, M. (2013). Controlled coalescence of MOVPE grown AlN during lateral overgrowth. Journal of Crystal Growth, 368, 83–86

[7] Cho, Y. S., Hardtdegen, H., Kaluza, N., Thillosen, N., Steins, R., Sofer, Z., & Lüth, H. (2006). Effect of carrier gas on GaN epilayer characteristics. Physica Status Solidi (c), 3(6), 1408–1411

[8] Das Bakshi, S., Sumner, J., Kappers, M. J., & Oliver, R. A. (2009). The influence of coalescence time on unintentional doping in GaN/sapphire. Journal of Crystal Growth, 311(2), 232–237

[9] Kappers, M. J., Moram, M. A., Sridhara Rao, D. V., McAleese, C., & Humphreys, C. J. (2010). Low dislocation density GaN growth on high-temperature AlN buffer layers on (0001) sapphire. Journal of Crystal Growth, 312(3), 363–367

[10] Bai, J., Wang, T., Parbrook, P. J., Lee, K. B., & Cullis, A. G. (2005). A study of dislocations in AlN and GaN films grown on sapphire substrates. Journal of Crystal Growth, 282(3-4), 290–296

[11] Weyher, J. ., Brown, P. ., Rouvière, J. ., Wosinski, T., Zauner, A. R. ., & Grzegory, I. (2000). Recent advances in defect-selective etching of GaN. Journal of Crystal Growth, 210(1-3), 151–156

[12] Weyher, J. L. (2006). Characterization of wide-band-gap semiconductors (GaN, SiC) by defect-selective etching and complementary methods. Superlattices and Microstructures, 40(4-6), 279–288

[13] Kyutt, R. N., & Dyshekov, A. A. (2011). Effect of epilayer microstructure on shape of X-Ray diffraction peaks. Technical Physics Letters, 37(4), 306–308

[14] Liu, B., Zhang, R., Xie, Z. L., Lu, H., Liu, Q. J., Zhang, Z., … Schaff, W. J. (2008). Erratum: “Microstructure and dislocation of epitaxial InN films revealed by high resolution x-ray diffraction” [J. Appl. Phys. 103, 023504, (2008)]. Journal of Applied Physics, 104(3), 039906

[16] Williamson, G. ., & Hall, W. . (1953). X-ray line broadening from filed aluminium and wolfram. Acta Metallurgica, 1(1), 22–31

Cutting force prediction in ball-end milling of NiTi alloy

M. Kowalczyk[a]
[a]Production Engineering Institute, Mechanical Faculty, Cracow University of Technology, Avenue Jana Pawła II 37, PL 31-864 Cracow, Poland;

ABSTRACT

Abstract: This paper presents a statistical model for prediction cutting components force in the ball-end milling of NiTi shape memory alloy (Nitinol). In experiment a ball-end mill (EB-A2 03-04C06E48) was used and a dynamometer Kistler was used for the measurement of cutting forces components. The research trials were conducted for two independent parameters (v_c, f_z,) affecting the cutting force in milling process. The choice of parameter configurations was performed by factorial design methods using orthogonal plan type L9, with two control factors, changing on three levels, developed by G. Taguchi. The model for the mathematical prediction of cutting force was developed in terms of feed per tooth and cutting speed. The computational model enabled to select optimal machining parameters for minimizing cutting forces values.

Keywords: NiTi Shape Memory Alloy, precise milling, Taguchi, cutting force

1. INTRODUCTION

Cutting forces which act on the tool and on the workpiece causes a certain change in the position of the tool relative to the workpiece. Any displacement of the tool relative to of the workpiece occurring during machining, can adversely affect accuracy dimension of the machined surface.

Prediction of cutting forces components before property machining can provide significant information to the planning and optimization of cutting process in particular such difficult to machine of NiTi alloys [16]. The shape memory materials belong to the new class of innovative materials featuring with high potential use. These materials can be used as the multifunctional materials and smart materials due to their memory shape and superelasticity properties. However, due to the immense ductility and heavy work hardening of the workpiece, the quality of the workpiece is repeatedly very low and more the tool wear is in unacceptable intensity. Therefore, a tailored process strategy connected with the prediction of cutting forces is pretty important when machining NiTi. The machining of this kind of alloy with shape memory by milling has not been studied so far, in particular, there is little information on the measurement and modeling of cutting force [2,7-8,12,16,19,23,24,25]. Because of the great number degrees of freedom, complex structures can be created by milling, which is important for the opening of new application areas for NiTi shape memory alloys.

In the literature there are many studies on the modeling of cutting forces, but for other materials than NiTi alloy. For example Sun et al. [21] showed a mechanistic method for calculating cutting force in ball-end milling of sculptured surfaces for any cases of tool paths and changing feed rate inclusion into a new chip thickness model. Naserian et al. [15] introduced a static rigid force model to evaluate cutting forces of sculptured surface in a direct way, without considering tool deflection, machine tool dynamic behavior and any vibration effects. Fontaine et al. [5] presented a milling force model based on a thermo-mechanical modelling of oblique cutting. Fujii and Iwabe [6] performed an experimental study to determine the relationship between the cutting force curve and the machining error. Wei et al. [22] carried out an approach to the prediction of cutting force in a 3-axis ball end milling of a surface processed with a Z contour tool path. A new approach for modelling and simulation of the cutting forces in helical end milling processes is presented by Li [11]. In this approach, the cutting forces in helical end milling are transformed based on the predictive machining theory. The theory allows to predict the machining characteristic factors from the input data of the basic material properties of the workpiece, tool geometry and cutting conditions.

*kowalczyk@mech.pk.edu.pl; phone +48 12 374 3245; fax +45 12 374 3202; mech.pk.edu.pl

Photonics Applications in Astronomy, Communications, Industry, and High-Energy Physics Experiments 2019, edited by Ryszard S. Romaniuk, Maciej Linczuk, Proc. of SPIE Vol. 11176, 1117650
© 2019 SPIE · CCC code: 0277-786X/19/$21 · doi: 10.1117/12.2536757

The research of Campatelli et al. [3] showed the effect of feed per tooth and cutting speed on cutting coefficients to create a model that allows reliable prediction of cutting force at various process parameters.

Experimental studies have shown that the shearing cutting coefficient is influenced not only by the instantaneous thickness of the chip, or the feed per tooth, but also by the cutting speed, this contribution has less influence on the tooth feed. The main purpose of this work is to develop a model based on the surface methodology of response to cutting force in relation to processing parameters, such as cutting speed and feed per tooth. The mathematical model helped us to research the direct and interaction effect of each parameter [1].

2. EXPERIMENTAL SETUP

All experimental tests were performed on 3 axes CNC milling machine tool Haas VF1 equipped with digital control unit. For experiments was used dry milling. Cutting tools was 4 mm diameter ball-end mill with two tooth (Iscar EB-A2 03-04C06E48) shown in Figure 1. For experiment was used a tough sub-micron PVD TiAlN coated grade. Used for machining of heat resistant alloys, austenitic stainless steel, hard alloys and carbon steel at medium to high cutting speed. The workpiece was NiTi (A_f =37°C) alloy shown in Figure 2, it is usually employed in the medical, aerospace and military industry to manufacture components. The dimension of the workpiece was diameter 20 mm and height 8 mm. In Table 1 the spectroscopy analysis of NiTi alloy with the austenite finish temperature A_f =37°C shown.

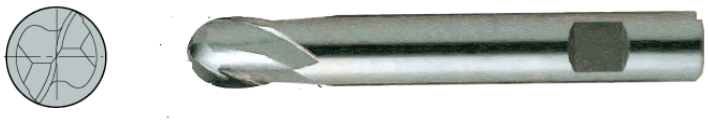

Figure 1. Ball-end solid carbide mill [26].

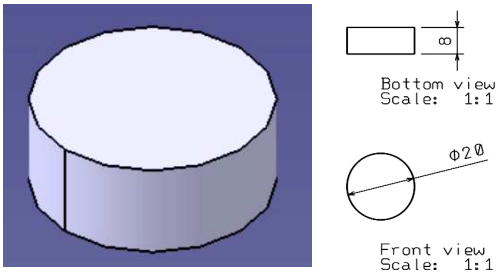

Figure 2. The pictures of workpiece.

Table 1. The spectroscopy (EDS) analysis [own results].

Material: β -TiNi		
Element	wt.%	at.%
TiK	42.76	47.79
NiK	57.24	52.21
Total	100	100

Milling tests were performed at two different cutting conditions. The design of experiment was according to L9 array based on Taguchi method while using the Taguchi orthogonal array would markedly reduce the number of experiments [4, 8-10, 13, 18].

The tests were conducted for two independent parameters (v_c and f_z) affecting the cutting force. This method uses a special design of orthogonal arrays to study the entire parameter space with small number of experiment only. Design of experiment is a powerful statistical method for determining the unknown properties of the machining parameters in the experiment process and for analyzing and modelling the interaction among the factors [4, 8-10, 13, 18]. For the experiment was used following cutting conditions show in Table2, depth and width of cut were constant equal a_p = 3.5 mm, a_e = 0.2 mm.

Table 2. Parameters and Levels in ball-end milling.

Parameters	**Notation**	**Units**	**Levels**		
			1	**2**	**3**
feed per tooth	f_z	mm/tooth	0.006	0.009	0.012
cutting speed	v_c	m/min	20	35	50

During the experiment, three components (max F_x, max F_y, max F_z) piezoelectric dynamometer Kistler 9257B was used to measure forces. The data are acquired in the data acquisition software and observations are tabulated to obtain the mathematical model. Schematic representation of experimental setup is shown in Figure 3. Obtained results of cutting force represent maximum measured values. The relationship between cutting forces (Infeed force F_x, Crossfeed force F_y and Thrust force F_z) and cutting parameters were analyzed.

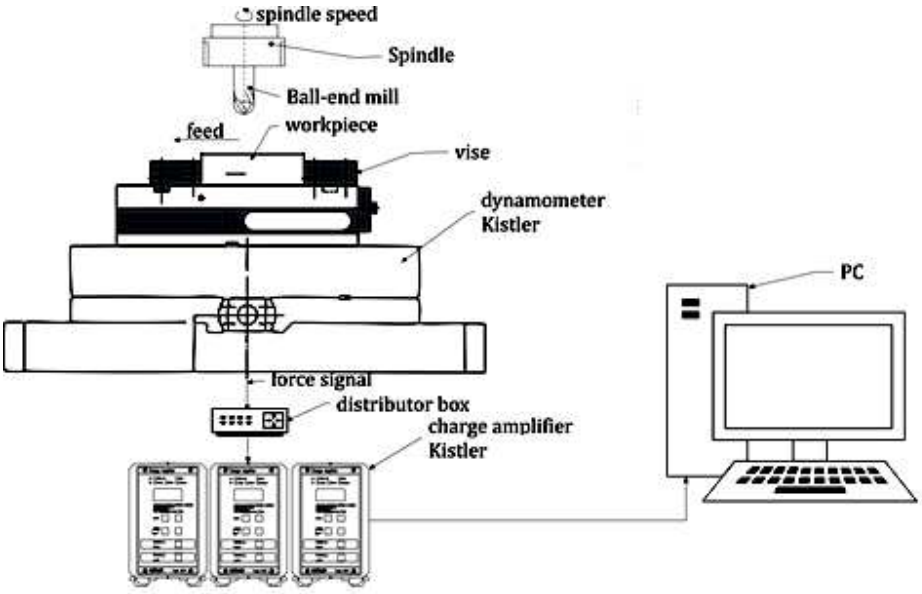

Figure 3. Schematic representation of experimental setup.

3. RESULTS AND ANALYSIS OF EXPERIMENT

The Taguchi method comes down to the fact that in practice it is not possible to monitor all the factors causing variability. All these uncontrollable factors are referred to as noise factors. The Taguchi method allows to identify controllable factors (control factors) that have an impact on the reduction of noise factors. Manipulating with noise factors during experiments allows for variability, which in turn allows to get the desired settings of the control factor. These actions allow the process to be resistant to changes depending on noise factors. In order to determine the influence of interactions of the milling process parameters on the cutting force, a plot of the response field for each force component was generated [4,8-10,18].Because the Taguchi method was used only for the analysis of the main factors that affect the parameters *Fx, Fy* and *Fz*, so without testing the connection between the factors, therefore the response surface regression was made in the correlation analysis between the factors. Response Surface Methodology (RSM) is a series of statistical and mathematical techniques useful for optimizing processes [14,20]. It is an effective tool for modelling and exploring the manufacturing problems. It provides more information with a small number of investigations. It is a research strategy to study the limits of input parameters and the emerging experimental statistical model for the measured response, by approximating the existing correlation between the response surface and input process parameters. The limit of the process parameters has to be defined in response surface method, and the first set of experiments was performed to identify machining parameters, which have an impact on the cutting force and to find selected range of cutting parameters [20]. In this study, the cutting speed and the feed per tooth were considered as cutting parameters for monitoring cutting conditions, and the cutting force is measured as a response variable (Table 3).

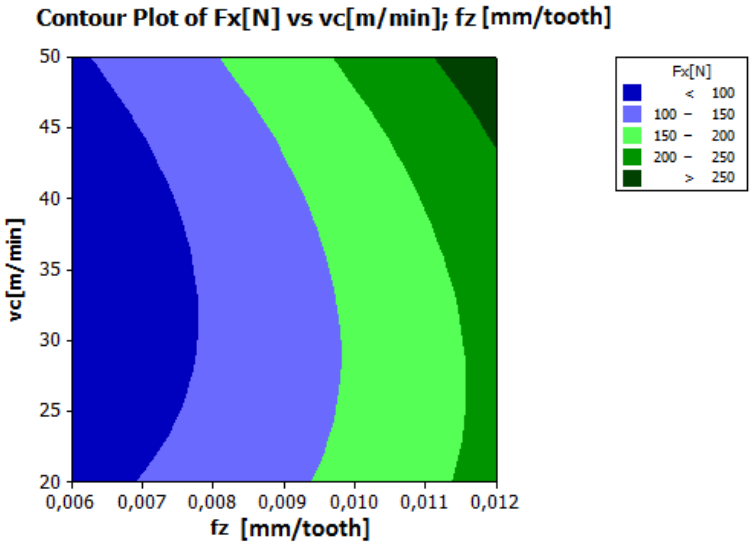

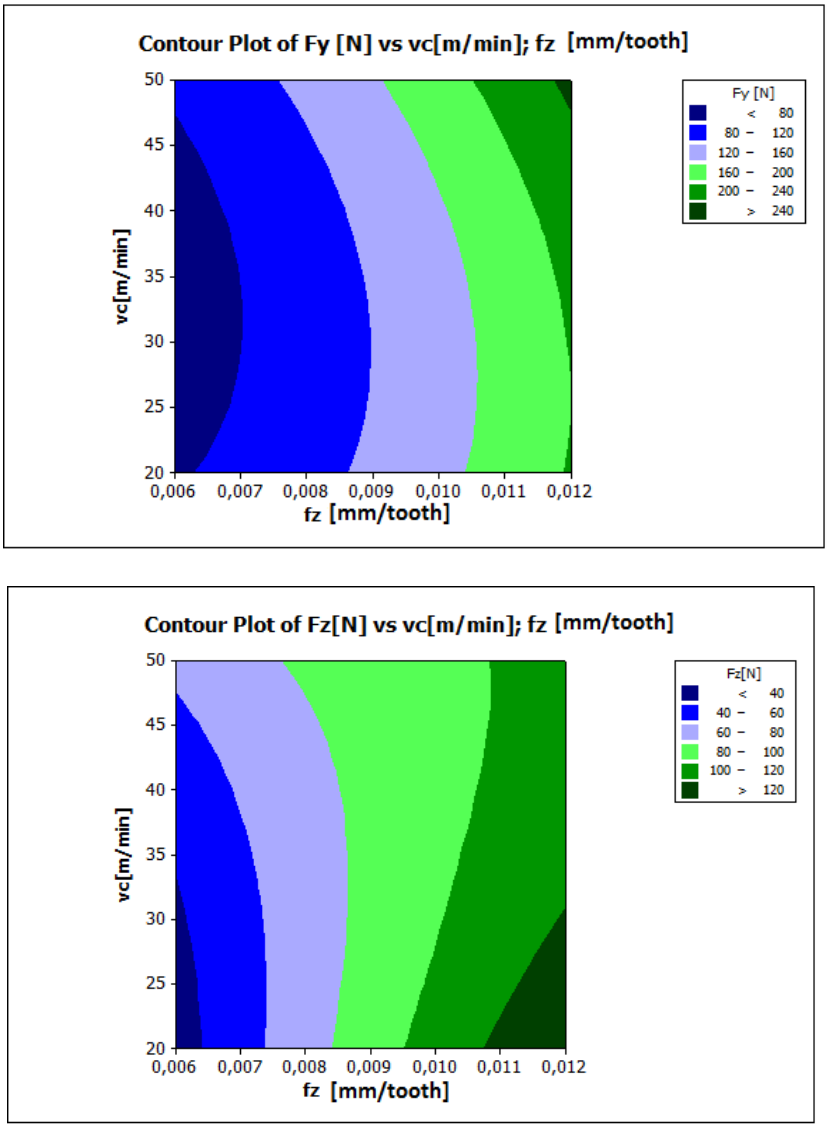

Figure 4. Sample contour Plots of parameter *Fx, Fy and Fz.*

The above analysis found that contour plots of parameters *Fx*, *Fy* and *Fz* are a curves. Therefore. mathematical model suitable for predicting suitable value is Quadratics model (equation 1) by considering the full quadratics model as shown in equation 2 (*Fx*), equation 3 (*Fy*) and equation 4 (*Fz*).

$$y = bo+b1x1+ b2x2+ b3x3+ b4x4+ b11x12+ b22x22+ b33x32+ b44x42+ b12x1x2+ b13x1x3+ b14x1x4+ b23x3x3+ b24x2x4+ b34x3x4 \quad (1)$$

Table 3. Experimental design matrix and results.

Test no.	Control factors		Max of Infeed force F_x			Max of Crossfeed force F_y			Max of Thrust force F_z		
	f_z	v_c	Measured value	Predicted value	%Error	Measured value	Predicted value	%Error	Measured value	Predicted value	
1	0.006	20	66.4	74.10	12%	59.5	69.19	16%	25.8	30.90	20%
2	0.006	35	83.97	82.79	1%	81.43	62.66	23%	47.84	41.60	13%
3	0.006	50	90.17	104.71	16%	83.97	93.05	11%	63.45	48.59	23%
4	0.009	20	154.1	158.88	3%	141.58	140.70	1%	92.69	84.09	9%
5	0.009	35	137.04	131.77	4%	121.56	122.94	1%	89.15	84.22	6%
6	0.009	50	159.32	159.89	0%	142.6	142.10	0%	83.1	96.63	16%
7	0.012	20	222.74	210.31	6%	204.14	195.33	4%	141.11	128.61	9%
8	0.012	35	194.17	221.67	14%	189.37	206.76	9%	103.47	114.64	11%
9	0.012	50	303.34	288.28	5%	263.71	255.13	3%	111.62	112.95	1%

The mathematical model was established by neglecting the insignificant coefficients of the cutting force F (Eq. 2-4):

$$Fx = 359.517 - 7408 * f_z - 5.59874 * v_c + 72612.4 * f_z^2 + 0.122748 * v_c^2 - 32.8882 * f_z * v_c \quad (2)$$

$$Fy = =309.319 - 6754.63 * f_z - 3.45113 * v_c + 64250.7 * f_z^2 + 0.0820593 * v_c^2 - 24.9612 * f_z * v_c \quad (3)$$

$$Fz = =216.826 - 4659.19 * f_z - 2.57735 * v_c + 37719.9 * f_z^2 + 0.0272963 * v_c^2 + 12.0504 * f_z * v_c \quad (4)$$

The mathematical model was used to predict cutting force by replacing the values of the machining parameters. The impact of cutting force machining parameters was examined using the developed model.

The information in Table 3 shows the result from the comparison between actual value and forecasting value which found that the forecasting values of max of Infeed force F_x has the maximum error of only 14%, for max of Crossfeed force F_y. – 23% and for max of Thrust force F_z – 23%.

Response surface (3D graph) of cutting forces in Figure 5-7 shows the relation between two main factors, cutting speed and feed per tooth which depend the cutting force resulting from ball-end milling. It is clear that force increase with the increase of feed per tooth (f_z) but it is not so obvious that as the cutting speed (v_c) of increases, cutting forces increase also. For feed per tooth f_z = 0.009 [mm/ tooth] and f_z = 0.012 [mm/ tooth], the component cutting forces *Fx*, *Fy* and *Fz* decrease. Therefore, the optimal combination of cutting conditions within testing area for ball-end mill should be minimum width of cut (a_e = 0,5mm) and minimum depth of cut (a_p = 0.5mm).

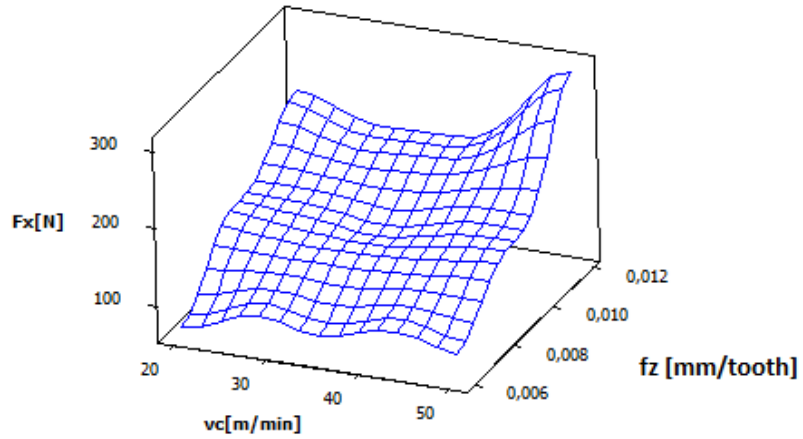

Figure 5. The response surface of cutting force *Fx* vs. cutting speed and feed per tooth.

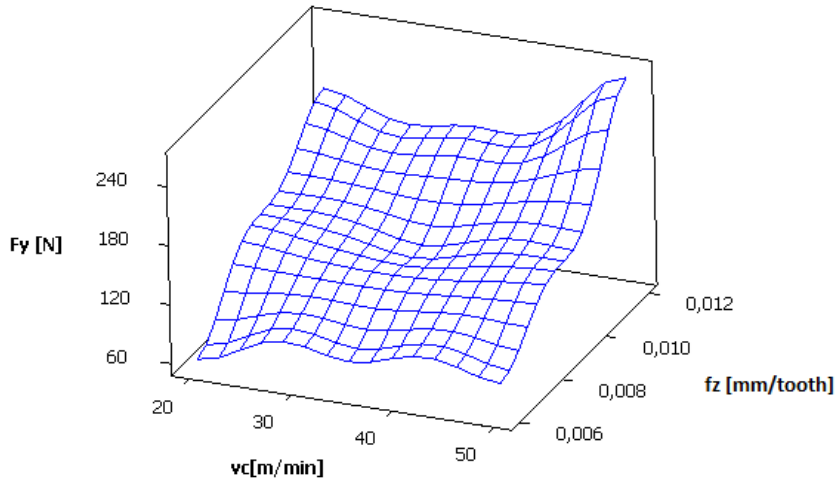

Figure 6. The response surface of cutting force *Fy* vs. cutting speed and feed per tooth.

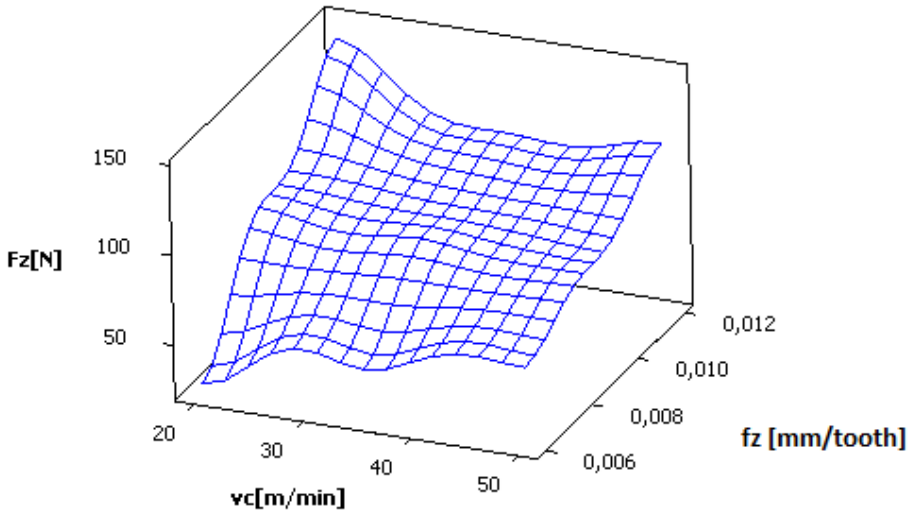

Figure 7. The response surface of cutting force *Fz* vs. cutting speed and feed per tooth.

The optimization plot for components cutting forces has been shown in Table 4 and Figure 8 also for Taguchi and RSM method. The desirability of optimization has been calculated as 0,81 all the parameters are within their working range.

Table 4. Optimum value of the ball-end milling.

Cutting force F [N]	**Taguchi method**		**Feed per tooth**	**Cutting speed**	**RSM method**	**Feed per tooth**	**Cutting speed**
	Value	**S/N ratio**	**f_z [mm/ tooth]**	**v_c [m/min]**		**f_z [mm/ tooth]**	**v_c [m/min]**
Infeed force Fx (tangential)	66.4	-36.4	0.006	25	67.5	0.006	27
Crossfeed (radial) force Fy	59.5	-35.5	0.006	25	65.05	0.006	27
Thrust (axial)force Fz	25.8	-28.2	0.006	25	34.5	0.006	27

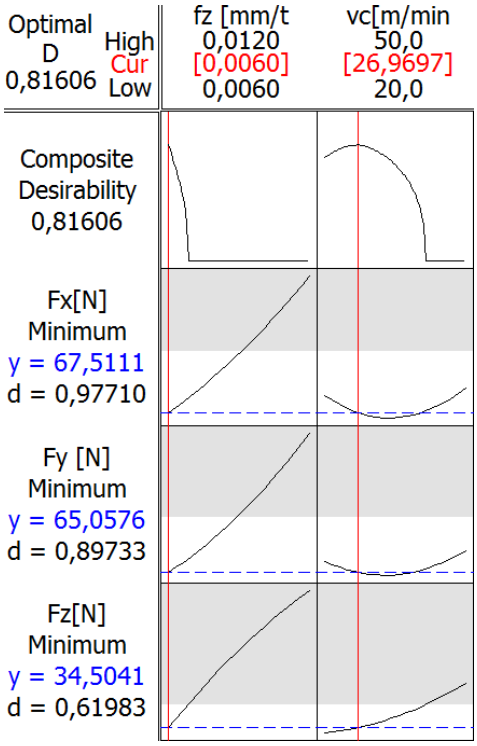

Figure 8. Optimization cutting force – RSM method.

From the S/N ratio analysis in Figure 9-11 the optimal machining conditions were 25 m/min cutting speed (level 1), 0.006 mm/ tooth feed rate (level 1), for components cutting force *Fx, Fy, Fz*.

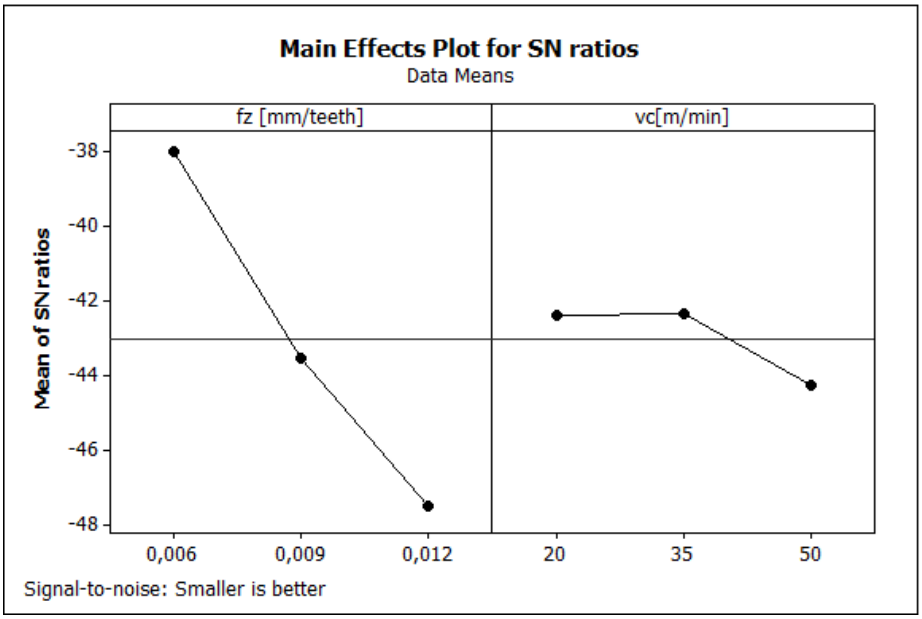

Figure 9. S/N ratio values for *Fx*.

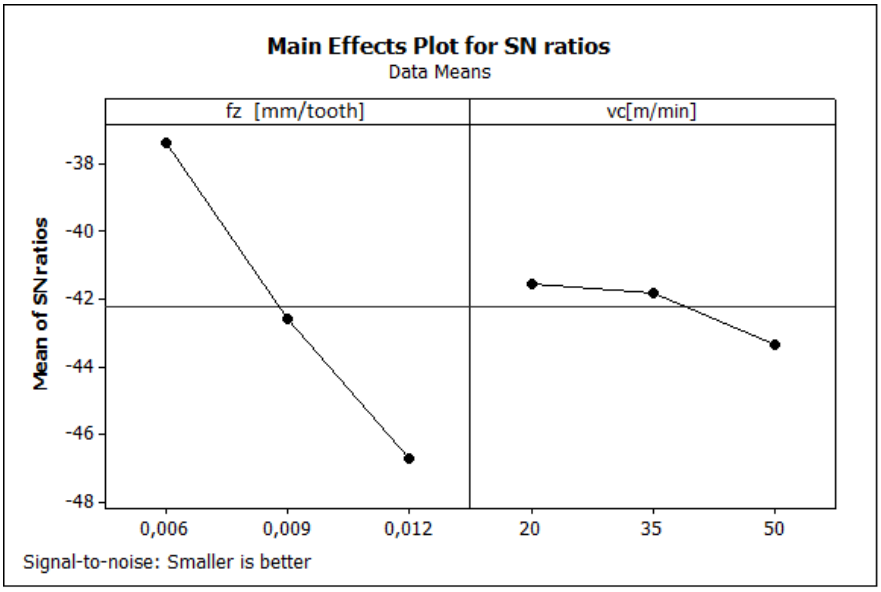

Figure 10. S/N ratio values for *Fy*.

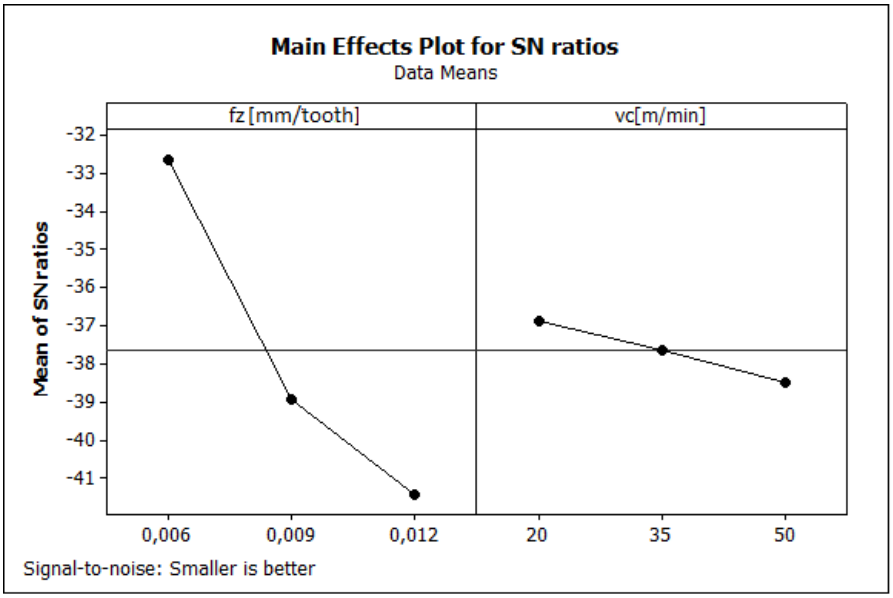

Figure 11. S/N ratio values for *Fz*.

4. CONCLUSION

The paper uses a surface response methodology to determine the optimal parameter of ball-end mill process, leading to the minimum cutting force under different cutting conditions. The surface response methodology for the cutting force regression model was developed by manipulating experimental measurements obtained from these cutting forces. The minimum cutting forces were obtained under these cutting conditions: a_e =0.2 mm, a_p = 3,5mm, v_c = 27 mm/min and feed per tooth f_z = 0.006 mm/ tooth. A comparison was made between the predicted results and experimental results and the deviation was found to be within the limit of 95% confidence level. It was found that the feed per tooth was the dominant factor during milling of NiTi alloy. The results also showed that the high cutting speed ensures better low cutting force.

REFERENCES

[1] Beňo, J., Stahovec J., Maňková I., Vrabel M., Kandráč L., "The Combined Approach to the Evaluation of the Cutting Force Data when Ball End Milling", Applied Mechanics and Materials, vol. 693, 2014, 352-357.

[2] Biermann D., Kahleyss F., Krebs E., Upmeier T., "A Study on Micro-Machining Technology for the Machining of NiTi: Five-Axis Micro-Milling and Micro Deep-Hole Drilling", JMEPEG, vol. 20, 2011, 745–751.

[3] Campitelli, G., Scippa, A., Prediction of milling cutting force coefficients for Aluminum 6082- T4, Procedia CIRP 1, 2012, 563- 568.

[4] Chomsamutr K., Jongprasithporn S., "Optimization Parameters of tool life Model Using the Taguchi Approach and Response Surface Methodology", Int. J. Comput. Inf. Sci., 93, 2012, 120-125.

[5] Fontaine M., Moufki A., Devillez A., Dudzinski D., "Modelling of cutting forces in ball-end milling with tool-surface inclination: Part I: Predictive force model and experimental validation", J. Mater. Process. Tech.,, vol. 189, 2007, 73–84.

[6] Fujii Y., Iwabe H., "Relationship between cutting force curve and working accuracy with ball-nose end mills", J. Japan Soc Prec Eng, vol. 48, 1982, 649–654.

[7] Guo Y., Klink A., Fu Ch., Snyder J., "Machinability and surface integrity of Nitinol shape memory alloy", CIRP Annals – Manu. Tech., vol. 62, 2013, 83–86.

[8] Kowalczyk M., "Application of Taguchi method to optimization of surface roughness during precise turning of NiTi shape memory alloy", Proc. of SPIE 104455, 2017, 1-10.

[9] Kolahan F., Manoochehri M., Hosseini A., "Application of Taguchi Method and ANOVA Analysis for Simultaneous Optimization of Machining Parameters and Tool Geometry in Turning", Eng. Tech., vol 74, 2011, 82-85.

[10] Kuram E. i in., "Optimization of the Cutting Fluids and Parameters Using Taguchi and ANOVA in Milling", Proceedings of the World Congress on Engineering, London, 2010, 1-5.

[11] Li H.Z., Zhang W.B., Li X.P., "Modelling of cutting forces in helical end milling using a predictive machining theory", Int Journal of Mech. Sci., vol. 43, 2001, 1711–1730.

[12] Lin H.C., Lin K.M., Chen Y.C., "A study on the machining characteristics of TiNi shape memory alloys", J. Mater. Process. Tech., vol. 105, 2000, 327-332.

[13] Motorcu A. R., "The Optimization of Machining Parameters Using the Taguchi Method for Surface Roughness of AISI 8660 Hardened Alloy Steel", J. Mech. Eng. Sci.,vol **56**, 2010, 391-401.

[14] Myers R. H., Mongomery D. C., "Response Surface Methodology: process and product optimization using designed experiment", A Wiley – Interscience Publication, 2002.

[15] Naserian R.S., Sadeghi M.H., Haghight H., "Static rigid force model for 3-axis ball-end milling of sculptured surfaces", Int. Journal of Machine Tools and Manufacture, vol. 47, 2007, 785–792.

[16] Piquard R., Acunto A. D, Laheurte P., Dudzinski D., "Micro-end milling of NiTi biomedical alloys, burr formation and phase transformation", Prec. Eng., vol. 38, 2014, 356–364.

[17] Ślusarczyk, Ł., "The construction of the milling process simulation models", Proc. of SPIE 10031, 2016, 1-10.

[18] Struzikiewicz, G., Zębla, W., Rumian K., "Application of Taguchi method to optimization of cutting force and temperature during turning of difficult to cut materials", Key Engineering Materials 686, 2016,1 14-118Weinert K.,

[19] Petzoldt V., Kotter D., "Turning and Drilling of NiTi Shape Memory Alloys", CIRP Annals – Manuf. Technol., vol. 53, Issue 1, 2004, 65–68.

[20] Subramanian M., Sakthivel M., Sooryaprakash K., Sudhakaran. "Optimization of Cutting Parameters for Cutting Force in Shoulder Milling of Al7075-T6 Using Response Surface R. Methodology and Genetic Algorithm", Procedia Engineering, 2013, 690-700.

[21] Sun Y., Ren F., Guo D., Jia Z., "Estimation and experimental validation of cutting forces in ball-end milling of sculptured" , International Journal of Machine Tools and Manufacture, vol. 49, 2009, 1238–1244.

[22] Wei Z.C., Wang M.J., Zhu J.N., Gu L.Y., "Cutting force prediction in ball end milling of sculptured surface with Z-level contouring tool path", International Journal of Machine Tools and Manufacture, vol. 51, 2011, 428–432.

[23] Weinert K., Petzoldt V., "Machining of NiTi based shape memory alloys", Mater, Sci. and Eng., vol. 378 ,2004, 180–184

[24] Weinert K., Petzoldt V., "Machining NiTi micro-parts by micro-milling", Mater, Sci. and Eng., vol. 481–482, 2008, 672–675.

[25] Wu S.K., Lin H.C., Chen C.C., "A study on the machinability of a Ti 49,6 Ni 50,4 shape memory alloy", Mater. Letters 40, 1999, 27–3.
[26] http://iscar.pl (access: 29.04.2019).

The application of high-speed camera registration for analysis of the chip breaking methods in the machining of nickel-based alloys

Grzegorz Struzikiewicz[*a]
[a]Production Engineering Institute, Cracow University of Technology, Al. Jana Pawła II 37
31-864 Cracow, Poland

ABSTRACT

The paper presents the results of application of the high-speed camera registration for the analysis of chip forming and chip breaking methods in the case of the nickel-based alloys turning. A process of chip formation in the cutting zone was recorded using the high speed camera Phantom 5.2. The experimental research was carried for two different materials ie. Inconel 718 and Inconel 625.The direction and speed of the chips flow were estimated in the computer program for analysis of the point movement.

Keywords: high-speed camera, chip creation and chip breaking process, turning, nickel-based alloys.

1. INTRODUCTION

Currently, intensive work is being carried out on the problem of chip evacuation from the treatment zone and identification of construction features and chip shape. This is closely related to the increasing degree of automation of machine tools and machining systems[1,2]. In addition, the process of chip formation and breaking falls under the supervision of material cutting processes, i.e. chip form control[3]. Obtaining a short, broken form of chips in the machining process is particularly important in the machining of difficult-to-cut materials, such as superalloys based on nickel, cobalt or titanium alloys[3,4,5]. These materials are widely used in aerospace applications, which puts high demands on the quality of manufactured parts as well as the stability of the machining process. Therefore, different methods and treatments that can meet these requirements are intensively looked for. Research is conducted on the optimization of cutting parameters of difficult-to-cut materials aimed at increasing the efficiency of machining processes while maintaining the assumed dimensional and shape accuracy and surface roughness[3,5,6,7]. The use of new tool materials such as ceramic tools or borazone in the machining of super alloys is being analyzed. New constructions of cutting tools, tool coatings as well as shapes of chip breakers and chip controllers on the tool surface are also implemented in the industry[8,9]. In the case of cutting with tools with a flat rake face one can distinguish three basic shapes of formed chips, i.e. linear in the rake's plane, circular obtained as a result of side or rising winding in a plane perpendicular to the rake surface. In industrial practice, there are more varieties of chip shapes that are the result of a combination of basic shapes. In the case of cutting tools with a shaped surface of rake, i.e. chip breaker or chip controller, chip shapes can take different forms[8,10,11,12]. The reason for this is the loss of continuity as well as the process of cracking and chip breaking. Classification of chips includes, banded, spiral, helical, arcing, elemental in short, long or entangled form chips. The process and mechanisms of chip formation are influenced by a number of factors related to the workpiece, tool and process (e.g. cooling method). In a broader sense, the chip formation process comprises three basic steps schematically shown in Fig. 1. The step of initial chip formation is first distinguished then followed by the step of controlling and breaking the chips. In turn, the process of chip breaking is presented in three ways and these are:- chip breaking as a result of contact (impact) of the chip with the work surface of the workpiece,- chip breaking as a result of contact of the chip with the transition surface (chip impact over the cutting tool), - chip breaking as a result of impact on the cutting edge surface (cutting insert)[9,10,11,12,13]. Basic cases of chip breaking are shown in Fig. 2.

[*] struzikiewicz@mech.pk.edu.pl

Photonics Applications in Astronomy, Communications, Industry, and High-Energy Physics Experiments 2019,
edited by Ryszard S. Romaniuk, Maciej Linczuk, Proc. of SPIE Vol. 11176, 1117651
© 2019 SPIE · CCC code: 0277-786X/19/$21 · doi: 10.1117/12.2536764

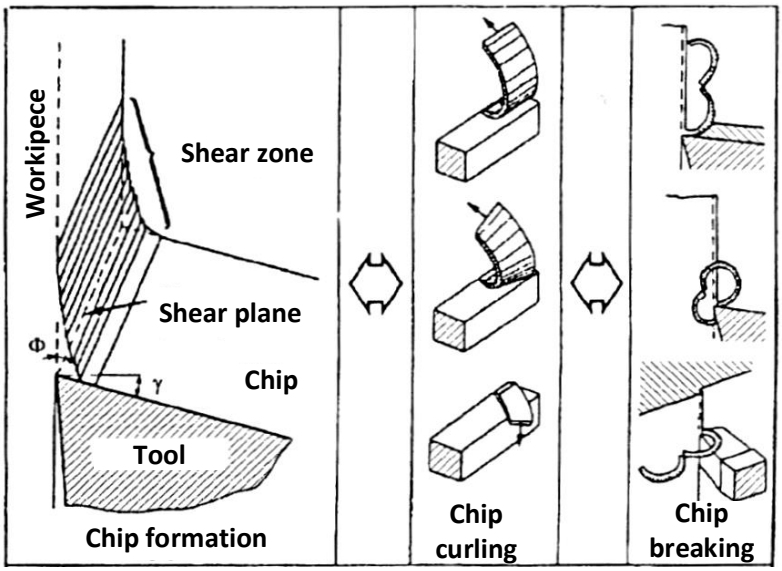

Figure 1. Stages of chip formation according to van Luttervelt[10,13]

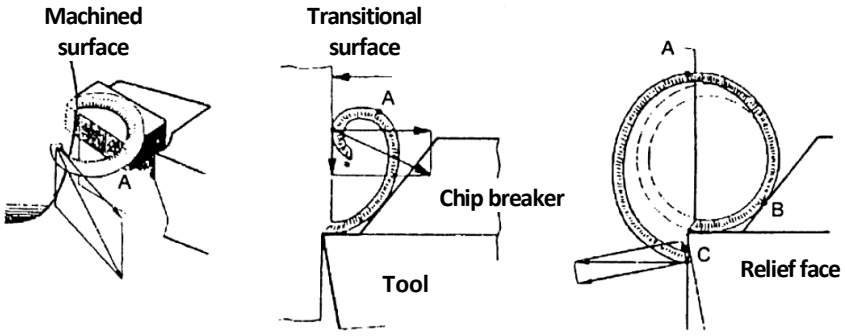

Figure 2. Basic case of chip breaking[10]

The chip breaking process is usually the result of the maximum bending stress at a certain point on its curvature. The radius of curvature of the chip depends on the geometry of the tool, the type of material to be machined and the cutting parameters like feed or depth of cut. Currently produced cutting tools (cutting inserts) usually have a shaped surface of rake[9,14,15,16]. Patterns of chip control for the case of a retractor with a straight and angled threshold, and with a flat section of the rake face and groove are shown in Fig. 3.

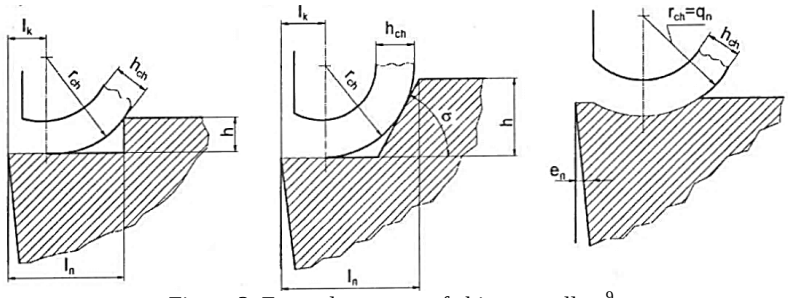

Figure 3. Exemplary types of chip controllers[9]

There are many methods (experiment, simulation, modeling) applied but none of them enables to explain and control chip creation phenomena[3,17]. The development of high speed camera technology enabled to record, observe and present particular phases of chip creation and breakage.

The recording system based on high speed camera can have various applications in machining. The main areas can include tests of chip breaking useful areas in local machining environment (revision of tool manufacturer recommendations), monitoring the operation of tools in actual machining process and testing theoretical models concerning chipbreaking phenomena. The purpose of the research was to use a high-speed camera to determine the shape of chips formed during longitudinal turning of nickel-based superalloys.

2. TEST STAND DESCRIPTION

The test stand was built on the basis of the Knuth Masterturn 400 lathe (table 1 presents basic lathe technical data). A measurement track was created in accordance with the diagram shown in Fig. 4. The measurement track included a high-speed camera, cold light lighting kit, lenses, necessary instrumentation (e.g. fastening systems, tripods) and a PC with software for recording and analysis of signals and film sequences. Fig. 5 shows photographs of the test stand together with the apparatus used. A Vision Fast Phantom v.5.2 camera from Vision Research has been directed to the cutting zone (Fig. 6). During registration two cold light spotlights were used from DEDOCOOL together with a 600 W power supply (Fig. 7). A Nikkor macro 200mm lens was used to register the chip formation process. The camera has been connected to the computer with a FireWire connector, used to transfer data from the camera directly to the computer's memory. Table 2 presents the basic technical parameters of a high-speed camera. The registrations of the chip forming and breaking processes were carried out at write speeds from 1000 to 3000 frames/s at a resolution of 512x512 to 1152x1152 pixels. Inconel 625 and Inconel 718 alloys were the processed materials. These are nickel based alloys characterized by high strength and resistance to various corrosion phenomena (including pitting). They are used in the aviation industry as elements of engines and turbines, chemical and shipbuilding apparatus industry and in nuclear reactors. The chemical composition of the materials used in the tests is shown in Table 3.
The tools used in the cutting tests were equipped with cutting inserts type WNMG080404 from Sandvik Coromant and VCMT 160404 from Iscar with chip breakers type 23 and SM. The technical data of the tools and the scores of the parameters are summarized in table 4. The machining was carried out with the cutting parameters recommended by the tool manufacturers for the areas of selected applications of chip controllers. Next, the individual film frames were extracted from the record, the images were processed and the selected sequences were compiled.

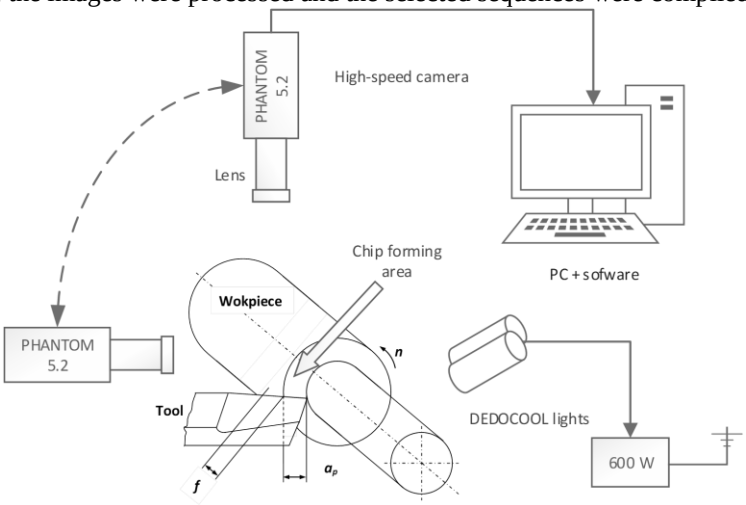

Figure 4. Block diagram of the measuring track

Table 1. Basic technical parameters of the Knuth Masterturn 400 lathe

Spindle speeds	Low 50-950; High 160-3000 rpm
Longitudinal feeds	0.038-0.678 mm/rev
Motor rating	7.5 kW
Center width	1000 mm
Tool holder	4-station
Dimensions (LxWxH)	2350x950x1250 mm
Weight	1500 kg

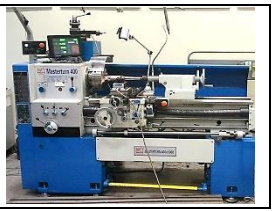

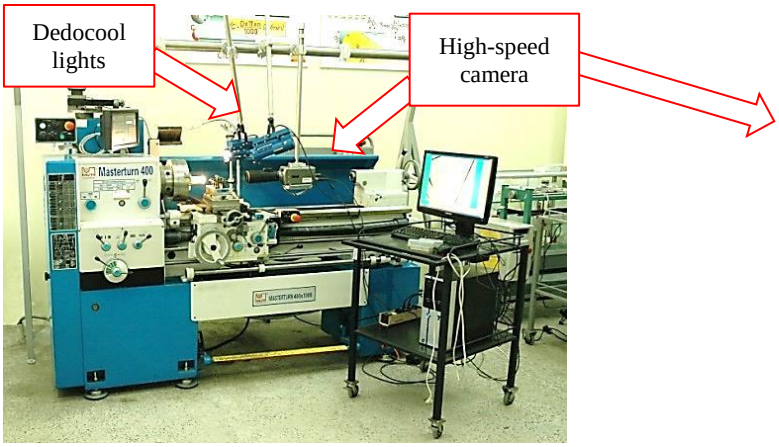

Figure 5. A photo of the test stand together with the measuring apparatus – PHANTOM v5.2 camera and DEDOCOOL illuminators

Figure 6. A high-speed camera Vision Researcher Phantom v5.2 with a lens Nikon AF Mikro-Nikkor 200

Figure 7. DEDOCOOL 600 W cold light spotlights

Table 2. Basic technical parameters of a high-speed camera PHANTOM v5.2.

	Sensor size	1.032.192 pixels
	Max. resolution	1156x896 pixels
	Frames-per second at full resolution	1,000 frame/s
	Max. frame rate	148.000 frame/s
	Exposure time (shutter speed)	min: 2 μs
	Bit depth	8, 10, 12 bit
	Communication	Ethernet
	Working temperature	10 to 40 ^{o}C

Table 3. The chemical composition of Inconel 718 and Inconel 625 alloys (%)

Material	**Al**	**C**	**Cr**	**Co**	**Fe**	**Mn**	**Mo**	**Ni**	**Nb**	**P**	**Si**	**S**	**Ti**
Inconel 718	0.5	0.07	20	1.0	17.0	0.3	2.9	54	5.1	0.015	0.35	0.015	1.1
Inconel 625	0.4	0.1	23	1.0	5.0	0.5	8.0	58	3.5	0.015	0.5	0.015	0.4

Table 4. Specification of tools used in cutting tests

Insert manufacturer	Sandvik Coromant	Iscar
Type	WNMG080404-23	VCMT160404-SM
Grade	GC1105	IC908
Toolholder	PWLNR2020K08	SVJCR2020K16
Recommended parameters	a_p = 0.5-4.0 mm, f = 0.1-0.3 mm/rev	a_p = 0.5-2.5 mm, f = 0.05-0.25 mm/rev

3. THE ANALYSIS OF RESULTS

Below (Fig. 8) there are examples of photographs of the formation of chips obtained in cutting tests. In both cases, machining of the tested materials resulted in a favorable form of chips (short, arched, broken) and an adverse form (long, spiral). It has been observed that the most important factor influencing the chip form is the feed f the depth of cut a_p. The cutting speed had no significant effect on the shape change and the intensity of chip breaking. The tests showed that for feed values above f = 0.15 mm / rev, for all tested cutting depths a favorable, short, arched form of chips was obtained for both tested materials.

Sample frames obtained from registered fast-changing sequences are presented below. Fig. 8 shows examples of photographs of long and preferred chips.

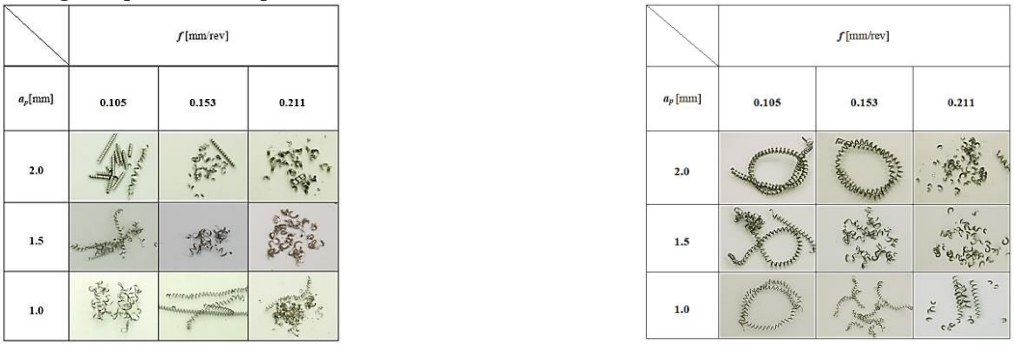

Fig. 8. Chips photos in turning a) Inconel 625 with chipformer -23, v_c = 75 m/min, b) Inconel 781 with chipformer -SM, v_c = 75 m/min

Sample frames obtained from registered fast-changing sequences are presented below. Fig. 9 shows examples of photographs of long and preferred chips.

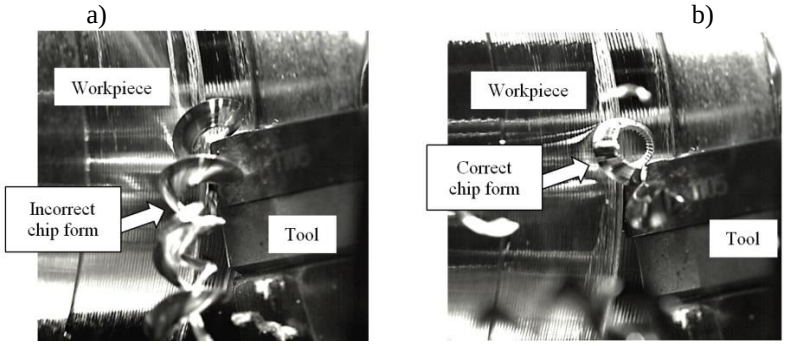

Figure 9. Example of incorrect and correct chip form, Inconel 625, v_c = 75 m/min, a_p = 1.5 mm, f = 0.345 mm/rev

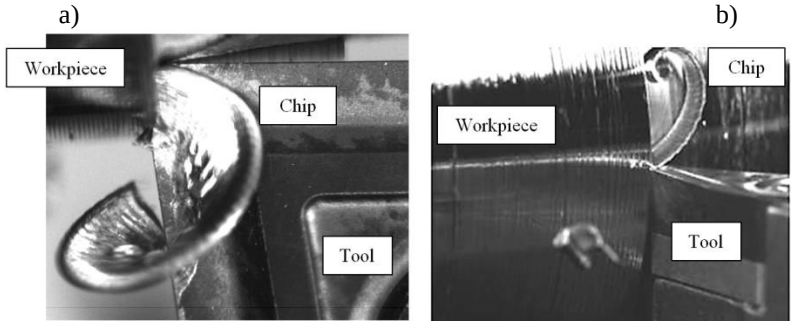

Figure 10. Examples of chip breaking sequences a) impact on the insert surface (relief face), Inconel 718 v_c = 75 m/min, a_p = 2.5 mm, f_n = 0,211 mm/reb) chip impact on the transition surface, Inconel 625 v_c = 75 m/min, a_p = 2.5 mm, f_n = 0.153 mm/rev

The analysis of registration showed that the most common reason for chip breaking is chip impact on the surface of the cutting insert (85% of chip breaking cases). Fig. 9b and 10a shows examples of such a method of chip breaking for both materials tested. In other cases, the chip impacted on the transition surface or chip breakage occurred as a result of

exceeding the material strength. This was the case with long, spiral chips, whose increasing mass and dimensions were the direct cause of breaking. Examples of frames from registered sequences representing different chip breaking methods are shown in Fig. 10b.

4. CONCLUSIONS

The obtained results showed the usefulness of using a high-speed camera to analyze the process of creating and breaking chips obtained in the process of turning super alloys. It has been shown that the dominating method of chip breaking is chip impact on the flank. Such a process was observed for 85% of cases of breaking and obtaining short arc chips.
Another method observed was the impact of the chip on the transition surface or the workpiece not yet processed. It should be remembered that collecting experimental film collections in photo sequences is not an easy task, and may be a limitation in industrial use. For example, it is possible to register only machining operations that do not require coolant. However, recordings of this type may supplement measuring apparatus, e.g. for measuring force and temperature in the cutting zone. They enable precise observation and explanation of various phenomena in the cutting zone, chip formation and material flow or the behavior of various tools in real processing.

Acknowledgements
The work was carried out as part of statutory research at Institute of Machine Technology and Production Automation at the Cracow University of Technology.

REFERENCES

[1] Matras, A., Zębala, W., Kowalczyk, R., "Precision milling of hardened steel with CBN tools," Key Engineering Materials 581, 182-187 (2014).
[2] Zębala, W., "Tool stiffness influence on the chosen physical parameters of the milling process," Bulletin of the Polish Academy of Sciences: Technical Sciences 60(3), 597-604 (2012).
[3] Słodki, B., Struzikiewicz, G., Slusarczyk, L., "Influence of cutting fluid conditions and cutting parameters on the chip form in turning of titanium and steel alloys," Key Engineering Materials 686, 74-79 (2016).
[4] Kowalczyk M., "Temperature distribution in the machining zone during precise turning of NiTi alloy," Proc. of SPIE 10808, 1-12 (2018).
[5] Kowalczyk M., "Application of Taguchi method to optimization of surface roughness during precise turning of NiTi shape memory alloy," Proc. of SPIE 104455, 1-10 (2017).
[6] Struzikiewicz, G., Otko, T., "Dependence of shape deviations and surface roughness in the hardened steel turning," Key Engineering Materials 581, 443-448 (2014).
[7] Kowalczyk, R., Matras, A., Zębala, W., "Analysis of the surface roughness after the sintered carbides turning with PCD tools," Proc. of SPIE 9290, 1-6 (2014).
[8] Ślusarczyk, Ł., Franczyk, E., "Development and verification of a measuring stand for recording the physical phenomena during turning," Proceedings of SPIE 10445, 1-6 (2017).
[9] Boothroyd, G., Knight, W.A., [Fundamentals of machining and machine tools], Marcel Dekker, New York, (1989).
[10] Van Luttervelt, C.A., "Neue entwicklungen in der spanuberwachung," VDI Berichte 988, 431-477 (1993).
[11] Davies, M.A., Chou, Y., Evans, C.J., "On Chip Morphology, Tool Wear and Cutting Mechanics in Finish Hard
[12] Turning," CIRP Annals – Manufacturing Technology 45(1), 77–82 (1996).
[13] Kluft, W., van Luttervelt, C.A., Nakayama, K., Pekelharing A.J., "Present knowledge of chip control," CIRP Annals - Manufacturing Technology 28(2), 441-455 (1979).
[14] Struzikiewicz, G., "The application of high-speed camera for analysis of chip creation process during the steel turning," Proc. of SPIE 10031, 1-6 (2016).
[15] Struzikiewicz, G., Zębla, W., Rumian K., "Chip flow analysis during the turning of an aircraft part made of stainless steel," Proc. of SPIE 10445, 1-6 (2017).
[16] Struzikiewicz, G., "Correlation of cutting forces measurements and high-speed camera registration in the analysis of the chip breaking process." Proc. of SPIE 10808, 1-6 (2018).
[17] Gawlik, J., Ryniewicz, A., Sioma, A., "The strategies and methods of measurement in multifunctional quality inspection," Measure and Quality Control in Production 1860, 649-662 (2004).

AC conductivity activation energy of composite cellulose - synthetic ester MIDEL 7131 - water nanodrops

Przemysław Rogalski*
Department of Electric Devices and High Voltage Technology, Lublin University of Technology
38A, Nadbystrzycka Street, Lublin, Poland

ABSTRACT

Paper presents the results of AC conductivity measurements of composite cellulose-synthetic ester-water nanodrops. Polynomial approximations made by using the new method, enabled numerical analysis of the obtained measurements. The mathematical analysis made it possible to determine the dependence of conductivity activation energy as a function of frequency. Obtained results of activation energy induce the presence of electric charges hopping exchange mechanism.

Keywords: synthetic ester, pressboard, AC conductivity, activation energy, moisture content, composite, water nanoparticle, power transformer

1. INTRODUCTION

Cellulose in combination with transformer oil has been used as an insulating material in energy transformers for more than a century. Despite of creation of many other modern materials, due to mainly economic reasons, so-called paper and oil insulation is still mainly used insulation material. The main threat to the durability of this type of insulation is an increase in its moisture level and temperature[1]. Initially, after production, the moisture level of the cellulose insulation in transformer does not exceed 0.8% by weight, however, over time it increases to a level of up to 5%, leading to the danger of losing its insulating properties. In order, among other things, to reduce the influence of moisture on cellulose, modern synthetic ester oils such as Midel 7131 are used. Oil of this type has many advantages such as, for example, greater ability to trap water molecules, thanks to which fewer of them reach cellulose. In order to determine moisture level of paper - oil insulation, non-destructive[2,3] electrical methods are used. They can be divided into two main groups. Time domain measurements[4]: PDC (Polarization and Depolarization Current) and RVM (Reverse Voltage Measurement). Measurements in the frequency domain[5,6]: FDS (Frequency Domain Spectroscopy). Recent research on water in paper insulation has shown its presence in the form of nanodrops[7,8]. Nanodrops embedded in the dielectric matrix, similar to nanocomposites[9–11], can create conditions for occurrence of hopping charge transfer in the form of tunneling. Currently used to describe phenomena occurring in the cellulose insulation, the ionic conductivity model in many aspects does not agree with the experimental results. When using a hopping charge transfer model, matching experimental data to mathematical calculations is much better.

The aim of this work was to develop a new method to determine the activation energy of AC conductivity of a composite cellulose - synthetic ester - water nanodrops in a wide range of frequencies. For testing, as an example, a sample of pressboard (cellulose) with a water content of 5% by weight was selected. Such a choice is due to the fact that reaching such moisture content of insulation threatens a catastrophic failure of the power transformer. To analyze obtained experimental results, the model of hopping conductivity (electron tunneling) on alternating current will be used, which proved excellent during the analysis of DC and AC current results of conductivity tests of the composite cellulose - mineral oil - water nanodrops.

*p.rogalski@pollub.pl

Photonics Applications in Astronomy, Communications, Industry, and High-Energy Physics Experiments 2019,
edited by Ryszard S. Romaniuk, Maciej Linczuk, Proc. of SPIE Vol. 11176, 1117652
© 2019 SPIE · CCC code: 0277-786X/19/$21 · doi: 10.1117/12.2536775

2. RESEARCH METHODOLOGY

2.1 Measurement samples

In research pressboard made my Weidmann company of thickness 1,5 mm and ester transformer oil Midel 7131, was used. After cutting the sample it was exposed for vacuum drying for 48 h in temperature of 80 °C. After drying, the weight of the sample was determined. The sample was then exposed to atmospheric air to increase its moisture content. By controlling the weight of the sample, it was possible to achieve a target moisture content of 5% by weight. When this happened, the sample was flooded with synthetic ester oil. In order to achieve a thermodynamic equilibrium between moisture, pressboard and oil, sample was aged in a hermetic container for 6 months in room temperature.

2.2 Test bench and measurements

In order to make reliable measurements, a capacitor equipped with three measuring electrodes shown in Figure 1 was used. A sample of synthetic ester oil impregnated pressboard was placed in measuring capacitor. Then, the measuring capacitor was placed in a hermetic vessel flooded with oil and inserted into a climatic chamber characterized by temperature stabilization accuracy of ± 0.1 ° C. Due to the large mass of the measuring capacitor, preliminary heating was performed at a given measurement temperature for a minimum of 5 hours. After this time, the temperature of the measuring capacitor stabilized, which made it possible to carry out measurements. The Agilent 34970A meter was used to control and record the temperature of measuring capacitor. A Dirana meter manufactured by Omicron was used for PDC and FDS measurements. The measurements of AC conductivity were made for 7 temperature values of, respectively: -20 °C, 0 °C, 10 °C, 20 °C, 30 °C, 40 °C and 50 °C.

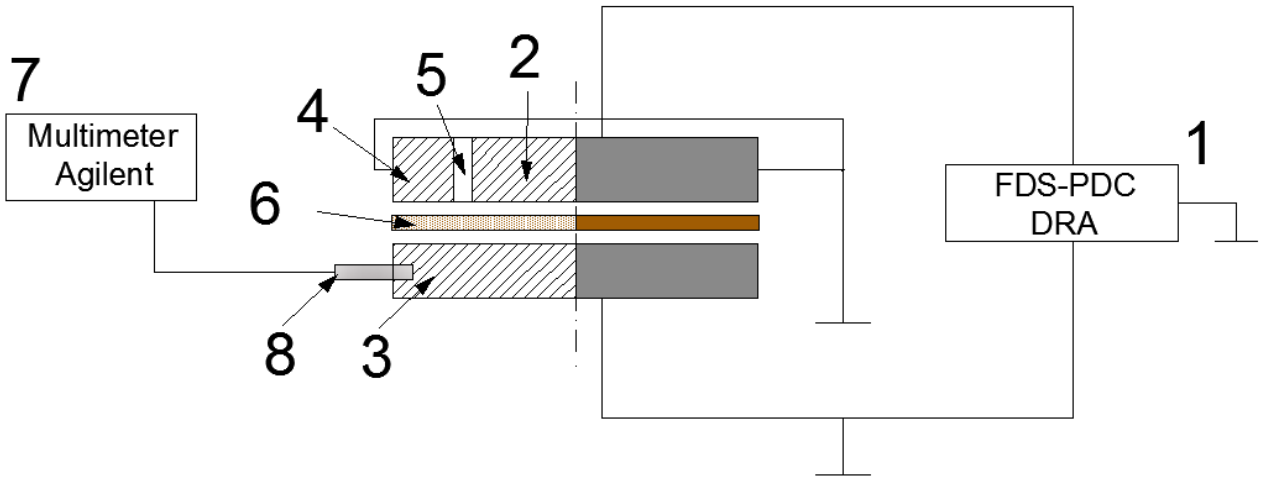

Figure 1. Test bench schematic: 1- FDS-PDC Dielectric Response Analyzer (Dirana meter); 2 - voltage electrode; 3 - measuring electrode; 4 - protective electrode; 5 - insulator; 6 - synthetic ester impregnated pressboard; 7 - temperature meter; 8 - PT 1000 temperature sensor.

2.3 Physical basis of the FDS method

The analysis of dielectric response (FDS) is based on the analysis of second Maxwell equation**.** It shows that in dielectric materials the electric current density consists of two components[12] i.e. conduction current density vector $\overrightarrow{J_R}$ and vector of the displacement current density $\overrightarrow{J_C}$:

$$\oint\left(\vec{H} * \vec{dl}\right) = \overrightarrow{J_C} + \overrightarrow{J_R} \tag{1}$$

where: $\oint$ – integral on a closed circuit that surrounds the current; $\vec{H}$ – vector of magnetic field strength; $\vec{dl}$– length vector, tangent to the integration circuit; $\overrightarrow{J_R}$ – conduction current density vector; $\overrightarrow{J_C}$ – vector of the displacement current density.

In the FDS method, the forcing electric field is sinusoidal. The instantaneous field strength value is described as:

$$E = E_0 \sin(\omega t) \tag{2}$$

where: E – instantaneous value of the electric field intensity; E_0 – amplitude of the electric field intensity; $\omega = 2\pi f$ – pulsation; t – time; f – frequency.

Density of the displacement current, entering the second Maxwell equation:

$$\overrightarrow{J_C}(\omega) = \frac{\partial \vec{D}}{\partial t} = \omega \varepsilon' \varepsilon_0 E_0 \sin\left(\omega t + \frac{\pi}{2}\right) \tag{3}$$

where: D – electric induction vector; ε_0 – dielectric permittivity of the vacuum; ε – relative dielectric permittivity.

Conductivity current density, entering the second Maxwell equation:

$$\overrightarrow{J_R}(\omega) = \sigma(\omega, T, X)E = \sigma(\omega, T, X)E_0 \sin(\omega t) \tag{4}$$

where: σ(ω) – conductivity; E_0 – amplitude of the electric field intensity; ω – pulsation; t – time.

For laboratory measurements using the FDS method, a parallel-plate capacitor system is most often used. The result of FDS measurement is the absolute value of impedance and the phase shift angle as a function of pulsation. Thanks to the knowledge of these two variables it is possible to determine the resistance value:

$$R = \frac{Z}{\cos \varphi} \tag{5}$$

where: Z – absolute value of impedance; φ - phase shift angle.

Knowing the geometrical dimensions of the measuring capacitor and value of sample resistance, it is possible to determine its conductivity:

$$\sigma(\omega, T, X) = \frac{d}{SR(\omega, T, X)} \tag{6}$$

where: σ(ω) – conductivity; R – resistance; d = 0.0015 m – thickness of the pressboard sample; S = 0.02 m^2 – surface area of the voltage electrode of the measuring capacitor.

3. DETERMINATION OF THE ACTIVATION ENERGY OF AC CONDUCTIVITY

Figure 2 shows in the form of points, calculated on the basis of measured values of Z and fi, conductivity values of composite pressboard-synthetic ester - water nanodrops for temperatures from -20 °C to 50 °C as a function of frequency. Measuring points visible in Figure 2 are characterized by a low density of only 3 points per decade. Due to this, a new approximation method presented in the paper[4] was used. As a result, approximation curves with a high coefficient of determination of average $R^2 = 0.9999967$ were obtained. As can be seen in Figure 2, the conductivity for all temperatures except for the lowest one shows the steady state. It should be noted that the steady state conductivity value increases with increasing temperature. This indicates the presence of temperature dependence of conductivity. The slope of the waveforms shown in Figure 3 that were plotted in double logarithmic coordinates can be determined using the equation:

$$\alpha(f) = \frac{\partial(log\sigma)}{\partial(logf)} \tag{7}$$

where: *α(f)* - frequency coefficient.

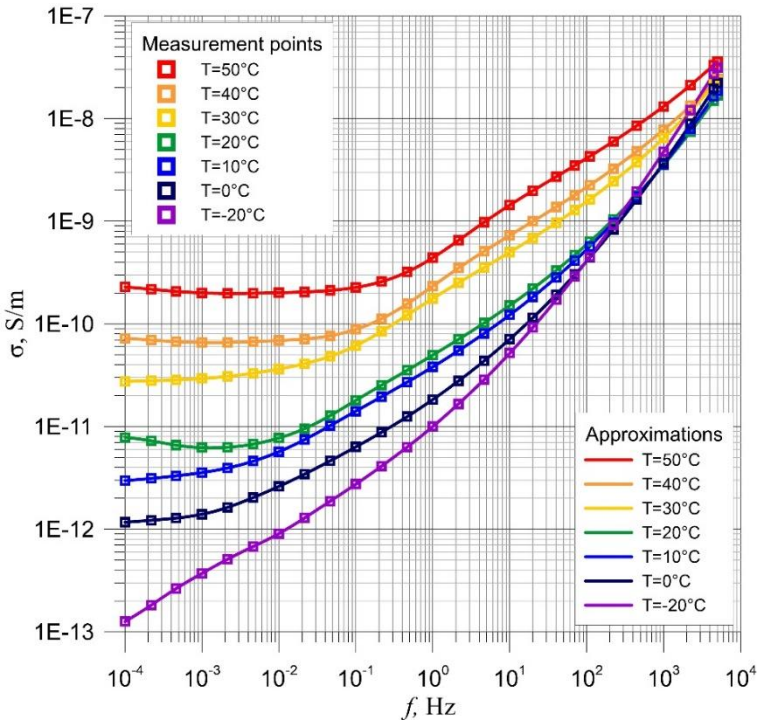

Figure 2. Conductivity of the composite cellulose - synthetic ester - water nanoparticles with a water content of 5% by weight as a function of frequency.

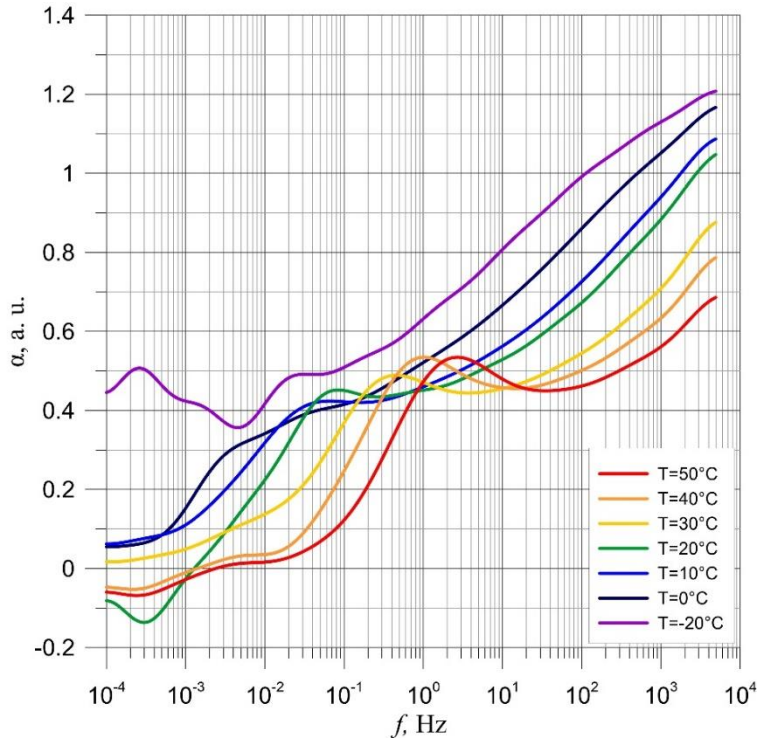

Figure 3. Frequency coefficient α(f) of composite cellulose - synthetic ester - water nanoparticles with a water content of 5% by weight as a function of frequency.

The location of the maxima in Fig.3 depends on the temperature and moves with its increase into the area of higher frequencies. This is caused by the temperature dependence of the relaxation time, described by the formula[13]:

$$\tau = \tau_0 \exp(\frac{\Delta W}{kT}) \quad (8)$$

where: τ_0 - numerical constant, ΔW - activation energy of relaxation time, k - Boltzmann constant, T – temperature.

From the diagrams of α(f) (Fig. 3), values of the relaxation time activation energy were determined, the values of which are for the low-frequency stage (0.816 ± 0.0268) eV and for the high-frequency stage (0.749 ± 0.0268) eV. These values are within the limits of the error the same, their average value is (0.783±0.0335) eV. The obtained mean value was used to shift the curves shown in figure 2 in X axis with respect to the curve obtained at 20° C, thanks to which the influence of relaxation time activation energy on the conductivity was eliminated. Results of approximated waveforms shift are shown in Figure 4.

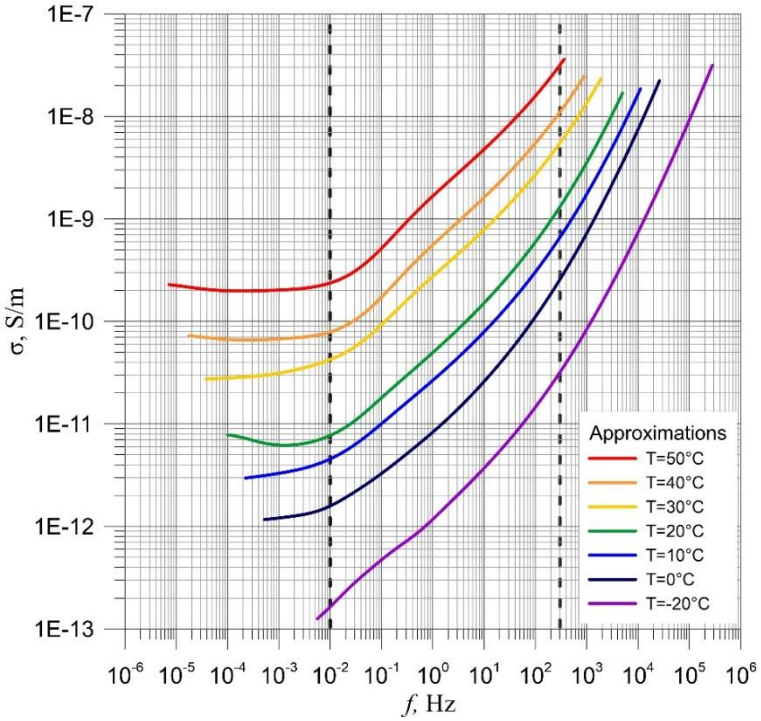

Figure 4. Frequency dependencies of approximated curves of the composite's cellulose - synthetic ester - water nanodrops with a moisture content of 5% by weight for measuring temperatures -20 °C, 0 °C, 10 °C, 20 °C, 30 °C, 40 °C and 50 °C, shifted by the activation energy of relaxation time to a temperature of 20 °C.

As can be seen from Figure 4, waveforms for temperatures, lower than 20 °C, are shifted to the higher frequency region, while for temperatures higher than 20 °C - to the lower frequency region. This means that all waveforms after shifting are in the range from about 0.01 Hz to about 300 Hz, marked in figure 4 in the form of vertical dashed lines. For five frequencies in this range, Arrhenius diagrams were drawn up, and shown in Figure 5. Approximations of Arrhenius graphs indicate their high accuracy, due to high value of determination coefficients, which range from 0.985 and higher (Table 1). On the basis of Arrhenius graphs, the activation energy of conductivity was determined for each of them, the values of which are presented in Table 1. The values of activation energy of conductivity for six frequencies in range of (0.01 - 300) Hz varies in a very narrow range from a minimum of 0.691 eV to a maximum of 0.733 eV. The average value of activation energy of conductivity is (0.714 ± 0.0141) eV.

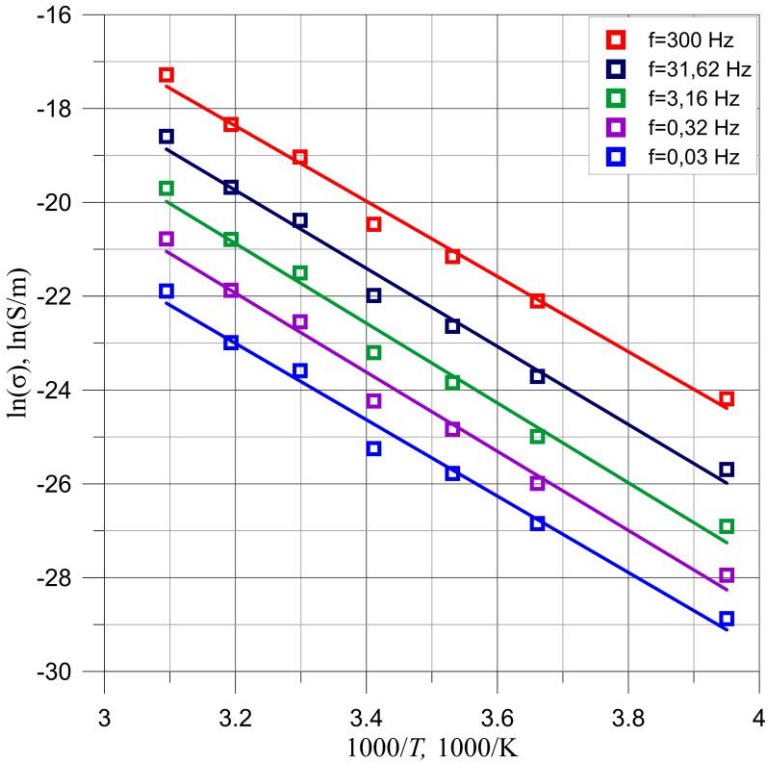

Figure 5. AC conductivity Arrhenius plots for selected frequencies.

Stability of conductivity activation energy in a wide range of measurement frequency indicates the presence of one charge transfer mechanism. On the basis of other works, it can be concluded that in such case hopping conduction through tunneling occurs.

Table 1. Values of conductivity activation energy, determination coefficient R^2 and standard deviation for 5 measuring frequencies.

***f*, Hz**	**Δ*E*, eV**	**R^2, a. u.**
0.03	0.701	0.987
0.32	0.726	0.986
3.16	0.733	0.985
31.62	0.717	0.987
300	0.691	0.991
Average value	0.714	0.987
Standard deviation	0.0141	0.0018

4. CONCLUSIONS

The article presents results of AC conductivity measurements of composite's cellulose - synthetic ester - water nanodrops with a moisture content of 5% by weight for measuring temperatures -20 °C, 0 °C, 10 °C, 20 °C, 30 °C, 40 °C and 50 °C 323 K. On the basis of the obtained measurement results, using the new approximation method, the activation energy of relaxation time was determined. The use of relaxation time activation energy allowed for shift of the conductivity curves in the frequency axis. This made it possible to eliminate the impact of relaxation time activation energy on conductivity, and thus to plot Arrhenius curves on the basis of which the activation energy of conductivity was calculated. The obtained

results of the conductivity activation energy indicate the occurrence of only one mechanism of conduction i.e. hopping charge transfer through tunneling..

REFERENCES

[1] Frivaldsky, M., Cuntala, J., Spanik, P. and Kanovsky, A., "Investigation of thermal effects and lifetime estimation of electrolytic double layer capacitors during repeated charge and discharge cycles in dedicated application," Electr. Eng. **100**(1), 11–25 (2018).

[2] Kabanau, D. M., Lebiadok, Y., Shpak, P., Zhuk, S. M. and Stashkevich, S. P., "Device based on GaInAsSb LEDs for measurement of water concentration in oil," Devices Methods Meas. **8**(2), 142–150 (2017).

[3] Alekseev, V. A., Usoltcev, V. P., Yuran, S. I. and Shulmin, D. N., "COMPLEX FOR MONITORING OF SEWAGE OPTICAL DENSITY CHANGES," Devices Methods Meas. **9**(1), 7–16 (2018).

[4] Żukowski, P., Kołtunowicz, T. N., Kierczyński, K., Subocz, J., Szrot, M. and Gutten, M., "Assessment of water content in an impregnated pressboard based on DC conductivity measurements. Theoretical assumptions," IEEE Trans. Dielectr. Electr. Insul. **21**(3), 1268–1275 (2014).

[5] Żukowski, P., Kołtunowicz, T. N., Kierczyński, K., Rogalski, P., Subocz, J., Szrot, M., Gutten, M., Sebok, M. and Jurcik, J., "Permittivity of a composite of cellulose, mineral oil, and water nanoparticles: theoretical assumptions," Cellulose **23**(1), 175–183 (2016).

[6] Żukowski, P., Kołtunowicz, T. N., Kierczyński, K., Rogalski, P., Subocz, J., Szrot, M., Gutten, M. and Sebok, M., "Dielectric losses in the composite cellulose-mineral oil-water nanoparticles: theoretical assumptions," Cellulose **23**(3), 1609–1616 (2016).

[7] Żukowski, P., Kierczyński, K., Kołtunowicz, T. N., Rogalski, P. and Subocz, J., "Application of elements of quantum mechanics in analysing AC conductivity and determining the dimensions of water nanodrops in the composite of cellulose and mineral oil," Cellulose **26**(5), 2969–2985 (2019).

[8] Żukowski, P., Kołtunowicz, T. N., Kierczyński, K., Subocz, J. and Szrot, M., "Formation of water nanodrops in cellulose impregnated with insulating oil," Cellulose **22**(1), 861–866 (2015).

[9] Pogrebnjak, A. D., Isakov, I. F., Opekunov, M. S., Ruzimov, S. M., Ligachev, A. E., Nesmelov, A. V. and Kurakin, I. B., "Increased wear resistance and positron annihilation in Cu exposed to high power ion beam," Phys. Lett. A **123**(8), 410–412 (1987).

[10] Pogrebnjak, A., Goncharov, A., Yunda, A., Shelest, I., Swic, A. and Lebedynskyi, I., "STRUCTURAL FEATURES OF THE FORMATION OF MULTICOMPONENT AND HIGH-ENTROPY TRANSITION METAL NITRIDE FILMS," High Temp. Mater. Process. An Int. Q. High-Technology Plasma Process. **22**(1), 7–15 (2018).

[11] Bondariev, V., Zukowski, P., Luhin, V. G. and Voitov, I. V., "THERMOGRAVIMETRIC ANALYSIS OF THE (FeCoZr)x(CaF2)(100–x) NANOCOMPOSITE," High Temp. Mater. Process. An Int. Q. High-Technology Plasma Process. **21**(4), 289–298 (2017).

[12] Landau, L. D., Ландау, Л. Д., Lifshits, E. M., Pitaevskiĭ, L. P., Лифшиц, Е. М. and Питаевский, Л. П., [Electrodynamics of continuous media] (1984).

[13] Psarras, G. C., Manolakaki, E. and Tsangaris, G. M., "Dielectric dispersion and ac conductivity in—Iron particles loaded—polymer composites," Compos. Part A Appl. Sci. Manuf. **34**(12), 1187–1198 (2003).

The numerical analysis of the electric field distribution behind the three-layer wall

Agnieszka Choroszucho[a], Adam Steckiewicz[a], Jacek M. Stankiewicz
[a]Bialystok University of Technology, Faculty of Electrical Engineering, Wiejska 45D, 15-351 Bialystok, Poland

ABSTRACT

The paper presents the influence of building materials (aerated concrete, plaster board) on the electromagnetic wave propagation. The relation between structures of three-layer wall and electric parameters like electric permittivity building materials and aerated concrete conductivity are examined. It was observed that when changing the aerated concrete conductivity in the range $\sigma = 0 \div 0.015$ S/m, the component of electric field (E_z) had higher values for permittivity $\varepsilon_r' = 2$. However, when the conductivity value increased (above 0.02 S/m), the max (E_z) values were higher for $\varepsilon_r' = 2.45$. The presented results give some information about field distribution around materials, which consist of some non-ideal, absorbing dielectrics. The finite-difference time-domain method (FDTD) was used. The delivered analysis may be useful for designers of wireless networks.

Keywords: electromagnetic wave propagation, finite-difference time-domain method (FDTD), wireless communications systems, building materials

1. INTRODUCTION

Wireless communication systems allow transferring data between computers without the necessity of installing complex cable networks. Through use of standard equipment the installation of wireless data transmission systems is easier and faster than installation of cable networks. Wireless communication systems may be used in places where it is impossible to install cables. Wireless data transmission systems allow connecting multiple devices relatively quickly, while retaining the possibility of dynamic and automated configuration of the group of communicating elements. The using wireless communication systems is decided also by less important factors, such as:

- the possibility of creating additional systems with overlapping areas of operation;
- the creation of an open and generally accessible communication system for users in the designated area;
- the increasing of reliability due to partial overlap in receivers' range (additional access points).

The wireless network system requires taking into account the number of access points and their proper placement. The discussed problems are especially important when installing wireless networks inside buildings. The cause is the effects occurring during the propagation of electromagnetic waves in area with complex geometry and material structure. Important factors determining the construction and functionality of wireless communication systems are:

- limiting the number of access points;
- fulfilling the limitations resulting from the allowed level of emitted signal (transmitter strength);
- limiting the number of placed transmitters due to difficult installation conditions and the need to minimize the cost connected with the network's structure.

The subjects in the scope of wireless communication systems (e.g. Wi-Fi) are discussed in many publications, taking into account aspects directly connected with the physical nature of the effects, as well as methods of their numerical modeling. In the available publications we can distinguish three main focus groups of discussed topics.

- The choice of numerical method used to determine the distribution of electromagnetic field, its formulation and practical implementation.

Photonics Applications in Astronomy, Communications, Industry, and High-Energy Physics Experiments 2019, edited by Ryszard S. Romaniuk, Maciej Linczuk, Proc. of SPIE Vol. 11176, 1117653
© 2019 SPIE · CCC code: 0277-786X/19/$21 · doi: 10.1117/12.2536786

- The assessment of building constructions' properties, including the multi-layered construction elements and complex materials (concrete, reinforced concrete). In case of numerical methods the selected subjects are directly connected with the method of the mathematical description of the structure and the properties of complex materials within the created models of building structures.
- Description of material data and material coefficients values characterizing electrical properties of building materials.

Due to a high specific gravity of concrete and the attempts to minimize surface strains for example acting on the ceiling construction, currently its lighter version is more often used – aerated concrete (autoclaved aerated concrete, suporex). It is used in the construction of detached houses and in large dimension constructs for construction of partition walls.
A basic set of ingredients includes [2, 8]:

- binding material – most often a mixture of cement and lime;
- aggregate – quartz sand or fly ash from incineration of coal, or a mixture of the two. For light concrete, mineral aggregate, industrial waste, aggregate from baked clay and rock material, organic fillers (mainly tree origin) and polymers are used;
- blowing agent – compounds of aluminum in the form of powder or paste;
- surfactants – removing the protective layer from the aluminum powder and reducing the surface tension of water;
- water and additives (ex. plaster).

The properties of aerated concrete are strictly dependent from its microstructure, which consists of two phases – solid occupying approx. 20-40% of material volume and gaseous (approx. 60-80%). The porous structure results in a low bulk density and shapes the electrical properties of the material.
The electrical parameters are similar to the properties of ceramic materials (ex. brick) [1, 2, 3].

2. FINITE-DIFFERENCE TIME-DOMAIN METHOD (FDTD)

This method allows to determine the distribution of the electromagnetic field inside the area where are used wireless communication systems like Wi-Fi. The FDTD method allows the analysis of complex structures, in which every material has a corresponding material property, which directly influences the correctness of the results. The FDTD method is based on the direct numerical integration of the Maxwell's curl equations in time and space [3, 4, 6, 7, 8].

$$\nabla \times \mathbf{E} = -\frac{\partial \mathbf{B}}{\partial t}, \tag{1}$$

$$\nabla \times \mathbf{H} = \mathbf{J} + \frac{\partial \mathbf{D}}{\partial t}, \tag{2}$$

$$\nabla \cdot \mathbf{D} = \rho, \tag{3}$$

$$\nabla \cdot \mathbf{B} = 0, \tag{4}$$

$$\nabla \cdot \mathbf{J} = -\frac{\partial \rho}{\partial t}, \tag{5}$$

where symbols in *bold* represent vector quantities, and symbols in *italics* represent scalar quantities and: **E** – electric field (vector), **H** – magnetic field (vector). The sources of these fields are electric charges and electric currents, which can be expressed as local densities namely charge density ρ and current density **J**.
In the classical approach, the cubic Yee cell is used (Figure 1) [3, 4, 6, 7, 8].

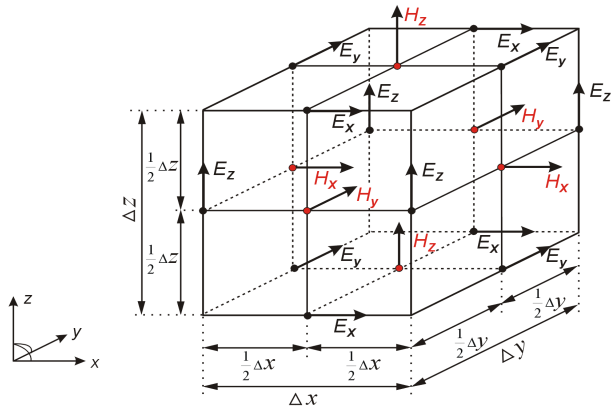

Figure 1. A Yee cell in the FDTD method.

For each cell three components are then assigned for both electric field (**E**) and magnetic (**H**) respectively. They are calculated in different points of space. The displacement of discreet time values by Δ_t /2 that appears in the calculations is used to determine the electric field with respect to the values, where the magnetic field is calculated. The components of the electromagnetic field are calculated in a different point in space. The E_x, E_y, E_z components which are associated with the Yee cell are anchored in mid-points of appropriate edges, and the H_x, H_y, H_z components – in the middle of the planes forming the sides of the cell. Appropriate component intensity vectors of the magnetic field circulating around it surround each component of intensity vector of the electric field. The presented record is analogical to calculate three component intensity vectors of the magnetic field.

The FDTD method allows the analysis of complex structures, in which every material has a corresponding electrical properly material. In order to obtain a simultaneous scalar equation describing the individual components of the field, the equations (1)-(2) are subjected to decomposition in the Cartesian coordinate system

$$\frac{\partial E_x}{\partial t} = \frac{1}{\varepsilon}\left(\frac{\partial H_z}{\partial y} - \frac{\partial H_y}{\partial z} - \sigma E_x\right), \tag{6}$$

$$\frac{\partial E_y}{\partial t} = \frac{1}{\varepsilon}\left(\frac{\partial H_x}{\partial z} - \frac{\partial H_z}{\partial x} - \sigma E_y\right), \tag{7}$$

$$\frac{\partial E_z}{\partial t} = \frac{1}{\varepsilon}\left(\frac{\partial H_y}{\partial x} - \frac{\partial H_x}{\partial y} - \sigma E_z\right), \tag{8}$$

$$\frac{\partial H_x}{\partial t} = \frac{1}{\mu}\left(\frac{\partial E_y}{\partial z} - \frac{\partial E_z}{\partial y}\right), \tag{9}$$

$$\frac{\partial H_y}{\partial t} = \frac{1}{\mu}\left(\frac{\partial E_z}{\partial x} - \frac{\partial E_x}{\partial z}\right), \tag{10}$$

$$\frac{\partial H_z}{\partial t} = \frac{1}{\mu}\left(\frac{\partial E_x}{\partial y} - \frac{\partial E_y}{\partial x}\right). \tag{11}$$

These equations are directly integrated in time and space domains, which were described in [3, 4, 6, 7, 8]. The integration of Maxwell's equations in time is based on using the two-step schematic. In selected moments in time, in which the distribution of the electrical field is determined, the component vector values of the intensity of the magnetic field are moved in time by $\Delta_t/2$ in relevance to them.

The determining of component intensity vectors of the electric field E_x, E_y, E_z is possible with the prior appointment of the component intensity vectors of the magnetic field H_x, H_y, H_z in the previous time step of this algorithm. Using the already calculated values H_x, H_y, H_z, the next values of the component vectors of the electric field are determined E_x, E_y, E_z. The described series of steps is called the time leapfrog (Figure 2).

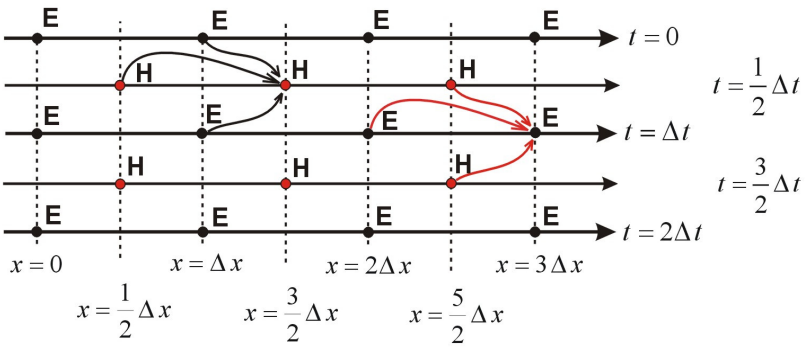

Figure 2. Determining the values of electric and magnetic fields' intensity in the FDTD algorithm.

As a result of the approximation of partial derivatives we received the Maxwell's equation in a differential form:

$$\frac{{}^{n+1}_{i,j,k}E_x - {}^{n}_{i,j,k}E_x}{\Delta_t} = \frac{1}{\varepsilon_{i,j,k}}\left(\frac{{}^{n+\frac{1}{2}}_{i,j+\frac{1}{2},k}H_z - {}^{n+\frac{1}{2}}_{i,j-\frac{1}{2},k}H_z}{\Delta_y} - \frac{{}^{n+\frac{1}{2}}_{i,j,k+\frac{1}{2}}H_y - {}^{n+\frac{1}{2}}_{i,j,k-\frac{1}{2}}H_y}{\Delta_z} - \sigma_{i,j,k}\,{}^{n+\frac{1}{2}}_{i,j,k}E_x \right), \tag{12}$$

$$\frac{{}^{n+1}_{i,j,k}E_y - {}^{n}_{i,j,k}E_y}{\Delta_t} = \frac{1}{\varepsilon_{i,j,k}}\left(\frac{{}^{n+\frac{1}{2}}_{i,j,k+\frac{1}{2}}H_x - {}^{n+\frac{1}{2}}_{i,j,k-\frac{1}{2}}H_x}{\Delta_z} - \frac{{}^{n+\frac{1}{2}}_{i+\frac{1}{2},j,k}H_z - {}^{n+\frac{1}{2}}_{i-\frac{1}{2},j,k}H_z}{\Delta_x} - \sigma_{i,j,k}\,{}^{n+\frac{1}{2}}_{i,j,k}E_y \right), \tag{13}$$

$$\frac{{}^{n+1}_{i,j,k}E_z - {}^{n}_{i,j,k}E_z}{\Delta_t} = \frac{1}{\varepsilon_{i,j,k}}\left(\frac{{}^{n+\frac{1}{2}}_{i+\frac{1}{2},j,k}H_y - {}^{n+\frac{1}{2}}_{i-\frac{1}{2},j,k}H_y}{\Delta_x} - \frac{{}^{n+\frac{1}{2}}_{i,j+\frac{1}{2},k}H_x - {}^{n+\frac{1}{2}}_{i,j-\frac{1}{2},k}H_x}{\Delta_y} - \sigma_{i,j,k}\,{}^{n+\frac{1}{2}}_{i,j,k}E_z \right), \tag{14}$$

$$\frac{{}^{n+\frac{1}{2}}_{i,j,k}H_x - {}^{n-\frac{1}{2}}_{i,j,k}H_x}{\Delta_t} = \frac{1}{\mu_{i,j,k}}\left(\frac{{}^{n}_{i,j,k+\frac{1}{2}}E_y - {}^{n}_{i,j,k-\frac{1}{2}}E_y}{\Delta_z} - \frac{{}^{n}_{i,j+\frac{1}{2},k}E_z - {}^{n}_{i,j-\frac{1}{2},k}E_z}{\Delta_y}\right), \tag{15}$$

$$\frac{{}^{n+\frac{1}{2}}_{i,j,k}H_y - {}^{n-\frac{1}{2}}_{i,j,k}H_y}{\Delta_t} = \frac{1}{\mu_{i,j,k}}\left(\frac{{}^{n}_{i+\frac{1}{2},j,k}E_z - {}^{n}_{i-\frac{1}{2},j,k}E_z}{\Delta_x} - \frac{{}^{n}_{i,j,k+\frac{1}{2}}E_x - {}^{n}_{i,j,k-\frac{1}{2}}E_x}{\Delta_z}\right), \tag{16}$$

$$\frac{{}^{n+\frac{1}{2}}_{i,j,k}H_z - {}^{n-\frac{1}{2}}_{i,j,k}H_z}{\Delta_t} = \frac{1}{\mu_{i,j,k}}\left(\frac{{}^{n}_{i,j+\frac{1}{2},k}E_x - {}^{n}_{i,j-\frac{1}{2},k}E_x}{\Delta_y} - \frac{{}^{n}_{i+\frac{1}{2},j,k}E_y - {}^{n}_{i-\frac{1}{2},j,k}E_y}{\Delta_x}\right). \tag{17}$$

3. CONSTRUCTION OF NUMERICAL MODELS

The subject of analysis was a model containing a three-layer wall made of commonly used building material. The analyzed wall model was composed of cement-lime plaster on the inside (0.015 m), a support layer made of aerated concrete 0.24×0.59×0.24 m blocks, insulated with 8 cm styrofoam, elevation layer of 0.12×0.59×0.24 cm aerated concrete tiles and cement-finished plaster finishing – limestone (0.015 m) (Figure 3).

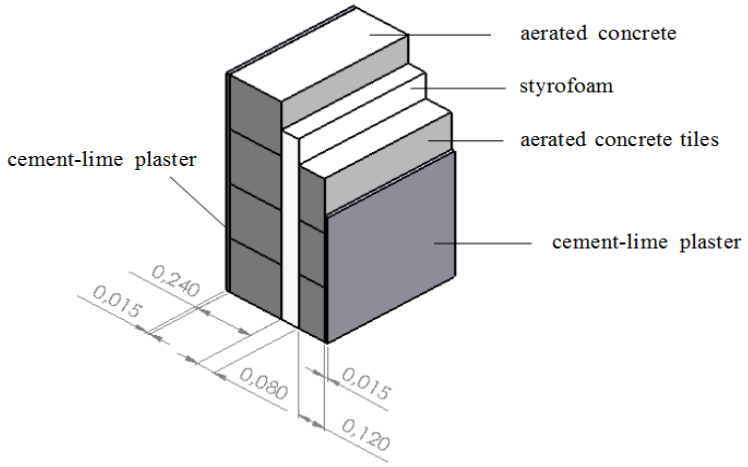

Figure 3. The geometry of the three-layer wall model made of aerated concrete.

The dimensions of the wall in the direction perpendicular to the propagating wave (the wall's width and height), are significantly larger than the length of the wave (f=2.4 GHz). Phenomena of wave propagation in open space were mapped by making the PML conditions at the edges perpendicular to the direction of the plane wave propagation [2]. The absorption of the propagated wave was obtained by assuming the PML layer, which was in line with the criteria assumed in declaring such conditions. In line with the chosen assumptions, on the surface of the model parallel to the direction of wave propagation,

conditions were chosen which would guarantee the extension of the area and repetitiveness (periodicity) of field distribution [9]. Due to proper mapping of periodic conditions, the crosswise dimensions and the internal structure of the created models underwent adjustments. The inducing of the field was by a sinusoidally plane wave at a frequency of f=2.4 GHz. The area of the analyzed models was subject to discretisation, by inscribing a uniform grid of Yee cells (Δ_x=Δ_y=0.001 m). With a chosen resolution of the difference grid, wave effects at a distance of one wavelength in air were modeled with 75 cells. The calculations for field distribution were conducted with the use of the finite difference time-domain method (FDTD) [3, 4, 5, 6, 7, 8].
In Table 1 the used model names and adopted electrical parameters of the analyzed wall construction elements have been presented.

Table 1. The electrical parameters of the building materials [2, 3].

Model	**Material**	**Electric permittivity** ε_r'	**Conductivity** σ **[S/m]**
g200	aerated concrete	2.00	0-0.1
	styrofoam	1.11	0.00001
	cement-lime plaster	2.44	0.001
g245	aerated concrete	2.45	0-0.1
	styrofoam	1.11	0.00001
	cement-lime plaster	2.44	0.001

4. RESULTS OF THE ANALYSIS

For the three-layer wall made mainly of aerated concrete, two cases differing in the electric permittivity value of aerated concrete were analyzed (Table 1). The results of the study on the g200 model show that when the conductivity value of aerated concrete changes in the range $\sigma \in \{0, 0{,}1\}$ [S/m], the E_z component obtained the highest value at σ=0 S/m (max (E_z) = 0.475). However, the lowest value at the highest conductivity value is 0.005 (Figure 4).

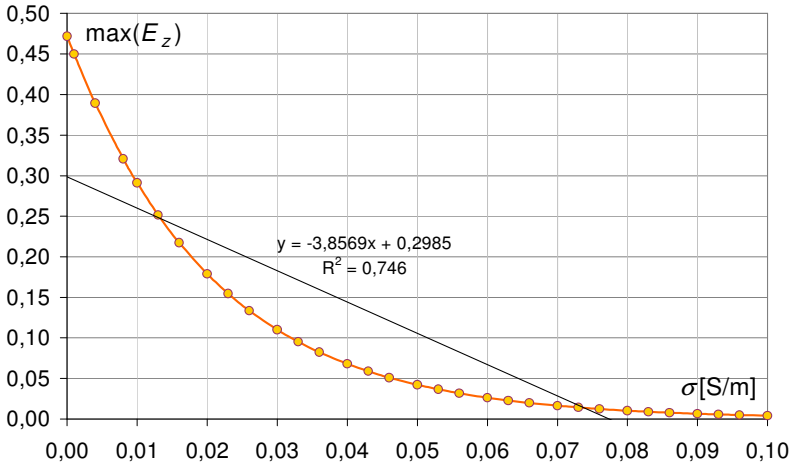

Figure 4. The relationship between max(E_z) and the conductivity of the aerated concrete for the g200 model.

The second analyzed variant concerned the same model with a different value of electric permittivity of aerated concrete (ε_r'=2.45). The results of the research on the g245 model show that when changing the conductivity value of aerated concrete in the range s $\sigma \in \{0, 0,1\}$ [S/m], the E_z component has the highest value obtained max(E_z)=0.43, while the lowest max(E_z)=0.008 (Figure 5). It can be noticed that with the increase of the relative value of electric permittivity, the value of the electric field intensity decreases, which is understandable from a physical point of view.

It was observed that when changing the conductivity value of aerated concrete in the range σ= 0÷0.015 S/m, the E_z component had higher values for permittivity ε_r'=2. However, when the conductivity value increased (above 0.02 S/m), the max(E_z) values were higher for ε_r'=2.45.

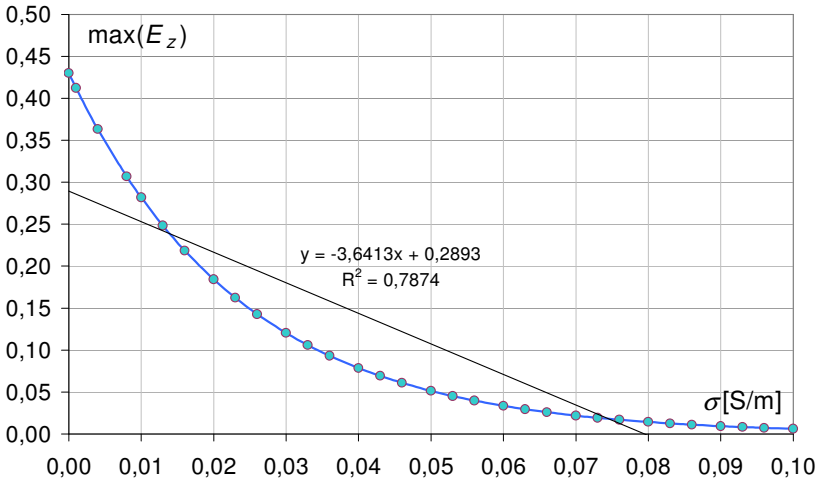

Figure 5. The relationship between max(E_z) and the conductivity of the aerated concrete for the g200 model.

5. CONCLUSIONS

The location of wireless communication systems (e.g. Wi-Fi, WIMAX) inside buildings requires a detailed analysis of the electromagnetic field distribution. The analysis of the wave propagation in the high frequency range is connected with the necessity to research the effects of the construction itself and the building materials with different electrical properties. The use the wireless communication systems require taking into account the effects that may lower the assumed quality of data transmission. The analysis of fields in wireless communication systems requires discussing the effects related with: multiple reflections, refractions, interference and wave damping caused by the geometry and complexity of the construction.

In article has been shown results the effect of the change in the conductivity of the aerated concrete on the values of the electric field intensity. For this purpose, the commonly used three-layer wall model was used. Based on the obtained results, it was observed that when propagating an electromagnetic wave with the frequency of 2.4 GHz, the value of electric permittivity of aerated concrete affects the maximum field values. The analysis of research shows that:

- with lower conductivity (σ=0÷0.015 S/m), the E_z component reaches higher values for the model in which the electric permeability value of aerated concrete is lower (g200);
- with a conductivity higher than (σ=0÷0.015 S/m, the E_z component achieves higher values for the model with higher permeability of aerated concrete (g245).

However, the construction of resistible communication networks requires at the stage of designing the system, to take into account the elements influencing the field distribution (among others: the geometry of the building, complex material structures in the path between the transmitter and receiver). The mentioned problems are especially visible in low range wireless networks (Wi-Fi), used in buildings. Taking into account the new and existing constructions is crucial in choosing the location of the network transmitters.

This work was prepared under scientific work S/WE/2/18 and supported by the Polish Ministry of Science and Higher Education.

REFERENCES

[1] Tan, S. Y., Tan, Y., Tan, H. S., "Multipath delay measurements and modeling for interfloor wireless communications," IEEE Transactions on Vehicular Technology Papers 49(4), 1334-13341 (2000).

[2] Stavrou, S., Saunders, S. R., "Review of constitutive parameters of building material," IEEE Transactions on Antennas and Propagation 1: 211-215 (2003).

[3] Choroszucho, A., "An analysis of the electromagnetic waves propagation in construction elements with a complex structure in the range of wireless communication (in Polish)," PhD dissertation, Bialystok (2014).

[4] Choroszucho, A., Butryło, B., "The numerical analysis of the influence the incidence angle of the plane wave on the values of the electric field intensity inside the models with the complex construction of a wall," Przegląd Elektrotechniczny Papers 90(12), 21-24 (2014).

[5] Pinhasi, Y., Yahalom, A., Petnev, S., "Propagation of ultra wide-band signals in lossy dispersive media," IEEE International Conference on Microwaves, Communications, Antennas and Electronic Systems, COMCAS: 1-10 (2008).

[6] Taflove, A., Hagness, S. C., [Computational electrodynamics, the finite-difference time-domain method], 3rd edn. Artech House, Norwood (2005).

[7] Oskooi, A. F., Roundyb, D., Ibanescua, M., Bermelc, P., Joannopoulosa, J. D., Johnson, S. G., "MEEP: A flexible free-software package for electromagnetic simulations by the FDTD method," Computer Physics Communications 181: 687-702 (2010).

[8] Elsherbeni, A. Z., Demir, V., [The finite-difference time-domain method for electromagnetics with MATLAB Simulations], 2nd edn. SciTech Publishing, Raleigh (2015).

Thin film capacitors made of various metals for impedance sensing technique

Zarzeczny D.
Lublin University of Technology, Electrical Engineering and Computer Science Faculty,
Institute of Electronics and Information Technology,
38 A Nadbystrzycka Str., 20-618 Lublin, Poland

ABSTRACT

The article is devoted to measuring matrices that can be used to determine the impact of a given material on a biological substance in BioMEMS devices. The focus is on the use of the ECIS system. The test consists in measuring the impedance of cells through which a low-current current is passed. As part of the conducted research, based on the commercial matrixes of the ECIS system, special test plates were designed and made on a biocompatible polycarbonate substrate. Titanium, nichrome, nickel and copper were used. The first measurements characterizing the structures made were carried out.

Keywords - technology, electronics, MEMS, Electric Cell-substrate Impedance, signals, comb capacitor, titanium, nichrome, nickel, copper, sputtering, photolithography

I. INTRODUCTION

Considering issues related to the difficulty of selecting material for applications in BioMEMS devices, the possibility of determining the impact of a given material on the examined cells was analyzed. Looking at current test methods performed on live cells, the ECIS system (Electric Cell-substrate Impedance) is of interest to measure cells impedance in real time. Its creators are the founders of Applied BioPhysics Inc., Dr. I. Giaever and Dr. C.R. Keese. It is a great alternative to experiments carried out using microscopes, consisting only of observing the changes taking place. The test consists in measuring the impedance of cells through which current flow is below 1 mA. The value of the frequency at which the measurements are carried is in the range from 100 Hz to 100 kHz. Individual values are plotted as points in ohms [Ω] or nanofarads [nF] within a certain time interval. For ideological simplification, using appropriate mathematical models, the cell can be represented as a parallel connection of the resistor and capacitor. Resistance describes the resistance of the current flowing. Capacity describes the polarity-inducing separation of electrons in the insulated layer of the cell membrane. Special matrices containing electrodes are used for the measurement. These elements are defined as very small holes in the thin metallization layer. Above each of them there is a special container in which the tissues immersed in the medium are placed. Such a set is located in a suitable incubator for providing cells. The whole is compatible with the ECIS system instruments [1-5].

II. TECHNOLOGY OF MEASURING ARRAYS

As part of the conducted research, special test plates were designed and made on a biocompatible polycarbonate substrate. For this purpose, a technology for the production of thin-film measuring structures has been developed. The first stage of works consisted in designing technological masks necessary for the photolithography process. Based on the commercial matrixes of the ECIS system, it was decided that the best results will be achieved using comb elements. Then, four materials were sputter in the magnetron sputtering process using a NANO 36 ™ sprayer from Kurt J. Lesker®. Titanium, nichrome, nickel and copper were used. In their layers, using the positive photolithography process, measuring electrodes were made. Titanium was chosen because of its very high biocompatibility and widespread use in implantology. Nichrome is characterized by high biocompatibility, which allows it to perform some surgical tools and other tools intended for contact with tissues of living organisms. Nickel that causes allergies in every fifth person was used due to the occurrence of its large amounts in stainless steel, used for the production of biomedical devices. The last material, which is copper, was selected because

Photonics Applications in Astronomy, Communications, Industry, and High-Energy Physics Experiments 2019,
edited by Ryszard S. Romaniuk, Maciej Linczuk, Proc. of SPIE Vol. 11176, 1117654
© 2019 SPIE · CCC code: 0277-786X/19/$21 · doi: 10.1117/12.2536787

it has excellent electrical parameters. Thanks to this, it is one of the most frequently used raw materials for the production of microelectronic devices. Despite its toxicity, it can be used in various types of sensor devices that do not require a long detection time [3-10].

III. RESULTS

The electrical parameters of the measuring plates were measured in order to check the possibility of using them to measure cell impedance. The measurements were carried out in the frequency range from 62.5 Hz to 64 kHz. Resistance, capacitance and impedance were tested. Differences in the values of individual results result from the different lead lengths of the electrodes.

The highest value of resistance and impedance is characterized by titanium electrodes. The value of the obtained results is several times higher than the results of other electrodes made of other metals. The resistance value ranged from about 6500 Ω to 11000 Ω, slightly decreasing with increasing frequency. The value of the measured capacitance ranged from 2E-6F to 4E-6F at low frequencies and dropped to zero as the frequency increased. However, it is possible to conduct research on cells using these structures, although the duration of the experiment is greatly extended. The resistance of electrodes from nichrome and nickel varies in the range from 600 Ω to over 1400Ω, slightly changing its value as the frequency increases. Bigger differences can be seen by analyzing the capacity value. In the case of electrodes made of nichrome, the value of the capacitance ranges from 4E-6F to 2E-5F. Nickel electrodes have a capacity ranging from 7E-6F to 9E-6F. While frequency increases in both cases, the capacity value drops to zero. However, the dynamics of changes is smaller in nickel electrodes. Electrodes made of copper have the largest discrepancies in the obtained results. At low frequencies, the resistance value is between approximately 1750 Ω and 3000 Ω. At higher frequencies, the resistance value decreases to about 250 Ω-400 Ω. Then the resistance value is stabilized. The capacity at low frequencies oscillates between 8E-7F and 1E-6F and decreases with increasing frequency. However, in this case the capacity value does not drop to zero.

The obtained results indicate that it is possible to conduct experiments using biological samples that have a specific resistance of several kilo ohms. Experiment with test plates can help assess the impact of individual metals on the living organism. The following graphs show examples of measurements of individual electrodes.

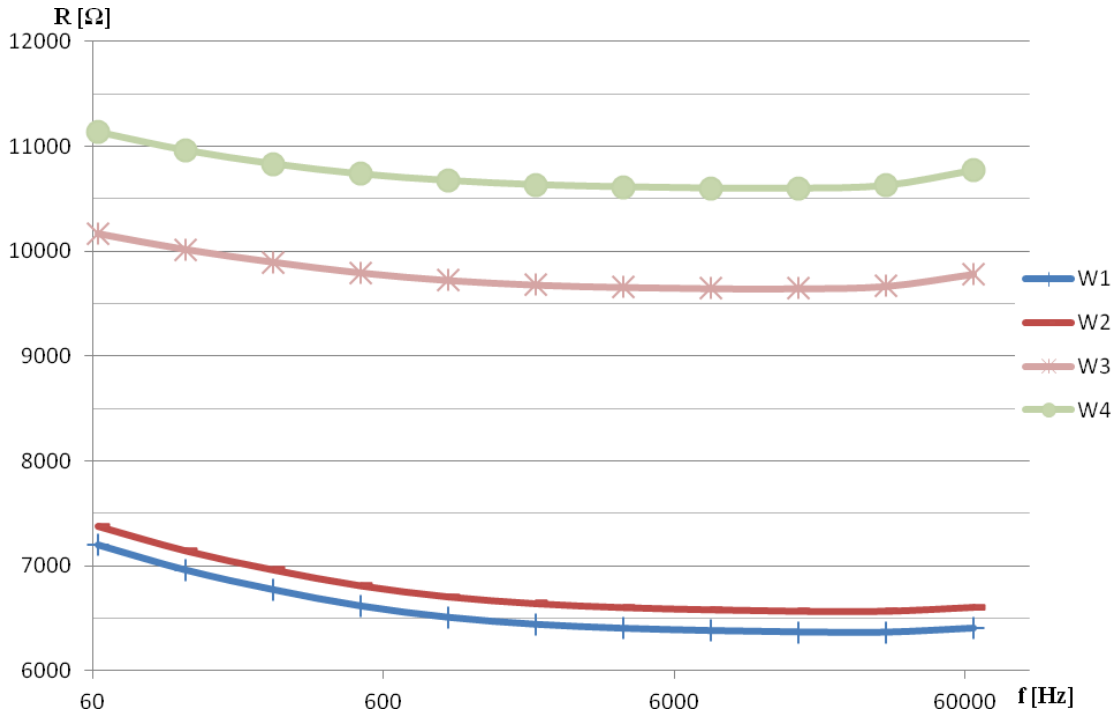

Figure 1. Characteristics of resistance as a function of the frequency of titanium electrodes

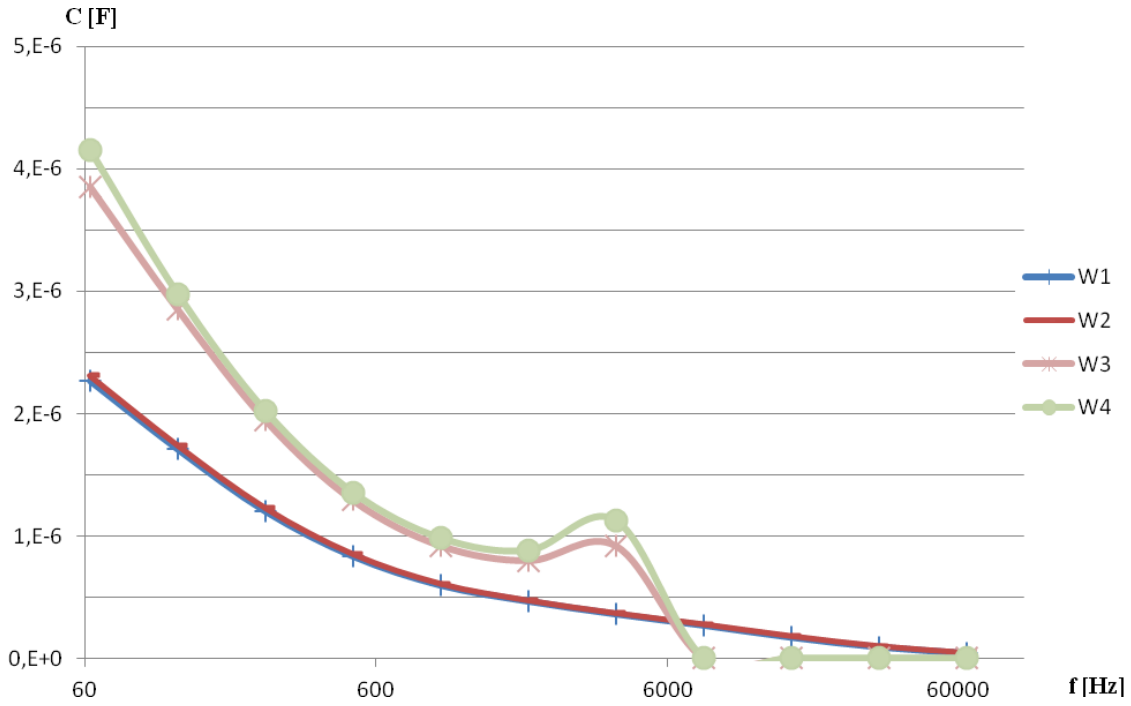

Figure 2. Characteristics of capacitance as a function of frequency titanium electrodes

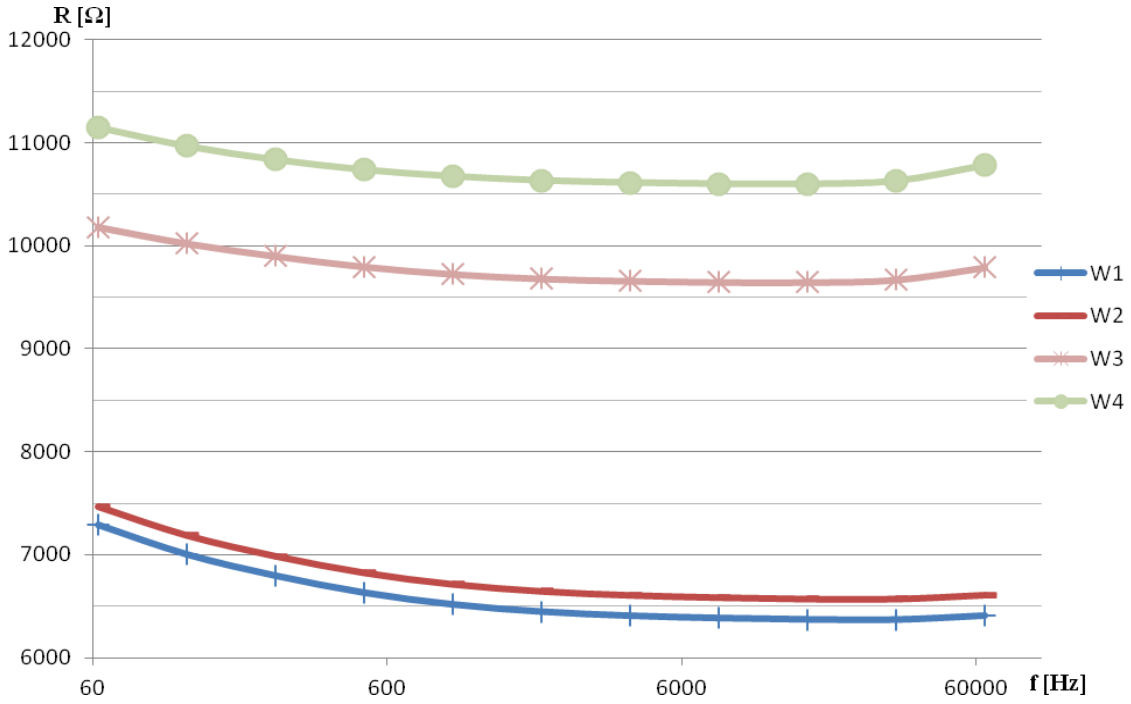

Figure 3. Characteristics of impedance as a function of frequency of titanium electrodes

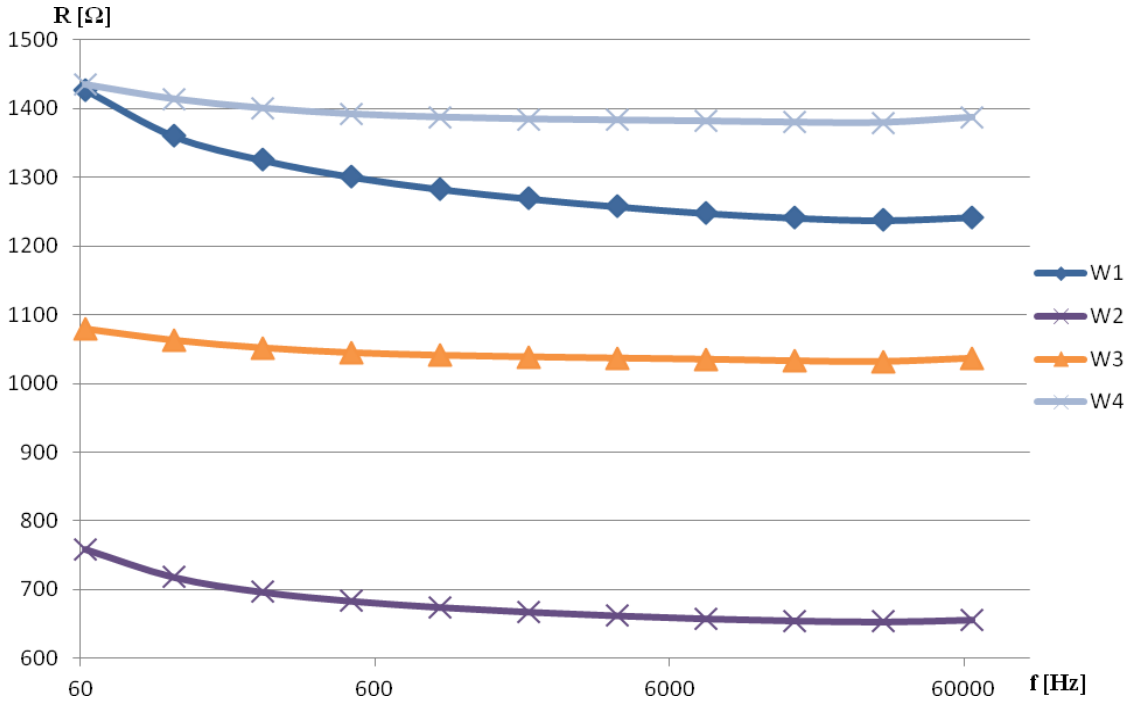

Figure 4. Characteristics of resistance as a function of the frequency of nichrome electrodes

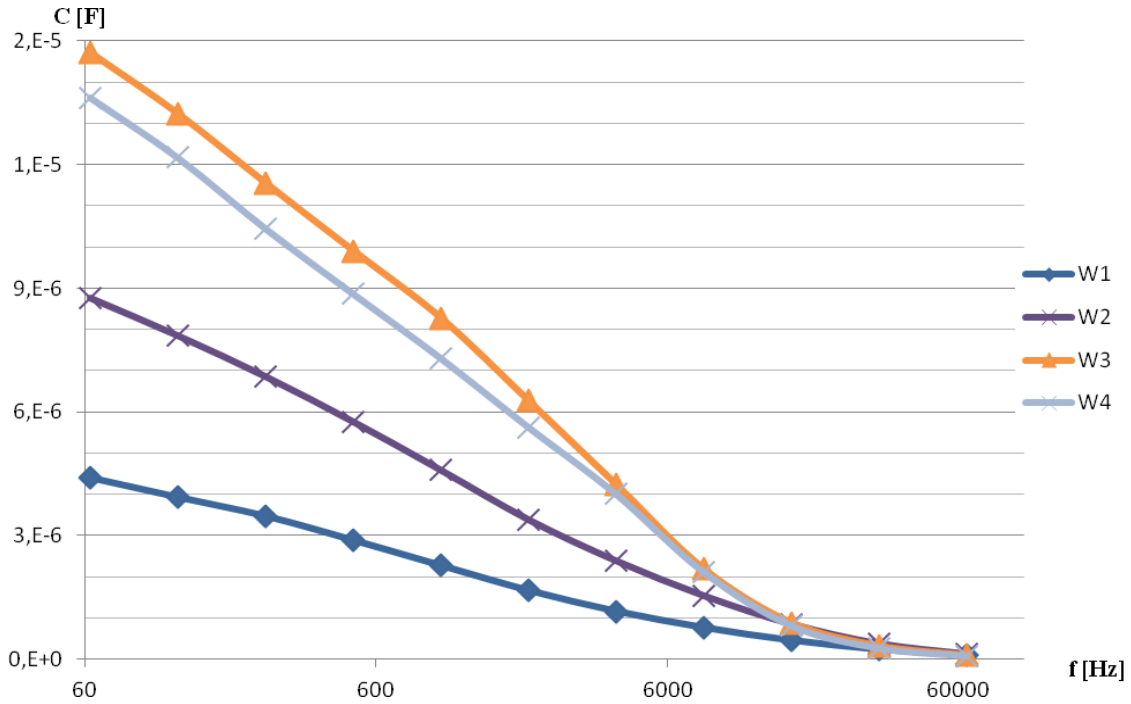

Figure 5. Characteristics of capacitance as a function of the frequency of nichrome electrodes

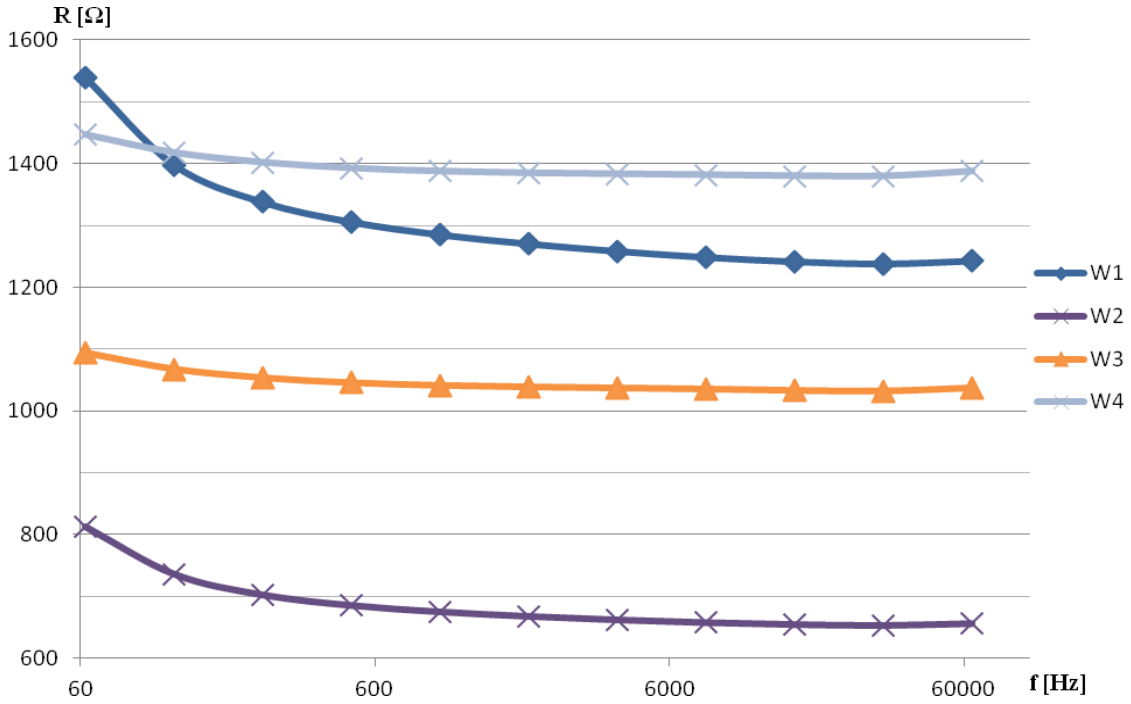

Figure 6. Characteristics of impedance as a function of the frequency of nichrome electrodes

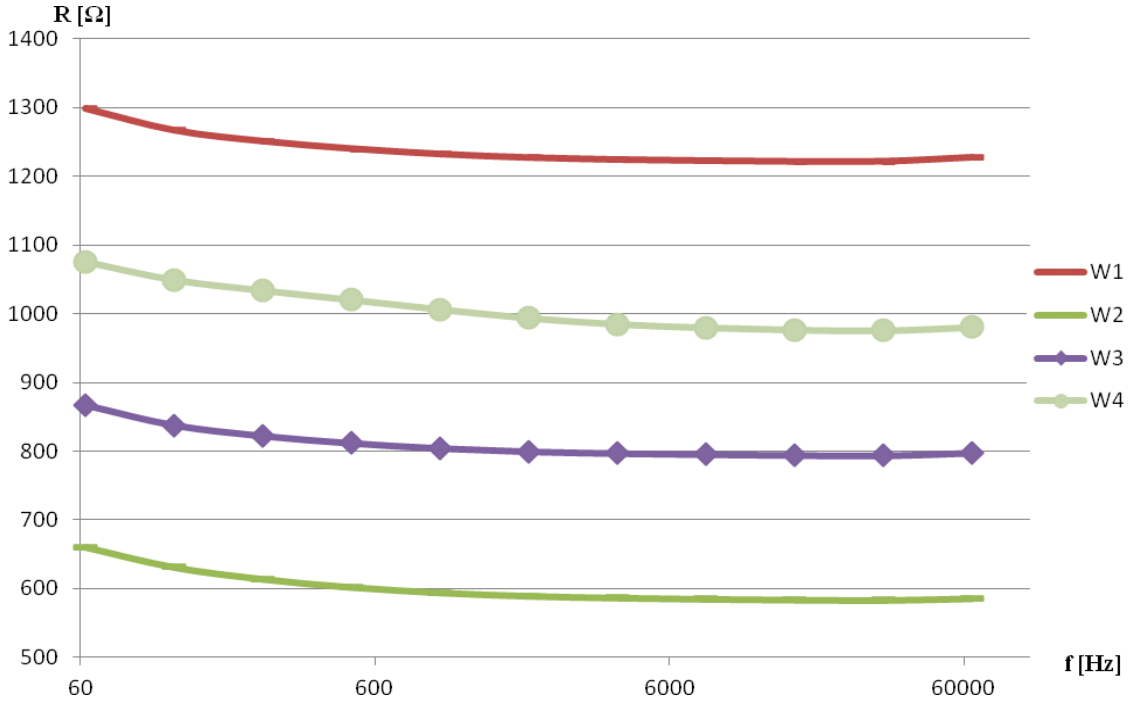

Figure 7. Characteristics of resistance as a function of the frequency of nickel electrodes

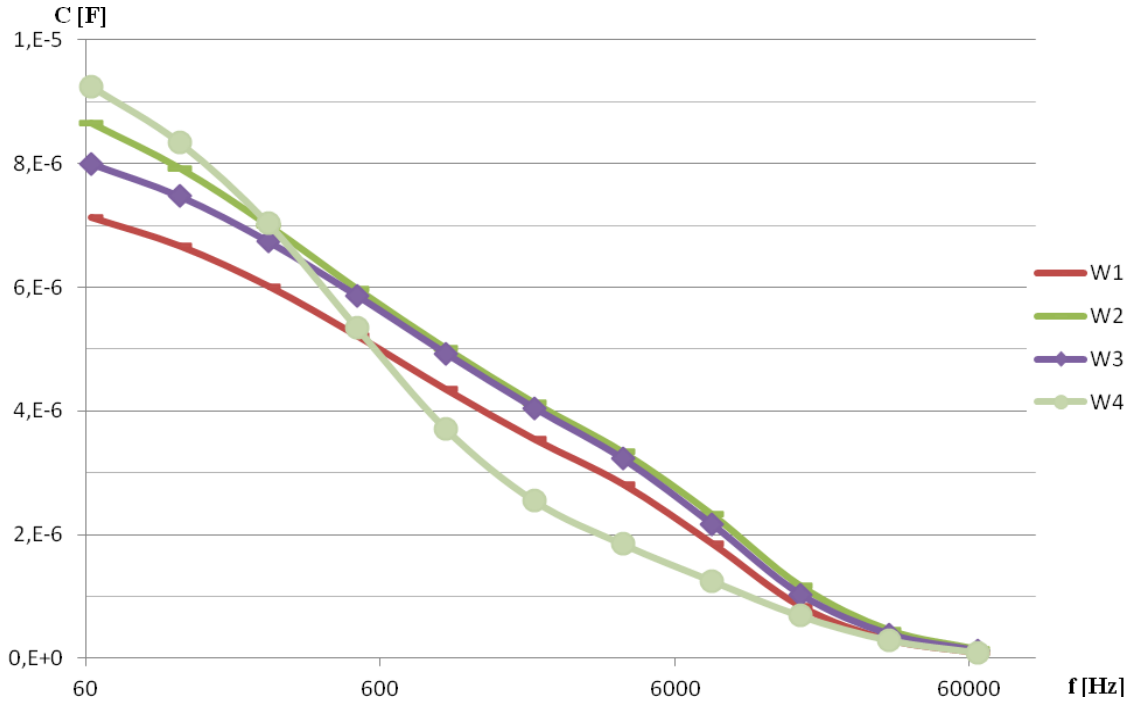

Figure 8. Characteristics of capacitance as a function of the frequency of nickel electrodes

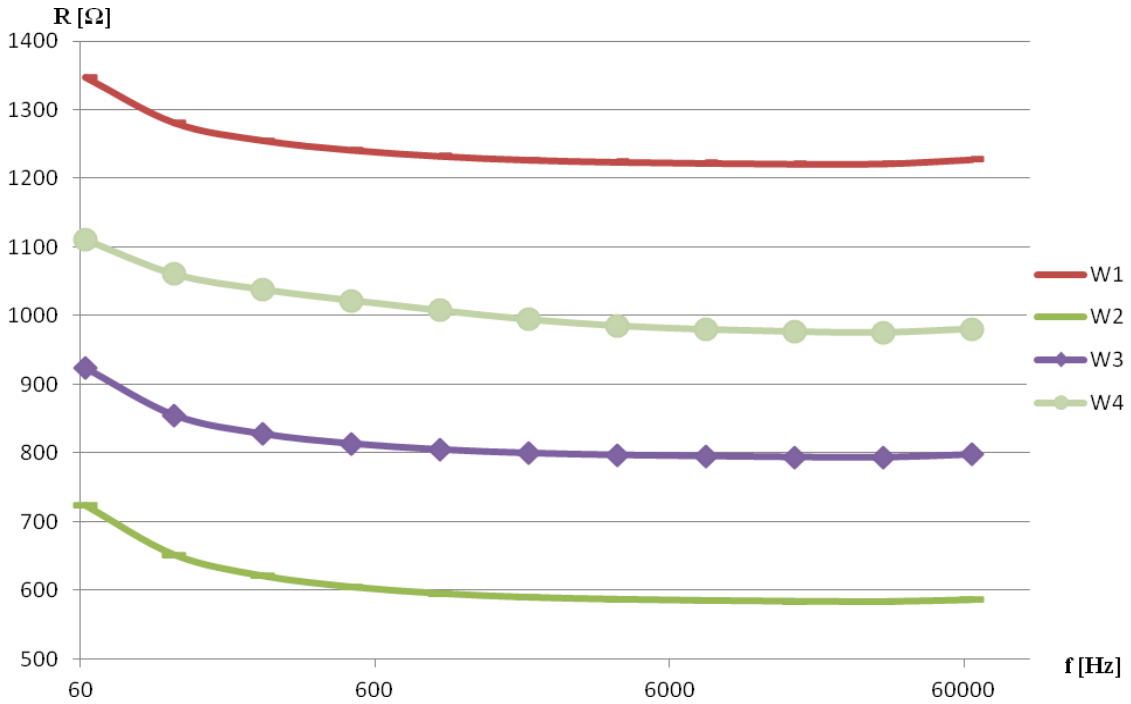

Figure 9. Characteristics of impedance as a function of the frequency of nickel electrodes

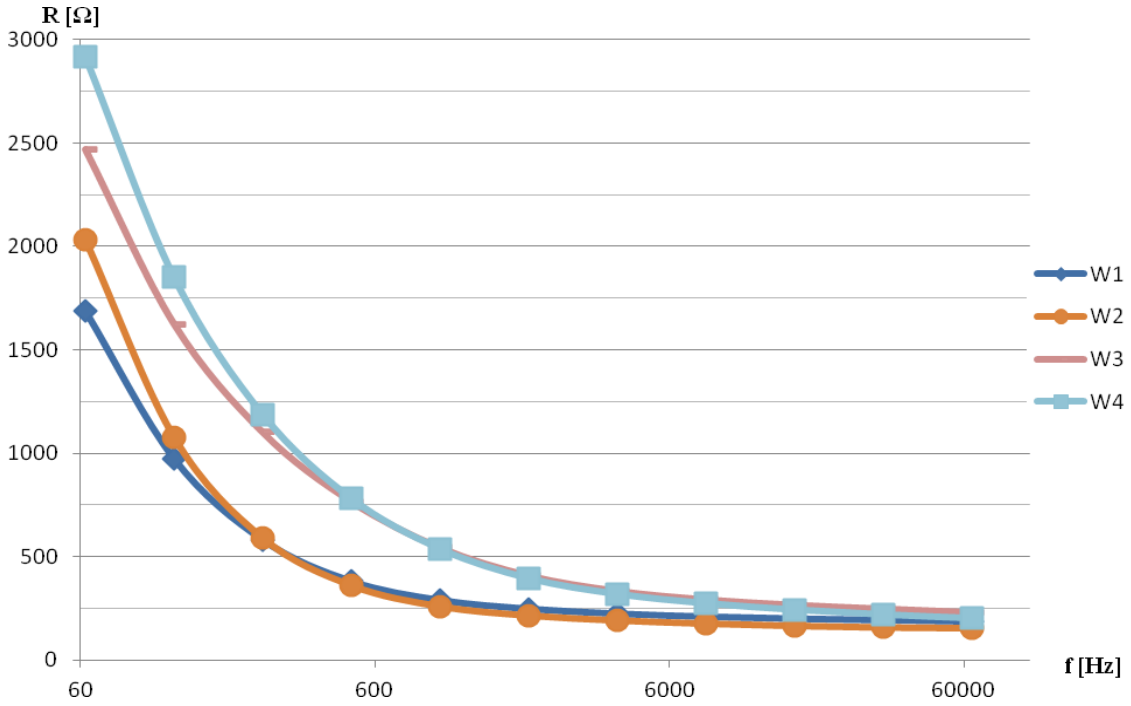

Figure 10. Characteristics of resistance as a function of frequency of copper electrodes

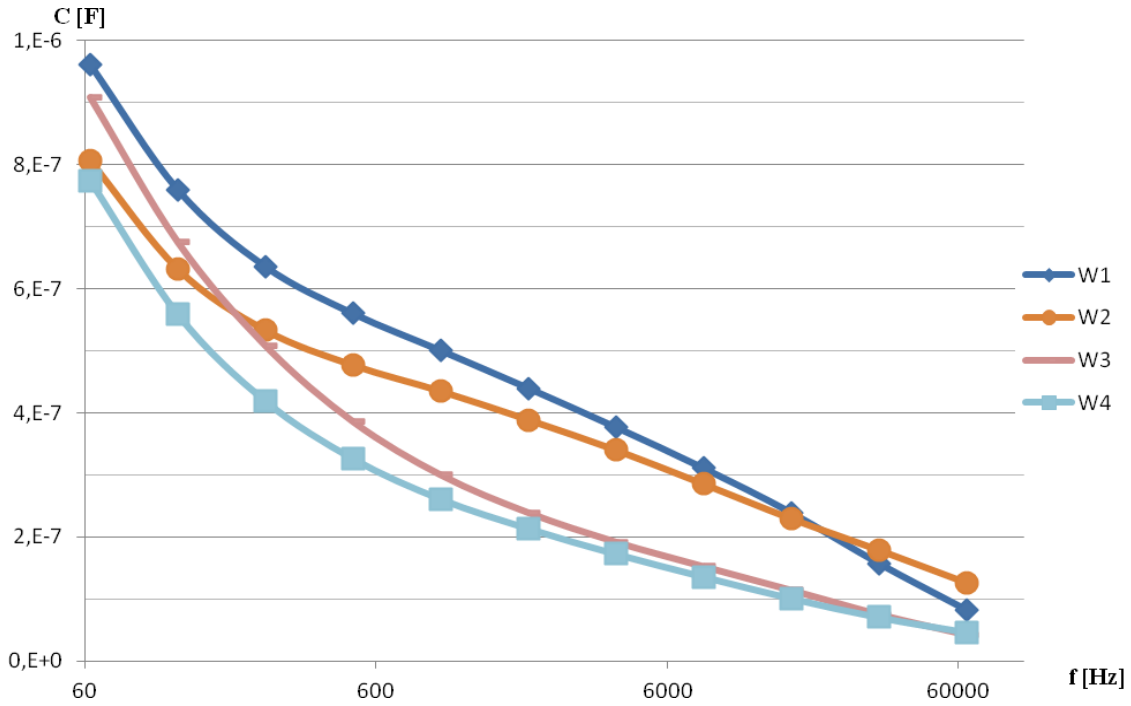

Figure 11. Characteristics of capacitance as a function of the frequency of copper electrodes

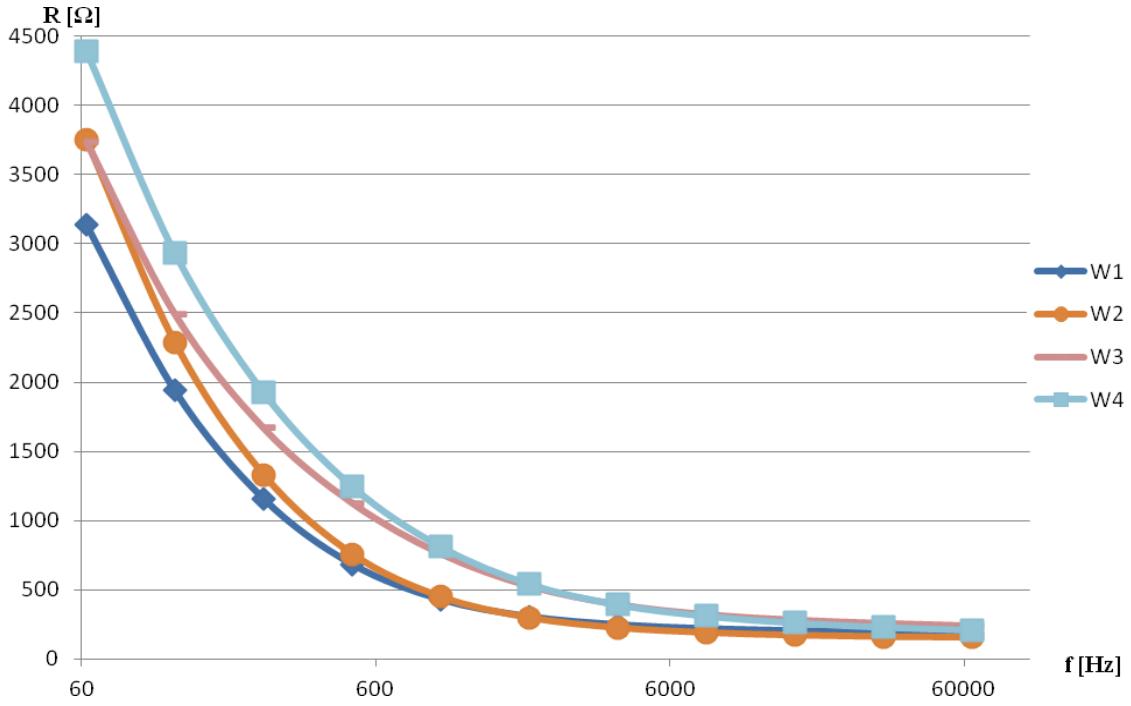

Figure 12. Characteristics of impedance as a function of frequency of copper electrodes

IV. RESULTS

As part of the presented work, test plates were designed, made and characterized. They are designed to measure the impedance of breeding cells in real time. They are compatible with ECIS instruments. The first attempts have shown that it is possible to use them and obtain reproducible results. Analyzing the received data, it can be concluded that it is possible to conduct studies assessing the impact of particular metallizations on biological material. Made instruments can be used to conduct research on the behavior of cells in the environment in which the given metal occurs. The generated plates will be used to extend the testing capabilities of the ECIS system, to analyze the impact of individual metals on the examined cells. The next stage of works will involve the cultivation of cells with the use of measuring matrices.

REFERENCES

[1] Applied BioPhysics, Product Guide, Corporate Headquarters: 185 Jordan Road • Troy, NY 12180 1-866-301-ECIS (3247).
[2] Napieralska M., Jabłoński G., "Research and Training Action for System on Chip Design", Podstawy Mikroelektroniki Łódź 2002, IST-2000-30193
[3] Kociubiński A., Zarzeczny D., Szypulski M., "Kondensatory grzebieniowe z miedzi do monitorowania funkcji życiowych komórek hodowlanych", Przegląd Elektrotechniczny.- 2018, nr 9, s. 59-61
[4] Zarzeczny D., Szypulski M., Lizak T., Muzyka K., Kociubiński A., Prendecka M., Małecka-Massalska T., "Design and technology of titanium comb capacitor" [W]: Photonics Applications in Astronomy, Communications, Industry, and High-Energy Physics Experiments 2018
[5] Kociubiński A., Szypulski M., Zarzeczny D., Lizak T., Muzyka K, Prendecka M., Małecka-Massalska T., "Design and technology of copper comb capacitors" [W]: Photonics Applications in Astronomy, Communications, Industry, and High-Energy Physics Experiments 2018

[6] Kociubiński A., Bieniek T, Janczyk G., "Design, Modeling and Simulation of MEMS Devices on Si, SiC, and Diamond for Harsh Environment Applications", Acta Physica Polonica, A. 125 (6)
[7] Geddes L.A., Roeder R., "Criteria for the Selection of Materials for Implanted Electrodes", Annals of Biomedical Engineering, Vol. 31, pp. 879–890, 2003
[8] Stensaas S.S., Stensaas L. J., "Histopathological Evaluation of Materials Implanted in the Cerebral Cortex", Acta neuropath. (Bed.) 41,145-155 (1978)
[9] Ullman D G, "The Mechanical Design Process", McGraw-Hill Education, 1992.
[10] Scholten K., Meng E., "Materials for Microfabricated Implantable Devices: A Review", Lab on a Chip, 15 September 2015, UNIVERSITY OF NEBRASKA

The investigation of transparent electrodes made with ultrasonic spray coater

L. Kołodziej, S. Ostrowski, M. Jakubowska, G. Wróblewski

Institute of Metrology and Biomedical Engineering, Warsaw University of Technology
A.Boboli St. 8, Warsaw, Poland

ABSTRACT

See-through layers of conductive material are used in many fields of science and technology for example on screens of electronic devices or heated car windows. An elaboration of a high-performance and economical method of producing transparent electrodes is one of the challenges of today's science.
This paper presents the results of spraying test of various conductive inks, performed on an ultrasonic spray coating station, leading to a development the optimal parameters of manufacturing the transparent conductive electrode.
Spray coating is one of the most common techniques of coating objects with thin films. The ultrasonic atomization used in this process allows the increase of the precision and thus decrease of thickness and higher homogeneity of applied layers. In this study, after the selection of the best carrier and coating parameters, a suspension of carbon nanotubes was created and used for coating. The prepared sample was subjected to electrical tests and the results of these studies have been described.
Keywords: Ultrasonic spray coating, conductive inks, transparent electrodes, conductive thin-films.

1. INTRODUCTION

Spray coating is well known and often used technique of imposition layers of materials on various surface, most often used to create protective coatings. Its most important advantages are wide range of coating materials, relatively low costs and possibility to create plain and uniform layer[1, 2]. Additionally, one of spray coating variety, which is not using high temperatures, called cold spray process, allows retaining phases of initial particles without exerting stress on the material[3] For precise applications standard drop-making system is replaced by ultrasonic atomization process, in which sprayed liquid material hits the vibrating (at frequency 18-100kHz) surface[4]. Thereby sharp, pointy structures are formed on the liquid surface, then micro-droplets come off the structures ends[5]. Combination of the spray coating technique with ultrasonic atomization increases precision, homogeneity and all above allows reduction the thickness of applied layers, while maintaining relatively low costs[6, 7].

One of the barriers to today`s optoelectronic industry is creating transparent, conductive material applicable for example in solar panels, displays or in various optical sensors[8–11]. Existing techniques of preparation such electrodes are expensive and often insufficiently efficient. As conductive layer the suspensions with carbon nanotubes are well suited, thanks to theirs excellent electrical conductivity[12–14]. Ultrasonic spray coating, thanks to its advantage is very promising method for making such electrodes[15]. Usage of thin PET foil as carrier of conductive layers enable making electrodes not only transparent, but also elastic, which further extends the possibilities of their applications, for examples in biosensors[17].

This paper presents results of tests carried out on special prepared ultrasonic spray coating station leading to making conductive layer on thin PET foil, with keeping it as transparent as possible. Part of test was done to determine optimal parameters of coating process with use of different solvents, then the test of atomization carbon nanotubes suspended in suitable solvents was performed. Finally, attempts were made to make the specific electrode.

The proper application of the conductive layer is influenced by many factors. The focus was on identifying the most important among them like: impact of using various substances, liquid flow speed, voltage of atomization, the effect of compressed air and the distance between the spray nozzle and the substrate. To determine the uniformity of the applied coating layers, visual evaluation was sufficient. Density of coverage were measured with multiplying covering time by flow rate and the conductivity was determinate as resistance measured with digital multimeter.

Photonics Applications in Astronomy, Communications, Industry, and High-Energy Physics Experiments 2019,
edited by Ryszard S. Romaniuk, Maciej Linczuk, Proc. of SPIE Vol. 11176, 1117655
© 2019 SPIE · CCC code: 0277-786X/19/$21 · doi: 10.1117/12.2536806

2. ULTRASONIC SPRAY COATING STATION

The tests were carried out on a research stand owned by the Institute of Metrology and Biomedical Engineering by Warsaw University of Technology. The station is presented on the picture 1.

Figure 1 Ultrasonic spray coating station

Most important part of station is spray nozzle, where the atomization takes place through ultrasonic generator from Spraying Systems Company, which allows to control voltage of atomization in range: 0-80V, frequency 75kHz. Substance for coating is given by syringe, mounted in infusion pump. It permits to control liquid flow velocity from 10 to 1200 ml/h and pressure in range 0-1500 mmHg. Nozzle is mounted on aluminum frame and attached servo motors allows to control station in 2 axis, additional servo under the table provides movement in third axis. Compressed air with low pressure (<0,2 bar) is also supplied to the head, ensuring the creation of the correct mist. The entire station is controlled through PC connected to microcontroller, which is linked to each part of stand.

3. PRELIMINARY RESEARCH

As mentioned at the beginning of the article, test have started from arrangements optimal parameters of atomization process. Influence of every parameter was measured and finest value has been chosen. The most important of them are presented below.

3.1 The effect of compressed air pressure

The impact of compressed air presence was presented on pictures 2 and 3. An absence of compressed air cause disorders in forming proper coating mist. Without compressed air or with low pressure – below 0,1 bar, mist deviated randomly in different directions and movement of spraying nozzle results in breaks of atomization process and as a result, bad coverage

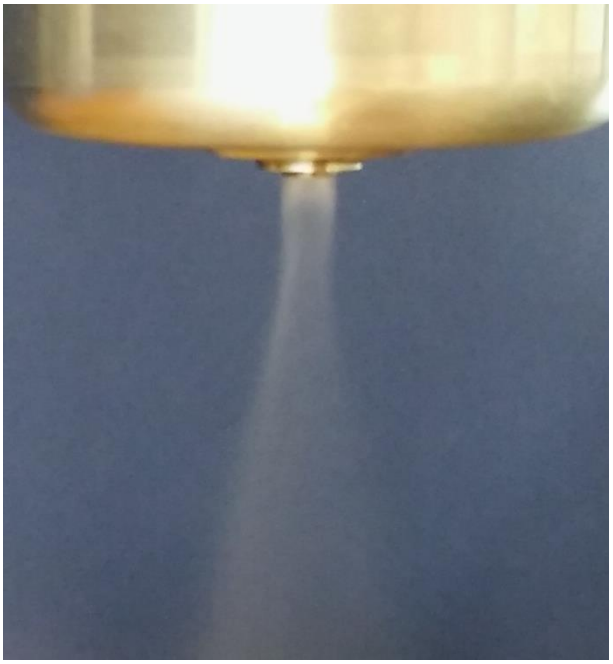

Figure 2 Compressed air presence

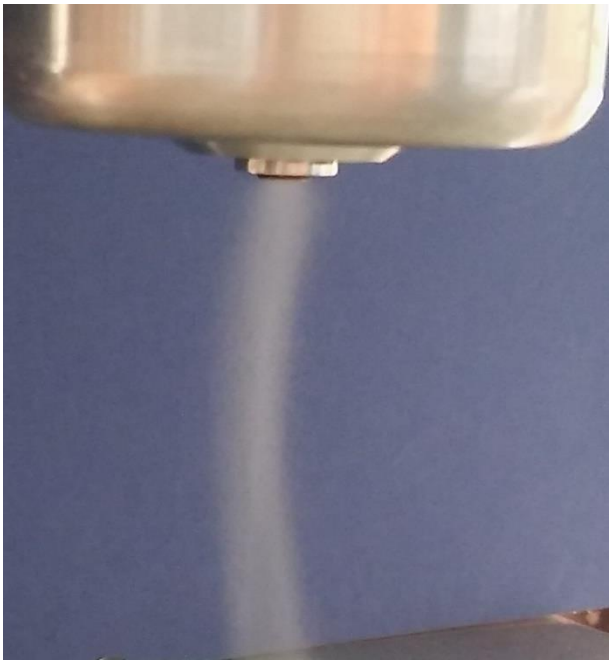

Figure 3 Absence of compressed air

No significant differences were observed while pressure was in range 0,1-0,2 bar, above this value mentioned mist forming disorders was also noticeable. Pressure of about 0,15 bar was considered to be optimal value.

3.2 Coating nozzle distance from substrate

Formed coating mist has shape of cane, so distance between head and foil have direct influence of sprayed paths width. It was determined that distance below 10 mm causes spot spraying of coating liquids, in the range of 10-20 mm paths was too thin and above 40 mm parts of fluids was diffused outside the right area. An optimal distance of 30 mm has been established. Each printed path had a width of 11.

3.3 Voltage of atomization process

Voltage of atomization is strongly related to liquid flow, greater flow requires higher voltage. Minimum stationary atomization process power was around 30-40V, for liquid flows 50-400 ml/h. However, a setting of about 2 times higher voltage was required to start atomization , which prevented the use of higher flows velocity. During the spraying nozzle movement, it was necessary to set about 20% more power. No significant influence of voltage value was observed so for further test 60 V of power was used.

3.4 Speed of liquid flow

As mentioned before liquids flow is limited by maximum voltage of atomization generator. Attempts to make transparent electrode force using relatively small flow velocity, so speed of 400 ml/h was not a significant obstacle. Measuring the coating area and spraying time in dependence of the liquid flow velocity, density of coating was designated. The results for the representative values are presented in table 1.

Tab. 1 Dependence of the coverage density on the flow velocity

liquid flow velocity [mm/h]	50	100	150	200	250	300	350	400
density of coating [ml/m^2]	20.9	41.7	62.6	83.5	104.3	125.2	146.1	167

3.5 Impact of using various substances

First atomization test was performed using distilled water, then 5 different popular solvents (Toluene, 2-Butanone 99%, 2-Pentanone 99%, Tetrahydrofuran, Methanol) were used to choose the best one to suspension carbon nanotubes in it. Liquids were sprayed on thin PET foil, with previously determined parameters. It was noted that due to higher viscosity of the solvents, they tend to form aggregations on carrier, which facilitates uniform coating. Below are the most important conclusions drawn from the spray tests of individual solvents:

- 2-Butanone 99% - very good coating, uniform layer with every liquid flow velocity;
- Toluene – medium quality of coating, when printing with small flows, breaks in sprayed layer was noticeable;
- 2 – Pentanone 99% - the same properties as 2 – Butanone;
- Methanol – a little better coating than with Toluene, but also small gaps in printed layer was noticeable;
- Tetrahydrofuran – after printing on PET foil some sort of sticky, solidified film was formed, instead of uniform coating.

Due to the best properties, 2-Butanone and 2-Pentanone solvents were chosen for further tests.

4. PRINTING THE TRANSPARENT CONDUCTIVE LAYER

4.1 Creating paints with carbon nanotubes

A series of samples solvent with different carbon nanotubes contents (0,01%, 0,05%, 0,1% wt.%) were made. The samples were then sonicated on Sonics VC505, 500W device. Setting of amplitude below 95% did not bring the expected results, so samples were sonicated with 100% amplitude, for 3 minutes, because of the strong heating of paints. The black clusters of CNTs were clearly visible in samples with 0,01% CNTs content in solvents, instead of a homogeneous liquid. Other paints had some stratification of individual ingredients, particularly visible on the bottom and surface of the liquids. The smallest stratification was noticed on 0,1% CNTs in 2-Butanone 99% samples, therefore, this paint was selected for subsequent tests.

4.2 Coating with the carbon nanotubes paints

For coating test 0,1wt% CNTs in 2-Butanone 99% was used, but also because of good result of carbon nanotubes dispersed in Toluene[16], paint of 78,2% 2 – Butanone, 21,7% Toluene and 0,1%CNTs wt.%, was created. PET carrier was coated with these 2 paints with different liquid flow settings and several applied layers. After the disposal samples was thermal cured in 100°C for 5 minutes. After drying, due to uneven prints of parts of the layers, every sample was cut for 10x10 mm squares and their resistance was tested by applying test leads to the ends of the squares. The samples that were the most different from the others were rejected. Average resistances of most important samples are presented in table 2, and examples of samples are shown in the figure 4.

Tab. 2 Average resistance of coated samples

Paint	Flow velocity [mm/h]	Average resistance [kΩ]
99% 2-Butanone 0.1%CNTs	100	700
	200	150
78.2% 2-Butanone 21.7% Toluene 0.1% CNTs	40 (2 layers)	930
	50 (2 layers)	170
	100	95
	200	1.16

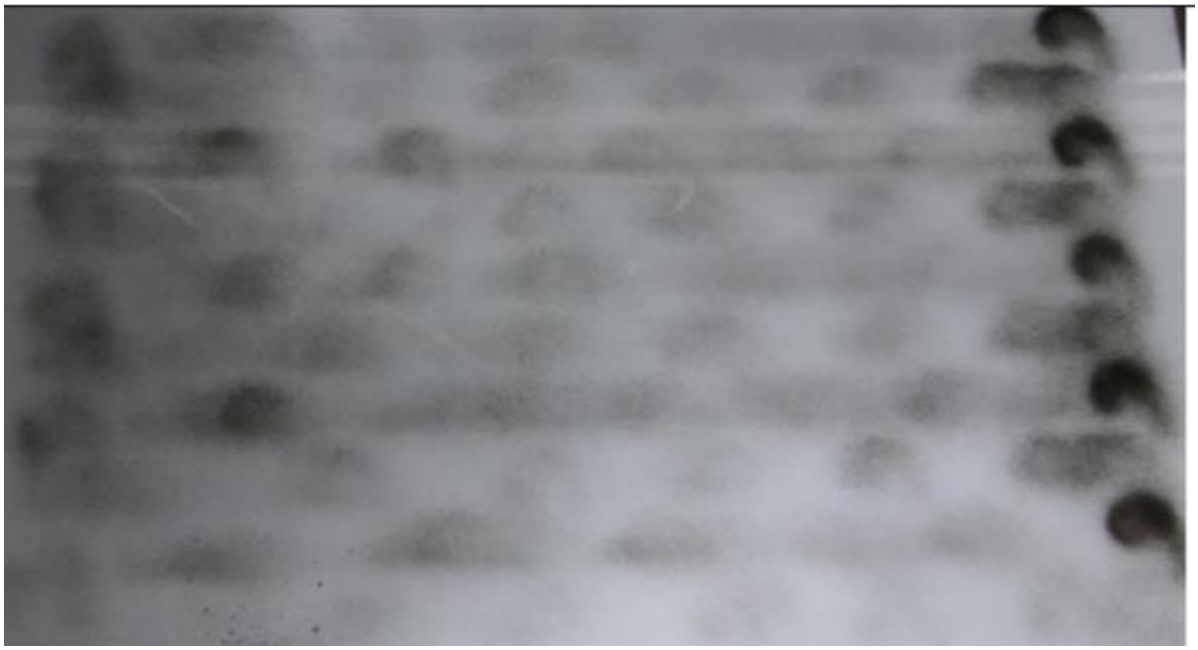

Figure 4 PET foil with 2 layers of 78.2% 2-Butanone, 21.7% Toluene, 0.1% CNTs paint coated with flow 50 ml/h

Carbon nanotubes dispersed in combination of 2-Butanone and Toluene turned out to be the best paint with lowest resistance results. However, the resistance of samples was worse than expected[20, 21]. To harden received printout and tie the nanotubes to lower their resistance, an attempt to cover them with a mixture PMMA/OKB 1wt% was made[18, 19]. Unfortunately, this substance was not suitable for ultrasonic spray coating, forming mist was not uniform and atomization process was often stopping itself, which prevented proper printing.

Unevenness of the printed layers was primarily result of inhomogeneous paints, CNTs was not properly dispersed in solvents. Mentioned stratification was also visible in pipes supplying inks to the printing head. As a result, almost clear solvent was sometimes printed on the foil. Moreover, the accumulation of paint on edges of the printout was a result of step change direction of print. Station driver software did not allow for smooth control of servomotors, and even relatively short stop of the head (below 0,5s) caused more ink to be printed in the edges.

Printed samples with flows below 40 ml/h, despite the increase in the number of applied layers, did not conduct electricity. Increasing flow velocity significantly reduces the resistance, but also reduces transparency. Most of samples printed with flow velocity above 80 ml/h did not let light through.

5. CONCLUSIONS

Demand for flexible, conductive, transparent electrodes is constantly growing, so developing an effective method of producing them is today's urgent need. Ultrasonic spray coating is a very promising method for manufacturing these electrodes, thanks to, among other, a wide range of applications or high process efficiency.

The correct printing parameters on ultrasonic spray coating station have been determined. To obtain electrode with lower resistance and greater transparency it is necessary to create the right paint. A solvent mixture of 2-Butanone with Toluene as a carrier for carbon nanotubes had the best result, however, further tests of properly the CNTs disperse, are required. Ultrasonic spray coating station should allow for a smooth head movement, because sudden stops disturb the atomization process. Printing several conductive layers one on the other, with low ink flow speeds seems to be a better way than printing more material at once, because it allows to have more control of the entire process and also allows to keep a higher electrode transparency.

6. REFERENCES

[1] Champagne, V. K., [The cold spray materials deposition process], Elsevier (2007).

[2] Girotto, C., Rand, B. P., Genoe, J. and Heremans, P., "Exploring spray coating as a deposition technique for the fabrication of solution-processed solar cells," Solar energy materials and solar cells 93(4), 454–458 (2009).

[3] Moridi, A., Hassani-Gangaraj, S. M., Guagliano, M. and Dao, M., "Cold spray coating. Review of material systems and future perspectives," Surface Engineering 30(6), 369–395 (2014).

[4] Dalmoro, A., Barba, A. A., Lamberti, G. and d'Amore, M., "Intensifying the microencapsulation process. Ultrasonic atomization as an innovative approach," European Journal of Pharmaceutics and Biopharmaceutics 80(3), 471–477 (2012).

[5] Rajan, R. and Pandit, A. B., "Correlations to predict droplet size in ultrasonic atomisation," Ultrasonics 39(4), 235–255 (2001).

[6] Bose, S., Keller, S. S., Alstrøm, T. S., Boisen, A. and Almdal, K., "Process Optimization of Ultrasonic Spray Coating of Polymer Films," Langmuir 29(23), 6911–6919 (2013).

[7] Lierke EG, "Techniques and applications of ultrasonic atomisation - 35 years of research and development in retrospect," Chem. Ing. Tech. 70(7), 815–826 (1998).

[8] De, S., Higgins, T. M., Lyons, P. E., Doherty, E. M., Nirmalraj, P. N., Blau, W. J., Boland, J. J. and Coleman, J. N., "Silver Nanowire Networks as Flexible, Transparent, Conducting Films. Extremely High DC to Optical Conductivity Ratios," ACS Nano 3(7), 1767–1774 (2009).

[9] Falco, A., Cinà, L., Scarpa, G., Lugli, P. and Abdellah, A., "Fully-Sprayed and Flexible Organic Photodiodes with Transparent Carbon Nanotube Electrodes," ACS Applied Materials & Interfaces 6(13), 10593–10601 (2014).

[10] Lee, S. M., Lee, J. H., Bak, S., Lee, K., Li, Y. and Lee, H., "Hybrid windshield-glass heater for commercial vehicles fabricated via enhanced electrostatic interactions among a substrate, silver nanowires, and an over-coating layer," Nano Research 8(6), 1882–1892 (2015).

[11] Krantz, J., Stubhan, T., Richter, M., Spallek, S., Litzov, I., Matt, G. J., Spiecker, E. and Brabec, C. J., "Spray-Coated Silver Nanowires as Top Electrode Layer in Semitransparent P3HT:PCBM-Based Organic Solar Cell Devices," Adv. Funct. Mater. 23(13), 1711–1717 (2013).

[12] Wu, H., Kong, D., Ruan, Z., Hsu, P.-C., Wang, S., Yu, Z., Carney, T. J., Hu, L., Fan, S. and Cui, Y., "A transparent electrode based on a metal nanotrough network," Nature Nanotechnology 8, 421 EP - (2013).

[13] Willey, A. D., Holt, J. M., Larsen, B. A., Blackburn, J. L., Liddiard, S., Abbott, J., Coffin, M., Vanfleet, R. R. and Davis, R. C., "Thin films of carbon nanotubes via ultrasonic spraying of suspensions in N-methyl-2-pyrrolidone and N-cyclohexyl-2-pyrrolidone," Journal of Vacuum Science & Technology B, Nanotechnology and Microelectronics: Materials, Processing, Measurement, and Phenomena 32(1), 11218 (2014).

[14] Zhao, Q., Tan, S., Xie, M., Liu, Y. and Yi, J., "A study on the CNTs-Ag composites prepared based on spark plasma sintering and improved electroless plating assisted by ultrasonic spray atomization," Journal of Alloys and Compounds 737, 31–38 (2018).

[15] Scardaci, V., Coull, R., Lyons, P. E., Rickard, D. and Coleman, J. N., "Spray Deposition of Highly Transparent, Low-Resistance Networks of Silver Nanowires over Large Areas," Small 7(18), 2621–2628 (2011).

[16] Penza, M., Antolini, F. and Antisari, M.V., "Carbon nanotubes as SAW chemical sensors materials," Sensors and Actuators B: Chemical 100(1), 47–59 (2004).

[17] Lipomi, D. J., Vosgueritchian, M., Tee, B. C.-K., Hellstrom, S. L., Lee, J. A., Fox, C. H. and Bao, Z., "Skin-like pressure and strain sensors based on transparent elastic films of carbon nanotubes," Nature Nanotechnology 6, 788 EP - (2011).

[18] Wróblewski, G. and Janczak, D., "Transparent electrodes based on carbon nanoforms for electroluminescent displays,".

[19] Wróblewski, G., Słoma, M., Janczak, D., Młozniak, A. and Jakubowska, M., "Influence of carbon nanoparticles morphology on physical properties of polymer composites," Acta Physica Polonica A 125(4), 861–863 (2014).

[20] Kim, S., Yim, J., Wang, X., Bradley, D. D.C., Lee, S. and deMello, J. C., "Spin- and Spray-Deposited Single-Walled Carbon-Nanotube Electrodes for Organic Solar Cells," Adv. Funct. Mater. 20(14), 2310–2316 (2010).

[21] Abdelhalim, A., Abdellah, A., Scarpa, G. and Lugli, P., "Fabrication of carbon nanotube thin films on flexible substrates by spray deposition and transfer printing," Carbon 61, 72–79 (2013).

Preparation of MoS_2 films for sensor applications

Bartłomiej Stonio, Piotr Firek, Andrzej Taube, Jan Szmidt
Warsaw University of Technology, Institute of Microelectronics and Optoelectronics,
Koszykowa 75, 00-662 Warszawa, Poland;

b.stonio@imio.pw.edu.pl

ABSTRACT

The paper presents a method of producing single layers of molybdenum disulphide on silicon substrates covered with a layer of 275nm silicon dioxide produced by means of thermal oxidation. MoS_2 was obtained using the CVD (Chemical Vapor Deposition) technique, and the process parameters were the heating temperatures of the substrates - sulfur and molybdenum oxide, the carrier gas flow in the reactor and the deposition time. Subsequently, the obtained layers were characterized using optical microscopy, atomic force microscopy and Raman spectroscopy. The obtained parameters of layers allow in the future to use them in sensory techniques.

Keywords: MoS_2, CVD, molybdenum disulphide,

1. INTRODUCTION

The production of silicon-based structures, devices, sensors is subject to various limitations, such as limited mobility or work temperature. Therefore, new solutions based on other materials and concepts are used [1], [2]. Limitations resulting from the physical and chemical properties of semiconductor materials do not allow for the implementation of systems or structures that fully meet market demand. The solution to this problem may be reaching for modern materials, called 2D materials. Their thickness is comparable to the thickness of one atom. In recent years, graphene focused the most attention of investigators. This material is built only from carbon atoms. His story begins very early. Already in 1940 P. R. Wallace presented the theoretical description of graphene [3]. However, at the same time, scientists R. E. Peierls and L. D. Landau argued that 2D structures are thermodynamic unstable and can not exist [4], [5]. This theory persisted until 2004, when the results of the experimental graphene discovery [6] were published. This event ultimately dispelled all doubts about the two-dimensional carbon layer and initiated increased research on the properties of this material. In addition, thanks to it, new layers with a two-dimensional structure were sought for. Experience shows that such materials may not only be stable, but also have different properties.

The graphene revolution that could be observed at the beginning of the twenty-first century brought with it a series of effects we can observe today. The scientific community has become interested in this material. What is more, they started to be interested in 2D materials in general. Two-dimensional material, like graphene, is a layer whose one dimension is compared to the thickness of one atom.

The transition metal chalcogens crystal is composed of single layers bound together by weak van der Waals forces [7]. The presence of the weak van der Waals bonds causes that it is possible to receive single layers of these materials, the amount of which affects their electron and optical properties [8]. For example, molybdenum disulphide MoS_2 in the form of a volume crystal has an oblique energy gap with a

Photonics Applications in Astronomy, Communications, Industry, and High-Energy Physics Experiments 2019,
edited by Ryszard S. Romaniuk, Maciej Linczuk, Proc. of SPIE Vol. 11176, 1117656
© 2019 SPIE · CCC code: 0277-786X/19/$21 · doi: 10.1117/12.2536814

width of approximately 1.3 eV. However, a single layer has a direct energy gap with a width of about 1.8 eV [9].

The construction of transient chalcogens is shown in Figure 1. Their atoms are on three levels, but as a compound, it is not possible to obtain a smaller thickness. General formula of such layers is MX_2 [7], [10]. The metal "M" in chalcogens can take atoms for example, Ti, Hf, Ta, Mo, W and Pt, while "X" are elements such as S, Se and Te. Depending on the relationship, we can point on materials with semiconductor properties, e.g. MoS_2, WS_2, $MoSe_2$, $MoTe_2$ or superconducting e.g. NbS_2, $NbSe_2$ [7], [8].

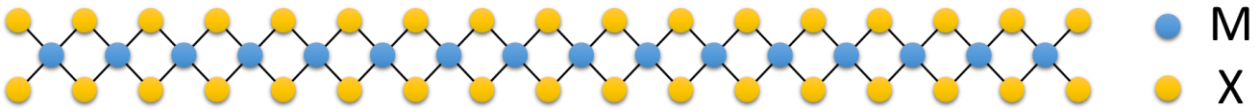

Figure 1. Chalcogens of transition materials - atomic structure.

The presence of a direct energy gap determines the possibility of using material in optoelectronics, e.g. as an active area of transistors or photodetectors. Due to bending strength it is possible to use it in flexible electronics. These properties make it possible to use this material successfully in optoelectronic applications, semiconductor devices as well as in sensors.

The first method of producing transitional metal chalcogens layers was mechanical exfoliation [7]–[9]. It is possible to obtain material with a thickness from single layers to thin films with a thickness of hundreds of nanometers. The size of individual flakes is around a few micrometers.

In addition to the exfoliation method, for the production of single layers of MoS_2, a chemical vapor deposition (CVD) method is used [8], [10]. Using this method, it is possible to create molybdenum disulphide layers with a much larger surface area than the previously described method. Such a material has equally excellent optical and electrical parameters. The thickness of one layer of molybdenum disulphide is 6.5 Å = 0.65 nm. Unlike other two-dimensional materials, MoS_2 has three planes on which atoms are located. Nevertheless, these layers are considered two-dimensional because they can not be divided.

MoS_2 is a very durable material. Its Young's modulus is 180 N/m. The bending module determined experimentally is 9.61 eV [11]. Due to the large surface area and light weight, this material is very well suited to the construction of nanoresistors. The thermal conductivity of a multi-layer molybdenum is 52 W/mK, however, the single layer MoS_2 has a conductivity of 800 W/mK [11]. Electrons in this material behave like fermions with a parabolic energy dispersion. The two-dimensional MoS_2 is a band gap-free semiconductor with 1.8 eV band width. As the number of layers increases, the band gap decreases to 1.2 eV [12]. Molybdenum very well absorbs visible light between 480 nm and 580 nm. The excitation energy of this material is (at 650 nm) 1.9 eV.

The described work presents the results of the synthesis of single layers of molybdenum disulphide by CVD method on silicon substrates and their characterization by means of optical microscopy, atomic force microscopy (AFM), Raman spectroscopy.

2. EXPERIMENTAL DETAILS

The single layers of molybdenum disulphide were made using the CVD method. The processes were carried out in a single-zone furnace for high-temperature processes. High-doped silicon with a thermal SiO_2 layer (275 nm thick) was used as the substrate. Substrates in the CVD process were: molybdenum

oxide (MoO_3) and sulfur (S). The precursors were placed in such a way that they were at their sublimation temperature. Argon (Ar) was used as the carrier gas. The growth temperature was set at 700 °C. The process duration was 20 minutes counted from reaching the set process temperature. The scheme of the technological process together with the dependence of temperature on time has been presented in Figure 2.

A)

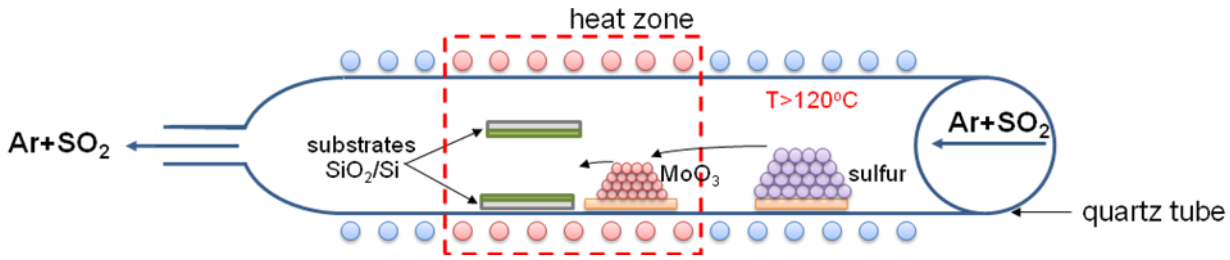

B)

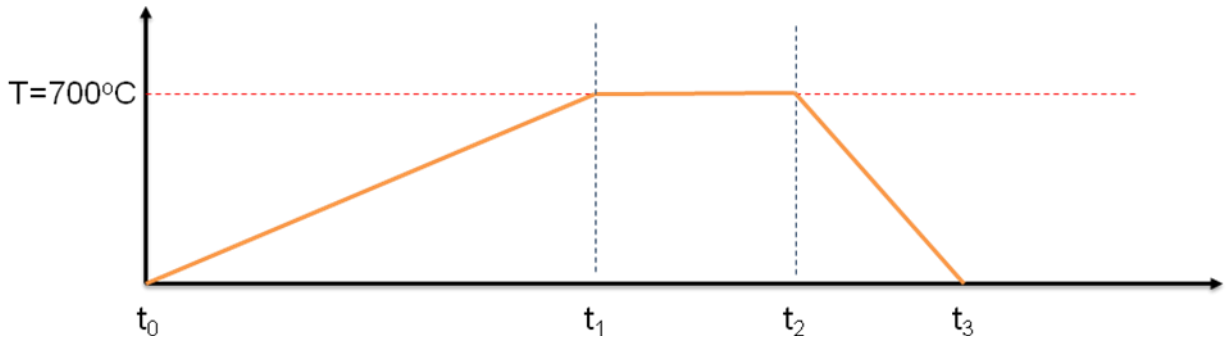

Figure 2. A) Setup for the manufacturing process of the MoS2 layer by CVD; B) Dependence of temperature vs. time during the layer synthesis process

Argon was used for substrates transport and to create an inert atmosphere needed during the process. After filling the entire quartz tube with working gas, it was possible to start heating the furnace. After the process temperature was reached, the reaction between the substrates begins. The reaction products was molybdenum disulphide and sulfur oxide. Sulfur oxide together with the working gas (Argon) is removed from the reactor.

After the process, the substrates with MoS_2 layer was cooled in an argon atmosphere and next characterized. Optical microscopy was chosen as the first method of characterization. Thickness of silicon oxide allow to identify MoS_2 due high contrast between the substrate and the produced layer. This allowed quick verification of the obtained material in terms of the size of the flakes. For the purpose of deeper verification measurements with atomic force microscope were carried out. The height profile of the layer was made. The final material verification was done by means of Raman spectroscopy measurement with excitation $\lambda = 514$ nm.

3. RESULTS

The first basic method to verify the correctness of the deposition process was optical microscopy. Figure 3 shows a picture taken with a confocal optical microscope. The MoS_2 flakes in the form of triangles are visible. This shape is characteristic for this type of material.

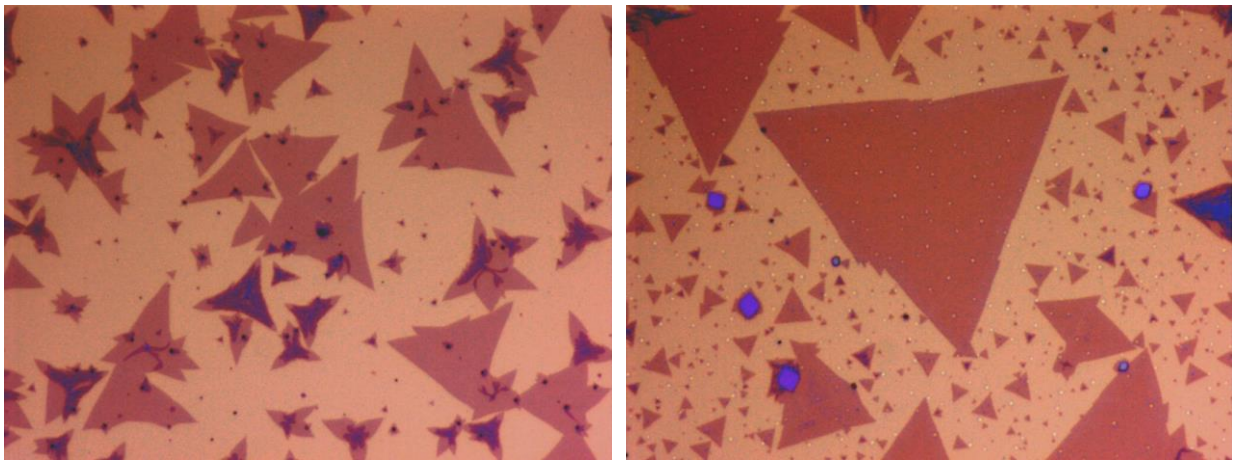

Figure 3. MoS_2 flakes pictures prepared by optical microscopy with magnification x 1000.

Triangular layers have different colors and shades. The colors depend on the thickness of the obtained layer. In addition, in the pictures it can be observed that part of the flakes, in the process, is combined to form a larger plane. The largest of the flakes presented in the figure have reached the value above 10um, which proves that this method can produce layers larger than the exfoliation method.

Figure 4 shows the atomic force microscope (AFM) picture of the surface of the sample after layer deposition process. The measure line is marked on one of investigated flakes. In Figure 5 AFM profile is presented.

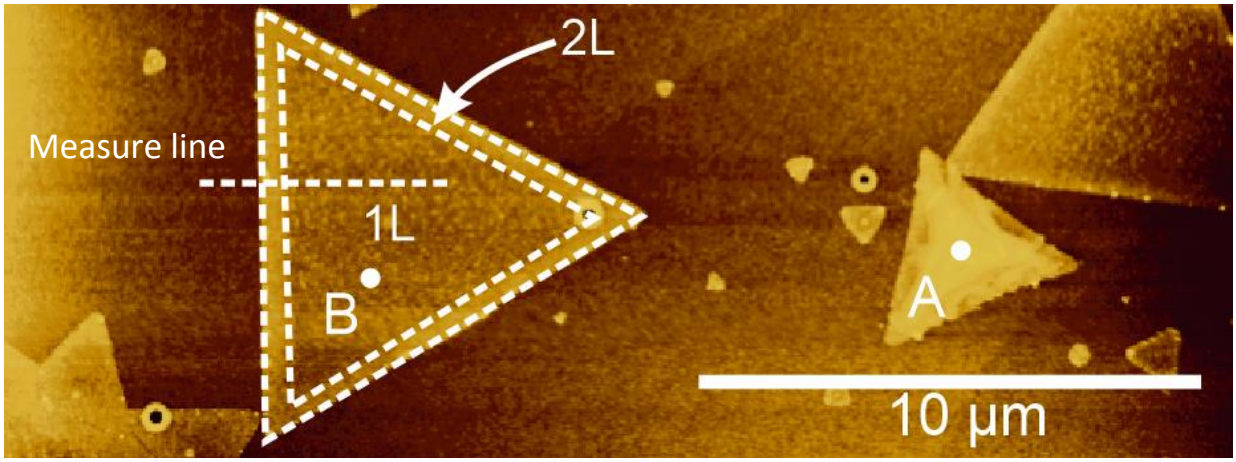

Figure 4. Morphology of obtained MoS_2 flakes on sample surface.

Figure 4 shows the triangular layer of MoS_2 with cross-section line along which the profile was made. The profile in Figure 5 shows that the obtained layer is two-dimensional. What's more, we can observe that on the edges of the layer, during the manufacturing process, a layer with a thickness of ~ 1.3 nm is formed. The thickness of the material formed at the edges corresponds to two single layers of MoS_2.

The technique used to confirm both the presence of MoS_2 and the thickness of the obtained layer was the measurement of the Raman spectra (excitation 514 nm). Measurement points are marked in the uppercase letters of the alphabet in Figure 4. Point A corresponds to a single layer and B to a bulk material. The spectral measurement results are shown in Figure 6.

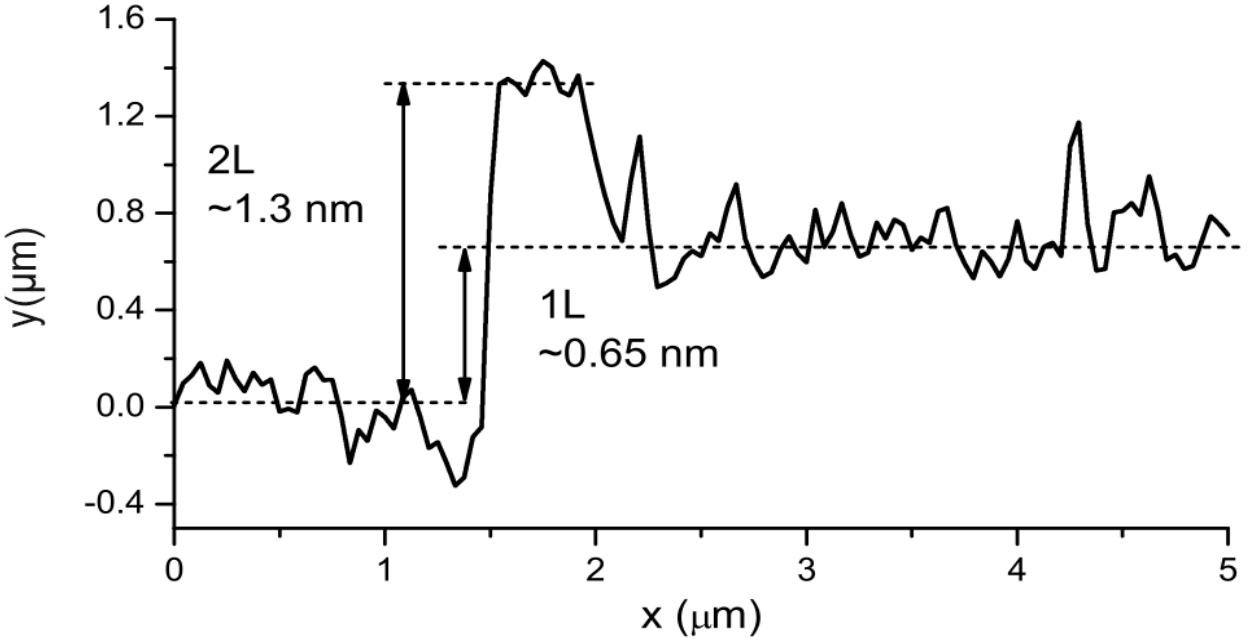

Figure 5. AFM profile of one and double layer of MoS_2.

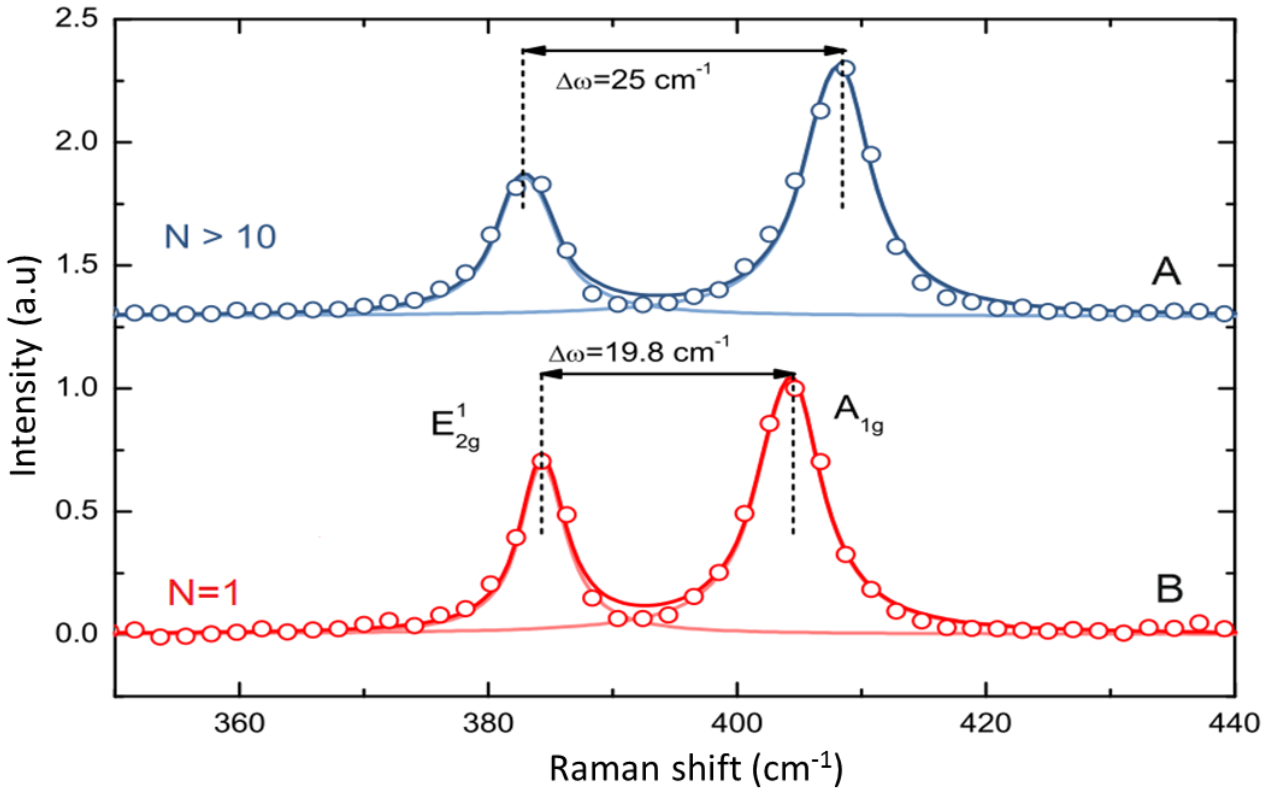

Figure 6. Raman spectra of MoS_2: bulk material (blue) and monolayer (red).

The distance between the Raman modes E^1_{2g} and A_{1g} ($\Delta\omega$), for the measurements at point B is 25.02 cm^{-1} which corresponds to the bulk material MoS_2. The spectrum for point A corresponds to a single layer and is equal $\Delta\omega = 19.7\ cm^{-1}$, which corresponds to the published results [8].

4. CONCLUSIONS

The described experiments show that it is possible to create single MoS_2 layers by CVD method. This method allows the production of large flakes over 10 μm. What is more, a lot of flakes of good quality are produced in one process. Analysis using the methods allow to accurately characterize the monolayer material. It is possible to find places where the obtained material reaches one, two or many layers. This is valuable during research on the properties of both single layers and a material composed of several layers. Taking into account the large surface area of the obtained flakes, the possibility of finding MoS_2 with a thickness of exactly one layer, as well as a simple energy break of this material. It is possible to create in the future photodetectors or extreme sensitive sensors

REFERENCES

[1] Borecki, M., Korwin-Pawlowski, M. L., Beblowska, M., Szmidt, J. and Jakubowski, A., "Optoelectronic Capillary Sensors in Microfluidic and Point-of-Care Instrumentation," Sensors 10(4), 3771–3797 (2010).

[2] Firek, P., Werbowy, A. and Szmidt, J., "MIS field effect transistor with barium titanate thin film as a gate insulator," Mater. Sci. Eng. B 165(1–2), 126–128 (2009).

[3] Wallace, P. R., "The Band Theory of Graphite," Phys. Rev. **71**(9), 622–634 (1947).

[4] Peierls, R., "Quelques propriétés typiques des corps solides," Ann. l'institut Henri Poincaré **5**(3), 177–222 (1935).

[5] Landau, L., "Zur Theorie der phasenumwandlungen II," Phys. Z. Sowjetunion **11**(545), 26–35 (1937).

[6] Novoselov, K. S., Geim, A. K., Morozov, S. V., Jiang, D., Zhang, Y., Dubonos, S. V., Crigorieva, I. V. and Firsov, A. A., "Electric Field Effect in Atomically Thin Carbon Films," Science, 306(5696), 666–669 (2004).

[7] Chhowalla, M., Shin, H. S., Eda, G., Li, L.-J., Loh, K. P. and Zhang, H., "The chemistry of two-dimensional layered transition metal dichalcogenide nanosheets," Nat. Chem. 5(4), 263–275 (2013).

[8] Wang, Q. H., Kalantar-Zadeh, K., Kis, A., Coleman, J. N. and Strano, M. S., "Electronics and optoelectronics of two-dimensional transition metal dichalcogenides," Nat. Nanotechnol. 7(11), 699–712 (2012).

[9] Lee, Y.-H., Yu, L., Wang, H., Fang, W., Ling, X., Shi, Y., Lin, C.-T., Huang, J.-K., Chang, M.-T., Chang, C.-S., Dresselhaus, M., Palacios, T., Li, L.-J. and Kong, J., "Synthesis and Transfer of Single-Layer Transition Metal Disulfides on Diverse Surfaces," Nano Lett. 13(4), 1852–1857 (2013).

[10] Lee, Y.-H., Zhang, X.-Q., Zhang, W., Chang, M.-T., Lin, C.-T., Chang, K.-D., Yu, Y.-C., Wang, J. T.-W., Chang, C.-S., Li, L.-J. and Lin, T.-W., "Synthesis of Large-Area MoS $_2$ Atomic Layers with Chemical Vapor Deposition," Adv. Mater. 24(17), 2320–2325 (2012).

[11] Jiang, J.-W., “Graphene versus MoS2: A short review,” Front. Phys. 10(3), 287–302 (2015).

[12] Park, J.-H., Park, J. C., Yun, S. J., Kim, H., Luong, D. H., Kim, S. M., Choi, S. H., Yang, W., Kong, J., Kim, K. K. and Lee, Y. H., “Large-Area Monolayer Hexagonal Boron Nitride on Pt Foil,” ACS Nano 8(8), 8520–8528 (2014).

Modeling of burrs during drilling of titanium alloy

Emilia Franczyk[a], Wojciech Zębala[a], Łukasz Ślusarczyk*[a]
[a]Production Engineering Institute, Cracow University of Technology, Al. Jana Pawła II 37, 31-864 Cracow

ABSTRACT

Drilling of difficult-to-cut materials like titanium alloy is a complex machining operation. Due to the tool trajectory, the chip thickness changes along the cutting edges and during the tool movement. The aim of this study is to develop a drilling simulation model depending on the tool geometry and cutting data in order to control the final quality of the machined borehole through the size of burrs. First the geometry of the chip is modelled taking into account the parameters defining the tool trajectory and its geometry. An experimental study validates the modelling through vision camera observations. From this modelling it is possible to optimize the cutting data and cutting tool geometry in order to control the burrs size and thus the final quality of the borehole.

Keywords: burr, drilling, modelling, simulation

1. INTRODUCTION

Machining of difficult-to-cut materials like stainless steel, titanium and nickel based alloys is a complex operation[1,14-15,19-20]. The phenomenon of burr formation on the edges of workpieces is one of the most onerous issues that occur during machining these kind of materials[2-5]. The cause of the phenomenon is the occurrence of elastic and plastic deformation on the edge formed as the tool exits the workpiece[6-8,18]. Burr is precisely defined in the ISO 13715 standard as a deviation beyond the ideal geometrical shape of the edge, as it is shown in Figure 1. Shape and size of burr are described by the parameters shown in Figure 2.

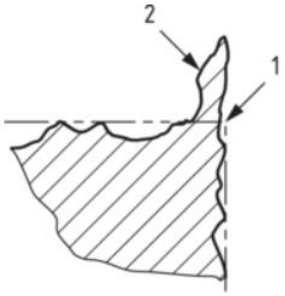

Figure 1. Edge with visible burr according to ISO 13715: 2017.
1-ideal shape of the edge, 2-burr

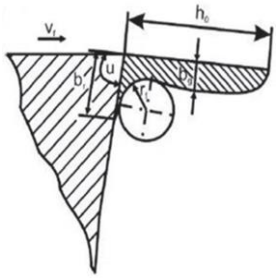

Figure 2. Burr geometry.
b_r – thickness of the base, h_o – height of burr,
r_f – radius of the base, b_g – thickness of burr

The problem of deburring or minimizing the phenomenon of their formation has already appeared in the scientific literature, on the basis of which it can be concluded, that there are a number of methods for removing them[3-4,11], which - due to the degree of their automation - can be divided into manual methods, manual-machine and machine methods. The most popular manual methods are those in which a file or a scraper are used. Manual-machine methods involve the use of grinding machines or other high-speed tools. Machine methods are based on edge machining using an abrasive medium. These are, for example, vibro-abrasive or rotary-abrasive methods. Authors[1,9,13] agree that effective deburring is an important technological problem, especially if future assembly is intended. Numerical FE modelling of machining processes is a popular method to predict the burr formation[10,12,16].
This paper presents a simulation model of drilling with the respect of the burr formation.

*slusarczyk@mech.pk.edu.pl; phone 12 374-32-14

Photonics Applications in Astronomy, Communications, Industry, and High-Energy Physics Experiments 2019, edited by Ryszard S. Romaniuk, Maciej Linczuk, Proc. of SPIE Vol. 11176, 1117657
© 2019 SPIE · CCC code: 0277-786X/19/$21 · doi: 10.1117/12.2536818

2. MODELLING OF BURR FORMATION

Simulation tests were carried out using software based on the finite element method (FEM)[17]. In the first stage of the research, a geometric model of the workpiece and the tool was built. The tool geometry was established on the basis of real tool measurements (twist, solid carbide drill, ϕ 10) on a Bressher laboratory microscope. It was determined: rake angle: γ=30°, face angle α=8°, cutting edge radius r_n=0,01 mm. The geometry of the model with the finite element mesh is shown in Figure 3.

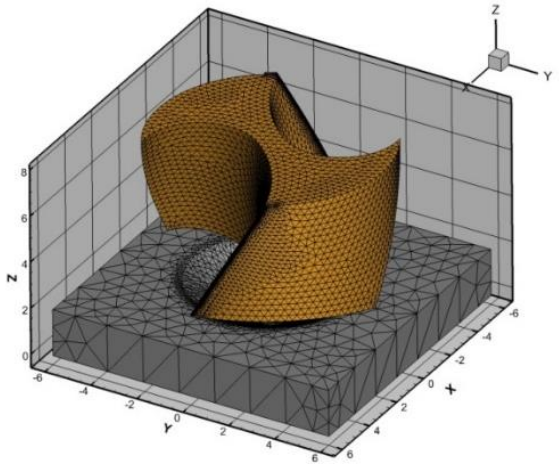

Figure 3. Geometry of a 3D model with the finite element mesh.

The process of burr formation was modeled in a cross-section perpendicular to the cutting edge, close to the external diameter of the drill, as a 2D flat model, Figure 4. Geometry of the 2D model with the finite element mesh is shown in Figure 5.

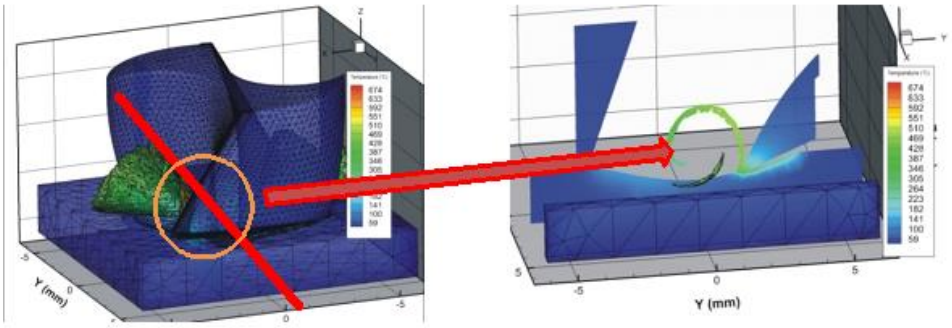

Figure 4. Method of construction of 2D burr formation model.

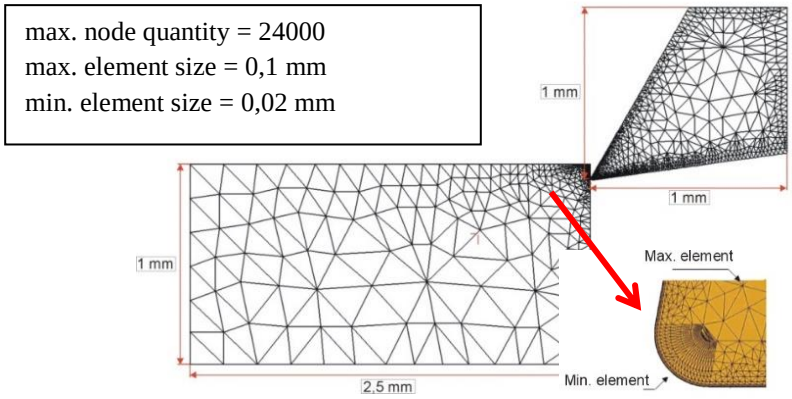

Figure 5. Geometry of a 2D model with the finite element mesh.

In the next stage of the research, material models of the tool and the workpiece were constructed, with the properties presented in Table 1 and Table 2. Sintered carbide was used as the tool material, and Ti-6Al-4V titanium alloy as the workpiece material.

Table 1. Basic material data for sintered carbides

Thermal expansion coefficient	4,7 μm /m°C
Density ρ	15000 kg·m^{-3}
Poisson's ratio ν	0,2
Specific heat c_p	203 J·kg^{-1}·K^{-1}
Thermal conductivity λ	46 W·m^{-1}·K^{-1}
Young modulus E	800 GPa

Table 2. Basic material data for Ti-6Al-4V alloy and values of J-C equation coefficients

Density ρ	4430 kg·m^{-3}
Poisson's ratio ν	0,33
Specific heat c_p	670 J·kg^{-1}·K^{-1}
Thermal conductivity λ	6,6 W·m^{-1}·K^{-1}
Young modulus E	115 GPa
A	782,7 MPa
B	498,4 MPa
C	0,028
n	0,28
m	1,0

Material model of the workpiece is based on Johnson - Cook's (1) constitutive equation.

$$\sigma(\varepsilon,\dot{\varepsilon},T) = (A + B\varepsilon^{n})\left(1 + C ln\left(\frac{\dot{\varepsilon}}{\dot{\varepsilon}_0}\right)\right)\left(1 - \left(\frac{T-T_R}{T_m-T_R}\right)^{m}\right) \quad (1)$$

where: A – yield point for the reference value: strain rate $\dot{\varepsilon}_o$ and T_R temperature,
B, n – strain hardening factors,
C – dynamic hardening factor,
T_m – melting temperature.

In order to identify burrs a 2D computer simulation of the machining process was carried out in accordance with Table 3. Figure 6 shows example simulation results.

Table 3. Machining parameters for individual models.

Trial no	v_c [m/min]	f [mm/rev]
1		0,08
2		0,11
3	18,8	0,14
4		0,17
5		0,2

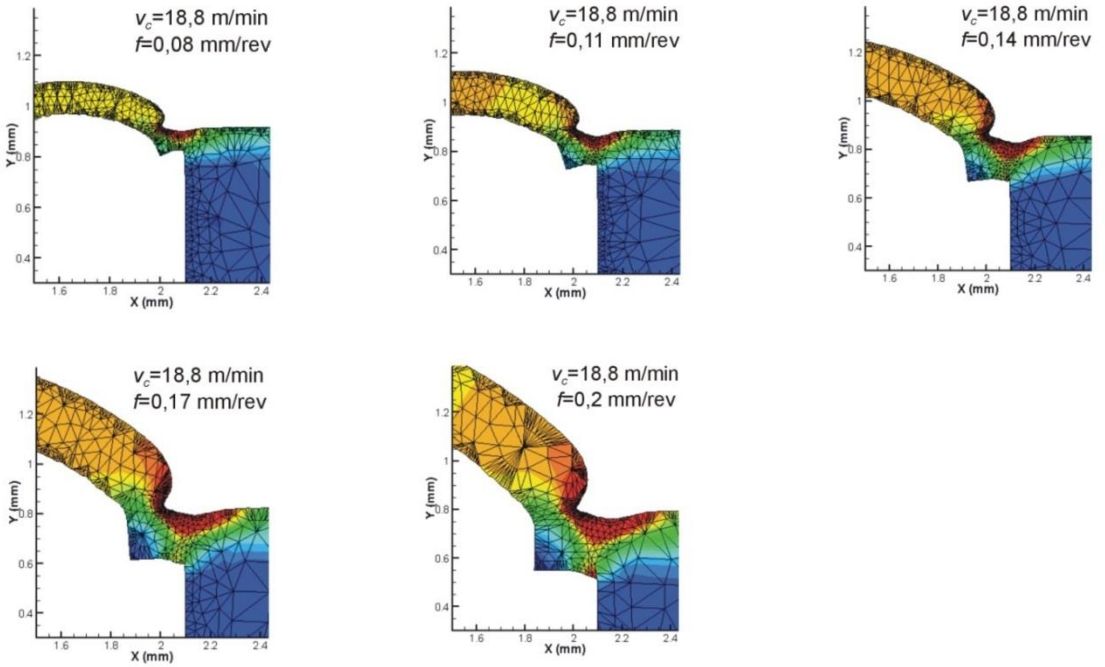

Figure 6. Simulation results for different feed rates f.

The distribution of plastic strain for different feed rates is shown in Figure 7.

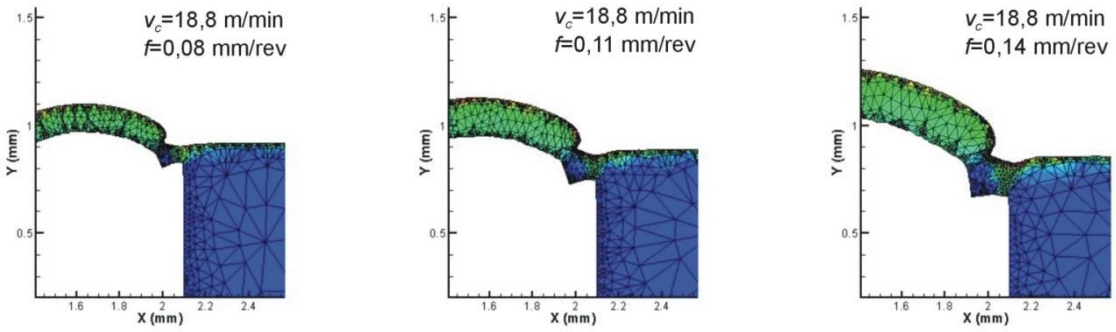

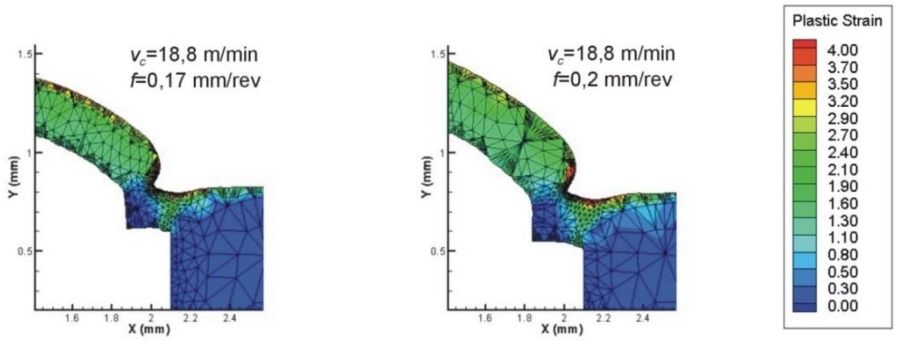

Figure 7. Simulation results of plastic strain for different feed rates f .

Geometrical values of burrs obtained on the basis of the simulation are shown in Figures 8 and 9.

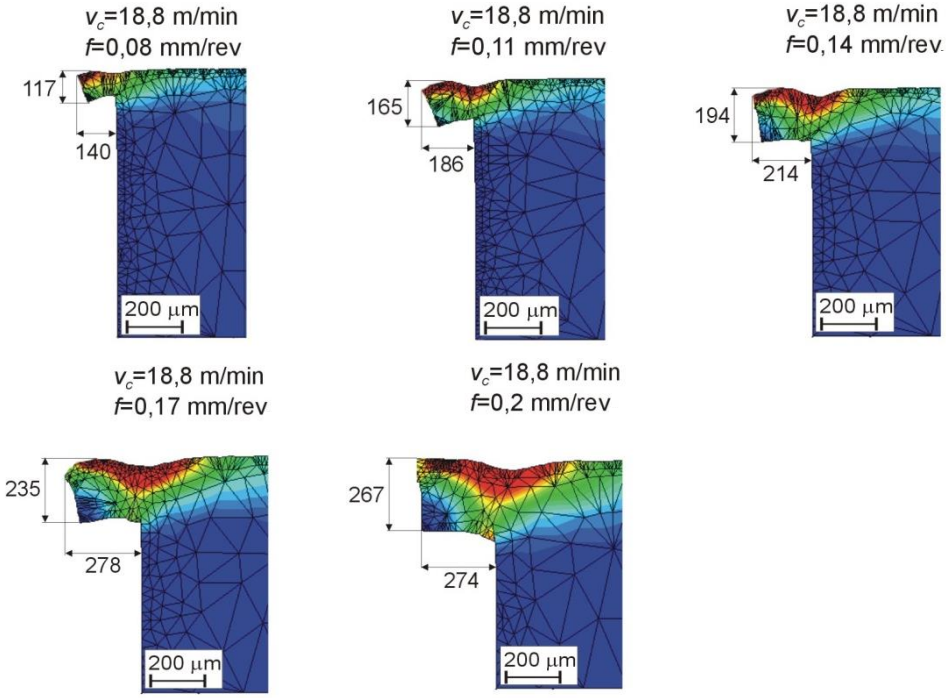

Figure 8. Burr geometry for different feed rates f.

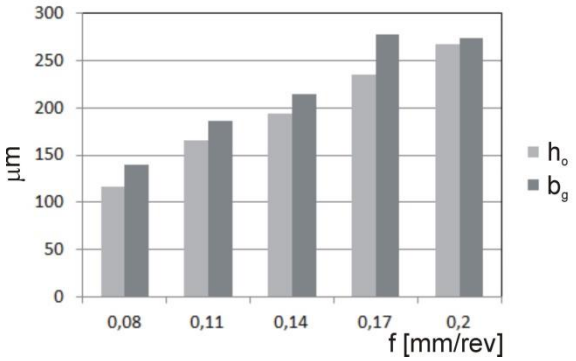

Figure 9. List of geometrical values of burrs (height h_o) and (width b_g).

Distributions of the maximum temperature and the *Fc* component of the total cutting force for different feed rates are shown in Figures 10 and 11.

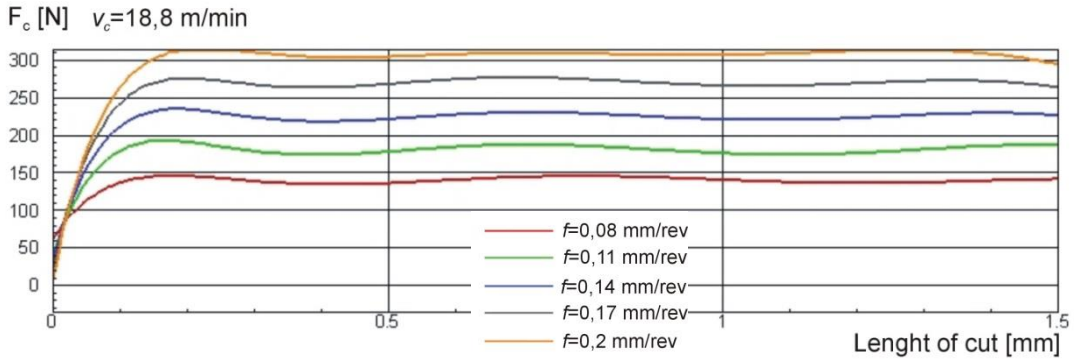

Figure 10. Cutting force values along the cutting path.

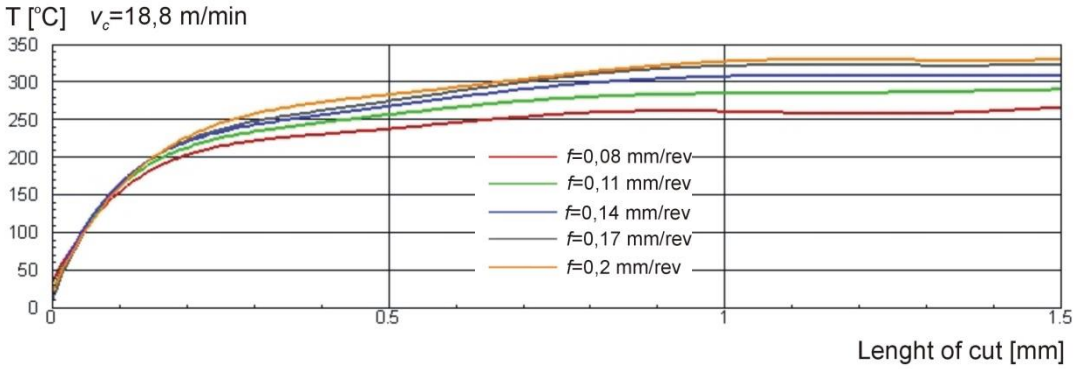

Figure 11. Maximum tool temperature values along the cutting path.

3. EXPERIMENTS

A flat bar made of Ti6Al4V titanium alloy, with composition shown in Table 4, was used for the tests. The entire process of burr formation was recorded by a camera equipped with Nikon AF Mikro-Nikkor 200 lens, and a set of Dedocool cold light spotlights. An example image of burr for feed f = 0,17 mm / rev is shown in Figure 12.

Table 4. Ti6Al4V titanium alloy chemical composition.

Element % by mass							
O	V	Al	Fe	H	C	N	Ti
<0,20	3,5	5,5	<0,30	<0,0015	<0,08	<0,05	balance

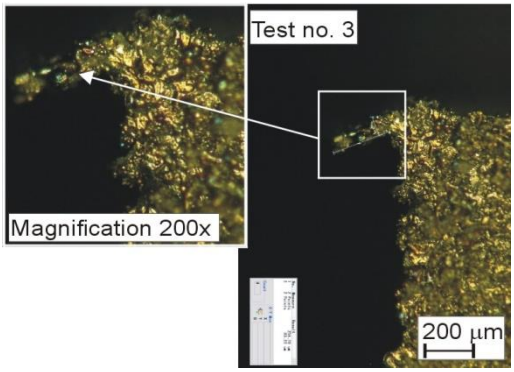

v_c=18,84 m/min
f=0,17 mm/rev

h_o: 260 µm

Figure 12. Burr image for feed rate f= 0,17 mm/rev.

4. CONCLUSION

Burr formation is particularly problematic where we want to achieve a good surface quality (SGP), produce parts, that do not have sharp edges breaking off or cause major failures. Minimizing the size of the burr can contribute to improving the efficiency of machining and the quality of the parts production. After research it can be assumed that with increasing the feed rate the burr arises (values of height and thickness of burr increase). The height of burr h_o changes from 140 µm till 274 µm and thickness changes from 117 µm till 267 µm. The main cutting forces and maximum tool temperature were in the range (150 – 300) N and (260-330) ^{o}C, respectively. Plastic strain also increases with the feed rate increase.
On the simulation model basis, it can be concluded that it is possible to optimize the drilling parameters (feed rate) so as to minimize the effect of burr formation.

REFERENCES

[1] Aurich, J.C., Dornfeld, D., Arrazola, P.J., Franke, V., Leitz, L., MIN S., "Burrs - Analysis, control and Removal," CIRP Annals – Manufacturing Technology 58, 2009.
[2] Chern, G.L., Dornfeld, D.A., "Burr/Breakout Development and Expe-rimental Verification," Trans. ASME, J. Eng. Mats. Tech., t. 118, nr 2, 201-206 (1996)
[3] Eder, S., Bacci, M., Machado, A., "Burr Produced on the Drilling Process as a Function of Tool Wear and Lubricant-Coolant Conditions", 2009.
[4] Gillespie, L.K., Blotter P.T. "The Formation and Properties of Machining Burr," Trans. of ASME, J. Eng. Ind., t. 98, nr 1, 66-74 (1976)
[5] Hashimura, M., Ueda, K., Dornfeld, D., Manabe, K., "Analysis of Three Dimensional Burr Formation in Oblique Cutting," Annals of CIRP, t. 44, nr 1, 27-30 (1995)
[6] Hashimura, M., Hassamontr, J., Dornfeld, D.A., "Effect of In-plane Exit Angle and Rake Angles on Burr Height and Thickness in Face Milling Operation," Transactions of the ASME Journal of Manufacturing Science and Engineering 121(1), 13–19 (1999)
[7] Ko, S.L., Dornfeld, D.A., "A Study of Burr Formation Mechanism," Trans. of ASME, J. Eng. Ind., t. 98, nr 1, 66-74 (1991)
[8] Leopold J., "From macroscopically scale to the microscopically scale in modeling and simulation of machining," International Users' Conference „Modeling Technology – Machining Solution" - Minneapolis MN, USA, 2, tom 4, 1-14 (2008)
[9] Niketh, S., Samuel, G.L., "Drilling performance of micro textured tools under dry, wet and MQL conditio," Jurnal of Manufacturing Processes 32, 254-268 (2018)
[10] Schulze, V., Zanger, F., "Numerical Analysis of the Influence of Johnson-Cook-Material Parameters on the Surface Integrity of Ti-6Al-4V", 2011.
[11] Słodki, B., Struzikiewicz, G., Ślusarczyk, Ł., "Influence of cutting fluid conditions and cutting parameters on the chip form in turning of titanium and steel alloys," Key Engineering Materials 686, 74-79 (2015)
[12] Sreenivasulu, R., Srinivasa, R.Ch., "Modelling, Simulation and Exprimental validation of Burr size in Drilling of Aluminium 6061 alloy," Procedia Manufacturing 20, 458-463 (2018)

[13] Stein, J.M., Dornfeld, D.A., “Burr Formation in Drilling Miniature Holes,” Annals of CIRP, t. 46, nr 1, 63-66 (1997)
[14] Struzikiewicz, G., Zębala, W., Rumian, K., “Application of Taguchi method to optimization of cutting force and temperature during turning of difficult to cut materials,” Key Engineering Materials, Vol. 686, 114-118 (2016)
[15] Ślusarczyk, Ł., Franczyk, E., “Development and verification of a measuring stand for recording the physical phenomena during turning,” Photonics Applications in Astronomy Communications Industry and High-Energy Physics Experiments Book Series: Proceedings of SPIE 10445, 104456G (2017)
[16] Ślusarczyk, Ł., “The construction of the milling process simulation models,” Photonics Applications in Astronomy Communications Industry and High-Energy Physics Experiments Book Series: Proceedings of SPIE 10031, 100310C (2016)
[17] User’s Manual of AdvantEdge v5.6 machining simulation software, Minneapolis, MN, 2010.
[18] Waldorf, D.J., DeVor, R.E., Kapoor, S.G., “An Evaluation of Ploughing Models for Orthogonal Machining,” Jour. Manufact. Science and Eng., Trans. of ASME, t. 121, 550-558 (1999)
[19] Zębala, W., Kowalczyk, R., Matras, A., “Analysis and optimization of sintered carbides turning with PCD tools,” Procedia Engineering, Vol. 100, 283-290 (2015)
[20] Zębala, W., Struzikiewicz, G., Rumian, K, Plaza, M., “Simulation and optimization of physical phenomena when engine block machining,” Case study. Proceedings of SPIE - The International Society for Optical Engineering, Vol. 10031, Article number 100310O (2016)

Fabrication antennas with 2D and 3D printing technologies: Review

Dariusz T. Grudziński[a], Marcin Słoma[a]
[a]Faculty of Mechatronics Warsaw University of Technology, Andrzeja Boboli 8, 02-525 Warsaw, Poland

ABSTRACT

The article contains a review of the achievements in the field of unconventional methods of antenna production. In particular, it concerns solutions based on 3D printing methods, screen printing, and ink-jet printing. The focus is on microwave antennas, whose widespread use in modern electronic devices for data transmission, as well as parasitic activity, allows us to assume faster implementation. Attention has been drawn to the new possibilities offered by the above-mentioned methods in terms of adjusting the shape and materials used. This, in turn, affects the change of mechanical properties of the antennas. It allows to use the resulting antennas for new devices, requiring adjustment to specific working conditions.

The paper also presents more classical ways of producing antennas with a similar range of operation. This, in turn, allows for easier comparison of the collected results with the results obtained for commonly used methods.

Keywords: Antenna, 3D printing, printed electronic, sreen-printing, FDM, DMLS.

1. INTRODUCTION

In now a day world of rich and growing societies, the market of devices which simplifies our everyday activities and entertainment is growing. When we moved away from the power supply of devices with mechanical energy of human origin, we moved on to freeing people from the role of operators or even supervisors. In this way, we were able to use a large number of independent devices. The use of many independent devices at one time forced people to devote a significant amount of time for inspection of each individual activity. The natural consequence was a short circuit in the computer system, which made it possible to centralize the management of individual processes. That's where ideas of intelligent buildings comes from. The same applies to the use of multiple sensors to control the work of the human body. The need to collect data form many sensors makes it necessary to provide an adequate communication network. Wired networks that can be used in buildings are not practical for monitoring living organisms. The natural answer is the use of wireless communication. There are also difficulties with access to power sources. One of the answers to this seems to be that the sensors may be parasitic on communication. The above requirements place particular demands on the antennas used to establish radio communication. They should adapt to changing body shape in motion, maintain functionality despite repeated bending, maintain adequate performance in pursuit of min. Their classic manufacturing methods, based on the digestion of the appropriate pattern in copper foil may not meet all requirements.

Wireless communication over short distances such as wi-fi, bluetooth or NFC operates in the range of gigahertz frequencies. This means waves length of several centimetres. The antenna's electrical parameters describing its ability to receive waves depend directly on its geometry. Classically used dipole antennas deteriorate their properties when the dimensions are limited below ¼ of the wavelength. It forces us to use more sophisticated geometry for very small antennas.

Currently, the market uses three basic types of antennas. Straight antennas, which are insulated conductors of length adjusted to the frequency of carrier wave. Usually they are a simple element of significant dimensions that stand out from the device. The second type are printed antennas, which are a part of a circuit on a printed circuit board. The third type is the so-called "chip antennas", i.e. antennas made similarly to printed antennas, but in the form of smd elements that can be soldered to the circuit board as single device. This reduces the need for independent antenna shape design[1].

Photonics Applications in Astronomy, Communications, Industry, and High-Energy Physics Experiments 2019, edited by Ryszard S. Romaniuk, Maciej Linczuk, Proc. of SPIE Vol. 11176, 1117658
© 2019 SPIE · CCC code: 0277-786X/19/$21 · doi: 10.1117/12.2536828

2. REVIEW OF MANUFACTURING METHODS

We will refer only to antennas used in portable electronic equipment for short-range communication, and proposals for their improvement. Looking at this way, we should first of all distinguish chemical etching with mask application by photolithography as a classical method. In addition, attempts are being made to produce antennas using the following methods: screen printing, ink-jet printing, flexography, FDM, DMLS and direct writing.

Let us now consider the possibilities and challenges of each of these methods.

2.1 Chemical etching

Chemical etching is the basic method of manufacturing passive elements on printed circuit boards in the copper layer. It allows to achieve a relatively high resolution and even edge of the antenna path. It is well-developed and enables the antenna to be made during manufacturing of circuit boards[2]. It is subtractive method causing relatively large amount of post-production waste. The thickness of the obtained layer corresponds to the thickness of the laminate from which it will be produced. It does not make it possible to make paths of large thickness and usually involves use of a flat antenna. Due to good mastery of this technology and mass use, relatively low unit costs can be achieved. This predestines this method in particular for use in standard and low-cost solutions.

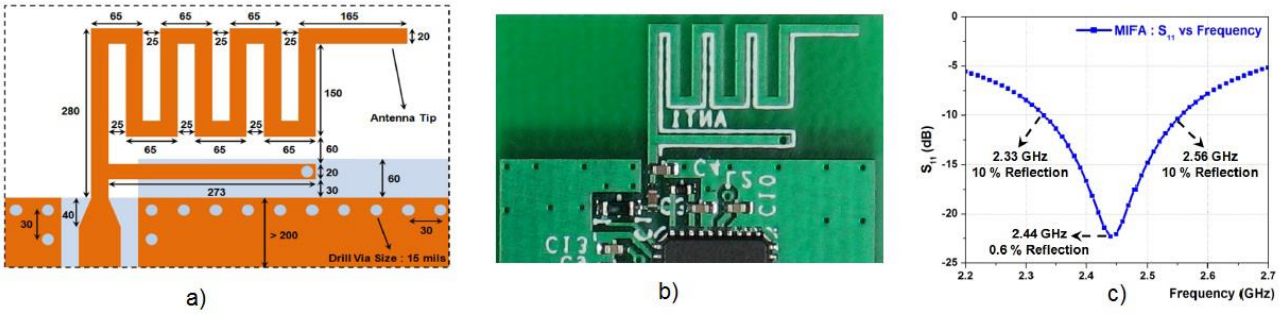

Figure 1. Antenna MIFA: a) antennas schematic b) prototype c) characteristic $\boldsymbol{S_{11}}$. [2]

2.2 2D printing methods

This category contain a few flat printing methods. Any of them allows production of shapes used in chemical etching. Screen printing, ink-jet printing and flexography should be distinguished as the basic ones. It also provides new possibility while there can be made many tinny layers one on the another.

Screen printing makes it possible to obtain relatively thick layers. In order to produce an antenna, it uses special pastes, which guarantee electric conductivity. In particular, tests are carried out with carbon nanotubes[3] or graphene nanoplatelets[4]. Their naturally high electrical conductivity and flexibility let us expect future application. A specially when consider flexible substrates.

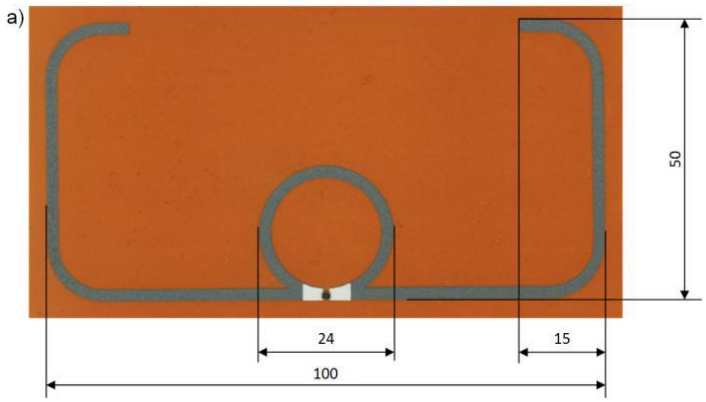

Figure 2. The GNP LD antenna on kapton foil of surface area of $\boldsymbol{100mm \times 50mm}$ with the loop ensuring impedance matching to the SL3S1213FTB0 RFID chip[4].

Ink-jet printing makes it easy to apply very thin layers, while at the same time provide a relatively high resolution. The aim is to use this method on cheap or flexible substrates. Special conductive inks are used to achieve the expected path mosaic. Especially those based on silver nanoparticles[5]. The main advantage of this method in comparison with chemical etch is, ultimately, a much wider choice of available substrate materials. At the same time, the method provides the possibility of greater shape adjustment. The main disadvantage is the smoothness of the path edge resulting from the method itself. What's more, it is quite difficult to obtain thick layer. The larger droplets of ink, the worst resolution of this technology.

Flexography is widely used in industry for printing on packaging. It can be use with conductive inks to provide very high production efficiency. In this way, products made with conductive inks could also compete in mass production applications. Unfortunately, this method places high demands on the carcasses used and the selection of appropriate technological parameters. It is necessary to use very low viscosity inks. Otherwise, the resulting paths may be discontinuous.[6,7]

Direct writing is a method from the borderline of flat and spatial printing. It assumes continuous ink application on the surface of the substrate. However, it is used in machines that allow application to spatial objects, not just flat objects. In combination with local laser sintering, it allows the creation of spatial elements that do not require a substrate.[8,9]

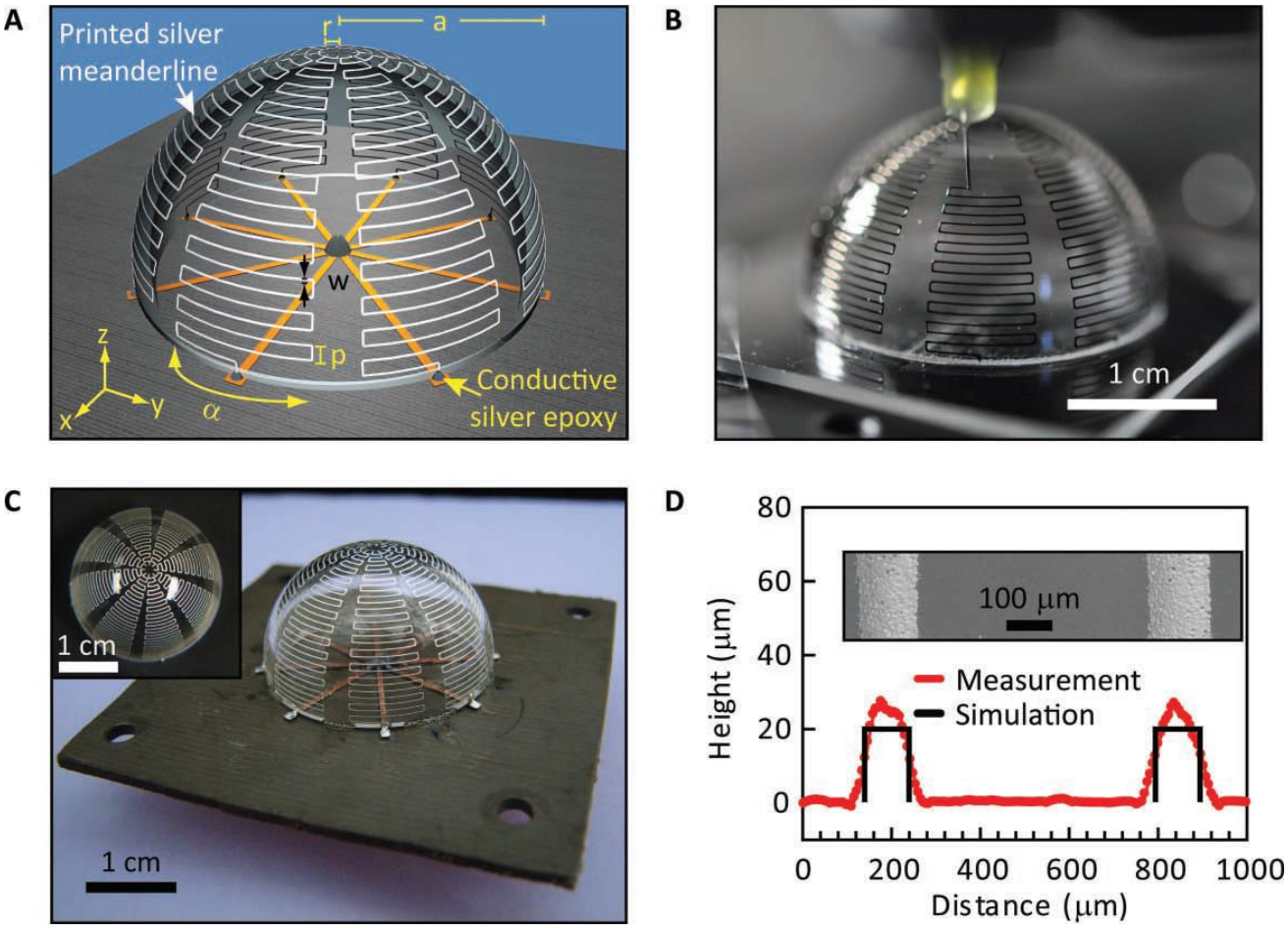

Figure 3. Direct writing[10] [16]

2.3 3D-printing methods

In this chapter we will describe a few additive methods of productions which final product also has a significant all three dimensions. All of them support not flat elements.

When 3D printing appear as a subject, it is widely identified with Fused Deposition Modeling (FDM) method. That's not correct, but due to its capability for ease of use, it has gained recognition among many amateurs. For a long time, it has been the subject of research work focused at making practical products. It took a lot of time before there could be made competitive electronic components. This method is distinguished by requirement of appropriate material. It must behave acceptable depending on temperature. It is required that the material has the widest possible temperature range at which it is plasticize, so that it does not degrade during processing. At the same time, it is also required that the processing temperature is not too high. Due to problems with conductive polymers, work is being carried out on composites whose matrix is based on a properly selected polymer and the functional phase of various metals[11]. The advantage of this method is that, it is relatively easy to obtain complex spatial shapes even on a relatively small scale without the need for human effort beyond modeling.

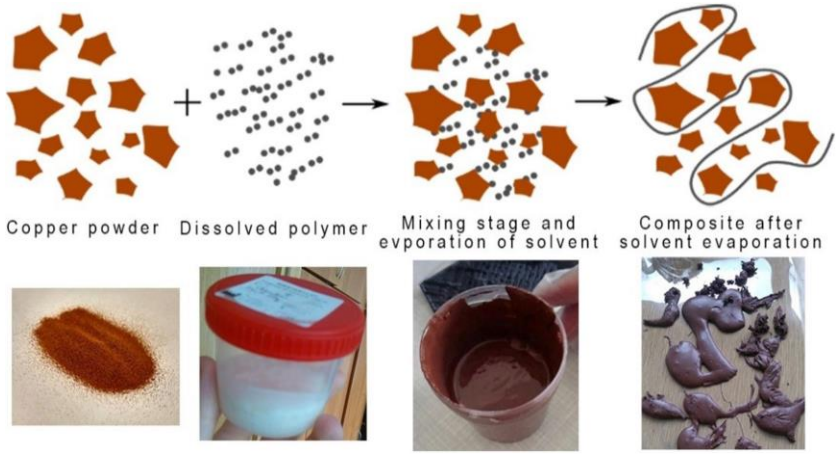

Figure 4. Solvent assisted processing method diagram. [11]

Direct Metal Laser Sintering (DMLS) is a technique that enables the production of electronic components from metal powders. Object is formed layer by layer. The subsequent powder layers must be applied and then sintered. This kind of manufacturing provides product with nearly pure metal. The limitation of this method are results of powder dimensions and how selective laser sintering can be. It can be used to manufacture complex shape antennas from classical materials.

Similar method was presented with "Laser-assisted direct ink writing"[8]. In this solution sintering powder is added selectively in a given place. In this case, the powder is sintered directly after application. It is possible to quickly obtain slender shapes. Does not demand as much powder as simple DMLS. It is kind of combination of both, DMLS and direct writing described above.

Figure 5. The DMLS-made conformal antenna.[12]

3. REASONS FOR USING PRINTING TECHNOLOGY

3.1 Flat printing techniques

In case of printing flat patterns, the main direction of investigations seems to be printing on any substrate. In particular, the aim is to use flexible materials. Such an approach is to constitute a competitive advantage in comparison with commonly used elements[4,13]. It can be used in the case of mobile solutions combined with dressings or sensors which are monitoring human body[14]. The requirement to use wireless sensors comes from the convenience of use as well as economy, where dressings should be disposable.

The second direction of development is the use of inks with special properties, which will allow to obtain new possibilities. This will be possible through local application of chosen's inks. An example is the use of vanadium dioxide[15,16]. Using it as a functional phase allowed to obtain an antenna with a changing frequency response, without a need for external interference in the geometry. Research is also being carried out into the introduction of good conductors alternative to copper, such as Carbon nanotubes[3].

3.2 3D printing

3D printing is seen as an opportunity to move away from flat antennas used in portable equipment. Spatial structures have a chance to get closer to the optimal shape of the antenna[10,17]. Optimizing this for specialized portable equipment can bring many benefits. It will be possible to obtain cheap antennas with a much larger range, with the same dimensions, or significantly extends the bandwidth. Another possibility resulting from greater production flexibility by these methods is to produce antennas with a variable and adaptable range. Of course, there are also problems. Elements with less smooth surface are obtained, which can lead to loss of amplification[18,19]. The problem may be visible in very high frequencies. Resolution of most of these methods limits the use of antennas for very high frequencies, because geometry is one of the most important parameters. There are also problems with relatively high resistance of conductive paths for FDM.

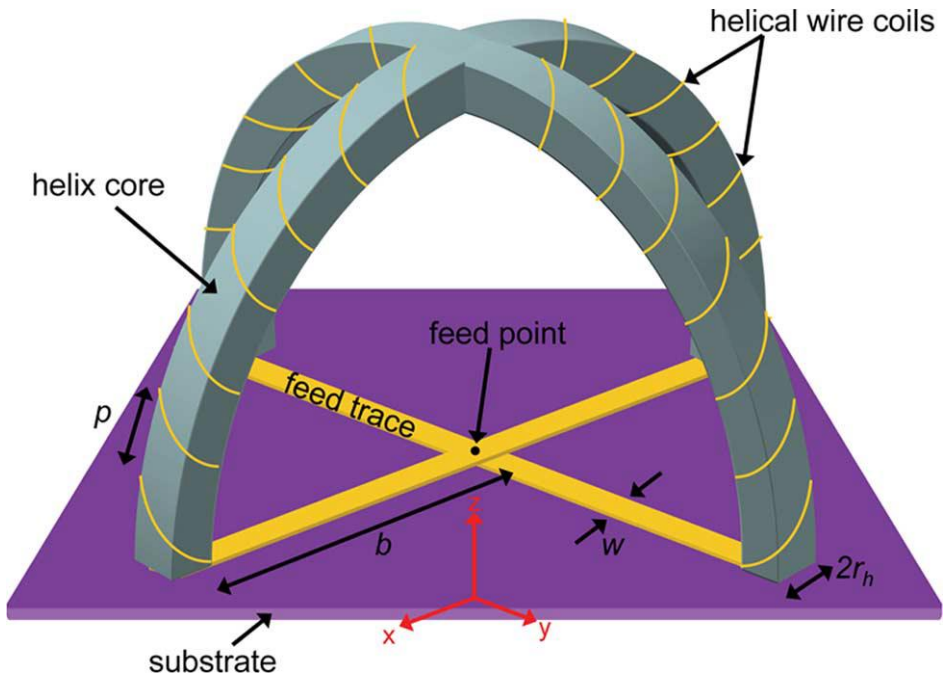

Figure 6. A monopole version of the 4-arm TM antenna.[17]

4. CONCLUSIONS

Relatively new production methods have proven that in the long term they can become very useful in the production of antennas. Especially for mobile and special purpose equipment. Screen printing, Ink-jet printing, flexography, FDM, SLS, EBM and others are able to significantly expand the range of available design solutions. Their use allows to meet the requirements of miniaturization or personalization of products. Further work on new inks, pastes and filaments as well as increased resolution can be expected in the near future. Due to the reduction of workload and good compatibility of prototypes with simulations, we can also expect further work on optimization of antennas geometry. In table below most important properties are shown. This data should be taken as indication of order of magnitude. Results always depends on many factors.

Table 1. Summary of the comparison[20]

	Materials that can be use	Resolution	Dimensions	Roughness
Chemical etching	Copper	High	2D	Plain
Ink-jet printing	Ink with: metals, graphene, carbon nanotubes, and other.	High (~20µm)	2D	Plain
Screen-printing	Paste with: metals, graphene, carbon nanotubes, and other	Low (~100µm)	2D	Plain
Flexography	Ink with: metals, graphene, carbon nanotubes, and other.	High (~20µm)	2D	Plain
Direct writing	Paste with: metals, graphene, carbon nanotubes, and other	Low	2D/3D	Plain
Fused Deposition Modeling	Filaments with metal powders	Low (~100µm)	3D	Rugged
Direct Metal Laser Sintering	Metals powders	Low (~100µm)	3D	Rugged
Direct writing with laser assistance	Paste with metals powders	-	3D	Rugged

REFERENCES

[1] Bogusz, J., "Anteny w urządzeniach przenośnych (1)," Elektronika Praktyczna, 3/2016, 102–106 (2016).

[2] Jagodzińska, K., "Zastosowanie anten drukowanych w miniaturowych urządzeniach radiokomunikacyjnych," ELECTROTECHNICAL REVIEW **1**(9), 116–119 (2016).

[3] Savi, P., Naishadam, K., Bayat, A., Giorcelli, M. and Quaranta, S., "Multi-Walled Carbon Nanotube thin film loading for tuning microstrip patch antennas," 2016 10th European Conference on Antennas and Propagation (EuCAP), 1–3 (2016).

[4] Kopyt, P., Salski, B., Olszewska-Placha, M., Janczak, D., Sloma, M., Kurkus, T., Jakubowska, M. and Gwarek, W., "Graphene-Based Dipole Antenna for a UHF RFID Tag," IEEE Transactions on Antennas and Propagation **64**(7), 2862–2868 (2016).

[5] Abutarboush, H. F. and Shamim, A., "A Reconfigurable Inkjet-Printed Antenna on Paper Substrate for Wireless Applications," IEEE Antennas and Wireless Propagation Letters **17**(9), 1648–1651 (2018).

[6] Sangoi, R., Smith, C. G., Seymour, M. D., Venkataraman, J. N., Clark, D. M., Kleper, M. L. and Kahn, B. E., "Printing Radio Frequency Identification (RFID) Tag Antennas Using Inks Containing Silver Dispersions," Journal of Dispersion Science and Technology **25**(4), 513–521 (2005).

[7] Guo, Z., Yang, G., Zhang, W., Liu, Q., Mo, L. and Li, L., "Application Research of Nano Silver Conductive Ink in Flexographic Printed RFID Antenna," Advances in Graphic Communication, Printing and Packaging, P. Zhao, Y. Ouyang, M. Xu, L. Yang, and Y. Ren, Eds., 480–487, Springer Singapore (2019).

[8] Skylar-Scott, M. A., Gunasekaran, S. and Lewis, J. A., "Laser-assisted direct ink writing of planar and 3D metal architectures," PNAS **113**(22), 6137–6142 (2016).

[9] Espera, A. H., Dizon, J. R. C., Chen, Q. and Advincula, R. C., "3D-printing and advanced manufacturing for electronics," Prog Addit Manuf (2019).

[10] Adams, J. J., Duoss, E. B., Malkowski, T. F., Motala, M. J., Ahn, B. Y., Nuzzo, R. G., Bernhard, J. T. and Lewis, J. A., "Conformal Printing of Electrically Small Antennas on Three-Dimensional Surfaces," Advanced Materials **23**(11), 1335–1340 (2011).

[11] "Heterophase materials for fused filament fabrication of structural electronics | SpringerLink.", <https://link.springer.com/article/10.1007/s10854-018-0391-4> (30 April 2019).

[12] Guennou-Martin, A., Quere, Y., Rius, E., Fourtinon, L., Person, C., Lesueur, G. and Merlet, T., "Design and manufacturing of a 3-D conformal slotted waveguide antenna array in Ku-band based on Direct Metal Laser Sintering," 2016 IEEE Conference on Antenna Measurements Applications (CAMA), 1–4 (2016).

[13] Colella, R., Michel, A. and Catarinucci, L., "Compact 3-D-Printed Circularly Polarized Antenna for Handheld UHF RFID Readers," IEEE Antennas and Wireless Propagation Letters **17**(11), 2021–2025 (2018).

[14] Pepłowski, A., "Tatuaże elektroniczne - elastyczne czujniki biomedyczne do monitorowania stanu zdrowia," ELECTROTECHNICAL REVIEW **1**(8), 137–139 (2017).

[15] Teeslink, T. S., Torres, D., Ebel, J. L., Sepulveda, N. and Anagnostou, D. E., "Reconfigurable Bowtie Antenna Using Metal-Insulator Transition in Vanadium Dioxide," IEEE Antennas and Wireless Propagation Letters **14**, 1381–1384 (2015).

[16] Vaseem, M., Su, Z., Yang, S. and Shamim, A., "Fully Printed Flexible and Reconfigurable Antenna With Novel Phase Change VO2 Ink Based Switch," 2018 International Flexible Electronics Technology Conference (IFETC), 1–2 (2018).

[17] Adams, J. J. and Bernhard, J. T., "Tuning Method for a New Electrically Small Antenna With Low Q," IEEE Antennas and Wireless Propagation Letters **8**, 303–306 (2009).

[18] Garcia, C. R., Rumpf, R. C., Tsang, H. H. and Barton, J. H., "Effects of extreme surface roughness on 3D printed horn antenna," Electronics Letters **49**(12), 734–736 (2013).

[19] Liang, M., Wu, J., Yu, X. and Xin, H., "3D printing technology for RF and THz antennas," 2016 International Symposium on Antennas and Propagation (ISAP), 536–537 (2016).

[20] Bahr, R., Tehrani, B. and Tentzeris, M. M., "Exploring 3-D Printing for New Applications: Novel Inkjet- and 3-D-Printed Millimeter-Wave Components, Interconnects, and Systems," IEEE Microwave Magazine **19**(1), 57–66 (2018).

Utilizing sugar based material in additive manufacturing

S. Ostrowski, L. Kołodziej, M. Słoma, M. Jakubowska, G. Wróblewski

Institute of Metrology and Biomedical Engineering, Warsaw University of Technology,
A. Boboli St. 8, Warsaw, Poland

ABSTRACT

Three dimensional structures made of sugar based materials can be utilized in tissue engineering since sugar serves as a nutrient for growing cells. It can also be applied in other areas of life like food industry or art. Following paper describes preparation of a material based on commonly used sucrose and proteins contained in chicken eggs. Furthermore a method of additive manufacturing with use of the mentioned material is also described. Method is based on a direct write 3D printing technology and was implemented by utilizing a low cost commercial 3D printer alongside with an industrial glue dispenser. The printed parts are then dried using UV light or a common oven and presented results are discussed.

Keywords: sugar, sucrose, additive manufacturing

1. INTRODUCTION

In an additive manufacturing process given materials are manipulated so they are successfully combined to a form of a desired object [1]. The final product of such process is constructed in a layer by layer fashion with each layer being deposited on top of the previous one. Three-dimensional CAD system is used in order to design a 3D model of an object. Later on this model is transferred into a CAM program which will process it into a set of commands for a 3D printer. On this stage all crucial process parameters are also determined. Among them, depending on a technology used, we can find height of each layer, temperature of a material, infill percentage, print speed, number of solid walls etc. Resulting set of commands can be put in a g-code format and usually contains information about manufacturing each layer with given z-axis movement in between layers.

Nowadays many additive manufacturing techniques utilizing different forms of materials can be found. Most accessible devices due to low cost and compact dimensions are Fused Deposition Modelling (FDM) printers. In that process a pre-manufactured polymer filament with fixed diameter is heated to a point of an increased plasticity and forced through a nozzle with a much smaller diameter. The movements of that nozzle combined with a movement of an extruding motor will draw an object one line at a time until a desired model is completed. Technique can utilize materials like polyactic acid (PLA), acrylonitrile butadiene styrene (ABS), thermoplastic polyurethane (TPU) [2]. Other processes use material in a form of powder. Selective laser melting (SLM) and Binder jetting are examples of that. In both of them the powder is distributed evenly on a flat surface. The former uses laser beam to selectively melt a portion of powder which hardens and adheres to the rest of a structure. The latter uses binding material to selectively glue together small portions of powder in order to create a solid structure. Both processes utilize a wide spectrum of materials like metal alloys and composite with Binder Jet being said to work with any kind of material that can be put in a form of powder [3]. Stereolithography (SLA) is a technology that utilizes photopolymer resin and an ultra violet laser in a 3D-printing process. UV laser selectively hardens the resin, therefore creating a 3D structure. SLA can deliver most accurate but usually relatively small and not very durable parts [4]. Finaly Direct Write is a technology in which viscous material usually put in some sort of container like a syringe is applied on substrate, for instance by a pneumatic system [5]. Resolution vary depending on a nozzle used. Solidification of a material can happen by solvent evaporation or cooling [6].

Utilizing additive manufacturing in food industry has been a goal of various studies [7,8]. Sweetest CNC machine [9] was developed as a part of educational workshop at Architectural Association Visiting school in Hong Kong. It showed approach similar to FDM printers with material in a form of powdered sugar being melted in a machine's head and then extruded through a nozzle. Candyfab [10] on the other hand in its approach is closest to SLM machines. Powdered sugar is distributed evenly on a flat surface and selectively hardened by applying heat, in that case with use of industrial heat

Photonics Applications in Astronomy, Communications, Industry, and High-Energy Physics Experiments 2019,
edited by Ryszard S. Romaniuk, Maciej Linczuk, Proc. of SPIE Vol. 11176, 1117659
© 2019 SPIE · CCC code: 0277-786X/19/$21 · doi: 10.1117/12.2536831

gun instead of laser. Chefjet [11] utilizes binder jet technology. It can produce accurate models with machine's head delivering adhesive for gluing material, along with RGB coloring and flavor additives.

2. MATERIAL DEVELOPMENT AND CHARACTERISTICS

2.1 Material development

Material utilized in the developed process was a mixture of powdered sugar and proteins contained in a common chicken egg white. It is already used in a food industry and called royal icing, however in case of this study it contained a higher concentration of sugar and did not have any additives beyond sugar and egg white like food coloring or lemon juice. These additives are considered optional but not crucial for the described additive method to function. Egg white contains 87.5% of water and 10.9% of proteins. Remaining 1.6% are carbohydrates and other substances [12].

Figure 1. Preparation of a material.

Material was prepared in a process of foaming egg white and successfully adding portions of powdered sugar. The goal was to achieve the highest possible concentration of sugar in a mixture. Final material contained 84% of powdered sugar and 16% of egg white, which could be divided into approximately 14% water and 2% proteins. Water would evaporate later in the curing process therefore hardening the material that should contain approximately 97.5% of sugar after curing. A common kitchen aid machine was used in the process of foaming egg white.

2.2 Material characteristics

Next stage was to test characteristics of made material. At this stage modified 3D-printer described later in this scope was not yet constructed. In order to check if material is possible to print with in Direct Write technology, it was put in a plastic syringe and then slowly applied on a paper substrate by hand. The results can be seen in figure 2. It was possible to doze the material through a syringe and it was dense enough to put several layers of it on top of each other without collapsing the structure. The bridge structure was also made by hand as it is often described as hard to print for instance in FDM technology. Bridge was visibly curved towards the bottom but remained stable.

Figure 2. Test with a bridge structure.

During tests also several disadvantages of working with such material were seen. Firstly it is worth mentioning that dozing material through a syringe was only possible while it still contained enough water. If it was left uncovered for as short as 5 minutes it was long enough for some water to evaporate rendering material useless for the printing process. Therefore it is important to either cover the material or keep it in a controlled environment with high humidity and decreased temperature.

Figure 3. Collapsed structure

Furthermore shortly after dozing material was not stiff enough to keep larger structures from collapsing, which is shown in figure 3. At that stage it already indicated that it will be required to at least partially cure the material while printing larger parts.

3. DEVICE DESCRIPTION

For the purpose of this study a modified FDM 3D-printer with an attachment of an industrial glue dispenser was utilized in order to additively manufacture test structures for the developed material. Printing station is shown in figure 4.

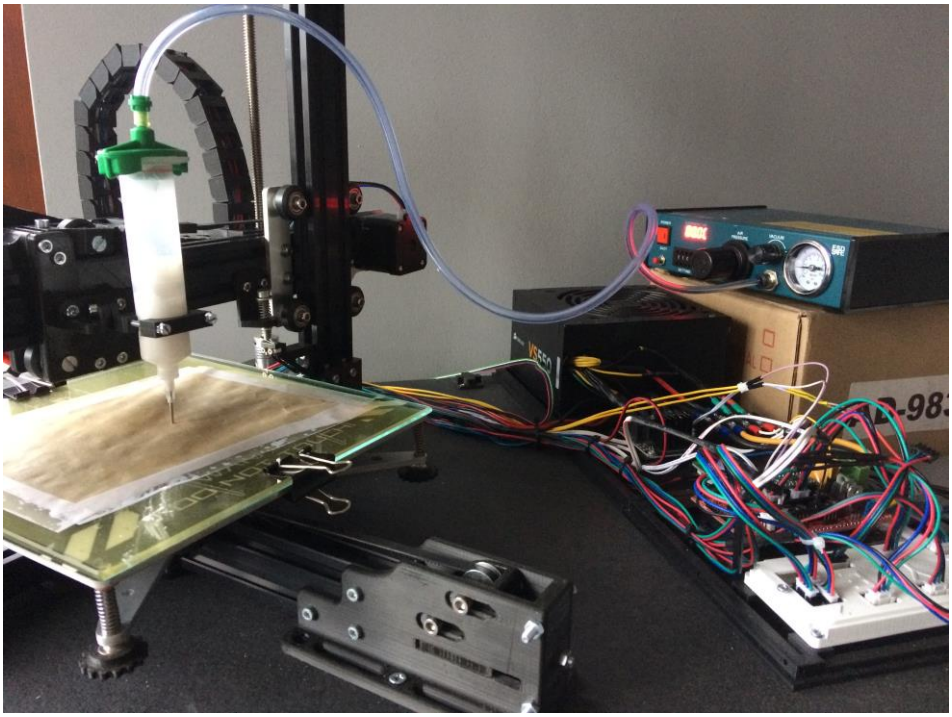

Figure 4. Printing station.

Main modification of the device consisted of replacing printer's head with a syringe and an extruder motor with a pneumatically controlled glue dispenser. Dispenser had an external socket for a mechanical switch which was used to connect it to the printer's mainboard. The intensity of material dosage had to be adjusted manually by changing pressure on a compressor. Pressure was set to 1.6 atm and was not changed throughout the process. Nozzle diameter was chosen to be 1.4mm.

Test models were processed through Cura engine – popular slicer designed for FDM printers. Its wide range of options and customization allowed to adjust it for the purpose of this study.

Table 1. Input parameters for Cura engine that were adjusted in relation to typical ones.

Parameter	Typical value	Used Value
Nozzle diameter	0.1 – 0.6 mm	1.4 mm
Print speed	20 – 100 mm/s	45 mm/s
Layer height	0.2 mm	0.8 mm
Printing temperature	180 – 250 °C	Not applicable
Top layers	1 – 4	0

4. RESULTS AND DISCUSSION

First trials were unsuccessful mainly due to air bubbles being contained in a syringe. It caused material to stop being continuously dispensed during the printing process, which rendered the final part empty in these points. Result is shown in figure 5. In order to avoid the problem, material has to loaded into the syringe in a way that minimizes the amount of air bubbles. Loading it first into the plastic bag and then extruding directly into the syringe proved sufficient.

Empty cylinder with a single layer foundation and a single line wall was printed in order to check how tall structures can be printed without any curing during the process. It is shown in figure 6. Structure had begun to fall down at the height of 15 mm and it collapsed completely later during the print. It clearly indicates that it is required to cure the material during the print just after it is released from a nozzle. In FDM printers it is common to use additional fan in order to cool material faster. Similar approach could be undertaken here in order to cure material with an increased temperature.

Figure 5. Print failed due to air bubbles.

Printed samples were cured in 80°C for 10 minutes which made them hard enough to take off a paper substrate and touch with a hand without damaging it. One sample was also dried using UV light which made its surface hard enough to support more material without collapsing.

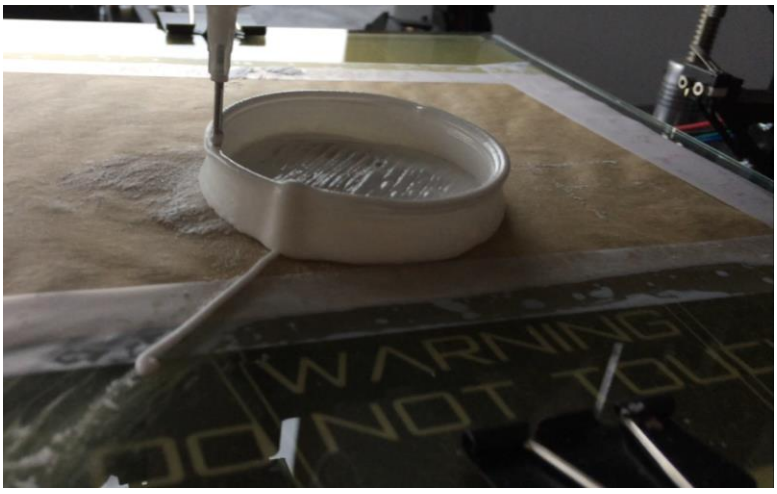

Figure 6. Height test.

Printed samples were cured in 80°C for 10 minutes which made them hard enough to take off a paper substrate and touch with a hand without damaging it. One sample was also dried using UV light which made its surface hard enough to support more material without collapsing. This shows that UV light treatment during the print might be an optimal way to maintain the process.

Rectangular shape sample was printed with commonly used line infill so the resolution could be easily compared to FDM printers. It is shown in figure 7. Part was then cured in an oven for 10 minutes and then left to completely dry at room temperature for several days. Sample was visibly harder than just after curing.

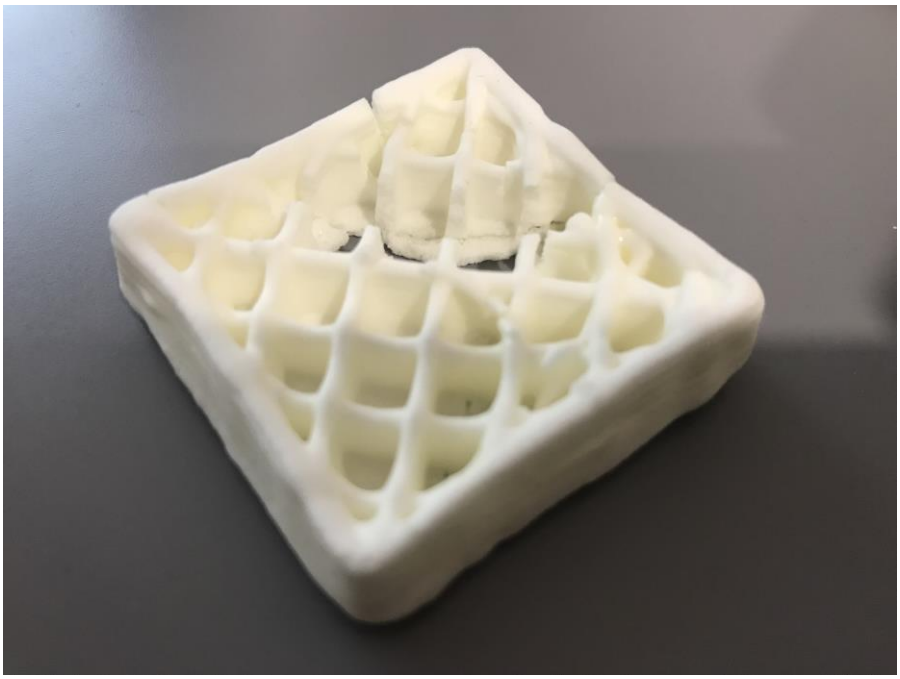

Figure 7. Sample after several days of drying at room temperature.

5. CONCLUSIONS

In this article a process of producing a sugar based material that is compatible with Direct Write 3D-printing technology is described. Furthermore a prototype device consisting of a FDM printer and an industrial glue dispenser is used to print sample parts to test the material. Several problems including material collapsing and air bubble contamination are described and solutions are proposed.

Presented method of additively manufacturing sugar parts is relatively fast. Applying an active curing during the printing process and increasing resolution by utilizing smaller nozzle diameters and possibly changing the dispensing system to mechanical or hydraulic should be the next steps in its further development.

REFERENCES

[1] Chua, C., Leong, K., Lim, C., Rapid prototyping, World Scientific, Singapore (2010).

[2] Yu, D., Zhu, C., Su, J., Wang, D., "Process Analysis and Application for Rapid Prototyping Based on Fused Deposition Modeling", Advanced Materials Research 179-180, 875-880 (2011).

[3] Gokuldoss, P., Kolla, S., Eckert, J., "Additive Manufacturing Processes: Selective Laser Melting, Electron Beam Melting and Binder Jetting—Selection Guidelines", Materials 10(6), 672 (2017).

[4] Bens, A., Seitz, H., Bermes, G., Emons, M., Pansky, A., Roitzheim, B., Tobiasch, E., Tille, C., "Non-toxic flexible photopolymers for medical stereolithography technology", Rapid Prototyping Journal 13(1), 38-47 (2007).

[5] Holzman, N., Francis, L., "Pneumatic System Design for Direct Write 3D Printing.", Research Gate (2017).

[6] Wu, W., Lewis, J., Lewis, J., White, S., Sottos, N., Braun, P., Direct ink writing of microvascular networks, University of Illinois, Urbana, IL. (2011).

[7] Lipton, J., Cutler, M., Nigl, F., Cohen, D., Lipson, H., "Additive manufacturing for the food industry", Trends in Food Science & Technology 43(1), 114-123 (2015).

[8] Sun, J., Peng, Z., Zhou, W., Fuh, J., Hong, G., Chiu, A., "A Review on 3D Printing for Customized Food Fabrication", Procedia Manufacturing 1, 308-319 (2015).

[9] "AAVS 2016 – Sweetest CNC Machine.", Victor Leung, 2019, <http://www.victorleung.info/post/aavs-2016-sweetest-cnc-machine/> (10 April 2019).

[10] "CandyFab | A DIY 3D Sugar Printer.", Candyfab.org, 2019, <https://candyfab.org/> (9 April 2019).

[11] "Culinary 3D Printing | 3D Systems.", 3D Systems, 2019, <https://www.3dsystems.com/culinary> (9 April 2019).

[12] "Food Composition Databases Show Foods -- Egg, white, raw, fresh.", Ndb.nal.usda.gov, 2019, <https://ndb.nal.usda.gov/ndb/foods/show/01124?n1=%7BQv%3D1%7D&fgcd=&man=&lfacet=&count=&max=25&sort=default&qlookup=egg+white&offset=&format=Full&new=&measureby=&Qv=1&ds=&qt=&qp=&qa=&qn=&q=&ing=> (5 April 2019).

Optimization of cutting data of nickel-based sintered materials turning

Ksenia Rumian[a] , Wojciech Zębala[a]
[a]Production Engineering Institute, Cracow University of Technology, Al. Jana Pawła II 37, 31-864 Cracow

ABSTRACT

The paper describes the method of cutting parameters optimization for the case of turning a sintered powder materials, which are based on nickel. During the cutting process the temperature, cutting force, tool wear and surface roughness Ra measurements were made. The test results are presented in the form of graphs, photos and tables.

Keywords: Turning, Taguchi, specific cutting force, sintered nickel alloy, optimization

1. INTRODUCTION

Machining is currently the most popular technology to create the tools. The development of machining is one of the factors which contributed to decreasing in production and machining costs [1,2,3]. The other factors which allowed such great decrease are the development of the new materials, tools and machine tools. At the same time, there is an ever increasing need for the greater efficiency of the machining process in numerous branched of the modern industry. This concerns particularly aircraft and automobile industries, which require higher quality of manufactured parts [4]. Machining process of difficult-to-cut materials must be digitally modelled and simulated. Computer software, which is based on the finite element method, is mostly used as optimization methods for the machining process. To improve the machining process, the control of the following parameters must be applied: cutting force, stresses and temperature within the chip formation zone. A special focus is directed towards the factors determining the quality of the machining process, such as surface roughness, force value and tool wear during the difficult-to-cut material machining [3,5-9].

The most important characteristics of nickel - alloys are high hardness, the ability to cure material inside the zone, high durability in high temperature, the susceptibility to reacting with tools (formation of the build-ups on the cutting edges) and low thermal conductivity [2]. The nickel based alloys are difficult to cut despite their good structural properties. Inconel 718 is characterized by high hardness in the increased temperature, which causes high resistivity during cutting. This alloy tends to harden within the surface layer. Low thermal conductivity results in high temperature in the cutting zone.

Cutting tools can be made of the following building materials: ceramics (oxide, non-oxide or mixed), cermets, ultra-small grain sintered carbonates, synthetic diamonds and cubic boron nitride (CBN). Polycrystalline cubic boron nitride is a material which is characterized with the exceptional hardness in the elevated temperatures and the compressive strength while still with a good fracture toughness. It is used during the machining of the nickel based materials and the parts with high development accuracy. CBN does not lose rapidly its hardness in the elevated temperatures in contrast to the diamond. The turning of the materials based on nickel, and the optimization of the machining of the Inconel 718 were analysed extensively by the scientists. The optimization of the machining of such materials was considered including different criteria of e.g. surface roughness [3,4,10], maximization of the durability period of the cutting edge and the minimization of the costs of the manufacturing [11]. The Taguchi Grey Relation Analysis (TGRA) approach was proposed by the authors [12,13,14] to optimize the high-speed turning. The problem of choosing the optimal cutting parameters is complicated because of the high number of limitations of the machining process (e.g. relating to the machine tool, tool required by the condition of the material surface). The majority of the authors is focusing in their research on the choice of the parameters

Photonics Applications in Astronomy, Communications, Industry, and High-Energy Physics Experiments 2019, edited by Ryszard S. Romaniuk, Maciej Linczuk, Proc. of SPIE Vol. 11176, 111765A
© 2019 SPIE · CCC code: 0277-786X/19/$21 · doi: 10.1117/12.2536835

for the moulded materials [14]. Only a few papers were published concerning the turning of the sintered materials based on nickel [15,16].
This paper presents investigations for the purpose to optimize the cutting data of nickel based sintered materials turning.

2. RESEARCH

The main thesis of this work is that there is a range of cross-section of the cutting layer, in which the specific cutting force of the cutting decreases with the increase of the volumetric productivity (Fig.1).

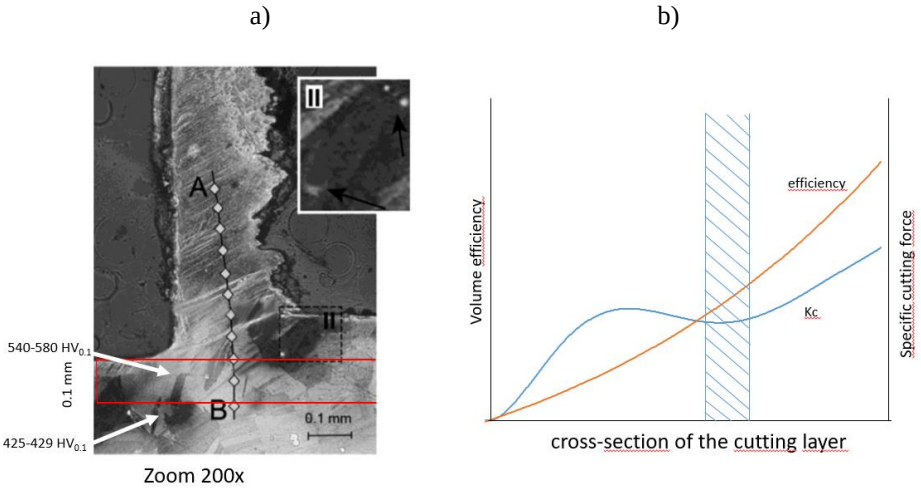

Figure 1. The photo of cutting zone (chip and surface layer) (a) and conceptual diagram of specific cutting force (b).

In order to achieve that goal, two main stages of the experiment were assumed. The first stage are preliminary experiments, which include a comparison of turning of the casted Inconel 718 alloy with the one prepared as a sintered nickel based material, Fig.2.

The basic characteristics of the machining tests are presented in the Table 1. Turning of the nickel based material was made with CBN tools.

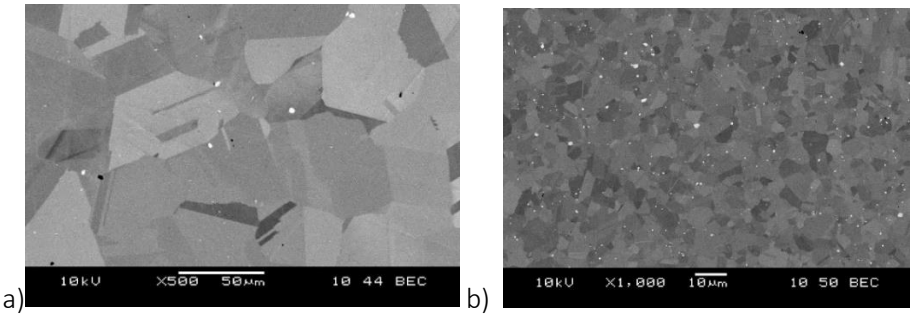

Figure 2. Microstructure a) Inconel 718 alloy, enl. 500x b) Sintered nickel material, mag. 1000x.

3. PLAN OF THE PRELIMINARY EXPERIMENTS

The Taguchi research plan was selected for the implementation of experimental research. The Taguchi method can be used for optimisation of both new process, as well as for perfecting of the process that already exists. The method offers a solution to three problems: how to estimate quality of efficient costs, how to keep the costs under control at an efficient level, and how to estimate quality. In our research, we use “the smaller is the better" (minimize) method.

The cutting speed, feed, cutting edge wear and corner rounding angle were changing. Data concerning cutting parameters, research plan and results are presented in Table 2.

Table 2. Taguchi’s experimental plan and input and output parameters

	v_c	f	VB	r_n	T_{sym_VBi}	Fc_{sym_VBi}	Ff_{sym_VBi}
	[m/min]	[mm/rev]	[mm]	[mm]	[°C]	[N]	[N]
1	160	0.05	0.0	0.01	1212	130	80
2	160	0.075	0.0	0.01	1192	160	148
3	160	0.1	0.0	0.01	1205	191	233
4	160	0.05	0.0	0.01	1219	202	264
5	180	0.075	0.0	0.01	1227	131	83
6	180	0.1	0.0	0.01	1223	154	149
7	180	0.05	0.0	0.01	1212	181	219
8	180	0.075	0.0	0.01	1217	197	264
9	200	0.1	0.0	0.01	1241	127	76
10	200	0.05	0.1	0.03	1245	159	158
11	200	0.075	0.1	0.03	1221	179	219
12	200	0.1	0.1	0.03	1228	203	266
13	160	0.05	0.1	0.03	1176	155	113
14	160	0.075	0.1	0.03	1191	174	170
15	160	0.1	0.1	0.03	1188	205	216
16	160	0.05	0.1	0.03	1156	249	283
17	180	0.075	0.1	0.03	1210	162	108
18	180	0.1	0.1	0.03	1216	195	188
19	180	0.05	0.2	0.05	1236	216	224
20	180	0.075	0.2	0.05	1204	250	284
21	200	0.1	0.2	0.05	1223	153	110
22	200	0.05	0.2	0.05	1222	194	182
23	200	0.075	0.2	0.05	1228	214	225
24	200	0.1	0.2	0.05	1206	248	282

	v_c	f	VB	r_n	T_{sym_VBi}	Fc_{sym_VBi}	Ff_{sym_VBi}
	[m/min]	[mm/rev]	[mm]	[mm]	[°C]	[N]	[N]
25	160	0.05	0.2	0.05	1174	247	197
26	160	0.075	0.2	0.05	1177	273	246
27	160	0.1	0.2	0.05	1158	302	293
28	160	0.05	0.3	0.07	1187	315	310
29	180	0.075	0.3	0.07	1192	239	190
30	180	0.1	0.3	0.07	1178	271	253
31	180	0.05	0.3	0.07	1174	303	289
32	180	0.075	0.3	0.07	1178	314	314
33	200	0.1	0.3	0.07	1209	244	183
34	200	0.05	0.3	0.07	1224	269	240
35	200	0.075	0.3	0.07	1216	305	288
36	200	0.1	0.3	0.07	1232	316	316

In order to carry out the experiments, a test bench based on lathe KNUTH Masterturn 400 was made (Fig.3). It allowed to verify experimentally the results of the simulation of the cutting process. A measurement of the components of the cutting force, parameters of the machined surface (roughness) and temperature within the machining zone was executed.

Measuring equipment:

- Thermographic camera Flir SC620 with software TermaCam Researcher Pro,
- Dynamometer of Kistler type 9257B, charge amplifier, Kistler, type 5070B together with the software DynoWare,
- High-speed camera Vision Researcher Phantom v5.2 equipped with lens Nikon AF Mikro-Nikkor 200 and Dedocool Cool Light Kit,
- Portable Surface Roughness Tester Surftest SJ-201P, Mitutoyo, profilometer Intra, Taylor-Hobson.

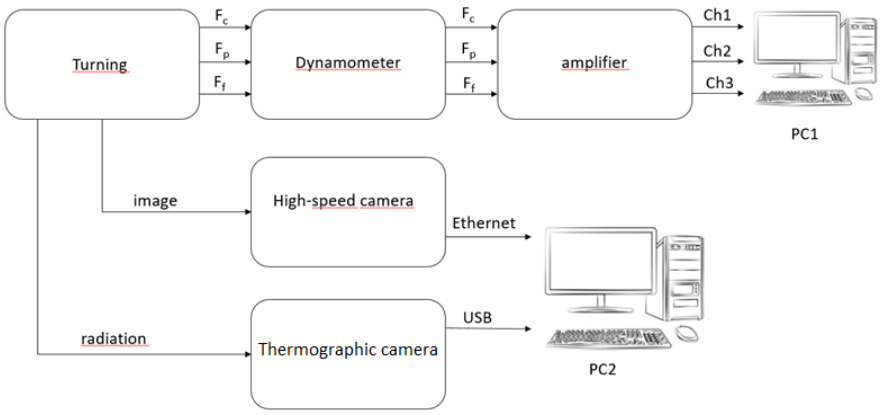

Figure 3. Research stand.

The development of the Johnson-Cook experimental equation (JC) was one of the most important achievements in the field of the theoretical research on the behaviour of the solids under dynamic loads [17]. This equation depicts the behaviour of the materials subjected to the dynamic loads. It includes the influence of the size of the deformation, the speed of the deformation and the temperature on the value of the yield point. The main reasons of the popularity of this equation are its simplicity, small number of the factors and relatively easy methods of their determination.

The material model was built based on the Johnson-Cook equation (1). The values of factors were taken from literature.

$$\sigma(\varepsilon, \dot{\varepsilon}, T) = (A + B\varepsilon^n)\left(1 + Cln\left(\frac{\dot{\varepsilon}}{\dot{\varepsilon}_0}\right)\right)\left(1 - \left(\frac{T-T_R}{T_m-T_R}\right)^m\right) \quad (1)$$

where: A - yield point for: deformation speed $\dot{\varepsilon}_o$ and temperature T_R,

B,n – the factor of strain strengthening,

C – dynamic strengthening factor

T_m – melting temperature.

4. RESULTS AND DISCUSSION

Simulations

Simulations of the cutting process were carried out in a program which uses the finite element method. The material model was built based on the Johnson-Cook equation. The results are presented in graphs below (Fig.4,5).

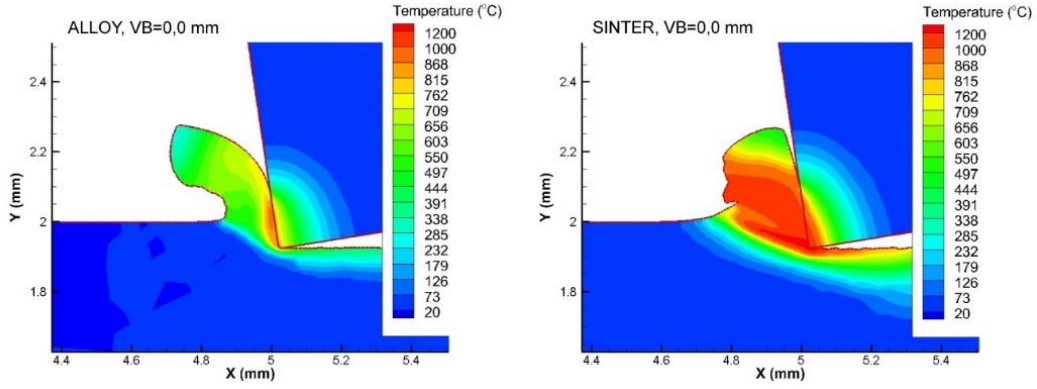

Figure 4. Distribution of temperature in the cutting zone for nickel alloy (left side) and sintered nickel based material (right side). Cutting parameters: v_c = 160 m/min; f = 0,075 mm/rev; a_p = 0,5 mm. Tool geometry: γ = - 8,5° and α =7°.

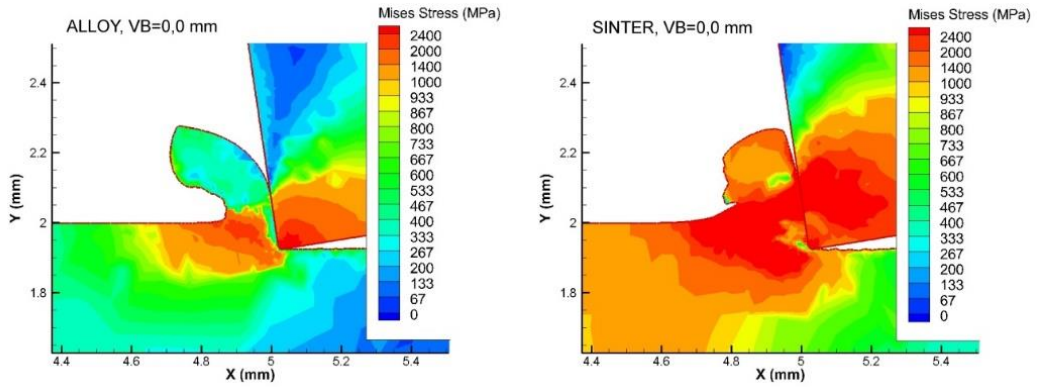

Figure 5. Distribution of stress according to Huber-Mises-Hencky (HMH) hypothesis in cutting zone for nickel alloy (left side) and sintered nickel base material (right side). Cutting parameters: v_c = 160 m/min; f = 0,075 mm/rev; a_p = 0,5 mm. Tool geometry: γ = - 8,5° and α =7°.

Experiments

For each shaft made of the sintered material based on nickel, 20 tests were carried out in accordance with the test plan and several additional tests for Inconel 718 alloy. Due to the large number of the results, only a part of them was presented below (Fig 6,7,8).

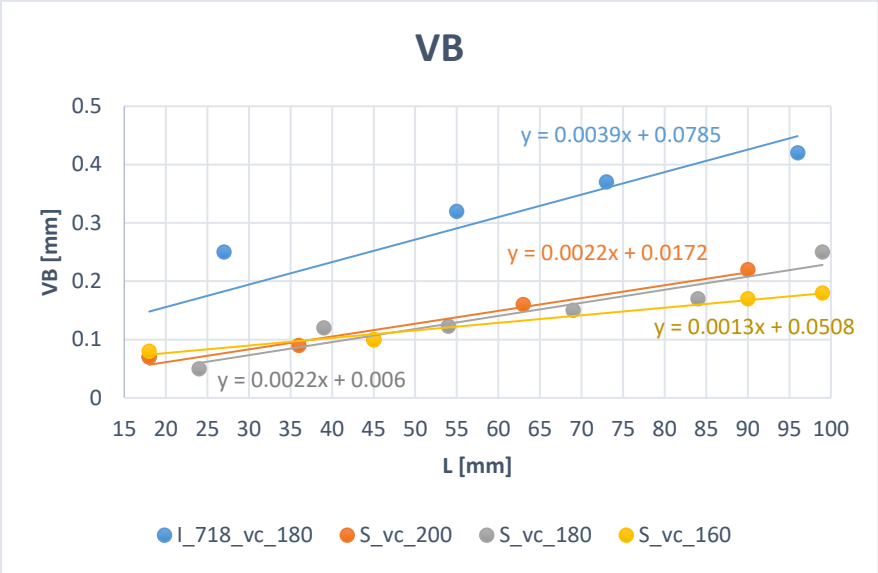

Figure 6. Cutting edge wear VB for sintered material for different cutting speed.

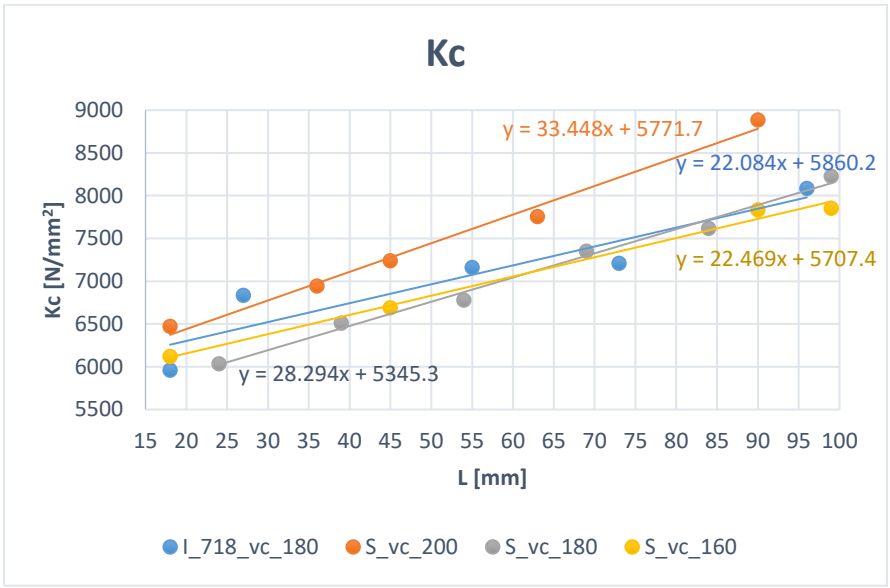

Figure 7. Specific cutting force *Kc* for sintered material for different cutting speed.

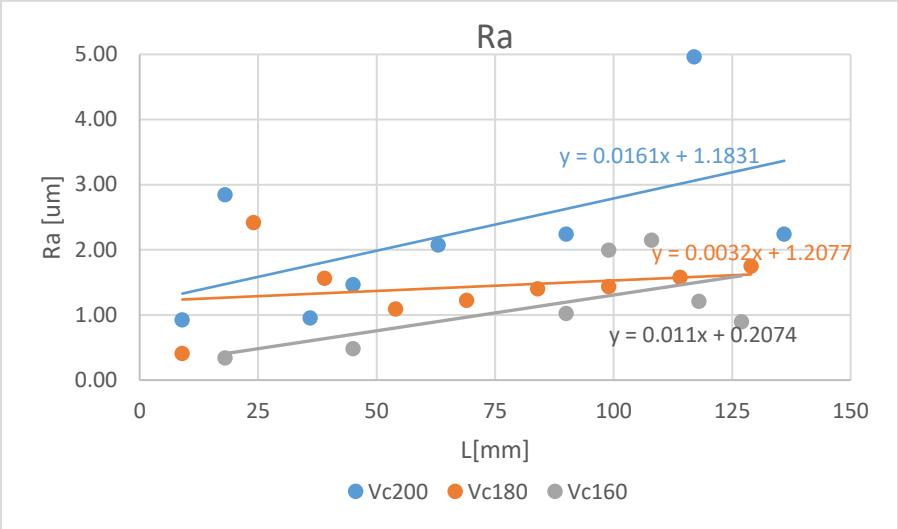

Figure 8. Surface roughness Ra for the sintered material for different cutting speed.

The figure above shows that the results are changing for different cutting parameters and different materials. The specific cutting force *Kc* is similar for each case for sintered materials. The surface roughness is different for every case, however for lower cutting speed it is better.

5. CONCLUSION

Based on the previous analyses, the following conclusions can be presented:

- Cutting edge wear is higher for Inconel 718 alloy in the initial phase of the cutting process.
- For sintered material the specific cutting force *Kc* is growing linearly together with the increase of the cutting length and the wear of the tools for higher cutting speed.
- In the case of the Inconel 718 alloy machining, the curve, which describes the dependency of the specific cutting force from the cutting length, is non-linear and is changing.
- Surface roughness Ra of the machined surface for the sintered material increases during the cutting, for the whole range of the cutting speed values.
- The sintered material treatment results in significantly higher temperatures and reduced strain according to Huber-Mises-Hencky (HMH) hypothesis.

REFERENCES

[1] Zębala, W., Kowalczyk, R., Matras, A., “Analysis and optimization of sintered carbides turning with PCD tools,” Procedia Engineering Vol. 100 p. 283-290 (2015)
[2] Szablewski, P., Weiss, E., Chwalczuk, T., "Rozwój obróbki materiałów trudnoskrawalnych, " Mechanik z. 8-9 (2016)
[3] Choudhoury, I. A., El-Baradic, M. A., “Machinability of nickel-base super alloys: a general review. Materials Processing Technology,” 77:278–284 (1998)
[4] Zębala, W., Struzikiewicz, G., Rumian, K., Plaza, M., “Simulation and optimization of physical phenomena when engine block machining: Case study,” Proceedings of SPIE - The International Society for Optical Engineering, Vol. 10031 Article number 100310O (2016)

[5] Arunachalam, R. M., Mannan, M. A., “Machinability of nickel-based high temperature alloys. Machining Science and Technology,” 4:127-168 (2000)
[6] Choudhoury, S. K., Appa Rao, I. V. K., “Optimization of cutting parameters for maximizing tool life,” International Journal of Machine Tools & Manufacture 39:343-353 (1999)
[7] D’Addona, D., Segreto, T., Simeone, A., Teti, R. ANN., “Tool wear modelling in the machining of nickel superalloy industrial products,” CIRP Journal of Manufacturing Science and Technology 4:33–37 (2011)
[8] Devillez, A., Schneider, F., Dominiak, S., Dudzinski, D., Larrouquere, D., “Cutting forces and wear in dry machining of Inconel 718 with coated carbide tools,” Wear 262:931–942 (2007)
[9] Narutaki, N., Yamane, Y., “Machining of difficult-to-cut materials. International Journal of the Japan Society for Precision Engineering,” 27:307-310(1993)
[10] El-Hossainy, T. M., El-Zoghby, A. A., Badr, M. A., Maalawi, K. Y., Nasr, M. F., “Cutting Parameter Optimization when Machining Different Materials,” Materials and Manufacturing Processes 25:1101-1114 (2010)
[11] Struzikiewicz, G., Otko, T., “Dependence of shape deviations and surface roughness in the hardened steel turning,” Key Engineering Materials 581, 443-448 (2014).
[12] Kowalczyk M., “Application of Taguchi method to optimization of surface roughness during precise turning of NiTi shape memory alloy,” Proc. of SPIE 104455, 1-10 (2017)
[13] Struzikiewicz, G., Zębala, W., Rumian K., “Application of Taguchi method to optimization of cutting force and temperature during turning of difficult to cut materials,” Key Engineering Materials 686, 114-118 (2016).
[14] Pawade, R. S., Joshi, S., “Mechanism of chip formation in high-speed turning of Inconel 718,” Machining Science and Technology 15:132-152 (2011)
[15] Fuys, R. A., Craig, R. G., Asgar, K., “Characterization of porosity of isostatically pressed and sintered nickel-base powdered metal,” Journal of Oral Rehabilitation, Volume 3, pages 217-226 (1976)
[16] Ergin, N., Ozdemir, O., Demirkiran, S., Sen, S., Sen U., “Synthesis of Inconel 718 Superalloy by Electric Current Activated Sintering,” Proceedings of the 4th International Congress APMAS2014, April 24-27, Fethiye, Turkey (2014)
[17] Johnson, G. R., Cook, W. H., “A constitutive Model and Data for Metals Subjected To Large Strains High Strain Rates and High Temperatures,” Proceedings of the 7th International Symposium on Ballistics, The Hauge, The Netherlands (1983)

Mechanical and thermal properties of ABS/iron composite for fused deposition modeling

B. Podsiadły*[a], A. Skalski [a], M. Słoma [a]
[a]Warsaw University of Technology, Faculty of Mechatronics, Institute of Metrology and Biomedical Engineering, Micro- and Nanotechnology Division, 8 sw. A. Boboli st., 02-525 Warsaw, Poland
*b.podsiadly@mchtr.pw.edu.pl

ABSTRACT

Fused deposition modeling is one of the most popular methods of additive manufacturing (AM). Typically, the thermoplastic polymer in the form of filament is melted in extrusion head and deposited layer by layer to fabricate object directly from 3D model data. Nowadays, FDM technology is also used to fabricate much more complex elements, like structural electronics or 3D printed electronics. Due to that, there is a necessity to develop new composite materials for this technology. In this work, an acrylonitrile butadiene styrene(ABS)/iron powder composite filament for use in 3D printing was fabricated by a two-stage solvent assisted processing method. Homogenously distributed iron powder in filaments with a filler content of 30 and 50 vol %, were fabricated using a single screw extruder machine. A static tensile test was carried out on samples printed from the developed composite materials. To demonstrate the thermal performance of 3D printed elements made with developed composites, exemplary heatsinks were printed. To exposed differences in thermal conductivity depending on iron powder contain, infrared thermography of printed objects was used. The results obtained were compared with the results for pure ABS prints. The research has shown that increasing filler content in composite filament decreases maximum engineering stress of materials but at the same time increase its thermal conductivity. Developed composites can be used to 3D print complicated and complex shaped heatsinks to improve thermal properties of 3D printed electronic circuits and objects.

Keywords: 3D printing, composites, additive manufacturing, fused deposition modeling, thermal properties, mechanical properties

1. INTRODUCTION

Additive manufacturing (AM) is dynamically and rapidly growing group of technologies used not only for prototyping reasons but also to produce complicated and complex components. The development of these technologies has had a huge impact on many industries.[1,2] In opposition of traditional, subtractive manufacturing methods, in additive manufacturing elements are made directly from a digital model, incrementally layer by layer. Thanks to that unique feature, AM technology allows producing complex and customized elements without the need for additional tooling, reducing the number of steps from project to ready component thereby cutting down manufacturing time and the cost. According to the addictive nature of this technology also the amount of waste is lowered.[3] Among all of the AM technologies, Fused Deposition Modeling (FDM) is the most popular and widely used printing technology. FDM is characterized with low cost of machines and materials, simplicity and a wide variety of available materials.[4] In FDM technology, thermoplastic material, in form of a filament, is melted in extrusion head and push through of the nozzle. The nozzle is moving in the X-Y axis and the layer of the object is put on the working platform. After that, the platform is moving down by the layer height and the next layer is deposited. Repeating this process allows to fabricate three-dimensional, physical element. Nowadays, the range of materials that can be used in this technology rapidly increase. To expend the applicability of 3D printing, new materials are developed including polymer matrix composites filaments with different fillers. Depending on the properties need to be improved, different fillers have to be added to the polymer matrix of composites. To improve the mechanical properties of 3D printed objects, for example, ABS/montmorillonite nanocomposite has been developed.[5] Other examples of composites with special properties are composites with enhanced dielectric properties - MWCNTs/BaTiO3/PVDF, ABS/BaTiO3 composites,[6,7] thermal properties – ABS/Cu, Nylon/Fe[8,9] but the largest number of researches has been carried out to develop filaments with low electrical resistivity. Composites with filler in form of copper powder,[10] graphene,[11] carbon nanotubes,[12,13] graphene oxide,[14] reduce graphene oxide[15] were developed and

Photonics Applications in Astronomy, Communications, Industry, and High-Energy Physics Experiments 2019, edited by Ryszard S. Romaniuk, Maciej Linczuk, Proc. of SPIE Vol. 11176, 111765B
© 2019 SPIE · CCC code: 0277-786X/19/$21 · doi: 10.1117/12.2536837

characterized with improved electrical properties and low resistivity. Thanks, due to the rising number of composites filaments, FDM technologies can be used to fabricate 3D printed and structural electronics.

In this paper, developing process of ABS/iron composite filament has been described. The aim of our research was to fabricate filament with enhanced thermal properties which can be used to 3D printing of complex heat sinks in structural electronics objects. While using special filaments to fabricate conductive elements with FDM technology, additional heat is produced when electrical current flow through it. As our previous research demonstrates, composite filaments have maximum current that can flow through it before it starts to melt and lost its electrical properties. [10] To improve the maximum power that can handle 3D printed conductive elements, heat sinks have to be used to dissipate the heat generated. An efficient solution to achieve that is using a composite with good thermal properties to 3D print heat sink directly on conductive paths, in the same process. To fabricate composite with optimal properties several challenges need to be overcome. First, microparticles of filler must be homogeneously distributed within the filament. Second, the composite filament has to be strong and not brittle such can be easily fed into the extrusion nozzle during the 3D printing process. Third, an increasing amount of filler causes an increase of composite viscosity when melted which cannot be too high as to cause a clogging the nozzle and stopping printing process.[16–18]

Bearing in mind above challenges, we report the development of new ABS/iron composite filaments containing up to 40 vol % of filler. To fabricate homogenous composite filament, multiple extrusion using single screw extruder has been performed. Investigated filaments demonstrate stable diameter, smooth surface, no porosity, and good printability. ABS/Fe composites were characterized by mechanical and thermal properties. To discover practical usability of fabricated filament, test heat sinks were printed and examine.

2. EXPERIMENTAL METHODS

2.1 Materials

ABS granulate was supplied by Plastspaw (Poland). The density of the used polymer is 1.05g/cm^3 and mass flow index is 6.6/10min (220 °C/10.0 kg). MH300.29 iron powder was purchased from Höganäs (Sweden). The iron powder was subjected to sieve analysis to assess the particle size distribution. In the process of developing composite filaments, only gradation less than 40 μm were used.

2.2 Pellet preparation

Composites were prepared by two-step solvent assisted process. Firstly, the right amount of ABS granulate was measured and acetone as dissolvent was added. The polymer was left in room temperature for 24 hours to dissolve. After polymer dissolve, the iron powder was added to the mixture. The solution was then mechanically mixed to achieve a homogenous composite. Composite prepared that way was poured out to glass container with big basis surface and put into the dryer set on 80 °C to rapidly evaporate the solvent. After solvent evaporation, pellets were manually formed. Two composites, containing 30 and 40 vol % of filler (denoted by ABS-30 and ABS-40, respectively), were prepared with that method.

2.3 Composite extrusion

The single-screw extrusion machine with two independent temperature zones was used to extrude composites. The extruded composite was air-cooled right after getting out of extruder nozzle. Extrusion temperatures were set at 160 and 190 °C, respectively. Chosen temperatures allowed to sufficient plasticity of the composite and, on the other hand, was not high enough to cause polymer degradation. To increase filament homogenous, extruded filament was pelleted and extruded the second time. After the second extrusion, the filament was smooth and did not show any signs of thermal degradation. Through controlling temperatures and speed of extrusion process, fabricated filaments have a diameter in the range between 1.7 and 1.9 mm which is good enough to use it on standard, nonmodified FDM printer.

2.4 Measurement of mechanical properties

Mechanical properties of printed objects with developed composites filaments were measured by preparing tensile testing using Cometech QC-506M2 machine. Due to the lack of standards in 3D printing, available standards for injection molding of thermoplastics were used. The condition and methods of the tensile test are specified in ISO 527-1:2012 and ISO 527-2:2012. The specimens designed according to ISO standards is shown in figure 1. All specimens were printed on CTC

Bizer 2X PRO printer. The printer was equipment with 0.8mm diameter nozzle, nozzle temperature was set to 200 °C, table temperature to 80 °C, layer height to 0.4mm and infill to 100 %. The speed of tensile testing was set to 2 mm/min.

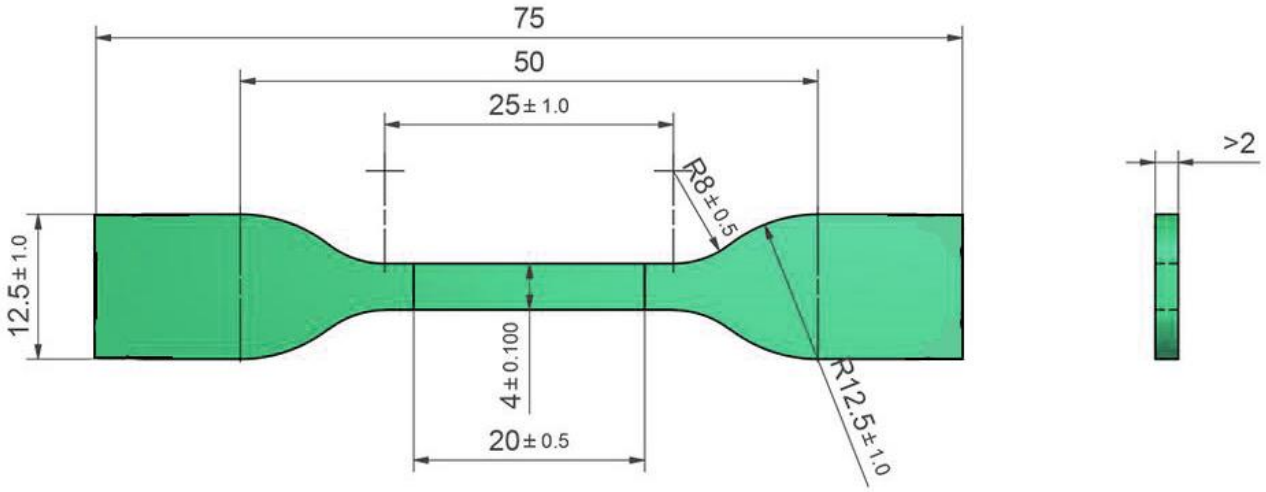

Figure 1 Sample element according to ISO 527-2 standard.

2.5 Measurement of thermal properties

The Lewis-Nielsen model was used to calculate the thermal conductivity of composites. The model was created for filler volume up to 40 %.[19] The effective thermal conductivity of a composite is given by the following equations:

$$k_C = \frac{1 + AB\phi}{1 - B\Psi\phi} \tag{1}$$

where

$$B = \left(\frac{k_1 / k_m - 1}{k_1 / k_m + A}\right) \tag{2}$$

$$\psi = 1 + \left(\frac{1 - \phi_m}{\phi_m^2}\right)\phi \tag{3}$$

In equations 1, 2, and 3 k_m is the thermal conductivity of matrix material, k_1 is the thermal conductivity of filler, ϕ is a filler volume. Additionally, ϕ_m is maximum filler volume fraction which is equal to 0.637 for particles in spheres shape and random close type of packing and A is shape coefficient equal to 1.5 for sphere particles.[20]

To experimentally determine the influence of iron filler in composite on thermal properties test heat sinks were printed using developed filaments and pure ABS filament. Fabricated elements were placed on a hotplate set at 100 °C and infrared camera Optris PI 200 was used to observe the temperature distribution and measure temperature of the top surface of the heat sinks. Increasing of thermal conductivity of composites can be noticed by increasing speed of heating top layer of heat sink and average temperature in the entire volume.

3. RESULTS AND DISCUSSION

3.1 Tensile properties

Force-displacement characteristics for both composites and pure ABS specimens are shown in figure 2. It has been observed that increasing contain iron powder in composite, decrease the breaking force of printed elements scientifically. Also, maximum elongation on break decrease when filler content increase.

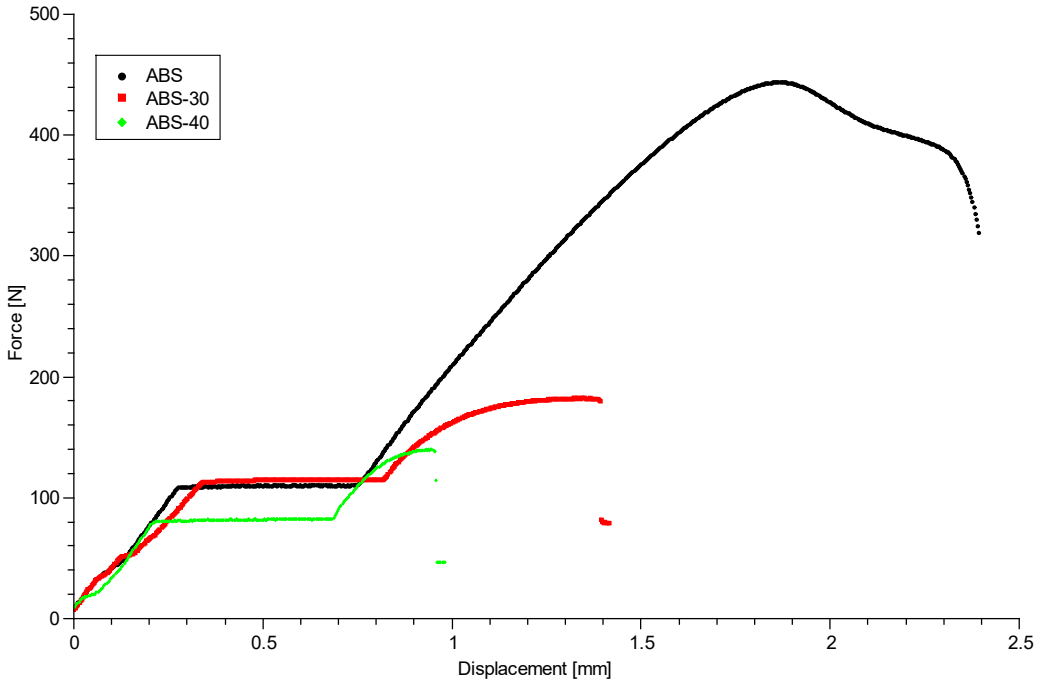

Figure 2 Exemplary force-displacement characteristics for ABS, ABS-30, and ABS-40.

Breaking force and elongation on break values, measured for 20 specimens for each material, are shown in figure 3. The average maximum force on break for ABS without iron particles was 393 N. For composite containing 30 vol % of iron powder maximum force decrease to 175 N and for composites containing 40 vol % of filler decrease to 152 N. The average elongation on break for pure ABS was 6.89 %. For composite containing 30 vol % of iron powder elongation on break decrease to 4.9 % and for composites containing 40 vol % of filler decrease to 3.3 %. It should be noticed, that heat sinks, especially in structural electronics circuits, are not supposed to carry the heavy load so mechanical properties are not so important. The mechanical parameters obtained for the developed materials are sufficient for the printing of objects that are not damaged if they do not carry significant loads.

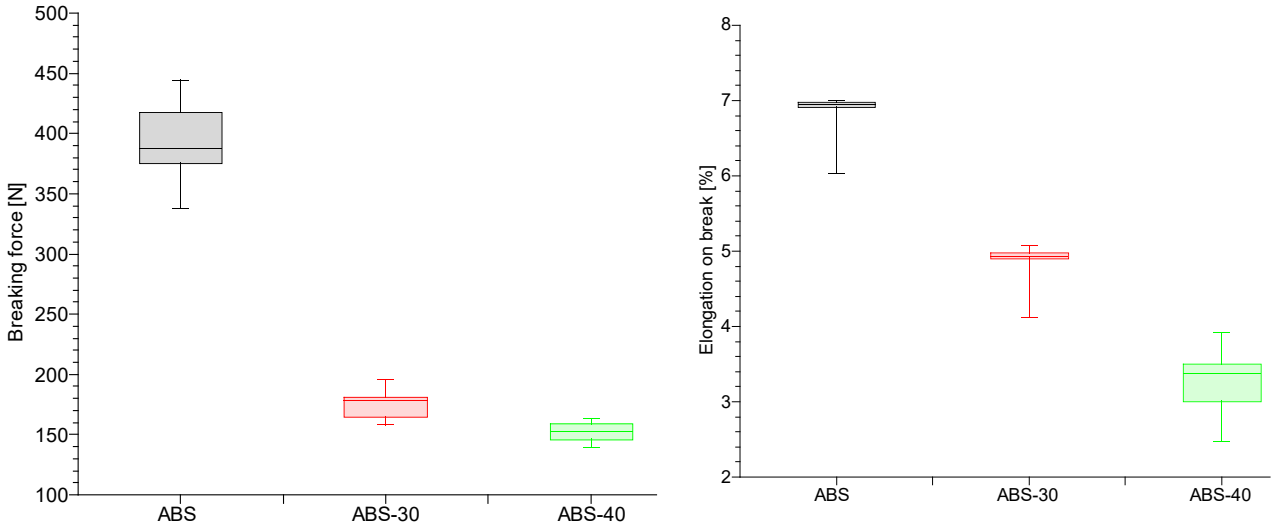

Figure 3 Average breaking force (left) and elongation on break (right) for ABS, ABS-30, and ABS-40.

3.2 Thermal conductivity

Over recent years, it has become obvious that electrical devices become smaller every year and there is a need to develop materials that allow to producing low cost and effective heat sinks to dissipate unwanted heat. Moreover, structural electronics devices also need this kind of materials to be fabricated to improve maximum electrical energy devices can generate. Adding metal powders to polymer matrix is one of the ideas to develop composites with a higher thermal conductivity that can be used in FDM technology.

According to the Lewis-Nielsen model theoretically thermal conductivity for both developed composites was calculated. The result has been shown in table 1.

Table 1 Thermal conductivity calculated with Lewis-Nielsen model.

Material	Thermal conductivity [W/(m·K)]
Iron	80.2
ABS	0.1
ABS-30	1.75
ABS-40	2.29

As shown calculated results, the thermal conductivity of ABS-30 and ABS-40 composites filaments increase approximately 175 % and 229 %, respectively, comparing to pure ABS. This improvement of the thermal conductivity with increasing content of iron powder particles shown that metal particles play an important role in developing composites filaments for FDM technology. The more metal particles in composites would provide better electrical and thermal conductivity.

Above calculations do not include different processes existing during printing that can also have an influence on thermal properties of composites. To examine the relationship between containing filler and thermal conductivity of physical elements, specimens in the form of heat sinks have been printed. Figure 4 shows a plot of time versus the top surface temperature of heat sinks printed with ABS and developed composites. It was observed that heat sink printed with ABS-40 composite had the highest temperature after 7 minutes of heating. Maximum temperatures recorded after 7 minutes for ABS, ABS-30, and ABS-40 were 50.9, 55.4, and 59.5 °C, respectively. Obtained results confirm theoretically calculations based on Lewis-Nielsen model.

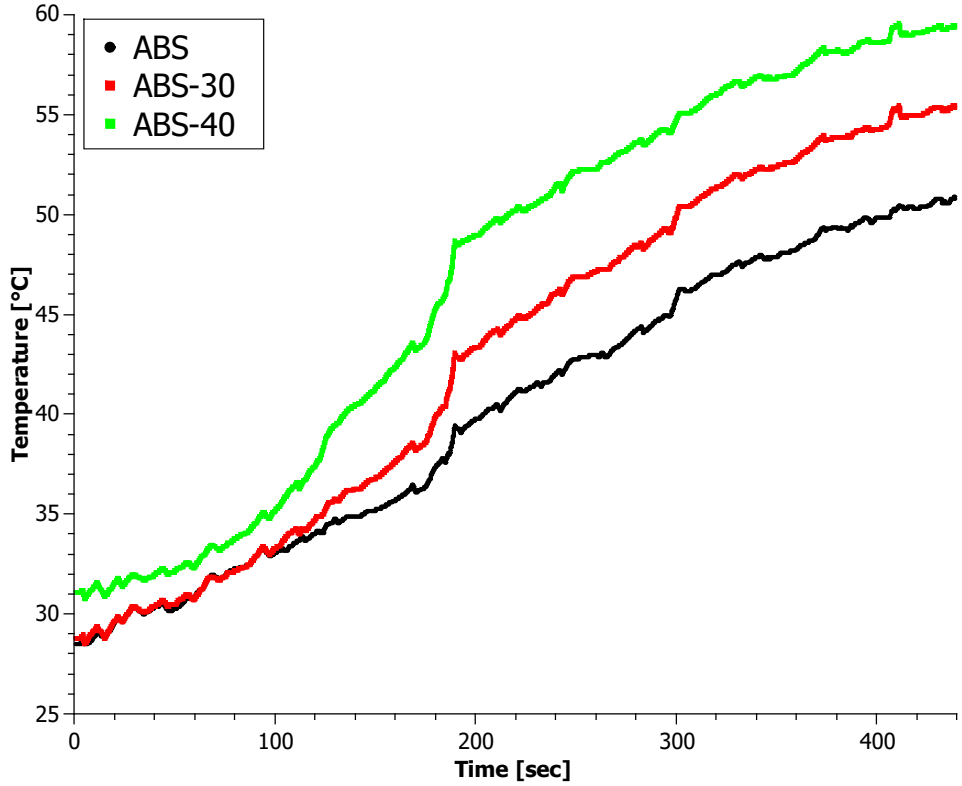

Figure 4 Temperature variation at the top surface of the 3D printed heat sinks.

The temperature differences and heat distributions of the three heat sinks were observed using a thermal imaging camera. The thermal images of heat sinks printed with ABS, ABS-30, and ABS-40 are shown in figure 5. The heat sinks were heated for 7 minutes on a hotplate set to 100 °C. The IR images showed that heat sink printed with ABS-40 had an average temperature around 7-8 °C higher comparing with heat sink printed with ABS. The highest temperature difference was observed at the top surface of heat sinks. The increase in temperature for the ABS-30 was equal to +8.8 % and for ABS-40 was equal to +16.9 % in comparison to the pure ABS heat sink.

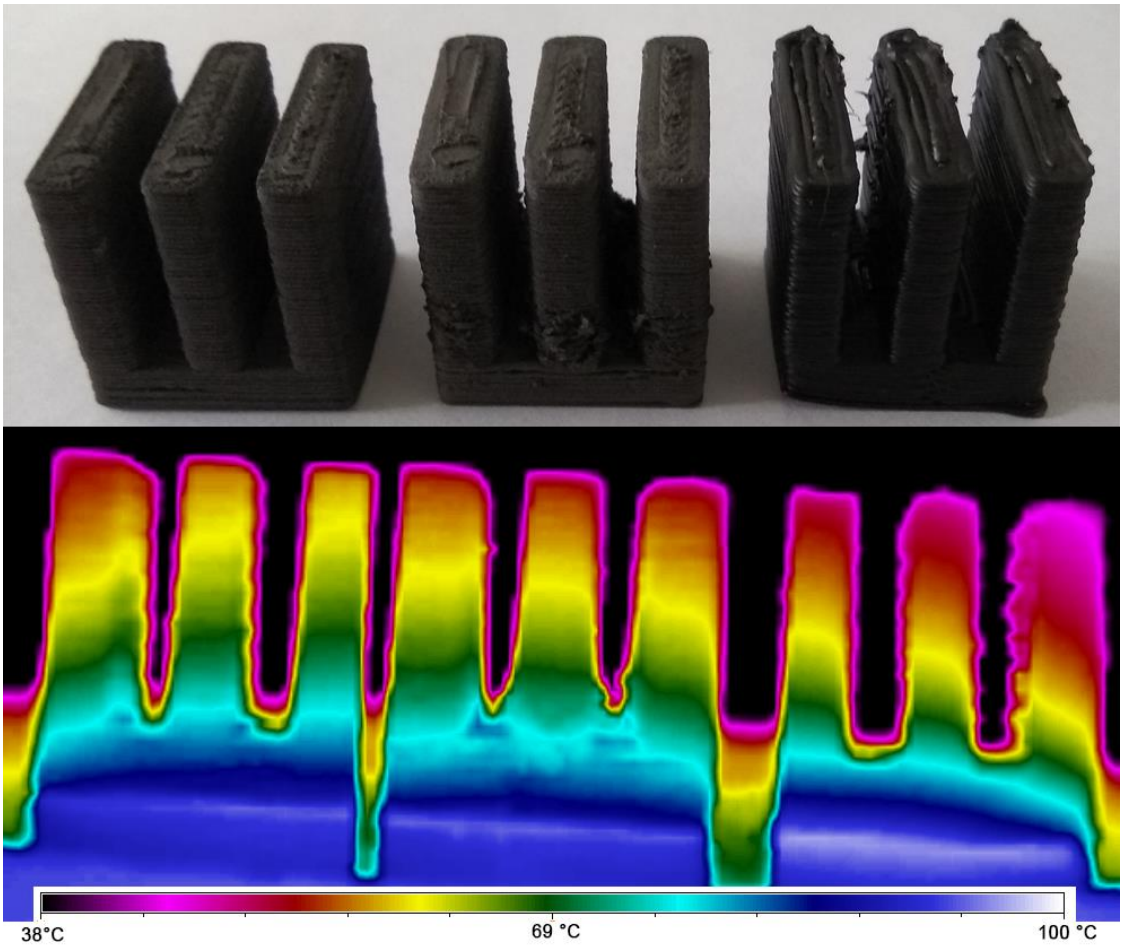

Figure 5 3D printed heat sinks with ABS-40, ABS-30, and ABS filaments (from left to right, respectively) with IR photograph showing temperature distribution after heating for 7 min.

4. CONCLUSION

This article presents the method of fabrication composites filaments for FDM technology with improved thermal properties. The ABS polymer was used as the matrix material and iron powder as filler. Composites with a filler content of 30 and 40 vol % were developed. Mechanical properties of developed composites in comparison with pure ABS were examined with the static tensile test. The obtained result showed that increasing volume on the filler in composites causes decreasing breaking force and elongation on the break of printed elements. Thermal conductivity of obtained composites was calculated theoretically. Influence of filler content in composite on thermal conductivity was also confirmed by infrared imaging. According to the Lewis-Nielson model, thermal conductivity of composite contenting 40 vol % of filler increases by 229% compared to pure ABS. Printed heat sinks also shown much better temperature distribution. What is also important, the developed composites are not difficult to print on an unmodified FDM printer. The obtained results confirm the possibility of using the developed composites as materials for the production of heat sinks with the use of FDM technology. They are characterized by much better thermal properties in comparison to commonly used polymers and at the same time, they are characterized by good printability.

5. ACKNOWLEDGMENTS

This work was financed by Warsaw University of Technology, Faculty Mechatronics, Institute of Metrology and Biomedical Engineering and Foundation for Polish Science project nr First TEAM/2016-1/7.

REFERENCES

[1] Gao, W., Zhang, Y., Ramanujan, D., Ramani, K., Chen, Y., Williams, C. B., Wang, C. C. L., Shin, Y. C., Zhang, S. and Zavattieri, P. D., "The status, challenges, and future of additive manufacturing in engineering," Computer-Aided Design **69**, 65–89 (2015).

[2] Thompson, M. K., Moroni, G., Vaneker, T., Fadel, G., Campbell, R. I., Gibson, I., Bernard, A., Schulz, J., Graf, P., Ahuja, B. and Martina, F., "Design for Additive Manufacturing: Trends, opportunities, considerations, and constraints," CIRP Annals **65**(2), 737–760 (2016).

[3] Gross, B., Lockwood, S. Y. and Spence, D. M., "Recent Advances in Analytical Chemistry by 3D Printing," Analytical Chemistry **89**(1), 57–70 (2017).

[4] Ligon, S. C., Liska, R., Stampfl, J., Gurr, M. and Mülhaupt, R., "Polymers for 3D Printing and Customized Additive Manufacturing," Chemical Reviews **117**(15), 10212–10290 (2017).

[5] Weng, Z., Wang, J., Senthil, T. and Wu, L., "Mechanical and thermal properties of ABS/montmorillonite nanocomposites for fused deposition modeling 3D printing," Materials & Design **102**, 276–283 (2016).

[6] Castles, F., Isakov, D., Lui, A., Lei, Q., Dancer, C. E. J., Wang, Y., Janurudin, J. M., Speller, S. C., Grovenor, C. R. M. and Grant, P. S., "Microwave dielectric characterisation of 3D-printed BaTiO3/ABS polymer composites," Scientific Reports **6**(1) (2016).

[7] Kim, H., Johnson, J., Chavez, L. A., Garcia Rosales, C. A., Tseng, T.-L. B. and Lin, Y., "Enhanced dielectric properties of three phase dielectric MWCNTs/BaTiO3/PVDF nanocomposites for energy storage using fused deposition modeling 3D printing," Ceramics International **44**(8), 9037–9044 (2018).

[8] Hwang, S., Reyes, E. I., Moon, K., Rumpf, R. C. and Kim, N. S., "Thermo-mechanical Characterization of Metal/Polymer Composite Filaments and Printing Parameter Study for Fused Deposition Modeling in the 3D Printing Process," Journal of Electronic Materials **44**(3), 771–777 (2015).

[9] Masood, S. H. and Song, W. Q., "Thermal characteristics of a new metal/polymer material for FDM rapid prototyping process," Assembly Automation **25**(4), J. Corney, Ed., 309–315 (2005).

[10] Podsiadły, B., Skalski, A., Wałpuski, B. and Słoma, M., "Heterophase materials for fused filament fabrication of structural electronics," J Mater Sci: Mater Electron **30**(2), 1236–1245 (2019).

[11] Gnanasekaran, K., Heijmans, T., van Bennekom, S., Woldhuis, H., Wijnia, S., de With, G. and Friedrich, H., "3D printing of CNT- and graphene-based conductive polymer nanocomposites by fused deposition modeling," Applied Materials Today **9**, 21–28 (2017).

[12] Gonçalves, J., Lima, P., Krause, B., Pötschke, P., Lafont, U., Gomes, J. R., Abreu, C. S., Paiva, M. C. and Covas, J. A., "Electrically Conductive Polyetheretherketone Nanocomposite Filaments: From Production to Fused Deposition Modeling," Polymers **10**(8), 925 (2018).

[13] Kim, K., Park, J., Suh, J., Kim, M., Jeong, Y. and Park, I., "3D printing of multiaxial force sensors using carbon nanotube (CNT)/thermoplastic polyurethane (TPU) filaments," Sensors and Actuators A: Physical **263**, 493–500 (2017).

[14] Wei, X., Li, D., Jiang, W., Gu, Z., Wang, X., Zhang, Z. and Sun, Z., "3D Printable Graphene Composite," Scientific Reports **5**(1), 11181 (2015).

[15] Zhang, D., Chi, B., Li, B., Gao, Z., Du, Y., Guo, J. and Wei, J., "Fabrication of highly conductive graphene flexible circuits by 3D printing," Synthetic Metals **217**, 79–86 (2016).

[16] Aumnate, C., Pongwisuthiruchte, A., Pattananuwat, P. and Potiyaraj, P., "Fabrication of ABS/Graphene Oxide Composite Filament for Fused Filament Fabrication (FFF) 3D Printing," Advances in Materials Science and Engineering, 2018, <https://www.hindawi.com/journals/amse/2018/2830437/> (19 November 2018).

[17] Nadgorny, M., Xiao, Z., Chen, C. and Connal, L. A., "Three-Dimensional Printing of pH-Responsive and Functional Polymers on an Affordable Desktop Printer," ACS Appl Mater Interfaces **8**(42), 28946–28954 (2016).

[18] Spinelli, G., Lamberti, P., Tucci, V., Kotsilkova, R., Tabakova, S., Ivanova, R., Angelova, P., Angelov, V., Ivanov, E., Di Maio, R., Silvestre, C., Meisak, D., Paddubskaya, A. and Kuzhir, P., "Morphological, Rheological and Electromagnetic Properties of Nanocarbon/Poly(lactic) Acid for 3D Printing: Solution Blending vs. Melt Mixing," Materials **11**(11), 2256 (2018).

[19] Pal, R., "On the Lewis–Nielsen model for thermal/electrical conductivity of composites," Composites Part A: Applied Science and Manufacturing **39**(5), 718–726 (2008).

[20] Pietrak, K. and Wiśniewski, T. S., "A review of models for effective thermal conductivity of composite materials," Journal of Power Technologies **95**(1), 14–24 (2014).

Manufacturing Stretchable Conductive Interconnects on Fabric Substrates, Development of a Technology

M. Zych*[a], D. Janczak [a], Ł. Dybowska-Sarapuk [a], A. Pepłowski [a], T. Raczyński [a], M. Jakubowska [a]

[a] Institute of Metrology and Bioengineering, Faculty of Mechatronics, Warsaw University of Technology, A. Boboli 8 St., 02-525 Warsaw, Poland
* marcin.j.zych@gmail.com

ABSTRACT

The paper includes description of a novel approach for producing stretchable, conductive interconnects for wearable electronics. At first the current state-of-the-art and market solutions were reviewed, and then we described our optimization of the composition of conductive pastes used in the screen printing technology. Namely, the ratios of TPU (Thermoplastic Polyurethane) dissolved in DMF (Dimethylformamide) as a carrier were empirically optimized, followed by adding silver flakes as a filler. To test the quality of the final paste, a number of tracks were printed on 100% cotton fabric substrate. Changes in the electrical resistance were measured while the samples were stretched, twisted, soaked, and washed. Despite being pushed to the limits of the substrate physical capabilities, printed interconnects still retained their conductive properties, with electrical resistance increasing by no more than 10x relative to initial, very low resistances of a few ohms, and then decreasing over time. We have also discovered that ironing the samples did not destroy the tracks. Instead, the ironing process regenerated them, and their electrical resistances returned to initial values or even decreased. The method described in this paper is innovative because it enables printing directly onto textiles and the usage of a non-synthetic textile substrate while still retaining robustness in electrical conductivity.

Keywords: stretchable electronics, wearable electronics, textronics

1. INTRODUCTION

The interest in wearable electronics has grown exponentially over recent years. The most popular applications are smartwatches and wristbands. On a third place there are electronics integrated with clothing, for which more than two-fold increase in the market share is expected in next three years[1]. Health monitoring systems, integrated heaters or gadgets are just few of promising applications[2-4]. Despite such interest, it is still developing technology with a lot of room for innovation. Devices integrated with clothing usually have to be placed in appropriate locations. Therefore, they usually require electrical connections to energy sources, signal analyzers or communication devices that are located in different places. A conventional approach is to run wires between them.

This solution has many disadvantages through which modified clothing cannot be treated as ordinary clothing. Wires cannot be washed or ironed, and the solution itself is uncomfortable for the user due to its rigidity. Currently, the most promising technologies for interconnects in wearables are conductive fibers woven into fabric or printed electronics[5]. The problems faced by electronics printed on textiles are usually lack of resistance to stretching or soaking. In order to avoid them, prints are made on polymeric substrate which is attached on clothing then, in example, by lamination[6]. To protect the printout, top layer of the polymer is used. Due to its stretchability, thermoplastic polyurethane (TPU) is often used as substrate. Printing on a stretchable substrate is not sufficient if the printing ink does not have the right parameters[13]. Printout may be damaged which is shown on figure 1 and 2. In our approach, we have developed an ink for printing that allows to make electric paths directly on textile substrate, using the same machines that are used in the clothing industry. Our samples made by screen printing method, had high bending and stretching strength and were resistant to other factors related to the use of clothing, such as washing and ironing.

Photonics Applications in Astronomy, Communications, Industry, and High-Energy Physics Experiments 2019, edited by Ryszard S. Romaniuk, Maciej Linczuk, Proc. of SPIE Vol. 11176, 111765C
© 2019 SPIE · CCC code: 0277-786X/19/$21 · doi: 10.1117/12.2536856

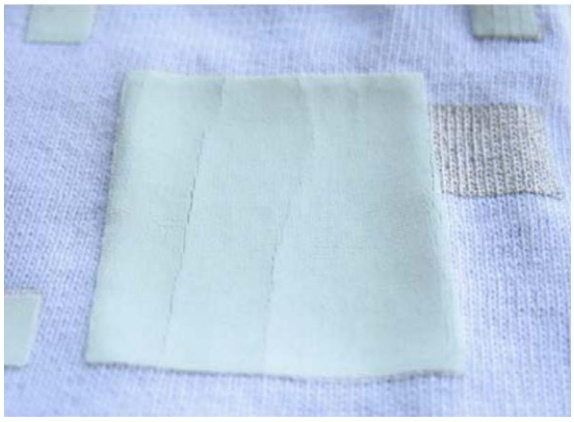

Figure 1. Visible damage of electroluminescence structure printed on cotton substrate using polymethacrylate based inks[4].

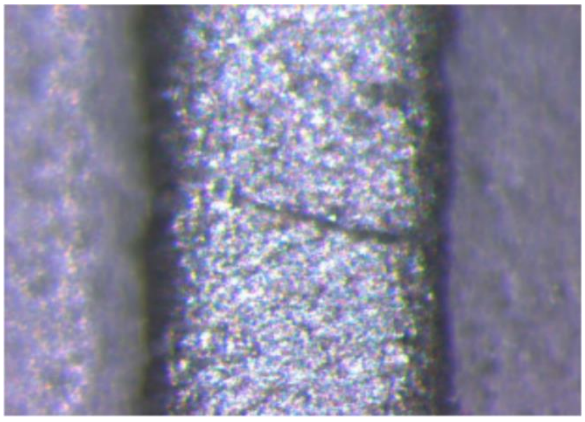

Figure 2. Microscope image of crack which emerged during the 70% strain test. Path was printed on TPU substrate[7]

1. EXPERIMENTAL METHODS

The conductive inks used for screen printing are usually composites of the solid particles of the conductor and the polymer as a carrier. As fillers, most often used are metallic nanoparticles or nanofibers, mainly silver and copper or carbon-based particles - graphene nanoflakes or carbon nanotubes[8]. Many different carries can be used depends on destiny of ink. Most common are silicons, acrylics or polyurethanes dissolved in organic solvents. Sometimes, conductive polymers such as PEDOT:PSS are also used to further increase the conductivity of the composite.

1.1. Materials

Focusing on the stretchability of the printout, we decided to examine various types of TPU as a carrier. Three types of TPU samples from BASF were tested. After initial inspection of its mechanical parameters, two of them were selected for further testing. Hardness of those materials was 37 and 72 Shore A, maximum elongation at break was successively 1150% and 850%. Both polymers are highly hygroscopic and require drying for 3 hours at 80-90°C.

The right choice of solvent is extremely important. In addition to the possibility of dissolving the selected polymer, boiling point should be noticed, which is related to the evaporation rate. Too fast evaporating solvent will prevent printing, because it will start to increase paste density. A very high evaporation temperature will result in a long drying time at high temperature which can damage the base material or the paste itself. The TPU we used is soluble in dimethylformamide (DMF), which has quite high boiling point of 153°C[9].

For the development of a suitable carrier, solutions of two types of TPU with different polymer to solvent ratios were made: 15%, 20%, 25% by weight. The samples were mixed for 24 hours with a magnetic stirrer. Rheology parameters of each carrier was examined with rotary rheometer. The study showed that solutions with TPU of hardness of 72 Shore A had too high viscosity to perform a rheometer measurement, thus they were excluded from further testing. Results for second type of TPU showed that solutions are Newtonian liquids and the higher the content of TPU in the solution, the greater its viscosity.

The most conductive are pastes containing silver nanoparticles due to the very high conductivity of this element. Therefore, we decided to use them. Two different silver powders with an average particle size of 2 μm and 10 μm were tested. Inks with different ratios of filler to carrier were prepared. For 10 μm silver it was 20, 30 and 40%, for 2 μm: 30, 40, 50, 60, 70 and 80%. Appropriate portions of powders were weighed, mixed with the 20% TPU solution and grinded in agate mortar for 10 minutes each. Then the mixtures were transferred into containers and mixed with use of high-speed mixer for 10 minutes at 3500 rpm.

1.2. Samples preparation method

To make samples for resistivity measurements, a polyester screen of mesh 77, with custom pattern was prepared. Straight lines of 1 mm in width and 20 mm at the length were printed on polymer film, eighteen samples for each paste. Printouts were dried in the oven at 120°C for 10 minutes. Then resistance of paths was measured. Average resistances are presented on figure 3.

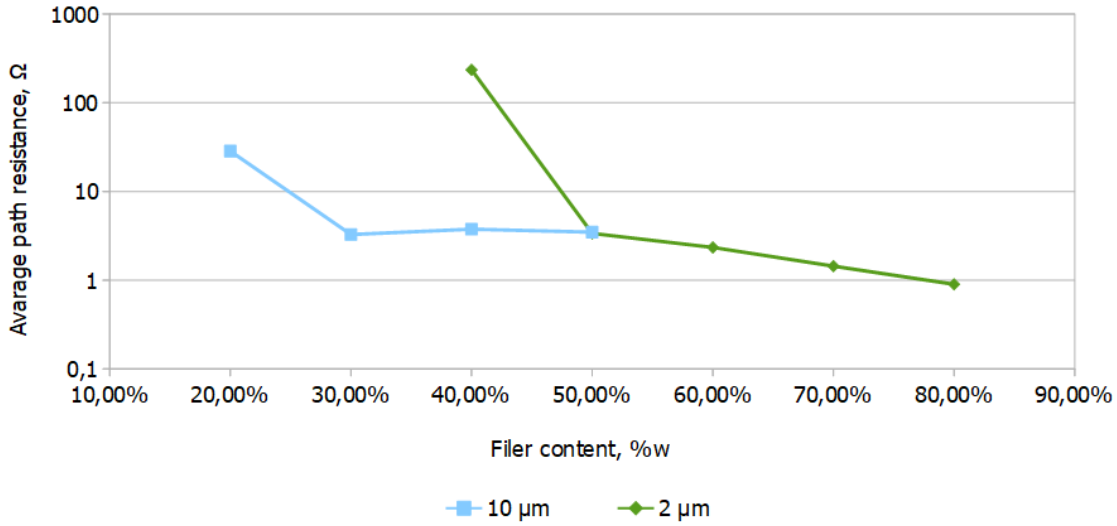

Figure 3. Average resistance of printed samples of pastes with different contents of 10µm and 2µm silver filler in 20% TPU-DMF carrier.

The results showed that the highest conductivity, while maintaining the appropriate density for printing, have 30% fillings for 10 µm silver and 70% for 2 µm silver. The paste based on 2 µm silver with 70% filling had several times greater conductivity than the 10 µm paste. Therefore 70% filling of 2 µm silver was used for further testing.

In order to check the effect of TPU content on the properties of the paste, three pastes with 15, 20 and 25% TPU carriers were made using analogous method to previously described. Rheological parameters were tested. The test consisted of continuously increasing the rotational speed of the rheometer cone and recording changes of paste viscosity. Results are shown on figure 4.

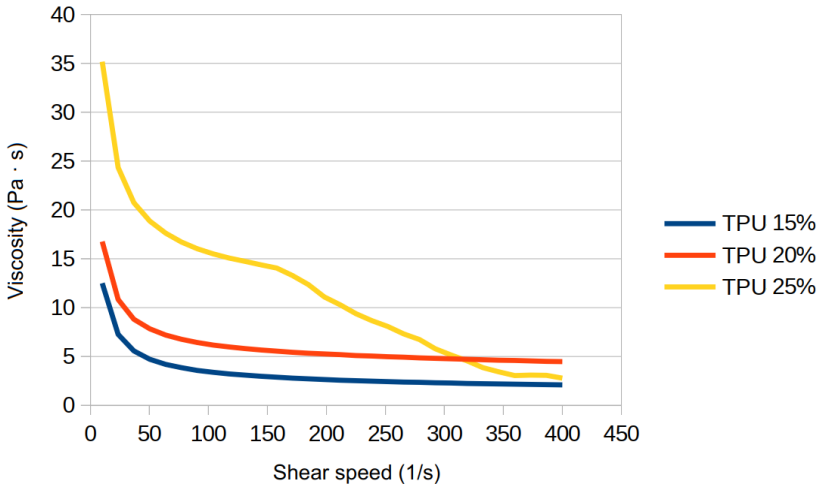

Figure 4. Results of viscosity measurements of three 70% silver pastes based on 15, 20 and 25% TPU carrier.

During screen printing, shear forces act on the paste. A well-made paste should have a higher viscosity in the absence of forces affecting it than during the printing process. All three pastes have rheology suitable for screen printing pastes[10].

A series of test prints were made to check the effect of TPU content in carrier on resistivity. As a substrate, 100% cotton was used. Before application of conductive paste, a substrate layer was printed with use of 25% TPU carrier. After printing conductive layer, samples were dried for 10 minutes in 120°C. During printing, it was noticed that the 25% paste had a tendency to clog the screen after one print. The 15% paste was well printable, but it melted slightly over the material, the printed paths had blurred edges. The most optimal for printing was the one with 20% of TPU content in the carrier. The initial tracks resistance has been measured. To facilitate stretching measurements and improve results[11], a larger, meandering path pattern was printed.

Some of the printouts were covered with a top protective layer of 25% TPU. Many different stretching tests were carried out. The effect of washing and ironing on the conductivity of the printout was also examined.

2. RESULTS AND DISCUSSION

The average track resistances were 2.06 Ω, 2.68 Ω and 4.96 Ω respectively for 15%, 20% and 25% of the TPU content. Initially, it was observed that after stretching and relaxing paths, the resistance increased about ten times and dropped with time, in many cases returning to the original resistance. In order to observe the physical change of the path structure before and during the stretching, microscopic photos were taken which are presented on figure 5.

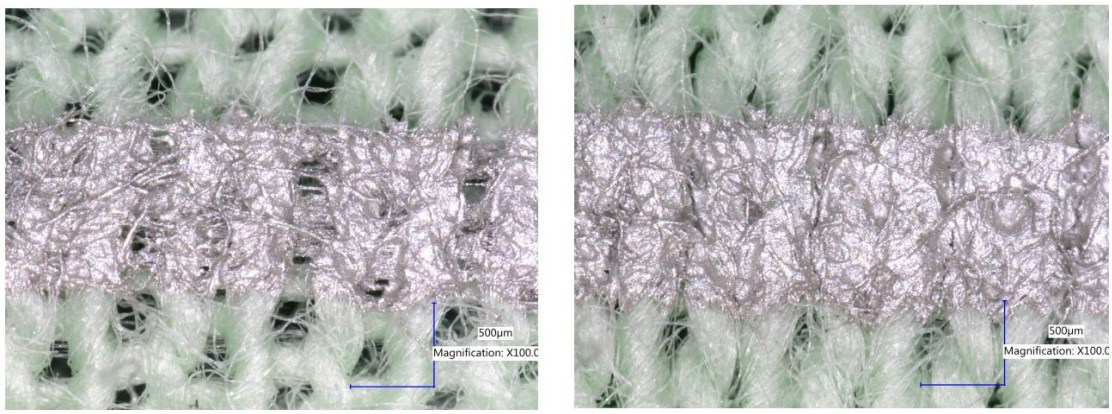

Figure 5. On the left image, printed path while stretched. On the right, after stretching relaxation. No cracks noticed on printout surface.

A meandering path with an initial resistance of 4 Ω was connected to the measuring apparatus, every 5 seconds the sample was stretched by 20% until it was 100%. After each step there was a rapid jump of resistance to stabilize after a while at a certain level. After stretching the sample to 100%, the tensile force was relaxed, the resistance stabilized around 18 Ω. The same sample has been subjected to ironing. After this, the path resistance dropped to the initial value of 4 Ω.

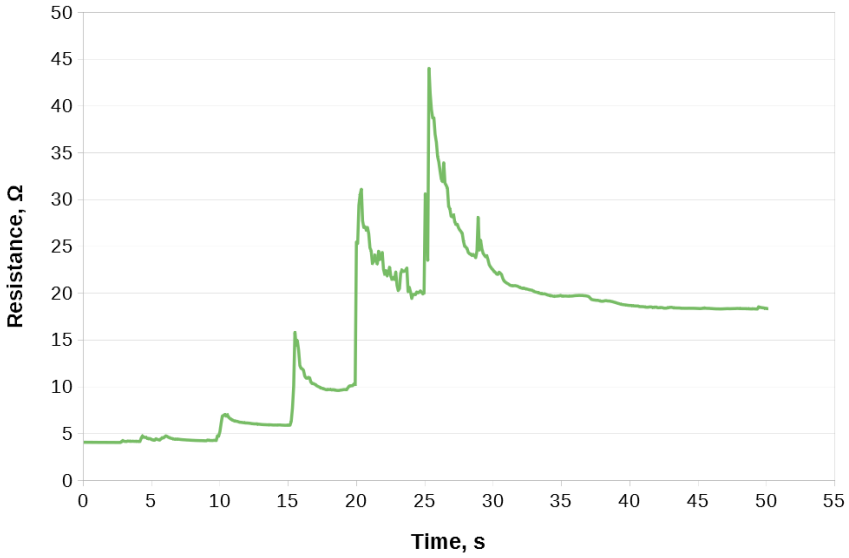

Figure 6. Influence of stretching on the resistance of meandering path. Stretching by 20% every 5 seconds to maximally 100% and then release.

During everyday use of clothes, the maximum stretch of the material is 20%[12], therefore a test of cyclical stretching and relaxation in this range was carried out. The graphs for paths without top layer and coated with TPU are shown on figure 7. Coated paths showed better conductivity during the tensile test from the uncoated tracks, despite a slightly higher initial resistance. In both cases the resistance jump occurred during stretching and relaxing, after which the resistance were dropping down constantly.

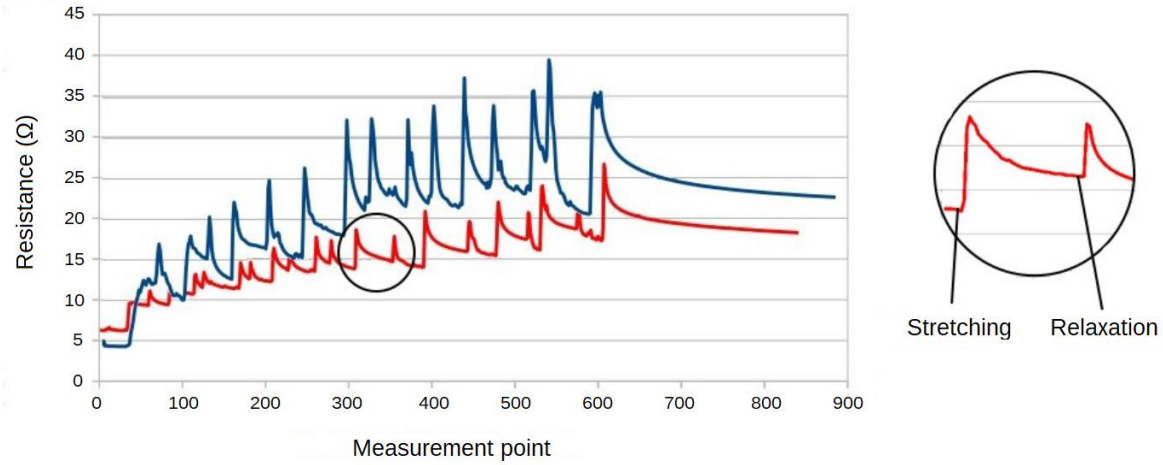

Figure 7. The result of a multiple stretching test by 20%, red - paths with TPU layer on top, blue - without top layer.

The influence of external factors such as bending, washing, ironing, soaking and wringing was tested. The bending of paths had a negligible impact on their conductivity. Soaking and wringing resulted in similar results as laundry. During initial experiments, it was determined that ironing causes the path's conductivity to regenerate, which is why it was decided to investigate it impact after performing various resistivity tests. For this purpose, pre-printed samples with a TPU surface layer and uncoated ones were used. The course of experiments and their effect on resistances are illustrated on figure 8.

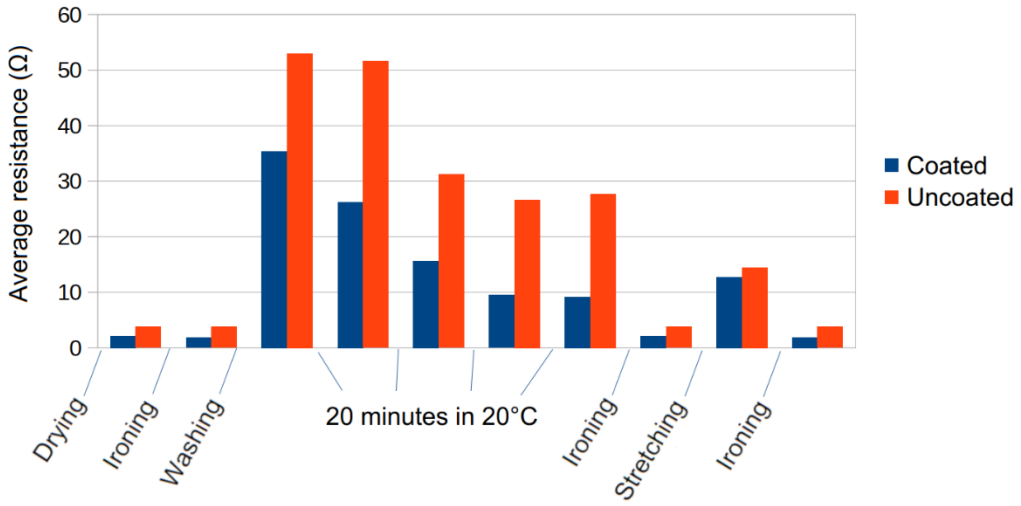

Figure 8. Influence of various physical factors on the resistances of printed tracks

Ironing had a negligible effect on the freshly produced path. Washing at 60 ° C for an hour with the use of detergents significantly increased the resistance, which decreased with time of drying in room temperature. Samples coated with TPU showed better resistance to washing than those uncoated. When the samples were considered dry, it was decided to iron them again. The resistance of the samples returned the initial values. Then the same samples were subjected to 100 stretching cycles by several percent. After ironing the resistances returned to the initial values. Some of the samples were subjected to multiple different fatigue tests, even after a few washing and stretching cycles, they remained conductive, and the ironing still resulted in lowering the resistance value.

3. CONCLUSION

The results show that the developed composite is suitable for the production of conductive paths for the garment technology. Best composition for this purpose is 20 %w TPU dissolved in DMF, filled by 70 %w 2 μm silver particles. The resistance of paths increases during tensile tests in a range that still allows the transmission of an electrical signal. Coating with the TPU surface layer significantly increased the stability of the resistance during stretching. The paths after washing and drying had about 5 times higher resistance than initial values, but after ironing the resistance returned to them. Regardless of the degree of damage to the path, the ironing regenerated it.

REFERENCES

[1] IDC Quarterly Wearable Device Tracker, September 2018
[2] Majumder, S., Mondal, T., & Deen, M. (2017). *Wearable Sensors for Remote Health Monitoring. Sensors, 17(12), 130.* doi:10.3390/s17010130
[3] “Electrically heated garment” patent US20180146510A1
[4] Słoma Marcin*, Janczak Daniel, Wróblewski Grzegorz [i in.]: Electroluminescent structures printed on paper and textile elastic substrates, w: Circuit World, vol. 40, nr 1, 2014, ss. 13-16, DOI:10.1108/CW-10-2013-0037
[5] Stoppa, M., & Chiolerio, A. (2014). *Wearable Electronics and Smart Textiles: A Critical Review. Sensors, 14(7), 11957–11992.*doi:10.3390/s140711957
[6] Vervust, T., Bossuyt, F., Axisa, F., & Vanfleteren, J. (2010). *Stretchable and Washable Electronics for Embedding in Textiles. MRS Proceedings, 1271.*doi:10.1557/proc-1271-jj04-03
[7] Screen-printed stretchable interconnects, Jari Suikkola, Timo Kankkunen, Pekka Iso-Ketola, Jukka Vanhala, and Matti Mäntysalo, Tampere University of Technology

Electronics and Communication Engineering
[8] Trung, T. Q., & Lee, N.-E. (2016). *Recent Progress on Stretchable Electronic Devices with Intrinsically Stretchable Components. Advanced Materials, 29(3), 1603167*.doi:10.1002/adma.201603167
[9] Valentine, A. D., Busbee, T. A., Boley, J. W., Raney, J. R., Chortos, A., Kotikian, A., … Lewis, J. A. (2017). *Hybrid 3D Printing of Soft Electronics. Advanced Materials, 29(40), 1703817*.doi:10.1002/adma.201703817
[10] „The rheological behaviors of screen-printing pastes", Hung-Wen Lin, Chang-Pin Chang, WenHwa Hwu, Ming-Der-Ger, 2008
[11] Design and fabrication of screen-printed silver circuits for stretchable electronics, Kwang-Seok Kim, Kwang-Ho Jung, Seung-Boo Jung, 2014
[12] „Printable stretchable interconnects" Wenting Dang, 2017
[13] Gralczyk Kinga, Janczak Daniel, Dybowska-Sarapuk Łucja [i in.]: Studies on possibilities of polymer composites with conductive nanomaterials application in wearable electronics, w: Proc. SPIE. 10445, Photonics Applications in Astronomy, Communications, Industry, and High-Energy Physics Experiments 2017 / Romaniuk Ryszard, Linczuk Maciej Grzegorz (red.), vol. 10445, 2017, ISBN 9781510613546, ss. 104455H-1 - 104455H-11, DOI:10.1117/12.2281067

Analysis of the creation process of the chip during the orthogonal turning of pure titanium using a high-speed camera

Łukasz Ślusarczyk*[a]
[a]Production Engineering Institute, Cracow University of Technology, Al. Jana Pawła II 37, 31-864 Cracow

ABSTRACT

Article presents the process of the chip creation during orthogonal turning of the pure titanium tube. During laboratory tests two tools were used, with different shape of the rakeface. The high-speed camera PHANTOM v 5.2, with NIKKOR 200 mm prime lens, was used to record the images. The obtained sequences significantly helped in the analysis of the process of chip creation, and allowed to carry out additionally analysis by using Tracker software.

Keywords: high-speed camera, chip creation, pure titanium, turning

1. INTRODUCTION

Machining is one of the most widely used manufacturing methods for machine and equipment parts. Currently, in addition to very high requirements in terms of dimensional and shape accuracy of manufactured objects, a huge emphasis is placed on productivity. With the application of CNC machine tools, the correct choice of machining parameters becomes a very important issue guaranteeing the achievement of high productivity[1-3]. Titanium and its alloys are widely used in the automotive and aerospace industries. Due to low thermal conductivity and tendency to harden under the impact of heat (precipitation hardening), titanium belongs to the group of difficult-to-cut materials. A lot of attention is given in the literature to the analysis of physical phenomena occurring in the cutting zone during the machining of difficult-to-cut materials[4-5]. This paper focuses on the issues relating to the chip creation and formation process. The chip form is a result of phenomena occurring in the cutting zone. The chip formation conditions and the chip form have a significant impact on the safety, reliability and efficiency of the machining process, and also on the workpiece surface properties[6]. Different forms are obtained, depending on the cutting conditions and the properties of machined material. Generally, the chips are classified as favourable, acceptable and unacceptable. The group of favourable chips includes short chips that leave the cutting zone in one, unchanged direction. Acceptable chips are short or mixed chips that do not have a specific flow direction (do not have a precisely defined dominating direction). Unacceptable chips are continuous, of a spiral shape, that might cause a catastrophic cutting tool point and workpiece damage[4]. The chip flow on the tool point's rake face is a very important issue during the design of cutting tools, particularly the chip curlers and chip breakers. The literature review indicates various chip flow models[7-8]. The most important ones include the Young's model that accounts for friction forces on the rake face for determination of the chip flow direction. In the Okushima's model, the resultant chip flow direction is an expression of the sum of speeds of individual elements of the formed chip along the cutting edge outline. The problem of chip curling is closely related to the chip flow direction. Three interconnected phases are distinguished in the chip formation process :

Phase I is an initial chip formation which takes places as a result of slippage, phase II includes the chip curling, and phase III the chip breaking. The literature review indicates that most authors describing the chip curling and breaking process quote the studies carried out by Jawahir who using a high-speed camera determined the process cyclicity and distinguished four chip deformation phases until the break:

- Phase I – initial: the chip loses contact with the tool point and starts to curl freely. No bending moment acts on the chip during that phase.
- Phase II: the chip curling above the point touches an external obstacle (outside workpiece surface). A small bending moment acts on the chip during that phase, and the chip shape resembles a semicircle.
- Phase III – intermediate: the bending moment increases. The chip takes the form of a spiral, and its point of contact with the obstacle moves slightly upward.

*slusarczyk@mech.pk.edu.pl; phone 12 374-32-14

Photonics Applications in Astronomy, Communications, Industry, and High-Energy Physics Experiments 2019, edited by Ryszard S. Romaniuk, Maciej Linczuk, Proc. of SPIE Vol. 11176, 111765D
© 2019 SPIE · CCC code: 0277-786X/19/$21 · doi: 10.1117/12.2536880

- Phase IV directly precedes the chip breaking. The maximum bending moment acts on the chip, and the point of contact reaches the uppermost position[7-10].

The chip formation process is a complex problem for analysis[6,11]. This is mainly caused by the variable contact surface between the chip and the cutting tool point. A rapid development in the area of chip breaking is also related to a dynamic development of multi-point inserts. The cutting tools manufacturers spent substantial amounts of money on research in order to improve the tool design and its specialization. Currently, a there is a huge emphasis on the development of new chip curlers of special shapes. The modern solutions intend to deflect the chip to the unmachined workpiece surface or towards the flank surface so that the chip breaks rapidly and has a favourable shape.

2. RESEARCHES

The test stand comprised a Knuth Masterturn 400 lathe, a Phantom v5.2 high-speed camera placed in front of the cutting zone, spot ilumination system Dedocool, and a computer with Cine 663 software (Figure 1).

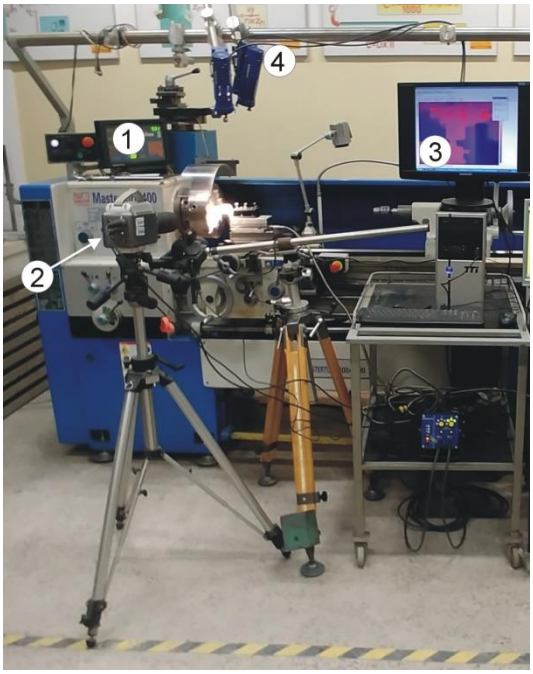

Figure 1. The test stand: 1 - Knuth Masterturn 400 lathe, 2 - Phantom v5.2 high-speed camera placed in front of the cutting zone, and 3 - computer with Cine 663 software, 4 - spot ilumination system Dedocool.

Table 1 presents the configuration parameters of the PHANTOM v 5.2 high-speed camera.

Table 1. The configuration parameters of the PHANTOM v 5.2 high-speed camera.

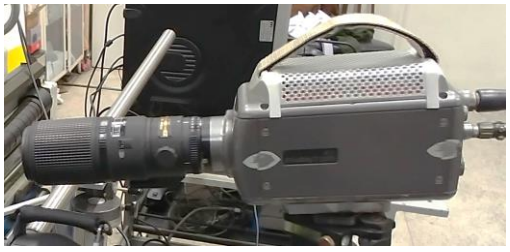

resolution	512x512 – 8 bit
sensor	CMOS
frame rate	3000 fps
memory	4 GB
distance measurement	1,0 m

Figure 2 shows a NIKKOR 200 mm prime lens with was used to record the fast-changing images, Figure 3 presents spot ilumination system Dedocool, model Coolt3.

Figure 2. NIKON Nikkor AF Micro 200 mm f/4D.

Figure 3. Spot ilumination system Dedocool, model Coolt 3.

The laboratory tests involved orthogonal turning of a pure titanium tube, diameter D=60 mm, wall thickness 2,77 mm (Figure 4).

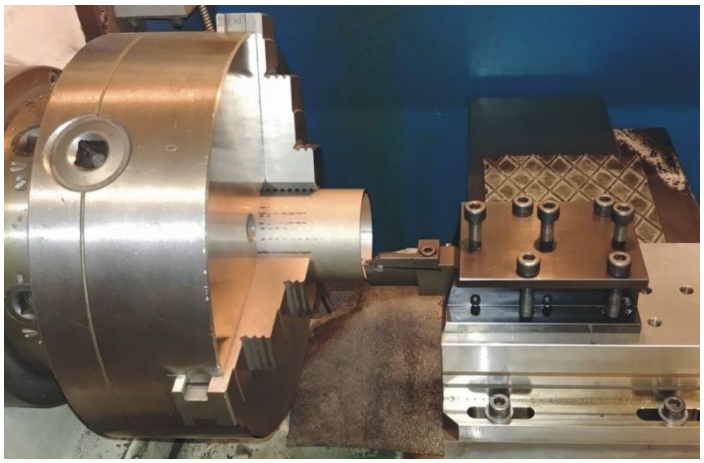

Figure 4. The orthogonal turning of a pure titanium tube.

The tube chemical composition is presented in Table 2.

Table 2. Workpiece chemical composition.

Element	Fe	O	C	N	H	Ti
Content	Max. 0,25%	Max. 0,25%	Max. 0,08%	Max. 0,03%	Max. 0,015%	Min. 99,375%

Two cutting tools were used during the tests (Figure 5):
- P10 sintered carbide tool with a flat rake face,
- Kennametal tool designated A3SAR2520M0425-075-100 with an A3G0500M05P04DF insert made of KC5010 sintered carbides, covered with a TiAlN coating. Not cutting fluid was used during the machining.

a) b)

Figure 5. Two cutting tools were used during the tests
a) P10 sintered carbide tool with a flat rake face,
b) Kennametal tool designated A3SAR2520M0425-075-100 with an A3G0500M05P04DF insert made of KC5010 sintered carbides, covered with a TiAlN coating.

The P10 sintered carbide tool has the rake angle γ of +10° and clearance angle α of +8°. The rake face photographs of the Kennametal tool were taken. The 2D photographs were taken with a Keyence VHX-600 laboratory microscope. Based on the 2D photographs, 3D images of the tool rake face were obtained. The figures below (Figure 6) show the side and top views of the rake face. A complex surface shape with a chip groove can be seen in the photographs.

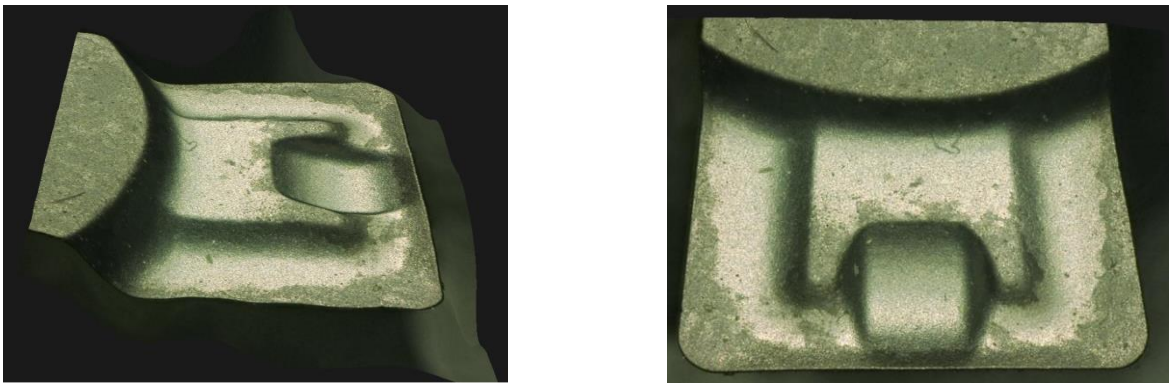

a) b)

Figure 6. The a) side and b) top views of the rake face.

The cutting speed and feedrate were chosen based on the recommended datasheet values. The parameters for individual trials are presented in Table 3. The cutting depth was the same in each case and equalled 2,77 mm – the tube wall thickness.

Table 3. Cutting parameters.

Symbol	Cutting parameter	Value		
A	v_c [m/min]	60	100	140
B	f [mm/rev]	0,048	0,153	0,249
	a_p [mm]	2.77		

The test plan, determined based on the Taguchi method, included 9 cutting trials for each of the two tools. The detailed plan is presented in Table 4.

Table 4. Test plan.

Trial no.	Parameters		Values		
	A	B	v_c [m/min]	f [mm/rev]	a_p [mm]
1	1	1	60	0,048	2,77
2	1	2	60	0,153	2,77
3	1	3	60	0,249	2,77
4	2	1	100	0,048	2,77
5	2	2	100	0,153	2,77
6	2	3	100	0,249	2,77
7	3	1	140	0,048	2,77
8	3	2	140	0,153	2,77
9	3	3	140	0,249	2,77

The chip formation process was recorded using a Phantom high-speed camera with a Nikor 200 mm lens. The recording time was 4 s, recording frequency 3000 frames/s., and the resolution 512x512 px. Fragments comprising a dozen frames were selected from the recorded sequences using the Cine application. Then, the Tracker application was used to analyse the point movement. The chip flow speed (v_{ch} m/min) on the tool rake face was determined using the "Point Mass" tool, based on the time-lapse analysis of a characteristic point on the chip. Shown below are examples of images from the analyses made for the two used tools (Figure 7). Please note that in order to correctly determine the chip flow speed, each time it was necessary to establish the characteristic dimension on the analysed photographs. The characteristic dimension was the length of the tool's working part.

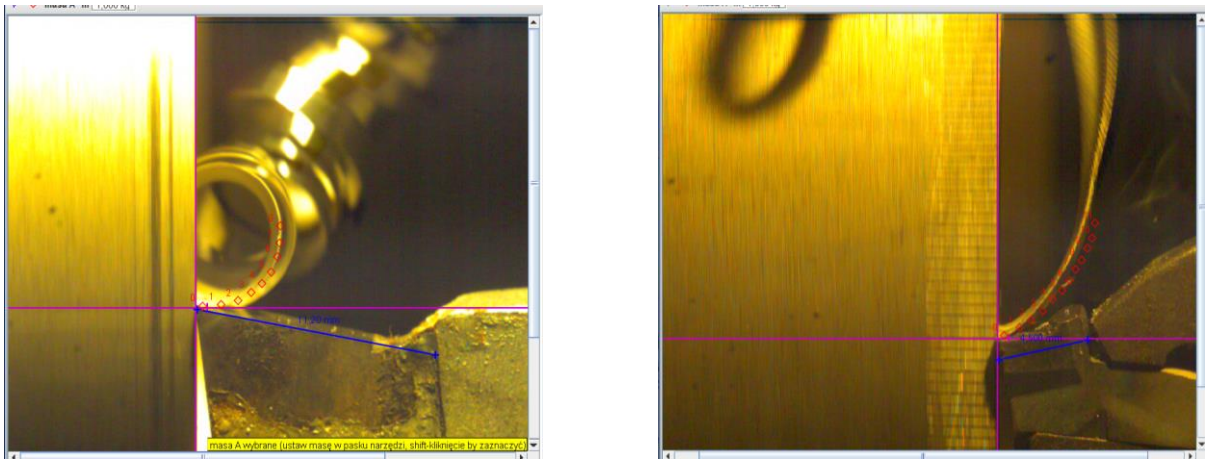

a) b)

Figure 7. Examples of images from the analyses made for the two used tools (v_c=100 m/min, f=0,048 mm/rev)
a) P10 sintered carbide tool,
b) Kennametal tool.

The table (Table 5) below presents the experimentally determined, average chip flow speeds on the rake face for the two cutting tools used in the tests.

Table 5. The experimentally determined, average chip flow speeds on the rake face for the two cutting tools used in the tests.

Trial no.	v_c [m/min]	f [mm/rev]	P10 sintered carbide tool	Kennametal tool
			v_{ch} [m/min]	v_{ch} [m/min]
1	60	0,048	48,2	43,1
2	60	0,153	64,4	59,3
3	60	0,249	126,8	118,8
4	100	0,048	40,9	38,4
5	100	0,153	62,8	53,8
6	100	0,249	124,4	114,3
7	140	0,048	38,4	34,5
8	140	0,153	61,9	61,7
9	140	0,249	122,2	113,2

On the basis the obtained measurement results, mathematical models with regression equations for the average chip flow speeds on the rake face were developed. The ANOVA analysis was used to perform the results analysis. Tables 6 and 7 present the results of ANOVA variance analysis. The impact of the cutting data (v_c and f) on the average chip flow speeds on the rake face is shown in Figures 8 and 9.

Table 6. Analysis of ANOVA variance for the average chip flow speeds on the rake face (P10 sintered carbide tool).

Source	DF	Adj SS	Adj MS	F-value	P-value
Linear					
f	1	48,200	48,200	18,110	0,013
v_c	1	10066,400	10066,400	3778,320	0,000
Square					
$v_c \cdot v_c$	1	833,700	833,700	312,900	0,000
Interaction					
$v_c : f$	1	7,000	7,000	2,620	0,181
Residual error	4	10,700	2,7		
Total	8	10979,000			

Table 7. Analysis of ANOVA variance for the average chip flow speeds on the rake face (Kennametal tool).

Source	DF	Adj SS	Adj MS	F-value	P-value
Linear					
f	1	24,130	24,130	1,600	0,750
v_c	1	8998,930	8998,930	594,950	0,000
Square					
$v_c \cdot v_c$	1	792,340	792,340	48,220	0,002
Interaction					
$v_c : f$	1	5,170	5,170	0,640	0,324
Residual error	4	60,500	15,130		
Total	8	9283,200			

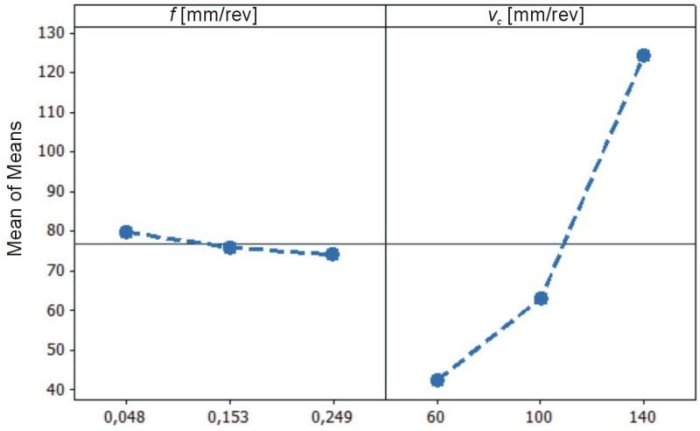

Figure 8. The relation between the average chip flow speeds on the rake face v_{ch} and feed f and cutting speed v_c for P10 sintered carbide tool.

The regression equation determined using the "linear + interactions" function for the average chip flow speeds on the rake face (v_{ch_P10}) during the turning P10 sintered carbide tool:

$$v_{ch_{P10}}(v_c, f) = 97{,}356 - 61{,}045 \cdot f - 1{,}576 \cdot v_c + 0{,}0127 \cdot {v_c}^2 + 0{,}3284 \cdot f \cdot v_c \quad (1)$$

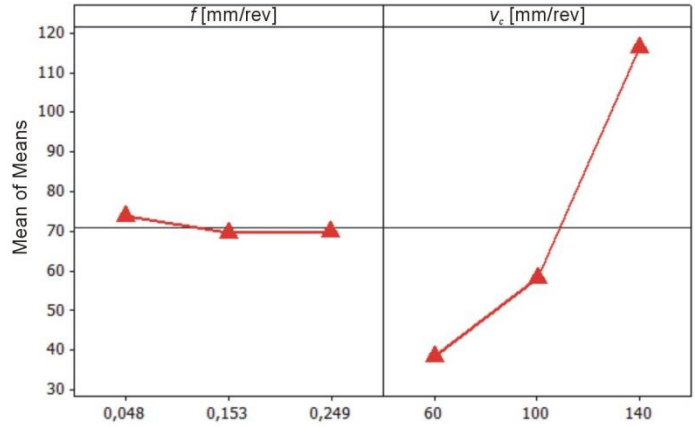

Figure 9. The relation between the average chip flow speeds on the rake face v_{ch} and feed f and cutting speed v_c for Kennametal tool.

The regression equation determined using the "linear + interactions" function for the average chip flow speeds on the rake face ($v_{ch_Kennametal}$) during the turning P10 sintered carbide tool:

$$v_{ch_{Kennametal}}(v_c, f) = 86{,}537 - 38{,}275 \cdot f - 1{,}445 \cdot v_c + 0{,}0119 \cdot {v_c}^2 + 0{,}1832 \cdot f \cdot v_c \quad (2)$$

Below is a 3D graphs (Figure 10) presenting the relationship between the average chip flow speeds on the rake face v_{ch} and feed f and cutting speed v_c for P10 sintered carbide tool, and for Kennametal tool.

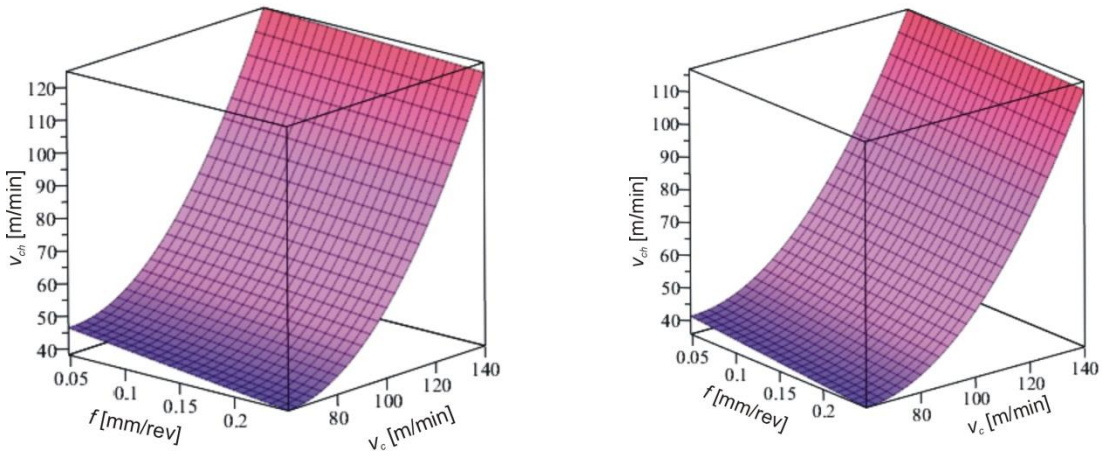

a) b)

Figure 10. The relationship between the average chip flow speeds on the rake face v_{ch} and feed f and cutting speed v_c for a) P10 sintered carbide tool, b) for Kennametal tool.

3. CONCLUSIONS

A measuring circuit was set up in the laboratory for recording the fast-changing phenomena in the cutting zone. The circuit consisted of a high-speed camera, Dedocool point lighting and a PC with specialist software. Continuous and spiral chips were obtained during the trials. Based on the performed analysis, it was determined that in the laboratory trials, the chip flow speeds on the Kennametal tool rake face are slightly lower. The maximum determined chip flow speed difference between the flat rake face tool and the Kennametal tool was 10 m/min. The lower chip flow speed is probably related to a larger chip compression as a result of using negative rake angles in the central part of the insert.

REFERENCES

[1] Benardos, P.G., Vosniakos, G.C., "Predicting surface roughness in machining: a review," International Journal of Machine Tools and Manufacture 43(8), 833–844 (2003).
[2] Struzikiewicz, G., Zębla, W., Rumian K., "Application of Taguchi method to optimization of cutting force and temperature during turning of difficult to cut materials," Key Engineering Materials 686, 114-118 (2016).
[3] Zębala, W., Kowalczyk, R., Matras, A., "Analysis and optimization of sintered carbides turning with PCD tools." Procedia Engineerin 100, 283-290 (2015).
[4] Słodki, B., Struzikiewicz, G., Slusarczyk, L., "Influence of cutting fluid conditions and cutting parameters on the chip form in turning of titanium and steel alloys," Key Engineering Materials 686, 74-79 (2016)
[5] Davies, M.A., Chou, Y., Evans, C.J., "On Chip Morphology, Tool Wear and Cutting Mechanics in Finish Hard Turning," CIRP Annals – Manufacturing Technology 45(1), 77–82 (1996).
[6] Ślusarczyk, Ł., Franczyk, E., "Development and verification of a measuring stand for recording the physical phenomena during turning," Photonics Applications in Astronomy Communications Industry and High-Energy Physics Experiments Book Series: Proceedings of SPIE 10445, 104456G (2017).
[7] Shamotoa, E., Aokia, T., Sencera, B., Suzukia, N., Hinoa, R., Koideb, T., "Control of chip flow with guide grooves for continuous chip disposal and chip-pulling turning," CIRP Annals - Manufacturing Technology 60(1), 125–128 (2011).
[8] Shaw, M.C., Vyas, A., "The Mechanism of Chip Formation with Hard Turning Steel," CIRP Annals - Manufacturing Technology 47(1), 77–82 (1998).
[9] Haglund, A.J., Kishawy, H.A., Rogers, R.J., "An Exploration of Friction Models for the Chip–Tool Interface Using an Arbitrary Lagrangian–Eulerian Finite Element Model," Wear 265, 452–460 (2008).

[10] Özel, T., Karpat, Y., “Identification of constitutive material model parameters for high-strain rate metal cutting conditions using evolutionary computational algorithms,” Materials and manufacturing processes 22(5), 659–667 (2007).
[11] Struzikiewicz, G., “The application of high-speed camera for analysis of chip creation process during the steel turning,” Proc. of SPIE 10031, 1-8 (2016).

Analysis of the material model of C45 steel for the simulation of the machining process

Łukasz Ślusarczyk*[a], Emilia Franczyk[a]
[a]Production Engineering Institute, Cracow University of Technology, Al. Jana Pawła II 37, 31-864 Cracow

ABSTRACT

Article presents the results of turning process simulation research, carried out with a use of specialized software based on FEM method. On the basis of test results, temperature distribution on the rake face of the cutting tool was determined. C45 steel was adopted as the workpiece material, and the sintered carbide, without a protective coating – as the tool material. Material models of the C45 steel were built using the Johnson-Cook constitutive equation and material constants available in the literature. Research scope included the simulation of the orthogonal turning process, considering different levels of rake face wear.

Keywords: Johnson-Cook model, simulation, temperature, FEM

1. INTRODUCTION

During the process of machining, large plastic deformations occur in the area of concentrated tangential stress. Part of the processed material moves along the rake face and the flank surface of the tool in the form of chip, and – under variable conditions of thermal and mechanical loads – forms a machined surface.
During the turning process, interrelated phenomena occur in the machining zone[1-4]:

- occurrence of stress, that leads to elastic and plastic deformations,
- occurrence of friction at the interface between the chip and the rake face, and between the flank surface and the workpiece,
- occurrence of internal friction within the workpiece,
- formation of the thermal zone, which leads to an increase in the temperature of the workpiece, chip and the tool,
- wear of the cutting edge.

Knowledge of the phenomena that occur in this processes, and of the relationships between them is a very important issue, as on its basis one can improve the planning system of the manufacturing process. It also facilitates making the right decision regarding the choice of the proper tool or cutting parameters under given conditions, which involve defining the thermal-mechanical state of the machining process[3-6]. During process design, including selection of tools, analysis of the cutting zone enables selection of appropriate material configuration between the workpiece and the tool, which allows determining the most effective tool stereometry[5-6]. Conducting analyzes of the critical stress-strain state of the tool material, which are based on theoretical models, allow for a more convenient initial analysis of the process, in a wider range of its variants, than with a use of experimental methods[7-9]. Strategies of building and conducting simulations of machining processes are constantly developed and expanded, starting from simple, flat analytical models in which a narrow, single slip plane is assumed, and ending with very complex models in a 3D coordinate system[8-9]. Using either simple or very complicated machining operation models, one can support the design and optimization of technological processes, perform simulations of chip formation for various machining parameters, which allows for a better control of the machining process. One of the most important issues in order to carry out the FEM simulation of the turning process correctly, is to adopt a suitable material model. Since the chemical composition, different for each material, translates into its physical properties, it is important that in order to obtain reliable and correct simulation results, it is essential to adopt a material model that accurately reflects the relationship between strain and stress in the areas of elastic and plastic deformation, up to the point of fracture. It is incorrect to use a linear-elastic model only, because the process of machining and formation of the chip takes place in the area of large plastic deformations. In the literature, one can often find many different models describing the relationships between plastic deformation and yield stress[7-9].

*slusarczyk@mech.pk.edu.pl; phone 12 374-32-14

Photonics Applications in Astronomy, Communications, Industry, and High-Energy Physics Experiments 2019, edited by Ryszard S. Romaniuk, Maciej Linczuk, Proc. of SPIE Vol. 11176, 111765E
© 2019 SPIE · CCC code: 0277-786X/19/$21 · doi: 10.1117/12.2536894

Most of the FEM simulation software (Abaqus, AdvantEdge, Ansys) has the option of choosing material model of a workpiece and tool from a built-in material library. Alternative solution is to create individual material model. During the construction of the material model, a constitutive equation based on the Jonhson-Cooke model was used. It takes the following form[9-12]:

$$\sigma(\varepsilon, \dot{\varepsilon}, T) = (A + B\varepsilon^n)\left(1 + C\ln\left(\frac{\dot{\varepsilon}}{\dot{\varepsilon}_0}\right)\right)\left(1 - \left(\frac{T - T_R}{T_m - T_R}\right)^m\right) \quad (1)$$

where: A – yield point for the reference value: strain rate $\dot{\varepsilon}_0$ and T_R temperature,
B, n – strain hardening factors,
C – dynamic hardening factor,
T_m – melting temperature.

The first part of the equation (1) describes the elastic-plastic characteristics of the material, the second expresses its viscosity and the third – the effect of thermal softening at high temperature. The Johnson-Cooke equation constants are determined experimentally. Parameters A, B and n are determined basing on the results of statistical research, and the values of constants C and m are the results of dynamic tests. Due to the difficulty and complexity of research aimed at determining material constants for a given material, a common solution is to calibrate a material model based on data obtained from real studies. Calibration consists in changing the values of material constants in such a way, that the results (e.g. cutting forces) obtained from the simulation coincide with the values obtained in an experimental way. It is a labor-intensive solution that requires knowledge of the entire machining process and dependencies between individual parameters.

2. RESEARCHES

The article presents the results a simulation of the machining process of an orthogonal C45 steel (AISI 1045) carried out with a tool made of uncoated, sintered carbide with a flat rake face. Chemical composition of C45 steel is presented in Table 1.

Table 1. The percentage chemical composition of the C45 steel.

Chemical composition [%]								
C	Mn	Si	P	S	Cr	Ni	Mo	Cu
0,42-0,5	0,5-0,8	0,1-0,4	max 0,04	max 0,04	max 0,3	max 0,3	max 0,1	max 0,3

Physical and chemical properties of the workpiece and the tool are shown below in Table 2.

Table 2. Physical and chemical properties of the workpiece and the tool.

Property	Steel C45	Sintered carbide
Density δ [kg/m^3]	7850	7850
Young's modulus E [GPa]	210	210
Poisson's ratio ν	0,3	0,3
Thermal conductivity λ [W/m·K]	49,4	38
Specific heat C_p [J/kg·K]	420	358

A 2D geometric model of an orthogonal turning process, with a finite element mesh, created in the AdvantEdge application is presented in the Figure 1 below. Presented profile of the rake face exemplifies new tool. It has been assumed, that the rake angle in the tool coordinate system equals γ=0º, the clearance angle α=8º, cutting edge radius r_n=0,02 mm, and the feed rate f=0,15 mm/rev. Machining process was simulated for two different cutting speed values: v_c=100 m/min and v_c=300 m/min. Cutting path length was l=3 mm.

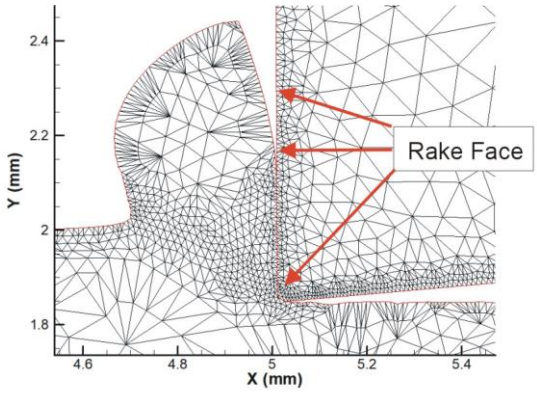

Figure 1. 2D geometric model of an orthogonal turning process, with a finite element mesh.

Material constants for C45 steel, obtained on the basis of literature analysis are shown in the Table 1.

Table 3. Material constants for C45 steel.

No.	A [MPa]	B [MPa]	C	n	M	T_t [°C]	T_o [°C]	ε_p^0 [s^{-1}]
1	553,10	600,80	0,0134	0,234	1,00	1538	20	1,00
2	451,60	819,50	$9* 10^{-7}$	0,1736	1,0955	1538	20	-
3	615,80	667,70	0,0134	0,225	1,078	1350	25	1,00
4	375,00	230	1260	0,430	0,9	1793	298	0,015

Smulations were carried out for three material models of C45 steel. After the initial verification, two models were created on the basis of coefficient sets from Table 3 (sets no. 1 and no. 3) and one using the data selected from the AdvantEdge database. The tool material was also selected from that database. The result of the cutting process simulation is the temperature distribution along the rake face, starting from the cutting edge. Results obtained for two cutting speed values are shown in Figure 2 (v_c=100 m/min) and Figure 3 (v_c=300 m/min).

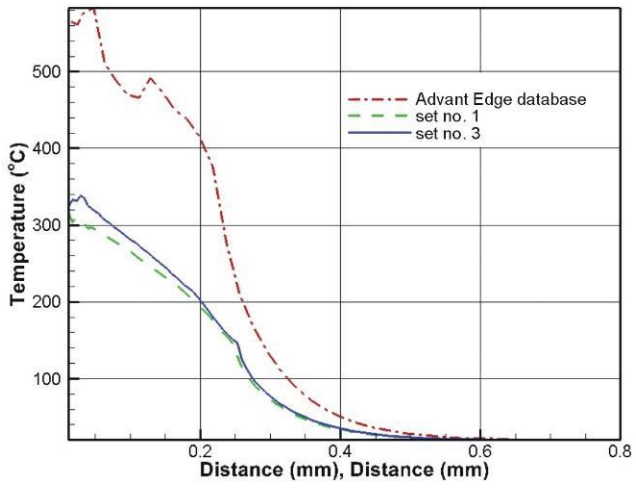

Figure 2. The temperature distribution along the rake face, starting from the cutting edge (v_c=100 m/min).

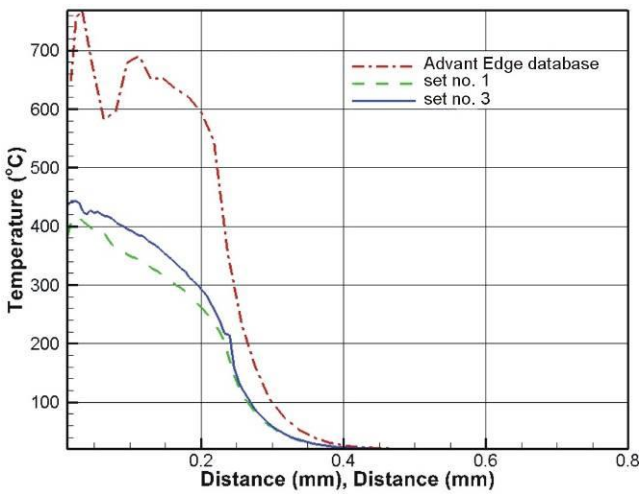

Figure 3. The temperature distribution along the rake face, starting from the cutting edge (v_c=300 m/min).

The temperature values obtained for models built on the basis of the Johnson-Cook equation are much lower than for the model selected from the software database. Results of laboratory tests, available in the literature and the results of own research, describing temperature values in the cutting zone during turning of the C45 steel were used to verify the correctness of the results obtained from the computer simulation. The results of available laboratory tests concern the temperature value in the cutting zone determined by contact (thermocouples) and contactless (thermovision cameras) methods. It should be assumed that the temperature at the rake face of the tool is higher. This assumption was adopted for initial verification of correctness of the computer simulation results. It was found that material models built in the Advant Edge application with the use of coefficient sets (1 and 3, Table 3) do not properly describe the C45 steel model, and the determined temperature at the rake face of the tool is significantly undervalued. In the case of a material model selected from the program database, obtained results of the temperature distribution were correct. For further analysis, a material model selected from the Advant Edge database was used.
Next stage of the research consisted in determining the impact of the rake face wear on the temperature values on it. To determine the geometrical wear indicators *KT* (mm) and *KB* (mm), and the shape of rake face contour, a series of 4 machining tests was carried out. The test stand and the process of an orthogonal turning are shown in Figure 4.

Figure 4. The test stand and the process of an orthogonal turning.

Tool geometry and process data were as in simulation tests. For two cutting speeds: v_{c1}=100 and v_{c2}=300 m/min, tool wear was determined after the cutting time of: t_{cut} = 90 s and t_{cut} = 180 s. A new tool was used to perform each trial. In order to measure the geometrical dimensions of the craters on the rake face, the tool was ground in a plane perpendicular to the cutting edge. The measurements of *KT* and *KB* values were carried out on a Bressher laboratory microscope. Exemplary tool profiles after the cutting time t_{cut} =90 s for v_c=100 and v_c=300 m/min are shown in Figure 5 and 6.

a) lateral view b) front view

Figure 5. Tool profiles after the cutting time t_{cut} =90 s for v_c=100 m/min.

a) lateral view b) front view

Figure 6. Tool profiles after the cutting time t_{cut} =90 s for v_c=300 m/min.

Exemplary tool profiles after the cutting time t_{cut} =180 s are shown in Figure 7 and 8.

a) lateral view b) front view

Figure 7. Tool profiles after the cutting time t_{cut} =180 s for v_c=100 m/min.

a) lateral view b) front view

Figure 8. Tool profiles after the cutting time t_{cut} =180 s for v_c=300 m/min.

Determined average values of geometric wear indicators *KT* and *KB* are presented in the Table 4 below.

Table 4. Average values of geometric wear indicators *KT* and *KB*.

	KT [mm]	*KB* [mm]
t_{cut} =90 s, v_{c1}=100 m/min	0,021	0,51
t_{cut} =90 s, v_{c1}=300 m/min	0,023	0,48
t_{cut} =180 s, v_{c1}=100 m/min	0,048	0,78
t_{cut} =180 s, v_{c1}=300 m/min	0,076	0,83

On the basis of obtained wear indicators values, in the graphical editor of the Advant Edge application, for both analyzed cutting speeds, tool profiles were created for a new tool, for a tool after time of t_{cut} = 90 s and for a tool after time of t_{cut} = 180 s. Exemplary tool profiles for v_c=100 m/min are shown in Figure 9.

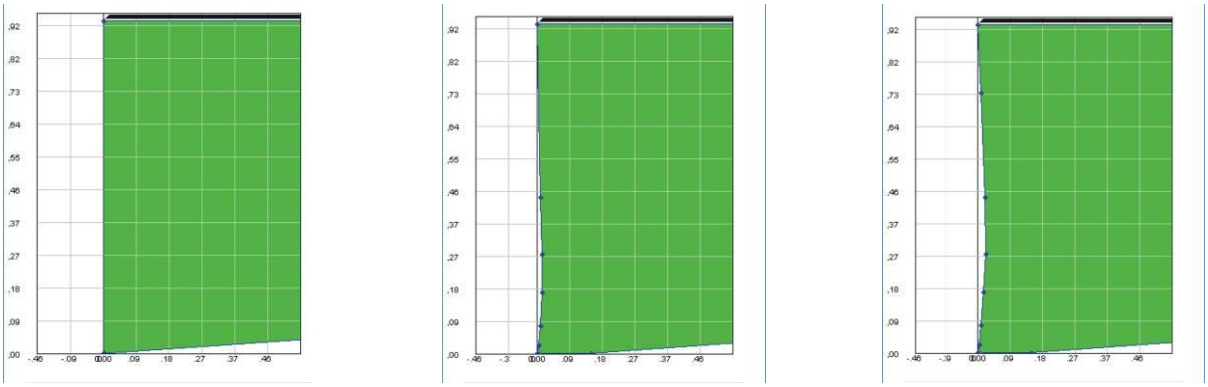

a) profile of a new tool b) profile of a tool after 90 s c) profile of a tool after 180 s

Figure 9. Exemplary tool profiles for v_{c1}=100 m/min.

On the basis of conducted simulations, temperature distributions were determined along the rake face of the tool, starting from the cutting edge, for two cutting speeds, and for three different levels of tool wear (Figure 10).

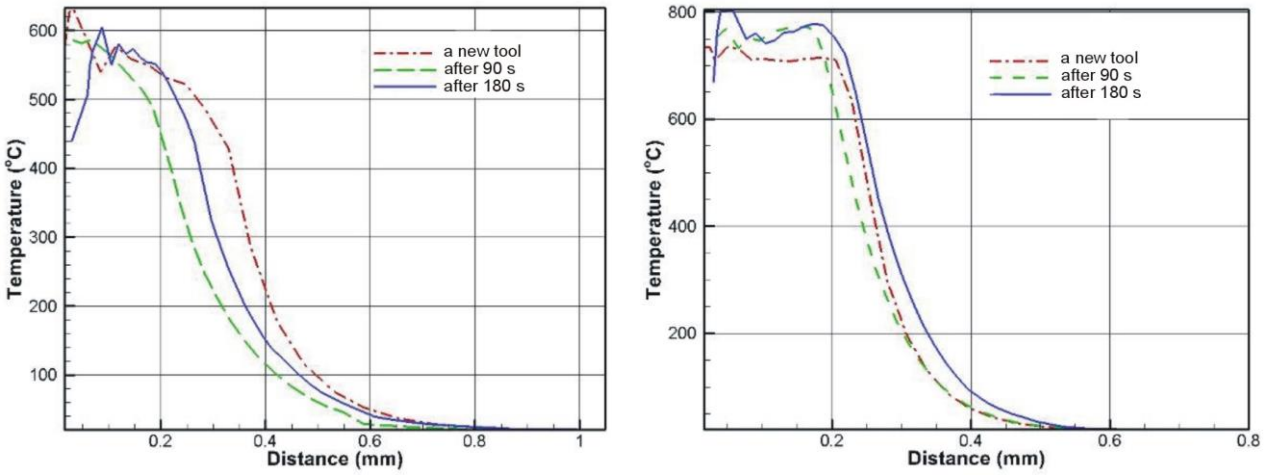

a) b)

Figure 10. Temperature distributions along the rake face of the tool, starting from the cutting edge, a) v_c=100 m/min, b) v_c=300 m/min

CONCLUSIONS

It can be seen that for v_c=100 m/min, the highest temperature occurs on the rake face of the new tool. At a distance of 0,3 mm from the cutting edge the difference between temperature values is approx. 300°C. The lowest temperature value occurs on the rake face after time of t_{cut} = 90 s. Lower temperature value for worn tools is probably due to the crater being formed and the tool geometry change from neutral to positive.

The temperature distribution on the rake face for v_c=300 m/min for different levels of tool wear is slightly different. The highest temperature occurs for a case with wear after time of 180 s, while the lowest temperature is similar to a case with v_c=100 m/min and wear after time of 90 s. As the cutting speed increases, a distinct increase in temperature can be observed, which confirms the literature data Preparation of the correct simulation model of the machining process and its proper calibration can significantly facilitate the analysis of physical phenomena in the cutting zone.

REFERENCES

[1] Johnson G.R., Cook W.H., “A constitutive model and data for metals subjected to large strain, high strain rate and high temperature,” Proceedings of the 7th International Symposium on Ballistics The Hague Netherlands, 541-547 (1983).

[2] Zębala, W., Kowalczyk, R., Matras, A., “Analysis and optimization of sintered carbides turning with PCD tools.” Procedia Engineerin 100, 283-290 (2015).

[3] Słodki, B., Zębala, W., Struzikiewicz, G., “Correlation between cutting data selection and chip form in stainless steel turning,” Machining Science and Technology, vol.19,Issue 2, 217-235 (2015).

[4] Zębala, W., Gawlik, J., Matras, A., Struzikiewicz, G., Ślusarczyk, Ł., “Research of Surface Finish during Titanium Alloy Turning,” Key Engineering Materials vol.581, 409-414 (2014).

[5] Ślusarczyk, Ł., Franczyk, E., “Development and verification of a measuring stand for recording the physical phenomena during turning,” Photonics Applications in Astronomy Communications Industry and High-Energy Physics Experiments Book Series: Proceedings of SPIE 10445, 104456G (2017).

[6] Jaspers S.P.F.C., Dautzenberg J. H., Taminiau D. A.”Temperature Measurement in Orthogonal Metal Cutting”. Int. J Advanced Manufacturing Technology, 14, 7-12 (1998).

[7] Ning, H., Zhigang, W., Chengyu, J., Bing, Z., "Finite element method analysis and control stratagem for machining deformation of thin-walled components," Journal of Materials Processing Technology 139, 332-336 (2003).

[8] Ślusarczyk, Ł., "The construction of the milling process simulation models," Photonics Applications in Astronomy Communications Industry and High-Energy Physics Experiments Book Series: Proceedings of SPIE 10031, 100310C (2016).
[9] Özel, T., "The Influence of Friction Models on Finite Element Simulations of Machining," International Journal of Machine Tools and Manufacture 46, 518–530 (2006).
[10] Haglund, A.J., Kishawy, H.A., Rogers, R.J., "An Exploration of Friction Models for the Chip–Tool Interface Using an Arbitrary Lagrangian–Eulerian Finite Element Model," Wear 265, 452–460 (2008).
[11] Ślusarczyk, Ł., "Analysis of the material model to simulation of the machining process," Photonics Applications in Astronomy Communications Industry and High-Energy Physics Experiments Book Series: Proceedings of SPIE 10808, 108085L (2018).
[12] User's Manual of AdvantEdge v5.6 machining simulation software, Minneapolis, MN, 2010.

Manufacturing methods and challenges in structural electronics

Bartłomiej Wałpuski*[a], Marcin Słoma [a]
[a]Faculty of Mechatronics Warsaw University of Technology, Andrzeja Boboli 8, 02-525 Warsaw, Poland;

ABSTRACT

Development of the three-dimensional printing made, that these techniques are more widely used. Initially, it was invented for quick prototypes manufacturing and models making, then adopted for final parts or even tools producing and nowadays even human organs and microstructures, smaller than human hair, can be 3D printed. It is not surprising, that these methods are adopted for electronics manufacturing, which gave the different approach of circuits producing called structural electronics. In this idea, electrical and mechanical modules are merged together what has great potential in building complex, multifunctional devices with limited sizes and weight. In this paper, a brief overview of structural electronics manufacturing methods are presented on both, industrial and academic, levels. Advantages and disadvantages of existing on the market systems are shown and the newest, often still under development, solutions are analysed. Potential and limitation of each method are presented and challenges of the whole branch of structural electronics manufacturing are shown.
Keywords: structural electronics, conductive inks, additive manufacturing.

1. INTRODUCTION

Electronic systems surround us from all sides. We find them not only in typical devices, such as consumer electronics, but more and more often they can be found in unusual places such as clothes, food (quality control) or even on teeth (to detect bacteria)[1,2]. What is more, electronics increasingly often extends the functionality of the device, and is not its only essence. More and more often we even talk about the Internet of Things (also known as smart things), where practically every object, apart from its basic function, additionally has electronic systems for mutual communication, data storage, gathering information from the environment or interaction with humans. Interest in this field is also manifested by the largest corporations such as Samsung, which acquires SmartThings for $200 million, or Google, which bought for $3.2 billion Nest company (both, SmartThings and Nest, are home automation producers) and whole IoT market value is estimated on $7.1 trillions[3–6]. The production of such devices has many extremes: on the one hand, due to the large scale, we want the production of these things to be cost-effective and environmentally friendly, and on the other hand, wireless communication (which is essential for this type of devices) and the large variety of devices requires precise and flexible manufacturing methods. What is more, it is also desirable that these electronics modules should be as small as possible, preferably not increase the size of traditional, non-smart, devices and with high reliability[7].

The group that fits in perfectly with these requirements is structural electronics (SE). Its main assumption is to break with the traditional approach, where the electronic circuit and the mechanical part of the device were made separately. In this technology there is a full integration of circuits and electronic components with mechanical structure in a single, monolithic device[8–10]. This technique was created by combining two, now very rapidly developing fields, namely additive manufacturing (AM) and printed electronics (PE). PE are techniques in which electronic circuits are produced using printing techniques (like inkjet printing, screen printing, flexography, etc.) by using special conductive inks and pastes. This allows for a very simple and cost effective production (vacuum, clean room or another special conditions are not required), and it is also environmentally friendly[11–15]. Therefore, it fits very well into the requirements for the production of SEs. Additive production, also known as 3D printing, consists in making objects from 3D models by joining or solidifying the material, usually layer by layer. This allows for full modification of the internal structure, and

*b.walpuski@mchtr.pw.edu.pl;

Photonics Applications in Astronomy, Communications, Industry, and High-Energy Physics Experiments 2019, edited by Ryszard S. Romaniuk, Maciej Linczuk, Proc. of SPIE Vol. 11176, 111765F
© 2019 SPIE · CCC code: 0277-786X/19/$21 · doi: 10.1117/12.2536953

the cost of production slightly depends on the level of complexity of the geometry[16–19]. These features are used in the SE to incorporate the electrical part of the inside of the internal structure produced in this way - it does not increase the cost of production or the dimensions of the device itself.

Although SE is a relatively new strain, there are many approaches to this problem, some are more related to printed electronics and others are closer to additive manufacturing. This paper presents the most common SE manufacturing techniques, their advantages and disadvantages, and the challenges they face.

2. PRINTING ON 3D

In this group, electrical circuits are applied only to the surface of a three-dimensional object. On the one hand, it increases the dimensions of the device, but usually this value is minimal, and on the other hand, it is often possible to place the electronics conformally on the internal walls of the housing. This solution also has a significant advantage, because it does not need a complete change in the manufacturing technique, but only extends the production chain, and adds many additional functions to produced devices (such as the ability to measure the environmental conditions, communication with other electronic devices, or change the working conditions). This group is quite closely related to printed electronics, often uses the same materials, but because the substrate in this case is not flat, it requires completely different production equipment.

2.1 3D Inkjet Printing

This technique was historically one of the first approaches to SE manufacturing. Traditional Inkjet is one of the most popular printing techniques, especially among the digital ones. It consists in forming a small drop of ink at the outlet of a nozzle with a diameter of less than 50 µm, and then separating it from the nozzle by an impulse produced by piezoelectric material, or thermal excitation. It has a very good resolution (even below 1 µm) and high surface efficiency (thanks to the high droplet generation frequency, up to 100 kHz), especially when the number of heads is multiplied. The conductivity of the paths obtained with this method is also a great advantage - the conductivity of produced paths is only slightly lower (less than 3 times) than for bulk silver. One of the disadvantages of this method is the low single layer thickness (single µm), which makes it difficult to apply at higher power. The mechanisms of formation and movement of drops require very precise observance of the distance between the nozzle and the substrate. Furthermore, small nozzle sizes require expensive inks with very small solid particles (e.g. nanoparticles) or even without any solids, because too large particles can cause nozzle clogging. Nevertheless, this technique was often used to produce RFID antennas or precise electronic circuits[20–23].

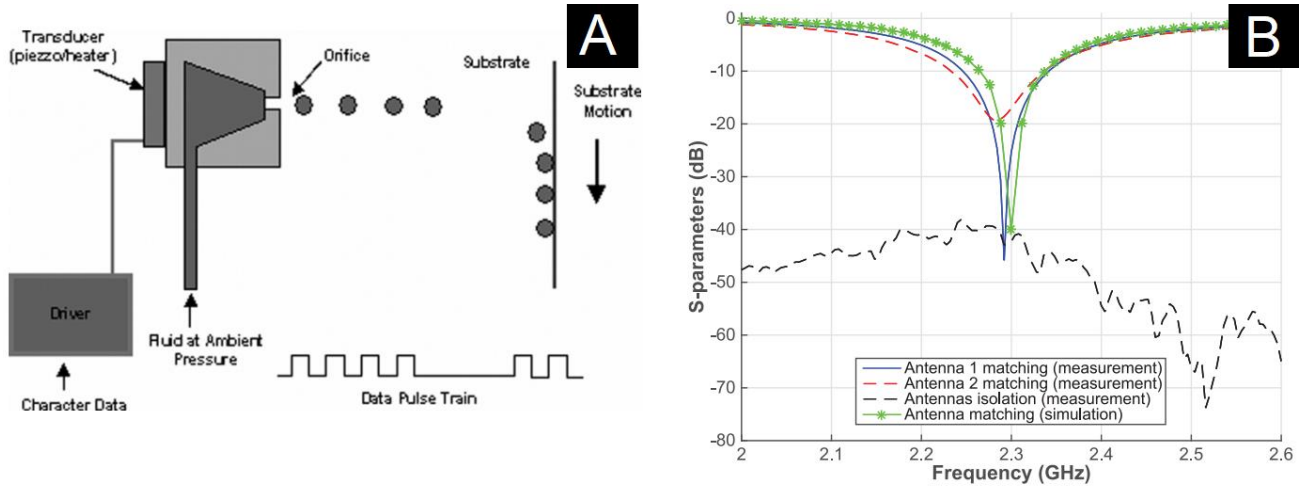

Figure 1. A- schematic of inkjet printing[23]; B- S-parameters of inkjet printed microwave antenna[22]

2.2 Aerosol Jet Printing

It was developed by Optomec, a company specialising in printed and structured electronics. It consists in forming an aerosol (using a piezoelectric element or a gas stream) from a conductive ink and then transporting it to the printing nozzle and forming it into a parallel beam using shielding gas. This allows to achieve a path with a diameter of less than 10 μm and the moulded jet is stable even over a distance of 2-5 mm (which reduces the requirement for accurate substrate movement). This also allows to made electrical connections even inside the vias, but the conductivity of such paths is worse than in the case of Inkjet printing - it was possible to achieve 1/10th of the conductivity of bulk silver. However, thanks to the greater thickness of a single layer (about 10 μm) it is possible to make connections that can provide 10 W of power or more. The disadvantages of this method include the need to control many technological parameters (such as aerosol or sheath gas flows) and the problem of using inks with low boiling point solvents. The efficiency of this method is also not the highest, especially when systems available on the market have only a single printing head. The disadvantages include the fact that Optomec is currently in a monopolistic position, which makes this systems one of the most expensive solutions[7,24–26].

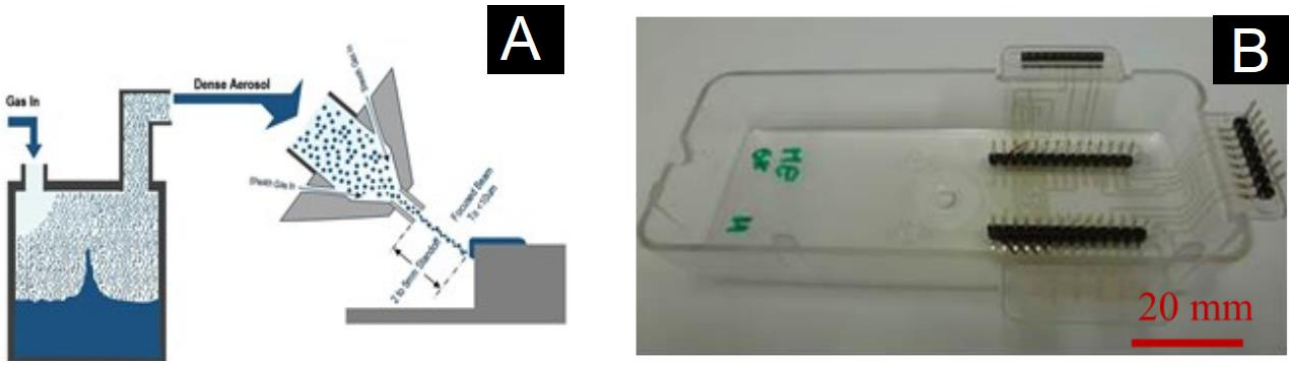

Figure 2. A- Aerosol Jet Printing scheme: aerosol generation and beam forming[25]; B- plastic case with 3D circuit made by AJP and attached connectors[7]

2.3 In-mold Electronics

In this approach, a different sequence was used compared to previous solutions: here, the electrical system is first printed on a flat film or polymer sheet surface and then it is formed into a three-dimensional structure, e.g. by vacuum thermoforming. Practically any PE technique can be used to create a circuit, but the materials must be more flexible to prevent damaged during the shaping process. Thanks to its simplicity, this technique is already used, for example, in the automotive industry, for the production of human-machine interface, which saves up to 70% in weight and up to 90% in thickness compared to traditional switches and buttons. At the same time, this technology reduces or even eliminates the need for assembly, and due to replacing of moving parts, the reliability of such panels is very high. The biggest drawbacks of this technique include geometric limitations of the manufactured object[27–29].

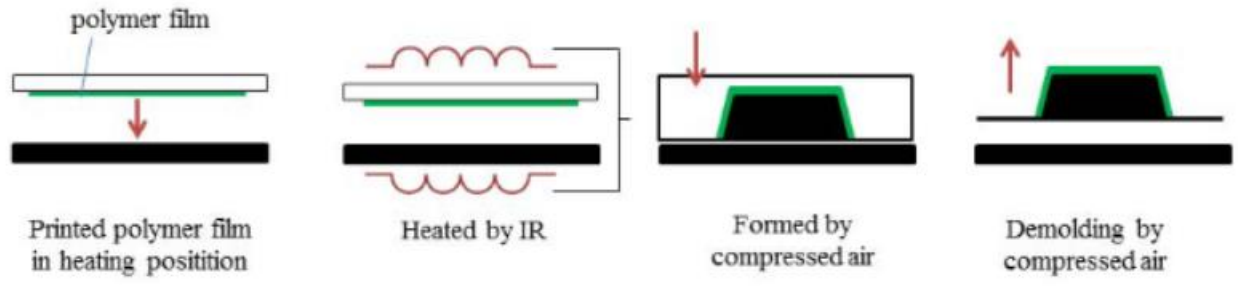

Figure 3. Steps of In-mold Electronics technique[28].

3. FULLY 3D PRINTED ELECTRONICS

This group is a kind of development of 3D printing: the standard additive manufacturing methods have been extended by producing of conductive paths, as well as the assembly of standard electronic components such as resistors, transistors and integrated circuits. A big advantage of these techniques is the possibility of merging the entire electrical module inside the mechanical elements (provided that they are large enough). The disadvantage of this group is the lower quality of the elements made in this way (e.g. prints in the fused deposition modelling technique have a significant roughness and lower strength in comparison to traditional methods). Due to the fixed production cost of each piece, these methods are also economically inefficient for large-scale and mass production.

3.1 3D printing + direct wright

In this technique, mechanical construction is performed using various additive manufacturing techniques (usually by fused deposition modelling technique (FDM), where thermoplastic filament is heated end extruded through nozzle or by stereolithography, where photosensitive resin is cured by UV laser) and the space for electronic circuitry and parts remains nonprinted. Electronic components (usually with surface connections) are placed just before the "closing" of their space, and the conductive paths, either, in each layer are filled with conductive inks or adhesives (heat cured if necessary), or at the end of the printout are filled with liquid conductive material (e.g. Galinstan-room temperature liquid alloy). The conductivity of the materials used is often 20 times worse than for solid silver or copper, but thanks to the thickness of each path, its resistance is comparable to a standard printed circuit board path. A big disadvantage is also the small resolution of such a method: the thinnest conductive paths usually have a width of 100 μm, which sometimes tries to be improved by milling the space under the electronic circuit. However, this technique was used to produce working devices such as wearable gadgets, sensors or heaters. Thanks to the high degree of integration and thus a significant reduction of the occupied space, this technique even made a part of the satellite, which was then sent into Earth's orbit[9,10,30–33].

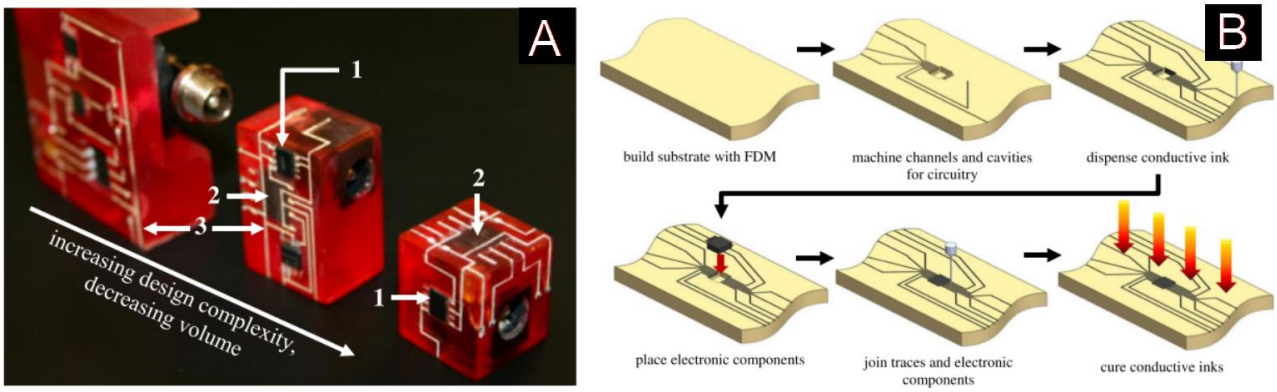

Figure 4. A- devices made by stereolithography and direct wright (1- Hall effect sensors, 2- microcontroller, 3- conductive paths)[32]; B- technological steps of manufacturing 3D printed electronics for satellite[32]

3.2 Conductive composite printing

This technique is by far the easiest to implement of all. It consists in using two materials for standard FDM production: one, being a dielectric and at the same time the main construction material (e.g. standard thermoplastic filament) and the other, a composite, being a electrical conductor. Advantage of this method is fact, that even the most common 3D printers, whose cost oscillates around $100, are sufficient for such production. The matrix of conductive composites are usually the same polymers that are used as dielectric, while the functional phase is usually different, allotropic carbon varieties (such as graphene, nanotubes or even carbon black) or metal powders. The biggest disadvantage of this technique is its low performance: the conductivity of such materials is even four orders of magnitude smaller than for bulk silver or copper. What is more obtained resolution is usually in the order of submillimeter and the connection of electronic components with such composite circuits is also problematic. Nevertheless, this technique can be used in very low cost application, like disposable sensors or gadgets[34–38].

CONCLUSION

Many manufacturing techniques, which can be used for the production of structural electronics, are presented. It is difficult to clearly indicate the best of them, because depending on the required performance or production scale, the result may be completely different. The spectrum of these techniques is quite wide, which is reflected in a large range of properties: e.g. resolution, or electrical conductivity are in the range of four orders of magnitude. Due to the relatively high innovativeness of these technologies, the reliability of such devices is often unknown, what can often block their introduction in market. The challenge is also to achieve high production efficiency (which would significantly reduce the cost): practically all the described techniques work best in small-scale applications. The only exception is In-mold Electronics, thanks to only this technology has now gone beyond the framework of academic experience. All the time the challenge is to design such devices: most often it is done manually, because there is no software on the market that would automatically generate three-dimensional electrical circuits.

ACKNOWLEDGEMENTS

This work was financed by Warsaw University of Technology, Faculty Mechatronics, Institute of Metrology and Biomedical Engineering and Foundation for Polish Science project nr First TEAM/2016-1/7.

REFERENCES

[1] Tan, E., Ng, W., Shao, R., Pereles, B., Ong, K., Tan, E. L., Ng, W. N., Shao, R., Pereles, B. D. and Ong, K. G., 'A Wireless, Passive Sensor for Quantifying Packaged Food Quality', Sensors **7**(9), 1747–1756 (2007).

[2] Mannoor, M. S., Tao, H., Clayton, J. D., Sengupta, A., Kaplan, D. L., Naik, R. R., Verma, N., Omenetto, F. G. and McAlpine, M. C., 'Graphene-based wireless bacteria detection on tooth enamel', Nat. Commun. **3**(1), 763 (2012).

[3] Wortmann, F. and Flüchter, K., 'Internet of Things: Technology and Value Added', Bus. Inf. Syst. Eng. **57**(3), 221–224 (2015).

[4] Gubbi, J., Buyya, R., Marusic, S. and Palaniswami, M., 'Internet of Things (IoT): A vision, architectural elements, and future directions', Futur. Gener. Comput. Syst. **29**(7), 1645–1660 (2013).

[5] Yang, S.-H., 'Internet of Things', Springer, London, 247–261 (2014).

[6] Tilley, A., 'Samsung Acquires SmartThings, A Fast-Growing Home Automation Startup', Forbes (2014).

[7] Stoukatch, S., Dupont, F., Seronveaux, L., Vandormael, D. and Kraft, M., 'Additive low temperature 3D printed electronic as enabling technology for IoT application', 2017 IEEE 19th Electron. Packag. Technol. Conf., 1–6, IEEE (2017).

[8] Lu, B.-H., Lan, H.-B. and Liu, H.-Z., 'Additive manufacturing frontier: 3D printing electronics', Opto-Electronic Adv. **1**(1), 17000401–17000410 (2018).

[9] Joe Lopes, A., MacDonald, E. and Wicker, R. B., 'Integrating stereolithography and direct print technologies for 3D structural electronics fabrication', Rapid Prototyp. J. **18**(2), 129–143 (2012).

[10] MacDonald, E., Salas, R., Espalin, D., Perez, M., Aguilera, E., Muse, D. and Wicker, R. B., '3D printing for the rapid prototyping of structural electronics', IEEE Access **2**, 234–242 (2014).

[11] Kamyshny, A. and Magdassi, S., 'Conductive Nanomaterials for Printed Electronics', Small **10**(17), 3515–3535 (2014).

[12] Aleeva, Y. and Pignataro, B., 'Recent advances in upscalable wet methods and ink formulations for printed electronics', J. Mater. Chem. C **2**(32), 6436–6453 (2014).

[13] Hoeng, F., Denneulin, A. and Bras, J., 'Use of nanocellulose in printed electronics: a review', Nanoscale **8**(27), 13131–13154 (2016).

[14] Ko, S. H., 'Low temperature thermal engineering of nanoparticle ink for flexible electronics applications', Semicond. Sci. Technol. **31**(7) (2016).

[15] Suh, Y. D., Kwon, J., Lee, J., Lee, H., Jeong, S., Kim, D., Cho, H., Yeo, J. and Ko, S. H., 'Maskless Fabrication

of Highly Robust, Flexible Transparent Cu Conductor by Random Crack Network Assisted Cu Nanoparticle Patterning and Laser Sintering', Adv. Electron. Mater. **2**(12) (2016).
[16] Weller, C., Kleer, R. and Piller, F. T., 'Economic implications of 3D printing: Market structure models in light of additive manufacturing revisited', Int. J. Prod. Econ. **164**, 43–56 (2015).
[17] Rayna, T. and Striukova, L., 'From rapid prototyping to home fabrication: How 3D printing is changing business model innovation', Technol. Forecast. Soc. Change **102**, 214–224 (2016).
[18] Campbell, I., Bourell, D. and Gibson, I., 'Additive manufacturing: rapid prototyping comes of age'.
[19] Gibson, I., Rosen, D. and Stucker, B. (Brent)., [Additive manufacturing technologies : 3D printing, rapid prototyping, and direct digital manufacturing].
[20] Sowpati, A. K., Palukuru, V. K., Pynttäri, V., Mäkinen, R., Kartikeyan, M. V and Jantunen, H., 'PERFORMANCE OF PRINTABLE ANTENNAS WITH DIFFERENT CONDUCTOR THICKNESS', Prog. Electromagn. Res. Lett. **13**, 59–65 (2010).
[21] Ready, S., Endicott, F., Whiting, G. L., Ng, T. N., Chow, E. M. and Lu, J., '3D Printed electronics', Jpn. J. Appl. Phys. **52**(5 PART 2), 9–12 (2013).
[22] Kimionis, J., Isakov, M., Koh, B. S., Georgiadis, A. and Tentzeris, M. M., '3D-Printed Origami Packaging With Inkjet-Printed Antennas for RF Harvesting Sensors', IEEE Trans. Microw. Theory Tech. **63**(12), 4521–4532 (2015).
[23] Junfeng Mei, Lovell, M. R. and Mickle, M. H., 'Formulation and processing of novel conductive solution inks in continuous inkjet printing of 3-D electric circuits', IEEE Trans. Electron. Packag. Manuf. **28**(3), 265–273 (2005).
[24] Wu, W., 'Inorganic nanomaterials for printed electronics: a review', Nanoscale **9**(22), 7342–7372 (2017).
[25] Paulsen, J. A., Renn, M., Christenson, K. and Plourde, R., 'Printing conformal electronics on 3D structures with Aerosol Jet technology', 2012 Futur. Instrum. Int. Work. Proc., 1–4, IEEE (2012).
[26] Krzeminski, J., Kanthamneni, A., Wagner, D., Detert, M., Schmidt, B. and Jakubowska, M., 'Microscale Hybrid Flexible Circuit Printed with Aerosol Jet Technique', IEEE Trans. Nanotechnol. **17**(5), 979–984 (2018).
[27] Giordano, G., 'Plastics Get Flexible for Electronics', Plast. Eng. **72**(2), 14–21 (2016).
[28] Wimmer, A., Reichel, H., Rauch, B., Schramm, R., Hörber, J. and Habler, B., 'Manufacturing of sandwich structures for the integration of electronics in in mold labelling components', 2016 12th Int. Congr. Molded Interconnect Devices, 1–4, IEEE (2016).
[29] Isohätälä, Anne; Sinivaara, Hasse; HEIKKINEN, M., 'Method for manufacturing an electronic assembly and an electronic assembly' (2017).
[30] Maalderink, H. H. H., Bruning, F. B. J., de Schipper, M. M. R., van der Werff, J. J. J., Germs, W. W. C., Remmers, J. J. C. and Meinders, E. R., '3D Printed structural electronics: embedding and connecting electronic components into freeform electronic devices', Plast. Rubber Compos. **47**(1), 35–41 (2018).
[31] Ota, H., Emaminejad, S., Gao, Y., Zhao, A., Wu, E., Challa, S., Chen, K., Fahad, H. M., Jha, A. K., Kiriya, D., Gao, W., Shiraki, H., Morioka, K., Ferguson, A. R., Healy, K. E., Davis, R. W. and Javey, A., 'Application of 3D Printing for Smart Objects with Embedded Electronic Sensors and Systems', Adv. Mater. Technol. **1**(1), 1600013 (2016).
[32] Espalin, D., Muse, D. W., MacDonald, E. and Wicker, R. B., '3D Printing multifunctionality: structures with electronics', Int. J. Adv. Manuf. Technol. **72**(5–8), 963–978 (2014).
[33] Lu, Y., Vatani, M. and Choi, J.-W., 'Direct-write/cure conductive polymer nanocomposites for 3D structural electronics', J. Mech. Sci. Technol. **27**(10), 2929–2934 (2013).
[34] Dul, S., Fambri, L. and Pegoretti, A., 'Fused deposition modelling with ABS–graphene nanocomposites', Compos. Part A Appl. Sci. Manuf. **85**, 181–191 (2016).
[35] Dul, S., Fambri, L., Pegoretti, A., Dul, S., Fambri, L. and Pegoretti, A., 'Filaments Production and Fused Deposition Modelling of ABS/Carbon Nanotubes Composites', Nanomaterials **8**(1), 49 (2018).
[36] Leigh, S. J., Bradley, R. J., Purssell, C. P., Billson, D. R. and Hutchins, D. A., 'A Simple, Low-Cost Conductive Composite Material for 3D Printing of Electronic Sensors', PLoS One **7**(11), J. Hong, Ed., e49365 (2012).
[37] Podsiadły, B., Skalski, A., Wałpuski, B. and Słoma, M., 'Heterophase materials for fused filament fabrication of structural electronics', J. Mater. Sci. Mater. Electron. **30**(2), 1236–1245 (2019).
[38] Wei, X., Li, D., Jiang, W., Gu, Z., Wang, X., Zhang, Z. and Sun, Z., '3D Printable Graphene Composite', Sci. Rep. **5**(1), 11181 (2015).

Effect of sonication process and solvent type on ageing of silver ink for aerosol jet printing

Kacper Skarżyński, Jakub Krzemiński, Marcin Słoma

Warsaw University of Technology, Faculty of Mechatronics, Institute of Metrology and Biomedical Engineering, Micro- and Nanotechnology Division, 8 sw. A. Boboli st., 02-525 Warsaw, Poland

ABSTRACT

Inks for printed electronics developed in the laboratory have several advantages over commercial ones – researchers have full information about the composition and are able to change its properties without the danger of undesirable interactions between the components. The requirement for this type of ink is long term stability in order to utilize its individuals features. Within this paper the difference between freshly created and 3-months old inks was examined to determine the effect of different sonication processes and solvents on the ageing of silver nano-particle ink. Ink was sonicated using a sonotrode and an ultrasonic bath. To examine inks printability in the aerosol jet printing process, their ability to create dense aerosol mist for 1 hour using an ultrasonic atomiser was investigated. Aerosol droplets diameters were measured to compare fresh and 3 months old printable inks.

Keywords: Aerosol Jet Printing, Inks, Printed Electronics

1. INTRODUCTION

Aerosol Jet Printing (AJP) is relatively new printing technique. It can reach the needs of high precision and easily modified technique to produce electronics on flexible or 3d substrates[1]. It is applied in fields where low resistivity, thin interconnects on non-planar and flexible substrates are required, for example in high speed controllers assembly, where AJP interconnects replaced wire bonding[2], or printed antennas[3], where 20 µm wide interconnects are required. Usage of this technique in creating micro patterns on glass for optical terahertz applications[4] and detection electrodes[5] is possible because of its accuracy. It potential is not used in mass production because of necessity of manual calibration and regulation due to the changing parameters during the process.

Schematic of AJP is shown in the Figure 1.[6] During the atomization process aerosol mist is created, and then transported to the printing head by atomisation gas (nitrogen or air). Inside the head jet is concentrated by sheath gas and printed thru the printing nozzle. The substrate can be placed up to 10mm below the nozzle, and because of that printing on 3d substrate is possible.[3]

Ultrasonic atomisation process is used for inks with viscosity up to 20cP. Liquid ink is atomised to create dense mist, containing droplets below 5µm.[7] In this process, shown in the picture 2, energy of ultrasonic is transferred from piezoelectric transducer to ink. When this energy is high enough, ink forms into the shape of standing wave. Kinetic energy of the wave ripped off the droplet's from its top, with the aid of cavitation process.[8] In ultrasonic atomisation stand made for Aerosol Jet Printing, calibration of the position of tube containing ink, power and frequency of piezoelectric transducer is required to obtain effectiveness of the process. Viscosity, solid loading, and surface tension of the ink also plays the crucial role in this process.[9] Dense mist allows usage of low total flow rate, which, with the proper focusing ratio (atomisation and sheat gas quotient), reduces path width.[10]

In this paper ability of ink to create dense aerosol mist for 1 hour, mist density and droplets mean diameters were measured to investigate effectiveness of fresh and 3-months old silver inks in aerosol jet printing process.

Photonics Applications in Astronomy, Communications, Industry, and High-Energy Physics Experiments 2019, edited by Ryszard S. Romaniuk, Maciej Linczuk, Proc. of SPIE Vol. 11176, 111765G
© 2019 SPIE · CCC code: 0277-786X/19/$21 · doi: 10.1117/12.2536963

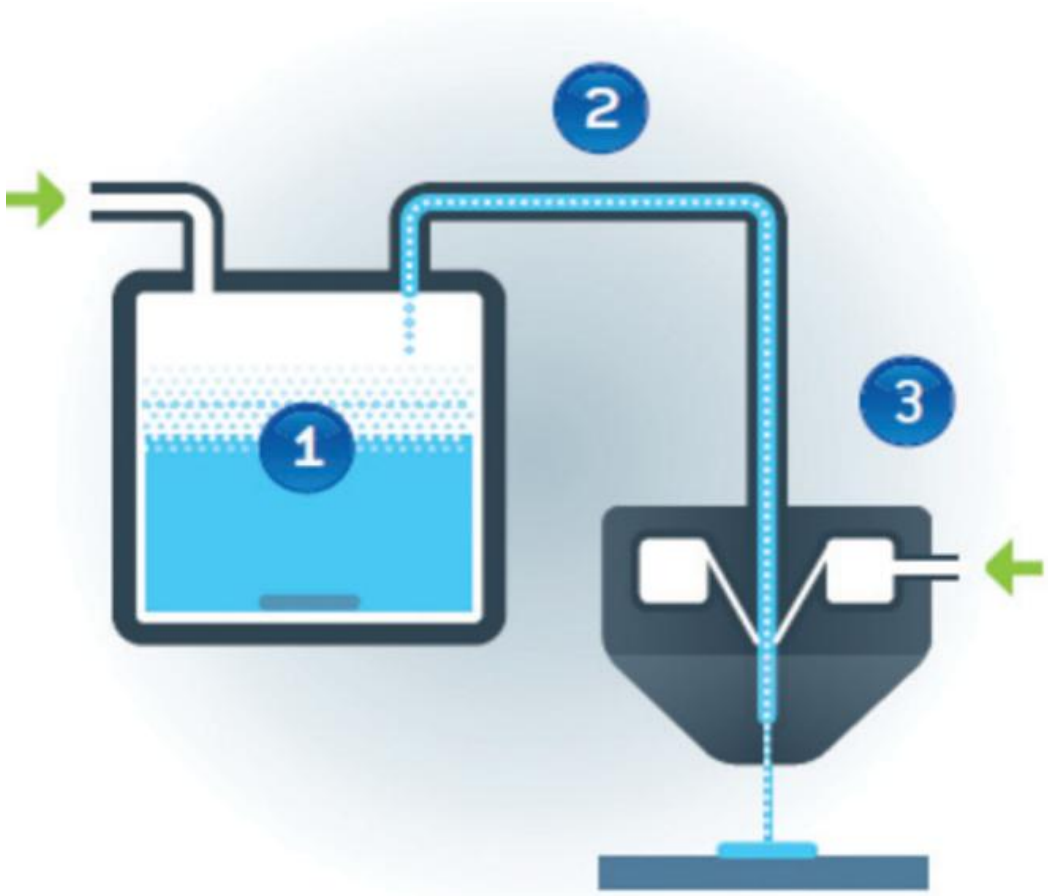

Figure 1. AJP schematics (1)Atomisation process (2)Aerosol mist transportation (3) collimation of aerosol jet in printing head[6]

2. METHODS

2.1 Materials and Ink mixing

An Ink recipes have been developed on faculty of Mechatronics, Warsaw University of Technology. They are based on silver nanoparticles and was created using processes of mixing, stirring and homogenization. To achieve homogenisation of mixture, two ultrasonic methods was used:

I. Sonotrode sonication
II. Bath sonication

Two solutions was used as solvents

A. Organic solution 1.1
B. Organic solution 1.2

There were three produced inks for two comparisons, shown in the table 1. All inks was stored in sealed tubes for aerosol jet printing ultrasonic atomisation stand.

Table 1 Produced Inks

Sample Number	Ultrasonic method	Type of solution	Weight composition
Sample 1	I	A	nAg: 8,748 g surfactant: 0,17433 g solvent: 26,25 g
Sample 2	I	B	nAg: 8,750 g surfactant: 0,17524 g solvent: 26,25 g
Sample 3	II	B	nAg: 8,748 g surfactant: 0,17505 g solvent: 26,25 g

2.2 Atomization process

Atomization process was made using ultrasonic atomizer build in Institute of Metrology and Biomedical Engineering and pneumatic system containing compressor, air filter and flow controller. Before the atomisation test each ink was manually stired and sonicated using ultrasonic bath for 2 minutes. One millilitre of inks was transferred to sample tubes which were mount in ultrasonic atomizer.

The atomizer was manually calibrated to achieve densest mist. If after an hour mist is still produced with similar density droplets was transferred onto paper filter mounted in mount used for sealing glass tube in AJP process (Figure 2) by carrier gas.

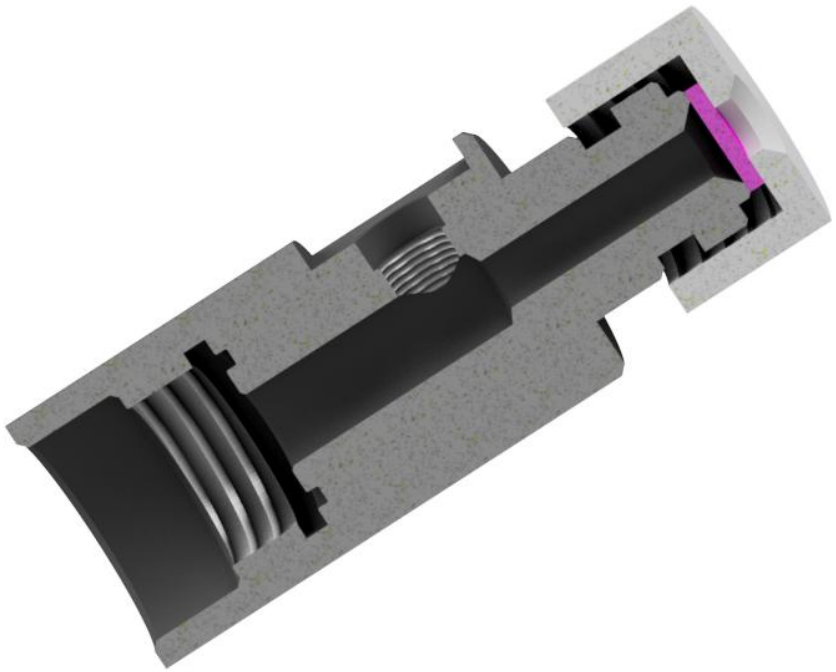

Figure 2. Mounting paper filter in AJP system part

2.3 Measurement

Time was measured by stopper. Visibility of droplets was investigated using a 50-fold magnification optical microscope and droplets diameters was measured by microscope VHX-900F Keyence build in software.

3. RESULTS AND DISCUSSION

Table 2 present the results of atomisation time of inks and visual comparison of density of their mists, measured as minimal carrier flow to achieve visibility of the droplets on filter paper, adjusted with 4 sccm step.

Table 2 Atomisation Time of samples and minimal carrier flow to achieve visibility of droplets on filter paper

	Fresh			3 months old		
	Sample 1	Sample 2	Sample 3	Sample 1	Sample 2	Sample 3
Atomisation time [hours]	>1	>1	>1	0	>1	>1
Carrier flow [sccm]	20	16	20		20	50

Lowest obtained carrier flow was measured for Sample 2, both between fresh samples and old samples. Old sample 1 was unable to atomize, as the result of evaporation of 35 wt.% of its solvent.

Table 3 show images of the droplets on filter papers and their mean planar diameter. Each mean planar diameter was calculated from 8 measured diameters.

Table 3 mean planar diameters of ink droplet marks and estimated diameters of droplets.

Sample Number	Mean planar diameter of ink droplet marks [µm]	Estimated mean diameter of droplets [µm]
Sample 1 fresh	10	10-20
Sample 2 fresh	9	9-18
Sample 3 fresh	10	10-20
Sample 2 old	16	16-32
Sample 3 old	14	14-28

According to literature[9], shape of ultrasonically atomised water droplets is spherical. To estimate droplets diameter, scaling factor for planar measured water droplets should be ~2. Silver Ink scaling factor, because of its solid loading, should be between 1 and 2.

Diameters of old samples are 1,5 times higher than diameters of fresh samples. Differences inside fresh and old groups are low enough to be considered as the result of choosing the measure areas on the surfaces of filter papers.\

Image samples of diameter measurement areas was shown in the Figures 3-7.

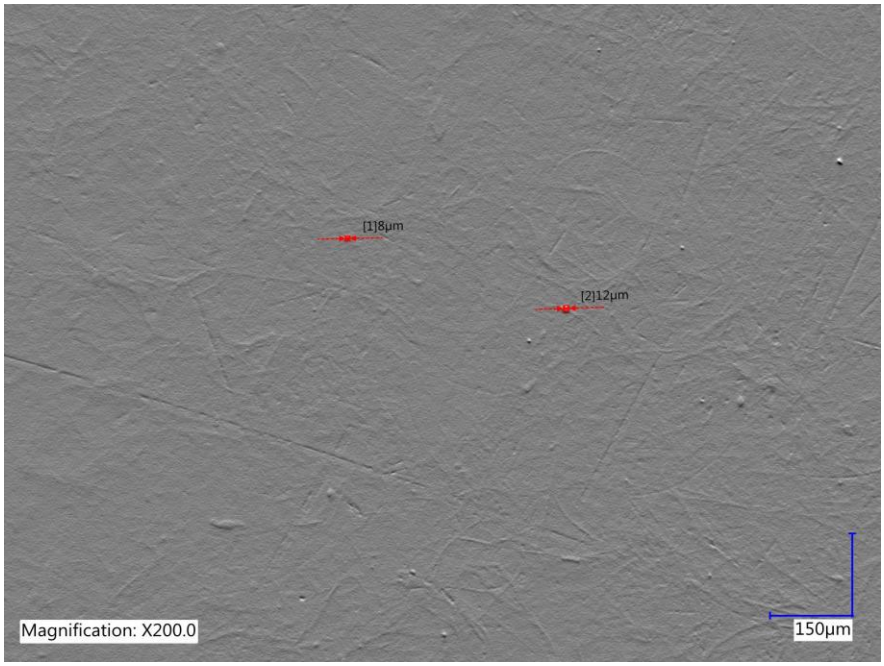

Figure 3. Sample measure area of planar diameter of fresh sample 1

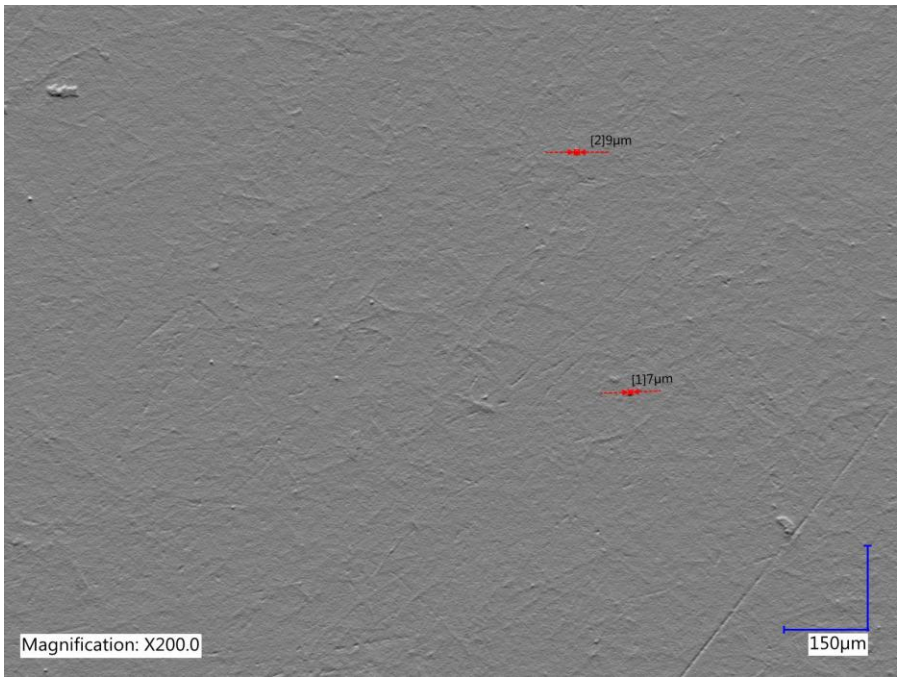

Figure 4. Sample measure area of planar diameter of fresh sample 2

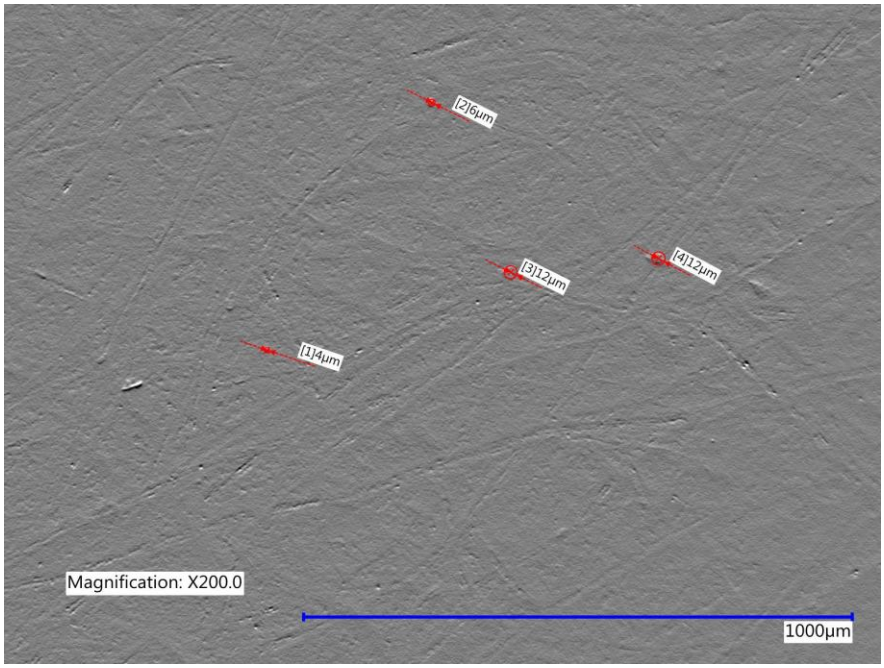

Figure 5. Sample measure area of planar diameter of fresh sample 3

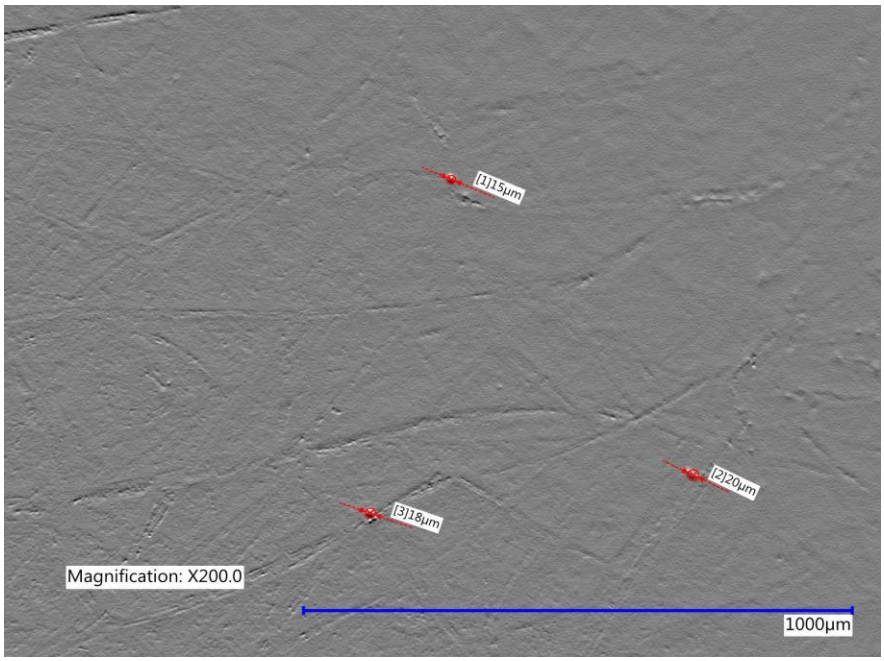

Figure 6. Sample measure area of planar diameter of old sample 2

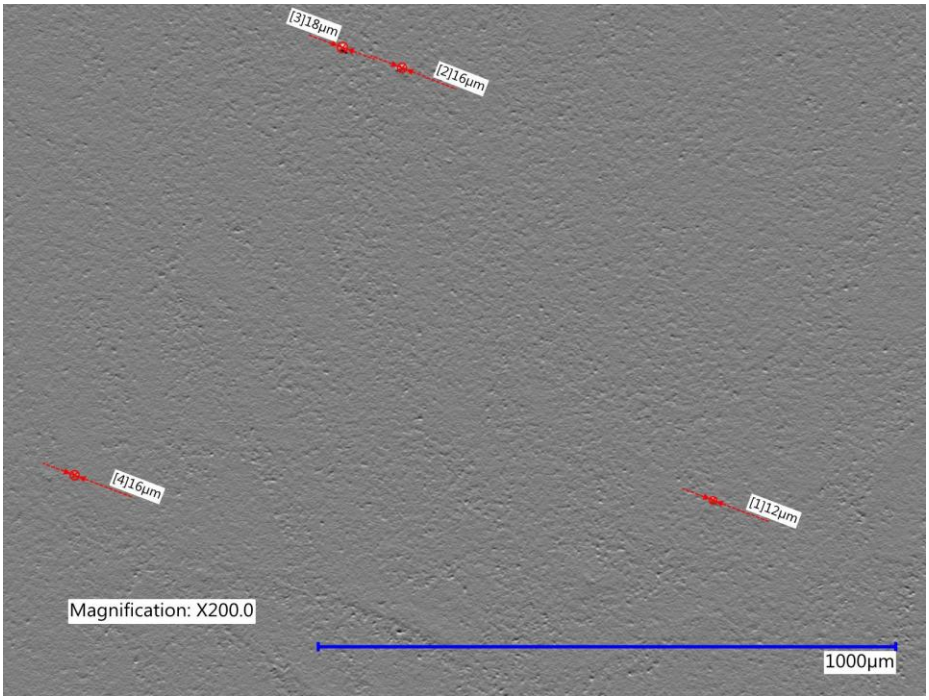

Figure 7. Sample measure area of planar diameter of old sample 3

4. CONCLUSION

In this article ageing process of silver nano-particle inks for aerosol jet printing process was presented. Inks can be used in Aerosol Jet Printing system with ultrasonic atomisation stand. Ink printability for aerosol jet printing process was investigate by measurement of its ability to create dense aerosol mist for an hour. Printable inks was then atomised and mists were applied on filter papers, transported by atomisation gas, which minimal flow required to obtain visible, using a 50-fold magnification optical microscope, droplet marks was investigated. The droplet marks size were measured using microscope X build-in software and diameter of the droplets were estimated.

Old ink droplets mean diameter was 1,5 times higher than diameter measured for fresh inks. Old inks require higher carrier gas flow to be applied on filter paper than fresh inks. Old Sample 1 was unable to atomise and old sample 3 using bath sonication has low mist density because of their solvent evaporation. The future tests should focused on evaluating technical capability to restore the parameters of the samples to their previous state and role of surfactant aging in the process.

ACKNOWLEDGMENTS

This research is part of the „Functional heterophase materials for structural electronics" project carried out within the First TEAM/2016-1/7 programme of the Foundation for Polish Science co-financed by the European Union under the European Regional Development Fund.

This work was financed by Warsaw University of Technology, Faculty Mechatronics, Institute of Metrology and Biomedical Engineering and Foundation for Polish Science project nr First TEAM/2016-1/7.

REFERENCES

[1] J. Navratil, A. Hamacek, J. Reboun, and R. Soukup, "Perspective methods of creating conductive paths by Aerosol Jet Printing technology," *Proc. Int. Spring Semin. Electron. Technol.*, vol. 2015-Septe, pp. 36–39, 2015.

[2] S. Stoukatch *et al.*, "Evaluation of aerosol jet printing (AJP) technology for electronic packaging and interconnect technique," *2012 4th Electron. Syst. Technol. Conf. ESTC 2012*, 2012.

[3] M. J. Renn, K. K. Christenson, D. Giroux, and D. Blazej, "Aerosol Jet® Printing of Conductive Epoxy for 3D Packaging," *Pan Pacific Microelectron. Symp.*, pp. 1–7, 2013.

[4] C. Oakley and P. Chahal, "Aerosol Jet Printed Quasi-Optical Terahertz Components," *IEEE Trans. Terahertz Sci. Technol.*, vol. 8, no. 6, pp. 765–772, Nov. 2018.

[5] E. Cantù, S. Tonello, G. Abate, D. Uberti, E. Sardini, and M. Serpelloni, "Aerosol Jet Printed 3D Electrochemical Sensors for Protein Detection," 2018.

[6] J. Q. Feng, "Mist flow visualization for round jets in Aerosol Jet® printing," *Aerosol Sci. Technol.*, vol. 53, no. 1, pp. 45–52, 2019.

[7] M. Renn, "Aerosol Jet Process Development Techniques," *Optomec North Am. User Gr. Meet.*, vol. 2010, 2010.

[8] B. Karl Sollner, "T H E MECHANISM OF T H E FORMATION O F FOGS BY ULTRASONIC WAVES."

[9] R. Rajan and A. B. Pandit, "Correlations to predict droplet size in ultrasonic atomisation."

[10] A. Mahajan, C. D. Frisbie, and L. F. Francis, "Optimization of aerosol jet printing for high-resolution, high-aspect ratio silver lines," *ACS Appl. Mater. Interfaces*, vol. 5, no. 11, pp. 4856–4864, 2013.

Controlling of gold nanoparticles by the help of transverse spin momentum of evanescent waves in biomedical applications

Oleg V. Angelsky*[a], Dmytro I. Ivanskyi[a], Waldemar Wójcik[b], Ainur Ormanbekova[c]
[a]Yuriy Fedkovych Chernivtsi National University; [b]Lublin University of Technology;
[c]Taraz State University after M.Kh.Dulaty

ABSTRACT

Additional approaches of gold nanoparticles manipulation in evanescent wave were proposed in the given paper. Vertical spin excited under the birefrigent biotissue section is transmitted to particles causing their complex motion in a surrounding fluid of tissue near the surface layer. The theoretical and experimental confirmation of the existence of the extraordinary spin momentum of the evanescent wave is proposed.

Keywors: evanescent wave, nanoparticles, biotissue

1. INTRODUCTION

Nanotechnology is widely used in biomedicine, including nanotherapy, transportation of medical products, biomarking, cancer diagnosis, bioprobing. All this is based on the use of non-invasive methods for evaluating and analyzing pathological changes in tissues with the search for new opportunities for treating diseases and possible pathologies by non-traumatic, easily accessible methods. As a rule, medical robots used for this aim are programmed to perform certain functions and are managed outside the human body. In this case, drugs are injected into nanoparticles, which imply side effects reduction, thereby overcoming the problems of solubility and toxicity. Thus, in particular, gold nanoparticles measuring 50 to 80 nm in size are effectively used[1, 2]. Thus using of gold nanoparticles is useful for diagnosing of optical fields[3,4,5], estimating their coherence and polarization properties, as well as for active elements in biomedical application[6]. These particles, being non-toxic to the body, can be introduced into the body in order to detect and destroy pathologically altered tissues in a non-invasive manner. Complex phase distribution of optical beam[7], subsequent phase recovery[8] form the promising picture of controlling and manipulation of gold nanoparticles in optical field of different nature. In this connection, evanescent waves are of particular interest, as they being limited by the size of thin layers propagate along the surface and are able to transmit their own angular momentum to the nanoparticles localized on the surface, thus setting a certain direction of their displacement[9].

Recent studies[10] of evanescent waves excited by linearly polarized waves of different azimuth demonstrate the possibility of realizing the transverse spin momentum in the plane above the section surface. For a linearly polarized wave with 45° polarization azimuth, falling on the interface of two media, the so-called vertical spin of the evanescent wave arises at an angle that ensures total internal reflection[8] (TIR). It is worth mentioning that by changing the incidence angle of light to the interface, it is possible to control the direction of the motion of nanoparticles, and, accordingly, of the entire nanostructure, which, depending on the problem being solved, can be a combination of different constituent components. Complex interaction mechanisms of different type of medium with internal radiation leads to creation of new memory system based on exciton[11] or plasmon excitation or evanescent wave[2] producing under the investigated structure.

The aim of this work is to search for optimal conditions for the formation of the vertical spin of the evanescent wave to control the mechanical displacements of gold nanosized particles localized on the surface of a section of a biological birefringent substance. We will assume that the medium, in which the evanescent wave is excited, is close in composition to a physiological one. It is proposed to use the so-called tissue fluid, which is based on water, amino acids, fatty acids, hormones and various waste cells, the dimensions of which are much smaller as compared with controlled gold nanoparticles. As a sample, a birefringent medium is selected, in which macroscopic anisotropy is caused by the fibrillar structure of partially oriented close-packed fibers[2]. Muscle tissue, tendon and derma, i.e. biotissues are the examples of such tissues[12].

* idmitrow@gmail.com

Photonics Applications in Astronomy, Communications, Industry, and High-Energy Physics Experiments 2019,
edited by Ryszard S. Romaniuk, Maciej Linczuk, Proc. of SPIE Vol. 11176, 111765H
© 2019 SPIE · CCC code: 0277-786X/19/$21 · doi: 10.1117/12.2536977

For a biotissue, in particular, muscle fiber, the derma thickness usually amounts to about 50–100 μm. For some other organs, the thickness may be about 300 μm. Such thickness values ensure the coherence and polarization of laser radiation as it penetrates deep into the structure. It is this fact that allows probing of the selected medium by polarized radiation. Moreover, choosing the wavelength of the laser radiation within the "transparency window" (800–1500 nm)[2] for biological tissues enables to achieve the total internal reflection at the biotissue-liquid interface. And this means it is possible to realize the vertical spin of an evanescent wave with further transportation of gold nanoparticles in the chosen direction.

2. MODEL OF OPTICAL ANISOTROPY OF BIOLOGICAL TISSUES

The optical anisotropy of the tissue is determined by the structural characteristics and the difference between the refractive indices of collagen fibers and the base material[13]. Using a two-component model with the representation of collagen fibers in the form of long cylinders[2], optical anisotropy Δn can be characterized as

$\Delta n = \frac{(n_{col}^2 - n_{bas}^2)(n_{col} + n_{bas})c(1-c)}{(1+c)n_{col}^2 + (1-c)n_{bas}^2}$, where c is the volume fraction of collagen fibers, n_{col}, n_{bas} – refractive indices for collagen and the base material respectively. Collagen has refractive index of 1.45, and is immersed in a dielectric medium with the refractive index of 1.37. Calculation of the refractive indices of ordinary (n_o) and extraordinary (n_e) rays in an anisotropic biotissue medium was carried out in the approximation of the model of parallel dielectric cylinders uniformly distributed in the interval from 80 to 120 nm with a volume fraction of cylinders equal to f = 0.8 and a radius of 50 nm, which is close to typical morphological parameters characterizing the fibrillar structure of the derma. Forming a denser packing of cylinders, i.e. realizing the model of a practically homogeneous medium, the scattering in the volume of the model section is reduced to minimum. Then, for an anisotropic, practically homogeneous medium, the orientation of the fast axis coincides with that of the collagen fibers of the muscle fiber.

To avoid the destruction of biological tissue when heated by laser radiation, it is necessary to select both the duration of the radiation pulse (the duration of the radiation exposure to minimize the damage zone and irreversible temperature changes) and the temperature interval of tissue heating.

For a laser with a depth of penetration into biological tissue up to 1 mm, the pulse duration is chosen to be approximately 1 μs, which provides the temperature of heating the biological tissue to 50–60°, while the optical properties of the tissue do not change.

According to Ref.[2], the refractive indices of ordinary and extraordinary beams are estimated as

$n_o = \sqrt{\varepsilon_o} = \sqrt{\varepsilon_{bas}(1+\frac{2\alpha f}{1-\alpha f})}$, $n_e = \sqrt{\varepsilon_e} = \sqrt{\varepsilon_{col} f + \varepsilon_{bas}(1-f)}$, where $\alpha = \frac{\varepsilon_{col} - \varepsilon_{bas}}{\varepsilon_{col} + \varepsilon_{bas}}$ – polarization ability of dielectric cylinders.

The simulation was carried out in the approximation when the vector of electric field intensity propagating in a medium of a linearly polarized monochromatic electromagnetic wave with unit amplitude was oriented parallel or perpendicular to the axes of the cylinders, respectively. The applied approach is based on using of the criterion for the equality of the energy of the electromagnetic field in the volume of the medium occupied by the model scattering center and the field energy in the equivalent volume of a spatially homogeneous medium[2].

3. ANALYSIS OF THE MECHANISM OF THE VERTICAL SPIN EXCITATION IN THE NEAR-SURFACE LAYER OF TISSUE FLUID

The evanescent wave, caused by the complete internal reflection of a linearly polarized wave of 45° azimuth at the interface “biotissue-liquid (water)”, is elliptically polarized, and the ellipticity is determined by the direction of propagation of the beam in the biotissue medium.

Let us consider the conditions for the formation of the vertical spin of the evanescent wave. Figure 1 shows the spreading of an optical flat parallel beam through a model section of the birefringent medium of a biotissue.

We will assume that the optical force produced by an elliptically polarized beam that propagates in the direction towards the interface "birefringent section-tissue fluid" ($\vec{F}_{br12}$), and the force acting in the opposite direction ($\vec{F}_{br21}$) are compensated. It was the case when the incidence angle of the beam on the section was determined, and the corresponding azimuth of the beam polarization at the input was selected in order to form the transverse polarization-dependent force of the evanescent wave.

Further we will use here the following terminology: the beam impinging on the first surface of the slice will be referred to as a probing beam, while the beam impinging on the second surface – the incident beam. Let us estimate the magnitude of the optical force for an elliptically polarized beam, which propagates in the birefringent section of the biotissue[2]. In the general case, for a plane elliptically polarized wave of circular frequency[14] ω, the optical force can be represented as the time-averaged Maxwell stress tensor $\vec{T}$ by integrating of the whole spatial element with consideration of the beam aperture r, as $\vec{F} = \int < \vec{T} > \hat{n} d^2 r$, where $< \vec{T}_{ij} >= [\varepsilon_0 \vec{E}_i \otimes \vec{E}_j^* + \frac{1}{\mu_0} \vec{B}_i \otimes \vec{B}_j^* - \frac{1}{2}(\varepsilon_0 |\vec{E}|^2 + \frac{1}{\mu_0} |\vec{B}|^2) I]$.

According to the figure, $i, j = y, z$; $\otimes$ is the dyadic product, I is the unit matrix, $\hat{n}$ is the surface-normal vector, $B = \sqrt{\varepsilon\varepsilon_0} E$ is the magnetic inductance vector, and ε is the media permittivity.

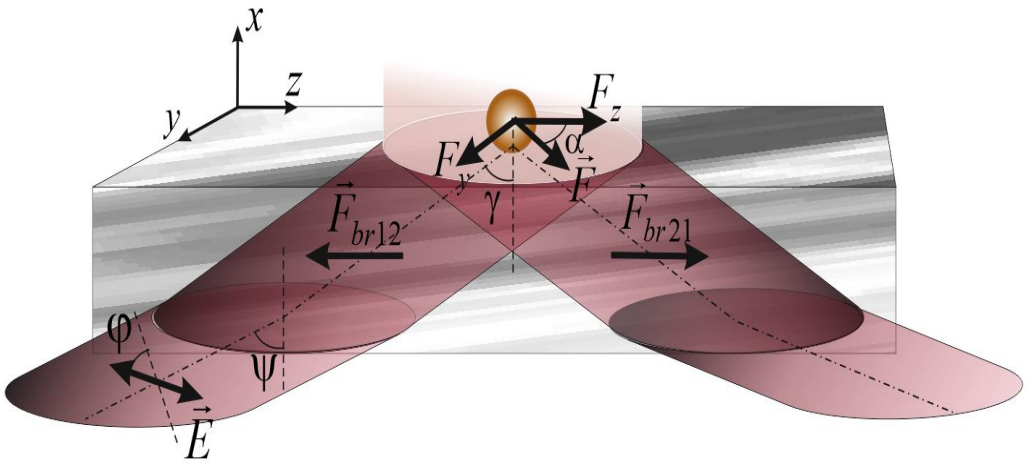

Figure1. Scheme showing the propagation of a beam through the birefringent section of biotissue during the formation of vertical spin of an evanescent wave above the surface of the section. Here, φ – the azimuth of polarization of the probing beam, ψ – the angle of incidence of the probing beam, γ – the angle determining the propagation direction of the incident beam. $\vec{F}_{br12}$ – optical force directed to the external surface of the section and $\vec{F}_{br21}$ – optical force acting in the opposite direction. F_y, F_z – the components of the optical force $\vec{F}$ determined by the action of the evanescent wave on the gold particles above the surface of the section, the resultant of which determines the direction of the particles motion (α).

In general, taking into account the optical path difference and the direction of beam propagation in the model section γ, the electrical vector of an incident elliptically polarized wave:

$$\vec{E}_{inc12} = \begin{pmatrix} 0 \\ E_y(\cos\Theta\cos\Phi + i\sin\Phi\cos\Theta)\exp(ikn_o d/\cos\gamma) \\ E_z(\cos\Theta\cos\Phi - i\sin\Phi\cos\Theta)\exp(ikn'_e d/\cos\gamma) \end{pmatrix} \times \exp i(ik\kappa d/\cos\gamma - \omega t) \quad (1)$$

Here Φ is the degree of ellipticity of the polarization defined as tangent of the ratio of the minor to major axes of an ellipse, and k is the free-space wavenumber, κ – extinction coefficient ($m = n + i\kappa$ (for birefringence n (n_o, n_e)). Here

$E_y = E_0 \sin\varphi(\cos\theta\cos\varphi + \sin\varphi\sin\theta)$, $E_z = E_0 \cos\varphi\cos\psi(\sin\theta\cos\varphi - \cos\theta\sin\varphi)$ – orthogonal components of linearly polarized beam with the azimuth φ, θ – angle between the main axis of the section and the direction of the electric field vector of the probing beam, ψ is the incidence angle of the probing beam.

While falling onto the second cut surface, the beam undergoes total internal reflection. The phase shift $\delta = \delta_p - \delta_s$ between the orthogonal components in the reflected beam is determined by the angle of the beam incidence on the second surface of a section. In this case, the electric vector of the reflected wave can be represented as:

$$\vec{E}_{inc21} = \begin{pmatrix} 0 \\ E_y(\cos\Theta\cos\Phi + i\sin\Phi\sin\Theta)\exp(i(2kn_o d/\cos\gamma + \delta)) \\ E_z(\sin\Theta\cos\Phi - i\cos\Theta\sin\Phi)\exp(i\,2kn'_e d/\cos\gamma) \end{pmatrix} \times \exp i(ik\kappa d/\cos\gamma - \omega t) \quad (2)$$

The absence of the torsion torque in a linearly polarized wave assumes the calculation of optical forces without taking into account the rotational motions of the sample, which is the basis for calculating the optical forces in the sample and determining the conditions enabling to realize the vertical spin.

According to (1), taking into account (2) and (3), we calculate the optical force for both beams propagating in two different directions – towards the upper surface of the section and in the opposite direction, which is determined by the condition of total internal reflection on this surface. Next, we determine the set of parameters under which these forces are compensated. When the vertical spin is realized, for the described conditions, the evanescent wave above the interface will be elliptically polarized, with the maximal values of the polarization components in the orthogonal directions. In this case, the manifestation of the transverse component of the optical force of the evanescent wave becomes obvious.

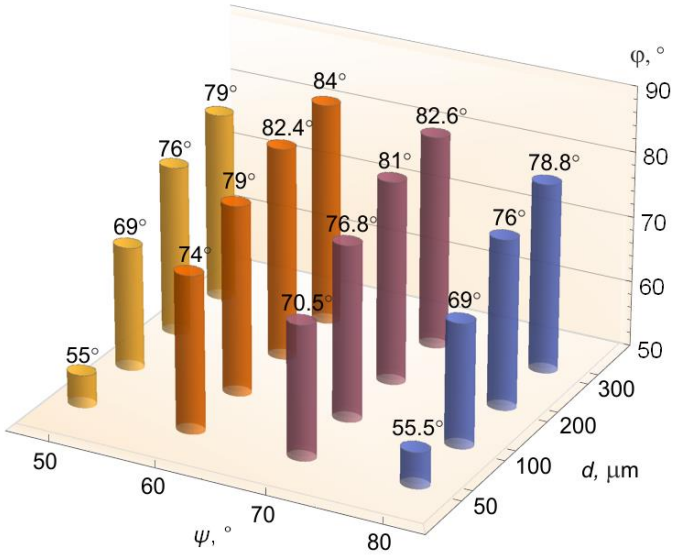

Figure 2. The constructed histogram is based on the condition of the optical forces (F_{br12}, F_{br21}) compensation at propagation of an elliptically polarized beam to the outer surface of the birefringent section and in the direction specified by the complete internal reflection. Here d is the thickness of the section, ψ – the incidence angle of the probing beam, φ – the polarization azimuth of the probing beam. The height of the columns corresponds to the value of polarization azimuth of the probing beam.

Figure 2 shows the results of modeling situations in which the optical force due to the beam propagating toward the outer surface of the section compensates the optical force produced by the reflected beam. Changing the angle of incidence ψ of the probing beam for different section thickness *d*, the polarization azimuth φ of this beam is selected, when the compensation of the optical forces (F_{br12}, F_{br21}) becomes possible.

Among the possible options for compensating the optical force in the volume of a biological section (Fig. 2), we choose the optimal one, concerning its experimental implementation. It can be shown that obtaining the polarization azimuth of the incident wave at 45° at the 'section-tissue fluid' interface is realized when the incidence angle of a linearly polarized probing beam on the first surface of the section with the polarization azimuth of 79° is about 60° for the thickness of the section 100 μm respectively. These parameters of the probing beam ensure complete internal reflection on the external surface of the section and the realization of an evanescent wave above the interface. This choice of parameters enables to experimentally visualize the transverse motion of gold particles in the surface layer of the tissue fluid, given by an evanescent wave.

The linearly polarized beam in the birefringent material is transformed into an elliptically polarized one and, as it propagates through the medium, the parameters of the polarization ellipse change[14]. The formation of an elliptically polarized wave is accompanied by the appearance of a spin angular momentum. At that, an optical force is generated, the cause of which consists in the change of the density of the spin moment of the propagating beam. As a consequence, the overall distribution of forces in the section can vary. However, the effect of this optical force is reduced to a minimum if the section is stationary. In the real conditions of the existence of biological tissues, reproduced in the experiment suggested in the work, the need to evaluate this optical force is no longer significant[14].

Thus, an evanescent wave, being excited above the interface, can be described by the following equation[14]

$$\vec{E}_{ev} = E \begin{pmatrix} \frac{1}{\sqrt{1+|m|^2}} \\ \frac{m}{\sqrt{1+|m|^2}} \frac{k}{k_z} \\ -i \frac{1}{\sqrt{1+|m|^2}} \frac{\kappa}{k_z} \end{pmatrix} \exp(-\kappa x) \exp(i(k_z z - \omega t)) .$$ Here $k_z = k \frac{n_o}{n} \sin\gamma$, $\kappa = k\sqrt{\left(\frac{n_o}{n}\right)^2 \sin^2(\gamma) - 1}$ is the exponential decay rate, $m = \frac{T_\perp}{T_{//}} m_1$ is the polarization state of an evanescent wave[15], where m_1 is the polarization state of the probing beam impinging on the interface plate–air being equal to unity for linear polarization with the azimuth of polarization 45º, γ is the incidence angle on the surface, where TIR takes place.

The electrical strength of the field of an evanescent wave is $E = k_z / k \sqrt{\frac{\mu_1}{\mu}} T E_0$, where $T = \frac{\sqrt{|T_{//}|^2 + |m_1|^2 |T_\perp|^2}}{\sqrt{1+|m_1|^2}} \exp[i \arg T_{//}]$ is the transmission coefficient[15], and $T_{//}$, $T_\perp$ are the Fresnel transmission coefficients[15].

The values of the optical force due to the evanescent wave in this experiment are not significant, since the controlled motion of particles by the evanescent wave in the near-surface layer of the section is of more interest. We estimate the magnitude of the density of the spin and orbital momentum in the transverse *y* and longitudinal *z* directions (Fig. 1), followed by the estimation of the value of the force in the corresponding directions. The spin momentum density in this case is expressed as[10] $p_s = \frac{1}{16\pi\omega} \nabla \times \mathrm{Im}[\vec{E}^*_{ev} \times \vec{E}_{ev}]$. It has both longitudinal and transversal components[10]. Thus, the resulting momentum density in the z-direction is given by

$p_z = p_{oz} + p_{sz} = \frac{A^2}{8\pi\omega}\left[\left(k_z + \frac{m^2k^2}{k_z} + \frac{\kappa^2}{k_z}\right) - 2\frac{\kappa^2}{k_z}\right]\exp(-2\kappa x)$ and the transversal momentum caused by the vertical spin is represented as $p_y = p_{sy} = \frac{A^2}{4\pi\omega}\frac{k\kappa}{k_z}\operatorname{Im} m\exp(-2\kappa x)$, where $A = E\frac{1}{\sqrt{1+|m|^2}}$. Gold nanoparticles are used as an object of research. Therefore, to calculate the optical force acting on the particles, we use Mie's scattering, in the approximation of which[18] $\vec{F} = \int_S \Delta\vec{p}dS$, where $\Delta\vec{p}$ is the change of momentum density. Simulation of the force affecting a plate and causing its motion presumes integration over the illuminated area assuming a beam aperture 6º.

The route of the nanoparticle motion is determined by the angle $\alpha = arctg\frac{F_y}{\sqrt{F_y^2 + F_z^2}}$ between the Poynting vector propagation along the *z* axis and the resultant direction of the particle motion, which does not coincide with either the longitudinal (F_z) or the transverse (F_y) directions of the optical force components action.

As modeling results show, it is possible to control the direction of nanoparticles motion due to the choice of the incidence angle of the probing beam on the first section surface (Fig. 3). So, for the chosen incidence angle of 60°, the angle determining the direction of nanoparticles motion is about 11° that is observed in the experiment.

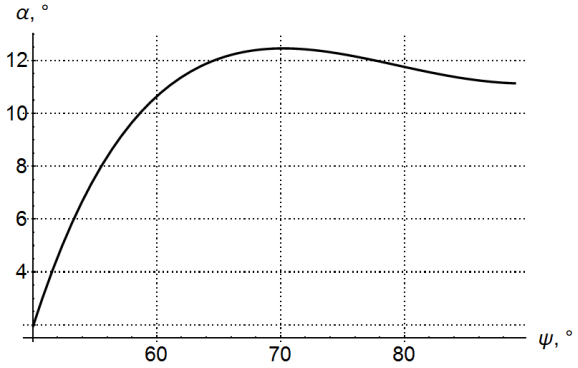

Figure 3 Dependence of the direction of motion of gold particles in the near-surface layer of the tissue fluid, depending on the change in the incidence angle of the probing beam at thickness of a section of 100 μm.

In general, the control of the nanoparticles motion by a homogeneous evanescent field is hampered by their Brownian motion. However, not the process of capturing particles by the evanescent wave, namely the displacement of the ensemble of nanoparticles by the evanescent field is demonstrated in this research work. Showing such a motion is rather a qualitative than a quantitative demonstration of the possibilities of using this phenomenon[16].

As a radiation source the semiconductor laser (980 nm 4000 mW Laser from Wavespectrum with the ability to control the beam power to 50–100 mW, which ensures the integrity of the biological tissue during irradiation) is used, which was focused on the interface of the section – physiological medium without spatial frequency filtration. The aperture of the beam was 6°. The use of a prism to form a condition for TIR is an alternative to other approaches associated with the use of waveguides, fluorescence technology or microspheres[14,15]. The availability of this optical element determining the simplicity of achieving the necessary conditions for total internal reflection which is accompanied by the evanescent wave creation forms a significant advantage of the experimental realization of the vertical spin. In the suggested experiment, the focal spot was of the nearly square shape, with a diagonal of about 50 μm.

The experimental conditions allowed regulating the azimuth of the linear polarization of the test and incident beams by rotating the light source. The receiver of the radiation was a 1.3-megapixel CCD camera without a protective glass, sensitive in the infrared (IR) region. This enabled to study both the particles, using the illumination in the visible region, and the position of the incident IR beam on the section. The radiation intensity of the laser was extracted with the power

typical of working with biological objects. To control the nanoparticles motion it is necessary to avoid the particle's interaction with the anisotropic mechanical environment nearby a solid interface[16]. Using an additional laser source (660 nm laser) provides an optical trapping mechanism with the displacement of particles from the surface. Nonetheless the particles remain in the area of the evanescent wave action. To reduce the surface tension of the tissue fluid used in the experiment and to demonstrate the action of the evanescent wave, thin, near-surface layers of fluid were used with the appropriate selection of the shape and curvature of the liquid meniscus. The radius of the meniscus was determined by the wettability of the section surface with the fluid and amounted to about 58 mm. On the other hand, the heating of the fluid also presupposed a decrease in the surface tension, which enabled to follow the action of the evanescent wave.

The flux of particles entrained by the evanescent wave moved in the transverse direction of the near-surface fluid layer, which is due to deviation from the original horizontal direction of motion. The deflection angle corresponds to the results obtained due to the theoretical approximation and amounts to about 11°. It was possible to approximate the average velocity of particle motion in our experiment that was about of 35 μm/s. It is natural to assume that by changing the parameters of the probing beam, we are able to control the movement of nanoparticles in the supersurface layer of the biological object, thereby increasing the possibilities of transporting the dosated portions of drugs to handle pathological biostructures.

4. CONCLUSIONS

The possibility of controlling the ensemble of nanosized gold particles with an evanescent wave excited in the surface layer of the surrounding fluid above the birefringent section of biological tissue is demonstrated. Selection of the parameters of the probing beam for which it is possible to realize a vertical spin above the section surface at the total internal reflection on the upper section boundary is proposed. The obtained results enable to expand the potentiality of controlled motion of microdoses of matter in biosystems, which is achieved by laser radiation of appropriate power.

REFERENCES

[1] Sabatini, D. M., [Leading Edge Nanotechnology Research Developments], Nova Science Publishers, (2007).
[2] Angelsky, O. V., Zenkova, C. Yu. and Ivansky, D. I., "Mechanical action of the transverse spin momentum of an evanescent wave on gold nanoparticles in biological objects media," Journal of Optoelectronics and Advanced Materials 20 (5-6), 217-223, (2018).
[3] Angelsky, O. V., Zenkova, C. Yu., Gorsky, M. P, Soltys, I. V. and Angelsky, P. O., 'The use of new approaches to estimating the coherence properties of mutually orthogonal beams," Open Opt. J. 7, 5-12, (2013).
[4] Zenkova, C. Yu., Gorsky, M. P., Soltys, I. V. and Angelsky, P. O., "Using inhomogeneity in light energy distribution for estimating the degree of coherence of superposing waves," Proc. SPIE 8411, 841108, (2012).
[5] Machulianskyi, O., Babych, B. and Machulianskyi, V., "Determination of the efficiency factors of the absorption and scattering of nickel nanoparticles," Informatyka, Automatyka, Pomiary w Gospodarce i Ochronie Srodowiska – IAPGOS 1, 4-7, (2018).
[6] Zenkova, C. Yu., Soltys, I. V. and Angelsky, P.O., "The use of motion peculiarities of particles of the Rayleigh light scattering mechanism for defining the coherence properties of optical fields," Optica Applicata 2, 297-312, (2013).
[7] Zenkova, C. Yu., Gorsky, M. P., Ryabiy, P. A. and Gruia, I., "Different approaches to phase restoration of distant complex optical fields," Optica Applicata 2, (2015).
[8] Zenkova, C. Yu, Gorsky, M.P. and Ryabiy, P.A., "Pseudo-phase mapping of speckle fields using 2D Hilbert transformation," Optica Applicata 1, 153-162. (2016).
[9] Zenkova, C. Yu., Gorsky, M. P., Ryabiy, P. A. and Angelskaya, A. O., "Additional approaches to solving the phase problem in optics," Applied optics 12, B78-B84, (2014).
[10] Bliokh, K. Y., Bekshaev, A.Y. and Nori, F., "Extraordinary momentum and spin in evanescent waves," Nature Communications 5, 4300, (2014).
[11] Maciejewski, M., Surtel, W., Wojcik, W., et al., "Telemedical systems for home monitoring of patients with chronic conditions in rural environment," Annals of Agricultural and Environmental Medicine 1, 167-173, (2014).

[12] Rovira, R. H, Pavlov, S. V., Kaminski, O. S. and Bayas, M. M., "Methods of Processing Video Polarimetry Information Based on Least-Squares and Fourier Analysis," Middle-East Journal of Scientific Research 9, 1201-1204, (2013).
[13] Kvyetnyy, R., Bunyak, Y., Sofina, O., et al., "Blur recognition using second fundamental form of image surface," Proc. SPIE 9816, 98161A, (2015).
[14] Azarov, O. D., Dudnyk, O. D., Duk, M. and Porubov, D., "Static and dynamic characteristics of the self-calibrating multibit ADC analog components," Proc. SPIE 8698, 86980N, (2013).
[15] Osadchuk, A., Osadchuk, I., Smolarz, A. and Kussambayeva, N., "Pressure transducer of the on the basis of reactive properties of transistor structure with negative resistance," Proc. SPIE 9816, 98161C, (2015).
[16] Kvyetnyy, R. N., Sofina, O. Yu., Lozun, A. V. et al., "Modification of fractal coding algorithm by a combination of modern technologies and parallel computations," Proc. SPIE 9816, 98161R, (2015).

Screen-printed ion-selective electrode for potassium determination

Izabella Piórek*[a], Andrzej Pepłowski[a], Małgorzata Jakubowska[a]
[a]Institute of Microtechnology and Nanotechnology, Faculty of Mechatronics, Warsaw University of Technology, 8 Boboli St., Warsaw, Poland, 02-525

*Author to whom correspondence should be addressed: izabella.piorek@gmail.com

ABSTRACT

Ion-selective electrodes, which detect activity of specific substances, are one of main analytical techniques in many fields e.g. medical and environmental analysis or process control in industries. This article describes manufacturing of screen-printed electrode for potassium determination, which can be used in potentiometric measurements. Electrode was made with usage of two conductive pastes. The first consists of silver nanoplatelets and thermoplastic polyurethane (TPU). The second contained PMMA matrix and graphene nanoplatelets as intermediate material. Two membranes for electrode coating, which differ in composition, were prepared and compared. For both membranes polyvinyl chloride (PVC) was used as a matrix and valinomycin was used as ionophore which binds potassium ions. Moreover, some of the prepared electrodes had an additional intermediate layer made of a conductive polymer - poly(3,4-ethylene-1,4-dioxythiophene) (PEDOT). Received calibration curves were linear. The curve slope for electrode with PEDOT intermediate layer in the physiological range (3,8-5,5 mM) was 62 mV/dec which exceed the Nernstian value.

Keywords: ion selective electrode, ISE, potentiometry, screen-printing, potassium

1. INTRODUCTION

Potassium is very important element for all living cells. In plants it regulates various of processes, including growth processes, protein synthesis and stomata regulation, which facilitates gas exchange [1]. In animal cells it is mostly used for creating electrical potential [2]. Therefore, it is also very important for human organism. It controls great amount of physiological processes and it is the basic component of intracellular fluid. Potassium ions are responsible for membrane potential which proper level is necessary for normal cell functioning. It also influences neurotransmission and muscle contraction. It is significant for energy transformation processes, amino acid transport and protein synthesis. [3] Normal potassium concentration in human blood varies between 3,8 and 5,5 mM [4]. In view of it is importance for proper organism functioning, analyzing level of potassium is one of main tests. For this purpose ion-selective electrodes are often used [5].

Ion-selective electrodes are often applied in chemical analyzing. Mostly, they are used in environmental and clinical analyzes. They can determine concentration of great amount of different ions. Characteristic for them is that their electrochemical respond is mostly dominated by one analyte ion [6]. However, there is also a group of interfering ions which can also have some influence on electrode potential. Despite that fact ion-selective electrodes have lots of advantages [7]. Influence of interfering ions can be not significant so sensor can indicate good selectivity and well accuracy. Moreover, these sensors are often used in analyzing samples due to their simplicity and low costs [8].

Ion-selective electrodes can differ in their structure. In conventional electrodes of this type membrane, which is responsible for selection of proper ion, is in electrical contact with inner reference solution that is also connected to inner reference electrode (Fig. 1). [9]

This kind of construction is hard to be miniaturize and to simplify it, a concept of eliminating an inner solution was introduced. That is how all-solid-state electrodes appear. However, eliminating inner solution brings additional issue [10]. In conventional design membrane has contact with environments with the same type of charge carrier. After eliminating inner solution membrane has contact with solid material which transfer electrons not ions. This is the reason of appearing so-called “blocked layer” which disturb potential of electrode [11]. To improve respond transition layer,

Photonics Applications in Astronomy, Communications, Industry, and High-Energy Physics Experiments 2019, edited by Ryszard S. Romaniuk, Maciej Linczuk, Proc. of SPIE Vol. 11176, 111765I
© 2019 SPIE · CCC code: 0277-786X/19/$21 · doi: 10.1117/12.2538088

which can transport charge by electrons and ions, is introduced. There are lots of different materials which can be used e.g. conductive polymers and carbon nanoparticles [12].

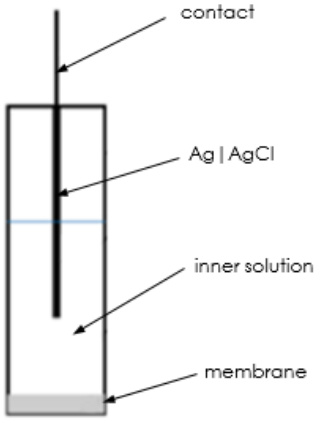

Figure 1 Conventional ion-selective electrode [9]

2. ELECTRODES MANUFACTURING

The process of manufacturing electrodes can be divided in two phases. The first part was screen-printing of sensor. The second was applying membrane.

2.1 Screen-printing

During this phase two kind of conductive pastes for screen-printing were prepared. The first was based on poly(methyl methacrylate) matrix. It was made as 8 wt% solution of PMMA in diethylene glycol buthyl ether acetate. The functional phase was graphene nanoplatelets GNPC from Cheap Tubes company (USA) of diameter between 5-25 μm and thickness below 10 nm. Content of graphene nanoplatelets in PMMA matrix was 12,5 wt%. The second paste consisted of silver nanoplatelets and thermoplastic polyurethane matrix. Used silver nanoplatelets AX 20LC of diameter 2μm were fabricated by AMEPOX company (Poland). Solution of 25 wt% TPU in diethylene glycol buthyl ether acetate was a matrix. Content of functional phase was 70 wt%.

First layer of electrode was a silver contact printed on PET 125 μm foil. It's shape is represented at Fig. 2. The print was placed in drier for 20 min in temperature 120 °C.

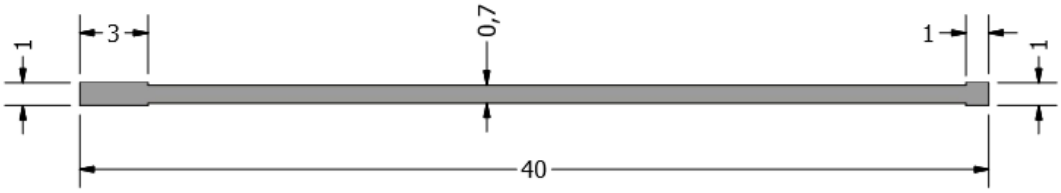

Figure 2 Silver contact

Second layer was made of graphene paste. It's shape is shown at Fig. 3. and placement at silver contact is represented at Fig. 4. It was dried in the same conditions as silver paste

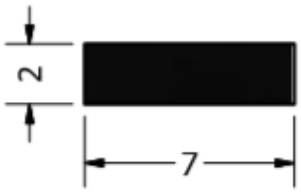

Figure 3 Graphene layer

Figure 4 Placement of graphene layer at silver electrode

Last layer was an isolation layer printed with commercial paste LOCTITE EDAG PF 455B, Henkel (Germany). Shape is shown at Fig. 5 and placement at Fig. 6. It was curing by ultra-violet light.

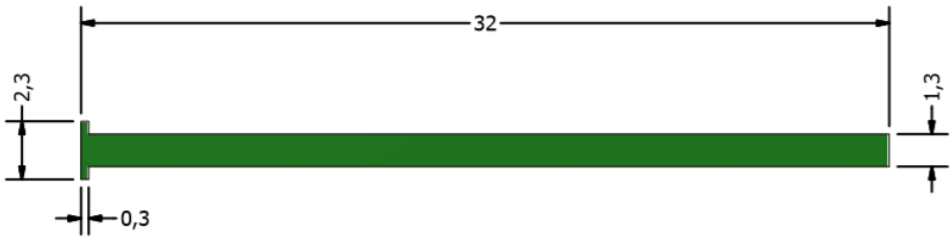

Figure 5 Isolation layer

Figure 6 Placement of isolation layer

2.2 Membranes

Two kind of membranes were prepared. They differed in ratio of polymeric matrix and plasticizer. Used matrix was polyvinyl chloride and plasticizer was bis(2-ethylhexyl) sebacate. Chosen ionophore, which binds potassium ions, was valinomycin. Used lipophilic additive was potassium tetrakis(3,5-bis(trifluoromethyl)phenyl)borate (KTFPB). All ingredients were dissolved in 3 ml of tetrahydrofuran (THF). The components of membranes are represented in Table 1.

Table 1. Membranes composition.

Ingredient	Membrane 1	Membrane 2
PVC	132 mg	66 mg
bis(2-ethylhexyl) sebacate	66 mg	132 mg
valinomycin	2 mg	2 mg
KTFPB	0,5 mg	0,5 mg

2.3 Coating screen-printed electrode

There were 4 types of electrodes prepared: with membrane 1, with membrane 2 and their combination with or without additional PEDOT layer. For applying PEDOT first it was dissolved in water in 1:2 volume ratio. Than 10 µl of solution was applied at graphene layer and left for 24 h air dry. Electrodes were coated with 10 µl of membranes solution and left for 0,5 h to dry. Processes of preparing electrodes are also represented as graphs at Fig. 7.

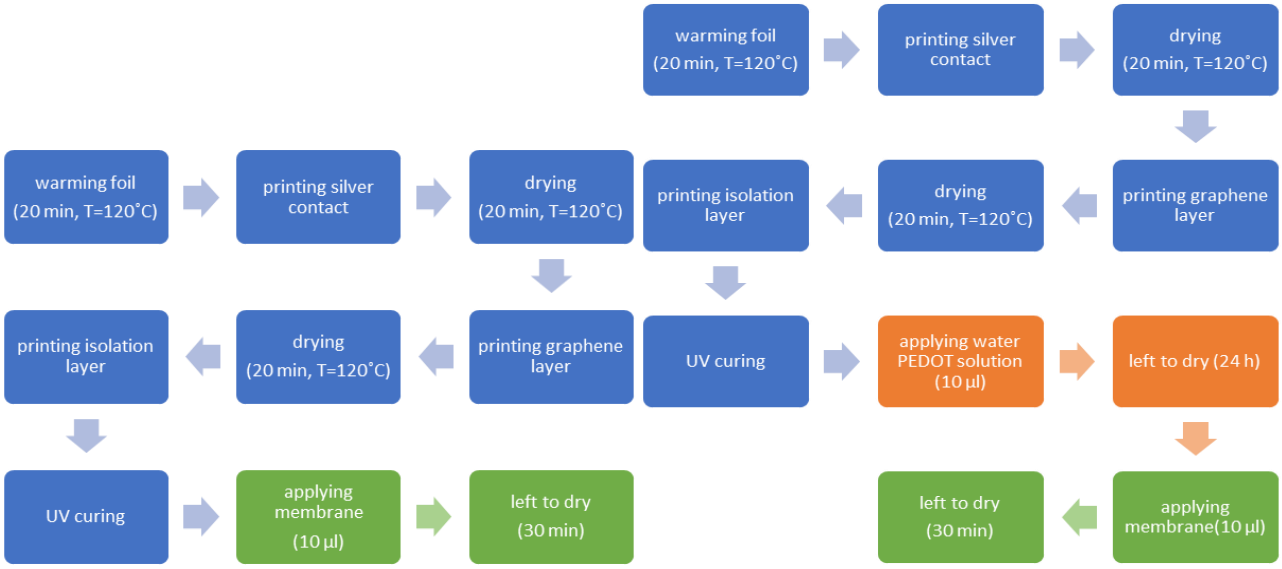

(a) (b)

Figure 7 Process of preparing electrode: a) without PEDOT layer, b) with PEDOT layer

3. MEASUREMENTS

Electromotive force of cell, which consisted of Ag|AgCl(s) electrode with 1M KCl inner solution (reference electrode) and screen-printed electrode (indicator electrode), was measured by EMF16 Interfce station from Lawson Labs, inc. Change in potassium ion concentration was provided by adding adequate volume of 1M potassium chloride (KCl) solution.

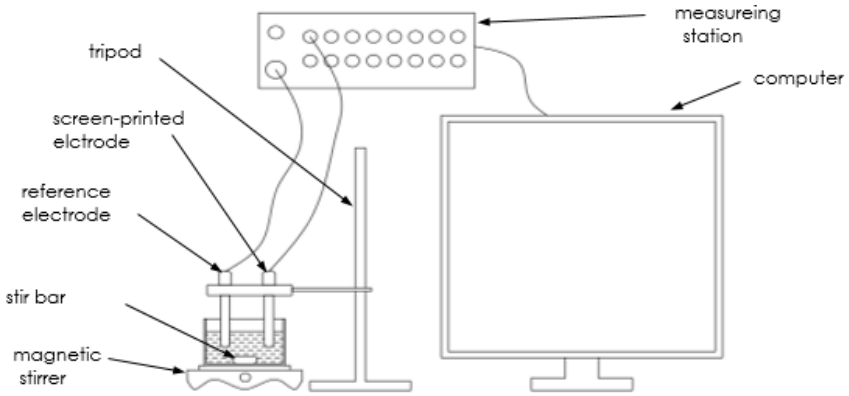

Figure 8 Scheme of measuring station

4. RESULTS

4.1 Symbols

For better readability symbols of electrodes were implemented. They are represented in Table 2.

Table 2. Electrodes symbols.

Membrane	Transition layer	Symbol
1	graphene	M1G
1	PEDOT	M1P
2	graphene	M2G
2	PEDOT	M2P

Some of results shows responds of electrodes after 24 h conditioning process executed in 0,01 M KCl solution.

4.2 Results and discussion

Majority of examined electrodes were characterized by plots similar to represented at Fig. 10 and M1G 3, M1G 4 Fig. 9. There was no response to change in potassium ion concentration determined for electrodes.

At fig there are two electrodes which respond to change in potassium ion concentration. Unluckily, their potential was not stable after initial increase. For this reason electrodes were conditioned. Responses of two indicator electrodes after this process is shown at Fig. 11. Potential of electrodes stabilized after some time.

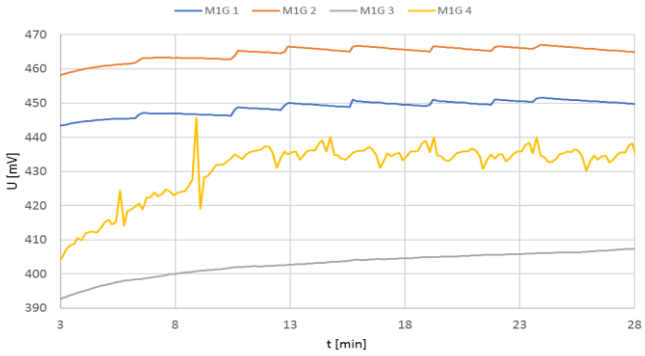

Figure 9 Response of M1G electrodes before conditioning

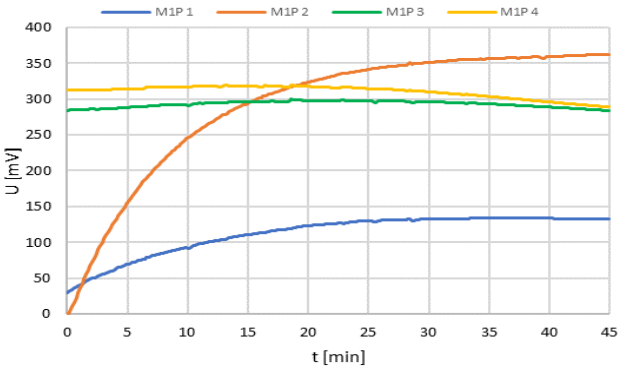

Figure 10 Response of electrodes M1P before conditioning

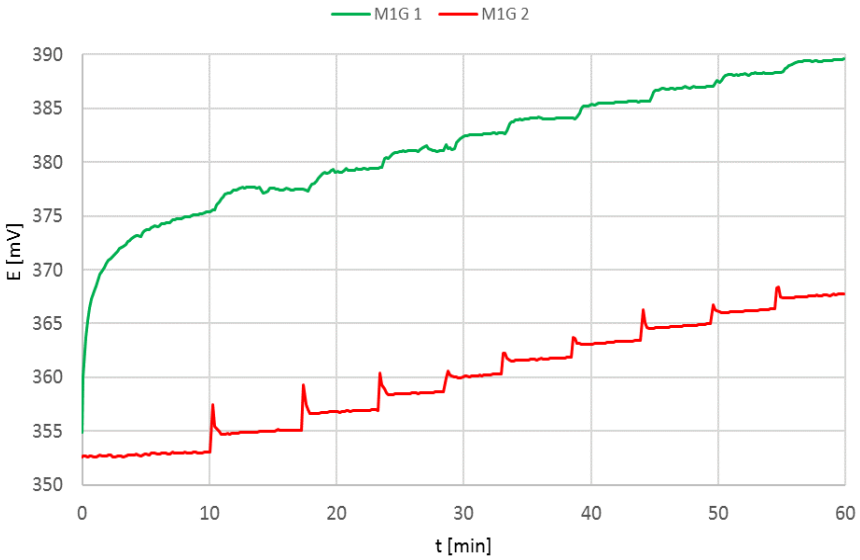

Figure 11 Response of M1G electrodes after conditioning process

Figure 12 represent calibration curves for electrodes M1G after conditioning process. Their character is linear, as predicted, but slope is lower than Nernstian value.

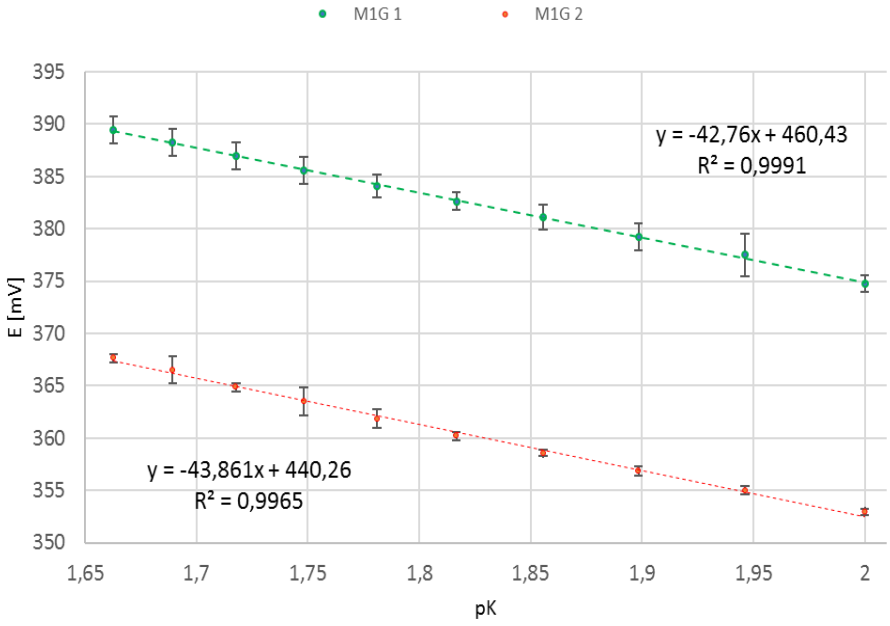

Figure 12 Calibration curves for M1G after conditioning

After conditioning also one of M1P electrodes exhibited deterministic response for changing potassium ion concentration (Fig. 13). Calibration curve for this electrode is shown at Fig. 14. The slope of the curve is approximately similar to electrodes M1G. Therefore, use of additional PEDOT layer with membrane 1 combination is questionable.

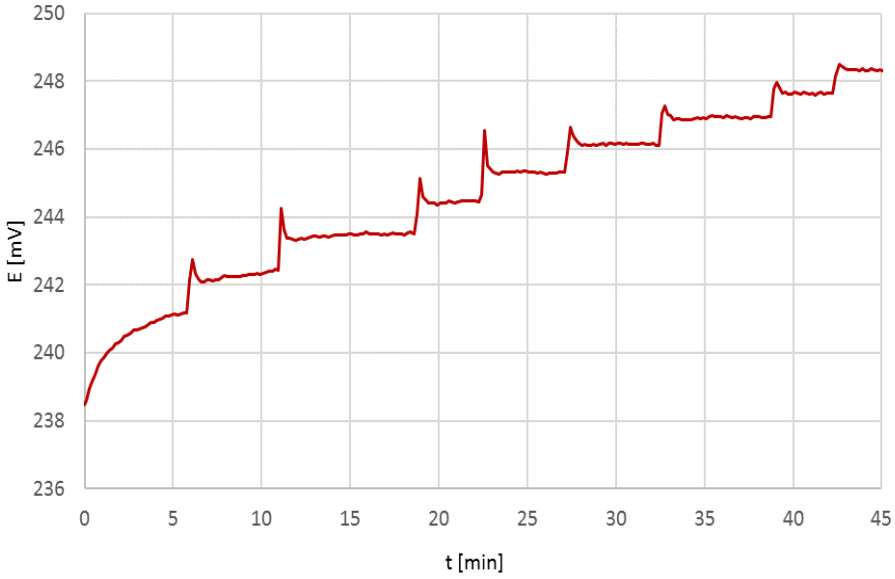

Figure 13 Response of M1P electrode after conditioning

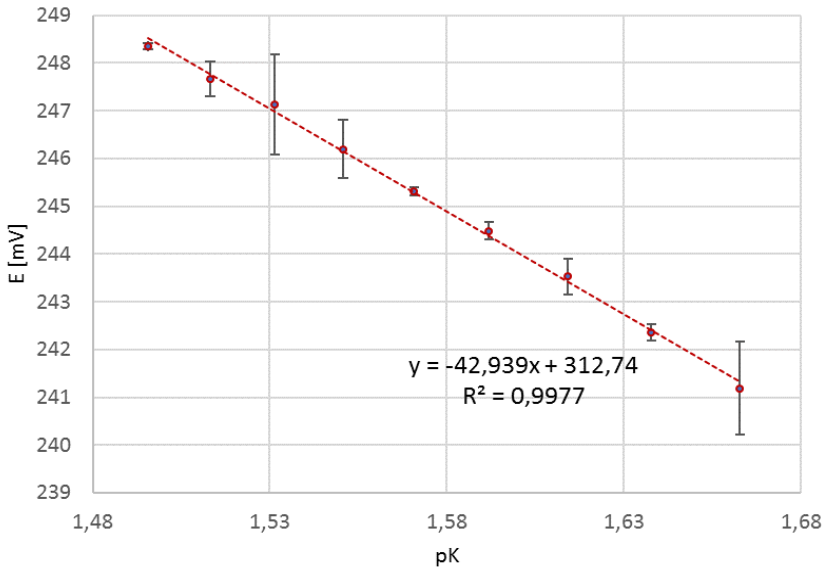

Figure 14 M1P - calibration curve after conditioning

Electrodes with membrane 2 were also subjected to conditioning. Their responses for change in potassium ion concentration is represented at Fig. 15. Difference between slopes of M2G and M2P is significant (Fig. 16). For M2G electrode value is more similar to electrodes M1G and M1P but for M2P is much lower. The same electrodes in range 2,2-3 pK are characterized by linear dependence with higher slope value (Fig. 17) and M2P slope is favorable. It is the only case when slope exceed Nernstian value (59,15 mV/dec).

Such significant difference in slope value in two ranges could indicate that previous experiments were performed near detection limit of sensor.

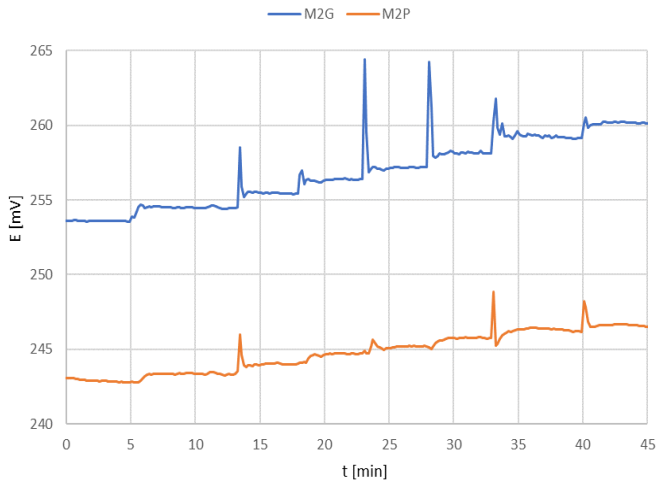

Figure 15 Response of M2G and M2P in range 16,2-23,7 mM after conditioning process

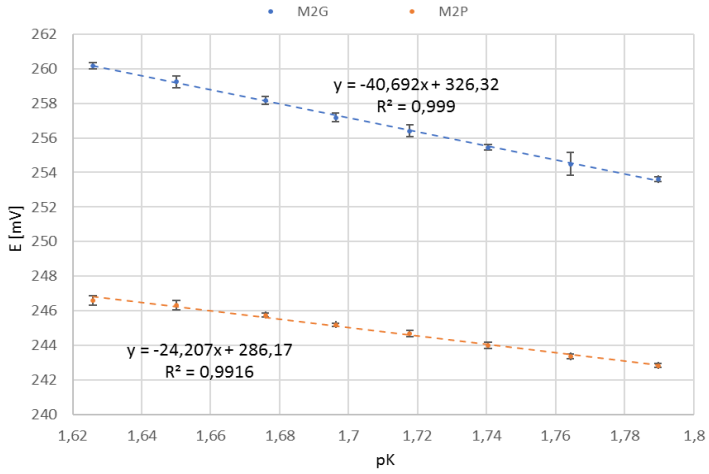

Figure 16 Calibration curve for M2G and M2P in range 16,2-23,7 mM after conditioning

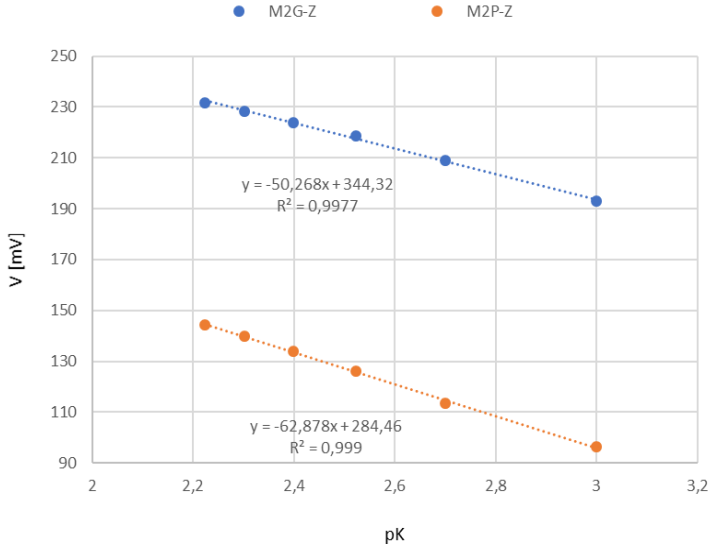

Figure 17 Calibration curve for M2G and M2P in range 1-6 mM after conditioning

Accuracy of linear regression was analyzed by using p-value test. It was calculated for each calibration curve and results are represented in Table 3. Statistical significance level was established at 5% value. Low p-value results indicate that linear regressions were adjusted with very high probability.

Table 3. P-value results.

Electrode	Range [mM]	Slope	p-value
M1G 1	10-21,7	-42,76	1,45 E-13
M1G 2	10-21,7	-43,86	4,01 E-11
M1P	21,7-31,9	-42,94	1,76 E-10
M2G	16,2-23,7	-40,69	2,69 E-10
M2P	16,2-23,7	-24,21	1,88 E-07
M2G	1-6	-50,27	2,04 E-06
M2P	1-6	-62,88	4,13 E-07

5. CONCLUSION

Only about 10% of manufactured electrodes where working. The main reason of this issue is probably lack of proper membrane adhesion to substrate. This problem could be solved by using other polymer for membrane matrix because polyvinyl chloride is distinguished with low adhesion to solid materials.

Despite issue with manufacturing results are promising. Received calibration curves are characterized with linear trend with very high probability. For graphene transition layer slope of curve is recurrent at potassium ion concentration range 1,62 2 pK. Moreover, graphene can also work well as mediating layer which binds ionic and electron conductivity and prevent blocking charge transfer.

In physiological range slope of calibration curve is higher than in other experiments. Electrode with graphene transition layer reached score 50,3 mV/dec which, in reference to theory, is still too low value, but electrode with additional PEDOT layer achieved value of 62,8 mV/dec which exceed Nernstian value. It indicates that device could be used in range 1-6 mM with well accuracy. It might give an opportunity to apply such kind of electrodes in blood tests if selectivity to potassium ion will be good.

REFERENCES

[1] Leigh R. A. and Wyn Jones R. G., "A hypothesis relating critical potassium concentration for growth to the distribution and functions of this ion in the plant cell" New Phytologist, 97(1), 1–13 (1984)

[2] Santos J.S., Asmar-Rovira G.A., Han G.W., Liu W., Syeda R., Cherezov V., Baker K. A., Stevens R. C., Montal M.. "Crystal structure of a voltage-gated K+ channel pore module in a closed state in lipid membranes". J Biol Chem. 287, 43063–70 (2012)

[3] Gerting H. and Przysławski J., [Bromatologia zarys nauki o żywności i żywieniu], Wydawnictwo Lekarskie PZWL, Warsaw (2006)

[4] Dembińska-Kieć A. and Naskalski J. W., [Diagnostyka laboratoryjna z elementami biochemii klinicznej], Elsevier Urban & Partner, Wrocław (2010)

[5] Neumeister B., Besenthal I. and Bohm B. O., [Diagnostyka laboratoryjna - poradnik kliniczny], Elsevier Urban & Partner, Wrocław, 215-216 (2013)

[6] Cygański A., [Podstawy metod elektroanalitycznych], Wydawnictwa Naukowo-Techniczne, Warszawa (1999)

[7] Fakhari A. R., Raji T. A. and Naeimi H. "Copper-selective PVC membrane electrodes based on salens as carriers", Sensors and Actuators B: Chemical 104(2), 317-323 (2005)

[8] Ping J., Wang Y., Wu J., Ying Y., "Development of an all-solid-state potassium ion-selective electrode using graphene as the solid-contact transducer", Electrochemistry Communications 13 (2011) 1529–1532
[9] Maksymiuk K. and Michalska A., „Elektrody jonoselektywne - klasyka i nowe koncepcje," Chemik 69, 373-382 (2015)
[10] James H., Carmack G. and Freiser H., „Coated Wire Ion Selective Electrodes," Analytical Chemistry 44(4), 856-857 (1972)
[11] Ping, J., Wang, Y., Wu, J., & Ying, Y., "Development of an all-solid-state potassium ion-selective electrode using graphene as the solid-contact transducer.", Electrochemistry Communications 13(12), 1529–1532 (2011)
[12] Khaled E., Hassan H., Girgis A., and Metelka R., "Construction of novel simple phosphate screen-printed and carbon paste ion-selective electrodes." Talanta, 77(2), 737–743 (2008)

The analysis of sensitivity and nonlinearity parameters of selected signal conditioners for resistance measurement

Wojciech Walendziuk*, Tomasz Siegieda, Anna Maria Dabrowska
Bialystok University of Technology, Dept. of Theoretical Electrotechnics and Metrology,
Wiejska Str. 45D, 15-351 Bialystok, Poland

ABSTRACT

One of the most important issues in the field of measurement techniques is measurement of resistance. This work focuses on the presentation of metrological properties of selected resistance measurement systems such as Voltage Divider, Wheatstone Bridge and Double Current Circuit. All the systems can be also used as simple and easy to use circuits for basic signal conditioners for resistance measurement. The performed analysis will be based on simulation and measurement tests of real electrical systems. In this paper, the sensitivity and non-linearity of selected resistance measurement systems will be analyzed.

Keywords: resistance, measurement system, sensitivity, strain gauge

1. INTRODUCTION

Many physical quantities can be reflected using resistance, e.g. temperature, strain or strength, illuminance, or relative humidity of the air.[1] These are non-electrical quantities that can be measured using sensors whose resistance changes with the change of the external factor. Due to the fact that the topic of resistance measurement, in spite of many studies, is still valid, it was decided to compare different measurement systems in one study. It is worth noticing that the dynamic development of the industry requires the use of many sensors that measure various non-electrical parameters, e.g. for controlling production processes. Performing measurements of the above values requires the use of a suitable measuring system or calibration procedures.[2–7]

Resistance measurements are not always carried out using the direct method. Very often, the measurement is made by indirect methods, using additional measuring systems.[8–11] These systems allow a greater accuracy of measurement by eliminating the influence of temperature on the measurement system or minimizing the influence of thermoelectric voltages.

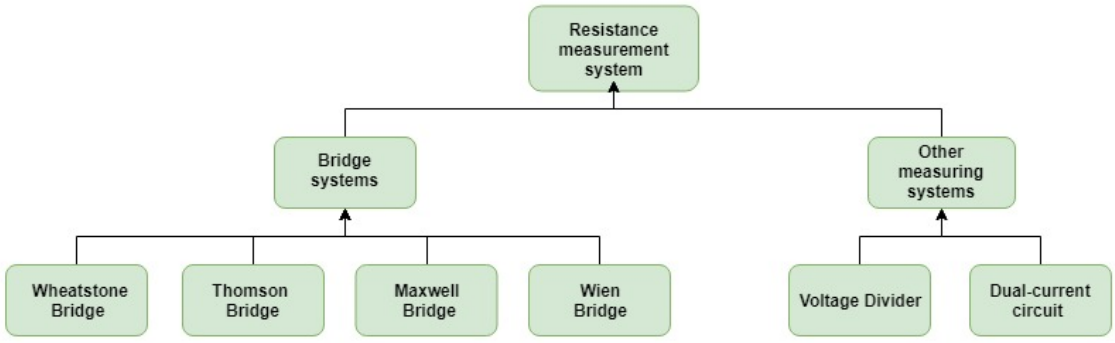

Figure 1. Resistance measurement systems.

Further author information: (Send correspondence to Wojciech Walendziuk)
Wojciech Walendziuk.: E-mail: w.walendziuk@pb.edu.pl, Telephone: +48 85 746 93 97

Photonics Applications in Astronomy, Communications, Industry, and High-Energy Physics Experiments 2019,
edited by Ryszard S. Romaniuk, Maciej Linczuk, Proc. of SPIE Vol. 11176, 111765J
© 2019 SPIE · CCC code: 0277-786X/19/$21 · doi: 10.1117/12.2536476

The aim of this work is to analyze the sensitivity and non-linearity of selected resistance measurement systems. Selected measuring systems will be supplied with various signals. The output parameters of the circuits for different values of the resistance variable will be determined. The analysis will be based on simulations and empirical tests that will be used to calculate the parameters of selected measurement circuits.

The following layout of the article has been adopted. The first part contains a review of literature. Next, the known measurement systems will be initially analyzed and will be subjected to simulation tests as well as real tests. The simulation tests will be performed in a SPICE (Simulation Program with Integrated Circuits Emphasis) type program. The last element is the presentation of the results of tests carried out on the developed laboratory bench with selected prototype systems. On the basis of the conducted simulation and actual tests, calculations of sensitivity and non-linearity parameters of the tested measurement systems will be performed.

2. BASIC SIGNAL CONDITIONER FOR RESISTANCE MEASUREMENT

2.1 Voltage divider

The voltage dividers can be based on resistive, capacitive or inductive passive elements which are usually used as components of measuring instruments and transducers.[8,12] A voltage divider is a simplest system that allows a measurement of the resistance changed in a parametric resistance sensor. A potential divider, as a passive linear circuit, can contain two resistors R_1 and R_2 connected in a series (Figure 2). It produces the output voltage (V_{out}) that is proportional to the input voltage (V_{in}) satisfying the following formula (1):

$$V_{out} = \frac{R_2}{R_1+R_2} \cdot V_{in} \tag{1}$$

It is worth stressing that the voltage divider can work with a current supply. In such a situation, providing a constant value of the supply current, the voltage V_{out} will be directly proportional to the resistance R_2 change.

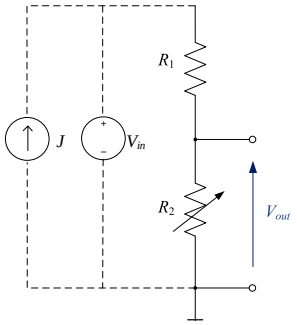

Figure 2. Resistive voltage divider circuit diagram.

2.2 Wheatstone bridge

Bridge systems are systems that use a parallel connection of at least two two-terminal networks. The response of the bridge system is the voltage that appears between the voltage divider output points. The advantage of bridge systems is the ability to bring them into equilibrium, this means that the output voltage of the bridge equals 0 V. Obviously, bridge systems can work in the state of imbalance, which is now more frequently used in measurement techniques. In this mode of the system operation, the unbalance voltage appearing at the output of the bridge allows to determine the resistance value in the bridge measuring branch. Figure 2 shows the circuit diagram of Wheatstone bridge that will be tested in this paper.

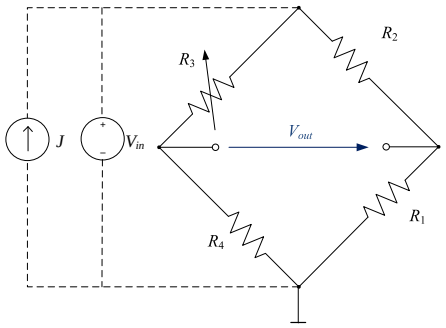

Figure 3. Wheatstone bridge circuit diagram.[8,10,13]

The bridge has two diagonals, one of them is connected to a power source V_{in} and the other has an equilibrium indicator. It is usually an Analog to Digital Converter or an analog device such as a magnetoelectric galvanometer. For a simple circuit connected to the ADC measurement device, V_{out} can be calculated as follow:

$$V_{out} = V_{in}\left(\frac{R_4}{(R_3+R_4)} - \frac{R_1}{(R_2+R_1)}\right), \tag{2}$$

In the case of supplying the bridge with the current source, the output voltage can be determined using the following formula (3):

$$V_{out} = J\left(\frac{R_2 \cdot R_4 - R_1 . R_3}{R_1+R_2+R_3+R_4}\right) \tag{3}$$

It is worth noticing that the previously presented cases, (2) and (3), concern the state of work of Wheatstone Bridge as unbalanced. This case occurs when we do not bring the bridge system to equilibrium during the measurement. During the measurement, we read from the so-called Voltage balance indicator. If the bridge system is working in the balance mode, the dependence (4) describes the relationship between the resistance in each branch of the bridge.

$$R_3R_4 - R_2R_3 = 0 \quad \rightarrow \quad R_3 = R_2\frac{R_3}{R_4}. \tag{4}$$

2.3 Double Current Circuit

The system presented in Figure 3, consisting of two current sources, is used for simultaneous measurement of two differences in resistance increments. The system includes resistive transducers connected into a four-armed bridge in such a way that two current sources J_1 and J_2 are connected to opposite vertices, while the other vertices are connected to the ground by reference resistors R_{r1} and R_{r2}. It should be noted that the currents of the sources must be directed to vertices A and B[14,1516].

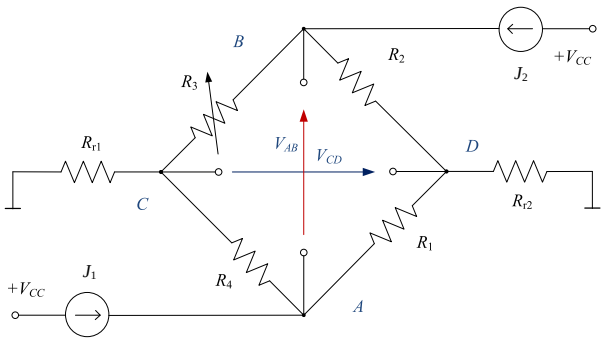

Figure 4. Circuit diagram of a double-current circuit.[15–18]

The system works by measuring the voltages at the vertices *A*, *B*, *C*, *D* or the difference in voltage between the vertices *D*-*C* and *A*-*B*. Formula (5), describing the relationship between electrical quantities in a dual-current system, looks as follows:

$$\begin{bmatrix} \frac{R_1+R_4}{R_1\cdot R_4} & \frac{R_2+R_3}{R_2\cdot R_3} & -\frac{1}{R_4} & -\frac{1}{R_1} \\ 0 & -\frac{1}{R_3} & -\frac{1}{R_2} & 0 \\ -\frac{1}{R_4} & -\frac{1}{R_3} & \frac{R_4\cdot R_3+(R_4+R_3)\cdot R_{r1}}{R_4\cdot R_3\cdot R_{r1}} & \frac{R_2\cdot R_1+(R_2+R_1)\cdot R_{r2}}{R_2\cdot R_1\cdot R_{r2}} \\ \frac{1}{R_1} & -\frac{1}{R_2} & 0 & 0 \end{bmatrix} \cdot \begin{bmatrix} V_A \\ V_B \\ V_C \\ V_D \end{bmatrix} = \begin{bmatrix} J_1 \\ J_2 \\ 0 \\ 0 \end{bmatrix} \tag{5}$$

It shows how the values of currents and measured voltages depend on the resistances in the system branches. The above mathematical description allows to derive a system of equations describing the dependence of resistance increments of individual bridge branches on the values of supply currents and voltages in the circuit nodes.

Assuming that the resistance of a single converter R_i equals the nominal resistance R_{i0} and the linear resistance increase ΔR_i, where i = 1, 2, 3, 4. Assuming that the current sources J_1 and J_2 are equal and represent current J and the resistance value reference values $R_{r1} = R_{r2} = R_0$ as well as the equality of the initial resistance of each of the resistive transducers placed in the bridge branches $R_{10} = R_{20} = R_{30} = R_{40}$, we obtain a set of equations:

$$\begin{cases} V_A - V_b \approx J\frac{(\Delta R_1-\Delta R_3)+(\Delta R_4-\Delta R_2)}{4} \\ V_D - V_C \approx J\frac{(\Delta R_1-\Delta R_3)-(\Delta R_4-\Delta R_2)}{6} \end{cases} \tag{6}$$

It should be noted that the system of equations is true for small resistance increments in relation to the value of the working resistance $R_0 >> \Delta R_i$ and assuming that small values of the resistance increments are small enough to be neglected. Dependencies (6) are true only for the measurement of resistance, in the case of impedance measurement, analogous formulas should be derived. Taking into account the above assumptions, the system of equations can be used in the practical implementation of a measuring bridge. It should be remembered that it is necessary to operate the measuring system in conditions ensuring small increments: ΔR_1, ΔR_2, ΔR_3, ΔR_4 of the resistance of the converters R_1, R_2, R_3, R_4. This will avoid the occurrence of nonlinearities in resistance difference gains.

The circuits presented in this chapter show that the measurement of resistance for direct current or impedance for alternating current is not so obvious. Proper measurement requires the selection of a suitable system. Before starting the selection of the measurement method, one should determine the range of resistance or impedance that we want to measure to select the appropriate system. If we specify what we want to measure then it is necessary to determine the system operation parameters so as not to exceed the permissible currents flowing in its branches, limited by the nominal power of

the elements used for its construction. The selection of an appropriate value of the supply voltage will allow satisfactory sensitivity of the bridge, which will be translated into high accuracy of measurement. The combination of bridge systems known for years with the currently developed microprocessor technology allows the construction of precision measuring equipment.

3. RESEARCH METOTHOLOGY

3.1 Simulation research

The simulation tests were performed in the National Instruments MULTISIM program[19]. The following systems for resistance measurement were tested: the Voltage Divider, the Wheatstone Bridge and the Double Current Circuit. Each of these systems has been supplied with a 5 V DC voltage source and a 12.5 mA DC source. The systems were analyzed for the system response to the resistance change R_x=R_3 with constant parameters of the power source. The simulation was carried out by changing the resistance of R_3 in the range of 0 Ω ÷ 200 Ω, with an increment of 10 Ω, after each change in the resistance value, the output voltage V_{out} was read.

The exception was the Double Current Circuit, which was powered only by a direct current source. The system was powered by two direct current sources with the value of J_1, J_2 = 12.5 mA. After each change of resistance on the output voltages V_1 (V_A - V_B) and V_2 (V_C - V_D) (Figure 4) were read, based on which the difference between these voltages was determined.

The characteristics obtained during the simulation do not differ from those obtained by measurements completed by the real systems shown in Figs. 7÷11.

3.2 Laboratory test bench

Executing tests on real systems required earlier implementation of the measurement test bench. The development was started with the preparation of the schematic diagram in the EAGLE program. The design used cheap and easily available elements, whose libraries were available in the program. The completed test bench (Fig. 5.) contained all three signal conditioner circuits described above, which were built based on 100 Ω resistors with a tolerance of 1% and the power of 0.5 W. The measuring stand also contained a permanently installed DC voltage source 5 V / 1 A based on an integrated stabilizer 7805 and two 12.5 mA current sources based on LM317 integrated circuits. Additionally, the circuits can be powered by external signals through connectors marked SIG1 and SIG2. It should be noted that during the measurement only one of the systems can work.

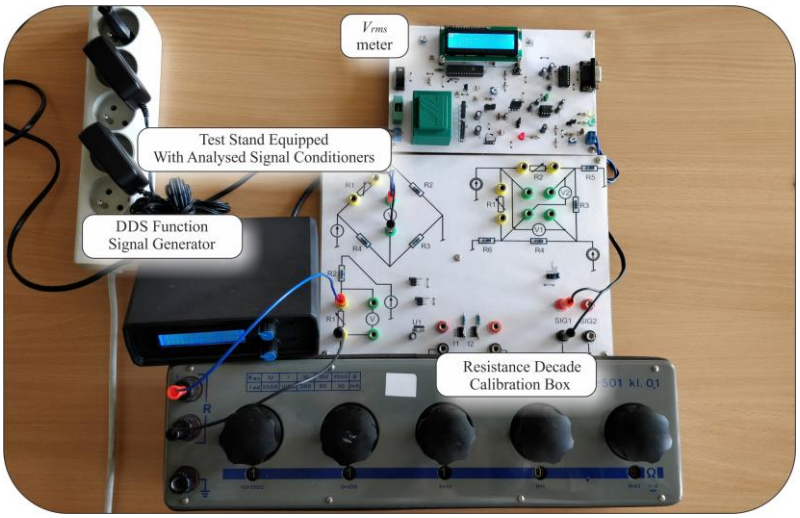

Fig. 5. General view of the finished measuring stand.

3.3 Data analysis achieved during simulation and empirical research

The performed simulations as well as the tests of real systems showed large convergence of practice with theory. In order to perform the analysis of metrological properties of the tested systems, their parameters should be determined (in the same way for each system). System parameters are considered based on the static properties of the analyzed systems. The static characteristics of each transducer is more or less non-linear. By applying appropriate measures in the design and application of correction systems, the non-linearity of the processing characteristics is minimized and is seek to be replaced by a linear characteristic burdened with a certain nonlinear error value. Calculation of the parameters of the measurement systems will be based on a two-point linear interpolation.[20–22] In this method, the interpolating straight line connects the points determined by the transducer range. Figure 6 shows an example of static processing characteristics $f(x)$ and its two-point linear interpolation function.

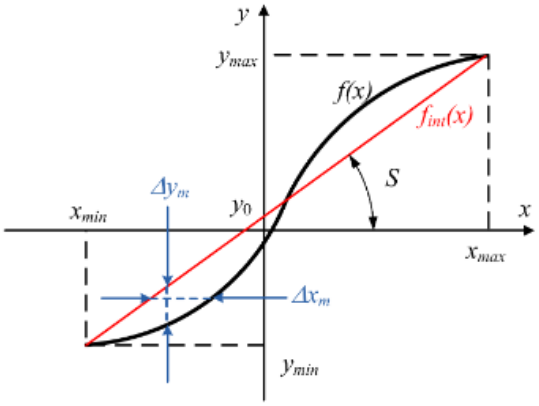

Figure 6. Definition of static parameters of the processing function.[20–22]

Sensitivity is a parameter defining the transducer response to the changes in the measured quantity, it is marked with letter S and is defined as follows:

$$S = \left|\frac{dy}{dx}\right| \tag{7}$$

where: dy - increase of the output quantity, dx - increase of the input quantity.

With non-linear processing characteristics, the sensitivity varies depending on the value of the measured quantity. For this reason, it is determined based on the measurement of the transmitter output value [17]:

$$x = f^{-1}(y) \tag{8}$$

The practical use of the non-linear processing function is awkward and requires the use of a microprocessor system that performs such calculations in the measuring system. Using interpolation of the non-linear processing function, we obtain a constant sensitivity value independent of the value of the measured value x.

$$y = S \cdot x + y_0 \tag{9}$$

where: y_0 - the transducer output value at zero measured value x.

The value of x is calculated after the transformation of the linear equation (9):

$$x = f_{int}^{-1}(y) = \frac{y - y_0}{S} \tag{10}$$

The determined value of the measured quantity *x* must have a determined error value related to the linear interpolation of the real, non-linear function of the measurement system processing. The value of the absolute non-linear error of the processing characteristics is determined in the field of the output size of the *y* converter:

$$\Delta y_m = \frac{max}{x}|f(x) - f_{int}(x)| \tag{11}$$

or in the field of measured quantity *x*:

$$\Delta x_m = \frac{max}{y}|f^{-1}(y) - f_{int}^{-1}(y)| \tag{12}$$

The value of the nonlinear error related to the measuring range allows to obtain a relative non-linear error:

$$\delta_{ny} = \left|\frac{\Delta y_m}{y_{max}-y_{min}} \cdot 100\%\right| \quad \text{or} \quad \delta_{nx} = \left|\frac{\Delta x_m}{x_{max}-x_{min}} \cdot 100\%\right| \tag{13}$$

where:

y_{min} - the value of the output voltage for the lower limit of the measuring range,

y_{max} - the value of the output voltage for the upper limit of the measuring range,

x_{min} - resistance value for the minimum value of the output voltage,

x_{max} - resistance value for the maximum value of the output voltage.

On the basis of the methodology used to determine the static parameters of the transducers, the sensitivity and non-linear error were calculated for each case and the measuring range was determined.

$$\Delta Vout = Vout_k - Vout_p \tag{14}$$

Sensitivity

$$S = tg(\alpha) = \left|\frac{\Delta V_{out}}{\Delta R_3}\right| \tag{15}$$

Non-linearity error

$$\Delta y_m = |Vout_u - Vout_d| \tag{16}$$

$$\delta_{ny} = \left|\frac{\Delta y_m}{Vout_k - Vout_p} \cdot 100\%\right| \tag{17}$$

The calculations were made by interpolating the linear characteristics of $Vout = f(R_3)$. The measuring range, due to the gentle curvature of the characteristics, was adopted within the limits of 0 Ω ÷ 200 Ω (Rp = 0 Ω, Rk = 200 Ω), hence $\Delta R_2 = Rk - Rp$=200 Ω -0 Ω =200 Ω.

4. RESEARCH RESULTS

4.1 Voltage Divider powered with DC voltage

The test was performed for the input data: $Vout_k$= 3.36 V, $Vout_p$ = 0 V, $Vout_d$ = 1.008 V, $Vout_u$ = 1.89 V. Using the above equations (8 ÷ 11), the following results were obtained: $\Delta Vout$ = 3.36 V, ΔR_2 = 200 Ω, S=0.0168 V/Ω, Δy_m= 0.882 V, δ_{ny}=26.2 %.

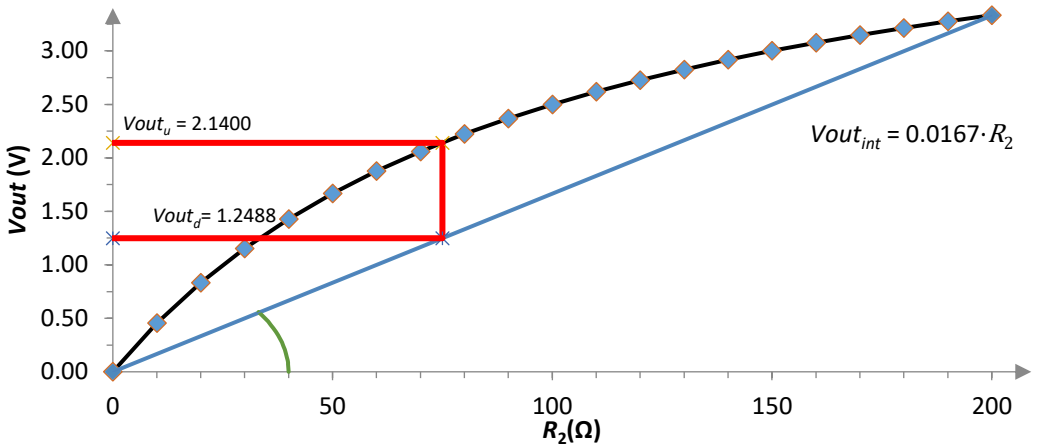

Figure 7. Two-points linear interpolation of the characteristic curve *Vout* = *f*(R_2) for DC voltage divider.

4.2 Voltage divider powered by DC current

Two-points interpolation coincides fully with the processing characteristics. The test was performed for the input data: $Vout_k$= 2.49 V, $Vout_p$ = 0 V, $Vout_d$ = 1.243 V, $Vout_u$ = 1.25 V. Using the above equations (8 ÷ 11), the following results were obtained: Δ $Vout$ = 2.49 V, S=0.01245 V/Ω, Δy_m= 0.007 V, δ_{ny}=0.3 %.

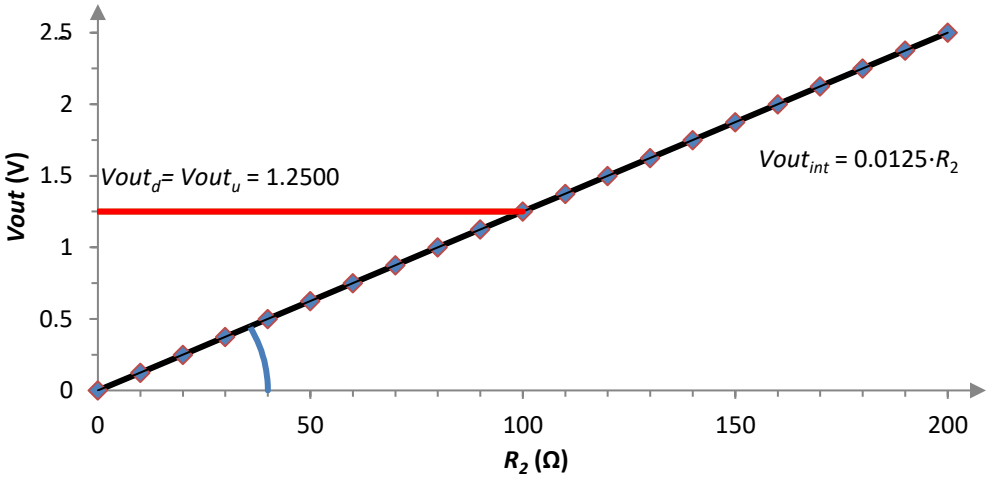

Figure 8. Two-points linear interpolation of the characteristic curve *Vout* = *f*(R_2) for DC voltage divider.

4.3 Wheatstone bridge powered with DC voltage

The test was performed for the following input data: $Vout_k$= -0.81V, $Vout_p$ = 2.51 V, $Vout_d$ = 1.182 V, $Vout_u$ = 0.3 V. Using the above equations (8 ÷ 11), the following results were obtained: Δ $Vout$ = -3.31 V, S=0.0155 V/Ω, Δy_m= 0.882 V, δ_{ny}=26.6 %.

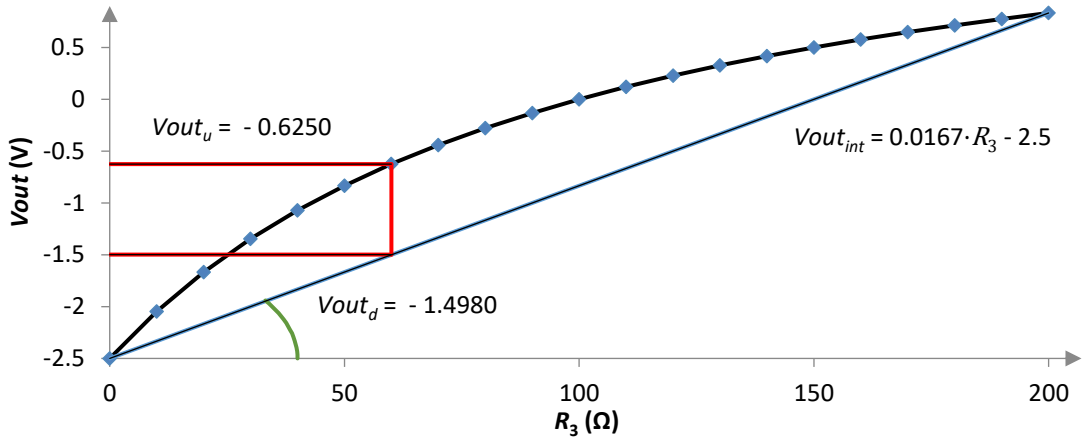

Figure 9. Two-points linear interpolation of the characteristic curve *Vout* = *f*(R_3) for Wheatstone bridge powered with DC voltage.

4.4 Wheatstone bridge powered with DC current

The test was performed for the following input data: $Vout_k$= -0.242 V, $Vout_p$ = 0.418 V, $Vout_d$ = 0.088 V, $Vout_u$ = 0.004 V. Using the above equations (8 ÷ 11), the following results were obtained: $\Delta\, Vout$ = -0.66 V, S=0.0033 V/Ω, Δy_m= 0.084 V, δ_{ny}=12.7 %.

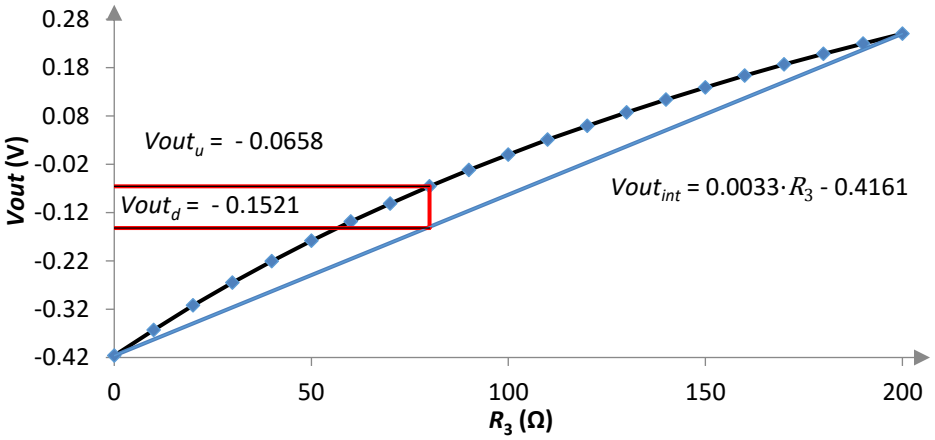

Figure 10. Two-points linear interpolation of the characteristic curve *Vout* = *f*(R_3) for Wheatstone bridge powered with DC current.

4.5 Double current circuit powered by direct current

The test was performed for the following input data: $(V_1 - V_2)_k = -0.393\ V$, $(V_1 - V_2)_p = 0.776\ V$, $(V_1 - V_2)_d$= 0.312 V, $(V_1 - V_2)_u$= 0.108 V. Using the above equations (8 ÷ 11), the following results were obtained: $\Delta\,(V_1 - V_2)_{rms1}$ = -1.169 V, ΔR_3 = 100 Ω, S = 0.01169 V/Ω, Δy_m= 0.204 V, δ_{ny}=17.4 %.

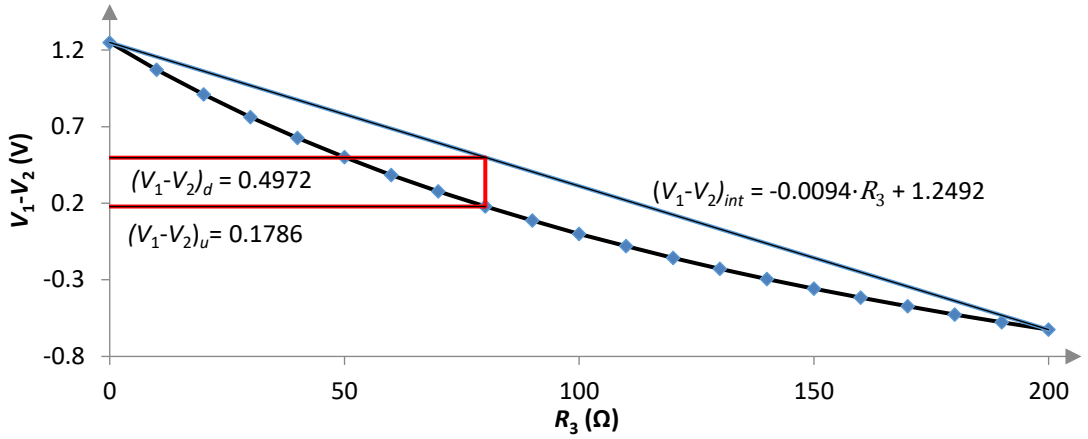

Figure 11. Two-points linear interpolation of the characteristic curve V_1-V_2 = $f(R_3)$ double current circuit powered by direct current.

As in the case of results from real systems, the following parameters for the results obtained in the simulation were determined: sensitivity and non-linear error. The characteristics obtained during the study of real systems and obtained in the simulation are practically identical, and their errors are presented in Table 1.

Table 1. Compilation of calculations.

Power source	**Voltage Divider**			**Wheatstone bridge**			**Double current circuit**		
	Range	Sensitivity	Non-linearity error	Range	Sensitivity	Non-linearity error	Range	Sensitivity	Non-linearity error
	(Ω)	(V/ Ω)	(%)	(Ω)	(V/ Ω)	(%)	(Ω)	(V/ Ω)	(%)
Results from simulation									
DC voltage	0 ÷ 200	0.01665	26.8	0 ÷ 200	0.01665	26.2	-	-	-
DC current	0 ÷ 200	0.0125	0.0	0 ÷ 200	0.00333	12.9	0 ÷ 200	0.0094	17.0
Calculations from empirical systems									
DC voltage	0 ÷ 200	0.0168	26.2	0 ÷ 200	0.0155	26.6	-	-	-
DC current	0 ÷ 200	0.01245	0.3	0 ÷ 200	0.0033	12.7	0 ÷ 200	0.0117	17.4

5. CONCLUSIONS

Simulation results are very similar to those of real systems. In the case of the sensitivity of the tested systems, the difference appears only in the fourth place after the decimal point, while the level of the nonlinear error has a discrepancy ranging within 1%. An additional behavior of the measuring systems under examination, as demonstrated in the analysis, is the decrease in the level of non-linear error together with the narrowing of the measurement range with the simultaneous increase in sensitivity. Such a dependence leads to implementation of measurement systems, adapted to the measurement of the target resistance, calculated at the design of the system, with small deviations of its value. Then the measurements performed will have high resolution and will be burdened with a small nonlinear error. The exception to this rule is the voltage divider. In such a set-up, the system allows the measurement of resistance in a fairly wide range, while the non-linear error remains small around 1%, where in other configurations of measurement systems, the nonlinearity error reaches even 26.8%. The average sensitivity of all measuring systems for the measuring range 0 Ω ÷ 200 Ω is at the level 0.0131 V / Ω narrowing the range to half narrower 0 Ω ÷ 100 Ω or 100 Ω ÷ 200 Ω allows to obtain an average sensitivity of 0.0028 V / Ω . This solution allows for a higher resolution of the measurement.

The practical application of the analysis performed is a helpful material in the selection of the type of measurement system for the implementation of systems using strain gauges.

Funding: This research was funded by Bialystok University of Technology, grant number S/WE/2/2018.

REFERENCES

[1] Anderson, K. F., “Your Successor to the Wheatstone Bridge? NASA’s Anderson Loop” (1998).
[2] Laurila, H., “Weighing scale calibration - How to calibrate weighing instruments” (2017).
[3] EURAMET., “Calibration Guidelines - EURAMET,” <https://www.euramet.org/publications-media-centre/calibration-guidelines/> (2 October 2018).
[4] Davidson, S, Fritsch, K, Grum, M, Malengo, A, Medina, N, Popa, G, Schnell, N., “Guidelines on the Calibration of Non-Automatic Weighing Instruments EURAMET Calibration Guide No. 18,” 2015, <www.euramet.org> (2 October 2018).
[5] European Accreditation Laboratory Committee., “EA-4/02 M: 2013 - Evaluation of the Uncertainty of Measurement In Calibration,” 2013, <www.european-accreditation.org> (2 October 2018).
[6] BEAMEX., “Weighing scale calibration-How to calibrate weighing instruments,” <www.beamex.com> (4 October 2018).
[7] Walendziuk, W., “Dynamic Outlier Detection in the Calibration by Comparison Method Applied to Strain Gauge Weight Sensors,” Sensors **18**, 4200 (2018).
[8] Hoffmann, K., “An Introduction to Stress Analysis using Strain Gauges,” <www.hbm.com> (25 October 2018).
[9] Pedersen, C., Jespersen, S. T., Krog, J. P., Christensen, C. and Thomsen, E. V., “Combined differential and static pressure sensor based on a double-bridged structure,” IEEE Sens. J. **5**(3), 446–454 (2005).
[10] Anderson, K. F., “Looking Under the Bridge (Wheatstone)” (2001).
[11] Cuenca, Á. D., Beltrán, L. O., Vilela, J. P. T. and Miranda, J. C., “Comparison of microstrain indicators measurements based on Anderson’s Loop and Wheatstone Bridge,” Proc. 16th IEEE Int. Conf. Electron. Commun. Comput. CONIELECOMP 2006 **2006**, 35, IEEE (2006).
[12] Walendziuk, W. and Idźkowski, A., “Portable acquisition system for domiciliary uroflowmetry,” J. Vibroengineering **11**(3), 592–596 (2009).
[13] Anderson, K. F., “A Conversion of Wheatstone Bridge to Current-Loop Signal Conditioning For Strain Gages,” Edwards, California (1995).
[14] Idźkowski, A., Walendziuk, W. and Świetochowski, Paweł, Warsza, Z. L., “Metrological Properties of a Two-Output Transducer for Measuring Sum and Difference of Small Resistances,” Elektron. ir Elektrotechnika **23**(5), 41–45 (2017).

[15] Idźkowski, A., Walendziuk, W. and Warsza, Z. L., "Unconventional double-current circuit for deflection and temperature simultaneous measurement," Elektron. ir Elektrotechnika **21**(1), 23–27 (2015).
[16] Idźkowski, A., Gołębiowski, J. and Walendziuk, W., "Analysis and application of two-current-source circuit as a signal conditioner for resistive sensors," J. Electr. Eng. **68**(3), 200–205 (2017).
[17] Warsza, Z. L., Idźkowski, A. and Walendziuk, W., "The parameters of unconventional double-current circuit, their accuracy measures and measurement of strain and temperature," Int. J. Electron. Telecommun. **60**(4), 327–330 (2014).
[18] Walendziuk, W., Gołębiowski, J. and Idźkowski, A., "Comparative evaluation of the two current source supplied strain gauge bridge," Elektron. ir Elektrotechnika **22**(6), 33–38 (2016).
[19] "What is Multisim™? - National Instruments.", <http://www.ni.com/pl-pl/shop/electronic-test-instrumentation/application-software-for-electronic-test-and-instrumentation-category/what-is-multisim.html> (20 May 2019).
[20] Carr, J. J. and Brown, J. M. (John M., [Introduction to biomedical equipment technology], Prentice Hall (1998).
[21] Aller, M. and Pennell, J., "The Measurement, Instrumentation and Sensors Handbook" (1999).
[22] Fraden, J., [Handbook of modern sensors : physics, designs, and applications.], Springer (2014).

Distributed measurement data collecting system with mobile packet transmission

Wojciech Wojtkowski
Faculty of Electrical Engineering, Bialystok University of Technology, Wiejska 45D, 15-351 Bialystok, e-mail: w.wojtkowski@pb.edu.pl.

ABSTRACT

The article presents a system for gathering measurement data. The system gathers the data from a number of distributed, across a wide area sensors, using mobile packet transmission. The data comes from a variety of digital sensors, including temperature sensors with 1-wire communication. The system allows to monitor many parameters for example temperatures of power semiconductors devices or any other signals from digital or analog sensors in the remote objects. The system is supplied with a data acquisition module which can store the important data for the further use and has a Wi-Fi module which allows for connection to the Internet and access to the data from any place. The described system may be used for recognition of anomalous behavior in the observed object, which may be caused by a semiconductor device failure. Such data is crucial for example in power electronic systems, remote solar plants or wind plants. The structure of the system as well as description of the system operation is presented in the paper.

Keywords: data acquisition, digital sensors, 3G/4G mobile network, MQTT, IoT, M2M

1. INTRODUCTION

Contemporary digital metrology systems usually provide a possibility of performing parallel measurements of many physical parameters like voltage, temperature, pressure, humidity and many others [1]. Frequently, it is crucial to measure all of the parameters at the same sampling point that allows for instance to detect some small asymmetries in the monitored system. It can be achieved by implementation of an FPGA chip and it was reported in the previous author's papers [2, 3]. The previous papers show the original concept of reading the temperatures from many 1- wire digital sensors, with as small as possible the time delay between the individual measurements and delivering the read data to the server through GPRS connection. This paper describes a more universal system than presented in [2, 3] that creates a complete M2M or IoT solution that allows remote parallel monitoring of different physical parameters and acquire measurements by a server system through MQTT protocol and contemporary 3G/4G mobile packet transmission. Access to the measurement data is realized using http protocol and a standard web browser application. MQTT protocol allows to minimize the amount of data transmitted through the mobile packet data service as well as provides high reliability. Web user interface allows to access data practically from any localization and any device with Internet access.

2. DESCRIPTION OF THE SYSTEM

The proposed system consists of several functional blocks. The block diagram, presenting main blocks of the system, is depicted in Fig 1. The presented diagram contains a set of specialized modules. The modules are installed on the client side. Each client module consists of digital sensors, FPGA device, UART / Bluetooth converter and a 3G/4G modem. The FPGA module reads the data from the sensors and periodically sends it, using MQTT protocol, to the server. The wireless transmission is accomplished by a WiFi module and the GSM modem. The measurements that are received by the data server are stored in the local or cloud data base. Later the results may be analyzed off-line be any dedicated software. The names t1-tn (Fig. 1) represent the temperature sensors. If necessary they can be replaced by any desirable kind of digital or analog sensor. If an analog sensor is needed, an additional translating or amplification circuit is required.

Photonics Applications in Astronomy, Communications, Industry, and High-Energy Physics Experiments 2019, edited by Ryszard S. Romaniuk, Maciej Linczuk, Proc. of SPIE Vol. 11176, 111765K
© 2019 SPIE · CCC code: 0277-786X/19/$21 · doi: 10.1117/12.2536496

2.1 Utilized sensors

In principle, any type of digital sensor can be directly used in the project. If there is a need to measure signals from analog sensors, a proper intermediary forming and amplifying circuit is necessary. The digital sensors may be connected to the system directly. For example to measure temperatures of the monitored semiconductor devices in the distributed monitored system, digital temperature sensors may be useful. A good example of a convenient in use digital temperature sensor is DS18B20. The sensor block diagram is presented in Fig. 2. It consists of a 64-bit read only memory which stores a unique serial code of the device. The code is used for addressing a particular device connected to the 1W bus. There is also a scratchpad memory which contains the temperature register storing the temperature value measured by the sensor. Additionally the scratchpad memory provides access to the alarm trigger registers (TH and TL , Fig. 2) and the configuration register. The configuration register may be used to set the resolution of the conversion. The maximal resolution is equal 12 bits and the minimal is equal 9 bits. The configuration registers are nonvolatile (EEPROM) and they will retain data during power off. The sensor uses 1W bus for communication, which simplifies the connection net. DS18B20 sensors are often utilized in a lot of the industrial systems [4-12]. The sensors may be powered by the data line (it is called parasitic power mode of operation) or by a separate power supply line. When the sensors are powered by a dedicated supply wire the solution is more reliable especially if the sensors are located close to some RF emission [13]. In a RF interferences environment, nonetheless, where some interferences or sensor malfunctions may occur, a special fault-tolerant signal processing or special decision algorithms supported by a sophisticated classification should be applied [14].

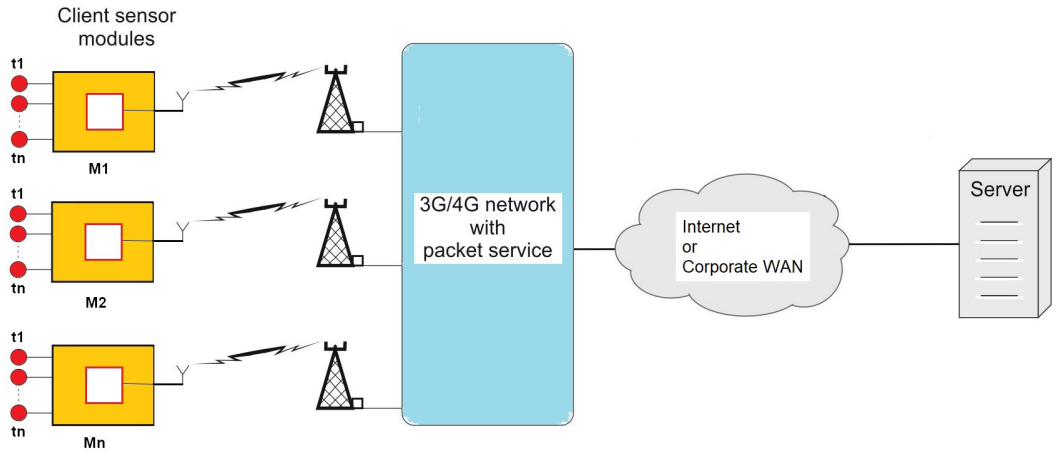

Figure 1. The block diagram of the system structure.

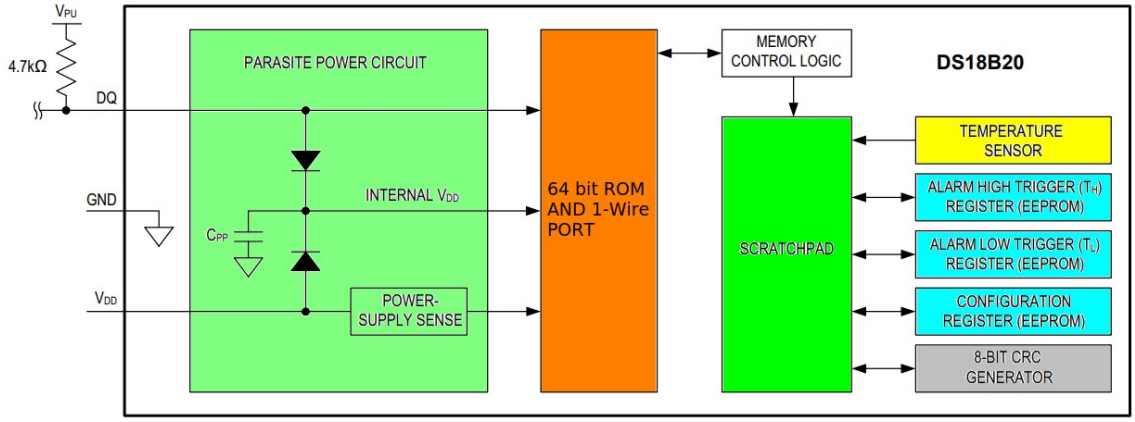

Figure 2. The sensor block diagram [15].

The sensor can measure the temperature in the range from -55 °C to +125 °C (declared minimum accuracy is equal ± 0.5 °C from - 10 °C to +85 °C and is equal ±2 °C from +85 °C to +125 °C [16]) The range is wide enough for the system. The sensor automatically generates an 8-bit CRC sum (Fig. 2, 8-bit CRC Generator) and provides this sum by the 1W line. The CRC allows validation of the transferred data. The 1-Wire communication consists of a special time slots representing low and high logical levels. The communication always begins with the RESET pulse. Next, the responding sensor sends the PRESENCE sequence. It is depicted in Fig. 3. On the 1W bus the data is transmitted least significant bit first. It can be seen in Fig. 4 (reset sequence, presence sequence and SKIP ROM command 0xCC. The complete list of the sensor commands can be found in [15].

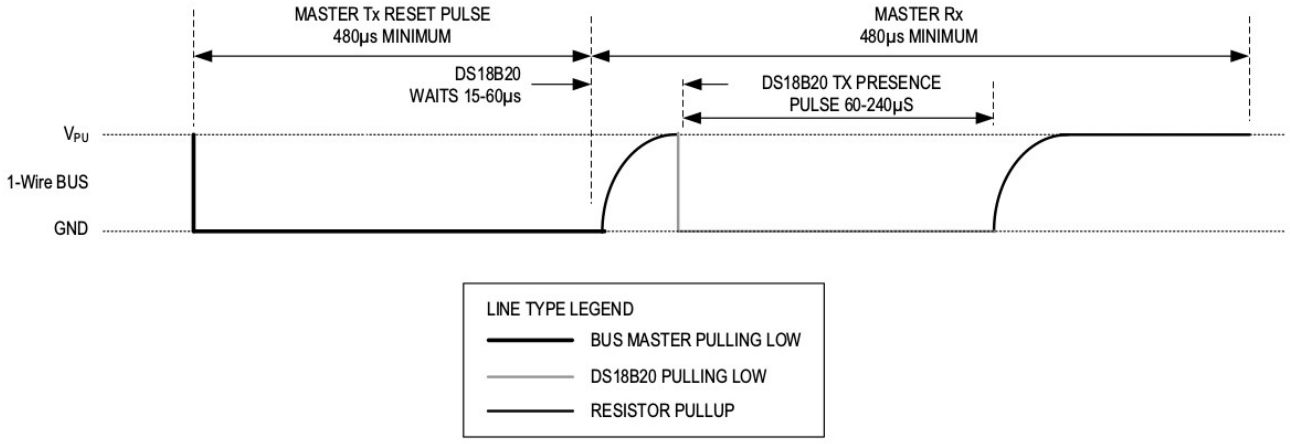

Figure 3. The 1-Wire sensor initialization timing [15].

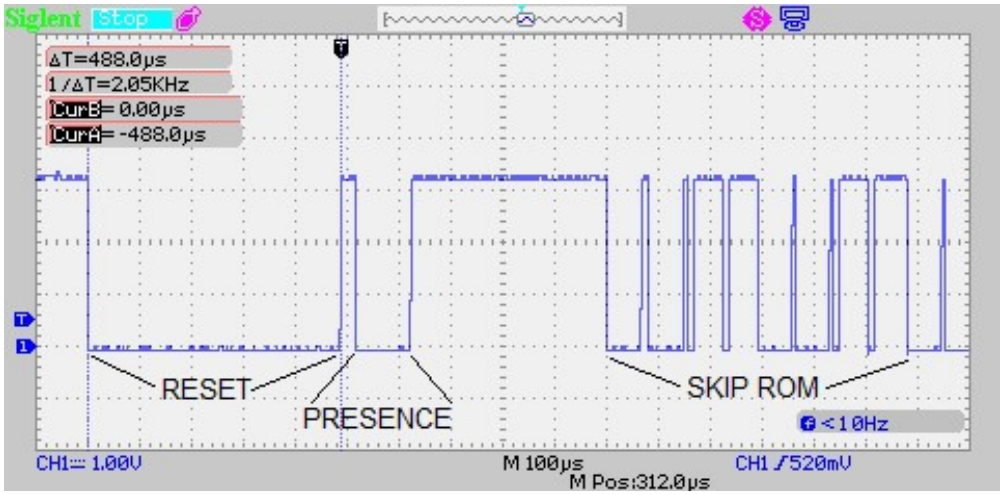

Figure 4. The 1W frame, 0xCC – “skip ROM” command.

In case, there is just a single sensor connected to a single bus, the communication sequence 0x0CC – Skip ROM, 0x044 – Convert T, begins the process of the temperature conversion. In case, there are multiple sensors attached to the 1W bus, each particular sensor has to be addressed before the further communication can start. The process of the serial communication with the sensor is lengthened, as a result of the fact that each sensor has a 64-bit serial number which should be transmitted to the sensor before further communication. A single temperature conversion sequence contains the following stages: sending command “Match ROM” from the bus master to the sensor, sending the serial number to the sensor, sending the temperature conversion starting sequence, waiting for completion of the conversion, starting

again communication with the DS18B20, reading the conversion result. The process of a single measurement will take almost 800 ms at the maximal resolution.

2.2 Client communication module

The client module is responsible for collecting data from a set of locally distributed sensors. The client block diagram is presented in Fig. 5. The communication with the available sensors is accomplished by the FPGA module. The module is able to conduct simultaneous reading of all the connected sensors because of the separate 1W buses. The module collects the data from the sensors and send it through the UART interface.

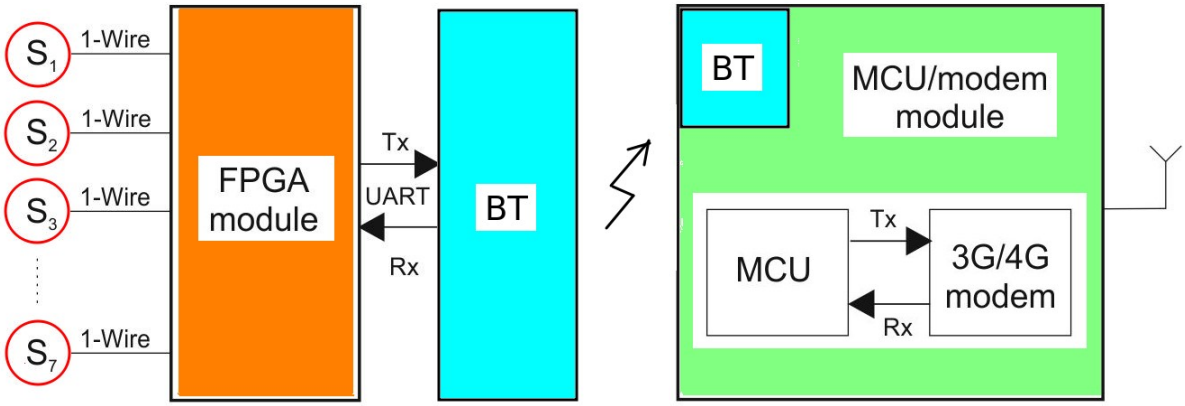

Figure 5. The block diagram of the structure of the client module.

Then this data is send through Bluetooth module which sends it to the server through the GSM modem. Instead of the 3G/4G integrated modem a simple cell phone may be used. The cell phone should have an active Internet connection. Its BT module should be activated and properly paired with the sensors board. The data is managed by a Mosquitto MQTT broker, which is installed on a small and relatively cheap single board micro-computer. Each additional 1-Wire sensor may be also connected to its own dedicated 1-Wire bus to allow simultaneous operation of all the available sensors. It is possible thanks to the implementation of the FPGA device. The FPGA communicates with the BT module through the standard UART interface. Because the MQTT protocol is relatively light weight it is ideal in the proposed solution because it is a hardware constrained environment. It is really important to save the network bandwidth in such case. During the laboratory testing of the client module, it turned out that a temperature simulator would be useful for testing the temperature sensors and the system operation. For this purpose, a set of semiconductor elements (triacs and transistors) loaded by regulated currents and with attached sensors was used. It is presented in Fig. 6.

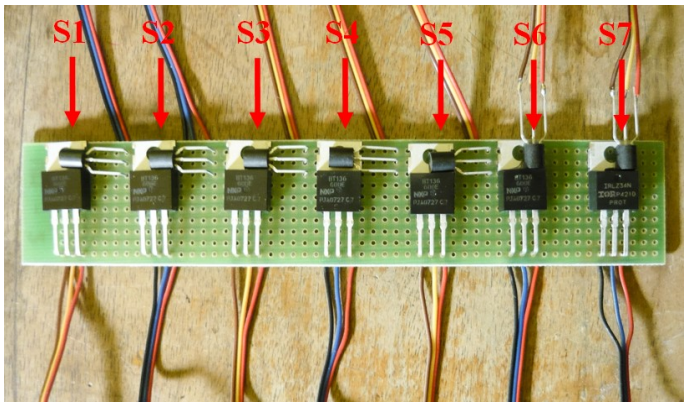

Figure 6. Laboratory simulator of heated transistors for testing the temperature measurements.

2.3 The server part

The server of the presented system is presented in form of a block diagram in Fig. 7. It is made on the base of Windows 2012R2 system. The Web server part is based on the ASP.NET technology. As a data base any SQL solution can be used, but in this example the MS SQL Express is implemented. The server is configured to listen to the incoming messages. The messages come from the clients modules. The server reads the data and stores them using the SQL database. The data can be used for generation of a webpage for presenting purpose and in a such case can be accessed through a standard web browser.

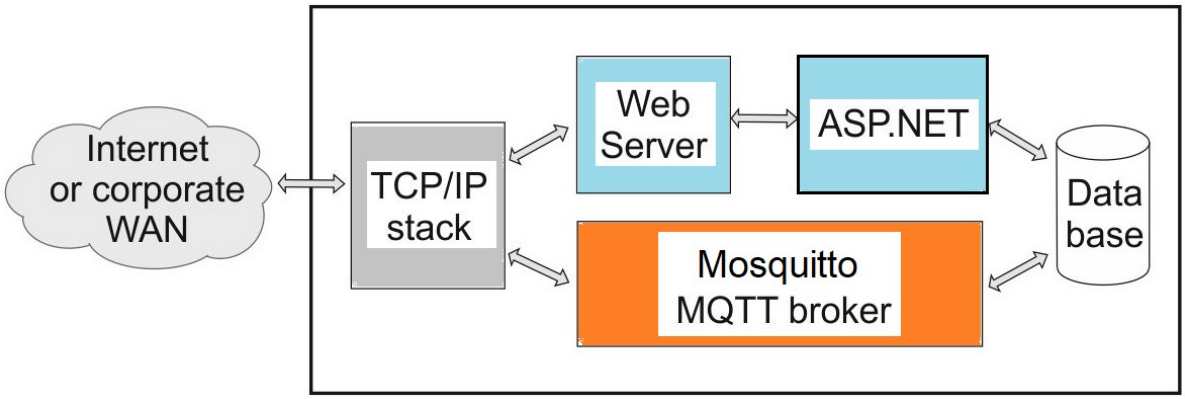

Figure 7. The diagram of the structure of the server.

3. MQTT TRANSPORT PROTOCOL

The MQTT is a short from message queue transport protocol. The protocol is used in a Client - Server communication structure with a typical pub/sub messaging . The MQTT is relatively light weight and what may be important in many implementations it is open. Because of the advantages the protocol is suitable for use in many practical situations, like small systems with hardware constrains typical for Machine to Machine scenario (M2M) and Internet of Things (IoT). In such systems it is really important to not block the network bandwidth and to fit in a small system's restricted program memory. The pub/sub messaging structure (publish/subscribe) is an interesting alternative to the traditional client-server connection architecture. In the traditional solution, the client should communicate directly with the server. The pub/sub solution isolates the publisher (pub) sending a message from the set of receivers that receiving the message (sub). The pub and sub nodes may never communicate directly. The communication between the publisher and the subscribents is realized by a kind of a server - the broker. The broker's responsibility covers filtering of the incoming messages and distributing them to proper subscribers. Really important advantage of the pub/sub structure is the decoupling of the receiver (subscriber) of the transmitted message from the publisher. This decoupling has three aspects: time, space and synchronization:

- Time – the subscriber and the publisher do not have to operate at the same time.
- Space – the subscriber and the publisher do not have to exchange their IP address and port.
- Synchronization - during receiving or publishing sequence, there is no need for interrupt the operation on the transmitter as well as on the receiver.

Thanks to the decoupling, the pub/sub model do not uses the direct communication between and the subscriber of the message. Because of the filtering possibility of the MQTT broker, it can control which client receives which message. The broker's admin can set necessary rules to control the data flow. Thanks to the Mosquitto implementation in the project, the number of connected clients is practically unrestricted and may be tuned to virtually any existing system. Additionally, the database may be duplicated and can be placed in different places across the World which dramatically improves security of the data.

4. SUMMARY

The presented measuring system gives the possibility to monitor many parameters in the controlled systems. For example voltages, currents and temperatures of the power semiconductors devices in the monitored distributed systems can be monitored and the data can be stored in the SQL database. The data is managed by a Mosquitto MQTT broker, which is installed on a small and relatively cheap single board micro-computer. Because the MQTT protocol is relatively light weight it is ideal in the proposed solution because it is a hardware constrained environment. The solution can be used for measurement of temperatures of semiconductor devices in power electronic systems. The information of power semiconductors temperatures may help in rapid detection of current flow asymmetry, usually associated with a specific hardware faults. The described temperature measurement system can be used for detection of several types of anomalies occurring in monitored power devices because many of them involve excessive heating of the endangered semiconductor elements. Practical advantage of the described solution is the remote acquisition of the measured data from many sensors which is important for remote monitoring of a distributed equipment. The system is scalable and each client equipment may be monitored for a lot of different important parameters.

Acknowledgement

This work was supported by the grant S/WE/1/2016 from Bialystok University of Technology founded by Ministry of Science and Higher Education.

REFERENCES

[1] V. Markevičius, D. Navikas, D. Andriukaitis, M. Čepėnas, A., Valinevičius, M. Žilys, R. Malekian, A. Janeliauskas, W. Walendziuk, A. Idzkowski, “Two thermocouples low power wireless sensors network”, AEU-International journal of electronics and communications, vol. 84, pp. 242–250, 2017. DOI: 10.1016/j.aeue.2017.11.032.

[2] Wojtkowski W., Zankiewicz A., Parallel RF Power Amplifiers Temperature Monitoring System Based on FPGA Device, IFAC-PapersOnLine, Vol. 51, No. 6, 2018, pp. 414-419.

[3] Wojtkowski W., Zankiewicz A., Data acquisition system with GPRS transmission for monitoring temperature of RF Power Amplifiers, 26th Telecommunications Forum: TELFOR 2018, Belgrade, November 20-21.

[4] W. Walendziuk, A. Sawicki, “Telemetric measurement system of beehive environment conditions”, Proceedings of SPIE, vol. 9290, 2014.

[5] S. Yan, Wang H., C. Liu, Design for Heater Control System Based on DS18B20 and Level Detector, 2011 International Conference on Multimedia and Signal Processing”, pp. 30-32, Guilin, 2011.

[6] Idzkowski, A., Walendziuk, W., and Warsza, Z. L., “Unconventional double-current circuit for deflection and temperature simultaneous measurement," *Elektronika ir Elektrotechnika* **Vol.21**(1), 23{27 (2015).

[7] Walendziuk, W., Idzkowski, A., and Golebiowski, J., “Reconfigurable two-current source supplied signal conditioner for resistive sensors," *Elektronika ir Elektrotechnika* **Vol.21**(4), 23{26 (2015).

[8] Vanus, J., Machacek, Z., Kozirek, J., Walendziuk, W., Kolar, V., and Jaron, Z., “Advanced energy management system in smart home care," *International Journal of Applied Electromagnetics and Mechanics* **Vol.52**, 517{524 (2016).

[9] W. Wojtkowski, Digital control of a bidirectional DC / DC converter for automotive applications, IFAC Papers Online, Vol. 51, Issue: 6, 2018, pp. 113-118.

[10] J. Kusznier, Reflectometric temperature sensor, Proceedings of SPIE, Volume: 8010, Article Number: 80100C, 2011.

[11] Z.L. Warsza, A. Idzkowski, Errors and uncertainties of imbalanced bridge-circuits as primary converters for RTD sensors, Advanced Mechatronics Solutions eds. Ryszard Jabłoński, Tomas Brezina, Volume 393 of the series Advances in Intelligent Systems and Computing, Springer, pp. 397-410, Cham 2016.

[12] W. Wojtkowski., R. Lewczuk, Parallel temperature measurement system for electric vehicle, Zeszyty Naukowe Wydziału Elektrotechniki i Automatyki Politechniki Gdańskiej, Vol. 54, 2017, pp. 237-244.

[13] A. Zankiewicz, Susceptibility of IEEE 802.11n networks to adjacent-channel interference in the 2.4GHz ISM band, Przeglad Elektrotechniczny, Vol. 88, No 9b, 2012, pp. 287-288.
[14] K. Konopko, D. Jańczak, Classification method based on multidimensional probability density function estimation dedicated to embedded systems, IFAC-PapersOnLine, Vol. 51, No. 6, 2018, pp. 318-323.
[15] Maxim Integrated, Programmable Resolution 1-Wire Digital Thermometer, Datasheet 19-7487; Rev 4; 1/15, 2015.

Multi-channel temperature measurement system with remote dashboard for electric vehicle

Wojciech Wojtkowski[a], Wojciech Walendziuk[b]
[a]Faculty of Electrical Engineering, Bialystok University of Technology, Wiejska 45D, 15-351 Bialystok, e-mail: w.wojtkowski@pb.edu.pl;
[b]Faculty of Electrical Engineering, Bialystok University of Technology, Wiejska 45D, 15-351 Bialystok, e-mail: w.walendziuk@pb.edu.pl.

ABSTRACT

A multi-channel temperature measurement system for an electric vehicle with a remote control dashboard capability is presented in the paper. The presented system is intended to be used for monitoring of batteries' temperatures in hybrid or electric vehicles. Generally it is necessary in case of charging or discharging a battery stack consisting of several batteries which should be monitored independently to avoid any malfunctions or catastrophic results caused by overvoltage, under-voltage or excessive heating. The presented system incorporates multi-channel temperature measurements with digital temperature sensors, a FPGA device which collects data from sensors and translates it to CAN bus frames. CAN bus is incorporated for communication with a Battery Management System. To allow the remote monitoring, the system is equipped with a single board micro-computer running Node RED software. The structure of the system as well as particular devices are described in the paper.

Keywords: Digital temperature sensor, temperature measurement, CAN, FPGA, electric vehicle.

1. INTRODUCTION

Automotive battery management systems, in general, should be equipped with temperature measurement devices. A good example showing the importance of the temperature measurement may be the battery stack utilized in electric vehicles (EV) or hybrid-electric vehicles (HEV). The lithium based batteries used in such systems should be monitored for the temperature. The batteries for the EV systems generate much heat during rapid charge and discharge cycles at the charging or discharging current levels exceeding the batteries rating, such as when the EV quickly starts consuming battery power or when recovering the inertia energy during sudden stops of the vehicle. Frequently, for recovering of the inertia energy, a super-capacitor or a set of super-capacitors is used for better performance. During these rapid charge and discharge cycles, the cell temperature may increase above the allowable limits [1-3]. Because there are a lot of the battery cells in a vehicle, just a single temperature sensor is definitely not enough. During some uncontrolled charging or discharging processes, batteries can get too hot which may be extremely dangerous and even cause fire [4]. In such case, a temperature measurement system should be multi-channel and should be able to work in parallel. Real parallel measurements give the possibility to control all the batteries at the same time. The opposite solution is to use many sensors communicating with a central processor unit in a strictly defined sequential order, one by one. The overall time needed to scan all the important temperatures in that case depends on the number of sensors, communication speed and the temperature conversion time of each sensor. In case of the parallel measurement the number of sensors does not influence the overall conversion time. Generally the temperature can be measured utilizing a variety of available temperature sensors. There are many different analog and digital temperature sensors on the market today. All the solutions have their pros and cons [5]. The digital sensors are convenient in use, do not need difficult or expensive calibration and are typically ready to use right out of the box. Such sensors feature a digital interface, which is typically more reliable in case of electromagnetic interferences. To proper operation they need a micro-controller for communication, but a micro-controller is already a part of almost every modern automation system. Typical digital buses used for such purpose are 1-Wire, Inter-Integrated Circuit bus (I^2C), Serial Peripheral Interface (SPI), Local Interconnect Network (LIN) and the Controller Area Network (CAN), the last one especially in the automotive systems. As a disadvantages of the digital sensors one can classify generally higher prices and greater complexity of the system software. In spite of this, some analog sensors are still in use and may be used in many different applications [6-10]. It is because of many reasons, one of them can be lower prices and the possibility to measure of more than one parameter at

Photonics Applications in Astronomy, Communications, Industry, and High-Energy Physics Experiments 2019, edited by Ryszard S. Romaniuk, Maciej Linczuk, Proc. of SPIE Vol. 11176, 111765L
© 2019 SPIE · CCC code: 0277-786X/19/$21 · doi: 10.1117/12.2536497

once (for example temperature and deflection) [11-13]. An interesting measurement system with multichannel temperature measurement is presented in [14]. This is an example of a distributed control and measurement system which, due to the utilized communication solution, is not fully synchronized (in terms of multi-point temperature measurement) compared to the system presented in this paper. The use of a field programmable gate array device (FPGA) allows the real parallel temperature measurement, which in many applications, including automotive electronics, is crucial. The presented solution allows for detection of abnormal states in the monitored battery stack, helps in proper balancing process and gives the possibility to test the maximal output power of the monitored system thanks to the temperature monitoring possibility. The system can be extended to monitor temperatures of power LEDs in the vehicle head lamps and power semiconductor devices in the onboard DC-DC converters as well [15]. This is crucial, because modern LEDs work in stress conditions and must be monitored to avoid any damage. The proposed monitoring system is based on the digital temperature sensors. The sensors are connected to a FPGA board, which collects the information about the measured temperatures. An additional single board microcomputer is implemented which operates Node-RED software to allow remote monitoring and remote control.

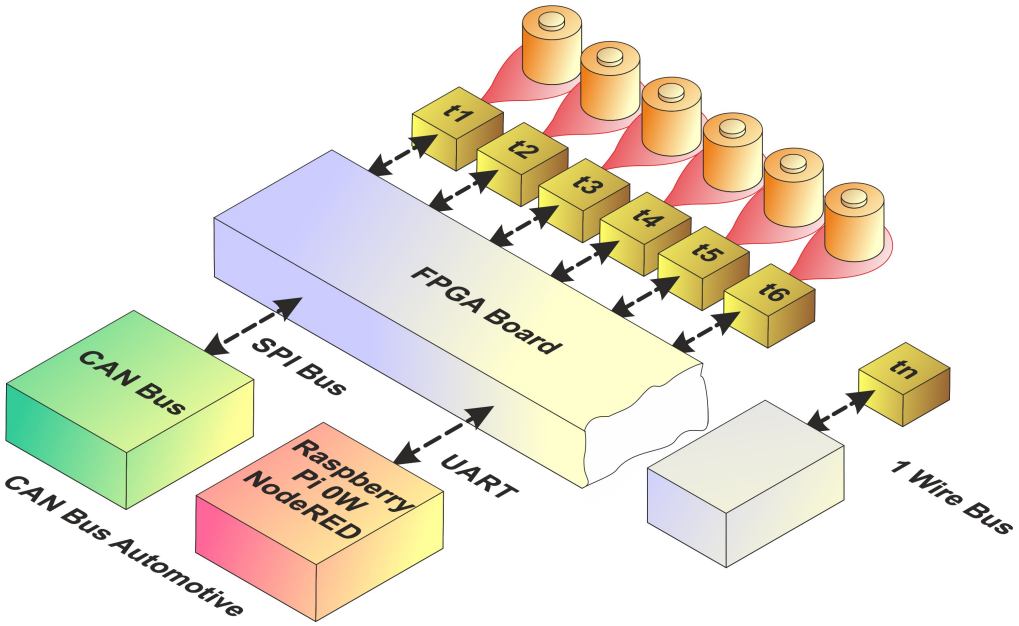

Figure 1. The temperature measurement system block diagram.

2. THE TEMPERATURE MEASUREMENT SYSTEM

The block diagram of the proposed temperature measurement system is presented in Fig. 1. The presented system is based on digital temperature sensors. They are connected to an FPGA to allow parallel temperature sampling, which is really important in the presented implementation. If all the measured temperatures are sampled at the same time, it is possible to discover all the existing irregularities, asymmetries and gives the possibility to properly balance the monitored battery stack. In our case it was achieved thanks to the implementation of many independent digital 1-Wire interfaces. Namely, each interface is connected directly to a single digital temperature sensor. Because of that, there are no delays, related to 1-Wire devices queue. Because of the complexity of the presented digital system, the softcore NIOS processor was implemented. The processor utilizes CAN communication with a vehicle through the external CAN controller (MCP2515). The CAN controller is connected to the vehicle bus through the CAN transceiver MCP2551. It supports 1 Mb/s operation and implements ISO-11898 standard physical layer requirements. The block diagram of the CAN transceiver is presented in Fig. 2. It is equipped with the externally-controlled slope control device (Fig. 2) for reduced RFI emissions. It makes the measurement system compatible with the vehicle requirements.

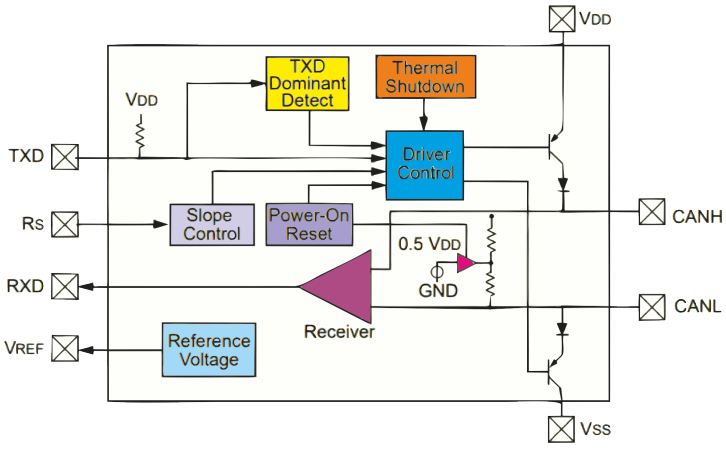

Figure 2. The CAN transceiver block diagram [16].

Thanks to the CAN bus implementation, from the vehicle side the system is visible as a typical CAN bus node and can send data frames with preset identifiers. The monitoring CAN node uses DS18B20 digital sensors which communicate with the NIOS microprocessor by 1-Wire serial interface. The microprocessor is implemented in Cyclone IV family FPGA device. It is important that each sensor has its own independent 1-Wire bus for parallel communication. The NIOS processor was specially configured for the project using Platform Designer module in Quartus 18.1 software. A fragment of the configuration, in graphical form, is presented in Fig. 3. The NIOS processor was equipped with Universal Asynchronous Receiver and Transmitter (UART) just for debugging purpose. It is also equipped with Serial Peripheral Interface for communication with the CAN bus controller. The whole system during laboratory tests is visible in Fig 3.

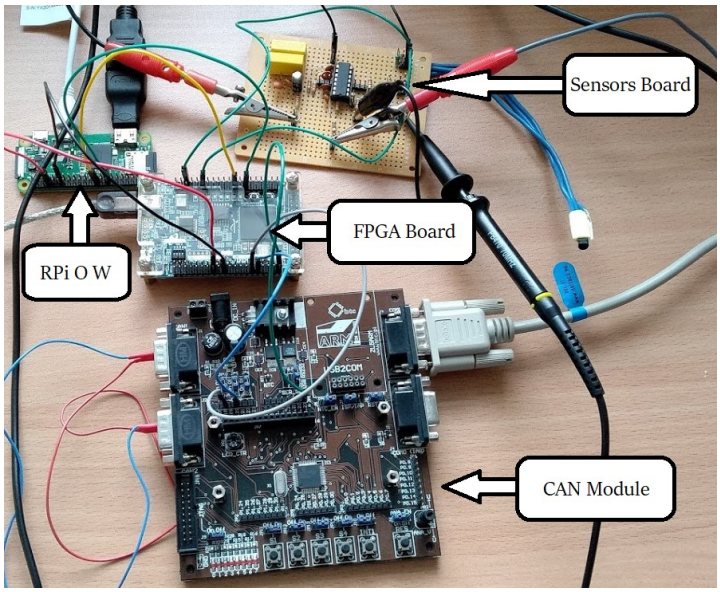

Figure 3. The laboratory system.

3. CAN BUS IMPLEMENTATION

The Controller Area Network (CAN bus) is a quasi real-time, serial, asynchronous bus, widely used in automotive and other industries. The main advantage which was considered during choosing of a proper bus for this project was high

level of security and compatibility with the automotive systems. The controller area network protocol is well suited to many high-level industrial protocols including the ISO-11898:2003 as their physical layer. Its performance, and upgradeability provide good flexibility in system design. Additional bus nodes can be easily added later to the already working system. That is why it is possible to add, to an existing vehicle network, some additional nodes. In particular case it may be the node which will monitor the EV battery stack. The robustness of CAN bus may be attributed to its abundant error-checking procedures and differential signaling. The CAN protocol incorporates five methods of error checking, and some of them are really robust to deceive. Three of the error checking methods operate at the message level and two at the bit level. Each bus node receives message that is broadcasted on the bus and if the message fails any one of these error detection methods, it is not accepted and an error frame is generated from the receiving node. This mechanism forces the transmitting node to resend the message until it is received correctly. So there is very low probability that a disrupted message can be received and interpreted. However, if a faulty node hangs up the bus by continuously repeating an error frame, its transmit capability is removed by its controller after an error limit is reached. For this purpose special error counters are implemented in bus controllers and there may be implemented separate counters for transmit errors and for receiving errors as well. If the number of errors during the transmission or receive process crosses preset threshold level, the CAN node is switched off the bus and remains in bus-off state (until necessary conditions appear). Because of the mentioned advantages, this project incorporates CAN bus for transmission of the measured temperatures from all the connected temperature sensors. The CAN protocol supports two message frame formats. These formats are presented in Fig 4 and Fig. 5. The only significant difference is the length of the identifier. The CAN standard frame, also known as CAN 2.0 A, supports a length of 11 bits for the identifier, and the CAN extended frame, also known as CAN 2.0 B, supports a length of 29 bits for the identifier. Depending on the vehicle type, the short format or the long may be incorporated. In this solution we have used the CAN standard frame format, but it is possible to switch to the long format if necessary – the used CAN controller is ready for it.

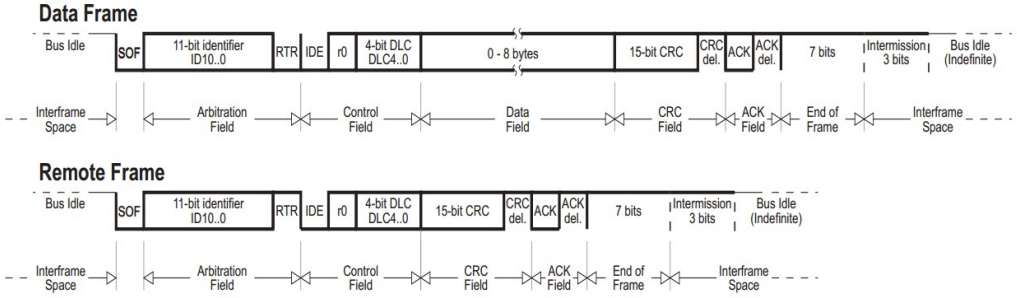

Figure 4. CAN Standard Frames [17].

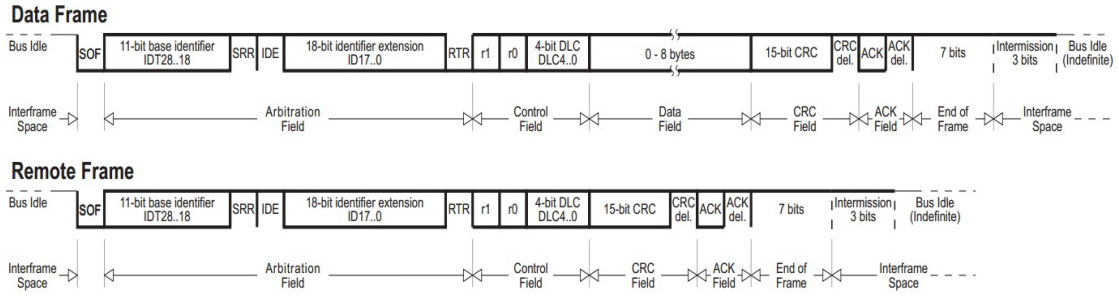

Figure 5. CAN Extended Frames [17].

Short explanation of the used abbreviations: SOF – Start Of Frame, RTR - Remote Transmission Request, IDE - Identifier Extension, DLC - Data Length Code, CRC - Cyclic Redundancy Check, del.-delimiter, ACK - Acknowledge. For the purpose of this project, the transmitted data is located at the specific locations in the CAN frames with

specific identifiers. Data allocation is presented in Fig. 6. As can be seen (Fig. 6), the 12 bits temperature value from each sensor uses two bytes of the CAN data frame. For example temperature from the sensor no 1 is named T1H (most significant byte) and T1L (least significant byte) and is located in data frame which has the identifier number 1. The identifier no 1 has a physical 11 bits value, which is dependent on the system needs. Each data frame broadcasted into the CAN bus has a time stamp information to allow the data consistency. The time stamp data format is also presented in Fig. 6. It uses 4 CAN data bytes from 4 (most significant byte of time stamp) to 7 (least significant byte of time stamp), so the time stamp information is 32 bit long (Fig. 6). It is the information from the 32 bit seconds counter located in the FPGA device. Any master device that receives the temperature data receives also the 32 bit seconds counter state and can properly interpret the data to achieve time consistency across the whole system. The main system controller which has to use the temperature data should know all the used identifiers values and the data allocation pattern inside them. To properly decode the data from the whole frame, additional stuffed bits should be removed. In CAN bus algorithm, after each five consecutive bits of the same polarity (00000 or 11111) an additional bit of an opposite polarity is always inserted into the frame. By reversing this procedure, these additional bits (stuffed bits) should be removed, which should be done at the receiver side. This technique, which is called bit-stuffing, implies that the actual number of transmitted bits may be larger than the size of the original frame. The bit stuffing should be taken into account during the frame decoding process from an oscilloscope screen. In the presented system this process is automatically executed inside the implemented CAN bus controller.

Identifier	Data0	Data1	Data2	Data3	Data4	Data5	Data6	Data7
1	T1H	T1L	T2H	T2L	Time3	Time2	Time1	Time0
2	T3H	T3L	T4H	T4L	Time3	Time2	Time1	Time0
3	T5H	T5L	T6H	T6L	Time3	Time2	Time1	Time0

Figure 6. Data allocation in CAN frames.

4. WIRELESS MONITORING OF THE TEMPERATURES

In the presented system, it is possible to monitor the temperatures remotely. The system is equipped with six temperature sensors. The number of sensors can be extended to measure more temperatures and also other parameters if necessary. The remote control panel is available on any device with an Internet browser. The temperatures are measured by DS18B20 digital sensors. They are connected to the FPGA board, which collects the data, and sends it to the Raspberry Pi board by UART interface (Fig. 1). The remote control panel is built based on the Node-RED software, node-red-dashboard and node-red-node-serial-port libraries. If the Raspberry Pi board has a static IP in the network, the control panel can be available not only locally but also from the entire Internet. The Node-RED flow of the proposed temperature monitoring system is presented in Fig. 7.

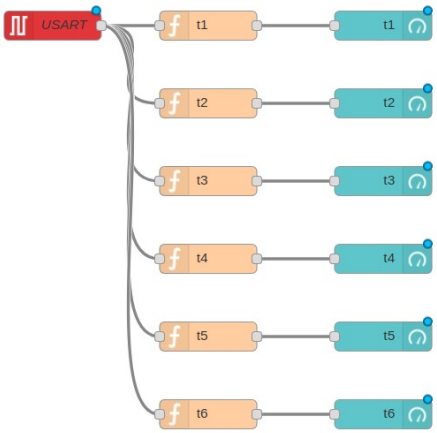

Figure 7. Node RED project flow.

Node USART (Fig. 7) is responsible for communication with the NIOS processor and allows for data collection. Nodes t1 – t6 (on the right side of Fig. 7) display the measured temperatures in a graphical form on the control panel. The Node-RED based temperature monitoring console is presented in Fig. 8. There are six visible temperature gauges t1-t6 (Fig. 8) showing the temperatures of the monitored battery radiators. The gauges can automatically change colors when the monitored temperature crosses predefined levels (in this case from green to yellow, orange and red). The gauges are refreshed every 2 seconds (it can be modified if necessary). There is also possibility to add some additional elements to the monitoring console. For example additional temperature charts may present the history of the chosen temperatures in set time interval and in set time horizon. Parameters of the temperature gauges like sampling interval, min, max or number of sampling points can be modified according to the user needs. The control panel can be configured for sending commands to the controlled system if predefined conditions occur.

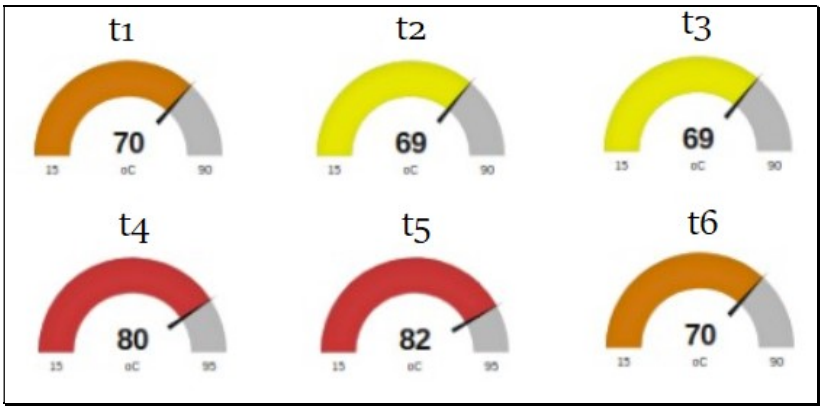

Figure 8. Monitoring console.

5. SUMMARY

A multi-channel temperature measurement system for monitoring temperatures of the automotive battery stack is presented in the paper. Lithium based batteries used in the EV or HEV systems should be monitored for temperature. In such systems, a single temperature sensor is not enough. During some uncontrolled charging or discharging process, the batteries can get hot what may be dangerous and even cause fire. The presented system is a complete battery temperature measuring system for hybrid or electric vehicles that incorporates multi-channel temperature measurements with digital temperature sensors communicating by 1-Wire buses, individual 1-Wire bus for each sensor for parallel computing (parallel measurements instead of sequential), FPGA device which collects the data from the sensors, translates it and sends the information through the vehicle CAN bus. The laboratory results show correct operation of the investigated system. CAN bus is incorporated for communication with the car BMS (Battery Management System). The described system can measure 6 or more temperatures and can be extended in case of additional needs. The structure of the system as well as particular devices are described in the paper. The system allows for remote monitoring of the temperatures. Thanks to the Node-RED which is installed on a Raspberry Pi single board microcomputer, the temperature monitoring console is available on any device which is connected to the local Wi-Fi network or to the Internet. The presented solution allows for detection of abnormal states in the monitored battery stack and gives possibility to test the maximal output power, thanks to the temperature monitoring. It is possible to increase the number of the temperature sensors for measuring temperatures of the vehicle power LEDs and to add another kinds of sensors to the system. Such an extension may be conducted with a minimal hardware modifications.

Acknowledgement

This work was supported by the grant S/WE/1/2016 from Bialystok University of Technology founded by Ministry of Science and Higher Education.

REFERENCES

[1] Onda, K., Ohshima, T., Nakayama, M., Fukuda, K., and Araki, T., "Thermal behavior of small lithium-ion battery during rapid charge and discharge cycles," *Journal of Power Sources* **158**(1), 535-542 (2006).

[2] Lewczuk R., Wojtkowski W., „Multi-channel temperature measurement system for automotive battery stack," Proceedings of SPIE - Photonics Applications in Astronomy, Communications, Industry, and HighEnergy Physics Experiments, vol. 10445, 1-8 (2017).

[3] Wojtkowski W., "SEPIC converter for high power LED lighting," Przeglad Elektrotechniczny, volume: 86, issue: 10, 260-263 (2010).

[4] Polak, A., Grzeczka, G., Swoboda, P., and Bakiera, P., "Aspects of safe operation of lithium based batteries in marine applications," *Scientific Journal of Polish Naval Academy* **LVII**(4(207)), 75-85 (2016).

[5] V. Markevičius, D. Navikas, D. Andriukaitis, M. Čepėnas, A., Valinevičius, M. Žilys, R. Malekian, A. Janeliauskas, W. Walendziuk, A. Idzkowski, "Two thermocouples low power wireless sensors network", AEU-International journal of electronics and communications, vol. 84, pp. 242–250, 2017. DOI: 10.1016/j.aeue.2017.11.032.

[6] Kusznier J., "Reflectometric temperature sensor," Proceedings of SPIE, volume: 8010, 2011.

[7] Wojtkowski W., "Wireless Monitoring of Semiconductor Switches' Temperatures in a Switching Power Converter," 26th Telecommunications Forum (TELFOR), Belgrade, SERBIA, 867-870 (2018).

[8] Kusznier J., "A multipoint optical fibre temperature sensor," Proceedings of SPIE, volume: 5775, 434-439 (2005).

[9] Gilewski M., Gryko L., Zajac A., "Digital controlling system to the set of high power LEDs," Proc. of SPIE, 8902, 89021D, (2013).

[10] Blaszczak U., Gryko L., Zajac A., "Tunable white light source for medical applications," Proc. of SPIE, 10445, 104453Y, (2017).

[11] Idzkowski, A., Walendziuk, W., and Warsza, Z. L., "Unconventional double-current circuit for deflection and temperature simultaneous measurement," *Elektronika ir Elektrotechnika* **Vol.21**(1), 23-27 (2015).

[12] Walendziuk, W., Idzkowski, A., and Golebiowski, J., "Reconfigurable two-current source supplied signal conditioner for resistive sensors," *Elektronika ir Elektrotechnika* **Vol.21**(4), 23-26 (2015).

[13] Wojtkowski W., Zankiewicz A., "Parallel RF Power Amplifiers Temperature Monitoring System Based on FPGA Device," 15th IFAC/IEEE Conference on Programmable Devices and Embedded Systems (PDeS), May 23-25, IFAC Papers Online, Volume: 51 Issue: 6, 414-419 (2018).

[14] Vanus, J., Machacek, Z., Kozirek, J., Waledziuk, W., Kolar, V., and Jaron, Z., "Advanced energy management system in smart home care," *International Journal of Applied Electromagnetics and Mechanics* **Vol.52**, 517{524 (2016).

[15] Wojtkowski W., "Digital control of a bidirectional DC / DC converter for automotive applications," 15th IFAC/IEEE Conference on Programmable Devices and Embedded Systems (PDeS), Ostrawa, May 23-25, IFAC Papers Online, Volume: 51 Issue: 6 Pages: 113-118 (2018).

[16] Microchip, MCP2551 datasheet, https://www.microchip.com/wwwproducts/en/MCP2551.

[17] Atmel-Microchip, AT90CAN128 datasheet, http://ww1.microchip.com/downloads/en/devicedoc/doc7679.pdf.

Influence of RES sources on the location of distribution points in the MV network

Karol Sidor*[a] ,Paweł Pijarski[a], Piotr Miller[a]

[a]Lublin University of Technology Faculty of Electrical Engineering and Computer Science Department of Electrical and Security Networks, Nadbystrzycka 38 A, Lublin, Poland

ABSTRACT

A dynamic increase in the share of renewable energy sources in the power industry may cause various changes related to the optimal functioning of the entire power system [7], [10]. A high concentration of renewable energy sources in the power system may force the need to reconfigure the network in order to ensure optimal work. The article presents the impact of renewable energy sources on the location of MV grid division points. As the function of the target, the minimization of active power losses in the network was selected. The research was carried out for a dozen or so variants of network operation to determine the magnitude of the impact of these sources on the location of optimal network partition points. The optimization calculations were carried out using the Cuckoo Search algorithm (cuckoo search).

Keywords: SN network optimization, renewable energy sources, network partition points

1. INTRODUCTION

The studies of the medium voltage network in terms of the selection of the location of the division points are not a new topic and have been widely described in the literature, among others [14]. However, this topic is now more important, especially in the case of medium voltage networks that work with a large number of renewable energy sources. Renewable energy sources such as solar farms or wind farms are characterized by high variability of generation in both the seasonal and the daily cycle [9], [14]. The unpredictability of renewable energy sources can be a serious problem for networks characterized by numerous branches [11]. In such networks, optimal split points can undergo radical changes, which is caused by the random nature of the work of renewable energy sources [13]. The article presents the impact of renewable energy sources on the optimal location of network dividing points. The tests were carried out on the actual fragment of the medium voltage distribution network. The purpose of the article was to quantify the impact of RES sources on the location of grid cut points. The research was carried out for ten different variants of network configuration with renewable energy sources. The calculations were made for a network operating without RES as well as for a network cooperating with various sources of different powers and connected to various points of the network under investigation. Research into the article was carried out using the Power World Simulator flow program. The optimization was carried out using the Cuckoo Search algorithm in the MATLAB program.

2. THE TEST NETWORK MODEL

A fragment of the medium voltage network, part of the energy region consisting of five GPZ 110 / 15kV substations, which was mapped in the Power World Simulator power calculation program, was used for the research. The network has 16MVA transformers installed. The network consists of 45 nodes, 50 sections of MV lines and 50 receptions with a total capacity of 45.6 MW. The model includes four renewable energy sources, three photovoltaic sources with the capacity of 0.2MW, 0.2MW and 0.5MW respectively, and a 1MW wind farm. The network is built of overhead lines made with AFL 6-70 cables with a total length of over 100 km.

* karolsidor11@wp.pl

Photonics Applications in Astronomy, Communications, Industry, and High-Energy Physics Experiments 2019, edited by Ryszard S. Romaniuk, Maciej Linczuk, Proc. of SPIE Vol. 11176, 111765M
© 2019 SPIE · CCC code: 0277-786X/19/$21 · doi: 10.1117/12.2536608

In the network model under consideration, five partition points are foreseen for various network configuration cases. The network model is presented in Fig.1.

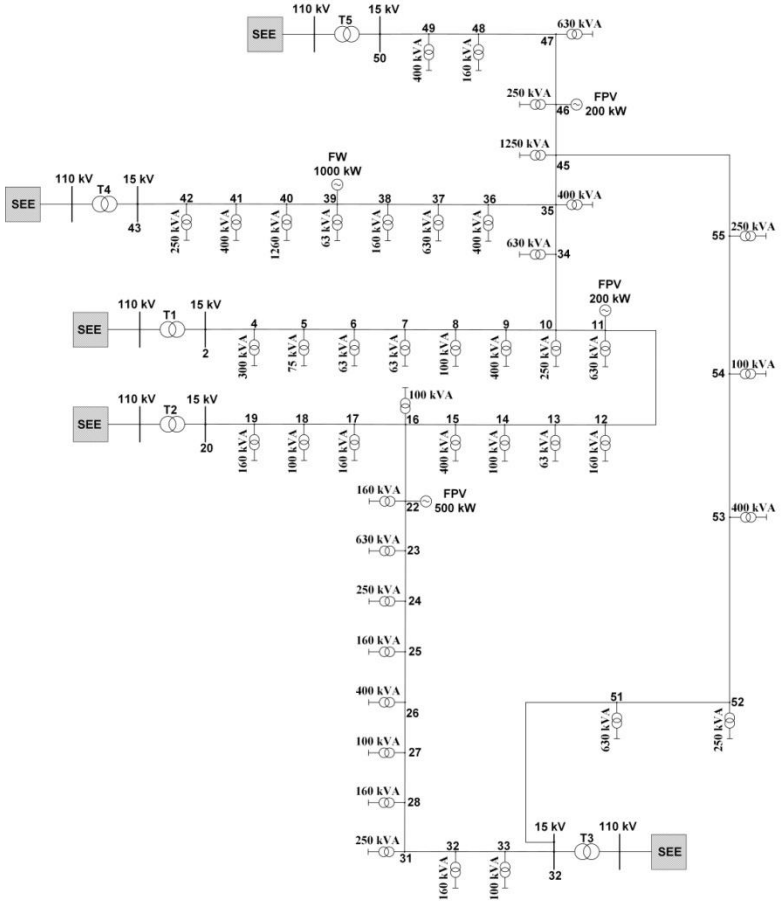

Figure1. Test network view [1]

3. RESEARCH METHODOLOGY

Research on the impact of RES sources on the location of network divisions was carried out in the Power World Simulator program. The optimization problem was the reduction of active power losses in the medium voltage network cooperating with renewable energy sources. The purpose of the task of finding the optimal location of network partition points was the loss of active power determined based on the analysis of power flows in the network. The function of the goal in a general form is presented below:

$$F_c = \Delta P \rightarrow min \tag{1}$$

The optimization was carried out using the cuckoo search algorithm (Cuccko Search). This algorithm mimics the behavior of certain species of cuckoos that toss their eggs to nests of other bird species [5],[6]. The idealization of cuckoo behaviors has been used to solve various optimization problems. The cuckoo search algorithm is based on three principles:

- each cuckoo folds one egg at a time in a randomly chosen nest,
- the best sockets are transferred to the next generation,
- the number of available nests is fixed, and foreign eggs are detected with the probability pα = [0,1].

The scheme of the cuckoo search algorithm is shown below.

begin

Draw the initial population **n** nests

while (x<MaxNumberOfGenerations)

Pick a cuckoo randomly by Levy's flight and evaluate **f (x)**

Choose a random cuckoo out of **n** cuckoos (**fj**)

if ($f_i > f_j$) **then**

Basics for j-th new value **end**

Part p_α of weak sockets was dropped to build a new one

Remember the best nest

Create a ranking of individuals from the population

end

end

The cuckoo search algorithm is extended with the "Levy flight" mechanism, ie jumping based on the Levy distribution. In the presented algorithm, problem solutions are represented by nests, the number of cuckoos is not important, so it can be assumed that it is equal to the number of nests. The choice of the cuckoo search algorithm to solve the problem was dictated by the robustness of the search space search and research, which suggests that this algorithm may outperform other popular algorithms [2],[3],[4].

In order to determine the impact of renewable energy sources on the location of the SN network partition points, 10 variants of network operation were analyzed, which are presented in Table 1.

Table 1. A list of networking options

Option	W1	W2	W3	W4	W5	W6	W7	W8	W9	W10
A	X	X	X	X	X	X	X	X	X	X
B		X	X	X		X	X			X
C			X	X				X		X
D				X		X			X	X
E					X		X	X	X	X

where:

A- base model - renewable energy sources do not work
B- a 0.2 MW photovoltaic power source works
C- a 0.2 MW photovoltaic power source works
D- a 0.5 MW photovoltaic power source works
E- a 1 MW wind farm is working

The research was carried out for each of the network variants. The aim of the research was to determine the optimal location of the 5 network partition points at which the lowest active power losses.

4. CALCULATION RESULTS FOR THE TEST NETWORK

Research on the impact of renewable energy sources on the level of active power losses in the network has been carried out in the PowerWorld Simulator program. The optimization task was solved using the MATLAB software, in which a script implementing the Cuccko Search (CS) algorithm was written. The algorithm connects to the PowerWorld program with the addition of SimAuto. 1000 optimization calculations were carried out for a network operating in various configurations. The results of calculations for individual variants of network operation are presented in Table 2.

Table 2.Set of optimal locations of network partition points for the minimum network load

Variant of network work	Location 1	Location 2	Location 3	Location 4	Location 5
W1	8-9	20-21	30-31	37-38	47-48
W2	8-9	25-26	28-29	36-37	48-49
W3	8-9	27-28	34-35	36-37	47-48
W4	8-9	27-28	30-31	37-38	46-47
W5	11-12	25-26	30-31	36-37	44-45
W6	10-11	25-26	28-29	36-37	48-49
W7	11-12	20-21	30-31	36-37	44-45
W8	8-9	25-26	30-31	37-38	47-48
W9	11-12	25-26	30-31	37-38	44-45
W10	8-9	2526	30-31	37-38	46-47

The obtained results confirm that the presence of renewable energy sources in electric power systems has an impact on active power losses and, consequently, on the location of the optimal network division point. The location of the best network division point depends primarily on the power of the source and its connection point in the power system. The conducted research will once again confirm the fact that the network partition points can change dynamically with changes taking place in the network. However, in the analyzed case, the changes in the network partition points do not show a large dispersion. This may be due to the fact that we are investigating a small fragment of the medium voltage distribution network and a relatively small number of renewable energy sources installed. On the basis of the obtained results, it can be concluded that the optimal places for the division of the tested network will be nodes marked as: 8-9, 25- 26, 30-31, 36-37, 47-48. Renewable energy sources cooperating with the power system always have an impact on its operation.

The magnitude of the impact of renewable energy sources on the power system depends primarily on the number of installed sources and their power. The type of source and its connection point to the network are also important. Whereas the power of generation from RES sources depends primarily on the season of the year as well as on the time of day and, above all, on weather conditions (wind, solar radiation). The location of the optimal network division point can change many times a day as a result of changes in generation from diffuse sources caused by changes such as insolation or windiness.

Table 3. List of power losses for the minimum network load condition

Variant of network work	Active power losses before optimization [kW]	Active power losses after optimization [kW]
W1	3,529	2,829
W2	7,696	7,053
W3	7,607	5,934
W4	9,769	8,971
W5	2,858	1,983
W6	9,858	8,661
W7	9,188	7,667
W8	2,769	2,086
W9	5,025	3,743
W10	9,010	8,902

Table 3 presents power losses for individual network operation variants before optimization (while maintaining fixed network partition points) as well as after optimization. The conducted research proves that the use of the Cuccko Search algorithm can reduce power losses by up to 25%. The results of the power losses analysis are presented in figure 2. The total active power losses for the network operating in different configurations has been determined. The obtained results confirm the possibility of reducing power losses in the network using reconfiguration.

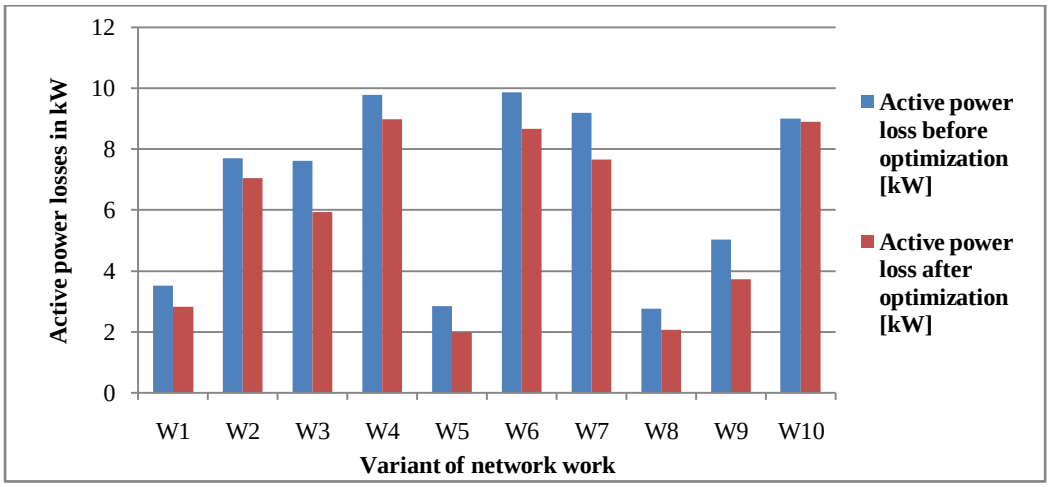

Fig. 2. Active power losses for individual variants of network operation with its minimum load

Table 4 presents the list of power losses for the maximum network load condition of Pmax = 0.9 p.u. The test results show that in the case of maximum network load, the active power losses in the network increased by two orders of magnitude compared to the network operation in the minimum load condition. The application of optimization in this case allowed to limit the losses of active power in the network up to 18% depending on the variant of the network operation. From the results obtained, it can be concluded that the network load status significantly influences the power flows and optimal locations of the network partition points.

Table 4. Set of optimal locations of network partition points for the maximum load condition

Variant of network work	Location 1	Location 2	Location 3	Location 4	Location 5
W1	7-8	14-15	30-31	36-37	46-47
W2	7-8	19-20	30-31	40-41	48-49
W3	8-9	19-20	30-31	36-37	48-49
W4	8-9	14-15	30-31	36-37	48-49
W5	7-8	19-20	30-31	36-37	48-49
W6	7-8	20-21	30-31	40-41	48-49
W7	7-8	19-20	30-31	36-37	48-49
W8	8-9	19-20	30-31	36-37	48-49
W9	7-8	20-21	30-31	36-37	48-49
W10	8-9	21-22	30-31	36-37	48-49

Table 5. List of active network power losses at its maximum load

Variant of network work	Active power losses before optimization [kW]	Active power losses after optimization [kW]
W1	307,49	258,31
W2	293,06	269,34
W3	283,33	234,26
W4	256,60	220,17
W5	297,92	245,95
W6	266,30	242,60
W7	279,08	255,40
W8	288,20	237,74
W9	271,09	234,65
W10	242,62	207,82

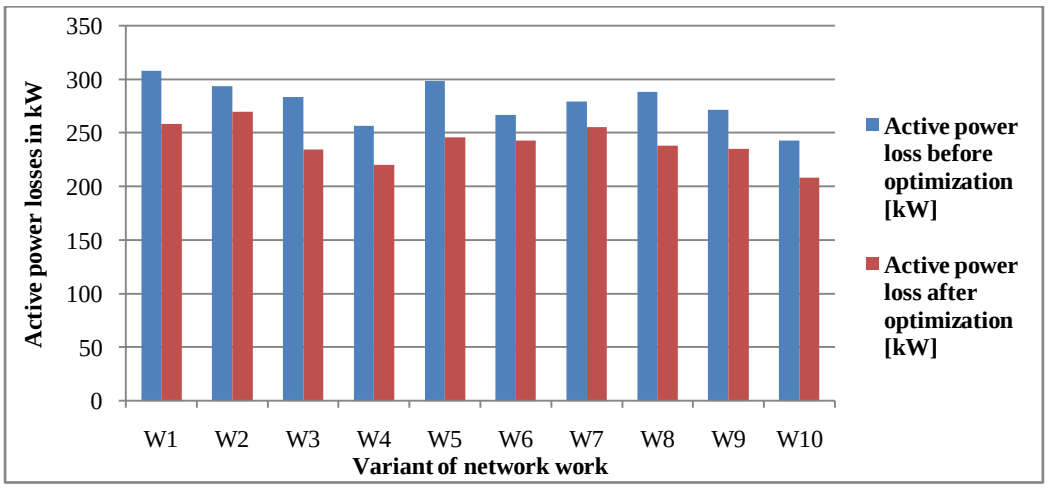

Figure 3. Power losses for individual network operation variants

In the case of dynamic network operation, both power losses and optimal network divisions radically change. The analysis of this case is presented below for a working network with variable load from 0.1 Pmax to 0.9 Pmax.

Table 6. List of optimal split point locations for dynamic network load status

Variant of network work	Location 1	Location 2	Location 3	Location 5	Location 6
W1	7-8	18-19	30-31	36-37	47-48
W2	7-8	18-19	30-31	36-37	48-49
W3	9-10	20-21	31-32	36-37	48-49
W4	9-10	20-21	30-31	36-37	48-49
W5	8-9	14-15	30-31	36-37	48-49
W6	8-9	24-25	31-32	40-41	48-49
W7	7-8	19-20	30-31	40-41	48-49
W8	8-9	19-20	30-31	40-41	48-49
W9	7-8	20-21	30-31	36-37	48-49
W10	8-9	22-23	30-31	36-37	48-49

Table 7. Set of active power losses for the dynamic load condition

Variant of network work	Active power losses before optimization [kW]	Active power losses after optimization [kW]
W1	311,0	121,0
W2	292,0	53,5
W3	283,2	45,7
W4	257,1	105,0
W5	297,4	85,0
W6	266,7	80,7
W7	278,9	85,7
W8	287,8	75,6
W9	271,4	75,4
W10	242,0	86,0

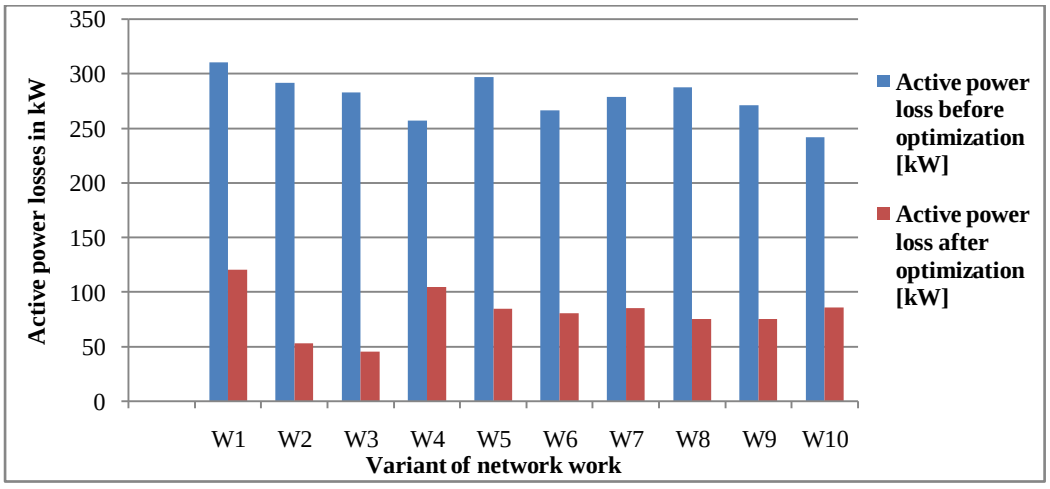

Figure 4. Active power losses for individual network operation variants with a dynamically changing load

5. CONCLUSIONS

The article analyzes the impact of renewable energy sources on the location of MV grid division points. Research shows that RES sources always affect the loss of active power in the network and, therefore, may necessitate the change of the network partition point to ensure optimal network operation. Reconfiguration of the network can reduce the active power loss by up to 25% in the case of network operation with its minimum load of Pmax = 0.1p.u. However, in the case of network operation at its maximum load of Pmax = 0.9p.u. optimization enabled the reduction of active power losses by 18%. In the case of a dynamically changing network load from Pmin to Pmax, optimization allowed to reduce the active power losses in the network by about 60%. This is caused by a dynamic change in both network load and RES sources. The dynamics of network operation has been simulated using a random number generator, in order to better reflect the dynamics of the network's operation, it would be worth using probabilistic methods [9], [14]. Connection to the growing network of renewable energy sources may cause an increase in the dynamics of changes in the network operating conditions and thus the need for frequent reconfiguration of the network to reduce the loss of electricity. In such conditions, the idea of changing the network configuration with regard to actual measurements is preferred. Monitoring the operation of the power system in terms of the optimal division of the network would allow to reduce the cost of energy losses [12], [13].

REFERENCES

[1] Pijarski, P.,Optymalizacja heurystyczna w ocenie warunków pracy i planowaniu rozwoju systemu elektroenergetycznego.Wydawnictwo Politechniki Lubelskiej, Lublin 2019.

[2] Findeisen, W., Szymanowski, J. and Wierzbicki, A., Teoria i metody obliczeniowe optymalizacji. WNT, Warszawa 1977.

[3] Michalewicz, Z. and Fogel,D. B., Jak to rozwiązać czyli nowoczesna heurystyka. WNT, Warszawa 2006.

[4] Seidler, J., Badach A. andMolisz, W., Metody rozwiązywania zadań optymalizacji. WNT, Warszawa 1980.

[5] Yang, X.S., Nature inspired metaheuristic algorithms. United Kingtom 2010, Luniver Press.

[6] Zhu, J., Optimization of power system operation. Wiley-IEEE Press, 2015.

[7] Pijarski, P., Wydra, M., Kacejko, P., „Optimal control of wind power generation", Advances in science and technology-research journal (1), 9-18(2018).

[8] Kacejko, P., Pijarski, P., „Cost sharing on the network upgrade individual investors applying for connection to a network of wind farms", Przeglad Elektrotechniczny (9A), 27-31(2012).

[9] Pijarski P., Miller P., Sidor K., „Probabilistic in power engineering", Proc. SPIE 1117, 108081 (2018).

[10] Pijarski P., Miller P., Sidor K., „Optimization of the selection of partition points in the MV network", Proc. SPIE 1117,108085 (2018).

[11] Pijarski P., Adamek S., Jędrychowski R., Sereja K., „Monitoring the impact of prosumer micro installations on the electrical parameters of low-voltage network systems", Przegląd Elektrotechniczny (2),59-62 (2019).

[12] Adamek S., Jędrychowski R., Pijarski P., Sereja K., „Economic justification for equipping LV network systems with energy storage units to enhance power supply parameters",15th International Conference on the European Energy Market ,8469213(2018).

[13] Jędrychowski R., Sereja K., Adamek S., Pijarski P., Wancerz M., „Evaluation of the impact of the rate of change of electrical parameters in the LV network on the operation of the distributed network control system" ,Progress in Applied Electrical Engineering 8441163 (2018).

[14] Wancerz M., Miller P.: „Problematyka pracy źródeł fotowoltaicznych przy zmianach i zanikach napięcia w sieci niskiego napięcia", Wiadomości Elektrotechniczne. (7), 3-9 (2017).

Development of a non-standard system of microwave quadripoles parameters

Andriy O. Semenov[a], Oleksandr M. Voznyak[a], Oleksandr V. Osadchuk[a], Serhii V. Baraban[a], Olena O. Semenova[a], Andrii V. Rudyk[b], Jacek Klimek[c], Sandugash Orazalieva[d]
[a]Vinnytsia National Technical University, 95 Khmelnitskoye Shose, Vinnitsya, 21021, Ukraine; [b]National University of Water and Environmental Engineering, Soborna Str., 11, Rivne, 33028 Ukraine; [c]Lublin University of Technology, 38D Nadbystrzycka Street, 20-618 Lublin, Poland; [d]Almaty University of Power Engineering and Telecommunications (AUPET)

ABSTRACT

In the work the non-standard system of w-parameters of the microwave quadripoles is proposed. a method of floating loads for the determination of w-parameters of microwave quadripoles is developed. the elements of the theory of the method of floating loads are proposed. new equations for determining the w-parameters of microwave quadripoles are obtained. the experimental setup for the determination of w-parameters of microwave quadripoles is developed. the results of experimental studies of w-parameters of the field transistor are obtained.

Keywords: microwave quadripole, W-parameters, non-standard system, floating loads, experimental equipment, short-circuit mode, idling mode

1. INTRODUCTION

To describe and define the parameters of radio-electronic devices in the microwave range, two systems of parameters of quadripoles are widely used: the system of parameters of the scattering matrix (*S*-parameters)[1], based on the representation of incident and reflected power waves, and the generalized W-parameters. There any of the four systems of parameters used in specific cases (*y*-, *z*-, *g*- and *h*-parameters)[2,14].

The advantage of the first system is the explicit physical content of its elements (coefficients of reflection and transmission), characteristic for schemes with distributed parameters, as well as simplicity and convenience of measurement in the microwave range using transmission lines with constant characteristic supports. To the disadvantages of this system of parameters can be attributed: the need to make measurements at coordinated loads (standing wave ratio < 1.05), which is practically not always possible to implement; growth of the measurement error in the determination of all parameters with the increase in the coefficient of standing wave of voltage in the measuring path[3]. The need for measurement of transmission and reflection arguments, which leads to the complication of the experimental installation. In addition, the calculated relations, expressed through *S*-parameters, are more complex and less visible than when using *W*-parameters.

In the microwave range, schemes with distributed parameters are predominantly used, but when designing, usually with certain assumptions, they are calculated as schemes with lumped parameters. This, on the one hand, simplifies the calculation, on the other hand, allows you to use the rich experience of designing low-frequency devices. In this case, the elements of the W-matrix[2] are used. The advantage of this matrix is the explicit physical content of its elements (*z* is resistance, *y* is conductivity), which is characteristic for schemes with lumped parameters. But for their measurement it is necessary to implement the short-circuit (SC) and idling (IM) mode, which is practically impossible to do in the microwave range due to the influence of parasitic reactive elements of the circuit.
In a detailed examination of these systems, one can conclude that their common disadvantage is the need for direct access to the investigated quadripole. This will not always be possible, in addition, the instability of the installation in the case of measuring the parameters of potentially unstable quadripole at frequencies that are usually unknown.
Based on the consideration of the advantages and disadvantages of the *S*- and *W*-parameters of the quadripole, one can formulate the requirements for a new system of parameters, which would have as much as possible the advantages of the *S*- and *W*-parameters and would not have their drawbacks. These requirements are as follows:

- the constituent elements of the new system must have an explicit physical content of the W-parameters;

Photonics Applications in Astronomy, Communications, Industry, and High-Energy Physics Experiments 2019, edited by Ryszard S. Romaniuk, Maciej Linczuk, Proc. of SPIE Vol. 11176, 111765N
© 2019 SPIE · CCC code: 0277-786X/19/$21 · doi: 10.1117/12.2536704

- the measurement error with increasing inconsistency of the quadripole with the measuring paths should be minimal;
- it measurement should be possible in the microwave range;
- the modes SC and IM should not be used for measurement;
- the measuring installation should have increased stability over a wide range of frequencies;
- calculated ratios for determining the required parameters should be as simple as possible.

This task can be solved by entering a new non-standard system of quadripole parameters. In microwave technology it is known to introduce non-standard parameters of quadripole systems. An example can be the non-standard system of *S*-parameters[3], through which the direct measurement of the coefficients of reflection of loads or complex-conjugate quantities with them. This eliminates the errors that arise in calculations with inaccurately measured standard *S*-parameters. This system, called the system of non-standard *S*-parameters (in the general case G_1, G_2, S_{12}, S_{21}), allows to carry out an unambiguous transition to the system of traditional *S*-parameters.

Non-standard parameters can be complete when their help is possible to identify all elements of the standard system of parameters, and partial (incomplete), when through them it is possible to express only a part of elements of the system of standard parameters. Not possessing the universality inherent in a complete system of non-standard parameters, the introduction of an incomplete system is appropriate in the case if it is sufficient for the calculation of a certain class of devices, while having significant advantages over the measurement of the complete system of parameters of the quadripole.

The main difficulty with the use of traditional *S*-parameters is that they are not measured with a sufficient degree of accuracy. Most of all, this is due to the lack of equipment, the inconsistency of the final loads, the presence of heterogeneous elements in the measuring path. Therefore, different system parameters can be uneven and the advantage must be given to one that guarantees the highest accuracy of the calculation. Systems of non-standard parameters, including directly the data necessary for design, are presented well-coordinated with the experiment and therefore it is expedient to use them.

2. DEVELOPMENT OF THE METHOD OF FLOATING LOADS

In the analysis of analytical expressions that determine the main low-signal parameters of broadband and frequency selective amplifiers (in the general case of quadripole) and used in the calculation, for example such parameters as working K_w and nominal $K_{w.n}$ the coefficients of the forward and inverse power transmission, the invariant coefficient of stability of $K_{s.in}$, the immitations of the matching schemes of ReW_{go}, ImW_{go}, ReW_{no}, ImW_{no}, it is clear that they can be calculated if a known part of the elements of the standard system of the *W*-parameters of the matrix of the quadripole and their derivatives[4] is:

$$\mathrm{Re}(W_{12}W_{21}),\ \mathrm{Im}(W_{12}W_{21}),\ W_{11},\ W_{22},\ |W_{12}|,\ |W_{21}|. \tag{1}$$

It is proposed to be used as a system of non-standard parameters of the quadripole[5].

System elements (1) determine the dependence of the input W_{in} and the output W_{out} immitations of the quadripole on the reactive immitations connected according to its output of $\mathrm{Im}W_l$ or $\mathrm{Im}W_g$ input, and the maximum steady-state gain of the quadripole[6] is:

$$K_{mS}=|W_{21}/W_{12}|. \tag{2}$$

In accordance with the theory of conformal mappings[7,8], dependence W_{in}=f($\mathrm{Im}W_l$) (W_{out}=f($\mathrm{Im}W_g$)) is displayed on the plane $W_{out}(W_{in})$ with a circle with a radius is:

$$\rho=|W-W_O|, \tag{3}$$

where W_O - center coordinates of the imitative circle (Fig. 1).

Expressing the radiuses through the imitations of the quadripole, we get:

$$\begin{cases} \rho_{out} = \dfrac{|W_{12}W_{21}|}{2\,\mathrm{Re}\,W_{11}}, \\ W_{out0} = \dfrac{W_{22} - W_{12}W_{21}}{2\,\mathrm{Re}\,W_{11}}, \\ \rho_{in} = \dfrac{|W_{12}W_{21}|}{2\,\mathrm{Re}\,W_{22}}, \\ W_{in0} = \dfrac{W_{22} - W_{12}W_{21}}{2\,\mathrm{Re}\,W_{22}}, \end{cases} \tag{4}$$

where ρ_{out} is a radius of the outgoing circle; W_{out0} is a coordinate of the center of the outgoing circle; ρ_{in} is a radius of input circle; W_{in0} is a coordinate of the center of the input circle[11,19,20].

The coordinates of the centers of the circle are respectively determined by the expressions:

$$\begin{cases} \mathrm{Re}\,W_{out0} = \mathrm{Re}\,W_{22} - \dfrac{\mathrm{Re}\left(W_{12}W_{21}\right)}{2\,\mathrm{Re}\,W_{11}}, \\ \mathrm{Im}\,W_{out0} = \mathrm{Im}\,W_{22} - \dfrac{\mathrm{Im}\left(W_{12}W_{21}\right)}{2\,\mathrm{Re}\,W_{11}}, \\ \mathrm{Re}\,W_{in0} = \mathrm{Re}\,W_{11} - \dfrac{\mathrm{Re}\left(W_{12}W_{21}\right)}{2\,\mathrm{Re}\,W_{22}}, \\ \mathrm{Im}\,W_{in0} = \mathrm{Im}\,W_{11} - \dfrac{\mathrm{Im}\left(W_{12}W_{21}\right)}{2\,\mathrm{Re}\,W_{22}}. \end{cases} \tag{5}$$

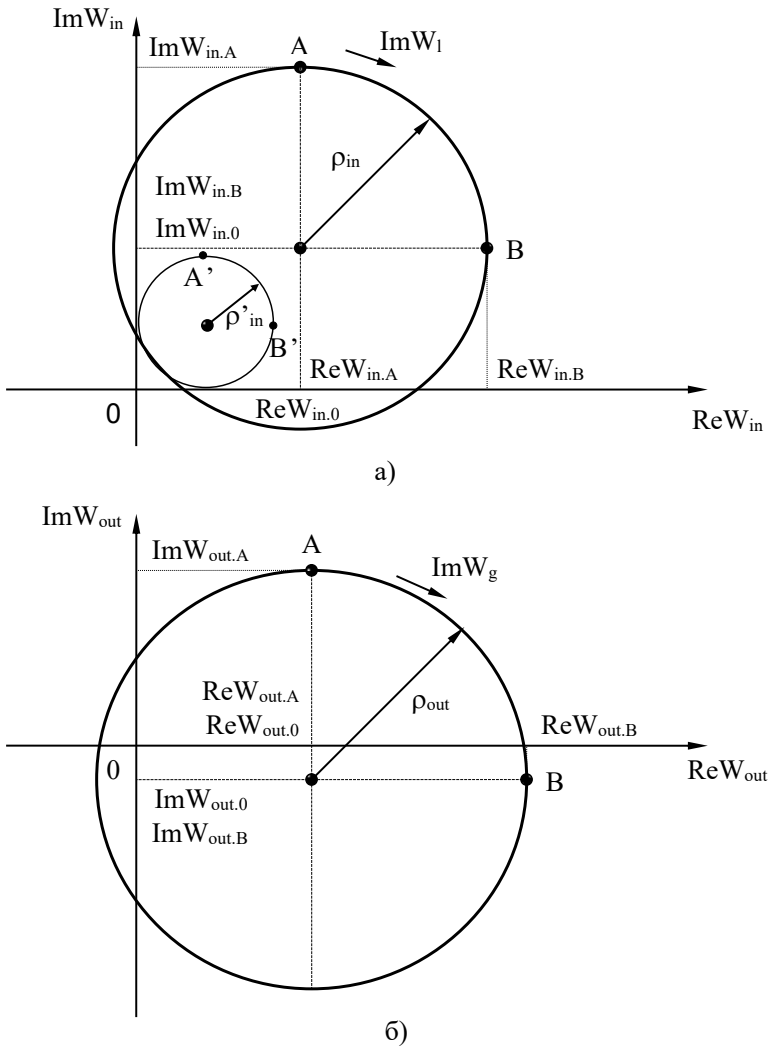

Figure 1. The dependences W_{in} = f(ImW_l) and W_{out} = f(ImW_g) on the complex plane.

Let Im$W_{in.A}$, Im$W_{out.A}$, Re$W_{in.B}$, Re$W_{out.B}$ define the coordinates of points A and B in the imitative circle corresponding to the maximum value of the components of the immittance of the quadripole. We express through these components the radii ρ_{in}, ρ_{out} and the coordinates of the centers of the circles (Fig. 1):

$$\begin{cases} \rho_{in} = \mathrm{Im}W_{in.A} - \mathrm{Im}W_{in.B} = \mathrm{Re}W_{in.B} - \mathrm{Re}W_{in.A}, \\ \rho_{out} = \mathrm{Im}W_{out.A} - \mathrm{Im}W_{out.B} = \mathrm{Re}W_{out.B} - \mathrm{Re}W_{out.A}, \\ \mathrm{Re}W_{in.0} = \mathrm{Re}W_{in.A}, \\ \mathrm{Re}W_{out.0} = \mathrm{Re}W_{\mathrm{out}.A}, \\ \mathrm{Im}W_{in.0} = \mathrm{Im}W_{in.\mathrm{B}}, \\ \mathrm{Im}W_{out.0} = \mathrm{Im}W_{out.\mathrm{B}}. \end{cases} \quad (6)$$

Systems of equations (24) and (35) are incomplete because

$$\frac{\mathrm{Re}W_{in.0}}{\rho_{in}} = \frac{\mathrm{Re}W_{out.0}}{\rho_{out}} = K_{s.\mathrm{in}}, \quad (7)$$

it does not allow to determine the parameters of the system (1). To find these parameters, we additionally connect to the output of the quadripole consecutive resistance $W_g=Z_g$ or parallel conductivity $W_g=Y_g$. In this case, the dependence of the input immittance W'_{in} of the newly formed quadripole on the reactive load $\mathrm{Im}W_l$ is a circle with a radius[12,21,22]

$$\rho'_{in} = \frac{|W_{12}W_{21}|}{2\,\mathrm{Re}\left(W_{22}+W_g\right)}, \tag{8}$$

where is:

$$\rho'_{in} = ImW'_{in.A} - ImW'_{in.B} = ReW'_{in.B} - ReW'_{in.A}, \tag{9}$$

where $W'_{in.A}$, $W'_{in.B}$ is a coordinate of points A and B corresponding to the maximum value of the components of the immitance on the circle W'_{in} (Fig. 1).

With a certain meaning of the immitance W_g, solving system of equations (4, 5) with taking (6), find some elements of the system (1) parameters W- matrix.

$$\begin{cases} \mathrm{Re}W_{22} = \dfrac{\rho'_{in}\,\mathrm{Re}W_g}{\left(\rho_{in}-\rho'_{in}\right)}, \\ \mathrm{Re}W_{11} = \dfrac{\rho_{in}}{\rho_{out}}\mathrm{Re}W_{22} = \dfrac{\rho_{in}\rho'_{in}}{\rho_{out}\left(\rho_{in}-\rho'_{in}\right)}\mathrm{Re}W_g, \\ |W_{12}W_{21}| = 2\rho_{in}\,\mathrm{Re}W_{22} = \dfrac{2\rho_{in}\rho'_{in}}{\left(\rho_{in}-\rho'_{in}\right)}\mathrm{Re}W_g, \\ \mathrm{Re}\left(W_{12}W_{21}\right) = 2\,\mathrm{Re}W_{22}\left(W_{11}-W_{in.A}\right), \\ \mathrm{Im}\left(W_{12}W_{21}\right) = \sqrt{|W_{12}W_{21}|^2 - \mathrm{Re}^2\left(W_{12}W_{21}\right)}, \\ \mathrm{Im}\left(W_{12}W_{21}\right) = |W_{12}W_{21}|\sin\left(\arccos\mathrm{Re}\left(\dfrac{\left(W_{12}W_{21}\right)}{|W_{12}W_{21}|}\right)\right), \\ \mathrm{Im}W_{11} = \mathrm{Im}W_{in.B} + \dfrac{\mathrm{Im}\left(W_{12}W_{21}\right)}{2\,\mathrm{Re}W_{22}}, \\ \mathrm{Im}W_{22} = \mathrm{Im}W_{out.B} + \dfrac{\mathrm{Im}\left(W_{12}W_{21}\right)}{2\,\mathrm{Re}W_{11}}. \end{cases} \tag{10}$$

To find these parameters, there is no need to implement CS and IM modes and use a consistent load, - it is enough to measure the input and output immitances of the quadripole at extreme points A and B, which correspond to $\mathrm{Im}W_g$ and $\mathrm{Im}W_l$ reactive immitations that may remain uncertain. From the above analysis it is obvious that the actual constituents of extreme parameters in the study of potentially unstable quadrupole with $K_{s.in} < 1$ are always positive, which guarantees the stability of measurements.

To find the parameters $|W_{21}|$ i $|W_{12}|$ we use familiar expressions for direct $K_{w.l.1}$ and the inverse $K_{w.l.2}$ nominal transmission coefficients of the quadripole power[2,23] is:

$$K_{w.l.1} = \frac{4|W_{21}|^2\,\mathrm{Re}W_{oscill.}\,\mathrm{Re}W_l}{\left|\left(W_{11}+W_{oscill.}\right)\left(W_{22}+W_l\right)-W_{11}W_{22}\right|^2}, \tag{11}$$

$$K_{w.l.2} = \frac{4|W_{12}|^2\,\mathrm{Re}W_{oscill.}\,\mathrm{Re}W_l}{\left|\left(W_{11}+W_{oscill.}\right)\left(W_{22}+W_l\right)-W_{22}W_{21}\right|^2}. \tag{12}$$

When the condition $W_g = W_l$ is fulfilled, dividing the expression (811) into (912), we find

$$\frac{K_{\text{w.}l1}}{K_{\text{w.}l2}} = \left|\frac{W_{21}}{W_{12}}\right|^2 = K_{mS}^2, \tag{13}$$

where K_{mS} is a maximum coefficient of stable amplification (transmission) of the quadripole power.

Using the obtained expression (1013) and previously defined parameters of the quadripole (710), we find:

$$|W_{21}| = \sqrt{K_{mS}\sqrt{\text{Re}^2\left(W_{12}W_{21}\right) + \text{Im}^2\left(W_{12}W_{21}\right)}} = \sqrt{K_{mS}\left|W_{12}W_{21}\right|}, \tag{14}$$

$$|W_{12}| = \sqrt{\frac{\sqrt{\text{Re}^2\left(W_{12}W_{21}\right) + \text{Im}^2\left(W_{12}W_{21}\right)}}{K_{mS}}} = \sqrt{\frac{\left|W_{12}W_{21}\right|}{K_{mS}}}. \tag{15}$$

From the above expressions (10), (14), (15) it is evident that in order to determine the system of W-parameters of the quadripole (1), convenient for finding the main parameters of the quadripole, it is necessary to determine a number of the following parameters[9] is:

$$W_{in.A},\ W_{out.A},\ W_{in.B},\ W_{out.B},\ K_{mS},\ W'_{in.A},\ W'_{in.B}. \tag{16}$$

We call this system a nonstandard extreme system of quadripole parameters, eliminating most of the disadvantages inherent in measuring the elements of the classical standard systems of the S- and W-parameters of the quadripole, the feature of which is the application of measuring non-fixed load (resistance or conductivity).

3. EXPERIMENTAL RESEARCH

In this work, an experimental equipment for the measurement of W-parameters of microwave quadripole was developed. The block diagram of the experimental equipment is shown on Fig. 2[11,24].

The measuring installation includes: measuring generator *MG*; solenoid valve *V*; reflectometer *R*; tee *T*; phase rotator *P*; investigated quadripole *IQ*, fixed in a special holder; two short-circuiting pistons *P1* and *P2*. The reflectometer *R* is used to determine the module of the reflectance coefficient *G* or the standing wave (ρ) in the measuring path. The piston *P1* is intended to compensate for the reactive component of the input (or output) immitance of the investigated quadripole, which is transformed into the plane of the *T* tee. The piston *P2* implements the required reactive load of the quadripole $\text{Im}W_l$ (or $\text{Im}W_g$). Phase rotator *P* reduces the electric length ℓ_2 of the measuring path from the investigated quadripole *IQ* to the *T* axis.

To eliminate the ambiguity of measurements, the characteristic immitance of the measuring path is chosen more than the minimum value of the actual component of the immitance $\text{Re}W_{in.B}$ (or $\text{Re}W_{in.B}$), that is measured. In this case, the reflection coefficient module *G* from the quadripole terminal is uniquely dependent on the immitance $\text{Re}W_{in}$ ($\text{Re}W_{out}$) (Fig. 3).

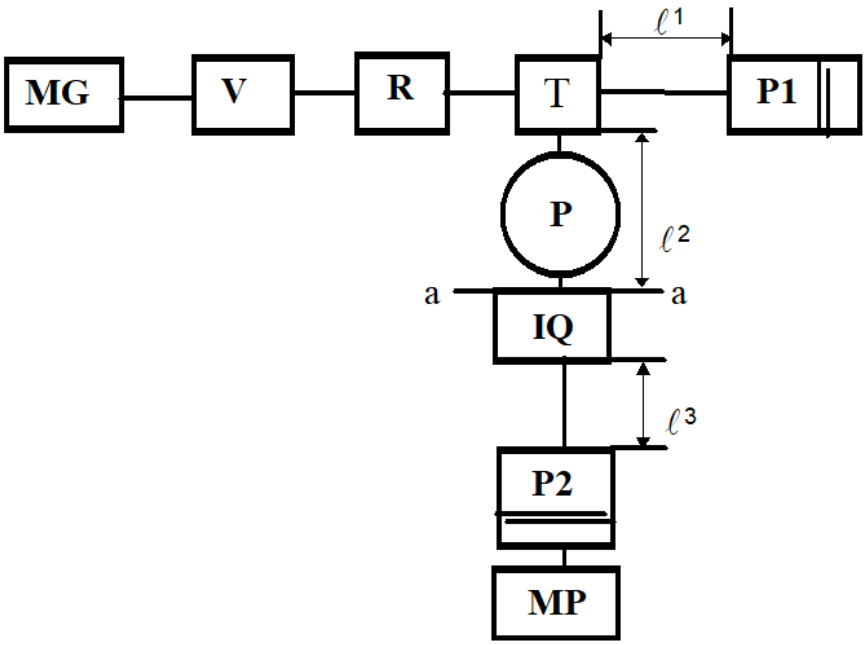

Figure 2. The block diagram of the experimental equipment to measure the non-standard system of parameters of microwave quadripole.

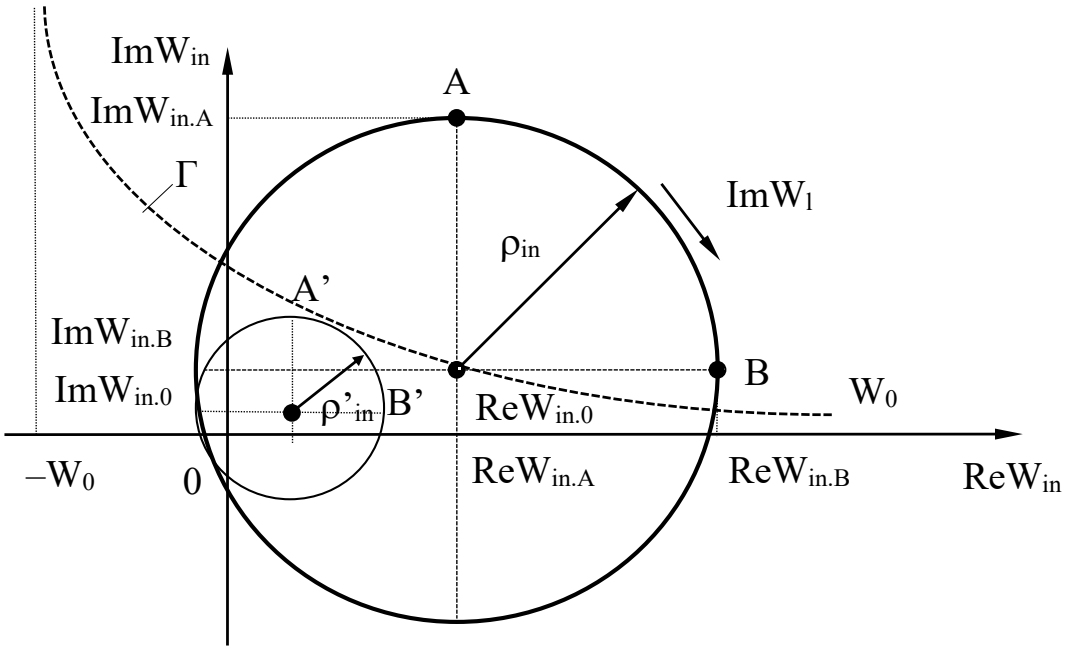

Figure 3. Comprehensive dependency plane Win= f(ImWl).

When calibrating the installation, the measurement of the measuring line in the plane A-A is shorted (Fig. 2). The length ℓ_1 of the piston *P1* is set to less than or more than a quarter of the wavelength in the measuring path. In this case, the ImW_{p1} reactive immittance implemented by the piston *P1* shunt the transmission line, providing $G<1$. By changing the phase shift produced by the phase shifter *P*, they obtain in the path of the coefficient of standing wave $G = 1$, which indicates the connection of the piston *P1* to the measuring path at a distance ℓ_2, the multiple half wavelength in the path $\ell_{02}=n\lambda/2$, which allows the measurement to pass the input (output) immitance of the quadripole in the plane of the piston *P1*. When

measuring at a fixed frequency, the preliminary installation of the piston *P1* at a distance ℓ_{02} from the plane of measurement A-A can be pre-installed, which allows to exclude the phase rotator P from the measuring circuit and refuse the calibration process[12,13].

To measure the required values, replace in the installation (Fig. 2) the piston with a power meter with an input impedance equal to W_0 and set the piston P_1 at a distance $\ell_1=\lambda/4$, which eliminates its influence. We measure power P_1. Then we turn the investigated quadripole on 180° and measure the power P_2. Based on these measurements we find the last extreme parameter K_{mS} is [14,15]:

$$K_{mS} = \sqrt{\frac{P_1}{P_2}}\ . \tag{17}$$

In the course of the experiment, the results of the dependence of the extreme parameters on the frequency for bipolar and field transistors were obtained. Table 1 shows the experimental results of the dependencies of the extreme parameters of the field transistor КП391. Practical application of research results in work[13] to measure humidity[16,17,18].

Table 1. The results of experimental research.

Parameters	**Frequency**				
$\times 10^{-2}$ (Om^{-1})	**1 GHz**	**0.8 GHz**	**0.6 GHz**	**0.4 GHz**	**0.3 GHz**
$ReY_{in.A}$	0.233	0.195	0.1	0.035	0.15
$ImY_{in.A}$	7.54	4.82	3.2	1.98	1.365
$ReY_{in.B}$	4.01	2.61	1.7	1.09	0.84
$ImY_{in.B}$	8.77	2.41	1.6	0.99	0.675
$ReY_{out.A}$	0.5	0.83	0.88	1.8	0.06
$ImY_{out.A}$	0.02	0.03	0.01	0.05	0.006
$ReY_{out.B}$	8.59	11.14	15.03	20.65	0.336
$ImY_{out.B}$	-8.07	-10.28	-14.4	-18.8	-0.27
K_{mS}	5.123	6.735	9.36	12.76	18.46

4. CONCLUSION

As a result of the conducted researches the method of determination of an extreme non-standard parameter system[5] has been developed, which allows to improve the accuracy of the measurement of the parameters of the quadripole. In developing this technique, three ideas were used:

1) the method of "floating loads"[10];
2) the method of differential measurements;
3) neutralization method.

Using the first two ideas allows for arbitrary (floating) loads to determine with high precision in the microwave range a system of non-standard parameters of a quadripole, sufficient for the calculation of most linear electronic devices.

The application of the neutralization method in conjunction with the method of "floating loads" ensures the stability of the experimental installation and measurement of the complete system of *W*-parameters of any quadripole.

According to the research materials given in this article, we can make the following conclusions:

1) The proposed methods are most effective in the microwave range, where so far the problem of measuring the *S*-parameters of a potentially unstable quadripole.

2) Mean-square errors were analyzed and their analytical expressions were obtained for each method. The analysis of these expressions showed a direct dependence of the methodological error on the error of measurement of incoming immitances.

3) The elements of the proposed non-standard extreme system of quadripole parameters have a dimension that corresponds to the dimensions of the elements of the standard *W*-parameters, but their measurements are carried out in the microwave range with an error of less than 5%, and to a lesser extent, depends on the KSVN of the measuring path, as measured by *S*-parameters.

4) To measure them there is no need to use the modes SC and IM or to make measurements in a coherent measuring path, which also increases the accuracy of the measurement and provides stability in the measurement of potentially unstable quadripole with $Ks > 0$.

REFERENCES

[1] Nekolaevskiy I. F. and Igumnov D. V., [Parametryi i predelnyie rezhimyi rabotyi tranzistorov], Sovetskoe radio, (1971).

[2] Medvedev, Y. A., Krukovskiy, Y. P., "Ustroystvo dlya opredeleniya koeffitsienta peredachi chetyirehpolyusnika, " Byul. Izobreteniy, (1977)

[3] Filinyuk, N. A. and Semerenko, M. M., "Aktivnyie chastotno-izbiratelnyie ustroystva SVCh diapazona," Dep. v Ukr NIINTI Vinnitsa, (1984).

[4] Podzharenko, V. A. and Kuharchuk, V. V., "Metrologicheskie osnovyi kompyuterno-izmeritelnoy tehniki," Sv. tamplan, (1989).

[5] Smit, F., [Krugovyie diagrammyi v radioelektronikę], Svyaz, (1976).

[6] Smogilev, K. A., [Rezonansnyie usiliteli na trehpolyusnikah], Sovetskoe radio, (1972).

[7] Nosov, Y. R., Petrosyants, K. O. and Shilin, V. A., [Matematicheskie modeli elementov integralnoy elektroniki], Sovetskoe radio, (1976).

[8] Zitkina, V. S., [Poluprovodnikovyie vhodnyie ustroystva SVCh], Sovetskoe radio, (1975).

[9] Bogachev, V. M., Volkov, V. M., Lyisenko, V. G. and Musyankov M. I ., "Raschet parametrov moschnyih vyisokochastotnyih tranzistorov," Radiotehnika i elektronika, 3, (1975).

[10] Filinyuk, N. A., [Nestandartnaya sistema parametrov chetyirehpolyusnika], Preprint Ukr NIINTI., (1984).

[11] Osadchuk, V. S., Osadchuk, A. V., Semenov, A. A., and Semenova, E. A., "Experimental research and modeling of the microwave oscillator based on the static inductance transistor structure with negative resistance," Proc. 20th International Crimean Conference Microwave and Telecommunication Technology Sevastopol, Ukraine, 187–188 (2010).

[12] Semenov, A., Semenova, O. and Osadchuk, O., "The UHF oscillators based on a HEMT structure with negative conductivity," Proc. 2015 SIBCON Conf., 1–4 (2015).

[13] Bereziuk, O. V., Lemeshev, M. S., Bohachuk, V. V. and Duk, M., "Means for measuring relative humidity of municipal solid wastes based on the microcontroller Arduino UNO R3," Proc. SPIE 10808, (2018)

[14] Vedmitskyi, Y. G., Kukharchuk, V. V. and Hraniak, V. F., "New non-system physical quantities for vibration monitoring of transient processes at hydropower facilities, integral vibratory accelerations," Przeglad Elektrotechniczny, 93(3), 69-72 (2017).

[15] Wojcik, W., "Application of fibre-optic flame monitoring systems to diagnostics of combustion process in power boilers," Bulletin Of The Polish Academy Of Sciences-Technical Sciences 56(2), 177-195 (2008).

[16] Wojcik, W. and Kisała, P., "The method for the recovery of the apodization function of the fiber Bragg gratings on the basis of its spectra," Przeglad Elektrotechniczny, 86(10), 127-130 (2010).

[17] Wojcik, J., Wojcik, W., Janoszczyk, B., et al. "Optical fibre system for flame monitoring in energetic boilers," Proc. SPIE 3189, 74-82 (1997).

[18] Kisała P., Skorupski K., Cięszczyk S., Panas P. and Klimek J., "Rotation and twist measurement using tilted fibre Bragg gratings," Metrology Measurement Systems, 25(3) 429-440 (2018).

[19] Azarov, O. D., Dudnyk, O, V., Kaduk, O. V., Smolarz, A. and Burlibay, A., "Method of correcting of the tracking ADC with weight redundancy conversion characteristic," Proc. SPIE 9816, (2015).
[20] Azarov, O. D., Murashchenko, O. G., Chernyak, O. I., Smolarz, A. and Kashaganova, G., "Method of glitch reduction in DAC with weight redundancy," Proc. SPIE 9816, (2015).
[21] Osadchuk V. S. and Osadchuk A. V., "The magneticreactive effect in transistors for construction transducers of magnetic field," Electronics and Electrical Engineering 3(109), 119-122 (2011).
[22] Pavlov, S. V. Kozhemiako, V. P. Kolesnik, P. F. et al. [Physical principles of biomedical optics], VNTU Vinnytsya, (2010).
[23] Valtchev, V. S, Teixeira, J. P. and Pavlov, S., "Energy harvesting: an interesting topic for education programs in engineering specialities," Internet, Education, Science (IES-2016), 149-156 (2016).
[24] Vasilevskyi, O. M., Yakovlev, M. Y. and Kulakov, P. I. "Spectral method to evaluate the uncertainty of dynamic measurements," Technical Electrodynamics, 4 72-78 (2017).
[25] Kvyetnyy, R. N., Sofina O. Y., Lozun, A. V. Smolarz, A. and Zhirnova, O., "Modification of fractal coding algorithm by a combination of modern technologies and parallel computations," Proc. SPIE 9816, (2015).

The role of equipotential bondings as a measure of protection against electric shock by the example of special installations

Anna Dąda*[a], Paweł Błaut[a], Karol Sidor[b]
[a]MGGP S.A., Krakow Branch, Juliusza Lea 112, Krakow, Poland
[b]Lublin University of Technology Faculty of Electrical Engineering and Computer ScienceDepartment of Electrical and Security Networks, Nadbystrzycka 38 A, Lublin, Poland

ABSTRACT

Equipotential bondings are low-resistance electrical connections of various conductive parts, which aim is to equalize their potentials. In Poland, equipotential bondings are required in each building to which electricity has been supplied. If equipotential bondings have not been carried out, users are exposed to dangerous touch voltage between the simultaneously accessible conductive parts.

This paper will include an analysis of the requirements for protection against electric shock for locations containing a bath or shower, based on the PN-HD 60364-7-701:2010 standard. A computer simulation will be performed to indicate the probable dangerous situations. On its basis, there will be made an attempt to identify solutions that will guarantee the highest effectiveness and reliability of the protection against electric shock. Particular attention will be paid to the protection measures of the additional shock protection in the form of equipotential bondings.

Keywords: equipotential bondings, protection against electric shock, electrical installations

1. INTRODUCTION

Beside electric installations there are water, sewage, central heating and gas installations in the majority of buildings and locations (rooms).Those installation mostly are made of metal pipes. Also some building's construction and reinforcement elements can be accessible. When failure occurs within installation or within supplying electric power public system, electric potential difference can appear between earth and conductive parts. Fault current threatening health and life can flow throughout human body when one or two conductive elements are touched. To avoid this, equipotential bondings are used. Those connections between various conductive parts causes that electric potentials of these parts are similar. Even if dangerous voltage to earth will appear within considered object, no electric shock will occur because there will be no conductive part with the earth potential accessi0ble within the arms' range.

Equipotential bondings can play a specific role in various protective systems, among others protection against: electric shock, lightning and surge, disturbances, explosion and fire, corrosion or static electricity [4]. According to standard [1] there are distinguished in against electric shock protection following types of equipotential bondings: protective equipotential bondings (clause 411.3.1.2), supplementary protective equipotential bondings (clause 415.2) and earth-free local equipotential bondings (clause C.2 in appendix C).

Protective equipotential bondings are part of fault protection for automatic disconnection of supply protective measure. Extraneous conductive parts, which does not belong to electrical installation, shall be connected to main earthing terminal of installation by means of protective equipotential bondings. Due to the place of execution of these connections i.e. in place where installations are introduced into the building, protective equipotential bondings are commonly referred to as main equipotential bondings.

Supplementary protective equipotential bondings provide additional protection against electric shock. They are established as complement to fault protection. These bonding should cover all simultaneously accessible exposed conductive parts of fixed connected electric equipment and extraneous conductive parts. Arrangement of supplementary equipotential bonding shall be also connected to protective conductors of all electric equipment including socket outlets.

*annadada0709@gmail.com; phone 796 312 722

Photonics Applications in Astronomy, Communications, Industry, and High-Energy Physics Experiments 2019, edited by Ryszard S. Romaniuk, Maciej Linczuk, Proc. of SPIE Vol. 11176, 111765O
© 2019 SPIE · CCC code: 0277-786X/19/$21 · doi: 10.1117/12.2536726

Most often supplementary equipotential bondings are used in special locations, such as bathroom. For that reason these connections are referred to as local equipotential bondings.

Earth-free local equipotential bonding is protective measure, which can be used when the installation is controlled or under supervision of qualified or instructed persons only. Such bonding system should not have electrical connection with the earth neither directly nor through exposed or extraneous conductive parts. Equipotential bonding conductors shall connect together all simultaneously accessible exposed and extraneous conductive parts.

All types of equipotential bonding shall cover only these of extraneous conductive parts which can bring to considered location a dangerous potential in relation to exposed conductive parts.

This article considers the mean of implementation of main and local equipotential bondings in the bathroom, that is in locations with increased threat of electric shock, so the protection against electric shock was as effectively as possible.

1.1 Main equipotential bonding

Regardless of the installation and electric power system main equipotential bonding are required in each of electrified building object in Poland [7]. Bonding should be carried out as close as possible to the point of power supply introduction to the building (possibly close to the main electric box) within ground floor storey (basement), in place which is accessible for inspection. Main equipotential bonding shall connect together through the main equipotential busbar at least: PE or PEN protective conductor of supply line, metal sheaths or screens of telecommunication cables introduced to the building, earth electrode of the building and/or other local earth electrodes if they are present, all metal pipelines covering the building (water, sewage, gas, heat, air condition etc.) and also metal construction and reinforcing elements of the building if they are accessible [5].

Clause 444.4.8 of standard [8] recommends that metal pipes and reinforced shelters of cables were connected to the main earthing terminal with conductors of as low impedance as possible. According to the remark no 2 to clause 542.1 in standard [3] main equipotential busbar can be used to carry out functional earthing, so it can simultaneously act as main earthing terminal. All metal pipes, power and signal cables should be introduced to the building in the same place. Thanks to that equipotential bondings can be arranged in a way that avoid long conductive loops in which dangerous voltage threatening electromagnetic interference and significant surges can be induced [6].

According to the clause 544.1 of standard [3] protective conductors of equipotential bonding intended for connection to the main earthing terminal (main equipotential busbar) should have cross-sectional area not smaller than half of largest cross-sectional area of the installation's earthing conductor and not less than: $6mm^2$ for copper, $16mm^2$ for aluminum, $50mm^2$ for steel. However, it should not exceed $25mm^2$ for copper or the equivalent cross-sectional area for other materials.

1.2 Local protective equipotential bonding (connected to earth)

In areas where the equipotentialisation provided by the main equipotential bondings is insufficient, local protective equipotential bondings are used. These kind of connections are obligatory in some specific conditions. This applies to the conditions discussed in this article, i.e. conditions of particular threat subjected to sheet no 7 of the PN-HD 60364 standard.

Local equipotential bondings shall cover exposed and extraneous conductive parts present within its extent. This arrangement shall be connected to protective conductors of all electric equipment including the socket outlets. In contrast to main equipotential bonding, local one can be arranged without local equipotential busbar, unless it is involved by additional requirements for the special conditions [4, 6].

Connections between individual conductive parts should be arranged in a manner which provides the lowest possible resistances and therefore in accordance with clause 415.2.2 of the standard [1] the resistance in alternative current systems (AC) should meet the condition:

$$R \leq 50/I_a \tag{1}$$

where:

I_a– switch off current of protection device equal to the rated switch off current of residual current protective device $I_{\Delta n}$ (RCD) or equal to the switch off current of overcurrent device within 5s.

In emergency conditions, through protective earthing and bonding conductors may flow currents of significant values, these conductors may also be liable to mechanical damage. For this reason, it is required that appropriate values of cross-sections of these conductors were picked. According to the clause 544.2 of standard [3], a local equipotential

bonding connecting two exposed conductive parts should have a conductivity at least as the conductivity of the protective conductor connected to these parts. Whereas, bonding conductor connecting the exposed and extraneous conductive parts should have a conductivity not lower than the half of the cross-sectional area of the corresponding protective conductor.

1.3 Equipotential bondings in bathroom

There is an increased risk of electric shock within the rooms equipped with a bathtub or shower due to the presence of moisture, splashing and penetration of water, and therefore much lower impedance of human body. Standards [2],[9]. specify three protection zones 0, 1, 2, defining the rules for the arrangement of electrical equipment in such locations.

Local equipotential bondings are required to apply in these conditions. According to clause 701.415.2 of standard [2] local bondings shall be carried out by connecting of protective conductor with the exposed and extraneous conductive parts. Possible extraneous parts are: metal parts structure (building) and following pipe systems: gas, water and sewage, heat and air condition.

Metal elements of equipment that do not bring extraneous (earth) potential, e.g. cabinets, handles, door and window frames or valves and taps on plastic pipelines, are not extraneous conductive parts and are not subject to equipotential bonding. Including such elements with equipotential bondings increases the risk of electric shock by giving them the potential of the earth.

2. COMPUTER SIMULATION

A computer simulation was carried out in the ATPDraw program in order to verify the theoretical considerations. As a result the values of current and paths of its flow in case of electric shock during assumed faults in electrical installation were determined. The subject of the analysis is the installation of a single-family house powered by a cable from the overhead low voltage network. From the main distribution board located in the hall, individual circuits are led out. Both the network and the installation are carried out in the TN system. The house has a foundation earthing. The other installations are made of metal pipes (central heating and gas pipes) and plastic pipes (hot water and sanitary).

In particular, the computer simulation model will include two independent circuits of the electrical installation: supplying the washing machine in the bathroom and supplying the heat boiler in the basement. In addition, the model will include a part of the central heating installation consisting of radiator in the bathroom and pipe between boiler and radiator. In the model under consideration, washing machine and heat boiler housings are exposed conductive parts, and the radiator and the metal pipe of central heating installation are extraneous conductive parts.

The simulation will include the following types of damage in the electric installation (or their combination): L-PE short circuit in the electrical device, break in the PE conductor and no local equipotential bonding. A simulation was carried out for six selected situations presented in Figures 2-4. These simulations will allow to determine the role of equipotential bonding for the safety of electrical installation's users with electric shock. In addition, simulation during normal operation of electric installation (with no faults) was also performed. This situation is shown in Figure 1.List of symbols and abbreviations is presented in table 1.

Table 1. List of symbols and abbreviations

Symbol	Description
FEE	Foundation earth electrode
EBB	Equipotential bonding busbar
MDB	Main distribution board
HB	Heat boiler
HP	Heating pipe
RAD	Radiator
GP	Gas pipe
GB	Gas box
WM	Washing machine
CC	Equipotential bonding conductor
PEN	Protective and neutral conductor
PE	Protective conductor
L	Phase conductor
N	Neutral conductor

2.1 Simulation model

For the needs of the simulation, the model of the considered object consisting of electrical and central heating installations elements was adopted. The model elements are presented in the table no 2. Depending on the type of fault (or the combination of considered faults), the model for individual simulations does not cover all elements.

Table 2. List of elements included in simulation model

Type of conductor or element	Relation	Cross section [mm^2]	Material	Length [m]	Resistance [mΩ]	Reactance [Ω]
CC (main)	FEE – EBB	10	Cu	2	3,7	omitted
	EBB – HP	10	Cu	2	3,7	omitted
	EBB - HB	10	Cu	2	3,7	omitted
	EBB - MDB	10	Cu	16	29,6	omitted
CC (Supplementary)	EBB - WM	10	Cu	10	18,5	omitted
	WM - RAD	4	Cu	2	9,2	omitted
Pipe 18x1mm	HP	53,4	Cu	10	3,35	omitted
L / N/ PE	MDB – HB MDB - WM	1,5	Cu	18	219,6	omitted
L / PEN	Public system	35	AL.	25	21,5	2,3
L / PEN	Public system	70	AL	250	110	45
Transformer 250kVA	Public system	-	-	-	11,8	26,2

Remarks:

- Resistance of foundation earthing - 10Ω
- Human body resistance: 750Ω in bathroom (wet skin)
- Electric power of devices: WM – 2kW, HB – 1kW
- Metal gas pipe was not included in simulation model because of insulation insert in gas box
- The water and drain pipes are made of plastic materials therefore they were not included in simulation model

Following faults or combination of faults in electric installation were considered:

1. L-PE short circuit within the washing machine,
2. Interruption of PE conductor,
3. No local equipotential bonding (or interruption of bondig's conductors),
4. L-PE short circuit within the heat boiler.

Simulations of following models were performed:

a) simulation 0 – no fault, main and local equipotential bonding are carried out; Model presented on a fig. 1,
b) simulation 1 – L-PE short circuit within the washing machine, main and local equipotential bonding are carried out; Human touches with hands the washing machine and radiator; Model presented on fig. 2 ,
c) simulation 2 – L-PE short circuit within the heat boiler (in basement), main and local equipotential bonding are carried out; Human touches with hands the washing machine and radiator (in bathroom); Model presented on fig. 2,
d) simulation 3 – L-PE short circuit within the washing machine, no local equipotential bonding (against requirements of standard [2]), main equipotential bonding are carried out; Human touches with hands the washing machine and radiator; Model presented on fig. 3,
e) simulation 4 – L-PE short circuit within the heat boiler (in basement), no local equipotential bonding (against requirements of standard [2]), main equipotential bonding are carried out; Human touches with hands the washing machine and radiator (in bathroom); Model presented on fig. 3,
f) simulation 5 – L-PE short circuit within the washing machine, PE conductor is interrupted, main and local equipotential bonding are carried out; Human touches with hands the washing machine and radiator; Model presented on fig. 4,

g) simulation 6 – L-PE short circuit within the washing machine, PE conductor is interrupted, no local equipotential bonding (against requirements of standard [2]), main equipotential bonding are carried out; Human touches with hands the washing machine and radiator; Model presented on fig. 4.

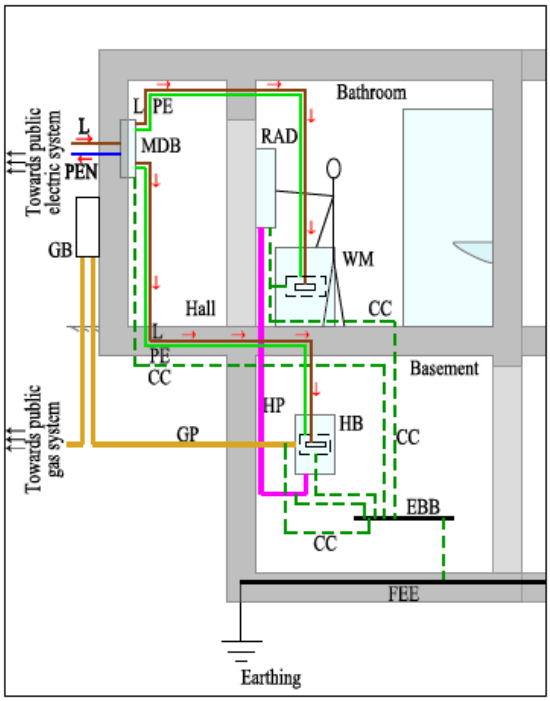

Figure 1. Model of simulation no 0

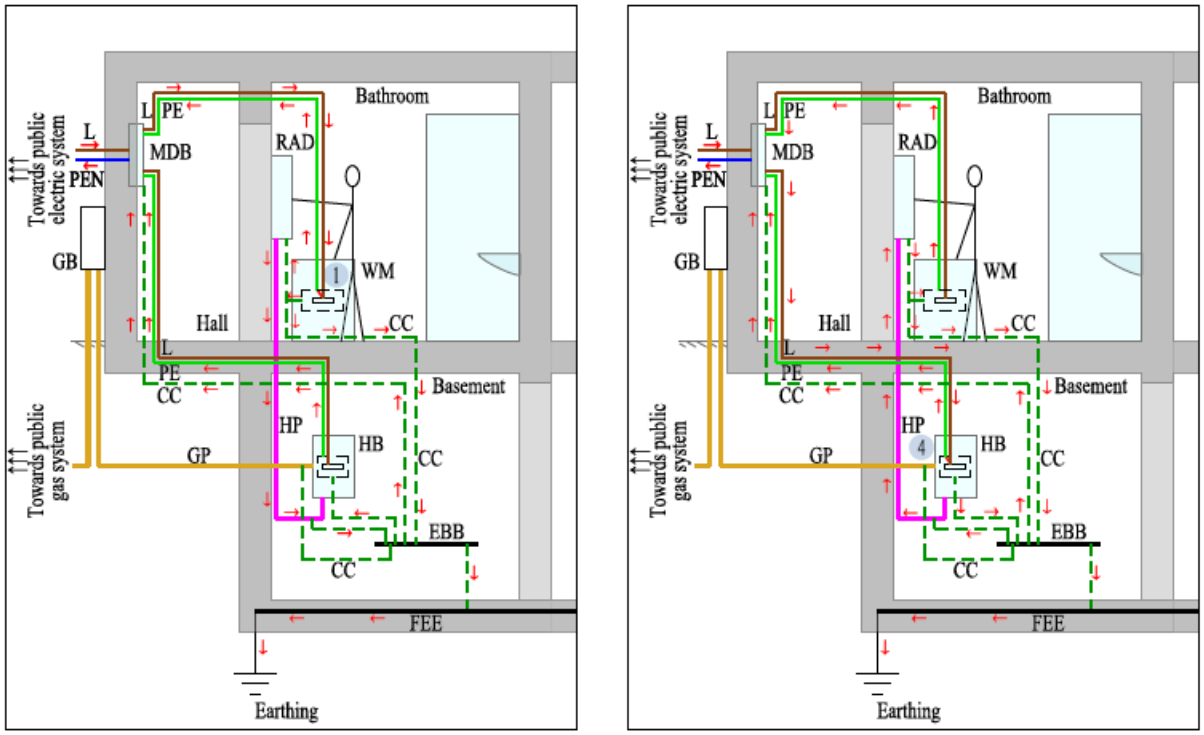

Figure 2. Models of simulation no 1 and 2

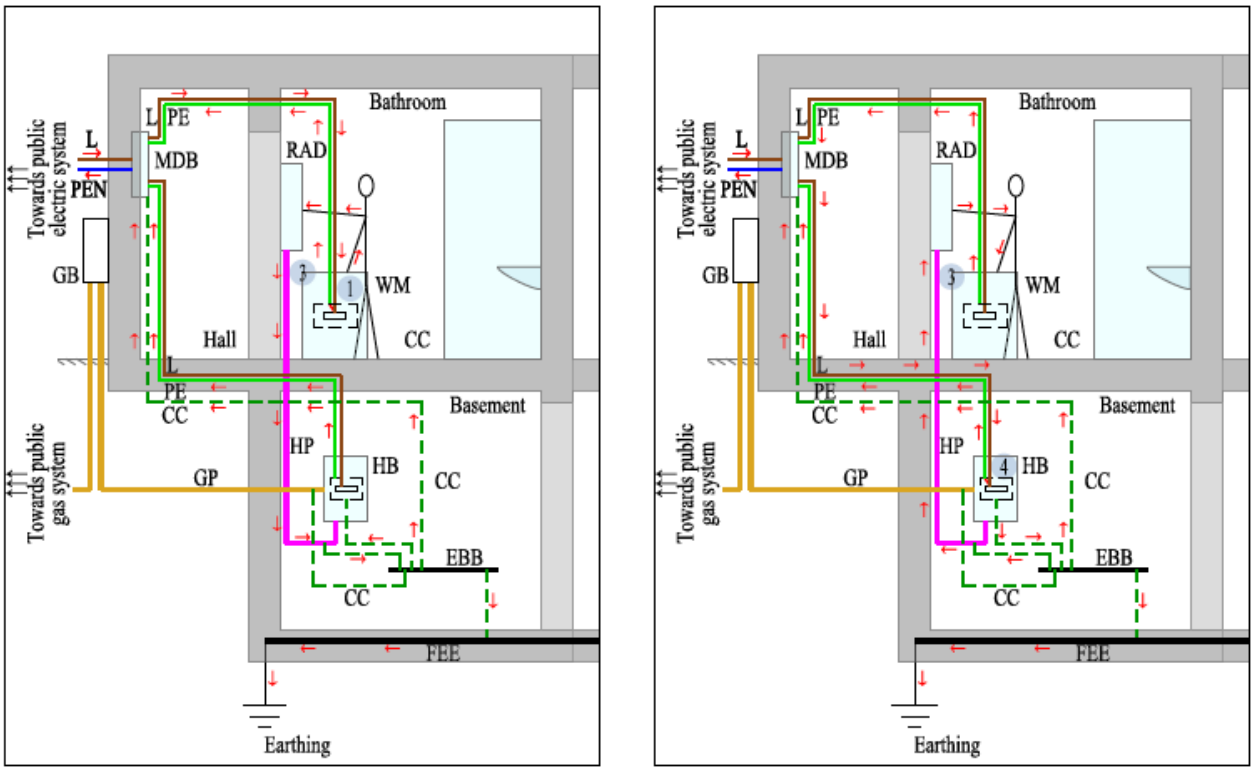

Figure 3. Models of simulation no 3 and 4

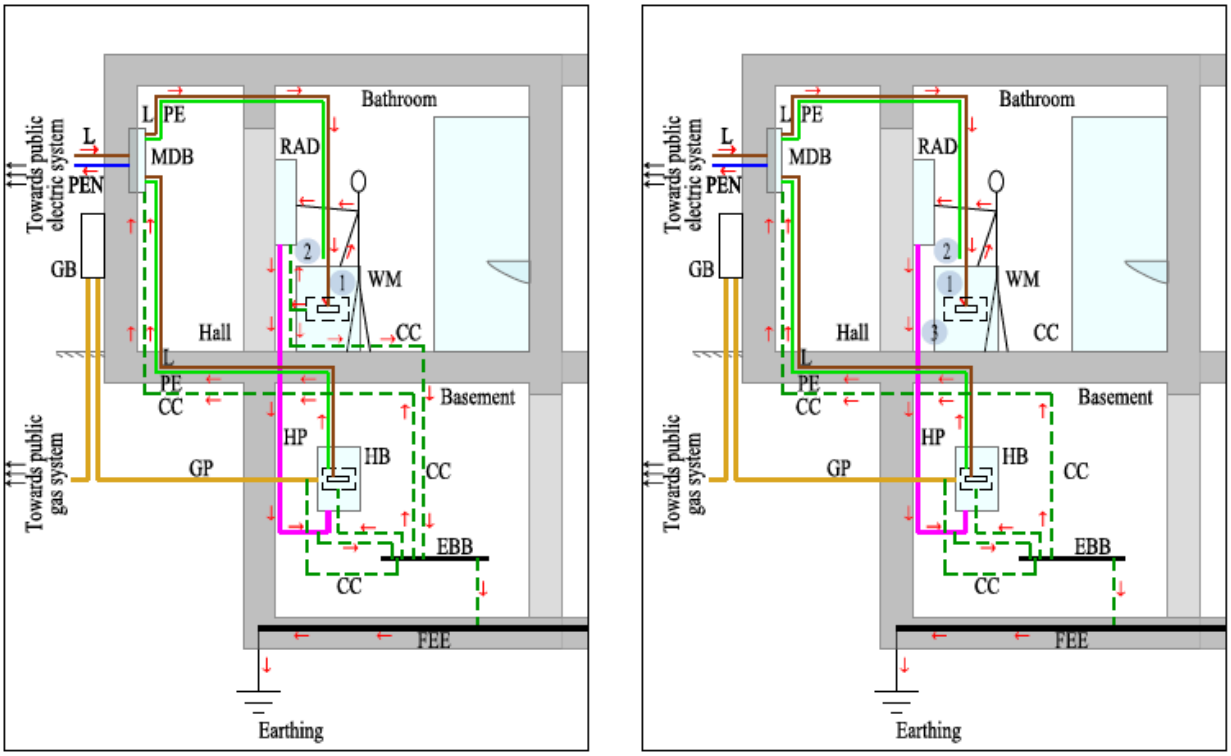

Figure 4. Models of simulation no 5 and 6

2.2 Results of simulations

As a result of the simulation, information on the distribution of currents in individual elements of the model was obtained. The results were collected and presented in tables 3a and 3b, while a summary of the performed simulations in table 4.

Table 3a. Current values obtained as a result of performed simulations no 0-3

Simulation no/ Conductors			**0**	**1**	**2**	**3**
-	human	mA	0,0001	3,00	-0,74	81,06
Phase (L)	system	A	12,68	530,31	459,18	417,24
	WM	A	8,44	528,61	4,10	414,98
	HB	A	4,23	1,71	455,08	2,26
(PEN)	system	A	12,61	527,10	456,38	415,06
Neutral (N)	WM	A	8,44	0,00	4,10	0,00
	HB	A	4,23	1,71	0,00	2,26
Protective (PE)	WM	mA	-9,55	99 058,68	67 252,27	414 896,40
	HB	mA	-6,65	52 068,09	48 303,23	-246,95
Bonding (CC)	FEE – EBB	mA	66,26	3 215,12	2 798,78	2 180,63
	EBB - MDB	mA	50,06	-374 264,00	-336 727,30	1 852,62
	EBB - HB	mA	5,82	96 199,64	173 044,00	164,01
	EBB - HP	mA	5,82	96 199,64	173 044,00	164,01
	EBB - WM	mA	4,55	185 079,80	-6 561,88	-
	WM - RAD	mA	4,99	244 464,40	-60 689,64	-
Pipes	HP	mA	4,99	244 467,40	-60 690,39	81,06

Table 3b. Current values obtained as a result of performed simulations– simulations no 4-6

Simulation no/ Conductors			**4**	**5**	**6**
-	human	mA	-16,46	3,64	306,25
Phase (L)	system	A	455,61	522,76	4,58
	WM	A	4,14	521,02	0,31
	HB	A	451,47	1,75	4,27
(PEN)	system	A	452,76	519,49	4,55
Neutral (N)	WM	A	4,14	0,00	0,00
	HB	A	0,00	1,75	4,27
Protective (PE)	WM	mA	16,46	-	-
	HB	mA	56 220,15	63 229,94	35,51
Equipotential bonding (CC)	FEE – EBB	mA	2 845,63	3 270,12	24,24
	EBB - MDB	mA	392 390,50	-454 516,60	-246,50
	EBB - HB	mA	197 618,10	116 649,70	135,37
	EBB - HP	mA	197 618,10	116 649,70	135,37
	EBB - WM	mA	-	224 487,30	-
	WM - RAD	mA	-	296 525,70	-
Pipes	HP	mA	-16,46	296 529,40	306,25

Table 4. Comparison of performed simulations

Specification / simulation	Main bonding	Local bonding	Combination of considered faults	Fault loop	Electric shock risk
0	yes	yes	-	-	-
1	yes	yes	1. Short circuit in WM	metallic	very low
2	yes	yes	4. Short circuit in HB	metallic	very low
3	yes	no	1. Short circuit in WM 3. No local bonding	metallic	medium
4	yes	no	3. No local bonding 4. Short circuit in HB	metallic	low
5	yes	yes	1. Short circuit in WM 2. PE conductor break	metallic	very low
6	yes	no	1. Short circuit in WM 2. PE conductor break 3. No local bonding	non-metallic	high

2.3 Analysis of results

– Simulation no 0

As it results from the simulation, if there is no fault in considered model, only operating currents flow through phase and neutral conductors. In protective and bonding conductors which are forming a closed electrical circuit, only small currents of a few tens of mA are flowing. These currents return through the ground to the power source without any risk of electric shock. The above currents constitute only approx. 0.5% of the operating current. They will not trigger residual current devices because the currents flowing through the phase and neutral wires of individual circuits (washing machine and boiler) are identical.

– Simulation no 1 and 2

The operating current in circuit of not damaged electric device is different than current when there is no fault because every change of voltage, current, impedance, etc. at any point in the power system, immediately causes changes in its other points. In the case of a short circuit in almost all points of the system, the voltage value changes, most often in a degree depending on the “electrical” distance from the fault location. With the voltage change, the value of the current also changes. This condition lasts until the protection devices disconnect the fault circuit from the power source. Then the voltage at each point of power system, except the disconnected circuit, returns to value close to the one before fault occurred.

As it results from the simulations, if main and local equipotential bonding is provided, the safety of the users of the electrical installation is significantly increased in case of fault.

In discussed situation, if fault occurs, almost all fault current flows through the metallic fault loop. This current has a significant value, so it can easily be switched off by both overcurrent and residual current protective devices. Even if both protection devices fail, through human flows a perceptible touch current, but it is small enough (less than 3mA) that a human is able to release his hands from the conductive parts and thus stop the electric shock.

For frequencies in the range of 50-60Hz, the human-perceived current is currents above the value of approx. 1mA, and the so-called the "self-release" current is below 6mA for women and 10mA for men [6].

– Simulation no 3

As it results from the simulation, if here is no local equipotential bonding in the bathroom, some risk of electric shock occurs in the case of fault (but without break of continuity of the protective conductor). Due to the metallic fault loop, fault current reaches a significant value (several hundred amps), so it can be easily switched off by overcurrent protection. The residual current protective device also should switch the voltage off at this kind of fault. However, until the power is switched off the current flows through a human, which is threat because at this current value (about 80 mA) there are already muscle contractions causing pain and preventing the human from self-releasing from electric shock [6].

If the overcurrent and residual current protection devices have failed (lack of power supply switch off), at times longer than 0.5s, the fault current can cause more serious effects, including increased pain, increase in blood pressure and tetanus contraction of the striated muscles and spasms of the respiratory muscles, which may cause hypoxia of the body, difficulty in breathing, increase in the amount of carbon dioxide in the blood and acidification of tissues, which may result in cyanosis of the skin and mucous membranes. In extreme cases, spasms of coronary vessels may occur and in result myocardial infarction. There may also be disturbances in the heartbeat (fibrillation).

– Simulation no 4

As it results from the simulation, if here is no local equipotential bonding in the bathroom, some risk of electric shock occurs in the case of fault in basement (but without break of continuity of the protective conductor). Due to the metallic fault loop, fault current reaches a significant value (several hundred amps), so it can be easily switched off by overcurrent protection. The residual current protective device also should switch the voltage off at this kind of fault. However, until the power is switched off the current flows through a human, which is threat because at this current value (about 16 mA) there are already muscle contractions causing pain and preventing the human from self-releasing from electric shock [6].

If the overcurrent and residual current protection devices have failed, the situation is similar to the simulation no 3. However, due to the lower value of the fault current, similar effects may occur at times longer than 1.5s. The differences that usually these are reversible physiological effects - without damage to the human body. In addition, in contrast to simulation no. 3,only a reversible disturbances in the heartbeat may occur (fibrillation or transient blockage) with a current at this value(16mA).

– Simulation no 5

As it results from the simulation, if the main and local equipotential bonding is carried out, this significantly increases the safety of the electric installation's users.

If fault occurs in discussed situation, thanks to bonding almost all fault current flows through the metallic fault loop despite the break in protective conductor. Therefore, the situation is analogous to cases of simulations no 1 and 2.

– Simulation no 6

As it results from the simulation, if there is no local equipotential bonding in the bathroom, the execution of main equipotential bonding does not fully provide the safety of users of electric installation in other rooms (not covered by bonding).

In discussed situation, in the case of fault within the room that is not covered by local equipotential bonding (bathroom), the human is electrocuted with a current of significant value (over 300mA). Overcurrent protection is not able to switch off such fault (fault current is too low), so if the residual current protective device failed, an electric shock would be a serious threat to health and life.

3. SUMMARY AND CONCLUSIONS

Equipotential bondings decline the expected touch voltage and touch current values during L-PE short circuits down to the level not exceeding the safe values. Moreover, they can also provide metallic fault loop if PE conductor is broken and thus high value of fault current enabling the triggering of overcurrent protective devices in a short time. Despite of the fact that correctly carried out equipotential bondings can provide the safety of the installation's users, even if the protection devices do not switch off the power supply, they should not be self-reliant or sole protective measure of fault protection against electric shock. They should provide protection against electric shock, until proper devices ensure automatic disconnection of supply.

As long as there are no accurate main equipotential bonding in the building, local bonding should not be carried out. Interferential conditions, such as the discussed L-PE short-circuit cases and breaking of the protective conductor, when there is no main equipotential bonding in the building, can cause significant thermal exposures to the local equipotential bonding conductors and also increase the risk of electric shock. Main equipotential bondings carried out solely does not provide the high level of safety of installation's users in rooms not covered with bondings. Only combinations of correctly carried out main and local bondings is able to provide safety, even in the case of complex faults of electric installations including the malfunction of protective devices. In particular, it applies to TT systems, in which despite the fact, that the residual current protective devices are circuit breakers with relatively high failure of operation, according to the standard [1] it is preferred in TT systems to this kind of protective devices as fault protection measure by automatic

disconnection of supply. Therefore equipotential bondings require due attention and range of their implementation should be preceded by a diligent analysis of determined installation.

Local and main equipotential bondings should be carried out in manner which provides reliable connection during long period of time. In consumer's installations, the TN system is preferred. In this system, in case of damage of the basic insulation (short circuit L-PE or L-PEN depending on the type of TN system), short-circuit current can achieve high values. Significant part of it (even 90%)may flow through the equipotential bonding conductors. For this reason, the cross-sections of these conductors, both main and local bondings, should be diligently picked, based on the requirements of the standard [3].

REFERENCES

[1] PN-HD 60364-4-41:2017 Low-voltage electrical installations – Part 4-41: Protection for safety – Protection against electric shock.

[2] PN-HD 60364-7-701:2010 Low-voltage electrical installations – Part 7-701: Requirements for special installations or locations – Locations containing a bath or shower.

[3] PN-HD 60364-5-54:2011 Low-voltage electrical installations – Part 5-54: Selection and erection of electrical equipment – Earthing arrangements and protective conductors.

[4] Musiał E., „Electric threats and protection against them. Selected issues – part 2", Monographs, book 55, COSiW SEP - INPE publishing company in Bełchatów, 30-55 (2016).

[5] Musiał E., „Equipotential bonding as additional protection against electric-shock" W: [Materials] Gdańsk International Fair 2002 „Electroinstallations". Association of Polish Electrical Engineers, Gdańsk Division, 5-26 (2002).

[6] Markiewicz H., ,,Safety in power engineering. Selected issues. Third edition changed" WNT Publishing company, Warsaw, 145-152 (2012).

[7] Regulation of Minister of Infrastructure of 12 April 2002 regarding technical conditions that should be met by buildings and their location (consolidated text Dz.U. 2015 pos. 1422 with later changes).

[8] PN-HD 60364-4-444:2012 Low-voltage electrical installations – Part 4-444: Protection for safety – Protection against voltage disturbances and electromagnetic disturbances.

[9] BS 7671:2018 Requirements for Electrical Installations, IET Wiring Regulations 18th Edition.

[10] Hanzelka Z., „Voltage sags and short interruptions", Automation – Electricity (2), 55-70.

An indoor tracking system and pattern recognition algorithms as key components of IoT-based entertainment industry

Radosław Belka*

The Faculty of Electrical Engineering, Automatic Control and Computer Science,
Kielce University of Technology, al. Tysiąclecia Państwa Polskiego 7, 25-314 Kielce, Poland,

ABSTRACT

The paper presents the key components of an innovative Integrated Visitor Support System (IVSS) for the distributed entertainment industry, based on Internet of Things (IoT) technology and classification analysis. Regarding the modern IoT layered models, including indoor tracking technologies and pattern recognition algorithm, the project of IVSS was presented. Simple tracking concepts based on chaining of Login Records to form a Path Vector (PV) by so-called poly-LR-isation process was proposed. The data generation model was also developed, where a Weibull and Poison distributions were adopted to generating Login Period and Entry Time parameters, respectively. The data in the form of PVs set was generated for a virtual theme park containing twenty monitored Points of Interest (POIs). The 5 different Visitors' profiles and 4 different behavior types were defined in the model. The efficiency of pattern recognition was calculated according to the Linear Discriminant Analysis concept. Influence of the set of independent variables on the efficiency of correctly classified labels was reported. It has been shown that high efficiency in recognizing the types of behavior can be obtained including the total number of logins in the POIs area and first login times, whereas the proper separation of profiles needs additional data as Login Period.

Keywords: Internet of Things, Entertainment Industry, indoor tracking, RTLS, BLE Beacon, pattern recognition, Linear Discriminant Analysis, Weibull distribution

1. INTRODUCTION

In recent years, the Internet of Things (IoT) term was understood as collectively describes technologies and IT solutions that enable the Internet to reach out into the physical world of device, sensors, controllers and actuators [1,2]. New solutions like Real Time Localisation System (RTLS), Distributed Sensor Networks, short and medium range wireless communications and IP-enable device can be treated as key enabling technologies for making the IoT a reality. Moreover, IoT can sometimes be synonymized with cyber-physical systems (CPS). Modern IoT solutions will open up the possibility to create novel value-added services across areas of science, technology, business, economy, and so on by dynamically combining different types of capabilities (e.g. sensing, communication, information processing, and actuation on physical resources). The IoT is expected to contribute towards the creation of a distributed, large-scale network of sensors, devices, machines, which are integrated with the traditional Internet. Moreover, data generated by a world of things will be available globally and in vast amounts to be shared among applications and devices for event detection, context and situational awareness based decision making, enhanced service creation and driving event-based actuation without human intervention.

One of the IoT application is making possible the exploitation of responsive device networks to create new ubiquitous information services for tourists [3-6]. In recent years, tourism and entertainment industry is a very dynamically developing area of business, especially associated with the theme and entertainment parks. Increased interest in this type of services is related to the growing awareness and direct human needs. It should be expected the IoT technology will be more and more often involved in the tourism industry. It is, no doubt, part of well-known concepts known as smart cities. Using some IoT technologies for electronic ticket & reservation systems, delivering of context-based information, smart monitoring, finding missed passengers or luggage and locating travelers in emergency situations, providing interactive tours are most popular

* r.belka@tu.kielce.pl

Photonics Applications in Astronomy, Communications, Industry, and High-Energy Physics Experiments 2019,
edited by Ryszard S. Romaniuk, Maciej Linczuk, Proc. of SPIE Vol. 11176, 111765P
© 2019 SPIE · CCC code: 0277-786X/19/$21 · doi: 10.1117/12.2536728

examples of new trends in tourism. Tourists should also be able to receive information about the point of interest (POI), local purchase opportunities and be informed about the location of nearby interesting places through their personal device or public display.

An increasing the potential of IoT technology will also be achieved thanks to the real-time location & tracking techniques [7-12]. Smart cities concepts typically implement the GPS-based solution for tourists' location and path monitoring. Unfortunately, this approach is limited to an outdoor open area and can not work properly in indoor locations. Meanwhile, many theme parks and other POIs like museums put some of their attractions and exhibitions inside large-sized buildings. In this situation, the problem can be solved by the integration of a Distributed Sensor Network (DSN) capable of indoors tracking. In both, outdoor/indoor cases, it can able to receive information in form of set so-called path vectors, which give the basic data regarding the client's behavior and preference. Another information as spatial distribution of the tourist load, most preferable sequences and many others can be further calculated based on path vector data.

One of the most valuable data is information about individual profile (preference) of every customer. Knowledge about preferable attraction or exhibition will allow the park managers to more effectively control the tourist traffic, provide more efficient customer service, optimize the distribution of attractions, allowing more efficient human or material resources management and, finally, targeted advertising in relation to individual clients. In last years, traditional forms of advertising, including billboards, newspapers, and radio, are progressively replaced by modern, client-oriented advertisements to target the most receptive audiences with certain traits. These traits are usually psychographic-focused, this means they are based on the consumer's values, personality, attitudes, opinions, lifestyles and interests. However, they can also be behavioral variables, such as path sequence, visiting history, and other recent activity. Targeted advertising is focused on certain traits and the client who is recognized to have a strong preference will receive the message instead of those who have no interest and/ or do not match an assumed profile. Through the emergence of new capabilities related to the implementation of IoT solution, the need for targeted advertising is increasing because managers aim to minimize wasted advertising. In other hands, discovering of clients' preference are related to well-known Market Basket Analysis concepts, where the retailer want to obtain information to understand the purchase behavior of a client. In practice, this often leads to the dividing the clients into groups or segments.

As the main goal, the authors intend to define a set of independent variables that ensure the most effective prediction of the visitors' profile in developed Integrated Visitor Support Systems (IVSS) known as "CyberMatrix". In addition, it is even more expedient to examine the effectiveness of customer profile recognition during the visit, i.e. based on incomplete data. This was achieved by defining the structure of relevant data records, creating a proper simulation model and performing a discriminant analysis.

2. GATHERING DATA IN IOT-BASED REAL-TIME LOCATING SYSTEM

The Real-Time Location System is a solution used to provide immediate or real-time tracking and management of both things and humans within all types of spaces and environments. The focused on indoor locations technology, it can be thought of as a type of "indoor GPS" as an alternative and supplement for well-known satellite-based locations. However, more than just locating assets, accurate locating technology that easily integrates with other IT solutions enables facilities to improve workflow, optimize traffic, reduce costs and increase service quality. The RTLS solutions comprise various tags and badges, technology platforms: 802.11 Wi-Fi, Infrared, Bluetooth Low Energy Beacons, Radio Frequency Identification (RFID), ZigBee, Ultra Wide Band, and others, hardware infrastructure (readers & exciters) and also other components like back-end servers, middleware edge-computing software, and frontend applications.

The RTLS systems provide asset-tracking capabilities in multiple industries including transportation, manufacturing, agriculture and healthcare. But recently the promising applications of advanced RTLS use cases lie in entertainment industry. However, the current degree of adaptation of RTLS solutions in distributed theme parks is relatively low, despite the numerous benefits of their applications. This is probably caused by factors such as: high implementation and maintenance cost or implementation complexity, but also insufficient awareness of benefits or incorrect definition of needs. It is enough to emphasize the fundamental difference between the exact position variant and proximity variant of RTLS solutions. Proximity based systems are simpler, less power-hungry, and usually cost much less than exact location based systems. To make RTLS applications more attractive, in our solutions we focus on less expensive variants based only on the approximate location of visitors. This can be done thanks to the integration of BLE beacon technology,

aspberry Pi 3 programmable microcomputers with Bluetooth and Wifi modules (or equivalents like EPS32 SBC solutions), distributed IPv6 wireless/wired networks and proper middleware and backend software.

2.1 Layered Model Of The Distributed Sensor Network

General structure of Distributed Sensor Network as key components of the "CyberMatrix" IVSS is presented in figure 1. It is based on BLE beacon and/or RFID–UHF solution controlled by SBC microcomputers, playing the IoT gateway role. The access/distributed network is based on proven IP technologies and should be scalable, reliable, secure and relatively cheap. It also applies the latest solutions in the field of programmable controllers and single-board microcomputers. This allows you to create an IoT-compatible edge-computing layer that supports the visitors' tracking. More information about Integrated Visitor Support System was reported in papers [12-14].

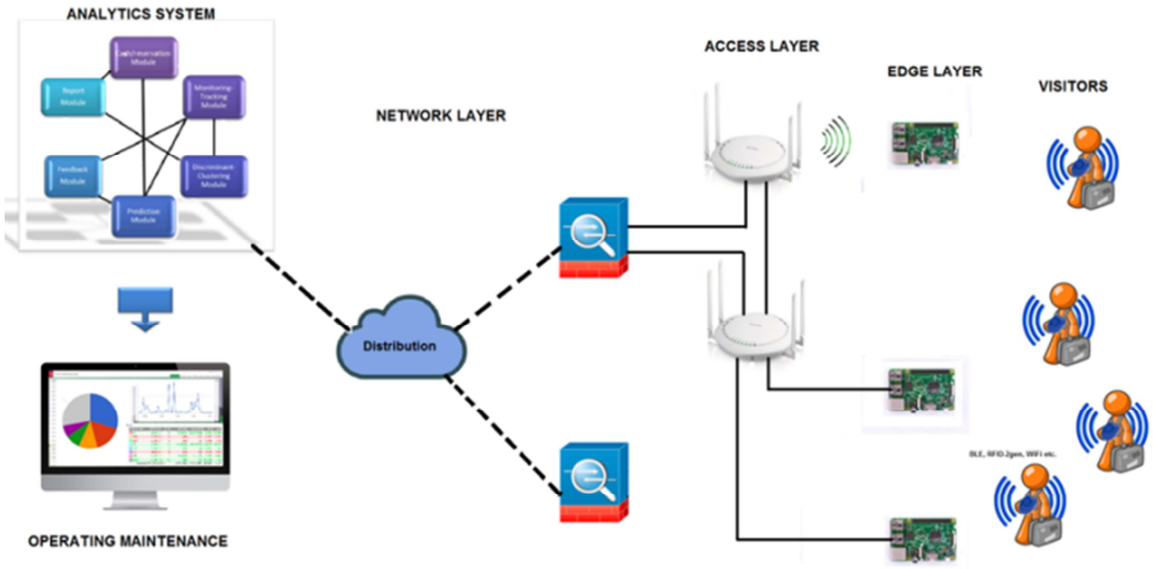

Figure 1. General structure of proposed IoT-based RTLS system.

The using of proximity beacons on the client's side and beacon scanner on the edge layer allows the system to collect information about the approximate location of a given person at a given time. We assume, the beacon scanner should be placed in the center of the POI and should receive signals from portable beacon emitter worn by and associated with a given customer. The visitors can be recognize by beacon UUID (Universally Unique Identifier) and /or by Major/Minor fields, depends on used types As the typical beacon time interval can be as low as 100ms, it can be simply to estimate so-called login time, and login period with high accuracy. Moreover, as the RSSI (Received Signal Strength Indicator) level in Bluetooth technology is typical monitored, it allows to estimate the beacon emitter to beacon scanner distance, which can be understood as a measure of the interests together with login period. It was based on the assumption that more interested persons are generally closer to POI and more often in its direct visibility, as a result the emitted signal is stronger. Thus, we propose the following method to calculate one of the most important factor called Interest Level (IL):

$$IL = T_{BI} \cdot \sum_{T_{in}}^{T_{out}} \left(1 - \frac{RSSI[dBm]}{100} \cdot \gamma\right) \quad (1)$$

where:

T_{BI} - Time interval between emitting two subsequent beacons (Beacon Interval)

γ – RSSI influence factor, if $\gamma = 0$ – no RSSI information are taken into account

T_{in} – time moment of receiving first UUID

T_{out} – estimated time moment of receiving last UUID

The T_{out} can be estimated based well-known keep-alive mechanism with , which can be implemented in SBC edge layer. We recommend to adopt hold time solution fairly often used in communication protocols.

2.2 Login Records and Path Vectors

The nowadays DSN solutions let to generate simple localization data record called further Login Record (LR). Its scalable structure is shown in Figure 2.

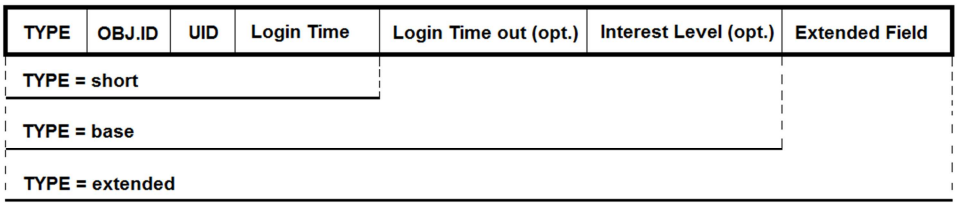

Figure 2. Proposed structure of Login Record.

Three variants of LR structure have been proposed. The variant is recognizable thanks to the *Type* field. The preferred variant is the base type, where following data is included:

- *OBJ.ID* - is a unique identifier of attraction (POI), defined by the manager and designer (known also as *k* index).
- *UID* – user identifier, is an anonymous user ID.
- *Login Time* (LT) – global time, the moment when the presence of the given beacon was softly detected in the beacon or RFID scanner.
- *Login Timeout* (LTout) - similarly, the moment when the no presence of the given beacon was found (beacon is no longer available).
- *Interest Level* (IL) – estimated interests according to formula (1). It is worth noting that if $\gamma = 0$, then IL=LP.

Alternatively, the LTout parameter can be replaced by an equivalent parameter known as Login Period (LP) – the interval time within the scope of the beacon scanner. However, not all IoT technologies have an acceptable form of the keep-alive mechanism and/or communication range is not too large. For such situations, a short LR variant has been proposed. Only the Login Time parameter is included in this type of LR. On the other hand, the expanding beacon capabilities as temperature, motion, vibrations detection, requires predicting an extended variant of Login Record for future use.

Visitors, moving freely around the entertainment park area, leaving behind a path in the form of sequences of visited attractions. The generated LRs form a new sequential structure (tuple), called as mentioned above Path Vector. The PV seems to be created by simply concatenations of LRs, but it should be emphasize it contains the more additional information about the related visitor, including his profile of interest (preferences) and type of behavior.

The PV contains higher information potential and the properties of the entire PV are slightly different from the properties of the individual LRs. The formation of PV can be considered as an analogy to the polymerization process - formation of polymers (PV) from single monomers (LR). According to the nomenclature of polymer chemistry, the tuple formation process was called as *poly-LR-isation* (fig. 3). It is well known that the properties of polymers are significantly different from the properties of monomers. In this case, the *poly-LR-isation* process provides new data, regarding not only to knowledge about the visitor's sequences (routes), but also the set of individual login timestamps allow estimating the LP value, if the average displacement times will be taken into account. This is particularly advantageous if the sensor layer does not provide information about the IL values directly.

The PV construction starts when the visitor enters the park, which is tantamount to a login into the entrance area (IN). The *PV-Id, UID, and Timestamp global in* fields can be filled immediately in PV header. Both *PV-Id* and *UID* (User Identifier) are used to identify and differentiate subsequent visitors. Wherein, the UID is rather related to a physical identifier (beacon UUID) meanwhile the *PV-Id* is the identifier of the PV tuple. This allows multiple uses of the same tag (beacon) for multiple paths. The *Timestamp Global out* field should be filled after reaching the OUT area. Before this happens, PV is in the so-called "in progress" state. After that, PV should go to "finished" state.

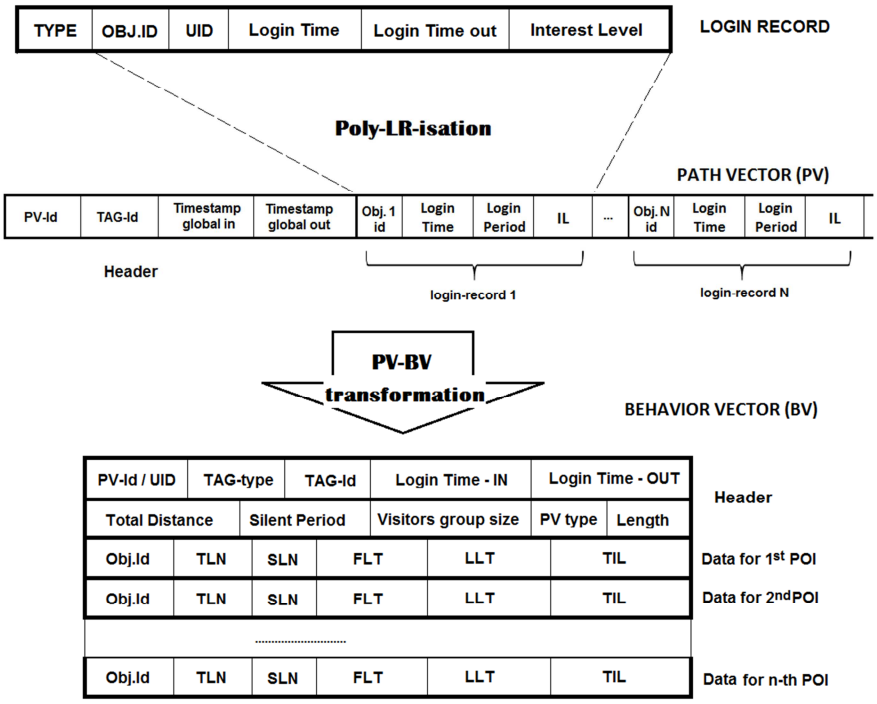

Figure 3. Poly-LR-isation and PV-BV transformation process.

2.3 Behavior Vectors

The PV in "finished" state is the basic candidate for transforming it into a relational data structure called Behavior Vector (BV) – fig. 3. Unlike PV, which can have basically any size, BV has a strictly defined size, depending on the number of currently monitored POIs. It can distinguish global information contained in the header, as well as local information about individual POIs in the records.

From the point of view of further analysis, the most important data are:

- *Login Time IN/OUT* - Time to log in to the entrance and exit area of the park, respectively. Their difference forms the parameters known as a *Total Visit Time* (TVT)
- *First Login Time* (FLT) – relative time that has elapsed since entering the part until the first login into the detection area of the given tourist attraction.
- *Total Distance* (TD) - estimated distance traveled by the visitor – knowledge about the locations of individual POIs are required and the proper metrics as Manhattan should be defined.
- *Silent Period* (SP) - a time spent out of range of any monitored POIs.
- *Total Interest Level* (TIL) - the sum of the total value of IL coefficients corresponding to the given OBJ.ID.
- *Separate Login Number* (SLN) - the number of independent logins - logins to the detection area of given POI separated by logins into the other detection area.

The other parameters, less important from the point of view of the conducted simulations, are Group Size (GS), PV type and Length (Hop Number – HN).

The PV with too few LRs can be an unreliable source of information. Referring to the earlier terminology of the polymer chemistry, the concept of an oligomer, i.e. a polymer composed of a relatively small number of monomers, can be adopted. Unlike polymers, an addition of another element to oligomers significantly influences their properties. As a result, formation of PV goes through the state of oligo-LR-ization to the quasi-stable state of poly-LR-ization. In the poly-LR-ization state, the addition of subsequent LRs to PV has a negligible effect on its analytical potential. Moreover,

receiving too many LRs in the case of expanded PV can contribute to the deterioration of its analytical potential according to rule “enough is enough”. This may mean, for example, that the visitor wanders aimlessly around the park.

3. SIMULATION MODEL

Recognizing the moment, when the PVs transform from the oligo- state to the poly- state can be a key issue for further analysis. For this reason, a simulation model was created due to the lack of a retrospective amount of experimental data. This model is a random data generator that represents the real parameters contained in LRs and PVs. The model was implemented in Mathcad software, using Programming Toolbar. The main steps of the data generations are following:

- Defining the Number of POIs (NoP) and their spatial arrangement, including IN and OUT positions.
- Defining the interest profiles and types of behavior.
- Generating a sequence of visits on the timeline for one visitor.
- Generating a data set for many visitors.

Step 1 required an adoption of the relevant metric for the considered cases. The Manhattan metric was chosen as the best representative of the real space situation. The 2-dimensional area of 100m x 100m size has been defined. The number of POIs was assumed to be equal to 20. The IN and OUT points are also taken into account as part of POI set.

In the 2nd step, the PROFILEs and TYPEs were defined. The PROFILE is understood as a priori distribution of visitors' preference of specific attraction set. This parameter can be represented in the form of a NoP-element vector whose components represent the expected ILs for related POIs. The five different profiles were generated named as: “UNIFORM”, “DESCENT”, “CENTRMAX”, “COMB” and “SAW” – fig. 4.

The TYPE is understood as a priori way of routing in the park area and method of selecting the next attractions in the sightseeing plan. The following criteria were accepted as the rules for the selection of the next hop: proximity of POIs (higher probability of choosing a closer POI), multiplicity of visits (preference for not yet visited POI), PROFILE (more chance of visiting of favored POI) and finally a fatigue (successively increasing a chance of choosing OUT during sightseeing). An exponential probability distribution was chosen to generate the selection of the next attraction in terms of the distance criterion. The four different models for TYPE generation were considered, depends on values of a, b and c coefficient. As a result, the so-called the route sequence (RS) as the ordered set of POI identifiers can be generated. Each proper RS should start at the IN point and ends at the OUT point.

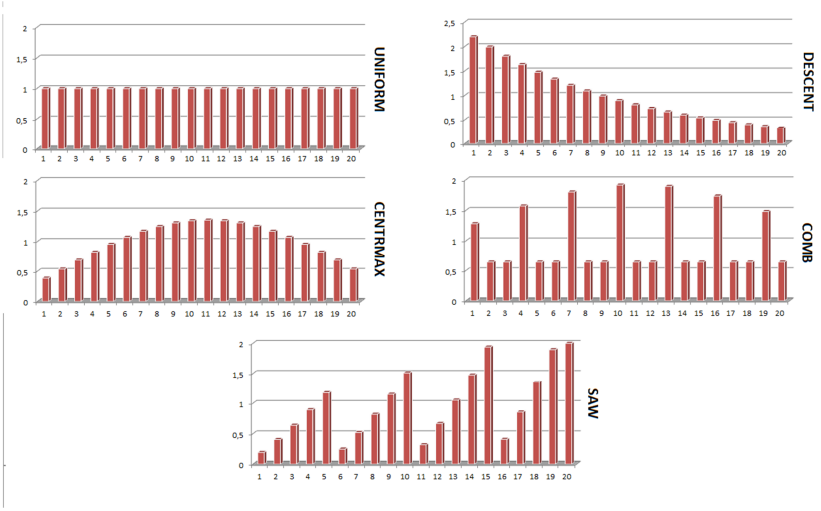

Figure 4. The model of the five visitors’ preference.

The next step of the simulation model is to generate a simple form of the PV vector, where IL = LP. It was accomplished by generating a route sequence, LP values and travel times (SPs) from one POI to another. Each route sequence starts at

the IN point and ends at the OUT point. Knowledge of the POIs location allows to easily calculate the *Total Distance* (TD) parameter corresponding to this RS.

The IL values were generated randomly, assuming they are related to a Weibull distribution - a three-parameter expression, which is widely used in reliability, failure rate, and survival analysis [15]. The using the Weibull statistics for evaluating Login Period values is a quite new idea. It was assumed that the fact that the visitor left the given POI is identified with the expiration (death) of interest. The SPs values were estimated based on related POI-POI distance and expected velocity. Ultimately, knowledge of LP and SP allows recreating Login Time on the timeline.

The one Route Sequence is generated for the individual visitor or organized group of visitors, where randomized PROFILE, TYPE, and average velocity were chosen. Generating a data set for many visitors requires to introduce the timeline to which the route sequences will be projected. These needs generate entry times for individual visitors. It was assumed that the number of visitors per unit time should satisfy the Poisson distribution. This means that the values of intervals between the appearance of two consecutive visitors should satisfy an exponential distribution. Then, the LT values relating to route sequences were simply time-shifted by the Entry Time values.

4. RESULTS AND DISCUSSION

4.1 Generation of LRs, PVs and BVs

Using the model presented above, testing data was generated by author, corresponding to the structure of BV. The output data set were generated for 1000 visitors, in range of 10 hours with 10s resolution (interval size) of a timeline. The following independent variables have been included in our further analysis:

- TLN, FLT, and TIL for all 20 POIs
- HN, TVT, TD, and TSP.

It should be emphasized that the received data is labeled with both PROFILE and TYPE, which act as dependent variables. This means that training sets are not necessary. In the generated dataset, it was found that 565 people visited each of 20 POIs once and only once. An additional 176 people visited the full set of POIs, some of them many times. The 117 people visited less than 20 POIs. The minimum, maximum and average numbers of visited POIs was 1, 60 and 22.7 respectively.

4.2 "Finished State" Data Discrimination

The effective way to assess the ability to predict profiles is to perform a Linear Discriminant Analysis (LDA). The objective of the LDA is to estimate discriminant functions that are a linear combination of independent variables that will discriminate between the categories of the dependent variable in a most effective manner. It also evaluates the accuracy of the classification. In the considered case, the Canonical Variate Analysis (CVA) method was used [16,17]. Calculations were performed using freeware software PAST 3.21 [18]. Details of the procedure are described according to the software manual.

The analyzes were carried out in three variants. In the first one, the Separate Login Number information was used (SLN only). It has been assumed that obtaining SLNs information from the Distributed Sensor Network should be relatively easy and also it is biased with the low uncertainty. In the second case, the analysis also included information about FLTs (SLN + FLT), because the FLT parameter should also be relatively easy to gather from the sensors. Finally, the last case includes all available information, including TILs and TD.

Figure 5 shows the coefficients of correctly classified labels for each PROFILE separately together with summary results. The total efficiency of discrimination was approximate ~45% for "SLN only" variants and was comparable to results if FLTs data were included. On the other hand, including the TIL data strongly influents the efficiency coefficient, changing it to more than 90%. It was noted that the SLN and FLT parameters are not sufficient to effectively recognize profiles behaviors. Only UNIFORM profile was recognized with reasonable efficiency where ~80% value was achieved.

As shown before, the proper recognition of visitors' profiles will require to receive reliable Interest Level data. This may result in having to surrender many popular location technologies, led by the RFID, QR scanners or optoelectronic sensors (optical barrier). Nevertheless, author proposes a solution that can significantly improve the efficiency of profile recognition without the need to directly obtain the TIL parameter. It consists in the fact that if the TIL data are absent, the appropriate values can be substituted based on Login Times only.

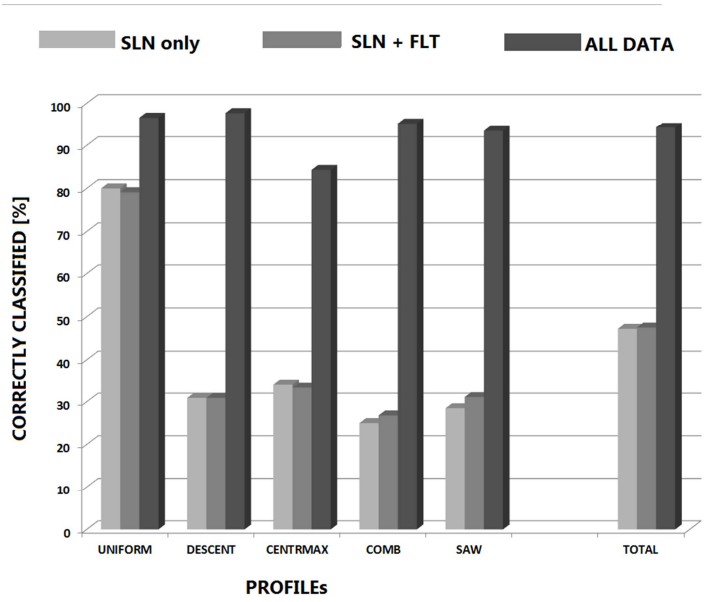

Figure 5. Coefficients of correctly classified PROFILE's label according to confusion matrix.

Note that IL can be estimated based on the following expression (2).

$$EIL(i) = LT(i+1) - LT(i) - \frac{D(POI_i, POI_{i+1})}{v_{avg}} \tag{2}$$

where: EIL - Expected IL, $D(POI_i, POI_{i+1})$ – a distance between i-th and (i+1)-th POIs, according to considered metric,

v_{avg} – average velocity of visitors, assumed to equal 1m/s.

New calculation was carried out in which the TIL values were replaced by the ETIL values calculated from the LT data. The results, shown in Figure 6, indicate that the TIL calculated in this way has comparable effect (94.2% vs 93.7%) on the efficiency of profile recognition. It was also noticed that more significant differences are observed in the case of more dynamic COMB and SAW profiles.

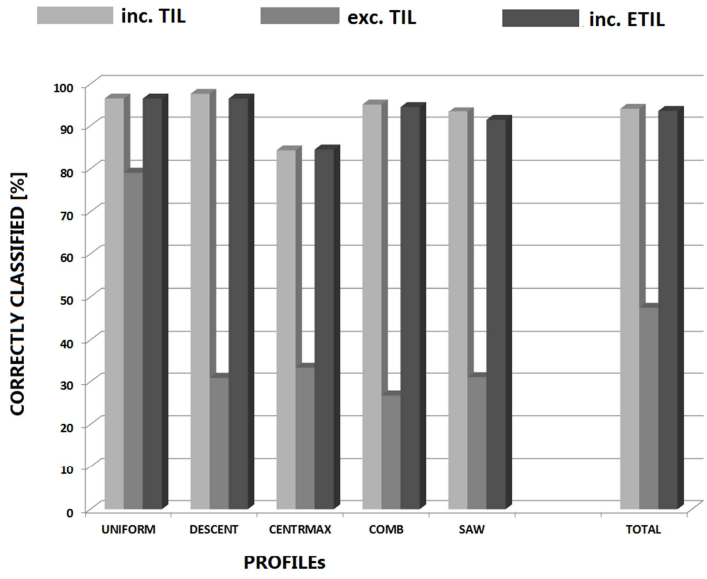

Figure 6. Coefficients of correctly classified PROFILE's label - ETIL influence

4.3 “In Progress” Data Discrimination

The effectiveness of linear discrimination for data obtained from PV in "in progress" mode was also investigated. In the first phase, a training set consisting of 10,000 labeled observations belonging to randomly selected profiles and types was generated. The data were used to generate four canonical axes (variation) to which these observations were projected, creating 5 reference data clusters corresponding to previously defined profiles. Next, a test set of 1000 PVs was generated. The corresponding BVs were obtained by accumulating data only a certain p number of first Login Records contained in the PVs. In this way, the situation where the visitors made the first p hops were considered. The received "in progress" BVs were also dropped onto the same canonical axes. In this way, the number of independent variables has been reduced from over 60 to 4 only. As before, the classification criterion was the minimum Mahalanobis distance of test observations from reference clusters.

The performed simulations showed that the total efficiency (TOTAL) of profile recognition was 88.6 % for the complete data set and it has a tendency to decreases with the depletion of the data set (decreasing p value), reaching the value of ~40.7 % for $p = 3$ – figure 7. However, it turns out that the relatively low overall effectiveness was caused by ineffective recognition of the UNIFORM profile. The other profiles were recognized with 90-99% efficiency for the complete data, and with ~ 52% for DESCENT profile, ~ 67% for SAW profile, and as much as ~ 78% for CENTRMAX profile if $p = 3$ only.

It was also found that 8.3% of all observations from the test set are outside the parent cluster. In other words, self-efficiency of total pattern recognition for complete test data was only 91.7%. It means that the obtained result of 88.6% efficiency using the training set should be satisfactory. Moreover, it is worth to notice that the UNIFORM profile concerns people who do not show particular preferences regarding the specificity of particular attractions, whereas the clients with particular preferences are much more valuable.

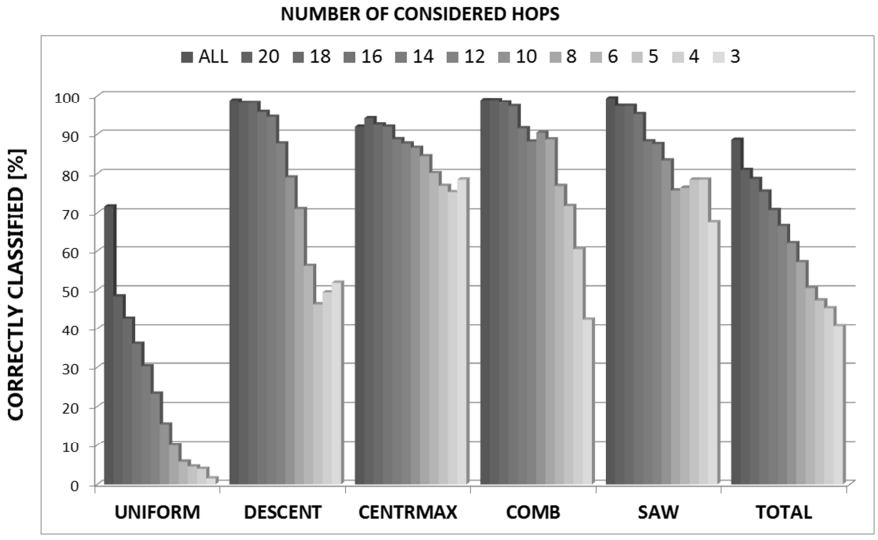

Figure 7. Efficiency of PROFILE recognitions for “in progress” data**.**

Performed study shown that some profiles, especially like SAW and COMB can be effectively recognized only after few hops. A 90% efficiency of recognition can be obtained after traveling around 2/3 of the route sequence, whereas 75% efficiency of recognition can be obtained after traveling only around 1/4 of the average route sequence length. These coefficients are the basis for defining the boundary between mentioned before the oligo- and poly-LR-isation process. Excluding the UNIFORM profile, this value has been estimated on average p ~ 15 LRs. Above this value, the efficiency of profile recognition changes only slightly. Moreover, analyzing the efficiency dependencies, it should be noted that they do not increase monotonically, but some anomalies are observed, related to suggested above overload (“enough is enough”) tendencies.

5. CONCLUSION

Concluding, it was shown that based solely on the knowledge of login times in the areas of individual POIs, it is possible to successfully recognize customer profiles. Using the simulation model, it was possible to easily obtain labeled observations, thanks to which we were able to determine the effectiveness of classification based on the confusion matrix returned by discriminant analysis algorithm. However, it should be added that in the real world, the labels will not be known. Moreover, we are aware that such a labeled dataset can never be obtained in real experiments. That's why it is necessary to refer to clustering algorithms, such as k-mean, DB-SCAN or ANN-based self-organized maps. It requires using, well-known unsupervised learning concepts based on a training set, and then validation of results based on test sets. Such a procedure will be most desirable for the treatment of actual data.

ACKNOWLEDGMENT

This paper was supported by the European Union's Smart Growth Operational Programme 2014-2020, under grant agreement no POIR.04.01.02-00-0041/17-00, „CyberMatrix - Integrated Visitors' Support Systems"

REFERENCES

[1] Siegel, J., Kumar, S. and Sarma, S.E., "The future Internet of Things: secure, efficient, and model-based", IEEE Internet of Things Journal 5 (4), 2386 – 2398 (2018).
[2] Zanella, A., Bui, N., Castellani, A., Vangelista, L. and Zorzi, M., "Internet of Things for smart cities," IEEE Internet Of Things Journal 1 (1), 22-32 (2014).
[3] Hu, G., "A research review on theme park," Business Manag Res 2 (4), 83-87 (2013).
[4] Davis, R., Campbell, R., Hildon, Z., Hobbs, L. and Michie, S., "Theories of behaviour and behaviour change across the social and behavioural sciences: a scoping review," Health Psych Rev 9 (3), 323–344 (2015).
[5] d'Amore, M., Baggio, R. and Valdani, E., "A practical approach to big data in tourism: A low cost raspberry pi cluster," Information and Communication Technologies in Tourism, 169-181 (2014).
[6] J Fisher, J.A. and Monahan, T. "Evaluation of real-time location systems in their hospital contexts, " International Journal of Medical Informations 81, 705–712 (2012).
[7] Scott, M.T., Scott, T. J. and Kelly, V.G. "The Validity and Reliability of Global Positioning Systems in Team Sport: A Brief Review," J Strength Cond Res. 30 (5), 1470-90 (2016).
[8] Yang, C. and Shao, H. "WiFi-based indoor positioning," IEEE Communications Magazine 53 (3), 150 – 157 (2015).
[9] Manikandan, G., Mathavan, N., Paramasivan, M. and Ashly, T. "RFID-Based Tracking System," International Journal Of Engineering And Computer Science 4 (3), 10755-10759 (2015).
[10] Feng, T., Yu,Y., Wu, L., Bai, Y., Xiao, Z. and Lu, Z., "A Human-Tracking Robot Using Ultra Wideband Technology," IEEE Access 6, 42541 – 42550 (2018).
[11] Lin, Y., Chen, H. and Su, M., "A cloud based Bluetooth Low Energy tracking system for dementia patients," Proc. of 8th Int. Conf. on Mobile Computing and Ubiquitous Networking, 88-89 (2015).
[12] Plaza, M., Belka, R., Plaza, M., Deniziak, S.R., Pięta, P. and Doszczeczko, S., "Analysis of feasibility and capabilities of RTLS systems in tourism industry, " Proc. SPIE 10808, 108080C (2018).
[13] Belka, R., Deniziak, S.R., Płaza, M., Hejduk, M., Pieta, P., Płaza, M., Czekaj, P., Wołowiec, P. and Ludwinek, K., "Integrated visitor support system for tourism industry based on iot technologies," Proc. SPIE 10808, 108081J (2018).
[14] Pieta, P., Deniziak, S.R., Belka, R., Plaza, M. and Plaza, M., "Multi-domain model for simulating smart IoT-based theme parks", Proc. SPIE 10808, 108082T (2018).
[15] Hallinan Jr. A.J., "A review of the Weibull distribution," J Quality Techn 25 (2), 85-93 (1993).
[16] Gittins, R. "Canonical variate analysis. In: Canonical Analysis," Biomathematics 12, Springer (1985).
[17] Peltier, C., Visalli, M. and Schlich, P., "Comparison of Canonical Variate Analysis and Principal Component Analysis on 422 descriptive sensory studies," Food Quality and Preference 40B, 326-333 (2015).
[18] Hammer, O., Harper, D.A.T. and Ryan, P.D., "PAST: Paleontological statistics software package for education and data analysis," Palaeontologia Electronica 4(1), 9 (2001).

Automatization of measurements in the stability and linearity tests of direct current-current transducer (DCCT)

Mateusz Sewiolo, Jaroslaw Makal
Bialystok University of Technology, Faculty of Electrical Engineering, Wiejska 45D,
15-351 Białystok, Poland

ABSTRACT

Since electrical measurement systems are becoming more and more vital part of an engineering and scientific worlds, it is crucial to test their quality in proper way. It is especially important in high-accuracy systems like the DCCTs. Different industrial conditions like a quality of used materials can determine if a device is good enough to use or not. But conducting such tests without proper applications would not be easy and convenient. This document describes such applications to conduct DCCTs quality check in a simple way, to gather data from DMM used in tests and most important DCCT tests which have a decisive impact on the rating of given DCCT.

Keywords*:* DCCT, doing measure, linearity test, stability test, testing system

1. INTRODUCTION

Nowadays in the science world the usage of the complex and precision machinery is growing at a fast pace. Because of that, in order to ensure that they are working properly, there is need to have a precise data about all processes which are taking place inside them, such as temperature and humidity of an environment. A particle accelerator is a good example of such machine. Since huge electromagnets are a foundation of their existence its urgent to give them a power of a precise quality. It is obvious that even a slight change in amount of current flowing in coil of the magnet can cause a loss of a beam of particles or even worse, makes a probability of damaging or destroying whole magnets, hit by the beam. That is why Zero Flux Direct Current-Current Transducers (in short DCCT) are used in power converters to supervise and assure the quality of current. In order to use in certain machine types, for example main dipole or quad magnets of accelerator, the power converter has to be of highest class. Regarding the value of total deviation of power converters they are attributed to three categories: 10 ppm for class 1, 50 ppm for class 2 and 100 ppm for class 3.
This total deviation is a sum of uncertainty of a DCCT (45%), quality of built-in ADC (45%) and some miscellaneous things (10%) such as an impact of external magnetic fields.
The DCCT is responsible for almost a half of an accuracy budget of a whole power converter. In this case, to fit in the strict requirements of quality classes, DCCTs must go through the procedure to see if their quality is good enough and then if they have to be necessary calibrated to reduce the uncertainty section.
To evaluate the quality of a DCCT the series of special tests to check its stability, repeatability and linearity are required.

2. TESTING SYSTEM

The testing system can be divided onto two parts: the *heavy devices* which includes DCCTs, cooling fan, current calibrator and voltage booster, and the *measurement and control* that contains three DMMs and laptop PC.
The one of the main components of the heavy part of the system current calibrator is capable of providing a precise value of current with the use of reference current source. It can be controlled through a USB port located in front panel, with the usage of serial port terminal. To Current Calibrator was attached Voltage Booster, which gets rid of the outputted voltage limitation of the current calibrator. It is because, on certain ranges calibrator can output only limited amount of the voltage, and if the voltage drop is bigger than allowed, there is no guaranteed that requested amount of current is outputted, which could be another source of errors if not handled.

Photonics Applications in Astronomy, Communications, Industry, and High-Energy Physics Experiments 2019,
edited by Ryszard S. Romaniuk, Maciej Linczuk, Proc. of SPIE Vol. 11176, 111765Q
© 2019 SPIE · CCC code: 0277-786X/19/$21 · doi: 10.1117/12.2536785

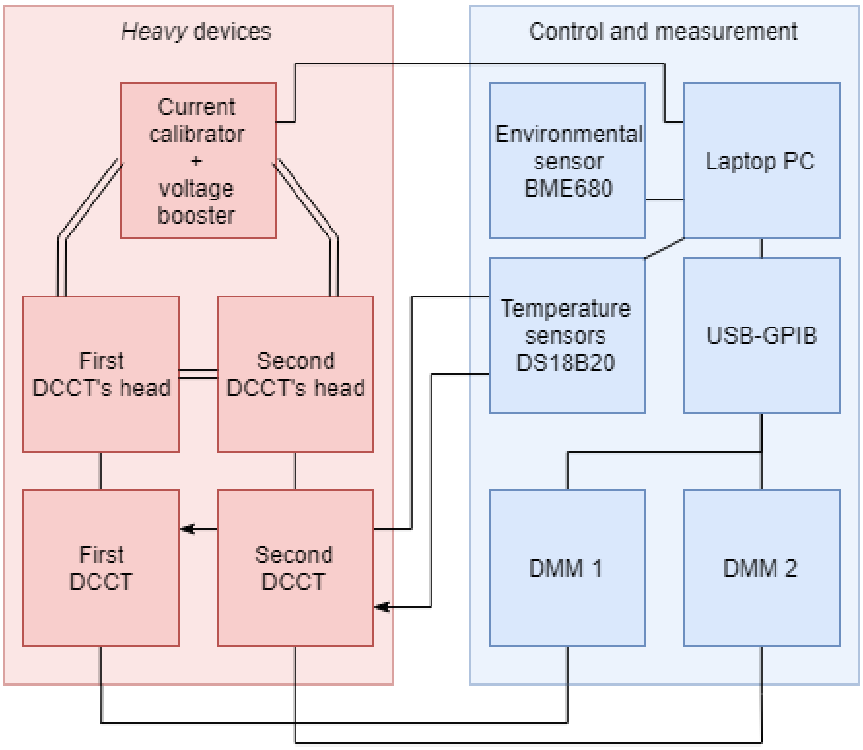

Figure 1. The testing system for DCCT.

In the picture above a full schematic of hardwire connections between parts of this project is presented. The laptop PC has been used as a main control device because of two reasons: (a) for the PC platform prototyping was fairly easy; (b) Windows OS has really good libraries to use serial communication.

The following DMMs was used within this system: Keithley 2001, 2002 and Keysight 3458a. The Keithley 2001 was used only to test if data acquisition is capable of dealing with two DMMs simultaneously, and later as a replacement before 3458a has arrived. Keithley 2002 and Keysight 3458a are both 8,5-digit DMMs with GPIB remote control output. Keysight's DMM has been also calibrated in certificated lab, so it was also used to calculate offset and gain error for the 2002. The Prologix USB-GPIB interface is used to make connection between DMMs and PC. It bases on FTDI chip, so there is serial communication, too.

In order to save time, almost all tests were conducted on two DCCTs simultaneously. The bundled cable which is used to flow current through the DCCTs heads, is a cluster of 20 wires which wraps around DCCT head couple of times, in order to fulfill the whole range of given head. For example, if DCCT head has 300 A range, to fulfill it completely, on the 5 A range of calibrator, there is need to wrap the head three times, because:

- *5 A (calibrator current) * 20 (wires in one bundle) * 3 (number of wraps) = 300 ampere-turns*

This wraps since now are going to be named ampere-turn.

3. DCCT CALIBRATOR SUITE

The application is written in C# language and designed for the Windows platform. This language was chosen because of following reasons. The C# contains really good serial port libraries and it has one of the best IDEs Microsoft Visual Studio, which simplifies the developing and debugging of an application. This language allows quick prototyping, so all mistakes and corrections could be made promptly. And also programs made in C# can be easily ported onto other platforms than PC, which is going to pay off in the future. The main idea behind this application was to replicate functions from existing application, but with addition of a couple features which are making carrying out tests easier and more convenient, and with the more user-friendly interface.

Application offers two modes of work, an automatic mode and a manual one. The manual mode allows the user to take full control of a current calibrator. The range and current are set by hand, but only in range allowed by the device. Internal functions checks if the current, which is about to be set, is not exceeding the set range and does not allow user to set current out of the range. Manual mode also offers a tool to precise adjust given output current, with the resolution of 0,1 μA.

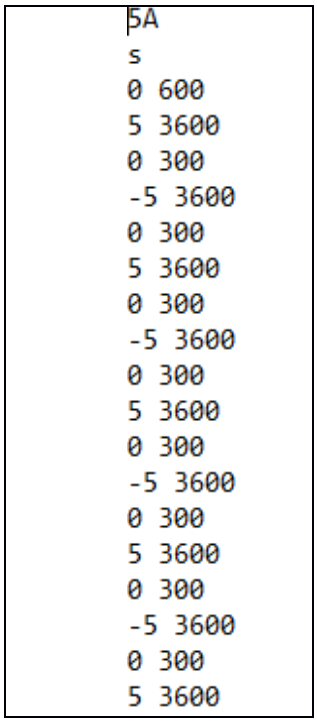

Figure 2. A structure of an exemplary batch file.

The automatic mode requires special prepared batch file, fulfilling a particular layout, to work. It may be generate in spreadsheet or text editors. The structure of batch file is fairly simple (Fig. 2.). First two lines at the beginning of the file make a header. First line contains data about range of operation. It cannot be changed during test, because there is no test that would require change of range during itself. Second line determines a unit of the number which determines a length of given step. Third and any other lines make the step sequence. In each line, the first number determines a current set during this step. Following steps are in further lines up to the end of file.

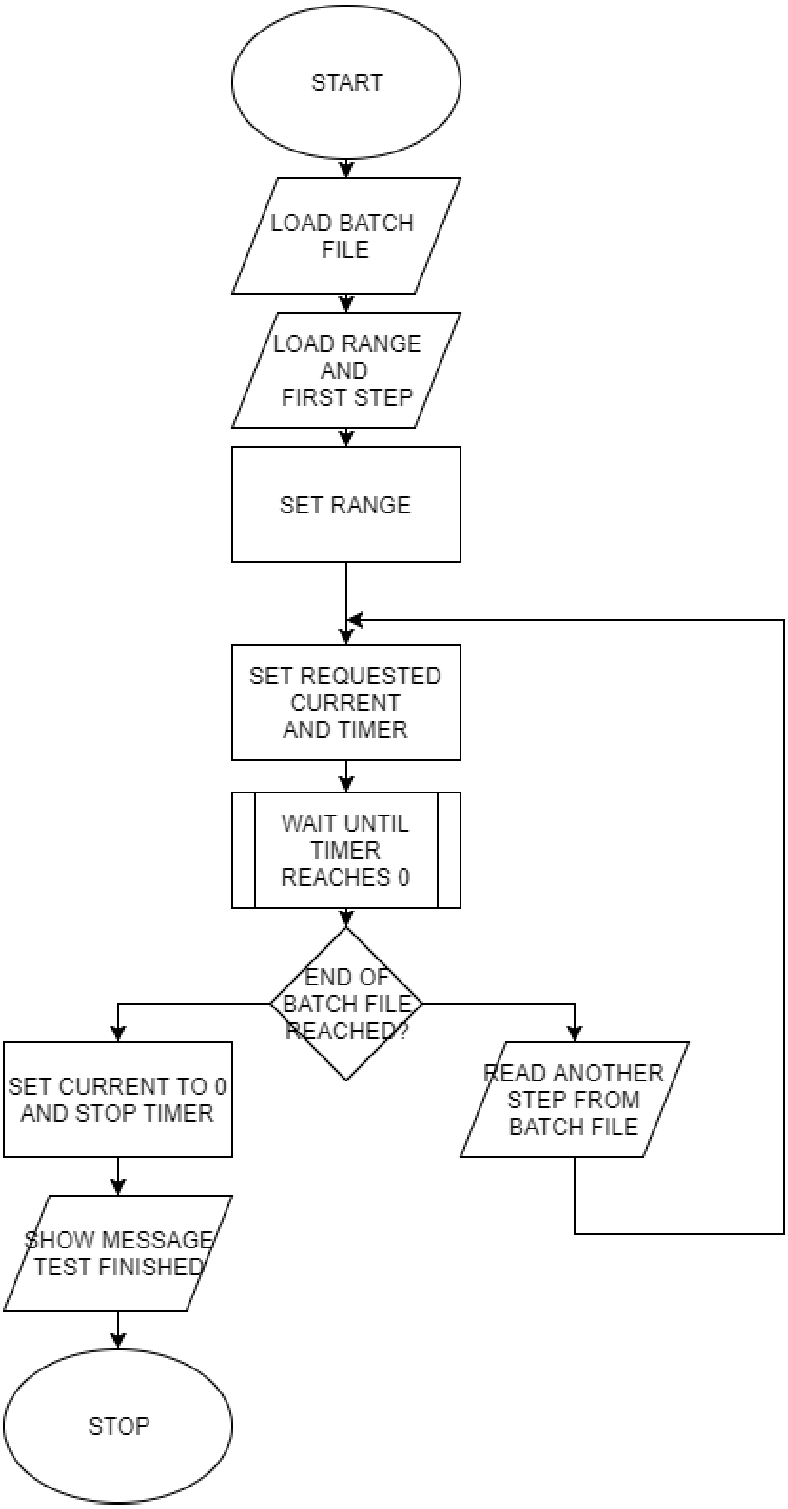

Figure 3. The algorithm of the automatic mode.

The automatic mode of the calibrator needed the dedicated application that has been elaborated for this purpose (Fig. 3.).

After selecting the right batch file, which contains settings for given test, the application waits until the start button is pressed. After that, application reads through the whole file, and loads and sets range setup, unless the status of the current calibrator prevents its functioning. If there is any problem with current calibrator, which can be outputted through the status check, special control on the interface turns red, immediately cuts off the current and range and shows appropriate message.
Another step is reading next line of the file, and loading and then setting requested amount of current for a given period of time. Then, during the waiting time, only thing the application is doing is the status checks. After waiting period, application checks if the end of file marker was encountered.
If yes, it shows the message that given task was completed and cuts off the current. If no, another line is read and the cycle repeats until the end of file is reached.

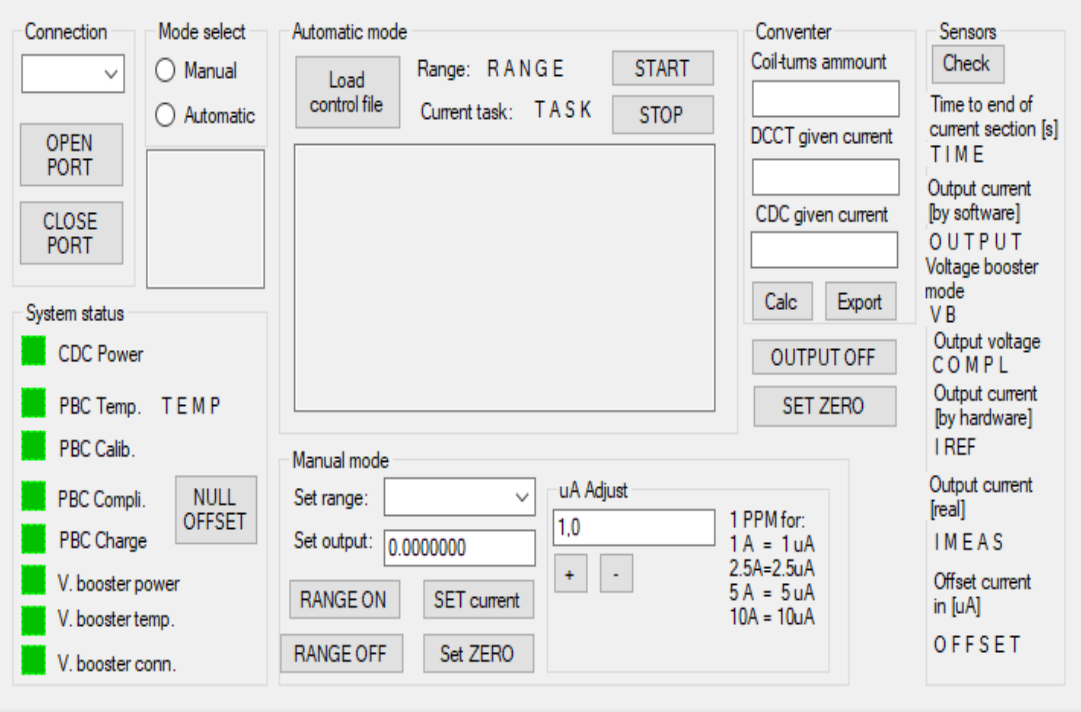

Figure 4. An interface of the current calibrator controller.

As can be seen in the picture above (figure 4), the user interface is built in the easy to understand way. All corresponding functions are grouped into separate categories, and lock themselves if they are not needed, for example tools from the manual mode cannot be used if the automatic mode is set. On the up-left side there is connection combo box, where a user must select the serial port, on which the current calibrator is operating. It can be easily checked in the device manager in computer settings. Without this, the user cannot proceed, because everything else is locked. On the bottom-left side there are status controls. Each control corresponds to its given function. It is green when everything is all right, and turns red if a device reports any problems. The only exception are the voltage booster controls, which turns gray if the voltage booster is disconnected. There is a list of all of them below:
CDC Power – indicates if the current calibrator is connected to the current.

1. PBC Temp. – turns red if the temperature of the 10 mA reference current source exceeds safe value, label next to it shows current temperature.

2. PBC Calib. – turns red if there is any problems with calibration of the 10 mA reference current source, or the reference current source is missing.

3. PBC Compli. – turns red if there is no short circuit between current outputs of the 10 mA reference current source, this is due to the specificity of work of such source[1].

4. PBC Charge – turns red if there are any issues with charging the 10 mA reference current source, which needs to be constantly charged in order to keep its load[2].

5. V. booster power – turns red if the voltage booster is connected to the current calibrator, but is not powered.

6. V. booster temp. – turns red if the temperature of the voltage booster exceeds safe value.

7. V. booster conn. – turns red if there are any issues with correct connection between the voltage booster and current calibrator.

If any of the controls turns red, program automatically shuts down the output and range of the current calibrator and does not allow any operation as long as the problem was eliminated. There are also "Null offset" button, which manually executes the internal nulling procedure [3].
Next to the connection field, right below the mode select menu, is the console window. Even though the application does not allow direct control of the calibrator through the console, it still has a console window only for the error messages purposes.
On the right side, there is sensors tab, where are presented data from all internal sensors of the calibrator. These are in order:

a) Time to end current instruction of the automatic mode.

b) Last current set by the user stated by an application.

c) Voltage booster indicator, it is '0' when voltage booster is offline and '1' when its online.

d) Output voltage, which is a reading from an internal voltmeter, it become dysfunctional, when voltage booster is online.

e) Last current set by the user stated by the calibrator, through special command.

f) Output current, read from internal amperemeter of the calibrator.

g) Offset measured through the internal null meter of the calibrator.

On the sensors tab, there is also button called "Check", which purpose is to manually execute sensor and status check. Such check is made every 6 seconds, but this button allows executing this manually in case of any inaccuracy.
Next to the sensors section, there is group of functions called "converter". It is simple build-in calculator which might be helpful when it comes to calculating right amount of current to flow through certain number of ampere-turns to fill the range of a DCCT. After writing the number of ampere-coils (or coil-turns like is in the GUI), and the given current the user is willing to let go through output, the application can calculate the current that has to be requested and can export it directly to the manual mode current request field.
Under converter there are two buttons, "output off" and "set zero". First one turns off the range and the second one sets the zero as a requested current. These buttons are always active, even during an automatic mode test, and should be used in emergency situation only.
Behind the scenes, all communication is made through the command line and virtual serial port. Even though it simplifies the whole communication between the device and the controller, it makes the communication really slow. Due to this fact, the status check-up need to be done no more often than 6 seconds, because it would overload the transfer capabilities of the serial interface. And even considering that, when application sets current, both in manual or automatic mode, and at the same time sensor check-up is done, all data received is "BBB…" due to the buffer overflow.

4. RESULTS

All tests have been provided in GSI and carried on DCCTs from third, 100 ppm, category. As it was mentioned earlier, these two applications were developed with one purpose, to simplify conducting DCCTs quality check and gathering data during tests. But before getting into tests, it should be talked about preparation. Before each test, a special procedure was conducted in order to gather the data from DMMs with as little uncertainty as possible. To achieve that, at first there was a 2-hour warm-up for the DMMs to let them stabilize and *autozero* themselves. It is called preconditioning. After that 3 measurements were carried on for each of the DMM. At first, there was an offset measure, where all DMMs had their outputs short circuited. An average from 10-minute offset test was counted and later was used, as an offset fix by just being subtracted from each result of the test. Second measure was 10-minute measurement of 10 V reference voltage source (IRef M75), and an average from results of this test, with the offset fix subtracted, become a fix of a gain error on the positive side of a scale, in short, an *upfix*. Because *upfix* was measured only for the 10 V point of a range, rest of the ranges received the same fix proportionally to its range, for example: 2 V point is one fifth of the 10 V, so the upfix for this point is 20% of the *upfix* for the 10 V. But to do such thing there was a need to make an assumption that the nonlinearity error was significantly lower compared to the gain error, that's why it was skipped. The third test, was almost the same like second, the very same object was measured, but in an opposite polarization to count the gain error for the negative scale, in short, a *downfix*.

Table 1. The main parameters of used DMMs: 3458a and 2002.

		3458a	2002
Offset fix	µV	0,0	0,9
Upfix	µV	-2,4	96,3
Downfix	µV	0,8	-99,6
10 V uncertainty	V	26,5*10E-6	103*10E-6

5. CONCLUSION

Described application met its assumptions. If it were not for the calibrator controller, all the tests would have to be carried out by hand. Easy way to control program is easy enough for anyone to understand and conduct his own test using a batch file templates filled with given steps. All of these would increase efficiency of making DCCTs quality check, because of automatic tests with no need of supervision.

But there is still so much to develop. In the future, this application will be ported into ARM based single board computer to get rid of the laptop PC. This is considered mainly to get over the PC limitations in the cheapest way possible. This also reduces the cost of this system and allows to make parallel measurements with single board computers clusters. A good example of such SBC is a Raspberry PI. It has all needed ports, has a C# compiler for its platform, its cheap, it has all needed ports and it is highly customizable. There are also humidity and temperature measurements going to be added, because environmental conditions have an impact on measurements, and this would allow seeing how rapid and big changes are because of the temperature changes. The last but not least is to use a database based system to store the batch files, in order to be easily found and compared to the other ones. The text file system is good enough for now, but the more different tests are conducted, the more text files are going to be stored and this can be inconvenient.

6. ACKNOWLEDGMENT

The authors would like to express their special thanks to the CSEP Department of GSI Helmholtzzentrum für Schwerionenforschung GmbH, Darmstadt (Germany), especially to Andrzej Stafiniak, Ph.D., for the help in providing the final tests of the described system.

REFERENCES

[1] Bastos, M. C., “Calibration System Quick User’s Guide”, CERN, Geneva (2014).

[2] User’s and Service Manual I-REF2 CERN Portable Very High Precision 10 Volt & 10 mA Reference Source, Metron Designs Ltd., The Old Rectory, Alderford, Norwich, NR9 5NF, U. K. (2008).

[3] Bastos, M. C., “CDC Programming Manual”, CERN, Geneva (2014).

[4] Myhrvold, N., “Confessions of a cybershaman,” Slate, 12 June 1997, <http://www.slate.com/CriticalMass/97-06-12/CriticalMass.asp> (19 October 1997). Prologix GPIB-USB Controller User Manual, http://prologix.biz/do-wnloads/PrologixGpibUsbManual-6.0.pdf, (2003).

[5] Model 2002 Multimeter User’s Manual, Keithley Instruments, Inc, Cleveland, Ohio, U.S.A. Fourth Printing, (1999).

[6] 3458A Multimeter User’s Guide, Agilent Technologies, Inc, Loveland, USA, (2014).

Acoustic Sensor Optimization for SMART Technologies

Jakub Kolarik, Radek Martinek, Zdenek Slanina, Radana Kahankova and Lukas Danys

Department of Cybernetics and Biomedical Engineering, Faculty of Electrical Engineering and Computer Science, VSB – Technical University of Ostrava, 17. listopadu 15, 708 33 Ostrava, Czech Republic

ABSTRACT

From the vibration analysis generated by biological and mechanical systems, it is possible to determine whether there has been a fundamental change in their time or frequency domain. This analysis can provide information about the internal state of the system and its dynamics without the need for invasive intervention. In addition, the measured data can be used together with advanced signal processing algorithms (neural networks or machine learning) to create a predictive maintenance and diagnostic system. According to the measured data diagnostics, it will be possible to identify a defective component (e.g. a damaged bearing, loose part or worn belt), replace it and prevent possible system failure. This work describes a modular measuring device based on closed acoustic tube. Acoustic tube parameters are measured and optimized for use in remote monitoring, which is part of a project dealing with measurement of vital signs in magnetic resonance.

Keywords: SMART sensor, Acoustic tube, Vibration measuring

1. INTRODUCTION

In this work, the issue of vibration measurement and sound analysis was chosen as an area that has a fundamental impact on the diagnosis of biological and mechanical systems. This idea was based on demand on development of sophisticated sensor systems as part of initiative of SMART technologies and Industry 4.0 (see [1][2] and [3]). According to current trends, the classical concept of electromechanical sensors is in decline and multiple sensor systems based on light and optical methods (optical gates, image recognition, etc.) have been preferred. One of the benefits of this development is that the captured image information can be further used to virtually reconstruct the work environment, robotic vision, etc. However, these technological trends can often overlook the possible synergy of outdated technologies along with new advanced signal processing methods (adaptive algorithms, neural networks, and methods of artificial intelligence and others).

The paper is a follow-up to previous work, which aims to develop a modular sensor system. Sensor modularity would be accomplished using replaceable sensor modules. The task of these modules would be to transfer the measured processes, in the sense of a basic physical quantity converter, to an acoustic and pneumatic signal, detectable by a measuring microphone. For each modification of the sensor system, it is necessary to determine the requirements for the sensor device according to the dynamics of the measured events. These requirements include the desired sampling rate, A/D converter range, or pre-processing and signal filtering to prevent aliasing. As rapid prototyping technology, 3D printing is suitable for sensor module design. The specific print material will be selected according to the application requirements (e.g. according to the flexibility or temperature resistance of the material). One of the goals of this project is to be competitive with optical fiber technology, while keeping the sensor cost of manufacturing low.

2. DESCRIPTION OF THE ACUSTIC SENSOR

This chapter describes the measuring equipment hardware. The device prototype was developed primarily for biomedical purposes, more specifically for the measurement of fetal phonocardiography. Later, this measuring platform has found

Photonics Applications in Astronomy, Communications, Industry, and High-Energy Physics Experiments 2019, edited by Ryszard S. Romaniuk, Maciej Linczuk, Proc. of SPIE Vol. 11176, 111765R
© 2019 SPIE · CCC code: 0277-786X/19/$21 · doi: 10.1117/12.2536825

use in other fields of our research by development of different sensor modules. These sensing modules are developed for the following applications:

- Biomedical applications,
- industrial applications,
- traffic applications,
- smart city and housing,
- construction industry.

To date, several prototype sensor modules have been built for biomedical and industrial applications. These sensor prototypes are listed in chapter 3.

2.1 Concept of the acoustic sensor

The block diagram (see Figure 1) describes the modular hardware design of the designed prototype sensor system. The sensor system consists of three probes, a microprocessor unit, a communication interface and a battery system. The probes contain one of the sensor modules that are specifically designed for each of the application areas, namely biomedical applications (see Figure 2, left), industrial applications (see Figure 2, right) and others. Sensing modules have been designed to use a microphone to measure different non-electrical quantities. In addition to the microphone, the probe also includes a built-in filter and amplifier to ensure the highest Signal-to-Noise ratio (SNR). The built-in microprocessor provides Analog-to-Digital convertor (ADC) and communication peripherals.

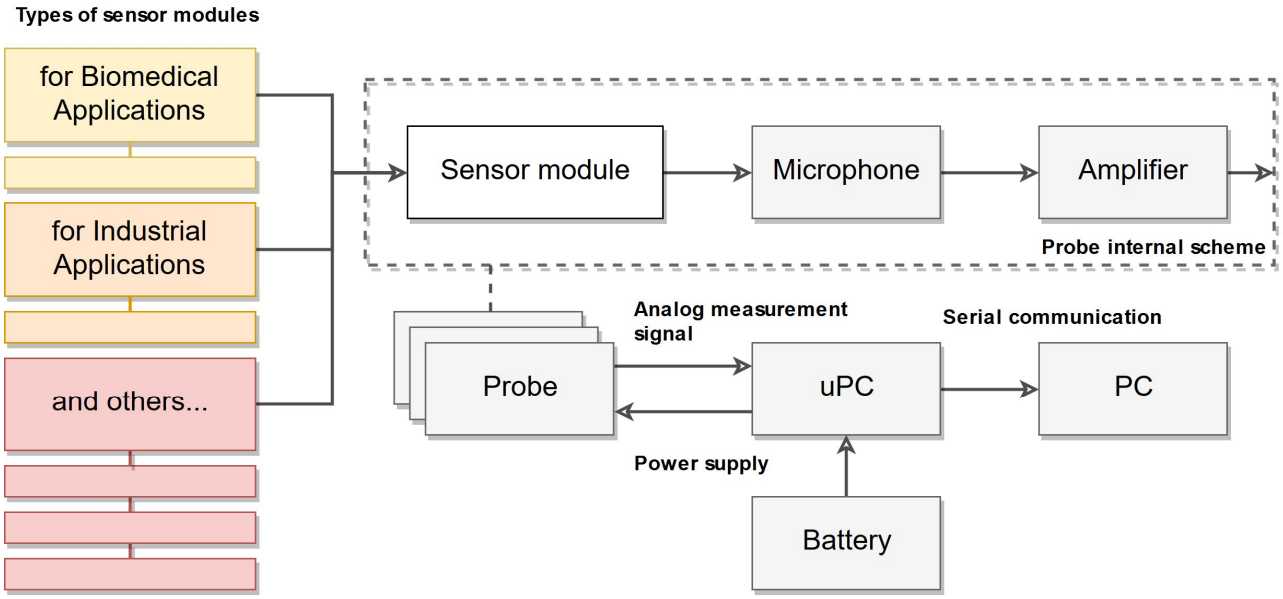

Figure 1. Block diagram of the acoustic sensor

2.2 Sensing system

The measuring system is based on a probe equipped with an electret microphone with a sensitivity of -50 ± 4 dB within a defined frequency range of 20 to 15 kHz. OPA172 Operational Amplifier is used to amplify the signal in the audible spectrum. The signal is amplified in the range of 16 to 20 kHz to provide signal resistance to induced interference, and also to maximize the efficiency of the ADC signal conversion.

Computing unit of measuring system consists of microcontroller STM32F373. The advantage of this microcontroller are three independent 16-bit sigma-delta analog-to-digital converters that are internally synchronized. After the desired use of the prototype sensor system, a sampling rate of 5 kHz was selected to prevent aliasing for accurate sensing of cardiac activity.

3. APPLICATION AREAS

This chapter describes the selection of signal measurement areas. Following the previously solved problems of analysis of mechanical and biological processes, the measurement of vital functions was chosen, namely the cardiac and respiratory cycle. To measure these vital signs, a measurement module adapted for measuring phonocardiography (PCG) and balistocardiography (BCG) will be used.

Several promising directions for sensor development have been defined in the prior art research group [4][5][6]. The first interesting area is non-invasive monitoring of the fetal heart cycle [7]. Another one of the interesting methods is the measurement of vital signs within magnetic resonance. When designing module for usage in magnetic resonance, the presence of strong interference must be taken into account. This fact limits the design of the vital function sensor, as it must not be constructed of metallic material. Another limitation of magnetic resonance measurement is strong acoustic interference in addition to induced currents [8].

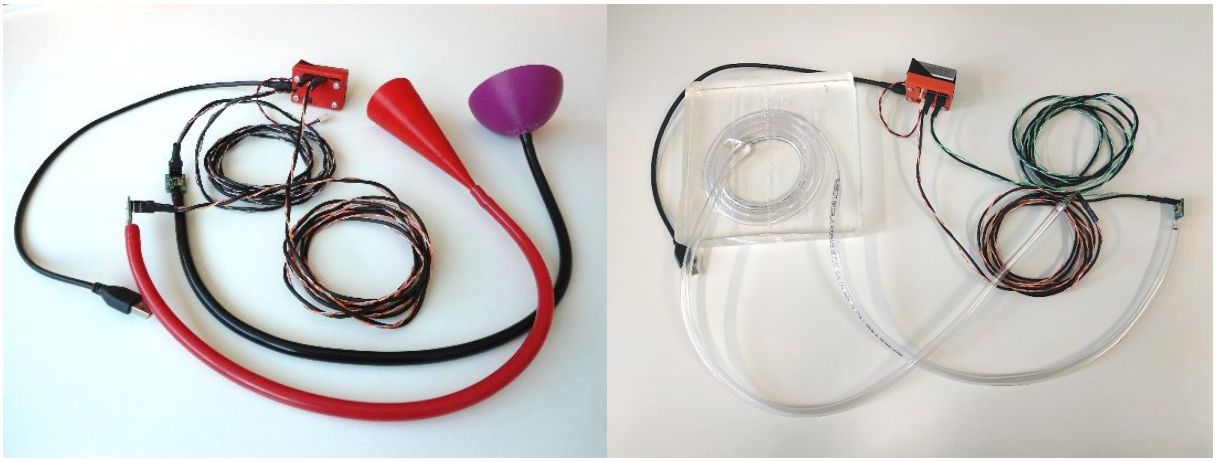

Figure 2. Sensor system for biomedical (Left image) and industrial application (Right image)

As stated at the beginning of the document, vibration measurement in industrial applications can have a major impact on predictive maintenance [9] and accident prevention, see [10]. Recent findings in science and research suggest that acoustic sensors (analysis of acoustic disturbances [11], predictive maintenance of engines and rotary machines [12], detection of defects in serial production based on natural frequency [13]) are very promising in terms of application of technology as predictive maintenance.

Advanced acoustic data processing also has a place in the transport sector and SMART city concept. Sensor acoustic data can be used for traffic classification and analysis [14]. These systems can analyze the acoustic performance of vehicles to determine their speed (see [15]), number or type of vehicles [16]. This information can be useful for traffic load analysis, detour scheduling and coastal rescue optimization. Another useful feature is the detection and classification of events such as traffic accidents [14] or exceeding noise limits [17].

4. EVALUATION OF ACUSTIC SYSTEM

In this chapter, the effects on the acoustic tube will be discussed. The acoustic system will be subjected to a measurement to determine the level of intrusion into the closed acoustic measurement system. The first issue will be a survey of the effect of acoustic interference on the measuring system. This effect occurs when the acoustic wave of the interfering signal (motor, moving machine, speech e.g.) penetrates inside the acoustic tube. When the acoustic wave passes between different density materials (air and tube material in our case), the sound wave is distributed (see Figure 3). The wave energy is then divided between the pervading wave, the absorbed wave, and the reflected wave. This phenomenon is dependent on the surface, internal structure, material and frequency of the sound wave.

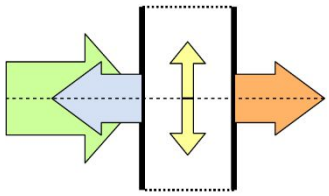

Figure 3. Separation of energy during the impact of a sound wave; green - incident wave, blue - reflected wave, yellow - absorbed wave, orange - pervading wave

Due to the requirement for the measuring system's resistance to ambient noise, an experiment was conducted to measure the damping of the closed sound line between the sensor module and the measurement microphone. The measurement used a sweep signal with a frequency range of 0 - 1 kHz for 10 seconds with a logarithmic frequency distribution. This sweep signal acted on the reference and measuring microphone, which was placed in an acoustically closed tube (microphone on one side and blank on the other). A loudspeaker with built-in tweeter and woofer was used to reproduce the signal (see Figure 4).

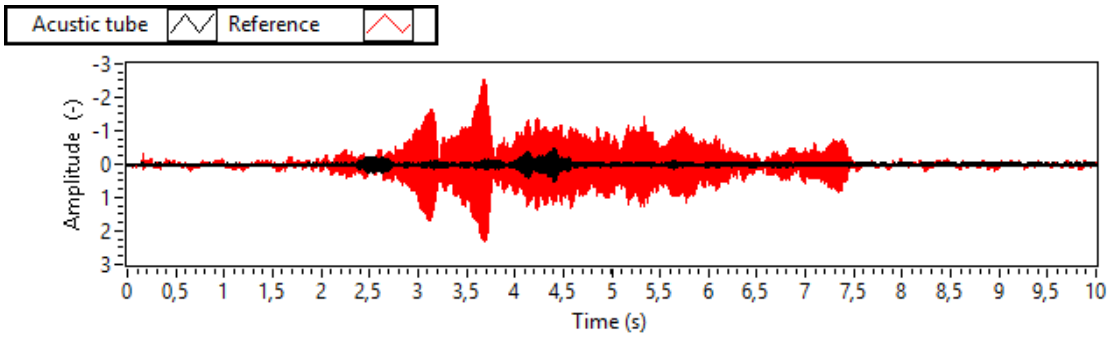

Figure 4. Signal measured inside tube (Acoustic tube) and outside (Reference) of the acoustic system in time domain

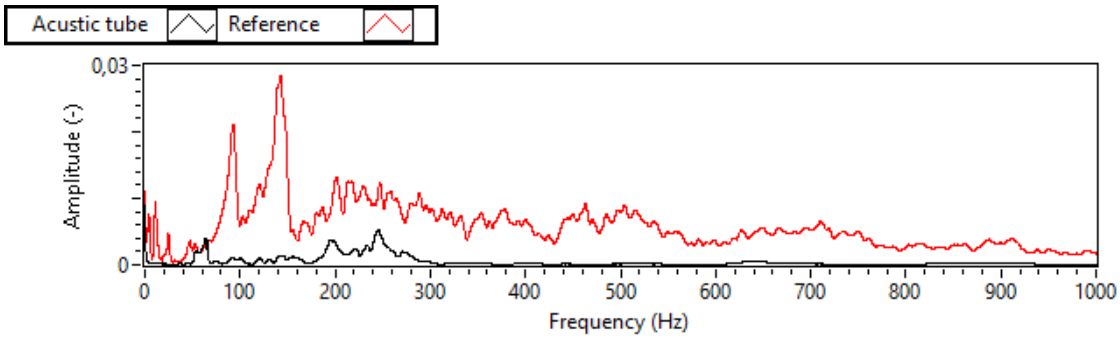

Figure 5. Signal measured inside tube (Acoustic tube) and outside (Reference) of the acoustic system in frequency domain

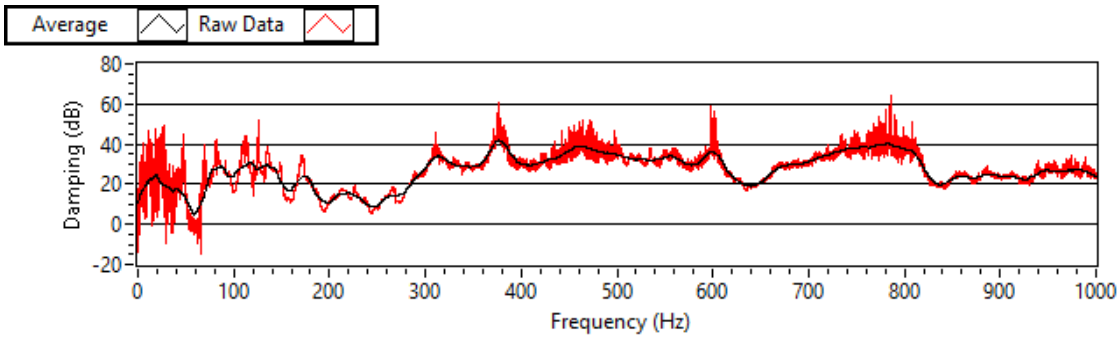

Figure 6. Difference in frequency domain on the opposite ends of the acoustic tube

Acoustic attenuation measurement confirmed the original assumption that this system is resistant to vibration. Furthermore, the measurement showed the system's sensitivity to vibrations transmitted by contact with the substrate or the material surrounding the measuring medium. The damping was measured using identical microphones inside and outside the measuring medium, and typically ranged from 20 to 40 dB (signals spectrum Figure 5 and tube dumping Figure 6). Airborne interference, such as speech or sounds produced as a by-product of electrical equipment and machinery (magnetic resonance, frequency converters, switched power supplies e.g.), has a negligible impact on this measuring system. This is due to the transmission of sound waves, vibrations, between materials of different density and the consequent attenuation of the sound wave energy due to the passage through this interface.

4.1 Distortion of the transmitted signal

Another phenomenon investigated will be the distortion of the signal for transmission through the acoustic tube. For this measurement, a modification of the sensor module for vital functions monitoring with two microphones was used. The first microphone was connected directly to the measuring sensor, and the other was connected through 20 meters of acoustic tube. Thirty minutes of recordings were measured and processed. An example of one of these signals is shown in Figures 7 for the time domain and Figure 8 for the spectral domain. As can be seen, the measured signal has not been substantially distorted in the frequency domain (see Figure 7). In contrast, a time delay was added in the time domain due to the limited propagation rate of the acoustic wave within the line (see Figure 8).

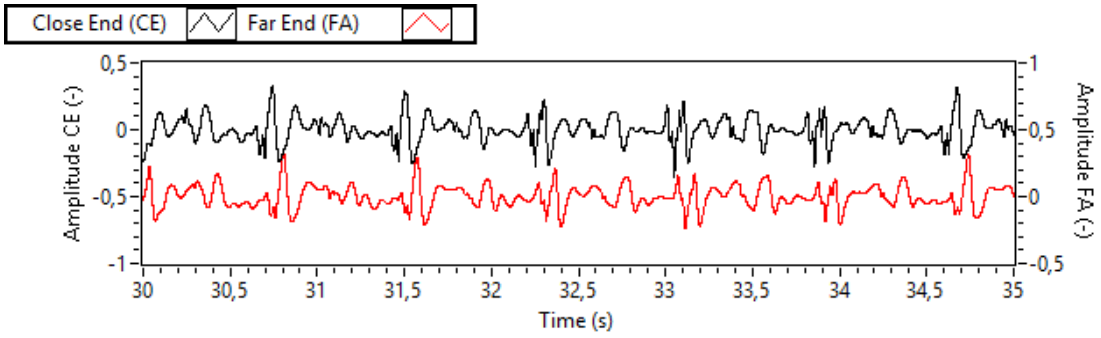

Figure 7. Hearth sound on close end (CE) and far end (FE) of the acoustic system in time domain

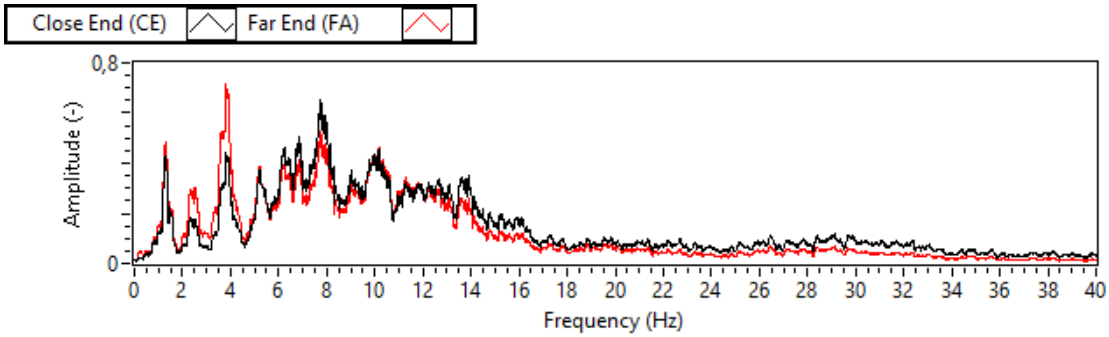

Figure 8. Hearth sound on close end (CE) and far end (FE) of the acoustic system in frequency domain

An additional measurement was made to determine the change in the delay variation over the acoustic tube length. The measurement started with acoustic tube by length of 10m, which was gradually shortened. The delay function of the wave in the acoustic tube was typically linear about 3.196 milliseconds, with sharp declination and nonlinearity in the range from 0 to 2 m. The computed speed of propagation was calculated as 312.92 ms^{-1}, contrary to typical speed of sound around 346.13 ms^{-1} for temperature 25°C.

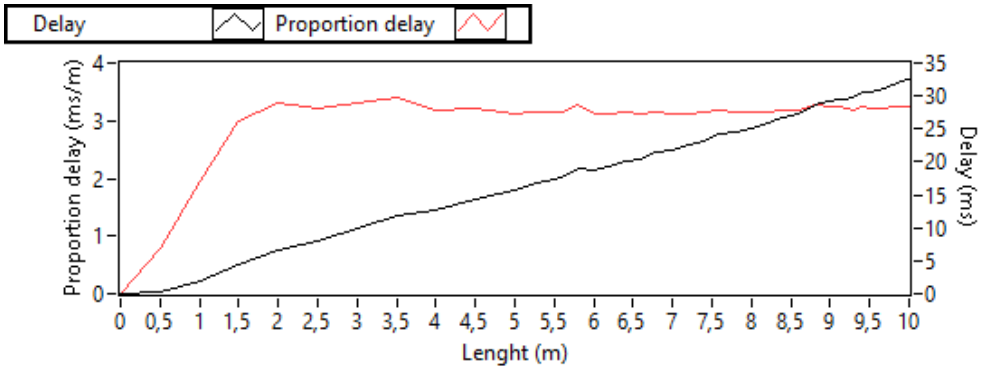

Figure 9. Dependence of time delay on acoustic tube length (Delay) and computed time delay on meter (Proportional delay)

Another interesting finding is the difference in amplitude reading at low frequencies. The signal at the far end of the acoustic tube is paradoxically amplified by up to 5dB than at the close end (see Figure 10). Other essential components of the heart sound spectrum (5-50Hz) are damped in the range of 0-5dB.

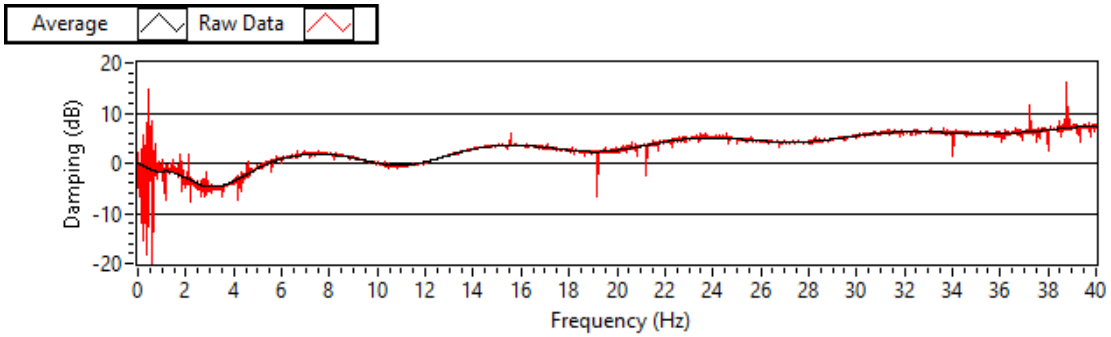

Figure 10. Difference in frequency domain on the opposite ends of the acoustic tube

5. CONCLUSION

Modern SMART sensors are the primary source of information for all downstream technologies. At present, it can be observed that sensors are becoming an essential element of a number of key concepts such as Intelligent Buildings, Intelligent City, Industry 4.0, Intelligent Home, Intelligent Networks, Intelligent Measurement, Internet of Things, Industrial Internet of Things, etc. Nowadays, the emphasis is on the cheapest but most robust solution to meet the requirements for durability, credibility and repeatability of measured data. In terms of implementability, the cost of deploying sensors within each of the concepts and technologies discussed above will also play a very important role. Obviously, for the widespread use of modern intelligent technologies in common practice, it will be necessary to apply advanced methods of signal processing at the lowest sensory layer.

To optimize the acoustic system of a modular measuring system, a particular application area from the biomedical field was chosen. The device was adapted for remote monitoring of cardiac activity. Acoustic conduction has proven its immunity to interference by acoustic interference and has retained the shape of the transmitted signal. The transmitted acoustic signal contained a time delay corresponding to the line length (in our case it was about 32,42 milliseconds). The key to the further development of this work will improve the sensitivity, noise reduction, acquisition of new information and extend the possible uses. A possible disadvantage of acoustic heart monitoring is the instability of the shape of the heart curve (which is dependent on the location of the probe). Compared to a standard ECG signal where the individual phases of the cardiac cycle are readily recognizable, multiple peaks during the S1 signal may cause a measurement error. However, this problem can be solved by using algorithms that include predictive elements when looking at the total energy or shape of previous S1 signals.

At the moment, we are also working on variations of the sensing module for measuring the speed of traffic, seismic activity and magnetic resonance imaging triggering.

ACKNOWLEDGMENTS

This article was supported by the Ministry of Education of the Czech Republic (Project No. SP2019/85). This work was supported by the European Regional Development Fund in the Research Centre of Advanced Mechatronic Systems project, project number CZ.02.1.01/0.0/0.0/16 019/0000867 within the Operational Programme Research, Development and Education. This work was supported by the European Regional Development Fund in A Research Platform focused on Industry 4.0 and Robotics in Ostrava project, CZ.02.1.01/0.0/0.0/17 049/0008425 within the Operational Programme Research, Development and Education.

This work was supported by the project SP2019/107, „Development of algorithms and systems for control, measurement and safety applications V" of Student Grant System, VSB-TU Ostrava.

REFERENCES

[1] Otahalova, T., Slanina, Z., and Vala, D., "Embedded sensors system for real time biomedical data acquisition and analysis", IFAC Proceedings Volumes (IFAC-PapersOnline) 11(part 1), 261-264 (2012).

[2] Nudzikova, P. and Slanina, Z., "User identification by biometric methods", Advances in Intelligent Systems and Computing 423, 181-190 (2016).

[3] Walendziuk, W., Sawicki, A. Telemetric measurement system of beehive environment conditions. Proceedings of SPIE - The International Society for Optical Engineering, 9290, art. no. 92901G, 2017. DOI: 10.1117/12.2073050

[4] Kolarik, J., Golembiovsky, M., Docekal, T., Kahankova, R., Martinek, R., & Prauzek, M., "A Low-cost Device for Fetal Heart Rate Measurement". *IFAC-PapersOnLine*, *51*(6), 426-431. (2018)

[5] Kolarik, J., Soustek, L., & Martinek, R., "Examination and Optimization of the Fetal Heart Rate Monitor: Evaluation of the effect influencing the measuring system of the Fetal Heart Rate Monitor". In *2018 IEEE 20th International Conference on e-Health Networking, Applications and Services (Healthcom)* (pp. 1-4). IEEE. (2018, September)

[6] R. Martinek, J. Brablik, L. Soustek, J. Kolarik, M. Fajkus, J. Nedoma, R. Kahankova, "A comparison of probes based on Bragg grating sensor and microphones for heart sounds measurement," Proc. SPIE 10801, Optical Materials and Biomaterials in Security and Defence Systems Technology XV, 108010G (8 October 2018)

[7] Rene Jaros, Radana Kahankova, Radek Martinek, Jan Nedoma, Marcel Fajkus, and Zdenek Slanina, "Fetal Phonocardiography Signal Processing from Abdominal Records by Non-Adaptive Methods", Proc. SPIE, Photonics Applications in Astronomy, Communications, Industry, and High-Energy Physics Experiments 2018, (2018).

[8] Amaro Jr, E., Williams, S. C., Shergill, S. S., Fu, C. H., MacSweeney, M., Picchioni, M. M., ... & McGuire, P. K. "Acoustic noise and functional magnetic resonance imaging: current strategies and future prospects". Journal of Magnetic Resonance Imaging: An Official Journal of the International Society for Magnetic Resonance in Medicine, 16(5), 497-510. (2002)

[9] Lee, J., Bagheri, B., & Kao, H. A. "A cyber-physical systems architecture for industry 4.0-based manufacturing systems". Manufacturing letters, 3, 18-23. (2015).

[10] Canito, A., Fernandes, M., Conceição, L., Praça, I., Santos, M., Rato, R., ... & Marreiros, G. "An architecture for proactive maintenance in the machinery industry". In International Symposium on Ambient Intelligence (pp. 254-262). Springer, Cham. (2017, June).

[11] Liao, Z., & Axinte, D. A. "On monitoring chip formation, penetration depth and cutting malfunctions in bone micro-drilling via acoustic emission". Journal of Materials Processing Technology, 229, 82-93. (2016)

[12] Lee, J., Kao, H. A., & Yang, S. "Service innovation and smart analytics for industry 4.0 and big data environment". Procedia Cirp, 16, 3-8. (2014)

[13] Van Tittelboom, K., De Belie, N., Lehmann, F., & Grosse, C. U. “Acoustic emission analysis for the quantification of autonomous crack healing in concrete”. Construction and Building Materials, 28(1), 333-341. (2012)

[14] Salamon, J., Jacoby, C., & Bello, J. P. “A dataset and taxonomy for urban sound research”. In Proceedings of the 22nd ACM international conference on Multimedia (pp. 1041-1044). ACM. (2014, November)

[15] Forssén, J., Kaczmarek, T., Alvarsson, J., Lundén, P., & Nilsson, M. E. “Auralization of traffic noise within the LISTEN project—Preliminary results for passenger car pass-by”. Euronoise 2009. (2009)

[16] Munich, M. E. “Bayesian subspace methods for acoustic signature recognition of vehicles”. In 2004 12th European signal processing conference (pp. 2107-2110). IEEE. (2004, September)

[17] Maisonneuve, N., Stevens, M., Niessen, M. E., Hanappe, P., & Steels, L. “Citizen noise pollution monitoring.” In Proceedings of the 10th Annual International Conference on Digital Government Research: Social Networks: Making Connections between Citizens, Data and Government (pp. 96-103). Digital Government Society of North America. (2009, May)

Comparative analysis of packet scheduling algorithms in IPv4 and IPv6 networks

Daniel Sawicki*[a], Jakub Słowik[b]
[a]Lublin University of Technology, 38A Nadbystrzycka Str, Lublin, Poland 20-618; [b]Second year computer science 2nd degree student, Lublin University of Technology, 38A Nadbystrzycka Str, Lublin, Poland 20-618

ABSTRACT

This paper focuses on researching and visualizing the differences of the quality of network connections between several network applications using popular scheduling algorithms. The aim of this work is to examine and compare the impact of application of scheduling algorithms for FIFO, DWRR, WFQ, PQ packets in IPv4 and IPv6 networks on the quality of data transmission. Using Riverbed Modeler Academic Edition version 17.5 software there was developed 10 research scenarios with different scheduling algorithms and IP protocols implemented on routers. Scenarios based on IP protocols in the fourth and sixth versions with implemented FIFO, PQ, DWRR and WFQ scheduling algorithms has been developed. Each scenario includes the operation of real-time VoIP and video conferencing applications as well as HTTP, FTP and e-mail applications. The research showed that there are significant differences in the quality of packet transmission of the tested applications using different configurations of the scheduling algorithms and network protocols.

Keywords: scheduling algorithms, IPv4, IPv6, quality of service, multimedia transmission, performance

1. INTRODUCTION

The quality of internet services is an important issue in terms of broadly understood internet communication. The increase in network traffic, forecast for 2019 2021, clearly shows that the lack of actions towards its regulation will cause a drop in the quality of services most susceptible to delays or various types of disruptions, such as real-time services such as internet telephony (VoIP), internet radio or live video broadcasts[1]. To prevent this problem, packet prioritization is used. Many algorithms (and their modifications) determine which packets have priority during data transmission and packet transmission quality which should be paid for packages with higher priority. Properly configured service (QoS. Quality of Service) allows for improvement in the transmission of one data stream, without significantly affecting the quality of other connections[2].

2. TRANSMISSION AND QOS

Communication in contemporary, extensive computer networks based on the OSI model is carried out by transferring small portions of data called packets. In addition to frames and segments, as the only all protocols data units (PDU), they are able to overcome the route on which routers are located, creating a complicated network of connections called the Internet. The speed and efficiency of packets transmitted via the network mainly affect the quality of connections.

The OSI reference model developed by the International Standards Organization was the first attempt at international standardization of protocols. The next was the four-layer TCP / IP model, which is currently in use[3].

The process of Encapsulation, preparation of data to be sent by the transmission medium, runs from the layer of the highest TCP / IP model, application, to the lowest layer, access to the medium. During this process, data headers and trailers of transport, network, and data link layers are added to the data generated by the applications. Portions of data are packed sequentially into segments, packets and frames ready to be sent by the transmission medium in the form of bits. Receiving sent data is carried out in a decapsulation process that includes previously added headers and trailers from the lowest layer to the top layer[3].

The TCP/IP reference model uses two addressing schemas for IPv4 and IPv6 devices. The IPv4 packet header consists of a fixed portion of 20 bytes long and part of the optional length of zero or more words. It is divided into fields defining the behavior of the packet in the network[4].

*d.sawicki@pollub.pl

Photonics Applications in Astronomy, Communications, Industry, and High-Energy Physics Experiments 2019, edited by Ryszard S. Romaniuk, Maciej Linczuk, Proc. of SPIE Vol. 11176, 111765S
© 2019 SPIE · CCC code: 0277-786X/19/$21 · doi: 10.1117/12.2536846

At today's pace of Internet development and the growing popularity of the Internet Things concept (IoT), the number of available addresses is insufficient. It is estimated that in 2020, 25 to 50 billion devices will be connected to the network[4]. The implementation of the IPv6 protocol systematically eliminates the problem of insufficient number of addresses, whose 128 bit structure allows to determine them 1028 times more than IPv4 addresses. This is the most important difference between the described versions of the IP protocol[5]. Such a large number of addresses should cover the demand of the growing Internet for many years.

The size of the IPv6 header is twice the size of the fixed IPv4 header portion. However, the construction of the IPv6 header is less complicated. In 40 bytes contained there are 8 fields, of which the majority of header volumes are 128-bit addresses, source and destination[5].

Network transmissions are divided into two types: connection and connectionless. Connection transmissions establish a session (logical connection) between two hosts. The TCP protocol uses three-way handshaking, which results in retransmits of incorrect data (all segments must reach the destination) and their order is maintained.The UDP protocol supports connectionless connections in which lost segments are not retransmitted and received in the order in which they were sent. There is no connection established before the datagram transmission[6].

The transport layer protocol, which is used most often for real-time data (audio, video), is RTP (Real Time Protocol). It was defined in the RFC 1889 document. The protocol was improved in 2003 and described in the RFC 3550. The segment with the RTP protocol header is encapsulated with the UDP protocol header allowing for effective communication and multimedia delivery, despite the fact that it does not guarantee the quality of services. TCP protocol cannot be used for this purpose, because all actions related to establishing and maintaining connections limit the possibilities of fast transmission and immediate responses. Real-time transmissions also do not need retransmission of lost packets because the retransmitted packet in streaming media becomes the expired. The basic functions of the RTP protocol are: multiplexing of multiple real-time flows to one UDP stream, detection of lost packets by their subsequent numbering and provides information on coding of transmitted data. It supports both unicast and multicast connections[7,8.]

Based on the client-server architecture, FTP (File Transfer Protocol) was created. It has been widely used before the increase in the popularity of the WWW (World Wide Web). Nevertheless, it is still used because of the simplicity of its use and configuration. It allows for two-way file transfer, file management and shared folders on the server, as well as for access to files through the ability to create user accounts and authorize connections. FTP protocol support is provided by two TCP connections. The FTP server can work in two modes. In active mode, one of the connections is responsible for file transfer (port 20) and the other for transferring control commands (port 21), which are responsible for the functionality of the FTP server. Passive mode allows you to change the data port to a port other than 20, usually above 1024. Thanks to this problematic network firewalls will not be so burdensome for the client[9].

Like the FTP protocol, the HTTP protocol is based on the transfer of files according to the assumptions of the client-server architecture. The difference is that data transfer is carried out with the same connection as is used for query transmission. Thanks to the universality of the HTTP protocol, queries are standardized and supported by websites servers. Such a query consists of a header containing an HTTP method, a URI (Uniform Resource Identifiers) address, and an HTTP protocol version. Immediately following the header, additional headers may be placed informing about another location of the requested resource, used to serve cookies or informing about the type and amount of data transferred. Behind the header is the body of the query containing the data sent by the client, e.g. the content of the completed HTML form. The HTTP request is coded using ASCII characters[10].

Each of the Internet services is characterized by a certain stringency of the quality of service connection. Data flow from source to destination may be affected at four levels: bandwidth, delay, jitter and loss. Ensuring a predictable quality of services, related to a greater or lesser extent with given parameters, is called QoS (Quality of Service)[11-14]. To achieve this purpose, a lot of technology, the use of which reduces the negative effects of disturbances, overloads and fluctuations.

The research conducted in this work is based on the implementation of QoS mechanisms in the third layer of the OSI model. In the proposed computer network model, all decisions regarding the prioritization of packages are made by routers.

3. TESTBED

To study the differences and comparison of scheduling algorithms for IPv4 and IPv6, a computer network topology

model was created in Riverbed Modeler Academic Edition 17.5 previously known as OPNET Modeler. It is the leading software in the field of modeling, simulation and analysis of computer networks. Creating computer network models in the simulator used consists of placing own or predefined models of workstations, servers, routers, etc. on the network plan and combining them with your own or predefined connection models. There are over 3000 different models of nodes, links and solutions found in modern computer networks available to the user.
The research was carried out on a computer with the following parameters: Intel Core i5-3230M 2.60 GHz processor, 4 GB RAM, integrated Intel HD Graphics 4000 graphics, motherboard compatible with Dell Latitude E6430 notebook computer, Windows 8.1 64-bit operating system.
Bearing in mind the license restrictions of the Riverbed simulator described above, the network topology model shown in Fig. 1 was created. including: two routers (model: ethernet4_slip8_gtwy), five switches (model: ethernet16_switch) - two main and three for the network of HTTP, FTP and e-mail clients, 10 for each of the above client workstation protocols (model: ethernet_wkstn), three VoIP customers (model: ethernet_wkstn), FTP, HTTP, email and VoIP server (model: ethernet_server), one pair of clients establishing video communication (model: ethernet_wkstn), link between routers A and B with a maximum bandwidth of 4 Mb / s (modified PPP model for simulation), connections between other devices with a bandwidth of 100 Mb / s (model: 100BaseT).
Limiting the main link between client stations and servers up to 4 Mb / s allows you to observe the behavior of packets in an overloaded network and also allows you to collect enough results with limited possibilities of the academic version of the Riverbed application.

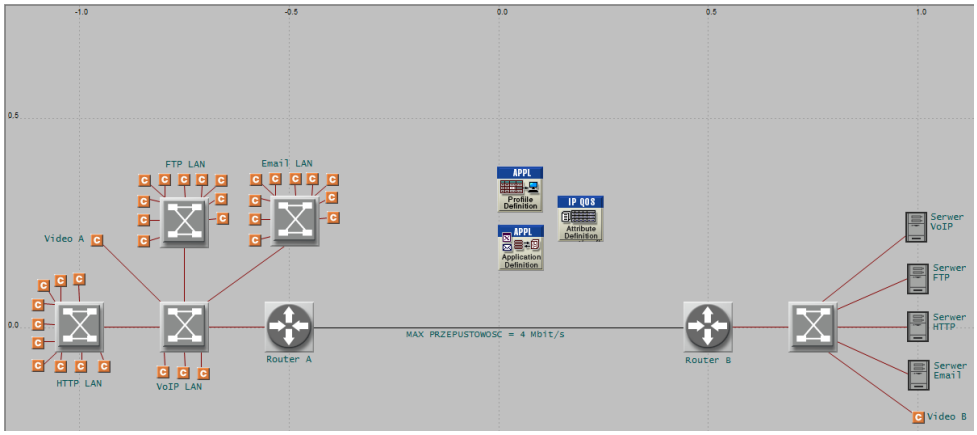

Figure 1. Testbed diagram.

4. RESULTS

Based on the topology presented above, 10 scenarios have been prepared that can collect the simulation results of the IPv4 and IPv6 networks with implemented on the interfaces connecting routers using the FIFO, PQ, DWRR and WFQ scheduling algorithms. Two scenarios are responsible for simulating network operation without implemented scheduling algorithms. Router priorities can be used by 98% of bandwidth. The Maximum Reserved Bandwidth attribute is responsible for this. The configuration of the prioritization algorithms is as follows. Queue buffers in the FIFO algorithm scenario can hold up to 500 packets. The WFQ algorithm buffer holds 1000 packets and its individual queues of 500 packages. The scales of five defined DWRR and WFQ queues have the values 5, 10, 20, 50, 100 which are assigned successively to traffic classes CS0 (FTP), CS1 (e-mail), CS2 (HTTP), CS3 (video conference) and CS4 (VoIP)). The queue priorities of the PQ algorithm are consistent with the above-mentioned values of the differentiated service fields. Queues of the PQ algorithm, in order from the highest to the lowest priority, contain: 20, 40, 60, 80 and 100 packets. All queues of the DWRR algorithm contain 500 packages.

During the simulation process, the following data is collected, based on which a comparative analysis will be made: FTP server response time, time to wait for the web page to load, time to wait for individual objects to load on the website, the response time of the email server, delay and fluctuation values of VoIP packet delays and videoconferences, the amount of data sent and received for individual protocols, routing CPU load, time to queue packets on the main link, percentage use of the main link, the number of rejected packages by individual routers, the amount of data transferred through links between routers and main switches.

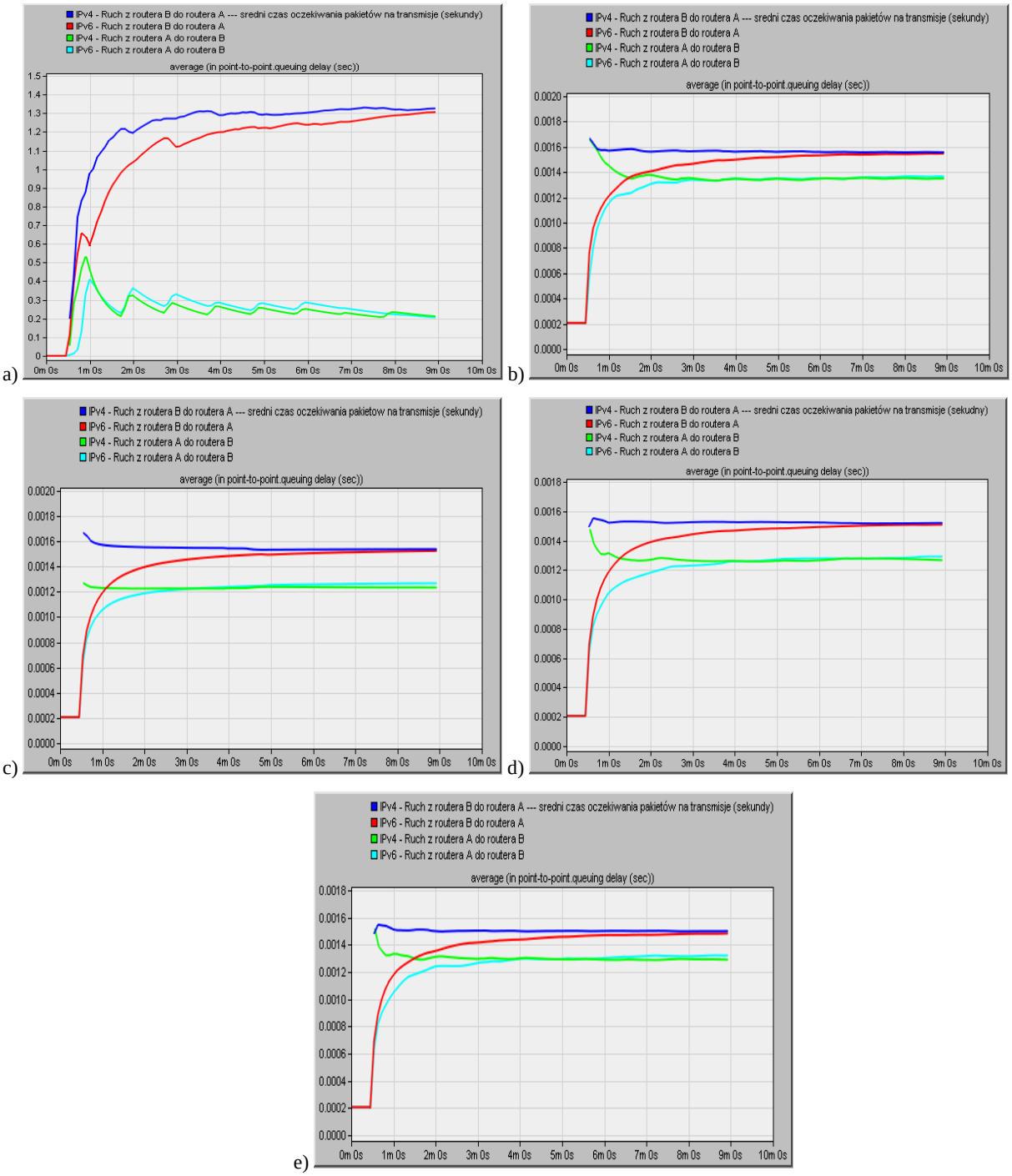

Figure 2. The average queuing time of packets on the main link with the algorithm used a)no scheduling, b)FIFO, c)PQ, d)DWRR, e)WFQ.

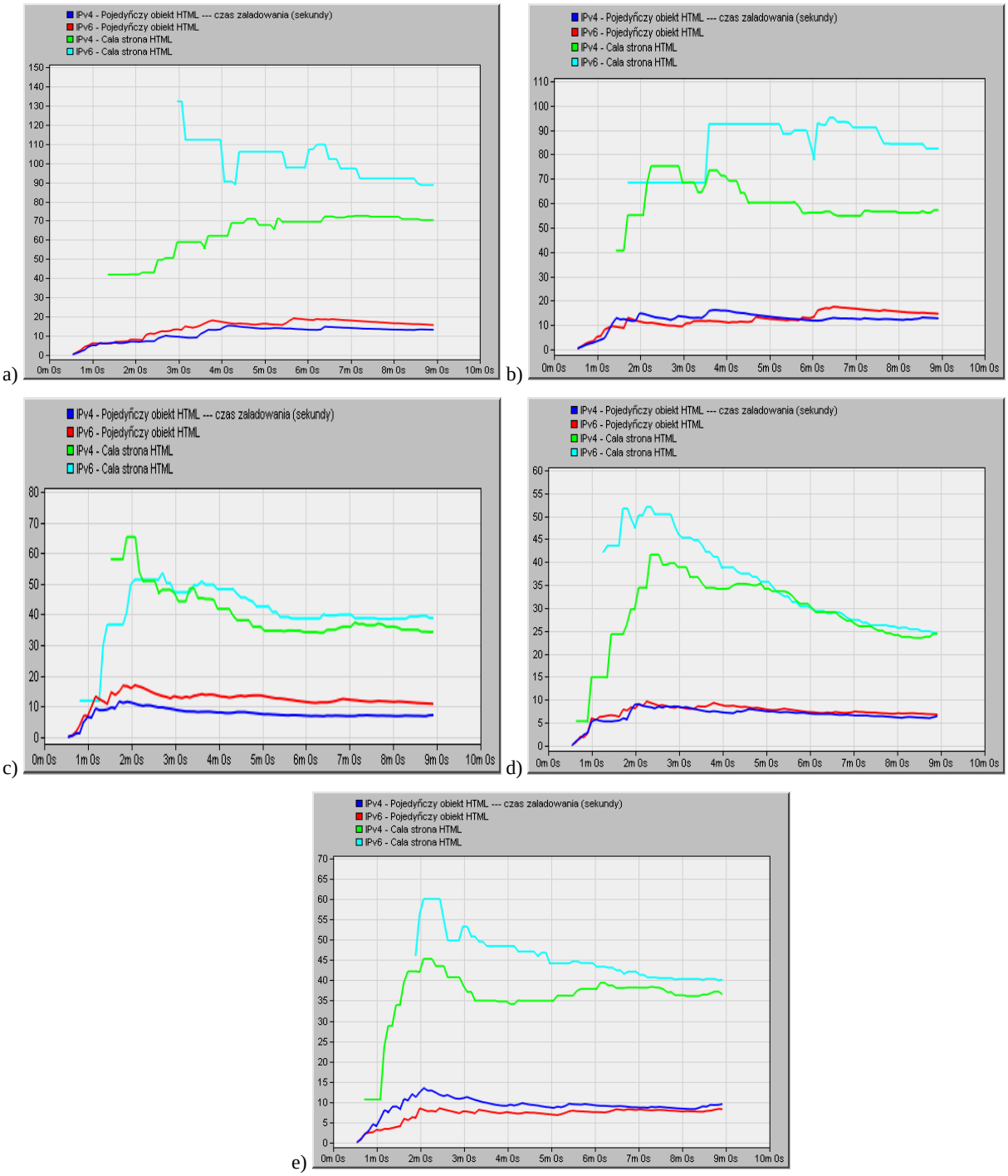

Figure 3. The average load time of page objects and entire HTML pages with the algorithm used a)no scheduling, b)FIFO, c)PQ, d)DWRR, e)WFQ.

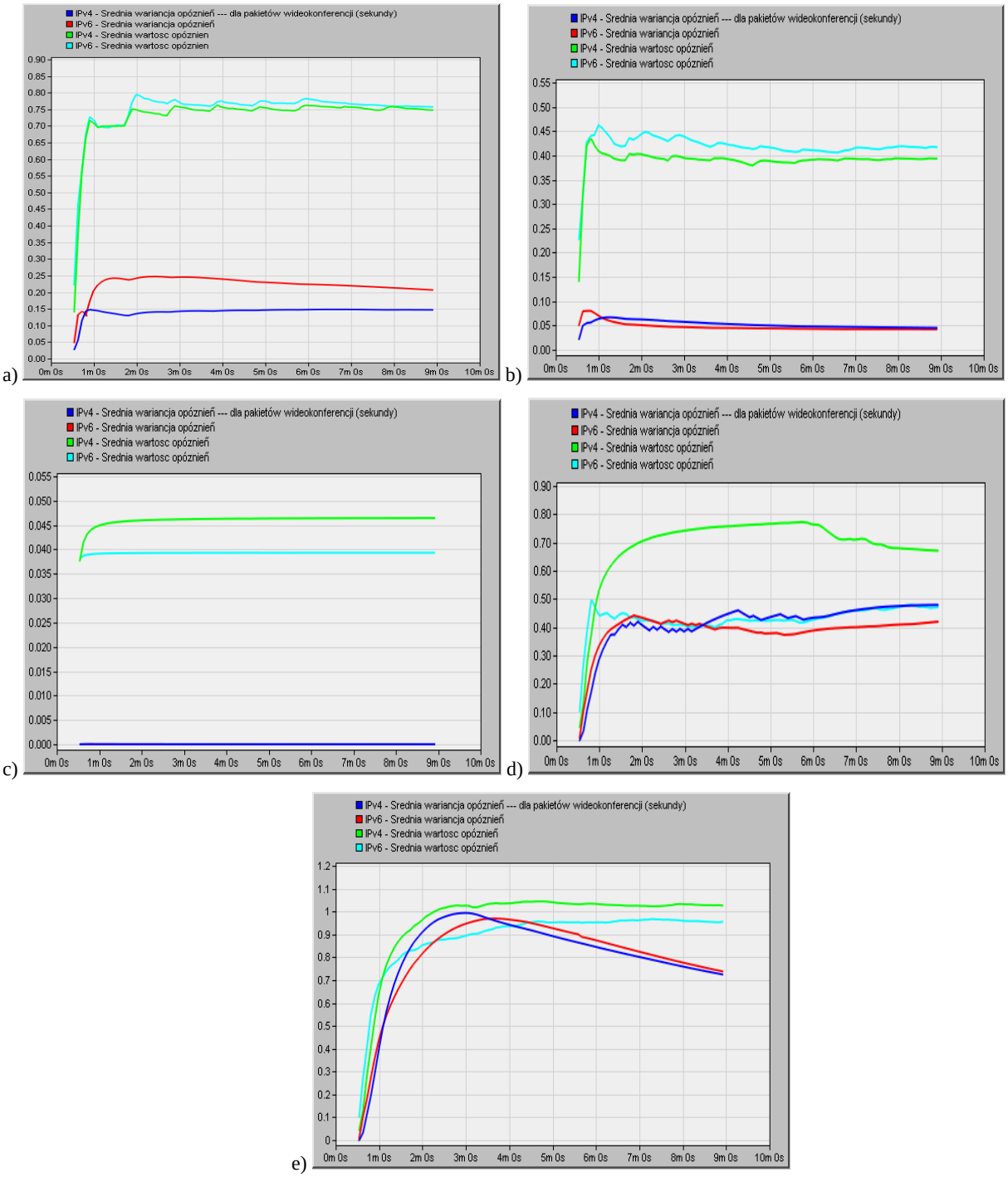

Figure 4. The average value and the variance of the video conferencing delay with the algorithm used a)no scheduling, b)FIFO, c)PQ, d)DWRR, e)WFQ.

In Fig. 2 presents the average queuing time of packets on the main link. The average time (Fig. 2a) of packet waiting for transmission towards the client network at the level of 1.3 seconds indicates overload of the link and the average IPv4 packet queuing time in this direction is higher by approximately 100 ms. In the opposite direction, the average queuing time for the IPv4 protocol is about 200 ms and for IPv6 it is 150 ms. Periodic latency fluctuations are also noticeable. In the Fig. 2b the average queuing time of packets in the first two minutes of simulation time is lower for the network based

on the IPv6 protocol (up to 0.5 ms). At the later stage of the simulation, the results become equal. On Fig. 2c differences in average packet waiting time for transmission with the previously described algorithm are insignificant (less than 0.1 ms). In the direction from the client to the server network, IPv6 packets are queued slightly longer (difference below 0.1 ms). IPv4 packets wait longer in the opposite direction with a difference similar to IPv6 packets. The average queuing times for packet routers, shown in Fig. 2d, are close to the times of the FIFO and PQ algorithms and are about 1.4 ms. Packet queuing times, illustrated in Fig. 2e, are similar to the results of research on previous algorithms.

The waiting time for loading the website is high (Fig. 3a). Despite similar average time to load each object on the side of the average time to load the whole page for IPv4 is 70 seconds and for IPv6 is 90 seconds. Such delays prevent a comfortable user's work. In Fig. 3b the IPv4 protocol in this case also has an advantage which confirms the difference in the average page load time of 24 seconds. An IPv6 network generates more data related to the HTTP protocol, but the amount received is lower. HTTP application packets in Fig. 3c reach recipients faster (the entire web page is loaded 21 seconds faster for IPv4 and 44 seconds faster for IPv6) than for the FIFO algorithm. Of all the scenarios described so far, the DWRR algorithm (Fig. 3d) provides the lowest average waiting time for HTML pages (about 25 seconds for IPv4 and IPv6) and their individual objects (about 6 seconds for IPv4 and IPv6). The delays shown in Fig. 3e are about 10 seconds higher for IPv4 and about 15 seconds for IPv6.

The average delay value (Fig. 4a) of 750 means that the connection is of poor quality. This is also confirmed by the variance of 150 ms for the IPv4 protocol and 200 ms for the IPv6 protocol. Fig. 4b shows that the average delay time in video conferencing in the IPv6 network is higher (about 25 ms), however, their variance is slightly lower than the network based on the IPv4 protocol by approx. 5 milliseconds. Delays at 400 milliseconds do not allow for comfortable communication. Overlapping graphs of data sent and received (Fig. 3c) confirm low delays. The IPv6 protocol in this case better deals with real-time transmission. In Fig.4d can be observed during the progressive discrepancy between the amount of data sent and received on the video conferencing carried out. The greater amount of data received for the IPv4 protocol may indicate a lower loss of packets of this protocol compared to IPv6. The Fig. 4e shows that more data has been received on the IPv4 network. As in the case of the DWRR algorithm, there is a discrepancy in the diagrams.

The FTP application, in which the priority of packet transfer is the lowest, in class algorithms (PQ, WFQ, DWRR), is characterized by the highest latencies, up to 250 seconds. Table 6.6 presents the average response time per request for sending and receiving files for all scenarios examined. For scenarios based on the PQ algorithm, a small number of responses, and in the case of IPv6-based networks, the lack of response caused by the large number of rejected packets indicates very low quality of FTP connections.

Table 1. Comparison of the results of the FTP application.

Scenario	The average time delay response to a request to send the file [ms]	Average response delay time on request to receive a file [ms]
IPv4 FIFO	25258	34859
IPv6 FIFO	27812	43366
IPv4 PQ	37474	26398
IPv6 PQ	---	---
IPv4 DWRR	111104	207412
IPv6 DWRR	123132	251821
IPv4 WFQ	71053	221592
IPv6 WFQ	51767	245493

In the case of email applications (table 2), the lowest delays were obtained in the DWRR scenarios (about 500 ms) and the highest, as in the case of FTP applications, in the IPv6 PQ scenario with a negligible value. The IPv6 protocol caused lower latency than IPv4 (about 160 ms) when waiting for downloading e-mails in the network with the implemented DWRR algorithm.

Table 2. Comparison of the results of the email application.

Scenario	Average waiting time to recive an email [ms]	Average waiting time to send an email [ms]
IPv4 FIFO	4682	5876
IPv6 FIFO	6480	7994
IPv4 PQ	121	3799
IPv6 PQ	9630	33107
IPv4 DWRR	625	209
IPv6 DWRR	465	514
IPv4 WFQ	1133	228
IPv6 WFQ	1645	500

Using IPv6 instead of IPv4 positively influenced the operation of the HTTP application (table 3) in the scenario with the implemented DWRR algorithm, which turned out to have the most positive effect on the waiting time for the HTML page to load. The use of the FIFO algorithm resulted in the highest delays.

Table 3. Comparison of the results of the HTTP application.

Scenario	Average waiting time for transmission from router B to router A [ms]
IPv4 FIFO	57754
IPv6 FIFO	82255
IPv4 PQ	36324
IPv6 PQ	39721
IPv4 DWRR	26307
IPv6 DWRR	26025
IPv4 WFQ	37027
IPv6 WFQ	41586

Table 4. Comparison of the results of the videoconferencing application.

Scenario	Average transmission delay time [ms]	Average transmission delay variance [ms]
IPv4 FIFO	394	44
IPv6 FIFO	417	41
IPv4 PQ	47	0,007
IPv6 PQ	39	0,001
IPv4 DWRR	674	374
IPv6 DWRR	462	383
IPv4 WFQ	1028	727
IPv6 WFQ	948	739

For real-time applications (table 4-5), the use of the PQ algorithm proved to be the best. It provides some support for videoconferencing applications and VoIP packages in front of others. The transmission quality of the VoIP application, for scenarios with the included class algorithms, is comparable. For video conferencing, the IPv6 protocol showed an advantage when using the PQ, DWRR and WFQ algorithms, causing in the last two a little more variation of delays (about 10 ms). This may be due to the fact that the IPv6 address has a fixed length of 40 bytes and the variable length of the IPv4 address forces the routers to take into account the field specifying the length of the packet.

Table 5. Comparison of the results of the VoIP application.

Scenario	Average transmission delay time [ms]	Average transmission delay variance [ms]	Jitter [ms]
IPv4 FIFO	497	34	0,024
IPv6 FIFO	535	25	0,026
IPv4 PQ	101	0,001	0
IPv6 PQ	102	0,001	0
IPv4 DWRR	102	0,001	0
IPv6 DWRR	102	0,001	0
IPv4 WFQ	102	0,006	0
IPv6 WFQ	102	0,01	0

Tables 6-8 present the results of the router operation.

Table 6. Comparison of the results of the VoIP application

Scenario	Average waiting time for transmission from router B to router A [ms]	Average waiting time for transmission from router A to router B [ms]
IPv4 FIFO	1,35	1,56
IPv6 FIFO	1,39	1,59
IPv4 PQ	1,23	1,54
IPv6 PQ	1,29	1,56
IPv4 DWRR	1,27	1,52
IPv6 DWRR	1,31	1,55
IPv4 WFQ	1,29	1,5
IPv6 WFQ	1,34	1,52

The average packet waiting time for transmissions on routers A and B is higher for IPv6 (on average by 0.04 ms). The lowest waiting times were achieved using the PQ algorithm (about 1.25 ms in the direction of the server network and 1.55 ms in the direction of the client network) and the highest using the FIFO algorithm (about 1.37 ms in the direction of the server network and 1 , 57 ms towards the client network). The number of rejected packets, in almost every performed scenario, is unequally higher for the IPv4 protocol depending on the used scheduling algorithm - the biggest difference, over 1000 packets dropped by router B, was noted by examining the FIFO algorithm. This number is lower for the FIFO and DWRR algorithm recorded on the more heavily utilization Router B. The most packets have been dropped by the routers from the implemented WFQ algorithm (7326 packages were discarded altogether). Differences in

the load of the calculating unit units are small (in the order of 0.01% to 0.10%). The highest values were recorded during the simulation of WFQ scenarios (from 2.64% to 2.73%) and the lowest for PQ simulations (from 2.47% to 2.51%).

Table 7. Comparison of the results of the VoIP application

Scenario	The number of packets dropped in the router A	The number of packets dropped in the router B
IPv4 FIFO	497	2264
IPv6 FIFO	397	3373
IPv4 PQ	16	413
IPv6 PQ	11	399
IPv4 DWRR	0	3189
IPv6 DWRR	0	3575
IPv4 WFQ	13	3747
IPv6 WFQ	0	3566

Table 8. Comparison of the results of the VoIP application

Scenario	Average percentage of router A processor utilization	Average percentage of router B processor utilization
IPv4 FIFO	2,64	2,67
IPv6 FIFO	2,6	2,67
IPv4 PQ	2,5	2,47
IPv6 PQ	2,51	2,48
IPv4 DWRR	2,6	2,57
IPv6 DWRR	2,67	2,65
IPv4 WFQ	2,65	2,67
IPv6 WFQ	2,64	2,73

5. CONCLUSIONS

The research showed that there are significant differences in the quality of packet transmission of the tested applications using different configurations of the scheduling algorithms and network protocols.

IPv6 protocol provides lower transmission delays of video conferencing applications with their comparable variances for packet scheduling algorithms (for PQ 17% lower, DWRR 31% lower, WFQ 8% lower). Differences are not large, but the need to scale the studied topology, enforced by licensing restrictions of the Riverbed Modeler program, requires their recording, because the difference in the results of research on a more complex topology can be proportionally higher.

On the basis of all dropped packets, from all scenarios, it can be concluded that IPv6 packets were dropped more frequently (about 11.5% of the difference). The IPv4 protocol showed an advantage in the scenarios with the applied FIFO algorithm (1109 fewer rejected packages) and DWRR (386 fewer rejected packages). This may be due to the larger amount of data transferred by one IPv6 packet.

Other results indicated an advantage of the IPv4 protocol over IPv6, which is proven by lower packet delay (about 8%), lower waiting times for server responses (30%) and better performance of network devices.

Applications whose DSCP fields had a value lower than the value of the real time application's DSCP fields (FTP, HTTP) in the FIFO algorithm scenario performed best because the transmission of their packets was not dependent on the transmission of application datagrams with a higher DSCP field value. E-mail application as the one that generated the smallest amount of data, characterized by the worst quality connection when using the PQ algorithm for the same reasons as the FTP application. Implementation of the weights of queues and WFQ algorithms DWRR enabled faster transmission of e-mail packages which resulted in the approx. 75% to 90% lower wait times to send and retrieve messages (up to two seconds).

REFERENCES

[1] Deshpande, H., Bawa, M. and Garcia-Molina, H., "Streaming live media over peer-to-peer network," Technical Report, Stanford University, (2001).

[2] Derecka, A. and Sawicki D., "Estimation of the impact of quality of service parameters on multimedia transmissions," Proc. SPIE 10808, (2018).

[3] Kurose, J. and Ross, K., [Computer Networking A Top-Down Approach], Pearson, New Jersey, (2013).

[4] Al-Ani, M. and Haddad, R., "IPv4/IPv6 Transition," International Journal of Engineering Science and Technology 4(12), 4815-4822 (2012).

[5] Al-Zobbi, M., "Comparison Between Ipv4 And Ipv6 In Adopting Differentiated Services, " International Journal of Scientific & Technology Research 3(2), 237-242 (2014).

[6] Okumus, I., Mantar, H., Hwang, J. and Chapin, S., "Inter-Domain Traffic Engineering on Diffserv Networks: A Region-based Approach," Przegląd Elektrotechniczny 85(10), 137-145 (2009).

[7] Asuquo, P., Aneke C. and Akpabio, I., "Qos Mechanism for RTP voice and RTP video based on Queuing Techniques, " International Journal of Scientific & Technology Research 3(5), 1421-1429 (2014).

[8] Schulzrinne, H., Casner, S., Frederick, R. and Ja-Cobson, V., "RTP: A Transport Protocol for Real-Time Applications, " Internet Engineering Task Force. Audio-Video Transport Working Group RFC- 1889, (1996).

[9] Kowalik, P., "Protokół IPv6 - Charakterystyka i proponowane metody wdrożenia w istniejących sieciach ipv4 korzystających z routerów CISCO," Informatyka, Automatyka, Pomiary w Gospodarce i Ochronie Środowiska 4(1), 58-61 (2014).

[10] Barkovska, O. and Serdechnyi, V., "Control model of data stream transmitted over a network based on proxying technology, " Informatyka, Automatyka, Pomiary w Gospodarce i Ochronie Środowiska 8(1), 8-11 (2018).

[11] Balogh, T. and Medvecky, M., "Performance evaluation of WFQ WF2Q and WRR queue scheduling algorithms," Proc. 2011 International Conference on Telecommunications and Signal Processing, 136-140. (2011).

[12] Balogh T. and Medvecky, M., "Average Delay and Queue Length Model for WRRPQ," WSEAS Transactions on Communications 13, 186-194 (2014).

[13] Balogh T. and Medvecky, M., "Comparison of Priority Queuing Based Scheduling Algorithms, " Elektrorevue 1(1), 1-8 (2010).

[14] Bennet, J. and Zhang, H., "Hierarchical Packet Fair Queueing Algorithms," IEEE/ACM Transactions on Networking 5(5), 675-689 (1997).

Analysis of wireless network security for data transmission performance

Daniel Sawicki*[a], Sebastian Smyk[b]
[a]Lublin University of Technology, 38A Nadbystrzycka Str, Lublin, Poland 20-618; [b]Second year computer science 2nd degree student, Lublin University of Technology, 38A Nadbystrzycka Str, Lublin, Poland 20-618;

ABSTRACT

In this work analysis of wireless network security for data transmission performance was performed. To carry out was chosen most currently popular wireless standards IEEE 802.11 family. Among the protocols used to secure local wireless networks, the most common protocols were selected. Four different test groups were tested, which tested the impact of wireless network security on: transfer depending on the network standard and frequency band for communication using TCP and UDP protocols, throughput depending on the size of the MTU parameter for communication using the TCP protocol, delay for communication using UDP protocol, delay depending on the type of data for communication using the UDP protocol. The best compromise between stability and network performance, and its protection is the standard IEEE 802.11n protected by WPA2 AES Enterprise version.

Keywords: wireless, security, transmission performance

1. INTRODUCTION

Recently, we can observe very fast development and progress in areas related to broadly understood information technologies. Thanks to the progressive miniaturization, easier access to the Internet and globalization, we have the ability to communicate with almost any person on earth in any place.

Wireless transmission in addition to the obvious convenience has one major disadvantage, it is a medium of transmission to which access is very difficult to control. By activating the access point, the possibility of limiting its coverage in such a way as to cover only the area that is required is very small, as a result of which the network is exposed to unauthorized access. The solution to this problem are methods and protocols that give the possibility to secure such networks. The constantly growing number of access points increases the possibilities of hacking computer networks. Serious network threats include the ability to steal personal data, impersonate other people, steal access to bank accounts, or take control of an attacker's computer[1-2].

The development of wireless networks requires that the network connection be as fast as possible to be stable and efficient, and at the same time properly secured. This will ensure the proper protection of privacy and data. Wireless network security negatively affects the quality of data transmission[3].

The IEEE 802.11 standard defines the physical layer PHY (the first layer of the OSI model) and the medium access control MAC (Media Access Control) sublayer which is contained in the DL data link layer (the second layer according to the OSI model). Depending on the wireless network standard, the IEEE 802.11 specification allows the use of physical layers such as: FHSS, DSSS and OFDM[3-5].

To enable simultaneous operation of devices from different manufacturers, the standards of wireless networks have been defined: 802.11a, 802.11b, 802.11g, 802.11n, 802.11ac, 802.11ad, 802.11ax[5-8].

Wireless LANs can be configured in several different topologies. The IEEE 802.11 standard defines the method of building a WLAN network, which is a group of communicating stations as BSS (Basic Service Set). Depending on the needs and possibilities, it is also possible to set up wireless connections directly between client stations in the IBSS (Independent Basic Service Set) mode, also known as ad-hoc mode. The area, which includes the BSS and IBSS networks, is called the basic service area of the BSA (Basic Service Area)[5-7].

*d.sawicki@pollub.pl

Photonics Applications in Astronomy, Communications, Industry, and High-Energy Physics Experiments 2019, edited by Ryszard S. Romaniuk, Maciej Linczuk, Proc. of SPIE Vol. 11176, 111765T
© 2019 SPIE · CCC code: 0277-786X/19/$21 · doi: 10.1117/12.2536848

Access points in addition to the basic mode of operation, in which they allow access to wireless client devices to the network infrastructure, may also offer other types of work. Depending on the model, manufacturer, needs and configurations can work like a normal network card or signal amplifier. They can also connect with each other, thus creating wireless network bridges. Access point can works with infrastructure, point-to-point, point-to-multipoint and repeater mode.

When considering the issue of wireless LAN security, it should be noted that both mechanisms for controlling access to such a network as the methods of encrypting the data sent by it. One of the first methods of wireless LAN security was to disable broadcasting of SSID (Service Set Identifier) by access point, that is, hiding the network name[6]. Most access devices have the ability to define a list of MAC addresses for network interfaces of devices that will be able to connect to a given wireless network. It is a form of protection, thanks to which only trusted, predefined devices will be able to connect to a given wireless network[7,8]. To eliminate communication between stations connected to one wireless network, the wireless client isolation mechanism can be used. Other security methods are WPS, WEP, WPA.WPA2[9,10].

2. TESTBED

In order to carry out tests and measurements of the impact of the type of wireless security on the transmission efficiency, an IP network with private address 192.168.1.0/24 was built and configured based on the following devices: switch: D-Link GO-SW-5E, RADIUS server: Raspberry Pi, Access point: Ubiquiti UniFi AP Pro, computer-client: Acer Switch laptop (Windows 10 64bit), computer-server: Lenovo X200 laptop (Windows 10 64bit).
the Riverbed application.

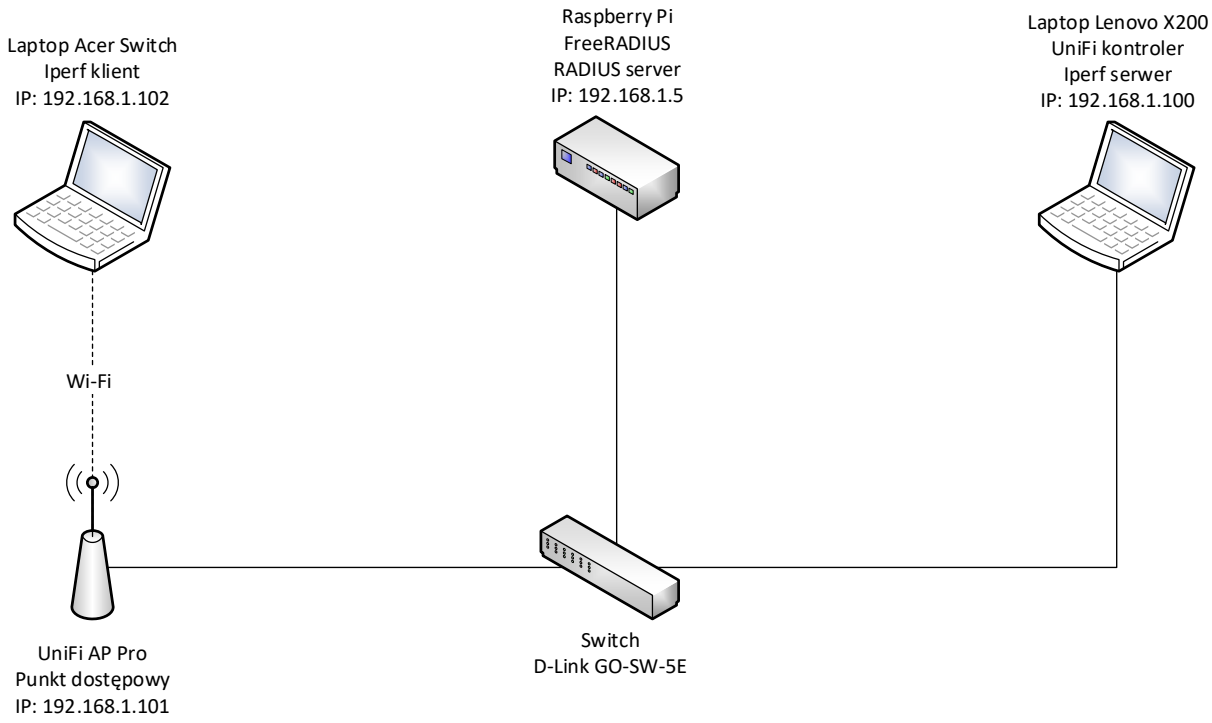

Figure 1. Testbed diagram.

Three types of software were used during the tests: configuration, measurement and authentication. Configuration software: The UniFi Controller is a software controller that allows configuration of the UniFi AP Pro access point. The use of such a controller was necessary, because only in this way was possible to configure UniFi AP Pro, changing settings directly on the device without the intermediation of such a controller is impossible. Configuration modifications made on this controller made it possible to carry out measurements for all the encryption options and wireless network operating standards necessary to carry out the measurements. Netsh is a command line tool that allows you to modify the computer's network configuration. It was used to change the value of the MTU parameter. Measurement software: Iperf3 is the main software used in the work to carry out measurements. It provides the ability to test throughput in IP networks,

giving the possibility of separate analysis of TCP and UDP protocols. It is required to be running on both the client and server side. StarTrinity Network Tester is software that has been used to measure the jitter parameter in relation to the UDP protocol. As with Iperf, the program must run on the server and the client. Authentication software: FreeRADIUS is software that was used to configure the RADIUS server. The use of this type of server was necessary to perform measurements when encrypting the WPA Enterprise and WPA2 Enterprise networks

3. RESULTS

The study of the assumed objective consisted in performing four different types of measurements in such a way as to check how the types of security of wireless networks affect various parameters related to the transmission of data in wireless networks. Each type of study consisted in the modification and measurement of other transmission parameters for various wireless network security protocols. Performed four tests:

- the wireless network standard and frequency band were changed, the transfer with the use of TCP and UDP protocols was measured,
- the value of the MTU parameter was changed, the transfer was measured using the TCP protocol with the IEEE 802.11n standard and the 5 GHz band,
- the value of the jitter parameter was measured in relation to the UDP protocol with the IEEE 802.11n standard and the 5 GHz band,
- the UDP protocol payload was changed, the value of the jitter parameter was measured in relation to the UDP protocol with the IEEE 802.11n standard and the 5 GHz band.

Transmission performance depending on the network standard. The test consisted in setting up a test connection between the server, which was a computer running the Iperf server, and the client, i.e. the second computer on which the Iperf application was launched in the client mode. The client computer on which the measurements were carried out was connected to the LAN using an access point whose configuration was modified so that it would be possible to measure all previously assumed work scenarios in inches. To see the extent to which wireless transmission performance is influenced by the way it is encrypted and the standard in which the measurements were performed: 802.11g, n with 2.4GHz, 5GHz frequencies for TCP and UDP transport protocols. Each single measurement lasted 60 seconds, during which the Iperf software measured the average transfer based on the amount of data sent during this time between the client and the server. For each type of encryption, ten single measurements were made in the band, and then the average was calculated based on them, which was the final result for a given type of encryption. The results are shown in the Fig. 2-7.

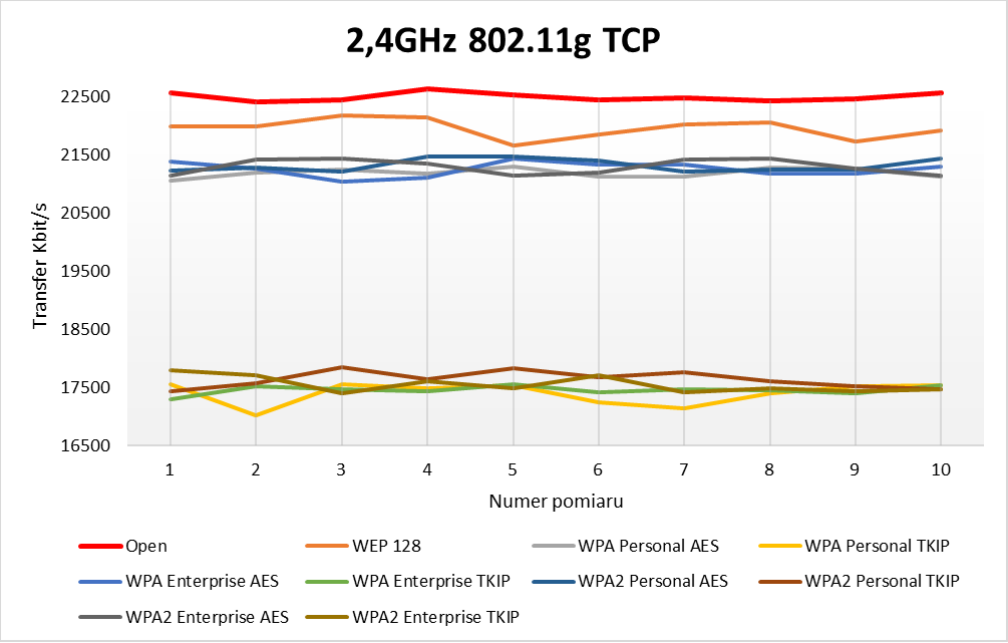

Figure 2. Throughput for TCP protocol using the 802.11g 2.4GHz standard.

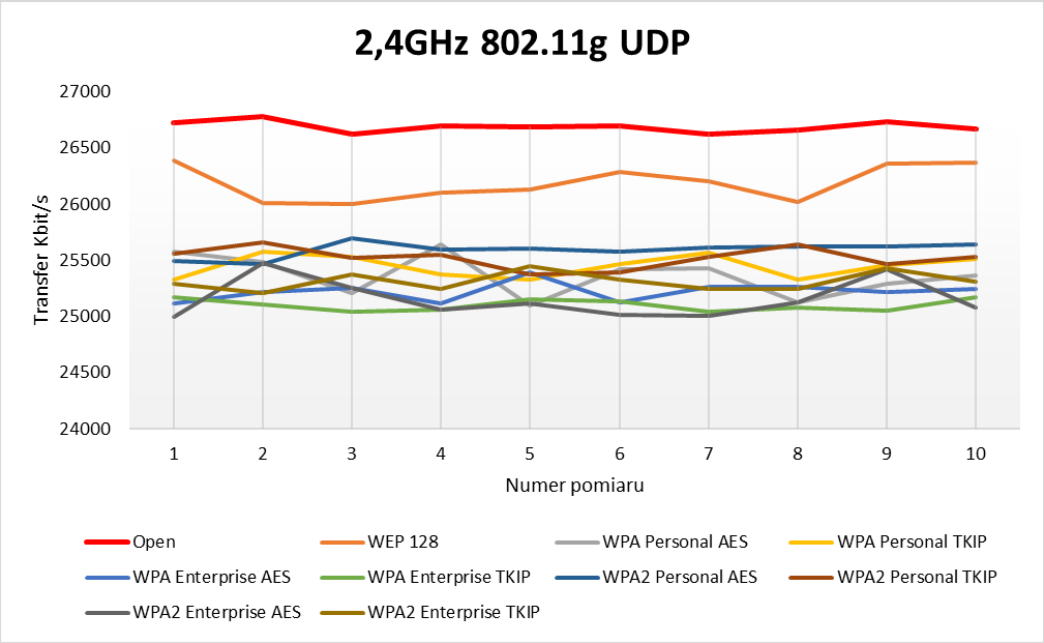

Figure 3. Throughput for UDP protocol using the 802.11g 2.4GHz standard.

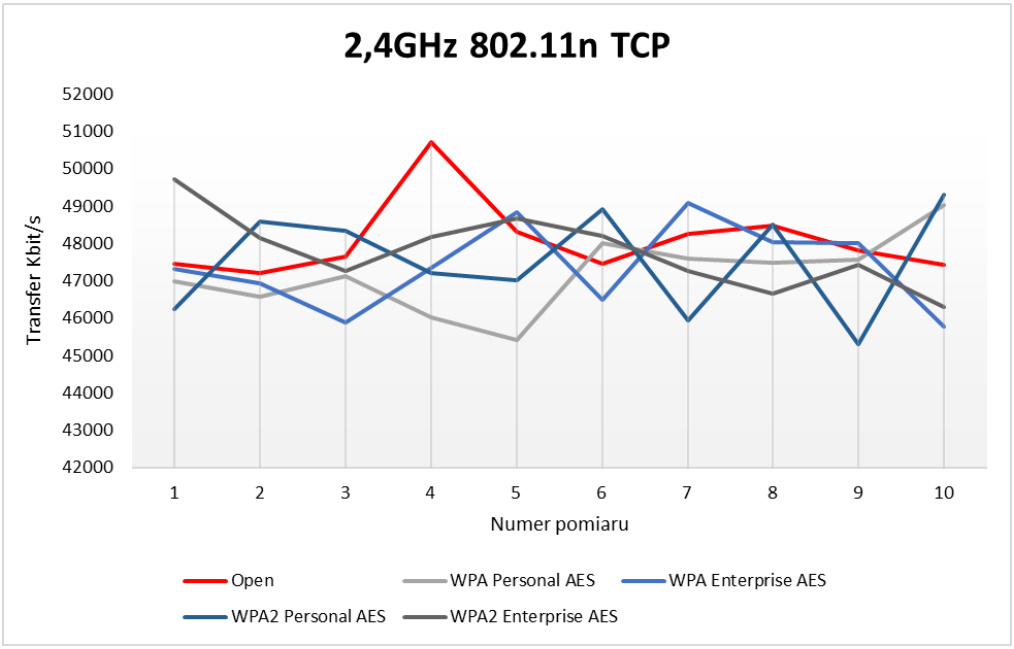

Figure 4. Throughput for TCP protocol using the 802.11n 2.4GHz standard.

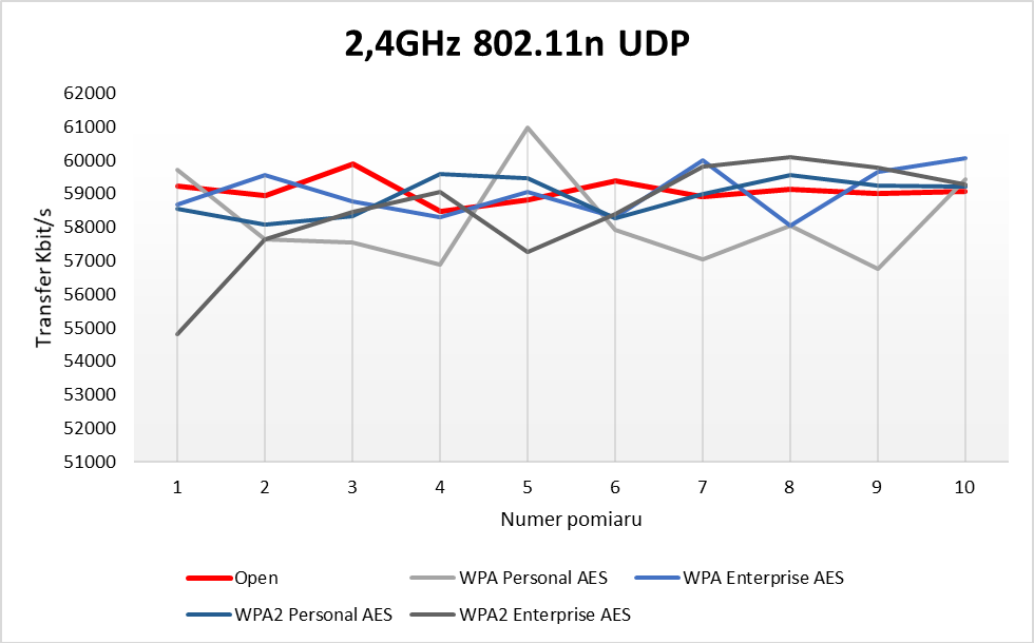

Figure 5. Throughput for UDP protocol using the 802.11n 2.4GHz standard.

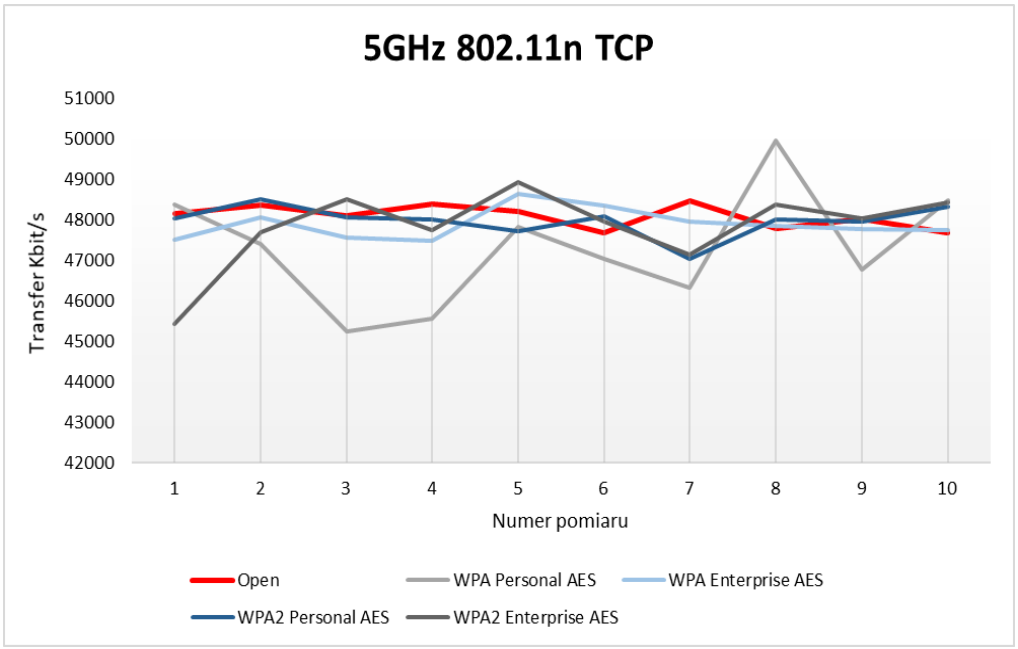

Figure 6. Throughput for TCP protocol using the 802.11n 5GHz standard.

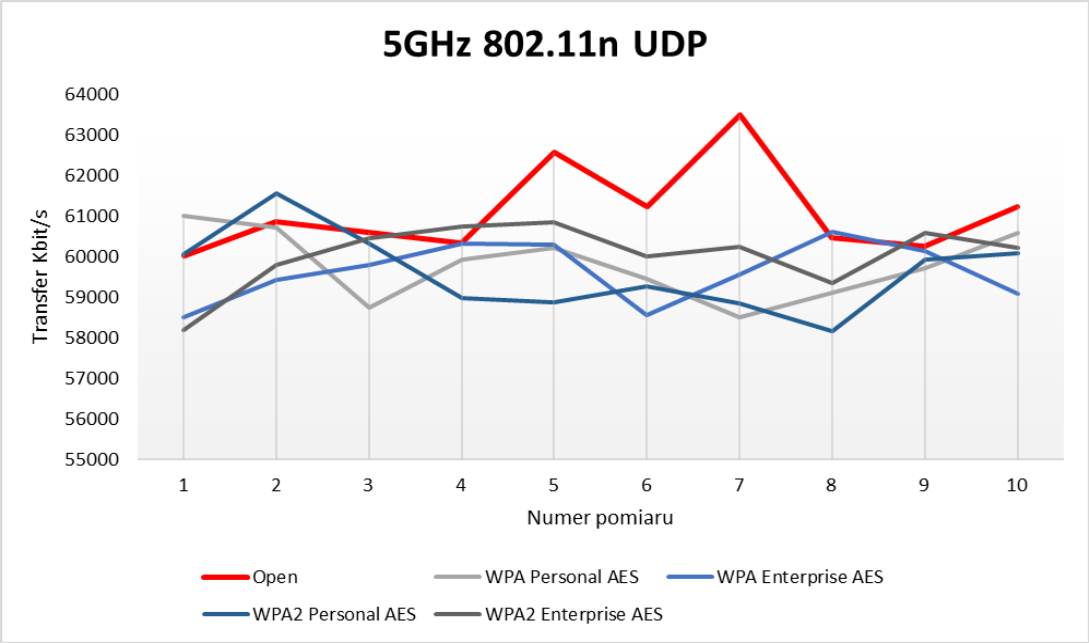

Figure 7. Throughput for UDP protocol using the 802.11n 5GHz standard.

During the measurements performed using the IEEE 802.11g standard, a significant negative impact of encryption, and thus the protection of the network on the transmission speed was observed. The TKIP protocol proved to have the most impact on the transmission speed, using it the connection speed based on the TCP protocol decreased by about 22%. The UDP protocol proved to be more resistant to this type of security, the transfer value in this case decreased by 5-6%. In the case of AES encryption, the drop in transmission speed was similar for both UDP and TCP, and amounted to around 5%. In the IEEE 802.11g standard the least adverse effect on the transmission speed was security based on the WEP protocol, in this case the average transfer decreased only by approx. 2%.

Because the IEEE 802.11n standard does not fully support TKIP and WEP encryption[11], measurements using these types of wireless network security have not been performed. In the case of the IEEE 802.11n standard, measurements were made for the 2.4 GHz and 5 GHz bands. In both cases, similar decreases in transfers were observed for the TCP and UDP protocol, which fluctuated within 1-2%.

In the case of the IEEE 802.11g standard, the highest measurement stability was achieved for the communication secured by WPA Enterprise TKIP for both TCP and UDP transmission where the standard deviation amounted to 78.41kb and 52.89kb respectively.

When testing the IEEE 802.11n standard, the stability of the measurements turned out to be lower than IEEE 802.11g. With regard to TCP communication, the best results were obtained for securing WPA Enterprise AES at the 5 GHz band where the standard deviation amounted to 248.4 kb. In the case of the UDP protocol, the most stable measurements were provided by the WPA2 Enterprise AES standard at the 5 GHz band, where the standard deviation amounted to 452.7kb.

Considering that the performance degradation of the secured network in the IEEE 802.11n standard is smaller than in the case of a secured network in the IEEE 802.11g standard, the IEEE 802.11n standard seems to be a much better choice, as compared to the IEEE 802.11g standard, in addition to higher performance also provides greater transfers. Protocols securing data transmissions operating on the IEEE 802.11n standard network in a similar and small way affect its performance, therefore it seems optimal to use their safest versions, ie WPA2 AES Personal or Enterprise protocols.

Transmission performance depending on the MTU value. The test was performed in the same way as before with the difference that the measurements were made only for the IEEE 802.11n standard, 5GHz band and UDP protocol, while the value of the MTU parameter was changed. The measurements were carried out for subsequent MTU values: 1500, 1461, 1460, 1300, 1100, 900, 700, 500, 300 and 100. The results are shown in the Fig. 8.

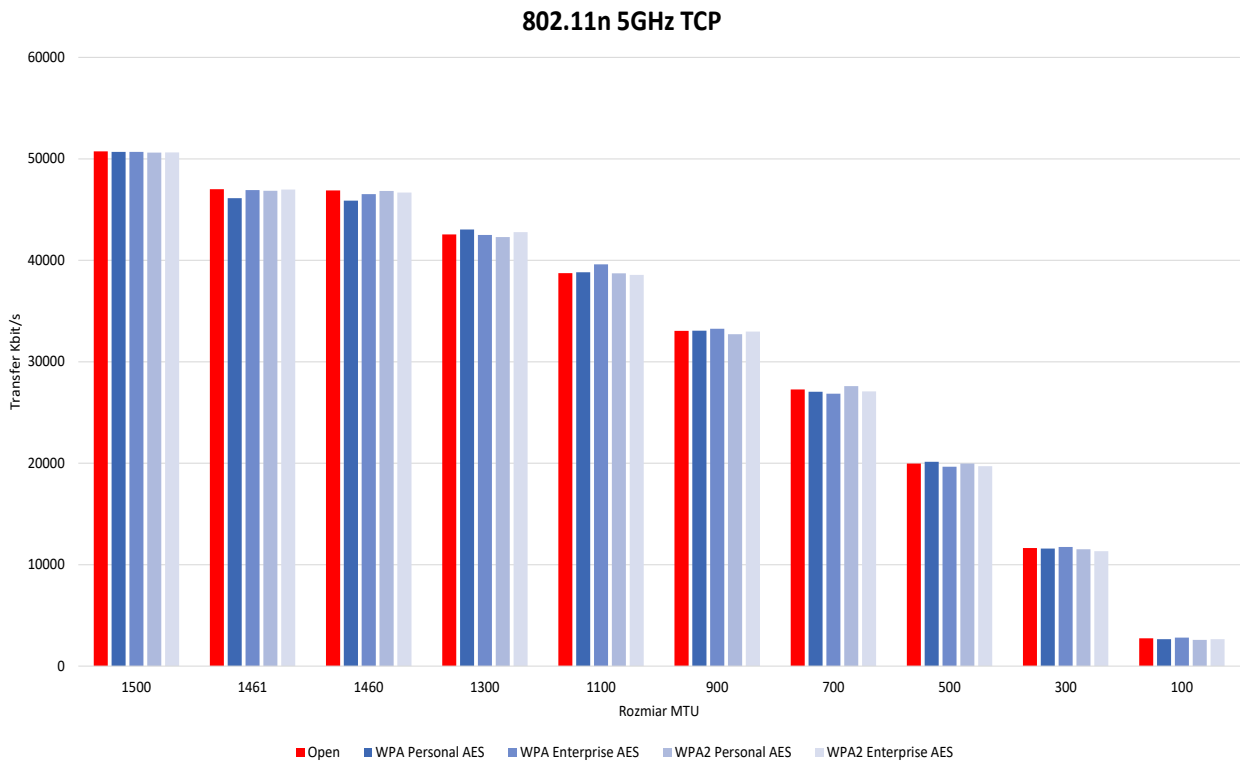

Figure 8. Measurement results for the TCP protocol at the 802.11n 5 GHz standard for different MTU values

Analyzing the measurements carried out in this study, it could be noted that protocols protecting wireless networks very much affect the transfer value regardless of the size of the MTU parameter. This was best observed for the MTU parameter of 1500 bytes, where the standard deviation of the average transfers of all tested protection protocols was only 30kb. It is difficult to clearly indicate which security protocol had the most negative impact on the transmission performance with respect to the unsecured network because at each size of the MTU parameter, the transfer decreased only by 1-2% which may be within the limits of measurement error.

Transmission performance depending on the delay value. The measurement method used in this study was similar to that used previously, but instead of the transfer value measurements, the value of the jitter parameter for the UDP protocol was measured. The results are shown in the Fig. 9.

This study showed that protections securing wireless networks have a negligible negative impact on the value of the jitter parameter. The differences in delays with respect to the unprotected network fluctuated between 0.05 ms and 0.15 ms. The WPA2 Personal AES protocol was the most unfavorable for the operation of the network, where the average value of the jitter parameter was 0.696 ms at the value of 0.547 ms for the unsecured network, which is an increase of 27.24% in relation to the unsecured network. Least adversely affected by the delay was the WPA Personal AES protocol, securing the wireless network in this way an increase in delay by 8.78% was achieved.

Analyzing the test results, it can be noticed that single measurements with secured transmission reached values much higher than the average, which was not the case with unsecured transmission. Each such measurement had an impact on increasing the value of the standard deviation and thus on the deterioration of transmission stability. It may be appropriate to conclude that the use of any wireless network security may cause a brief, temporary and significant increase in delay, which is undesirable.

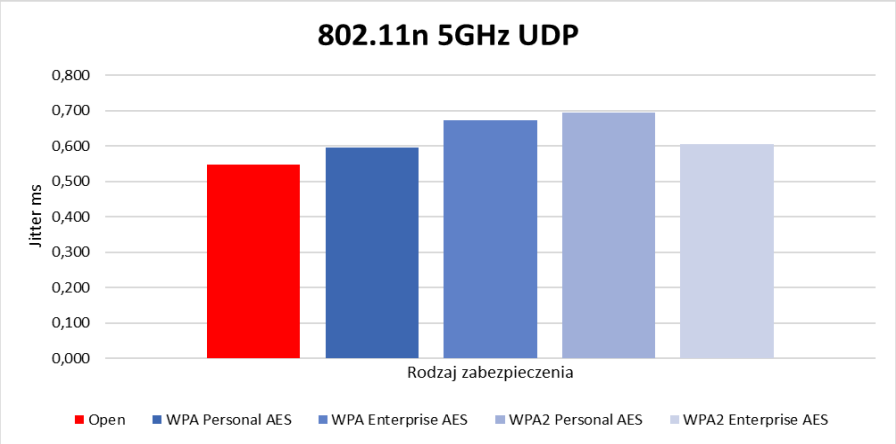

Figure 9. Measurement results for the UDP protocol using the 802.11n 5 GHz standard.

Transmission performance depending on the type of data. In this test, the StarTrinity Network Tester measurement software was used. Test software for proper operation required launching both on the server and client side. The measurements made in this study consisted in examining the value of the jitter parameter in relation to the UDP protocol at different UDP load values, which were successively 1500, 1461, 1460, 1300, 1100, 900, 700, 500, 300 and 100. StarTrinity Network Tester software allows you to perform many consecutive series of measurements. In order to carry out the test, for each UDP charge value and for each type of security, five one-minute measurements were made.

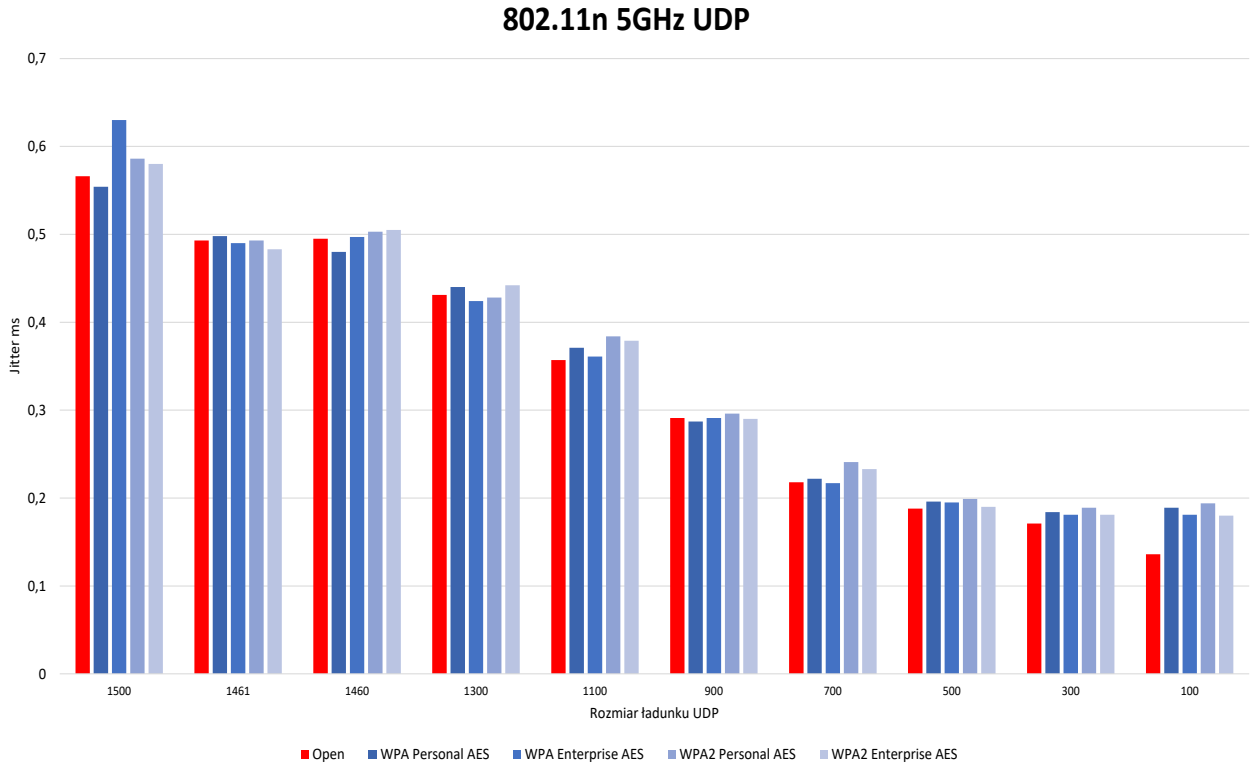

Figure 10. Measurement results for the TCP protocol at the 802.11n 5 GHz standard for different UDP load values.

It should be noted that the study concerned only the UDP protocol by means of which multimedia transmissions are carried out, among others. It is important due to the current increase in popularity of both voice and video streaming.

The study showed the low impact of protocols securing wireless networks on transmission performance. The most negative impact on the jitter parameter in the studied UDP could be observed for UDP load size of 100 bytes, where the average delay value for the network secured with respect to an unsecured network was higher by 30-40%.

4. CONCLUSIONS

The implementation of all the measurements assumed turned out to be very difficult to implement. In the 2.4 GHz and 5 GHz radio frequencies in which the measurements were carried out, there are currently a very large number of devices whose work disrupted the course of the research, and thus the collection of reliable results. It was not until all the devices to which physical access was possible and which could interfere with the tests allowed to carry out the measurements. As it turned out, the time of day had a key impact on research. In the evening and at night it was possible to notice greater stability of measurements than during the day. It resulted from a much smaller use and load of the surrounding, largely home wireless networks just in the evening and night. All of the following observations regarding the percentage reduction in transmission speed refer to measurements relative to an unprotected network operating in the open mode.

Taking into account the results of all the tests carried out and analyzed at work, it can be concluded that wireless network security has a small but negative impact on data transmission efficiency in terms of data transmission speed when using the IEEE 802.11n standard, both in the 2.4 range GHz and 5 GHz. In such configurations, the drop in data transfer was 1-2% for both TCP and UDP. However, when deciding to use the IEEE 802.11g standard, it should be noted that simultaneous use of TKIP encryption is associated with significant decreases in data transmission speed, which are within 22%.

The use of encryption protocols may also adversely affect the stability of the transmission performed using the UDP protocol. Analyzing the results of tests on secured networks recorded, it can be noticed that single measurements in which large changes in delay were recorded in relation to the average value from the entire measurement. In the measurement results, in the case of unsecured network testing, no such large delay changes were noticed.

The best compromise between stability and network performance, and its protection is the standard IEEE 802.11n protected by WPA2 AES Enterprise version

REFERENCES

[1] Zhou, L. and Haas, Z., "Securing Ad Hoc Networks," IEEE Network Magazine 13(6), 24–30 (1999).
[2] Kurose, J. and Ross, K., [Computer Networking A Top-Down Approach], Pearson, New Jersey, (2013).
[3] Boukerche, A., [Algorithms and protocols for wireless, mobile ad hoc networks], John Wiley & Sons Inc, New Jersey, (2009).
[4] Derecka, A. and Sawicki D., "Estimation of the impact of quality of service parameters on multimedia transmissions," Proc. SPIE 10808, (2018).
[5] Oksiiuk, O. and Krotov, V., "Analysis and choice of routing protocols in wireless ad hoc networks based on the use the neural network, "Informatyka, Automatyka, Pomiary w Gospodarce i Ochronie Środowiska 9(1), 53-55 (2019).
[6] Bilski, T., "New Challenges in Network Security," Przegląd Elektrotechniczny 1(12), 230-234 (2016).
[7] Kurdziel, M. T. and Alvermann, J. A., "Information security trades in tactical wireless networks," Proc. SPIE 9497, (2015).
[8] Uher, J., Harper, J., Mennecke, R., Patton, P. and Farroha, B., "Investigating end-to-end security in the fifth generation wireless capabilities and IoT extensions, " Proc. SPIE 9826, (2016).
[9] Ahmad, M., Taj, S., Mustafa, T. and Asri, M., "Performance analysis of wireless network with the impact of security mechanisms," 2012 International Conference on Emerging Technologies, Islamabad, 1-6 (2012).
[10] Akram, R. N., Markantonakis, K., Mayes, K., Bonnefoi, P., Sauveron, D. and Chaumette, S., "Security and performance comparison of different secure channel protocols for Avionics Wireless Networks," 2016 IEEE/AIAA 35th Digital Avionics Systems Conference (DASC), 1-8 (2016).
[11] Agarwal, A. K. and Wang, W., "Measuring performance impact of security protocols in wireless local area networks," 2nd International Conference on Broadband Networks 1, 581-590 (2005).

Strain Gauge Sensor for the Internet of Things

Zdenek Slanina[a], Radovan Hajovsky[a], Michal Cepelak[a], and Wojciech Walendziuk[b]

[a]VSB-TU Ostrava, 17. listopadu 15, Ostrava-Poruba, Czech Republic
[b]Bialystok University of Technology, Wiejska 45D, Bialystok, Poland

ABSTRACT

The aim of this article is to design and implement smart devices for measuring roof loads and then early warning system. The resulting measurement unit consists of a resistance strain gauge whose analog output is converted to a 24-bit digital value using the Avia Semiconductor's HX711 A/D converter, which is further processed in a Raspberry Pi microcomputer. The processed data are supplemented with the current temperature measurement at the strain gauge to check its temperature dependence and sent to the InfluxDB database. The warning and data monitoring system is then handled by the Chronograph interface. This article includes a small research for the use of strain gauge for this type of measurement.

Keywords: strain gauge, smart device, internet of things, database

1. INTRODUCTION

Nowadays, the Internet of Things and the Industry 4.0 are becoming a trend of contemporary digitization.[1–4, 6] This work deals with current issues of adding devices to the Internet of Things and subsequent data processing in cloud technologies. First, the norms related to the load of roof structures and individual types of loads are discussed. Furthermore, the basic types of strain gauges are described and the most suitable strain gauge is chosen for the required type of measurement. Part of the work is also design and realization of unit, which would guarantee to use available resistance strain gauges in reasonable range for conventional bridge connections.

Next chapter describes software for connection of suitable digitization of analogue data from strain gauges using a suitable range of A/D converter. Last but not least, the thesis also contains a description of the Raspberry Pi single-board computer used, the reason for its choice, and its function in the Internet of Things Unit, or a replacement for this comprehensive control system. The results of testing with the InfluxDB database and its extensions are listed at the experimental work description.

2. REDUCING CONSTRUCTION FEATURES PREDICTION

Leaving aside the human factor, defects in projection and unsuitable building procedures, it is precisely the overload or uneven load of roof structures that is one of the most common causes of roof accidents in the Czech Republic. Using strain gauges for roof weighing and early warning, we can avoid reaching the ultimate limit states of roofs and effectively prevent accidental and property damage.[7–9]

Currently, we do not see much monitoring of roof loads in the Czech Republic, but rather companies and universities are mainly concerned with measuring the load and deformation of bridge structures. Institutions use fiber-based FBG sensors (fiber Bragg grating) to monitor roof loads.

First of all, it is necessary to get acquainted with phenomena that can affect safety for prediction of emergency states. The general load on structures is discussed in more detail in CSN EN 1991-1-1 (730035). Snow load is the main load component on which roof structures are designed. Therefore, and for a simpler description of the load on roof structures, this work is using mainly the third part of the mentioned standard, namely CSN EN 1991-1-3 Eurocode 1: Actions of structures - Part 1-3: General actions - Snow loads. It specifies the nationally determined parameters valid for the territory of the Czech Republic. The National Annex also contains a map of snow areas in the Czech Republic, which sets the characteristic snow load values, see picture 1. It specifies the

Photonics Applications in Astronomy, Communications, Industry, and High-Energy Physics Experiments 2019,
edited by Ryszard S. Romaniuk, Maciej Linczuk, Proc. of SPIE Vol. 11176, 111765U
© 2019 SPIE · CCC code: 0277-786X/19/$21 · doi: 10.1117/12.2536882

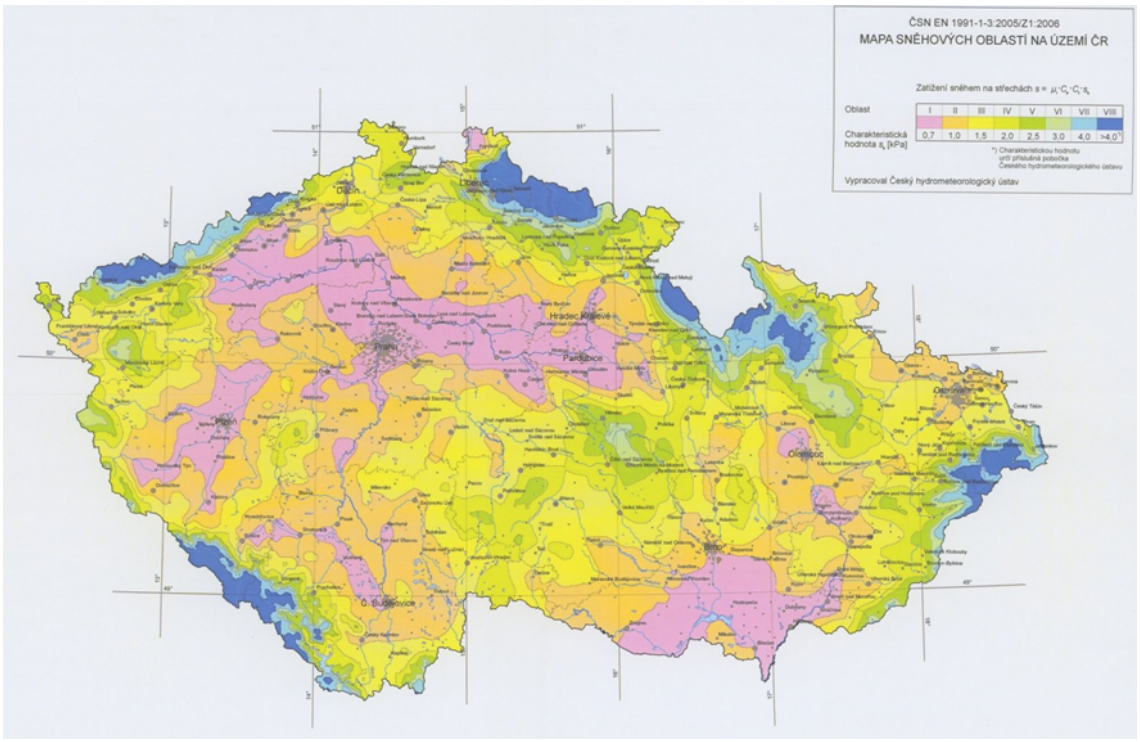

Figure 1. Map of snow load regions in the Czech Republic.

standard snow load in the areas. The characteristic snow load values are values that can be reached or exceeded every fifty years. Table 1 describes the standard load in the color-coded areas of the snow area map.

For example, according to the map of snow areas, the city of Ostrava is located in area II. According to the standard load values in table 1, snow loads of $80kg/m^2$ can be expected in area II. Roof structures in a given area should be projected to this area from the period of validity of the standard to this load per square meter according to the aforementioned ČSN EN 1991-1-3 standard. The previous standard ČSN 73 00 35, valid until November 2006, used a different characteristic load calculation and generally considered less load.

The constant load of the roof structure includes the weight of the supporting structure itself, the roofing and other roof components. The constant load acts on the structure with the same intensity throughout the construction. This type of load should not pose any risk to the roof structure.

Random or variable loads act only in some situations and change over time. These include snow, ice, wind, traffic, or machine loads. In the event of an accidental load, emergency situations may already occur in some situations, as, for example, $1m^3$ of snow may have a density of 100 to 400 kg depending on the type of snow. Excessive loads can occur, for example, even in flat roofs when the drainage paths are clogged.

Exceptional events such as catastrophic events, such as earthquakes, explosions, disruptions, can be an extraordinary burden. This load variant is usually not easy to prevent.

3. STRAIN GAUGE SENSORS

At present, we can encounter a large number of different types of strain gauges, which are more or less suitable for measuring the load of roof structures. The principle of strain gauges consists in measuring the change of distance of two points on the body surface due to its load. Indirectly, it measures the mechanical stress on the body surface by measuring its deformation.

Further author information: (Send correspondence to Z.S.)
Z.S.: E-mail: zdenek.slaniana@vsb.cz

Table 1. Standard load of buildings in individual snow areas according to CSN EN 1991-1-1.

Snow area	Snow density (kg/m^3)	I	II	III	IV	V	VI	VII	VIII
Characteristic value of snow load on the ground (kPa)		0.7	1	1.5	2	2.5	3	4	individual designation
Snow weight on roof determined from characteristic value (kg/m^2)		56	80	120	160	200	240	320	individual designation
Fresh snow	100	56 cm	80 cm	120 cm	160 cm	200 cm	240 cm	320 cm	
Relaxed (hours or days after snowfall)	200	28 cm	40 cm	60 cm	80 cm	100 cm	120 cm	160 cm	
Old (weeks or months after snowfall)	300	19 cm	27 cm	40 cm	53 cm	67 cm	80 cm	107 cm	
Wet snow	400	14 cm	20 cm	30 cm	40 cm	50 cm	60 cm	80 cm	

String strain gauges - as the name suggests, the strain gauge is a steel string that is tense between two points. As a result, the distance of these two points is measured. Even with a slight change in the distance of the points due to deformation, the tension of the steel string changes and thus the actual frequency of the string is changed. A similar change in string frequency can be observed, for example, when tuning stringed musical instruments. The resulting string frequency is evaluated by a special device that excites the string with an electrical pulse and then measures the duration of the N periods. This strain gauge is not very suitable for load measurement.

Pneumatic strain gauges - the principle of this strain gauge is to measure the change in pressure inside the strain gauge due to its deformation.

Mechanical strain gauges - generally known as a load cell, it consists of a spring and a measuring hand moving along a scale of digits, depending on the type of strain gauge.

Photoelasticimetric strain gauges - these are strain gauges also referred to as FBG. Their principle lies in the reflection of light from the Bragg grid. The Bragg grid has a wavelength equal to one wavelength at rest. After deformation of the strain gauge, the Bragg lattice is deformed and thus its pitch and reflected wavelength change. The resulting wavelength is evaluated by a spectrometer.

Electrical strain gauges are divided into inductive, capacitive, resistive and semiconductor based. It is the most commonly used type of strain gauge since it directly converts the elongation to an electrical quantity in this case. Depending on the type of electrical strain gauge, the coil impedance changes in the case of inductive strain gauge, or the capacitor capacity of the capacitive strain gauge, by varying the length. Resistance strain gauges are further divided into semiconductor, carbon and metal strain gauges. The semiconductor strain gauge uses so-called piezoresistance of some materials, such as silicon. Depending on the mechanical pressure, the electrical resistance changes.

Carbon strain gauges consist of two carbon surfaces, which are pressed against each other by the load and the pressure of the carbon plates, and thus the electrical resistance between them, also change with a change in load. Today, this type of strain gauge is no longer used.

This work deals with the weighting of roofs using resistive metal strain gauges because they have the most advantages in this respect. The benefits of using resistance strain gauges include their availability, cost, and output signal processing. Compared to semiconductor strain gauges, it offers less resistivity, but accuracy is sufficient for this type of utilization. Resistance strain gauges can be used to monitor (A) for roof structure monitoring, as well as to measure roof deflection or deflection due to load (B) as is shown at figure 2.

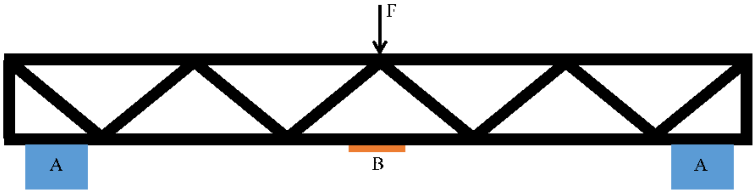

Figure 2. Strain gauge placement options for roof load monitoring.

The most commonly used strain gauges currently include resistance metal and semiconductor strain gauges. For the realization of the measuring unit, a resistance metal strain gauge was chosen mainly due to its relatively low purchase price, despite very good availability in various measuring ranges and last but not least for relatively easy output signal processing while maintaining acceptable measurement accuracy.

The resistance strain gauge is a passive electrical component that is used to convert a non-electrical quantity into an electrical component. In the case of a strain gauge, the deformation of the measured material is measured. The principle of the strain gauge is based on the change of the length Δl and the change in the cross-section of the conductor ΔS caused by the mechanical deformation of the material with which the strain gauge is firmly connected. The strain gauge glued to the surface of the object to be measured is thus deformed in the same way as the stressed object. When the strain gauge is stretched with force F, its length l increases and the S-section decreases as shown in figure 3, thus changing the strain gauge electrical resistance.

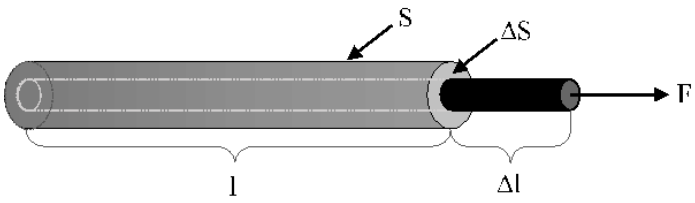

Figure 3. Changes in conductor caused by deformation.

The resultant phenomenon can also be supported by the relation, which describes the dependence of the conductor resistance R on its length, cross-section and material.

$$R = \varrho \frac{l}{S} [\Omega]$$

where l represents the conductor length, S the conductor cross section with the specific electrical resistance ϱ.

In the case of metal resistance strain gauges, we can neglect the change in the resistivity ϱ caused by microstructural changes in the material. The change in the specific electrical resistance ϱ due to deformation is considered to be zero. The change of electrical resistance in one conductor due to deformation is too small, and

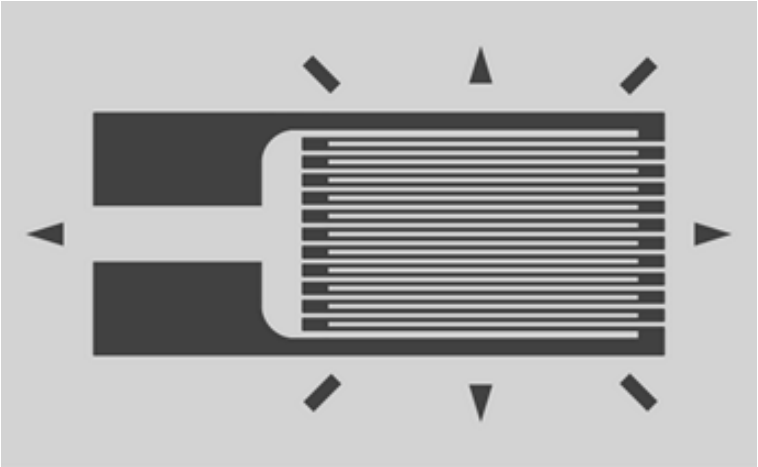

Figure 4. Conductor distribution on foil strain gauge.

there would be problems with its evaluation. Therefore, a series of parallel parallel conductors are used whose resistance change is summed up as shown at figure 4. In the case of resistance strain gauges, a suitably shaped metal foil is usually used, attached to a flexible insulating pad.

By evaluating correctly, it is also possible to obtain uneven roof load data. In this variant, for example, the Zemic HM9B-C3-xxt strain gauge can be used, where xx denotes the weighing capacity of this product between 10 and 50 tons according to the chosen variant. When used according to variant (B) (figure 2) it is possible to monitor the deflection of the roof structure. Due to the weight on the roof, the lower part of the structure is slightly longer. The extension can be detected by a correctly mounted strain gauge.

With the use of strain gauges for roof weighing, it is often necessary to calculate when designing the roof structure. Furthermore, it is important to dimension the strain gauges so that their capacity is not exceeded and the equipment is not damaged.

The optimal direction of deformation is in the horizontal direction. Perpendicular deformation is undesirable. The shape of the conductors is chosen so that the short transverse sections with a larger cross section are as sensitive as possible to the deformation perpendicular to the optimum direction of deformation. The resulting foil strain gauge can be used alone and stuck to the surface to be measured, or adhered to the finished deformation member used, for example, in scales. The change in the resistance of this conductor is therefore proportional to the deformation:

$$\frac{\Delta R}{R} = K \cdot \epsilon[-]$$

where $R[\Omega]$ corresponds to the strain gauge resistance at initial mechanical load, $\Delta R[\Omega]$ is the strain gauge resistance gain, $K[-]$ is a constant expressing the strain gauge sensitivity (according to the metal layer material), $\epsilon[\%]$ relative elongation, where $\epsilon = \frac{\Delta l}{l}$ where Δl is the change of the conductor length and l is the conductor length. Dependence of resistance change on deformation change in resistance strain gauges is usually linear in given measuring range, thus complicated evaluation of output signal is not necessary.

Typically, resistance strain gauges are produced with typical unloaded values corresponding to standard resistance ranges of 120, 350, 600 and 1000 Ω. However, changes in resistance due to deformation are very small, so it is important to use an accurate A/D converter for signal processing. When measuring the strain gauges, the temperature is also affected by the temperature, as the temperature also affects the conductivity of the strain gauge material, and thus the electrical resistance. For the dependence of the electrical resistance of the metal conductor on the temperature, the relation:

$$R = R_{20} \cdot (1 + \alpha \cdot \Delta t)$$

Where R is the conductor resistance at t temperature, R_20 is the resistance of the conductor material at reference temperature $t = 20°C$, α is the temperature coefficient of electrical resistance, Δt corresponds to the temperature difference $t - t_{20}$.[10–14]

The temperature also causes thermal expansion of the strain gauge itself. The most common way to compensate for the influence of temperature is to use multiple strain gauges and connect them to the Wheatstone bridge. The Wheatstone bridge can be composed of four strain gauges, with some strain gauges being replaced by fixed resistors in the bridge. More strain gauges and possibly also solid resistors are usually part of already manufactured strain gauges.

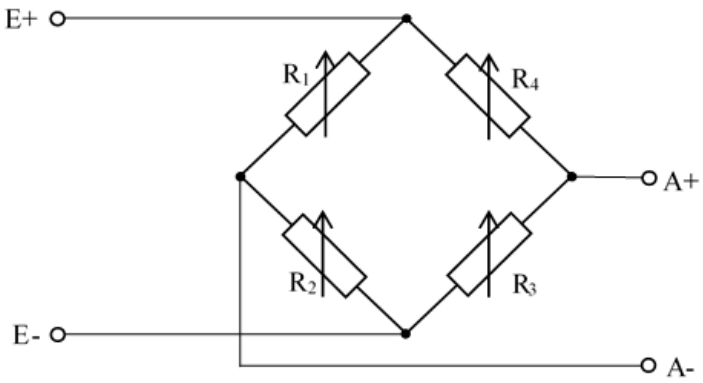

Figure 5. Schematic diagram of the full Wheatstone bridge.

Figure 5 shows a schematic diagram of the so-called full Wheatstone bridge, that is, using a strain gauge on each bridge bridge. This type of connection offers advantages such as quadruple sensitivity, non-linearity suppression, almost zero temperature error and negligible lead length. The inputs labeled $E+$ and $E-$ represent the supply of the bridge, ie the strain gauge itself. The outputs $A+$ and $A-$ then represent the strain gauge output voltage.

4. MEASUREMENT UNIT DESIGN

This part is focused on the design of the strain gauge unit. The description of the design proceeds in the direction of the electrical signal from the sensor used, through processing in a particular microcomputer or microprocessor, to sending it to the database on the Internet.[5]

First of all, it was necessary to select a suitable sensor for weighing roof structures, ie one that would be able to weigh up to tens of tons. A resistance metal strain gauge is best suited for this type of application. Its indisputable advantage is that the connection of a strain gauge with a weighing range up to 1 kg is practically identical with a tensometer with a range in tons. Therefore, it is possible to simulate and test the real use of the measuring unit in the school premises for this bachelor thesis. Another advantage of resistive metal strain gauges is the fact that in most cases they are produced as complete internal wiring devices to suppress negative environmental influences such as temperature.

To build a resistance strain gauge unit, it is important to know how the strain gauge works and what the strain gauge output signal is. According to this knowledge, a suitable A/D converter is selected and then a device capable of processing the resulting signal.

4.1 Measurement convertor

The HX711 is a 24-bit Analog to Digital converter manufactured in a 16-pin housing called SOP-16L. The total transducer module is named according to the A/D converter used. The HX711 integrated circuit is directly designed for weighing and bridge application industrial applications. The input of the integrated circuit is an input multiplexer that switches between channel A or B. Behind the multiplexer is a low-noise PGA amplifier

Figure 6. Used resistance metal strain gauge.

with a programmable gain of 32, 64, or 128 dB, corresponding to a differential input of the full range of 20 mV or 40 mV at a 5 volt power supply. It is possible to use lower power supply voltage for optimal connection with Raspberry Pi because GPIO pins supports only 3.3V logic.

The HX711 converter works on the principle of Sigma-Delta conversion. Sigma-Delta transducers provide very high linearity at up to 24 bit resolution, up to 16777216 levels. The analog portion of the converter includes a comparator, a reference voltage source, one or more integrators, and circuits for combining analog signals. Sigma-Delta transmitters use a much higher sampling frequency than the Nyquist frequency for digitization. They get a high number of samples, which are then reduced by filtering and averaging. Thus, on digital DOUT output, the averaged digital n-bit data is resampled to the frequency given by the clock signal. The clock signal can be supplied from an external source, or an internal oscillator can be used in the integrated circuit. In this work, the clock signal is applied to the any pin of Raspberry Pi.

4.2 Raspberry Pi

The Raspberry Pi microcomputer is much more suitable for creating models of different devices than the microprocessors themselves. The advantage over microprocessors is that Raspberry Pi can work independently and it is not necessary to add additional expansion cards to it, for example to connect to the Internet. Raspberry Pi contains all the important components to use as a measuring unit with a strain gauge for the Internet of Things. A more powerful RPi 3 Model B has been used for this work, but a lower power consumption system is required for actual battery power usage, as is the case with mains power.

The whole unit is composed of a Raspberry Pi microcomputer, HX711 A/D converter and temperature sensor for measuring the current ambient temperature to verify the temperature dependence of the strain gauge. Since the Raspberry Pi microcomputer does not have a built-in A/D converter in its basic configuration, the MAXIM DS18B20 digital temperature sensor was selected. The measuring range of this temperature sensor is from $-55°C$ to $125°C$, so it is fully sufficient for measurements under normal conditions. The DS18B20 is a three-pin TO-92 sensor and needs a $4.7k\Omega$ resistor connected between the digital output and the power lead for proper operation.

5. MEASUREMENT SOFTWARE DESIGN

Raspberry Pi microcomputers support running on many different operating systems. In our case, the real-time operating system Linux was used, which allows applications to run in soft real-time mode, which is sufficient for demonstration purposes. In any case, the system can be expanded to include hard real time for truly critical measurements.

The system setting corresponds to the measurement period required to diagnose the load on the ceiling structures. Running the measurement application is controlled by the system service and triggered by the CRON daemon. In the absence of a system library to connect to the InfluxDB database (InfluxData provides

the leading time series platform to instrument, observe, learn and automate any system, application and business process across a variety of use cases), the same script was used to retrieve stored values directly in the file system storage space using CURL-based basic system calls. With this method, all data can be sent to the target database platform without the need for specialized libraries. Also, the possibility of writing to the standard MySQL database, over which the Grafan system operated, was tested. Due to the special features of InfluxDB, the entire system has been redesigned for this target platform.

As mentioned earlier, the HX711 communicates on its own communication protocol. Fortunately, the manufacturer of the HX711 converter, Avia semiconductor provides an unusually detailed datasheet with a detailed description of the transmitter communication principle. The communication works on a simple principle, where the converter announces that it is not busy by setting the DOUT pin to logic 0, and then receiving the pin labeled PD_SCK. For example, the number of pulses on the PD_SCK determines what gain the transmitter should set for the next conversion, whereby at each pulse the converter matches the bits of the converted value in order from the most important bit, using the DOUT wire. PD_SCK thus serves as such clock signal input. Setting PD_SCK to logic 1 for more than $60\mu s$ will reset the converter. When creating a program for working with the HX711 converter, it is important to pay attention to the timing given in the datasheet.

Recalculation of raw value per weight is designed in such a way that the resulting weight is in units that were used in the calibration. If the weight in grams is entered during calibration, then the displayed weight is also in grams. The same applies if the value is given in kilograms, tons or even pounds.

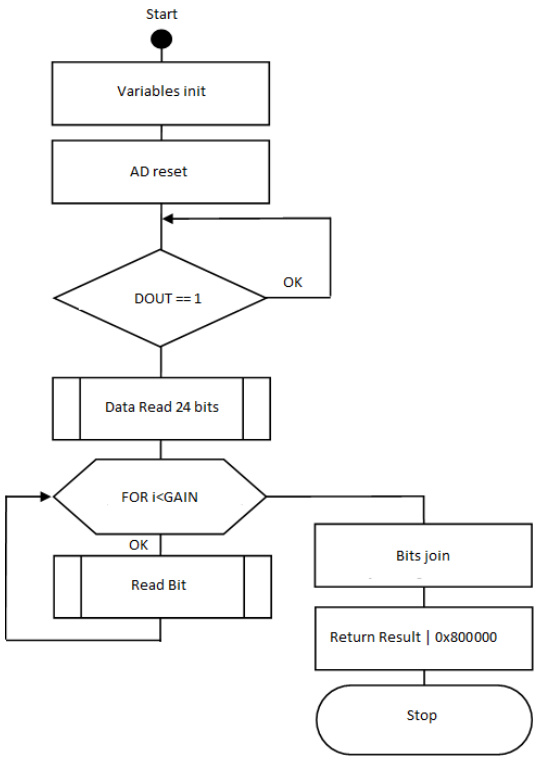

Figure 7. Simplified flowchart of hx711 library.

To process data from the DS18B20 temperature sensor, a ds18b20 library containing the function ds18b20_lib with a return temperature value is created. The ds18b20_lib function is called from the main program when sending data to the database.

To add data to a database, Influx offers a number of ready-made libraries in many programming languages, such as Python, Java, Haskell, Matlab, PHP, and more. Unfortunately, for C, the current library does not exist. The first plan to connect the unit of measurement with the strain gauge was to use a library written in Python

followed by data transfer, or another kind of link, with C. After a few failures and lack of knowledge of the C-Python connection, it was easier to find a different kind of communication. Fortunately, Influx also offers an HTTP API that supports HTTP requests. To test the functionality of sending data was first used the command line tool curl.

Programmatic adding of data to the database is ensured by the help of the same name library curl in the C language. This library is able to send queries called HTTP POST which contain data to the database. Therefore, sending data to InfluxDB works as expected, so there is time for further data processing such as visualization and gambling alerts. Other components of the Influxdata family are used for these purposes, see figure 8. The Chronograph is a user interface for monitoring data from InfluxDB databases and also for displaying notifications from Capacitor. The final appearance of the data visualization is shown in the picture **??**.

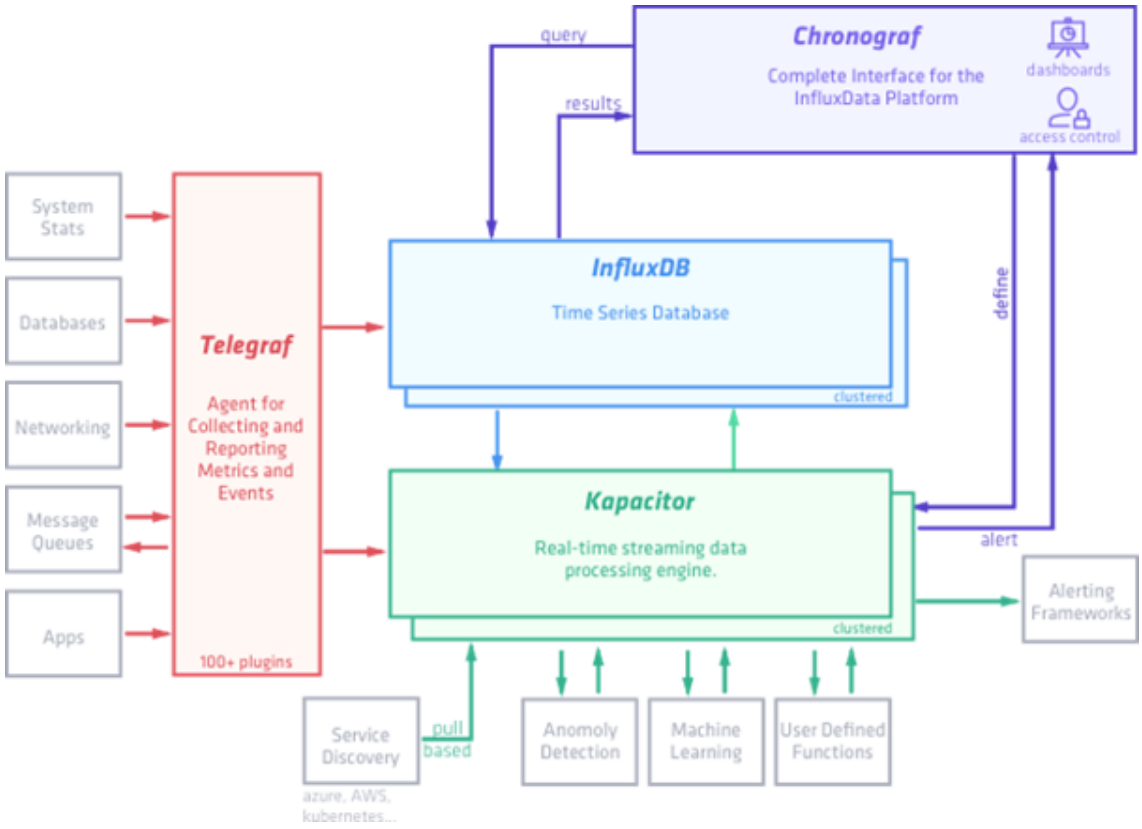

Figure 8. InfluxData product architecture.

6. TESTING RESULTS

Since it is a measuring unit designed for long-term monitoring of roof loads, it must be operated independently and without external intervention. Testing took place by connecting the unit to a database located on the VŠB network using VPN and sending the measured data to enviro.vsb.cz. The monitoring interface is located at this address. Chronograph, where the data visualization for the selected time period is displayed in the picture 9. For the Chronograph visualization, it is possible to observe the current load on the strain gauge. Appendix II shows the visualization progress of the tensiometer testing using weights of different weights - 50 g, 500 g, 1 kg and 2 kg. According to the graph shown, it can be concluded that the unit operates as expected at room temperature.

7. CONCLUSION

This work contains a description of the problem of roof loads, especially snow load, because snow load is one of the most common causes of roof structure accidents. In the next part, the thesis dealt with a brief description

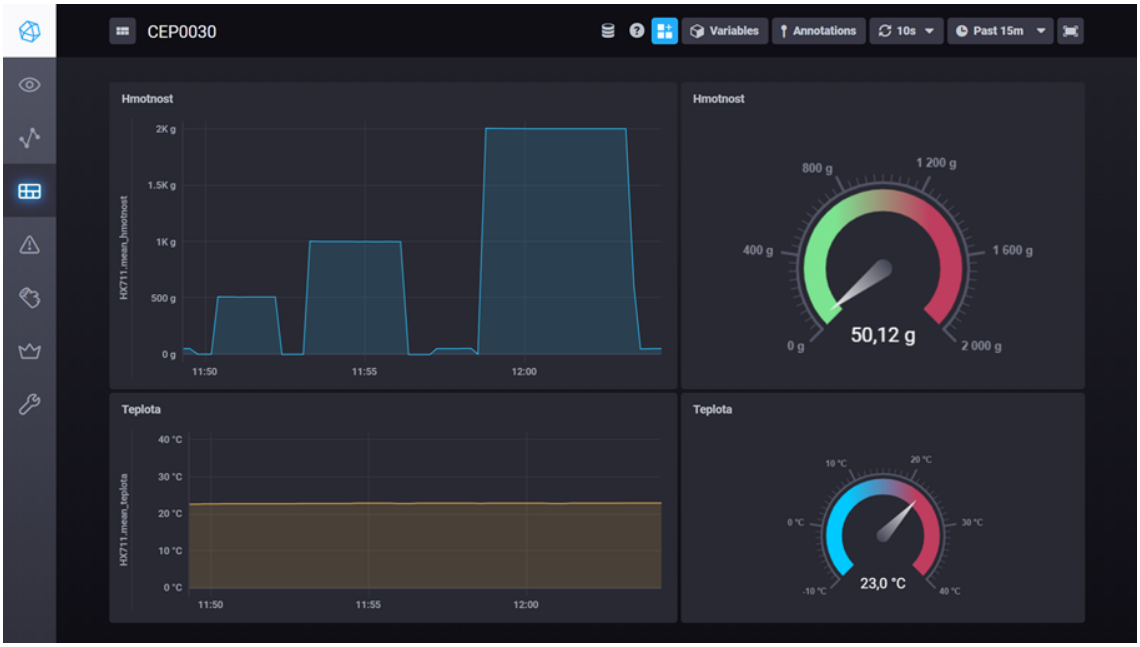

Figure 9. Chronograf visualization.

of the various types of strain gauges and the selection of the most suitable type for this kind of use.

A metal resistance strain gauge with its own deformation member was used to verify the measurement principle. In addition, a 24-bit analogue to digital converter, called HX711, and a Raspberry Pi 3 model B microcomputer were used.

Measured data from the unit was sent for later processing to the InfluxDB database, where measured data monitoring and various visualization options are performed with the Chronograph application. The chronograph further comprises an extension called a Capacitor for indicating the achieved gambling values of the load and the possibility of triggering warnings when they are exceeded.

ACKNOWLEDGMENTS

This work was supported by the project SP2019/107, Development of algorithms and systems for control, measurement and safety applications V of Student Grant System, VSB-TU Ostrava. This work was also supported by the projects of the Ministry of Industry and Trade - MPO FV20519 and by the project No. CZ.01.1.02/0.0/0.0/15 019/0004694 of European structural funds.

REFERENCES

[1] Zhang, J., Wen, H., Teng, Z., Martinek, R., and Bilik, P., "Power system dynamic frequency measurement based on novel interpolated stft algorithm," *Advances in Electrical and Electronic Engineering* **15**(3), 365–375 (2017).

[2] Martinek, R., Brablik, J., Soustek, L., Kolarik, J., Fajkus, M., Nedoma, J., and Kahankova, R., "A comparison of probes based on bragg grating sensor and microphones for heart sounds measurement," *Proceedings of SPIE - The International Society for Optical Engineering* **10801** (2018).

[3] Kolarik, J., Golembiovsky, M., Docekal, T., Kahankova, R., Martinek, R., and Prauzek, M., "A low-cost device for fetal heart rate measurement," *IFAC-PapersOnLine* **51**(6), 426–431 (2018).

[4] Marcon, P., Diedrich, C., Zezulka, F., Schroder, T., Belyaev, A., Arm, J., Benesl, T., Bradac, Z., and Vesely, I., "The asset administration shell of operator in the platform of industry 4.0," *Proceedings of the 18th International Conference on Mechatronics* (2019).

[5] Jirgl, M., Bradac, Z., and Fiedler, P., "Testing the e-peas energy management circuit for embedded systems," *IFAC-PapersOnLine* **51**(6), 432–437 (2018).

[6] Zezulka, F., Marcon, P., Bradac, Z., Arm, J., Benesl, T., and Vesely, I., "Communication systems for industry 4.0 and the iiot," *IFAC-PapersOnLine* **51**(6), 150–155 (2018).

[7] Misik, S., Bradac, Z., and Cela, A., "Reducing usage of the computational resources by event driven approach to model predictive control," *Journal of Electrical Engineering* **68**(4), 290–298 (2017).

[8] Misik, S., Cela, A., and Bradac, Z., "Optimal predictive control - a brief review of theory and practice," *IFAC-PapersOnLine* **49**(25), 324–329 (2016).

[9] Ozana, S. and Pies, M., "Predictive protective control for flexible energy system," *IFAC-PapersOnLine* **51**(6), 1–6 (2018).

[10] Walendziuk, W., "Dynamic outlier detection in the calibration by comparison method applied to strain gauge weight sensors," *Sensors (Switzerland)* **18**(12) (2018).

[11] Idzkowski, A., Walendziuk, W., and Warsza, Z., "Unconventional double-current circuit for deflection and temperature simultaneous measurement," *Elektronika ir Elektrotechnika* **21**(1), 23–27 (2015).

[12] Walendziuk, W., Idzkowski, A., and Golebiowski, J., "Reconfigurable two-current source supplied signal conditioner for resistive sensors," *Elektronika ir Elektrotechnika* **22**(2), 27–32 (2016).

[13] Walendziuk, W., Golebiowski, J., and Idzkowski, A., "Comparative evaluation of the two current source supplied strain gauge bridge," *Elektronika ir Elektrotechnika* **22**(6), 33–38 (2016).

[14] Idzkowski, A., Walendziuk, W., Swietochowski, P., and Warsza, Z., "Metrological properties of a two-output transducer for measuring sum and difference of small resistances," *Elektronika ir Elektrotechnika* **23**(5), 41–45 (2017).

Generalized model of optimal development of the production system based on optimal aggregation methodology

Taisa M. Borovska*[a], Inna V. Vernigora[a], Dmitry I. Grishin[a], Victor A. Severilov[a], Waldemar Wójcik[b], Mashat Kalimoldayev[c]
[a]Vinnytsia National Technical University, 95 Khmelnitsky Shose str., 21000 Vinnytsia, Ukraine; [b]Lublin University of Technology, Nadbystrzycka 38A, 20-618 Lublin, Poland; [c]Institute Information and Computational Technologies CS MES RK, Almaty, Kazakhstan

ABSTRACT

The paper is devoted to the development and research of new mathematical models of the functioning and development of modern production systems. The development is based on the methodology of optimal aggregation and the solution of a variational problem of optimal development applying the maximum principle method. The following modules have been developed: operators of optimal aggregation of the "production, development", "innovation" structures. The simulation model of the active external environment has been modified: "producers, products, consumers". The decomposition of the development process has been made into intervals where correction of the optimal development strategy is performed. The analysis of the existing integral criteria of optimality of the "accumulated output" type has been made. The criterion of the generalized stability of the optimally aggregated production system on the given classes of environment is selected and implemented in the software environment. Examples of modelling are given.

Keywords: optimal aggregation, variational problem, production function, simulation modeling

1. INTRODUCTION

For this work, a significant number of analogs were found by keywords, that indicates the constant relevance of the subject. There are few analogs on models and methods: "external" [16–23] and "internal" [1–8] – are works on the area of research of the T. Borovska group. This work is a continuation and development of this scientific direction. The essence of work in the field of optimal aggregation methodology is the integration of mathematical models and software modules into "working models".

Characteristics of optimal aggregation methodology are the following: the presence of the mathematical base – the algebra of optimal aggregation, which is similar to the algebra of transfer functions in control theory, where the operands are transfer functions, and operators are sums, products of transfer functions. In optimal aggregation algebra, operands are functions of the "cost, release" class – production functions; operators are binary operators for parallel, sequential, and other resource structures of production systems. The essential difference between algebra of optimal aggregation and known algebras is the optimization of resource distribution, embedded in binary operators. The operand of the aggregation result is the production function, which for each resource cost value gives the distribution maximizing the output of the production system. Optimal aggregation methods eliminate the "dimension problem". Computational costs for solving optimization problems increase no more than linearly as the dimension of the problem increases. For optimization, the direct iteration method is used, which eliminates the problem of searching in multidimensional phase spaces. The methodology of optimal aggregation allows you to set and solve problems of analysis and synthesis of control systems that are not solved by classical methods.

The aim of the development is to obtain a parametrized model of production and enterprise development, enabling parametric adjustment for a specific production, providing optimal adaptive control. **Development tasks:** solving the problem of optimal aggregation for structures with parametric links; formulation and solution of the problem of optimal aggregation of multilevel structures with parametric links.

*taisaborovska@gmail.com

Photonics Applications in Astronomy, Communications, Industry, and High-Energy Physics Experiments 2019, edited by Ryszard S. Romaniuk, Maciej Linczuk, Proc. of SPIE Vol. 11176, 111765V
© 2019 SPIE · CCC code: 0277-786X/19/$21 · doi: 10.1117/12.2536889

2. ANALYSIS OF BASIC MODELS OF OPTIMAL PRODUCTION DEVELOPMENT

In [5] presents an adaptive optimally aggregated production system. Two examples of the production system working the testing input "required total output" are presented. The content of adaptation: the optimal distribution of the current input is calculated online for the current input and the current values of the parameters of production functions and the dynamics of the subsystems. Adaptive system – non-searching, analytical. This example is the confirmation of the operability of the optimal control model. The result, presented in [5] allows you to set and solve more significant survivability problem – the optimal control of the production system in case of subsystem failures. In [4] presents the concept of such a control system. Vitality is ensured by the optimal redistribution of the resource (or the load of the production system) between the subsystems by the method of optimal aggregation. The implementation of the control concept in case of failures and accidents allowed us to set and solve the problem of developing a unified model of efficiency and survivability [4]. In the model for analyzing and optimizing efficiency and survivability, these tasks are combined as efficiencies in nominal and non-nominal conditions. For this article, this is an example of solving the problem of optimizing the future state of a production system operating in conditions of passive and active, external and internal disturbances. In the framework of classical models and methods, a satisfactory solution of the problem of optimal development is impossible.

Fig. 1 shows the structure and tasks of the basic analogue [3] of the optimal development problem. The original source of the base analog is the solution of the variational "distribution problem" by R. Bellman [13, 15], who investigated this problem, applying purely analytical methods, but did not solve the problem of high dimensionality. Three steps of the method for solving the development problem based on optimal aggregation methods are presented: formalization and testing of the rationality of the resource structure of production; optimal aggregation, obtaining optimal equivalent functions of production and development; solving a variational optimal development problem for an equivalent one-dimensional object.

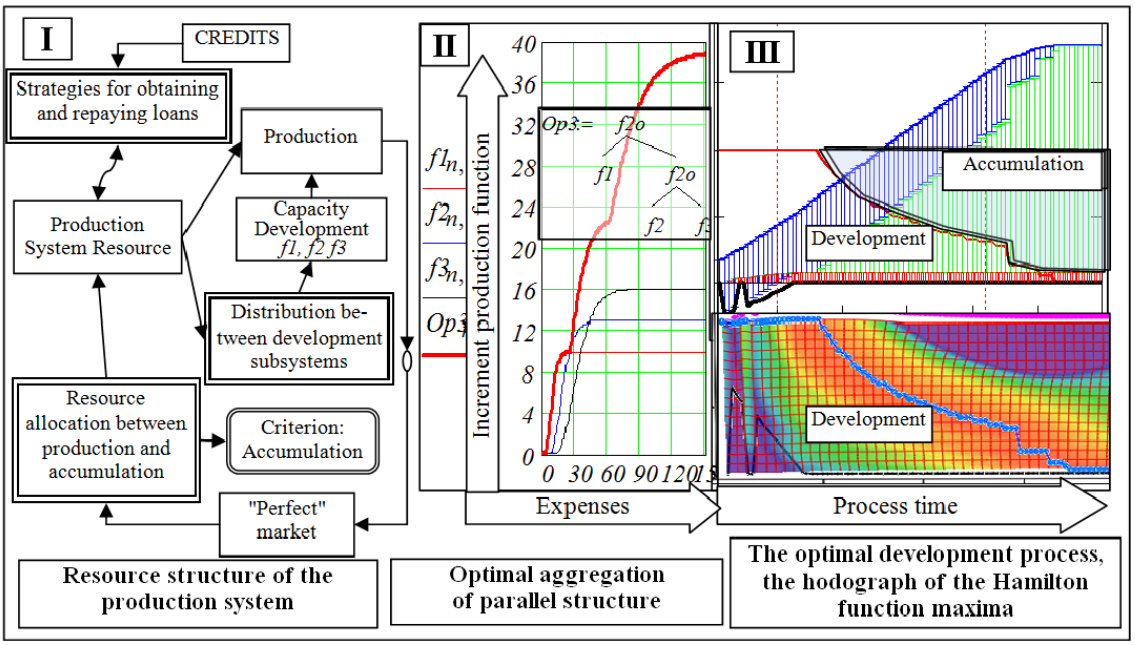

Fig. 1. Basic analogue: resource structure, optimal aggregation, optimal development strategy

The selected research and development subject has always been and remains relevant. High technologies and globalization have significantly changed the properties of production systems, from aircraft to the agricultural sector. The existing scientific support for production does not in essence take advantage of modern information and computing systems in solving problems of analysis and synthesis of production systems. In the considered analogues and prototypes [4, 5], the possibilities of vectorization and other possibilities of parallelization of computations are used. The methods of optimal aggregation have a significant advantage with search methods, and the methodology of optimal aggregation allows you to set and obtain effective solutions to new actual problems, in particular the generalized problem of the functioning and development of production systems.

3. FORMULATION AND ANALYSIS OF DEVELOPMENT TASKS

Fig. 1 presented the scheme of the basic analogue. Fig. 2 shows a diagram of a new generalized development model. This diagram is filled with test production data of the system. Natural problem of scaling the mathematical model appears. In optimal aggregation, this is a routine operation. In [3] the examples of systems are presented: "corporation" – 24 elements and "region" – 128 elements. The novelty and lack of the direct analogs stipulate the necessity of the development of a mathematical model in conjunction with a software module – a test working model of the production system.

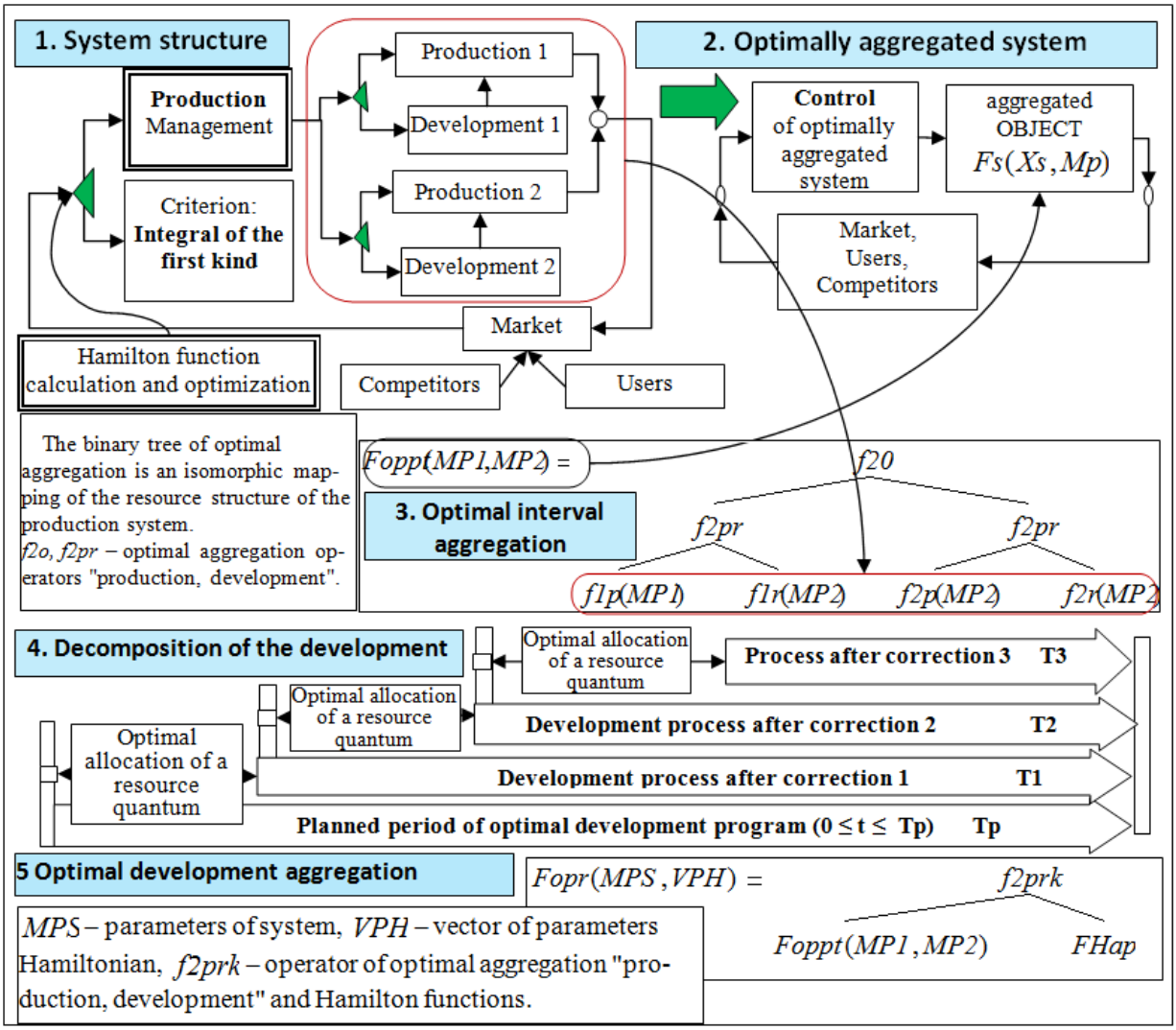

Fig. 2. Structure of the complex development tasks. Proposed new solution

Fig. 2 presents five problems their solution is necessary for creation of a generalized model of optimal development. It should be noted that when using classical methods for solving variational problems of development, the central problem is the solution of nonlinear algebraic and differential equations higher than the second order. When using the methodology of optimal aggregation, it is the development of efficient resource models based on "generating mechanisms" [10–12]. Fig. 2 also presents the connections between tasks 1–5. In general, this is the structure of the "tools" for the construction of the generalized model of functioning and development of modern production. In this paper, the generalization is not the result of expanding the model, introduction of new subsystems, but obtaining of a compact form – an optimal equivalent production function (OEPF), which allows to solve the control problems taking into account all the essential factors. The base for generalization is a theorem on the isomorphic mapping of the resource

structure of the production system into a binary tree of optimal aggregation [3, 16]. Fig. 3 presents the informational aspect of the generalized model: increasing the efficiency of using heterogeneous information on the state of production.

In the application plan, the result is trivial: the elements of the scheme I, II, III are user functions with the parameters MP and V, respectively, the matrix of parameters and the vector of perturbations. The issues of measurement, obtaining of estimations and statistics are not considered in this article. Let us compare this scientific result with analogues based on search methods in multidimensional phase spaces (theories of optimality, adaptability, sensitivity, dynamics of nonlinear systems, statistical methods). Classical methods: – complex mathematical apparatus and too simplified models and tasks. All this was fundamental and effective in the pre-computer era and did not lose its importance today. The methods of optimal aggregation do not have limitations on the object model, they allow to "automate" the operations of mappings and implement an online solution of optimization problems when the parameters of the production system change.

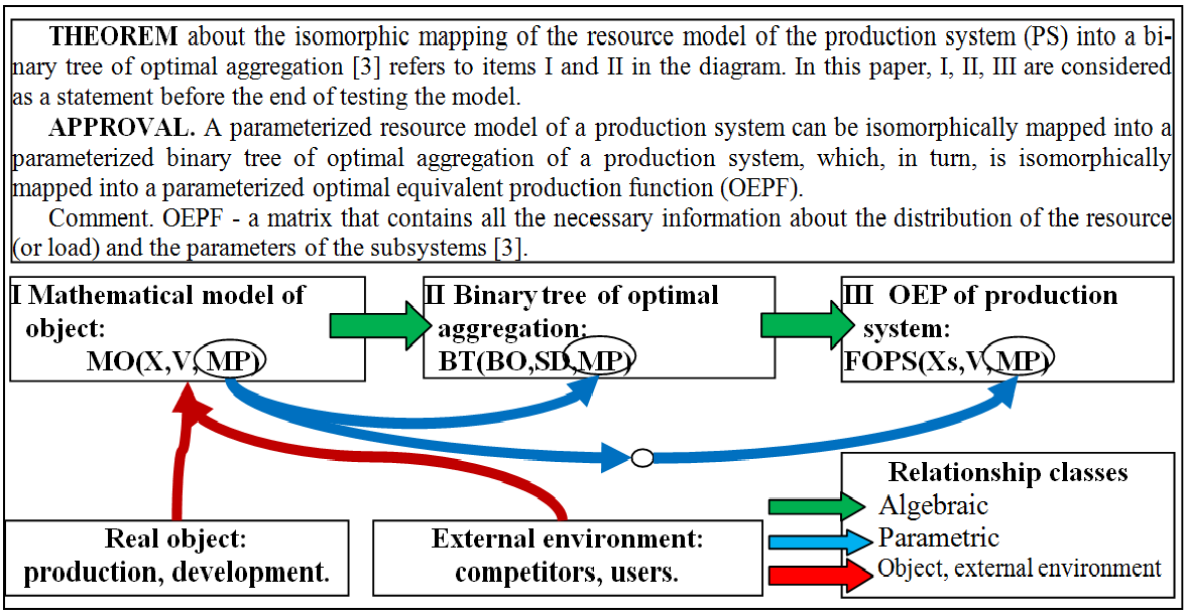

Fig. 3. New scientific result: isomorphic mapping of a parameterized production model into a parameterized optimal equivalent production system function

4. INFORMATION TECHNOLOGY OF CONSTRUCTION OF THE GENERALIZED MODEL

The methodology of optimal aggregation is based on the creation of a working model already at the first steps of management system development. For constant control over the development process of substantially non-linear discretized stochastic systems, modeling and corresponding systems of models are required. Such technology is essentially an implementation of prototyping technologies in various areas of technology that have not lost their effectiveness today. Testing and research on models provide new knowledge about the properties of the object – real or designed. Classical science makes great efforts to control the adequacy of the model to a natural object. Today, *de facto*, there is a direction "modification of a natural object according to the results of modeling". To move from an abstract idea (Fig. 3) to a working model, a comprehensive study of all aspects of optimal aggregation of parameterized objects is necessary. Further (Figs. 4–8) the sequence of steps for the development of a parameterized generalized model of the functioning and development of the production system is presented.

Fig. 4 shows the optimal system aggregation. Fig. 4 – test model of small dimension, but it includes all typical resource binary structures: parallel, sequential, resource feedback, "production, development". The diagram shows the blocks IMS and "SERVICES" without specifying links. We are considering a "clean production" model. The methodology of optimal aggregation allows you to create rational structures of IMS. In the lower part of fig. 4 shows a binary tree of optimal aggregation. This is not a drawing, but a formula in structural form. Assignments are recorded in several nodes: PAR7 = , PAR12 = , PAR14 = – reminder of the operation, the result of which is the optimal equivalent function of the

corresponding subsystem. In a software environment, this is a matrix that contains information about input operands and a result operand. The result of the first step: solving the problem of nonlinear programming, presented as a function of the total cost of production resources and the matrix of parameters. Parameters can be scalar, matrix, user functions.

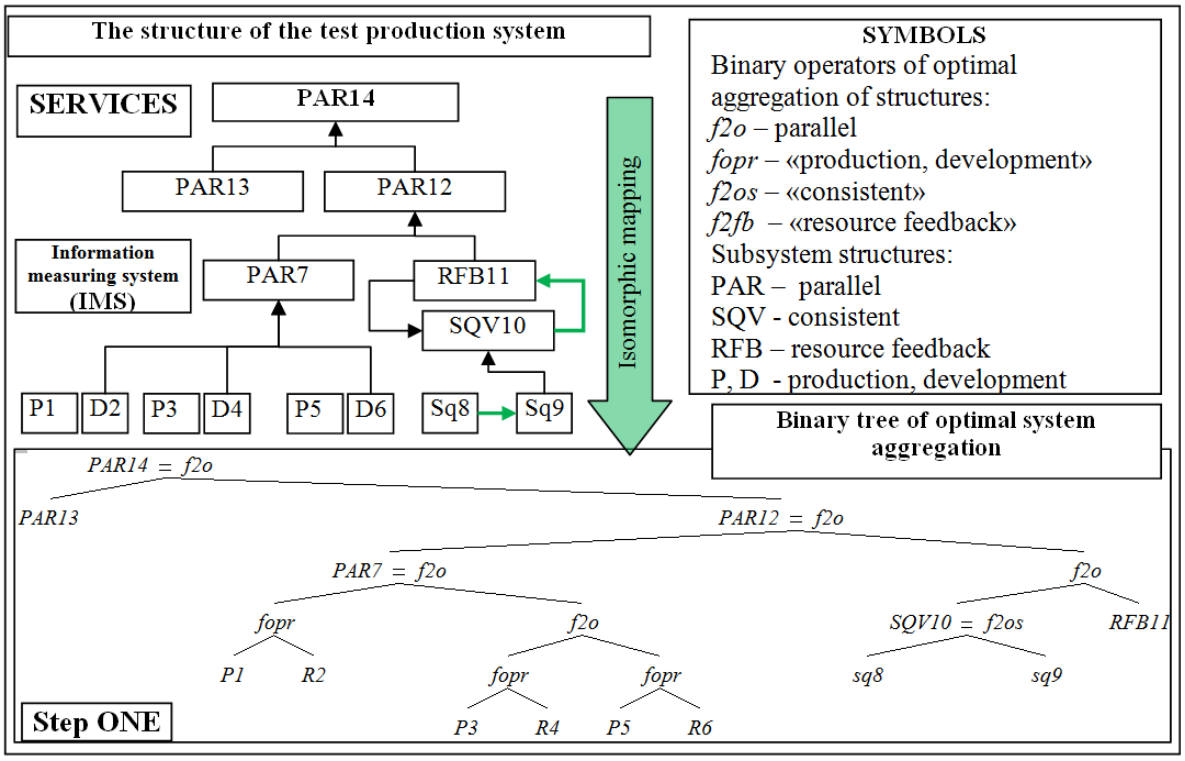

Fig. 4. Isomorphic mapping of the resource structure into a binary tree of optimal aggregation

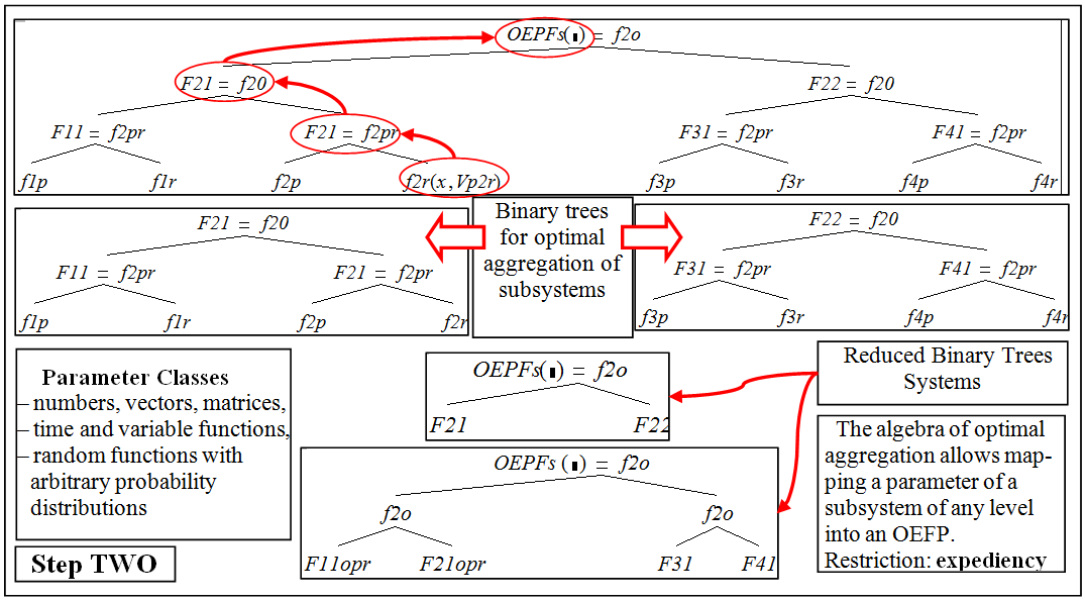

Fig. 5. Multi-level optimal aggregation. Passing of the parameters between the levels

Fig. 5 shows the second development stage: optimal aggregation of the structure of the four integrated subsystems "production, development". The binary aggregation tree consists of four aggregations "production, development" at the

lower level and three aggregations of parallel structures. In this diagram f*2pr, f2o* – aggregation operators of structures: "production, development" and "parallel". At the top of Fig. 5 shows the diagram of displaying the parameter of the lower level of aggregation to the upper level is shown. In the lower part of Fig. 5 the examples of the analysis of binary aggregation trees are shown.

Fig. 6 considered the problem of optimal aggregation of systems with sequential parametric resource relations. Interpretation of the structure "production, development": we have an integrated subsystem of the elements "production" and "development". At the beginning of a certain planning interval, the resource is distributed among the elements so as to maximize certain criterion at the end of the interval. The resource relationship between the elements: the costs in the "development" element are converted into increments of production capacity and an increase in the efficiency of the "production" element. Thus, the element "development" changes the parameters of the element "production". This is essentially only a concept, but if we ask a specific production, for example: "dairy", "agricultural enterprise", "garment factory", then one can get a satisfactory solution of the problem, based on the methodology of modeling and optimal aggregation. In modern production, the structures "production, development, innovations" can be formed. This article presents an approach to the solution of such problems on the basis of a modification of the optimal aggregation algorithm (bottom part of Fig. 6). The content of the modification is the calculation of the new values of the parameters of the corresponding element of the binary structure [24–26].

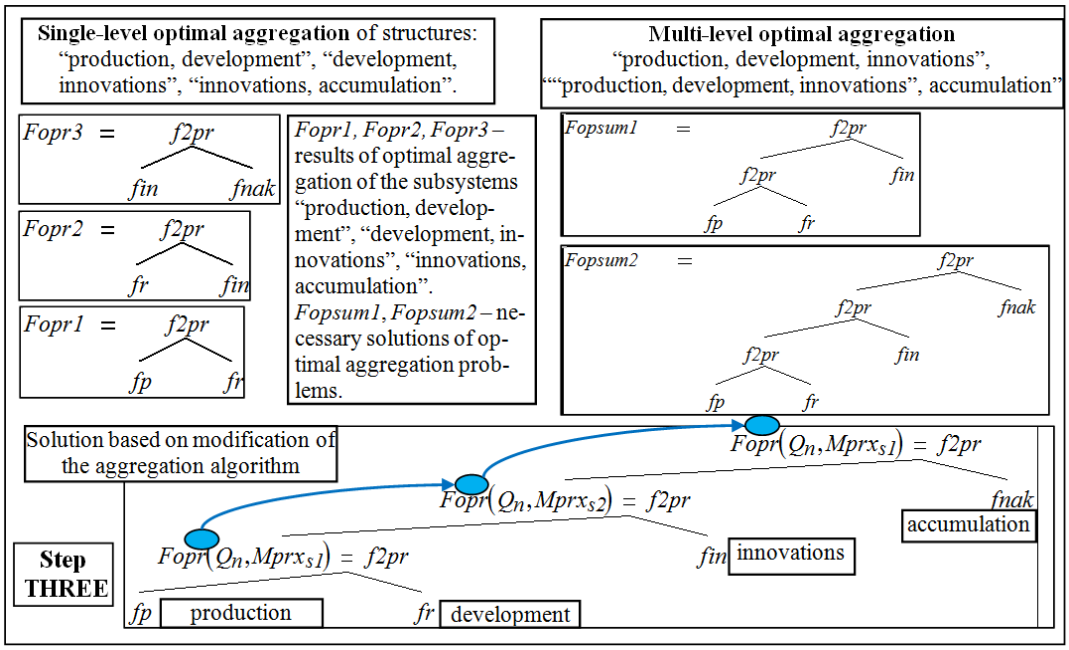

Fig. 6. Optimal aggregation of the sequential structures with parametric operand connections

Parametric links are difficult to formalize, identify, but they are real and "naturally" arise in developing systems. In [14], such structures are called "model towers" and their study was conducted. The difference of structures in Fig. 5 and 6: in Fig. 5 selected chain – displaying of the lower level parameters transfer of the lower level to the upper one, and in Fig. 6 – changes of the functions of production parameters values according to the results of the performed aggregation.

Fig. 7 shows the elaboration of the task of developing a parameterized transition operator between the intervals of the development process. In the upper part of Fig. 7 – the structure of the process of optimal functioning and development of the production system (PS) is shown. At the initial moment, on the basis of the initial state of the production system, the optimal development strategy for the "planned period" (0, *TP*) is calculated. Further, after the expiration of a certain interval ΔT, the optimal strategy for the period (ΔT, *Tn*) is calculated taking into account the actual current state of the PS, the environment and the updated forecasts for the future. The control at the current interval is formed as some autonomous task, for which the "resource quantum" ΔXsn , the initial state of the substation and the initial values of the subsystems parameters are set to perform the optimal aggregation of "production, development" [1, 2]. The result of optimal aggregation gives the initial data for the next interval. The specified strategic management and development of

"resource quanta" are implemented at the operational management level. In the framework of classical methods, stable and high-quality control of an essentially nonlinear non-stationary stochastic system in its general form is an almost insoluble task. However, optimal aggregation allows to distribute the management of the production system among the elements of a binary tree of optimal aggregation. In the lower part of Fig. 7 the example of a complex system dynamics model is shown. The *smt* state vector and the state transition operator *Ypur*, a software module whose structure is consistent with the state structure, is shown. Such models are designed for dynamic systems of the classes "queuing system", "Optimal development", "product market", "Inventory management" [7].

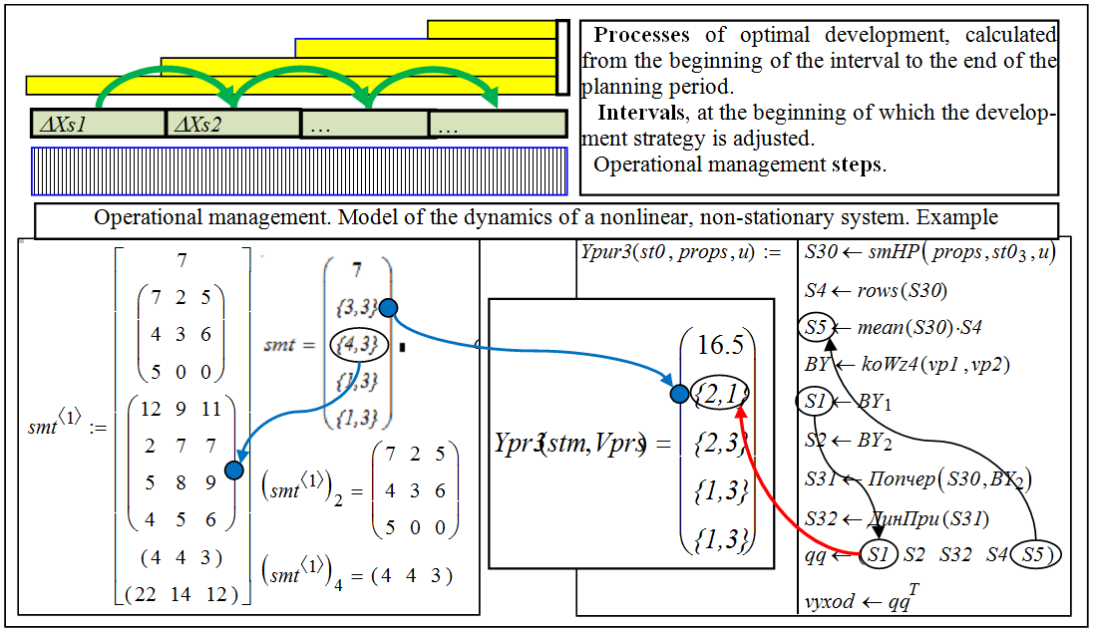

Fig. 7. Development of a parameterized transition operator between the development process intervals

The methodology of optimal aggregation makes it possible to form models of the dynamics of production systems in a new way, namely, to implement, on the software level, optimality, adaptability, vitality, resistance to random perturbations and failures more effectively than in classical models and methods [17–24]. Using the methodology of optimal aggregation not only solves the problem of optimal control, but also determines the rational hierarchical structure of the control system. Fig. 8 presents the operational control scheme. Block of strategic management issues the required level of the output Ys. The block of optimal aggregation in real time solves the problem of optimal aggregation using the current values of parameters (prices, credits, efficiency, etc.). The result of the optimization is the optimal equivalent production function of the *Fops* ((Xs, Mps) of the production system. On the basis of this optimal equivalent function of the production system, the equations of dynamics of all subsystems are formed. This is a key point of transition from the global task of enterprise management to local tasks of subsystem management. At the same time, this information control structure provides a solution of survivability problem not only for the production task, but also for the systems of service, inventory management, retail, product lines. These tasks are still satisfactorily solved by practitioners with insufficient scientific support. The optimal equivalent production function actually provides solutions for a pair of conjugate tasks of nonlinear programming: – *direct task*: the objective function *Ys* = *Fop* (*Xs*, *Mp*), the constraint on the resource *Xs*, to find the distribution of the resource *Xs*, giving maximum output to the products *Ys*; – *conjugate task*: the objective function *Xs* = *Fobr* (*Ys*, *Mp*), the restriction on the release of *Ys*, to find the distribution of the resource *Xs*, which gives the minimum cost of production *Xs*. Note, that the solution of optimal aggregation problem is a function, but not a point. The numbers and graphs in Fig. 8 is the result of the work of the program module. The matrix (fragment) in the right part of Fig. 8 is an information structure similar to an entry in relational databases. The graph is constructed according to the column number 1. These data are used to construct schemes for solving conjugate optimization problems. The optimal equivalent production function (OEPF) contains the solution – the optimal normalized resource distribution between the subsystems. For the value of costs *Xs* = 47, we have the optimal resource allocation: (0.29 + 0.7 + 0.01+ 0.0 = 1). These are the input data of operational control in the subsystems.

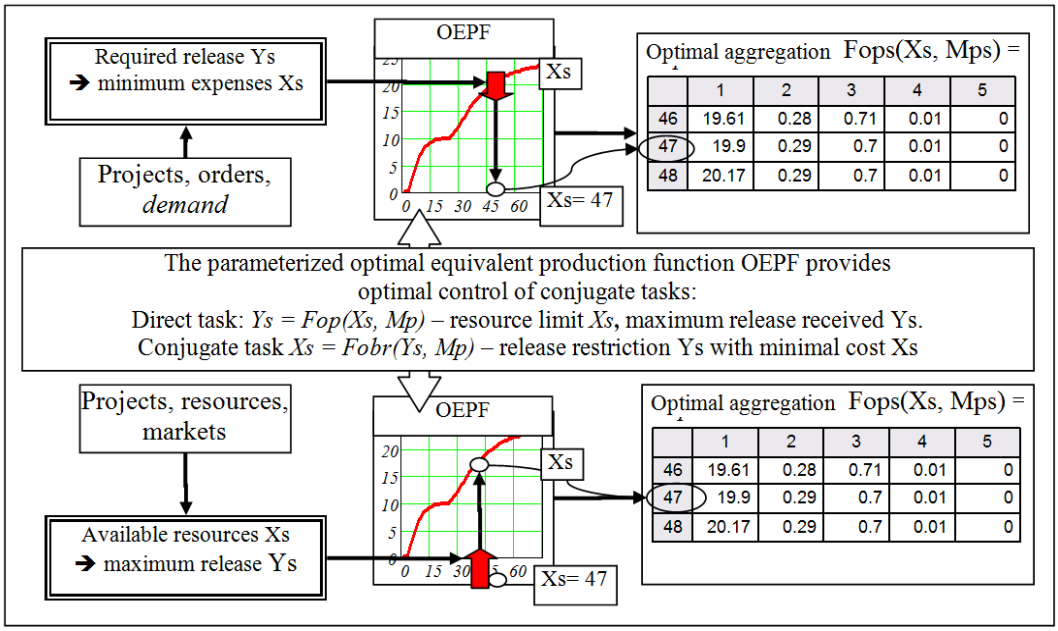

	1	2	3	4	5
46	19.61	0.28	0.71	0.01	0
47	19.9	0.29	0.7	0.01	0
48	20.17	0.29	0.7	0.01	0

Fig. 8. Operational optimal control of the production system for the conjugate tasks

In the methodology of optimal aggregation, the development of a working mathematical model is a smaller part of the costs. Greater part of the costs – testing of the model and model research carrying out. Research tasks are selected from what is relevant, but unacceptable in natural systems.

5. CONCLUSIONS

On the basis of the analysis of the known solutions of the variational development problem, the goal of development is defined: a generalized model of optimal functioning and development of a production enterprise. Specific development tasks have been set and a justification has been made for choosing the optimal aggregation methodology. The methods of optimal aggregation of the production system typical resource structures allow the model to be tuned to a new control object due to the operands parameterization. The difference between the method of optimal aggregation and analogs is that it gives, as a solution of the optimization problem, the "optimal equivalent production function" of the aggregated system. The same property of methods of optimal aggregation allows to create an analytical (non-search) adaptive automatic control system (ACS). We set new tasks to achieve the goal. The basis of development and the standard for controlling the adequacy of the model is the classical formulation of the variational problem of developing a production system and its solution using the methods of maximum principle and methods for optimal aggregation of parallel structures of development subsystems. The problem of optimal aggregation of arbitrary resource structures of the production system, in particular, the structures "production, development", "production, innovations" is solved. The result of aggregation is the optimal equivalent production function and development of the production system. The relevance on the theoretical level is the effective solution of development process optimization problem. Relevance in practical terms – testing of a complete, optimal, adaptive management system of the operation and development of production.

REFERENCES

[1] Borovska, T., Vernigora, I., Severilov, V., Kolesnik, I., and Shestakevych, T., "Model of Innovative Development of Production Systems Based on the Methodology of Optimal Aggregation," Selected Papers from International Conference on Computer Science and Information Technologies, CSIT 2018, 171-181 (2018).

[2] Borovska, T., Vernigora, I., Kolesnyk I., Kushnir A., "Control of multi-channel multiphase queuing system based on optimal aggregation methodology", Selected Papers from International Conference on Computer Science and Information Technologies, CSIT 2018, 259-265 (2018).

[3] Borovska, T. M. [Mathematical models of functioning and development of production systems based on optimal aggregation methodology], VNTU, Vinnitsa, Ukraine, (2018)
[4] Borovska, T.M., Bevz, I.S., Kolesnyk, I.S., Severilov, V.A., Kobylianskyi, O.V., Gromaszek, K., Rakhmetullina, S., "Model for the analysis and optimization of the efficiency and survivability of an enterprise based on optimal aggregation methodology," Proc. SPIE 10808, 1080824 (2018).
[5] Borovska, T.M., Vernigora, I.V., Grishin, D.I., Severilov, V.A., Gromaszek, K., Aizhanova, A., "Adaptive production control system based on optimal aggregation methods," Proc. SPIE 10808, 108086O (2018).
[6] Borovska, T. N., Kolesnik, I. C., Severilov, V. A., [Optimal aggregation method in optimization problems], Universum, Vinnitsa, (2009).
[7] Borovska T. N., Badera, S. P., Severilov, V. A., Severilov, P. V., [Modeling and optimization processes of production systems with the use of external resources and the effects of development], VNTU Vinnitsa, Ukraine, (2009).
[8] Borovska, T., "Generalized model of optimal development, based on the integration of production and development subsystems", Proc. CSIT'2017, 446-449 (2017).
[9] Mukha Ap.A., "Control of the process of complex engineering systems and processes development. Characteristic features of FMEA-analysis application," Mathematical machine and systems 2012(2), 168–176 (2012).
[10] Forrester J. [Fundamentas of cybernetics of the enterprise (Industrial dynamics)], Probgress, Moscow (1971).
[11] Opoitsev, V. I. [Equilibrium and stability in models of collective behavior], World Publishing House, Moscow (1977).
[12] Mashkov, V., Smolarz, A., Lytvynenko, V., Gromaszek, K., "The problem of system fault-tolerance," Informatyka, Automatyka, Pomiary w Gospodarce i Ochronie Srodowiska – IAPGOS 4(4), 41-44 (2014).
[13] Bellman, R. E., Kalaba, R. E., [Dynamic programming and modern control theory], "Nauka", Moscow, (1969).
[14] Leontiev V., "Theoretical assumptions and non-observable facts," USA: Economy, ideology, politics 9, 15 (1972).
[15] Bellman, R.E., [Certain problems of mathematical control theory], Publishing House of Foreign Literature, Moscow, (1962).
[16] Fagin, R., Kumar, R., Sivakumar, D., "Efficient similarity search and classification via rank aggregation," Proceedings of the 2003 ACM SIGMOD international conference on Management of data – SIGMOD '03, 301 (2003).
[17] Rüttimann, B. [Introduction to Modern Manufacturing Theory], Springer International Publishing, (2016).
[18] Rüttimann, B., Stockli, M., "Going beyond triviality: The Toyota production system—lean manufacturing beyond Muda and Kaizen,". J. Serv. Sci. Manag. 9, 140–149 (2016).
[19] Nersessian, N. J., & Chandrasekharan, S., "Hybrid analogies in conceptual innovation in science, "Cognitive Systems Research 10, 178–188. (2009).
[20] Murayama. T, Devis, P., "Optimal aggregation of noisy observations," Journal of Physics: Conference Series, 233(1), 301-312 (2003).
[21] Zaritskyi, O., "Information system for assessing the professional activities complexity – theoretical and practical aspects of implementation," Informatyka, Automatyka, Pomiary w Gospodarce i Ochronie Srodowiska – IAPGOS 8(4), 52-55 (2018).
[22] Dai, W., Jin, G.Z., Lee, J., Luca, M., "Aggregation of Consumer Ratings: An Application to Yelp.com," National Bureau of Economic Research Working Paper Series 18567, 12–23 (2012).
[23] Xinxin L, "Self-Selection and Information Role of Online Product Reviews," Information Systems Research 19(4), 56-64 (2008).
[24] Wojcik, W., Lach, Z., Smolarz, A., et al., "Power supply via optical fibre in home telematic networks," Przeglad Elektrotechniczny 84(3), 277-279 (2008).
[25] Wojcik, W., Gromaszek, K., Kotyra, A., et al., "Pulverized coal combustion boiler efficient control," Przeglad Elektrotechniczny 88(11B), 316-319 (2012).
[26] Wojcik W., Romaniuk, R., „Optical fiber technology development in Poland," Proc. of SPIE 7745, 774508 (2010).

High speed buffer devices on the base of push-pull current amplifiers

Olexiy D. Azarov[1], Sergii V. Bogomolov[1], Svitlana A. Kyrylashchuk[1],
Olexiy J. Stakhov[1], Mariusz Duk[2] , Yedilkhan Amirgaliyev[3]
[1] Vinnytsia National Technical University, Vinnytsa
[2] Lublin University of Technology
[3] Institute Information and Computational Technologies CS MES RK

ABSTRACT

Method of structural-functional organization of high speed buffer devices on the base of push-pull current amplifiers is considered. The importance and practical expediency of the creation of such types of voltage buffers for obtaining the low error of linearity and high operation speed is substantiated. Push-pull voltage buffers with the input amplifying stages and input current compensation are considered and analyzed. Analytical relations, describing static transfer characteristic, taking into account the circuit core parameters, are given. The components, leading to the linearity error occurrence are determined, ways of its reduction are shown. Voltage buffers with the decreased output resistance are suggested, for this purpose, push pull DC amplifiers are additionally introduced in the circuit, they have profound negative feedback. Computer simulation of the static and dynamic characteristics of the suggested schemes of the voltage buffers has been carried out, the comparative analysis of the results obtained has been performed, the possibility of the construction of high speed buffer devices on the base of push pull current amplifiers has been proved.
Key words: high speed, buffer device, push pull current amplifier.

1. INTRODUCTION

Buffer devices are the analog blocks, used in various electronic devices, in particular, multidigit system ADC and DAC, which in their turn, are parts of the high accurate information-measuring systems [1-5]. Buffer devices are power amplifiers and are intended for matching the resistance of the signal generator with the load resistance [4]. Voltage buffer (VB) performs the function of the resistance transformer with high input and low output resistance. Voltage transfer ratio of VB equals one. Current, supplied by VB in the load, can be far greater than the input current. Such buffer devices are called voltage repeaters [6]. Current buffer (CB), on the contrary, has low input and high output resistances. CB current transfer ratio of CB, as a rule, equals one and does not depend on the load.

Many varieties of the precision buffer devices are known both by their circuit engineering organization and designation. The most widely-used is the construction of the buffer devices on the base of the operational amplifiers [1,2,4]. However, such an approach limits their operational rate.

2. RELEVANCE OF THE RESEARCH

Nowadays special attention is paid to push-pull circuits of the buffer devices. They are able to provide high linearity of the transfer characteristics and the required operation speed [2,4,5]. It should be noted that the known circuit engineering solutions of the buffer devices with the push-pull structure, which provide high operation speed and minor nonlinearity are unbalanced, have low accuracy of zero shift , have high temperature drift. Also it is known that the static errors of the VB first of all are determined by the linearity of the volt-ampere characteristics of the transistors [7], on which they are constructed . For achieving high dynamic characteristics of VB the principle of the conversion and amplification of currents must be used to the maximum . It is stipulated by the fact that greater part of the stray parameters of the integrated circuit are capacitances [8, 9, 13]. That is why, if the current but not voltage is chosen as the signal carrier, then the application of large voltage increments to the stray capacitances can be avoided. Also, it should be noted, that even when voltage amplification has to be done, it is expedient to convert the voltage of the input signal into the current, then amplify it, and at the output of the circuits the current will be converted into voltage again. The bipolar transistor can be successfully used up to the boundary frequency. At the same time, the material, devoted to the construction of the buffer devices on the base of push-pull symmetric structures, is presented in scientific-technical literature occasionally and is non-structured. That is why, the subject of the paper, devoted to the construction of high speed buffer devices on the base of push-pull current amplifiers, is important.

Photonics Applications in Astronomy, Communications, Industry, and High-Energy Physics Experiments 2019,
edited by Ryszard S. Romaniuk, Maciej Linczuk, Proc. of SPIE Vol. 11176, 111765W
© 2019 SPIE · CCC code: 0277-786X/19/$21 · doi: 10.1117/12.2536902

Aim. Creation of the high speed buffer devices on the base of the push-pull current amplifier with minimized linearity errors, high operation speed and the increased loading capacity.

3. STATEMENT OF THE PROBLEM

1. Analyze the suggested method of structural functional organization of the high speed buffer devices on the base of push-pull current amplifiers with the increased loading capacity.
2. Propose and analyze the circuits of the VB cores on the base of push-pull symmetric structures.
3. Compose the mathematical models of the static characteristics of VB cores, small signal coefficient of voltage transfer, error of the transfer characteristic scale, input resistance and loading capacity at the preset scale error.
4. Propose and analyze the circuits of the push-pull VB with the decreased static errors.
5. Perform the computer simulation of the static and dynamic characteristics of the considered VB circuits, evaluate the quantitative values of the transfer characteristic linearity error, zero shifts current and voltage, ra te of input signal growth, time of the transient characteristic setting, carry out the comparative analysis of the results obtained.

4. SOLUTION OF THE SET PROBLEMS

VB on the base of the push-pull symmetric structures must provide the possibility of the operation in the mode, when the input U_{IN} and output U_{OUT} voltages are bipolar and the output current I_{OUT} can both flow in and flow from the load. Conventionally, circuit, constructed on the base of the operation amplifier meets these requirements, however, it cannot provide high operation speed, when $\pm U_{IN}$ varies in a step change manner [14,15].

This is connected with the fact, that the input differential stage of the operation amplifier leaves the linear mode and some time is needed to restore the balance between the input and output. Such an approach does not provide necessary loading capacity.

The authors propose another approach to the construction of the buffer devices, enabling to increase the loading capacity and not influencing the preset linearity of the base of the push-pull symmetric structures [5]. The generalized structure of such buffer device is shown in Fig.1.

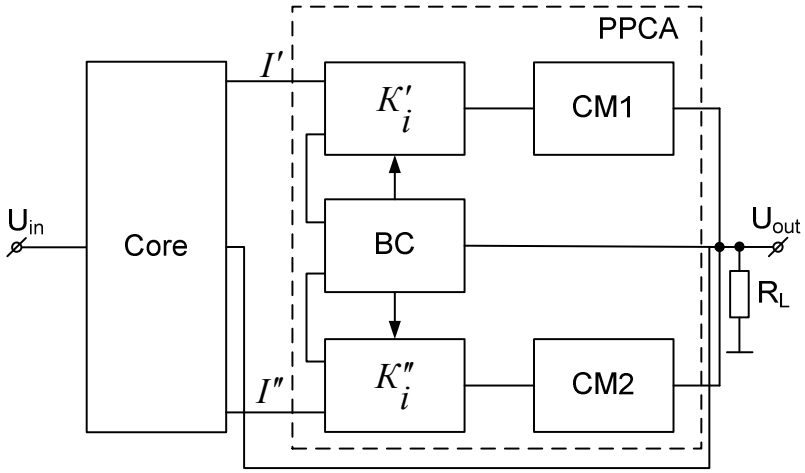

Fig. 1 – Structural-functional organization of the high speed buffer device on the base of push-pull current amplifier

The device consists of the amplifying stages K'_i i K''_i, balancing circuit (BC) and current mirrors CM1 and CM2. Balancing circuit enables to obtain the proportional dependence between the resulting transfer coefficients and equalizing of their values in the signal range. The condition of the self- balancing is the performing of the equality: $\frac{I'}{Iw} = \frac{Iw}{I''}$, where Iw – the current of the working point. In this case: $K'_i = K''_i$.

The introduction of the push-pull current amplifier (PPCA) in the feedback circuit, namely between the core and the load, allows to decrease the output resistance to the level:

$$r_{out} = \frac{r_e}{K_i},$$

where K_i – general coefficient of PPCA amplification, determined as:

$$K_i = \frac{2 \cdot K_i' \cdot K_i''}{K_i' + K_i''}.$$

Special attention should be paid to the core of the circuit, also built according to the push-pull structure.

Several approaches can be mentioned , regarding the constructions of the VB on the base of push-pull symmetric structures. One of such approaches is the circuit, shown in Fig. 2, a, its prototype is described in [4,15].

The circuit additionally contains the input push-pull stage on T1 and T2 transistors and the output stage on T3 and T4 transistors. Besides, T′C, T″C and biased -diodes D1, D2 are introduced in the circuit additionally to block the changes of the collector-emitter voltages T1 and T2, as well as for the balancing of their working points relatively T3 and T4. We will evaluate the static characteristics of this VB. It should be noted, that the input resistance will increase as the amplifying transistors T1 and T2 are introduced additionally in the circuit. Its value will be equal to:

$$r_{IN} = R_L \cdot K_i.$$

where, taking into account [10], we will have:

$$K_i = \frac{2 \cdot (\beta' \cdot \beta'') \cdot (\beta' \cdot \beta'')}{\beta' \cdot \beta'' + \beta' \cdot \beta''} = \beta' \cdot \beta'',$$

where β', β'' – small signal current amplification factors of the transistors n-p-n and p-n-p, correspondingly.

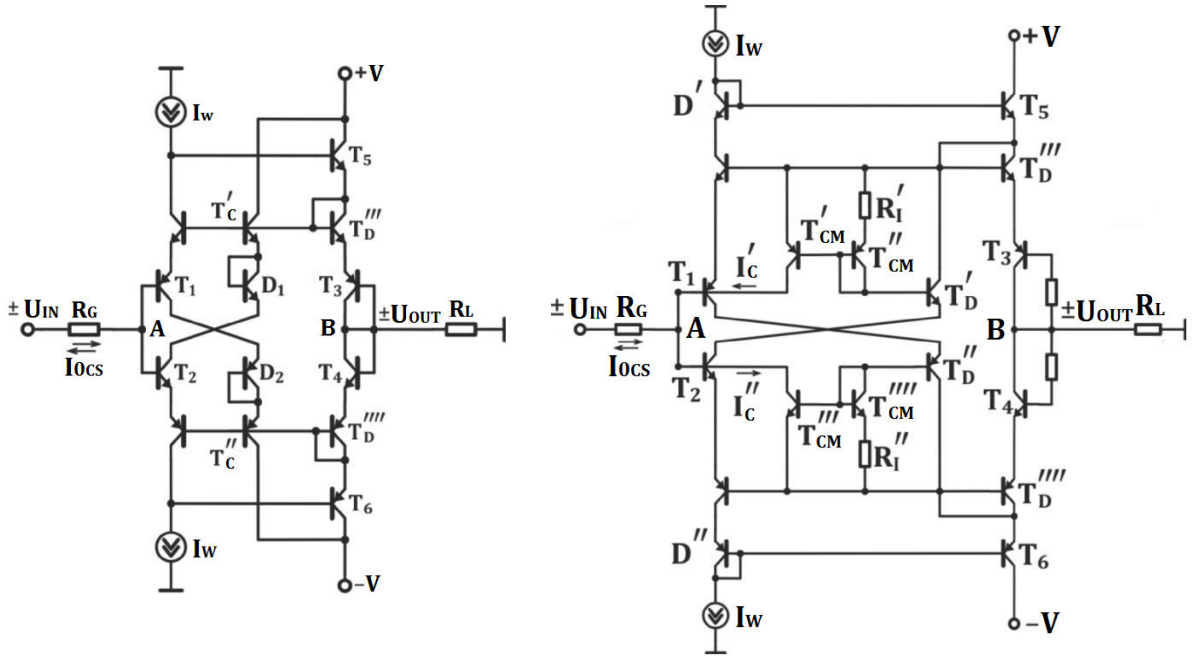

a) b)

Fig. 2 – Cores of the push-pull VB: a) without compensation I_{0cs} ; b) with the compensation of I_{0cs}.

The output resistance can be determined:

$$r_{OUT} = r_e + \frac{r_{b3} + r_{b4}}{K_i},$$

where $r_e = \frac{\varphi_T}{I_e}$ – small signal resistance of the emitter junctions T3 and T4, φ_T – thermal potential, r_{b3}, r_{b4} – resistances of the base junctions. If $I_W = 1 мА$, $r_{OUT} \approx 30\ Ohm$.

It should be noted, that the important drawback of the circuit is the availability of the direct current zero shift I_{0cs}, which appears as a result of the difference (1,5÷2 times) of the static transfer coefficients β', β'' of the output transistors T1 and T2 [16,17]. Voltage drop at R_G as a result of the current flow will lead to the appearance of the additional methodical error of the zero shift. By means of the compensation of the base currents T1 and T2 it is possible to decrease the value of I_0 considerably (by 2 orders), at it is realized in the circuit of VB, shown in Fig.2, b. It additionally contains two generators of the compensating currents I'_C and I''_C, sensors of which are the transistors T'_D and T''_D. The bases of these transistors are connected to the current sensors, built on the transistors T'_{CM}, T''_{CM} i T'''_{CM}, T''''_{CM} , correspondingly. Resistors R'_I i R''_I serve for fine adjustment of the values I'_C i I''_C. The value of I_0 will move to zero on condition of achieving the equality:

$$I_{B1} + I'_C = I_{B2} + I''_C,$$

This can be realized by the selecting the values of R'_I i R''_I . In this case, it should be noted that one of these resistors may not be used at all. The resistors in the bases of T3, T4 transistors provide the correction of the zero voltage shift.

For the determination of the VB input resistance we will note that in the input circuits of the scheme the positive two-contour current feedback functions, which considerably increases the value of r_{IN} as compared with the circuit, shown in Fig.1, a. In accordance with the theory of the feedbacks [6] the resistance in the point A can be determined in the form:

$$r = \frac{r^*_{IN}}{1 - \frac{1}{2} \cdot \chi_1 - \frac{1}{2} \cdot \chi_2},$$

where r^*_{IN} – value of the input resistance without the impact of the feedbacks; χ_1, χ_2 – depths of the feedbacks in the first and second circuits, correspondingly. The first circuit consists of the transistors T_1 and T''_D and the second current mirror on the transistors T'''_{CM} and T''''_{CM}, and the second circuit consists of the transistors T_2 and T'_D and the first current mirror on the transistors T'_{CM} and T''_{CM}. It should be noted, that the input current I_{IN} in the point A in a small signal mode is divided into two and this substantiates the appearance of the coefficients 1/2 before χ_1, χ_2 .If:

$$\chi_1 = \frac{\Delta I_{OUT}}{\Delta I''_C}.$$

Going around the low input circuit we have small signal relation:

$$\Delta I''_C = \Delta I''_{BD} \cdot K''_{CM} = \frac{\Delta I''_{ED}}{1+\beta''_D} \cdot K''_{CM} = \frac{\Delta I''_{B1} \cdot \beta_1}{1+\beta''_D} \cdot K''_{CM} = \frac{\Delta I''_{IN} \cdot \beta_1}{1+\beta''_D} \cdot K''_{CM}.$$

Substituting the obtained value of $\Delta I''_C$ in the expression for χ_1 and taking into account that the transistors T1 and T''_D are realized in the integral execution and have the same β_1 and β''_D, i.e., $\Delta I''_{BD} = \Delta I''_{B1}$, we have:

$$\chi_1 = \frac{1}{K''_{CM}} \approx 1,$$

where K''_{CM} – the current amplification coefficient of the current mirror (CM2). Similarly, it can be shown that:

$$\chi_2 = \frac{1}{K'_{CM}} \approx 1.$$

Thus, the denominator in the formula for r_{IN} may have rather low value. Regulating K'_{CM} i K''_{CM} by means of selecting the resistors R'_I and R''_I theoretically it is possible to make r_{IN} infinitely large and the input current I_{IN} approach to zero [18,19].

We will evaluate the loading capacity of the considered cores of the VB, which can be determined by means of the output resistance, which can be presented in the form of the function $r_{OUT} = f(I_W, R_G)$. This is stipulated by the fact that the level of the working current I_W sets the small signal resistances of the output diodes, realized on the transistors T3 and T4. It also should be added that as a result of the low internal coefficient of the current amplification K_i, set by the amplification transistors T1 and T2, the value of the resistance of the input voltage generator will also influence the loading capacity. Taking into account that T3 and T4 in the diode connection are set on parallel operation, finally we may write:

$$r_{OUT} = r'_D \parallel r''_D + \frac{R_G}{K_i},$$

where $r'_D = r'_E + \frac{r_{B3}}{\beta_3}$ and $r'_D = r''_E + \frac{r_{B4}}{\beta_4}$ – small signal resistances of the emitter junctions of T3 and T4, r_{B3} i r_{B4} – resistances of the base junctions, $K_i = \frac{2 \cdot (\beta' \cdot \beta'')}{\beta' + \beta''}$ – small signal coefficients of the current amplification. Substituting the value r'_D, r''_D, K_i in the output formula, finally we obtain:

$$r_{OUT} = r_E \cdot \frac{r_E \cdot \beta_3 \cdot \beta_4 + r_{B4} \cdot \beta_3 + r_{B3} \cdot \beta_4 + \frac{r_{B3} + r_{B4}}{r_E}}{r_E \cdot \beta_3 \cdot \beta_4 + \frac{r_{B4} \cdot \beta_3 + r_{B3} \cdot \beta_4}{2}} + R_G \cdot \frac{\beta_3 \cdot \beta_4}{\beta_3 + \beta_4}.$$

If $I_W = 1 мА$, $r_{OUT} \approx 30\ Ohm$.

It is obvious, that the loading capacity of the considered cores of VB is not high and if the current in the load increases, the voltage difference between the input and output will grow, where:

$$\Delta U_{AB} = r_{OUT} \cdot I_L.$$

Non zero value of ΔU_{AB} characterizes the errors of zero shift and the scale in the range of $\pm U_{OUT}$. Decrease of the output resistance will enable to provide the decrease of errors and achieve high linearity, maintain the level of the operation rate and increase loading capacity. It is possible to achieve due to the introduction of PPCA which contain negative feedback (see Fig. 1) [5, 10, 11]. Scheme of such solution is shown in Fig.3 [21,22].

It should be noted that if PPCA from BC is available and as a result of the feedback action, the input resistance considerably decreases.

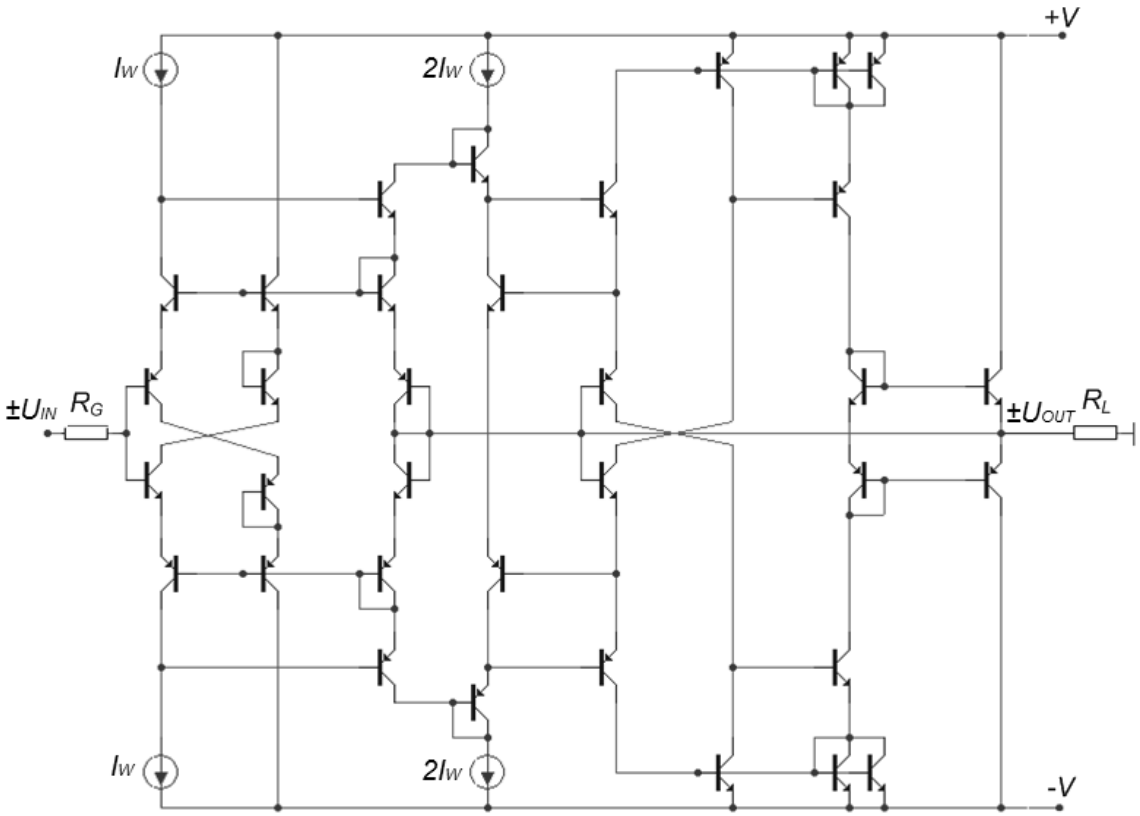

Fig. 3 – Scheme of VB with the output PPCA

By means of the computer simulation of VB cores without PPCA and with PPCA, built on the integrated circuit transistors [12], the comparative data, shown in Table 1, are obtained. The data are obtained on the condition of the input voltage change in the range of $U_{OUT}=\pm 1V$.

Table 1 – Comparison characteristics

Parameters		$I_{OUT}(\mu A)$	$U_{AB}(\mu V)$	$\Delta I_{OUT}(nA)$	$\Delta U_{AB}(\mu V)$	$r_{IN}(GOhm)$	$r_{OUT}(Ohm)$
Circuit	Fig. 2, a	8,94	201	16,6	100	0,12	29,8
	Fig. 2, б	0,5	157	1,05	141	1,96	30
	Fig. 3	0,5	83	1,22	124	7200	$1{,}3\cdot 10^{-3}$

Here ΔI_{IN}, ΔU_{AB} are linearity errors in the range of the input signal. Dynamic properties of VB cores may be evaluated by the transient characteristics. The graph of the transient characteristic for the circuit in Fig.2,b is shown in Fig. 4.

Fig. 4 – Transient characteristic of VB core with I_{0cs} compensation

In this case rather high rate of the input voltage growth ≈1800-2000V/μs should be noted.

CONCLUSIONS

1. Structural-functional organization of the buffer device with the increased loading capacity is considered. It is proved, that the suggested approach enables to decrease the output resistance by 2÷3 orders.
2. The suggested circuits of the push-pull VB on the base of the push-pull current amplifiers are analyzed. It is shown that the application of the voltages stabilization of the collector-emitter junctions of the cores transistors enables to improve considerably (by 1÷2orders) the metrological characteristics of the circuits.
3. Mathematical models of the static characteristics, in particular, small signal coefficient of voltage transfer, input and output resistances are composed, it enabled to set the requirements to PPCA which must be added to the core of VB.
4. Circuits of the push-pull VB with the decreased zero shift current are suggested and analyzed. It is shown that the decrease of the output resistance allows to achieve high linearity and maintain the level of the operation rate and increase the loading capacity.
5. Computer simulation of the static and dynamic characteristics of the suggested circuits of VB cores with PPCA and without PPCA is performed, the results of the simulation prove the possibility of the construction of the high speed buffer devices on the base of the push-pull current amplifiers.

Authors: *D.Sc., Prof. Oleksyi D. Azarov, Vinnytsa National Technical University, 95 Khmelnitske Sh., Vinnitsa 21021, Ukraine, E-mail: azarov2@vntu.edu.ua, PhD. Sergii V. Bogomolov , docent of the Department of Computer Engineering, Vinnytsia National Technical University, 95 Khmelnitske Sh., Vinnitsa 21021, Ukraine, E-mail: sergiy.bogomolov1987@gmail.com, PhD. Svitlana A. Kyrylashchuk, docent of the Department of Higher Mathematics, Vinnytsia National Technical University, 95 Khmelnitske Sh., Vinnitsa 21021, Ukraine, E-mail: ksa07750@gmail.com,*

PhD. Oleksiy J. Stakhov, post-graduate student of the Department of Computer Engineering, Vinnytsia National Technical University, 95 Khmelnitske Sh., Vinnitsa 21021, Ukraine.Mariusz Duk, Lublin University of Technology, E-mail: mariusz.duk@o2.pl. Yedilkhan Amirgaliyev, Institute Information and Computational Technologies CS MES RK, E-mail: amir_ed@mail.ru.

REFERENCES

[1] Kesler, W., [ANALOG-DIGITAL CONVERSION], ADI Central Application Department (2004).
[2] Grebene, A. B.. [Bipolar and MOS analog integrated circuit design], Whiley Classic Library, New Jercy (2002).
[3] Azarov, O. D., Obertiukh, M. R., "High linear push-pull balancing voltage buffers on bipolar transistors," Information technologies and computer engineering, Vinnytsia, VNTU, No. 1 (41), 34-41 (2018).
[4] Bakhtiarov, G. D., Malinin, V. V., Shkolin, V. P., "Analog-digital converters", M .: Soviet Radio (1980).
[5] Azarov, O. D., Bogomolov, S. V., [Fundamentals of the theory of high-line analog devices on the base of the push-pull amplification circuits,] UNIVERSUM-Vinnytsia (2013).
[6] Stepanenko, I. P., [Fundamental of the theory of the transistors and transistor circuits], M.: Energy (1973).
[7] Azarov, O. D., Garnaga, V. A., Jatsyk, V. E., "Current mirrors for the analog devices with the improved static and dynamic characteristics", Information technologies and computer engineering, Vinnytsia, VNTU, T. 2, 48-55 (2012).
[8] Grebene, A. B., [Design of the analog integrated circuits], M: Energy (1976).
[9] Grebene, A. B., [Bipolar and MOS Analog Integrated Circuit Design], Wiley-Interscience, New York (2003).
[10] Azarov, O. D., Teplytskyi, M. Yu., Bilichenko, N. O., [High-speed push pull direct current amplifiers with balancing feedback], VNTU, Vinnitsa (2016).
[11] Azarov, O. D., Garnaga, V. A., [Push pull direct current amplifiers for multidigital self-calibrating information form converters] , VNTU, Vinnitsa (2011).
[12] HFA3046/3096/3127/3128 Transistor Array SPICE Models, Intersil Corporation™ – https://www.intersil.com/content/dam/Intersil/documents/mm30/mm3046.pdf.
[13] Osadchuk, V.S., Osadchuk, A.V., "The Microelectronic Radiomeasuring Transducers of Magnetic Field with a Frequency Output," Electronics and Electrical Engineering, Kaunas, Technologija, No. 4 (110), 67-70 (2011).
[14] Osadchuk, V.S., Osadchuk, A.V., "The magneticreactive effect in transistors for construction transducers of magnetic field," Electronics and Electrical Engineering, Kaunas, Technologija, No. 3 (109), 119-122 (2011).
[15] Osadchuk, V.S., Osadchuk, A.V., "The microelectronic transducers of pressure with the frequency," Electronics and Electrical Engineering, Kaunas, Technologija, No. 5 (121), 105-108 (2012).
[16] Osadchuk, V.S., Osadchuk, A.V., "Radiomeasuring Microelectronic Transducers of Physical Quantities," Proceedings of the 2015 International Siberian Conference on Control and Communications (SIBCON), Omsk, 21-23 May (2015).
[17] Osadchuk, A.V., Osadchuk, I.A., "Frequency transducer of the pressure on the basis of reactive properties of transistor structure with negative resistance," Proceedings of the 2015 International Siberian Conference on Control and Communications (SIBCON), Omsk, 21-23 May (2015).
[18] Wojcik, W., Bieganski, T., Kotyra, A., et al., "Application of algorithms of forecasting in the optical fibre coal dust burner monitoring system," Proc. SPIE 3189, 100- 109 (1997).
[19] Wojcik, W., Kotyra, A., Lawicki, T., "A quality factor of combustion of pulverized coal based on image analysis using the curvelet transform," PRZEGLAD ELEKTROTECHNICZNY, Volume: 88, Issue: 10B, 82-84, (2012).
[20] Lach, Z., Smolarz, A., Wojcik, W., et al., "Optically powered system for automatic protection of a fiber segment," PRZEGLAD ELEKTROTECHNICZNY, Volume: 84, Issue: 3, 259-262 (2008).
[21] Koprowski, R., Korzynska, A., Wrobel, Z., et al., "Influence of the measurement method of features in ultrasound images of the thyroid in the diagnosis of Hashimoto's disease," BIOMEDICAL ENGINEERING ONLINE, Volume: 11, Article Number: 91 (2012).
[22] Zyska, T., Wojcik, W., Imanbek, B., et al., Diagnosis of the thermocouple in the process of gasification of biomass," ROCZNIK OCHRONA SRODOWISKA, Volume: 18, Part: 2, 652-666, (2016).

High Directivity Microstrip Couplers for Impedance Transforming

Arkadiusz Gołaszewski, Mateusz Żukociński, Adam Abramowicz
Warsaw University of Technology
Institute of Electronic Systems
Warsaw, Poland
A.Golaszewski@stud.elka.pw.edu.pl

ABSTRACT

Abstract - The paper describes the design method and simulations results of high directivity planar directional couplers with impedance transformation between the main and the coupled ports. Presented couplers are realized in microstrip line technology. The basic idea is to allow for coupling between two different impedance transmission lines. The coupling is realized by lumped capacitors soldered at two ends of coupled lines section. The proposed directional couplers are narrowband and high directivity. Wide range of coupling factors is easy to achieve. The example structures presented in the paper have a few levels of coupling factors and have been designed for operating frequencies 1.3 GHz and 3.0 GHz. The directivity of the couplers is better than 30 dB in the narrow bandwidth and the impedance matching is better than 25 dB at any port.

Keywords: directional couplers, high directivity, impedance transforming coupler, microstrip couplers

1. INTRODUCTION

The directional couplers are indispensable components in today's complex microwave circuits and systems. It is necessary to use couplers if one needs to split or combine signals [1-4]. Also when control of power levels of signals is needed [1-4] one can use directional couplers to tap and sample the signals. This paper is intended to show the new exceptional impedance transforming structure of directional coupler. The new structure is based on the coupler concept from [5]. Unlike the coupler from [5] the new structure has two different impedance microstrip lines in coupled section which allow integrating different impedance systems [14], e.g. we can connect high power signal source which output impedance is equal to 50 Ω to transmission line which impedance is 75 Ω. The coupler simplified model is shown in Fig. 1. The input port is denoted by P1, the transmission port by P2, the coupled port by P3 and the isolated port is denoted by P4. Z1 and Z2 are values of the characteristic impedances of each line. The L is a length of microstrip line section.

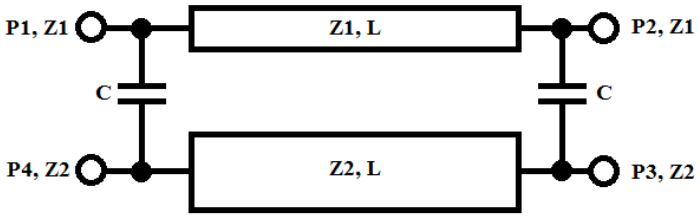

Figure 1. The basic model of the narrowband high directivity directional coupler for impedance transforming.

The coupler model from Fig. 1 is based on two-hole waveguide coupler described in [6]. In the paper [5] the authors introduced a modified concept of narrowband high directivity planar couplers. That paper has presented design formulas and simulated results for couplers having equal port impedances. The idea was to use weakly coupled lines section and produce the actual coupling between the lines by applying lumped capacitors connected to the two ends of the coupled lines section. This concept allows producing high directivity structures with easily adjustable coupling factor and excellent port matching. These high directivity couplers with weakly coupled lines section and lumped coupling capacitors provide a unique solution different from many other couplers published recently [7-13]. To design a coupler

Photonics Applications in Astronomy, Communications, Industry, and High-Energy Physics Experiments 2019,
edited by Ryszard S. Romaniuk, Maciej Linczuk, Proc. of SPIE Vol. 11176, 111765X
© 2019 SPIE · CCC code: 0277-786X/19/$21 · doi: 10.1117/12.2536924

for impedance transforming some modifications of formulas from [5] are needed to include lines of different impedances. The paper presents example designs of the new couplers and their modeling results. The example structures manufacturing process is in progress.

2. REQUIREMENTS

The most important parameters which were taken into account when designing the example couplers are: high directivity better than 30 dB and excellent matching, also better than 30 dB. The mentioned parameters must be optimal at frequencies: 1.3 GHz and 3.0 GHz because these two frequencies are used in our couplers application systems. The levels of coupling factors are: 10 dB and 15 dB. Also it is necessary to achieve the size of couplers as small as possible and to design them in microstrip technology to allow easier integration with PCBs. It is worth to mention that these couplers were designed to be used on PCB modules of the Low-Level RF (LLRF) control system for European X-ray Free Electron Laser (E-XFEL).

3. BASIC FORMULAS AND SIMULATIONS RESULTS

The basic formulas shown in paper [5] can be supplemented with the special mathematical formulas describing transformation of characteristic impedance of lossless transmission line over the length l (1). Also one should remember to make some modification to formulas from [4] because in this case the couplers have two different port impedances.

$$Z_{in} = Z_0 \frac{Z_L + jZ_0 \tan(\beta l)}{Z_0 + jZ_L \tan(\beta l)} \quad (1)$$

Where:

Z_0 – line impedance

Z_L – load impedance

β – wavenumber

l – line length

The preliminary couplers design parameters have been calculated using NI AWR Microwave Office (MWO). TXLine, a module of MWO, was used to find lengths and widths of microstrip sections of particular characteristic impedances. Then the initial circuit based on Fig. 1 has been created for circuit modelling in MWO. Using optimization algorithms for frequency characteristics of the couplers the circuit parameters of lines, lengths and widths as well as capacitors values, have been found.

The parameters of four trial couplers are shown in Table 1. Two couplers with the coupling factor values: 10 dB and 15 dB, are designed for operation frequency 1.3 GHz, and two couplers with the same coupling values are designed for frequency of 3.0 GHz.

Table 1. Calculations results of basics couplers parameters.

Center frequency [GHz]	Coupling [dB]	First line impedance [Ω]	Second line impedance [Ω]	Lines length [mm]	Capacitance [pF]
1.3	10	49.6821	75.6922	26.5	0.7
1.3	15	49.8295	75.3193	29.83	0.37
3.0	10	49.6725	75.6626	11.38	0.3
3.0	15	49.8198	75.29	12.925	0.15

These circuit modeling results are excellent starting points for calculation of final geometry of real microstrip couplers. This is done using an electromagnetic solver, e.g. MWO Axiem solver which is based on method of moments (MoM). The simulated frequency characteristics based on coupler model from Fig. 1 and parameters from Table 1 are presented in the next chapter.

4. SIMULATIONS

High directivity 1.3 GHz coupler

The simulated frequency characteristics of S-parameters for 1.3 GHz couplers have been shown below. Fig. 2 presents 10dB coupler and Fig. 3 presents 15 dB coupler. As one can see the couplers have the directivity much better than 30 dB in the narrow band around the center frequency of 1.3 GHz in which the port impedance matching $|S_{xx}|$ is better than 25 dB in >200 MHz bandwidth. Also, the level of coupling factor $|S_{13}|$ meets the design assumptions.

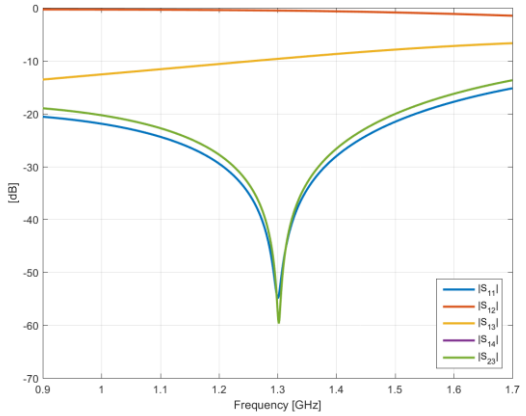

Figure 2. Simulated S-parameter characteristics of the 10 dB coupler designed for 1.3 GHz.

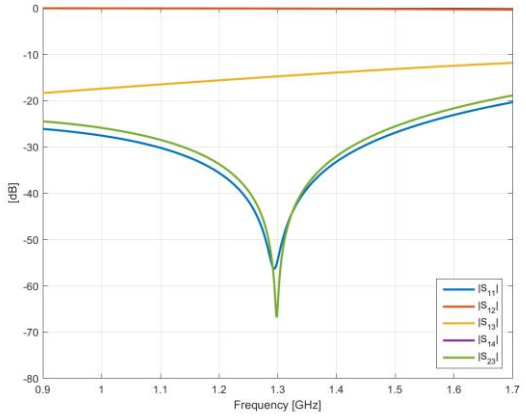

Figure 3. Simulated S-parameter characteristics of the 15 dB coupler designed for 1.3 GHz.

On the next page impedance matching characteristics have been shown for every port of the couplers. Good matching is very important to achieve high directivity. Also if we want the coupler to make precise impedance transformation, high matching is necessary.

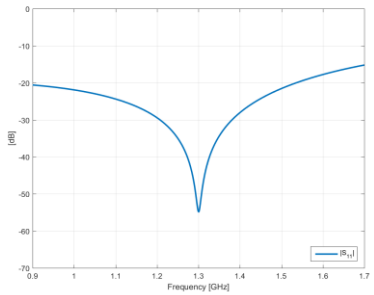

Figure 4.1. Simulated $|S_{11}|$ 10 dB 1.3 GHz coupler.

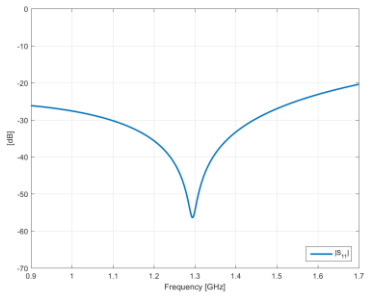

Figure 5.1. Simulated $|S_{11}|$ 15 dB 1.3 GHz coupler.

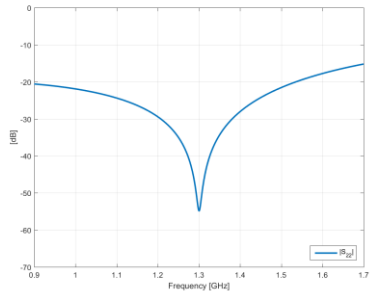

Figure 4.2. Simulated $|S_{22}|$ 10 dB 1.3 GHz coupler.

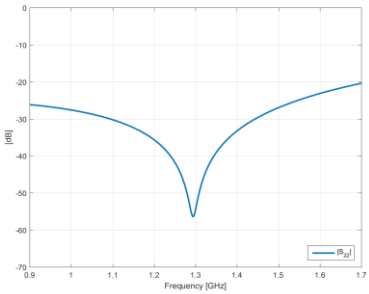

Figure 5.2. Simulated $|S_{22}|$ 15 dB 1.3 GHz coupler.

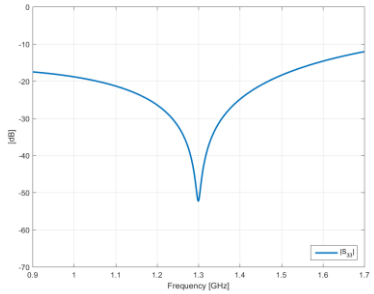

Figure 4.3. Simulated $|S_{33}|$ 10 dB 1.3 GHz coupler.

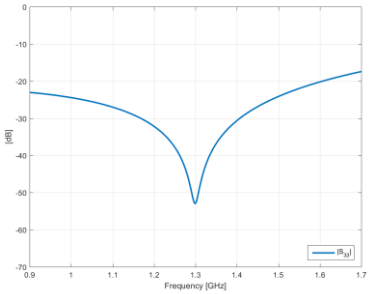

Figure 5.3. Simulated $|S_{33}|$ 15 dB 1.3 GHz coupler.

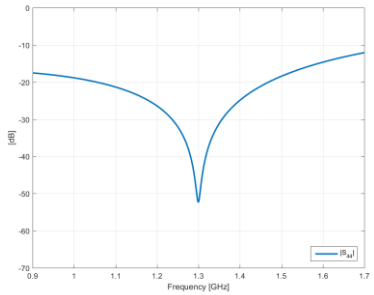

Figure 4.4. Simulated $|S_{44}|$ 10 dB 1.3 GHz coupler.

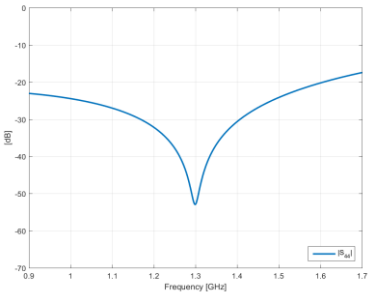

Figure 5.4. Simulated $|S_{44}|$ 15 dB 1.3 GHz coupler.

In the above figures (4-5) one can see that impedance matching at operating frequency is better than 50 dB at every port of each of the couplers. This is great result but one should remember that these are only simulations results and results from the real structures measurements may be worse.

High directivity 3.0 GHz coupler

The simulated S-parameters characteristics for 3.0 GHz couplers have been presented in Fig. 6 for 10 dB coupler and in Fig. 7 for 15 dB coupler. The directivity of these couplers is much better than 30 dB near the operating frequency which is 3.0 GHz. The matching is also very good and achieves 25 dB in >300 MHz bandwidth. All the parameters of presented couplers meet the design specification.

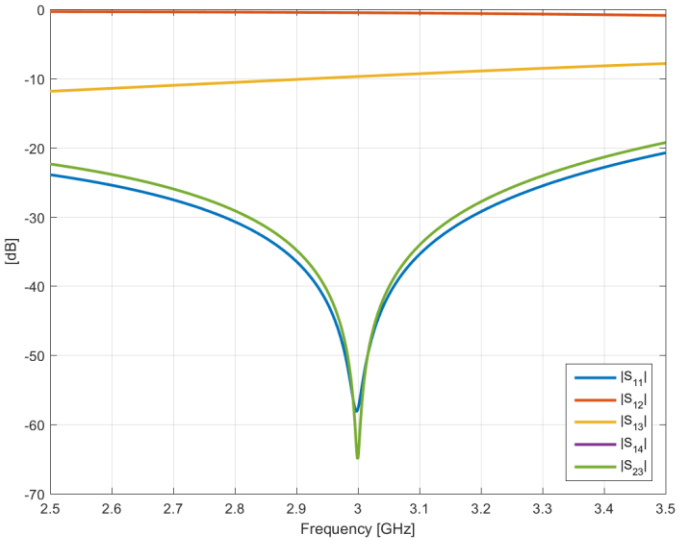

Figure 6. Simulated S-parameter characteristics of the 10 dB coupler designed for 3.0 GHz.

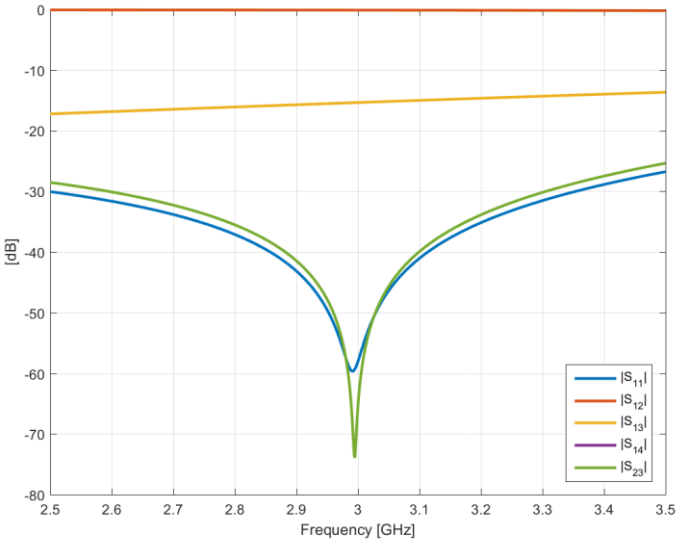

Figure 7. Simulated S-parameter characteristics of the 15 dB coupler designed for 3.0 GHz.

Next figures show impedance matching characteristics at each port of 3.0 GHz couplers.

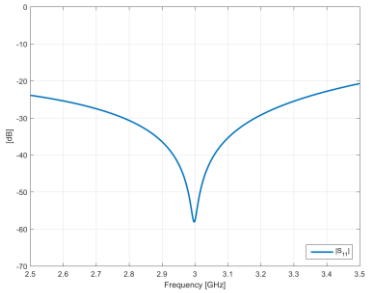

Figure 8.1. Simulated $|S_{11}|$ 10 dB 3.0 GHz coupler.

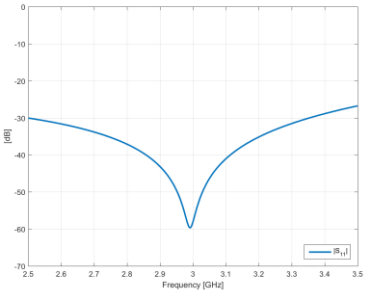

Figure 9.1. Simulated $|S_{11}|$ 15 dB 3.0 GHz coupler.

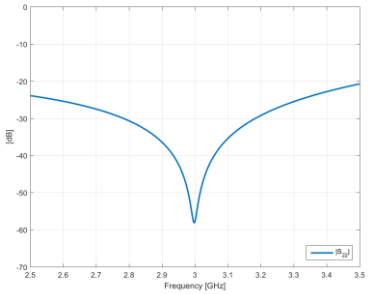

Figure 8.2. Simulated $|S_{22}|$ 10 dB 3.0 GHz coupler.

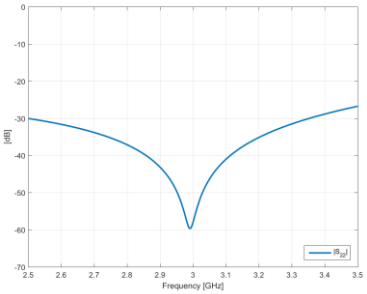

Figure 9.2. Simulated $|S_{22}|$ 15 dB 3.0 GHz coupler.

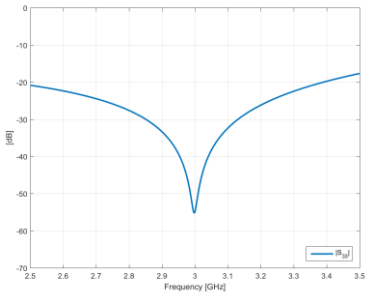

Figure 8.3. Simulated $|S_{33}|$ 10 dB 3.0 GHz coupler.

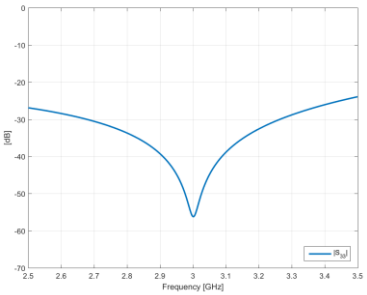

Figure 9.3. Simulated $|S_{33}|$ 15 dB 3.0 GHz coupler.

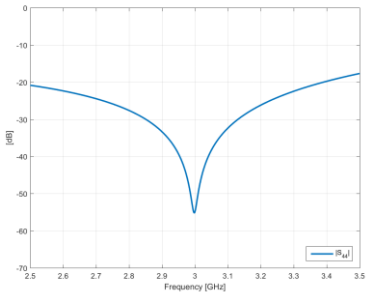

Figure 8.4. Simulated $|S_{44}|$ 10 dB 3.0 GHz coupler.

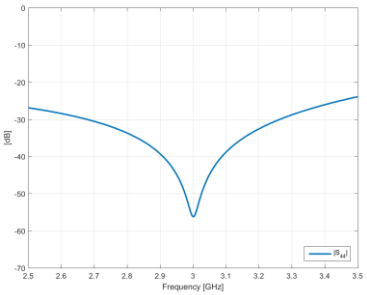

Figure 9.4. Simulated $|S_{44}|$ 15 dB 3.0 GHz coupler.

As in previous examples the figures (8-9) show extremely good matching at both 50 Ω ports and 75 Ω ports. Impedance matching better that 30 dB is often a desire in high power systems or in systems sensitive to backscattered waves which cause interference and produce hard to control standing waves in the signal transmission systems. These novel directional couplers seems to be predisposed for such demanding applications.

5. CONCLUSIONS

The novel realization of high directivity microstrip directional coupler for impedance transforming has been presented. This structure facilitates integration of different line impedance systems. The achieved results prove the concept of these new directional couplers. Furthermore excellent port matching of the presented structures allows combining many sensitive components in one complex system. Not only the great matching but also extremely high directivity and thus high port isolation improves signal integrity conditions in a system which uses these directional couplers. The form factor of the presented couplers is small comparing to classical quarter-wavelength structures. The ease of designing of these couplers in planar technology allows convenient and flexible integration with complex PCBs.

REFERENCES

[1] R.Mongia, I.Bahl and P.Bhartia, "RF and Microwave Coupled-Line Circuits", Boston, Artech House, 1999 IEEE

[2] O.P.Gandhi, "Microwave Engineering and Applications", Pergamon Press, New York1981

[3] G.Mattahei, E.M.T.Young, L.Jones, "Microwave Filters, Impedance-Matching Networks, and Coupling Structures", Artech House, 1964

[4] A. Grebennikov, "Power Combiners, Impedance Transformers and Directional Couplers: Part III", High Frequency Electronics, March 2008

[5] A. Golaszewski, A. Abramowicz , "Design Method for High Directivity Couplers", 2018 International Conference on Signals and Electronic Systems (ICSES), Krakow 2018, pp. 185-190

[6] N.Marcuwitz, "Waveguide Handbook", McGraw-Hill, New York1951

[7] A.Golaszewski, A.Abramowicz, "Properties of High Directivity Microstrip Couplers", 2017Signal Processing Symposium (SPSympo), Jachranka, 2017, pp. 1–4

[8] S.L.Mar, "Phase Velocity Compensation in Parallel-Coupled Microstrip", IEEE MTT-S Symp. Dig., June 1982, pp. 410–412

[9] A.Podell, "A High Directivity Microstrip Coupler Technique", IEEE MTT-S Symp. Dig., May 1970, pp. 33–36

[10] G.Schaller, "Optimization of Microstrip Directional Couplers with Lumped Capacitors", Arch. Elek. Uebertrag. Tech., vol. 31, pp. 301–307

[11] M.Dydyk, "Microstrip Directional Couplers with Ideal Performance Via Single-Element Compensation", IEEE Trans. Microwave Theory Tech., vol. 47, No. 6, June 1999, pp. 956–964 https://doi.org/10.1109/22.769332

[12] Y.D.Wu, M.L.Her, Y.Z.Wang, M.W.Hsu, "Stepped-Impedance Directional Coupler with Enhanced Isolation Using Interdigital Capacitance Compensation", Electron. Lett., vol. 41, Issue 10, 2011, pp. 598–599

[13] Y.Wu, W.Sun, S.-W.Leung, Y.Diao, K.H.Chan, Y.-M.Siu, "Single-Layer Microstrip High-Directivity Coupled-Line Coupler with Tight Coupling", IEEE Trans. Microwave Theory Tech., vol. 61, Feb. 2013, pp. 746–752

[14] H.-R. Ahn , Bumman Kim, "Transmission-Line Directional Couplers for Impedance Transforming", IEEE Microwave and Wireless Components Letters (Volume: 16 , Issue: 10 , Oct. 2006), pp. 537 - 539

Numerical method for processing frequency measuring signals from microelectronic sensors based on transistor structures with negative differential resistance

Alexander V. Osadchuk*[a], Andriy A. Semenov[a], Oleksander S. Zviahin[a],
Anton Y. Savytskyi[a], Paweł Komada[b], Karlygash Nurseitova[c]
[a]Vinnytsia National Technical University; [b]Lublin University of Technology;
[c]East Kazakhstan State Technical University named after D. Serikbayev

ABSTRACT

The application of the proposed mathematical tools, that can be used for signal processing self-generating transducers of physical quantities, are considered. Its operating mechanism is based on frequency modulation, when the frequency deviation depends on the intensity of exposure measurement parameter. It is shown that the action for leveling additive errors in the channel the signal generator is highly stable enough to use approximating second order polynomial.

Keywords: self-oscillator transducer; additive error; noise; definite integral; measurement accuracy; sensor; negative differential resistance

1. INTRODUCTION

The quality of oil and fuel and lubricants is largely determined by the accuracy of their moisture content. Water present in hydraulic and lubricating liquids, causes significant damage to technological units requiring lubrication of parts. Without proper devices and controls, it is difficult to see their current destruction. The water available in oil contributes to corrosion, during transportation it can distort the displays of flowmeters, as well as leads to premature wear of equipment and the emergence of emergency situations. Therefore, it is very important to develop systems for measuring and controlling this parameter of liquid hydrocarbons[1,2,3].

Currently, there are used measuring systems the quantity and quality parameters of crude oil (MSPCO), intended for automated accounting at delivery of commodity oil from the supplier to the consumer, for qualitative definition indicators of oil refinings, as well as at carrying out of accounting and settlement operations at transportation oil and petroleum products[4]. MSPCO performs automatic calculation of the mass of petroleum products and sampling to determine such parameters as temperature, pressure, viscosity, humidity; and transfer of measurement results to a computerized control panel[5,6,7].

2. THEORETICAL AND EXPERIMENTAL RESEARCH

It can be seen a block diagram of MSPCO (Fig. 1). It includes: measurement and control unit, block of filters (BF) and block of the stationary pipe-piston installation (BPI)[8,9].

In turn, the measuring and control unit includes a measuring unit for quality indicators that provides measurement of density, viscosity, flow rate, humidity, pressure and temperature of oil (Fig. 2).

As a humidity analyzer in the unit of measurement of quality indicators, a system for measuring and controlling the humidity of oil and petroleum products, the structural scheme of which is given in Fig. 3. The system works in follow way: the humidity change of the liquid to be studied leads to the change in the humidity-sensitive capacitance of the condenser cylindrical structure (CCS)[10] and, accordingly, to the change of oscillations frequency at the output of FM oscillator (FMO)[11], then the signal is digitized and means of displaying information (LCD-display, PC screen) displays the value of the oil product humidity.

* osadchuk.av69@gmail.com

Photonics Applications in Astronomy, Communications, Industry, and High-Energy Physics Experiments 2019,
edited by Ryszard S. Romaniuk, Maciej Linczuk, Proc. of SPIE Vol. 11176, 111765Y
© 2019 SPIE · CCC code: 0277-786X/19/$21 · doi: 10.1117/12.2536942

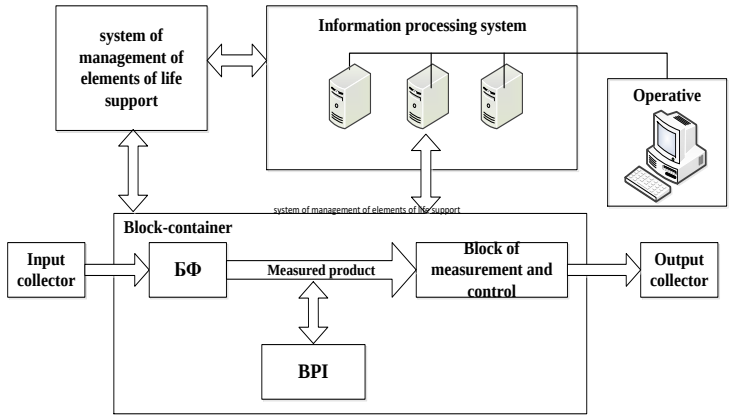

Figure 1. Block diagram of MSPCO.

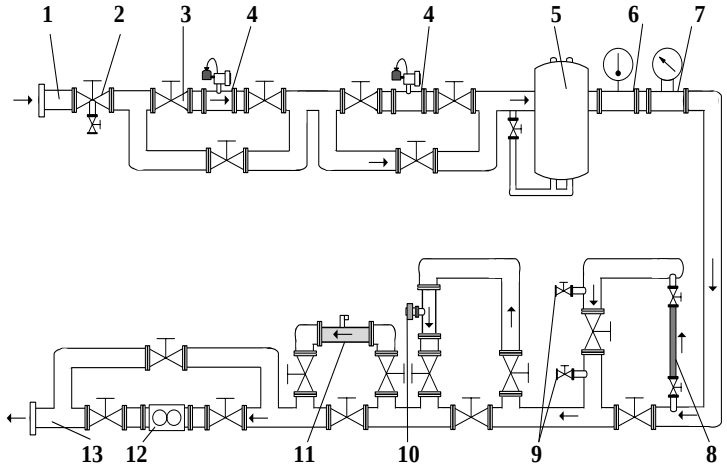

Figure 2. Block of measurement of quality indicators: 1 – oil from sampling device; 2 – manual sampler; 3 – stop valves; 4 – sampler automatic; 5 – cylinder thermostat for the hydrometer; 6 – temperature sensor; 7 – pressure gauge; 8 – density sensor; 9 – place of connection of the pycnometer; 10 – Viscosimeter; 11 – a moisture meter; 12 – flow meter; 13 – oil output.

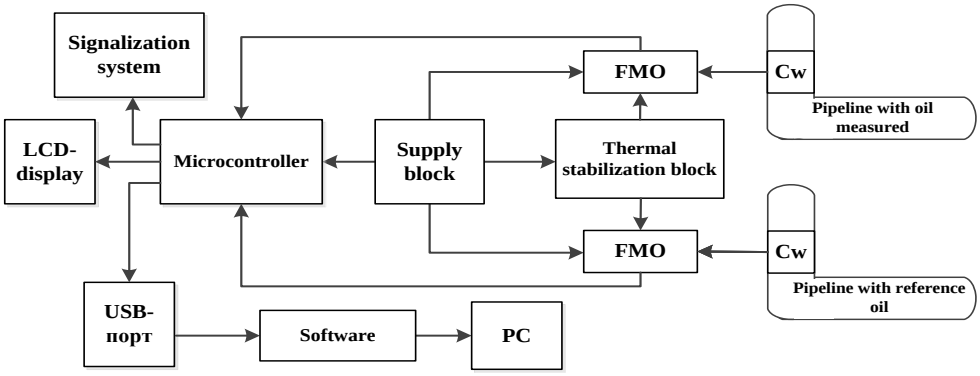

Figure 3. Structural scheme of the system for measuring and controlling the humidity of oil and petroleum products.

Discribed system allows not only to measure and store the humidity values for a certain time, but also to control the permissible humidity value given by the executable program. When the permissible humidity value is exceeded, the signaling device is triggered and a message is displayed that the petroleum product does not correspond to the tolerance value (on the screen the user sees the inscription "norm" or "abnormality").

The schematic diagram of the developed system is shown in Fig. 4 consists of a 8-bit microprocessor with a USB interface PIC18F4550, a PC, a FMO, an LCD display WH1602C-YGH-CTK, and also contains a thermostabilization system. The system of thermostabilization consists of the first thermochemical detector, which is installed with FMO and controls the value of the temperature within the limits of 53°C ± 0,5°C. If the temperature becomes less than 52.5°C, then the heating element is switched on and the FMO is heated to 53,5°C. The second and third thermocouples are installed on a humidity sensitive CCS to take into account the influence of temperature, in particular to select a certain conversion function, from the list of those prescribed in the program at different temperatures[12]. The used DS18B20 thermocouples are connected in parallel.

The information on the FMO, the sensory elements (CCSs) are installed in the pipeline in such a way that one is in the measuring line, and the other in the reference, through the input nodes enters the microcontroller where the frequency measurement takes place and their difference is calculated. The result of the difference in the frequency of data signals based on the conversion function, recorded in the microcontroller, shows the percentage of water in the oil. Indication of the results of the measurement of humidity is possible in two versions: the first with an LCD display, the second on the screen of the PC monitor.

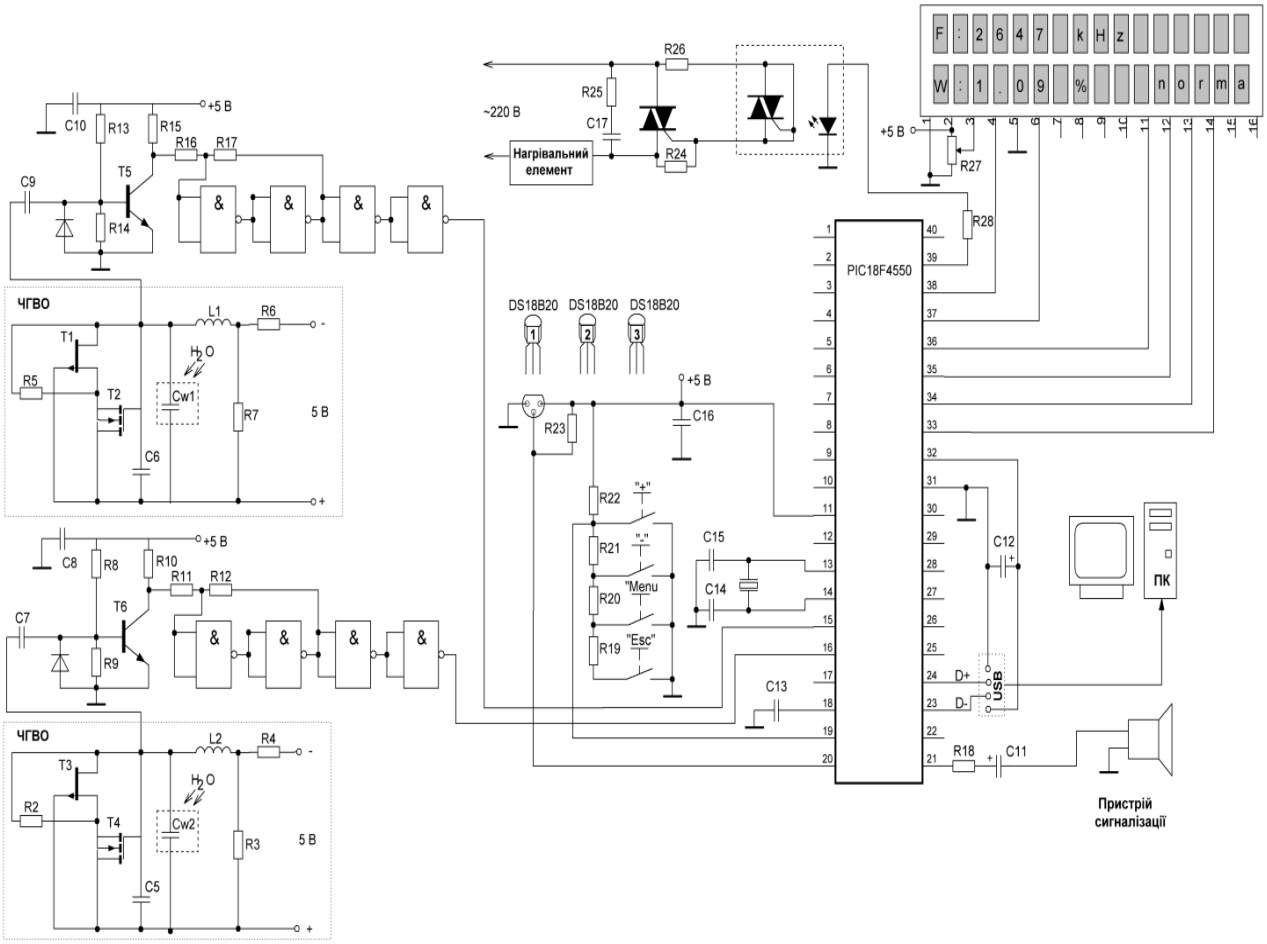

Figure 4. Principal scheme of the system for measuring and controlling the humidity of oil and petroleum products

In the system for oil and petroleum products humidity measuring and controlling, FMO is used on the basis of the structure of two field-effect transistors[4] with CCS based on cylindrical electrodes.

The advantage of the described system is the application of the frequency modulation of the information signal, which allows significantly increase the noise immunity of the data transmission channel[13-16].

The FMO transformation function is described by the expression:

$$F = \frac{\sqrt{2}\sqrt{LC_{s2}C_i(W,T)\cdot\left(\left(R_{ds2}{}^2C_{ds2}-L\right)\cdot C_{s2}C_i(W,T)+R_{ds2}{}^2A_1+\sqrt{A_2}\right)}}{4\pi LC_i(W,T)C_{s2}R_{ds2}C_{ds2}}, \quad (1)$$

where $A_1 = C_{ds2}{}^2\left(C_{s2}+C_i(W,T)\right)$;

$$A_2 = R_{ds2}{}^4C_{ds2}{}^2C_{s2}{}^2C_i{}^2(W,T)+2R_{ds2}{}^4C_{ds2}{}^3C_{s2}C_i(W,T)\left(C_{s2}+C_i(W,T)\right)-$$
$$-2LR_{ds2}{}^2C_{ds2}C_{s2}{}^2C_i{}^2(W,T)+R_{ds2}{}^4C_{ds2}{}^4\left(C_{s2}{}^2+2C_{s2}+C_i{}^2(W,T)\right)+$$
$$+2LR_{ds2}{}^2C_{ds2}{}^2C_{s2}C_i(W,T)\left(C_{s2}+C_i(W,T)\right)+L^2C_{s2}{}^2C_i{}^2(W,T),$$

R_{ds2} – MOSFET's drain-sourse resistance; L – inductor; C_{s2}, C_{ds2} – MOSFET's drain-gate and drain-sourse capacitances; $C_i(W,T)$ – capacitance of humidity-sensitive CCS.

Fig. 5 and Fig. 6 show the theoretical and experimental dependences of the transformation functions, namely, the frequency of FMO generation due to humidity of petroleum products[17,18].

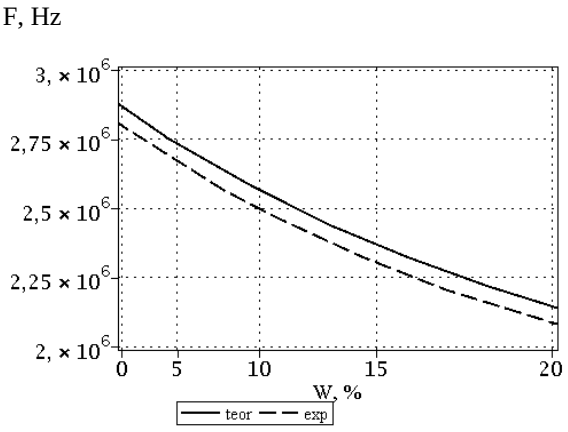

Figure 5. Conversion functions for motor oil 5W40.

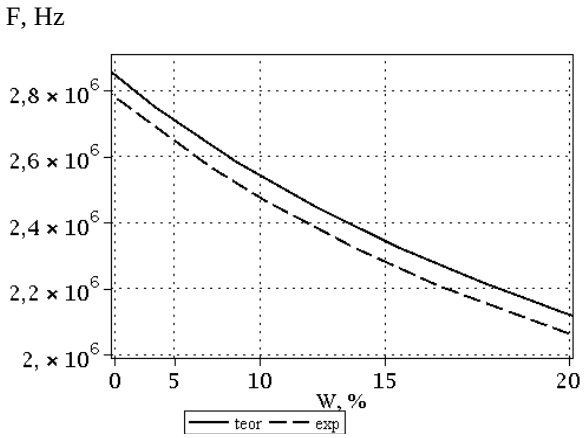

Figure 6. Conversion functions motor oil M8V.

As can be seen from Fig. 5 and Fig. 6 FMO transformations are nonlinear, but they can be easily approximated. The sensitivity of FMO in the range of changes in the humidity of petroleum products from 0% to 20% is from 25.7 kHz/% to 43 kHz /%. The difference between the theoretical and experimental results for FMO is not exceed 3%.

In the case of measuring the humidity content of petroleum products, this accuracy is not always sufficient. In order to improve metrological characteristics by reducing the additive error, the averaging method is used[17]. In the case where the information signal is represented as a discrete sample, the need for the application of numerical methods arises. In this article, the authors present a method of applying numerical methods for signal averaging.

Let the measurement result be a quasi-stationary value provided that the measuring parameter of the object is constant $a_f(t)$ is a quasistationary value a_f, and the sum of all cascades the frequency display error is "white noise", which is described by the function $\varepsilon(t)$. Then at each moment of time a signal that is a signal of frequency and noise, which is a function of frequency instability can be described $y(t) = a_f + \varepsilon(t)$. Apply the accumulation effect through the use of integral signal processing, which will be observed for some time of research T_D. Thus at the output of the integrator a signal is formed[19,20]:

$$Y(t) = \int_0^{T_D} y(t)dt = \int_0^{T_D} [a_f + \varepsilon(t)]dt = a_f T_C + \int_0^{T_D} \varepsilon(t)dt\,. \quad (2)$$

In this case, the signal / noise ratio will determine the error from the effect of the additive interference after the frequency/amplitude conversion to the interval of the frequency detector-indicator device:

$$n = \frac{P_{a_f}}{P_n} = \frac{\left(a_f \cdot T_D\right)^2}{\mathrm{D}\left[\int_0^{T_D} \xi(\mathrm{t})\mathrm{dt}\right]}, \tag{3}$$

where P_{a_f} i P_n – signal strength and interference respectively.

Provided that the measuring system corresponds to Kotelnikov's theorem, we can give the following properties of this system:

- the calculation method is valid for systems in which the information signal is quasi-constant, or periodic (including pulse);
- the information signal, as well as the signal interference can be represented as a sum of samples with the corresponding sampling rate;
- the variance of the sum of random variables (offset distances) will also be a random variable.

Based on the above statements, the following expressions can be written:

$$\int_0^{T_D} \varepsilon(t)dt \cong \sum_{i-1}^{k} \varepsilon(t_i)\tau_0 \,, \tag{4}$$

where $k = T_D / \tau_0 ; \tau_0$ – period of noise autocorrelation function.

The dispersion of the noise at the output of the integrator is determined by the expression:

$$D\left[\int_0^{T_D} \varepsilon(t)dt\right] \cong D\left[\sum_{i=1}^{k} \varepsilon(t_i)\tau_0\right] \approx \tau_0^2 \cdot D\left[\sum_{i=1}^{k} \varepsilon(t_i)\right] = \varepsilon_0 \cdot n \cdot D(\varepsilon) = T_D \cdot \tau_0 \cdot D(\varepsilon). \tag{5}$$

Reducing interference is determined by the signal / noise ratio at the input and output of the integrator:

$$\frac{P_{a_f .вих}}{P_{n.вих}} \cong \frac{(a_f \cdot T_D)^2}{T_D \cdot \tau_0 \cdot D(\varepsilon)} = \frac{T_D \cdot {a_f}^2}{\tau_0 \cdot D(\varepsilon)} = \frac{T_D}{\tau_0} \cdot \frac{P_{a_f .вх}}{P_{n.вх}} \,. \tag{6}$$

As can be seen from the last expression, the signal / noise gain increases with increasing integration time (observation) and the frequency of the auto-correlation function of the interference.

In this case, for the Kotelnikov theorem to run the system, there is a problem of ensuring the speed of the integrator with the simultaneous provision of the necessary accuracy of the measurement. In[18], the possibility of applying the curvilinear approximation of the table-defined function by the arc segment was shown (Fig. 7), which is essentially a curvilinear refinement of the known trapezoidal method. The essence of the method is to assume that the graph of the approximated function on each reference in the curvilinear and refinement of the trapezoid method is due to the finding of an area limited by the straightforward approximation of the trapezium and the segment of the arc by the radius proposed in[19,20]. In this case, unlike the Simpson formula, it is eliminated the need to replace the segment of the desired straight line with two parabolas with intersection points in the middle of this segment, since this point can be found with some probability[21-23].

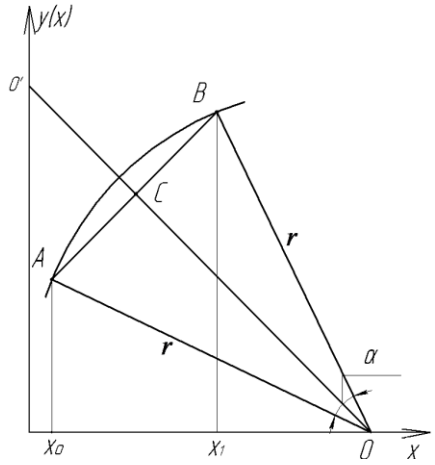

Figure 7. Graphic interpretation of the integration method.

The mathematical apparatus of the proposed integration techniques is given below[5,24]:

$$r_n = \sqrt{\left(\frac{(t_n^2 - t_{n-1}^2) + \left(y^2(t_n) - y^2(t_{n-1})\right) - 2ht_{n-1}}{2h}\right)^2 + y^2(t_{n-1})}\,. \tag{7}$$

$$\sin\alpha_n = \sqrt{1 - \left[1 - \left(\frac{(t_n - t_{n-1})^2 + (a_{f.n} - a_{f.n-1})^2}{2r_n^2}\right)\right]^2}\,; \tag{8}$$

$$\alpha_n = \left|\arcsin(\sin\alpha_n)\right|; \tag{9}$$

$$S_{segm.n} = \frac{r_n^2}{2}\left(\pi\frac{\alpha_n}{180^0} - \sin\alpha_n\right). \tag{10}$$

Area, contoured by function graphs $t = t_0$, $t = t_n$, $y(t)$ is replaced by an integral sum:

$$\int_{t_0}^{t_n} y(t)dt = \sum_{i=1}^{m} S_{trap.i} + \sum_{i=1}^{m} S_{segm.i}; \tag{11}$$

$$\sum_{i=1}^{m} S_{trap.i} = h\left(\frac{y(t_0) + y(t_n)}{2} + y(t_1) + y(t_2) + \ldots\right); \tag{12}$$

$$\sum_{i=1}^{m} S_{segm.i} = \sum_{i=1}^{m} \frac{r_i^2}{2}\left(\pi\frac{\alpha_i}{180^0} - \sin\alpha_i\right). \tag{13}$$

The accuracy of numerical integration depends on the degree of integrable polynomial. So, with substitution of original function y(t) with a line segment (the method of tangents, the trapezoid method), the integration error is determined by the residual term[21-23]:

$R(t) = \frac{(t_n - t_{n-1})^3}{12} y''(\varsigma)$, where $\varsigma \in [x_{n-1}; x_n]$ midpoint of the cut-off.

In this case, the total error of measurement equals the sum of errors for each reference[24]:

$$R(t)_\Sigma = \sum_{i=1}^{n} \frac{(t_i - t_{i-1})^3}{12} y''(\varsigma_{i-1})\,. \tag{14}$$

The application of numerical integration with higher order polynomials reduces the error of integration. In this case, the remainder of the integral equality described by expression[25-27]:

$$R(t) = \left(\frac{t_n - t_{n-1}}{2} \right)^5 \frac{y^{(IV)}(\varsigma)}{90}. \quad (15)$$

Similarly, for this case, the total error of numerical integration can be determined by remainder member[28]:

$$R(t)_\Sigma = \sum_{i=1}^{n} \left(\frac{t_i - t_{i-1}}{2} \right)^5 \frac{y^{(IV)}(\varsigma_{i-1})}{90}. \quad (16)$$

An algorithm has been developed for calculating a definite integral for averaging the results of measuring the humidity of oil and petroleum products. On the basis of this algorithm, the software of the microcontroller system for processing the information signal was developed.

3. CONCLUSIONS

The microprocessor system for monitoring the humidity concentration in petroleum products, which can be used in the system for control systems of crude oil at refineries, is developed. Dependences of the transformation function for different petroleum products are obtained. The sensitivity of the measuring instrument in the range of changes in the humidity of petroleum products from 0% to 20% is from 25.7 kHz /% to 43 kHz /%. Absolute error of measuring the humidity of petroleum products is not more than 5 ppm. This result has been achieved by using the mathematical apparatus of the averaging of the results of the measurement of the humidity of petroleum products on the basis of numerical integration methods. In this work a mathematical apparatus was developed that was used for implementation MSPCO.

REFERENCES

[1] Sergey, Y. Y., "Sensors and Transducers: Frequency Output Versus Voltage Output," Sensors & Transducers Magazine 11, 302-305, (2004).
[2] Sergey, Y. Y., [Digital and Intelligent Sensors and Sensor Systems: Practical Design], Tutorial, Rome, (2012).
[3] Osadchuk, V. S., Osadchuk, A. V. and Yushchenko, Y. A., "Radiomeasuring thermal flowmeter of gas on the basis of transistor structure with negative resistance," Elektronika ir Elektrotechnika 4, 89-93, (2008).
[4] Osadchuk, V. S., Osadchuk, A. V., "Radiomeasuring Microelectronic Transducers of Physical Quantities," Proc. International Siberian Conference on Control and Communications – SIBCON, (2015), doi: 10.1109/SIBCON.2015.7147167.
[5] Osadchuk, V. S. and Osadchuk, A. V., "The microelectronic transducers of pressure with the frequency," Elektronika ir Elektrotechnika 5, 105-108, (2012), doi: 10.5755/j01.eee.121.5.1661.
[6] Pidchenko, S. K., "Dual-frequency temperature-compensated Quartz Crystal Oscillator," Proc. 23rd International Crimean Conference Microwave and Telecommunication Technology, 669-670, (2013).
[7] Taranchuk, A. A., Pidchenko, S. K. and Khoptinskiy, R. P., "Dynamics of temperature-frequency processes in multifrequency crystal oscillators with digital compensations of resonator performance instability," Radioelectronics and Communications Systems 6, 250-257, (2015).
[8] Leonov, A. V., Malykh, A. A., Mordkovich, V. N., and Pavlyuk, V. I., "Sensors with SOI FET Primary Transducers and Frequency Output," Proc. SENSOR 2015 and IRS2 2015, 864-867, (2015).
[9] Azcona Murillo Cristina, Calvo Lopez Belén and Celma Pueyo Santiago, [Voltage-to-Frequency Converters: CMOS Design and Implementation], Springer Science+Business Media, New York, (2013).
[10] Osadchuk, A., Koval, K., Semenov, A. and Prutula, M., "Mathematical model of transistor equivalent of electrical controlled capacity," Proc. International Conference TCSET 2008, 35-36, (2008).
[11] Osadchuk, A.V. and Osadchuk, I.A., "Frequency transducer of the pressure on the basis of reactive properties of transistor structure with negative resistance," Proc. International Siberian Conference on Control and Communications – SIBCON, (2015), doi: 10.1109/SIBCON.2015.7147168.

[12] Taranchuk, A. A., Pidchenko, S. K., and Khoptinskiy, R. P., "Determination of bulk density of the source of heat in the analysis of thermodynamic processes in the quartz piezoelectric element," Proc. 24rd International Crimean Conference Microwave and Telecommunication Technology, 716-717, (2014).
[13] Mahajan Ajay, Oesch Christopher, Padmanaban Haricharan, Utterback Lucas, Chitikeshi Sanjeevi and Figueroa Fernando, "Physical and Virtual Intelligent Sensors for Integrated Health Management Systems," International Journal on Smart Sensing and Intelligent Systems 3, 559-575, (2012).
[14] Kwang-Jow Gan, Kuan-Yu Chun, Wen-Kuan Yeh, "Design of Dynamic Frequency Divider using Negative Differential Resistance Circuit," International Journal on Recent and Innovation Trends in Computing and Communication 8, 5224-5228, (2015).
[15] Kychak V. and Kychak V., "Computer-aided design of digital radio devices with frequency representation of information," Proc. 11th International Conference Modern Problems of Radio Engineering, Telecommunications and Computer Science, 405, (2012).
[16] Frankiewicz, M. and Kos, A., "Thermal analysis of CMOS voltage-controlled oscillators," Informatyka, Automatyka Pomiary w Gospodarce i Ochronie Srodowiska – IAPGOS 4b, 3-6, (2012).
[17] Dogadin, N. B., [Fundamentals of radio engineering], Lan, St. Petersburg, (2007).
[18] Maplesoft, [Maple User Manual], Waterloo Maple Inc., (2014).
[19] Berezin, I. S. and Zhydkov, N. P., [Metody vychyslenyi], State publishing house of physical and mathematical literature, Moscow, (1962).
[20] Osadchuk, O. V., Zviahin, O. S. and Savitsky, A. Yu., " Processing of the sensor's measurement signal using parabolic interpolation," Journal of Khmelnitsky National University 2, 153-158, (2015).
[21] Bronstein, I. N., Semendyayev, K. A., [Handbook of mathematics for engineers and students of technical colleges], The main editors of physical and mathematical literature, Moscow, (1986).
[22] Chernyshova, T. I. and Chernyshov, N. G., [Simulation of electronic circuits], TSTU, Tambov, (2010).
[23] Vedmitskyi, Y. G., Kukharchuk, V. V. and Hraniak, V. F., "New non-system physical quantities for vibration monitoring of transient processes at hydropower facilities, integral vibratory accelerations," Przeglad Elektrotechniczny 3, 69-72, (2017).
[24] Kukharchuk, V. V., Kazyv, S. S. and Bykovsky, S. A., "Discrete wavelet transformation in spectral analysis of vibration processes at hydropower units," Przeglad Elektrotechniczny 5, 65-68, (2017).
[25] Kukharchuk, V. V., Hraniak, V. F., Vedmitskyi, Y. G., Bogachuk, V. V., et al., "Noncontact method of temperature measurement based on the phenomenon of the luminophor temperature decreasing," Proc. SPIE 10031, 100312F, (2016).
[26] Kukharchuk, V. V., Bogachuk, V. V., Hraniak, V. F., Wójcik, W., Suleimenov, B. and Karnakova, G., "Method of magneto-elastic control of mechanic rigidity in assemblies of hydropower units," Proc. SPIE 10445, 104456A, (2017).
[27] Azarov, O. D., Dudnyk, O. D., Duk, M. and Porubov, D., "Static and dynamic characteristics of the self-calibrating multibit ADC analog components," Proc. SPIE 8698, 86980N, (2013).

Forecasting and evaluation of voltage conditions in a low-voltage power grid with a large share of prosumer installations

Klara Sereja*, Piotr Miller
Department of Electrical Networks and Security, Lublin University of Technology,
Nadbystrzycka 38A, 20-618 Lublin, Poland

ABSTRACT

The increase in the number of photovoltaic installations connected to the low-voltage power grid, in addition to obvious benefits, under certain circumstances also adversely affects the network's operating conditions. Power generation from photovoltaic sources, strongly dependent on insolation, on the one hand is not able to cover the energy demand in the daily load peaks, and on the other hand - in another part of the day it exceeds the current demand, causing excess energy production. The randomness of photovoltaic generation negatively influences the voltage in the network.

The article attempts to model the variability of network with PV sources operation conditions, using probabilistic methods for this purpose. The analyzes were carried out, based on actual measurement data, for a low-voltage test network with photovoltaic microinstallations. The result of the conducted research is the analysis of voltage levels in selected periods of the year and the day.

Keywords: distributed generation, distributed energy resources (DERs), photovoltaic micro-sources, probabilistic models

1. INTRODUCTION

Distributed energy resources (DERs) appeared in Poland more than a dozen years ago and their number has been growing ever since. The presence of renewable sources in the electricity generation structure contributes to increasing the efficiency and energy independence of the country and to minimizing the negative impact of energy industry on the natural environment. This trend is also visible on a global scale. Poland, as a member of the European Union, obliges international agreements that impose ever new requirements on reducing the level of carbon dioxide emissions by, among other things, replacing conventional energy sources with renewable sources. One of them is a directive requiring a 15% share of energy from renewable sources in total energy consumption in Poland by 2020 [1]. Therefore, it is necessary to undertake new investments in the area of renewable energy, including photovoltaics. In the future, you can expect further forms of support for investors and prosumers, as well as a drop in the cost of the investment itself. Forecasts, both those for the coming years and long-term ones, assume further and even more dynamic development of renewable energy in Poland.

The growing number of renewable sources affects the functioning of the power grid. Particularly troublesome seem to be the sources connected to the low-voltage network classified as prosumer microinstallations - up to 50 kW [2]. In Polish conditions, in built-up areas, these are predominantly photovoltaic installations (PV). The infrastructure of the low-voltage network in its current form does not allow for accurate monitoring of electrical parameters, and even more so as affecting their value.

In the situation of increasing saturation with microinstallations, a number of new technical aspects related to the cooperation of prosumer installations with the low-voltage power grid should be considered. Among them, changes in power flows, imbalance, voltage and current surges, deterioration of power quality indicators, changes in short-circuit currents values, issues related to island operation of microsources or the problem of optimal source location in the network are mentioned most often [3, 4]. The paper focuses on the impact of PV sources operation on the voltage profile in the LV network.

*k.sereja@pollub.pl

Photonics Applications in Astronomy, Communications, Industry, and High-Energy Physics Experiments 2019,
edited by Ryszard S. Romaniuk, Maciej Linczuk, Proc. of SPIE Vol. 11176, 111765Z
© 2019 SPIE · CCC code: 0277-786X/19/$21 · doi: 10.1117/12.2536975

2. IMPACT OF DISPERSED SOURCES ON LOW-VOLTAGE NETWORK

Connecting energy sources to a low-voltage network affects the way it operates. These networks have been designed to work in a radial structure. After connecting prosumer installations, the network configuration changes and the power flows are bidirectional. Changes in the power flow affect the voltage values at the network nodes. According to national regulations [5], based on the PN-EN 50160 standard [6], the obligation of the distribution system operator (DSO) is to provide the customer with a voltage between 0,9 V_n and 1,1 V_n (95% of samples from the set of 10-minute average values during the week). Meeting this requirement has generally been limited so far to determining the maximum network load and on its basis an adequate selection of network infrastructure parameters so that the voltage drop at any of the consumption points does not exceed 10% of the nominal value. In the case of a significant share of microgeneration installations connected to the network, it is not enough to maintain the voltage above the lower limit, but also to prevent exceeding the upper limit. As research shows, the problem of voltage boost is already noticeable in Poland as well. In spite of the still relatively small share of photovoltaics in the total energy production structure in the country, there are areas where generation from PV sources exceeds locally energy consumption in certain periods of the year or the day. The relation between the power consumed and returned to the network determines the way in which distributed sources affect the network. This impact can be positive, when generation reduces voltage drops, or negative, when in periods of high insolation and at the same time low network load there is a voltage rise that causes exceeding the permissible value. This results in the activation of overvoltage protections and disconnection of the PV installation, thus causing a drop in the profitability of the prosumer investment in a wider perspective. Negative voltage impact, although it may occur only in a short period of time throughout the year, will limit the possibility of connecting further prosumer installations to the network.

Another issue related to the emergence of distributed generation is the partial unpredictability of network operation resulting from changing weather conditions. Generation from renewable sources requires further analysis and selection of models that will allow prediction of generation levels. In the research carried out so far [7], the generation from PV sources is dependent on solar radiation, which depends on the position of the sun on a given day of a given month (deterministic variable) and cloudiness expressed as the so-called clear-sky index. Clear-sky index can be treated as a random variable and modeled using the probability distribution. Examples of distributions for modeling clear-sky index include: Gamma, Boltzmann, bi-exponential, double Normal distributions, double beta distributions, double Boltzmann distributions, logistic combined with Weibull and triple Normal distribution [7].

Energy consumption is also characterized by a certain randomness, showing partial repeatability in diurnal and annual perspective, related to the lifestyle and habits of recipients, weather conditions, natural daylight lighting, etc. The literature presents attempts to model household load profiles using the following distributions: Normal, Log-Normal, Gamma, Gumbel, Inverse-Normal, Beta, Exponential, Rayleigh or Weibull [7, 8]. The unpredictability of network operation will be additionally exacerbated by the introduction of electric vehicles on a larger scale, constituting receivers with variable and difficult to predict the nature of energy consumption. All this means that conventional methods of power flow calculations seem to be insufficient. A new approach to forecasting network operating conditions is necessary, taking into account uncertainties and random changes in both generation and load. This article attempts to model network conditions with distributed generation using probabilistic tools. It presents the possibilities of MATLAB and Statistica packages in this area and indicates areas for further research.

3. RESEARCH RESULTS

3.1 Assumptions of simulation

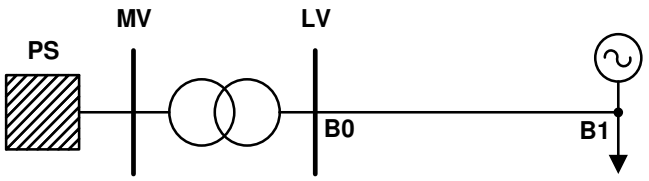

Figure 1. Diagram of a simplified test network

The calculations and simulations carried out in the framework of the research are based on real measurement data collected throughout the year in the network in which the occurrence of a negative phenomenon of voltage boost was

noted. In order to simplify the calculations and to keep the results clear, the actual network diagram has been simplified to the form shown in Fig. 1.

The test network consists of a MV/LV power transformer with a power of 63 kVA and a 450 m long low-voltage circuit supplied from it, made of an overhead aluminum cables with a cross-section of 70 mm^2. The network load and all PV sources connected to it were replaced with substitute load and source connected at the end of the circuit (at node B1). In B0, on the LV side of the transformer, a nominal voltage of 400 V was assumed. It was assumed that only active power is consumed and generated. Distribution of network load is presented in the form of a surface plot, showing the frequency of occurrence of a given value of consumed power *PL* in a given hour throughout the whole year (Fig. 2).

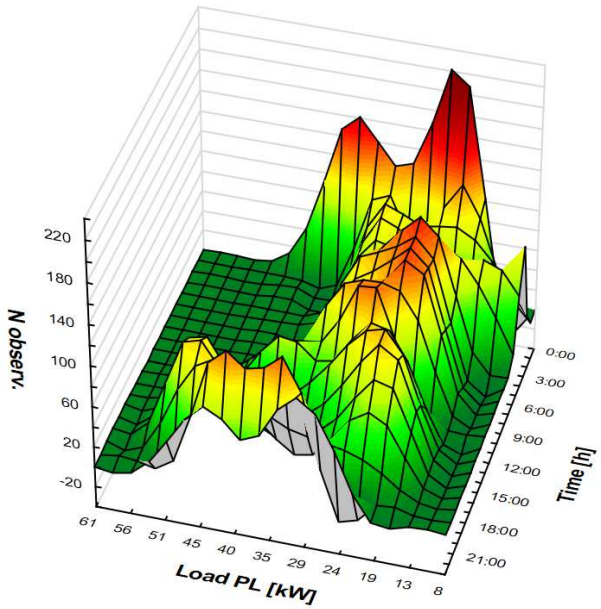

Figure 2. Surface plot of power consumption for each hour of the day throughout the year

The total installed power in microsources is 100 kW. Generation variation during the year was depicted on surface plots (Fig. 3) showing the frequency of a given value of generated power *PPV* at specific hours of the day throughout the year.

The purpose of the simulation was to determine the voltage value on the LV side of the transformer (node B0) and at the end of the line (node B1). One summer month, July, was chosen for the analysis. Several calculation options have been carried out. First, in variant A, the voltage levels were determined based only on real measurement data. In option B an attempt was made to replace the actual load with the matching probability distribution. Option C, however, shows the results of determining voltage levels in the network when both load and generation from PV sources are treated as random variables with a given probability distribution. Variant A will therefore present the most accurate results, but with the simultaneous need to provide a large amount of input data. Option C will allow to obtain results with lower accuracy, but with the introduction of relatively few information on network operating conditions.

Calculations related to matching probability distributions to data were made using the Statistica package. Whereas, the Newton-Raphson method was used for power flow calculations, using the MATLAB package and the power system simulation tool, Simscape Power Systems.

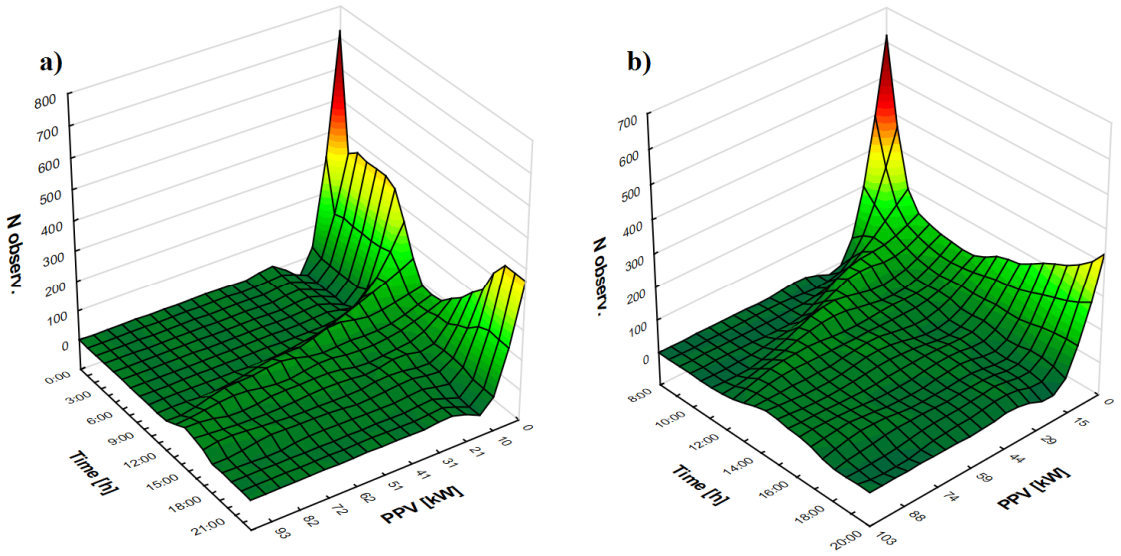

Figure 3. Surface plots of power generation for each hour of the day throughout the year; a – for the whole day; b – for the daytime from 8 a.m. up to 8 p.m.

3.2 Simulation results for the summer month (July)

Problems related to exceeding the upper voltage limit in networks with photovoltaic dispersed sources occur primarily in the summer months, when the generated power reaches high values. This is related to favorable weather conditions for the generation as well as lower power consumption from the grid in relation to winter months. The analyzes were carried out for July, additionally reduced to the daytime (8 a.m. - 8 p.m.), when the generation from PV sources is non-zero.

3.2.1 Variant A - measurement data of generated and consumer power

The first variant of the calculation is based solely on the measurement data - the active consumed power *PL* and the generated *PPV*. The variation in power during the month is shown in Fig. 4.

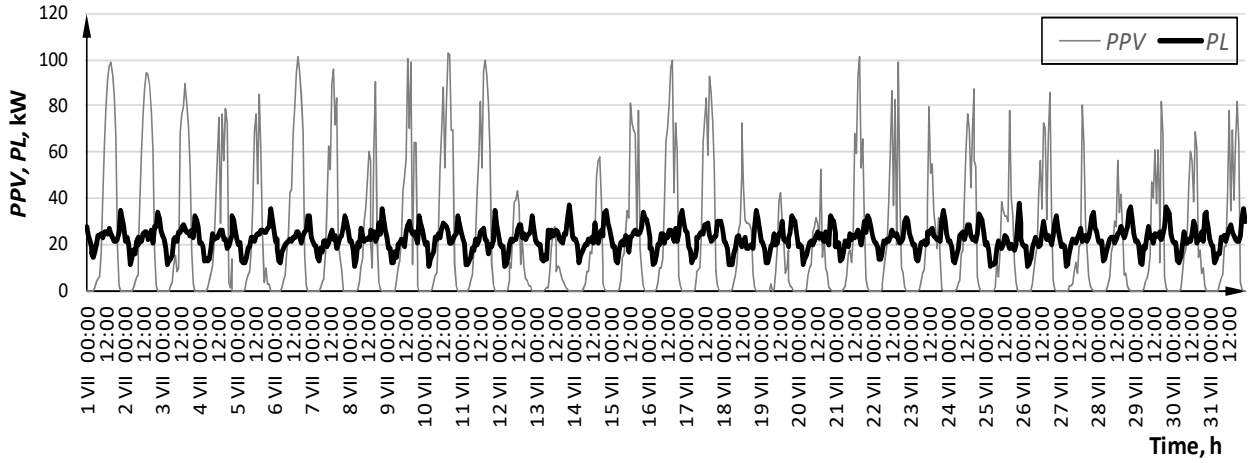

Figure 4. Variability of generation and consumption of electric power in July

The consumption and generation profile was used in the test network, counting power flows for each of over 400 sets of values. As a result of the calculations, the voltage values at the B0 and B1 nodes were obtained. The results were grouped in ascending order and plotted as a plot (Fig. 5). The upper voltage limit $V_{\text{lim_up}} = 1{,}1\ V_{\text{n}}$ is additionally marked.

As the results show, the voltage on the LV side of the transformer varies within small limits. Over half of the value is higher than the rated voltage $V_{\text{n}} = 400$ V = 1 p.u., however, none of the results exceeds the permissible level. The voltage

at the end of the line is characterized by greater variability. There were also voltage jumps above the acceptable limit, occurring most frequently from 1 p.m. up to 4 p.m. These overruns, however, constitute a relatively small part, about 7% of all measurements.

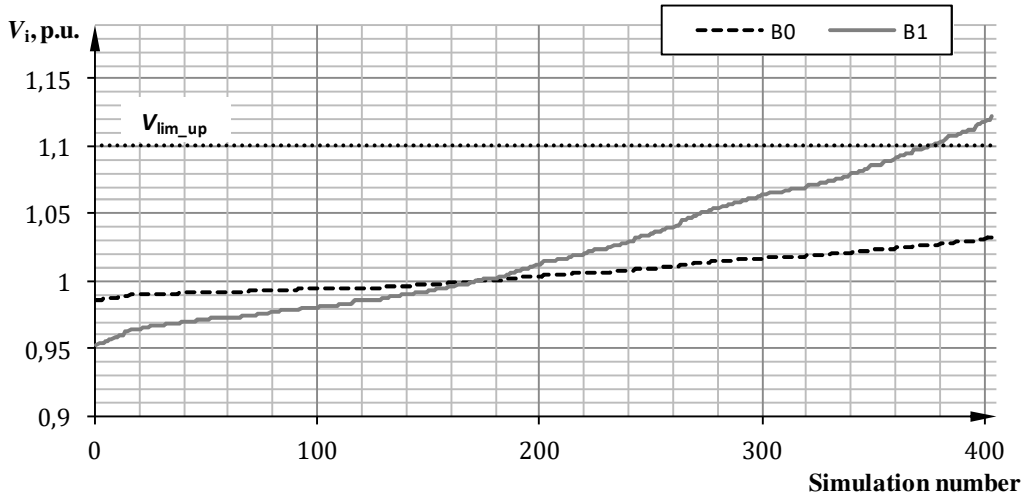

Figure 5. Simulation results – variant A

3.2.2 Variant B – measurement data of generated power, power consumption values in accordance with the Gamma distribution

In the second variant of the simulation, the actual load data was replaced with data according to the adjusted probability distribution. Gamma distribution was chosen to represent electricity consumption based on Kolmogorov-Smirnov goodness-of-fit test. The probability density function (PDF) was estimated using the Statistica package using the method of moments [9]. The random variable X has a Gamma distribution when its PDF is given by:

$$f_X(x,k,\lambda) = \frac{\lambda^k x^{k-1} e^{-\lambda x}}{\Gamma(k)}, x > 0 \quad (1)$$

where Γ is Γ-function, $k > 0$ is called the shape parameter and $\lambda > 0$ is called the scale parameter.

The Gamma distribution with the following parameters was adapted to the data: $k = 79{,}66$, $\lambda = 0{,}29$. The matching of the probability density function (PDF) and the cumulative distribution function (CDF) are shown in Fig. 6.

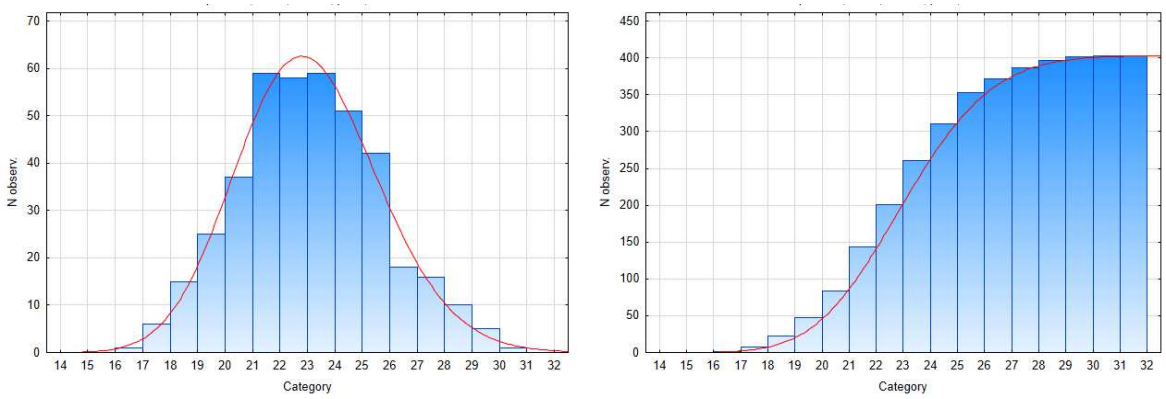

Figure 6. Histograms of electricity consumptions data with a Gamma PDF and CDF

For the assumed data, power flow calculations were made and the obtained voltage results in B0 and B1 nodes, as before, were ordered in ascending order and presented in the form of a plot (Fig. 7).

The obtained plot has a similar course as in the case of the use of measurement data in the previous variant. Voltage surges above $V_{\text{lim_up}}$ account for 8% of all results.

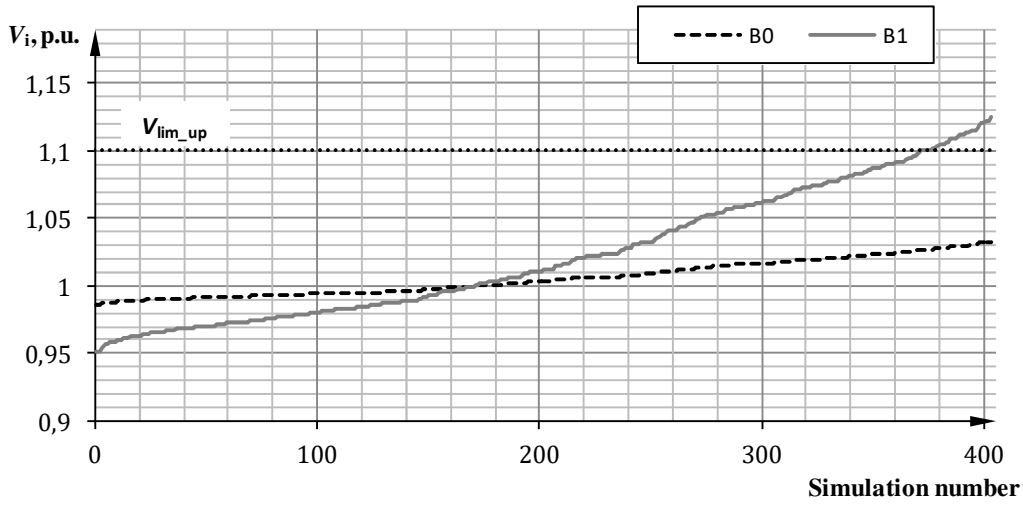

Figure 7. Simulation results – variant B

3.2.3 Variant C – generated power values in accordance with the uniform distribution, power consumption values in accordance with the Gamma distribution

In the last calculation variant, it was assumed that the power generated in photovoltaic sources is a random variable with a uniform distribution defined for the interval <0, 100 kW>. This assumption allows to consider the most unfavorable conditions of network operation and it seems justified in the case of forecasting well in advance and the high uncertainty of the generated power [10]. This approach has the advantage of not requiring complicated clear-sky index models. On the other hand, it is also associated with low accuracy of obtained results. The load profile was adopted in accordance with the Gamma distribution, described in the previous section. The voltage values determined on the basis of the simulations are shown in Fig. 8.

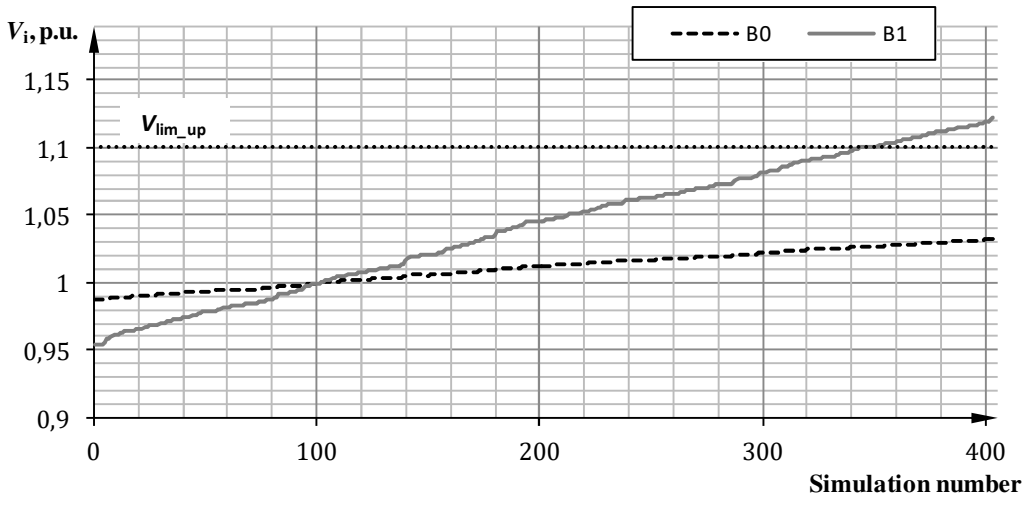

Figure 8. Simulation results – variant C

4. CONCLUSION

The paper presents three variants of the approach to modeling the operating conditions of a low-voltage power network with a large share of distributed generation. The purpose of the simulation was to determine the voltage in the network and its evaluation in terms of the risk of voltage boost. The results are presented in the form of a table (Tab. 1). The share of individual voltage groups in the total number of simulations was presented. The results in the first two variants are almost identical, which means that in order to estimate the voltage levels in the network, instead of data from measurements, you can use stochastic models, which would simplify calculation algorithms and allow you to forecast network conditions. The results obtained in option C differ from the other two. The uniform distribution used to model the generated power level allowed to limit the input data to the minimum, but at the cost of the obtained accuracy.

Table 1. Summary of simulation results in individual calculation variants

	Variant A	Variant B	Variant C
$V_i \geq 1{,}0\ V_n$	58% (233)	58% (232)	75% (302)
$V_i \geq 1{,}05\ V_n$	33% (131)	33% (132)	47% (191)
$V_i \geq 1{,}1\ V_n$	7% (29)	8% (31)	15% (60)

Simulations were carried out for one month. In order to accurately predict the voltage conditions in the network, it would be necessary to model the entire year. For this purpose, you should use data from at least a few years, but these data are difficult to obtain. However, this situation is changing due to the gradual implementation in Poland of smart energy meters.

As presented in the article, distributed generation may have a negative impact on the network voltage, especially at the consumption points furthest from the transformer substation. For this reason, the possibilities of connecting further prosumers are limited. To remedy this, appropriate actions should be taken based on the knowledge of the nature of the network's operation and anticipating changes in its functioning throughout the year. This topic was taken up in the article and is subject to further research. The remedies that can be taken include [11], for example, partial modernization of the network, including increasing the transformer power, installing the on-load tap-changer or increasing the line cross-sections. On the other hand, one can influence also the nature of microinstallation operation by activating other operating modes of the inverter, assuming the consumption/generation of reactive power or smooth limitation of generated active power (modes $Q(P)$, $Q(U)$, $P(U)$) [12]. Another approach assumes influencing not only on generation, but also on the variability and nature of the load, e.g. through DSR (demand side response) systems.

REFERENCES

[1] Directive 2009/28 / EC of the European Parliament and of the Council of 23 April 2009 on the promotion of the use of energy from renewable sources and amending and subsequently repealing Directives 2001/77 / EC and 2003/30 / EC.

[2] Act of June 7, 2018 amending the act on renewable energy sources and certain other acts, (2018).

[3] Conti, S., Raiti, S., Tina, G., Vagliasindi, U., “Study of the impact of PV generation on voltage profile in LV distribution networks,” Power Tech Proceedings IEEE, Portugal, (2001).

[4] Montusiewicz, J., Gryniewicz-Jaworska, M., Pijarski, P., "Looking for the optimal location for wind farms," Advances in science and technology research journal 9 (27), 135-142 (2015).

[5] Regulation of the Minister of Economy of 4 May 2007 on detailed conditions for the operation of the power system, Dz.U.2007 No. 93, item. 623.

[6] PN-EN 50160:2010, “ Parameters of supply voltage in public electric power networks,” (2014).

[7] Munkhammar, J., Widen, J., Ryden, J., “On a probability distribution model combining household power consumption, electric vehicle home-charging and photovoltaic power production,” Applied Energy, 142, 135-143 (2015).

[8] Munkhammar, J., Ryden, J., Widen, J., “Characterizing probability density distributions for household electricity load profiles from high-resolution electricity use data,” Applied Energy, 135, 382-390 (2014).

[9] Pluciński, E., Plucińska, A., [Probability. Stochastic processes. Mathematical statistics. Theory of probability], WNT, Warsaw, (2015).
[10] Sobierajski, M., "Pseudo-random simulation of node voltages in medium and low voltage grids with photovoltaic micro-installations," Acta Energetica 2 (31), 203-208 (2017).
[11] Kacejko, P., Adamek, S., Wancerz, M., Jędrychowski, R., "Possibilities of mitigation of overvoltage caused by intensive PV development in LV grid," Wiadomości Elektrotechniczne 85(9), 20-26 (2017).
[12] Jędrychowski, R., Pijarski, P., Adamek, S., Sereja, K., "Evaluation of the impact of PV generation on the voltage regulation efficiency in low-voltage networks," Rynek Energii 3(136), 43-47 (2018).

Logic correctness of control algorithms for mechatronic discrete systems with parallel processes

Aleksandr P. Gubarev*[a], Oksana S. Hanpantsurova[a] , Konstantin A. Belikov[a], Konrad Gromaszek[b], Azat Turgunbekov[c]
[a]National Technical University of Ukraine "Sikorsky Kyiv Polytechnic Institute", 37 Prosp.Peremohy, Solomyanskyi district, Kyiv, Ukraine, 03056; [b]Lublin University of Technology, ul. Nadbystrzycka 28A, 20-618 Lublin, Poland; [c]L. N. Gumilyov Eurasian National University, Satpayev Str., 2, 010008 Astana, Kazakhstan

ABSTRACT

Systems, consisted of fixed quantity of operating devices and actuators, were considered in case of determined functional algorithm. It's shown, for binary description of system's state, including variability of transition states, can be applied a given memory criterion. Memory zero-values correspond to undetermined operating logic of a system. Whenever states, when memory equal to zero, pointing on process stage, where unregistered information was appeared. The design procedure of the relative memory calculation is shown. The construction of the process structure and functional graph is represented by the example of the assemble technology of a pneumatic cylinder. It is shown that the use of reduced memory allows reducing the laboriousness of logical synthesis of systems and control algorithms for parallel processes, as compared with Petri nets and cyclograms.

Keywords: system, branched process, closed-loop process, logic, actuator

1. INTRODUCTION

Raising of production speed and flexibility leads to complication of manufacturing processes and algorithms of PLC's programs [1 – 5]. It's clear to see from the increased quantity of actuating devices, also it complicates ensurance of their correct interaction. Such systems pass many transition states during operating, due to aperiodic features of actuating devices and actuators' characteristics, additionally, are destabilized by environment conditions [6, 7]. The known description methods for such systems use sequence of determined states in binary form [8, 9]. Parallel processes are used to increase production values, but the same time these methods are limited in this case. Separation of entire algorithm on several subprograms corresponds to partition of operating object and regroup of system structure. Ineffective methods of the parallel processes description are replaced by coordination among actuating parts of a system. The deviation and error searching usually are made by checking of all possible actuating variants, e.g. reachability graph of Petri Nets [8, 10]. Additional relations among system's actions are inserted into algorithm to ensure the correctness. But these relations don't define the nature of actuating process and ensure the correctness (maybe there are no needs in additional relations), also it could create new error. Using of PLC's allow to provide pseudo-parallel control of processes, during transition processes in the mechanic part of a system (fig. 1). Operational algorithm is based logic functions, which take into account temporal indeterminate states of actuators. Functions are made via method of cycle-modular approach [11, 12]. The algorithm is established as full list of possible functions, which change periodically, according to PLC's input states. The main aim of the presented researches is the reduction of time of control algorithms creation and research of logical certainly of systems with parallel processes [13,14].

2. A CRITERION OF COMPLETENESS SYSTEM

System evaluation is made via system features like a reachability, coverability, termination etc. [8, 9, 13]. But these features can be determined for existing model and cannot be ensured in development of system. Known formal methods

*gubarev@i.ua,

Photonics Applications in Astronomy, Communications, Industry, and High-Energy Physics Experiments 2019, edited by Ryszard S. Romaniuk, Maciej Linczuk, Proc. of SPIE Vol. 11176, 1117660
© 2019 SPIE · CCC code: 0277-786X/19/$21 · doi: 10.1117/12.2537074

well describe the branched process path and are used for operational programs, e.g. CoDeSys. However, they don't give a criterion of the complete system in case of the aperiodic objects design and performing operational algorithms for PLC's.

In case of automated production system, it is mean the system's "intelligence" (memory + algorithm) knows, in each operational moment, about following action on a product. When the product will ready the system's memory "S" will reach a maximum value and includes all actions, were done.

For example, the system consists of n steps of manufacturing process. The finished product corresponds to the value S of system memory, which is equal to:

$$S_{n/0} = \int_{\tau_0}^{\tau_n} \Phi(\tau) d\tau = \sum_{i=0}^{n-1} [\Phi(\tau_{i+1}) - \Phi(\tau_i)] > \sum_{i=0}^{n-(1+k)} [\Phi(\tau_{i+1}) - \Phi(\tau_i)], \quad (1)$$

herein $S_{n/0}$ – the value of system memory in the beginning of step n relatively to the beginning of step 0, Φ – the function of execution of actions by system elements, τ – discrete time, n – the number of steps of the production process, 0 – initial state of the system (zero reference point) [15,16].
So, if memory depends on the initial point (coordinates) and system repeats production cycle, than (1) is satisfied for each other point along fixed cycle length: :

$$S_{n+j/j} = \int_{\tau_j}^{\tau_{n+j}} \Phi(\tau) d\tau = \sum_{i=j}^{n+j-1} [\Phi(\tau_{i+1}) - \Phi(\tau_i)] > \sum_{i=j}^{n+j-(1+k)} [\Phi(\tau_{i+1}) - \Phi(\tau_i)], \quad (2)$$

herein $S_{n+j/j}$ - the value of system memory in the beginning of step n+j relatively to the beginning of step j. .

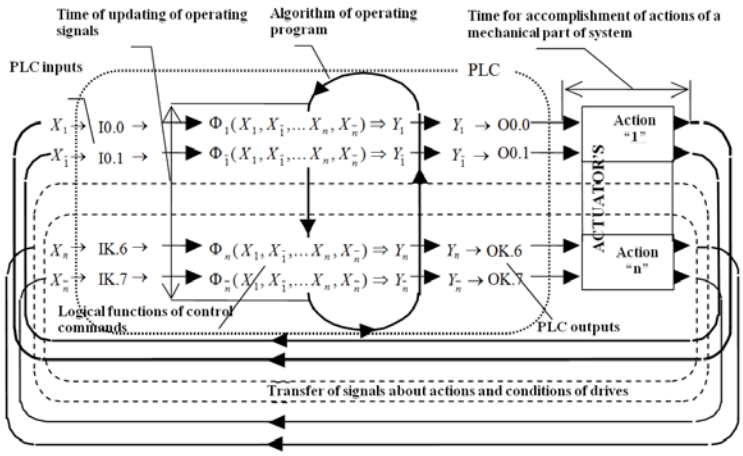

Figure 1. Function process and structure of the main algorithm for management of a mechatronic system in "pseudo-parallel" alternative.

The system's memory consists of many elements – flags or triggers, memorized each separate action. Minimal distance, used for assessment of the memory change, is complete action, state or transition, which bind several aperiodic actions. Each of flags has been in initial state "0"/"FALSE" before action and became "1"/"TRUE" after. In case of considering actuating device, it has two possible actions: direct and reverse. At the moment, state of actuator is described as "0"/"FALSE", for direct action, after appearing signal of command "ON", actuator state became "1"/"TRUE". The reached state is kind of memory about direct action were done. Hence, actuator returns into initial state on signal of command "OFF", reverse action, and waits for next command "ON". So, state of the direct action returns to "0"/"FALSE". It is need to remember about direct action were done, in case of several direct action of actuator for a cycle. If actuating device, on one command provides action and for another returns in "stand by" – mode, this change in memory is provided by one flag's/trigger's state [17,18,19].

For example, the system consists of 7 elements (fig. 2). We can define system memory at any moment of this manufacturing cycle. For example, at the time moment T1 devices No 1, 2 and 3 are already have executed some actions

(values of their states is “1”), device No. 4 is now executing an action (has value “*”) and actions of devices No. 5, 6 and 7 is not begun (they have values “0”). At this time moment the value of system memory is equal to:

$$S_{4/0} = \{1, 1, 1, *, 0, 0, 0\}.$$

Therefore, at the time moment T2 the value of system memory is equal:

$$S_{6/0} = \{1, 1, 1, 1, 1, *, 0\}.$$

Conclusion #1: the memory is divine value and depends on the initial point (node).

Conclusion #2: the memory consists of the real part (“0” or “1”) and the image part (marked with “ * ”).

Proposing method is based on hypothesis: function of each object in the system can be described by states of determined quantity of binary elements [9]. Each device are considered as binary element, but the same time they have transition state “ * ”, that corresponds to actions:

$$O(\tau) = \{Z_i\}_n : \forall \tau \in T \exists j : Z_j(\tau) \in \{0,1\} \wedge Z_j(\tau+1) = \overline{Z_j(\tau)}, \quad (3)$$

herein $O(\tau)$ – an object; n – a number of elements; τ – discrete time; $Zj(\tau)$ – an element.

In the Figure 2 memory consists of actuating devices’ states: complete direct actions and “stand by” modes.

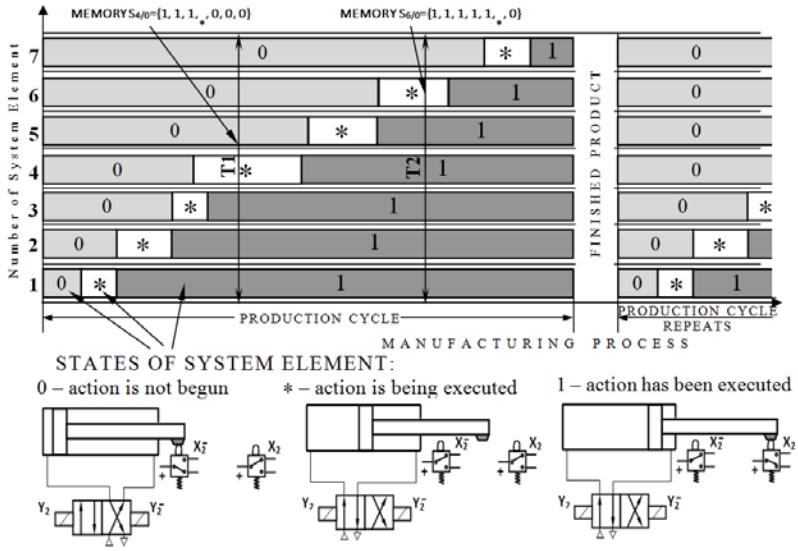

Figure 2. Simplified diagram of memory stacking in production cycle (a) and execution of action by system element No. 2 (b).

Actions can represent technological, supporting, transporting etc. processes. When memory obtain some value, e.g. “S_6”, it means the system have done (6/K)% of the production cycle, herein K – overall quantity of actions in the production cycle. Also, it means that ((K-6)/K) % is left to do in cycle. According to value “S_6”, as initial point, system will start cycle from point of (6/K) % product completeness. However, if memory value “S_i” is equal to “S_6” than system might start execution from point of (6/K) % instead of (i/K) %. If there are two or more point in the cycle, having the same value of memory, then it leads to uncontrollable executing of cycle segment between these points – incorrect control [20,21,27,28].

Difference between two segments can be determined by states of elements, which are inactive in these segments, transitions. Comparing two transitions, there are different actions for each segments, but memory of elements on transitions cannot be compared:

$$\Delta S(\tau_i,\tau_j)=S_{j/i}=\{s_k\}_m:\begin{cases}s_k=1:[s_k(\tau_j)=1\wedge s_k(\tau_i)=0]\vee[s_k(\tau_j)=0\wedge s_k(\tau_i)=1]\\ s_k=0:[s_k(\tau_j)=1\wedge s_k(\tau_i)=1]\vee[s_k(\tau_j)=0\wedge s_k(\tau_i)=0],\\ s_k=*:[s_k(\tau_j)=*]\vee[s_k(\tau_i)=*]\end{cases} \quad (4)$$

herein s_k - the state of system element № k, m – total number of system elements.

S_i {1, 1, 0, 1, 0, 0, 0, 1, 1, 0, *, *, 0, 1, 0, 1, 1, *}

S_j {1, *, 0, *, 0, 1, 0, *, 1, *, 1, 1, 0, 1, 0, 0, 1, *}

$S_{j/i}$ {0, *, 0, *, 0, 1, 0, *, 0, *, *, *, 0, 0, 0, 1, 0, * }

Figure 3. Example of calculating specific memory value for two transition (i and j) with undetermined states of elements.

Taking into account undetermined states of devices #12 and #8, the memory value of transition #15 is:

$$S_{15}^{\text{var}}=\{1,_,3,4,5,6,7,8,9,_,_,12,_,_,15,_,17,18\}$$
$$\Downarrow \quad , \quad (5)$$
$$S_{15}^{\text{var}}=\{*,_,*,*,*,*,*,*,*,_,_,*,_,_,*,_,*,*\}$$

herein "*" - system elements, which execute actions in parallel with transition #15 (these are elements No. 1, 3-9, 12, 15, 17, 18); "_" - system elements, which do not change its state during execution of transition #15 (these are elements 2, 10, 11, 13, 14, 16).

It's value doesn't depend on initial point. Low lines replace elements' states, which depend on the initial point "A". According to (4) a memory of the transition "X" consists of determined and undetermined parts. At the initial point, undetermined part also exists, similar to (5). All undetermined elements, at the "A" or the "X", have unknown increment between "A"→"X". If "k" – device was inactive, then memory increment will be equal "0", other way – "1". State "1" can be caused by command "ON" (direct action) or "OFF" (reverse), both possible. So , if number of "k"-device actions is even, then increment is "0", in case of odd – increment is "1".

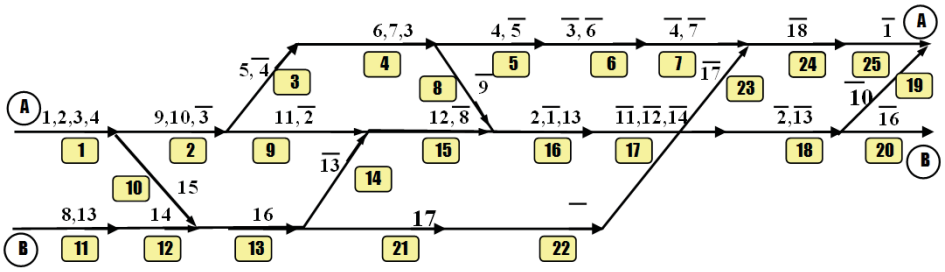

Figure 4. Graph of parallel processes: 18 devices, 25 transitions, 42 actions, 2…5 parallel processes, 1…4 asynchrony actions for trasitions.

If initial point was on transition #1, then action between "#1" →"#15" have been done:

$$P_{1\to 15}=|\,9,10,\bar{3},11,\bar{2},15,16,\overline{13}\,|\,. \quad (6)$$

Undetermined part of memory for #1 is:

$$S_1^{\text{var}}=\{*,*,*,*,_,_,_,*,_,_,_,_,*,*,_,*,_,_\}\,. \quad (7)$$

Relative memory value on transition “#1” →”#15” in “string-state” form:

$$S_{15/1} = \{*,*,*,*,*,*,*,*,*,*,1,1,*,*,*,*,*,*,*,*,*\}. \quad (8)$$

Increment in memory system of binary devices (3):

$$S_{15/1} = |10,11|. \quad (9)$$

Memory’s increment for segment can be defined: A) by memory quantities at the beginning and at the end of segment; B) by memory increment at a segment [24,25,27].

Thus, transition from string-states to direct calculation of memory increment reduces amount of information in several times (in our example in 9 times).

From the operating beginning elements start change their states. For each moment, result of system operating can defined by difference between initial and current state of elements:

$$S_{j/0} = \{Z_i(\tau_j)/Z_i(\tau_0)\}_n = \{Z_1(\tau_j)/Z_1(\tau_0),...,Z_n(\tau_j)/Z_n(\tau_0)\}_n. \quad (10)$$

In case of “0” as result, the system returns to the initial point and ready to begin new cycle.

In case of τ_k as initial point and (10) is equal to “0”, it means that system returns to τ_k and will repeat cycle of segment (τ_k, τj) periodically.

In case of existing two transitions (τ_{k1}, τ_{k2}) and $S(\tau_{k1}, \tau_{k2}) = 0$, then system is logically incorrect and production cycle, e.g. assembly (Fig.5), won’t be executed. Relative quantity of memory definition for closed-loop process have to be made according to rules for marks i and j, which bind transitions $P_{i \to j}$:

$$S_{i/j} = \overline{S}_{j/i} = \left(\left(\sum_{i+1<k<j+1} (Z_l \in \{\mu_k\} + Z_{\bar{l}} \in \{\mu_k\}) \right) / Z_l \in \{\mu_i\} \vee \{\mu_j\} \right) / Z_{\bar{l}} \in \{\mu_i\} \vee \{\mu_j\}. \quad (11)$$

Relative memory is a criterion of system logic correctness:

- relative memory doesn’t equal to “0” for any segment, that shorter then cycle:

$$\begin{cases} \forall(\tau_i, \tau_j) : \tau_j = \tau_i \pm (k+1) \Rightarrow S_{i/j} \neq 0 \\ \forall \tau_k \overline{\exists} Z : (Z(\tau_k) = 1) \wedge (Z(\tau_k + 1) = 0) \vee (Z(\tau_k) = 0) \wedge (Z(\tau_k + 1) = 1) \end{cases}. \quad (12)$$

- relative memory equal to “0” for any cycle in process:

$$\forall \tau_i : (S(\tau)\Big|_{\tau_i}^{\tau_i + 1} + S(\tau)\Big|_{\tau_i + 1}^{\tau_i}) \equiv 0. \quad (13)$$

- if there there are two similar (unrecognizable) transition “k” and “t”, then process structure is splited up on two independent systems: $P_{k \to t}$ and $P_{t \to k}$.

Definition method of relative memory between transitions “β” and “ω”:

1. Define the undetermined part of transition “β”.

2. Define the undetermined part of transition “ω”.

3. Make a list of actions $P_{\beta \to \omega}$ between “β” and “ω”.

4. Subtract undetermined parts of «β» and «ω» from the list $P_{\beta \to \omega}$.

5. Subtract elements with even-number of i-device actions from the list $P_{\beta \to \omega}$.

6. In case of $P_{\beta\to\omega}=\{0\}$, system is logically incorrect.

To eliminate "0" – memory between transitions "β" and "ω" it must be added a new device Zn+1 to the system, consists on n-devices, as flag/trigger. Command "ON" for Z_{n+1} must be placed on cycle segment from "β" to "ω"; command "OFF" – on segment from "ω" to "β".

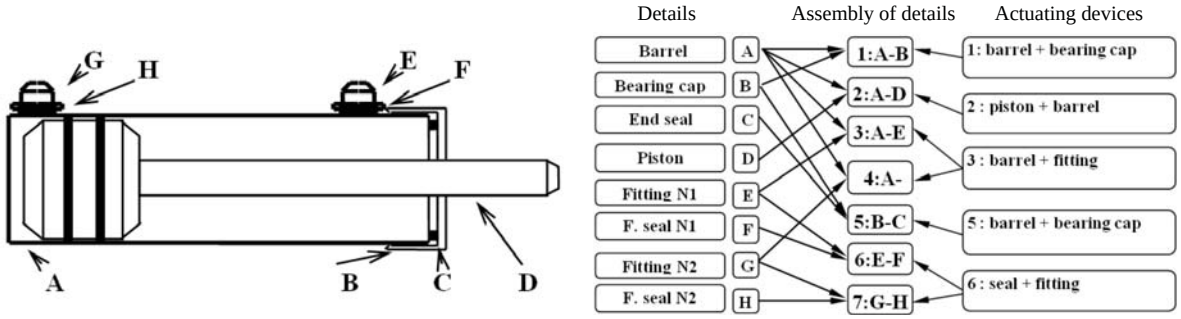

Figure 5. Simplified scheme of product (pneumatic cylinder) and assembling operations.

3. EXAMPLE OF THE PROCESS STRUCTURE CONSTRUCTION

Center As an example we will observe automatic line of assemblage of the pneumatic cylinder. Pneumatic cylinder consists of 8 details, must be assembled (Fig. 5). Some detail can be assembled in parallel processes; other must be assembled consequence, one by one. To simplify assembly, let it be that each action corresponds to one actuating device, additionally there are actions "pick/grab" and "drop/release" detail, plus outload of complete assembly. Design scheme of product transforms into the list of actuating device actions. Each actuator has two types of action – "direct" and "reverse".

Taking into account requirements of details assembling order: seal +fitting must be done before fitting + barrel, structure of product (Fig. 6.a) transforms into process chart (Fig. 6.b).

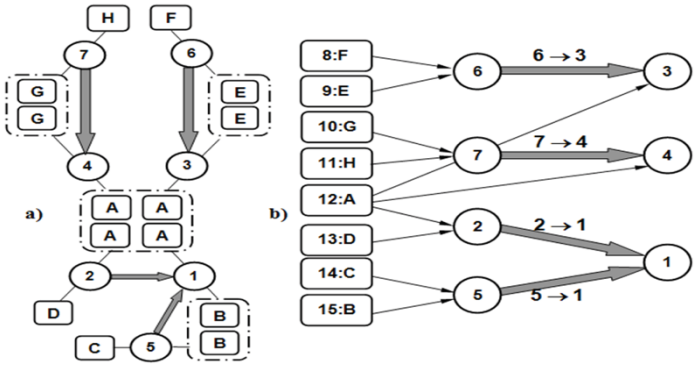

Figure 6. Figure captions are indented 5 spaces and justified. If you are familiar with Word styles, you can insert a field code called Seq figure which automatically numbers your figures.

Similar actions 3, 4 (fitting + barrel) and 6, 7 (fitting + seal) will be provided by one actuating device. Instead of action 4, there will be action 3 repeated twice (A-E then A-G), same for 6 and 7 – action 6 will be repeated (E-F, then G-H). Parallel processes of the assembly (Fig. 7) are described by binary element system with undetermined memory quantity on transitions (similar to Fig. 2). General description are used for actuating devices and logic control components (flag, timer, subprogram etc.) [9, 11]. The relative memory, as criterion of correctness (12) and (13), can be applied to the considering cycle [25,26,28]. Locus of memory lost between I and II points on missed action. Analyze of process data ensures, that between the 1st and 2nd fitting attachments, assembly zone for action must be changed.

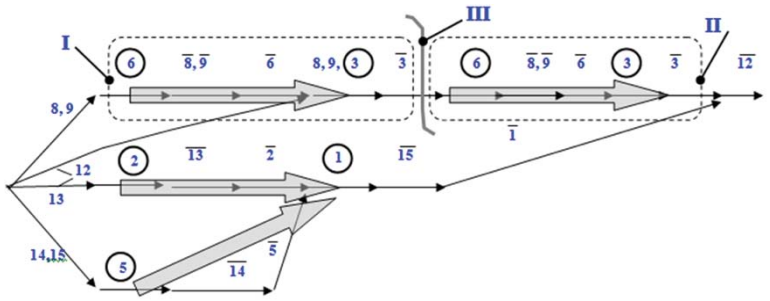

Figure 7. Closed-loop assembly process: pathes are subscribed with direct and reverse actions 1, 2, 3, 5, 6 and supplementary actions 8, 9, 12, 13, 14, 15; I and II – segments with "0" memory increment, III – location of memory lost.

To carry out the relative memory quantity chart (Fig. 7) is changed to the functional graph (Fig. 8). All transitions are marked. Quantities of required relative memory on consequence non-adjacent transitions can be obtained, according to method and using (4). In case of Si/j = "0", system splits on two logically independent parts. Line, that connect two transitions with similar memory quantity (Fig. 8). Obtained results:

$S_{4/1} = S_{9/1} = S_{11/1} = 0;\ S_{8/5} = S_{9/5} = S_{11/5} = S_{28/5} = 0;\ S_{11/8} = S_{28/8} = 0;\ S_{19/12} = S_{20/12} = S_{21/12} = S_{22/12} = S_{23/12} = S_{24/12} = 0;\ S_{16/13} = S_{17/13} = S_{19/13} = S_{20/13} = S_{21/13} = S_{23/13} = S_{24/13} = 0;\ S_{20/14} = S_{21/14} = S_{22/14} = 0;\ S_{21/15} = S_{22/15} = S_{23/15} = 0;\ S_{20/16} = S_{22/16} = S_{23/16} = S_{24/16} = 0;\ S_{20/17} = S_{23/17} = S_{24/17} = 0;\ S_{23/20} = S_{24/20} = 0.$

Number and location of obtained "0" quantities show that process seems like a complex of actions, instead of logic process of the assembly. In fact, memory must to be an indicator of product completeness level, however product completeness in one period of process increase, and in another decrease. It's because system memorize locations and states of actuating devices instead of changes have been made in product structure. For example, the 1st fitting were installed to barrel, released by gripper and actuator returned to initial state (I, Fig. 6). End switch and position sensor will detect the same state before and after action. Relative memory hasn't increased. It is need to memorize this action with an additional flag or trigger. It can bind several system's segments, e.g. connection line of flag #14 (fig. 8) crosses 6 lines of undetermined states, each one split system on logically independent segments. But the parallel processes do not lie in one plane and the graph of parallel processes must be considered as 3D-structure (Fig. 8).

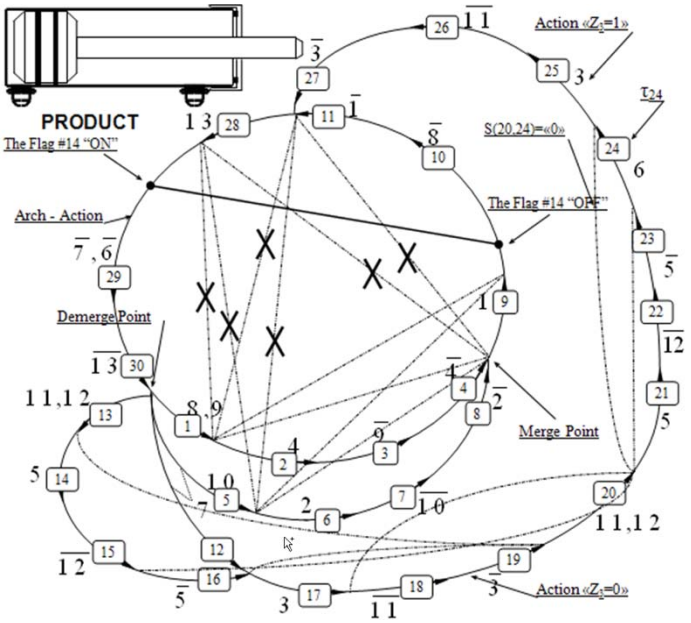

Figure 8. Functional graph of parallel process of pneumatic cylinder assemblage with lines of zero memory values (shown by a dot line), example of the Flag #14 addition, cut lines of indeterminacy (crossed out).

For each parallel process must be inserted flag or trigger, that can bind two parallel processes and can be used by another process as indicator. The flag can logically unite some fragments of system. As system elements are elementary cyclic processes $\{1\cdots\to\bar{1}\cdots\to,2\cdots\to\bar{2}\cdots\to,...,k\cdots\to\bar{k}\cdots\to\}_n$), and to them there match means of realization (modules), amount of information about structure of process and system is reduced in four times (2 – due to the uniqueness of "process - module", 2 – due to the cyclic recurrence of process "main action – back action"). Thus, testing logic correctness using diagrams, Petri's Nets or functional plans requires 8 times more data, to be analyzed, than relative memory criterion. Number of tests will be equal the square of data quantity and it will continue raise during testing. Method of relative memory criterion allow to test massive systems without these decomposing. Compactness of system description allows to find out causes of memory lost on subject level.

4. CONCLUSIONS

1. The proposed approach was originally designed for tasks of construction of discrete industrial systems with the cyclic or closed algorithms of functioning, that include fixed number of alternative branches of process.

2. The approach provides obtaining of the minimal form of logic control commands and a minimal quantity of memory elements without execution of minimization procedures.

3. The approach guarantees the preservation of logic of process at any change of time of separate actions execution. It reduces complexity of developed circuit diagrams (there is no blocking or duplication), control algorithms, localizes search of errors, allows to build more effective (reliable) and economic (less elements) systems.

4. The proposed approach has shown an efficiency by working out of electro-pneumatic systems and control algorithms for PLC for parallel processes with (10…50) asynchronous elements and (20…100) transitions

REFERENCES

[1] Ebel F. and von Terzi M., [Festo Didactic. Mechatronics], Festo Didactic GmbH&Co., Denkendorf 73-770(2000).
[2] Schmid, D., [Mechatronika], REA, Warszawa, 35-73 (2002).
[3] Bliesener, R., Ebel, F. and, Loeffler, C., [Programmable Logic Controllers], Festo Didactic, 67-89(2002).
[4] ElMaraghy, H.A. and AlGeddawy, T., "Co-evolution of products and manufacturing capabilities and application in auto-parts assembly," Flexible Services and Manufacturing Journal., 24(2), 142–170(2012).
[5] Bauernhansl T., ten Hompel M. and Vogel-Heuser B., [Industrie 4.0 in Produktion, Automatisierung und Logistik: Anwendung • Technologien • Migration], Springer, Wiesbaden, 1-648(2014).
[6] Polishchuk, L.K., Kozlov, L.G. and Piontkevych, O.V., "Study of the dynamic stability of the conveyor belt adaptive drive," Proc. SPIE 10808, 108-116 (2018).
[7] Burennikov, Y., Kozlov, L., Pyliavets, V. and Piontkevych, O., "Mechatronic hydraulic drive with regulator, based on artificial neural network," IOP Conference Series: Materials Science and Engineering, 209(1), 012-071(2017).
[8] Peterson, J. L., [Petri net theory and the modeling of systems], Prentice Hall 135-186(1981).
[9] Chałajdży, W., Iakymchuk, M. and Gavva, A., "Strukturalna synteza sprzętu do pakowania zbiorczego", Opakowanie, 8(1), 65-70(2014).
[10] Gubarev, A., Yakhno, O. and Ganpantsurova, O., "Control algorithms in mechatronic systems with parallel processes," Solid State Phenomena, 164(1), 105-110(2010).
[11] Yakhno, O., Gubarev, A., and Ganpantsurova, O., "Flexible control for the discrete systems presented in the form of cyclic modules," International scientific conference "UNITECH'12", 2(1), 244-252(2012).
[12] Kozlov. L.G., Bogachuk, V.V., Bilichenko, V.V. and Tovkach, A.O., "Determining of the optimal parameters for a mechatronic hydraulic drive," Proc. SPIE 10808, 64-72(2018).
[13] Vedmitskyi, Y.G., Kukharchuk, V.V. and Hraniak, V.F., "New non-system physical quantities for vibration monitoring of transient processes at hydropower facilities, integral vibratory accelerations," Przeglad Elektrotechniczny, 93(3), 69-72(2017).
[14] Wojcik, W., "Application of fibre-optic flame monitoring systems to diagnostics of combustion process in power boilers, " Bulletin of the Polish Academy of Sciences- Technical Sciences, 56 (2), 177-195(2008).

[15] Wojcik, W., and Kisala, P., "The method for the recovery of the apodization function of the fiber Bragg gratings on the basis of its spectra," Przeglad Elektrotechniczny, 86(10), Pages: 127-130(2010).
[16] Wojcik, J., Wojcik, W., Janoszczyk, B., et al., "Optical fibre system for flame monitoring in energetic boilers," Proc. SPIE 3189 Pages: 74-82(1997).
[17] Azarov, O.D., Dudnyk, O.V., Kaduk, O.V., Smolarz, A. and Burlibay, A, "Method of correcting of the tracking ADC with weight redundancy conversion characteristic", Proc. SPIE 9816, 136-144(2015).
[18] Azarov, O.D., Murashchenko, O.G., Chernyak, O.I., Smolarz, A. and Kashaganova, G., "Method of glitch reduction in DAC with weight redundancy", Proc. SPIE 9816, 15-26, (2015).
[19] Osadchuk V.S. and Osadchuk A.V., "The magnetic reactive effect in transistors for construction transducers of magnetic field," Electronics and Electrical Engineering, 3(109), 119-122(2011).
[20] Pavlov, S.V., Kozhemiako, V.P. and Kolesnik, P.F, [Physical principles of biomedical optics: monograph], VNTU, Vinnytsya, 1-152(2010).
[21] Vassilenko, S., Valtchev, S., Teixeira, P. and Pavlov, S., "Energy harvesting: an interesting topic for education programs in engineering specialities," Internet, Education, Science (IES-2016), 149-156(2016).
[22] Vasilevskyi, O.M., Yakovlev, M.Y. and Kulakov, P.I., "Spectral method to evaluate the uncertainty of dynamic measurements," Technical Electrodynamics, 4(1), 72-78(2017).
[23] Kvyetnyy, R. N., Sofina, O.Y. and Lozun, A.V. "Modification of fractal coding algorithm by a combination of modern technologies and parallel computations", Proc. SPIE 9816, 98-1161(2015).
[24] Polishchuk, L.K., Kozlov, L.G., and Piontkevych,, O.V. "Study of the dynamic stability of the conveyor belt adaptive drive", Proc. SPIE 10808, 117-125(2018).
[25] Obertyukh, R.R., Slabkyi, A.V., Marushchak, M.V., Koval L.G. and Koval L.G., "Dynamic and mathematical models of the hydraulic-pulse device for deformation strengthening of materials", Proc. SPIE 10808, 84-92(2018).
[26] Ogorodnikov, V.A., Zyska, T., Sundetov, S,. "The physical model of motor vehicle destruction under shock loading for analysis of road traffic accident," Proc. SPIE 10808, 245-253(2018).
[27] Sawicki, D. and Kotyra, A., "Porównanie wybranych metod wyznaczania obszaru płomienia w wizyjnym systemie diagnostycznym, " Informatyka, Automatyka, Pomiary w Gospodarce i Ochronie Środowiska, 4:14-17(2013).
[28] Zyska, T., Wójcik, W., Imanbek, B. and Zhirnova, O., "Diagnostyka stanu czujnika termoelektrycznego w procesie zgazowania biomasy, " Rocznik Ochrona Środowiska, 18, 652–666(2016).

Comparison of high-level programming languages efficiency in embedded systems

Agnieszka Choroszucho, Piotr Golonko, Jakub Bednarek, Mateusz Sumorek, Jakub Żukowski
Bialystok University of Technology, Faculty of Electrical Engineering, Wiejska 45D,
15-351 Białystok, Poland

ABSTRACT

Conducting research, especially in technical field often binds with necessity of making device prototype or specialized tools. In such situations implementing solution using hardware microcontroller-based platform is best way to reach set goal. Choice of development platform and software environment decides about success of project or allows saving significant amount of time. In article have been tested 3 common development platforms based on different microcontrollers and two high-level programming languages, C/C++ and new solution based on Python. Chosen testing process is based on mathematical procedures used in control, analysis and automation. Results of research should allow to selection of optimal hardware platform as well programming language according to planned use and requested computing power.

Keywords: ESP32, Python, C/C++, MicroPython, STM32, ARM, AVR

1. INTRODUCTION

Conducting research often binds with necessity of implementing developed solutions on hardware platform based on modules with microcontroller units. In past years number of platforms was limited to 2-3 popular solutions with full technical documentation and big Internet community. Such platforms as AVR or PIC or even 8051 family nevertheless continuous development are unable to offer enough computing power and 8-bit architecture itself is barrier in case of usage fast memories and peripherals.

Lately microcontrollers market came with new solutions, which were enthusiastically accepted by engineers, forasmuch they are fully documented, supported by manufacturers as well as by Internet community. These solutions are microcontroller units based on 32-bit architecture with ARM [8] core. Main advantage is that, it is efficient computing unit equipped with massive memory (which is unavailable for 8-bit units) and wireless connectivity interfaces, such as LoRa, WiFi and BLE.

Having regard to the above facts appears a problem with platform selection. Older platforms, such as Arduino [7], based on 8-bit AVR microcontroller have well-established position on market, massive amount of documentation, many examples, libraries and large support from community. Programming environment is also stable and ready for professional solutions. From the other hand, 32-bit platforms are developmental, more efficient and technical documentation is more than acceptable. It is important to note that programming environments become more stable and functional.

Because of 8-bit architecture limitations solutions based on it, are gradually displaced by 32-bit solutions based on ARM [8] architecture. Due to that software written in Assembler becomes less significant in favor of high-level languages, such as C, C++ [2] or MicroPython [1, 4]. Although C and C++ is commonly used on 8-bit platforms while MicroPython is still not implemented.

In order to facilitate implementation of solutions based on microcontrollers in research has been presented analysis of hardware platforms efficiency using two programming languages: C/C++ and MicroPython. Choice of C/C++ language is obvious, while application of Python-based solution might raise doubts. Python [5] is interpreted language (fig. 4), while C/C++ is compiled (fig. 4), that might majorly decrease efficiency of used algorithm. It is important to note that Python has also a number of advantages: ease of learning, large libraries resources, no need for compiling. Python also allows implementing significant part of PC software solutions on microcontroller units.

Photonics Applications in Astronomy, Communications, Industry, and High-Energy Physics Experiments 2019,
edited by Ryszard S. Romaniuk, Maciej Linczuk, Proc. of SPIE Vol. 11176, 1117661
© 2019 SPIE · CCC code: 0277-786X/19/$21 · doi: 10.1117/12.2537143

2. TESTING PLATFORMS

In the age of popularizing embedded systems and its dynamic development, low-cost rapid prototyping platforms became very common. In tests have been used Arduino Uno (fig. 1) board equipped with Atmel's Atmega328p MCU (MicroController Unit), LOLIN D32 (fig. 2) fitted with Espressif's ESP32-WROVER module. Atmeag328p MCU is 8-bit microcontroller working with clock rated at 16 MHz. Second platform used in research is using Tensilica Xtensa LX6 [3] 32-bit processor rated at 240 MHz. Last platform used for tests is Discovery board (fig. 3) with STM32f407 [10] MCU with clock rated at 168MHz.

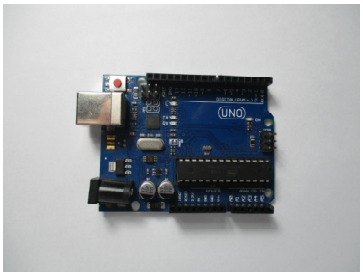

Figure 1. Arduino UNO board.

Efficiency of both tested languages has been conducted on hardware test platforms through measurement of time used for realization of given task. The considered test tasks are:

- calculation of pi number with accuracy of six numbers after the decimal point,
- calculation of 10 000 determinants random-generated 4x4 matrices,
- sorting 5 000 random generated numbers using bubble sorting algorithm.

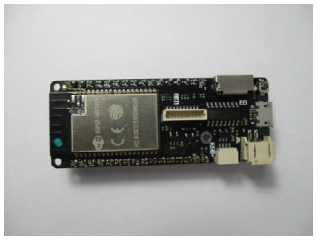

Figure 2. Lolin D32 board.

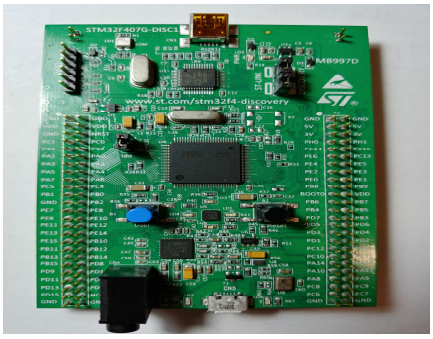

Figure 3. STM32 Discovery board.

Table 1. List of used platforms.

Board	MCU	RAM	Flash	Operating frequency	Architecture
Arduino UNO	Atmeag328p	2 KB	32 KB	16 MHz	8-bit
Lolin D32	ESP-32	320 KB	4 MB	240 MHz	32-bit
STM32F4 DISCOVERY	STM32f407	192 KB	1 MB	168MHz	32-bit

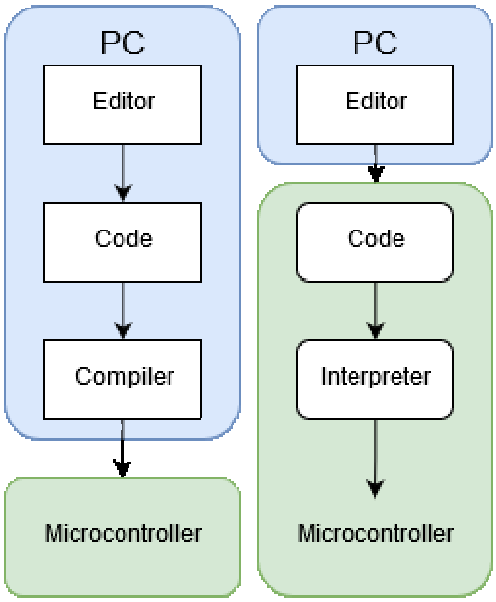

Figure 4. Graphic presentation of code implementation (left side – C, right side – Python).

3. ASSUMPTIONS

In order to determine π number Lebniz formula for π has been used (Equation 1), which isn't efficient for numerical methods due to its slowly rate of convergence [6]. This method requires significant amount of iterations to reach acceptable result of π number approximation. For this reason it's proper method for conducted research, where the main goal is to study how high-level languages behave when large number of operations is extorted.

$$\pi = 4 \cdot \sum_{n=1}^{\infty} \frac{(-1)^{n-1}}{2n-1} = 4 \cdot \left(1 - \frac{1}{3} + \frac{1}{5} - \frac{1}{7} + \frac{1}{9} - \ldots\right) \quad (1)$$

Another task in analysis was to determine determinants of 10 000 quasi randomly generated 4x4 matrices (Equation 2). Every single element in matrix took value in range of 0 to 4096. In this case for calculating determinants has been used Leibniz formula for determinants (Equation 3). Usually this formula isn't used when matrix dimensions are bigger than 3x3, that's because of large amount of calculations required for reaching result, number of calculations in the size of matrix function is non-linear.

$$\det|\mathbf{A}| = \det\begin{bmatrix} a_{11} & \cdots & a_{14} \\ \vdots & \ddots & \vdots \\ a_{41} & \cdots & a_{44} \end{bmatrix} \tag{2}$$

$$\det(A) = \sum_{\tau \in S_n} \operatorname{sgn}(\tau) \prod_{i=1}^{n} a_{i,\tau(i)} = \sum_{\sigma \in S_n} \operatorname{sgn}(\sigma) \prod_{i=1}^{n} a_{i(i),i} \tag{3}$$

Where: **A** – matrix with dimensions *n* by *n*, **det(A)** – matrix **A** determinant, a_{ij} – matrix element in i^{th} row and j^{th} column, sgn(σ) – sign function.

As last task used in research has been chosen bubble sorting algorithm [9], which is simple sorting algorithm. Its operation is based on comparing adjacent numbers and swapping them depending whether they in proper order or not. Because of its simple principle of operation it is inefficient way for sorting because, in worst case, computational complexity is $O(n^2)$ where *n* is number of elements to be sorted. Set of numbers used for this task is quasi random-generated.

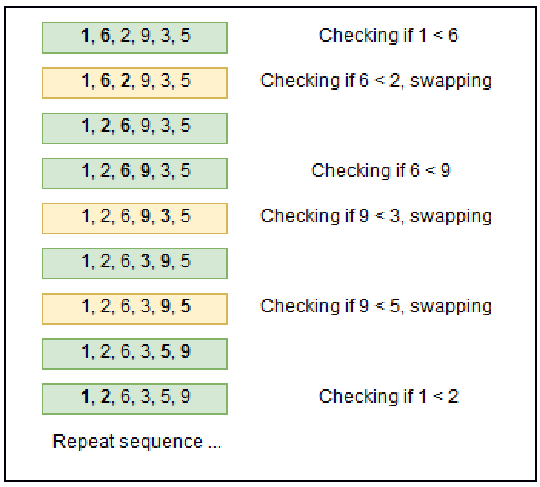

Figure 5. Graphic presentation of bubble sorting algorithm operation

4. USED ALGORITHMS

```
import urandom
import time
row = 0
column = 0
value = 0
m = [[0, 0, 0, 0], [0, 0, 0, 0], [0, 0, 0, 0], [0, 0, 0, 0]]
start = time.ticks_ms()
for matrix in range(10000):
  for i in range(16):
    value = urandom.getrandbits(12)
    if row==4:
        row=0
        column += 1
    if column==4: column = 0
    m[column][row] = value
    row += 1
    determinant = (
      m[0][3] * m[1][2] * m[2][1] * m[3][0] - m[0][2] * m[1][3] * m[2][1] * m[3][0] -
      m[0][3] * m[1][1] * m[2][2] * m[3][0] + m[0][1] * m[1][3] * m[2][2] * m[3][0] +
      m[0][2] * m[1][1] * m[2][3] * m[3][0] - m[0][1] * m[1][2] * m[2][3] * m[3][0] -
      m[0][3] * m[1][2] * m[2][0] * m[3][1] + m[0][2] * m[1][3] * m[2][0] * m[3][1] +
      m[0][3] * m[1][0] * m[2][2] * m[3][1] - m[0][0] * m[1][3] * m[2][2] * m[3][1] -
      m[0][2] * m[1][0] * m[2][3] * m[3][1] + m[0][0] * m[1][2] * m[2][3] * m[3][1] +
      m[0][3] * m[1][1] * m[2][0] * m[3][2] - m[0][1] * m[1][3] * m[2][0] * m[3][2] -
      m[0][3] * m[1][0] * m[2][1] * m[3][2] + m[0][0] * m[1][3] * m[2][1] * m[3][2] +
      m[0][1] * m[1][0] * m[2][3] * m[3][2] - m[0][0] * m[1][1] * m[2][3] * m[3][2] -
      m[0][2] * m[1][1] * m[2][0] * m[3][3] + m[0][1] * m[1][2] * m[2][0] * m[3][3] +
      m[0][2] * m[1][0] * m[2][1] * m[3][3] - m[0][0] * m[1][2] * m[2][1] * m[3][3] -
      m[0][1] * m[1][0] * m[2][2] * m[3][3] + m[0][0] * m[1][1] * m[2][2] * m[3][3])
end = time.ticks_ms()
print(end - start)
print(determinant)
```

Figure 6. MicroPython algorithm calculating matrices determinants.

```
while (count < 1):
  start = time.ticks_ms()
  a=0

  for i in range (250000):
    a += ((-1)**i)/(2*i+1)

  end = ticks_ms()
  print(end-start)
  print(4*a)
  count = 1
```

Figure 7. MicroPython algorithm calculating pi number.

```
import urandom
import time

data = [0 for x in range(5000)]
start = time.ticks_ms()

def sort(data):
    for i in range(len(data) - 1, 0, -1):
        for j in range(i):
            if data[j] > data[j + 1]:
                data[j], data[j + 1] = data[j + 1], data[j]

for size in range(5000):
    value = urandom.getrandbits(12)
    data[size] = value
sort(data)

end = time.ticks_ms()
print(end-start)
```

Figure 8. MicroPython algorithm sorting random-generated number array.

```
int m[4][4] = {
              {0,0,0,0},
              {0,0,0,0},
              {0,0,0,0},
              {0,0,0,0}
              };
Serial.println(millis());
for(unsigned long start = 0; start<10000;start++)
{

  for(uint8_t i =0; i<16; ++i)
    {
      value = random(0,4096);
      if(row == 4)
      {
        row=0;
        column++;
      }
      if(column==4) column=0;
      m[column][row] = value;
      row++;
      cnt++;
      determinant = (
       m[0][3] * m[1][2] * m[2][1] * m[3][0] - m[0][2] * m[1][3] * m[2][1] * m[3][0] -
       m[0][3] * m[1][1] * m[2][2] * m[3][0] + m[0][1] * m[1][3] * m[2][2] * m[3][0] +
       m[0][2] * m[1][1] * m[2][3] * m[3][0] - m[0][1] * m[1][2] * m[2][3] * m[3][0] -
       m[0][3] * m[1][2] * m[2][0] * m[3][1] + m[0][2] * m[1][3] * m[2][0] * m[3][1] +
       m[0][3] * m[1][0] * m[2][2] * m[3][1] - m[0][0] * m[1][3] * m[2][2] * m[3][1] -
       m[0][2] * m[1][0] * m[2][3] * m[3][1] + m[0][0] * m[1][2] * m[2][3] * m[3][1] +
       m[0][3] * m[1][1] * m[2][0] * m[3][2] - m[0][1] * m[1][3] * m[2][0] * m[3][2] -
       m[0][3] * m[1][0] * m[2][1] * m[3][2] + m[0][0] * m[1][3] * m[2][1] * m[3][2] +
       m[0][1] * m[1][0] * m[2][3] * m[3][2] - m[0][0] * m[1][1] * m[2][3] * m[3][2] -
       m[0][2] * m[1][1] * m[2][0] * m[3][3] + m[0][1] * m[1][2] * m[2][0] * m[3][3] +
       m[0][2] * m[1][0] * m[2][1] * m[3][3] - m[0][0] * m[1][2] * m[2][1] * m[3][3] -
       m[0][1] * m[1][0] * m[2][2] * m[3][3] + m[0][0] * m[1][1] * m[2][2] * m[3][3]);
    }
}
  Serial.println(millis());
  Serial.println(determinant);
```

Figure 9. C algorithm calculating matrices determinants.

```
Serial.println(millis());
float pi_value = 4;
int flag = 0;
unsigned long cnt;
for(unsigned long i=3; i<500000; i+=2){
  cnt++;
  if(flag){
    pi_value = pi_value + (4.0/i);
  }
  else{
    pi_value = pi_value - (4.0/i);
  }
 flag= !flag;
}
Serial.println(millis());
Serial.println(pi_value, 6);
```

Figure 10. C algorithm calculating pi number.

```
int a[5000];
uint16_t t;
uint16_t value;

void setup() {
    Serial.begin(9600);
    Serial.println(millis());

    for(unsigned long start = 0; start<5001; start++) {
    value = random(4096);
    a[start] = value;
    }

for (uint16_t j =0 ; j < 5001; j++){
        for (uint16_t i = 0; i < 5001 - 1; i++) {
                if (a[i] > a[i + 1]){
                        t = a[i];
                        a[i] = a[i + 1];
                        a[i + 1] = t;
                }
        }
  }
Serial.println(millis());
}
```

Figure 11. C algorithm sorting random-generated number array.

5. TEST RESULTS

Basing on obtained test results it can be said that MicroPython is not proper choice when implemented algorithm requires intense calculations. We can notice that C is incomparably faster in most tasks, especially when MCU is forced to do many jumps in executed algorithm. In order to avoid inaccuracy of measurements caused by time of generating random numbers and matrices additional tests has been conducted. In all cases time was short enough to omit its influence.

Table 2. Arduino UNO results.

Arduino UNO		
Language	**C**	**MircoPython**
Clock rate [MHz]	16	
Time of calculation π [ms]	10 776	Not involved
Time of determinants calculation [ms]	14 760	Not involved
Time of sorting [ms]	Unable to complete task, lack of memory	Not involved

Table 3.LOLIN D32 results.

LOLIN D32		
Language	**C**	**MircoPython**
Clock rate [MHz]	240	
Time of calculation π [ms]	827	5895
Time of determinants calculation [ms]	182	129 682
Time of sorting [ms]	1588	97 484

Table 4. STM32 Discovery results.

STM32 Discovery		
Language	**C**	**MircoPython**
Clock rate [MHz]	168	
Time of calculation π [ms]	9	7872
Time of determinants calculation [ms]	56	184 309
Time of sorting [ms]	2580	150 086

6. SUMMARY

In article has been shown results of efficiency high-level programming languages with use of various testing platforms. Main goal of used algorithms was to test how examined programming languages handle with tasks requiring significant amount of computing power. Research will be continued with usage of other development platforms and libraries specialized in specific tasks.

This work was prepared under scientific work S/WE/2/18 and supported by the Polish Ministry of Science and Higher Education.

REFERENCES

[1] Tollervey N. H., Programming with MicroPython: Embedded Programming with Microcontrollers and Python, O'Reilly Media (2017).
[2] Oualline S., Practical C programming, O'Reilly Media (1997).
[3] Espressif Systems. espressif.com [Online]. Access, (11th April 2019): https://espressif.com/sites/default/files/documentation/esp32_technical_reference_manual_en.pdf.
[4] Norris D., Python for Microcontrollers: Getting Started with MicroPython,McGraw-Hill Education TAB (2017).
[5] Martelli A., Ascher D., Martelli Ravenscroft A., Python Cookbook, Third edition, O'Reilly Media, (2013).
[6] Borwein J.M., Borwein P.B., Bailey D.H., "The American Mathematical Monthly", 96(3), 201-219, Mathematical Association of America, (Mar., 1989).
[7] Syed Omar Faruk Towaha, Learning C for Arduino, Packt Publishing (2017).
[8] Yiu J., The Definitive Guide to the ARM Cortex-M0, Newnes 2011.
[9] Thomas H. Cormen, Charles E. Leiserson, Ronald L. Rivest, Clifford Stein, Introduction to Algorithms, The MIT Press (1989).
[10] STMicroelectronics. st.com [Online]. Access: https://www.st.com/resource/en/reference_manual/dm00031020.pdf (14th April 2019).

Selection of the calculus system base for ADC and DAC with weight redundancy

Alexey D. Azarov*[a], Svitlana A. Kyrylashchyk[a], Sergey V. Bogomolov[a], Oleksiy Y. Stakhov[a], Andrzej Kotyra[b], Orken Mamyrbaev[c]
Vinnytsia National Technical University, 95 Khmelnytske shose, Vinnytsia, Ukraine 21021; [b]Lublin University of Technology, Nadbystrzycka 38a, 20-618 Lublin, Poland; [c]Institute Information and Computational Technologies CS MES RK, 1/1 Abylai Khan St., Kaskelen, Almaty, Kazakhstan 040900

ABSTRACT

It is well known that the application of the weight redundancy in self-calibrating DAC enables to lower considerably, the requirements regarding the accuracy of digits weight formation, particularly in multidigit code-current converters and the idea of laser adjustment of the resistor matrices nominals. It is also known, that the construction of ADC of the bit-wise balancing on the base of such DAC additionally enables to increase (by an order or more) the operation speed as a result of a considerable reduction of the balancing cycle duration.

Keywords: analog to digital converter, circuit of the resistive matrices, weight redundancy

1. INTRODUCTION

It should be noted that the improvement of the above-mentioned characteristics greatly depends on the level of weight redundancy of the calculus, used in these information converters. In analog-digital converters (ADC) it is expedient to spent the smaller part of this redundancy to lower the requirements, concerning the manufacturing technology of digital to analog converters (DAC), in particular, for the correction of the statistical errors and greater part– for the compensation of the dynamic errors of the I and II kinds to increase the operation speed[1-2]. It is worth mentioning that the selection of the calculus is the key issue. For convenience adaptability to manufacture of ADC and DAC, the system must be positional to provide the regularity of the structure[4]. Besides, it is necessary that the base of the calculus α(relation of the weights of the neighboring bits)

$$\alpha = \frac{Q_i}{Q_{i-1}},$$

(where $Q_i=\alpha^i \cdot Q_0$ – weight of the i-th bit, $Q_0 = 1$ – weight of the lower zero bit) was a constant number. This will give the possibility to have constant ratio between the weights of bits, especially discharge currents or voltages, in its turn, this will provide the regularity of the circuits of the resistive or capacitor arrays of DAC. Another requirement for DAC construction is minimization of the number of nominals of the discharge resistors or capacitors, depending on the method of the realization[5]. The above-method requires complex approach to the solution of the calculus or calculation of the calculus base[6,7]. In spite of the fact, that there exists scientific-engineering literature on this subject, the problem of the system selection of the calculus and calculation of the calculus base was not considered separately. In this connection the subject of the paper dealing with the problem of the selection of calculus system base for ADC and DAC with the weight redundancy is relevant.

The aim of the research is systematization of the calculus system selection and its base calculation for high performance ADC and DAC with weight redundancy. The task of the research are as follows:

- Propose the set of the characteristic polynomials of the k^{th} degree, solutions of which would enable to obtain the necessary value of α;
- systematization of the set of the α values obtained according to the level of the set weight redundancy;

*azarov2@vntu.edu.ua

Photonics Applications in Astronomy, Communications, Industry, and High-Energy Physics Experiments 2019, edited by Ryszard S. Romaniuk, Maciej Linczuk, Proc. of SPIE Vol. 11176, 1117662
© 2019 SPIE · CCC code: 0277-786X/19/$21 · doi: 10.1117/12.2537197

- assessing the level of the redundancy, depending on the value of the calculus system base α;
- providing the examples of ADC and DAC with weight redundancy construction.

2. THE METHOD

In the positional calculus system, the real number is accurately presented[1] in the form

$$D = \sum_{i=-\infty}^{n-1} a_i \cdot \alpha^i , \tag{1}$$

where α_i – bit coefficients, $a_i \in \{0,1\};\{\overline{1},1\};\{\overline{1},0,1\}$ – binary number in the i^{th} bit (bit coefficient); α – basic calculus system, i – the number of bit. In the systems with natural base (the set of bit weights) α is a constant number unlike the artificial base, where the value ofα can vary from bit to bit[8].

As such form of the presentation requires the usage of the infinitely long bit grid, for ADC and DAC it is not real. It is expedient to pass from the real numbers to natural numbers. It was shown[9] that if a is a fractional irrational number, for instance, golden p-proportion, then any natural number is presented in the form:

$$N = \sum_{i=-n}^{n-1} a_i \cdot \alpha_p^i \tag{3}$$

where $a_p^i = a_p^{i-1} + a_p^{i-p-1}$ denotes i^{th} degree of the golden p-proportion. It should be noted that in such calculus system each successive term of series (weight of i^{th} bit) equals the sum of the weights of the neighboring bit and the bit located in p. Such recurrent connection allows to obtain minimize in DAC the values of the nominal of elements (resistors or capacitors) which set the discharge currents or voltages by means of their parallel or serial connection, that is convenient in the process of microelectronic realization[10,4]. The value of golden p-proportion[11,12,16] is calculated as the real positive root of the polynomial

$$x^{p+1} - x^p - 1 = 0 \tag{3}$$

We will consider the form of the polynomial for certain specific p and calculate the corresponding α, in the form of real positive roots, i.e. $\alpha > 0$ (calculations are carried out in Mathcad 15). The values of α_p for the calculus system of the golden p-proportion are presented in the Table 1.

Table 1. Values of α_p for calculus system of the golden p-proportion.

p	0	1	2	3	4	5	6	…	∞
α_p	2	1.618	1.466	1.380	1.324	1.285	1.256	…	1

Apart from "golden" p-proportions, "golden" s-sections are also redundant. In golden s-proportions every i^{th} member is the sum of the antecedents $i-1$, $i-2$,…, $i-s$. In golden s-proportions real positive values of α_s are calculated as the root of the following polynomial:

$$x^{s+1} - \sum_{0}^{s} x^i = 0. \tag{4}$$

The values of α_s are shown in the Table 2.

Table 2. Values of α_s for NS of the golden s-section.

s	1	2	3	4	5	6	…	∞
α_s	1.618	1.839	1.928	1.966	1.984	1.992	…	2

It should be noted that the values of the golden s-proportions is the continuation of the numerical series from 1.618 to 2.00[17]. At the same time, besides the golden p-proportions and s-proportions additionally golden s-p-proportions can be used. In such proportions s is the number of neighboring weight bits after $(i-1)^{th}, (s = 2,3,4,...,n)$; p – is the distance

between the group of s bits and high of low order bits. In golden s-p-proportions real positive values of α_s are calculated from the following polynomial:

$$\sum_{p+1}^{s+p+1} x^i - 1 = 0. \tag{5}$$

The values of $\alpha_{s\text{-}p}$ are presented in Table 3.

Table 3. Values of $\alpha_{s\text{-}p}$ for the calculus system of the golden s-p-proportion for $s = 2$ and $s = 3$.

p	0	1	2	3	4	5	6	…	∞
$s = 2$									
$\alpha_{s\text{-}p}$	1.8393	1.7549	1.7049	1.6737	1.6536	1.6407	1.6324	…	1
$s = 3$									
$\alpha_{s\text{-}p}$	1.9276	1.88852	1.8668	1.85455	1.84772	1.84392	1.84182	…	1

It should be noted, that these calculus systems have natural redundancy and meet the requirements:

$$\alpha^i < \sum_{0}^{i-1} \alpha^j \tag{6}$$

For the i^{th} bit the absolute WR is set by the expression:

$$\Delta\tilde{Q}_i = \sum_{j=0}^{i-1} Q_j - Q_i. \tag{7}$$

Relative WR is considered as the ratio of the absolute WRt o the sum of the all bit weights from 0^{th} to i^{th} and is evaluated from the expression:

$$\delta Q_i^* = \frac{\sum_{j=0}^{i-1} \alpha^j - \alpha^i}{\sum_{j=0}^{i} \alpha^j}. \tag{8}$$

For its simplification the following transformations can be made:

$$\sum_{j=0}^{i-1} \alpha^j = \alpha^{i-1} \cdot \frac{1-\left(\frac{1}{\alpha}\right)^i}{1-\frac{1}{\alpha}} = \alpha^{i-1} \cdot \frac{\alpha^i - 1}{\alpha^i} \cdot \frac{\alpha}{\alpha - 1} = \frac{\alpha^i - 1}{\alpha - 1}.$$

Thus,

$$\delta Q_i^* = \frac{\frac{\alpha^i - 1}{\alpha - 1} - \alpha^i}{\frac{\alpha^{i+1} - 1}{\alpha - 1}} = \frac{\alpha^i - 1 - \alpha^{i+1} + \alpha^i}{\alpha - 1} \cdot \frac{\alpha - 1}{\alpha^{i+1} - 1} = \frac{2\alpha^i - \alpha^{i+1} - 1}{\alpha^{i+1} - 1}.$$

As α = const, it can be assumed that:

$$\delta Q_i^* = \frac{2 - \alpha}{\alpha} \tag{9}$$

Such value of WR should be taken for the assessment of the possibility of the static error correction in the process of self-calibration. Relative WR reduced to the i^{th} bit is calculated in the form:

$$\delta Q_i{}^{**} = \frac{\sum_{j=0}^{i-1}\alpha^j - \alpha^i}{\alpha^i} = \sum_{j=0}^{i-1}\alpha^{j-i} - 1 = \alpha^{-1}\cdot\frac{1-\left(\frac{1}{\alpha}\right)^i}{1-\frac{1}{\alpha}} - 1 = \frac{\alpha^i - 1}{\alpha^i(\alpha-1)} - 1 = \frac{1}{\alpha-1} - \frac{\alpha^{-i}}{\alpha-1} - 1.$$

For the separate *p*, within the frame of the "golden" *p*-proportions, the relative WR corresponds to the values as shown in Table 4 and for the separate *s* in Table 5, respectively.

Table 4. Value of the weight redundancy for CS of golden *p*-proportions.

p	0	1	2	3	4	5	6	..	∞
α_p	2	1.618	1.466	1.380	1.324	1.285	1.256	..	1
δQ_s* (%)	0	23.61	36.43	44.93	51.06	55.64	59.24	..	1
δQ_s** (%)	0	61.81	114.59	163.16	208.64	250.88	290.62	..	∞

Table 5. Values of the weight redundancy for the calculus system of golden *s*-proportions.

s	1	2	3	4	5	6	..	∞
α_s	1.618	1.839	1.928	1.966	1.984	1.992	..	2
δQ_p* (%)	23.61	8.75	3.73	1.73	0.81	0.4	..	0
δQ_p** (%)	61.81	19.19	7.76	3.52	1.63	0.8	..	0

With the increase of *i*, the last term rapidly changes, that is why, we may assume

$$\delta Q_i{}^{**} = \frac{1}{\alpha-1} - 1 = \frac{2-\alpha}{\alpha-1}. \tag{10}$$

This index characterizes the level of WR. It is used for the calculation of the dynamic characteristics in the process of the accelerated bit-wise analog-to-digital conversion[13]. Solving the inverse problem we will find the value of the calculus system base α for the target δQ_i* and δQ_i**:

$$\alpha = \frac{2}{\delta Q_i{}^* + 1}, \tag{11}$$

$$\alpha = \frac{2 + \delta Q_i{}^{**}}{1 + \delta Q_i{}^{**}}. \tag{12}$$

For “golden” s-proportions, if *s*=2 and 3 we have (table 6)

Table 6.Value of weight redundancy for the calculus system of golden *s-p* proportions.

P	0	1	2	3	4	5	6	…	∞
s = 2									
$\alpha_{s\text{-}p}$	1.8393	1.7549	1.7049	1.6737	1.6536	1.6407	1.6324	…	1
δQ_l* (%)	8.74	13.97	17.31	19.5	20.95	21.9	22.52	…	∞
δQ_l** (%)	19.15	32.47	41.86	48.43	53	56.08	58.13	…	∞
s = 3									
$\alpha_{s\text{-}p}$	1.928	1.8885	1.8668	1.85455	1.84772	1.84392	1.8418	…	1
δQ_l* (%)	3.76	5.9	7.14	7.84	8.24	8.46	8.59	…	∞
δQ_l** (%)	7.81	12.55	15.37	17.02	17.96	18.49	18.79	…	∞

3. PRACTICAL REALIZATION

Weight redundancy gives the possibility to eliminate gaps in the characteristic of transformations. Application of the calculus system(CS) with WR can be demonstrated on the example of the resistive matrices, which are the part of DAC[3].The output signal of this code-current converter (CCC) is set by the input code:

$$I_{out} = I \cdot \sum_{i=0}^{n-1} a_i \cdot \alpha^{i-(n-1)} \tag{13}$$

where α_i – bit coefficients K*inp*; $I = U_{res} / R$ – current of the high $(n-1)^{th}$ bit, which is for the circuit (Fig. 1b) U_{res} and $\frac{\alpha}{\alpha - 1} \cdot R$. Fig. 1a shows the diagram of *n*-bit code-current converter (CCC) on the base of the resistive matrix of ladder type in the inverse switching with α =1,839 for *s* = 2.

$$\frac{\alpha}{\alpha - 1} R = 2{,}192R\,;\ (\alpha - 1)R = 0{,}839R\,;\ \alpha R = 1{,}839R$$

where *R* – basic nominal of the matrix; $\alpha_i \in \{0,1\}$- bit coefficients.

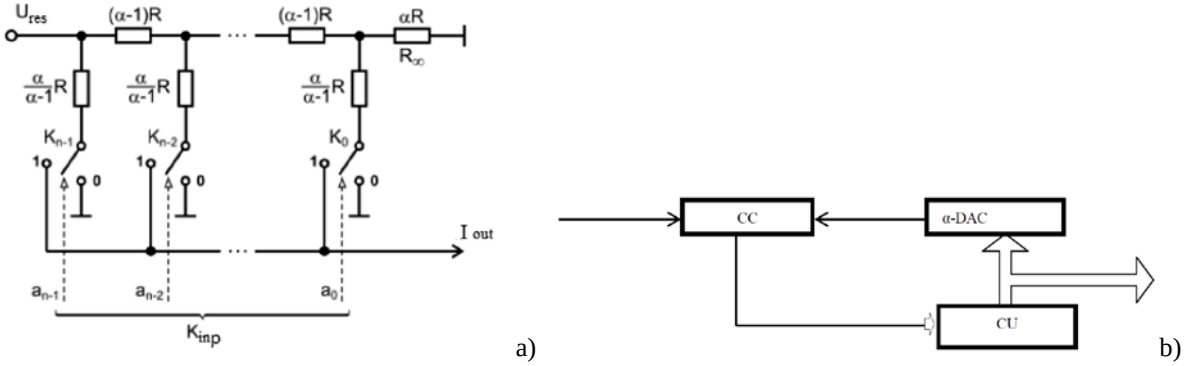

Figure 1. a) code-current converter on the base of the resistive matrix with the inverse switching; b) generalized structural diagram of ADC.

Table 6. Codes of the initial sequence of numbers for golden *s*-proportion for α=1,839, *s*=2.

bit order		6	5	4	3	2	1	0	-1	-2	-3	-4	-5	-6
Weights of bits		α^6	α^5	α^4	α^3	α^2	α^1	α^0	α^{-1}	α^{-2}	α^{-3}	α^{-4}	α^{-5}	α^{-6}
Digital equivalent	0	0	0	0	0	0	0	0	0	0	0	0	0	0
	1	0	0	0	0	0	0	1	0	0	0	0	0	0
		0	0	0	0	0	0	0	1	1	1	0	0	0
	2	0	0	0	0	0	0	1	1	1	1	0	0	0
		0	0	0	0	0	1	0	0	0	1	0	0	0
	3	0	0	0	0	0	1	1	0	0	1	0	0	0
		0	0	0	0	0	1	1	0	0	0	1	1	1
		0	0	0	0	0	1	0	1	1	1	1	1	1
	4	0	0	0	0	0	1	1	1	1	1	1	1	1

The diagram (Fig. 1a) contains the resistive matrix with the nominals $(\alpha - 1)R$, $\alpha R/(\alpha - 1)$ and αR, and the source of the reference voltage U_{res} and key elements $K_{n-1} - K_{n-1}$. During the serial supply of K_{inp} such correspondence of the conversion $K_{inp} \rightarrow A_{out}$ (I_{inp}) is formed. ADC contains the comparison circuit (CC) of the analog signals; α-DAC- digital analog converter on the base of CS with WR; CU – control unit.

In the process of the analog – digital conversion the input analog signal is sent to the first input of α-DAC. After the instruction of CU, α-DAC generates the compensation signal, that enters the second input of CC and balances A_{inp}. In the process of the conversion code K_{out} is formed at the conversion output, which is a digital equivalent of the input signal A_{inp} in the form[18,19]:

$$K_{out} = \alpha_{n-1}, \alpha_{n-2}, ..., \alpha_1, \alpha_0,$$

where $\alpha_i \in \{0,1\}$ digit coefficients of the code, formed at the input of α-DAC[14,20]. Operations of convolution and scanning can be performed over the bits of codes digits in the given system. Convolution is the replacement of zero in the i^{th} and ones in $(i - 1)^{th}$, $(i - 2)^{th}$ and $(i - 3)^{th}$ bits by their inversions. Scanning is an operation, inverse to convolution[15]. Presentation of the initial section of the natural numbers in golden calculus system is convenient to perform by means of convolution and scanning operations in the form as in Table 7[21,22].

4. CONCLUSIONS

The set of the characteristic polynomials of the k^{th} degree is suggested, their solution enables to obtain the value of α which is the base of CS, which correspond to the redundant "golden" *p*-proportion, *s*-proportions and *s-p* proportions. The set of the obtained values of α_p, α_s and α_{s-p} is systematized according to the level of the set weight redundancy if: $1 \le \alpha \le 2$. The level of the redundancy, depending on the value of the calculus system base α is determined. The examples of the construction of the code-current converter with weight redundancy of α=1,839 for s=2 on the base of the resistive matrix in the inverse switching and analog-digital converter, containing DAC with weight redundancy (WR) are given.

REFERENCES

[1] Azarov, O. D., [Fundamentals of the theory of analog-digital conversion on the base of redundant positional numerical system], Universum, Vinnytsia, 50-135 (2004).

[2] Azarov, O. D., [Analog-digital bit-wise conversion on the base of the redundant numerical system with weight redundancy], VNTU, Vinnitsia, 158-189 (2010).

[3] Azarov, O. D. (ed.), [Analog-digital self-calibration systems for measurements and processing of low-frequency signals], Universum, Vinnytsia, 53-160 (2003).

[4] Azarov, A. D., Chernyak, A. I. and Chernyak, P. A., "The class of numerical systems for pipeline bit sequential development of multiple optoelectronic data streams", Proceedings of SPIE 4425, 406-409 (2001).

[5] Stakhov, A. P., "The Generalized Principle of the Golden Section and its applications in mathematics, science, and engineering", Chaos, Solitons& Fractals, 26(2), 263-289 (2005).

[6] Stakhov, A. P., "The “golden” matrices and a new kind of cryptography", 2(3), 1138-1146 (2007).

[7] Stakhov A. P., [Fibonacci microprocessors as one of the basic innovations of the future technological pattern, changing the level of information security of the systems], Academy of Trinitarism, Moscow, 2011.

[8] Azarov, O. D., Pavlov, S. V. Chernyak, O. I., Ivasyuk, I. D., Wójcik, W., Syzdykpayeva, A., "Principles of fast count in modified Fibonacci numerical system", Proc. SPIE 10808, 1080829 (2018).

[9] Stakhov, A. P., [Golden section codes], Radio and Communication, Moscow, 15-152 (1984).

[10] Stakhov, A. P., "The golden section in the measurement theory", Computers & Mathematics with Applications, 17(4-6), 613-638 (1989).

[11] Bergum, G. E., Philippou, A. N. and Horadam A. F. (eds), [Applications of Fibonacci Numbers], Springer, Dordrecht, 393-399 (1998).

[12] Azarov, A., Zakharchenko, S., Arkhipchuk, A., "New method of reduction of a methodical error of self-calibration for ADC on the basis of redundant positional number systems", Proceedings of SPIE 4425, 22-26 (2001).

[13] Azarov, O. D., Chernyak, O. I. and Muraschenko, O. G., "Information aspects of count in the modified Fibonacci numerical system", Information Technologies and Computer Engineering 1 (38), 48-52 (2017).
[14] Azarov O. D., Chernyak, O. I. and Muraschenko, O. G., "Methods of the transfer and borrowing in fast acting Fibonacci counters", Information Technologies and computer engineering 2(42), p. 55-63 (2018).
[15] Zegarmistrz, P. and Galias, Z., "Application and comparison of metaheuristic and optimization algorithms for reconstruction of conductances in resistive grids", IAPGOŚ 2(3), 19-24 (2012).
[16] Osadchuk, V. S. and Osadchuk, A.V., "The Microelectronic Radiomeasuring Transducers of Magnetic Field with a Frequency Output", Electronics and Electrical Engineering 4(110), 67-70 (2011).
[17] Osadchuk, V.S. and Osadchuk A.V., "The microelectronic transducers of pressure with the frequency", Electronics and Electrical Engineering", Technologija 5(121), 105-108 (2012).
[18] Osadchuk A.V. and Osadchuk I.A., "Frequency transducer of the pressure on the basis of reactive properties of transistor structure with negative resistance", Proceedings of the International Siberian Conference on Control and Communications (SIBCON), 46-52 (2015).
[19] Wojcik, W. Komada, P. Cieszczyk, S. et al., "ECTL application for carbon monoxide measurements", Proceedings of SPIE 5958, 595837 (2005).
[20] Zabolotna, N. I.; Wójcik, W.; Pavlov, S. V. et al., "Diagnostics of pathologically changed birefringent networks by means of phase Mueller matrix tomography", Proceedings of SPIE 8698, 86980E (2013).
[21] Chepurna, O., Shton, I., Kholin, V. et al., "Photodynamic therapy with laser scanning mode of tumor", Proceedings of SPIE 9816, 98161F (2015).

Correlation method for calculation of weight coefficients of artificial neural-like networking hydraulic units' diagnostic systems

Valerii F. Hraniak*[a], Vasyl V. Kukharchuk [a], Victor V. Bilichenko [a], Volodymyr V. Bogachuk [a], Samoil Sh. Katsyv [a], Serhii V. Tsymbal[a], Waldemar Wójcik[b], Mashat Kalimoldayev[c]
[a]Vinnytsia National Technical University, Vinnytsia, Ukraina; [b]Lublin University of Technology, Lublin, Poland; [c]Institute Information and Computational Technologies CS MES RK, Almaty, Kazakhstan;

ABSTRACT

The paper proposes a new method for calculating the weight coefficients of an artificial neural network in the systems of technical diagnostics of hydro aggregates, in which it is proposed to use the coefficients of correlation between vibration signals in spatially distributed points of a hydro aggregate. A mathematical model and algorithm for calculation of weight coefficients of an artificial neural network are developed. The expediency of use of wavelet transformation of time realizations of a vibration signal is shown, as a result of which the received vibration signal is divided into amplitude-frequency-time spectrum, which leads to increase its informativeness. Experimentally confirmed the presence of strong inter-correlation links between spatially distributed points of the hydro aggregate and their dependence on the nature and place of application of disturbing forces. The dependence of the correlation coefficients on the load of the hydro aggregate and the water pressure in the reservoir is established. The obtained results can be considered as an experimental confirmation of the expediency of using the proposed method for calculating the weight coefficients of an artificial neural network.

Keywords: artificial neural network, amplitude-frequency-time spectrum, frequency band, vibration factor, probability index, correlation coefficient, weight coefficient

1. INTRODUCTION

The system of automatic diagnostics and forecasting of hydraulic units' defects development (SADF-HUDD)[1] is based on a modified frequency technology of vibration diagnostics, being hardware and software complex composed of vibration measurement channels, a sub-system for routine monitoring of vibration and a sub-system for diagnostics and forecasting. Commercial operation of vibration measurement channels and sub-system for routine monitoring commenced at Nyzhnyodnistrovs'ka HPP (Ukraine), with the test operation of diagnostics and forecasting sub-system being commenced in a stage-by-stage manner[2-9]. The diagnostic sub-system is based on a three-layer artificial neural-like network (ANLN). Each vibroacoustic signal received from the routine monitoring sub-system by way of discrete wavelet transformation (DWT) is decomposed in the amplitude-frequency-time spectrum (AFTS). Further on, all AFTS arrive at the entry point of ANLN[10-11]. The mathematical model of ANLN is shown in detail in[1-2],that is why we will turn our attention to the results of its operation – by determining the probability of the fact that certain vibration factor may cause excessive vibration displacement.

The informative probability indicator of $PV_{k\tau}$ factor that corresponds to k^{th} neuron, as of the time point τ ,is determined as follows:

$$\forall k = 1,6 \forall i = 1,4 \forall j \in \Psi_k \left(PV_{k\tau} = \sum_{i,j} w_{kij} d_{kij\tau}^{norm} \right), \quad (1)$$

where w_{kij} – weight coefficients that define the significance of accounting for wavelet coefficients of AFTS's j^{th} frequency band of the i^{th} vibration signal at the probability level of the k^{th} neuron; $d_{kij\tau}^{norm}$ – standardized values of wavelet coefficients of AFTS's j^{th} frequency band of the i^{th} vibration signal at the probability level of the k^{th} neuron as of the time point τ ; Ψ_k – the multitude of frequency bands' numbers, where the influence of vibration factor exists, which

*titanxp2000@ukr.net

Photonics Applications in Astronomy, Communications, Industry, and High-Energy Physics Experiments 2019, edited by Ryszard S. Romaniuk, Maciej Linczuk, Proc. of SPIE Vol. 11176, 1117663
© 2019 SPIE · CCC code: 0277-786X/19/$21 · doi: 10.1117/12.2537215

corresponds to the k^{th}neuron[12,13].

The task of this research paper lies in development of the correlation method for determination of weight coefficients w_{kij} as the coefficients of cross-correlation; it presents the analysis of their dependence on the hydraulic generator's load and water pressure head in water reservoir.

2. THEORETICAL RESEARCH RESULTS AND ANALYSIS THEREOF

The mathematical model for determination of cross-correlation coefficients is shown in detail in[3-6]. Let us recall its main provisions.

The hydraulic unit is shown as a relatively stationary distributed quasi-linearized inseparable elastic system with space-variant stiffness coefficients[7]. Another specificity of a controlled unit (CU) lies in its exposure to k spatially distributed uncompensated forces of different physical nature, amplitude and vector direction that vary randomly with time function. Generalized structure of such CU may be shown as follows (fig. 1).

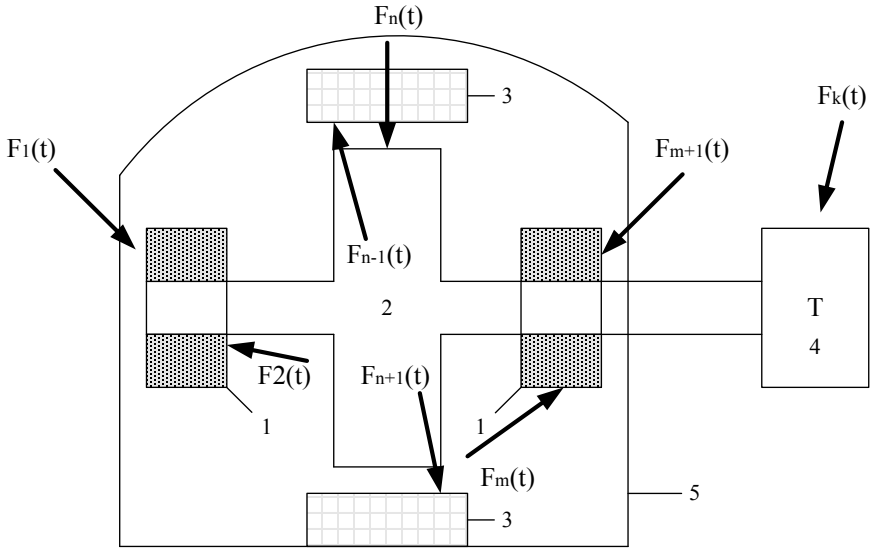

Fig. 1 Generalized structural diagram of hydraulic unit (1 – bearings; 2 – rotor; 3 – stator; 4 – turbine; 5 – housing)

In view of such system's inseparability, any of k external uncompensated disturbing forces will evoke in the system's randomly chosen point (assembly) the occurrence of k^{th} component of vibration signal (response), the amplitude of which will be different than zero. This being the case, in view of the system's quasi-linearity, the vector-similar force, the resultant of which is applied to one and the same point of electrical machine with time delay Δt will cause the occurrence of the system's identical response with the same time delay in any randomly selected unit assembly. Hence, for a randomly selected controlled assembly in relation to each of k possible disturbing forces, one can obtain a link function. For a randomly selected assembly A being a part of CU, the following equation system will be true:

$$\begin{cases} \psi_{A1}(t) = F_1(t) \cdot H_{A1}(t), \\ \psi_{A2}(t) = F_2(t) \cdot H_{A2}(t), \\ \ldots\ldots\ldots\ldots\ldots\ldots\ldots\ldots \\ \psi_{Ak}(t) = F_k(t) \cdot H_{Ak}(t), \end{cases} \tag{2}$$

where $F_1(t) - F_k(t)$ – uncompensated force affecting an electrical machine; $H_{A1}(t) - H_{Ak}(t)$ – link functions in relation to disturbing forces $F_1(t) - F_k(t)$, respectively; $\psi_{A1}(t) - \psi_{Ak}(t)$ – system's response at point A to the disturbing action in the form of $F_1(t) - F_k(t)$ force, respectively.

Such being the case, the resulting vibration signal to be observed at point A may be obtained on the basis of superposition principle $\psi_A(t) = \sum_{i=1}^{k} \psi_{Ai}(t) = \sum_{i=1}^{k} F_i(t) \cdot H_{Ai}(t)$.

On similar grounds for point B, the dependence between vibration signal response and disturbing forces will be written in the following form $\psi_B(t) = \sum_{i=1}^{k} \psi_{Bi}(t) = \sum_{i=1}^{k} F_i(t) \cdot H_{Bi}(t)$, and the dependence between each system response at point B and system response at point A will appear as: $\psi_{Bi}(t) = \frac{H_{Bi}(t)}{H_{Ai}(t)} \psi_{Ai}(t)$.

Hence, general system response at point B is defined as

$$\psi_B(t) = \sum_{i=1}^{k} \frac{H_{Bi}(t)}{H_{Ai}(t)} \psi_{Ai}(t). \tag{3}$$

In a similar way, other points belonging to the CU may be interconnected.

Since in view of a stochastic nature of disturbing uncompensated forces $F_1(t) – F_k(t)$ the analyzed CU may be considered a stochastic system, presented expressions serve the theoretical substantiation for presence of cross-correlation connections between vibration signal responses at various points of the electrical machine under research.

A considerable challenge in the use of proposed approach lies in obtaining of cross-correlation coefficients' instantaneous values. Since vibration processes in electrical machines' controlled assembles are of occasional nature, precise evaluation of linear relationship between two values $\psi_A(t)$ and $\psi_B(t)$ would require the use of the following expression[8].

$$K_\psi(t_1, t_2) = \int_{-\infty}^{\infty} \int_{-\infty}^{\infty} (\psi_1 - m_A(t_1))(\psi_2 - m_B(t_2)) \cdot f(\psi_1, \psi_2, t_1, t_2)\, d\psi_1 d\psi_2, \tag{4}$$

where $m_A(t_1)$, $m_B(t_2)$ are the mathematical expectations of functions $\psi_A(t)$ and $\psi_B(t)$ at time points t_1 and t_2., respectively; $f(\psi_1, \psi_2, t_1, t_2)$ is the two-dimensional probability of occasional process $\psi(t)$, which preconditions the occurrence of vibration signals in A and B assemblies.

In its turn, $f(\psi_1, \psi_2, t_1, t_2) = \frac{\partial^2 F(\psi_1, \psi_2, t_1, t_2)}{\partial \psi_1 \partial \psi_2}$, where $F(\psi_1, \psi_2, t_1, t_2)$ is a two-dimensional function of occasional process probability distribution $\psi(t)$, which assigns the value of probability of the fact that at time pointt1inequality $\psi_A \leq \psi_1$ is implemented, with inequality $\psi_B \leq \psi_2$ being implemented at time point t_2, that is

$$F(\psi_1, \psi_2, t_1, t_2) = P(\psi_A(t_1) \leq \psi_1, \psi_B(t_2) \leq \psi_2). \tag{5}$$

Considering the particularity of CU, the auto-correlation coefficient between signals $\psi_A(t)$ and $\psi_B(t)$ would be advisable to be determined for one and the same time point $t_1 = t_2$, that is $K_\psi(t_1, t_2) = K_\psi(t_1)$.

Given stationary external disturbances $F_1(t) – F_k(t)$ signals $\psi_A(t)$ and $\psi_B(t)$ may be considered ergodic, that is why, following the chain of transformations, the required quasi-instantaneous cross-correlation coefficient can be obtained as $K^*_\psi(t_1) = \frac{1}{T} \int_0^T (\psi^*_A(t_1))(\psi^*_B(t_1)) dt_1$, and for discrete time implementations, with due regard to known Pearson's equation, one can write the following correlation:

$$K^*_\psi(t_1) = \frac{\sum_{i=1}^{n} \psi^*_{Ai} \psi^*_{Bi}}{\sqrt{\sum_{i=1}^{n} \psi^{*2}_{Ai} \cdot \sum_{i=1}^{n} \psi^{*2}_{Bi}}}, \tag{6}$$

where ψ^*_{Ai} and ψ^*_{Bi} are the i^{th} values of time implementations of $\psi_A(t)$ and $\psi_B(t)$ functions.

3. METHODFOR CALCULATION OFCROSS-CORRELATION COEFFICIENTS

Based on the foregoing mathematical model, the calculation method was developed, the algorithm for which implementation is shown below:

1. Selection of synchronized time implementations of vibration signals of the support ψ_A and tested assemblies ψ_B with the length of n and starting at time moment *t*.
2. Calculation of amplitude-frequency-time spectra of supporting assembly's vibration signal.
3. Calculation of amplitude-frequency-time spectra of tested assembly's vibration signal.
4. Assignment of the initial value (*j*=1) to the control mark.
5. Calculation of neuron's j^{th} weight coefficient responsible for the tested assembly using formula (6).
6. Recording the calculated j^{th} weight coefficient in ANLN.
7. Raising the control mark by one (*j*=*j*+1) and in the case when the value obtained does not exceed the number of tested harmonics, going on to item 5, otherwise – termination of the calculation.

This algorithm was implemented by the example of real archived values of vibration signals obtained from the sensors installed at journal-and-thrust bearing and turbine bearing of the other hydraulic unit of Nyzhnyodnistrovs'ka HPP (Ukraine) in the process of its commercial operation[14,15].

4. RESULTS OFEXPERIMENTAL INVESTIGATION AND ANALYSIS THEREOF

Experimental investigations were carried out in two stages. Matrices of AFTS wavelet coefficients were designed, using discretewavelettransformation[9], for archival values of vibration signals in equal time periods for each of the vibration sensors installed at turbine and journal-and-thrust bearings along the horizontal and the vertical axes. At the first stage of the experimental investigation, required stacks of archival data were selected for hydrogenerator load parameters of 6.1MW and 3.7MW with the pressure head values that differed from each other by no more than 20%.

An example of such a matrix is shown infig.2.

0,00058	0,01155	0,01438	0,01576	0,01212	-0,00096	0,00346	0,00287	-0,0078	-0,00846	-0,00734	-0,0045	0,0
0,03872	0,00872	-0,0115	-0,03566	-0,04232	-0,03	-0,00131	0,05437	0,05372	0,05523	-0,00306	-0,03252	-0,0
0,15454	-0,16133	0,0555	0,04689	-0,05505	0,13334	-0,04775	0,07545	-0,19004	0,24963	-0,12663	0,18934	-0
-0,72517	0,73477	-1,05508	0,97104	-0,03406	0,97215	0,03884	0,87108	-3,94973	0,66259	-0,78816	0,78332	(
-7,78715	13,04255	4,62815	-3,72211	-1,1116	5,23574	3,05388	-10,54587	2,24375	6,12588	-1,75158	0,41051	
-2,21957	-3,53178	-3,16962	-3,55569	-3,21698	-2,80924	-2,85577	0,47871	0,65359	-1,20723	-0,96873	0,16932	
1,28836	0,67028	0,38083	1,1104	2,32887	1,49697	-0,74232	-1,60403	0,99532	-0,71171	1,34484	-0,09773	1,1
1,5978	-1,66826	3,41903	-1,30703	-0,19206	-1,09668	2,10297	-0,0658	-1,43045	-0,73242	-0,67391	0,06276	-(
-1,96601	0,10126	0,7241	-1,8216	0,34918	-1,18097	2,15002	-0,08153	-1,42263	-0,73579	-0,67224	0,06198	-0
-1,96604	0,10127	0,72411	-1,82159	0,34918	-1,18097	2,15002	-0,08153	-1,42263	-0,73579	-0,67224	0,06198	
-1,96604	0,10127	0,72411	-1,82159	0,34918	-1,18097	2,15002	-0,08153					
-1,96604	0,10127	0,72411	-1,82159									
-1,96604	0,10127											
-1,96604												

Fig.2. Example of AFTS wavelet-coefficients' matrix for the journal-and-thrust bearing (axis Y, load – 4.1MW, water pressure head 4.85 m)

Further on (according to the calculation algorithm proposed), cross-correlation coefficients were determined for the third through the fourteenth frequency bands. Moreover, to generate time implementations of the third frequency band, 4 consecutive values were used, with eight ones used for the fourth band and ten ones for the remainder. Coefficients determined on the basis of experimental data are summarized in tables 1 and 2.

Table 1 – Computer simulation results (load – 6.1 MW)

Place of receipt and input signal axis	Frequency band No.											
	3	4	5	6	7	8	9	10	11	12	13	14
Support bearing, axis Y – turbine bearing, axis Y	0,821	0,707	0,73	0,953	0,703	0,879	0,693	0,527	0,64	0,754	0,53	0,699
Support bearing, axis Y – support bearing, axis X	0,851	0,83	0,862	0,864	0,846	0,794	0,683	0,699	0,763	0,849	0,64	0,68
Support bearing, axis X – turbine bearing, axis X	0,642	0,658	0,612	0,688	0,606	0,846	0,753	0,688	0,585	0,816	0,668	0,57
Turbine bearing, axis X – turbine bearing, axis Y	0,625	0,524	0,691	0,877	0,905	0,741	0,831	0,765	0,781	0,641	0,634	0,29

Table 2 – Computer simulation results (load – 3.7 MW)

Place of receipt and input signal axis	Frequency band No.											
	3	4	5	6	7	8	9	10	11	12	13	14
Support bearing, axis Y – turbine bearing, axis Y	0,908	0,6939	0,767	0,75	0,565	0,68	0,485	0,46	0,75	0,908	0,526	0,755
Support bearing, axis Y – support bearing, axis X	0,611	0,614	0,765	0,744	0,626	0,637	0,791	0,598	0,774	0,646	0,698	0,62
Support bearing, axis X – turbine bearing, axis X	0,891	0,588	0,517	0,288	0,475	0,68	0,728	0,684	0,63	0,381	0,882	0,389
Turbine bearing, axis X – turbine bearing, axis Y	0,815	0,73	0,636	0,703	0,696	0,511	0,758	0,83	0,678	0,536	0,722	0,177

At the second stage of experimental investigation, stacks of archival data required for the same-type hydraulic unit were selected for the time periods corresponding to hydrogenerator load of 4.1MW with water pressure head of 4.85m and the load of 4.7MW with water pressure head of 6.35m. Coefficients determined on the basis of experimental data are summarized in tables3 and 4.

Table3– Results of cross-correlation coefficients' calculation (load – 4.1 MW, pressure head 4.85 m)

Place of receipt and input signal axis	Frequency band No.											
	3	4	5	6	7	8	9	10	11	12	13	14
Support bearing, axisY – turbine bearing, axis Y	0,57	0,677	0,678	0,678	0,706	0,523	0,65	0,871	0,548	0,864	0,659	0,808
Support bearing, axisY – support bearing, axis X	0,479	0,539	0,537	0,537	0,528	0,629	0,622	0,664	0,555	0,7	0,648	0,77
Support bearing, axisX– turbine bearing, axis X	0,534	0,512	0,511	0,511	0,641	0,801	0,677	0,791	0,646	0,722	0,527	0,931
Turbine bearing, axis X – turbine bearing, axis Y	0,654	0,742	0,757	0,757	0,794	0,556	0,633	0,893	0,603	0,79	0,47	0,819

Table4 – Results of cross-correlation coefficients' calculation (load – 4,7 MW, pressure head 6.35 m)

Place of receipt and input signal axis	Frequency band No.											
	3	4	5	6	7	8	9	10	11	12	13	14
Support bearing, axis Y – turbine bearing, axis Y	0,679	0,796	0,732	0,732	0,809	0,697	0,71	0,949	0,673	0,619	0,778	0,789
Support bearing, axis Y – support bearing, axis X	0,636	0,703	0,662	0,662	0,882	0,78	0,765	0,704	0,69	0,687	0,915	0,931
Support bearing, axis X – turbine bearing, axis X	0,854	0,803	0,772	0,772	0,667	0,884	0,75	0,702	0,544	0,632	0,608	0,627
Turbine bearing, axis X – turbine bearing, axis Y	0,833	0,861	0,836	0,836	0,801	0,716	0,722	0,425	0,459	0,648	0,736	0,877

5. ANALYZING THE RESULTS OF EXPERIMENTAL INVESTIGATIONS

It was demonstrated in research papers[1] and [9] that each line of AFTS wavelet coefficients' matrix corresponds to certain frequency band of the spectrum.

The upper limit of the spectrum, according to Kotelnikov-Shannon theorem, equals to a half of vibration measurement channels' sampling frequency. Since sampling frequency for vibration measurement channels at Nyzhnyodnistrovs'ka HPP (Ukraine), as used during experimental investigation, equals to 913.92 Hz, the upper limit of spectrum is 456.96 Hz.

The contraction coefficient of discrete wavelet transformation, which was used in the course of the above-mentioned investigation, equaled to 2, that is why each subsequent frequency band was twice as wide as the preceding one and, according to the algorithm of discrete wavelet transformation, the number of calculated frequency bands in AFTS equals to 14. Calculation of AFTS frequency bands was performed in Excel environment (see [1], [9]) with the calculation results shown infig.3.

	A	B	C	D	E
1	*Fd*	*Frequency band*	*Band width*	*Band start*	*Band end*
2	*913,9*	*1*	*0,027892327*	*0*	*0,027892327*
3	*dF*	*2*	*0,055784655*	*0,027892327*	*0,083676982*
4	*k*	*3*	*0,11156913*	*0,083676982*	*0,195246112*
5	*2*	*4*	*0,223138619*	*0,195246112*	*0,418384731*
6	*M*	*5*	*0,446277239*	*0,418384731*	*0,86466197*
7	*14*	*6*	*0,892554477*	*0,86466197*	*1,757216447*
8		*7*	*1,785108954*	*1,757216447*	*3,542325401*
9		*8*	*3,570217909*	*3,542325401*	*7,11254331*
10		*9*	*7,140435818*	*7,11254331*	*14,25297913*
11		*10*	*14,28087164*	*14,25297913*	*28,53385077*
12		*11*	*28,56174327*	*28,53385077*	*57,09559404*
13		*12*	*57,12348654*	*57,09559404*	*114,2190806*
14		*13*	*114,2469731*	*114,2190806*	*228,4660537*
15		*14*	*228,4939462*	*228,4660537*	*456,9599999*

Fig.3 AFTS frequency band of vibration signal at Dnistrovs'ka HPP -2hydraulic unit with contraction coefficient of 2

It is known that rotor speed f_g (generator speed) of hydraulic units at Nyzhnyodnistrovs'ka HPP (Ukraine) equals to 1.785Hz. As shown in[1], electrodynamic components of vibration are directly proportional to hydrogenerator load, and their main effects are focused on the generator speed (f_r) and on the nearest harmonic ($2f_r$) and sub-harmonic($f_r/2$).

It follows from fig. 4 that generator speed is confined to the beginning of the seventh frequency band, with the nearest harmonic respectively being in the eighth band and the nearest sub-harmonic – in the sixth one.

It also follows from tables 1 and 2 that these very frequency bands are the place where, with the increase in hydrogenerator load, cross-correlation coefficients grow significantly. This confirms the hypothesis set forth in research papers[5] and [6]

that coefficients of cross-correlation between vibration signals in the assemblies investigated will grow with the approach of external disturbance's significant component application point to the conditional point of the mechanical center between them, being also proportional to the this disturbing force's relative contribution to formation of general vibration signal [14,15].

Let us analyze the results of experimental investigation's stage two.

Considering that, during the above-mentioned experimental investigation, the hydraulic unit's capacity differed by no more than 15% and the pressure head by more than 30 %, and given that the investigations were performed in the course of one day according to hydraulic unit's standard operating procedure, which disables any considerable influence on the results of changes in the system's mechanical stiffness or other considerable mechanical changes, these are the hydrodynamic factors that can be considered the primary drivers of change invibrationcharacteristics[16,17].

It was demonstrated in research papers [1] and [9] that hydrodynamic vibrations are characterized by rotor speed $f_r = 1.785\text{Hz}$ (which is confined to the beginning of the seventh frequency band), and its harmonics and sub-harmonics, which corresponds to the frequency bands 3 (minimum frequency 0.08 Hz) through 9 (maximum frequency 14.25 Hz), as well as higher frequencies in the case when vibration originates from pressure pulsations or cavitation phenomena. These papers also prove that hydrodynamic vibrations are occasional, characterized by poor autocorrelation and poor cross-correlation between their axial projections, and they also grow with reduction in flow laminarity, which is typical for pressure head reduction. On the other side, paper [5] contains theoretical and computer-simulated proofs of the fact that, with considerable disturbing force's estrangement from a conventional point of mechanical center between them (the said effect occurs with zooming of hydrodynamic vibration signal, since hydrodynamic forces' application points are located at the hydroturbine),their cross-correlation coefficients will decrease[18-21].

When analyzing the results of experimental investigations set forth in tables 1 and 2, one can observe a distinct trend to reduction of cross-correlation coefficients with pressure head decrease at frequency bands 3 through 9 and 13, which entirely corresponds to the theoretical assumptions set forth in papers[1], [5] and [9]. However, as already mentioned, the change in load was also significant during the experiment, which was inevitably reflected in hydraulic unit's overall vibration.

When analyzing the data obtained at stage one of experimental investigations, one can note that, given almost unchanged pressure head of hydraulic unit of examined type, with reduction of its load observed was the reduction in cross-correlation coefficients between investigated assemblies at frequency bands 6 through 8. Given that, concurrently with pressure head reduction, hydraulic unit's load also decreased, one can assume that reduction of cross-correlation coefficients at frequency bands 6 through 8 was conditioned both hydro-dynamically and electromagnetically, with both factors acting in the same direction and magnifying the effect revealed during the experiment.

Based on the above, it would be advisable to state that cross-correlation coefficients may be used not only as ANLN weight coefficients, but also as an additional diagnostic attribute of one or another vibration components' presence in particular frequency bands.

6. CONCLUSIONS

1. It was experimentally proven that there are powerful correlation relationships between vibration signal's time implementations (vibration acceleration) at spaced points and in hydraulic unit's different coordinate axes in stationary operating conditions.
2. It was proved advisable to determine ANLN weight coefficients for vibration diagnostics of hydraulic units' defects using the correlation method, i.e. considering them as cross-correlation coefficients. This procedure's input data are represented by numerical values of wavelet coefficients of particular AFTS frequency bands.
3. It was found that, in the frequency bands, where electrodynamic components of vibration are concentrated, with the increase of hydrogenerator load, cross-correlation coefficients of vibration signals grow significantly at hydraulic unit's spaced quasi-symmetric points. This enables us to consider cross-correlation coefficients as an additional sign of electrodynamic vibration component's presence in particular frequency band.
4. It was experimentally proven that, with pressure head reduction, observed is the decrease of cross-correlation coefficients between vibration signals at support and turbine bearings within frequency bands, where hydrodynamic disturbing forces are concentrated.

REFERENCES

[1] Kukharchukandother, V. V., [Monitoring, diagnosing, and forecasting of vibration state of hydraulic aggregates], VNTU, Vinnitsa Ukraine, 168, (2014).

[2] Kolesnitsky, O. K., Gordyshevskaya, E. O. and Lukash, S. I., "Computer modeling of the method of recognition of signals of multi-sensors of gases on the basis of pulsed neural network," Information-measuring systems and complexes in technological processes 1, 121-126, (2013).

[3] Broersen, P. M. T., [Automatic autocorrelation and spectral analysis], GB: Springer-Verlag London Limited, London, 298, (2006).

[4] Rao, S. S., [Vibration of continuous systems], Jon Wiley & Sons, New York USA, 720, (2007).

[5] Hraniak, V. F., Kukharchuk, V. V., Kucheruk, V. and Khassenov, A., "Using instantaneous cross-correlation coefficients of vibration signals for technical condition monitoring in rotating electric power machines," Bulletin of the Karaganda University: PHYSICS Series 1 (89), 72 –80 (2018).

[6] Hraniak, V. F., Katsyv, S. Sh. and Kukharchuk, V. V., "Correlation approach to determination of weight coefficients of artificial neural network for vibration diagnostics of hydro aggregates," Bulletin of the Engineering Academy of Ukraine 4, 100–105 (2017).

[7] ChongH., Su, W. Xi, K. T., "Vibration signal analysis for electricalfault detection of induction machine using neural networks," International Symposium on ISITC, 188-192 (2007).

[8] Broersen, P. M. T., "Automatic autocorrelation and spectral analysis", Springer-Verlag London Limited, (2006).

[9] Kukharchuk, Vasyl V., et al. "Discrete wavelet transformation in spectral analysis of vibration processes at hydropower units," Przegląd Elektrotechniczny 93(3), 65-68 (2017).

[10] Azarov, O.D., Troianovska, T.I. et al., "Quality of content delivery in computer specialists training system," Proc. SPIE 10445, 104452S (2017).

[11] Azarov, O.D., Krupelnitskyi, L.V. and Komada, P., "AD systems for processing of low frequency signals based on self calibrate ADC and DAC with weight redundancy," Przeglad Elektrotechniczny 93(5), 125-128, (2017).

[12] Azarov, O.D., Dudnyk, O.V., Kaduk, O.V., Smolarz, A. and Burlibay, A., "Method of correcting of the tracking ADC with weight redundancy conversion characteristic," Proc. SPIE 9816, 98161V (2015).

[13] Vedmitskyi, Y.G., Kukharchuk, V.V., Hraniak, V.F., Vishtak, I.V., Kacejko, P. and Abenov, A., "Newton binomial in the generalized Cauchy problem as exemplified by electrical systems," Proc. SPIE 10808, 108082M (2018).

[14] Vyatkin, S.I., Romanyuk, O.N., Pavlov, S.V. et al.,, "Offsetting and blending with perturbation functions", Proc. SPIE 10808, 108082Y (2018).

[15] Smolarz, A., Wojcik, W., Ballester, J., et al. "Fuzzy controller for a lean premixed burner," Przeglad Elektrotechniczny 86 (7), 287-289, (2010).

[16] Kaczmarek, C.,Wojcik, W. et al., "Measurement of pressure sensitivity of modal birefringence of birefringent optical fibers using a Sagnac interferometer," Optica Applicata 45 (1), 5-14 (2015).

[17] Wojcik, W., "Application of fibre-optic flame monitoring systems to diagnostics of combustion process in power boilers," Bulletin of The Polish Academy of Sciences-Technical Sciences 56 (2), 177-195 (2008).

[18] Osadchuk, V.S. and Osadchuk, A.V., "Radiomeasuring Microelectronic Transducers of Physical Quantities" Proceedings of the 2015 International Siberian Conference on Control and Communications (SIBCON), (2015).

[19] Osadchuk, A.V. and Osadchuk, I.A., "Frequency transducer of the pressure on the basis of reactive properties of transistor structure with negative resistance," Proceedings of the 2015 International Siberian Conference on Control and Communications (SIBCON), (2015).

[20] Kłosowski, G., Rymarczyk, T., " Using neural networks and deep learning algorithms in electrical impedance tomography," Informatyka, Automatyka, Pomiary w Gospodarce i Ochronie Srodowiska – IAPGOS 7 (3), 99-102 (2017).

[21] Temich, S. and Grzechca, D., " Application of Neural Network for Testing selected specification parameters of Voltage-Controlled Oscillator," Journal of Electronics and Telecommunications 64(2), 203-207, (2018).

Mobile Distribution Point Architecture Concept of ICT Infrastructure

Grzegorz H. Kasprowicz [1a], Krzysztof T. Poźniak[a], Wojciech M. Zabołotny[a], Zbigniew M. Wawrzyniak[a], Andrzej Wojeński[a], Agata Tyburska[b], Jarosław Kamiński[b], Jarosław Struniawski[b], Jacek Iwański[b], Sebastian Brawata[c], Waldemar Szymajda[c], Piotr Markowski[c], Mariusz Kotlik[c] Piotr Mrozowski[c], Ewelina Katewicz[c], Andrzej Grabowski[d], Krzysztof Małkiewicz[d]

[a]Institute of Electronic Systems, Warsaw University of Technology, ul. Nowowiejska 15/19, 00-665 Warszawa, Poland;
[b]Police Academy in Szczytno, ul. Marszałka Józefa Piłsudskiego 111, 12-100 Szczytno, Poland
[c]Vortex Ltd., ul. Grunwaldzka 28/6, 80-229 Gdańsk, Poland
[d]Longevity, ul. Bernardyńska 16B/88, 02-904Warszawa, Poland

ABSTRACT

Mobile Distribution Point of ICT Infrastructure (MPDIT) is an innovative mobile device that integrates modern ICT solutions with advanced hardware architecture with a modular design. The primary function of MPDIT is to effectively increase public safety and counteract and reduce many types of threats, such as natural disasters. The article discusses considered hardware architecture construction solutions for the MPDIT project. It must ensure high reliability of operation in severe operating conditions, ICT performance in terms of throughput information through a variety of communication channels that cooperate, and low latency. Critical is the ability to modify the hardware layer by implementing a modular construction and based solutions based on modern standards and technologies.

Keywords: communication systems; telecommunications technologies; processing and integration of images, sounds, data; performance; latency

1. INTRODUCTION

It is particularly challenging to conduct practical actions in the area of ensuring security

- in areas with a low level of ICT infrastructure or deprived of this infrastructure, such as non-urbanized areas,
- in the event of a technical failure in critical infrastructure facilities or facilities subject to mandatory protection,
- in the event of natural disasters such as floods, fires, landslides, storms, and whirlwinds,
- during large-scale communication incidents such as air or rail accidents and mainly occurring in remote and hard-to-reach places,
- possible terrorist attacks.

The lack of such infrastructure hinders, in particular, the cooperation of entities involved in rescue, search, pursuit, and detection operations that often accompany crises. The concept of a mobile point presented in this article as a node that integrates technologically advanced ICT services will allow in such situations:

- increasing the efficiency and effectiveness of the tasks carried out,
- improving the personal safety of the participants of the measures taken, i.e., uninterrupted communication, precise location, the transmission of information, data, voice, and image,

[1] G.Kasprowicz@elka.pw.edu.pl; phone +48 22 234 7729; fax +48 22-825-23-00.

Photonics Applications in Astronomy, Communications, Industry, and High-Energy Physics Experiments 2019, edited by Ryszard S. Romaniuk, Maciej Linczuk, Proc. of SPIE Vol. 11176, 1117664
© 2019 SPIE · CCC code: 0277-786X/19/$21 · doi: 10.1117/12.2537988

- improvement of the command system, as well as facilitating and streamlining the creation of procedural documents (including visual inspection of the incident site, securing materials that constitute evidential value), and as a consequence will improve safety and public order.

Not without significance, in this case, will be the savings arising for users resulting from the rational use of their forces and resources and adapting their use to the actual needs. From state security, MPDIT will be a reserve enabling temporary replacement of damaged or destroyed key infrastructure.

Part of the project is analyzing the tele-information services used by the Police and emergency services in rescue and special operations (rescue and search, handling mass events, natural disasters and communications, outdoor events, technical disasters, and other police activities and operations, including special ones, during the activities ensuring the maintenance of state security). The opinion research tools will be used, including expert interviews to define the assumptions of the research and methodology for the evaluation of existing technical solutions and necessary directions of systemic development and verification of the pilotage carried out among Police officers [1]-[3].

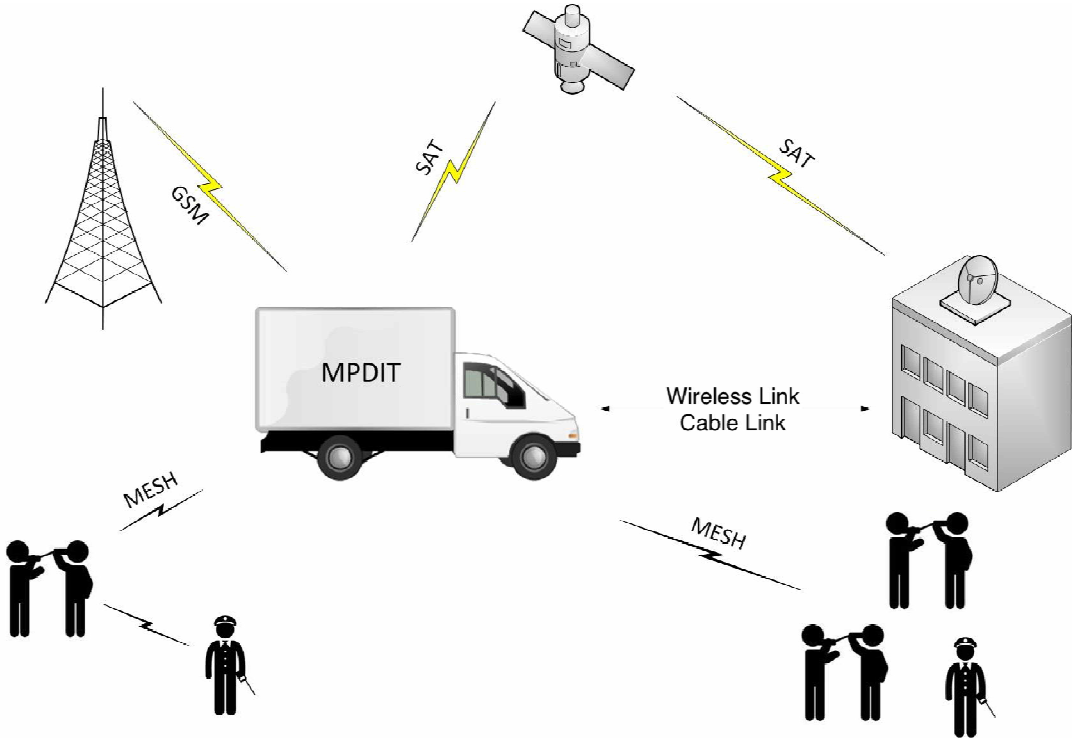

Figure 1. Diagram of integration of communication means using MPDIT

The main goal of the MPDIT project is a prototype system developed for the 9th PGT that integrates various means of communication on an operational vehicle, which shown in Figure 1.

The system will consist of three essential components:

- A van with specialized conversion enabling the integration of various communication channels to be implemented and managed by the operator,
- Stationary equipment allowing communication with MPDIT,
- Patrol Communications System based on terminals with implemented software operating in the MESH system.

The next chapter presents the key concept for the integration of the ICT structure for the MPDIT project. In particular, the current technological conditions and commercially available solutions in the context of the ICT performance and reliability of the discussed technical solutions were taken into account.

2. CONCEPT OF THE ICT INFRASTRUCTURE ARCHITECTURE FOR MPDIT

The solution proposed in this paper covers the integration of various communication systems in the form of a hybrid system, which is shown in figure 2.

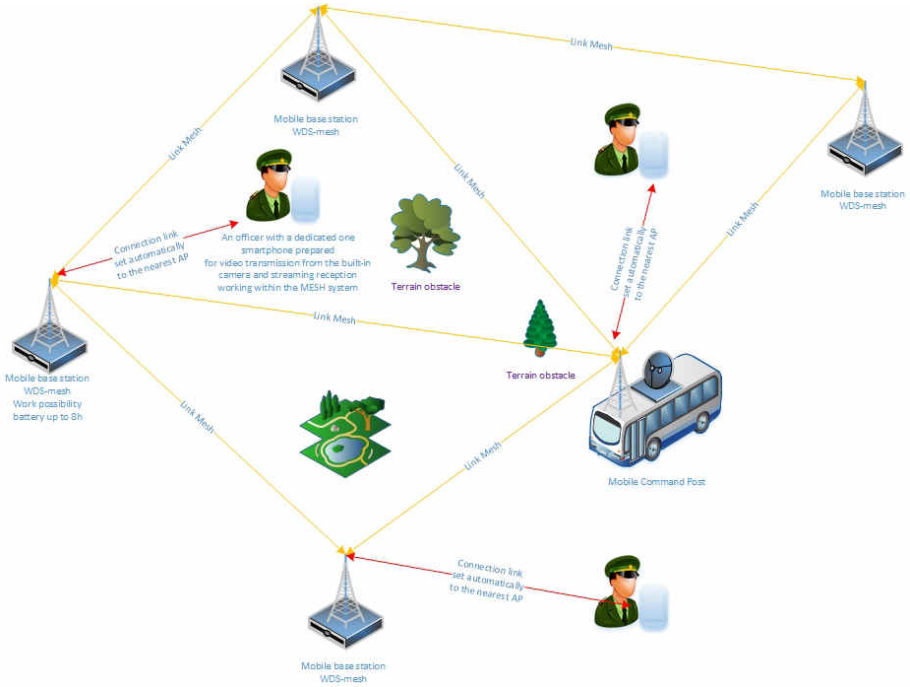

Figure 2. Diagram of integration of communication means using MPDIT

The proposed solution is characterized by the following main features [4]-[7]:

- Portable terminals are based on tablets/smartphones and individual wearable communication devices– they are points of the MESH network;
- WDS-mesh masts perform main direct links using low-range NIC cards working in the 868MHz band (long-range) and wireless network module (for example with OFDM modulation) for communication with terminals operating in the configured MESH network operating system;
- Terminals are COTS mobile devices with one of the popular operating systems. They have a built-in screen and camera and provide transmission and reception of the video stream. If necessary, it will be required to transcode the video stream if the selected video codec is different from the one natively supported by the device;
- Terminals communicate with WDS-mesh masts using the built-in network module.

The solution presented in Figure 1 assumes the establishment of appropriate functions and roles for individual elements of the solution to implement the technical assumptions of the integrated communication system. The main functional element is a unique vehicle with communication systems, which manages communication (including commutation) for various types of communication channels, including the MESH network. At the same time, the system has portable access points, implemented by devices of various types, which ensure the propagation of connectivity and functions of the MESH network along with increasing the coverage of this network. Portable wearable points can quickly create a MESH type network and provide it with the required functions.

It is also possible to create permanent connections to the MESH network based on portable functional masts serving as range extenders. Masts allow increasing the coverage of the network through the use of sector and directional antennas located at a much higher altitude and management of connections according to the MESH network functions. Also, this option allows the use in the field of high-rise buildings with flat roofs, elevations and other places allowing to increase the range of the operating MESH network significantly.

Technical conditioning resulting from specific technical solutions of the devices used will be consulted and reviewed regularly by the Gestor, in particular regarding the impact of transmission power and environmental conditions causing weakening of signal strength and reduction of transmission bandwidth for specific communication frequencies. Aforementioned may have an impact on the bandwidth and secondary quality of the signal, especially information transmitted in the form of streaming video signals in the field of unknown propagation characteristics (forest area, urbanization facilities, concrete obstacles, and such). Also, the applied solutions of the type of modulation, adaptation mechanisms, and signal protection (coding) will consist in adapting in the technical area. In particular, they will be:

- The coding and use of specific codecs will be selected the optimal solution meeting the requirements of the Project's objectives, depending on the needs and the need for specific technical solutions, which may occur after technical consultation with Gestor and the Beneficiary. We assume that will use the standard codecs and other necessary (required) interfaces to obtain access and distribution of video signals;
- Technical conditions and solutions for various frequency ranges used in MDPI communication systems will be selected for transmission technology after establishing with the Gestor. We will take into account the innovative validity of the proposed solutions and parameters resulting from the cooperation of individual network standards and devices performing transmission functions.

The concept of architecture has been divided into functional levels, discussed in successive subsections, respectively.

2.1 The level of the MESH network architecture

The level of MESH network architecture consists of:

- Central access point equipped with an Ethernet interface is the MESH network node. This point will be an integral element of MPDIT;
- MESH network controllers, both distributed and the central controller which are managing all devices (in the TaskManager standard). It is an element of a network that has the functionality of managing the MESH network. Also, each network node (repeater) works with the main network controller. It sends basic information about the working network resulting from the needs of management and network security, organization and necessary notification. For example, alarm mode is encrypted as messenger messages or commands from information exchange portal);
- Dynamic nodes of the network also called wearable repeaters would be placed in the vests. These devices allow to extend the coverage of the MESH network fulfilling its functions, including network management and configuration functions;
- Portable terminals are based on mobile devices with a built-in camera and software allowing to transmit and receive a video signal.

2.2 Level of the ICT streams concentrator

The concept of a part of the MPDIT system including the MESH system assumes the use of a technical solution in the form of a modular system of CPCIS(Compact PCI Serial) / MTCA in the form of a hardware cassette with functional extension boards [8]. The device constructed in this way will be autonomously powered (by own source in the car) and equipped with interchangeable communication interfaces realizing protocols for various communication channels (types). In the case of the MESH network, the integration will take place via a standard Gigabit Ethernet link along with a dedicated network card. Integration will ensure individual packet routing between the MESH network and other elements of the communication and event management system via MPDIT.

The hardware layer proposed by the authors includes:

- Miniature CPCIS/MTCA cassette [8] providing power supply and switching of Ethernet and PCI Express serial interfaces;
- CPCI/AMC-based computer modules with FMC connectors [9];
- Gigabit Ethernet network modules in the FMC or CPCIS standard [9];
- Radio communication modules in the CPCIS or RTM AMC standard [10].

The MPDIT project is assumed to be a mobile communication node integrating into one common communication system, at least the following communication subsystems allowing their integration with the Police radio communication systems:

- SATCOM communications subsystem,
- GSM/GPRS/LTE subsystem,
- radiotelephone communication subsystem,
- WAN / LAN network subsystem,
- communication subsystem with patrols in the MESH system,
- radio link subsystem,
- Wi-Fi subsystem.

The operator layer proposed by the authors includes:

- Operator's command console equipped with a multi-monitor system that allows configuring of individual subsystems into one common communication system;
- VIK terminal allowing to set up videoconferences;
- GUI software (dashboard system) consisting of five function panels:
  - The network status and console options panel,
  - Interactive map panel,
  - Event history panel,
  - A panel of function buttons,
  - The status panel and support for current transmissions in the system.

3. INTEGRATION CONCEPT OF TELEINFORMATION INFRASTRUCTURE FOR MPDIT

Figure 3 presents a preliminary functional flowchart of interactions between individual communication subsystems along with the proposed network interfaces.

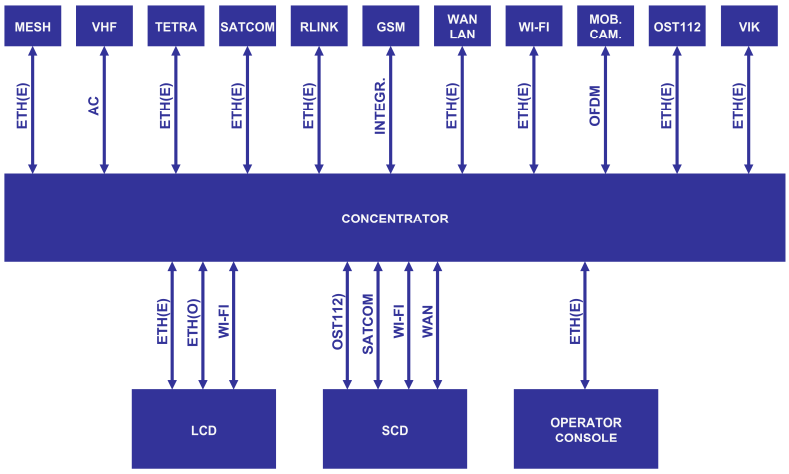

Figure 3. Block functional diagram of ICT connections in the MPDIT system

The concept of integration has been segmented into the following levels of integration functionalities, as appropriate:

- At the concentrator level, the MESH network consists of network node devices and an access device that provides communication with other networks as well as manages the traffic of transmission packets and the organization of the mesh network. The proposed integration of the MESH network will be based on the connection of the CPCIS/MTCA hub with the MESH network access device using Gigabit Ethernet interfaces and the configuration of network interfaces, routing tables and applications that manage data transmission on the upper layers of IP protocols;
- At the MESH network level, functional integration assumes a combination of all devices included in the system, namely terminals, portable WDS masts, a stationary mast with an access point and MESH network management software, both at the access point and in portable WDS masts. Configuration of devices, network interfaces, verification of interoperability will be made. The verification includes compatibility of the video codec version, compatibility of the application version with the operating system, compatibility of the version of the drivers with the OS version, and other similar technical conditions.

4. CONCLUSIONS

The article presents solutions for hardware architecture for the MPDIT project, which must ensure high reliability of MPDIT operation in severe operating conditions, ICT performance in terms of information through various communication channels and low latency, and the ability to modify the hardware layer through the implementation of a modular structure and solutions based on modern standards and technologies. Based on the analyses carried out, the following conclusions can be formulated:

- It is proposed to move away from the concept of various popular smartphones equipped with a mobile application working in various OS systems for dedicated terminals equipped with professional radio interfaces, reinforced housing, and a video camera, and a network security system;
- A dedicated terminal is proposed, equipped with a reinforced housing, a battery and an external antenna working in the range of low radio frequencies ensuring optimal signal propagation, with dedicated software being the optimal and recommended solution;
- It is required to conduct analysis and technical examination of the impact of technical and operational conditions of the MPDIT system on technical solutions of a unique vehicle, including the problem of an autonomous power source.

ACKNOWLEDGMENTS

This work was partially supported by National Center for Research and Development of Poland - grant no DOB-BIO9/02/01/2018.

REFERENCES

[1] Babbie, Earl, (2003). Badania społeczne w praktyce, Warszawa PWN.
[2] Nowak, Stefan, (2006). Metodologia badań społecznych, Warszawa PWN.
[3] Sztabiński, Franciszek, (1997). Ankieta pocztowa i wywiad kwestionariuszowy, Warszawa Wydawnictwo ISFiS, PAN.
[4] https://www.octoscope.com/English/Collaterals/Articles/octoScope_MeshTesting_RFDesign_20060601.pdf
[5] https://www.researchgate.net/publication/295403088_WIRELESS_MESH_NETWORKS_THROUGHPUT_CAPACITY_ANALYSIS
[6] http://wpage.unina.it/pescape/cit/QShine06.pdf
[7] https://www.ncbi.nlm.nih.gov/pmc/articles/PMC3279226/
[8] https://www.nateurope.com/products/technologies/technologies_mtca.html
[9] https://www.vita.com/fmc
[10] https://www.picmg.org/openstandards/advanced-mezzanine-card/